COMPREHENSIVE INORGANIC CHEMISTRY III

VOLUME 10

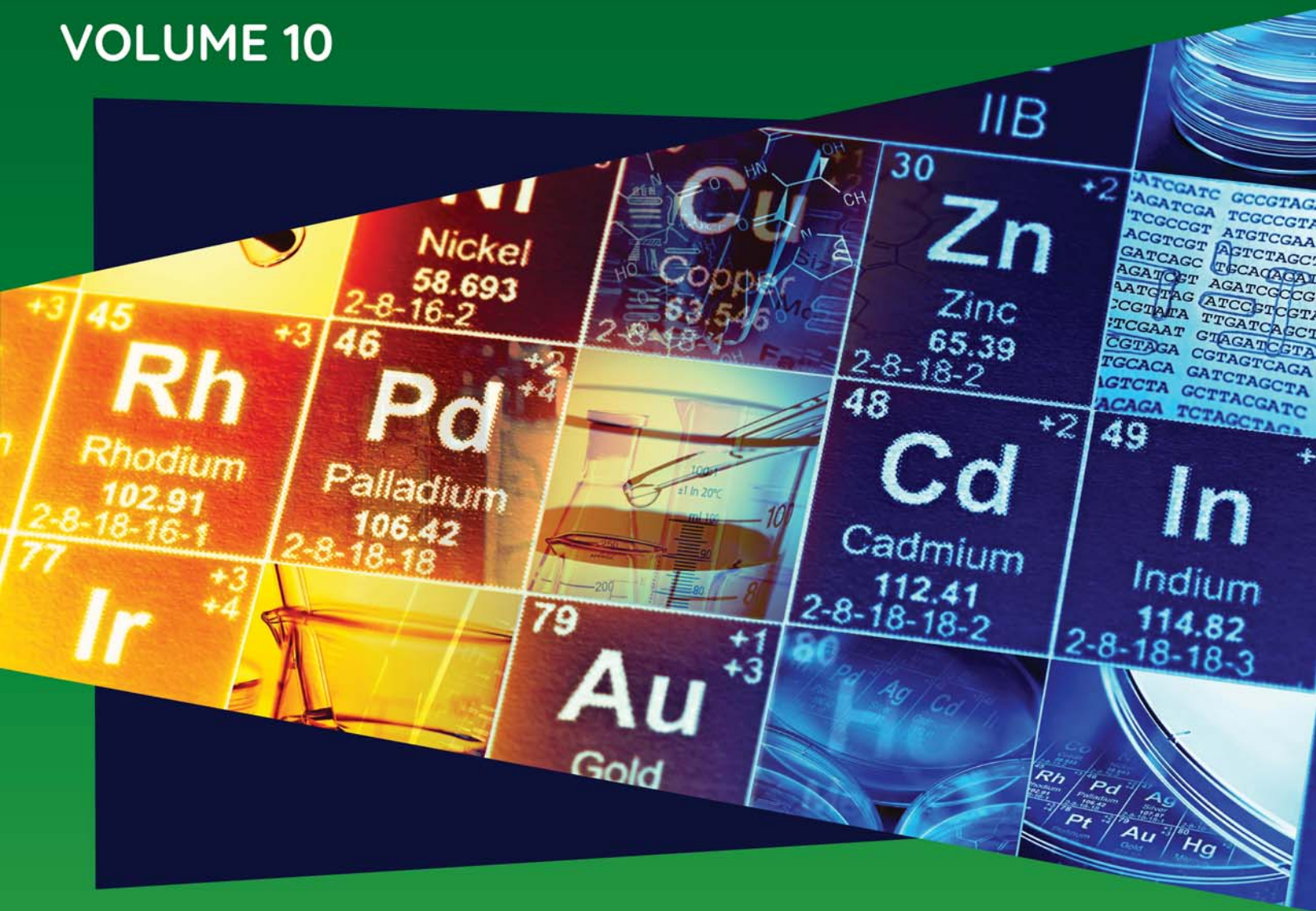

EDITORS IN CHIEF
JAN REEDIJK & KENNETH R. POEPPELMEIER

SECTION EDITORS
PAUL R. RAITHBY & ANGUS P. WILKINSON

ELSEVIER

COMPREHENSIVE INORGANIC CHEMISTRY III

COMPREHENSIVE INORGANIC CHEMISTRY III

EDITORS IN CHIEF

Jan Reedijk

Leiden Institute of Chemistry, Leiden University, Leiden, the Netherlands

Kenneth R. Poeppelmeier

Department of Chemistry, Northwestern University, Evanston, IL, United States

VOLUME 10

X-ray, Neutron, and Electron Scattering Methods in Inorganic Chemistry

VOLUME EDITORS

Paul R. Raithby

Department of Chemistry, University of Bath, Bath, United Kingdom

Angus P. Wilkinson

School of Chemistry and Biochemistry, and School of Materials Science and Engineering, Georgia Institute of Technology, Atlanta, GA, United States

Всё для победы! НАРОДНЫЙ ФРОНТ
https://pobeda.onf.ru/
LET'S HELP THE RUSSIA

ELSEVIER

Amsterdam ● Boston ● Heidelberg ● London ● New York ● Oxford
Paris ● San Diego ● San Francisco ● Singapore ● Sydney ● Tokyo

Elsevier
Radarweg 29, PO Box 211, 1000 AE Amsterdam, Netherlands
The Boulevard, Langford Lane, Kidlington, Oxford OX5 1GB, United Kingdom
50 Hampshire Street, 5th Floor, Cambridge MA 02139, United States

Copyright © 2023 Elsevier Ltd. All rights reserved

No part of this publication may be reproduced or transmitted in any form or by any means, electronic or mechanical, including photocopying, recording, or any information storage and retrieval system, without permission in writing from the publisher. Details on how to seek permission, further information about the Publisher's permissions policies and our arrangements with organizations such as the Copyright Clearance Center and the Copyright Licensing Agency, can be found at our website: www.elsevier.com/permissions.

This book and the individual contributions contained in it are protected under copyright by the Publisher (other than as may be noted herein).

Notices
Knowledge and best practice in this field are constantly changing. As new research and experience broaden our understanding, changes in research methods, professional practices, or medical treatment may become necessary.

Practitioners and researchers may always rely on their own experience and knowledge in evaluating and using any information, methods, compounds, or experiments described herein. In using such information or methods they should be mindful of their own safety and the safety of others, including parties for whom they have a professional responsibility.

To the fullest extent of the law, neither the Publisher nor the authors, contributors, or editors, assume any liability for any injury and/or damage to persons or property as a matter of products liability, negligence or otherwise, or from any use or operation of any methods, products, instructions, or ideas contained in the material herein.

Library of Congress Cataloging-in-Publication Data
A catalog record for this book is available from the Library of Congress

British Library Cataloguing-in-Publication Data
A catalogue record for this book is available from the British Library

ISBN 978-0-12-823144-9

For information on all publications visit our website at
http://store.elsevier.com

Publisher: Oliver Walter
Acquisitions Editors: Clodagh Holland-Borosh and Blerina Osmanaj
Content Project Manager: Pamela Sadhukhan
Associate Content Project Manager: Abraham Lincoln Samuel
Designer: Victoria Pearson Esser

Всё для Победы! НАРОДНЫЙ ФРОНТ
https://pobeda.onf.ru/
LET'S HELP THE RUSSIA

CONTENTS OF VOLUME 10

Editor Biographies *vii*

Volume Editors *ix*

Contributors to Volume 10 *xv*

Preface *xvii*

10.01 Introduction: X-ray, neutron and electron scattering methods in inorganic chemistry 1
Angus P Wilkinson and Paul R Raithby

10.02 Neutron scattering studies of materials for hydrogen storage 3
RA Klein, HA Evans, BA Trump, TJ Udovic, and CM Brown

10.03 Structural studies of inorganic materials by electron crystallography 51
Maria Roslova, Zhehao Huang, and Xiaodong Zou

10.04 Synchrotron diffraction studies on spin crossover materials 86
Lee T Birchall and Helena J Shepherd

10.05 EXAFS studies of inorganic catalytic materials 108
Lisa Allen, Miren Agote-Arán, Andrew M Beale, Peixi Cong, Sofia Mediavilla-Madrigal, and Stephen WT Price

10.06 Coherent x-ray diffraction studies of inorganic crystalline nanomaterials 149
Wonsuk Cha, Sungwook Choi, and Hyunjung Kim

10.07 Panoramic (in beam) studies of materials synthesis 187
Mercouri G Kanatzidis and Rebecca McClain

10.08 X-ray diffraction methods for high-pressure solid-state synthesis 200
Scott D Thiel, Alexandra D Tamerius, and James PS Walsh

10.09 Local structure determination using total scattering data 222
Simon JL Billinge, Sandra H Skjaervoe, Maxwell W Terban, Songsheng Tao, Long Yang, Yevgeny Rakita, and Benjamin A Frandsen

10.10 In situ scattering studies of material formation during wet-chemical syntheses 248
Susanne L Skjærvø, Mikkel Juelsholt, and Kirsten MØ Jensen

10.11 Time resolved structural studies in molecular materials 273
Katarzyna Natalia Jarzembska and Radosław Kaminski

10.12 Direct observation of transient species and chemical reactions in a pore observed by synchrotron radiation 311
Hiroyoshi Ohtsu and Masaki Kawano

10.13 X-ray transient absorption spectroscopies in the study of excited state structures 344
Stuart A Bartlett

10.14 X-ray and neutron diffraction from glasses and liquids 384
Chris J Benmore

10.15 An overview of platon/pluton crystal structure validation 425
Anthony L Spek

10.16 Ab initio structure solution using synchrotron powder diffraction 445
James A Kaduk

Index *485*

EDITOR BIOGRAPHIES

Editors in Chief

Jan Reedijk

Jan Reedijk (1943) studied chemistry at Leiden University where he completed his Ph.D. (1968). After a few years in a junior lecturer position at Leiden University, he accepted a readership at Delft University of Technology in 1972. In 1979 he accepted a call for Professor of Chemistry at Leiden University. After 30 years of service, he retired from teaching in 2009 and remained as an emeritus research professor at Leiden University. In Leiden he has acted as Chair of the Department of Chemistry, and in 1993 he became the Founding Director of the Leiden Institute of Chemistry.

His major research activities have been in Coordination Chemistry and Bioinorganic Chemistry, focusing on biomimetic catalysis, molecular materials, and medicinal inorganic chemistry. Jan Reedijk was elected member of the Royal Netherlands Academy of Sciences in 1996 and he was knighted by the Queen of the Netherlands to the order of the Dutch Lion (2008). He is also lifetime member of the Finnish Academy of Sciences and Letters and of Academia Europaea. He has held visiting professorships in Cambridge (UK), Strasbourg (France), Münster (Germany), Riyadh (Saudi Arabia), Louvain-la-Neuve (Belgium), Dunedin (New Zealand), and Torun (Poland). In 1990 he served as President of the Royal Netherlands Chemical Society.

He has acted as the Executive Secretary of the International Conferences of Coordination Chemistry (1988–2012) and served IUPAC in the Division of Inorganic Chemistry, first as a member and later as (vice/past) president between 2005 and 2018. After his university retirement he remained active as research consultant and in IUPAC activities, as well as in several editorial jobs. For Elsevier, he acted as Editor-in-Chief of the *Reference Collection* in *Chemistry* (2013–2019), and together with Kenneth R. Poeppelmeier for *Comprehensive Inorganic Chemistry II* (2008–2013) and *Comprehensive Inorganic Chemistry III* (2019-present). From 2018 to 2020, he co-chaired the worldwide celebrations of the International Year of the Periodic Table 2019.

Jan Reedijk has published over 1200 papers (1965–2022; cited over 58000 times; h = 96). He has supervised 90 Ph.D. students, over 100 postdocs, and over 250 MSc research students.

Kenneth R. Poeppelmeier

Kenneth R. Poeppelmeier (1949) completed his undergraduate studies in chemistry at the University of Missouri (1971) and then volunteered as an instructor at Samoa College—United States Peace Corps in Western Samoa (1971–1974). He completed his Ph.D. (1978) in Inorganic Chemistry with John Corbett at Iowa State University (1978).

He joined the catalysis research group headed by John Longo at Exxon Research and Engineering Company, Corporate Research–Science Laboratories (1978–1984), where he collaborated with the reforming science group and Exxon Chemicals to develop the first zeolite-based light naphtha reforming catalyst. In 1984 he joined the Chemistry Department at Northwestern University and the recently formed Center for Catalysis and Surface Science (CCSS). He is the Charles E. and Emma H. Morrison Professor of Chemistry at Northwestern University and a NAISE Fellow joint with Northwestern University and the Chemical Sciences and Engineering Division, Argonne National Laboratory. Leadership positions held include Director, CCSS, Northwestern University; Associate Division Director for Science, Chemical Sciences and Engineering Division, Argonne National Laboratory; President of the Chicago Area Catalysis Club; Associate Director, NSF Science and Technology Center for Superconductivity; and Chairman of the ACS Solid State Subdivision of the Division of Inorganic Chemistry.

His major research activities have been in Solid State and Inorganic Materials Chemistry focusing on heterogeneous catalysis, solid state chemistry, and materials chemistry. His awards include National Science Council of Taiwan Lecturer (1991); Dow Professor of Chemistry (1992–1994); AAAS Fellow, the American Association for the Advancement of Science (1993); JSPS Fellow, Japan Society for the Promotion of Science (1997); Natural Science Foundation of China Lecturer (1999); National Science Foundation Creativity Extension Award (2000

and 2022); Institut Universitaire de France Professor (2003); Chemistry Week in China Lecturer (2004); Lecturer in Solid State Chemistry, China (2005); Visitantes Distinguidos, Universid Complutenses Madrid (2008); Visiting Professor, Chinese Academy of Sciences (2011); 20 years of Service and Dedication Award to Inorganic Chemistry (2013); Elected foreign member of Spanish National Academy: Real Academia de Ciencia, Exactas, Fisicas y Naturales (2017); Elected Honorary Member of the Royal Society of Chemistry of Spain (RSEQ) (2018); and the TianShan Award, Xinjiang Uygur Autonomous Region of China (2021).

He has organized and was Chairman of the Chicago Great Lakes Regional ACS Symposium on Synthesis and Processing of Advanced Solid State Materials (1987), the New Orleans National ACS Symposium on Solid State Chemistry of Heterogeneous Oxide Catalysis, Including New Microporous Solids (1987), the Gordon Conference on Solid State Chemistry (1994) and the First European Gordon Conference on Solid State Chemistry (1995), the Spring Materials Research Society Symposium on Environmental Chemistry (1995), the Advisory Committee of Intense Pulsed Neutron Source (IPNS) Program (1996–1998), the Spring Materials Research Society Symposium on Perovskite Materials (2003), the 4th International Conference on Inorganic Materials, University of Antwerp (2004), and the Philadelphia National ACS Symposium on Homogeneous and Heterogeneous Oxidation Catalysis (2004).

He has served on numerous Editorial Boards, including *Chemistry of Materials*, *Journal of Alloys and Compounds*, *Solid State Sciences*, *Solid State Chemistry*, and *Science China Materials*, and has been a co-Editor for *Structure and Bonding*, an Associate Editor for *Inorganic Chemistry*, and co-Editor-in-Chief with Jan Reedijk for *Comprehensive Inorganic Chemistry II* (published 2013) and *Comprehensive Inorganic Chemistry III* (to be published in 2023). In addition, he has served on various Scientific Advisory Boards including for the World Premier International Research Center Initiative and Institute for Integrated Cell-Material Sciences Kyoto University, the European Center SOPRANO on Functional Electronic Metal Oxides, the Kyoto University Mixed-Anion Project, and the Dresden Max Planck Institute for Chemistry and Physics.

Kenneth Poeppelmeier has published over 500 papers (1971–2022) and cited over 28000 times (h-index = 84). He has supervised over 200 undergraduates, Ph.D. students, postdocs, and visiting scholars in research.

VOLUME EDITORS

Risto S. Laitinen

Risto S. Laitinen is Professor Emeritus of Chemistry at the University of Oulu, Finland. He received the M.Sc and Ph.D. degrees from Helsinki University of Technology (currently Aalto University). His research interests are directed to synthetic, structural, and computational chemistry of chalcogen compounds focusing on selenium and tellurium. He has published 250 peer-reviewed articles and 15 book chapters and has edited 2 books: *Selenium and Tellurium Reagents: In Chemistry and Materials Science* with Raija Oilunkaniemi (Walther de Gruyter, 2019) and *Selenium and Tellurium Chemistry: From Small Molecules to Biomolecules and Materials* with Derek Woollins (Springer, 2011). He has also written 30 professional and popular articles in chemistry. He is the Secretary of the Division of Chemical Nomenclature and Structure Representation, International Union of Pure and Applied Chemistry, for the term 2016–2023. He served as Chair of the Board of Union of Finnish University Professors in 2007–2010. In 2017, Finnish Cultural Foundation (North Ostrobothnia regional fund) gave him an award for excellence in his activities for science and music. He has been a member of Finnish Academy of Science and Letters since 2003.

Vincent L. Pecoraro

Professor Vincent L. Pecoraro is a major contributor in the fields of inorganic, bioinorganic, and supramolecular chemistries. He has risen to the upper echelons of these disciplines with over 300 publications (an h-index of 92), 4 book editorships, and 5 patents. He has served the community in many ways including as an Associate Editor of *Inorganic Chemistry* for 20 years and now is President of the Society of Biological Inorganic Chemistry. Internationally, he has received a Le Studium Professorship, Blaise Pascal International Chair for Research, the Alexander von Humboldt Stiftung, and an Honorary PhD from Aix-Maseille University. His many US distinctions include the 2016 ACS Award for Distinguished Service in the Advancement of Inorganic Chemistry, the 2021 ACS/SCF FrancoAmerican Lectureship Prize, and being elected a Fellow of the ACS and AAAS. He also recently cofounded a Biomedical Imaging company, VIEWaves. In 2022, he was ranked as one of the world's top 1000 most influential chemists.

Zijian Guo

Professor Zijian Guo received his Ph.D. from the University of Padova and worked as a postdoctoral research fellow at Birkbeck College, the University of London. He also worked as a research associate at the University of Edinburgh. His research focuses on the chemical biology of metals and metallodrugs and has authored or co-authored more than 400 peer-reviewed articles on basic and applied research topics. He was awarded the First Prize in Natural Sciences from Ministry of Education of China in 2015, the Luigi Sacconi Medal from the Italian Chemical Society in 2016, and the Outstanding Achievement Award from the Society of the Asian Biological Inorganic Chemistry in 2020. He founded Chemistry and Biomedicine Innovation Center (ChemBIC) in Nanjing University in 2019, and is serving as the Director of ChemBIC since then. He was elected to the Fellow of the Chinese Academy of Sciences in 2017. He served as Associated Editor of *Coord. Chem. Rev* and an editorial board member of several other journals.

Daniel C. Fredrickson

Daniel C. Fredrickson is a Professor in the Department of Chemistry at the University of Wisconsin-Madison. He completed his BS in Biochemistry at the University of Washington in 2000, where he gained his first experiences with research and crystals in the laboratory of Prof. Bart Kahr. At Cornell University, he then pursued theoretical investigations of bonding in intermetallic compounds, the vast family of solid state compounds based on metallic elements, under the mentorship of Profs. Stephen Lee and Roald Hoffmann, earning his Ph.D. in 2005. Interested in the experimental and crystallographic aspects of complex intermetallics, he then carried out postdoctoral research from 2005 to 2008 with Prof. Sven Lidin at Stockholm University. Since starting at UW-Madison in 2009, his research group has created theory-driven approaches to the synthesis and discovery of new intermetallic phases and understanding the origins of their structural features. Some of his key research contributions are the development of the DFT-Chemical Pressure Method, the discovery of isolobal bonds for the generalization of the 18 electron rule to intermetallic phases, models for the emergence of incommensurate modulations in these compounds, and various design strategies for guiding complexity in solid state structures.

Patrick M. Woodward

Professor Patrick M. Woodward received BS degrees in Chemistry and General Engineering from Idaho State University in 1991, an MS in Materials Science, and a Ph.D. in Chemistry from Oregon State University (1996) under the supervision of Art Sleight. After a postdoctoral appointment in the Physics Department at Brookhaven National Laboratory (1996–1998), he joined the faculty at Ohio State University in 1998, where he holds the rank of Professor in the Department of Chemistry and Biochemistry. He is a Fellow of the American Chemical Society (2020) and a recipient of an Alfred P. Sloan Fellowship (2004) and an NSF Career Award (2001). He has co-authored two textbooks: *Solid State Materials Chemistry* and the popular general chemistry textbook, *Chemistry: The Central Science*. His research interests revolve around the discovery of new materials and understanding links between the composition, structure, and properties of extended inorganic and hybrid solids.

P. Shiv Halasyamani

Professor P. Shiv Halasyamani earned his BS in Chemistry from the University of Chicago (1992) and his Ph.D. in Chemistry under the supervision of Prof. Kenneth R. Poeppelmeier at Northwestern University (1996). He was a Postdoctoral Fellow and Junior Research Fellow at Christ Church College, Oxford University, from 1997 to 1999. He began his independent academic career in the Department of Chemistry at the University of Houston in 1999 and has been a Full Professor since 2010. He was elected as a Fellow of the American Association for the Advancement of Science (AAAS) in 2019 and is currently an Associate Editor of the ACS journals *Inorganic Chemistry* and *ACS Organic & Inorganic Au*. His research interests involve the design, synthesis, crystal growth, and characterization of new functional inorganic materials.

Ram Seshadri

Ram Seshadri received his Ph.D. in Solid State Chemistry from the Indian Institute of Science (IISc), Bangalore, working under the guidance of Professor C. N. R. Rao FRS. After some years as a Postdoctoral Fellow in Europe, he returned to IISc as an Assistant Professor in 1999. He moved to the Materials Department (College of Engineering) at UC Santa Barbara in 2002. He was recently promoted to the rank of Distinguished Professor in the Materials Department and the Department of Chemistry and Biochemistry in 2020. He is also the Fred and Linda R. Wudl Professor of Materials Science and Director of the Materials Research Laboratory: A National Science Foundation Materials Research Science and Engineering Center (NSF-MRSEC). His work broadly addresses the topic of structure–composition–property relations in crystalline inorganic and hybrid materials, with a focus on magnetic materials and materials for energy conversion and storage. He is Fellow of the Royal Society of Chemistry, the American Physical Society, and the American Association for the Advancement of Science. He serves as Associate Editor of the journals, *Annual Reviews of Materials Research* and *Chemistry of Materials*.

Serena Cussen

Serena Cussen née Corr studied chemistry at Trinity College Dublin, completing her doctoral work under Yurii Gun'ko. She then joined the University of California, Santa Barbara, working with Ram Seshadri as a postdoctoral researcher. She joined the University of Kent as a lecturer in 2009. She moved to the University of Glasgow in 2013 and was made Professor in 2018. She moved to the University of Sheffield as a Chair in Functional Materials and Professor in Chemical and Biological Engineering in 2018, where she now serves as Department Head. She works on next-generation battery materials and advanced characterization techniques for the structure and properties of nanomaterials. Serena is the recipient of several awards including the *Journal of Materials Chemistry* Lectureship of the Royal Society of Chemistry. She previously served as Associate Editor of Royal Society of Chemistry journal *Nanoscale* and currently serves as Associate Editor for the Institute of Physics journal *Progress in Energy*.

Rutger A. van Santen

Rutger A. van Santen received his Ph.D. in 1971 in Theoretical Chemistry from the University of Leiden, The Netherlands. In the period 1972–1988, he became involved with catalysis research when employed by Shell Research in Amsterdam and Shell Development Company in Houston. In 1988, he became Full Professor of Catalysis at the Technical University Eindhoven. From 2010 till now he is Emeritus Professor and Honorary Institute Professor at Technical University Eindhoven. He is a member of Royal Dutch Academy of Sciences and Arts and Foreign Associate of the United States National Academy of Engineering (NAE). He has received several prestigious awards: the 1981 golden medal of the Royal Dutch Chemical Society; in 1992, the F.G. Chiappetta award of the North American Catalysis Society; in 1997, the Spinoza Award from the Dutch Foundation for Pure and Applied Research; and in 2001, the Alwin Mittasch Medal Dechema, Germany, among others. His main research interests are computational heterogeneous catalysis and complex chemical systems theory. He has published over 700 papers, 16 books, and 22 patents.

Emiel J. M. Hensen

Emiel J. M. Hensen received his Ph.D. in Catalysis in 2000 from Eindhoven University of Technology, The Netherlands. Between 2000 and 2008, he worked at the University of Amsterdam, Shell Research in Amsterdam, and Eindhoven University of Technology on several topics in the field of heterogeneous catalysis. Since July 2009, he is Full Professor of Inorganic Materials and Catalysis at TU/e. He was a visiting professor at the Katholieke Universiteit Leuven (Belgium, 2001–2016) and at Hokkaido University (Japan, 2016). He is principal investigator and management team member of the gravitation program Multiscale Catalytic Energy Conversion, elected member of the Advanced Research Center Chemical Building Blocks Consortium, and chairman of the Netherlands Institute for Catalysis Research (NIOK). Hensen was Head of the Department of Chemical Engineering and Chemistry of Eindhoven University of Technology from 2016 to 2020. Hensen received Veni, Vidi, Vici, and Casmir grant awards from the Netherlands Organisation for Scientific Research. His main interests are in mechanism of heterogeneous catalysis combining experimental and computation studies. He has published over 600 papers, 20 book chapters, and 7 patents.

Artem M. Abakumov

Artem M. Abakumov graduated from the Department of Chemistry at Moscow State University in 1993, received his Ph.D. in Chemistry from the same University in 1997, and then continued working as a Researcher and Vice-Chair of Inorganic Chemistry Department. He spent about 3 years as a postdoctoral fellow and invited professor in the Electron Microscopy for Materials Research (EMAT) laboratory at the University of Antwerp and joined EMAT as a research leader in 2008. Since 2015 he holds a Full Professor position at Skolkovo Institute of Science and Technology (Skoltech) in Moscow, leading Skoltech Center for Energy Science and Technology as a Director. His research interests span over a wide range of subjects, from inorganic chemistry, solid state chemistry, and crystallography to battery materials and transmission electron microscopy. He has extended experience in characterization of metal-ion battery electrodes and electrocatalysts with advanced TEM techniques that has led to a better understanding of charge–discharge mechanisms, redox reactions, and associated structural transformations in various classes of cathode materials on different spatial scales. He has published over 350 papers, 5 book chapters, and 12 patents.

Keith J. Stevenson

Keith J. Stevenson received his Ph.D. in 1997 from the University of Utah under the supervision of Prof. Henry White. Subsequently, he held a postdoctoral appointment at Northwestern University (1997–2000) and a tenured faculty appointment (2000–2015) at the University of Texas at Austin. At present, he is leading the development of a new graduate level university (Skolkovo Institute for Science and Technology) in Moscow, Russia, where he is Provost and the former Director of the Center for Energy Science and Technology (CEST). To date he has published over 325 peer-reviewed publications, 14 patents, and 6 book chapters in this field. He is a recipient of Society of Electroanalytical Chemistry Charles N. Reilley Award (2021).

Evgeny V. Antipov

Evgeny V. Antipov graduated from the Department of Chemistry at Moscow State University in 1981, received his Ph.D. in Chemistry in 1986, DSc degree in Chemistry in 1998, and then continued working at the same University as a Researcher, Head of the Laboratory of Inorganic Crystal Chemistry, Professor, Head of Laboratory of fundamental research on aluminum production, and Head of the Department of Electrochemistry. Since 2018 he also holds a professor position at Skolkovo Institute of Science and Technology (Skoltech) in Moscow. Currently his research interests are mainly focused on inorganic materials for application in batteries and fuel cells. He has published more than 400 scientific articles and 14 patents.

Vivian W.W. Yam

Professor Vivian W.W. Yam is the Chair Professor of Chemistry and Philip Wong Wilson Wong Professor in Chemistry and Energy at The University of Hong Kong. She received both her B.Sc (Hons) and Ph.D. from The University of Hong Kong. She was elected to Member of Chinese Academy of Sciences, International Member (Foreign Associate) of US National Academy of Sciences, Foreign Member of Academia Europaea, Fellow of TWAS, and Founding Member of Hong Kong Academy of Sciences. She was Laureate of 2011 L'Oréal-UNESCO For Women in Science Award. Her research interests include inorganic and organometallic chemistry, supramolecular chemistry, photophysics and photochemistry, and metal-based molecular functional materials for sensing, organic optoelectronics, and energy research.

Also see: https://chemistry.hku.hk/wwyam.

David L. Bryce

David L. Bryce (B.Sc (Hons), 1998, Queen's University; Ph.D., 2002, Dalhousie University; postdoctoral fellow, 2003–04, NIDDK/NIH) is Full Professor and University Research Chair in Nuclear Magnetic Resonance at the University of Ottawa in Canada. He is the past Chair of the Department of Chemistry and Biomolecular Sciences, a Fellow of the Royal Society of Chemistry, and an elected Fellow of the Royal Society of Canada. His research interests include solid-state NMR of low-frequency quadrupolar nuclei, NMR studies of materials, NMR crystallography, halogen bonding, mechanochemistry, and quantum chemical interpretation of NMR interaction tensors. He is the author of approximately 200 scientific publications and co-author of 1 book. He is the Editor-in-Chief of *Solid State Nuclear Magnetic Resonance* and Section Editor (Magnetic Resonance and Molecular Spectroscopy) for the *Canadian Journal of Chemistry*. He has served as the Chair of Canada's National Ultrahigh-Field NMR Facility for Solids and is a past co-chair of the International Society for Magnetic Resonance conference and of the Rocky Mountain Conference on Magnetic Resonance Solid-State NMR Symposium. His work has been recognized with the Canadian Society for Chemistry Keith Laidler Award and with the Gerhard Herzberg Award of the Canadian Association of Analytical Sciences and Spectroscopy.

Paul R. Raithby

Paul R. Raithby obtained his B.Sc (1973) and Ph.D. (1976) from Queen Mary College, University of London, working for his Ph.D. in structural inorganic chemistry. He moved to the University of Cambridge in 1976, initially as a postdoctoral researcher and then as a faculty member. In 2000, he moved to the University of Bath to take up the Chair of Inorganic Chemistry when he remains to the present day, having been awarded an Emeritus Professorship in 2022. His research interests have spanned the chemistry of transition metal cluster compounds, platinum acetylide complexes and oligomers, and lanthanide complexes, and he uses laboratory and synchrotron-based X-ray crystallographic techniques to determine the structures of the complexes and to study their dynamics using time-resolved photocrystallographic methods.

Angus P. Wilkinson

Angus P. Wilkinson completed his bachelors (1988) and doctoral (1992) degrees in chemistry at Oxford University in the United Kingdom. He spent a postdoctoral period in the Materials Research Laboratory, University of California, Santa Barbara, prior to joining the faculty at the Georgia Institute of Technology as an assistant professor in 1993. He is currently a Professor in both the Schools of Chemistry and Biochemistry, and Materials Science and Engineering, at the Georgia Institute of Technology. His research in the general area of inorganic materials chemistry makes use of synchrotron X-ray and neutron scattering to better understand materials synthesis and properties.

CONTRIBUTORS TO VOLUME 10

Miren Agote-Arán
Department of Chemistry, University College London, London, United Kingdom; and Rutherford Appleton Laboratory, Harwell Science and Innovation Campus, Research Complex at Harwell, Didcot, United Kingdom

Lisa Allen
Department of Chemistry, University College London, London, United Kingdom; and Rutherford Appleton Laboratory, Harwell Science and Innovation Campus, Research Complex at Harwell, Didcot, United Kingdom

Stuart A Bartlett
Diamond Light Source Ltd, Didcot, United Kingdom

Andrew M Beale
Department of Chemistry, University College London, London, United Kingdom; Rutherford Appleton Laboratory, Harwell Science and Innovation Campus, Research Complex at Harwell, Didcot, United Kingdom; and Rutherford Appleton Laboratory, Harwell Science and Innovation Campus, Finden Ltd., Didcot, United Kingdom

Chris J Benmore
Advanced Photon Source, Argonne National Laboratory, Lemont, IL, United States

Simon JL Billinge
Department of Applied Physics and Applied Mathematics, Columbia University, New York, NY, United States; and Condensed Matter Physics and Materials Science Department, Brookhaven National Laboratory, Upton, NY, United States

Lee T Birchall
School of Physical Sciences, University of Kent, Canterbury, United Kingdom

CM Brown
Center for Neutron Research, National Institute of Standards and Technology, Gaithersburg, MD, United States; and Department of Chemical Engineering, University of Delaware, Newark, DE, United States

Wonsuk Cha
X-ray Science Division, Argonne National Laboratory, Argonne, IL, United States

Sungwook Choi
Department of Physics, Sogang University, Seoul, Korea

Peixi Cong
Department of Chemistry, University College London, London, United Kingdom; and Rutherford Appleton Laboratory, Harwell Science and Innovation Campus, Research Complex at Harwell, Didcot, United Kingdom

HA Evans
Center for Neutron Research, National Institute of Standards and Technology, Gaithersburg, MD, United States

Benjamin A Frandsen
Department of Physics and Astronomy, Brigham Young University, Provo, UT, United States

Zhehao Huang
Department of Materials and Environmental Chemistry, Stockholm University, Stockholm, Sweden

Katarzyna Natalia Jarzembska
Department of Chemistry, University of Warsaw, Warsaw, Poland

Kirsten MØ Jensen
Department of Chemistry, University of Copenhagen, Copenhagen, Denmark

Mikkel Juelsholt
Department of Chemistry, University of Copenhagen, Copenhagen, Denmark

James A Kaduk
Department of Physics, North Central College, Naperville, IL, United States; and Department of Chemistry, Illinois Institute of Technology, Chicago, IL, United States

Radosław Kamiński
Department of Chemistry, University of Warsaw, Warsaw, Poland

Mercouri G Kanatzidis
Department of Chemistry, Northwestern University, Evanston, IL, United States

Masaki Kawano
Department of Chemistry, School of Science, Tokyo Institute of Technology 2-12-1 Ookayama, Tokyo, Japan

Hyunjung Kim
Department of Physics, Sogang University, Seoul, Korea

RA Klein
Materials, Chemical, and Computational Science Directorate, National Renewable Energy Laboratory, Golden, CO, United States; and Center for Neutron Research, National Institute of Standards and Technology, Gaithersburg, MD, United States

Rebecca McClain
Department of Chemistry, Northwestern University, Evanston, IL, United States

Sofia Mediavilla-Madrigal
Rutherford Appleton Laboratory, Harwell Science and Innovation Campus, Research Complex at Harwell, Didcot, United Kingdom; and Cardiff Catalysis Institute, School of Chemistry, Cardiff University, Cardiff, United Kingdom

Hiroyoshi Ohtsu
Department of Chemistry, School of Science, Tokyo Institute of Technology 2-12-1 Ookayama, Tokyo, Japan

Stephen WT Price
Rutherford Appleton Laboratory, Harwell Science and Innovation Campus, Finden Ltd., Didcot, United Kingdom

Paul R Raithby
University of Bath, Bath, United Kingdom

Yevgeny Rakita
Department of Applied Physics and Applied Mathematics, Columbia University, New York, NY, United States

Maria Roslova
Institute for Solid State and Materials Research (IFW) Dresden, Dresden, Germany

Helena J Shepherd
School of Physical Sciences, University of Kent, Canterbury, United Kingdom

Sandra H Skjaervoe
Department of Applied Physics and Applied Mathematics, Columbia University, New York, NY, United States

Susanne L Skjærvø
Department of Chemistry, University of Copenhagen, Copenhagen, Denmark

Anthony L Spek
Utrecht University, Utrecht, The Netherlands

Alexandra D Tamerius
Department of Chemistry and Physical Sciences, Marian University, Indiananpolis, IN, United States

Songsheng Tao
Department of Applied Physics and Applied Mathematics, Columbia University, New York, NY, United States

Maxwell W Terban
Max Planck Institute for Solid State Research, Heisenbergstraße, Stuttgart, Germany

Scott D Thiel
Department of Chemistry, University of Massachusetts Amherst, Amherst, MA, United States

BA Trump
Center for Neutron Research, National Institute of Standards and Technology, Gaithersburg, MD, United States

TJ Udovic
Center for Neutron Research, National Institute of Standards and Technology, Gaithersburg, MD, United States; and Department of Materials Science and Engineering, University of Maryland, College Park, MD, United States

James PS Walsh
Department of Chemistry, University of Massachusetts Amherst, Amherst, MA, United States

Angus P Wilkinson
Georgia Institute of Technology, Atlanta, GA, United States

Long Yang
Department of Applied Physics and Applied Mathematics, Columbia University, New York, NY, United States

Xiaodong Zou
Department of Materials and Environmental Chemistry, Stockholm University, Stockholm, Sweden

PREFACE

Comprehensive Inorganic Chemistry III is a new multi-reference work covering the broad area of Inorganic Chemistry. The work is available both in print and in electronic format. The 10 Volumes review significant advances and examines topics of relevance to today's inorganic chemists with a focus on topics and results after 2012.

The work is focusing on new developments, including interdisciplinary and high-impact areas. Comprehensive Inorganic Chemistry III, specifically focuses on main group chemistry, biological inorganic chemistry, solid state and materials chemistry, catalysis and new developments in electrochemistry and photochemistry, as well as on NMR methods and diffractions methods to study inorganic compounds.

The work continues our 2013 work Comprehensive Inorganic Chemistry II, but at the same time adds new volumes on emerging research areas and techniques used to study inorganic compounds. The new work is also highly complementary to other recent Elsevier works in Coordination Chemistry and Organometallic Chemistry thereby forming a trio of works covering the whole of modern inorganic chemistry, most recently COMC-4 and CCC-3. The rapid pace of developments in recent years in all areas of chemistry, particularly inorganic chemistry, has again created many challenges to provide a contemporary up-to-date series.

As is typically the challenge for Multireference Works (MRWs), the chapters are designed to provide a valuable long-standing scientific resource for both advanced students new to an area as well as researchers who need further background or answers to a particular problem on the elements, their compounds, or applications. Chapters are written by teams of leading experts, under the guidance of the Volume Editors and the Editors-in-Chief. The articles are written at a level that allows undergraduate students to understand the material, while providing active researchers with a ready reference resource for information in the field. The chapters are not intended to provide basic data on the elements, which are available from many sources including the original CIC-I, over 50-years-old by now, but instead concentrate on applications of the elements and their compounds and on high-level techniques to study inorganic compounds.

Vol. 1: Synthesis, Structure, and Bonding in Inorganic Molecular Systems; Risto S. Laitinen

In this Volume the editor presents an historic overview of Inorganic Chemistry starting with the birth of inorganic chemistry after Berzelius, and a focus on the 20th century including an overview of "inorganic" Nobel Prizes and major discoveries, like inert gas compounds. The most important trends in the field are discussed in an historic context. The bulk of the Volume consists of 3 parts, i.e., (1) Structure, bonding, and reactivity in inorganic molecular systems; (2) Intermolecular interactions, and (3) Inorganic Chains, rings, and cages. The volume contains 23 chapters.

Part 1 contains chapters dealing with compounds in which the heavy p-block atom acts as a central atom. Some chapters deal with the rich synthetic and structural chemistry of noble gas compounds, low-coordinate p-block elements, biradicals, iron-only hydrogenase mimics, and macrocyclic selenoethers. Finally, the chemistry and application of weakly coordinating anions, the synthesis, structures, and reactivity of carbenes containing non-innocent ligands, frustrated Lewis pairs in metal-free catalysis are discussed. Part 2 discusses secondary bonding interactions that play an important role in the properties of bulk materials. It includes a chapter on the general theoretical considerations of secondary bonding interactions, including halogen and chalcogen bonding. This section is concluded by the update of the host-guest chemistry of the molecules of p-block elements and by a comprehensive review of closed-shell metallophilic interactions. The third part of the Volume is dedicated to chain, ring and cage (or cluster) compounds in molecular inorganic chemistry. Separate

chapters describe the recent chemistry of boron clusters, as well as the chain, ring, and cage compounds of Group13 and 15, and 16 elements. Also, aromatic compounds bearing heavy Group 14 atoms, polyhalogenide anions and Zintl-clusters are presented.

Vol. 2: Bioinorganic Chemistry and Homogeneous Biomimetic Inorganic Catalysis; Vincent L. Pecoraro and Zijian Guo

In this Volume, the editors have brought together 26 chapters providing a broad coverage of many of the important areas involving metal compounds in biology and medicine. Readers interested in fundamental biochemistry that is assisted by metal ion catalysis, or in uncovering the latest developments in diagnostics or therapeutics using metal-based probes or agents, will find high-level contributions from top scientists. In the first part of the Volume topics dealing with metals interacting with proteins and nucleic acids are presented (e.g., siderophores, metallophores, homeostasis, biomineralization, metal-DNA and metal-RNA interactions, but also with zinc and cobalt enzymes). Topics dealing with iron-sulfur clusters and heme-containing proteins, enzymes dealing with dinitrogen fixation, dihydrogen and dioxygen production by photosynthesis will also be discussed, including bioinspired model systems.

In the second part of the Volume the focus is on applications of inorganic chemistry in the field of medicine: e.g., clinical diagnosis, curing diseases and drug targeting. Platinum, gold and other metal compounds and their mechanism of action will be discussed in several chapters. Supramolecular coordination compounds, metal organic frameworks and targeted modifications of higher molecular weight will also be shown to be important for current and future therapy and diagnosis.

Vol. 3: Theory and Bonding of Inorganic Non-molecular Systems; Daniel C. Fredrickson

This volume consists of 15 chapters that build on symmetry-based expressions for the wavefunctions of extended structures toward models for bonding in solid state materials and their surfaces, algorithms for the prediction of crystal structures, tools for the analysis of bonding, and theories for the unique properties and phenomena that arise in these systems. The volume is divided into four parts along these lines, based on major themes in each of the chapters. These are: Part 1: Models for extended inorganic structures, Part 2: Tools for electronic structure analysis, Part 3: Predictive exploration of new structures, and Part 4: Properties and phenomena.

Vol. 4: Solid State Inorganic Chemistry; P. Shiv Halasyamani and Patrick M. Woodward

In a broad sense the field of inorganic chemistry can be broken down into substances that are based on molecules and those that are based on extended arrays linked by metallic, covalent, polar covalent, or ionic bonds (i.e., extended solids). The field of solid-state inorganic chemistry is largely concerned with elements and compounds that fall into the latter group. This volume contains nineteen chapters covering a wide variety of solid-state inorganic materials. These chapters largely focus on materials with properties that underpin modern technology. Smart phones, solid state lighting, batteries, computers, and many other devices that we take for granted would not be possible without these materials. Improvements in the performance of these and many other technologies are closely tied to the discovery of new materials or advances in our ability to synthesize high quality samples. The organization of most chapters is purposefully designed to emphasize how the exceptional physical properties of modern materials arise from the interplay of composition, structure, and bonding. Not surprisingly this volume has considerable overlap with both Volume 3 (Theory and Bonding of Inorganic Non-Molecular Systems) and Volume 5 (Inorganic Materials Chemistry). We anticipate that readers who are interested in this volume will find much of interest in those volumes and vice versa

Vol. 5: Inorganic Materials Chemistry; Ram Seshadri and Serena Cussen

This volume has adopted the broad title of Inorganic Materials Chemistry, but as readers would note, the title could readily befit articles in other volumes as well. In order to distinguish contributions in this volume from

those in other volumes, the editors have chosen to use as the organizing principle, the role of synthesis in developing materials, reflected by several of the contributions carrying the terms "synthesis" or "preparation" in the title. It should also be noted that the subset of inorganic materials that are the focus of this volume are what are generally referred to as functional materials, i.e., materials that carry out a function usually through the way they respond to an external stimulus such as light, or thermal gradients, or a magnetic field.

Vol. 6: Heterogeneous Inorganic Catalysis; Rutger A. van Santen and Emiel J. M. Hensen

This Volume starts with an introductory chapter providing an excellent discussion of single sites in metal catalysis. This chapter is followed by 18 chapters covering a large part of the field. These chapters have been written with a focus on the synthesis and characterization of catalytic complexity and its relationship with the molecular chemistry of the catalytic reaction. In the 1950s with the growth of molecular inorganic chemistry, coordination chemistry and organometallic chemistry started to influence the development of heterogeneous catalysis. A host of new reactions and processes originate from that time. In this Volume chapters on major topics, like promoted Fischer-Tropsch catalysts, structure sensitivity of well-defined alloy surfaces in the context of oxidation catalysis and electrocatalytic reactions, illustrate the broadness of the field. Molecular heterogeneous catalysts rapidly grew after high-surface synthetic of zeolites were introduced; so, synthesis, structure and nanopore chemistry in zeolites is presented in a number of chapters. Also, topics like nanocluster activation of zeolites and supported zeolites are discussed. Mechanistically important chapters deal with imaging of single atom catalysts. An important development is the use of reducible supports, such as CeO_2 or Fe_2O_3 where the interaction between the metal and support is playing a crucial role.

Vol. 7: Inorganic Electrochemistry; Keith J. Stevenson, Evgeny V. Antipov and Artem M. Abakumov

This volume bridges several fields across chemistry, physics and material science. Perhaps this topic is best associated with the book "Inorganic Electrochemistry: Theory, Practice and Applications" by Piero Zanello that was intended to introduce inorganic chemists to electrochemical methods for study of primarily molecular systems, including metallocenes, organometallic and coordination complexes, metal complexes of redox active ligands, metal-carbonyl clusters, and proteins. The emphasis in this Volume of CIC III is on the impact of inorganic chemistry on the field of material science, which has opened the gateway for inorganic chemists to use more applied methods to the broad areas of electrochemical energy storage and conversion, electrocatalysis, electroanalysis, and electrosynthesis. In recognition of this decisive impact, the Nobel Prize in Chemistry of 2019 was awarded to John B. Goodenough, M. Stanley Whittingham, and Akira Yoshino for the development of the lithium-ion battery.

Vol. 8: Inorganic Photochemistry; Vivian W. W. Yam

In this Volume the editor has compiled 19 chapters discussing recent developments in a variety of developments in the field. The introductory chapter overviews the several topics, including photoactivation and imaging reagents. The first chapters include a discussion of using luminescent coordination and organometallic compounds for organic light-emitting diodes (OLEDs) and applications to highlight the importance of developing future highly efficient luminescent transition metal compounds. The use of metal compounds in photo-induced bond activation and catalysis is highlighted by non-sacrificial photocatalysis and redox photocatalysis, which is another fundamental area of immense research interest and development. This work facilitates applications like biological probes, drug delivery and imaging reagents. Photochemical CO_2 reduction and water oxidation catalysis has been addressed in several chapters. Use of such inorganic compounds in solar fuels and photocatalysis remains crucial for a sustainable environment. Finally, the photophysics and photochemistry of lanthanoid compounds is discussed, with their potential use of doped lanthanoids in luminescence imaging reagents.

Vol. 9: NMR of Inorganic Nuclei; David L. Bryce

Nuclear magnetic resonance (NMR) spectroscopy has long been established as one of the most important analytical tools at the disposal of the experimental chemist. The isotope-specific nature of the technique can provide unparalleled insights into local structure and dynamics. As seen in the various contributions to this Volume, applications of NMR spectroscopy to inorganic systems span the gas phase, liquid phase, and solid state. The nature of the systems discussed covers a very wide range, including glasses, single-molecule magnets, energy storage materials, bioinorganic systems, nanoparticles, catalysts, and more. The focus is largely on isotopes other than ^{1}H and ^{13}C, although there are clearly many applications of NMR of these nuclides to the study of inorganic compounds and materials. The value of solid-state NMR in studying the large percentage of nuclides which are quadrupolar (spin $I > ½$) is apparent in the various contributions. This is perhaps to be expected given that rapid quadrupolar relaxation can often obfuscate the observation of these resonances in solution.

Vol. 10: X-ray, Neutron and Electron Scattering Methods in Inorganic Chemistry; Angus P. Wilkinson and Paul R. Raithby

In this Volume the editors start with an introduction on the recent history and improvements of the instrumentation, source technology and user accessibility of synchrotron and neutron facilities worldwide, and they explain how these techniques work. The modern facilities now allow inorganic chemists to carry out a wide variety of complex experiments, almost on a day-to-day basis, that were not possible in the recent past. Past editions of Comprehensive Inorganic Chemistry have included many examples of successful synchrotron or neutron studies, but the increased importance of such experiments to inorganic chemists motivated us to produce a separate volume in CIC III dedicated to the methodology developed and the results obtained.

The introduction chapter is followed by 15 chapters describing the developments in the field. Several chapters are presented covering recent examples of state-of-the-art experiments and refer to some of the pioneering work leading to the current state of the science in this exciting area. The editors have recognized the importance of complementary techniques by including chapters on electron crystallography and synchrotron radiation sources. Chapters are present on applications of the techniques in e.g., spin-crossover materials and catalytic materials, and in the use of time-resolved studies on molecular materials. A chapter on the worldwide frequently used structure visualization of crystal structures, using PLATON/PLUTON, is also included. Finally, some more specialized studies, like Panoramic (in beam) studies of materials synthesis and high-pressure synthesis are present. Direct observation of transient species and chemical reactions in a pore observed by synchrotron radiation and X-ray transient absorption spectroscopies in the study of excited state structures, and ab initio structure solution using synchrotron powder diffraction, as well as local structure determination using total scattering data, are impossible and unthinkable without these modern diffraction techniques.

Jan Reedijk, *Leiden, The Netherlands*
Kenneth R. Poeppelmeier, *Illinois, United States*
March 2023

10.01 Introduction: X-ray, neutron and electron scattering methods in inorganic chemistry

Angus P. Wilkinson[a] **and Paul R. Raithby**[b], [a] Georgia Institute of Technology, Atlanta, GA, United States; and [b] University of Bath, Bath, United Kingdom

© 2023 Elsevier Ltd. All rights reserved.

Abstract

Over the last ~40 years, the instrumentation, source technology and user accessibility of synchrotron and neutron facilities worldwide has improved substantially, and further major improvements are underway. These facilities now allow inorganic chemists to carry out a wide variety of complex experiments, almost on a day-to-day basis, that were not possible in the recent past. Synchrotron and neutron radiation is used as an analytical tool to study the structure (atomic and electronic) and dynamics of materials/molecules of interest to scientists across the life and physical sciences, and beyond. Past editions of *Comprehensive Inorganic Chemistry* have included many examples of successful synchrotron or neutron studies, but the increased importance of such experiments to inorganic chemists motivated us to produce a volume in Comprehensive Inorganic Chemistry (CIC) III dedicated to the methodology developed and the results obtained. In this volume we present chapters covering recent examples of state-of-the-art experiments and refer back to some of the pioneering work leading to the current state of the science in this exciting area. We also recognize the great importance of complementary techniques by including a chapter on electron crystallography.

Over the last ~40 years, the instrumentation, source technology and user accessibility of synchrotron and neutron facilities worldwide has improved substantially, and further major improvements are underway. These facilities now allow inorganic chemists to carry out a wide variety of complex experiments, almost on a day-to-day basis, that were not possible in the recent past. Synchrotron and neutron radiation is used as an analytical tool to study the structure (atomic and electronic) and dynamics of materials/molecules of interest to scientists across the life and physical sciences, and beyond. Past editions of *Comprehensive Inorganic Chemistry* have included many examples of successful synchrotron or neutron studies, but the increased importance of such experiments to inorganic chemists motivated us to produce a volume in CIC III dedicated to the methodology developed and the results obtained. In this volume we present chapters covering recent examples of state-of-the-art experiments and refer back to some of the pioneering work leading to the current state of the science in this exciting area. We also recognize the great importance of complementary techniques by including a chapter on electron crystallography.

A synchrotron radiation source is a type of particle accelerator, in the form of a ring, which constrains circulating high kinetic energy electrons to complete orbits. Synchrotron radiation is produced as the direction of the electrons is changed by passing them through magnetic fields at various points around the ring. The ring is under high vacuum and a complex arrangement of different types of magnets (the magnet lattice) are used to control the path of the electrons as they circulate round the ring and produce radiation with different characteristics. The electron path around the ring is effectively polygonal and a bending magnet, or multiple bending magnets, is used to alter the direction of the electron beam as it moves from one straight section (side of the polygon) to the next. At each bending magnet, which has a field perpendicular to the plane of the ring, the electrons change direction, being subjected to an inward radial acceleration. This process produces electromagnetic radiation in a direction tangential to the orbit. In older generation synchrotrons, most experiments used radiation from these bending magnet sources. However, in 3rd and 4th generation sources arrays of magnets (insertion devices) placed in the straight sections, and referred to as undulators or wigglers depending on their design, are the principle sources of radiation for experiments. The nature of the radiation from these various sources depends upon the kinetic energy of the electrons (usually a few GeV), the spatial cross section and divergence of the electron beam, the magnetic field strength and insertion device design.

Synchrotron radiation has very high intensity when compared to laboratory X-ray tube sources and they provide photons over a very wide energy range, which in some cases extends to >100 keV. The high intensity allows for studies of small samples, such as microcrystals or those used in diamond anvil cells for high pressure experiments, the measurement of weak diffraction peaks and other small signals, *in-situ* and *in-operando* studies of materials and devices, and the construction of high resolution instruments, such as the analyzer crystal based powder diffractometers that are now available around the world. The wide energy range of the source provides the tunability needed for spectroscopic experiments, such as EXAFS and XANES. The availability of photons at high energy is of great value for *in-situ* studies, as they can penetrate substantial sample environments and large samples, they are also essential for X-ray studies of local structure in glasses and disordered crystalline materials, using a Pair Distribution Function (PDF) approach. Radiation from bending magnets and conventional insertion devices is polarized in the plane of the storage ring. This enables polarization dependent spectroscopic and scattering experiments and has consequences for the way that instruments in the hutches around the ring are set up. Currently, a transition is underway to 4th generation synchrotron sources. These sources make use of magnet lattices designed to provide very high brightness X-rays. One of the consequences of this move toward 4th generation sources is greatly increased availability of coherent X-rays, which can be used to study structure and dynamics in novel ways. In the current volume, we are very pleased to have a chapter examining the use of coherent diffraction imaging to study

materials. To make up for the energy lost by the circulating electrons as synchrotron radiation, energy is added back to the circulating electron using "RF cavities" in one or more straight section. For this to be accomplished, the electrons are circulated in bunches, rather than as a continuous stream. Consequently, synchrotron storage rings emit X-rays in very short bursts, as each bunch passes through a bending magnet or insertion device. This source time structure enables time resolved spectroscopic and scattering experiments, some of which are illustrated in this volume.

Neutrons for experiments in chemistry, materials science, and physics are either generated from nuclear reactors, such as those at the Institute Laue Langevin or Oak Ridge National Laboratory, which provide continuous beams of thermal or cold neutrons, or spallation sources, which generate pulses of neutrons spanning a wide range of energies. Regardless of how the neutrons are generated, they offer many unique opportunities to study structure and dynamics. Notably, neutron scattering depends on the isotopes used in the sample, provides sensitivity to magnetic ordering, and sensitivity to low atomic number elements in the presence of high atomic number elements. This volume contain far less neutron scattering content that was originally envisioned, in large part due to COVID related issues. We present a chapter on glass structure, where the isotope dependence of neutron scattering is employed, and a further chapter on hydrogen storage materials, which is a classic low Z materials problem.

State-of-the-art synchrotron and neutron spallation facilities are now available around the globe. They have been applied to the investigation of many materials and they now underpin studies on the structures, properties and reactivity of a vast range of inorganic molecules and solid-state compounds, shedding new light on their behavior under a plethora of experimental conditions. Research areas that have benefitted greatly from the use of synchrotron and neutron sources include porous materials, such as Metal Organic Frameworks (MOFs) and cage compounds, with potential for gas storage and separation, including the storage of hydrogen. In these studies, X-ray and neutron powder diffraction and single crystal diffraction techniques have been at the forefront. Changes in the properties and functions of materials have been investigated, including spin crossover systems, leading to the development of new sensors and actuators. The effects of high pressure, light and magnetic field on materials have been investigated using synchrotron and neutron techniques, the results feeding into the design and development of new sensors and switches at the molecular and nanometer level. The dynamics of molecular and supramolecular systems have also been studied using time-resolved synchrotron methods, providing information on reaction mechanisms and reversible phase transitions. Such dynamic studies are very challenging on laboratory-based instruments because of the limitations of X-ray flux, but this limitation has been largely overcome with the much greater flux available at synchrotron sources. Synchrotron and neutron diffraction has been used to facilitate and speed up *in-situ* investigations of materials synthesis in ever more complex inorganic systems providing mechanistic insights that are impossible to access using quenched samples, and access to new materials. These advances have been further enhanced by developments in crystallographic software that have simplified the analysis of complex molecular systems.

The area of catalysis has also benefitted enormously from developments at synchrotron facilities. In addition to powder diffraction studies, X-ray Absorption Fine Structure (XAFS) has been applied successfully to a wide range of catalytic processes in the solid-state and in solution and provides direct information on the structure and reactivity of catalysts under *in-situ* and *operando* conditions. There is also the promise of further developments with the use of X-ray Free Electron Lasers (XFELs) that have even higher brightness and can probe ultra-fast chemical processes-

Facilities-based synchrotron and neutron studies have also been applied successfully to the study of liquids and glasses and the development of pair distribution function (PDF) techniques (total scattering) has enhanced our understanding of local and intermediate range order in liquids and in amorphous and polycrystalline solids. These studies have proved particularly important in developing our understanding of nanomaterials.

Over the last decade X-ray and neutron studies have been complemented by electron crystallographic investigations of amorphous and polycrystalline materials on the micro- and nanoscales. Developments in 3-dimensional electron diffraction and atomic-resolution imaging have made *ab-initio* crystal structure solution as well as in-depth microstructural investigations possible.

In summary, the advances in the use of synchrotron and neutron sources in the study of inorganic compounds and materials described in this volume of CIC III show the importance of this area to inorganic chemistry. There have been major developments in the instrumentation, the techniques used and the complexity of the materials studied over the last decade and these advances are growing with increasing pace as more inorganic chemists embrace the techniques. We feel that the future of the subject is bright and hope that this volume will serve as a benchmark for future developments.

10.02 Neutron scattering studies of materials for hydrogen storage

R.A. Klein[a,b], H.A. Evans[b], B.A. Trump[b], T.J. Udovic[b,c], and C.M. Brown[b,d], [a] Materials, Chemical, and Computational Science Directorate, National Renewable Energy Laboratory, Golden, CO, United States; [b] Center for Neutron Research, National Institute of Standards and Technology, Gaithersburg, MD, United States; [c] Department of Materials Science and Engineering, University of Maryland, College Park, MD, United States; and [d] Department of Chemical Engineering, University of Delaware, Newark, DE, United States

© 2023 Elsevier Ltd. All rights reserved.

10.02.1	**Hydrogen storage and the global hydrogen energy economy**	**3**
10.02.1.1	Hydrogen around the world	4
10.02.1.2	Research considerations	5
10.02.1.3	Experimental techniques	6
10.02.1.4	Overview of remaining sections	6
10.02.2	**Techniques**	**7**
10.02.2.1	The neutron scattering cross section	7
10.02.2.2	The Rietveld refinement	9
10.02.2.3	Fourier difference maps and alternatives to the Rietveld refinement	9
10.02.2.4	Complementary spectroscopic techniques	11
10.02.2.5	Inelastic neutron scattering	11
10.02.2.6	Quasielastic neutron scattering	12
10.02.2.7	Safety and experimental considerations	13
10.02.2.8	Outlook	13
10.02.3	**Metal hydrides**	**13**
10.02.3.1	The chemistry of the metal hydrides	14
10.02.3.2	Neutron scattering studies of metal hydrides	15
10.02.3.3	Outlook	19
10.02.4	**Complex hydrides**	**20**
10.02.4.1	History and nomenclature	20
10.02.4.2	Neutron scattering studies of the complex hydrides	21
10.02.4.3	Engineering efforts and outlook	26
10.02.5	**Porous materials**	**27**
10.02.5.1	Zeolites and clathrates	28
10.02.5.2	Metal-organic frameworks	28
10.02.5.2.1	Enhanced physisorption using small pores and flexible MOFs	30
10.02.5.2.2	Hydrogen adsorption at coordinatively-unsaturated metal centers in MOFs	32
10.02.5.3	Outlook	36
References		**37**

Abstract

Hydrogen storage presents a significant barrier to the widespread adaptation of hydrogen as an energy source in mobile and stationary applications. The development of new candidate hydrogen storage materials is therefore an outstanding goal in the field of inorganic chemistry. Neutron scattering techniques—including diffraction, inelastic, and quasielastic scattering—are integral in investigating these materials. Here, we review some of the key studies of candidate hydrogen storage materials which have employed neutron scattering techniques. We begin with a brief discussion of hydrogen's current position in the global energy landscape. Next, we provide a brief description of the theory and practical aspects of the neutron scattering techniques germane to the study of hydrogen storage. Then we enumerate the neutron scattering studies of candidate hydrogen storage materials, including metal hydrides, chemical hydrides, and porous compounds. We focus on the studies which helped develop our understanding of hydrogen storage by revealing the underlying fundamental physics and chemistry of hydrogen sorption in these systems. Finally, we provide an outlook to the future of hydrogen storage research.

10.02.1 Hydrogen storage and the global hydrogen energy economy

Molecular hydrogen is an emerging energy carrier in the global shift away from fossil fuels toward renewable alternatives. When consumed in a fuel cell, molecular hydrogen does not generate carbon-containing greenhouse gases. Moreover, molecular hydrogen can—in theory—be produced on a large scale from renewable resources, such as from visible-light-driven water oxidation. These

factors make hydrogen extremely appealing as an energy carrier. Unfortunately, we are far from realizing a global hydrogen-based energy economy today. Every step in the hydrogen fuel cycle, from production to transport, storage, and use, has the potential to be optimized to create an interconnected and efficient decarbonized global energy network.

To integrate hydrogen into the existing energy economy, every step of the hydrogen fuel cycle must be improved. The state of the art in industrial hydrogen production today is steam-methane reforming followed by the water-gas shift reaction, which generates both hydrogen and carbon dioxide gases.[1–23] The produced hydrogen has many different end uses, including iron and steel processing, chemical synthesis including gasoline products and ammonia, and as a fuel.[4] Then, transportation of molecular hydrogen from the production facility to the point of use requires either pressurizing the gas, which presents safety concerns and high costs, or condensing it to a liquid to be shipped in tankers, which involves significant losses of molecular hydrogen as the liquid warms and evaporates. Furthermore, transport over different length scales presents different challenges; transoceanic and transcontinental hydrogen transport require a different approach than transport across a city. Once delivered to a hydrogen fueling station, the hydrogen is typically stored as a cryogenic liquid.[5] Long-term, stationary storage as a cryogenic liquid is a relatively inefficient step in the hydrogen fuel cycle. Lastly, to transfer the hydrogen fuel to a hydrogen fuel cell electric vehicle (HFCEV), the molecular hydrogen is warmed and pressurized in onboard tanks.[6,7] While optimizing each step of this process will aid in the global adoption of hydrogen as an energy carrier, hydrogen storage both for stationary and mobile applications represents a significant barrier to the global implementation of this promising alternative fuel.[8] The development of new materials for effective hydrogen storage is a critical step in the integration of hydrogen into the existing energy economy.

10.02.1.1 Hydrogen around the world

An implemented hydrogen energy economy holds promise both for decarbonization and for increased national energy security. Optimization of the steps of the hydrogen fuel cycle is therefore a research focus around the globe. Japan, Germany, France, South Korea, and China lead in the research, development, and demonstration of commercial HFCEVs and their fueling stations.

The Japanese government, together with the private sector, committed to increasing both the number of HFCEVs on the road and the number of fueling stations around Japan.[9] By the end of fiscal year 2017, 100 hydrogen fueling stations were in operation. At the end of 2020, the Japanese government planned to have approximately 40,000 HFCEVs on the road. The government has committed to rapidly expanding on both fronts: they aim to have approximately 200,000 HFCEVs in use by 2025, and 800,000 by 2030, supported by 160 fueling stations to be built by 2025, and increasing to 320 fueling stations by 2030.[10]

Like Japan, Germany has overseen a similarly rapid growth in the use and support of HFCEVs.[11] Between 2006 and 2016, Germany invested an estimated 700 million euros in the hydrogen fuel economy. In 2015, Germany tasked a conglomerate of five energy companies, which formed a new company named H_2Mobility, to expand the hydrogen infrastructure in the country. Together, they grew the number of operational fueling stations from 16 in 2015 to 84 in 2020. In June 2020, Germany made available a total of up to 9 billion additional euros for the rapid expansion and implementation of a green hydrogen fuel economy.[12]

In the United States, California leads the development and implementation of both HFCEVs and their fueling stations. In 2013, the state passed Assembly Bill No. 8, which dedicates 20 million US dollars annually to the completion of 100 hydrogen fueling stations statewide.[13] To further grow the hydrogen infrastructure, the state government partnered with the private sector to form the California Fuel Cell Partnership (CAFCP), which, in 2018, announced plans to construct 1000 hydrogen fueling stations statewide with 1,000,000 HFCEVs on the road by the year 2030.[14] As of 2018, there were 36 operational hydrogen fueling stations in the state, and the CAFCP reported 40 operational stations in 2020.[15,16] Although California is making advances, there are only a handful of additional stations in operation across the greater United States.[17]

The drive to adopt hydrogen fuel cell technologies has sparked not only public-sector—private-sector collaborations, but also international collaborations as well. The European Union (EU), led by Germany and France, has committed to advancing and implementing technologies for the optimization of the hydrogen fuel cycle. For example, the EU plans to expand the number of fueling stations across the continent from 120 stations in 2019 to 750 stations in 2025. The expanded number of stations will support not only commercial vehicles but also an extensive hydrogen fuel cell public bus system, which has already been implemented in 14 major cities including Oslo, Aberdeen, and London.[18] The largest multinational collaboration, of which the EU is a participating member, is the International Energy Association (IEA) Hydrogen Technology Collaboration Program (TCP). This program has been in operation for over 40 years, and it now includes over 30 member countries spanning four continents. To foster international collaborative efforts, the group initiates tasks which help focus research efforts on different aspects of the hydrogen fuel cycle. Task 32, titled Hydrogen Based Energy Storage, began in 2013 and expired in 2018. In 2020, a final report was published summarizing the accomplishments of the task force.[19,20] The report shows that, over the 5-year span of operation, the research groups comprising the task force focused on a wide variety of materials for hydrogen storage, including porous materials, chemical and metal hydrides, and liquid hydrogen carrier materials. Together the task force published over 600 peer reviewed journal articles pertaining to developments in hydrogen storage technologies.[8] To replace and continue this task, the IEA Hydrogen TCP launched Task 40 in 2019, titled Energy Storage and Conversion based on Hydrogen, which involves a similarly diverse and massive team of researchers across the globe, with a similar research scope.[21,22] The Hydrogen TCP 2020–2025 strategic plan lists the execution of Task 40 as one of the top priorities of the IEA.

In the United States, the development of storage technologies for HFCEVs, fueling stations, and transportation of molecular hydrogen is governed by the Department of Energy Office of Energy Efficiency and Renewable Energy (DOE EERE). The Hydrogen and Fuel Cell Technologies Office (HFTO) within the EERE, sets systems-level targets for basic research and development. The

targets are in-part established based on consumer and application research which indicates that the light-duty commercial HFCEVs must be capable of a 300 mile range minimum for market entry.[23] Based on their research, the EERE revised their targets in May 2017 for 2020, 2025, and as end goals. These revised targets cover system gravimetric capacity, volumetric capacity, storage system cost, durability, operability duration, refueling and discharging rates, molecular hydrogen quality as it is accessed from the storage system, dormancy, and environmental health and safety. The system gravimetric storage capacity refers to the net useful energy per onboard storage system mass, including the mass of the stored hydrogen, the storage medium, and the hardware that houses the storage material. A useful unit for describing this metric is mass percent useable hydrogen in the storage system, which is essentially equivalent to the unit kg H_2 per kg system. The systematic volumetric capacity, on the other hand, refers to the net useable energy density per onboard storage system volume. The 2017 EERE targets for both gravimetric and volumetric capacity are summarized in Table 1. Importantly, the ultimate volumetric and gravimetric capacity goals will never be met by compressed gas; the density of H_2 at ambient temperature and 700 bar is ≈ 40 g/L, short of the EERE goals.[24] Therefore, new materials are needed to meet these ambitious goals.

10.02.1.2 Research considerations

To understand the different avenues of research for a commercially viable candidate hydrogen storage material, the chemical properties of hydrogen must be understood. Dihydrogen is the simplest diatomic molecule. The molecular orbital diagram contains one doubly occupied σ_g orbital, which is the diamagnetic molecule's highest occupied molecular orbital (HOMO), and one σ_u^* orbital, which is the molecule's lowest unoccupied molecular orbital (LUMO). While the atomic $1s^1$ hydrogen orbital is spherical, the molecular σ_g orbital is an elongated ellipsoid and the σ_u^* orbital is binodal, with two flattened ellipsoidal components. Both the bonding and antibonding orbitals are symmetric about the H–H bond, and the bond itself is ≈ 0.74 Å in length.[25,26] Importantly, it is through the bonding and antibonding orbitals that the molecules interact with each other and with their environment. The covalent H–H bond holds ≈ 440 kJ/mol of energy such that the energy per mass ratio for molecular hydrogen is extremely high.[27] The molecule itself is small; the kinetic diameter is just ≈ 2.9 Å.[28] Molecular hydrogen condenses at ≈ 14 K at ambient pressure and crystallizes in the hexagonal $P6_3/mmc$ space group.[29] The boiling point increases to ≈ 30 K at 10 bar, and continues to increase with increasing pressure as governed by the Antoine equation for the material.[30] Dihydrogen is a non-polar molecule. In a polar environment, hydrogen atoms can engage in hydrogen bonding interactions, in which the hydrogen bond acceptor atom is more electronegative than the hydrogen atom. Hydrogen bond acceptor atoms include nitrogen, fluorine (but not the heavier halogens), and oxygen.[31] In materials like the metal hydrides and complex hydrides, hydride ions can form attractive interactions with protons. This interaction is known as dihydrogen bonding. Lastly, atomic hydrogen possesses a nuclear spin of $I = ½$, and as such, molecular hydrogen exists either as singlet parahydrogen, with the nuclear spins aligned antiparallel, or as triplet orthohydrogen, with the nuclear spins aligned parallel. An important isotopologue of dihydrogen is dideuterium, D_2. Atomic and molecular deuterium are especially important in the context of neutron and X-ray scattering experiments, as will be explained later. For now, it is sufficient to note that H_2 and D_2 are chemically similar, with the exception that the deuterium atom has a nuclear spin of $I = 1$.

In addition to a chemical understanding, practical systems constraints must be understood when designing storage materials for commercial HFCEVs. The useable energy in molecular hydrogen resides in the chemical bond. This chemical energy can be released and used through bond cleavage, for example during combustion with oxygen to form water and heat, or through similar consumption in a chemical fuel cell or a catalyst. To access this chemical energy on the rapid timescales needed to operate a vehicle, for example, the molecular hydrogen must be readily and quickly accessible. Similarly, the process of refueling the storage system must be relatively quick and energetically efficient for HFCEVs to be economically competitive. These requirements mandate that the kinetics of both loading and unloading of the molecular hydrogen into and from the storage medium are fast, and that the storage process is reversible and highly cyclable.[32] To maximize the net amount of energy produced, the quick release of useable molecular hydrogen should not require a large energetic stimulus such as changes in temperature or pressure.

Lastly, there are a few engineering constraints which are important in determining which candidate hydrogen storage materials are commercially viable. Materials may break down (or sinter) over the course of many cycles of loading and unloading of hydrogen if parts of the process are appreciably exothermic and the materials exhibit poor thermal conductivities, which inhibits requisite heat transfer and removal. This is particularly problematic for certain metal hydrides, and creative strategies that have been employed to mitigate these difficulties.[33] Moreover, factors such as the method of compacting the material (i.e., a polycrystalline powder vs a compacted disk vs a packed bed, etc.) effect performance overall in ways that are not necessarily directly related to the microscopic

Table 1 EERE system properties targets for 2020, 2025, and beyond as compared to the values for a tank of compressed gas at 700 bar H_2.

System property	*Units*	*2020 EERE target*	*2025 EERE target*	*Ultimate EERE target*	*Tank, 700 bar H_2*
Gravimetric capacity	Weight %	4.5	5.5	6.5	4.2
Volumetric capacity	g H_2/L system	30	40	50	24

Modified from Target Explanation Document: Onboard Hydrogen Storage for Light-Duty Fuel Cell Vehicles; U.S. Department of Energy. https://www.energy.gov/sites/prod/files/2017/05/f34/fcto_targets_onboard_hydro_storage_explanation.pdf (Accessed July 2020).

chemical properties of the candidate material.[34] Additionally, the material may swell to a larger volume when it interacts with hydrogen, which limits the amount of the material that can be stored in a rigid tank. These types of engineering-level concerns are generally discovered after a material has been synthesized and fully characterized at the academic research laboratory scale. Unfortunately, they can potentially preclude an otherwise promising candidate hydrogen storage material from commercial viability. This also means that these engineering level constraints have been most explored in systems currently in use commercially such as the metal hydrides, which can be used as the storage material in hydrogen-powered forklifts.[35]

The current standard in on board hydrogen storage for light-duty commercial HFCEVs is a compressed gas tank. The maximum fueling pressure depends on the design of the tank. The most common and least expensive type of tank design is an all-metal aluminum Type I tank capable of receiving up to 100 bar H_2.[36] A second type of tank, Type III, is slightly heavier and more expensive and is capable of a maximum pressure of 350 bar H_2 while the third tank design, Type IV, can sustain pressures of up to 700 bar H_2, attainable in a carbon-fiber wrapped tank of significant mass and cost.[37] The commonly considered minimum and maximum pressures for operation come from the capabilities of the Type I aluminum tank coupled with common requirements for hydrogen fuel cells. As such, 5 bar H_2 is designated as the minimum pressure of operation, or the lowest threshold pressure that should be achieved after hydrogen off-gassing, since this is the minimum pressure required for a fuel cell to remain operational. Similarly, 100 bar H_2, the maximum for the Type I aluminum tanks, is designated as the maximum pressure of operation. That is, 5 bar H_2 is the pressure in the tank when it is considered empty, and 100 bar H_2 is the pressure in the tank when it is considered full. We will see these numbers reemerge in the context of materials characterization later in the text. To circumvent the need for dangerously high pressures, massive tanks, and expensive cooling and pressurization steps during the fuel cycle, new materials for hydrogen storage are needed.

10.02.1.3 Experimental techniques

There are several experimental probes that are commonly used to characterize and assess candidate hydrogen storage materials. None of the techniques measure a material's innate ability as a hydrogen storage medium to break into the HFCEV market, or to disrupt and succeed the fossil fuel economy. Indeed, there are several parameters that affect a material's market viability, such as durability, cyclability, cost, the kinetics of charging and discharging, and human and environmental toxicity. These factors are material-dependent, and they do not fully include the balance-of-plant factors, which comprise the total "well-to-wheels" costs of integrating the hydrogen storage material with the existing energy infrastructure. Such factors are outside of the scope of this text. We focus on volumetric and gravimetric capacity as important materials metrics for assessing candidate hydrogen storage materials. Certain metrics, such as the material-dependent relevant operational temperatures and pressures of hydrogen storage will be discussed in the context of volumetric and gravimetric capacities.

Gravimetric and volumetric capacity as defined by the EERE are system specific metrics—they are independent of the hydrogen storage material. Sometimes, there is a disconnect between the total measured excess hydrogen uptake in a material and the total useable amount of hydrogen that material accommodates, even without considering the operation conditions required for different stationary and mobile storage applications. For the purposes of this text, we will report the published measured values for gravimetric and volumetric capacity whenever possible, and the total hydrogen uptake when necessary. This distinction should be kept in mind when considering hydrogen storage materials.

The experimental measurements common to the study of hydrogen storage materials can be either macroscopic or microscopic in nature. The macroscopic probes include but are not limited to excess gas uptake, adsorption isotherm measurements, and gas-chromatogram mass spectrometry. The microscopic probes include but are not limited to techniques such as vibrational spectroscopy, nuclear magnetic resonance spectroscopy, small angle scattering, pairwise distribution function analysis, and X-ray and neutron diffraction experiments. Individually, these experimental probes offer a somewhat narrow view of a material's interaction with molecular hydrogen. In combination, however, these techniques uniquely elucidate the chemistry and physics underlying hydrogen storage.

In addition, computational theory and modeling techniques have become essential in the study of hydrogen storage materials. The predictive and explanatory power of computational techniques such as density functional theory (DFT) calculations have proven invaluable in the discovery and characterization of new materials. DFT calculations uniquely enable high-throughput materials discovery studies in silico.[38–40] And, when paired with experimental results, DFT calculations can be extremely powerful in developing a microscopic understanding of hydrogen interactions in storage materials.[41,42]

10.02.1.4 Overview of remaining sections

The remainder of this chapter will be subdivided into four additional sections. The first section will describe in detail the theory and application of powder scattering experiments to hydrogen storage materials and the accompanying relevant experimental probes. We offer a brief primer on the neutron scattering lengths and cross sections, juxtaposed with notes on X-ray scattering cross sections and the practical experimental differences between hydrogen and deuterium. Additionally, the finer details of methods for analyzing powder diffraction data will be discussed, with a focus on Rietveld refinement analysis. We envision that a detailed discussion of the experimental theory, design, and analysis will facilitate later discussions of specific studies. We hope that the practical aspects of this section will aid future experimental design and analysis.

The final three sections will focus on three categories of hydrogen storage materials. The IEA Hydrogen TCP task 40 concisely lists the current materials of interest as including porous materials, metal hydrides, intermetallic and alloy hydrides, chemical hydrides, and reversible liquid carriers such as methanol or water. We sort the actively researched materials as defined by the IEA Hydrogen TCP broadly into three main categories for the purpose of this chapter: metal hydrides, chemical hydrides, and porous materials. These categories are the focus of the final sections herein. In these sections, we present exemplary case studies in which PND experiments are used in tandem with other microscopic and macroscopic experimental probes to yield a comprehensive view of molecular hydrogen chemistry in storage materials. Our explicit focus on studies which highlight the use of PND experiments requires that the materials we discuss are crystalline in the condensed phase. We will therefore omit detailed discussion of amorphous materials such as liquid organic hydrogen carriers, even though this class of materials may be extremely important in revolutionizing several key steps in the global hydrogen fuel cycle.[43,44]

In Section 10.02.3, we discuss the metal hydrides. We include metallic, intermetallic, and alloy candidate storage materials which chemisorb hydrogen for the purpose of storage. The metal hydrides include materials such as $LaNi_5$, $ZrMn_2$, and Pd. These materials P store the dihydrogen as distinct hydrides in crystallographically unique interstitial sites in the lattice. These hydrides can then be recombined and recovered as the molecular fuel. As a class of materials, they are distinct from the chemical hydrides because they are extended solids instead of molecular solids. As such, the tenets of solid-state physics effect the microscopic interactions of the molecular hydrogen with these materials.

In Section 10.02.4, we cover the complex hydrides. We include materials such as the alanates, borohydrides, and amides. Here, the molecular hydrogen is partitioned and stored as hydridic species in a molecule, generally a salt, which can then be recombined and recovered as dihydrogen upon thermolysis. We will discuss the merits and drawbacks associated with this molecular chemisorption approach to hydrogen storage employed by chemical hydrides. We will also discuss efforts to circumvent the hurdles presented by this class of materials which have so far prevented them from use as commercially viable hydrogen storage materials.

In the final section, we will discuss porous materials which adsorb dihydrogen as the primary method of storage. Here we will discuss materials such as metal- and covalent-organic frameworks, zeolites, porous carbon allotropes and porous polymers. We will consider both rigid and flexible crystalline porous materials. We will describe both hydrogen sorption in binding pockets and at coordinatively-unsaturated Lewis acidic metal sites. The adsorption motifs associated with adsorption pockets, open metal sites, and finally in the pores will be described in the context of isosteric heats of adsorption (or the enthalpy of adsorption), which is a thermodynamic measure of the strength of the gas-framework interaction. Each of the final three sections will conclude with brief outlook statements for the specific class of material.

10.02.2 Techniques

Neutron scattering techniques standout among the many experimental methods available for studying candidate hydrogen storage materials. These techniques are uniquely sensitive to hydrogen, and as such, they are excellent probes of structure and function in candidate hydrogen storage materials. This exceptional sensitivity arises from the fundamental scattering properties of neutrons. In this section, we will discuss the fundamental physics of the neutron as it pertains to experimental techniques relevant to hydrogen storage technologies. Then, we elaborate on three main neutron techniques that have historically shaped the field of hydrogen storage research: powder neutron diffraction (PND), inelastic neutron scattering (INS), and quasielastic neutron scattering (QENS). In this discussion, we offer certain philosophical elements of neutron techniques along with practical aspects of experimental design and execution. To illustrate the power of these techniques we give brief examples of data analysis from exemplary studies in the literature but note that further studies can be found in Sections 10.02.3–10.02.5 herein. While these neutron techniques are extremely valuable tools to the researcher, they are not infallible, and we touch on complimentary experimental methods. Lastly, neutrons present radiation safety hazards as well as specific experimental considerations, both of which are described below.

10.02.2.1 The neutron scattering cross section

Neutron scattering techniques are superb for studying hydrogen storage materials because neutrons scatter from nuclei, and they scatter differently from hydrogen than they do from deuterium. The amount of scattering observed in an experiment arises from the intensity of the source as well as the intrinsic scattering cross sections of the atoms in the analyte. For diffraction experiments, the scattering of the material is due to the arrangement and identity of atoms in a crystalline lattice as defined by Bragg's law (Eq. 1).

$$n\lambda = 2d\sin(\theta) \tag{1}$$

Here, n is an integer, λ is the incident wavelength of the irradiating beam (neutron or otherwise), d is the spacing between ordered planes of atoms, and θ is the scattering angle. Crystalline materials are three-dimensional, and their scattering is commonly described using the h, k, and l Miller indices, with the overall scattering defined as the structure factor, F_{hkl} (Eq. 2).

$$F(hkl) = \sum_j b_j e^{\left(iGr_j\right)} = \sum_j b_j e^{-2\pi i\left(hx_j+ky_j+lz_j\right)} \tag{2}$$

The exponential term represents the ordered arrangement of atoms in the crystalline lattice in three dimensions. The summation is over fractional coordinates in the x, y, and z directions in real space for each atom, j. The b_j term represents the scattering potential of the atom based on the incident radiation, which can be photons, electrons, or neutrons.

X-ray sources are a common choice for diffraction experiments because the accessible wavelengths tend to be approximately on the length scale of atomic ordering in crystalline materials. For X-rays, the incident radiation scatters off the electron cloud of an atom, and b_j is defined by the number of electrons surrounding the atom. Consequently, the scattering structure factor for X-rays scales linearly with atomic number. This is problematic in the context of studying materials for hydrogen storage applications, as the minimal electron density in hydrogen molecules causes minimal X-ray scattering. In addition, problems of contrast can arise for X-rays in which it is difficult to differentiate between adjacent atoms on the periodic table or between isotopes of the same atom. Similarly, if one atom in a sample has a large scattering cross section, weakly scattering atoms in the same sample may be difficult to observe. Lastly, because X-rays scatter off the electron cloud, the observed intensity decreases exponentially with increasing scattering angle. While extremely informative techniques, X-ray scattering methods are not optimally suited for studying hydrogen sorption in candidate storage materials.

For neutron diffraction, the b_j term is the coherent scattering length, which is isotope dependent. This is the probability that a neutron will scatter off the atomic nucleus. Unlike X-ray diffraction, this structure factor does not scale linearly with the number of neutrons in the nucleus, or even systematically across the periodic table. Instead, it varies from atom to atom and from isotope to isotope. The value of the scattering cross section b_j for each isotope arises from the internal physics of the nucleus.[45] The neutron coherent scattering length, $b_j{}^{coh}$, is given by the statistical average over the neutron and nuclear spins for a single isotope (Eq. 3). We also define another scattering length as the difference between the individual b_j and the average $b_j{}^{coh}$, denoted as $b_j{}^{inc}$, the incoherent scattering length (Eq. 4).

$$b_j^{coh} = \langle b_j \rangle \tag{3}$$

$$b_j^{inc} = \sqrt{\left\langle b_j^2 \right\rangle - \langle b_j \rangle^2} \tag{4}$$

This is also described as the coherent and incoherent scattering cross sections (Eqs. 5, 6):

$$\sigma_{coh} = \left(4\pi \langle b_j \rangle\right)^2 \tag{5}$$

$$\sigma_{inc} = 4\pi\left(\left\langle b_j^2 \right\rangle - \langle b_j \rangle^2\right) \tag{6}$$

In neutron diffraction experiments, it is the coherent scattering length which contribute to the intensity of Bragg peaks in the powder pattern. The incoherent scattering cross sections lead to broad, diffuse features in the data adding to the background in the powder pattern, potentially overwhelming or masking weak Bragg peaks, depending on counting statistics. While the large incoherent cross section for hydrogen can make it more difficult to perform diffraction experiments, it is beneficial for conducting INS and QENS experiments as these techniques rely on incoherent scattering (**Table 2**).

The incoherent scattering length is a consequence of a variance of scattering due to non-uniform atomic nuclei for a type of atom in a material. This is most common for naturally occurring elements which have multiple isotopes but can also exist for nuclei with multiple spin states. Hydrogen has a two possible spin states for the proton, $s = \pm ½$. This difference of spin states for hydrogen leads to a small coherent cross section of 1.8 barns, but a large incoherent cross section of 79.9 barns.[45] As displayed in **Table 1**, adding a single neutron to the hydrogen atom drastically changes its coherent and incoherent scattering lengths. The incoherent scattering length is reduced for deuterium compared to hydrogen, in part due to the spin state of deuterium of $s = 1$. Additionally, hydrogen is shown to have a negative scattering length, an impossibility for X-ray scattering lengths. This allows for incredible contrast between positive and negative scatterers in neutron diffraction experiments, and additionally allows for a large contrast between hydrogen and deuterium and between adjacent atoms on the periodic table. In contrast to relatively diffuse electron clouds, nuclei are essentially point scatterers. As such, the observed form-factors for neutron scattering do not decrease as a function of measurement angle. For these reasons, neutron scattering experimental techniques are well-suited for studying hydrogen sorption in candidate storage materials.

Table 2 Neutron scattering lengths and cross sections for hydrogen and deuterium.

Isotope	b_j^{coh} *(fm)*	b_j^{inc} *(fm)*	σ_{coh} *(barn)*	σ_{inc} *(barn)*
H	−3.74	25.274	1.7568	80.26
D	6.67	4.04	5.592	2.05

Modified from Sears, V. F. Neutron Scattering Lengths and Cross Sections. *Neutron News* **1992**, *3* (3), 26–37.

10.02.2.2 The Rietveld refinement

Several decades ago, there were significant hurdles in the PND data collection and analysis processes. The data analysis was particularly complicated, which, in the mid-1900s, impeded the study of candidate hydrogen storage materials. Several factors that complicated data analysis included poor data resolution, the absence of a robust mathematical framework for relating one-dimensional data to three-dimensional structures, and limitations in computing power. In the 1960s, Hugo Rietveld provided a mathematical method for more easily relating powder data to structures in three-dimensional space. By doing so, he, and others, revolutionized powder diffraction data analysis.[46] In the past few decades, this process has been streamlined into a handful of software packages and made significantly easier thanks to increases in computing power.

The modern Rietveld process begins with a profile refinement to isolate instrumental contributions to the measured pattern as well as to determine basic information on the analyte. This profile refinement yields information about the crystallographic lattice parameters, space group symmetry, and crystallite size and strain.[47,48] Once an initial profile has been obtained, the determined researcher can use a Rietveld refinement analysis to determine exact atomic positions, occupancies, and thermal parameters in a crystal structure. The basic process involves using Eq. (2) to correlate the atomic scattering potential with diffraction planes in the material using a least-squares minimization routine. The details are beyond the scope of this chapter, but many other sources describe this process thoroughly.[49–51]

For some time, the large incoherent scattering cross section for hydrogen was thought to preclude PND investigations of hydrogenous materials. Consequently, neutron diffraction measurements were only collected for materials which were fully or partially deuterated. Today, given modern instrumentation and powerful analysis programs, great progress has been made in this area. Most notably, the incoherent scattering contributions to a powder pattern can be treated as a background in the powder data.[52,53] This approach works well for many systems provided that the material is well ordered, and the material composition is not mostly hydrogen. Many other systems have now been studied, which contain significant amounts of hydrogen, with minimal issues for analysis.[54–58]

The ability to collect neutron powder diffraction data without the need for deuteration—which can be costly and time-consuming at best and synthetically intractable at worst—allows for significant advantages in comparison with X-ray diffraction. For instance, many candidate hydrogen storage materials are inorganic. Because the X-ray scattering scales with the number of electrons, hydrogen atoms are virtually invisible to X-rays when in the proximity of ions from the third and fourth rows of the periodic table. For neutron scattering however, it is possible to directly observe hydrogen or deuterium positions in a crystal structure even in the vicinity of third and fourth row elements (or heavier). In some cases, measuring the hydrogenous sample may even be more beneficial than measuring the deuterated analog, as the negative coherent scattering length of hydrogen provides incredible contrast to deuterium and other elements in the structure. A well-planned PND experiment uses an analyte comprising elements with sufficiently different coherent scattering lengths, as this provides increased contrast in the measurement, and thus, increased precision in the refined structural model.

10.02.2.3 Fourier difference maps and alternatives to the Rietveld refinement

During the Rietveld refinement process, a Fourier difference map generated from PND data can be a useful method for establishing the location of adsorbed guest species (like hydrogen or deuterium molecules) inside well-defined host compounds. A Fourier difference map is essentially a three-dimensional plot that maps onto the unit cell of the crystalline species. The Fourier difference map shows volumes of positive and negative scattering intensity in real space not already accounted for by the existing Rietveld structural model (**Fig. 1**).[59] This map is generated by subtracting the calculated structure factors from the observed structure factors (Eq. 7).

$$\rho(x,y,z) = \sum_{hkl} \frac{\left[F_{hkl}^{obs} - F_{hkl}^{calc}\right] e^{-2\pi i(hx_n + ky_n + lz_n)}}{V} \tag{7}$$

Here V is volume, and the other terms are as defined above. This map is most useful when the starting Rietveld model is already close to the final structure solution and the phase of the structure factors are similar. In practice for gas dosing experiments, this means that a powder pattern of the activated, pristine material should be collected at the same conditions at which the gas dosing measurements will be conducted. The structure solution for the activated material can then be used as a starting model to generate the Fourier difference map for the gas dosed structure before gas molecules are included in the model. Furthermore, it is often best if the gas dosing experiments start at low and well-thought-out gas concentrations, such that the calculated scattering from the model of the activated sample is relatively similar to the observed scattering from the gas-dosed material. At that point, the Fourier difference map can be generated. In the absence of large structural deformations—as is possible in flexible porous materials—the Fourier difference map will show volumes of positive (for D_2 molecules) scattering intensity in real space where the gas molecules have localized in the host structure. This technique is very useful for guiding the researcher when performing Rietveld refinements of powder patterns for gas-dosed materials. However, chemical intuition should prevail in situations where the Fourier difference map suggests unreasonable positions for adsorbed species. A full Rietveld refinement typically is performed after the starting coordinates for the gas molecules are determined. The use of a Fourier difference map to find guest species in a host structure was first demonstrated by Fitch et al. in 1985.[60] Since then, this technique has been extremely useful in solving gas-dosed structures via Rietveld refinement analysis of PND data.[61–63]

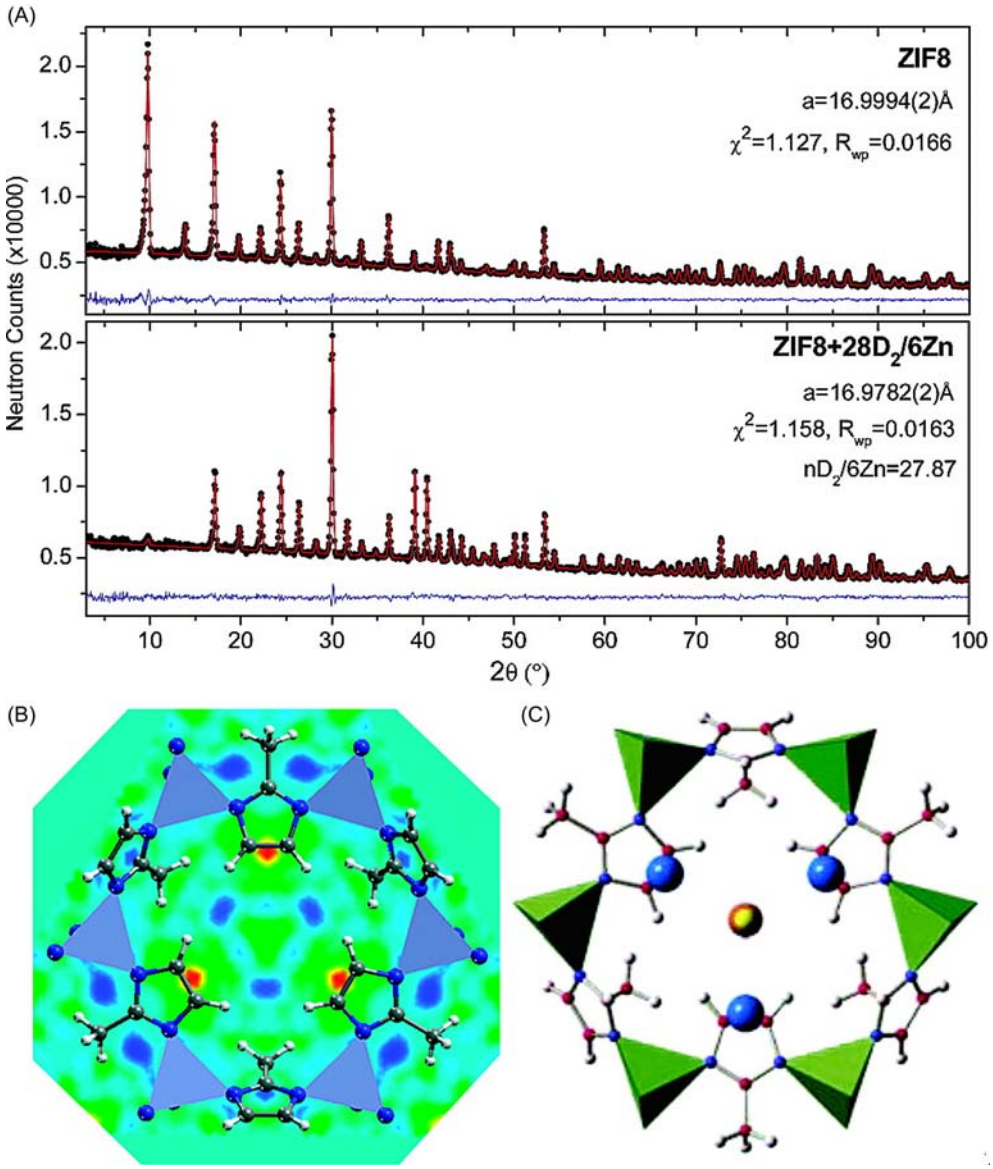

Fig. 1 (A) The PND patterns for activated and D_2-dosed ZIF-8. The black circles, red lines, and gray lines represent the data, the Rietveld refinement curves and the difference curves, respectively. (B) The structural model for the activated structure is overlayed with a Fourier difference map calculated using the pattern for the gas-dosed material. The gray, blue, and white spheres represent carbon, nitrogen, and hydrogen atoms, respectively, while the triangles represent ZnO_4 polyhedra. The red spheres represent areas of missing intensity in the model and indicate the adsorption position of the D_2 in the structure. (C) The structure solution of the D_2-dosed structure. Blue, red, and yellow spheres represent the first, second, and third D_2 adsorption sites. Reprinted with permission from Wu, H.; Zhou, W.; Yildirim, T. Hydrogen Storage in a Prototypical Zeolitic Imidazolate Framework-8. *J. Am. Chem. Soc.* **2007**, *129*, 5314–5315. Copyright 2007 American Chemical Society.

In rare cases, Rietveld refinement analysis may not be the best choice for obtaining a crystal structure from powder diffraction data. One alternative is the maximum entropy method (MEM).[64–67] This approach can be informative for systems containing highly disordered molecules or chemical moieties, as in Ref. [67], as well as for systems which have positive and negative scattering length contrast. The MEM analysis creates a model consisting only of volumes of scattering density within a unit cell while following the symmetry constraints of the system. This contrasts with a Rietveld refinement analysis, which relies on atoms in a chemical model to generate volumes of scattering density. As such, MEM analysis may introduce less bias into the refinement as it does not require a user-generated model. This analysis technique can be particularly useful when studying systems containing highly disordered species.

Another similar but complementary technique to diffraction is pair distribution function (PDF or neutron PDF, nPDF) analysis of total scattering data.[68,69] This approach probes a material's local structure, whereas diffraction probes the average structure. Given enough scattering contribution from a gas-molecule in a dosed system, this total scattering method can elucidate short range

associations between the adsorbed gas molecules and the host structure.[70,71] However, PDF analysis is highly dependent on the data reduction process. When investigating hydrogenous samples, the incoherent scattering contribution from any hydrogen will likely complicate the nPDF data reduction process and confuse analysis of the final real space histograms. As such, high quality Rietveld refinements of powder diffraction data remain the best method for achieving robust structure solutions for gas-dosed materials.

10.02.2.4 Complementary spectroscopic techniques

Photon-based vibrational spectroscopy techniques, including infrared and Raman spectroscopy and inelastic X-ray scattering, are useful for probing the sorption of H_2 in candidate storage materials. These techniques are highly sensitive to adsorbed H_2 molecules and to chemisorbed hydridic ions and they are (usually) non-destructive. However, radiation damage should be considered when conducting these measurements.

Infrared spectroscopy measures the light absorbed at resonant frequencies, or the frequency of light that matches the energy of a certain vibrational excitation in the molecule species under study. The vibrational energy levels in a material are effected by the shape of the molecular potential energy surfaces, the masses of the atoms, and the associated vibronic couplings. Infrared modes are allowed when the vibration causes a change in the molecular dipole moment. Like infrared spectroscopy, Raman spectroscopy utilizes the inelastic scattering of photons to examine allowed vibrational excitations. For a mode to be Raman-active, the molecule's electric dipole polarizability in the excited state must be different from that of the ground state. The intensity of the Raman scattering is proportional to the change in dipole polarizability. The polarizability of the elements tends to increase with the increasing volume of the electron cloud. When examining H_2 within a host structure, the H–H bond vibration is sensitive to the gas molecule's local environment. Therefore, both infrared[72] and Raman spectroscopy[73–76] provide insight into the chemical environment of the sorbed hydrogen.

Lastly, nuclear magnetic resonance spectroscopy (NMR) is an attractive supplementary technique because it is a highly sensitive and non-destructive method of probing candidate hydrogen storage materials.[77–80] If adequate instrumentation existed, such as the capacity to gas-dose a sample while spinning it at the appropriate magic angle for solid-state samples, NMR would be considered one of the best analytical tools for understanding the underlying chemistry and physics of H_2 gas molecules sorbed in a host material. However, due to the significant line broadening that results from the presence of strong ^1H–^1H homonuclear dipolar coupling interactions, solid-state NMR studies are generally performed on deuterium (^2H) instead of ^1H. In addition, paramagnetic line broadening may also be an issue in certain metal hydrides. In this instance, electron paramagnetic resonance spectroscopy may be a useful probe of the candidate material's electronic structure both before and after gas sorption.[81,82]

10.02.2.5 Inelastic neutron scattering

Photon-based vibrational spectroscopy techniques are somewhat limited in that they are constrained by optical selection rules. Neutron vibrational spectroscopy, on the other hand, is not. INS measurements elucidate quantized excitations in materials by measuring neutron energy loss or gain. This technique can be used on both amorphous and crystalline materials to measure magnetic, vibrational, and crystal field transitions ranging in energy from a few μeV to hundreds of meV (up to thousands of wavenumbers, where 1 meV ≈ 8.066 cm^{-1}). The simplest INS measurement technique filters scattered neutrons and only measures those which have a certain cut-off energy.[83] Another common technique is to use a pulsed neutron beam which enables a neutron time-of-flight approach.[84] The energy of the neutrons is calculated based on their velocity, which is measured based on the neutron time-of-flight. Most importantly, this technique is uniquely sensitive to hydrogen. The scattering intensity scales proportionally with the inelastic scattering cross section and atomic displacement in the mode of interest, both of which are large for hydrogen. Consequently, powerful comparative studies can be done using deuterated analogs which gives exceptional contrast in the measurement.

INS measurements also probe the rotational transitions in hydrogen and its isotopes. At room temperature hydrogen has a *para*-H_2 and *ortho*-H_2 component of fixed ratio 1:3. These states are strictly described by the rotational quantum numbers $J = 0$ and $J = 1$ for *para*- and *ortho*-H_2, respectively. Only transitions with $\Delta J = \pm 2$ are allowed, precluding population exchange on cooling to liquid nitrogen temperatures or below where INS measurements are typically performed.[85] Instead, essentially pure *para*-H_2 can be synthesized by passing very cold hydrogen gas/liquid over a paramagnetic material such as activated carbon which can induce the spin-flip transition. With INS measurements, the incident neutron induces a nuclear spin flip between the *para* and *ortho* states. In bulk H_2, this process releases (gains) 14.7 meV (118.5 cm^{-1}). As hydrogen is adsorbed in a material, it experiences an asymmetric local adsorption potential formed by the solid surface of the adsorbent. The interaction between gaseous H_2 and the potential surface of the adsorbent creates an energy barrier to molecular rotation and the H_2 molecular rotations become "hindered." For solid-gas interactions of moderate strength (*ca.* 10's of kJ/mol), the molecule becomes weakly activated (i.e., the H–H bond becomes longer), and the energy degeneracy of the $J = 1$ level is split. In the simplest case, the center of energy of the $J = 1$ manifold is maintained, and the first two transitions out of the m_j ground state manifest as features in the INS spectra centered around 14.7 meV.[86] Thus, the nature of hydrogen adsorption can be indirectly probed by measuring the H_2 rotational energy levels using INS. Unlike diffraction measurements, this technique is not restricted to crystalline materials and has been used to probe the local adsorption environment of hydrogen in many candidate hydrogen storage materials to date.

10.02.2.6 Quasielastic neutron scattering

Neutrons are extremely beneficial for elastic scattering (i.e., diffraction) as well as inelastic scattering (i.e., spectroscopy) measurements. In addition, neutron scattering can be used to measure diffusive dynamic motion in materials, either due to diffusion (translation or rotational motion) or thermal effects. This motion results in a broadened signal located at the elastic line and the technique for measuring the dynamic motion is known as QENS. Fig. 2 demonstrates typical quasielastic scattering data and fits.[87] Again, this technique is extremely sensitive to hydrogen as the intensity scales with the incoherent neutron scattering cross section and the number of atoms participating in the dynamic motion.

The total combined intensity of the elastic and quasielastic scattering remains constant (besides a damping from an effective Debye-Waller contribution), however the amount of each might change as a function of temperature, as is typical for activated dynamic motion. A quick probe to gauge the onset of this motion is to conduct a fixed window scan experiment which measures only the intensity of the elastic line. In these measurements, the observed elastic intensity decreases as more dynamic motion is present.

QENS data are typically collected across a wide range of both scattering angles and temperatures. By collecting data across multiple scattering angles, the length- and timescales of the dynamic motion can be determined. The broadening of the quasielastic contribution is measured as a function of scattering angle, Q. If the diffusive motion is rotational, the line broadening is roughly constant as a function of Q, following the form of $\mathrm{HWHM} = \hbar/\tau_1$. Here, HWHM is the half-width at half-max broadening of the Lorentzian function used to model the quasielastic scattering, $\hbar$ is the reduced Planck constant, and τ_1 is the residency time. The residency time is a measure of the time the diffusing species remains in one position before moving. If the diffusive motion is translational, the HWHM will change as a function of Q. One common mathematical framework used to model this behavior is the Chudley-Elliot model, $\mathrm{HWHM} = \frac{\hbar}{\tau_1}\left(1 - \frac{\sin(Ql)}{Ql}\right)$.[88] Here l is the jump length, or the length in real space the molecule moves from one crystallographic site to another. In this way, the characteristic residency time can be determined as well as the length scale of such motion and finally the diffusion constant D can be calculated as $D = l^2/6\tau_1$.

By collecting data across multiple temperatures, the energy scale of the diffusive motion can also be determined. The plot of τ_0 as a function of temperature can be typically fit using the Arrhenius equation. Modeled all together, the analysis yields detailed information about the diffusive mechanism of the analyte through the host compound. Hence QENS can be an extremely powerful technique for understanding any sort of dynamic motion in candidate hydrogen storage materials. More detail regarding the analysis of QENS data can be found elsewhere.[89–91]

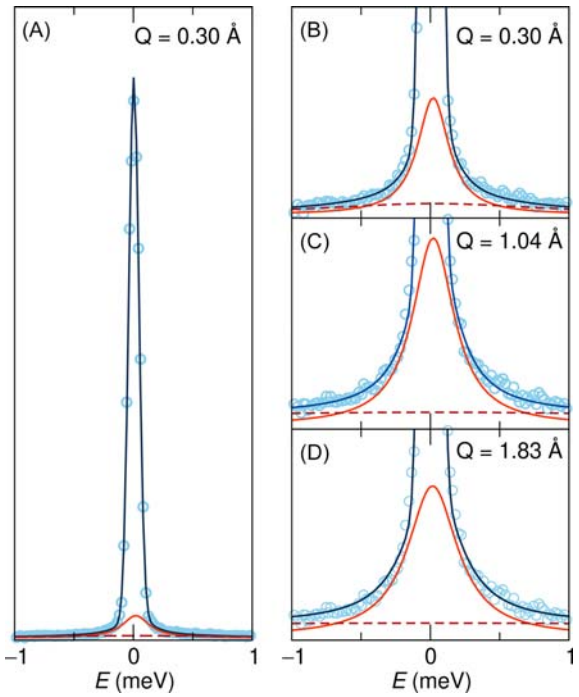

Fig. 2 QENS spectra of H_2 adsorption in Mg_2(dobdc) at various wavevectors, Q. The dotted line denotes the background fit with a sloped line, the solid dark blue curve shows the fit envelope including the delta function convoluted with the resolution function, which accounts for the elastic scattering, and the solid red line is a Lorentzian curve representing the quasielastic scattering from adsorbed diffusing hydrogen. (A) shows the full spectrum, while (B), (C), and (D) show the QENS dependence on Q. Adapted from Sumida, K.; Brown, C. M.; Herm, Z. R.; Chavan, S.; Bordiga, S.; Long, J. R. Hydrogen Storage Properties and Neutron Scattering Studies of Mg_2(dobdc)—A Metal–Organic Framework With Open Mg^{2+} Adsorption Sites. *Chem. Commun.* **2011**, *47* (4), 1157–1159.

The analysis of QENS data is often phenomenological and as such constrained to describing relatively simple dynamics. The advent of powerful computational tools enabled QENS studies in much more complicated systems. Advances in molecular dynamics simulations have allowed for the development of more complicated models for systems with rich dynamical motion of the diffusive species. Molecular dynamics simulations can be directly related to QENS data using various correlation functions and transforms employed with the use of the convolution of a resolution function. These developments have allowed for even the most complicated systems to be well understood, as will be seen in the following sections of this chapter.

10.02.2.7 Safety and experimental considerations

Safety is the most important aspect of conducting any experiment. When conducting neutron experiments, careful consideration must be given to the induced activation of a sample. After exposure to a neutron beam, samples are assumed to be radioactive, with decay half-lives that are specific to each isotope in the sample. After exposure to a neutron beam, samples are considered "hot" and must "cool off" before they can be safely handled. The amount of time required for a sample to cool off sufficiently can be calculated based on the composition of the sample, the duration and intensity of exposure, and time since the sample was removed from the beam. A radiation or health physics professional at the neutron facility is required to assess samples after exposure to neutrons. In addition, gas-dosing experiments or hydride syntheses involve pressurized gasses, which may be flammable, corrosive, and/or explosive. Samples may also be air or oxygen sensitive and suitable handling and storage precautions should be an integral part of any plan for experimenting. Adequate safety training and contingency planning is necessary when conducting these experiments.

Performing experiments *in situ* presents several advantages compared to performing experiments *ex situ*. For *in situ* measurements, all experiments can be done on one sample under varying conditions. Chemical insights can be gleaned from the series of measurements under these disparate conditions on the same exact sample. While this approach is still possible for *ex situ* experiments, sample variability from synthetic batch to synthetic batch, or uncertainties in sample handling, may introduce ambiguity and error into the study. Furthermore, performing an experiment *in situ* allows the researcher to update the experimental data collection plan in real time while the data are being collected.

Lastly, in contrast to X-ray experiments, the fluxes from neutron sources are relatively low. With only a few milligrams of a sample, laboratory X-ray data collection may take several minutes. For that same material, it might take several hours with 100 s of milligrams of material to collect similar quality data on a neutron instrument. Hence careful planning and contact with instrument scientists are an important part of any neutron scattering experiment. Specific care should be made to ensure sample purity, stability, and a solid experimental plan to ensure that the limited time for a neutron instrument is used wisely.

10.02.2.8 Outlook

Neutron scattering techniques have been instrumental in driving our understanding of hydrogen sorption in candidate storage materials. As we will explore in the upcoming sections, the field of hydrogen chemisorption began over a century ago. The development of new neutron sources around the world in the mid-1950s made neutron scattering experiments readily available for the first time. At the same time, investigations into hydrogen storage in metal hydrides erupted, and the results of neutron scattering measurements on these materials quickly formed the cutting edge of knowledge on hydrogen absorption. Later, chemical hydrides came into focus. Here, again, neutron scattering experiments played—and continue to play—an important role in determining the underlying chemistry and physics in these intriguing systems. Most recently, porous compounds showed promise as candidate hydrogen storage materials. It should not be surprising that neutron scattering experiments are now essential measurement techniques for investigating the hydrogen sorption interactions in candidate storage materials of any kind. In the remaining three sections, we will illustrate how neutron scattering measurements uniquely contributed to advancing the science of hydrogen storage.

10.02.3 Metal hydrides

Studies of hydrogen absorption in metals date back to the 19th century.[92] The advent of more easily accessible neutron sources in the mid-20th century revolutionized the study of metal hydrides. These studies coincided with a renewed excitement in metal hydrides as, among other things, potential materials for energy storage.[93,94] The utility of the metal hydrides as candidate hydrogen storage materials comes from their ability to store molecular hydrogen as hydride ions in the interstitial spaces in crystalline lattices. This leads to high volumetric capacities, which are comparable to those of liquid and pressurized gaseous hydrogen, at moderate operational temperatures and pressures. Because of their mild operating conditions, metal hydrides can represent a safer alternative to liquid or compressed gas storage systems. Another advantage of these systems is that the hydriding process can be relatively quick and reversible over many cycles. Because of these benefits, there are already metal hydride storage systems in use in niche applications today. For example, metal hydrides are used as the hydrogen storage system in some forklifts.[95,96] Forklifts powered by traditional fuels emit carbon monoxide during operation, which in confined spaces such as warehouses, presents serious health hazards. Moreover, hydrogen-fueled forklifts provide the same operational capacity as their fossil-fuel powered counterparts. As of 2018, there were over 21,000 fuel cell powered forklifts deployed or ordered for deployment in the United States, however, a majority of these operate using compressed gas tanks.[97] However, despite the adoption of metal hydride hydrogen storage systems in certain

commercial sectors, there are still significant barriers which have so far precluded the adoption of metal hydrides as commercially viable storage materials. In this section, we will give a brief overview of the general chemistry of metal hydride formation and then review select works in which neutron experiments advanced our understanding of the hydride chemistry and hydrogen storage properties in metal hydrides.

10.02.3.1 The chemistry of the metal hydrides

Here we give a synopsis of metal hydride chemistry, from separate H_2 gas and metal phases to the fully formed β-hydride phase. At the beginning of the hydriding process, the H_2 gas physisorbs to the metal at the interface to form a gas-metal monolayer, with additional gas-gas layers formed away from the metal surface. The predominant physisorption interactions are van der Waals in nature.[91] The gas molecules physisorbed to the surface can then chemisorb to the metal ions, through a somewhat complex, metal-dependent mechanism.[98] The chemical interaction of these two phases was first considered in the context of heterogeneous hydrogenation catalysis. In this context, *M*-H_2 intermediates (where *M* is a metal) were invoked, although crystallographic evidence supporting these reactive intermediates was naturally lacking.[99] The details of the interaction of gaseous molecular hydrogen with a metal ion were elucidated in 1984, when Kubas and coworkers crystallized the $W(CO)_3(P^iPr_3)_2(H_2)$ complex and characterized it using X-ray and neutron diffraction experiments (**Fig. 3**).[100] These experiments revealed that hydrogen can interact with electropositive metal ions by donating the electrons in the H–H σ bond into an empty *d* orbital, in this case to form a side-on, η^2-H_2–M bond.[26,101–103] The hydrogen in these complexes is distinct from the gaseous molecule: the H_2 is "activated," meaning the H–H bond is elongated and weakened. The experimental determination of the individual H atoms in the complex indicate that the molecule has lost the quantum rotational degeneracy that it possesses in the gas phase. The elongation is evidenced by neutron diffraction in the determined H–H distance for $W(CO)_3(P^iPr_3)_2(H_2)$ of ≈ 0.89 Å, about a 20% extension relative to the H–H bond in free H_2 (0.74 Å).[29] Proof of the intramolecular bond remaining intact came from NMR studies of the HD isotopologue that shows a 1:1:1 triplet with a coupling $J_{HD} = 33.5$ Hz, compared to 43.2 Hz in the gas phase.[100]

Qualitatively, the dissociative process at a discrete metal center in a coordination complex and at a bulk metal surface are similar: electron density from the H_2 σ_g orbital is donated into the metal orbitals (bands), and electron density from the metal populates the H_2 σ_u^* orbital, leading eventually to bond cleavage. The precise nature of the initial interaction depends on the metal and on the surface features where the hydrogen is adsorbed and can resemble a range of hydrogen states from the Kubas dihydrogen, to a stretched dihydrogen, and to a compressed dihydride state.[104] Spectroscopic experiments of hydrogen interaction with the stepped Ni(510) edge suggest that the η^2-H_2–M σ-complex motif is present during hydride formation in this specific context.[105,106] Due to the transient nature of these intermediates, there is somewhat limited experimental evidence regarding the precise initial interactions of H_2 with metal surfaces. However, extensive theoretical work has shed light in this area. These works illustrate the different modes of interaction of dihydrogen with a flat metal surface, including the Kubas-type side-on, η^2-H_2–M bonding motif, end-on interactions, and scenarios in which the H_2 molecule interacts with multiple metal atoms simultaneously.[98,107–114]

Once the H_2 molecules are adsorbed to the metal surface, sufficient overpressures of hydrogen gas leads to H–H bond cleavage on the metal surface, and the resulting anions migrate into the metal.[83] At low hydride concentrations in the metal (i.e., $< \approx 0.1$ H:M molar ratio), the α-metal-hydride phase forms (**Fig. 4**). The α-metal-hydride phase is a solid solution of hydrogen intercalated into the interstitial sites in the metal crystalline lattice. At increasing external H_2 pressures, the hydride concentration in the metal increases, leading to the formation of the β-phase. In contrast to the solid-solution nature of the α-phase, the β-phase has a discreet, ordered chemical structure: the metal hydride. The α- and β-phases coexist over a material-dependent pressure interval. In this interval, the concentration of hydrogen in the metal hydride increases rapidly for a small change in H_2 gas overpressure. The change in the hydrogen concentration over this pressure interval determines the amount of useable hydrogen that can be stored in the metal

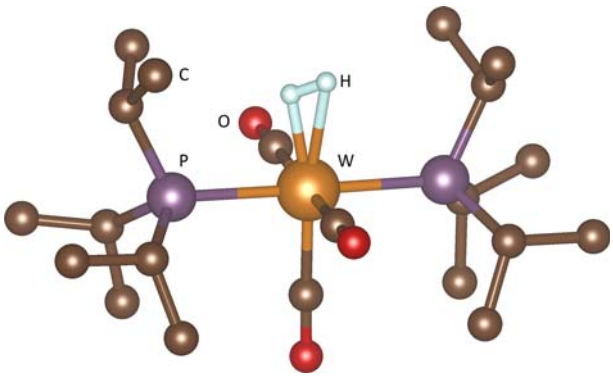

Fig. 3 The $W(CO)_3(P^iPr_3)_2(H_2)$ complex, as derived from neutron and X-ray diffraction experiments, displays side-on η^2-H_2–M bonding. Hydrogen atoms on the ligands are omitted of clarity. Adapted from Kubas, G. J.; Ryan, R.; Swanson, B.; Vergamini, P.; Wasserman, H. Characterization of the First Examples of Isolable Molecular Hydrogen Complexes, $M(CO)_3(PR_3)_2(H_2)$(M = Molybdenum or Tungsten; R = Cy or Isopropyl). Evidence for a Side-on Bonded Dihydrogen Ligand. *J. Am. Chem. Soc.* **1984**, *106* (2), 451–452.

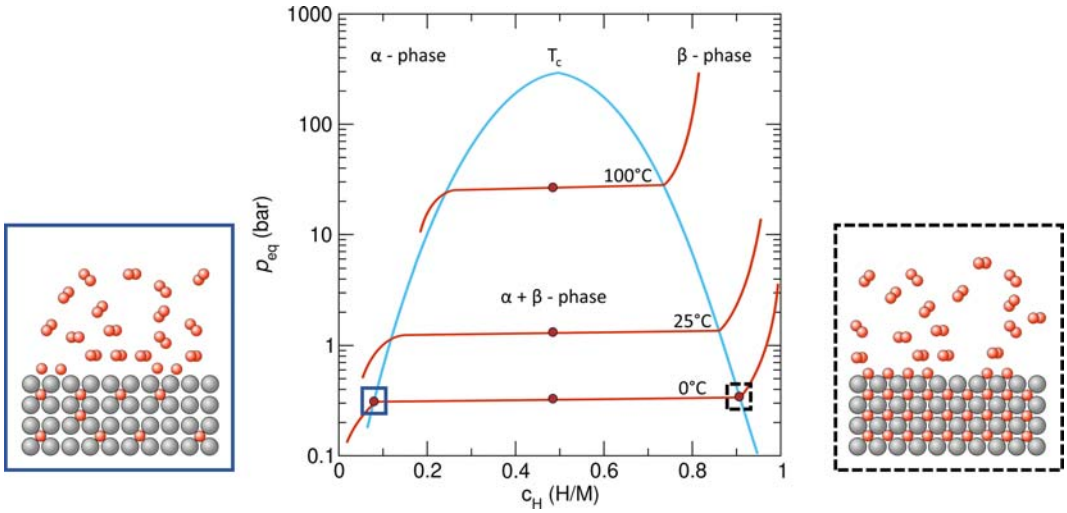

Fig. 4 The pressure-composition phase diagram shows the region of phase space where the two metal hydride phases coexist. Adapted from Züttel, A. Materials for Hydrogen Storage. *Mater. Today* **2003**, *6* (9), 24–33.

given a small pressure swing at a specific operation temperature. During the formation of the α- and β-phases, there can be an appreciable change in crystal volume, which presents engineering challenges in designing storage tanks for these materials.[115] In addition, incorporation of the H ions into the material sometimes leads to complex changes in the crystal and band structures, which can lead to interesting phase changes including metallic-non-metallic[116] and magnetic transitions.[117] Once the pure β-phase is achieved, the amount of H_2 overpressure required to cause a small change in the hydrogen concentration in the hydride material increases drastically.

The phenomenological microscopic description of hydride formation above is also well understood from a thermodynamic perspective. As the molecular hydrogen chemisorbs onto the metal surface and then dissipates into the metal, there is a large change in entropy, roughly equal to the standard entropy of hydrogen, $\Delta S^0 \approx 130$ J/K/mol. This decrease in entropy in the system is often more than offset by the enthalpic energy change from the formation of the metal hydride, which is dictated by the strength of the M–H bonds. Metal hydride formation can therefore be quite exothermic, which presents a problematic tradeoff. The same amount of heat is needed to both hydride and dehydride metals. Over years of study, an empirical rule emerged that states that the materials with the highest volumetric capacities tend to form strong ionic M–H bonds and have the highest enthalpies of formation. These materials are known as the high-temperature hydrides and, unsurprisingly, they often operate at restrictively high temperatures. Conversely, the low-temperature (i.e., near ambient temperature) hydrides generally form weaker covalent M–H bonds, leading to both lower operating temperatures and, unfortunately, lower volumetric capacities of useable hydrogen.

Several common types of hydrides are tabulated in **Table 3**, grouped by formula and with archetypal examples given for these groups. This serves as a table of contents for this section, where we discuss the history and current state of the field for the AB_5, AB_2, A_2B, and A type metal hydrides. We note that the field of metal hydrides has been sufficiently reviewed in the context of hydrogen storage.[94,118–122] Additionally, several reviews specifically focus on the neutron studies of molecular and solid-state metal hydrides.[123–125] Here, we focus on neutron scattering studies of solid-state metal hydrides as candidate materials for hydrogen storage applications, and how these studies have advanced our understanding of these promising materials.

10.02.3.2 Neutron scattering studies of metal hydrides

Since the first observation of hydrogen absorption in a metal in the 1800s,[92] there have been many outstanding fundamental questions regarding the metal hydriding and dehydriding processes. These included questions regarding the location of the hydrogen in metal hydride structures, the effects of hydrogen absorption on the structure and thus on the physical properties, the chemical

Table 3 Common types of metal hydrides studied as candidate hydrogen storage materials.

Formula	*Archetype*	*Hydride*	*Structure*
AB_5	$LaNi_5$	$LaNi_5H_7$	Haucke phase
AB_2	$ZrMn_2$	$ZrMn_2H_3$	C14, C15 Laves phases
A_2B	Mg_2Ni	Mg_2NiH_4	Cubic
A	Mg, Pd	MgH_2, PdH	Tetragonal

nature of hydride formation including hydrogen dynamics in the lattice, and the chemical factors that favor high hydrogen concentrations in a material. Neutron diffraction and scattering experiments were crucial in answering these questions.

The AB_5 compounds generally crystallize in the $CaCu_5$ structure type (*P6/mmm*) and are named after Werner Haucke, who discovered $CaCu_5$ in 1940.[126] The best-known material in this class is $LaNi_5$, along with its alloys and congener species, which have been extensively studied.[127–131] In 1970, $LaNi_5$ was shown to uptake hydrogen with a very promising volumetric capacity of 115 g/L.[132,133] The phase diagram for the $LaNi_5$-H_x system contains several phases, including the parent $LaNi_5$ (non-standardly named the α-phase), $LaNi_5H_3$ (the β-phase), and the fully hydrided $LaNi_5H_7$ (the γ-phase). The structure of $LaNi_5$ can be described by three atomic sites: one for La and two for Ni, in which planes of La and Ni, parallel to (001), alternate with planes of Ni. The γ-phase was the first hydride phase to be structurally investigated using PND experiments. For about 10 years, several PND studies were published, constituting a debate over the crystal symmetry of the γ-phase as well as the position of the hydride (deuteride) ions in the lattice.[134–139] Anisotropic line broadening from a degradation in sample crystallinity caused by the hydriding process initially hindered these studies. Eventually, advancements in Rietveld refinement methods and a finer understanding of the effects of stoichiometry on structure allowed the correct assignment of the space group (*P6/mmm* after all) and D ion site positions, occupancies, and anisotropic thermal parameters as measured at room temperature (**Fig. 5**).[140] The thermal parameters shed light on local thermal vibrations while the occupancies revealed which sites are relatively thermodynamically more favorable for hydride absorption. In the crystallographically ordered compound $LaNi_5D_{6.7}$, there are five distinct absorption sites of varying D occupancy, with the highest occupancy site identified as a Ni_4 tetrahedron. The D ions sit nearly in the center of this Ni_4 tetrahedral site, which is in the basal (001) plane, and the ions have an approximately isotropic thermal parameter indicating isotropic thermal motion at this site. Alternatively, this structure can be viewed as having Ni ions centered in NiD_4 tetrahedra (**Fig. 5**). One year later, another PND study detailed the structure of the β phase, in which the D ions occupy tetrahedral and trigonal bipyramidal interstitial sites.[141]

The structure of the metal hydride was further probed using INS experiments. INS measurements on $LaNi_5H_{4.3}$ and on the Al-substituted compound $LaNi_4AlH_{4.3}$ helped corroborate the crystallographically determined H positions in the $LaNi_5$ hydrides.[142–145] In addition, neutrons were also used to further study the dynamics of hydride diffusion during the hydriding and dehydriding processes and the phase transitions. The hydride diffusion through α-$LaNi_5$ was studied using QENS and INS experiments. At low concentrations of H, these studies found that the hydride ions diffuse through the material via a complex anisotropic mechanism involving three modes of hydride jump diffusion.[145,146] Previous NMR measurements had hinted at this ionic motion, but neutron spectroscopic techniques uniquely elucidated the microscopic details of hydride dynamics in $LaNi_5$.[147–149] The important phase transition from the α-phase to the β-phase was studied in depth using PND experiments, and it was shown that the anisotropic change in volume at this phase transition causes the particles to decrepitate at the phase boundaries.[150,151] This results in a powder of particle size on the micron scale and some loss of hydrogen absorption capacity. While the pure, unalloyed $LaNi_5$ compound was being thoroughly investigated, it was found that some of the practical properties of the hydriding/dehydriding process could be improved in related Haucke compounds and their alloys. These compounds were also extensively studied using PND experiments.[152–161]

$LaNi_5$ and the other AB_5 Haucke compounds showed extreme potential as hydrogen storage candidate materials for use in HFCEVs due to their high volumetric capacities near ambient temperatures and at moderate pressures of hydrogen, their limited hysteresis of absorption and desorption, and their cyclability. Unfortunately, the downfall of these materials has so far been their gravimetric capacities. Because of the large atomic masses of the formula units of the parent materials, the gravimetric capacities are prohibitively low for mobile applications. For example, the gravimetric capacity for $LaNi_5$ is 1.4 mass %, far below the EERE target value of 4.5 mass % by 2020.

As the hydrogen absorption properties of $LaNi_5$ were under study, the hydrogen absorbing properties of the Laves phase AB_2 type compounds were also being investigated.[162–165] The Laves phase compounds that show exceptional hydrogen absorption

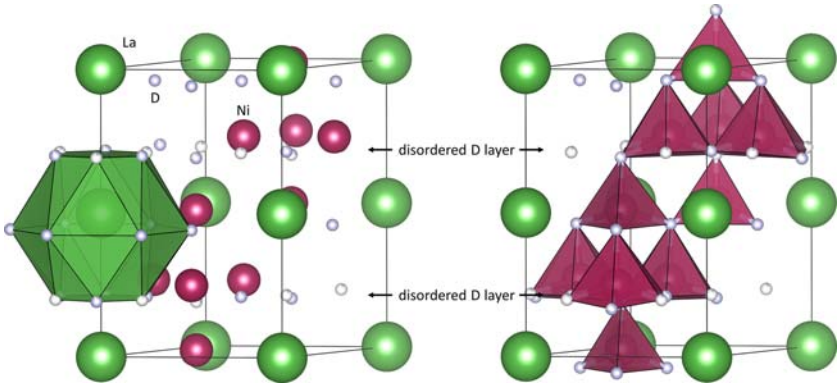

Fig. 5 The structure of hypothetically fully deuterided $LaNi_5D_7$ as derived from Rietveld refinements of PND data. Adapted from Lartigue, C.; Le Bail, A.; Percheron-Guegan, A. A New Study of the Structure of $LaNi_5D_{6.7}$ Using a Modified Rietveld Method for the Refinement of Neutron Powder Diffraction Data. *J. Less Common Metals* **1987**, *129*, 65–76.

properties crystallize in either the hexagonal C14 or the cubic C15 structure types.[166] Neutron scattering experiments were quickly carried out on these materials to determine the D position in the deuterides and to investigate the nature of the chemical bonding and hydride diffusion in these materials.

The archetypal representative of the hexagonal C14 materials is the $ZrMn_2H_3$ Laves compound. PND experiments on the deuterated congener of this material showed that, out of 24 possible interstitial sites in the parent metal lattice, the D ions occupy only four crystallographically distinct sites, each a Zr_2Mn_2 tetrahedral interstitial position.[167,168] The occupied interstices create an intricate network of hexagons within the parent metal lattice (**Fig. 6**). The occupancy and thermal parameters in this network at various temperatures hinted at a possible H(D) diffusion mechanism through the metal during hydride formation. QENS measurements again proved invaluable in elucidating the diffusion mechanism for the deuteride ions through the C14 Laves compounds.[169–172] These studies found that the hydride ions move through the metal lattice following two mechanisms of different time scales: a quick, localized mechanism in which the hydride ions jump back and forth between pairs of 24*l* crystallographic sites within the same hexagon of sites, and a slower diffusive mechanism whereby the hydride ions migrate to different hexagons of sites through the material. Here the time scale for the slow process at 300 K was found to be $\tau^{-1} = 1.8 \times 10^{10}\ s^{-1}$ and the time scale for the fast process at 300 K was measured to be $\tau^{-1} = 2.7 \times 10^{11}\ s^{-1}$ (i.e., jumps on the order of every ≈ 60 and ≈ 4 ps, respectively).

Neutron experiments were also carried out on the cubic C15 Laves compounds.[173–181] These experiments again showed that the hydride (deuteride) ions preferentially occupy A_2B_2 type tetrahedral interstitial sites. In $ZrCr_2H_x$, it was found that the hydride ions also occupy $ZrCr_3$ interstices in low occupancies when $x > 3.1$. Here again, the occupied A_2B_2 sites form a complex network of hexagons, interspersed with AB_3 type sites. The diffusion processes in the cubic Laves phases, as revealed by QENS experiments, again followed two mechanisms of different time scales.[171,176–178,180,182] The hydride ions move between A_2B_2 sites, and the rate and nature of their movement is determined by the distance between the A_2B_2 sites. Like the measurements on the C14 Laves compounds, these experiments again found a faster hopping mechanism of diffusion between sites in the same hexagon and a slower diffusive process between sites on adjacent hexagons. The characteristic values of τ^{-1} for the fast and slow processes in these materials are also on the order of tens to hundreds of picoseconds, depending on the temperature of the measurement, similar to the τ^{-1} values for the C14 Laves compounds.

Interestingly, PND and magnetic measurements also revealed magnetic phase transitions in which the magnetic properties were dependent on hydride concentration in the C14 and C15 Laves materials.[183–185] In general, the absorption of hydrogen leads to an expansion of the lattice and thus a decrease in the magnetic ordering temperature of the magnetic Laves materials. But in certain cases, such as in $ZrMn_2H_3$, the hydride ions impact the crystal structure and band structure in such a way as to induce a transition

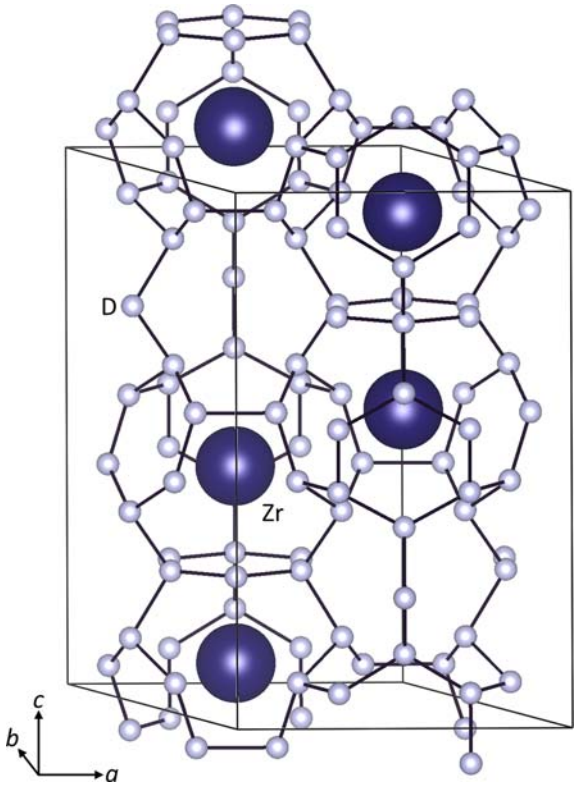

Fig. 6 The complex network of D atoms is connected by hexagons in the structure of $ZrMn_2D_3$. This structure was derived from Rietveld refinements of PND data. Mn ions omitted for clarity. Adapted from Didisheim, J.-J.; Yvon, K.; Shaltiel, D.; Fischer, P. The Distribution of the Deuterium Atoms in the Deuterated Hexagonal Laves-Phase $ZrMn_2D_3$. *Solid State Commun.* **1979**, *31* (1), 47–50.

from a Pauli paramagnet in the non-hydride to a ferromagnet with an ordering temperature of $T_C = 148$ K upon hydriding.[186–188] This discovery in part helped develop a field of study centering around the interplay of structure and magnetism in metal hydrides, particularly in the AB_2H_x compounds in which both A and B are magnetic ions. Because neutrons are also an excellent probe of magnetic properties, the combined studies of magnetism, structure, and hydriding function in the C14 and C15 Laves compounds led to a proliferation of PND studies on these materials and their alloys which continues today.[179,181,189–206]

The A_2B-type hydrides also showed promise as candidate hydrogen storage materials. These included compounds such as Mg_2Ni and Sn_2Co.[207–209] Here, Mg_2Ni is the most studied example of materials in this structure type, in part because of its gravimetric capacity of 3.8 mass % of useable hydrogen, accessible at 518 K and 1 bar H_2.[210–212] Diffraction experiments revealed a temperature-induced phase transition in the Mg_2NiH_4 hydride, in which the high-temperature cubic phase transforms into a monoclinic low-temperature phase below 508 K. Initially, these studies were hindered by factors such as low crystallinity of the hydride phase, low resolution of the available powder diffractometers, anisotropic line broadening, and incompletely developed refinement techniques for analyzing the data.[134] Over time, a series of PND experiments elucidated the structures of both phases.[213–221] Extensive work has also been conducted investigating the macroscopic properties of hydriding, particularly the mechanochemical properties, and these investigations are ongoing.[222–225]

Today, perhaps the most promising class of metal hydrides are the elemental (A) metal hydrides of form AH_x (**Fig. 7**). While many metals form hydrides of type AH_x, MgH_2 has been of particular interest due to its gravimetric capacity of 7.6 mass %.[226–250] However, practical issues such as the high temperatures required to access the stored hydrogen and the rates of absorption and release of hydrogen preclude MgH_2 as a realistic candidate material for commercial applications. As such, neutron measurements on this material and its alloys were limited to more fundamental studies.[251–254]

Another example of the elemental hydrides is PdH_x. PND studies played a crucial role in understanding the underlying physics and chemistry in this system. Pd was found to absorb large amounts of hydrogen as early as 1866, and the hydride and deuteride of Pd continue to be investigated today.[92,124,125] References [124, 125] effectively review the numerous neutron experiments on PdH_x. This system contains an α-phase, a β-phase, an intermediate region on the phase diagram in which both phases coexist, and a supercritical phase at high temperature and pressure conditions.[255–258] The top of the α-phase+β-phase dome in the pressure-composition phase diagram of PdH_x occurs near $p \approx 10^6$ Pa H_2 and $x \approx 0.25$, and the dome terminates near $p \approx 10^2$ Pa H_2 at $x \approx 0$ and $x \approx 0.65$. While pure Pd is a Pauli paramagnet, the paramagnetism is suppressed as the concentration of the hydride(deuteride) increases, and the β-phase is a diamagnet that superconducts below $T_C \approx 1.3$ K at sufficient concentrations of H(D).[259–261]

For several decades, it was thought that the H(D) ions only occupy octahedral interstitial sites, and not the tetrahedral sites, in Pd's cubic lattice.[262,263] More recent PND experiments revealed that the tetrahedral interstitial sites also become occupied at sufficiently high temperatures and pressures.[264,265] QENS measurements showed that the H(D) atoms move through the lattice by a jump diffusion mechanism between adjacent octahedral sites which are adjoined by a tetrahedral site.[266] At low temperatures, an anomaly in the specific heat and resistivity measurements was observed at ≈ 50 K, with the temperature of the anomaly being

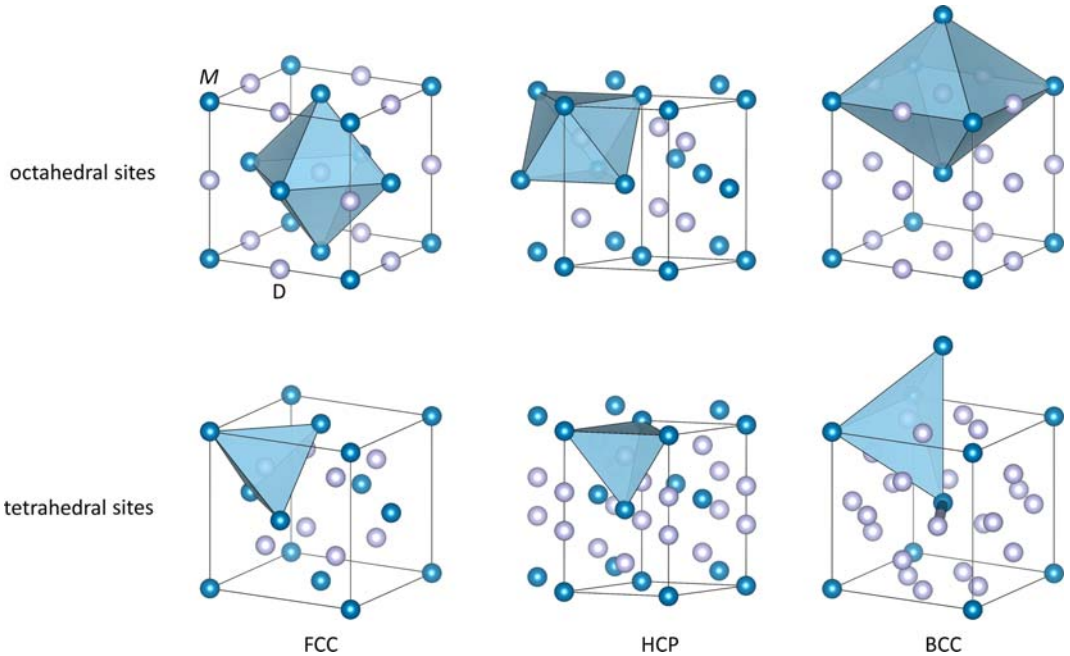

Fig. 7 The tetrahedral and octahedral interstices are highlighted in three common types of metal lattices. Adapted from Otomo, T.; Ikeda, K.; Honda, T. Structural Studies of Hydrogen Storage Materials With Neutron Diffraction: A Review. *J. Phys. Soc. Japan* **2020**, *89* (5), 51001.

dependent on the concentration of the hydride in the lattice. This anomaly was attributed to the freezing of the jump diffusion of hydrogen, leading to the formation of a glass.[267] In addition to measurements on bulk $PdH(D)_x$, the hydriding ability of Pd nanoparticles has been of interest recently.[268,269] It was found that the $PdH(D)_x$ nanoparticles of particular size do not display the 50 K anomaly in the heat capacity data. Moreover, the nanoparticles display significantly different hydrogen absorption properties from bulk Pd. Diffraction, INS, and QENS measurements have probed the physics in the nanoparticles thoroughly. Succinct summaries of these works are given in Refs. [113, 114] and the references therein.

Lastly, a handful of AH_x type hydrides have been studied using single crystal neutron diffraction (SCND) measurements. These include VD_x, HfD_x, and TiD_x.[270–272] The single crystal measurements in the VD_x system elucidated the behavior of the D atoms in the parent lattice in the α-phase at temperatures above an order-disorder transition at $T_C = 210$ K. It should be noted that single crystal studies of metal hydrides are generally particularly difficult due to decrepitation of the materials upon hydriding.

Finally, several high-entropy alloy hydrides have been investigated using neutron diffraction and scattering techniques.[273] These are materials in which there are five or more elements of roughly equal molar proportion that form an alloy. These materials greatly benefit from dual neutron and X-ray diffraction experiments analyzed in tandem, as some of the constituent atoms have low coherent neutron scattering cross sections. The high-entropy alloys generally possess deceptively simple crystal structures and can display exceptional physical properties, including hydrogen absorption.[274–277] In some cases, the high-entropy alloys have been demonstrated to absorb more hydrogen than their bulk constituent elements. One example of a high-entropy alloy characterized by neutron diffraction is HfNbTiVZr.[278] In the neutron study, it was shown that the deuteride ions occupy both the octahedral and the tetrahedral interstitial sites in the BCC lattice, albeit at high temperatures and pressures. In other studies, it has been hypothesized that chemical strain in the lattice lowers the energy for hydride occupation for some of the otherwise thermodynamically unfavorable interstitial sites, enhancing hydrogen adsorption overall.[175]

10.02.3.3 Outlook

For decades, neutron experiments have pushed our understanding of metal hydride chemistry. The PND experiments on the Haucke and Laves phase compounds, the A_2B type metal hydrides, the elemental hydrides and the high-entropy alloy hydrides all helped address the fundamental chemical questions regarding the hydriding process. Questions like, where does the hydrogen go in the lattice, by what mechanism does the hydrogen move through the lattice, and what is the nature of the *M*–H bond were all answered using neutron techniques. The aggregate of these studies has revealed general rules for hydride absorption in metals. For example, the hydride ions prefer specific geometries and sizes for the interstitial sites.[134] There are also empirical trends within the periodic table that designate which elements—among them, La, Zr, Ti, Ca, Y, and others[122] tend to absorb hydrogen more readily. Additionally, the Switendick criterion was developed, which states that H⋯H contact distances in metal lattices cannot be shorter than ≈ 2.1 Å.[279,280]

The Switendick criterion is as an empirical rule that defines how close H ions may be in a metal hydride due to H⋯H Coulombic repulsion. This repulsion can lead to lower-than-expected occupancies of otherwise thermodynamically stable neighboring interstitial sites as a function of hydride concentration in the metal lattice. This effectively lowers the volumetric and gravimetric capacities of the metal hydrides. Interestingly, there are only a handful of metal hydrides that violate the Switendick criterion. Among these, the $RNiInH_x$ compounds (R = La, Ce, Nd, Pr) have been studied using a suite of techniques including NMR spectroscopy, PND, and DFT calculations.[281–284] The PND experiments showed that the deuterides occupy adjacent, face-sharing R_3Ni tetrahedra, leading to a D⋯D distance of ≈ 1.6 Å, far below the Switendick criterion distance of ≈ 2.1 Å. Together, the studies showed that the negative charge on the hydrides is polarized toward the electropositive rare earth ions in the structure, thereby screening the H⋯H Coulombic repulsion and allowing the hydride ions to simultaneously occupy close interstitial sites. Additionally, a recent combined INS and DFT study also provided experimental evidence suggesting very close H⋯H contacts in the C15 Laves compound ZrV_2H_3, which was crystallographically characterized by neutron diffraction experiments in 1979 and 1980.[285–287] The earlier neutron diffraction studies hinted at possible close H⋯H contacts, but found low occupancies for all occupied sites, indicating that adjacent sites were not simultaneously occupied. The INS study found features in the spectra that the authors claim arise from simultaneous occupation of adjacent sites, suggesting H⋯H contacts of < 2.1 Å. The authors note that the feature may also arise from an amorphous VH_X impurity possibly present in the sample that was not observed in the diffraction experiments. Similarly, low occupancies in close H sites explained an apparent violation of the Switendick criterion in K_2ReH_9.[134,288]

Several obstacles still hinder metal hydrides from being commercially viable candidate materials for hydrogen storage application in HFCEVs. Namely, the gravimetric capacities are lower than the EERE targets, and the thermodynamic stability of the hydrides needs to be further tuned to control the operational temperatures for these materials. There are several approaches which try to circumvent these obstacles. One is the pursuit of hydrides containing lower-Z elements. Examples of such materials that have already benefited from neutron diffraction characterization include alloy hydrides of Li, Ca, and Mg with Si and Ge, and lighter-element perovskite hydrides such as $NaMgH_3$, $RbMgH_3$, and $RbCaH_3$.[289–302] Another approach to circumvent practical issues with the metal hydrides includes confinement of metal nanoparticles in porous materials, which prevents sintering during hydriding.[303–305]

Today, metal hydrides face an uphill battle as viable commercial materials for both stationary and mobile hydrogen storage applications because of the tradeoffs between volumetric capacity, gravimetric capacity, and operating conditions. Innovative material science techniques for circumventing these issues are under investigation. Yet, improved methods—or entirely new metal hydrides—are needed to overcome these hurdles if these materials are to break into the energy market. These difficulties may be less of an

issue for potential stationary applications such as backup power storage, or for material handling and manufacturing-based applications.

10.02.4 Complex hydrides

The complex hydrides are an exciting class of candidate materials for potential hydrogen storage applications. These materials are molecular salts that store molecular hydrogen as individual atoms in multiatomic anions. The non-hydrogen atoms in the anion are usually light elements from groups 1, 2, or 3 of the periodic table. The cations can be inorganic or organic, and generally also comprise light elements. As such, the gravimetric capacities for these materials can be exceptionally high while the operational pressures remain modest. In an ideal complex hydride hydrogen storage material, release of molecular hydrogen occurs via thermal decomposition of the ionic compound, whereas complex-hydride regeneration occurs via reaction of molecular hydrogen with the decomposed byproduct. In this section, we first provide a brief discussion of the classifications and history of chemical research in the complex hydrides. Then we review selected studies in which PND experiments have augmented our understanding of complex hydrides as candidate hydrogen storage materials for use in commercial applications. Note that, compared to the metal hydrides, the chemistry of the complex hydrides is extremely intricate and system dependent.[32,118,306–312] Typically, the unsolvated complex hydrides have several polymorphs as a function of temperature and pressure. After thermolysis to evolve hydrogen gas, the resulting species often further decompose along labyrinthian reaction coordinates. Worse, the reaction pathways may dead-end irreversibly with thermodynamically stable byproducts. As such, the discussion of the hydriding chemistry in complex hydrides will be specific and confined to the individual subsections on each class of material. Despite their complicated chemistry, the complex hydrides still show great promise as candidate hydrogen storage materials.

10.02.4.1 History and nomenclature

The complex hydrides are categorized first by their anion and then by their cation. The three main classes of complex hydrides by anion are the borohydrides (BH_4^-), the alanates (AlH_4^-), and the amides/imides (NH_2^-, NH^{2-}). These categories are further subdivided by the type of cation, which is either organic or inorganic. The space for cations is naturally large. Historically, complex hydrides with inorganic cations have been researched extensively, with materials containing organic cations coming into focus relatively recently. In addition, mixed-cation hybrid materials and materials containing neutral or charged additives have been investigated to improve detrimental hydriding/dehydriding properties, as will be discussed below. At the end of this section, we will return to some of the contemporary methods for circumventing the challenges still presented by this promising class of materials.

The neutral boranes and ionic borohydrides have a fascinating chemical history dating back to World War II and before.[306,313] Early in their history, the work on boranes was pioneered at the University of Chicago in the laboratory of Prof. Hermann Schlesinger by Schlesinger, Herbert Brown, Anton Burg, and others. They discovered the reducing properties of a series of boranes and organoboranes—Brown later received the Nobel Prize for these contributions.[314] As part of the Manhattan Project, Brown, Schlesinger, and Burg developed $U(BH_4)_4$ as a material for volatile uranium isotope separations.[315] The trio discovered numerous metal borohydrides, including $LiBH_4$ and $NaBH_4$.[316–319] $NaBH_4$ was among the first complex hydride materials used for condensed phase hydrogen storage. Upon hydrolysis, $NaBH_4$ irreversibly evolves hydrogen gas which can then be used, for example, in weather balloons.[320]

Research interest in complex hydrides began in the mid-20th century, starting with investigations into synthesis and then thermolysis to yield hydrogen gas. But facile reversibility to recover the complex hydride remains as a key issue in this field today. As early as 1960, it was shown that $NaAlH_4$ can be solvothermally synthesized using NaH, Al, and H_2 in a variety of solvents, or via a solid-state reaction from the melt.[321,322] Similarly, it was known that $NaAlH_4$ thermally decomposes in a two-step reaction to give off 5.5 mass % H_2. At the first thermal dissociation, hydrogen gas evolves concomitantly with the formation of the hexahydride, Na_3AlH_6, and Al metal. Upon further heating, additional hydrogen is released and NaH and additional Al metal form.[a] [323,324] Dymova et al. showed that the reaction can be driven backwards under harsh conditions. They recovered $NaAlH_4$ from NaH and Al metal by treating the solid reagents with 175 bar H_2 at $\approx$ 543 K for 3 h.[325] While the reaction is technically reversible, these conditions are not ideal for vehicular applications. In 1997, Bogdonavić and Schwickardi demonstrated that Ti-doped $NaAlH_4$ can be recovered at $\approx$ 440 K and 150 bar, and the hydriding and dehydriding process can be cycled at least 100 times with minimal loss of hydrogen storage capacity.[326] Furthermore, the Ti-doped system also evolves hydrogen gas at lower temperatures. While the reported catalysts $TiCl_3$ and $Ti(OMe)_4$ were imperfect, this discovery reinvigorated the field of complex hydrides as potential hydrogen storage candidate materials for stationary and mobile energy storage applications.

[a]NaH can thermally decompose to give off additional hydrogen gas, but it does so at $\approx$ 730 K at ambient pressure, so this reaction is usually neglected. Below, we use the term "theoretical mass % H_2" to encapsulate the hydrogen gas from the thermolysis of all products, even those that require excess heat.

10.02.4.2 Neutron scattering studies of the complex hydrides

The initial report describing the catalyzed reversibility of Ti-doped $NaAlH_4$ shed light on the macroscopic details of this process, yet several questions remained regarding the microscopic details. Neutron studies of Ti-doped $NaAlH_4$ and other pure and doped alanates helped illuminate the microscopic details of the hydriding and dehydriding processes at the atomic level.[327–329] The structure of pure $NaAlH_4$ ($NaAlD_4$) was determined by single crystal X-ray diffraction (SCXRD) experiments,[330,331] and later, by PND experiments. The X-ray experiments showed that the material crystallizes in the $CaWO_4$ structure type within the $I4_1/a$ space group. The neutron diffraction experiments confirmed this and pinpointed the position of the deuteride ions (Fig. 8).[332] The sodium ions have eight nearest neighbor deuteride ions from eight distinct AlD_4^- anions, forming a distorted square antiprism geometry for the cation. The crystal structure of Ti-doped $NaAlD_4$ was also investigated using PND experiments, which showed an expansion of the lattice parameters as a function of doping concentration, but which were unable to locate the Ti atoms in the compound.[333] A combined DFT and INS study investigated the Ti-doping processes and resulting structure.[334] This study showed that Ti atoms replaced Na atoms in the structure. The study also suggested that the Ti atoms then activate the surrounding Al–H bonds. Additionally, a joint PXRD and PND study monitored the crystalline species during the hydriding and dehydriding processes in Ti-doped $NaAlH_4$.[335] This study helped elucidate the mechanism for regeneration of $NaAlH_4$ and supported the INS/DFT study by showing an expansion of the Na_3AlH_6 unit cell upon Ti substitution for the Na atoms. The precise mechanistic role of the Ti ions in facilitating reversibility remained somewhat unclear until recently. In 2015, a DFT study—informed by the previous neutron studies—suggested that the Ti ions bridge two alanate groups and minimize charge separation as the hydride ions are transferred to form the hexahydride.[336] Notably, the proposed mechanism is symmetric such that it is consistent with the Ti ions catalyzing both the forward and backward reactions in this system.

In an attempt to further improve the hydriding and dehydriding kinetics, many other doped $NaAlH_4$ systems have been investigated, where the dopants included Sc, Ce, La, Zr, C, and combinations thereof.[337–340] Additionally, several other pure and doped metal alanates received intense interest as candidate hydrogen storage materials. Many have been characterized using PND experiments, including $LiAlH_4$,[341] $KAlH_4$,[342] $Mg(AlH_4)_2$,[343] and $Ca(AlH_4)_2$.[329,344] Also of interest are the mixed-cation tetrahydride and hexahydride systems. An example is Na_2LiAlH_6, which holds ≈ 3.5 mass % H_2. Na_2LiAlD_6 is synthesized mechanochemically by ball milling $LiAlD_4$ and $NaAlD_4$ in an Ar atmosphere. PND experiments revealed that the material crystallizes in a double perovskite

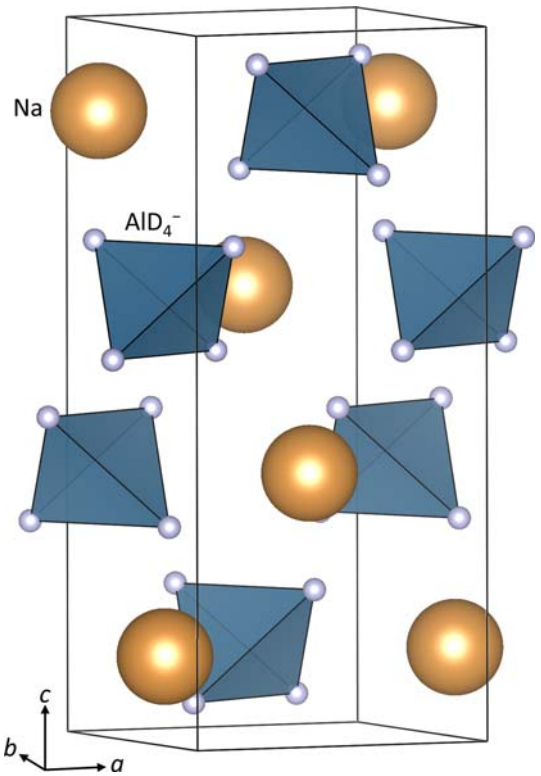

Fig. 8 The structure of $NaAlD_4$ as elucidated by powder neutron diffraction experiments. Large gold spheres and small grey spheres represent Na and D atoms, respectively, while the Al atoms sit at the center of the polyhedra. Adapted from Hauback, B.; Brinks, H.; Jensen, C.; Murphy, K.; Maeland, A. Neutron Diffraction Structure Determination of $NaAlD_4$. *J. Alloys Compd.* **2003**, *358* (1–2), 142–145.

structure with Na ions charge balancing the ordered [LiD_6] and [AlD_6] octahedra.[345] Today, extensive research efforts aim to lower the operational temperatures of the pure, doped, and mixed-cation alanates.

The discovery of catalyzed reversibility in Ti-doped $NaAlH_4$ inspired renewed research efforts in a range of complex hydride materials including the borohydrides. The chemistry of the borohydrides is complex and has been reviewed extensively.[306,311,346,347] The modern research efforts into the borohydrides were bolstered by the 2002 discovery that SiO_2-doped $LiBH_4$ evolves 13.5 mass % H_2 at $\approx$ 473 K, around 270 K colder than the pure parent material.[348–350] $LiBH_4$ holds a remarkable 18.5 theoretical mass % H_2 combined with a volumetric capacity of 121 kg H_2 m^{-3}. While the gravimetric and volumetric capacities exceed even the strictest requirements for a hydrogen storage material as outlined by the EERE, the hydrogen is not readily accessible near ambient conditions. Moreover, these materials are air-sensitive and must be handled in inert environments. Lowering the operational temperatures for this material and for related complex hydrides remains as a central research focus today.

Even though $LiBH_4$ was first discovered by Brown and Schlesinger in 1940, the crystal structure remained unknown for decades. This is in part due to the neutron absorption cross sections for naturally occurring Li and B, which are $\approx$ 71 barn and $\approx$ 770 barn, respectively. These values are large compared to the neutron absorption cross section for deuterium, 5.2×10^{-4} barn.[45] Paired with the low sensitivity for lighter elements inherent to X-rays, this material presents a unique crystallographic challenge. Nonetheless, the structure was studied using both laboratory source and synchrotron X-ray radiation.[351,352] These studies showed that the material undergoes a phase transition from an orthorhombic structure (*Pnma* space group) to a hexagonal structure at high temperature ($P6_3mc$ space group). The synchrotron X-ray derived structure displays very large thermal ellipsoids for the H ions about the molecular C_3 axis, parallel with the crystallographic *c*-axis. However, the structures derived from the X-ray studies have a wide range of bond lengths and angles that are likely nonphysical. The structures show highly distorted $[BH_4]^-$ tetrahedra with B–H bonds ranging from 1.04(2) Å to 1.28(1) Å and a similarly broad range of distorted H–B–H angles. Later, full isotopic labeling with ^7Li and ^{11}B (neutron absorption

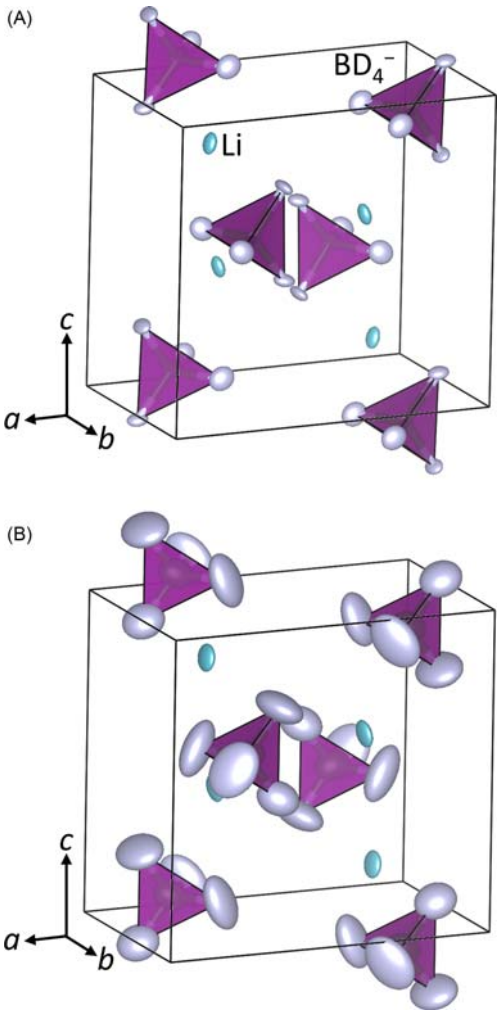

Fig. 9 The structure of $^7Li^{11}BD_4$ at 3.5 K (A) and 360 K (B) as elucidated by PND experiments. The refined thermal ellipsoids are shown with 80% probability. Purple, gray, and blue ellipsoids represent B, D, and Li atoms, respectively. Adapted from Hartman, M. R.; Rush, J. J.; Udovic, T. J.; Bowman Jr, R. C.; Hwang, S.-J. Structure and Vibrational Dynamics of Isotopically Labeled Lithium Borohydride Using Neutron Diffraction and Spectroscopy. *J. Solid State Chem.* **2007**, *180* (4), 1298–1305.

cross sections of $\approx 4.5 \times 10^{-2}$ and $\approx 5.5 \times 10^{-3}$ barn, respectively) along with partial isotopic labeling with D enabled a joint PND and INS study of both the low- and high-temperature phases.[353] The low temperature structure derived from the PND experiments displayed significantly less distorted $[BH_4]^-$ tetrahedra with B–H bond lengths of 1.226(5) Å and H–B–H angles ranging from 107.2(3)° to 111.7(3)° (Fig. 9). These values agree well with those from structures derived from PND experiments on related alkali borohydrides, MBD_4 (M = Na, K, Rb, Cs), and were corroborated in subsequent studies.[354,355] At higher temperatures, the B–D bond length and the size of the thermal ellipsoids increase significantly. The B–D bond is 1.3(1) Å in length and the thermal displacement ellipsoids for the D atoms are quite large in the high-temperature $P6_3mc$ phase.

The large thermal ellipsoids observed in both the X-ray and the neutron studies suggested dynamical reorientational motion for the $[BH_4]^-$ anions (Fig. 9). The dynamic motion was investigated through a series of QENS studies at various temperatures, both on pure $LiBH_4$ and on mixed systems like $LiBH_4$–LiI. [356–362] At low temperatures in the orthorhombic phase, the BH_4^- anions reorient predominantly by three-fold (120°) jumps of three of the four H atoms about a particular anion C_3 symmetry axis with indications that the fourth H atom increasingly participates in the anion reorientations as the orthorhombic-hexagonal phase transition is approached. At higher temperatures in the hexagonal phase, the reorientational mobility increases dramatically. In this phase, the anions predominantly undergo facile and delocalized reorientations around the $[BH_4]^-$ C_3 axis parallel with the crystallographic c-axis together with much slower jump exchanges of these three H atoms with the remaining apical H atom.

In addition to ongoing studies on $LiBH_4$, there are many other borohydride systems under investigation.[354,363–369] Notable among these are $Mg(BH_4)_2$ and $Ca(BH_4)_2$, which display gravimetric capacities of 14.9 theoretical mass % H_2 and 11.5 theoretical mass % H_2, respectively.[370–373] More importantly, some degree of reversible hydriding/dehydriding has been demonstrated at moderate conditions for these materials.[374,375] Both $Mg(BH_4)_2$ and $Ca(BH_4)_2$ have several polymorphic phases. For example, there are seven polymorphs for $Mg(BH_4)_2$: the α-, β-, β′-, γ-, δ-, ε-, and ζ-phases.[311,347] Due to the similar ground state energies for the polymorphs, computational studies of $Mg(BH_4)_2$ are difficult. In addition, diffraction experiments are challenging due to the X-ray and neutron absorption and scattering cross sections involved. As a result, some of the structures were debated. At ambient pressure, the polymorphs crystallize in the $P6_122$ (α-phase), $Fddd$ (β-phase), $Ia\bar{3}d$ (γ-phase), $P4_2nm$ (δ-phase), and $P3_112$ (ζ-phase) space groups, respectively.[376–382] The β′- and ε-phases have been observed via synchrotron PXRD measurements, but the space groups for these phases remain unidentified.[383,384] The thermal decomposition pathway to evolve hydrogen from $Mg(BH_4)_2$ is complicated and polymorph dependent.[302] Often, the decomposition ends with the evolution of poisonous diborane gas, which renders the system boron-deficient and which strongly hinders reversibility. Understanding the evolution of the structure and the resulting thermal decomposition pathways for each polymorph remains as an important goal today.

The structure of unsolvated α-$Mg(BH_4)_2$ was studied using SCXRD, PXRD, and PND experiments.[381,385,386] Perhaps unsurprisingly, these diffraction studies reveal a complicated crystal structure. Four distinct $[BH_4]^-$ anions coordinate each Mg cation along

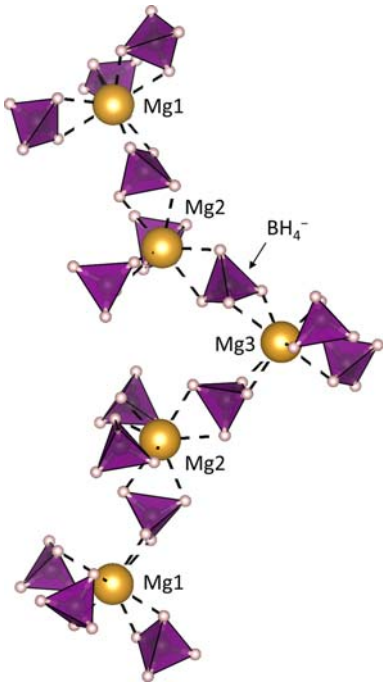

Fig. 10 The coordination spheres for the Mg ions in $Mg(BH_4)_2$ are shown as derived from Rietveld refinements of synchrotron PXRD data. The gold, purple, and gray spheres depict Mg, B, and H atoms, respectively. The positions of the H atoms are idealized. Adapted from Filinchuk, Y.; Cerny, R.; Hagemann, H. Insight Into $Mg(BH_4)_2$ With Synchrotron X-Ray Diffraction: Structure Revision, Crystal Chemistry, and Anomalous Thermal Expansion. *Chem. Mater.* **2009**, *21* (5), 925–933.

the H–H edge of the $[BH_4]^-$ tetrahedra. This creates an eightfold coordination environment for the Mg ions which have a slightly distorted snub disphenoid geometry. Due to the edge-on coordination, Mg-$[BH_4]$-Mg chains run through the structure. These chains are not linear; Mg–B–Mg angles range from 148° to 170°. Lastly, the α-polymorph displays five-membered rings of $[Mg\text{-}BH_2]_5$ units. The Mg–B–Mg chains are common to the crystallographically characterized polymorphs of $Mg(BH_4)_2$ (**Fig. 10**). Some of the other polymorphs have been characterized using powder X-ray and neutron diffraction experiments.[387] Interestingly, the γ-polymorph is porous, and some of the polymorphs display anomalous thermal expansion. The anomalous thermal expansion hints at complex dynamic motion of the anions. This dynamical motion of the ions in $Mg(BH_4)_2$ was studied as a function of temperature using a suite of techniques, including QENS, on the α-, β-, and γ-polymorphs.[388–391] The QENS studies showed that the anions move via jump rotations about the Mg–B–Mg C_2 axis and about the $[BH_4]$ C_3 axis on different time scales. Yet, the temperature dependence for these activated motions are quite different for the different polymorphs, which may correlate the observed differences in phase stability with temperature. Similarly, a recent combined INS and DFT study showed that the $Mg(BH_4)_2$ polymorphs display distinct phonon densities of states.[392]

The structure and dynamics of $Ca(BH_4)_2$ were also probed using neutron techniques. $Ca(BH_4)_2$ has four polymorphs. These are denoted as the α-, α′-, β-, and γ-phases of the material, and they crystallize in the *F2dd*, $I\bar{4}2d$, $P\bar{4}$, and *Pbca* space groups, respectively.[393–397] Each polymorph displays distorted octahedral coordination of the Ca ion by six $[BH_4]^-$ anions. In β-$Ca(BH_4)_2$, jump reorientations about $[BH_4]^-$ C_2 and C_3 axes were detected using QENS measurements coupled with DFT calculations.[398] Similar to the results found for the $Mg(BH_4)_2$ polymorphs, INS measurements found that differences in the vibrational density of states may help explain differences in thermal stability of the $Ca(BH_4)_2$ polymorphs.[399,400]

The third class of complex hydride materials by anion are the amides and imides.[401] These materials store hydrogen covalently bound to a nitrogen atom in the anion. Like the alanates and borohydrides, these materials usually have inorganic cations, and they can have high gravimetric capacities. For example, the Li–N–H system stores a theoretical 10.4 mass % H_2.[402] Note that, to achieve the full theoretical yield of hydrogen, temperatures near 590 K are required. Practically, the set of reversible reactions at more tractable temperatures have a total gravimetric capacity of ≈ 5.5 mass % H_2. The chemistry of the Li–N–H system is rich, and some of the crystalline species therein have been investigated via X-ray and neutron diffraction experiments.[403–406] PND measurements showed that Li_2NH crystallizes in the anti-fluorite structure type ($F\bar{4}3m$ space group).[407] The structure of the amide was also solved using powder X-ray and neutron diffraction experiments.[408–411] $LiNH_2$ crystallizes in the tetragonal space group $I\bar{4}$, and features covalent bonding (in the NH_2^- anion) and ionic bonding with the metal ion to form the salt. In addition, in situ neutron diffraction experiments played a significant role in determining the reaction pathways in the Li–N–H system under different conditions.[412–414] Similarly, the structure and chemistry of many other amide and imide systems have been investigated using PND measurements.[415–423] Yet, the evolution of ammonia gas as a side product hinders reversibility in these systems and the temperatures to liberate hydrogen gas remain undesirably high for vehicular applications.

To destabilize the monometallic metal amide systems and suppress ammonia production, mixed cation systems have been investigated. Of these, materials in the Li–Mg–N–H and Li–Ca–N–H systems show promise as candidate hydrogen storage materials. The Li–Mg–N–H system has a gravimetric capacity of 5.6 mass % H_2 and a suppressed operational temperature of ≈ 420 K. Here, again, PND experiments were invaluable in determining the hydrogen evolution reaction pathways and the structure of key intermediate species. The structure of $Li_2Mg(NH)_2$ was determined by a joint powder X-ray and neutron diffraction study.[424,425] The compound has three polymorphs as a function of temperature: α-, β, and γ-$Li_2Mg(NH)_2$. Because Li^+ and Mg^{2+} have similar ionic radii, the unit cell of α-$Li_2Mg(NH)_2$ resembles a supercell of the cubic phase of the parent compound, $Li_2(NH)$, with ordered cation substitutions.[426] In the Li–Ca–N–H system, $Li_2Ca(NH)_2$ crystalizes in the $P\bar{3}m1$ space group. Due to the larger ionic radius of Ca^{2+}, the structure of $Li_2Ca(NH)_2$ is significantly different from that of the Mg congener or the parent imide.[427,428] Instead, $Li_2Ca(NH)_2$ comprises $Ca[NH]_6$ octahedra and $Li[NH]_4$ tetrahedra. These polyhedra are reminiscent of those in the Ca(NH) and Li_2NH structures, such that the structure of $Li_2Ca(NH)_2$ can be described as a combination of these two parent materials. The hydrogenation (dehydrogenation) reaction mechanism was in part elucidated through these detailed PND experiments. The suppressed operational temperature is attributed to an increased H^- mobility in the bimetallic material compared to the pure imide.

Today, the main detriments precluding the complex hydrides from breaking into the HFCEV market as hydrogen storage materials are the thermodynamic stability of the hydrides with high operating temperatures and the slow kinetics of the hydriding and dehydriding processes. A fundamental understanding of structure and molecular dynamics in the complex hydrides is required before these materials can be rationally designed to operate at lower temperatures. PND and neutron spectroscopy experiments have greatly augmented our understanding of the structure and dynamics in these systems. Based on the results of these experiments, researchers developed several methods for destabilizing the alanates, borohydrides, and amides. These include the development of hybrid materials, the use of additives like coordinating solvents, and techniques such as nanoscaffolding.

One exemplary hybrid materials system is the B–N–H family.[429] In this family, ammonia borane boasts a gravimetric capacity of 19.6 mass % H_2 accessible at operational temperatures between 350 and 410 K.[430–432] The structure, reaction pathway, and dynamic molecular motion have been studied using neutron techniques.[433–438] The structure of NH_3BH_3 was elucidated using PND experiments, after some debate in the literature (**Fig. 11**).[439] This study shed light on a new bonding motif known as dihydrogen bonding.[440] Dihydrogen bonds comprise hydrogen bond acceptors and donors, but here both may be H atoms. Generally, the dihydrogen bond arises from electrostatic attraction between a proton and a hydride ion. The dihydrogen bond leads to close H⋯H contacts of *ca.* 1.7–2.2 Å, which can be much shorter than the Switendick criterion for hydrides in solid state metal hydrides. In the case of NH_3BH_3, the δ^+ nitrogen-bound hydrogen is the hydrogen bond donor and the δ^- B–H σ-bond acts as the hydrogen

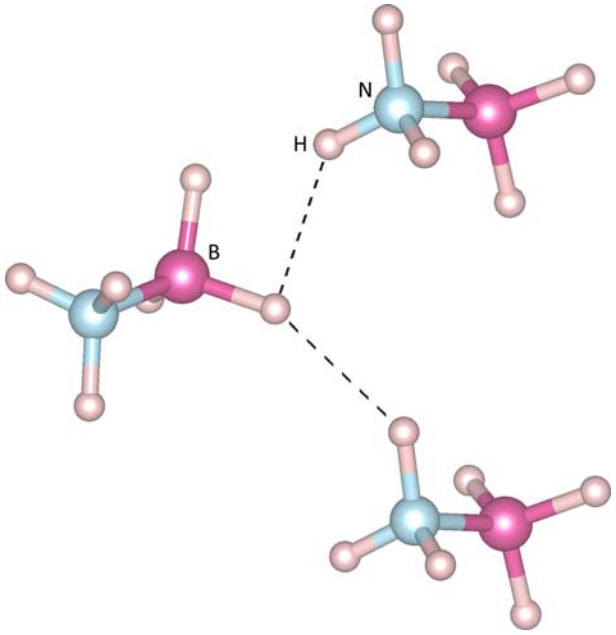

Fig. 11 The dihydrogen bonding interaction is highlighted between neighboring NH_3BH_3 molecules. This structure was derived from Rietveld refinements of PND data. Adapted from Klooster, W. T.; Koetzle, T. F.; Siegbahn, P. E.; Richardson, T. B.; Crabtree, R. H. Study of the N-H···H-B Dihydrogen Bond Including the Crystal Structure of BH_3NH_3 by Neutron Diffraction. *J. Am. Chem. Soc.* **1999**, *121* (27), 6337–6343.

bond acceptor. The H···H contact is ≈ 2.0 Å with a non-linear N–H···H angle of ≈ 156° and a bent B–H···H angle of ≈ 106°. The presence of a strong dihydrogen bond network leads to a melting point for NH_3BH_3 that is ≈ 280 K higher than that of isoelectronic ethane and ≈ 240 K higher than that of polar CH_3F. In a later study, it was shown that confining NH_3BH_3 within mesoporous silica destabilizes the material and lowers the operating temperature significantly compared to the bulk material.[441] A subsequent QENS study showed that the suppressed operational temperature may in part arise from a decrease in the activation energy barrier for proton mobility in the nanoscaffolded material.[442] In addition to its high operational temperature, one unfortunate issue with ammonia borane is that it produces borazine upon thermal decomposition, which is toxic to fuel cell catalysts.

Also in the B–N–H family of compounds is ammonium borohydride. Ammonium borohydride suffers from the opposite issue of ammonia borane—the salt is unstable at low temperature. NH_4BH_4 has a gravimetric capacity of 24.5 mass % H_2, a volumetric capacity of 157 g H_2 L^{-1}, and, unfortunately, undergoes thermolysis at ≈ 230 K.[443] Neutron studies of this material help develop the necessary fundamental understanding required to improve the operational temperature.[444] A recent QENS paper highlighted the dynamic interaction between the $[NH_4]^+$ and the $[BH_4]^-$ ions. The cations reorient via a tetrahedral tumbling mechanism at low and moderate temperatures, and then potentially via cubic or isotropic mechanisms at higher temperatures. The anions are relatively static at low temperatures compared to the cations and then reorient via a cubic tumbling mechanism at moderate temperatures. Interestingly, the timescale for the cation reorientations is rapid compared to the anion reorientations, such that the $[BH_4]^-$ polyhedra appear motionless in the $[NH_4]^+$ frame of reference. As such, the anions play a large role in orienting the cations.

In addition to materials in the B–N–H group, *M*-B–N–H quaternary and higher order mixed-metal and mixed-anion systems have been investigated as candidate hydrogen storage materials.[445–452] These systems simultaneously display lowered operational temperatures and suppressed off gassing of byproducts that poison fuel cell catalysts. Li–B–N–H system shows depressed ammonia off-gassing and a theoretical gravimetric capacity of 11.9 mass % H_2. At least four distinct crystalline intermediates have been observed in this family.[453] Yet the crystal structure for these intermediates have been difficult to solve due to the neutron and X-ray scattering cross sections of natural Li, B, and H. Isotopic labeling enabled the structural elucidation of $Li[BH_4]_x[NH_2]_{1-x}$ ($x = 0$, 0.25, 0.5, 1) using PND and INS measurements.[454] All four structures comprise $\{Li[BH_4^-]_n[NH_2^-]_{4-n}\}$ building blocks. The compounds Li_2BNH_6 and $Li_4BN_3H_{10}$ can be described as solid solutions in which $[BH_4]^-$ tetrahedra are gradually substituted with $[NH_2]^-$ anions, moving between the two end members. Together with the end members, these structures provide insight into the potential mechanism of formation for these compounds, and possible clues as to the structure and stoichiometry of the intermediates that have yet to be fully characterized.

The two key issues which plague ammonia borane, namely the high dehydrogenation temperatures and the evolution of toxic byproducts, are ameliorated in certain classes of nitrogen and boron containing species. One such class of materials is the metal amidoboranes, which show enhanced dehydrogenation properties while at the same time demonstrating suppressed borazine off-gassing.[455,456] $Li(NH_2BH_3)$ and $Na(NH_2BH_3)$ were shown to release ≈ 10.9 mass % and ≈ 7.5 mass % H_2 at ≈ 90 °C with minimal borazine emission.[457] These materials, along with $Ca(NH_2BH_3)\cdot THF$ (THF = tetrahydrofuran), were structurally characterized using PXRD measurements augmented by accompanying DFT calculations (**Fig. 12**).[445,450] These studies suggested that the

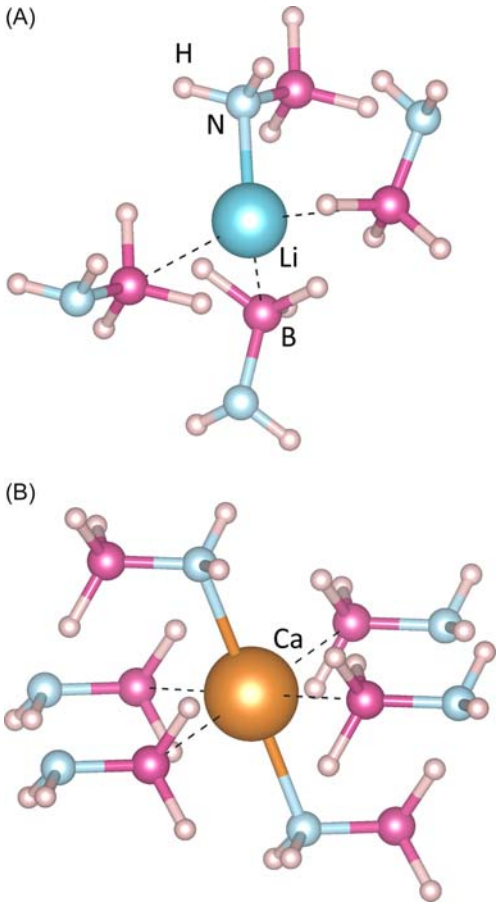

Fig. 12 The crystal structures of (A) $Li(NH_2BH_3)$ and (B) $Ca(NH_2BH_3)_2$ as derived from Rietveld refinements of PXRD patterns. Adapted from Wu, H.; Zhou, W.; Yildirim, T. Alkali and Alkaline-Earth Metal Amidoboranes: Structure, Crystal Chemistry, and Hydrogen Storage Properties. *J. Am. Chem. Soc.* **2008**, *130* (44), 14834–14839.

change in the electronic structure from neutral NH_3BH_3 moiety to $[NH_2BH_3]^-$ anion leads to an increased polarization of the protonic and hydridic ions in the amidoboranes. The resulting increased propensity for the $N–H^{\delta+}\cdots H^{\delta-}–B$ interaction to produce H_2 gas upon decomposition in turn explains the decrease in dehydrogenation temperature. Later, INS measurements further shed light on the nature of the ionic interactions and on the thermal decomposition of $Li(NH_2BH_3)$.[458] Efforts to synthetically tune the electrostatic balance between the $H^{\delta+}$ and $H^{\delta-}$ have included substituting and mixing the cations in the amidoboranes, and experimenting with additives such as solvents, ammonia, and ammonia borane.[306] Some additional classes of promising candidate hydrogen storage materials are the metal borohydride ammonia boranes,[459] the metal amidoborane hydrazinates,[460] and the metal hydrazinoboranes.[461] These three classes of materials show promise for hydrogen storage applications due to their depressed thermal dehydrogenation temperatures and their suppressed emission of toxic byproducts like ammonia, hydrazine, or borazine. Yet, these materials sometimes suffer from irreversibility and they are difficult to study using diffraction techniques due to the component atomic scattering cross sections.

10.02.4.3 Engineering efforts and outlook

As shown for the metal amidoboranes, the hydriding and dehydriding properties of certain alanates, borohydrides, and imides/amides can be improved by the addition of a Lewis basic coordinating solvent to the system.[462] These include, for example, ethylenediamine, ammonia, water, or THF. A recent neutron study investigated the molecular dynamics in $Mg(BH_4)_2\cdot(THF)_3$ using PND, QENS, and INS measurements coupled with DFT calculations.[463] This study demonstrated that low concentrations of THF led to a relatively strong Mg-THF interaction, which the authors posit may be beneficial for destabilizing the borohydride. Other examples of solvated complex hydrides studied using neutron techniques include THF-solvated ammonia borane and water-solvated sodium borohydride.[366,464]

Lastly, particle size control (e.g., nanoconfinement) has been demonstrated as an efficient route to tune certain hydriding and dehydriding properties.[305,465] Nanoconfinement improves the kinetics of charging and discharging by shortening the diffusion pathways. Moreover, the particle surface-gas interactions are affected as well as the solid-solid phase boundaries inside the

particles.[466,467] As the nanoparticle absorbs H_2 gas, the chemical species change as a function of depth and time, leading to nano-interfaces within the particles. This can destabilize and eliminate certain intermediate species from the phase diagram. In the case of nanoconfined Li–N–H, nanoscaffolding Li_3N in nano-porous carbon yields two immediate changes upon hydriding and dehydriding.[468] The first is that the Li_2NH and α-Li_3N phases are destabilized and not observed under conditions that generate these phases in the bulk. In their place, metastable β-Li_3N is observed in the particles. Second, the kinetics of hydriding the particles is greatly enhanced and becomes reversible at much milder conditions. The improved kinetics and emerging reversibility arise from the direct conversion of $LiNH_2$ and LiH to β-Li_3N and H_2 gas. This reaction is only possible when the more stable intermediates have been squeezed out of the phase diagram due to nanoconfinement. Nanoconfinement is a highly tunable method for engineering hydriding properties; the nanoconfined material, particle size, and the scaffolding material can all be adjusted and optimized. Today, numerous complex hydrides have been reinvestigated upon nanoconfinement, including $LiBH_4$, $NaBH_4$, $LiAlH_4$, $Li_3BN_2H_8$, and many others.[469–473]

The complex hydrides possess extremely high gravimetric and volumetric hydrogen storage capacities thanks to their light constituent elements and high hydrogen content. The field of complex hydrides as candidate hydrogen storage materials was reinvigorated by the discovery of reversible hydriding behavior in $NaAlH_4$. Since then, great progress has been made in developing these materials and in combating their sub-optimal kinetics, reversibility, and operating temperatures. A deep fundamental understanding of complex hydride chemistry is required to rationally design and engineer new systems that overcome these barriers and simultaneously satisfy all the DOE hydrogen storage material requirements. This includes understanding the structure of the complex hydrides, their thermolysis reaction pathways, the mechanism for hydrogen evolution and reversibility, the ion dynamics as a function of temperature, and the nature of chemical bonding in these systems. Neutron diffraction and scattering techniques have been invaluable in developing our current understanding of the complex hydrides, and they remain integral tools to the research community today.

10.02.5 Porous materials

The two classes of hydrogen storage materials discussed so far, metal hydrides and chemical hydrides, store the gas as hydridic ions. In this section, we discuss a third class of promising materials: porous compounds. These materials adsorb molecular hydrogen gas allowing for rapid and reversible adsorption and desorption properties. Porous materials such as high-surface area allotropes of carbon, zeolites, clathrates, metal-organic frameworks, covalent-organic frameworks, and porous polymers all adsorb hydrogen gas. As with metal and chemical hydrides, research in the field of porous materials for hydrogen storage applications aims to generate materials which satisfy and exceed the EERE criteria for gravimetric and volumetric storage capacities. Neutron scattering studies reveal the underlying chemistry and physics of adsorption in these systems and deliver valuable microscopic insight into the hydrogen storage properties of these compounds. The results of these studies are often used to update the existing design criteria for compounds that may meet the EERE standards. In this section, we highlight the unique way in which PND, INS, and QENS methods have advanced our knowledge of hydrogen storage in candidate porous materials. We begin this section with a brief discussion of the chemistry of adsorption. Then we discuss hydrogen adsorption in amorphous carbons, zeolites, and clathrates, followed by a discussion of hydrogen storage in metal-organic frameworks. We conclude this section, and the chapter, with an outlook on the future of the field of hydrogen storage materials.

The chemical process of adsorption is distinct from that of chemisorption. Adsorption of H_2 molecules onto solid surfaces typically occurs through weak van der Waals interactions with differential enthalpies of adsorption (ΔH_{ads}) close to -5 kJ/mol. As a result, significant hydrogen uptake in adsorbents can often only be achieved at cryogenic temperatures. Initial work in this field focused on improving hydrogen uptake by systematically increasing the internal surface area and pore volume in porous materials.[474–477] From these studies, several empirical rules were developed which relate the hydrogen storage capacity to pore volume, surface area, pore-size distribution, the operating temperature, and theoretical enthalpy of adsorption in porous materials. The enthalpy of adsorption values thought to yield optimal hydrogen storage capacities at room temperature range between -15 and -20 kJ/mol.[478] Hydrogen enthalpies of adsorption in this range indicate solid-gas interactions of insufficient strength to break the dihydrogen chemical bond, but strong enough to allow for reversible adsorption and desorption at room temperature. Several strategies have been developed to increase the enthalpy of adsorption from the relatively low values generated by individual van der Waals interactions into this optimal range. An example of a strategy to increase the enthalpy of adsorption—and therefore the hydrogen storage capacities at technology-relevant operating conditions—is to include stronger adsorption sites in the solid like coordinatively-unsaturated Lewis acidic cations.[57,479–482] The inclusion of Lewis acidic cations leads to much higher enthalpies of adsorption compared to those that arise from individual van der Waals interactions alone. As will be shown below, neutron scattering techniques were instrumental in illuminating the underlying mechanism that leads to this increased enthalpy of adsorption. On the other end of the hydrogen sorption spectrum, the enthalpy of sorption is very large—*ca.* -40 kJ/mol and above—for the direct chemical bonds observed in the Kubas complex and similar organometallic species.[26] Today, an open question in the field remains as to whether there is a continuously accessible range of enthalpies up to -40 kJ/mol that bridges between hydrogen physisorption and Kubas-type complexation.

The study of hydrogen storage in porous materials began in the late 20th and early 21st century. The push to incorporate lighter and lighter elements in candidate hydrogen storage materials, stemming from work in the metal hydrides and then in the chemical hydrides, led researchers to amorphous porous carbon allotropes[483–489] and the carbon aerogels.[490–495] Activated carbon aerogels

are attractive materials for gas storage applications because they can be highly porous and comprise light constituent elements. One study of activated carbon aerogels found an internal surface area of up to 3200 m^2/g and a gravimetric capacity of up to 5 mass % H_2 at 77 K.[474] Similarly, amorphous carbon materials, such as the zeolite-templated carbons, have recently garnered interest as candidate hydrogen storage materials.[496–498] Yet, these materials are often intrinsically difficult to study using traditional diffraction measurements. While the aerogels and porous carbon allotropes were being investigated for their hydrogen storage properties, research efforts into porous, crystalline materials—such as zeolites, clathrates, and framework materials—erupted.

10.02.5.1 Zeolites and clathrates

Zeolites were among the first adsorbents examined for their hydrogen storage capabilities. Zeolites are porous compounds comprising corner sharing SiO_4 and AlO_4 tetrahedra. Also known as molecular sieves, zeolites today are commercially relevant for catalysis, adsorption, and ion exchange applications.[499,500] The pores can be emptied via a process called activation and can contain additional cations and/or small molecules. In the early 1990s, it was recognized that these porous compounds may be useful candidate hydrogen storage materials.[501] Neutron scattering techniques were quickly deployed to understand the chemistry and physics underlying the adsorption processes in these and related compounds.[502–505] PND experiments conducted on AlPO-5 showed that, at high-dosing concentrations of D_2, the gas molecules formed a lattice fluid-like structure without deforming the aluminophosphate framework. The resulting liquid-like structure had D_2 molecules localized and disordered within certain pores.[506] Typically a lattice-fluid structure has distinct crystallographic positions (solid-like) but contains disorder over these positions (liquid-like) representing molecular jumps between distinct crystallographic sites. Later, results from QENS experiments corroborated this finding, showing translational motion of HD molecules along the 1-D pores.[507] Similar dynamics studies on other zeolites, like zeolite 13X and zeolite A, also observed a liquid-like H_2 phase below 60 K.[508] Notably, the lattice-fluid like structure forms well above the condensation temperature at ambient pressure.[509] Some zeolites have stronger hydrogen molecule interactions, such as Fe-ZSM5 which can adsorb hydrogen at temperatures as high as 110 K.[510]

Clathrates also showed promise as candidate hydrogen storage materials.[511–519] Clathrates are porous, crystalline materials that can adsorb hydrogen via a host-guest interaction. Like zeolites and amorphous carbons, van der Waals interactions are the main driving forces for hydrogen adsorption in clathrates.[520] Interestingly, it was found that clathrates formed by very light small molecules encasing hydrogen molecules could be synthesized at high pressure and temperature conditions. Many such compounds were synthesized at high pressure, including the H_2–CH_4[521] and H_2–Ar[522] clathrates. Unfortunately, these materials are often metastable and are not recoverable to ambient conditions. In addition, high pressure studies generally require the use of very small sample sizes which hinders PND measurements. Nevertheless, successful in situ high pressure PND measurements were conducted on the D_2–D_2O deuterated clathrate hydrate.[523] Rietveld refinement analysis of the PND data revealed that the structure contains two types of deuterium gas-containing cages formed by hydrogen bonding of the water molecules: a larger hexadecahedral cage and a smaller dodecahedral cage. The larger cage can accommodate between two and four D_2 molecules at temperatures below 160 K while the smaller cage adsorbs a single equivalent of D_2 at these conditions. The distance between the four D_2 molecules in the large cage is 2.93(1) Å, and the occupancy of the D_2 molecules in the larger cage decreases with increasing temperature. Another in situ high pressure PND study structurally characterized the D_2–d_8-THF clathrate[524] which complemented earlier INS studies of this material.[525] More recently, hydrogen adsorbed in a β-hydroquinone clathrate was investigated using QENS and INS measurements at ambient pressure.[526] These high-resolution measurements observed distinct excitations in the INS spectra, possibly indicating large energy barriers for rotation for localized hydrogen molecules in the clathrate. The INS excitations were strong enough to assign distinct rotational and translational excitations for both the *ortho* and *para* hydrogen states.

The neutron scattering studies on zeolites and clathrates invigorated the scientific community and revealed the promise of using porous, crystalline compounds as candidate hydrogen storage materials.[527–541] New materials, namely metal-organic frameworks, came into focus in the mid and late 1990s. These materials immediately attracted intense interest as candidate hydrogen storage materials. Once again, neutron scattering techniques were instrumental in understanding the underlying chemistry and physics of hydrogen adsorption in these materials.

10.02.5.2 Metal-organic frameworks

Metal-organic frameworks (MOFs) are porous compounds comprising organic linkers and metal nodes.[542] MOFs have a multitude of applications but are best known for pursuits where their high porosity is effectively leveraged, including gas adsorption and small molecule separations. Because the frameworks are often rigid and crystalline, neutron diffraction studies are extremely useful for elucidating the nature of H_2 adsorption in MOFs.[543–546] The location of H_2 adsorption in the frameworks is critically important information in the synthetic design feedback loop. Knowledge of the adsorption positions coupled with the chemical information derived from INS and QENS measurements reveals the underlying mechanism of hydrogen adsorption in these porous materials. This detailed understanding of the hydrogen adsorption chemistry enables the rational design of the next generation of adsorbent materials. As will be shown in the following sections, this precise chemical knowledge curated from neutron scattering experiments guided the evolution of the field of hydrogen adsorption in MOFs.

The prototypical MOF may well be IRMOF-1 [MOF-5; $Zn_4O(bdc)_3$ bdc = 1,4-benzenedicarboxylate].[547,548] The structure of IRMOF-1 consists of a cubic array of Zn_4O clusters connected by phenylenecarboxylate linkers crystallizing in a ReO_3-type structure (Fig. 13).[549] IRMOF-1 was one of the first MOFs studied for gas adsorption, as it contained both larger pores volumes

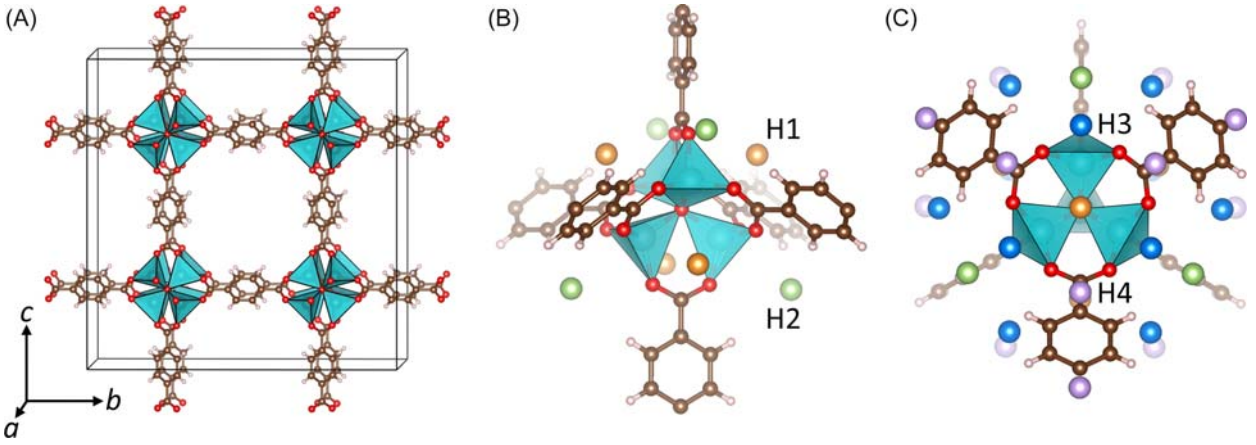

Fig. 13 The crystal structure of activated MOF-5 structure was derived from Rietveld refinements of powder neutron diffraction data (A). Rietveld refinements of powder patterns for the gas-dosed material reveal the primary adsorption sites for D_2 (H1, deemed the "cup site," orange; H2, called the "ZnO_3 site," green). Higher order sites, H3 and H4, are shown around the cluster and organic ligands when the structure is fully saturated with D_2 gas (C) (H3, the "ZnO_2 site," blue; H4, the so-called "hex site," purple). Here, the brown, red, and light blue spheres represent carbon, oxygen, and zinc atoms, respectively. The remaining colored spheres represent D_2 molecules. Adapted from Yildirim, T.; Hartman, M. Direct Observation of Hydrogen Adsorption Sites and Nanocage Formation in Metal-Organic Frameworks. *Phys. Rev. Lett.* **2005**, *95* (21), 215504.

(0.54–0.61 cm^3/cm^3) and a larger surface area (2900 m^2/g) compared to zeolites.[545] In order to examine possible adsorption sites, initial SCXRD studies were conducted dosing with Ar. Eight Ar adsorption sites were identified: three sites associated with the Zn_4O cluster, two with the phenyl ring, and three in the pores in a fluid-like structure reminiscent of those observed in zeolites.[550] Once these initial possible adsorption sites were identified, the location and underlying adsorption chemistry of hydrogen in IRMOF-1 was probed using SCND and INS measurements. Initial INS measurements of the hydrogen gas dosed IRMOF-1 revealed two possible adsorption sites: at the Zn-cluster and on the linker.[479] A subsequent study re-analyzed the INS data and proposed that both the hydrogen gas absorption is associated with the $(CO_2)_3$ "cup" sites, with edges of the ZnO_4 tetrahedron (the "ZnO_2 site"), and with the phenyl ring (the "C_6 site").[551] The location of the ZnO_4 tetrahedron adsorption site was clarified by a SCND study of D_2 adsorption in IRMOF-1. The authors modeled the second D_2 adsorption site over the face of the ZnO_4 tetrahedron at the ZnO_3 site, which contradicted the proposed site from the INS studies.[552]

Subsequent PND measurements on the D_2-dosed perdeuterated MOF-5 illuminated the location of ZnO_4 tetrahedron adsorption sites (Fig. 13B and C).[553] The structure derived from Rietveld refinement of the powder data showed that the ZnO_4 cluster adsorbs several equivalents of hydrogen and that there is some minor adsorption occurring via van der Waals interactions at the organic linkers. The primary adsorption cup site is formed by the $(CO_2)_3$ adsorption pocket while secondary adsorption occurs at the ZnO_3 site. With additional gas dosing, two additional sites populate equally: the ZnO_2 and C_6 positions. When these four sites are full the gravimetric capacity for IRMOF-1 is 6.8 mass % H_2. When these primary adsorption sites are saturated, the porous material can still adsorb additional equivalents of H_2 gas in the pores through a fluid-like mechanism like that of the zeolites. The MOF-5 lattice has enough space to hold H_2 gas molecules up to a gravimetric capacity of 11 mass % at cryogenic temperatures by forming a D_2 "nanocage" with D_2 intermolecular contacts of about 3 Å—much shorter than those found in solid H_2 ($\approx$ 3.6 Å).[29] PND studies of hydrogen adsorption in other MOFs also observed this D_2 liquid-like nanostructure in the pores.[554] Similar close associations of H_2 to coordinatively available metal ions were seen for the dobdc system [CPO-27; $Zn_2(dobdc)_2$ dobdc = 2,5-dioxido-1,4-benzenedicarboxylate], as well as an increased packing density relative to liquid/solid H_2.[555] From these careful gas-dosing studies, it was shown that the strongest adsorption sites usually fills before the secondary sites.[556,557]

These above conclusions were drawn mostly from PND results. But it is interesting to compare how the single-crystal and powder diffraction data were analyzed in determining the characteristics of the adsorbed D_2 species. The neutron single crystal work and SCXRD data taken on another MOF (CPL-1; $Cu_2(pzdc)_2(pyz)$ pzdc = pyrazine-2,3-dicarboxylate, pyz = pyrazine) were modeled with an H_2 dimer.[558] In yet another SCXRD study the residual electron density was directly attributed to the ordered H_2 molecule.[559] This view of H_2 as a classical molecule is incompatible with quantum mechanics.[86] The quantum rotating nature of the diatomic species is clearly evidenced by the rotational transitions observed in INS measurements. The rotational lines for adsorbed H_2 occur at energies distinct from that of a free rotor, indicating hindered rotating molecules.[504] As performed in the analysis of the PND patterns, and subsequently rationalized in greater detail,[560] the D_2 molecules are hence treated as point scatterers with double occupancy and large thermal parameters to account for the rotation and vibration of the molecule. This is the so-called "super-atom" approach.

The relative importance of the H_2-ligand interactions were further illustrated by a study by Yildirim, Wu and Zhou, who utilized PND measurements at 3.5 K to locate the adsorption sites in the zeolitic imidazolate framework Zn(methylimidazolate)$_2$, ZIF-8 (Fig. 1).[59] The authors used a super-atom approach to model the D_2 molecules that were quantified through Rietveld refinement analysis. Here, the primary D_2 adsorption site was located closest to the imidazolate linker—unlike the case of the D_2 binding near

the metal-oxo cluster in MOF-5. The stability of this ligand-adjacent site was borne out by density functional theory (DFT) calculations using the plane-wave implementation of the local-density approximation, where binding energies for the first two sites are −16.4 and −14.2 kJ/mol, respectively, resulting in only a 2.2 kJ/mol difference in the binding energies. At dosing concentrations approaching D_2 saturation, the authors located six different D_2 adsorption sites that formed a nanocage like that observed for MOF-5, with short nearest-neighbor distances of only ≈3.04 Å, again supporting better H_2 storage and packing efficiency in MOFs compared to simply pressurizing H_2 gas.

The PND studies described thus far revealed D_2 adsorption sites of moderate strength arising from framework-adsorbate and adsorbate-adsorbate interactions. Generally, these interactions are insufficient to result in an optimum enthalpy of adsorption. Hence, new material design criteria were needed to synthetically tune the enthalpy of adsorption into the optimal range between −15 and −20 kJ/mol. One new design criterion inspired by these initial diffraction studies is that the enthalpy of adsorption can be increased by combining multiple additive weak interactions. In practice, this means synthesizing materials with smaller pores which fit the kinetic diameter of the gas molecule, or by creating new flexible frameworks that conform to size-match with the gas molecules.

10.02.5.2.1 Enhanced physisorption using small pores and flexible MOFs

There are a few notable examples of neutron studies on MOFs which leverage smaller pores and flexible MOFs in which enhanced enthalpies of adsorption were realized. For example, PND measurements on the rare earth material Y(btc) (btc = 1,3,5-benzenetricarboxylate) illustrated the differences in enthalpies of adsorption associated with differing pore sizes.[561] Fourier difference map analysis followed by subsequent Rietveld refinement analysis of the powder data indicated four different D_2 adsorption sites. While the Y^{3+} is pseudo-octahedrally coordinated by the btc linkers, the ion is sufficiently large that it can accommodate larger coordination numbers. This is the case when the MOF is hydrated, which suggests that possible primary gas adsorption may occur at the Lewis acidic metal ions. It was somewhat surprising then that the first adsorption site is near the btc linkers instead of at the metal polyhedra. In Y(btc), the four adsorption sites are within van der Waals distances to the framework instead of adsorbing at the metal center. The observed −7.3 kJ/mol enthalpy of adsorption arises from the sum of these van der Waals interactions. These results suggested that an optimal pore size of ≈6 Å strengthens the gas-framework interaction beyond what is possible for individual van der Waals contacts.

Another MOF which attempted to increase $|\Delta H_{ads}|$ by utilizing small pores and open metal sites is Zn(trz)(tftph), which has Zn^{2+} ions coordinated by 1,2,4-triazole (trz) and tetrafluoroterephthalate (tftph) ligands.[562] The experimental H_2 isosteric enthalpy of adsorption value for this MOF is ≈−8.0 kJ/mol. INS spectra for this MOF show high energy barriers to H_2 rotation. The H_2 rotational excitations were observed at ≈5.4 meV, ≈6.2 meV, and ≈7.8 meV (corresponding to ≈44, ≈50, and ≈63, respectively) suggesting relatively strong H_2 adsorption. At low loadings (1.7 equivalents of H_2 gas per formula unit), the peak at 6.2 meV (≈50 cm^{-1}) is the most intense. At a higher loading concentration of 2.7 H_2 per formula unit, the 5.4 meV (≈44 cm^{-1}) peak intensity increases significantly and the peak at 6.2 meV (≈50 cm^{-1}) virtually disappears. This low-energy peak signifies a high rotational energy barrier for the physisorbed H_2 molecules. However, it should be noted that high energy barriers to rotation do not directly correlate with strong enthalpies of adsorption. From structural simulations based on these INS results, the primary sorption site in the MOF is a small volume where an H_2 molecule can simultaneously interact with an exposed fluorine atom from a tftph linker, a carboxylate group of another tftph linker, and a Zn-coordinated H_2O molecule. This work further supports the hypothesis that small pores with diameters tailored to the kinetic diameter of hydrogen lead to increased enthalpies of adsorption. Furthermore, this study provided evidence that, alongside small pores, fluorination may prove to be a useful materials design criterion for enhancing physisorption of H_2. Other small-pore materials that may be attractive candidate hydrogen storage materials include MIL-100 and MIL-101, as they are small-pore adsorbents.[563] These compounds adsorb large amounts of hydrogen at 77 K, with a gravimetric capacity of ≈6.1 mass % for MIL-101 and a high enthalpy of adsorption of ≈−10 kJ/mol at low hydrogen gas pressure. The higher observed enthalpy of adsorption appears to be a result H_2 confinement within the small pores, but neutron diffraction measurements are needed to test this hypothesis.

The small-pore approach is unfortunately ineffective by itself as a mechanism to drastically increase $|\Delta H_{ads}|$ while maximizing gravimetric capacities at realistic operational temperatures. One alternative is to use flexible materials that provide large pore sizes with optimized van der Waals adsorption pockets. These compounds undergo a reversible structural transition with temperature as shown by PND results.[564] This structural transition involves the collapsing (with decreasing temperature, T) and expanding (with increasing T) of the porous cavities within the crystal structure. These structural changes manifest in the gas-adsorption isotherm data as large, step-like jumps, resulting in Type *V* adsorption isotherms. The different regions in the isotherm data are sometimes described as the pre-step regime, in which the structure is typically collapsed, and the post-step regime, where the structure is typically expanded. The pre-step and post-step regimes correspond to discrete phases while the step itself denotes the pressure- or temperature-induced phase transition.

Notable examples of flexible candidate hydrogen storage materials are the MIL-53 compounds (*M*-1,4-benzenedicarboxylate, $M = Cr^{3+}$, Al^{3+}). These compounds undergo similar structural changes, or breathing modes, when exposed to polar solvents like H_2O,[565] or nonpolar compounds like alkanes.[566] Breathing modes were observed when hydrogen gas was adsorbed in Cr-MIL-53.[567] This MOF displays a gravimetric capacity of up to ≈5.5 mass % reversible hydrogen loading.[568] Though previously studied from a macroscopic viewpoint,[569] the microscopic nature of H_2 adsorption in Cr-MIL-53 was not well known. Similarly, the relationship between hydrogen adsorption and the breathing modes remained open to debate. PND and INS measurements revealed four different adsorption sites in Cr-MIL-53.[568] In the post-step phase, the primary adsorption site occurs

near the Cr–O clusters. The adsorption interactions near the Cr–O clusters are predominantly facilitated by the CO_2 moieties of adjacent linkers with the H_2 molecules. Secondary and tertiary sites were observed near the phenyl rings in the center of the pores, respectively. The step in the hydrogen adsorption isotherm is both temperature and pressure dependent. At temperatures above the boiling point of hydrogen, the breathing mode of the crystal structure is associated with the larger pore openings—a direct contrast for the structural changes observed during the breathing modes induced by H_2O uptake.[565] At even higher temperatures, due to the weak interaction between host structure and D_2, the structure only contracts slightly through the phase transition.

PND measurements were also used to examine D_2 uptake in Al(OH)(bdc) (Al-MIL-53) at 77 K.[570] Unlike Cr-MIL-53, Al-MIL-53 exhibits a completely closed-pore pre-step structure when activated. The framework expands to an open phase upon loading with D_2 at pressures above ≈ 2 bar up to a pressure of ≈ 10 bar (**Fig. 14**). The primary and secondary D_2 adsorption sites in Al-MIL-53 are in similar positions to those found in the Cr congener. Also similar to the Cr congener, evacuation of the pores by application of a vacuum and subsequent heating was incomplete. Some portion of D_2 was retained in the structure after the initial dose, even at temperatures above 100 K. Subsequent QENS measurements supported this conclusion and revealed far slower H_2 mobility in the pre-step, closed-pore phase compared to the post-step, open-pore phase. These results suggested that small amounts of H_2 are kinetically trapped within the framework in the pre-step regime.

Another flexible material shown to adsorb hydrogen is CAU-1 $[Al_4(OH)_2(OCH_3)_4(O_2C\text{-}C_6H_3NH_2\text{-}CO_2)_3]$ which reaches a gravimetric capacity of ≈ 4 mass % at 70 K. In a study utilizing PND measurements combined with DFT calculations and adsorption isotherm measurements, the authors describe how hydrogen sorption is facilitated by cooperative adsorbate–adsorbate interactions and associations between guest hydrogen molecules and organic linkers.[571] There are two types of microporous cages in the structure of CAU-1: the first is an ≈ 10 Å diameter octahedral cage and the second is an ≈ 5 Å diameter tetrahedral cage. Here, the large hydrogen adsorption arises from a hydrogen gas pressure-induced phase transition. Hydrogen adsorption onto the organic linkers induces a contraction of the host framework, which in turn alters the electronic potential surface locally inside the pores. This structural change further causes cooperative rearrangement of the molecules already adsorbed, helping facilitate additionally occupied positions and more hydrogen uptake.

Lastly, a uranium-based MOF, $U(bdc)_2$, was recently shown to achieve high hydrogen enthalpies of adsorption.[572] Within the measured pressure-temperature phase space, this material displays a Type I hydrogen adsorption isotherm indicative of a rigid crystalline framework. Thus, the results of the PND measurements, which showed pore flexibility, were somewhat surprising. The structures derived from Rietveld refinements of the powder data showed that the material self-adjusts to size-match the kinetic diameter of the guest, be it D_2 gas, CD_4 gas, or dimethylformamide solvent molecules. The material self-adjusts to tailor the adsorption pocket for the guest species, leading to isosteric heats of adsorption of -8.6 and -24.8 kJ/mol for H_2 and CH_4, respectively. These high enthalpies of adsorption arise from the sum of the gas-framework van der Waals interactions in the tailored adsorption pockets in this flexible material. This study again highlights flexible frameworks as a design criterion for synthetically tuning hydrogen enthalpies of adsorption. While it may be intractable to rationally design and synthesize a new adsorbent with micropores tailored for each adsorbate, flexibility such as that observed in $U(bdc)_2$ provides a synthetic route to materials that inherently conform to accommodate gas molecules within optimized adsorption pockets.

As shown, the design criteria of utilizing small pores and flexible frameworks allowed for the realization of materials with enhanced enthalpies of adsorption. However, as of yet, these design criteria alone do not provide a synthetically tractable handle for easily tuning hydrogen enthalpies of adsorption into the optimal range of -15 and -20 kJ/mol. Toward this end, an additional design criterion has been developed: the inclusion of coordinatively-unsaturated Lewis acidic metal ions within the framework. The coordinatively-unsaturated metal centers provide a platform for direct, Kubas-complex-like adsorption of the hydrogen gas molecules to the metal ions. Unlike the original $W(CO)_3(P^iPr_3)_2H_2$ Kubas complex, excess steric bulk is not required to stabilize

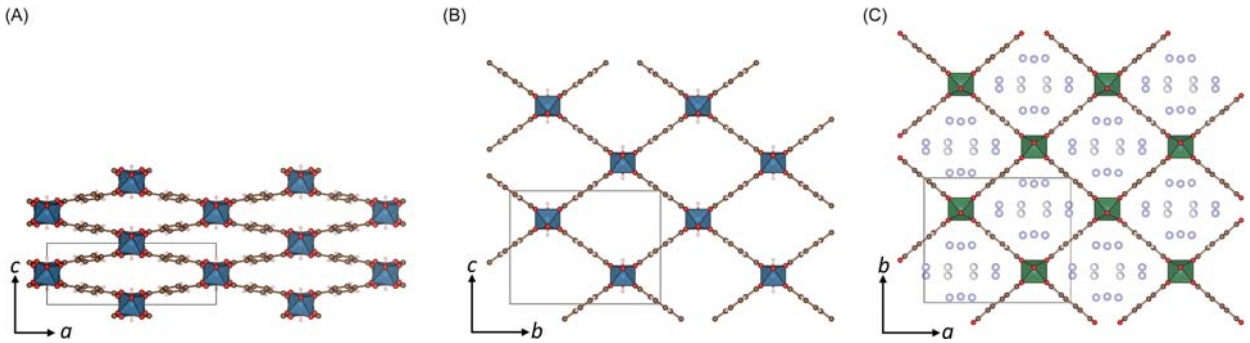

Fig. 14 (A) Al-MIL-53 in the completely collapsed phase. (B) Al-MIL-53, in the expanded phase. (C) The D_2 gas-dosed structure of Cr-MIL-53. The D_2 super-atom approach was used to model the gas molecules. The structures are drawn to scale to illustrate volumetric change in these flexible materials through the phase transition. Blue, red, brown, and white spheres represent aluminum, oxygen, and carbon atoms and D_2 molecules, respectively. Adapted from Liu, Y.; Her, J.-H.; Dailly, A.; Ramirez-Cuesta, A. J.; Neumann, D. A.; Brown, C. M. Reversible Structural Transition in MIL-53 With Large Temperature Hysteresis. *J. Am. Chem. Soc.* **2008**, *130* (35), 11813–11818; Mulder, F. M.; Assfour, B.; Huot, J.; Dingemans, T. J.; Wagemaker, M.; Ramirez-Cuesta, A. Hydrogen in the Metal-Organic Framework Cr-MIL-53. *J. Phys. Chem. C* **2010**, *114* (23), 10648–10655.

the η^2-H_2–M σ-complexes, as the coordinatively-unsaturated metal ions within the framework are crystallographically isolated and thus cannot dimerize. Below, we enumerate the neutron scattering studies of materials which display enhanced hydrogen adsorption at coordinatively-unsaturated metal centers.

10.02.5.2.2 Hydrogen adsorption at coordinatively-unsaturated metal centers in MOFs

Perhaps the first example of enhanced hydrogen enthalpies of adsorption in a MOF with coordinatively-unsaturated metal sites comes from the complex $Cu_6O(tzi)_3(H_2O)_9(NO_3)$ (tzi = 5-tetrazolylisophthalate).[573] This MOF contained both very large and small pores in the same structure and an exposed Cu paddlewheel containing two square-planar CuO_4 groups. The enhanced enthalpy of adsorption of −9.5 kJ/mol was rationalized to originate from adsorption to the metal ions. It decreased in magnitude to −4.7 kJ/mol on higher loadings. However, direct evidence for D_2 adsorption at open metal sites in this MOF and similar materials was lacking.[569,574–579]

Direct evidence for enhanced hydrogen adsorption at a coordinatively-unsaturated metal site came from the work of Brown, Long, and coworkers, who used PND measurements to discover the D_2 sorption sites in $Mn_3[(Mn_4Cl)(btt)_8(CH_3OH)_{10}]_2$ (btt = 1,3,5-benzenetristetrazolate).[57] The framework contains chloride-centered square-planar $[Mn_4Cl]^{7+}$ units linked by btt^{3-} ligands to form the anionic, three-dimensional sodalite-like cubic structure. Partially occupied, extra-framework Mn^{2+} balance the framework's negative charge. Though full framework activation proved challenging, the material showed a gravimetric capacity of ≈6.9 mass % at 77 K and 90 bar H_2, and an equivalent single-crystal storage density 85% of that of liquid hydrogen. PND measurements revealed four different adsorption sites. Two primary adsorption sites occur near the metal nodes of the framework and two weaker adsorption sites become occupied near the π-orbitals of the ligands at higher gas pressures. Here again, the D_2 molecules were treated as super-atoms. Based on the structures derived from Rietveld refinement analysis of the PND patterns, the primary adsorption site (site I) was only ≈30% occupied at high gas-dosing concentrations due to steric hinderance from residual solvent molecules left over after incomplete activation. Still, the refinements clearly indicated a strong adsorption interaction as the center of the D_2 super-atom sat only ≈2.27 Å away from the exposed Mn^{2+} ion. The D_2 molecules at the secondary adsorption site are positioned inside the sodalite-like cages and are supported by van der Waals contacts of ≈3.47 and ≈3.66 Å with a chloride anion and four equidistant tetrazolate rings, respectively. This site gradually becomes fully occupied with increasing gas-dosing. The sum of the attractive interactions in the adsorption pocket leads to a significant enthalpy of adsorption at site II, which contributes to the overall enthalpy of adsorption of −10.1 kJ/mol for the MOF.

Exchanging the Mn^{2+} ion for Cu^{2+} in the btt MOF allowed for more thorough activation (over 90% complete) and higher D_2 occupancy at the metal center. PND on the Cu congener found the primary sorption site to be adsorption at the metal center with a Cu-D_2 distance of ≈2.47 Å.[580] These results indicated that the identity of the metal center strongly influences the nature of the hydrogen adsorption. As such, a series of MOFs with different metal ions was then investigated for their hydrogen adsorption properties. The synthesis initially proved unwieldy, and ultimately a high-throughput approach was required to discover the synthetic path to the Fe^{2+} congener.[581] Activating the framework by removing methanol prior to decomposition was again difficult, and subsequent PND measurements revealed residual solvent molecules at the Fe^{2+} sites with ≈30% occupancy. The D_2-dosed structures were obtained from Rietveld refinements of the PND data. Analysis of these structures showed that the D_2 adsorption sites are similar to those identified in the Mn^{2+} and Cu^{2+} compounds but with differing rates of occupation. The first and only adsorption site occupied at low dosing concentration is adsorption at the metal center with an Fe–D_2 centroid distance of 2.17(5) Å. At saturation there are 98 D_2 molecules per formula unit at 10 crystallographically distinct adsorption sites, corresponding to a gravimetric capacity of ≈6 mass %. Another member of this series, the isostructural btt MOF with a softer Cr^{2+} ion, was also synthesized by the Long group, $Cr_3[(Cr_4Cl)_3(btt)_8]_2$. This MOF was robust to activation with no residual solvents apparent in the structure refinements from the PND data.[582] The enthalpy of adsorption for the primary adsorption site is −10.0 kJ/mol, and the open Cr^{2+} cations adsorb D_2 with a Cr–D_2 centroid distance of 2.57(3) Å. This distance is longer than the rest of the series due to the large ionic radius of Cr^{2+} and the significant Jahn-Teller axial elongation displayed by the $3d^4$ metal center. Recent work on the related compound, Cu-BTTri [$Cu_3(BTTri)_2$ TTri = 1,3,5-benzenetristriazolate], revealed four separate sorption sites, with a Cu–D_2 centroid distance of 2.73(4) Å.[583] In total, these compounds present an interesting comparison showing the effect of metal and ligand variation on D_2 adsorption.

The metal paddlewheel motif is common to several classes of MOFs that adsorb hydrogen. Some of these have been spectroscopically investigated. Specifically, IR spectroscopy studies on HKUST-1 [$Cu_3(btc)_2$, also known as $Cu_3(tma)_2$] were used to probe the local structure upon adsorption of H_2 at 15 K.[584,585] The results supported the hypothesis that the activation process did not perturb framework crystallinity and revealed a shrinking of the Cu-paddlewheel with the copper atoms sinking into the plane of carboxylic oxygens upon activation and subsequent gas-dosing. An IR signature vibrational frequency of ≈4100 cm^{-1} measured at 15 K was ascribed to that of a Cu(II)–H_2 adduct.[574] Results from PND experiments determined the progressive filling of six distinct D_2 sorption sites (**Fig. 15**).[58] At a loading of 4 D_2 molecules per Cu in the material, the location of the primary adsorption site for D_2 was just 2.39(1) Å away from the Cu^{2+} ion, confirming the association inferred from the IR data. From INS studies, the hydrogen at this site has a rotational barrier consistent with the estimated binding energy of ≈−6 to −10 kJ/mol.[586] This association arises from a classical Coulomb interaction that is unscreened due to the open metal site.[560] This results in a propensity for the H_2 to lie in a plane perpendicular to the Cu–Cu axis. This was corroborated by measurements conducted by Callear et al., who used higher-resolution PND data to refine an anisotropic displacement resulting in Cu–D_2 distances of 2.4633(4) Å for a gas-dosing concentration of 0.5 D_2/Cu ion, 2.4893(4) Å for 2 D_2/Cu, and 2.3542(4) Å at a loading of 6 D_2/Cu, compatible with the previous results.[575] Peterson et al.[587] also reported a high D_2 dosing concentration series of PND experiments where the response of the

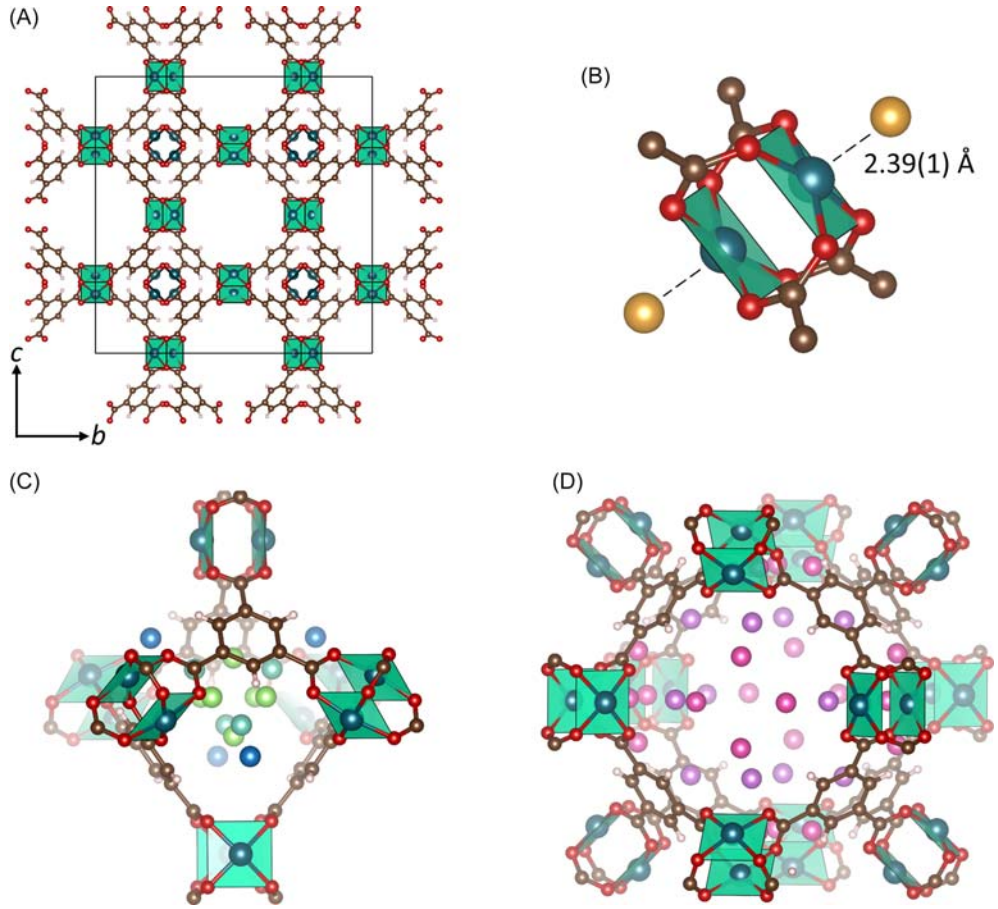

Fig. 15 (A) The structure of activated HKUST-1. (B) The primary adsorption site in HKUST-1 is the coordinatively unsaturated Cu metal site, where D_2 adsorbs at the metal at a distance of 2.39(1) Å. (C) and (D) show the other five D_2 adsorption sites in HKUST-1 at a gas dosing concentration of 4 D_2 molecules per Cu ion. Each site is drawn with full occupancy for clarity. Here, the brown, red, and white spheres, and the green-blue spheres in the green squares, represent carbon, oxygen, hydrogen, and copper atoms, respectively. The other colored spheres represent D_2 molecules in crystallographically distinct positions in the structure. Adapted from Peterson, V. K.; Liu, Y.; Brown, C. M.; Kepert, C. J. Neutron Powder Diffraction Study of D_2 Sorption in Cu_3(1,3,5-Benzenetricarboxylate)$_2$. *J. Am. Chem. Soc.* **2006**, *128* (49), 15578–15579.

system to the total deuterium loading is a redistribution of population of D_2 among the various possible sorption sites. There is only a small response from the framework as the gas is accommodated, as confirmed by Callear et al.[582] This is interesting when compared to the structurally analogous compound, $Cr_3(btc)_2$,[588] in which the Cr^{2+} open metal site is only partially occupied below loadings of 1 D_2 per metal site. Here most of the adsorption occurs at the apertures of the structure's octahedral microporous cages. Above this D_2 gas dosing concentration there is a marked elongation of the Cr–Cr internuclear distance in the paddlewheels, which results in a displacement of Cr^{2+} out of the oxygen plane and full population of D_2 at the open metal sites.

Other Cu paddlewheel carboxylate MOFs have been studied for their hydrogen storage properties. PND studies of MFM-101 (NOTT-101, Cu_2(tptc) $tptc^{4-}$ = terphenyl-3,3″,5,5″-tetracarboxylate) reveal a primary adsorption site at the Cu ions with a Cu–D_2 centroid distance of 2.50(3) Å, slightly longer than that observed in HKUST-1.[589] MFM-112 (NOTT-112, Cu_3(btpi) $btpi^{6-}$ = 1,3,5-tris(3′,5′-dicarboxy[1,1′-biphenyl]-4-yl)benzene) however, revealed that there are differences in the exposed Cu(II) sites in this framework.[590] The strongest sorption site here is within the cuboctahedral microporous cage and has a short Cu–D_2 centroid distance (≈ 2.23 Å). Presumably, the adsorption here is stronger as this site is preferentially occupied at low gas dosing concentrations. The second site is on the same paddlewheel but outside the cage, and adsorbs with a slightly longer Cu–D_2 centroid distance of ≈ 2.41 Å. Both measured distances are quite short given the low initial ΔH_{ads} of −6.7 kJ/mol.

The importance of the coordinatively-unsaturated metal center's identify for hydrogen sorption was further investigated in a series of metal dobdc MOFs [MOF-74, CPO-27, M_2(dobdc) M = Ni, Co, Mg, Fe, Zn, Mn, and Cu].[87,591,592] The results of the PND and INS measurements on these compounds emphasize the importance of open-metal sites in porous materials that are candidates for use in hydrogen storage applications. Sumida, Long, and coworkers gave direct evidence that Mg_2(dobdc) can adsorb H_2 strongly at the coordinatively-unsaturated Mg^{2+} ion, with a distance of 2.45(4) Å. Isotherm data indicated an initial isosteric heat of adsorption as high as −10.3(2) kJ/mol, which then was reduced to −7.9(2) kJ/mol at higher loading concentrations. A second site was also observed interacting with the oxido moiety of the dobdc linker. QENS measurements on Mg_2(*m*-dobdc) included in this

study probed the diffusion of H_2 on the surface of this MOF over a range of equilibrium H_2 pressures (Fig. 2). The results of the measurements showed that, at low loading concentrations, there is a lack of H_2 diffusion on the picosecond timescale due to strong adsorption at the metal centers. At higher loadings, the QENS scattering is fit with two Lorentzian functions, one narrow (slower diffusion) and one broad (faster diffusion). These correspond to H_2 diffusion along the pore surfaces and to bulk-like H_2 diffusion within the pores, respectively. It was observed that the mean jump length and average diffusivity of the slow surface hydrogen are reduced with increasing hydrogen adsorption such that, at 77 K and ≈ 1 bar, the diffusion coefficient is an order of magnitude lower than the one observed for one-dimensional H_2 diffusion in Cr(OH)(bdc) (MIL-53(Cr)) and *VO*(bdc) (MIL-47(V)).[593]

Later, the authors synthesized a related class of compounds using the *meta* version of the dobdc linkers instead of the *para* version, M_2(*m*-dobdc) (M = Mg, Mn, Fe, Co, Ni) (Fig. 16). This seemingly innocuous substitution led to an ≈ 2 kJ/mol difference in the enthalpy of adsorption. These PND studies also revealed that the distance between the metal center and the D_2 centroid decreases from 2.32(2) Å to 2.23(5) Å when going from dobdc to *m*-dobdc for M = Co (Fig. 17). This shortened M-D_2 distance corresponded with a ΔH_{ads} of ≈ − 0.7 kJ/mol. The decreased adsorption distance, corresponding to an increase in the strength of the adsorption interaction, stems from increased electron donation from the *m*-dobdc ligands into the metal site, and thus increased electron density at the coordinatively-unsaturated metal ion. Hence the increased enthalpy of adsorption shows both a direct relationship with the identity of the metal ion and the identity of the ligand.

The hydrogen storage capacities for M_2(dobdc) and M_2(*m*-dobdc) with M = Ni, Co were then evaluated at temperature and pressure conditions relevant to real world mobile applications. The authors of this study combined PND measurements with adsorption isotherm data and variable-pressure and -temperature IR spectroscopy measurements.[62] The results of the adsorption isotherm measurements showed record high H_2 uptake for Ni_2(*m*-dobdc) with a useable H_2 volumetric capacity of 11 g H_2 L^{-1} at ≈ 298 K for a pressure swing between 5 and 100 bar. The PND measurements were conducted on the Co_2(*m*-dobdc)—due to

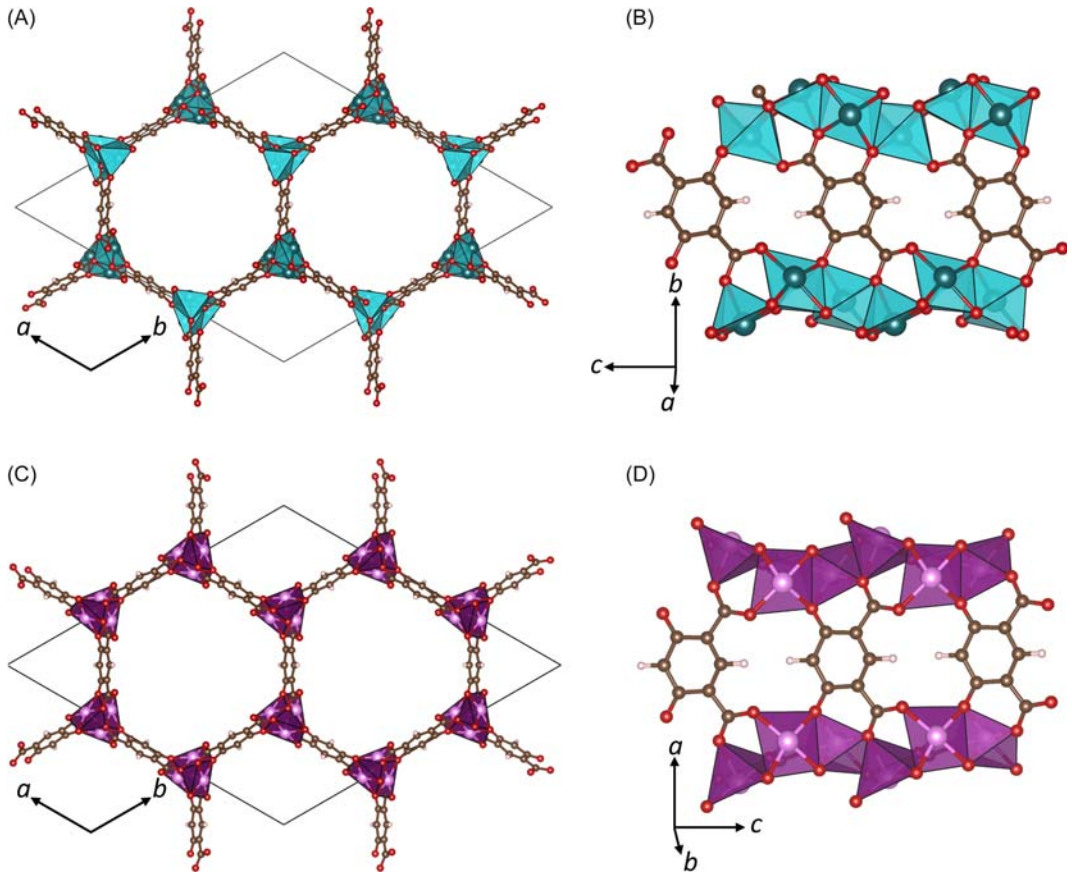

Fig. 16 M_2(dobdc) and M_2(*m*-dobdc) are very closely related compounds; M_2(dobdc) contains *para*-dobdc ligands, whereas M_2(*m*-dobdc) utilizes the *meta* version of the ligand. (A) Activated Zn_2(dobdc) structure. (B) Zn_2(dobdc) open metal site chain, showing the bonding of the *p*-dobdc ligand. (C) Activated Co_2(*m*-dobdc) structure. (D) Co_2(*m*-dobdc) open metal site chain, showing the bonding of the *m*-dobdc ligand. Adapted from Sumida, K.; Brown, C. M.; Herm, Z. R.; Chavan, S.; Bordiga, S.; Long, J. R. Hydrogen Storage Properties and Neutron Scattering Studies of Mg_2(dobdc)—A Metal–Organic Framework With Open Mg^{2+} Adsorption Sites. *Chem. Commun.* **2011**, *47* (4), 1157–1159; Kapelewski, M. T.; Geier, S. J.; Hudson, M. R.; Stück, D.; Mason, J. A.; Nelson, J. N.; Xiao, D. J.; Hulvey, Z.; Gilmour, E.; FitzGerald, S. A.; Head-Gordon, M.; Brown, C. M.; Long, J. R. M_2(m-dobdc) (M = Mg, Mn, Fe, Co, Ni) Metal–Organic Frameworks Exhibiting Increased Charge Density and Enhanced H_2 Binding at the Open Metal Sites. *J. Am. Chem. Soc.* **2014**, *136* (34), 12119–12129.

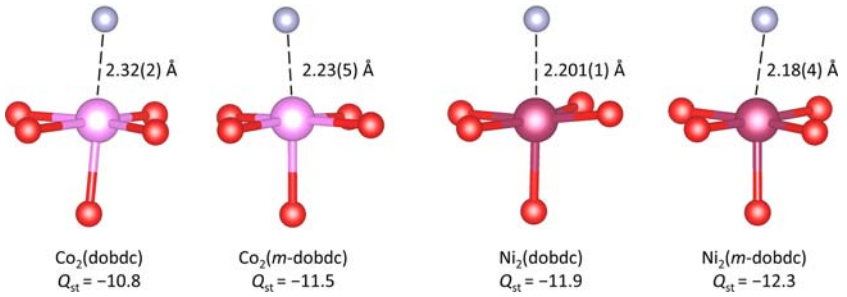

Fig. 17 Experimentally obtained distances between the D_2 centroids and metal centers in the M_2(dobdc)] and M_2(*m*-dobdc) MOFs. The increasingly negative isosteric heats of adsorption of D_2 correlates with shorter distances between the D_2 molecules and the metal centers. For the Ni varieties, the heat of adsorption values are similar, and the experimentally measured distances are the same within error. Here, red, pink, maroon, and white spheres represent oxygen, cobalt, and nickel atoms and deuterium molecules, respectively. Adapted from Sumida, K.; Brown, C. M.; Herm, Z. R.; Chavan, S.; Bordiga, S.; Long, J. R. Hydrogen Storage Properties and Neutron Scattering Studies of Mg_2(dobdc)—A Metal–Organic Framework With Open Mg^{2+} Adsorption Sites. *Chem. Commun.* **2011**, *47* (4), 1157–1159; Kapelewski, M. T.; Geier, S. J.; Hudson, M. R.; Stück, D.; Mason, J. A.; Nelson, J. N.; Xiao, D. J.; Hulvey, Z.; Gilmour, E.; FitzGerald, S. A.; Head-Gordon, M.; Brown, C. M.; Long, J. R. M_2(m-dobdc) (M = Mg, Mn, Fe, Co, Ni) Metal–Organic Frameworks Exhibiting Increased Charge Density and Enhanced H_2 Binding at the Open Metal Sites. *J. Am. Chem. Soc.* **2014**, *136* (34), 12119–12129.

its high degree of crystallinity compared to the Ni species—at 77 K and 79 bar D_2 to somewhat approximate the isotherm measurement conditions. Rietveld refinement analysis of the data from the high pressure in situ PND measurements revealed seven crystallographically unique adsorption sites for D_2 in the framework. These included adsorption at the metal, as previously observed, and adsorption sites at the ligands and in the pores. The D_2 molecules adsorbed in the pores formed close gas-gas contacts shorter in length than those found in solid D_2, reminiscent of the liquid-like structure found in the zeolites and other MOFs. Importantly, this study found good quantitative agreement between the number of D_2 molecules adsorbed in the structure as derived from the analysis of the PND data with the amount of hydrogen adsorbed in the material as derived from analysis of the adsorption isotherm data obtained under the same temperature and pressure conditions. This study illustrates how macroscopic and microscopic measurement techniques combine to yield a detailed understanding of the underlying chemistry and physics of hydrogen sorption. Moreover, the results from this study helped validate the design criteria of using coordinatively-unsaturated metal centers in MOFs to enhance the enthalpy of adsorption, and ultimately, to improve the volumetric capacity in these porous materials.[594]

The importance of metal center identity for hydrogen adsorption was further investigated using additional PND and INS measurements on M_2(dobdc) (M = Ni, Co, Mg, Fe, Zn, Mn, and Cu). Upon evaluating this system, it was clear that the hydrogen affinity with the metal site follows the Ni > Co > Mg > Fe > Zn ≈ Mn > Cu order.[595] Most surprisingly, the Cu(II) congener had a much lower affinity for H_2 than would be expected based on other MOFs with Cu(II) centers. This is explained by the Jahn-Teller distorted coordination environment, which is less favorable for H_2 adsorption when compared to the square-pyramidal Cu(II) sites in a MOF with the paddle-wheel geometry such as HKUST-1. The Cu-D_2 centroid distance in Cu-MOF-75 is 3.03(2) Å, whereas it is as short as 2.3542(4) Å in HKUST-1.[586]

In recent work on $Cu_xZn_{5-x}Cl_{4-x}$(btdd)$_3$ (H_2btdd = bis(1H-1,2,3-triazolo[4,5-b],[4′,5′-i])dibenzo[1,4]dioxin), also known as Cu-MFU-4l, the MOF exhibited a difference between H_2 and D_2 enthalpies of adsorption of ≈ 2.3 kJ/mol, with D_2 being the preferred molecule).[596–598] The difference in binding energy difference could be used to filter H_2 gas from D_2 gas under the correct conditions. At low enough temperatures (77 K), however, the kinetic effects eliminate the capacity for selectivity. On closer examination using PND experiments on the interaction between D_2 and the Cu-MFU-4l MOF, it was shown that there are 3 possible D_2 sorption sites depending on the temperature of dosing (**Fig. 18**).[599] This includes one weakly physisorbed site, nestled within the Zn-btdd nodes, a site close to the Cu(I) ions, and a third site slightly farther from the Cu(I) ions. The third site can be viewed as a precursor site to the site close the Cu(I) site. At low dosing temperature (40 K), the physisorbed site is the primary sorption site even though the enthalpy of adsorption for this site is the lowest of the three. However, if the gas dosing is performed at ≈ 300 K and then the gas-dosed material is cooled to ≈ 10 K, the site closest to the Cu(I) metal center becomes the most populated site, with no discernable D_2 density at the physisorbed site. Interestingly, at both ≈ 77 and ≈ 10 K, the precursor site has a significant occupancy. The presence of this precursor site was further confirmed by temperature programmed D_2 desorption data, X-ray adsorption spectroscopy, and DFT calculations.

Finally, there are many other types of porous extended framework and molecular species which represent important candidate hydrogen storage materials. These include covalent organic frameworks,[600–603] hypercrosslinked porous polymers,[604–606] and polymers of intrinsic microporosity.[607–610] While these materials may play a critically important role in the future of hydrogen storage, they are inherently difficult to study using traditional diffraction techniques. As such, they are outside of the scope of this chapter. One exception are the amorphous molecular coordination cages, called porous coordination compounds (PCCs). PCCs have recently gained interest for their hydrogen storage properties, perhaps because of their similarities to MOFs.[611] A series of cages involving triangular Fe_3O metal polyhedra connected by carboxylate phenyl organic linkers were among the first PCCs studied for possible gas storage application.[612] This study examined isoreticular metal-organic polyhedra (IRMOPs), and an exemplary

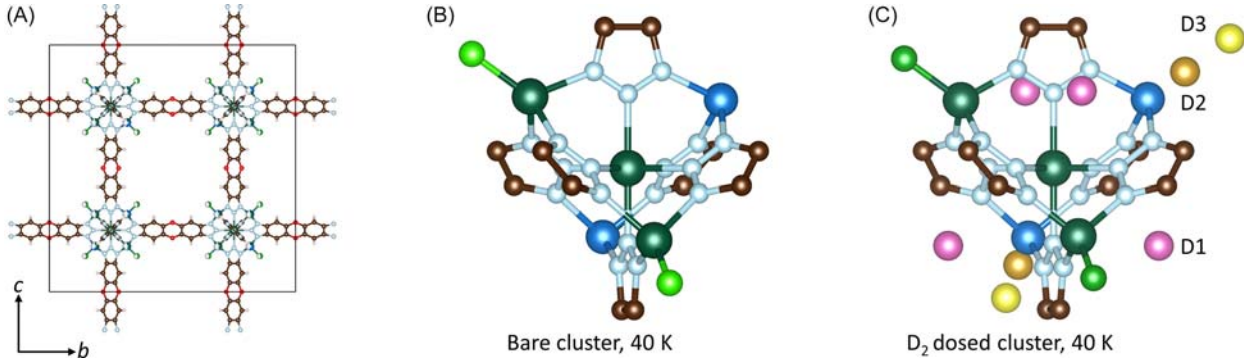

Fig. 18 (A) The crystallographically averaged structure of activated Cu-MFU-4l at 40 K. (B) Idealized bare cluster, showing a likely view of single cluster containing two chloride-ligated Zn ions and two coordinatively-unsaturated, active Cu ions. For clarity, the atoms are shown fully occupied in an idealized image of the structure. This idealized image is averaged over the entire crystal structure. (C) Structure of the idealized, D_2 gas-dosed cluster illustrating the three experimentally resolved D_2 sites. The "D1" site is the physisorption site nestled within the nodes of the cluster, the "D2" site is the site close to the Cu(I) atom (distance of 1.56(13) Å), and the "D3" site is the precursor site to "D2" (distance of 2.88(9) Å). Brown, red, blue, white, light green, and dark green spheres represent carbon, oxygen, nitrogen, hydrogen, chlorine, and copper atoms, respectively. The orange, pink, and yellow spheres represent D_2 molecules. Adapted from Denysenko, D.; Grzywa, M.; Jelic, J.; Reuter, K.; Volkmer, D. Scorpionate-Type Coordination in MFU-4l Metal–Organic Frameworks: Small-Molecule Binding and Activation Upon the Thermally Activated Formation of Open Metal Sites. *Angew. Chem. Int. Ed.* **2014**, *53* (23), 5832–5836.

compound from this work is IRMOP-51 [$Fe_6O_2(bpdc)_3(SO_4)_6(py)_6$ bpdc = 4,4′ biphenyldicarboxylate, py = pyridine]. The volumetric capacity for IRMOP-51 is ≈ 5 g/L at pressures below 1 bar H_2 and a temperature of 78 K. Since these initial works, more gas adsorption studies have been conducted on other PCCs. Unfortunately, their inherent lack of long-range structural ordering still precludes diffraction experiments. Nevertheless, recent PND measurements were conducted on structurally analogous MOFs with pillared isostructural cages to identify the adsorption sites in the amorphous PCCs.[613,614] In one study, the PCC—and the cages pillared into the MOF—were constructed using tricarboxylate linkers bound to metal paddlewheels to give $M_{24}(bdc)_{24}$ (M = Mo, Cr, Cu, Fe, Zn, Co). The authors compared the crystal structures of the CD_4-dosed pillared MOF with the methane gas-dosed structures of HKUST-1 and concluded that the fundamental nature of the gas adsorption in the PCC is similar to that observed in the solid-state compounds.[588] These studies illustrate that PCCs have the same chemical tunability, pore size, and similar gas-solid interactions as observed in MOFs. As such, the emerging field of study focusing on gas storage in PCCs shows promise for the discovery of new candidate hydrogen storage materials.

10.02.5.3 Outlook

Today, the effort to improve gravimetric and volumetric capacities in porous materials at realistic operating temperatures is ongoing. To this end, there is a push in the research community to develop methods for synthetically tuning hydrogen enthalpies of adsorption. Besides the use of small pores, flexible frameworks, and unsaturated metal centers, other methodologies have been attempted to tune the enthalpy of hydrogen adsorption in these compounds. One such approach is introducing polar functionalities at the linkers in a framework: the hydroxyl-decorated framework MFM-300(In) [$In_2(OH)_2(bptc)$ ($bptc^{4-}$ = biphenyl-3,3′,5,5′-tetracarboxylate)] exhibits a differential enthalpy for H_2 adsorption of ≈ −6.8 kJ/mol.[615] PND measurements revealed that the first adsorption site was indeed located 2.54(1) Å away from the bridging hydroxyl group and the second site between phenyl rings of adjacent ligands. Increasing the D_2 loading further resulted in the population of two more sites accompanied by slight rearrangement of the adsorbed molecules at the primary and secondary adsorption sites. Lastly, an additional three adsorption sites were populated upon saturation, giving rise to a liquid-like packing of D_2-molecules in the pores.

Some efforts to improve the capacities in MOFs include work to design materials that adsorb multiple equivalents of hydrogen gas at a single coordinatively-unsaturated metal ion, and to increase the concentration of coordinatively-unsaturated metal ions in the frameworks. The former has been observed only once in a MOF. PXRD and PND measurements on gas-dosed, activated $Mn_2(dsbdc)$ ($dsbdc^{4-}$ = 2,5-disulfido-1,4-benzenedicarboxylate) reveal multiple D_2 adsorption events at the Mn^{2+} ions, with the crystallographically equivalent Mn–D_2 centroid distance of 3.40(4) Å.[616] A polymorph of this compound, $Zn_2(dobdc)$, known as UTSA-74, has been shown to have two crystallographically distinct, coordinatively-unsaturated Zn^{2+} ions in the framework, which seems to be very promising for possible multi-sorption events at these ions. However, only the solvated structure has been investigated to date.[617] Lastly, one possible route to increasing the density of coordinatively-unsaturated metal centers in MOFs is through the intentional inclusion of linker defects followed by activation to expose the metal centers. This creates both potential open metal sites but also linker defect sites for adsorption as well. Synthetic tunability of linker defect concentration has been demonstrated to be a useful handle on macroscopic gas adsorption properties in UiO-66.[618]

The lack of a commercially viable hydrogen storage materials represents a significant impediment in implementing an efficient and green hydrogen fuel economy. Governments and private companies around the globe are investing heavily in every aspect of

the hydrogen fuel cycle. The development of the infrastructure of a hydrogen economy is underway in the United States, EU, Japan, South Korea, and elsewhere, in anticipation of the next generation of commercial HFCEVs. The research and development of a commercially viable hydrogen storage material that meets the EERE-specified targets will enable the development of this next generation of vehicles. Already, great progress toward this goal has been achieved. Investigations of materials we now know are commercially inviable as storage media serve as invaluable steppingstones in the development of materials design criteria and lead us closer to commercially competitive materials. Along the way, neutron scattering studies investigating candidate hydrogen storage materials have uncovered beautiful fundamental chemistry in a diversity of molecular and solid-state systems. We hope that this text—and the studies enumerated within—inform and inspire future generations of researchers to guide us toward a realized green global hydrogen energy economy.

References

1. Fuel Cell Technology Office Multi-Year Research, Development, and Demonstration Plan; U.S. Department of Energy Office of Energy Efficiency and Renewable Energy. https://www.energy.gov/sites/prod/files/2015/06/f23/fcto_myrdd_production.pdf (Accessed July 2020).
2. Kalamaras, C. M.; Efstathiou, A. M. Hydrogen Production Technologies: Current State and Future Developments. Conference Papers in Energy, Hindawi.
3. Sun, P.; Young, B.; Elgowainy, A.; Lu, Z.; Wang, M.; Morelli, B.; Hawkins, T. Criteria Air Pollutants and Greenhouse Gas Emissions From Hydrogen Production in US Steam Methane Reforming Facilities. *Environ. Sci. Technol.* **2019,** *53* (12), 7103–7113.
4. H2@Scale: Enabling Affordable, Reliable, Clean, and Secure Energy Across Sectors; U.S. Department of Energy Office of Energy Efficiency and Renewable Energy. https://www.energy.gov/sites/prod/files/2019/09/f67/fcto-h2-at-scale-handout-2019.pdf (Accessed July 2020).
5. Liu, X.; Reddi, K.; Elgowainy, A.; Lohse-Busch, H.; Wang, M.; Rustagi, N. Comparison of Well-to-Wheels Energy Use and Emissions of a Hydrogen Fuel Cell Electric Vehicle Relative to a Conventional Gasoline-Powered Internal Combustion Engine Vehicle. *Int. J. Hydrog. Energy* **2020,** *45* (1), 972–983.
6. Allendorf, M. D.; Hulvey, Z.; Gennett, T.; Ahmed, A.; Autrey, T.; Camp, J.; Cho, E. S.; Furukawa, H.; Haranczyk, M.; Head-Gordon, M.; et al. An Assessment of Strategies for the Development of Solid-State Adsorbents for Vehicular Hydrogen Storage. *Energy Environ. Sci.* **2018,** *11* (10), 2784–2812.
7. Durbin, D.; Malardier-Jugroot, C. Review of Hydrogen Storage Techniques for on Board Vehicle Applications. *Int. J. Hydrog. Energy* **2013,** *38* (34), 14595–14617.
8. Wieliczko, M.; Stetson, N. Hydrogen Technologies for Energy Storage: A Perspective. *MRS Energy Sustain.* **2020,** *7*, E41.
9. The Strategic Road Map for Hydrogen and Fuel Cells; Japanese Ministry of Economy, Trade, and Industry, Hydrogen and Fuel Cell Strategy Council. https://www.meti.go.jp/english/press/2019/pdf/0312_002b.pdf (Accessed 2020).
10. Basic Hydrogen Strategy; Japanese Ministry of Economy, Trade, and Industry, Ministerial Council on Renewable Energy. https://www.meti.go.jp/english/press/2017/pdf/1226_003b.pdf (Accessed July 2020).
11. Staffell, I.; Scamman, D.; Abad, A. V.; Balcombe, P.; Dodds, P. E.; Ekins, P.; Shah, N.; Ward, K. R. The Role of Hydrogen and Fuel Cells in the Global Energy System. *Energy Environ. Sci.* **2019,** *12* (2), 463–491.
12. *The National Hydrogen Strategy, Germany Federal Ministry for Economic Affairs and Energy*. https://www.bmwi.de/Redaktion/EN/Publikationen/Energie/the-national-hydrogen-strategy.pdf?__blob=publicationFile&v=6.
13. AB-8 Alternative Fuel and Vehicle Technologies: Funding Programs; State of California. https://leginfo.legislature.ca.gov/faces/billNavClient.xhtml?bill_id=201320140AB8 (Accessed July 2020).
14. The California Fuel Cell Revolution: A Vision for Advancing Economic, Social, and Environmental Priorities; California Fuel Cell Partnership. https://cafcp.org/sites/default/files/CAFCR.pdf (Accessed July 2002).
15. 2018 Annual Evaluation of Fuel Cell Electric Vehicle Deployment & Hydrogen Fuel Station Network Development; California Air Resources Board. https://ww2.arb.ca.gov/sites/default/files/2019-11/AB8_report_2018_print_ac.pdf (Accessed July 2020).
16. Joint Agency Staff Report on Assembly Bill 8: 2018 Annual Assessment of Time and Cost Needed to Attain 100 Hydrogen Refueling Stations in California; California Air and Resources Board. https://ww2.energy.ca.gov/2018publications/CEC-600-2018-008/CEC-600-2018-008.pdf (Accessed July 2020).
17. Melaina, M. W.; Bush, B. W.; Muratori, M.; Zuboy, J.; Ellis, S. *National Hydrogen Scenarios: How Many Stations, Where, and When?*; U.S. Department of Energy National Renewable Energy Laboratory, 2017. https://doi.org/10.2172/1461868 (Accessed July 2020).
18. Hydrogen Roadmap Europe: A Sustainable Pathway for the European Energy Transition; European Union Fuel Cells and Hydrogen Joint Undertaking. https://www.fch.europa.eu/sites/default/files/Hydrogen%20Roadmap%20Europe_Report.pdf (Accessed July 2020).
19. 2013 Annual Report, Task 32 Hydrogen-Based Energy Storage, International Energy Agency Hydrogen Technology Collaboration Program. http://ieahydrogen.org/PUBLICATIONS,-REPORTS-PRESENTATIONS/Annual-Reports-(1)/2013/Task32_2013.aspx (Accessed July 2020).
20. Hirscher, M.; Yartys, V. A.; Baricco, M.; von Colbe, J. B.; Blanchard, D.; Bowman, R. C., Jr.; Broom, D. P.; Buckley, C. E.; Chang, F.; Chen, P.; et al. Materials for Hydrogen-Based Energy Storage – Past, Recent Progress and Future Outlook. *J. Alloys Compd.* **2020,** *827,* 153548.
21. Strategic Plan 2020–2025; International Energy Agency Hydrogen Technology Collaboration Program. http://ieahydrogen.org/pdfs/Strategic-Plan-One-pager_v32-_A4.aspx (Accessed July 2020).
22. End-of-Term Report 2015–2020; International Energy Agency Hydrogen Technology Collaboration Program. http://ieahydrogen.org/pdfs/EOTH2T_v11_OnlineVersion.aspx (Accessed July 2020).
23. Target Explanation Document: Onboard Hydrogen Storage for Light-Duty Fuel Cell Vehicles; U.S. Department of Energy. https://www.energy.gov/sites/prod/files/2017/05/f34/fcto_targets_onboard_hydro_storage_explanation.pdf (Accessed July 2020).
24. Schlichtenmayer, M.; Hirscher, M. The Usable Capacity of Porous Materials for Hydrogen Storage. *Appl. Phys. A* **2016,** *122* (4), 379.
25. Oxtoby, D. W.; Gillis, H. P.; Butler, L. J. *Principles of Modern Chemistry*, Cengage Learning, 2015.
26. Kubas, G. J. Fundamentals of H_2 Binding and Reactivity on Transition Metals Underlying Hydrogenase Function and H_2 Production and Storage. *Chem. Rev.* **2007,** *107* (10), 4152–4205.
27. Lide, D. R. *CRC Handbook of Chemistry and Physics*; vol. 85; CRC Press, 2004.
28. Mehio, N.; Dai, S.; Jiang, D.-e. Quantum Mechanical Basis for Kinetic Diameters of Small Gaseous Molecules. *J. Phys. Chem. A* **2014,** *118* (6), 1150–1154.
29. Ishmaev, S.; Sadikov, I.; Chernyshov, B.; Vindryaevskii, V.; Sukhoparov, A.; Kobelev, G. Neutron Structural Investigations of Solid Parahydrogen at Pressures up to 24 kbar. *J. Exp. Theor. Phys.* **1983,** *84,* 228.
30. Van Itterbeek, A.; Verbeke, O.; Theewes, F.; Staes, K.; De Boelpaep, J. The Difference in Vapour Pressure Between Normal and Equilibrium Hydrogen. Vapour Pressure of Normal Hydrogen Between 20 K and 32 K. *Physica* **1964,** *30* (6), 1238–1244.
31. Jeffrey, G. A.; Saenger, W. *Hydrogen Bonding in Biological Structures*, Springer Science & Business Media, 2012.
32. Yang, J.; Sudik, A.; Wolverton, C.; Siegel, D. J. High Capacity Hydrogen Storage Materials: Attributes for Automotive Applications and Techniques for Materials Discovery. *Chem. Soc. Rev.* **2010,** *39* (2), 656–675.
33. Smith, K. C.; Fisher, T. S. Models for Metal Hydride Particle Shape, Packing, and Heat Transfer. *Int. J. Hydrog. Energy* **2012,** *37* (18), 13417–13428.

34. Jehan, M.; Fruchart, D. McPhy-Energy's Proposal for Solid State Hydrogen Storage Materials and Systems. *J. Alloys Compd.* **2013,** *580,* S343–S348.
35. Lototskyy, M. V.; Tolj, I.; Davids, M. W.; Klochko, Y. V.; Parsons, A.; Swanepoel, D.; Ehlers, R.; Louw, G.; van der Westhuizen, B.; Smith, F.; et al. Metal Hydride Hydrogen Storage and Supply Systems for Electric Forklift With Low-Temperature Proton Exchange Membrane Fuel Cell Power Module. *Int. J. Hydrog. Energy* **2016,** *41* (31), 13831–13842.
36. Program 2015 Annual Merit Review Proceedings: Project ST004; U.S. Department of Energy, Hydrogen and Fuel Cells https://www.hydrogen.energy.gov/pdfs/review15/st004_anton_2015_o.pdf (Accessed July 2020).
37. Hua, T.; Ahluwalia, R.; Peng, J.-K.; Kromer, M.; Lasher, S.; McKenney, K.; Law, K.; Sinha, J. Technical Assessment of Compressed Hydrogen Storage Tank Systems for Automotive Applications. *Int. J. Hydrog. Energy* **2011,** *36* (4), 3037–3049.
38. Lin, L.-C.; Berger, A. H.; Martin, R. L.; Kim, J.; Swisher, J. A.; Jariwala, K.; Rycroft, C. H.; Bhown, A. S.; Deem, M. W.; Haranczyk, M.; et al. In Silico Screening of Carbon-Capture Materials. *Nat. Mater.* **2012,** *11* (7), 633–641.
39. Wilmer, C. E.; Leaf, M.; Lee, C. Y.; Farha, O. K.; Hauser, B. G.; Hupp, J. T.; Snurr, R. Q. Large-Scale Screening of Hypothetical Metal–Organic Frameworks. *Nat. Chem.* **2012,** *4* (2), 83.
40. Goldsmith, J.; Wong-Foy, A. G.; Cafarella, M. J.; Siegel, D. J. Theoretical Limits of Hydrogen Storage in Metal–Organic Frameworks: Opportunities and Trade-Offs. *Chem. Mater.* **2013,** *25* (16), 3373–3382.
41. First, E. L.; Floudas, C. A. MOFomics: Computational Pore Characterization of Metal–Organic Frameworks. *Microporous Mesoporous Mater.* **2013,** *165,* 32–39.
42. Haldoupis, E.; Nair, S.; Sholl, D. S. Pore Size Analysis of >250000 Hypothetical Zeolites. *Phys. Chem. Chem. Phys.* **2011,** *13* (11), 5053–5060.
43. He, T.; Pachfule, P.; Wu, H.; Xu, Q.; Chen, P. Hydrogen Carriers. *Nat. Rev. Mater.* **2016,** *1* (12), 1–17.
44. Preuster, P.; Papp, C.; Wasserscheid, P. Liquid Organic Hydrogen Carriers (LOHCs): Toward a Hydrogen-Free Hydrogen Economy. *Acc. Chem. Res.* **2017,** *50* (1), 74–85.
45. Sears, V. F. Neutron Scattering Lengths and Cross Sections. *Neutron News* **1992,** *3* (3), 26–37.
46. Rietveld, H. M. A Profile Refinement Method for Nuclear and Magnetic Structures. *J. Appl. Crystallogr.* **1969,** *2* (2), 65–71.
47. Pawley, G. Unit-Cell Refinement From Powder Diffraction Scans. *J. Appl. Crystallogr.* **1981,** *14* (6), 357–361.
48. Le Bail, A.; Duroy, H.; Fourquet, J. Ab-Initio Structure Determination of LiSbWO6 by X-Ray Powder Diffraction. *Mater. Res. Bull.* **1988,** *23* (3), 447–452.
49. West, A. R. *Basic Solid State Chemistry*, John Wiley & Sons Incorporated, 1999.
50. Warren, B. E. *X-Ray Diffraction*, Courier Corporation, 1990.
51. Suryanarayana, C.; Norton, M. G. *X-Ray Diffraction: A Practical Approach*, Plenum Press: New York City, NY, USA, 1998.
52. Weller, M. T.; Henry, P. F.; Ting, V. P.; Wilson, C. C. Crystallography of Hydrogen-Containing Compounds: Realizing the Potential of Neutron Powder Diffraction. *Chem. Commun.* **2009,** *21,* 2973–2989.
53. Wilson, C. C.; Henry, P. F.; Schmidtmann, M.; Ting, V. P.; Williams, E.; Weller, M. T. Neutron Powder Diffraction–New Opportunities in Hydrogen Location in Molecular and Materials Structure. *Crystallogr. Rev.* **2014,** *20* (3), 162–206.
54. Queen, W. L.; Hudson, M. R.; Bloch, E. D.; Mason, J. A.; Gonzalez, M. I.; Lee, J. S.; Gygi, D.; Howe, J. D.; Lee, K.; Darwish, T. A.; et al. Comprehensive Study of Carbon Dioxide Adsorption in the Metal–Organic Frameworks M_2(dobdc)(M = Mg, Mn, Fe, Co, Ni, Cu, Zn). *Chem. Sci.* **2014,** *5* (12), 4569–4581.
55. Rowland, C. A.; Lorzing, G. R.; Gosselin, E. J.; Trump, B. A.; Yap, G. P.; Brown, C. M.; Bloch, E. D. Methane Storage in Paddlewheel-Based Porous Coordination Cages. *J. Am. Chem. Soc.* **2018,** *140* (36), 11153–11157.
56. Salles, F.; Jobic, H.; Devic, T.; Guillerm, V.; Serre, C.; Koza, M. M.; Férey, G.; Maurin, G. Diffusion of Binary CO_2/CH_4 Mixtures in the MIL-47 (V) and MIL-53 (Cr) Metal–Organic Framework Type Solids: A Combination of Neutron Scattering Measurements and Molecular Dynamics Simulations. *J. Phys. Chem. C* **2013,** *117* (21), 11275–11284.
57. Dincă, M.; Dailly, A.; Liu, Y.; Brown, C. M.; Neumann, D. A.; Long, J. R. Hydrogen Storage in a Microporous Metal-Organic Framework With Exposed Mn^{2+} Coordination Sites. *J. Am. Chem. Soc.* **2006,** *128* (51), 16876–16883.
58. Peterson, V. K.; Liu, Y.; Brown, C. M.; Kepert, C. J. Neutron Powder Diffraction Study of D_2 Sorption in Cu_3(1,3,5-Benzenetricarboxylate)$_2$. *J. Am. Chem. Soc.* **2006,** *128* (49), 15578–15579.
59. Wu, H.; Zhou, W.; Yildirim, T. Hydrogen Storage in a Prototypical Zeolitic Imidazolate Framework-8. *J. Am. Chem. Soc.* **2007,** *129,* 5314–5315.
60. Fitch, A. N.; Jobic, H.; Renouprez, A. The Localization of Benzene in a Y-Zeolite. *J. Chem. Soc. Chem. Commun.* **1985**, (5), 284–286.
61. Hulvey, Z.; Vlaisavljevich, B.; Mason, J. A.; Tsivion, E.; Dougherty, T. P.; Bloch, E. D.; Head-Gordon, M.; Smit, B.; Long, J. R.; Brown, C. M. Critical Factors Driving the High Volumetric Uptake of Methane in Cu_3(btc)$_2$. *J. Am. Chem. Soc.* **2015,** *137* (33), 10816–10825.
62. Herm, Z. R.; Wiers, B. M.; Mason, J. A.; van Baten, J. M.; Hudson, M. R.; Zajdel, P.; Brown, C. M.; Masciocchi, N.; Krishna, R.; Long, J. R. Separation of Hexane Isomers in a Metal-Organic Framework With Triangular Channels. *Science* **2013,** *340* (6135), 960–964.
63. Queen, W. L.; Brown, C. M.; Britt, D. K.; Zajdel, P.; Hudson, M. R.; Yaghi, O. M. Site-Specific CO_2 Adsorption and Zero Thermal Expansion in an Anisotropic Pore Network. *J. Phys. Chem. C* **2011,** *115* (50), 24915–24919.
64. Gilmore, C.; Shankland, K.; Bricogne, G. Applications of the Maximum Entropy Method to Powder Diffraction and Electron Crystallography. *Proc. R. Soc. Lond. A Math. Phys. Sci.* **1914,** *1993* (442), 97–111.
65. Livesey, A. K.; Skilling, J. Maximum Entropy Theory. *Acta Crystallogr. A: Found. Crystallogr.* **1985,** *41* (2), 113–122.
66. Sakata, M.; Sato, M. Accurate Structure Analysis by the Maximum-Entropy Method. *Acta Crystallogr. A: Found. Crystallogr.* **1990,** *46* (4), 263–270.
67. Wang, F.; Evans, H. A.; Kim, K.; Yin, L.; Li, Y.; Tsai, P.-C.; Liu, J.; Lapidus, S. H.; Brown, C. M.; Siegel, D. J.; Chiang, Y.-M. Dynamics of Hydroxyl Anions Promotes Lithium Ion Conduction in Antiperovskite Li_2OHCl. *Chem. Mater.* **2020,** *32* (19), 8481–8491.
68. Toby, B.; Egami, T. Accuracy of Pair Distribution Function Analysis Applied to Crystalline and Non-Crystalline Materials. *Acta Crystallogr. A: Found. Crystallogr.* **1992,** *48* (3), 336–346.
69. Proffen, T.; Billinge, S.; Egami, T.; Louca, D. Structural Analysis of Complex Materials Using the Atomic Pair Distribution Function—A Practical Guide. *Z. Kristallogr.* **2003,** *218* (2), 132–143.
70. Olds, D.; Lawler, K. V.; Paecklar, A. A.; Liu, J.; Page, K.; Peterson, P. F.; Forster, P. M.; Neilson, J. R. Capturing the Details of N_2 Adsorption in Zeolite X Using Stroboscopic Isotope Contrasted Neutron Total Scattering. *Chem. Mater.* **2017,** *30* (1), 296–302.
71. Chapman, K. W.; Chupas, P. J.; Maxey, E. R.; Richardson, J. W. Direct Observation of Adsorbed H_2-Framework Interactions in the Prussian Blue Analogue $Mn^{II}_3[Co^{III}(CN)_6]_2$: The Relative Importance of Accessible Coordination Sites and Van Der Waals Interactions. *Chem. Commun.* **2006**, (38), 4013–4015.
72. Kapelewski, M. T.; Runčevski, T.; Tarver, J. D.; Jiang, H. Z.; Hurst, K. E.; Parilla, P. A.; Ayala, A.; Gennett, T.; FitzGerald, S. A.; Brown, C. M.; et al. Record High Hydrogen Storage Capacity in the Metal–Organic Framework Ni_2(m-dobdc) at Near-Ambient Temperatures. *Chem. Mater.* **2018,** *30* (22), 8179–8189.
73. Panella, B.; Hirscher, M. Raman Studies of Hydrogen Adsorbed on Nanostructured Porous Materials. *Phys. Chem. Chem. Phys.* **2008,** *10* (20), 2910–2917.
74. Lee, S. M.; Park, K. S.; Choi, Y. C.; Park, Y. S.; Bok, J. M.; Bae, D. J.; Nahm, K. S.; Choi, Y. G.; Yu, S. C.; Kim, N.-g.; et al. Hydrogen Adsorption and Storage in Carbon Nanotubes. *Synth. Met.* **2000,** *113* (3), 209–216.
75. Centrone, A.; Brambilla, L.; Zerbi, G. Adsorption of H_2 on Carbon-Based Materials: A Raman Spectroscopy Study. *Phys. Rev. B* **2005,** *71* (24), 245406.
76. Centrone, A.; Siberio-Pérez, D. Y.; Millward, A. R.; Yaghi, O. M.; Matzger, A. J.; Zerbi, G. Raman Spectra of Hydrogen and Deuterium Adsorbed on a Metal–Organic Framework. *Chem. Phys. Lett.* **2005,** *411* (4–6), 516–519.
77. Wong, Y. A.; Martins, V.; Lucier, B. E.; Huang, Y. Solid-State NMR Spectroscopy: A Powerful Technique to Directly Study Small Gas Molecules Adsorbed in Metal–Organic Frameworks. *Chem. Eur. J.* **2019,** *25* (8), 1848–1853.
78. Li, G.; Kobayashi, H.; Taylor, J. M.; Ikeda, R.; Kubota, Y.; Kato, K.; Takata, M.; Yamamoto, T.; Toh, S.; Matsumura, S.; et al. Hydrogen Storage in Pd Nanocrystals Covered With a Metal–Organic Framework. *Nat. Mater.* **2014,** *13* (8), 802–806.

79. Shen, K.; Pietraß, T. ^{2}H Nuclear Magnetic Resonance Spectroscopy of Deuterium Adsorption on Single-Walled Carbon Nanotubes. *Appl. Phys. Lett.* **2004,** *84* (9), 1567–1569.
80. Shen, K. NMR Spectroscopy of Hydrogen Adsorption on Single-Walled Carbon Nanotubes After Exposure to High Pressure. *Solid State Nucl. Magn. Reson.* **2006,** *29,* 125–131.
81. Hoang, T. K.; Webb, M. I.; Mai, H. V.; Hamaed, A.; Walsby, C. J.; Trudeau, M.; Antonelli, D. M. Design and Synthesis of Vanadium Hydrazide Gels for Kubas-Type Hydrogen Adsorption: A New Class of Hydrogen Storage Materials. *J. Am. Chem. Soc.* **2010,** *132* (33), 11792–11798.
82. Hoang, T. K.; Morris, L.; Rawson, J. M.; Trudeau, M. L.; Antonelli, D. M. Multivalent Manganese Hydrazide Gels for Kubas-Type Hydrogen Storage. *Chem. Mater.* **2012,** *24* (9), 1629–1638.
83. Udovic, T.; Brown, C.; Leao, J.; Brand, P.; Jiggetts, R.; Zeitoun, R.; Pierce, T.; Peral, I.; Copley, J.; Huang, Q.; et al. The Design of a Bismuth-Based Auxiliary Filter for the Removal of Spurious Background Scattering Associated With Filter-Analyzer Neutron Spectrometers. *Nucl. Instrum. Methods Phys. Res. Sect. A* **2008,** *588* (3), 406–413.
84. Mitchell, P. C. H. *Vibrational Spectroscopy With Neutrons: With Applications in Chemistry, Biology, Materials Science and Catalysis*; vol. 3; World Scientific, 2005.
85. Silvera, I. F. The Solid Molecular Hydrogens in the Condensed Phase: Fundamentals and Static Properties. *Rev. Mod. Phys.* **1980,** *52* (2), 393.
86. Young, J. A.; Koppel, J. U. Slow Neutron Scattering by Molecular Hydrogen and Deuterium. *Phys. Rev.* **1964,** *135* (3A), A603.
87. Sumida, K.; Brown, C. M.; Herm, Z. R.; Chavan, S.; Bordiga, S.; Long, J. R. Hydrogen Storage Properties and Neutron Scattering Studies of Mg_2(dobdc)—A Metal–Organic Framework With Open Mg^{2+} Adsorption Sites. *Chem. Commun.* **2011,** *47* (4), 1157–1159.
88. Chudley, C.; Elliott, R. Neutron Scattering From a Liquid on a Jump Diffusion Model. *Proc. Phys. Soc.* **1961,** *77* (2), 353.
89. Bée, M. *Quasielastic Neutron Scattering*, Adam Hilger: Philadelphia, PA, USA, 1988.
90. Hempelmann, R. *Quasielastic Neutron Scattering and Solid State Diffusion*, Clarendon Press: Oxford, England, 2000.
91. Yildirim, T. Structure and Dynamics From Combined Neutron Scattering and First-Principles Studies. *Chem. Phys.* **2000,** *261* (1–2), 205–216.
92. Graham, T. XVIII. On the Absorption and Dialytic Separation of Gases by Colloid Septa. *Philos. Trans. R. Soc. Lond.* **1866**, (156), 399–439.
93. Møller, K. T.; Sheppard, D.; Ravnsbæk, D. B.; Buckley, C. E.; Akiba, E.; Li, H.-W.; Jensen, T. R. Complex Metal Hydrides for Hydrogen, Thermal and Electrochemical Energy Storage. *Energies* **2017,** *10* (10), 1645.
94. Züttel, A. Materials for Hydrogen Storage. *Mater. Today* **2003,** *6* (9), 24–33.
95. Garland, N. L.; Papageorgopoulos, D. C.; Stanford, J. M. Hydrogen and Fuel Cell Technology: Progress, Challenges, and Future Directions. *Energy Procedia* **2012,** *28,* 2–11.
96. Mukherjee, U.; Maroufmashat, A.; Ranisau, J.; Barbouti, M.; Trainor, A.; Juthani, N.; El-Shayeb, H.; Fowler, M. Techno-Economic, Environmental, and Safety Assessment of Hydrogen Powered Community Microgrids; Case Study in Canada. *Int. J. Hydrog. Energy* **2017,** *42* (20), 14333–14349.
97. Devlin, P.; Moreland, G. *DOE Hydrogen and Fuel Cells Program Record # 18002*. https://www.hydrogen.energy.gov/pdfs/18002_industry_deployed_fc_powered_lift_trucks.pdf.
98. Saillard, J. Y.; Hoffmann, R. Carbon-Hydrogen and Hydrogen-Hydrogen Activation in Transition Metal Complexes and on Surfaces. *J. Am. Chem. Soc.* **1984,** *106* (7), 2006–2026.
99. Halpern, J. The Catalytic Activation of Hydrogen in Homogeneous, Heterogeneous, and Biological Systems. *Adv. Catal.* **1959,** *11,* 301–370. Elsevier.
100. Kubas, G. J.; Ryan, R.; Swanson, B.; Vergamini, P.; Wasserman, H. Characterization of the First Examples of Isolable Molecular Hydrogen Complexes, $M(CO)_3(PR_3)_2(H_2)$(M = Molybdenum or Tungsten; R = Cy or Isopropyl). Evidence for a Side-on Bonded Dihydrogen Ligand. *J. Am. Chem. Soc.* **1984,** *106* (2), 451–452.
101. Kubas, G. J. Molecular Hydrogen Complexes: Coordination of a σ Bond to Transition Metals. *Acc. Chem. Res.* **1988,** *21* (3), 120–128.
102. Kubas, G. J. *Metal Dihydrogen and S-Bond Complexes: Structure, Theory, and Reactivity*, Springer Science & Business Media, 2001.
103. Crabtree, R. H. Transition Metal Complexation of σ Bonds. *Angew. Chem. Int. Ed.* **1993,** *32* (6), 789–805.
104. Crabtree, R. H. Dihydrogen Complexation. *Chem. Rev.* **2016,** *116* (15), 8750–8769.
105. Mårtensson, A.-S.; Nyberg, C.; Andersson, S. Adsorption of Hydrogen on a Stepped Nickel Surface. *Surf. Sci.* **1988,** *205* (1–2), 12–24.
106. Mårtensson, A.-S.; Nyberg, C.; Andersson, S. Observation of Molecular H_2 Chemisorption on a Nickel Surface. *Phys. Rev. Lett.* **1986,** *57* (16), 2045.
107. Hammer, B.; Nørskov, J. Electronic Factors Determining the Reactivity of Metal Surfaces. *Surf. Sci.* **1995,** *343* (3), 211–220.
108. Ferrin, P.; Kandoi, S.; Nilekar, A. U.; Mavrikakis, M. Hydrogen Adsorption, Absorption and Diffusion on and in Transition Metal Surfaces: A DFT Study. *Surf. Sci.* **2012,** *606* (7–8), 679–689.
109. Groß, A. Hydrogen on Metal Surfaces: Forever Young. *Surf. Sci.* **2012,** *606* (7–8), 690–691.
110. Wilke, S.; Scheffler, M. Potential-Energy Surface for H_2 Dissociation Over Pd (100). *Phys. Rev. B* **1996,** *53* (8), 4926.
111. Upton, T. Activation of Single-Bond Cleavage Processes on Metal Surfaces: A Comparison of Dissociative Hydrogen Adsorption With Simple Gas-Phase Exchange Reactions. *J. Am. Chem. Soc.* **1984,** *106* (6), 1561–1571.
112. Groß, A. Hydrogen Dissociation on Metal Surfaces–A Model System for Reactions on Surfaces. *Appl. Phys. A* **1998,** *67* (6), 627–635.
113. Lischka, M.; Groß, A. Hydrogen Adsorption on an Open Metal Surface: H_2/Pd (210). *Phys. Rev. B* **2002,** *65* (7), 75420.
114. Groß, A.; Scheffler, M. Ab Initio Quantum and Molecular Dynamics of the Dissociative Adsorption of Hydrogen on Pd (100). *Phys. Rev. B* **1998,** *57* (4), 2493.
115. Lototskyy, M.; Yartys, V.; Pollet, B.; Bowman, R., Jr. Metal Hydride Hydrogen Compressors: A Review. *Int. J. Hydrog. Energy* **2014,** *39* (11), 5818–5851.
116. Barnes, R.; Chang, C.-T.; Belhoul, M.; Torgeson, D.; Schoenberger, R.; Beaudry, B.; Seymour, E. Magnetic Resonance Determination of the Electronic Density of States and the Metal-Non-Metal Transition in the LaH_2–LaH_3 System. *J. Less-Common Met.* **1991,** *172,* 411–418.
117. Baranowski, B. Metal-Hydrogen Systems in the High Pressure Range. *Z. Phys. Chem.* **1979,** *114* (114), 59–81.
118. Mohtadi, R.; Orimo, S.-i. The Renaissance of Hydrides as Energy Materials. *Nat. Rev. Mater.* **2016,** *2* (3), 1–15.
119. Schlapbach, L.; Züttel, A. Hydrogen-Storage Materials for Mobile Applications. *Nature* **2002,** *414,* 353–358.
120. Stavila, V.; Klebanoff, L. Metal Hydrides. In *Fuel Cells: Data, Facts, and Figures*, John Wiley and Sons, 2016.
121. Yvon, K.; Fischer, P. Crystal and Magnetic Structures of Ternary Metal Hydrides: A Comprehensive Review. In *Hydrogen in Intermetallic Compounds I*, Springer, 1988; pp 87–138.
122. Abe, J.; Popoola, A.; Ajenifuja, E.; Popoola, O. Hydrogen Energy, Economy and Storage: Review and Recommendation. *Int. J. Hydrog. Energy* **2019,** *44* (29), 15072–15086.
123. Bau, R.; Drabnis, M. H. Structures of Transition Metal Hydrides Determined by Neutron Diffraction. *Inorg. Chim. Acta* **1997,** *259* (1–2), 27–50.
124. Kofu, M.; Yamamuro, O. Dynamics of Atomic Hydrogen in Palladium Probed by Neutron Spectroscopy. *J. Phys. Soc. Jpn.* **2020,** *89* (5), 51002.
125. Otomo, T.; Ikeda, K.; Honda, T. Structural Studies of Hydrogen Storage Materials With Neutron Diffraction: A Review. *J. Phys. Soc. Jpn.* **2020,** *89* (5), 51001.
126. Haucke, W. Kristallstruktur von $CaZn_5$ und $CaCu_5$. *Z. Anorg. Allg. Chem.* **1940,** *244* (1), 17–22.
127. Buschow, K.; Bouten, P.; Miedema, A. Hydrides Formed From Intermetallic Compounds of Two Transition Metals: A Special Class of Ternary Alloys. *Rep. Prog. Phys.* **1982,** *45* (9), 937.
128. Zijlstra, H.; Westendorp, F. Influence of Hydrogen on the Magnetic Properties of SmCo5. *Solid State Commun.* **1969,** *7* (12), 857–859.
129. Gupta, M. Electronic Properties of $LaNi_5$ and $LaNi_5H_7$. *J. Less-Common Met.* **1987,** *130,* 219–228.
130. Liang, G.; Huot, J.; Boily, S.; Van Neste, A.; Schulz, R. Hydrogen Storage in Mechanically Milled Mg–$LaNi_5$ and MgH_2–$LaNi_5$ Composites. *J. Alloys Compd.* **2000,** *297* (1–2), 261–265.
131. Belkbir, L.; Gerard, N.; Percheron-Guegan, A.; Achard, J. Kinetics of Hydrogen Absorption and Desorption by Ternary $LaNi_5$-Type Intermetallic Compounds. *Int. J. Hydrog. Energy* **1979,** *4* (6), 541–557.
132. Van Vucht, J.; Kuijpers, F.; Bruning, H. Reversible Room-Temperature Absorption of Large Quantities of Hydrogen by Intermetallic Compounds. *Philips Res. Rep.* **1970,** *25,* 133–140.
133. Chen, P.; Zhu, M. Recent Progress in Hydrogen Storage. *Mater. Today* **2008,** *11* (12), 36–43.

134. Yvon, K. Structural Aspects of Ternary Metal Hydrides: A Critical Review. *J. Less-Common Met.* **1984,** *103* (1), 53–70.
135. Fischer, P.; Furrer, A.; Busch, G.; Schlapbach, L. Neutron Scattering Investigations of the $LaNi_5$ Hydrogen Storage System. *Helv. Phys. Acta* **1977,** *50,* 421–430.
136. Lartigue, C.; Percheron-Guégan, A.; Achard, J.; Soubeyroux, J. Hydrogen (Deuterium) Ordering in the β-$LaNi_5D_{x>5}$ Phases: A Neutron Diffraction Study. *J. Less-Common Met.* **1985,** *113* (1), 127–148.
137. Thompson, P.; Reilly, J.; Corliss, L.; Hastings, J.; Hempelmann, R. The Crystal Structure of $LaNi_5D_7$. *J. Phys. F: Met. Phys.* **1986,** *16* (6), 675.
138. Percheron-Guegan, A.; Lartigue, C.; Achard, J. Correlations between the Structural Properties, the Stability and the Hydrogen Content of Substituted $LaNi_5$ Compounds. *J. Less-Common Met.* **1985,** *109* (2), 287–309.
139. Percheron-Guégan, A.; Lartigue, C.; Achard, J.; Germi, P.; Tasset, F. Neutron and X-Ray Diffraction Profile Analyses and Structure of $LaNi_5$, $LaNi_{5-x}Al_x$ and $LaNi_{5-x}Mn_x$ Intermetallics and their Hydrides (Deuterides). *J. Less-Common Met.* **1980,** *74* (1), 1–12.
140. Lartigue, C.; Le Bail, A.; Percheron-Guegan, A. A New Study of the Structure of $LaNi_5D_{6.7}$ Using a Modified Rietveld Method for the Refinement of Neutron Powder Diffraction Data. *J. Less-Common Met.* **1987,** *129,* 65–76.
141. Hayakawa, H.; Nomura, K.; Ishido, Y.; Akiba, E.; Shin, S.; Asano, H.; Izumi, F.; Watanabe, N. Time-of-Flight Neutron Powder Diffraction Study of the $LaNi_5D_3$ Structure. *J. Less-Common Met.* **1988,** *143* (1–2), 315–324.
142. Hempelmann, R.; Richter, D.; Eckold, G.; Rush, J.; Rowe, J.; Montoya, M. Localized Hydrogen Modes in $LaNi_5H_x$. *J. Less-Common Met.* **1984,** *104* (1), 1–12.
143. Achard, J.; Lartigue, C.; Percheron-Guégan, A.; Dianoux, A.; Tasset, F. Hydrogen Mobility in $LaNi_5$ Hydride and Its Aluminium-and Manganese-Substituted Hydrides. *J. Less-Common Met.* **1982,** *88* (1), 89–96.
144. Gray, E. M. A.; Kemali, M.; Mayers, J.; Norland, J. Interstitial Site Occupation in α-$LaNi_5$-H Studied by Deep Inelastic Neutron Scattering. *J. Alloys Compd.* **1997,** *253,* 291–294.
145. Schönfeld, C.; Hempelmann, R.; Richter, D.; Springer, T.; Dianoux, A.; Rush, J.; Udovic, T.; Bennington, S. Dynamics of Hydrogen in α-$LaNi_5$ Hydride Investigated by Neutron Scattering. *Phys. Rev. B* **1994,** *50* (2), 853.
146. Ross, D. Neutron Scattering Studies of Metal Hydrogen Systems. In *Hydrogen in Metals III*, Springer, 1997; pp 153–214.
147. Karlicek, R., Jr.; Lowe, I. Hydrogen Diffusion in β-$LaNi_5$ Hydride. *J. Less-Common Met.* **1980,** *73* (2), 219–225.
148. Karlicek, R., Jr.; Lowe, I. A Modified Pulsed Gradient Technique for Measuring Diffusion in the Presence of Large Background Gradients. *J. Magn. Reson.* **1980,** *37* (1), 75–91.
149. Majer, G.; Kaess, U.; Bowman, R., Jr. Nuclear Magnetic Resonance Studies of Hydrogen Diffusion in $LaNi_{5.0}H_{6.0}$ and $LaNi_{4.8}Sn_{0.2}H_{5.8}$. *Phys. Rev. B* **1998,** *57* (21), 13599.
150. Kisi, E.; Gray, E. M. A.; Kennedy, S. A Neutron Diffraction Investigation of the LaNi5D Phase Diagram. *J. Alloys Compd.* **1994,** *216* (1), 123–129.
151. Pitt, M.; Gray, E. M.; Kisi, E.; Hunter, B. Neutron Diffraction Study of the $LaNi_5$–D System During Activation. *J. Alloys Compd.* **1999,** *293,* 118–123.
152. Moze, O.; Buschow, K. Neutron Diffraction Investigation of Preferred Site Occupation in Several $CaCu_5$-Type Compounds of Cerium. *J. Magn. Magn. Mater.* **1995,** *146* (1–2), 111–116.
153. Bobet, J.; Pechev, S.; Chevalier, B.; Darriet, B. Structural and Hydrogen Sorption Studies of $NdNi_{5-x}Al_x$ and $GdNi_{5-x}Al_x$. *J. Alloys Compd.* **1998,** *267* (1–2), 136–141.
154. Zlotea, C.; Isnard, O. Neutron Powder Diffraction and Magnetic Phase Diagram of RCo_4Ga Compounds (R = Y and Pr). *J. Alloys Compd.* **2002,** *346* (1–2), 29–37.
155. Pitt, M.; Brinks, H.; Jensen, J. O.; Hauback, B. An In-Situ Neutron Diffraction Study of the Ageing of $CaNi_5D_x$ at 80 C and 9 Bar. *J. Alloys Compd.* **2004,** *372* (1–2), 190–196.
156. Nakamura, J.; Iwase, K.; Hayakawa, H.; Nakamura, Y.; Akiba, E. Structural Study of La_4MgNi_{19} Hydride by In Situ X-Ray and Neutron Powder Diffraction. *J. Phys. Chem. C* **2009,** *113* (14), 5853–5859.
157. Roquefere, J.-G.; Matar, S. F.; Huot, J.; Bobet, J.-L. X-Ray/Neutron Diffraction Studies and Ab Initio Electronic Structure of $CeMgNi_4$ and Its Hydride. *Solid State Sci.* **2009,** *11* (11), 1971–1978.
158. Burnasheva, V.; Semenenko, K.; Fadeeva, N.; Solov'ev, S.; et al. Crystal Chemistry of $RT_5H(D)_x$, $RT_2H(D)_x$ and $RT_3H(D)_x$ Hydrides Based on Intermetallic Compounds of $CaCu_5$, $MgCu_2$, $MgZn_2$ and $PuNi_3$ Structure Types. *Int. J. Hydrog. Energy* **1982,** *7* (12), 957–965.
159. Latroche, M.; Rodriguez-Carvajal, J.; Percheron-Guégan, A.; Bourée-Vigneron, F. Structural Studies of $LaNi_4CoD_{6.11}$ and $LaNi_{3.55}Mn_{0.4}Al_{0.3}Co_{0.75}D_{5.57}$ by Means of Neutron Powder Diffraction. *J. Alloys Compd.* **1995,** *218* (1), 64–72.
160. Gurewitz, E.; Pinto, H.; Dariel, M.; Shaked, H. Neutron Diffraction Study of $LaNi_4Co$ and $LaNi_4CoD_4$. *J. Phys. F: Met. Phys.* **1983,** *13* (3), 545.
161. Fultz, B.; Witham, C.; Udovic, T. Distributions of Hydrogen and Strains in $LaNi_5$ and $LaNi_{4.75}Sn_{0.25}$. *J. Alloys Compd.* **2002,** *335* (1–2), 165–175.
162. Shaltiel, D.; Jacob, I.; Davidov, D. Hydrogen Absorption and Desorption Properties of AB2 Laves-Phase Pseudobinary Compounds. *J. Less-Common Met.* **1977,** *53* (1), 117–131.
163. Shaltiel, D. Hydride Properties of AB_2 Laves Phase Compounds. *J. Less-Common Met.* **1978,** *62,* 407–416.
164. Pebler, A.; Gulbransen, E. Thermochemical and Structural Aspects of the Reaction of Hydrogen With Alloys and Intermetallic Compounds of Zirconium. *Electrochem. Technol.* **1966,** *4,* 211.
165. Pebler, A.; Gulbransen, E. Equilibrium Studies on the Systems $ZrCr_2H_2$, ZrV_2H_2, and $ZrMo_2H_2$ Between 0° and 900°C. *Trans. Metall. Soc. AIME* **1967,** *239* (10), 1593–1600.
166. Laves, F.; Witte, H. Die Kristallstruktur des $MgNi_2$ und seine Beziehungen zu den Typen $MgCu_2$ und $MgZn_2$. *Metallwirtsch. Metallwiss. Metalltech.* **1935,** *14* (33), 645–649.
167. Didisheim, J.-J.; Yvon, K.; Shaltiel, D.; Fischer, P. The Distribution of the Deuterium Atoms in the Deuterated Hexagonal Laves-Phase $ZrMn_2D_3$. *Solid State Commun.* **1979,** *31* (1), 47–50.
168. Didisheim, J.; Fischer, P. Structural and Magnetic Phase Transitions in $ZrMn_2D_3$. *J. Less-Common Met.* **1984,** *103* (2), 267–275.
169. Skripov, A.; Udovic, T.; Rush, J. Hydrogen Jump Diffusion in C14-Type $ZrMn_2H_3$: Quasielastic Neutron Scattering Study. *Phys. Rev. B* **2007,** *76* (10), 104305.
170. Skripov, A.; Soloninin, A.; Buzlukov, A.; Voyevodina, L.; Cook, J.; Udovic, T.; Hempelmann, R. Hydrogen Motion in C14-Type $HfCr_2H_x$: Quasielastic Neutron Scattering and NMR Studies. *J. Phys. Condens. Matter* **2005,** *17* (33), 5011.
171. Skripov, A.; Pionke, M.; Randl, O.; Hempelmann, R. Quasielastic Neutron Scattering Study of Hydrogen Motion in C14-and C15-Type $ZrCr_2H_x$. *J. Phys. Condens. Matter* **1999,** *11* (6), 1489.
172. Cappelletti, R.; Udovic, T.; Chowdhuri, Z.; Hauback, B.; Maeland, A.; Dimeo, R. Diffusive Hydrogen Motion in $ZrBe_2H_{0.56}$: A Quasielastic Neutron Scattering Study. *Phys. B Condens. Matter* **2006,** *385,* 208–211.
173. Fruchart, D.; Rouault, A.; Shoemaker, C.; Shoemaker, D. Neutron Diffraction Studies of the Cubic $ZrCr_2D_x$ and $ZrV_2D_x(H_x)$ Phases. *J. Less-Common Met.* **1980,** *73* (2), 363–368.
174. Skripov, A.; Paul-Boncour, V.; Udovic, T. J.; Rush, J. J. Hydrogen Dynamics in Laves-Phase Hydride $YFe_2H_{2.6}$: Inelastic and Quasielastic Neutron Scattering Studies. *J. Alloys Compd.* **2014,** *595,* 28–32.
175. Skripov, A. V.; Udovic, T. J.; Rush, J. J.; Uimin, M. A Neutron Scattering Study of Hydrogen Dynamics in Coarse-Grained and Nanostructured $ZrCr_2H_3$. *J. Phys. Condens. Matter* **2011,** *23* (6), 65402.
176. Skripov, A.; Buzlukov, A.; Kozhanov, V.; Udovic, T.; Huang, Q. Hydrogen in $Nb(V_{1-y}Cr_y)_2$ Laves-Phase Compounds: Neutron Diffraction and Nuclear Magnetic Resonance Studies. *J. Alloys Compd.* **2003,** *359* (1–2), 27–34.
177. Skripov, A.; Cook, J.; Udovic, T.; Gonzalez, M.; Hempelmann, R.; Kozhanov, V. Quasielastic Neutron Scattering Study of Hydrogen Motion in C15-Type YMn_2H_x. *J. Phys. Condens. Matter* **2003,** *15* (21), 3555.
178. Skripov, A.; Cook, J.; Udovic, T.; Kozhanov, V.; Hempelmann, R. Quasielastic Neutron Scattering Studies of H Motion in Laves-Phase Compounds. *Appl. Phys. A* **2002,** *74* (1), s948–s950.
179. Kohlmann, H.; Fauth, F.; Yvon, K. Hydrogen Order in Monoclinic $ZrCr_2H_{3.8}$. *J. Alloys Compd.* **1999,** *285* (1–2), 204–211.
180. Skripov, A.; Cook, J.; Udovic, T.; Kozhanov, V. Quasielastic Neutron Scattering Study of Hydrogen Motion in C15-type $HfMo_2H_{0.26}$. *Phys. Rev. B* **2000,** *62* (21), 14099.

181. Skripov, A.; Udovic, T.; Huang, Q.; Cook, J.; Kozhanov, V. Neutron Diffraction Study of the Location of Deuterium in the Deuterium-Stabilized $ZrTi_2D_{3.83}$ Phase. *J. Alloys Compd.* **2000,** *311* (2), 234–237.
182. Skripov, A.; Cook, J.; Sibirtsev, D.; Karmonik, C.; Hempelmann, R. Quasielastic Neutron Scattering Study of Hydrogen Motion in C15-Type $TaHf_2H_x$. *J. Phys. Condens. Matter* **1998,** *10* (8), 1787.
183. Fish, G.; Rhyne, J.; Sankar, S.; Wallace, W. Effect of Hydrogen on Sublattice Magnetization of Laves-Phase Rare Earth Iron Compounds. *J. Appl. Phys.* **1979,** *50* (B3), 2003–2005.
184. Pourarian, F.; Wallace, W.; Malik, S. Magnetic Behavior of Laves Phase $RCo_{2-x}Fe_x$ (R = Ho, Er) Compounds and Their Hydrides. *J. Magn. Magn. Mater.* **1982,** *25* (3), 299–306.
185. Li, X.; Chiba, A.; Takahashi, S.; Aoki, K.; Masumoto, T. Changes in Magnetic Properties of C15 Laves Compound RCo_2 Due to Hydrogenation. *Intermetallics* **1999,** *7* (2), 207–211.
186. Fujii, H.; Pourarian, F.; Wallace, W. Influence of Hydrogen Absorption on Magnetic Ordering in Some Zirconium-Based Laves Phase Compounds. *J. Less-Common Met.* **1982,** *88* (1), 187–193.
187. Wiesinger, G.; Hilscher, G. Magnetism of Hydrides. *Handb. Magn. Mater.* **1991,** *6,* 511–584.
188. Pourarian, F.; Fujii, H.; Wallace, W.; Sinha, V.; Smith, H. K. Stability and Magnetism of Hydrides of Nonstoichiometric $ZrMn_2$. *J. Phys. Chem.* **1981,** *85* (21), 3105–3111.
189. Didisheim, J.-J.; Yvon, K.; Fischer, P.; Tissot, P. Order-Disorder Phase Transition in ZrV_2D_3. 6. *Solid State Commun.* **1981,** *38* (7), 637–641.
190. Soubeyroux, J.; Bououdina, M.; Fruchart, D.; Pontonnier, L. Phase Stability and Neutron Diffraction Studies of Laves Phases $Zr(Cr_{1-x}M_x)_2$ with M = Mn, Fe, Co, Ni, Cu and $0 < x < 0.2$ and Their Hydrides. *J. Alloys Compd.* **1995,** *219* (1–2), 48–54.
191. Paul-Boncour, V.; Guénée, L.; Latroche, M.; Percheron-Guégan, A.; Ouladdiaf, B.; Bourée-Vigneron, F. Elaboration, Structures, and Phase Transitions for YFe_2D_x Compounds (x = 1.3, 1.75, 1.9, 2.6) Studied by Neutron Diffraction. *J. Solid State Chem.* **1999,** *142* (1), 120–129.
192. Irodova, A.; Glazkov, V.; Somenkov, V.; Shilstein, S. S. Hydrogen Ordering in the Cubic Laves Phase HfV_2. *J. Less-Common Met.* **1981,** *77* (1), 89–98.
193. Irodova, A.; Andre, G.; Bouree, F. Phase Transition Between Hydrogen Superstructures With k = (001) and k = 0 Via Incommensurate Phase in ZrV_2D_x ($2.8 \leq x \leq 3.9$). *J. Alloys Compd.* **2000,** *302* (1–2), 159–168.
194. Fruchart, D.; Soubeyroux, J.; Hempelmann, R. Neutron Diffraction in $Ti_{1.2}Mn_{1.8}$ Deuteride: Structural and Magnetic Aspects. *J. Less-Common Met.* **1984,** *99* (2), 307–319.
195. Kohlmann, H.; Fauth, F.; Fischer, P.; Skripov, A.; Kozhanov, V.; Yvon, K. Low-Temperature Deuterium Ordering in the Cubic Laves Phase Derivative α-$ZrCr_2D_{0.66}$. *J. Alloys Compd.* **2001,** *327* (1–2), L4–L9.
196. Kohlmann, H.; Yvon, K. Revision of the Low-Temperature Structures of Rhombohedral $ZrCr_2D_x$ ($x \sim 3.8$), and Monoclinic ZrV_2D_x ($1.1 < x < 2.3$) and HfV_2D_x ($x \sim 1.9$). *J. Alloys Compd.* **2000,** *309* (1–2), 123–126.
197. Fischer, P.; Fauth, F.; Skripov, A.; Podlesnyak, A.; Padurets, L.; Shilov, A.; Ouladdiaf, B. Neutron Diffraction Study of Deuterium Ordering in C15 Type TaV_2D_x ($x > 1$) in the Temperature Range of 1.5–295 K. *J. Alloys Compd.* **1997,** *253,* 282–285.
198. Bououdina, M.; Soubeyroux, J.; Fruchart, D. Study of the Hydrogenation/Dehydrogenation Processes of $ZrCr_{0.7}Ni_{1.3}$, a Laves Phase-Rich Multi-Component System, by In-Situ Neutron Diffraction Under Hydrogen Gas Pressure. *J. Alloys Compd.* **2001,** *327* (1–2), 185–194.
199. Ouyang, Z.; Wang, F.; Hang, Q.; Liu, W.; Liu, G.; Lynn, J.; Liang, J.; Rao, G. Temperature Dependent Neutron Powder Diffraction Study of the Laves Phase Compound $TbCo_2$. *J. Alloys Compd.* **2005,** *390* (1–2), 21–25.
200. Latroche, M.; Paul-Boncour, V.; Percheron-Guégan, A.; Bourée-Vigneron, F. Temperature Dependence Study of $YMn_2D_{4.5}$ by Means of Neutron Powder Diffraction. *J. Alloys Compd.* **1998,** *274* (1–2), 59–64.
201. Götze, A.; Möllmer, J.; Kohlmann, H. From the Laves Phase $CaRh_2$ to the Perovskite $CaRhH_3$–In Situ Investigation of Hydrogenation Intermediates $CaRh_2H_x$. *Inorg. Chem.* **2018,** *57* (17), 10925–10934.
202. Werwein, A.; Maaß, F.; Dorsch, L. Y.; Janka, O.; Pöttgen, R.; Hansen, T. C.; Kimpton, J.; Kohlmann, H. Hydrogenation Properties of Laves Phases $LnMg_2$ (Ln = La, Ce, Pr, Nd, Sm, Eu, Gd, Tb, Ho, Er, Tm, Yb). *Inorg. Chem.* **2017,** *56* (24), 15006–15014.
203. Rönnebro, E.; Noréus, D.; Tsukahara, M.; Sakai, T. Neutron Diffraction Study of the New Hexagonal Laves Phase $(Hf,Ti)(Ni,V)_2$ and Its Deuteride. *J. Alloys Compd.* **1999,** *293,* 169–173.
204. Gross, K.; Chartouni, D.; Fauth, F. A New Hexagonal Laves Phase Deuteride $CeMn_{1.5}Al_{0.5}D_x$ ($0 < x < 4$): Investigated by In Situ Neutron Diffraction. *J. Alloys Compd.* **2000,** *306* (1–2), 203–218.
205. Andresen, A. Structure and Phase Relations in Metal Hydrides Studied by Neutron Diffraction. *J. Less-Common Met.* **1982,** *88* (1), 1–8.
206. Makarova, O.; Goncharenko, I.; Irodova, A.; Mirebeau, I.; Suard, E. Interplay of Magnetic and Hydrogen Ordering in the Hexagonal Laves Hydrides. *Phys. Rev. B* **2002,** *66* (10), 104423.
207. Reilly, J. J., Jr.; Wiswall, R. H., Jr. Reaction of Hydrogen With Alloys of Magnesium and Nickel and the Formation of Mg_2NiH_4. *Inorg. Chem.* **1968,** *7* (11), 2254–2256.
208. Buchner, H.; Gutjahr, M. A.; Beccu, K. D.; Saufferer, H. Wasserstoff in Intermetallischen Phasen Am Beispiel Des Systems Titan-Nickel-Wasserstoff. *Z. Metalkunde* **1972,** *63,* 497–500.
209. Wu, H.; Skripov, A.; Udovic, T.; Rush, J.; Derakhshan, S.; Kleinke, H. Hydrogen in Ti_3Sb and Ti_2Sb: Neutron Vibrational Spectroscopy and Neutron Diffraction Studies. *J. Alloys Compd.* **2010,** *496* (1–2), 1–6.
210. Sandrock, G. A Panoramic Overview of Hydrogen Storage Alloys From a Gas Reaction Point of View. *J. Alloys Compd.* **1999,** *293,* 877–888.
211. Schefer, J.; Fischer, P.; Hälg, W.; Stucki, F.; Schlapbach, L.; Didisheim, J.; Yvon, K.; Andresen, A. New Structure Results for Hydrides and Deuterides of the Hydrogen Storage Material Mg_2Ni. *J. Less-Common Met.* **1980,** *74* (1), 65–73.
212. Dornheim, M.; Doppiu, S.; Barkhordarian, G.; Boesenberg, U.; Klassen, T.; Gutfleisch, O.; Bormann, R. Hydrogen Storage in Magnesium-Based Hydrides and Hydride Composites. *Scr. Mater.* **2007,** *56* (10), 841–846.
213. Noréus, D.; Werner, P.-E. Structural Studies of Monoclinic Mg_2NiD_4. *J. Less-Common Met.* **1984,** *97,* 215–222.
214. Noreus, D.; Olsson, L. The Structure and Dynamics of Hydrogen in Mg_2NiH_4 Studied by Elastic and Inelastic Neutron Scattering. *J. Chem. Phys.* **1983,** *78* (5), 2419–2427.
215. Soubeyroux, J.; Fruchart, D.; Mikou, A.; Pezat, M.; Darriet, B. Etude structurale du systeme Mg_2Ni–H_2: I – La solution solide Mg_2NiH_x (x = 0.30). *Mater. Res. Bull.* **1984,** *19* (7), 895–904.
216. Soubeyroux, J.; Fruchart, D.; Mikou, A.; Pezat, M.; Darriet, B.; Hagenmuller, P. Etude structurale du system Mg_2Ni–H_2: II – La variete haute temperature de Mg_2NiH_4 de symetrie cubique. *Mater. Res. Bull.* **1984,** *19* (8), 969–978.
217. Soubeyroux, J.; Fruchart, D.; Mikou, A.; Pezat, M.; Darriet, B. Etude structurale du systeme Mg_2Ni–H_2: III—La variete monoclinique de Mg_2NiH_4. *Mater. Res. Bull.* **1984,** *19* (9), 1119–1128.
218. Yvon, K.; Schefer, J.; Stucki, F. Structural Studies of the Hydrogen Storage Material $Mg_2NiH_{4.1}$. Cubic High-Temperature Structure. *Inorg. Chem.* **1981,** *20* (9), 2776–2778.
219. Zolliker, P.; Yvon, K.; Baerlocher, C.; Jorgensen, J.; Rotella, F. Low Temperature Structure of Mg_2NiD_4: A Combined Study of High Resolution X-Ray and Neutron Diffraction. *J. Less-Common Met.* **1987,** *129,* 208–209.
220. Zolliker, P.; Yvon, K.; Jorgensen, J.; Rotella, F. Structural Studies of the Hydrogen Storage Material Magnesium Nickel Hydride (Mg_2NiH_4). 2. Monoclinic Low-Temperature Structure. *Inorg. Chem.* **1986,** *25* (20), 3590–3593.
221. Zolliker, P.; Yvon, K. Comments on the Structure Ambiguity of Cubic Mg_2NiH_4 as Found by Neutron Powder Diffraction Analysis. *Mater. Res. Bull.* **1986,** *21* (4), 415–419.
222. Martinez-Coronado, R.; Retuerto, M.; Alonso, J. Simplified Mechano-Synthesis Procedure of Mg_2NiH_4. *Int. J. Hydrog. Energy* **2012,** *37* (5), 4188–4193.
223. Konstanchuk, I. G.; Ivanov, E. Y.; Boldyrev, V. V. Interaction of Alloys and Intermetallic Compounds Obtained by Mechanochemical Methods With Hydrogen. *Russ. Chem. Rev.* **1998,** *67* (1), 69–79.

224. Bergemann, N.; Pistidda, C.; Uptmoor, M.; Milanese, C.; Santoru, A.; Emmler, T.; Puszkiel, J.; Dornheim, M.; Klassen, T. A New Mutually Destabilized Reactive Hydride System: $LiBH_4$–Mg_2NiH_4. *J. Energy Chem.* **2019,** *34,* 240–254.
225. Tran, X. Q.; McDonald, S. D.; Gu, Q.; Yamamoto, T.; Shigematsu, K.; Aso, K.; Tanaka, E.; Matsumura, S.; Nogita, K. In-Situ Investigation of the Hydrogen Release Mechanism in Bulk Mg_2NiH_4. *J. Power Sources* **2017,** *341,* 130–138.
226. Anderson, I.; Berk, N.; Rush, J.; Udovic, T. Concentration and Temperature Dependence of Hydrogen Vibrations Along the c Axis for Hydrogen in Yttrium: Evidence of Dynamically Coupled Hydrogen Pairs. *Phys. Rev. B* **1988,** *37* (9), 4358.
227. Anderson, I.; Rush, J.; Udovic, T.; Rowe, J. Hydrogen Pairing and Anisotropic Potential for Hydrogen Isotopes in Yttrium. *Phys. Rev. Lett.* **1986,** *57* (22), 2822.
228. Rundle, R.; Shull, C.; Wollan, E. O. The Crystal Structure of Thorium and Zirconium Dihydrides by X-Ray and Neutron Diffraction. *Acta Crystallogr.* **1952,** *5* (1), 22–26.
229. Udovic, T.; Rush, J.; Anderson, I. Neutron Spectroscopic Evidence of Concentration-Dependent Hydrogen Ordering in the Octahedral Sublattice of β-TbH_{2+x}. *Phys. Rev. B* **1994,** *50* (10), 7144.
230. Udovic, T.; Huang, Q.; Rush, J. Characterization of the Structure of YD_3 by Neutron Powder Diffraction. *J. Phys. Chem. Solids* **1996,** *57* (4), 423–435.
231. Udovic, T.; Huang, Q.; Rush, J. Characterization of the Structure of $LaD_{2.50}$ by Neutron Powder Diffraction. *J. Solid State Chem.* **1996,** *122* (1), 151–159.
232. Vajda, P.; André, G.; Udovic, T.; Erwin, R.; Huang, Q. Magnetic Structure of β-ErD_2: Long-Range and Short-Range Order From Powder Neutron Diffraction. *Phys. Rev. B* **2005,** *71* (5), 54419.
233. Udovic, T.; Rush, J.; Anderson, I. Neutron Spectroscopic Comparison of β-Phase Rare Earth Hydrides. *J. Alloys Compd.* **1995,** *231* (1–2), 138–143.
234. Udovic, T.; Rush, J.; Hempelmann, R.; Richter, D. Low-Energy Vibrations and Octahedral Site Occupation in $Nb_{95}V_5H(D)_y$. *J. Alloys Compd.* **1995,** *231* (1–2), 144–146.
235. Berk, N.; Rush, J.; Udovic, T.; Anderson, I. Anomalous Hydrogen Dynamics in Rare Earth Metals. *J. Less-Common Met.* **1991,** *172,* 496–508.
236. Udovic, T.; Huang, Q.; Rush, J. A Neutron-Powder-Diffraction Study of the Rare-Earth Deuteride Two-Phase Region. *J. Alloys Compd.* **2003,** *356,* 41–44.
237. Glagolenko, I.; Carney, K.; Kern, S.; Goremychkin, E.; Udovic, T.; Copley, J.; Cook, J. Quantitative Analysis of UH_3 in U Metal and UO_2 Matrices by Neutron Vibrational Spectroscopy. *Appl. Phys. A* **2002,** *74* (1), s1397–s1399.
238. Huang, Q.; Udovic, T.; Rush, J.; Schefer, J.; Anderson, I. Characterization of the Structure of $TbD_{2.25}$ at 70 K by Neutron Powder Diffraction. *J. Alloys Compd.* **1995,** *231* (1–2), 95–98.
239. Udovic, T.; Huang, Q.; Rush, J.; Schefer, J.; Anderson, I. Neutron-Powder-Diffraction Study of the Long-Range Order in the Octahedral Sublattice of $LaD_{2.25}$. *Phys. Rev. B* **1995,** *51* (18), 12116.
240. Udovic, T.; Rush, J.; Anderson, I. Local-Mode Dynamics in YH_2 and YD_2 by Isotope-Dilution Neutron Spectroscopy. *Phys. Rev. B* **1994,** *50* (21), 15739.
241. Udovic, T.; Rush, J.; Anderson, I.; Daou, J.; Vajda, P.; Blaschko, O. Vibrations of Hydrogen and Deuterium in Solid Solution With Lutetium. *Phys. Rev. B* **1994,** *50* (6), 3696.
242. Hauer, B.; Hempelmann, R.; Udovic, T.; Rush, J.; Jansen, E.; Kockelmann, W.; Schäfer, W.; Richter, D. Neutron-Scattering Studies on the Vibrational Excitations and the Structure of Ordered Niobium Hydrides: The ε Phase. *Phys. Rev. B* **1998,** *57* (18), 11115.
243. Hauer, B.; Hempelmann, R.; Udovic, T.; Rush, J.; Kockelmann, W.; Schäfer, W.; Jansen, E.; Richter, D. Neutron Scattering Studies on the Vibrational Excitations and the Structure of Ordered Niobium Hydrides: The λ Phases. *J. Phys. Condens. Matter* **2004,** *16* (29), 5205.
244. Hauer, B.; Hempelmann, R.; Udovic, T.; Rush, J.; Kockelmann, W.; Jansen, E.; Schäfer, W.; Richter, D. Structure and Microdomain Structure of Ordered Niobium Hydrides and Deuterides by Means of Neutron Scattering. *J. Alloys Compd.* **1997,** *253,* 258–259.
245. Udovic, T.; Huang, Q.; Lynn, J.; Erwin, R.; Rush, J. Neutron-Scattering Study of the Nuclear and Magnetic Structure of DyD_3 and Associated Vibrational and Magnetic Excitations. *Phys. Rev. B* **1999,** *59* (18), 11852.
246. Udovic, T.; Rush, J.; Anderson, I. Characterization of the Vibrational Dynamics in the Octahedral Sublattices of $LaD_{2.25}$ and $LaH_{2.25}$. *J. Phys. Condens. Matter* **1995,** *7* (35), 7005.
247. Numakura, H.; Koiwa, M.; Asano, H.; Izumi, F. Neutron Diffraction Study of the Metastable γ Titanium Deuteride. *Acta Metall.* **1988,** *36* (8), 2267–2273.
248. Anderson, I.; Berk, N.; Rush, J.; Udovic, T.; Barnes, R.; Magerl, A.; Richter, D. Rapid Low-Temperature Hopping of Hydrogen in a Pure Metal: The ScH_x System. *Phys. Rev. Lett.* **1990,** *65* (12), 1439.
249. Udovic, T.; Huang, Q.; Karmonik, C.; Rush, J. Structural Ordering and Dynamics of LaH_{3-x}. *J. Alloys Compd.* **1999,** *293,* 113–117.
250. Udovic, T.; Rush, J.; Anderson, I.; Barnes, R. Hydrogen Vibrational Modes and Anisotropic Potential in α-ScH_x. *Phys. Rev. B* **1990,** *41* (6), 3460.
251. Zachariasen, W.; Holley, C.; Stamper, J. Neutron Diffraction Study of Magnesium Deuteride. *Acta Crystallogr.* **1963,** *16* (5), 352–353.
252. Moser, D.; Bull, D.; Cowpe, J.; Roach, D.; Ross, D.; Noréus, D.; Tucker, M. An *In Situ* Neutron Diffraction Measurement of the Pressure–Temperature Evolution of a MgD_2:TiD_2 Mixture. *High Pressure Res.* **2010,** *30* (4), 643–652.
253. Vajeeston, P.; Ravindran, P.; Hauback, B.; Fjellvåg, H.; Kjekshus, A.; Furuseth, S.; Hanfland, M. Structural Stability and Pressure-Induced Phase Transitions in MgH_2. *Phys. Rev. B* **2006,** *73* (22), 224102.
254. Bortz, M.; Bertheville, B.; Böttger, G.; Yvon, K. Structure of the High Pressure Phase γ-MgH_2 by Neutron Powder Diffraction. *J. Alloys Compd.* **1999,** *287* (1–2), L4–L6.
255. Nicol, J. M.; Udovic, T. J.; Rush, J.; Kelley, R. D. Isotope Dilution Neutron Spectroscopy: A Vibrational Probe of Hydrogen/Deuterium Adsorbate Interactions on Palladium Black. *Langmuir* **1988,** *4* (2), 294–297.
256. Carstanjen, H.-D.; Huang, X.; Kieninger, W.; Kirchheim, R.; Rush, J.; Udovic, T.; Glinka, J.; Petry, A. A Neutron Scattering Study of Deuterium Trapping by Dislocations. *Z. Phys. Chem.* **1989,** *163* (1), 203–204.
257. Frieske, H.; Wicke, E. Magnetic Susceptibility and Equilibrium Diagram of PdH_n. *Ber. Bunsenges. Phys. Chem.* **1973,** *77* (1), 48–52.
258. Manchester, F.; San-Martin, A.; Pitre, J. The H-Pd (Hydrogen-Palladium) System. *J. Phase Equilib.* **1994,** *15* (1), 62–83.
259. Kawae, T.; Inagaki, Y.; Wen, S.; Hirota, S.; Itou, D.; Kimura, T. Superconductivity in Palladium Hydride Systems. *J. Phys. Soc. Jpn.* **2020,** *89* (5), 51004.
260. Bennemann, K.; Garland, J. Theory for Superconductivity in Pd-H and Pd-D Systems. *Z. Phys. A: Hadrons Nucl.* **1973,** *260* (5), 367–374.
261. Jamieson, H.; Manchester, F. The Magnetic Susceptibility of Pd, PdH and PdD Between 4 and 300 K. *J. Phys. F: Met. Phys.* **1972,** *2* (2), 323.
262. Worsham, J.; Wilkinson, M.; Shull, C. Neutron-Diffraction Observations on the Palladium-Hydrogen and Palladium-Deuterium Systems. *J. Phys. Chem. Solids* **1957,** *3* (3–4), 303–310.
263. Nelin, G. A Neutron Diffraction Study of Palladium Hydride. *Phys. Status Solidi B* **1971,** *45* (2), 527–536.
264. McLennan, K.; Gray, E. M.; Dobson, J. Deuterium Occupation of Tetrahedral Sites in Palladium. *Phys. Rev. B* **2008,** *78* (1), 14104.
265. Pitt, M.; Gray, E. M. Tetrahedral Occupancy in the Pd-D System Observed by In Situ Neutron Powder Diffraction. *Europhys. Lett.* **2003,** *64* (3), 344.
266. Kofu, M.; Hashimoto, N.; Akiba, H.; Kobayashi, H.; Kitagawa, H.; Tyagi, M.; Faraone, A.; Copley, J. R.; Lohstroh, W.; Yamamuro, O. Hydrogen Diffusion in Bulk and Nanocrystalline Palladium: A Quasielastic Neutron Scattering Study. *Phys. Rev. B* **2016,** *94* (6), 64303.
267. Akiba, H.; Kobayashi, H.; Kitagawa, H.; Kofu, M.; Yamamuro, O. Glass Transition and Positional Ordering of Hydrogen in Bulk and Nanocrystalline Palladium. *Phys. Rev. B* **2015,** *92* (6), 64202.
268. Stuhr, U.; Wipf, H.; Udovic, T.; Weißmüller, J.; Gleiter, H. Inelastic Neutron Scattering Study of Hydrogen in Nanocrystalline Pd. *Nanostruct. Mater.* **1995,** *6* (5–8), 555–558.
269. Stuhr, U.; Wipf, H.; Udovic, T.; Weissmuller, J.; Gleiter, H. The Vibrational Excitations and the Position of Hydrogen in Nanocrystalline Palladium. *J. Phys. Condens. Matter* **1995,** *7* (2), 219.
270. Sugizaki, Y.; Yamaguchi, S. Neutron Diffraction Study on the Short-Range Order in a $VD_{0.81}$ Single Crystal. *J. Alloys Compd.* **1995,** *231* (1–2), 126–131.
271. Reidinger, F.; Reilly, J.; Stoenner, R. Single Crystal Studies of Cubic Phases of VD_X by Neutron Diffraction. In *Superionic Conductors*, Springer, 1976; pp 427–428.
272. Sidhu, S.; Heaton, L.; Zauberis, D. Neutron Diffraction Studies of Hafnium–Hydrogen and Titanium–Hydrogen Systems. *Acta Crystallogr.* **1956,** *9* (7), 607–614.
273. Chuang, A. C.-P.; Liu, Y.; Udovic, T. J.; Liaw, P. K.; Yu, G.-P.; Huang, J.-H. Inelastic Neutron Scattering Study of the Hydrogenated $(Zr_{55}Cu_{30}Ni_5Al_{10})_{99}Y_1$ Bulk Metallic Glass. *Phys. Rev. B* **2011,** *83* (17), 174206.

274. Sahlberg, M.; Karlsson, D.; Zlotea, C.; Jansson, U. Superior Hydrogen Storage in High-Entropy Alloys. *Sci. Rep.* **2016,** *6,* 36770.
275. Kunce, I.; Polanski, M.; Bystrzycki, J. Microstructure and Hydrogen Storage Properties of a TiZrNbMoV High-Entropy Alloy Synthesized Using Laser Engineered Net Shaping (LENS). *Int. J. Hydrog. Energy* **2014,** *39* (18), 9904–9910.
276. Kunce, I.; Polanski, M.; Bystrzycki, J. Structure and Hydrogen Storage Properties of a High-Entropy ZrTiVCrFeNi Alloy Synthesized Using Laser Engineered Net Shaping (LENS). *Int. J. Hydrog. Energy* **2013,** *38* (27), 12180–12189.
277. Kunce, I.; Polański, M.; Czujko, T. Microstructures and Hydrogen Storage Properties of LaNiFeVMn Alloys. *Int. J. Hydrog. Energy* **2017,** *42* (44), 27154–27164.
278. Karlsson, D.; Ek, G.; Cedervall, J.; Zlotea, C.; Møller, K. T.; Hansen, T. C.; Bednarcik, J.; Paskevicius, M.; Sørby, M. H.; Jensen, T. R.; et al. Structure and Hydrogenation Properties of a HfNbTiVZr High-Entropy Alloy. *Inorg. Chem.* **2018,** *57* (4), 2103–2110.
279. Switendick, A. *Bandstructure Calculations for Metal Hydrogen Systems*, Sandia Labs: Albuquerque, NM, USA, 1979.
280. Rao, B.; Jena, P. Switendick Criterion for Stable Hydrides. *Phys. Rev. B* **1985,** *31* (10), 6726.
281. Sen, M.; Ghoshray, A.; Ghoshray, K.; Sil, S.; Chatterjee, N. Ordered Arrangement of Proton Pairs in the $PrNiInH_{1.29}$ System. *Phys. Rev. B* **1996,** *53* (21), 14345.
282. Yartys, V.; Denys, R.; Hauback, B.; Fjellvåg, H.; Bulyk, I.; Riabov, A.; Kalychak, Y. M. Short Hydrogen–Hydrogen Separations in Novel Intermetallic Hydrides, $RE_3Ni_3In_3D_4$ (RE = La, Ce and Nd). *J. Alloys Compd.* **2002,** *330,* 132–140.
283. Sen, M.; Giri, S.; Ghoshray, K.; Bandyopadhyay, B.; Ghoshray, A.; Chatterjee, N. Study of Magnetic Susceptibility & Lattice Parameters of $CeNiInH_x$ Systems. *Solid State Commun.* **1994,** *89* (4), 327–330.
284. Ghoshray, K.; Bandyopadhyay, B.; Sen, M.; Ghoshray, A.; Chatterjee, N. Observation of a Pake Doublet in the ^1H Nuclear-Magnetic-Resonance Spectrum of $CeNiInH_x$. *Phys. Rev. B* **1993,** *47* (13), 8277.
285. Borgschulte, A.; Terreni, J.; Billeter, E.; Daemen, L.; Cheng, Y.; Pandey, A.; Łodziana, Z.; Hemley, R. J.; Ramirez-Cuesta, A. J. Inelastic Neutron Scattering Evidence for Anomalous H–H Distances in Metal Hydrides. *Proc. Natl. Acad. Sci.* **2020,** *117* (8), 4021–4026.
286. Didisheim, J.-J.; Yvon, K.; Fischer, P.; Shaltiel, D. The Deuterium Site Occupation in ZrV_2D_x as a Function of the Deuterium Concentration. *J. Less-Common Met.* **1980,** *73* (2), 355–362.
287. Didisheim, J.-J.; Yvon, K.; Shaltiel, D.; Fischer, P.; Bujard, P.; Walker, E. The Distribution of the Deuterium Atoms in the Deuterated Cubic Laves-Phase $ZrV_2D_{4.5}$. *Solid State Commun.* **1979,** *32* (11), 1087–1090.
288. Abrahams, S.; Ginsberg, A.; Knox, K. Transition Metal-Hydrogen Compounds. II. The Crystal and Molecular Structure of Potassium Rhenium Hydride, K_2ReH_9. *Inorg. Chem.* **1964,** *3* (4), 558–567.
289. Wu, H.; Zhou, W.; Udovic, T. J.; Rush, J. J.; Yildirim, T. Structure and Hydrogen Bonding in $CaSiD_{1+x}$: Issues About Covalent Bonding. *Phys. Rev. B* **2006,** *74* (22), 224101.
290. Rönnebro, E.; Noréus, D.; Kadir, K.; Reiser, A.; Bogdanovic, B. Investigation of the Perovskite Related Structures of $NaMgH_3$, $NaMgF_3$ and Na_3AlH_6. *J. Alloys Compd.* **2000,** *299* (1–2), 101–106.
291. Wu, H.; Zhou, W.; Udovic, T. J.; Rush, J. J. Hydrogen Storage in a Novel Destabilized Hydride System, Ca_2SiH_x: Effects of Amorphization. *Chem. Mater.* **2007,** *19* (2), 329–334.
292. Mamontov, E.; Kolesnikov, A. I.; Sampath, S.; Yarger, J. L. Hydrogen Mobility in the Lightest Reversible Metal Hydride, $LiBeH_3$. *Sci. Rep.* **2017,** *7* (1), 1–7.
293. Andrada-Chacón, A.; Alonso, J.; Pomjakushin, V.; Sánchez-Benítez, J. High-Pressure Synthesis and Structural Characterization of $Na_{1-x}K_xMgH_3$ Perovskite Hydrides. *J. Alloys Compd.* **2017,** *729,* 914–920.
294. Wu, H.; Hartman, M. R.; Udovic, T. J.; Rush, J. J.; Zhou, W.; Bowman, R. C., Jr.; Vajo, J. J. Structure of the Novel Ternary Hydrides Li_4Tt_2D (*Tt* = Si and Ge). *Acta Crystallogr. Sect. B: Struct. Sci.* **2007,** *63* (1), 63–68.
295. Gingla, F.; Vogt, T.; Akiba, E.; Yvon, K. Cubic $CsCaH_3$ and Hexagonal $RbMgH_3$: New Examples of Fluoride-Related Perovskite-Type Hydrides. *J. Alloys Compd.* **1999,** *282* (1–2), 125–129.
296. Bertheville, B.; Fischer, P.; Yvon, K. High-Pressure Synthesis and Crystal Structures of New Ternary Caesium Magnesium Hydrides, $CsMgH_3$, $Cs_4Mg_3H_{10}$ and Cs_2MgH_4. *J. Alloys Compd.* **2002,** *330,* 152–156.
297. Wu, H.; Zhou, W.; Udovic, T. J.; Rush, J. J.; Yildirim, T. Crystal Chemistry of Perovskite-Type Hydride $NaMgH_3$: Implications for Hydrogen Storage. *Chem. Mater.* **2008,** *20* (6), 2335–2342.
298. Renaudin, G.; Bertheville, B.; Yvon, K. Synthesis and Structure of an Orthorhombic Low-Pressure Polymorph of Caesium Magnesium Hydride, $CsMgH_3$. *J. Alloys Compd.* **2003,** *353* (1–2), 175–179.
299. Wu, H.; Zhou, W.; Udovic, T. J.; Rush, J. J.; Yildirim, T. Structural Variations and Hydrogen Storage Properties of Ca_5Si_3 with Cr_5B_3-Type Structure. *Chem. Phys. Lett.* **2008,** *460* (4–6), 432–437.
300. Werwein, A.; Kohlmann, H. Synthesis and Crystal Structure of $BaLaSi_2H_{0.80}$. *Z. Anorg. Allg. Chem.* **2020,** *646* (14), 1227–1230.
301. Wu, H.; Zhou, W.; Udovic, T. J.; Rush, J. J.; Yildirim, T. Crystal Chemistry and Dehydrogenation/Rehydrogenation Properties of Perovskite Hydrides $RbMgH_3$ and $RbCaH_3$. *J. Phys. Chem. C* **2009,** *113* (33), 15091–15098.
302. Auer, H.; Yang, F.; Playford, H. Y.; Hansen, T. C.; Franz, A.; Kohlmann, H. Covalent Si–H Bonds in the Zintl Phase Hydride $CaSiH_{1+x}$ ($x \leq 1/3$). *Inorganics* **2019,** *7* (9), 106.
303. Wu, H. Strategies for the Improvement of the Hydrogen Storage Properties of Metal Hydride Materials. *ChemPhysChem* **2008,** *9* (15), 2157–2162.
304. Liu, Y.; Yang, Y.; Gao, M.; Pan, H. Tailoring Thermodynamics and Kinetics for Hydrogen Storage in Complex Hydrides Towards Applications. *Chem. Rec.* **2016,** *16* (1), 189–204.
305. Yu, X.; Tang, Z.; Sun, D.; Ouyang, L.; Zhu, M. Recent Advances and Remaining Challenges of Nanostructured Materials for Hydrogen Storage Applications. *Prog. Mater. Sci.* **2017,** *88,* 1–48.
306. Paskevicius, M.; Jepsen, L. H.; Schouwink, P.; Černý, R.; Ravnsbæk, D. B.; Filinchuk, Y.; Dornheim, M.; Besenbacher, F.; Jensen, T. R. Metal Borohydrides and Derivatives – Synthesis, Structure and Properties. *Chem. Soc. Rev.* **2017,** *46* (5), 1565–1634.
307. Orimo, S.-I.; Nakamori, Y.; Eliseo, J. R.; Züttel, A.; Jensen, C. M. Complex Hydrides for Hydrogen Storage. *Chem. Rev.* **2007,** *107* (10), 4111–4132.
308. Jain, I.; Jain, P.; Jain, A. Novel Hydrogen Storage Materials: A Review of Lightweight Complex Hydrides. *J. Alloys Compd.* **2010,** *503* (2), 303–339.
309. Schüth, F.; Bogdanović, B.; Felderhoff, M. Light Metal Hydrides and Complex Hydrides for Hydrogen Storage. *Chem. Commun.* **2004,** *20,* 2249–2258.
310. Rossin, A.; Peruzzini, M. Ammonia–Borane and Amine–Borane Dehydrogenation Mediated by Complex Metal Hydrides. *Chem. Rev.* **2016,** *116* (15), 8848–8872.
311. Zavorotynska, O.; El-Kharbachi, A.; Deledda, S.; Hauback, B. C. Recent Progress in Magnesium Borohydride $Mg(BH_4)_2$: Fundamentals and Applications for Energy Storage. *Int. J. Hydrog. Energy* **2016,** *41* (32), 14387–14403.
312. Callini, E.; Atakli, Z.Ö. K.; Hauback, B. C.; Orimo, S.-I.; Jensen, C.; Dornheim, M.; Grant, D.; Cho, Y. W.; Chen, P.; Hjörvarsson, B.; et al. Complex and Liquid Hydrides for Energy Storage. *Appl. Phys. A* **2016,** *122* (4), 353.
313. Brown, H. C. *Boranes in Organic Chemistry*, Cornell University Press: Ithaca, New York, 2019.
314. Brown, H. C. From Little Acors to Tall Oaks—From Boranes Through Organoboranes. *Science* **1980,** *210,* 485.
315. Schlesinger, H. I.; Brown, H. C. Uranium (IV) Borohydride. *J. Am. Chem. Soc.* **1953,** *75* (1), 219–221.
316. Schlesinger, H.; Sanderson, R. T.; Burg, A. Metallo Borohydrides. I. Aluminum Borohydride. *J. Am. Chem. Soc.* **1940,** *62* (12), 3421–3425.
317. Burg, A. B.; Schlesinger, H. Metallo Borohydrides. II. Beryllium Borohydride. *J. Am. Chem. Soc.* **1940,** *62* (12), 3425–3429.
318. Schlesinger, H.; Brown, H. C. Metallo Borohydrides. III. Lithium Borohydride. *J. Am. Chem. Soc.* **1940,** *62* (12), 3429–3435.
319. Schlesinger, H. I.; Brown, H. C.; Abraham, B.; Bond, A.; Davidson, N.; Finholt, A.; Gilbreath, J. R.; Hoekstra, H.; Horvitz, L.; Hyde, E. K.; et al. New Developments in the Chemistry of Diborane and the Borohydrides. I. General Summary. *J. Am. Chem. Soc.* **1953,** *75* (1), 186–190.

320. Schlesinger, H.; Brown, H. C.; Finholt, A.; Gilbreath, J. R.; Hoekstra, H. R.; Hyde, E. K. Sodium Borohydride, Its Hydrolysis and its Use as a Reducing Agent and in the Generation of Hydrogen. *J. Am. Chem. Soc.* **1953,** *75* (1), 215–219.
321. Ashby, E.; Brendel, G.; Redman, H. Direct Synthesis of Complex Metal Hydrides. *Inorg. Chem.* **1963,** *2* (3), 499–504.
322. Clasen, H. Alanat-Synthese aus den Elementen und ihre Bedeutung. *Angew. Chem.* **1961,** *73* (10), 322–331.
323. Ashby, E.; Kobetz, P. The Direct Synthesis of Na_3AlH_6. *Inorg. Chem.* **1966,** *5* (9), 1615–1617.
324. Dilts, J.; Ashby, E. Thermal Decomposition of Complex Metal Hydrides. *Inorg. Chem.* **1972,** *11* (6), 1230–1236.
325. Dymova, T.; Eliseeva, N.; Bakum, S.; Dergachev, Y. M. Direct Synthesis of Alcali Metal Alumohydrides in Melts. *Dokl. Akad. Nauk SSSR* **1974,** *215* (6), 1369–1372.
326. Bogdanović, B.; Schwickardi, M. Ti-Doped Alkali Metal Aluminium Hydrides as Potential Novel Reversible Hydrogen Storage Materials. *J. Alloys Compd.* **1997,** *253,* 1–9.
327. Suárez-Alcántara, K.; Tena-Garcia, J. R.; Guerrero-Ortiz, R. Alanates, a Comprehensive Review. *Materials* **2019,** *12* (17), 2724.
328. Neumann, D. A. Neutron Scattering and Hydrogenous Materials. *Mater. Today* **2006,** *9* (1–2), 34–41.
329. Milanese, C.; Garroni, S.; Gennari, F.; Marini, A.; Klassen, T.; Dornheim, M.; Pistidda, C. Solid State Hydrogen Storage in Alanates and Alanate-Based Compounds: A Review. *Metals* **2018,** *8* (8), 567.
330. Lauher, J.; Dougherty, D.; Herley, P. Sodium Tetrahydroaluminate. *Acta Crystallogr. B Struct. Crystallogr. Cryst. Chem.* **1979,** *35* (6), 1454–1456.
331. Bel'skii, V. K.; Bulychev, B. M.; Golubeva, A. V. *Zh. Neorg. Khim.* **1983,** *28,* 2694–2696.
332. Hauback, B.; Brinks, H.; Jensen, C.; Murphy, K.; Maeland, A. Neutron Diffraction Structure Determination of $NaAlD_4$. *J. Alloys Compd.* **2003,** *358* (1–2), 142–145.
333. Ozolins, V.; Majzoub, E.; Udovic, T. Electronic Structure and Rietveld Refinement Parameters of Ti-Doped Sodium Alanates. *J. Alloys Compd.* **2004,** *375* (1–2), 1–10.
334. Íñiguez, J.; Yildirim, T.; Udovic, T.; Sulic, M.; Jensen, C. Structure and Hydrogen Dynamics of Pure and Ti-Doped Sodium Alanate. *Phys. Rev. B* **2004,** *70* (6), 60101.
335. Humphries, T. D.; Makepeace, J. W.; Hino, S.; David, W. I.; Hauback, B. C. Regeneration of Sodium Alanate Studied by Powder *In Situ* Neutron and Synchrotron X-Ray Diffraction. *J. Mater. Chem. A* **2014,** *2* (39), 16594–16600.
336. Atakli, Z.Ö. K.; Callini, E.; Kato, S.; Mauron, P.; Orimo, S.-I.; Züttel, A. The Catalyzed Hydrogen Sorption Mechanism in Alkali Alanates. *Phys. Chem. Chem. Phys.* **2015,** *17* (32), 20932–20940.
337. Bogdanović, B.; Sandrock, G. Catalyzed Complex Metal Hydrides. *MRS Bull.* **2002,** *27* (9), 712–716.
338. Zidan, R. A.; Takara, S.; Hee, A. G.; Jensen, C. M. Hydrogen Cycling Behavior of Zirconium and Titanium–Zirconium-Doped Sodium Aluminum Hydride. *J. Alloys Compd.* **1999,** *285* (1–2), 119–122.
339. Wang, J.; Ebner, A.; Zidan, R.; Ritter, J. Synergistic Effects of Co-Dopants on the Dehydrogenation Kinetics of Sodium Aluminum Hydride. *J. Alloys Compd.* **2005,** *391* (1–2), 245–255.
340. Lee, G.-J.; Kim, J. W.; Shim, J.-H.; Cho, Y. W.; Lee, K. S. Synthesis of Ultrafine Titanium Aluminide Powders and their Catalytic Enhancement in Dehydrogenation Kinetics of $NaAlH_4$. *Scr. Mater.* **2007,** *56* (2), 125–128.
341. Hauback, B.; Brinks, H.; Fjellvåg, H. Accurate Structure of $LiAlD_4$ Studied by Combined Powder Neutron and X-Ray Diffraction. *J. Alloys Compd.* **2002,** *346* (1–2), 184–189.
342. Hauback, B.; Brinks, H.; Heyn, R.; Blom, R.; Fjellvåg, H. The Crystal Structure of $KAlD_4$. *J. Alloys Compd.* **2005,** *394* (1–2), 35–38.
343. Fossdal, A.; Brinks, H.; Fichtner, M.; Hauback, B. Determination of the Crystal Structure of $Mg(AlH_4)_2$ by Combined X-Ray and Neutron Diffraction. *J. Alloys Compd.* **2005,** *387* (1–2), 47–51.
344. Sato, T.; Sørby, M.; Ikeda, K.; Sato, S.; Hauback, B.; Orimo, S. Syntheses, Crystal Structures, and Thermal Analyses of Solvent-Free $Ca(AlD_4)_2$ and $CaAlD_5$. *J. Alloys Compd.* **2009,** *487* (1–2), 472–478.
345. Brinks, H.; Hauback, B.; Jensen, C.; Zidan, R. Synthesis and Crystal Structure of Na_2LiAlD_6. *J. Alloys Compd.* **2005,** *392* (1–2), 27–30.
346. Ravnsbæk, D. B.; Filinchuk, Y.; Černý, R.; Jensen, T. R. Powder Diffraction Methods for Studies of Borohydride-Based Energy Storage Materials. *Z. Krist.* **2010,** *225* (12), 557–569.
347. Lohstroh, W.; Heere, M. Structure and Dynamics of Borohydrides Studied by Neutron Scattering Techniques: A Review. *J. Phys. Soc. Jpn.* **2020,** *89* (5), 51011.
348. Züttel, A.; Wenger, P.; Rentsch, S.; Sudan, P.; Mauron, P.; Emmenegger, C. $LiBH_4$ a New Hydrogen Storage Material. *J. Power Sources* **2003,** *118* (1–2), 1–7.
349. Züttel, A.; Rentsch, S.; Fischer, P.; Wenger, P.; Sudan, P.; Mauron, P.; Emmenegger, C. Hydrogen Storage Properties of $LiBH_4$. *J. Alloys Compd.* **2003,** *356,* 515–520.
350. Chen, J.; Kuriyama, N.; Xu, Q.; Takeshita, H. T.; Sakai, T. Reversible Hydrogen Storage via Titanium-Catalyzed $LiAlH_4$ and Li_3AlH_6. *J. Phys. Chem. B* **2001,** *105* (45), 11214–11220.
351. Harris, P.; Meibohm, E. The Crystal Structure of Lithium Borohydride $LiBH_4$. *J. Am. Chem. Soc.* **1947,** *69* (5), 1231–1232.
352. Soulié, J.-P.; Renaudin, G.; Černý, R.; Yvon, K. Lithium Boro-Hydride $LiBH_4$: I. Crystal Structure. *J. Alloys Compd.* **2002,** *346* (1–2), 200–205.
353. Hartman, M. R.; Rush, J. J.; Udovic, T. J.; Bowman, R. C., Jr.; Hwang, S.-J. Structure and Vibrational Dynamics of Isotopically Labeled Lithium Borohydride Using Neutron Diffraction and Spectroscopy. *J. Solid State Chem.* **2007,** *180* (4), 1298–1305.
354. Renaudin, G.; Gomes, S.; Hagemann, H.; Keller, L.; Yvon, K. Structural and Spectroscopic Studies on the Alkali Borohydrides MBH_4 (M = Na, K, Rb, Cs). *J. Alloys Compd.* **2004,** *375* (1–2), 98–106.
355. Buchter, F.; Łodziana, Z.; Mauron, P.; Remhof, A.; Friedrichs, O.; Borgschulte, A.; Züttel, A.; Sheptyakov, D.; Strässle, T.; Ramirez-Cuesta, A. Dynamical Properties and Temperature Induced Molecular Disordering of $LiBH_4$ and $LiBD_4$. *Phys. Rev. B* **2008,** *78* (9), 94302.
356. Verdal, N.; Udovic, T. J.; Rush, J. J.; Liu, X.; Majzoub, E. H.; Vajo, J. J.; Gross, A. F. Dynamical Perturbations of Tetrahydroborate Anions in $LiBH_4$ Due to Nanoconfinement in Controlled-Pore Carbon Scaffolds. *J. Phys. Chem. C* **2013,** *117* (35), 17983–17995.
357. Remhof, A.; Züttel, A.; Ramirez-Cuesta, T. A.; García-Sakai, V.; Frick, B. Hydrogen Dynamics in the Low Temperature Phase of $LiBH_4$ Probed by Quasielastic Neutron Scattering. *Chem. Phys.* **2013,** *427,* 18–21.
358. Verdal, N.; Udovic, T. J.; Rush, J. J. The Nature of BH4—Reorientations in Hexagonal $LiBH_4$. *J. Phys. Chem. C* **2012,** *116* (1), 1614–1618.
359. Udovic, T. J.; Verdal, N.; Rush, J. J.; De Vries, D. J.; Hartman, M. R.; Vajo, J. J.; Gross, A. F.; Skripov, A. V. Mapping Trends in the Reorientational Mobilities of Tetrahydroborate Anions via Neutron-Scattering Fixed-Window Scans. *J. Alloys Compd.* **2013,** *580,* S47–S50.
360. Remhof, A.; Łodziana, Z.; Martelli, P.; Friedrichs, O.; Züttel, A.; Skripov, A. V.; Embs, J. P.; Strässle, T. Rotational Motion of BH_4 Units in MBH_4 (M = Li, Na, K) from Quasielastic Neutron Scattering and Density Functional Calculations. *Phys. Rev. B* **2010,** *81* (21), 214304.
361. Verdal, N.; Udovic, T. J.; Rush, J. J.; Wu, H.; Skripov, A. V. Evolution of the Reorientational Motions of the Tetrahydroborate Anions in Hexagonal $LiBH_4$–LiI Solid Solution by High-Q Quasielastic Neutron Scattering. *J. Phys. Chem. C* **2013,** *117* (23), 12010–12018.
362. Martelli, P.; Remhof, A.; Borgschulte, A.; Ackermann, R.; Strässle, T.; Embs, J. P.; Ernst, M.; Matsuo, M.; Orimo, S.-I.; Züttel, A. Rotational Motion in $LiBH_4$/LiI Solid Solutions. *J. Phys. Chem. A* **2011,** *115* (21), 5329–5334.
363. Kitchen, B. B.; Verdal, N.; Udovic, T. J.; Rush, J. J.; Hartman, M. R.; DeVries, D. J. Investigation of an Unusual Low-Temperature Phase Transformation in $RbBH_4$ by Neutron Diffraction. *J. Solid State Chem.* **2013,** *203,* 51–54.
364. Moussa, G.; Moury, R.; Demirci, U. B.; Şener, T.; Miele, P. Boron-Based Hydrides for Chemical Hydrogen Storage. *Int. J. Energy Res.* **2013,** *37* (8), 825–842.
365. Sirsch, P.; Clark, N. L.; Onuţ, L.; Burchell, R. P.; Decken, A.; McGrady, G. S.; Daoud-Aladine, A.; Gutmann, M. J. Insights Into Metal Borohydride and Aluminohydride Bonding: X-Ray and Neutron Diffraction Structures and a DFT and Charge Density Study of $[Na(15\text{-Crown-5})][EH_4]$(E = B, Al). *Inorg. Chem.* **2010,** *49* (24), 11395–11402.
366. Zhou, Y.; Yamaguchi, T.; Ikeda, K.; Yoshida, K.; Otomo, T.; Fang, C.; Zhang, W.; Zhu, F. Dihydrogen Bonds in Aqueous $NaBD_4$ Solution by Neutron and X-Ray Diffraction. *J. Phys. Chem. Lett.* **2020,** *11* (5), 1622–1628.
367. Frommen, C.; Aliouane, N.; Deledda, S.; Fonneløp, J. E.; Grove, H.; Lieutenant, K.; Llamas-Jansa, I.; Sartori, S.; Sørby, M. H.; Hauback, B. C. Crystal Structure, Polymorphism, and Thermal Properties of Yttrium Borohydride $Y(BH_4)_3$. *J. Alloys Compd.* **2010,** *496* (1–2), 710–716.

368. Verdal, N.; Udovic, T. J.; Rush, J. J.; Skripov, A. V. Quasielastic Neutron Scattering Study of Tetrahydroborate Anion Dynamical Perturbations in Sodium Borohydride Due to Partial Halide Anion Substitution. *J. Alloys Compd.* **2015,** *645,* S513–S517.
369. Ravnsbæk, D. B.; Frommen, C.; Reed, D.; Filinchuk, Y.; Sørby, M.; Hauback, B.; Jakobsen, H. J.; Book, D.; Besenbacher, F.; Skibsted, J.; et al. Structural Studies of Lithium Zinc Borohydride by Neutron Powder Diffraction, Raman and NMR Spectroscopy. *J. Alloys Compd.* **2011,** *509,* S698–S704.
370. Wiberg, E.; Bauer, R. Zur Kenntnis eines Magnesium-bor-wasserstoffs $Mg(AlH_4)_2$. *Z. Naturforsh. B* **1950,** *5* (7), 397–398.
371. Chłopek, K.; Frommen, C.; Léon, A.; Zabara, O.; Fichtner, M. Synthesis and Properties of Magnesium Tetrahydroborate, $Mg(BH_4)_2$. *J. Mater. Chem.* **2007,** *17* (33), 3496–3503.
372. Nakamori, Y.; Miwa, K.; Ninomiya, A.; Li, H.; Ohba, N.; Towata, S.-I.; Züttel, A.; Orimo, S.-I. Correlation Between Thermodynamical Stabilities of Metal Borohydrides and Cation Electronegativites: First-Principles Calculations and Experiments. *Phys. Rev. B* **2006,** *74* (4), 045126.
373. Miwa, K.; Aoki, M.; Noritake, T.; Ohba, N.; Nakamori, Y.; Towata, S.-I.; Züttel, A.; Orimo, S.-I. Thermodynamical Stability of Calcium Borohydride $Ca(BH_4)_2$. *Phys. Rev. B* **2006,** *74* (15), 155122.
374. Severa, G.; Rönnebro, E.; Jensen, C. M. Direct Hydrogenation of Magnesium Boride to Magnesium Borohydride: Demonstration of >11 Weight Percent Reversible Hydrogen Storage. *Chem. Commun.* **2010,** *46* (3), 421–423.
375. Kim, J.-H.; Shim, J.-H.; Cho, Y. W. On the Reversibility of Hydrogen Storage in Ti-and Nb-Catalyzed $Ca(BH_4)_2$. *J. Power Sources* **2008,** *181* (1), 140–143.
376. Bil, A.; Kolb, B.; Atkinson, R.; Pettifor, D.; Thonhauser, T.; van der Kolmogorov, A. Waals Interactions in the Ground State of $Mg(BH_4)_2$ from Density Functional Theory. *Phys. Rev. B* **2011,** *83* (22), 224103.
377. Pitt, M. P.; Webb, C. J.; Paskevicius, M.; Sheptyakov, D.; Buckley, C. E.; Gray, E. M. In Situ Neutron Diffraction Study of the Deuteration of Isotopic $Mg^{11}B_2$. *J. Phys. Chem. C* **2011,** *115* (45), 22669–22679.
378. Zhou, X.-F.; Oganov, A. R.; Qian, G.-R.; Zhu, Q. First-Principles Determination of the Structure of Magnesium Borohydride. *Phys. Rev. Lett.* **2012,** *109* (24), 245503.
379. Ozolins, V.; Majzoub, E.; Wolverton, C. First-Principles Prediction of a Ground State Crystal Structure of Magnesium Borohydride. *Phys. Rev. Lett.* **2008,** *100* (13), 135501.
380. Vitillo, J. G.; Bordiga, S.; Baricco, M. Spectroscopic and Structural Characterization of Thermal Decomposition of γ-$Mg(BH_4)_2$: Dynamic Vacuum Versus H_2 Atmosphere. *J. Phys. Chem. C* **2015,** *119* (45), 25340–25351.
381. Filinchuk, Y.; Cerny, R.; Hagemann, H. Insight into $Mg(BH_4)_2$ with Synchrotron X-Ray Diffraction: Structure Revision, Crystal Chemistry, and Anomalous Thermal Expansion. *Chem. Mater.* **2009,** *21* (5), 925–933.
382. Paskevicius, M.; Pitt, M. P.; Webb, C. J.; Sheppard, D. A.; Filsø, U.; Gray, E. M.; Buckley, C. E. In-Situ X-Ray Diffraction Study of γ-$Mg(BH_4)_2$ Decomposition. *J. Phys. Chem. C* **2012,** *116* (29), 15231–15240.
383. David, W.; Callear, S.; Jones, M.; Aeberhard, P.; Culligan, S.; Pohl, A.; Johnson, S.; Ryan, K.; Parker, J.; Edwards, P.; et al. The Structure, Thermal Properties and Phase Transformations of the Cubic Polymorph of Magnesium Tetrahydroborate. *Phys. Chem. Chem. Phys.* **2012,** *14* (33), 11800–11807.
384. Zavorotynska, O.; Deledda, S.; Vitillo, J. G.; Saldan, I.; Guzik, M. N.; Baricco, M.; Walmsley, J. C.; Muller, J.; Hauback, B. C. Combined X-Ray and Raman Studies on the Effect of Cobalt Additives on the Decomposition of Magnesium Borohydride. *Energies* **2015,** *8* (9), 9173–9190.
385. Her, J.-H.; Stephens, P. W.; Gao, Y.; Soloveichik, G. L.; Rijssenbeek, J.; Andrus, M.; Zhao, J.-C. Structure of Unsolvated Magnesium Borohydride $Mg(BH_4)_2$. *Acta Crystallogr. Sect. B: Struct. Sci.* **2007,** *63* (4), 561–568.
386. Černỳ, R.; Filinchuk, Y.; Hagemann, H.; Yvon, K. Magnesium Borohydride: Synthesis and Crystal Structure. *Angew. Chem. Int. Ed.* **2007,** *119* (30), 5867–5869.
387. Filinchuk, Y.; Chernyshov, D.; Dmitriev, V. Light Metal Borohydrides: Crystal Structures and Beyond. *Z. Krist.* **2008,** *223* (10), 649–659.
388. Blanchard, D.; Maronsson, J. B.; Riktor, M.; Kheres, J.; Sveinbjörnsson, D.; Gil Bardají, E.; Léon, A.; Juranyi, F.; Wuttke, J.; Lefmann, K.; et al. Hindered Rotational Energy Barriers of BH_4–Tetrahedra in β-$Mg(BH_4)_2$ From Quasielastic Neutron Scattering and DFT Calculations. *J. Phys. Chem. C* **2012,** *116* (2), 2013–2023.
389. Silvi, L.; Zhao-Karger, Z.; Röhm, E.; Fichtner, M.; Petry, W.; Lohstroh, W. A Quasielastic and Inelastic Neutron Scattering Study of the Alkaline and Alkaline-Earth Borohydrides $LiBH_4$ and $Mg(BH_4)_2$ and the Mixture $LiBH_4+Mg(BH_4)_2$. *Phys. Chem. Chem. Phys.* **2019,** *21* (2), 718–728.
390. Silvi, L.; Röhm, E.; Fichtner, M.; Petry, W.; Lohstroh, W. Hydrogen Dynamics in β-$Mg(BH_4)_2$ on the Picosecond Timescale. *Phys. Chem. Chem. Phys.* **2016,** *18* (21), 14323–14332.
391. Heere, M.; Hansen, A.-L.; Payandeh, S.; Aslan, N.; Gizer, G.; Sørby, M. H.; Hauback, B. C.; Pistidda, C.; Dornheim, M.; Lohstroh, W. Dynamics of Porous and Amorphous Magnesium Borohydride to Understand Solid State Mg-Ion-Conductors. *Sci. Rep.* **2020,** *10* (1), 1–11.
392. Dimitrievska, M.; White, J. L.; Zhou, W.; Stavila, V.; Klebanoff, L. E.; Udovic, T. J. Structure-Dependent Vibrational Dynamics of $Mg(BH_4)_2$ Polymorphs Probed With Neutron Vibrational Spectroscopy and First-Principles Calculations. *Phys. Chem. Chem. Phys.* **2016,** *18* (36), 25546–25552.
393. Buchter, F.; Łodziana, Z.; Remhof, A.; Friedrichs, O.; Borgschulte, A.; Mauron, P.; Züttel, A.; Sheptyakov, D.; Palatinus, L.; Chłopek, K.; et al. Structure of the Orthorhombic γ-Phase and Phase Transitions of $Ca(BD_4)_2$. *J. Phys. Chem. C* **2009,** *113* (39), 17223–17230.
394. Buchter, F.; Łodziana, Z.; Remhof, A.; Friedrichs, O.; Borgschulte, A.; Mauron, P.; Züttel, A.; Sheptyakov, D.; Barkhordarian, G.; Bormann, R. D.; et al. Structure of $Ca(BD_4)_2$ β-Phase From Combined Neutron and Synchrotron X-Ray Powder Diffraction Data and Density Functional Calculations. *J. Phys. Chem. B* **2008,** *112* (27), 8042–8048.
395. Filinchuk, Y.; Rönnebro, E.; Chandra, D. Crystal Structures and Phase Transformations in $Ca(BH_4)_2$. *Acta Mater.* **2009,** *57* (3), 732–738.
396. Barkhordarian, G.; Jensen, T. R.; Doppiu, S.; Bösenberg, U.; Borgschulte, A.; Gremaud, R.; Cerenius, Y.; Dornheim, M.; Klassen, T.; Bormann, R. Formation of $Ca(BH_4)_2$ From Hydrogenation of CaH_2+MgB_2 Composite. *J. Phys. Chem. C* **2008,** *112* (7), 2743–2749.
397. Riktor, M.; Sørby, M.; Chłopek, K.; Fichtner, M.; Buchter, F.; Züttel, A.; Hauback, B. In Situ Synchrotron Diffraction Studies of Phase Transitions and Thermal Decomposition of $Mg(BH_4)_2$ and $Ca(BH_4)_2$. *J. Mater. Chem.* **2007,** *17* (47), 4939–4942.
398. Blanchard, D.; Riktor, M.; Maronsson, J. B.; Jacobsen, H. S.; Kehres, J.; Sveinbjornsson, D.; Bardaji, E. G.; Leon, A.; Juranyi, F.; Wuttke, J.; et al. Hydrogen Rotational and Translational Diffusion in Calcium Borohydride From Quasielastic Neutron Scattering and DFT Calculations. *J. Phys. Chem. C* **2010,** *114* (47), 20249–20257.
399. Tomkinson, J.; Waddington, T. C. Inelastic Neutron Scattering From the Alkali Metal Borohydrides and Calcium Borohydride. *J. Chem. Soc. Faraday Trans. 2 Mol. Chem. Phys.* **1976,** *72,* 528–538.
400. Fichtner, M.; Chlopek, K.; Longhini, M.; Hagemann, H. Vibrational Spectra of $Ca(BH_4)_2$. *J. Phys. Chem. C* **2008,** *112* (30), 11575–11579.
401. Ichikawa, T. Amides, Imides and Mixtures. In *Handbook of Hydrogen Storage: New Materials for Future Energy Storage*, John Wiley and Sons, 2010; pp 159–185.
402. Chen, P.; Xiong, Z.; Luo, J.; Lin, J.; Tan, K. L. Interaction of Hydrogen With Metal Nitrides and Imides. *Nature* **2002,** *420* (6913), 302–304.
403. Weidner, E.; Bull, D.; Shabalin, I.; Keens, S.; Telling, M.; Ross, D. Observation of Novel Phases During Deuteration of Lithium Nitride From In Situ Neutron Diffraction. *Chem. Phys. Lett.* **2007,** *444* (1–3), 76–79.
404. David, W. I.; Jones, M. O.; Gregory, D. H.; Jewell, C. M.; Johnson, S. R.; Walton, A.; Edwards, P. P. A Mechanism for Non-Stoichiometry in the Lithium Amide/Lithium Imide Hydrogen Storage Reaction. *J. Am. Chem. Soc.* **2007,** *129* (6), 1594–1601.
405. Balogh, M. P.; Jones, C. Y.; Herbst, J.; Hector, L. G., Jr.; Kundrat, M. Crystal Structures and Phase Transformation of Deuterated Lithium Imide, Li_2ND. *J. Alloys Compd.* **2006,** *420* (1–2), 326–336.
406. Ichikawa, T.; Isobe, S. The Structural Properties of Amides and Imides as Hydrogen Storage Materials. *Z. Krist.* **2008,** *223* (10), 660–665.
407. Ohoyama, K.; Nakamori, Y.; Orimo, S.-I.; Yamada, K. Revised Crystal Structure Model of Li_2NH by Neutron Powder Diffraction. *J. Phys. Soc. Jpn.* **2005,** *74* (1), 483–487.
408. Yang, J.; Zhou, X.; Cai, Q.; James, W. J.; Yelon, W. B. Crystal and Electronic Structures of $LiNH_2$. *Appl. Phys. Lett.* **2006,** *88* (4), 41914.
409. Juza, R.; Opp, K. Metallamide Und Metallnitride, 24. Mitteilung. Die Kristallstruktur Des Lithiumamides. *Z. Anorg. Allg. Chem.* **1951,** *266* (6), 313–324.
410. Jacobs, H.; Juza, R. Neubestimmung Der Kristallstruktur Des Lithiumamids. *Z. Anorg. Allg. Chem.* **1972,** *391* (3), 271–279.
411. Grotjahn, D. B.; Sheridan, P.; Al Jihad, I.; Ziurys, L. M. First Synthesis and Structural Determination of a Monomeric, Unsolvated Lithium Amide, $LiNH_2$. *J. Am. Chem. Soc.* **2001,** *123* (23), 5489–5494.

412. Bull, D. J.; Sorbie, N.; Baldissin, G.; Moser, D.; Telling, M. T.; Smith, R. I.; Gregory, D. H.; Ross, D. K. In Situ Powder Neutron Diffraction Study of Non-Stoichiometric Phase Formation During the Hydrogenation of Li_3N. *Faraday Discuss.* **2011,** *151,* 263–270.
413. Bull, D. J.; Weidner, E.; Shabalin, I. L.; Telling, M. T.; Jewell, C. M.; Gregory, D. H.; Ross, D. K. Pressure-Dependent Deuterium Reaction Pathways in the Li–N–D System. *Phys. Chem. Chem. Phys.* **2010,** *12* (9), 2089–2097.
414. Hansen, T. C.; Kohlmann, H. Chemical Reactions Followed by In Situ Neutron Powder Diffraction. *Z. Anorg. Allg. Chem.* **2014,** *640* (15), 3044–3063.
415. Müller, M.; Asmussen, B.; Press, W.; Senker, J.; Jacobs, H.; Büttner, H.; Kockelmann, W.; Ibberson, R. Dynamics of the Amide Ions in Potassium Amide: Orientational Order and Disorder. *Phys. B Condens. Matter* **1997,** *234,* 45–47.
416. Dolci, F.; Napolitano, E.; Weidner, E.; Enzo, S.; Moretto, P.; Brunelli, M.; Hansen, T.; Fichtner, M.; Lohstroh, W. Magnesium Imide: Synthesis and Structure Determination of an Unconventional Alkaline Earth Imide From Decomposition of Magnesium Amide. *Inorg. Chem.* **2011,** *50* (3), 1116–1122.
417. Müller, M.; Senker, J.; Asmussen, B.; Press, W.; Jacobs, H.; Kockelmann, W.; Mayer, H.; Ibberson, R. Orientational Order and Rotational Dynamics of the Amide Ions in Potassium Amide. I. Neutron Diffraction. *J. Chem. Phys.* **1997,** *107* (7), 2363–2373.
418. Müller, M.; Asmussen, B.; Press, W.; Senker, J.; Jacobs, H.; Büttner, H.; Schober, H. Orientational Order and Rotational Dynamics of the Amide Ions in Potassium Amide. II. Quasielastic Neutron Scattering. *J. Chem. Phys.* **1998,** *109* (9), 3559–3567.
419. Senker, J.; Jacobs, H.; Müller, M.; Press, W.; Mayer, H.; Ibberson, R. Structure Determination of a Low Temperature Phase of Calcium and Strontium Amide by Means of Neutron Powder Diffraction on $Ca(ND_2)_2$ and $Sr(ND_2)_2$. *Z. Anorg. Allg. Chem.* **1999,** *625* (12), 2025–2032.
420. Juza, R.; Weber, H. H.; Opp, K. Kristallstruktur des natriumamids. *Z. Anorg. Allg. Chem.* **1956,** *284* (1–3), 73–82.
421. Nagib, M.; Kistrup, H.; Jacobs, H. Neutronenbeugung am Natriumdeuteroamid. *Atomkernenergie* **1975,** *26,* 87–90.
422. Day, D.; Sinclair, R. Studies of Vibration Spectra of Bonded Hydrogen Atoms Using a Pulsed Neutron Source. *J. Chem. Phys.* **1971,** *55* (6), 2807–2811.
423. Sørby, M.; Nakamura, Y.; Brinks, H.; Ichikawa, T.; Hino, S.; Fujii, H.; Hauback, B. The Crystal Structure of $LiND_2$ and $Mg(ND_2)_2$. *J. Alloys Compd.* **2007,** *428* (1–2), 297–301.
424. Huq, A.; Richardson, J. W.; Maxey, E. R.; Chandra, D.; Chien, W.-M. Structural Studies of Deuteration and Dedeuteration of Li_3N by Use of In Situ Neutron Diffraction. *J. Phys. Chem. C* **2007,** *111* (28), 10712–10717.
425. Nakamura, Y.; Hino, S.; Ichikawa, T.; Fujii, H.; Brinks, H.; Hauback, B. Dehydrogenation Reaction of Li–Mg–N–H Systems Studied by In Situ Synchrotron Powder X-Ray Diffraction and Powder Neutron Diffraction. *J. Alloys Compd.* **2008,** *457* (1–2), 362–367.
426. Shannon, R. D. Revised Effective Ionic Radii and Systematic Studies of Interatomic Distances in Halides and Chalcogenides. *Acta Crystallogr. Sect. A: Cryst. Phys., Diffr., Theor. Gen. Crystallogr.* **1976,** *32* (5), 751–767.
427. Wu, H. Structure of Ternary Imide $Li_2Ca(NH)_2$ and Hydrogen Storage Mechanisms in Amide-Hydride System. *J. Am. Chem. Soc.* **2008,** *130* (20), 6515–6522.
428. Wu, G.; Xiong, Z.; Liu, T.; Liu, Y.; Hu, J.; Chen, P.; Feng, Y.; Wee, A. T. Synthesis and Characterization of a New Ternary Imide – $Li_2Ca(NH)_2$. *Inorg. Chem.* **2007,** *46* (2), 517–521.
429. Huang, Z.; Autrey, T. Boron–Nitrogen–Hydrogen (BNH) Compounds: Recent Developments in Hydrogen Storage, Applications in Hydrogenation and Catalysis, and New Syntheses. *Energy Environ. Sci.* **2012,** *5* (11), 9257–9268.
430. Baitalow, F.; Baumann, J.; Wolf, G.; Jaenicke-Rössler, K.; Leitner, G. Thermal Decomposition of B–N–H Compounds Investigated by Using Combined Thermoanalytical Methods. *Thermochim. Acta* **2002,** *391* (1–2), 159–168.
431. Demirci, U. B. Ammonia Borane, a Material With Exceptional Properties for Chemical Hydrogen Storage. *Int. J. Hydrog. Energy* **2017,** *42* (15), 9978–10013.
432. Parvanov, V. M.; Schenter, G. K.; Hess, N. J.; Daemen, L. L.; Hartl, M.; Stowe, A. C.; Camaioni, D. M.; Autrey, T. Materials for Hydrogen Storage: Structure and Dynamics of Borane Ammonia Complex. *Dalton Trans.* **2008,** *33,* 4514–4522.
433. Bowden, M. E.; Gainsford, G. J.; Robinson, W. T. Room-Temperature Structure of Ammonia Borane. *Aust. J. Chem.* **2007,** *60* (3), 149–153.
434. Yang, J.; Lamsal, J.; Cai, Q.; James, W.; Yelon, W. Structural Evolution of Ammonia Borane for Hydrogen Storage. *Appl. Phys. Lett.* **2008,** *92* (9), 91916.
435. Hess, N. J.; Schenter, G. K.; Hartman, M. R.; Daemen, L. L.; Proffen, T.; Kathmann, S. M.; Mundy, C. J.; Hartl, M.; Heldebrant, D. J.; Stowe, A. C.; et al. Neutron Powder Diffraction and Molecular Simulation Study of the Structural Evolution of Ammonia Borane from 15 to 340 K. *J. Phys. Chem. A* **2009,** *113* (19), 5723–5735.
436. Hess, N. J.; Hartman, M. R.; Brown, C. M.; Mamontov, E.; Karkamkar, A.; Heldebrant, D. J.; Daemen, L. L.; Autrey, T. Quasielastic Neutron Scattering of $–NH_3$ and $–BH_3$ Rotational Dynamics in Orthorhombic Ammonia Borane. *Chem. Phys. Lett.* **2008,** *459* (1–6), 85–88.
437. Kathmann, S. M.; Parvanov, V.; Schenter, G. K.; Stowe, A. C.; Daemen, L. L.; Hartl, M.; Linehan, J.; Hess, N. J.; Karkamkar, A.; Autrey, T. Experimental and Computational Studies on Collective Hydrogen Dynamics in Ammonia Borane: Incoherent Inelastic Neutron Scattering. *J. Chem. Phys.* **2009,** *130* (2), 24507.
438. Kumar, R. S.; Ke, X.; Zhang, J.; Lin, Z.; Vogel, S. C.; Hartl, M.; Sinogeikin, S.; Daemen, L.; Cornelius, A. L.; Chen, C.; et al. Pressure Induced Structural Changes in the Potential Hydrogen Storage Compound Ammonia Borane: A Combined X-Ray, Neutron and Theoretical Investigation. *Chem. Phys. Lett.* **2010,** *495* (4–6), 203–207.
439. Klooster, W. T.; Koetzle, T. F.; Siegbahn, P. E.; Richardson, T. B.; Crabtree, R. H. Study of the N-H $\cdots$H-B Dihydrogen Bond Including the Crystal Structure of BH_3NH_3 by Neutron Diffraction. *J. Am. Chem. Soc.* **1999,** *121* (27), 6337–6343.
440. Liu, Q.; Hoffmann, R. Theoretical Aspects of a Novel Mode of Hydrogen-Hydrogen Bonding. *J. Am. Chem. Soc.* **1995,** *117* (40), 10108–10112.
441. Gutowska, A.; Li, L.; Shin, Y.; Wang, C. M.; Li, X. S.; Linehan, J. C.; Smith, R. S.; Kay, B. D.; Schmid, B.; Shaw, W.; et al. Nanoscaffold Mediates Hydrogen Release and the Reactivity of Ammonia Borane. *Angew. Chem. Int. Ed.* **2005,** *117* (23), 3644–3648.
442. Brown, C. M.; Jacques, T. L.; Hess, N. J.; Daemen, L. L.; Mamontov, E.; Linehan, J. C.; Stowe, A. C.; Autrey, T. Dynamics of Ammonia Borane Using Neutron Scattering. *Phys. B Condens. Matter* **2006,** *385,* 266–268.
443. Parry, R.; Schultz, D.; Girardot, P. The Preparation and Properties of Hexamminecobalt(III) Borohydride, Hexamminechromium(III) Borohydride and Ammonium Borhydride1. *J. Am. Chem. Soc.* **1958,** *80* (1), 1–3.
444. Ryan, K. R. *A Study of Ammonia Borane and Its Derivatives*, Oxford University: UK, 2011.
445. Castilla-Martinez, C. A.; Moury, R.; Demirci, U. B. Amidoboranes and Hydrazinidoboranes: State of the Art, Potential for Hydrogen Storage, and Other Prospects. *Int. J. Hydrog. Energy* **2020,** *45* (55), 30731–30755.
446. Wu, H.; Zhou, W.; Pinkerton, F. E.; Meyer, M. S.; Yao, Q.; Gadipelli, S.; Udovic, T. J.; Yildirim, T.; Rush, J. J. Sodium Magnesium Amidoborane: The First Mixed-Metal Amidoborane. *Chem. Commun.* **2011,** *47* (14), 4102–4104.
447. Burankova, T.; Duchêne, L.; Łodziana, Z.; Frick, B.; Yan, Y.; Kühnel, R.-S.; Hagemann, H.; Remhof, A.; Embs, J. P. Reorientational Hydrogen Dynamics in Complex Hydrides With Enhanced Li^+ Conduction. *J. Phys. Chem. C* **2017,** *121* (33), 17693–17702.
448. Pei, Z.; Bai, Y.; Wang, Y.; Wu, F.; Wu, C. Insight to the Thermal Decomposition and Hydrogen Desorption Behaviors of $NaNH_2$–$NaBH_4$ Hydrogen Storage Composite. *ACS Appl. Mater. Interfaces* **2017,** *9* (37), 31977–31984.
449. Chua, Y. S.; Wu, H.; Zhou, W.; Udovic, T. J.; Wu, G.; Xiong, Z.; Wong, M. W.; Chen, P. Monoammoniate of Calcium Amidoborane: Synthesis, Structure, and Hydrogen-Storage Properties. *Inorg. Chem.* **2012,** *51* (3), 1599–1603.
450. Wu, H.; Zhou, W.; Yildirim, T. Alkali and Alkaline-Earth Metal Amidoboranes: Structure, Crystal Chemistry, and Hydrogen Storage Properties. *J. Am. Chem. Soc.* **2008,** *130* (44), 14834–14839.
451. Bai, Y.; Pei, Z.; Wu, F.; Wu, C. Role of Metal Electronegativity in the Dehydrogenation Thermodynamics and Kinetics of Composite Metal Borohydride–$LiNH_2$ Hydrogen Storage Materials. *ACS Appl. Mater. Interfaces* **2018,** *10* (11), 9514–9521.
452. Xia, G.; Tan, Y.; Chen, X.; Guo, Z.; Liu, H.; Yu, X. Mixed-Metal (Li, Al) Amidoborane: Synthesis and Enhanced Hydrogen Storage Properties. *J. Mater. Chem. A* **2013,** *1* (5), 1810–1820.
453. Meisner, G. P.; Scullin, M. L.; Balogh, M. P.; Pinkerton, F. E.; Meyer, M. S. Hydrogen Release From Mixtures of Lithium Borohydride and Lithium Amide: A Phase Diagram Study. *J. Phys. Chem. B* **2006,** *110* (9), 4186–4192.

454. Wu, H.; Zhou, W.; Udovic, T. J.; Rush, J. J.; Yildirim, T. Structures and Crystal Chemistry of Li_2BNH_6 and $Li_4BN_3H_{10}$. *Chem. Mater.* **2008,** *20* (4), 1245–1247.
455. Myers, A. G.; Yang, B. H.; David, K. J. Lithium Amidotrihydroborate, a Powerful New Reductant. Transformation of Tertiary Amides to Primary Alcohols. *Tetrahedron Lett.* **1996,** *37* (21), 3623–3626.
456. Diyabalanage, H. V.; Shrestha, R. P.; Semelsberger, T. A.; Scott, B. L.; Bowden, M. E.; Davis, B. L.; Burrell, A. K. Calcium Amidotrihydroborate: A Hydrogen Storage Material. *Angew. Chem.* **2007,** *119* (47), 9153–9155.
457. Xiong, Z.; Yong, C. K.; Wu, G.; Chen, P.; Shaw, W.; Karkamkar, A.; Autrey, T.; Jones, M. O.; Johnson, S. R.; Edwards, P. P.; et al. High-Capacity Hydrogen Storage in Lithium and Sodium Amidoboranes. *Nat. Mater.* **2008,** *7* (2), 138–141.
458. Ryan, K. R.; Ramirez-Cuesta, A.; Refson, K.; Jones, M. O.; Edwards, P. P.; David, W. I. A Combined Experimental Inelastic Neutron Scattering, Raman and Ab Initio Lattice Dynamics Study of α-Lithium Amidoborane. *Phys. Chem. Chem. Phys.* **2011,** *13* (26), 12249–12253.
459. Wu, H.; Zhou, W.; Pinkerton, F. E.; Meyer, M. S.; Srinivas, G.; Yildirim, T.; Udovic, T. J.; Rush, J. J. A New Family of Metal Borohydride Ammonia Borane Complexes: Synthesis, Structures, and Hydrogen Storage Properties. *J. Mater. Chem.* **2010,** *20* (31), 6550–6556.
460. He, T.; Wu, H.; Wu, G.; Li, Z.; Zhou, W.; Ju, X.; Xie, D.; Chen, P. Lithium Amidoborane Hydrazinates: Synthesis, Structure and Hydrogen Storage Properties. *J. Mater. Chem. A* **2015,** *3* (18), 10100–10106.
461. Wu, H.; Zhou, W.; Pinkerton, F. E.; Udovic, T. J.; Yildirim, T.; Rush, J. J. Metal Hydrazinoborane $LiN_2H_3BH_3$ and $LiN_2H_3BH_3 \cdot 2N_2H_4BH_3$: Crystal Structures and High-Extent Dehydrogenation. *Energy Environ. Sci.* **2012,** *5* (6), 7531–7535.
462. Chong, M.; Autrey, T.; Jensen, C. M. Lewis Base Complexes of Magnesium Borohydride: Enhanced Kinetics and Product Selectivity Upon Hydrogen Release. *Inorganics* **2017,** *5* (4), 89.
463. Dimitrievska, M.; Chong, M.; Bowden, M. E.; Wu, H.; Zhou, W.; Nayyar, I.; Ginovska, B.; Gennett, T.; Autrey, T.; Jensen, C. M.; et al. Structural and Reorientational Dynamics of Tetrahydroborate (BH_4^-) and Tetrahydrofuran (THF) in a $Mg(BH_4)\cdot 3THF$ Adduct: Neutron-Scattering Characterization. *Phys. Chem. Chem. Phys.* **2020,** *22* (1), 368–378.
464. Ingram, D. J.; Headen, T. F.; Skipper, N. T.; Callear, S. K.; Billing, M.; Sella, A. Dihydrogen Vs. Hydrogen Bonding in the Solvation of Ammonia Borane by Tetrahydrofuran and Liquid Ammonia. *Phys. Chem. Chem. Phys.* **2018,** *20* (17), 12200–12209.
465. Nielsen, T. K.; Besenbacher, F.; Jensen, T. R. Nanoconfined Hydrides for Energy Storage. *Nanoscale* **2011,** *3* (5), 2086–2098.
466. de Jongh, P. E.; Allendorf, M.; Vajo, J. J.; Zlotea, C. Nanoconfined Light Metal Hydrides for Reversible Hydrogen Storage. *MRS Bull.* **2013,** *38* (6), 488.
467. Vajo, J. J. Influence of Nano-Confinement on the Thermodynamics and Dehydrogenation Kinetics of Metal Hydrides. *Curr. Opinion Solid State Mater. Sci.* **2011,** *15* (2), 52–61.
468. Wood, B. C.; Stavila, V.; Poonyayant, N.; Heo, T. W.; Ray, K. G.; Klebanoff, L. E.; Udovic, T. J.; Lee, J. R.; Angboonpong, N.; Sugar, J. D.; et al. Nanointerface-Driven Reversible Hydrogen Storage in the Nanoconfined Li–N–H System. *Adv. Mater. Interfaces* **2017,** *4* (3), 1600803.
469. Liu, X.; Majzoub, E. H.; Stavila, V.; Bhakta, R. K.; Allendorf, M. D.; Shane, D. T.; Conradi, M. S.; Verdal, N.; Udovic, T. J.; Hwang, S.-J. Probing the Unusual Anion Mobility of $LiBH_4$ Confined in Highly Ordered Nanoporous Carbon Frameworks via Solid State NMR and Quasielastic Neutron Scattering. *J. Mater. Chem. A* **2013,** *1* (34), 9935–9941.
470. Chong, L.; Zeng, X.; Ding, W.; Liu, D.-J.; Zou, J. $NaBH_4$ in "Graphene Wrapper:" Significantly Enhanced Hydrogen Storage Capacity and Regenerability Through Nano-encapsulation. *Adv. Mater.* **2015,** *27* (34), 5070–5074.
471. Wang, L.; Rawal, A.; Quadir, M. Z.; Aguey-Zinsou, K.-F. Nanoconfined Lithium Aluminium Hydride ($LiAlH_4$) and Hydrogen Reversibility. *Int. J. Hydrog. Energy* **2017,** *42* (20), 14144–14153.
472. Wu, H.; Zhou, W.; Wang, K.; Udovic, T. J.; Rush, J. J.; Yildirim, T.; Bendersky, L. A.; Gross, A. F.; Van Atta, S. L.; Vajo, J. J.; et al. Size Effects on the Hydrogen Storage Properties of Nanoscaffolded $Li_3BN_2H_8$. *Nanotechnology* **2009,** *20* (20), 204002.
473. Gadipelli, S.; Ford, J.; Zhou, W.; Wu, H.; Udovic, T. J.; Yildirim, T. Nanoconfinement and Catalytic Dehydrogenation of Ammonia Borane by Magnesium-Metal–Organic-Framework-74. *Chem. Eur. J.* **2011,** *17* (22), 6043–6047.
474. Kabbour, H.; Baumann, T. F.; Satcher, J. H.; Saulnier, A.; Ahn, C. C. Toward New Candidates for Hydrogen Storage: High-Surface-Area Carbon Aerogels. *Chem. Mater.* **2006,** *18* (26), 6085–6087.
475. Zhao, D.; Yuan, D.; Zhou, H.-C. The Current Status of Hydrogen Storage in Metal–Organic Frameworks. *Energy Environ. Sci.* **2008,** *1* (2), 222–235.
476. Nijkamp, M.; Raaymakers, J.; Van Dillen, A.; De Jong, K. Hydrogen Storage Using Physisorption–Materials Demands. *Appl. Phys. A* **2001,** *72* (5), 619–623.
477. Wong-Foy, A. G.; Matzger, A. J.; Yaghi, O. M. Exceptional H_2 Saturation Uptake in Microporous Metal-Organic Frameworks. *J. Am. Chem. Soc.* **2006,** *128* (11), 3494–3495.
478. Bhatia, S. K.; Myers, A. L. Optimum Conditions for Adsorptive Storage. *Langmuir* **2006,** *22* (4), 1688–1700.
479. Rosi, N. L.; Eckert, J.; Eddaoudi, M.; Vodak, D. T.; Kim, J.; O'Keeffe, M.; Yaghi, O. M. Hydrogen Storage in Microporous Metal-Organic Frameworks. *Science* **2003,** *300* (5622), 1127–1129.
480. Vitillo, J. G.; Regli, L.; Chavan, S.; Ricchiardi, G.; Spoto, G.; Dietzel, P. D.; Bordiga, S.; Zecchina, A. Role of Exposed Metal Sites in Hydrogen Storage in MOFs. *J. Am. Chem. Soc.* **2008,** *130* (26), 8386–8396.
481. Zhou, W.; Wu, H.; Yildirim, T. Enhanced H_2 Adsorption in Isostructural Metal-Organic Frameworks With Open Metal Sites: Strong Dependence of the Binding Strength on Metal Ions. *J. Am. Chem. Soc.* **2008,** *130* (46), 15268–15269.
482. Oh, H.; Savchenko, I.; Mavrandonakis, A.; Heine, T.; Hirscher, M. Highly Effective Hydrogen Isotope Separation in Nanoporous Metal–Organic Frameworks With Open Metal Sites: Direct Measurement and Theoretical Analysis. *ACS Nano* **2014,** *8* (1), 761–770.
483. Yushin, G.; Dash, R.; Jagiello, J.; Fischer, J. E.; Gogotsi, Y. Carbide-Derived Carbons: Effect of Pore Size on Hydrogen Uptake and Heat of Adsorption. *Adv. Funct. Mater.* **2006,** *16* (17), 2288–2293.
484. Purewal, J.; Keith, J.; Ahn, C.; Fultz, B.; Brown, C.; Tyagi, M. Adsorption and Melting of Hydrogen in Potassium-Intercalated Graphite. *Phys. Rev. B* **2009,** *79* (5), 54305.
485. Haas, O.-E.; Simon, J. M.; Kjelstrup, S.; Ramstad, A. L.; Fouquet, P. Quasi-Elastic Neutron Scattering Investigation of the Hydrogen Surface Self-Diffusion on Polymer Electrolyte Membrane Fuel Cell Catalyst Support. *J. Phys. Chem. C* **2008,** *112* (8), 3121–3125.
486. Narehood, D.; Pearce, J.; Eklund, P.; Sokol, P.; Lechner, R.; Pieper, J.; Copley, J.; Cook, J. Diffusion of H_2 Adsorbed on Single-Walled Carbon Nanotubes. *Phys. Rev. B* **2003,** *67* (20), 205409.
487. Panella, B.; Hirscher, M.; Roth, S. Hydrogen Adsorption in Different Carbon Nanostructures. *Carbon* **2005,** *43* (10), 2209–2214.
488. Ritschel, M.; Uhlemann, M.; Gutfleisch, O.; Leonhardt, A.; Graff, A.; Täschner, C.; Fink, J. Hydrogen Storage in Different Carbon Nanostructures. *Appl. Phys. Lett.* **2002,** *80* (16), 2985–2987.
489. Minuto, F. D.; Balderas-Xicohténcatl, R.; Policicchio, A.; Hirscher, M.; Agostino, R. Assessment Methodology of Promising Porous Materials for Near Ambient Temperature Hydrogen Storage Applications. *Int. J. Hydrog. Energy* **2018,** *43* (31), 14550–14556.
490. Pekala, R. Organic Aerogels From the Polycondensation of Resorcinol With Formaldehyde. *J. Mater. Sci.* **1989,** *24* (9), 3221–3227.
491. Zhang, S.; Gross, A. F.; Van Atta, S. L.; Lopez, M.; Liu, P.; Ahn, C. C.; Vajo, J. J.; Jensen, C. M. The Synthesis and Hydrogen Storage Properties of a MgH_2 Incorporated Carbon Aerogel Scaffold. *Nanotechnology* **2009,** *20* (20), 204027.
492. Biener, J.; Stadermann, M.; Suss, M.; Worsley, M. A.; Biener, M. M.; Rose, K. A.; Baumann, T. F. Advanced Carbon Aerogels for Energy Applications. *Energy Environ. Sci.* **2011,** *4* (3), 656–667.
493. Tian, H.-Y.; Buckley, C.; Wang, S.; Zhou, M. Enhanced Hydrogen Storage Capacity in Carbon Aerogels Treated With KOH. *Carbon* **2009,** *47* (8), 2128–2130.
494. Pekala, R.; Alviso, C.; LeMay, J. Organic Aerogels: Microstructural Dependence of Mechanical Properties in Compression. *J. Non-Cryst. Solids* **1990,** *125* (1–2), 67–75.
495. Shane, D. T.; Corey, R. L.; McIntosh, C.; Rayhel, L. H.; Bowman, R. C., Jr.; Vajo, J. J.; Gross, A. F.; Conradi, M. S. $LiBH_4$ in Carbon Aerogel Nanoscaffolds: An NMR Study of Atomic Motions. *J. Phys. Chem. C* **2010,** *114* (9), 4008–4014.

496. Yang, Y.; Brown, C. M.; Zhao, C.; Chaffee, A. L.; Nick, B.; Zhao, D.; Webley, P. A.; Schalch, J.; Simmons, J. M.; Liu, Y.; et al. Micro-Channel Development and Hydrogen Adsorption Properties in Templated Microporous Carbons Containing Platinum Nanoparticles. *Carbon* **2011,** *49* (4), 1305–1317.
497. Yang, Z.; Xia, Y.; Mokaya, R. Enhanced Hydrogen Storage Capacity of High Surface Area Zeolite-Like Carbon Materials. *J. Am. Chem. Soc.* **2007,** *129* (6), 1673–1679.
498. Stadie, N. P.; Vajo, J. J.; Cumberland, R. W.; Wilson, A. A.; Ahn, C. C.; Fultz, B. Zeolite-Templated Carbon Materials for High-Pressure Hydrogen Storage. *Langmuir* **2012,** *28* (26), 10057–10063.
499. Weitkamp, J. Zeolites and Catalysis. *Solid State Ionics* **2000,** *131* (1–2), 175–188.
500. Wang, S.; Peng, Y. Natural Zeolites as Effective Adsorbents in Water and Wastewater Treatment. *Chem. Eng. J.* **2010,** *156* (1), 11–24.
501. Weitkamp, J.; Fritz, M.; Ernst, S. Zeolites as Media for Hydrogen Storage. Proceedings From the Ninth International Zeolite Conference, Elsevier, 1993; pp 11–19.
502. De Lara, E. C.; Kahn, R.; Tarek, M. Neutron Scattering Studies of Host-Guest Interaction in Zeolites. *Mol. Cryst. Liq. Cryst. Sci. Technol. Sect. A* **1994,** *248* (1), 5–11.
503. Eckert, J.; Nicol, J. M.; Howard, J.; Trouw, F. R. Adsorption of Hydrogen in Ca-Exchanged Na-A Zeolites Probed by Inelastic Neutron Scattering Spectroscopy. *J. Phys. Chem.* **1996,** *100* (25), 10646–10651.
504. Philip, C.; et al. Probing the Internal Structure of a Cobalt Aluminophosphate Catalyst. An Inelastic Neutron Scattering Study of Sorbed Dihydrogen Molecules Behaving as One- and Two-Dimensional Rotors. *Chem. Commun.* **2000**, (14), 1257–1258.
505. Jobic, H.; Theodorou, D. N. Quasi-Elastic Neutron Scattering and Molecular Dynamics Simulation as Complementary Techniques for Studying Diffusion in Zeolites. *Microporous Mesoporous Mater.* **2007,** *102* (1–3), 21–50.
506. Coulomb, J.; Martin, C.; Grillet, Y.; Tosi-Pellenq, N. Structural Analysis by Neutron Diffraction of Simples Gases (H_2, Ar, CH_4 and CF_4) Sorbed Phases in AlPO4-5. *Stud. Surf. Sci. Catal.* **1994,** *84,* 445–452. Elsevier.
507. Martin, C.; Coulomb, J.; Ferrand, M. Direct Measurement of the Translational Mobility of Deuterium Hydride Molecules Confined in a Model Microporous Material: AlPO4-5 Zeolite. *Europhys. Lett.* **1996,** *36* (7), 503.
508. Ji, Y.; Sullivan, N.; Hamida, J. Dynamics of HD Molecules Trapped in Cages of Zeolite. *J. Low Temp. Phys.* **2011,** *162* (3–4), 121–126.
509. Ho, T.-L.; Ma, M. Quasi 1 and 2d Dilute Bose Gas in Magnetic Traps: Existence of Off-Diagonal Order and Anomalous Quantum Fluctuations. *J. Low Temp. Phys.* **1999,** *115* (1–2), 61–70.
510. Mojet, B. L.; Eckert, J.; van Santen, R. A.; Albinati, A.; Lechner, R. E. Evidence for Chemisorbed Molecular Hydrogen in Fe-ZSM5 From Inelastic Neutron Scattering. *J. Am. Chem. Soc.* **2001,** *123* (33), 8147–8148.
511. Mao, W. L.; Mao, H.-K. Hydrogen Storage in Molecular Compounds. *Proc. Natl. Acad. Sci.* **2004,** *101* (3), 708–710.
512. Veluswamy, H. P.; Kumar, R.; Linga, P. Hydrogen Storage in Clathrate Hydrates: Current State of the Art and Future Directions. *Appl. Energy* **2014,** *122,* 112–132.
513. Englezos, P. Clathrate Hydrates. *Ind. Eng. Chem. Res.* **1993,** *32* (7), 1251–1274.
514. Culp, J. T.; Natesakhawat, S.; Smith, M. R.; Bittner, E.; Matranga, C.; Bockrath, B. Hydrogen Storage Properties of Rigid Three-Dimensional Hofmann Clathrate Derivatives: The Effects of Pore Size. *J. Phys. Chem. C* **2008,** *112* (17), 7079–7083.
515. Mao, W. L.; Mao, H.-K.; Goncharov, A. F.; Struzhkin, V. V.; Guo, Q.; Hu, J.; Shu, J.; Hemley, R. J.; Somayazulu, M.; Zhao, Y. Hydrogen Clusters in Clathrate Hydrate. *Science* **2002,** *297* (5590), 2247–2249.
516. Strobel, T. A.; Hester, K. C.; Sloan, E. D.; Koh, C. A. A Hydrogen Clathrate Hydrate With Cyclohexanone: Structure and Stability. *J. Am. Chem. Soc.* **2007,** *129* (31), 9544–9545.
517. Strobel, T. A.; Koh, C. A.; Sloan, E. D. Hydrogen Storage Properties of Clathrate Hydrate Materials. *Fluid Phase Equilib.* **2007,** *261* (1–2), 382–389.
518. Patchkovskii, S.; John, S. T. Thermodynamic Stability of Hydrogen Clathrates. *Proc. Natl. Acad. Sci.* **2003,** *100* (25), 14645–14650.
519. Strobel, T. A.; Sloan, E. D.; Koh, C. A. Raman Spectroscopic Studies of Hydrogen Clathrate Hydrates. *J. Chem. Phys.* **2009,** *130* (1), 14506.
520. Struzhkin, V. V.; Militzer, B.; Mao, W. L.; Mao, H.-K.; Hemley, R. J. Hydrogen Storage in Molecular Clathrates. *Chem. Rev.* **2007,** *107* (10), 4133–4151.
521. Somayazulu, M.; Finger, L.; Hemley, R.; Mao, H. High-Pressure Compounds in Methane-Hydrogen Mixtures. *Science* **1996,** *271* (5254), 1400–1402.
522. Loubeyre, P.; Letoullec, R.; Pinceaux, J.-P. Compression of Ar (H2) 2 up to 175 GPa: A New Path for the Dissociation of Molecular Hydrogen? *Phys. Rev. Lett.* **1994,** *72* (9), 1360.
523. Lokshin, K. A.; Zhao, Y.; He, D.; Mao, W. L.; Mao, H.-K.; Hemley, R. J.; Lobanov, M. V.; Greenblatt, M. Structure and Dynamics of Hydrogen Molecules in the Novel Clathrate Hydrate by High Pressure Neutron Diffraction. *Phys. Rev. Lett.* **2004,** *93* (12), 125503.
524. Hester, K. C.; Strobel, T. A.; Sloan, E. D.; Koh, C. A.; Huq, A.; Schultz, A. J. Molecular Hydrogen Occupancy in Binary THF-H_2 Clathrate Hydrates by High Resolution Neutron Diffraction. *J. Phys. Chem. B* **2006,** *110* (29), 14024–14027.
525. Tait, K. T.; Trouw, F.; Zhao, Y.; Brown, C. M.; Downs, R. T. Inelastic Neutron Scattering Study of Hydrogen in D_8-THF/D_2O Ice Clathrate. *J. Chem. Phys.* **2007,** *127* (13), 134505.
526. Strobel, T. A.; Ramirez-Cuesta, A. J.; Daemen, L. L.; Bhadram, V. S.; Jenkens, T. A.; Brown, C. M.; Cheng, Y. Quantum Dynamics of H_2 Trapped in Organic Clathrate Cages. *Phys. Rev. Lett.* **2018,** *120,* 120402.
527. Fu, H.; Trouw, F.; Sokol, P. A Quasi-Elastic and Inelastic Neutron Scattering Study of H_2 in Zeolite. *J. Low Temp. Phys.* **1999,** *116* (3–4), 149–165.
528. Ulivi, L.; Celli, M.; Giannasi, A.; Ramirez-Cuesta, A.; Zoppi, M. Inelastic Neutron Scattering From Hydrogen Clathrate Hydrates. *J. Phys. Condens. Matter* **2008,** *20* (10), 104242.
529. De Lara, E. C.; Kahn, R. Diffusivity of Hydrogen and Methane Molecules in a Zeolites: Neutron Scattering Measurements and Comparison. *Zeolites* **1992,** *12* (3), 256–260.
530. Cohen De Lara, E.; Kahn, R. Diffusivity of the Deuterated Hydrogen Molecule HD in NaA Zeolite by Neutron Scattering Experiment. Comparison With H_2 in NaA. *J. Chem. Phys.* **1992,** *96* (1), 862–863.
531. MacKinnon, J. A.; Eckert, J.; Coker, D. F.; Bug, A. L. Computational Study of Molecular Hydrogen in Zeolite Na–A. II. Density of Rotational States and Inelastic Neutron Scattering Spectra. *J. Chem. Phys.* **2001,** *114* (22), 10137–10150.
532. DeWall, J.; Dimeo, R.; Sokol, P. Slow Diffusion of Molecular Hydrogen in Zeolite 13X. *J. Low Temp. Phys.* **2002,** *129* (3–4), 171–184.
533. Tam, C. N.; Trouw, F. R.; Iton, L. E. Inelastic Neutron Scattering Study of the Activation of Molecular Hydrogen in Silver-Exchanged a Zeolite: First Step in the Reduction to Metallic Silver at Low Temperature. *J. Phys. Chem. A* **2004,** *108* (21), 4737–4743.
534. Georgiev, P. A.; Albinati, A.; Eckert, J. Room Temperature Isosteric Heat of Dihydrogen Adsorption on Cu(I) Cations in Zeolite ZSM-5. *Chem. Phys. Lett.* **2007,** *449* (1–3), 182–185.
535. Ramirez-Cuesta, A.; Mitchell, P.; Ross, D.; Georgiev, P.; Anderson, P.; Langmi, H.; Book, D. Dihydrogen in Zeolite CaX—An Inelastic Neutron Scattering Study. *J. Alloys Compd.* **2007,** *446,* 393–396.
536. Ramirez-Cuesta, A.; Mitchell, P. Hydrogen Adsorption in a Copper ZSM5 Zeolite: An Inelastic Neutron Scattering Study. *Catal. Today* **2007,** *120* (3–4), 368–373.
537. Kang, L.; Deng, W.; Han, K.; Zhang, T.; Liu, Z. A DFT Study of Adsorption Hydrogen on the Li-FAU Zeolite. *Int. J. Hydrog. Energy* **2008,** *33* (1), 105–110.
538. Acatrinei, A.; Hartl, M.; Eckert, J.; Falcao, E. H.; Chertkov, G.; Daemen, L. Hydrogen Adsorption in the Ti-Doped Mesoporous Silicate SBA-15. *J. Phys. Chem. C* **2009,** *113* (35), 15634–15638.
539. Coulomb, J.-P.; Floquet, N.; Dufau, N.; Llewellyn, P.; André, G. Structural and Dynamic Properties of Confined Hydrogen Isotopes (H_2, HD, D_2) in Model Porous Materials: Silicalite-I, AlPO4-N Family (N = 5, 8, 11, 54) and MCM-41 ($\varnothing$ = 25 Å). *Microporous Mesoporous Mater.* **2007,** *101* (1–2), 271–278.
540. Edler, K. J.; Reynolds, P. A.; Branton, P. J.; Trouw, F. R.; White, J. W. Structure and Dynamics of Hydrogen Sorption in Mesoporous MCM-41. *J. Chem. Soc. Faraday Trans.* **1997,** *93* (8), 1667–1674.
541. Glanville, Y.; Pearce, J.; Sokol, P.; Newalker, B.; Komarneni, S. Study of H_2 Confined in the Highly Ordered Pores of MCM-48. *Chem. Phys.* **2003,** *292* (2–3), 289–293.
542. Zhou, H.-C.; Long, J. R.; Yaghi, O. M. Introduction to Metal–Organic Frameworks. *Chem. Rev.* **2012,** *112,* 673–674.

543. Rowsell, J. L.; Yaghi, O. M. Strategies for Hydrogen Storage in Metal–Organic Frameworks. *Angew. Chem. Int. Ed.* **2005,** *44* (30), 4670–4679.
544. García-Holley, P.; Schweitzer, B.; Islamoglu, T.; Liu, Y.; Lin, L.; Rodriguez, S.; Weston, M. H.; Hupp, J. T.; Gómez-Gualdrón, D. A.; Yildirim, T.; et al. Benchmark Study of Hydrogen Storage in Metal–Organic Frameworks Under Temperature and Pressure Swing Conditions. *ACS Energy Lett.* **2018,** *3* (3), 748–754.
545. Langmi, H. W.; Ren, J.; North, B.; Mathe, M.; Bessarabov, D. Hydrogen Storage in Metal-Organic Frameworks: A Review. *Electrochim. Acta* **2014,** *128,* 368–392.
546. Murray, L. J.; Dincă, M.; Long, J. R. Hydrogen Storage in Metal–Organic Frameworks. *Chem. Soc. Rev.* **2009,** *38* (5), 1294–1314.
547. Li, H.; Eddaoudi, M.; O'Keeffe, M.; Yaghi, O. M. Design and Synthesis of an Exceptionally Stable and Highly Porous Metal-Organic Framework. *Nature* **1999,** *402* (6759), 276–279.
548. Snurr, R. Q.; Hupp, J. T.; Nguyen, S. T. Prospects for Nanoporous Metal-Organic Materials in Advanced Separations Processes. *AICHE J.* **2004,** *50* (6), 1090–1095.
549. Evans, H. A.; Wu, Y.; Seshadri, R.; Cheetham, A. K. Perovskite-Related ReO_3-Type Structures. *Nat. Rev. Mater.* **2020,** 1–18.
550. Rowsell, J. L.; Spencer, E. C.; Eckert, J.; Howard, J. A.; Yaghi, O. M. Gas Adsorption Sites in a Large-Pore Metal-Organic Framework. *Science* **2005,** *309* (5739), 1350–1354.
551. Rowsell, J. L.; Eckert, J.; Yaghi, O. M. Characterization of H_2 Binding Sites in Prototypical Metal-Organic Frameworks by Inelastic Neutron Scattering. *J. Am. Chem. Soc.* **2005,** *127* (42), 14904–14910.
552. Spencer, E. C.; Howard, J. A.; McIntyre, G. J.; Rowsell, J. L.; Yaghi, O. M. Determination of the Hydrogen Absorption Sites in Zn_4O(1,4-Benzenedicarboxylate) by Single Crystal Neutron Diffraction. *Chem. Commun.* **2006**, (3), 278–280.
553. Yildirim, T.; Hartman, M. Direct Observation of Hydrogen Adsorption Sites and Nanocage Formation in Metal-Organic Frameworks. *Phys. Rev. Lett.* **2005,** *95* (21), 215504.
554. Lee, H.; Choi, Y. N.; Choi, S. B.; Kim, J.; Kim, D.; Jung, D. H.; Park, Y. S.; Yoon, K. B. Liquid-Like Hydrogen Stored in Nanoporous Materials at 50 K Observed by In Situ Neutron Diffraction Experiments. *J. Phys. Chem. C* **2013,** *117* (6), 3177–3184.
555. Liu, Y.; Kabbour, H.; Brown, C. M.; Neumann, D. A.; Ahn, C. C. Increasing the Density of Adsorbed Hydrogen With Coordinatively Unsaturated Metal Centers in Metal-Organic Frameworks. *Langmuir* **2008,** *24* (9), 4772–4777.
556. Liu, Y.; Brown, C. M.; Neumann, D. A.; Kabbour, H.; Ahn, C. C. Hydrogen Adsorption in MOF-74 Studied by Inelastic Neutron Scattering. *MRS Online Proc. Libr. Archive* **2007,** *1041*. 1041-R02−R03.
557. Pham, T.; Forrest, K. A.; Banerjee, R.; Orcajo, G.; Eckert, J.; Space, B. Understanding the H_2 Sorption Trends in the M-MOF-74 Series (M = Mg, Ni, Co, Zn). *J. Phys. Chem. C* **2015,** *119* (2), 1078–1090.
558. Kubota, Y.; Takata, M.; Matsuda, R.; Kitaura, R.; Kitagawa, S.; Kato, K.; Sakata, M.; Kobayashi, T. C. Direct Observation of Hydrogen Molecules Adsorbed Onto a Microporous Coordination Polymer. *Angew. Chem.* **2005,** *117* (6), 942–945.
559. Takamizawa, S.; Nakata, E.-i. Direct Observation of H-2 Adsorbed State Within a Porous Crystal by Single Crystal X-Ray Diffraction Analysis. *CrystEngComm* **2005,** *7,* 476–479.
560. Brown, C. M.; Liu, Y.; Yildirim, T.; Peterson, V. K.; Kepert, C. J. Hydrogen Adsorption in HKUST-1: A Combined Inelastic Neutron Scattering and First-Principles Study. *Nanotechnology* **2009,** *20* (20), 204025.
561. Luo, J.; Xu, H.; Liu, Y.; Zhao, Y.; Daemen, L. L.; Brown, C.; Timofeeva, T. V.; Ma, S.; Zhou, H.-C. Hydrogen Adsorption in a Highly Stable Porous Rare-Earth Metal-Organic Framework: Sorption Properties and Neutron Diffraction Studies. *J. Am. Chem. Soc.* **2008,** *130* (30), 9626–9627.
562. Forrest, K. A.; Pham, T.; Georgiev, P. A.; Pinzan, F.; Cioce, C. R.; Unruh, T.; Eckert, J.; Space, B. Investigating H_2 Sorption in a Fluorinated Metal–Organic Framework With Small Pores Through Molecular Simulation and Inelastic Neutron Scattering. *Langmuir* **2015,** *31* (26), 7328–7336.
563. Latroche, M.; Surblé, S.; Serre, C.; Mellot-Draznieks, C.; Llewellyn, P. L.; Lee, J.-H.; Chang, J.-S.; Jhung, S. H.; Férey, G. Hydrogen Storage in the Giant-Pore Metal–Organic Frameworks MIL-100 and MIL-101. *Angew. Chem.* **2006,** *118* (48), 8407–8411.
564. Li, P.; Liu, L.; Xiao, H.; Zhang, W.; Wang, L.; Tang, B. A New Polymer Nanoprobe Based on Chemiluminescence Resonance Energy Transfer for Ultrasensitive Imaging of Intrinsic Superoxide Anion in Mice. *J. Am. Chem. Soc.* **2016,** *138* (9), 2893–2896.
565. Serre, C.; Mellot-Draznieks, C.; Surblé, S.; Audebrand, N.; Filinchuk, Y.; Férey, G. Role of Solvent-Host Interactions That Lead to Very Large Swelling of Hybrid Frameworks. *Science* **2007,** *315* (5820), 1828–1831.
566. Trung, T. K.; Trens, P.; Tanchoux, N.; Bourrelly, S.; Llewellyn, P. L.; Loera-Serna, S.; Serre, C.; Loiseau, T.; Fajula, F.; Férey, G. Hydrocarbon Adsorption in the Flexible Metal Organic Frameworks MIL-53 (Al, Cr). *J. Am. Chem. Soc.* **2008,** *130* (50), 16926–16932.
567. Liu, Y.; Her, J.-H.; Dailly, A.; Ramirez-Cuesta, A. J.; Neumann, D. A.; Brown, C. M. Reversible Structural Transition in MIL-53 with Large Temperature Hysteresis. *J. Am. Chem. Soc.* **2008,** *130* (35), 11813–11818.
568. Mulder, F. M.; Assfour, B.; Huot, J.; Dingemans, T. J.; Wagemaker, M.; Ramirez-Cuesta, A. Hydrogen in the Metal-Organic Framework Cr-MIL-53. *J. Phys. Chem. C* **2010,** *114* (23), 10648–10655.
569. Férey, G.; Latroche, M.; Serre, C.; Millange, F.; Loiseau, T.; Percheron-Guégan, A. Hydrogen Adsorption in the Nanoporous Metal-Benzenedicarboxylate $M(OH)(O_2C–C_6H_4–CO_2)$($M = Al^{3+}$, Cr^{3+}), MIL-53. *Chem. Commun.* **2003**, (24), 2976–2977.
570. Pollock, R. A.; Her, J.-H.; Brown, C. M.; Liu, Y.; Dailly, A. Kinetic Trapping of D_2 in MIL-53(Al) Observed Using Neutron Scattering. *J. Phys. Chem. C* **2014,** *118* (31), 18197–18206.
571. Schlegel, M.-C.; Többens, D.; Svetogorov, R.; Krüger, M.; Stock, N.; Reinsch, H.; Wallacher, D.; Stewart, R.; Russina, M. Conformation-Controlled Hydrogen Storage in the CAU-1 Metal–Organic Framework. *Phys. Chem. Chem. Phys.* **2016,** *18* (42), 29258–29267.
572. Halter, D. P.; Klein, R. A.; Boreen, M.; Trump, B. A.; Brown, C. M.; Long, J. R. Self-Adjusting Binding Pockets Enhance H_2 and CH_4 Adsorption in a Uranium-Based Metal–Organic Framework. *Chem. Sci.* **2020,** *11,* 6709–6716.
573. Nouar, F.; Eubank, J. F.; Bousquet, T.; Wojtas, L.; Zaworotko, M. J.; Eddaoudi, M. Supermolecular Building Blocks (SBBs) for the Design and Synthesis of Highly Porous Metal-Organic Frameworks. *J. Am. Chem. Soc.* **2008,** *130* (6), 1833–1835.
574. Chen, B.; Eddaoudi, M.; Reineke, T.; Kampf, J.; O'keeffe, M.; Yaghi, O. $Cu_2(ATC)\cdot 6H_2O$: Design of Open Metal Sites in Porous Metal-Organic Crystals (ATC: 1,3,5,7-Adamantane Tetracarboxylate). *J. Am. Chem. Soc.* **2000,** *122* (46), 11559–11560.
575. Kaye, S. S.; Long, J. R. Hydrogen Storage in the Dehydrated Prussian Blue Analogues $M_3[Co(CN)_6]_2$ (M = Mn, Fe, Co, Ni, Cu, Zn). *J. Am. Chem. Soc.* **2005,** *127* (18), 6506–6507.
576. Hartman, M. R.; Peterson, V. K.; Liu, Y.; Kaye, S. S.; Long, J. R. Neutron Diffraction and Neutron Vibrational Spectroscopy Studies of Hydrogen Adsorption in the Prussian Blue Analogue $Cu_3[Co(CN)_6]_2$. *Chem. Mater.* **2006,** *18* (14), 3221–3224.
577. Ma, S.; Zhou, H.-C. A Metal-Organic Framework With Entatic Metal Centers Exhibiting High Gas Adsorption Affinity. *J. Am. Chem. Soc.* **2006,** *128* (36), 11734–11735.
578. Rowsell, J. L.; Yaghi, O. M. Effects of Functionalization, Catenation, and Variation of the Metal Oxide and Organic Linking Units on the Low-Pressure Hydrogen Adsorption Properties of Metal-Organic Frameworks. *J. Am. Chem. Soc.* **2006,** *128* (4), 1304–1315.
579. Dincă, M.; Yu, A. F.; Long, J. R. Microporous Metal-Organic Frameworks Incorporating 1, 4-Benzeneditetrazolate: Syntheses, Structures, and Hydrogen Storage Properties. *J. Am. Chem. Soc.* **2006,** *128* (27), 8904–8913.
580. Dincă, M.; Han, W. S.; Liu, Y.; Dailly, A.; Brown, C. M.; Long, J. R. Observation of Cu^{2+}–H_2 Interactions in a Fully Desolvated Sodalite-Type Metal–Organic Framework. *Angew. Chem. Int. Ed.* **2007,** *46* (9), 1419–1422.
581. Sumida, K.; Horike, S.; Kaye, S. S.; Herm, Z. R.; Queen, W. L.; Brown, C. M.; Grandjean, F.; Long, G. J.; Dailly, A.; Long, J. R. Hydrogen Storage and Carbon Dioxide Capture in an Iron-Based Sodalite-Type Metal–Organic Framework (Fe-BTT) Discovered via High-Throughput Methods. *Chem. Sci.* **2010,** *1* (2), 184–191.
582. Bloch, E. D.; Queen, W. L.; Hudson, M. R.; Mason, J. A.; Xiao, D. J.; Murray, L. J.; Flacau, R.; Brown, C. M.; Long, J. R. Hydrogen Storage and Selective, Reversible O_2 Adsorption in a Metal–Organic Framework With Open Chromium(II) Sites. *Angew. Chem.* **2016,** *128* (30), 8747–8751.

583. Asgari, M.; Semino, R.; Schouwink, P.; Kochetygov, I.; Trukhina, O.; Tarver, J. D.; Bulut, S.; Yang, S.; Brown, C. M.; Ceriotti, M.; et al. An In-Situ Neutron Diffraction and DFT Study of Hydrogen Adsorption in a Sodalite-Type Metal–Organic Framework, Cu-BTTri. *Eur. J. Inorg. Chem.* **2019,** *2019* (8), 1147–1154.
584. Chui, S. S.-Y.; Lo, S. M.-F.; Charmant, J. P.; Orpen, A. G.; Williams, I. D. A Chemically Functionalizable Nanoporous Material $[Cu_3(TMA)_2(H_2O)_3]_n$. *Science* **1999,** *283* (5405), 1148–1150.
585. Prestipino, C.; Regli, L.; Vitillo, J. G.; Bonino, F.; Damin, A.; Lamberti, C.; Zecchina, A.; Solari, P.; Kongshaug, K.; Bordiga, S. Local Structure of Framework Cu(II) in HKUST-1 Metallorganic Framework: Spectroscopic Characterization Upon Activation and Interaction With Adsorbates. *Chem. Mater.* **2006,** *18* (5), 1337–1346.
586. Callear, S. K.; Ramirez-Cuesta, A. J.; David, W. I.; Millange, F.; Walton, R. I. High-Resolution Inelastic Neutron Scattering and Neutron Powder Diffraction Study of the Adsorption of Dihydrogen by the Cu(II) Metal–Organic Framework Material HKUST-1. *Chem. Phys.* **2013,** *427,* 9–17.
587. Peterson, V. K.; Brown, C. M.; Liu, Y.; Kepert, C. J. Structural Study of D_2 Within the Trimodal Pore System of a Metal Organic Framework. *J. Phys. Chem. C* **2011,** *115* (17), 8851–8857.
588. Sumida, K.; Her, J.-H.; Dinca, M.; Murray, L. J.; Schloss, J. M.; Pierce, C. J.; Thompson, B. A.; FitzGerald, S. A.; Brown, C. M.; Long, J. R. Neutron Scattering and Spectroscopic Studies of Hydrogen Adsorption in $Cr_3(BTC)_2$—A Metal-Organic Framework With Exposed Cr^{2+} Sites. *J. Phys. Chem. C* **2011,** *115* (16), 8414–8421.
589. Lin, X.; Telepeni, I.; Blake, A. J.; Dailly, A.; Brown, C. M.; Simmons, J. M.; Zoppi, M.; Walker, G. S.; Thomas, K. M.; Mays, T. J.; et al. High Capacity Hydrogen Adsorption in Cu(II) Tetracarboxylate Framework Materials: The Role of Pore Size, Ligand Functionalization, and Exposed Metal Sites. *J. Am. Chem. Soc.* **2009,** *131* (6), 2159–2171.
590. Yan, Y.; Telepeni, I.; Yang, S.; Lin, X.; Kockelmann, W.; Dailly, A.; Blake, A. J.; Lewis, W.; Walker, G. S.; Allan, D. R.; Barnett, S. A.; Champness, N. R.; Schröder, M. Metal-Organic Polyhedral Frameworks: High H_2 Adsorption Capacities and Neutron Powder Diffraction Studies. *J. Am. Chem. Soc.* **2010,** *132* (12), 4092–4094.
591. Kapelewski, M. T.; Geier, S. J.; Hudson, M. R.; Stück, D.; Mason, J. A.; Nelson, J. N.; Xiao, D. J.; Hulvey, Z.; Gilmour, E.; FitzGerald, S. A.; Head-Gordon, M.; Brown, C. M.; Long, J. R. M_2(m-dobdc) (M = Mg, Mn, Fe, Co, Ni) Metal–Organic Frameworks Exhibiting Increased Charge Density and Enhanced H_2 Binding at the Open Metal Sites. *J. Am. Chem. Soc.* **2014,** *136* (34), 12119–12129.
592. Queen, W. L.; Bloch, E. D.; Brown, C. M.; Hudson, M. R.; Mason, J. A.; Murray, L. J.; Ramirez-Cuesta, A. J.; Peterson, V. K.; Long, J. R. Hydrogen Adsorption in the Metal–Organic Frameworks Fe_2(dobdc) and $Fe_2(O_2)$(dobdc). *Dalton Trans.* **2012,** *41* (14), 4180–4187.
593. Salles, F.; Kolokolov, D. I.; Jobic, H.; Maurin, G.; Llewellyn, P. L.; Devic, T.; Serre, C.; Férey, G. Adsorption and Diffusion of H_2 in the MOF Type Systems MIL-47(V) and MIL-53(Cr): A Combination of Microcalorimetry and QENS Experiments With Molecular Simulations. *J. Phys. Chem. C* **2009,** *113* (18), 7802–7812.
594. Li, H.; Li, L.; Lin, R.-B.; Zhou, W.; Zhang, Z.; Xiang, S.; Chen, B. Porous Metal-Organic Frameworks for Gas Storage and Separation: Status and Challenges. *EnergyChem* **2019,** *1* (1), 100006.
595. Rosnes, M. H.; Opitz, M.; Frontzek, M.; Lohstroh, W.; Embs, J. P.; Georgiev, P. A.; Dietzel, P. D. C. Intriguing Differences in Hydrogen Adsorption in CPO-27 Materials Induced by Metal Substitution. *J. Mater. Chem. A* **2015,** *3* (9), 4827–4839.
596. FitzGerald, S. A.; Mukasa, D.; Rigdon, K. H.; Zhang, N.; Barnett, B. R. Hydrogen Isotope Separation Within the Metal–Organic Framework Cu(I)-MFU-4l. *J. Phys. Chem. C* **2019,** *123* (50), 30427–30433.
597. Denysenko, D.; Grzywa, M.; Jelic, J.; Reuter, K.; Volkmer, D. Scorpionate-Type Coordination in MFU-4l Metal–Organic Frameworks: Small-Molecule Binding and Activation Upon the Thermally Activated Formation of Open Metal Sites. *Angew. Chem. Int. Ed.* **2014,** *53* (23), 5832–5836.
598. Weinrauch, I.; Savchenko, I.; Denysenko, D.; Souliou, S. M.; Kim, H.-H.; Tacon, M. L.; Daemen, L. L.; Cheng, Y.; Mavrandonakis, A.; Ramirez-Cuesta, A. J.; Volkmer, D.; Schütz, G.; Hirscher, M.; Heine, T. Capture of Heavy Hydrogen Isotopes in a Metal-Organic Framework With Active Cu(I) Sites. *Nat. Commun.* **2017,** *8* (1).
599. Barnett, B.; Evans, H. A.; Su, G. M.; Jiang, H. Z.; Chakraborty, R.; Banyeretse, D.; Hartman, T.; Martinez, M.; Trump, B. A.; Tarver, J.; Dods, M.; et al. Observation of an Intermediate to H_2 Binding in a Metal–Organic Framework. *ChemRxiv* **2020.** https://doi.org/10.26434/chemrxiv.13208207.v1. Preprint.
600. Waller, P. J.; Gándara, F.; Yaghi, O. M. Chemistry of Covalent Organic Frameworks. *Acc. Chem. Res.* **2015,** *48* (12), 3053–3063.
601. Han, S. S.; Furukawa, H.; Yaghi, O. M.; Goddard Iii, W. A. Covalent Organic Frameworks as Exceptional Hydrogen Storage Materials. *J. Am. Chem. Soc.* **2008,** *130* (35), 11580–11581.
602. Chandra, S.; Roy Chowdhury, D.; Addicoat, M.; Heine, T.; Paul, A.; Banerjee, R. Molecular Level Control of the Capacitance of Two-Dimensional Covalent Organic Frameworks: Role of Hydrogen Bonding in Energy Storage Materials. *Chem. Mater.* **2017,** *29* (5), 2074–2080.
603. Li, Z.; Zhi, Y.; Feng, X.; Ding, X.; Zou, Y.; Liu, X.; Mu, Y. An Azine-Linked Covalent Organic Framework: Synthesis, Characterization and Efficient Gas Storage. *Chem. Eur. J.* **2015,** *21* (34), 12079–12084.
604. Germain, J.; Hradil, J.; Fréchet, J. M.; Svec, F. High Surface Area Nanoporous Polymers for Reversible Hydrogen Storage. *Chem. Mater.* **2006,** *18* (18), 4430–4435.
605. Wood, C. D.; Tan, B.; Trewin, A.; Niu, H.; Bradshaw, D.; Rosseinsky, M. J.; Khimyak, Y. Z.; Campbell, N. L.; Kirk, R.; Stöckel, E.; et al. Hydrogen Storage in Microporous Hypercrosslinked Organic Polymer Networks. *Chem. Mater.* **2007,** *19* (8), 2034–2048.
606. Xu, S.; Luo, Y.; Tan, B. Recent Development of Hypercrosslinked Microporous Organic Polymers. *Macromol. Rapid Commun.* **2013,** *34* (6), 471–484.
607. McKeown, N. B.; Budd, P. M. Polymers of Intrinsic Microporosity (PIMs): Organic Materials for Membrane Separations, Heterogeneous Catalysis and Hydrogen Storage. *Chem. Soc. Rev.* **2006,** *35* (8), 675–683.
608. Ramimoghadam, D.; Gray, E. M.; Webb, C. Review of Polymers of Intrinsic Microporosity for Hydrogen Storage Applications. *Int. J. Hydrog. Energy* **2016,** *41* (38), 16944–16965.
609. Germain, J.; Fréchet, J. M.; Svec, F. Nanoporous Polymers for Hydrogen Storage. *Small* **2009,** *5* (10), 1098–1111.
610. Budd, P. M.; Butler, A.; Selbie, J.; Mahmood, K.; McKeown, N. B.; Ghanem, B.; Msayib, K.; Book, D.; Walton, A. The Potential of Organic Polymer-Based Hydrogen Storage Materials. *Phys. Chem. Chem. Phys.* **2007,** *9* (15), 1802–1808.
611. Meaghan, M. D.; Dworzak, M. R.; Gosselin, A. J.; Korman, K. J.; Bloch, E. D. Gas Storage in Porous Molecular Materials. *Chem. Eur. J.* **2021,** *27,* 1–18.
612. Sudik, A. C.; Millward, A. R.; Ockwig, N. W.; Cote, A. P.; Kim, J.; Yaghi, O. M. Design, Synthesis, Structure, and Gas (N_2, Ar, CO_2, CH_4, and H_2) Sorption Properties of Porous Metal-Organic Tetrahedral and Heterocuboidal Polyhedra. *J. Am. Chem. Soc.* **2005,** *127,* 7110–7118.
613. Gosselin, E. J.; Lorzing, G. R.; Trump, B. A.; Brown, C. M.; Bloch, E. D. Gas Adsorption in an Isostructural Series of Pillared Coordination Cages. *Chem. Commun.* **2018,** *54,* 6391.
614. Lorzing, G. R.; Gosselin, A. J.; Trump, B. A.; York, A. H. P.; Sturluson, A.; Rowland, C. A.; Yap, G. P. A.; Brown, C. M.; Simon, C. M.; Bloch, E. D. Understanding Gas Storage in Cuboctahedral Porous Coordination Cages. *J. Am. Chem. Soc.* **2019,** *141,* 12128–12138.
615. Savage, M.; da Silva, I.; Johnson, M.; Carter, J. H.; Newby, R.; Suyetin, M.; Besley, E.; Manuel, P.; Rudić, S.; Fitch, A. N.; et al. Observation of Binding and Rotation of Methane and Hydrogen Within a Functional Metal–Organic Framework. *J. Am. Chem. Soc.* **2016,** *138* (29), 9119–9127.
616. Runčevski, T.; Kapelewski, M. T.; Torres-Gavosto, R. M.; Tarver, J. D.; Brown, C. M.; Long, J. R. Adsorption of Two Gas Molecules at a Single Metal Site in a Metal–Organic Framework. *Chem. Commun.* **2016,** *52* (53), 8251–8254.
617. Luo, F.; Yan, C.; Dang, L.; Krishna, R.; Zhou, W.; Wu, H.; Dong, X.; Han, Y.; Hu, T.-L.; O'Keeffe, M.; Wang, L.; Luo, M.; Lin, R. B.; Chen, B. USTA-74: A MOF-74 Isomer With Two Accessible Binding Sites per Metal Center for Highly Selective Gas Separation. *J. Am. Chem. Soc.* **2016,** *138,* 5678–5684.
618. Wu, H.; Chua, Y. S.; Krungleviciute, V.; Tyagi, M.; Chen, P.; Yildirim, T.; Zhou, W. Unusual and Highly Tunable Missing-Linker Defects in Zirconium Metal–Organic Framework UiO-66 and Their Important Effects on Gas Adsorption. *J. Am. Chem. Soc.* **2013,** *135* (28), 10525–11053.

10.03 Structural studies of inorganic materials by electron crystallography

Maria Roslova*, Zhehao Huang, and Xiaodong Zou, Department of Materials and Environmental Chemistry, Stockholm University, Stockholm, Sweden

© 2023 Elsevier Ltd. All rights reserved.

10.03.1	**Introduction**	**52**
10.03.2	**Structure determination by electron diffraction**	**53**
10.03.2.1	Formation of electron diffraction	53
10.03.2.2	Protocols for the acquisition of electron diffraction data	56
10.03.2.2.1	Various techniques of zonal-axis 2D electron diffraction acquisition	56
10.03.2.2.2	Three-dimensional electron diffraction	57
10.03.2.2.3	Serial electron diffraction	58
10.03.2.3	Structure determination and phase analysis	59
10.03.2.3.1	Data processing	59
10.03.2.3.2	Structure solution	61
10.03.2.3.3	Structure refinement	62
10.03.2.3.4	Phase analysis	62
10.03.3	**Decoding atomic arrangements from high resolution images**	**64**
10.03.3.1	A conceptual picture of HRTEM image formation and contrast transfer	64
10.03.3.1.1	Image formation	64
10.03.3.1.2	Contrast transfer function (CTF)	64
10.03.3.2	Retrieval of structure projection by CTF correction and structure determination from HRTEM images by crystallographic image processing	65
10.03.3.3	STEM for electron crystallography applications: Imaging modes and different types of image contrast	67
10.03.3.3.1	Crewe's Z-contrast	67
10.03.3.3.2	Z^{2-x} contrast	68
10.03.3.3.3	ABF-STEM	68
10.03.3.3.4	Integrated differential phase-contrast (iDPC)	68
10.03.3.4	How can 3D crystallographic information be obtained from 2D high resolution images?	69
10.03.3.5	Advantages of aberration correction for HRTEM and HRSTEM investigations	71
10.03.4	**Applications of electron crystallography for studies of inorganic and functional materials**	**73**
10.03.4.1	Ab initio structure determination of perfectly periodic crystals by 3D ED and imaging	73
10.03.4.2	Outside the realm of perfectly periodic crystals	74
10.03.4.2.1	Mixed occupancies and vacancies	74
10.03.4.2.2	Planar discontinuities: Stacking disorder and nano-twinning	75
10.03.4.2.3	Superstructures and aperiodic structures	76
10.03.4.3	Detecting light elements by 3D ED and imaging	77
10.03.4.4	2D materials and thin films	78
10.03.4.5	Electron pair-distribution function analysis (ePDF) for amorphous materials	78
10.03.4.6	Orientation and secondary phases maps	81
10.03.4.7	Phase analysis and serial ED	81
10.03.5	**Conclusions and future prospects**	**82**
References		**83**

Abstract

The advance of electron crystallographic techniques during the last decade has had a significant impact on the structural analysis of micro- and nanocrystalline materials. 3D electron diffraction and atomic-resolution imaging are cornerstones of electron crystallography. In the chapter "Structural studies of inorganic materials by electron crystallography" we cover a broad range of topics, from the principles of image and diffraction pattern formation inside a transmission electron microscope, to recent advances in data collection and processing, making possible *ab-initio* crystal structure solution as well as in-depth microstructural investigations from μm- and nm-size regions of inorganic materials. We focus on obtaining detailed

*Current affiliation: Institute for Solid State and Materials Research (IFW) Dresden, Dresden, Germany

structural information at atomic resolution, which is essential for developing new materials, optimizing their properties and utilizing their full functionality.

10.03.1 Introduction

Electron crystallography has been widely applied to structural studies of inorganic materials. One of the recent trends, changing the landscape of modern crystallography, is a reduction in the crystal size required for structure determination. Micro- and nanocrystals that were once considered too small to be of use, are now delivering high-resolution structural data, thanks to the implementation and development of electron crystallographic methods. Decoding of atomic arrangement in solids from high resolution imaging and electron diffraction datasets has become a valuable alternative to conventional X-ray and neutron diffraction. It is worth noting that the scope of electron crystallography is significantly broader than that of X-ray or neutron crystallography, and includes nearly any use of electron diffraction, electron scattering, or direct imaging with the purpose of obtaining structural information.

Various imaging modes can be integrated with electron diffraction and, if necessary, with spectroscopic techniques in a transmission electron microscope (TEM) to gain comprehensive structural and compositional information from a specimen with very high spatial (<1 Å) resolution. TEM is the main working instrument for solving electron crystallography tasks. Standard TEMs designed for materials analysis are typically equipped with a Schottky type or a cold field emission gun (FEG) and operate at an accelerating voltage between 80 and 300 kV. Tungsten and LaB_6 filaments are still common, but they are less bright, and produce a less coherent electron probe. Using condenser electromagnetic lenses, we shape the incoming electron beam onto the specimen. The specimen scatters and diffracts electrons, and the magnetic field created by the pole piece of the objective lens focuses them on its back focal plane. Then, using intermediate and final projector lenses, we magnify and focus the projected pattern to a camera, see Fig. 1. We are able to control the electron's ray path when forming either an image or a diffraction pattern, by changing the parameters of the electron gun, positioning apertures along the optical path, and changing the current in the electromagnetic lenses. There are different ways to shape the electron beam onto the specimen, as shown in Fig. 1. In the high-resolution transmission electron microscopy (HRTEM) mode, a larger probe with parallel illumination is formed (convergence angle is ≤ 0.1 mrad), analogous to conventional optical microscopes. In the scanning transmission electron microscopy (STEM) mode, the electron beam converges to a small probe with a large convergence angle (typically 20–30 mrad) and this probe is scanned across a sample driven by a set of scan coils. For a thin specimen the incident beam is transmitted, and several signals can be detected simultaneously by STEM detectors. The high-angle annular dark-field (HAADF) detector collects Rutherford scattering from the atomic nuclei, producing an image

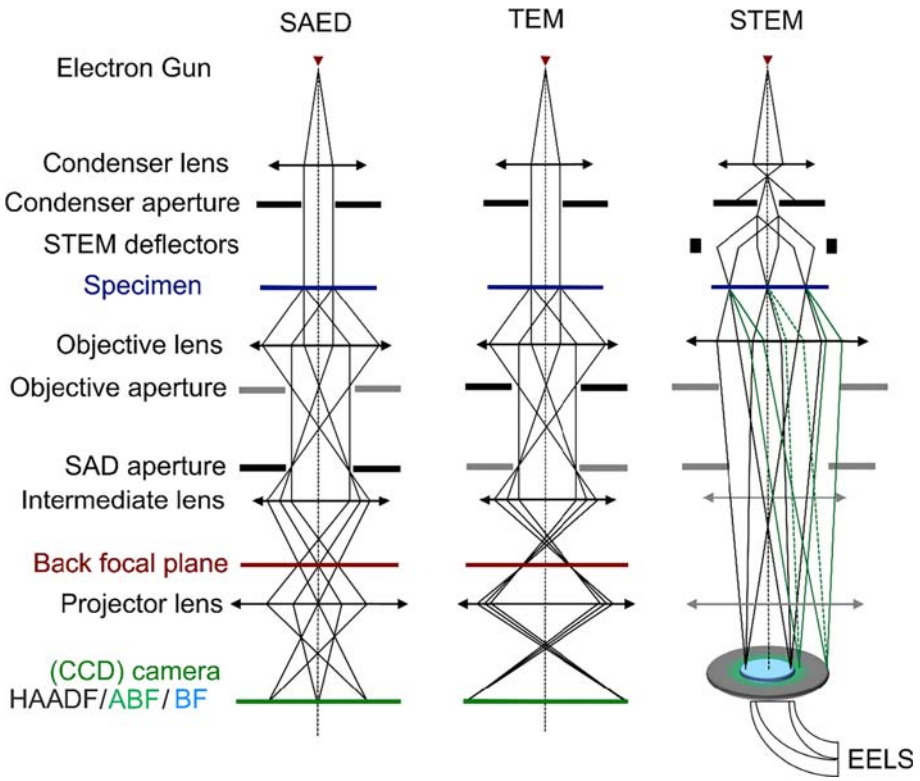

Fig. 1 Schematic showing the electron ray paths in different modes relevant for electron crystallography: selected area diffraction (SAED), conventional transmission electron microscopy imaging (TEM), scanning transmission electron microscopy (STEM).

with a strong sensitivity to atomic number Z, often called a *Z*-contrast. Columns of light atoms are weakly visible in HAADF images, but they may be seen in a bright-field (BF) image or an annular bright-field (ABF) image. If we extract the BF detector, the electrons can reach the entrance of an electron energy loss spectrometer (EELS) and provide elemental maps and electronic structure information. High-resolution imaging offers numerous possibilities to determine crystal structures. The structural information in the image, however, is prone to many factors that can alter the phase relationships between the scattered beams[1]:

(1) thickness of the crystal is crucial, in thick specimens dynamical effects can dominate;
(2) unless exactly at the zone axis, crystal tilt can be a problem in image interpretation;
(3) lens aberrations can alter dramatically the relative phases of the scattered beams, especially at high resolution.

Nevertheless, a great deal of success came from images and crystallographic image analysis, retrieving phases from images and relating these directly to the structure factor phases, starting first with biological molecules[2] and later organic and inorganic crystals.[3–6]

A diffraction pattern, in turn, is formed in the objective lens' focal plane and represents the Fourier transform of the transmitted wave function, as explained by the theory of Fourier optics. Thus, an individual 2D diffraction pattern can be taken by projecting the back focal plane of the image to the camera. Compared to imaging, diffraction has the unique advantages that the data resolution is not affected by lens aberrations and much thicker crystals can be used. Images are also hardly interpretable if they are not taken exactly at certain zone-axes and no prior knowledge of the crystal structure is available.

Moving from 2D to 3D, in order to obtain a dataset suitable for 3D reconstruction, we rotate the crystal under investigation around an arbitrary axis, either in steps or continuously, and record a diffraction pattern at each step or at certain tilt intervals. A 3D ED data set is essentially a sequence of diffraction patterns recorded at different tilt angles of a crystal. It is worth noting that different research groups working in the field of electron crystallography tend to use different acronyms, depending on experimental set-ups for data acquisition, such as automated diffraction tomography (ADT),[7–9] electron diffraction tomography (EDT),[10] precession-assisted electron diffraction tomography (PEDT),[11,12] rotation electron diffraction (RED),[13] continuous rotation electron diffraction (cRED),[14] and microcrystal electron diffraction (MicroED).[15,16] The generic term 3D ED is used when broadly referring to all of them.

Diffraction is remarkably useful for solving structures from micro- and nanocrystals of different materials. In the pioneering works of Pinsker and Vainshtein,[17,18] the first proof-of-principle structure solution for an inorganic compound was undertaken, although at the early stages mostly organic crystals were studied, where undesirable dynamical effects are less significant. Zvyagin et al. applied electron diffraction to clay minerals analysis in 1967,[19] later the first examples of *ab-initio* solved inorganic structures appeared, e.g. MCM-22 zeolite[20] (1995), $(Ga, In)_2SnO_5$[21,22] (1998), a metastable alloy phase Al_mFe[23] with 90 Al and 20 Fe atoms (1998), β-Ti_2Se and several other related metal-rich compounds (2000).[24] Beginning in 2016, several reviews have been published summarizing case studies by 3D ED for different classes of materials. Gemmi et al. reviewed existing data collection protocols and gave a broad overview of structures solved by 3D ED, including functional materials, porous materials, minerals, proteins and other structures of biological relevance.[25] The recent review article by Huang et al. focuses on metal-organic and covalent organic frameworks solved by 3D ED.[26] Structure determination by electron crystallography of porous materials, such as zeolites and MOFs, was reviewed by Zou's group.[27–29] Methods and approaches for handling disordered nanocrystalline materials have been reviewed by Mugnaioli and Gorelik[30] as a contribution to a special issue of Acta Cryst. B devoted to electron crystallography. 3D ED data acquisition can be performed at cryogenic temperatures using a cryo-sample holder or in a cryo-TEM. It collects electron diffraction data as the crystals are continuously rotated in the beam under very low electron doses. It facilitates the structure determination of proteins, peptides, and radiation sensitive organic molecules. The topic cannot be sufficiently covered in this chapter, but an interested reader may wish to consult review papers published by Nannenga[16] and Clabbers and Xu.[31] A fundamental description of electron diffraction can be found in the books by Zuo and Spence[32] and Zou et al. [33]

In this chapter we will cover a broad range of electron crystallography topics, from principles of image and diffraction formation in the TEM in **Section 10.03.1**, to recent advances in data collection and processing, and complex cases of structure determination. Before entering into a critical review of recent structural studies in the **Section 10.03.4**, we will give a brief overview and present the methodology of electron diffraction as well as high resolution image analysis in **Sections 10.03.2 and 10.03.3**, respectively. We will describe several advanced techniques for diffraction experiments, including precession electron diffraction (PED), 3D electron diffraction as represented by ADT, RED, continuous rotation electron diffraction (cRED), Serial electron (rotation) diffraction (SerialED/RED) and cluster analysis for phase identification. We will also give a pictorial introduction to crystallographic image processing, including the extraction of phases and amplitudes from images, structure projection reconstruction by image processing, and 3D reconstruction from HRTEM and STEM images. Finally, **Section 10.03.5** addresses some of the outstanding experimental and theoretical problems that still confront the method, in order to give a further idea of the present-day limitations of electron crystallography as well as the prospects for its continued development and improvement.

10.03.2 Structure determination by electron diffraction

10.03.2.1 Formation of electron diffraction

Diffraction is a phenomenon that lends itself directly to detailed mathematical modelling. Recent developments and applications of 3D ED have shown that accurate atomic structures can be obtained from 3D ED data using a refinement that assumes kinematical

3D ED intensities. However, almost uniformly across all the structure refinements using 3D ED, the final R factors, which are used to ascertain the quality of the structure determination, have remained far higher than those for most equivalent X-ray diffraction refinements. To understand the origin of that, we have to ask how electron diffraction fundamentally differs from X-ray diffraction, and derive equations that form a basis for further discussion of 3D ED.

Electrons interact with the nuclei and electrons of solids through electrostatic Coulomb interactions. An incident electron can pass straight through the specimen with no interactions, can be scattered by the Coulomb potential in the sample with no energy loss (elastic scattering), and with a loss of energy (inelastic scattering). Generally, electron scattering in solids can be reduced to an effective one-body Schrödinger equation for the incident electron

$$\left[-\frac{\hbar^2}{2m}\nabla^2+\varphi(\mathbf{r})\right]\Psi(\mathbf{r})=E\Psi(\mathbf{r}) \tag{1}$$

where $\Psi(\mathbf{r})$ is the wave function of an incident electron, $\varphi(\mathbf{r})$ is the electrostatic Coulomb potential, m is the electron mass, $\hbar$ is the Planck constant. This equation can be solved numerically by different methods.[34–41] The simplest approach to describe the electrostatic potential of a specimen is by linear superposition of the spherically symmetric electrostatic potentials of each atom in it, neglecting any effect resulting from a charge redistribution in bringing together isolated atoms, which is known as an "independent atom model." The electron charge distribution can be computed from the knowledge of the atomic wave function, which can be obtained by numerically solving the Dirac equation under suitable approximations. For a single isolated atom, the atomic potential is related to the atomic charge distribution via Poisson's equation:

$$\nabla^2\varphi(\mathbf{r})=-4\pi\{\rho_n(\mathbf{r})-\rho_e(\mathbf{r})\} \tag{2}$$

yielding

$$\varphi(r)=\int\frac{e^2\rho_e(\mathbf{r}')}{|\mathbf{r}-\mathbf{r}'|}d\mathbf{r}'-\sum\frac{Ze^2}{|\mathbf{r}-R_n|} \tag{3}$$

for an assemble of scatters sitting at R_n.[42]

It contains a first contribution, $\rho_n(\mathbf{r})$, from the nucleus with the charge Ze and a second contribution, $\rho_e(r)$, from the charge distribution of the electrons in the atom (which is the electron density function as determined from X-ray scattering). Next, the atomic scattering factor is defined as the three-dimensional Fourier transform of the $\varphi(\mathbf{r})$. The Fourier transform is a unifying concept in X-ray and electron diffraction (and also in optical and neutron diffraction).

$$f^{(e)}(u)=K.\mathscr{F}\{\varphi(\mathbf{r})\}, \tag{4}$$

where K is a constant and in SI units $K=\frac{2\pi\varepsilon_0}{a_0e}$, e is the electron charge, ε_0 is the vacuum permittivity and a_0 is the Bohr radius, 0.0529 nm. In Fourier space, this then yields the atomic scattering factor given by the Mott–Bethe formula relating the atomic scattering factors of electrons to those of X-rays (detailed equation derivation is given in[43])

$$f^{(e)}(q)=\frac{\mathrm{m}e^2}{8\pi\varepsilon_0\hbar^2}\,\frac{\left[Z-f^{(X)}(q)\right]}{q^2}=\frac{0.0239\left[Z-f^{(X)}(q)\right]}{q^2} \tag{5}$$

where $q=\sin\theta/\lambda$, θ is the half of the scattering angle, and λ is the wavelength.

The Fourier transform of the electron density distribution yields the X-ray scattering factor, $f^{(X)}$. By accounting for the contribution of the nuclei to the X-ray scattering factor using the Mott–Bethe formula, one can then calculate the electron scattering factor. Resulting tabulated data are available for both X-ray and electron scattering factors for all the neutral atoms.[44,45] These numerical values for the scattering factors are used in all structure refinements by 3D ED. In addition to the scattering factor approach describing the low angle elastic scattering ($\theta\leq\sim3^{\circ}$), for some applications (e.g. computations of scattering into higher-order Laue zones) we need also to include scattering at very high angles. In these cases, the numerical values of atomic scattering factors can be taken from Lobato and van Dyck.[46]

Most physical process of electron diffraction can be described mathematically by a Fourier transform. For a crystal with a periodic lattice repeating according to basis vectors $\vec{a}$, $\vec{b}$, $\vec{c}$, the Fourier coefficients Φ_{hkl} are non-zero only when $\mathbf{u}=ha^*+kb^*+lc^*$, $\mathbf{u}$ is a spatial frequency corresponding to a reciprocal lattice vector in the crystal

$$\Phi_{hkl}=\int_{\mathrm{V}}\varphi(r)\cdot e^{-2\pi\mathbf{u}\cdot\mathbf{r}_i}\,dr \tag{6}$$

where h, k, l are the Miller indices of the reflecting net planes and V is the volume of the unit cell. These Fourier coefficients represent electron plane waves that are scattered by the electrostatic potential in the crystal in directions that are defined by Bragg's law.[47] Bragg's law states that for in-phase arrival of two electron waves scattered from successive "planes" within the crystal, at the observation point, the path length difference between them must be equal to an integer number of wavelengths

$$2d_{hkl}sin\theta=\lambda \tag{7}$$

where d_{hkl} is the inter-planar spacing involved ($d_{hkl}=1/|\mathbf{u}_{hkl}|$) and θ is the angle between the incident (or diffracted) ray and the relevant crystal planes, also known as Bragg angle. While Bragg's equation in direct space is simple and elegant, it is not very useful

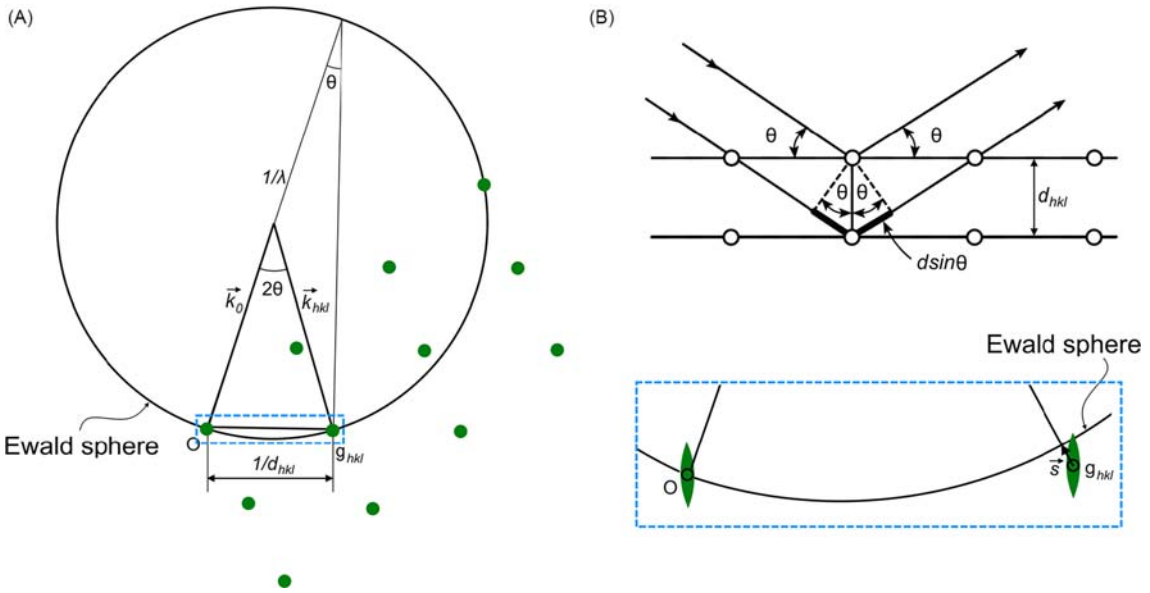

Fig. 2 (A) Ewald sphere construction, geometric relationship between k_{hkl}, k_0, θ, and λ. (B) The excitation error. The sign of s is negative when g_{hkl} is outside the Ewald sphere and positive is inside the Ewald sphere. We can change *s* by tilting the specimen or tilting the beam above the specimen.

for determination of the absolute direction of a diffracted wave, since both incident beam direction and crystal orientation must be specified with respect to some reference frame. To incorporate absolute wave directions, we may want to think about Bragg's condition in reciprocal space. In reciprocal space a plane wave can be represented by its wave vector $\vec{k}$, fully characterizing the direction and the wavelength of the wave with respect to the crystal reference frame. In Fig. 2, the incident wave vector $\vec{k}_0$ has length of $1/\lambda$, starts at the crystal points in the direction of the incident beam and ends at the origin O of the reciprocal lattice. The scattered wave vector $\vec{k}_{hkl}$ has the same length $1/\lambda$ since we deal with an elastic scattering event with no energy loss. The difference between two wave vectors is

$$|k_{hkl} - k_0| = \frac{1}{d_{hkl}} = \frac{2sin\theta}{\lambda} \tag{8}$$

which is the same as Bragg's law in direct space. Hence, each reciprocal lattice vector $\vec{g}_{hkl} = \vec{k}_{hkl} - \vec{k}_0$ will lie on a sphere with a radius $1/\lambda$, called the Ewald sphere, passing through the origin of the reciprocal lattice. When combined with the Ewald sphere construction, the reciprocal lattice is a very convenient way of thinking about diffraction. When the sphere exactly cuts through a point, Bragg's law is exactly satisfied. Here, a fundamental difference between X-ray and electron diffraction appears – for electrons the Ewald sphere radius of curvature is very large when compared to the reciprocal-lattice vectors (e.g. for 200 keV electrons, $k \simeq 40\ \text{Å}^{-1}$). For a very thin crystal each reciprocal-lattice point is effectively extended into a spike or rod, and many spikes usually intersect the nearly flat Ewald sphere. Hence a typical electron diffraction pattern contains many diffraction spots, but *not all of them exactly satisfy Bragg's condition*. This differs significantly from X-ray diffraction where each beam is an "arranged event", since the radius of curvature of the Ewald sphere is small (typically $k \simeq 1\ \text{Å}^{-1}$) and the crystal has to be oriented very precisely to fulfil the Bragg condition for a given reflection.

Bragg's law gives us the geometric conditions for diffraction to occur. It does not treat the diffraction intensity. However, the intensity can be easily calculated if we assume the idealized case of single scattering for electrons by the crystal. This is the conceptual basis for kinematical scattering, which can be reasonably well adhered to while recording experimental data from very thin specimens,[48] when the nanocrystals are less than 50–100 nm, do not contain heavy atoms (such as, e.g., Pb or Au), and possess crystal structures where not all the atoms scatter in phase (e.g. face-centered cubic close-packed structure with space group *Fm*-3 *m*).[49]

The kinematical approximation implies that diffracted intensity is proportional to the amplitude square of the corresponding structure factor F_{hkl},

$$F_{hkl} = \frac{2\pi me}{\hbar^2}\Phi_{hkl} = \sum_i f_i^{(e)} T_i \exp(2\pi i \mathbf{u}\cdot\mathbf{r}_i) \tag{9}$$

$$I_{hkl} \propto |F_{hkl}|^2 \tag{10}$$

where $f_i^{(e)}$ is the atomic scattering factor for electrons, $T_i = \exp(-Bu^2)$, B is the Debye-Waller factor or B-factor.[50] Note that the Debye-Waller factor describes the exponential decay of the diffraction amplitudes with increasing scattering angle since $u \propto \sin\theta/\lambda$. Note also that while the first Born approximation ensures that the atomic scattering factors are real numbers, the structure factors are

complex numbers with a modulus and phase (angle). The Fourier series method similar to that used for X-rays crystallography can be employed to obtain an electrostatic potential map, containing well defined maxima at atom positions.

With increasing crystal thickness (>150 nm), electrons will be scattered multiple times in the crystal, i.e. dynamical scattering, which alters the intensities of the diffracted electron beams so that the kinematical approximation as given in Eq. (10) no longer holds. The effects of dynamical scattering depend on the atomic structure, and the thickness and orientation of the crystal, which determine the number of reflections that are excited simultaneously at the Bragg conditions. An important parameter is the excitation error s, which is a measure how far a reflection deviates from the exact Bragg condition (vector s in **Fig. 2**B). The excitation error is important for electron diffraction theory because if a reflection is measured out of its exact Bragg conditions, severe underestimation of the intensity may occur. To have an idea of the impact of excitation error on the correct estimation of structure factor amplitudes, we can calculate how far from a perfect Bragg condition the intensity drops off by 50%. For a specimen with a thickness of 200 Å, this happens at $s = 0.0022$ Å^{-1}. Such an excitation error corresponds to a tilt of 0.35° off from Bragg condition for a reflection of 3 Å periodicity, and to smaller tilts for higher resolution reflections.[51]

In practice, dynamical effects can be reduced by collecting off-zone axis diffraction data. This was first shown by Vincent and Midgley in precession electron diffraction (PED) data where the electron beam is tilted away from a zone axis by a small angle (0.5–2°) and processed around the zone axis while the data are collected.[52] However, it cannot eliminate completely the dynamical effects, and some residual effects may manifest themselves either through increased dynamic interactions at, or near, zone-axes and strong systematic rows, or by changes in the probability of multiple scattering with an increase in thickness as the sample is tilted.[53] It might look superfluous to use dynamical-diffraction theory together with PED, but in practice this combination is very helpful[54] since the dynamical-diffraction theory provides a solid background for such residual dynamical diffraction effects to be taken into account and corrected for, refining in a first step only the experimental parameters: sample thickness, individual scale and fine orientation of each diffraction pattern. More examples and explanation of PED will be given later in this chapter.

Summing up, atoms in crystals are weakly scattering objects for X-rays, but strongly scattering objects for electrons. The atomic scattering factors for electrons are about 3–4 orders of magnitudes larger than those for X-rays ensuring that there will be sufficiently high diffraction intensities even from nanosized crystals made of light elements. On the other hand, it follows that multiple scattering is much more important for electrons than that for X-rays. While structure solution of unknown crystals from electron diffraction data has proven to be as successful as for X-rays, structure refinement, assuming the intensities are kinematical and not taking into account the multiple scattering, consistently leads to high R factors. The likely major reason for this, in the vast majority of cases, is that individual intensities, indeed all electron diffraction intensities in general, are not kinematical. Other factors to be taken into account are:

(1) Systematic errors in integration of diffraction intensity if a reflection is measured out of its exact Bragg conditions;
(2) Missing wedge of 3D ED data due to limited tilt range in a TEM; It is often necessary to merge data collected from different crystals.
(3) Beam damage. For beam sensitive samples the incident beam can cause structural changes or amorphization, sometimes even under cryogenic conditions.

10.03.2.2 Protocols for the acquisition of electron diffraction data

10.03.2.2.1 Various techniques of zonal-axis 2D electron diffraction acquisition

Selected area electron diffraction (SAED) is one of the most common techniques for acquiring two-dimensional (2D) electron diffraction patterns. A selected area aperture, which is located at the imaging plane below the sample, is typically used to limit the area used for obtaining an SAED pattern. When the intermediate lens is focused on the back focal plane, an SAED pattern is displayed. Depending on the type of sample, the SAED pattern can contain sharp spots from single crystal, ring patterns from nanocrystalline powders, or diffused ring patterns from amorphous samples. An example SAED pattern is shown in **Fig. 3**A. Because of the short wavelength of electrons, the Ewald sphere is almost flat when cutting through the reciprocal lattice of a crystal. Therefore, it is difficult to obtain 3D information from a single SAED pattern. Thus, SAED is mostly used for analyzing known materials. In order to determine the unit cell parameters of an unknown crystal, it is necessary to tilt the crystal and collect SAED patterns from different orientations.

Precession electron diffraction (PED) is a unique technique to collect ED patterns.[52] Unlike using a stationary incident beam in conventional ED, PED applies a tilted incident electron beam around the optical axis of the microscope, and uses a double conical scanning system where the beam is de-scanned below the sample. In this way, PED patterns contain more reflections cut by the Ewald sphere, and the intensities of most reflections are integrated. As fewer reflections are excited simultaneously when the beam is tilted, dynamical effects are reduced (**Fig. 3**). However, similar to conventional ED patterns, it is difficult to obtain 3D information from a single PED pattern and therefore determine the unit cell of unknown materials.

Convergent beam electron diffraction (CBED) applies a focused and convergent beam to the specimen. The resulting diffraction patterns consist of discs, instead of sharp diffraction spots. In CBED patterns, it is possible to obtain information from high order Laue zones (HOLZ), which can be used to determine the unit cell and space group of unknown materials from a single CBED pattern.

Nanobeam electron diffraction (NBED) is another technique to obtain 2D electron diffraction patterns by using a nanosized, and ideally, parallel electron beam to select the crystal instead of selected area aperture. In modern TEMs, such an electron

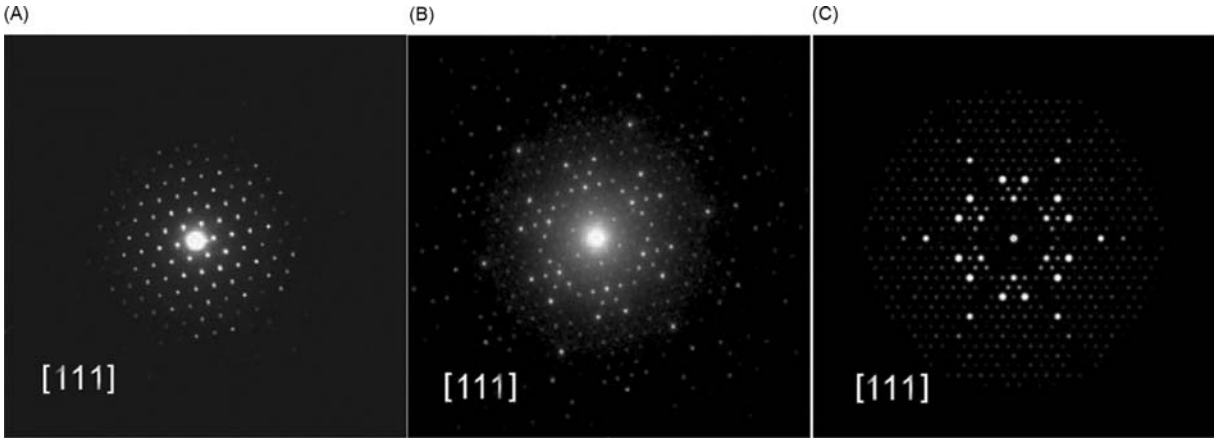

Fig. 3 Electron diffraction patterns of uvarovite, $Ca_3Cr_2(SiO_4)_3$, with precession (A) off and (B) on. (C) Simulated diffraction pattern, using the kinematical approximation.[55] Reproduced from ref. Gemmi, M.; Nicolopoulos, S. *Ultramicroscopy* **2007**, *107*, 483–494, with permission from the International Union of Crystallography, copyright 2007.

beam is achieved using the C3 condenser lens. Nowadays, a coherent electron beam with diameter < 1 nm can be obtained using spherical aberration-corrected (Cs-corrected) TEMs.

10.03.2.2.2 Three-dimensional electron diffraction

As mentioned, it is difficult to study unknown materials using a single SAED or PED pattern, and CBED typically requires a high electron dose which damages the sample. Although it is possible to combine a series of zonal-axis SAED patterns to study new materials,[56–58] it is often demanding in terms of expertise and time to collect SAED patterns from many zone axes, and data merging is also problematic. Three-dimensional electron diffraction (3D ED) techniques have been developed to overcome this challenge (**Table 1**).

The first data collection strategy to obtain a 3D ED dataset involved stepwise tilting of the sample at fixed angular steps. This is referred to as automated diffraction tomography (ADT)[7,8] and rotation electron diffraction (RED).[13,60] The goniometer stops at each tilt step to enable the acquisition of an ED pattern (**Fig. 4**A and B). After sequentially collecting a series of ED patterns, the 3D reciprocal lattice can be reconstructed from the collected sequence, which provides crucial information for structure determination. While ADT works in STEM mode using a nanosized quasi-parallel beam, RED works in TEM mode using a parallel beam. Regardless of the TEM setup, however, there is a gap between two step positions (typically 0.5–2°), which results in missing information in the datasets. This missing information can be filled by beam precession using PED[52] or using fine beam tilting (RED)[13] (**Fig. 4**C and D). In precession-assisted electron diffraction tomography (PEDT), the beam is tilted away from the optical axis of the microscope and scanned around the axis on a vertex fixed on the sample (**Fig. 4**). In RED, the beam tilt step can be accurately adjusted to typically 0.01–0.10° by using the TEM deflection coils (**Fig. 4**D). Therefore, to collect a RED dataset, it combines large goniometer tilt steps (i.e. 2.0°) followed by a series of beam tilt steps (i.e. 0.10°) to fill the gap (i.e. 2.0°). During the goniometer tilt, the crystal may move out of the electron beam. Thus, it is important to check the crystal position and re-center the crystal back to the beam. In PEDT and RED, crystal tracking and re-centering are done in image mode, ensuring the maximum reciprocal space coverage.

The most recently developed 3D ED techniques are based on a continuous rotation data acquisition strategy, including continuous rotation electron diffraction (cRED),[14,66] integrated electron diffraction tomography (Fast-EDT)[65] and microcrystal electron

Table 1 Comparison of different 3D ED protocols.

Protocol name	*Data collection strategy*	*Data collection speed*	*EM mode*	*Beam tilt*	*Beam procession*	*Publication year*	*References*
ADT/PEDT	Stepwise	Slow	STEM	No	Yes	2007	7,59
RED	Stepwise	Slow	TEM	Yes	No	2010	13,60
EDT	Stepwise	Slow	TEM	Yes	No	2013	10
MicroED	Stepwise	Slow	TEM	No	No	2013	61
Rotation electron diffraction	Continuous	Fast	TEM	No	No	2013	62
MicroED	Continuous	Fast	TEM	No	No	2014	63
Fast-ADT/EDT	Continuous	Fast	TEM	No	No	2015	64,65
cRED	Continuous	Fast	TEM	No	No	2018	14

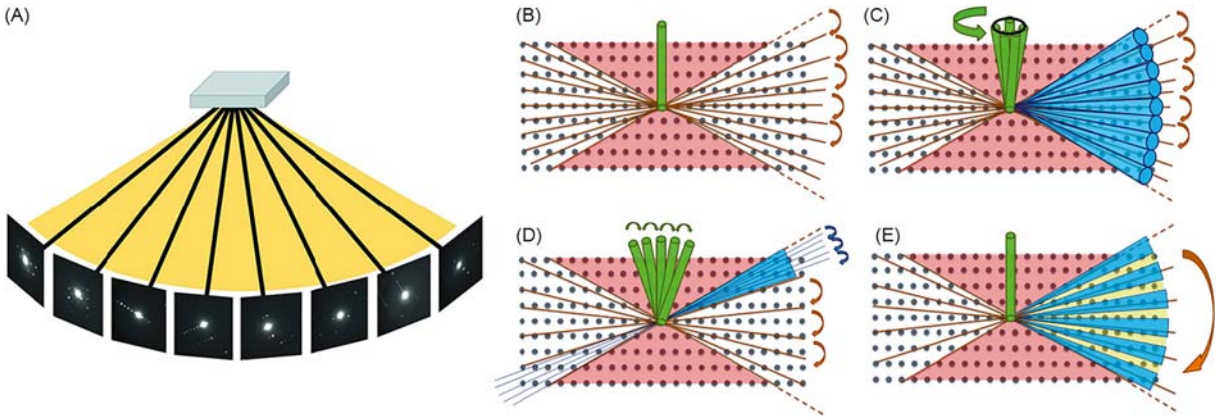

Fig. 4 (A) Schematic illustrations of 3D ED data collection.[13] 3D ED data collected on a crystal by goniometer tilt. ED frames of arbitrary orientations are collected at different rotation angles. The stepwise acquisition performed by (B) goniometer tilt only, (C) combination of goniometer tilt and precession electron beam, and (D) combination of goniometer tilt and beam tilt. (E) The continuous rotation acquisition. The sample is tilted within the entire goniometer range while a sequence of ED patterns are recorded. Brown, goniometer tilt; green, electron beam; blue, data range; yellow, detector readout time.[25] Reproduced from refs. Wan, W.; Sun, J.; Su, J.; Hovmöller, S.; Zou, X. *J. Appl. Crystallogr.* **2013**, *46*, 1863–1873 and Gemmi, M.; Mugnaioli, E.; Gorelik, T. E.; Kolb, U.; Palatinus, L.; Boullay, P.; Hovmöller, S.; Abrahams, J. P. *ACS Cent. Sci.* **2019**, *5*, 1315–132963, with permission from the International Union of Crystallography and American Chemical Society, copyright 2013 and 2019, respectively.

diffraction (MicroED).[61,63] In contrast to the stepwise 3D ED methods, in the continuous rotation data acquisition, the goniometer rotates continuously at a constant speed during the entire data acquisition (Fig. 4E). Therefore, the angular step between frames in a continuous rotation dataset is determined by the detector exposure time combined with the goniometer rotation speed. However, because most detectors require a readout time for saving each image, no data will be collected during the data readout period. A detector with a fast readout time would be beneficial to reduce the loss of reciprocal space sampling. The most significant advantage of continuous rotation methods is that a high goniometer rotation speed can be applied for data collection. As a result, one major obstacle in electron diffraction, the beam damage, can be minimized, which allows 3D ED to study beam sensitive materials. This is because the beam damage is related to the total electron dose the sample is exposed to, as defined by.

$$D = T \bullet I \tag{11}$$

where D denotes electron dose per $Å^2$, T is exposure time, and I is dose rate or beam current. It is clear that decreasing the data collection time can reduce the total electron dose on the sample exposed in electron beam. This has been enhanced by the development of direct detectors, which have very short readout times. Exploiting the recording speed of such detectors, for example, a complete dataset obtained by continuous rotation methods can be achieved within one minute, and the electron dose rate can be kept below 0.1 e s^{-1} $Å^{-2}$. Furthermore, because the reciprocal lattice is completely sampled, the continuous rotation methods provide more accurate integrated intensities. However, the crystal can easily move out of the beam during the rotation caused by the alignment and instability of the goniometers. Because the data collection is performed continuously without any interruption, it is difficult to re-center the crystal as in stepwise methods. This problem is solved in the data acquisition program *Instamatic*.[14,67] By using *Instamatic*, diffraction pattern can be defocused at a regular interval (e.g., after every 10 diffraction patterns), and the crystal of interest can be visualized in the defocused image. In this way, re-centering of crystals can be achieved without stopping the crystal rotation.

10.03.2.2.3 Serial electron diffraction

Serial electron diffraction (SerialED) is an emerging technique that provides new opportunities for the study of polycrystalline materials, particularly those that only form nano-sized crystals and are sensitive to beam damage. In a SerialED experiment, ED patterns are collected on a vast number of randomly oriented crystals, each of which is exposed only once, and an ED pattern is acquired before beam damage occurs. After combining diffraction patterns from many different crystals (typically 100–1000), a complete 3D dataset can be obtained and used for structural analysis. This requires effort to collect data from a large number of crystals. Therefore, automation of data collection is becoming increasingly important to increase the throughput of identifying suitable crystals, and acquiring ED patterns. *Instamatic* was developed for automated collection of SerialED data.[14,67] It utilizes software-controlled stage translation and beam shift to identify, track, and collect ED patterns on a large number of crystals. Practically, parallel illumination is used in imaging mode to identify and track crystals. In diffraction mode, the electron beam is focused to approximately 400 nm using the first condenser lens to collect ED patterns (Fig. 5A). Besides using a TEM setup for data collection by *Instamatic*, STEM-based SerialED has been developed as well.[68] In STEM mode, a low magnification image with an overview of the TEM grid is first recorded, followed by mapping of the positions of the crystals. ED patterns are then recorded from each mapped crystal (Fig. 5B). After completion of data acquisition from the mapped region, the TEM stage is moved to an adjacent new region and

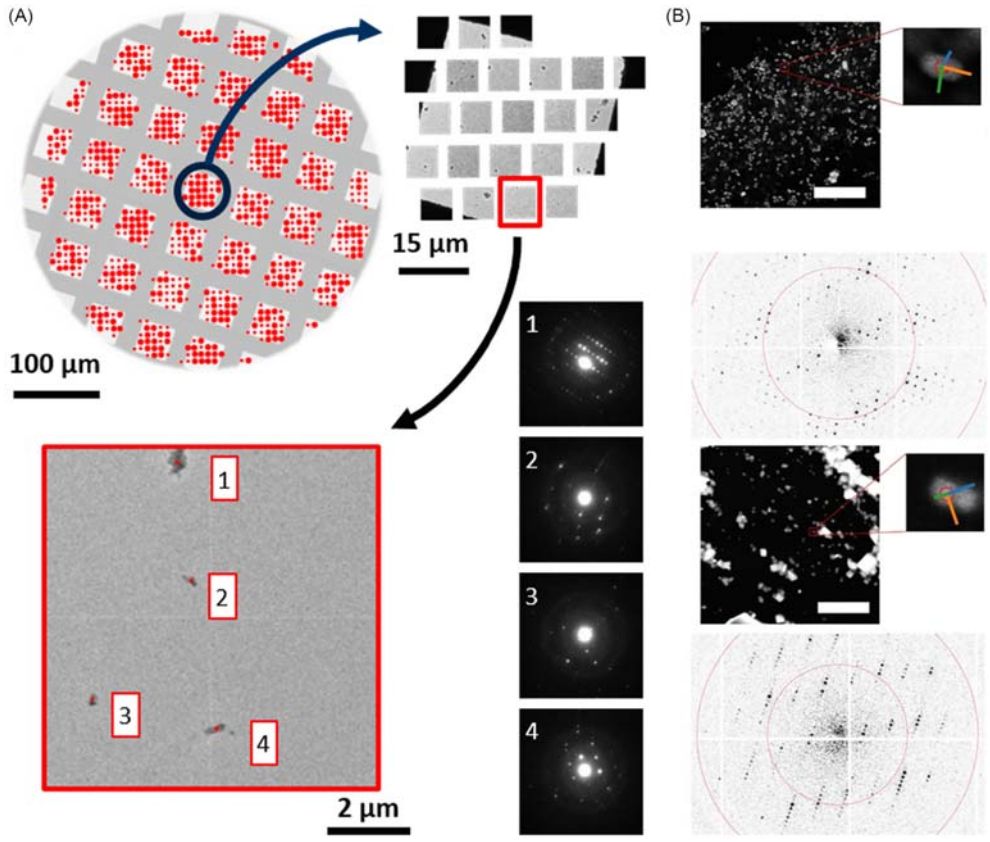

Fig. 5 SerialED performed in (A) TEM mode,[14] and (B) STEM mode.[68] The same core concept is shared in these two protocols, where a low magnification image is first taken to identify the positions of crystals, and ED patterns are thereby recorded from each mapped crystal. Reproduced from ref. Cichocka, M. O.; Ångström, J.; Wang, B.; Zou, X.; Smeets, S. *J. Appl. Crystallogr.* **2018**, *51*, 1652–1661 and ref. Bücker, R.; Hogan-Lamarre, P.; Mehrabi, P.; Schulz, E. C.; Bultema, L. A.; Gevorkov, Y.; Brehm, W.; Yefanov, O.; Oberthür, D.; Kassier, G. H.; Dwayne Miller, R. J. *Nat. Commun.* **2020**, *11*, 996, with permission from the International Union of Crystallography and Springer Nature, respectively, copyright 2018 and 2020.

a new data acquisition sequence starts until the desired number of ED patterns are obtained. As high-throughput approaches, both methods can achieve a data collection rate of at least several thousands of crystals per hour.

Indexing SerialED data is challenging, particularly when the crystal is an unknown material. On the other hand, continuous collection of 3D ED data has an important advantage that each dataset can be collected within a few minutes. Therefore, built on SerialED technique, a new approach, serial rotation electron diffraction (SerialRED), has recently been developed.[69] Rather than collecting single ED patterns, SerialRED can achieve automated collection of 3D ED data. Besides the benefits from high-throughput analysis, which is capable to screen up to 500 crystals per hour, the obtained different 3D datasets can be merged to achieve high data completeness and improve data quality.

10.03.2.3 Structure determination and phase analysis

Electron diffraction can be used for crystal structure determination and phase analysis. Once a 3D ED dataset is collected from a crystal, the unit cell parameters and space group of the crystal can be determined. The intensities of the reflections can be extracted and used for structure determination. A structure determination includes two steps: structure solution and structure refinement, which is similar to those for single crystal X-ray diffraction. The unit cell and space group can be also used to identify the crystal phases in a sample.

10.03.2.3.1 Data processing

The described 3D ED protocols share the same concept that 3D reciprocal space is sampled by a sequence of hundreds of 2D ED frames. Several software suites, such as *REDp*,[13] *ADT3D*,[70] *PETS*,[12] and *EDT-PROCESS*,[10] have been developed for 3D ED data processing. They reconstruct and visualize 3D reciprocal space, determine the unit cell parameters and space group, index diffraction spots, and extract integrate diffraction intensities (Fig. 6). Moreover, with the recent development of continuous 3D ED data collection protocols, software developed for X-ray crystallography, such as XDS,[71,72] DIALS,[73,74] and MOSFLM,[75] can also be directly adapted for analyzing 3D ED datasets.

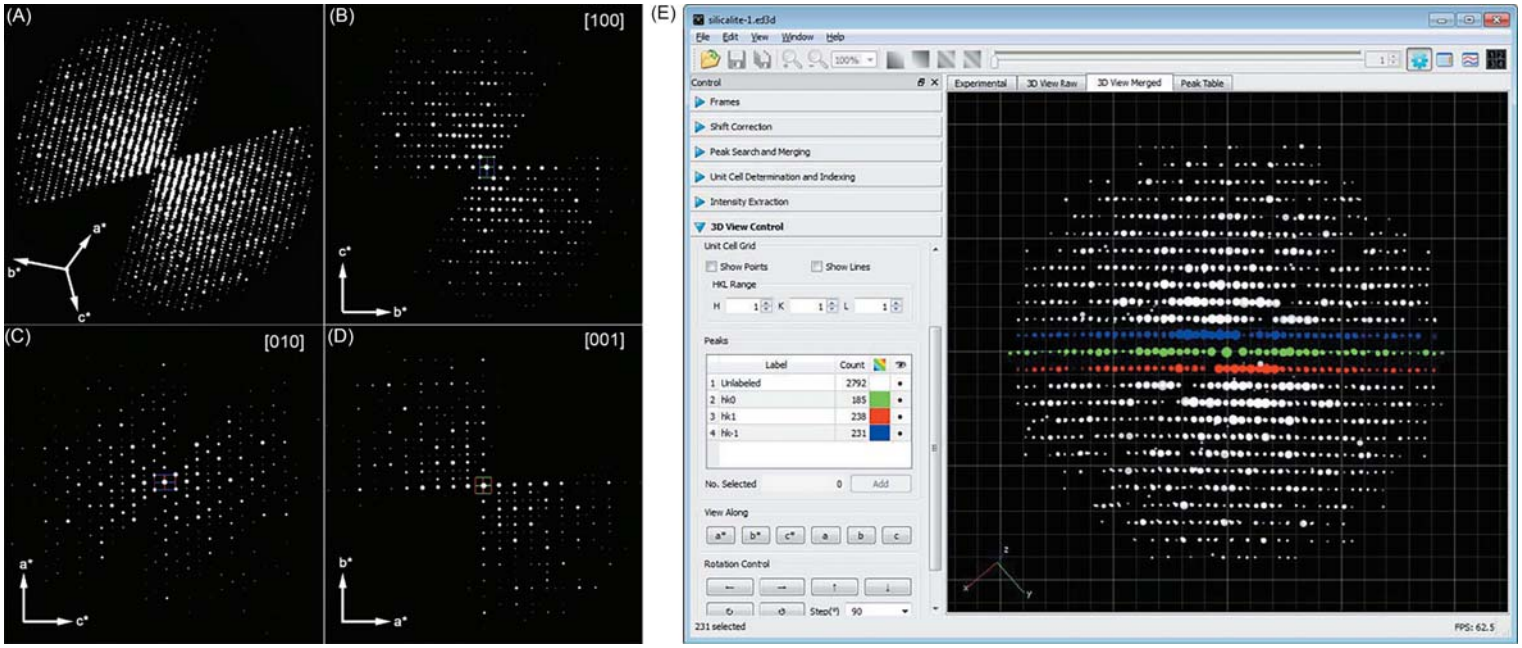

Fig. 6 (A) The reconstructed 3D reciprocal lattice of zeolite silicalite-1 from the RED data. (B)–(D) Slice cuts from the reconstructed 3D reciprocal lattice showing the (B) 0*kl*, (C) *h*0*l* and (C) *hk*0 planes. (E) The graphical user interface of the RED data processing program.[13] Reproduced from ref. Wan, W.; Sun, J.; Su, J.; Hovmöller, S.; Zou, X. *J. Appl. Crystallogr.* **2013**, *46*, 1863–1873, with permission from the International Union of Crystallography, copyright 2013.

Importantly, due to the space limitation of the objective lens pole pieces, the angular tilt range of the goniometer is limited. In a typical setup, the tilt range is restricted to 140° (±70°) by using a tomography TEM holder. Depending on the crystal symmetry, this could lead to low completeness, especially for crystals with preferred orientation, i.e., 2D crystals. Merging data from crystals with different orientations can effectively improve the completeness.[76]

10.03.2.3.2 Structure solution

All the described 3D ED protocols share a common concept that ED patterns are collected through a range of arbitrary orientations rather than along zone axes. This reduces the probability of multiple scattering of electrons that pass through the crystal. Consequently, dynamical effects are reduced drastically, and intensities extracted from 3D ED data can be treated as kinematical intensities for ab initio structure solution.

A crystal structure can be described as a Bravais lattice where the arrangement of atoms around each lattice point is identical. For a perfect crystal, the Fourier transform of the real-space crystal lattice gives the reciprocal lattice, which determines the positions of diffraction spots. The Fourier transform of the electrostatic potential in the crystal is represented by structure factors $\boldsymbol{F}_{hkl}$, which are the vector sums of contributions from all atoms within the unit cell, see Eqs. (9), (10). It can be expressed as,

$$\mathbf{F}_{hkl} = F_{hkl}\exp(i\alpha_{hkl}) = \sum_{j}^{N} f_j \exp\left[2\pi i\left(hx_j + ky_j + lz_j\right)\right] \tag{12}$$

where F_{hkl} and α_{hkl} are the amplitude and phase of the structure factor respectively, f_j is the atomic scattering factor of the j^{th} atom, and x_j,y_j,z_j are the fractional atomic coordinates of the j^{th} atom.[77]

The electrostatic potential distribution in the crystal can be directly obtained by an inverse Fourier transformation of structure factors, where high potential peaks correspond to atomic positions in the crystal. Therefore, once the structure factors, including both their amplitudes and phases, are obtained, the crystal structure can be solved. While the intensity of a diffracted beam is directly related to the amplitude of the structure factor, the phase information of the structure factors is lost for electron diffraction in the same way as for X-ray diffraction. A crystal structure is regarded solved when most atoms in the unit cell can be located. This requires that the structure factor phases of enough strong reflections can be determined. Similar to X-ray crystallography, there are several methods to solve the phase problem for structure determination of inorganic crystals using electron diffraction data. The most commonly used method is the direct methods, which use probability relationships to assign phases.[78] Modern direct methods use a combination of various methods to generate phases, which initially start from a random phase set and then refine the phases. Patterson method, initially developed in 1935,[79] is another method that is still in use for structure solution of inorganic crystals. Rather than calculating an electrostatic potential map by inverse Fourier transformation of structure factors $\mathbf{F}$, which requires phase information, a Patterson map is generated by Fourier transformation of the measured $|\mathbf{F}|^2$. Instead of atomic positions, the peaks in a Patterson map correspond to vectors between atoms. Positions for the heaviest atoms can be deduced from the highest peaks in the Patterson map and then the positions can be used to calculate initial phases for the structure factors. The remaining atoms can be obtained by iterative Fourier refinement. The Patterson method is mainly of use for structures containing heavy atoms.

It is worth mentioning that the direct methods and Patterson method generally require data at atomic resolution (better than 1.2 Å). For low resolution data, structure solution can be conducted using real space methods. Real-space methods are ideal for organometallic compounds because the organic components of the structure are normally known from the synthesis or they can be characterized by other spectroscopic techniques (e.g. NMR) before determining the crystal structure. Moreover, organic molecules have well defined bond distances and angles, which are independent of crystal structures. Therefore, structure solution by real-space methods is commonly applied to determine the linkage between metals and organic molecules and the spatial configuration (torsion angles) of organic molecules. Simulated annealing is one of the most effective real-space methods to solve structures from low resolution electron diffraction data. It can be considered as a simulation process analogous to the solidification of a melt. A slow enough process can lead to a crystalline solid while a fast quench will result in an amorphous form. During the simulation, parameters are randomly assigned to give a possible structural model, from which structure factors are calculated and compared to those obtained from the electron diffraction data. The parameters are kept if good agreement is reached. The program is run for thousands of iterations to find a best set of parameters.[80]

Charge flipping,[81,82] which belongs to the class of dual-space methods, is another structure solution method for electron diffraction data. The key step of charge flipping method is the charge flipping operation. In this step, the pixel values that are below a small positive threshold δ in an electron density/electrostatic potential map are multiplied by -1, i.e., flipped. The initial map is calculated by inverse Fourier transform of the structure factors, where the amplitudes are obtained from experimental diffraction data and phases are assigned randomly. After each iteration of charge flipping operation, new structure factors are calculated from the modified map by charge flipping. Then a new map is calculated using the phases of the new structure factors and the experimental amplitudes. The process is iterated until a converging solution is found.

The above described methods are implemented in software packages such as SHELX,[83,84] SIR,[85] JANA,[86] etc. Notably, most software has set default values of parameters optimized for X-ray crystallography. Thus, it is important to ensure all the parameters, such as wavelength, and atomic scattering factors are chosen for electrons.

10.03.2.3.3 Structure refinement

A structural model obtained from an initial structure solution may be incomplete and some atoms in the unit cell may be missing. The missing atoms can be located by so called Fourier refinement. Typically, a set of structure factors can be calculated from the atom types and positions of the initial model. An electrostatic potential map can then be obtained using the amplitudes $|\mathrm{F_o}|$ and the phases calculated from the model. Practically, it is more useful to calculate difference Fourier maps using coefficients of ($|\mathrm{F_o}|$ - $|\mathrm{F_c}|$) with the calculated phases. In the difference maps, missing atoms are shown as positive peaks, while negative peaks indicate wrong assignment of atom types. In this way, missing atoms can be located from the map and added to the model, and atom types can be modified. This process is repeated until all non-hydrogen atoms are found and there are no extra high positive and negative peaks in the difference map. Meanwhile, the structure factor amplitudes are calculated from the models and compared with those experimentally observed. Refinement procedures are made to minimize the difference between calculated and experimental amplitude squares. To assess the quality of refinement for inorganic compounds, wR_2 and $\mathrm{R_1}$ are the common indicators. They are defined as,

$$wR2 = \sqrt{\frac{\sum\left[w\left(\mathrm{F}_o^2 - \mathrm{F}_c^2\right)^2\right]}{\sum\left[w\left(\mathrm{F}_o^2\right)^2\right]}} \tag{13}$$

$$R1 = \frac{\sum||\mathrm{F}_o| - |\mathrm{F}_c||}{\sum|\mathrm{F}_o|} \tag{14}$$

where w is the weighting factor, $\mathrm{F_o}$ is the observed structure factors and $\mathrm{F_c}$ is the calculated structure factors.[87] The Goodness of Fit (Goof) also describes how well the structural model fits the observations. It can be expressed as

$$\mathrm{Goof} = \sqrt{\frac{\sum\left[w\left(F_o^2 - F_c^2\right)^2\right]}{n-p}} \tag{15}$$

where n is the number of reflections and p is the total number of parameters refined.[87]

Although dynamical scattering is significantly reduced in 3D ED data, electron diffraction intensities are still dynamical. Therefore, structure refinements based on kinematical approximation still result in much higher R values when compared to those for X-ray diffraction. This has been a major concern for electron diffraction. However, recent studies on inorganic compounds have proved that accurate structural models can be obtained from 3D ED data, with average deviations of atomic positions by less than 0.1 Å compared to those determined by X-ray diffraction.[88–90] Structure refinement software developed for X-ray diffraction compare observed dynamical 3D ED intensities with kinematical intensities calculated from the structural model. A high R_1-value does not necessarily mean that the structural model is inaccurate, but instead indicates the ED intensities are dynamical. It is possible to take dynamical scattering into account in the structure refinement. An alternative refinement procedure was developed for dynamical refinement,[91] where the model intensities are calculated using the dynamical diffraction theory of electrons.[92] In this procedure, the Bloch-wave method is used to calculate the intensities, which are extracted frame by frame and are treated independently for each frame. Moreover, the thickness of the crystal is also refined because of its close association to the dynamical scattering.

10.03.2.3.4 Phase analysis

Typically, there are hundreds of thousands of crystals on a TEM grid, so phase analysis can be performed by collecting ED patterns for many crystals. Phase analysis can be performed using either single electron diffraction patterns or 3D ED data. From a single electron diffraction pattern, the 2D repeating lattice can be determined. The 2D lattice is compared to all possible 2D lattices generated from the unit cell and lattice type of each known crystal structure in the database. The phase is identified when there is a good match between the experimental and calculated 2D lattice. Programs, such as *PhIDO*,[33] have been developed for phase analysis from one or a few ED patterns collected from both zonal-axis and off-axis. A drawback of phase analysis using single ED patterns is that more than one phases may match the same ED pattern and the phase analysis can be ambiguous. This drawback has been overcome with the development of 3D ED techniques. Phase analyses can be made by comparing the 3D unit cell and lattice type determined from the 3D ED data with those in a database. Moreover, each 3D ED dataset can be collected in less than a few minutes. Thus, it is possible to collect datasets from many different individual crystals for phase analysis. To analyze a huge number of datasets, an automated data processing pipeline has been developed.[69] The data processing pipeline includes functions for automatically running ED data processing software, such as XDS or DIALS, on all the datasets, extracting lattice parameters and integration statistics, and analyzing the results using hierarchical cluster analysis (HCA). Based on lattice parameters and reflection intensities, HCA can automatically group different crystal phases in the sample. For unknown phases, HCA can find the best matching datasets for structural analysis (**Fig. 7**). Combined with the high throughput data collection techniques such as SerialRED,[69] this method allows high-throughput phase analysis, which is especially powerful for studies of phase mixtures.

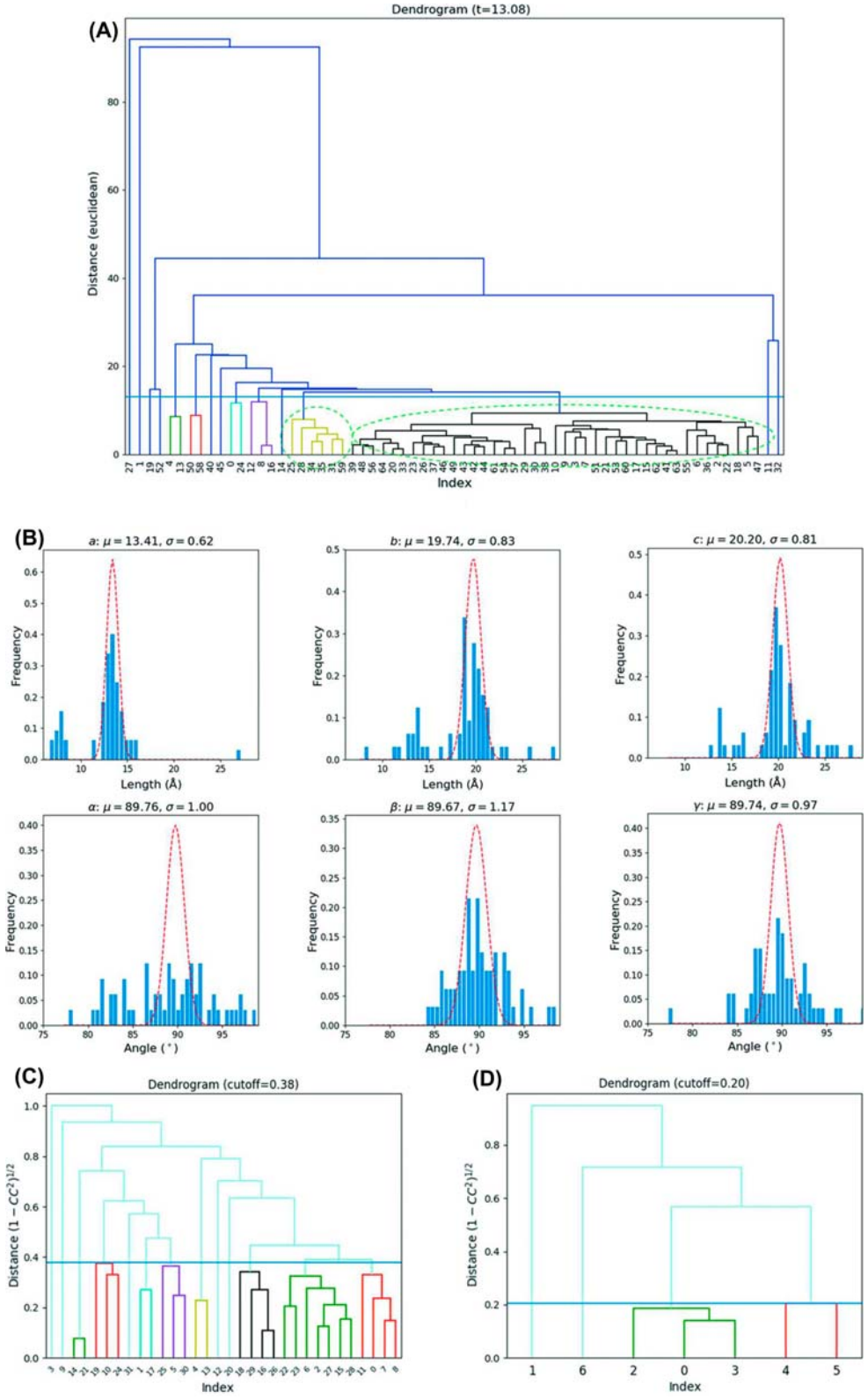

Fig. 7 (A) Dendrogram of a hierarchical cluster analysis (HCA) based on unit cells. Two clusters are identified, corresponding to ZSM-5 and mordenite, shown as black and yellow cluster respectively (marked by circles). (B) Histogram of the lattice parameters. Dendrogram of the reflection-based cluster analysis for (C) ZSM-5 and (D) mordenite.[69] Reproduced from ref. Wang, B.; Zou, X.; Smeets, S. *IUCrJ* **2019**, *6*, 854–867, with permission from the International Union of Crystallography, copyright 2019.

10.03.3 Decoding atomic arrangements from high resolution images

Taking good high resolution images may be more demanding than collecting electron diffraction data, but it is often more rewarding. High resolution images have several benefits over diffraction techniques. Some of the key advantages are given below:

(1) Images always contain information about crystallographic structure factor phases, which is of utmost importance for structure determination.
(2) Images provide local information, whereas diffraction experiments are limited to sufficiently large periodic structures, and hence, exclude the study of individual interfaces or point defects.
(3) Images deliver structural information not biased by any assumption of periodicity, which is crucial when studying e.g. disordered materials. The occurrence of disorder in crystals creates diffuse scattering which in many cases obstructs ab initio structure solution from diffraction data.

As was mentioned before, the two most relevant imaging modes for electron crystallography are HRTEM and STEM. Both of them can give sub-Ångström resolution when equipped with spherical aberration (C_s) correctors. In this section, we aim to provide a conceptual picture of image formation for non-TEM specialists, with the focus on HRTEM and STEM. Many important topics related to wave optics, physics of the probe formation and in-depth aspects of imaging theory will not be covered here. We reference C&W[93] quite often and highly recommend it as further reading.

10.03.3.1 A conceptual picture of HRTEM image formation and contrast transfer

10.03.3.1.1 Image formation

As shown in Fig. 1B, a HRTEM image is formed via coherent parallel beam illumination. When we hit a specimen with a plane wave of electrons, it causes a modulation of the wave amplitude and phase depending on the local electron density of the specimen. This process is governed by the relativistic Schrödinger equation describing the motion of the electron wave $\psi(\mathbf{r})$ in the potential $V(\mathbf{r})$ of the specimen (see Eq. 1).[93] Propagating from the bottom of the specimen through the lens towards the image plane, the exit wave is affected by imperfections of the objective lens (spherical aberration, defocus, coma, astigmatism and higher order aberrations) as well as those of other lenses on its optical path. This results in a blurring of the exit wave function, which can be written as a convolution with a point-spread function, P(r), and what is actually measured in the image plane is the intensity of this convolution,[94]

$$I(\mathbf{r}) = |P(\mathbf{r}) \otimes \psi(\mathbf{r})|^2 \tag{16}$$

meaning that the scattering from spatially separated parts of the specimen can interfere in the blurring process. Conventional HRTEM is a coherent mode of imaging though.

10.03.3.1.2 Contrast transfer function (CTF)

In reciprocal space, the equivalent to the point-spread function is a contrast transfer function $T(u)$ (Fig. 8). CTF contains two parts, an envelope part which dampens the amplitudes of the high resolution components, and an oscillating part which determines the contrast of the image.[95] Simplifying and only considering spherical aberration C_s (see also Section 10.03.3.5) and defocus ε, we can write the contrast transfer function as

$$T(u) = D(u)sin\chi(u) = D(u)sin\left[\pi\left(\tfrac{1}{2}C_s\lambda^3u^4 + \varepsilon\lambda u^2\right)\right] \tag{17}$$

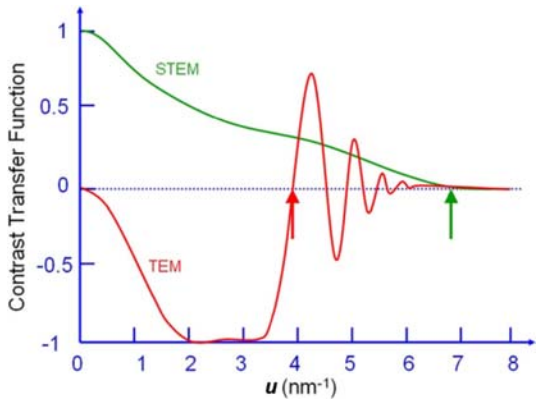

Fig. 8 Comparison of transfer functions in HRTEM (in red) and STEM (in green) modes for the same objective lens and aperture. For HRTEM imaging, the higher frequencies should be excluded by a proper objective aperture marked by the red arrow because they introduce contrast reversals. For STEM imaging, a proper probe-forming aperture should be applied to match the spatial frequency marked by the green arrow.

where $D(u) = \exp.[-\frac{1}{2}\pi^2\Delta^2\lambda^2u^4]\exp.[-\pi^2\alpha^2u^2(\varepsilon + C_s\lambda^2u^2)^2]$, u is spatial frequency, C_s coefficient of spherical aberration, λ electron wavelength, and ε defocus, Δ the focus spread and α the electron beam convergence. Scherzer was the first to realize that, in practice, the oscillations of the CTF result in dramatic fluctuations of the image intensity, since $T(u)$ is changed by changing the focus, for instance.[96] Contrast reversals can occur depending on whether constructive or destructive interference is occurring. There is uncertainty over whether atoms should appear as bright or dark contrast in the image, which can change depending on the focusing condition. However, there is a defocus setting where the contrast remains almost constant. This is so called Scherzer focus, given by

$$\varepsilon_s = -1.155\sqrt{C_s\lambda} \tag{18}$$

The first zero crossover of the CTF at the Scherzer defocus is called the point resolution d_p of the TEM and sets the limit for a straightforward interpretation of a HRTEM image of a thin object.

$$d_p = 0.667C_s^{1/4}\lambda^{3/4} \tag{19}$$

It is worth mentioning that the CTF only holds for very thin specimen where the projected potential is much smaller than the inverse of the interaction constant σ, i.e. weak-phase approximation (WPOA). σ is a function of wavelength and decreases with the increasing accelerating voltage. For $U = 200$ kV, $\sigma = 7.288 \times 10^{-4}\,\mathrm{V}^{-1}\,\mathrm{Å}^{-1}$ and $\varphi(xyz)$ is typically 5–30 V.

For an image taken at Scherzer defocus, where $\mathrm{T(u)} \approx -1$ over a large range of resolution, the structure factor $\mathrm{F}(\mathbf{u})$ can be obtained from the Fourier transform of the HRTEM image, $\mathrm{I_{im}}(\mathbf{u})$.[33]

$$\mathrm{F}(\mathbf{u}) \approx -\frac{1}{\mathrm{k}'}\mathrm{I_{im}}(\mathbf{u}) = \frac{1}{\mathrm{k}'}\exp(\mathrm{i}\pi)\mathrm{I_{im}}(\mathbf{u}) \tag{20}$$

where $I(\mathbf{u})$ is the Fourier transform of the image and k' is a constant. Section 10.03.3.2 The amplitudes of the crystallographic structure factors are proportional to the amplitudes of the corresponding Fourier components of the Fourier transform $\mathrm{I_{im}}(\mathbf{u})$ of the image. All the phases in the Fourier transform $\mathrm{I_{im}}(\mathbf{u})$ of the image, within the Scherzer resolution limit are shifted by 180° from the structure factor phases.

Summing up, in HRTEM mode the exit wave function generally cannot be directly interpreted in terms of the specimen structure. Often an approach is taken where images are simulated from trial structural models and are systematically compared with the experimental data (e.g. EMS software, Stadelman 1987[97]). The situation is further complicated by the existence of dynamical scattering, which can also have a strong effect on the coherent HRTEM image contrast, causing, for instance, contrast reversals as the thickness is changed. Nevertheless, the majority of TEM imaging at atomic resolution has been performed using conventional high-resolution TEM, and there is a huge range of applications.[98]

10.03.3.2 Retrieval of structure projection by CTF correction and structure determination from HRTEM images by crystallographic image processing

The structure projection of a crystal can be directly obtained from HRTEM images by crystallographic image processing. The structure projection, as given by the projected potential of the crystal can be calculated using

$$\varphi(\mathbf{r}) = \frac{1}{2\sigma N_z}\sum_{\mathbf{u}}\left\{\frac{\mathrm{I_{im}}(\mathbf{u})}{\mathrm{T}(\mathbf{u})}\exp[-2\pi\mathrm{i}(\mathbf{u}\cdot\mathbf{r})]\right\} \tag{21}$$

Eq. (21) shows that the projected potential can be obtained from the Fourier transform of the image, if the contrast transfer function $\mathrm{T}(\mathbf{u})$ can be determined. $\mathrm{T}(\mathbf{u})$ can be estimated from the Fourier transform of the HRTEM image, using an amorphous region of the specimen. Knowing the defocus values, the effects of the CTF can be partially compensated for by image post-processing.[33] Crystallographic image processing program can be used to retrieve the structure projection.[6]

The structure projection can also be reconstructed from through-focus series of HRTEM images using, for example, the software QFocus.[99] The defocus values are determined jointly from the through-focus series of HRTEM images with a known defocus step by comparing the phase values α of $F(\mathbf{u})$ over all u-values (pixels) in the Fourier transforms of the HRTEM images, where the structure factor $F(\mathbf{u})$ is

$$F(\mathbf{u}) = |F(\mathbf{u})|\exp[i\alpha(\mathbf{u})] \tag{22}$$

which can be calculated from Fourier transform of the HRTEM image according to Eq. (20) using a trial defocus value for the first image in the series

$$F(\boldsymbol{u}) = \frac{I(\boldsymbol{u})}{2\sigma T(\boldsymbol{u})}\ (\text{for } T(\boldsymbol{u}) \neq 0) \tag{23}$$

The defocus values for other images are calculated from the trial defocus value and the defocus step. The trial defocus value that gives the best agreement of the phase values among all images will be the correct defocus. The twofold astigmatism in the HRTEM images can also be estimated. A projected electrostatic potential image is obtained from each HRTEM image in the series by the CTF correction based on Eq. 23. An example is shown in Fig. 9.

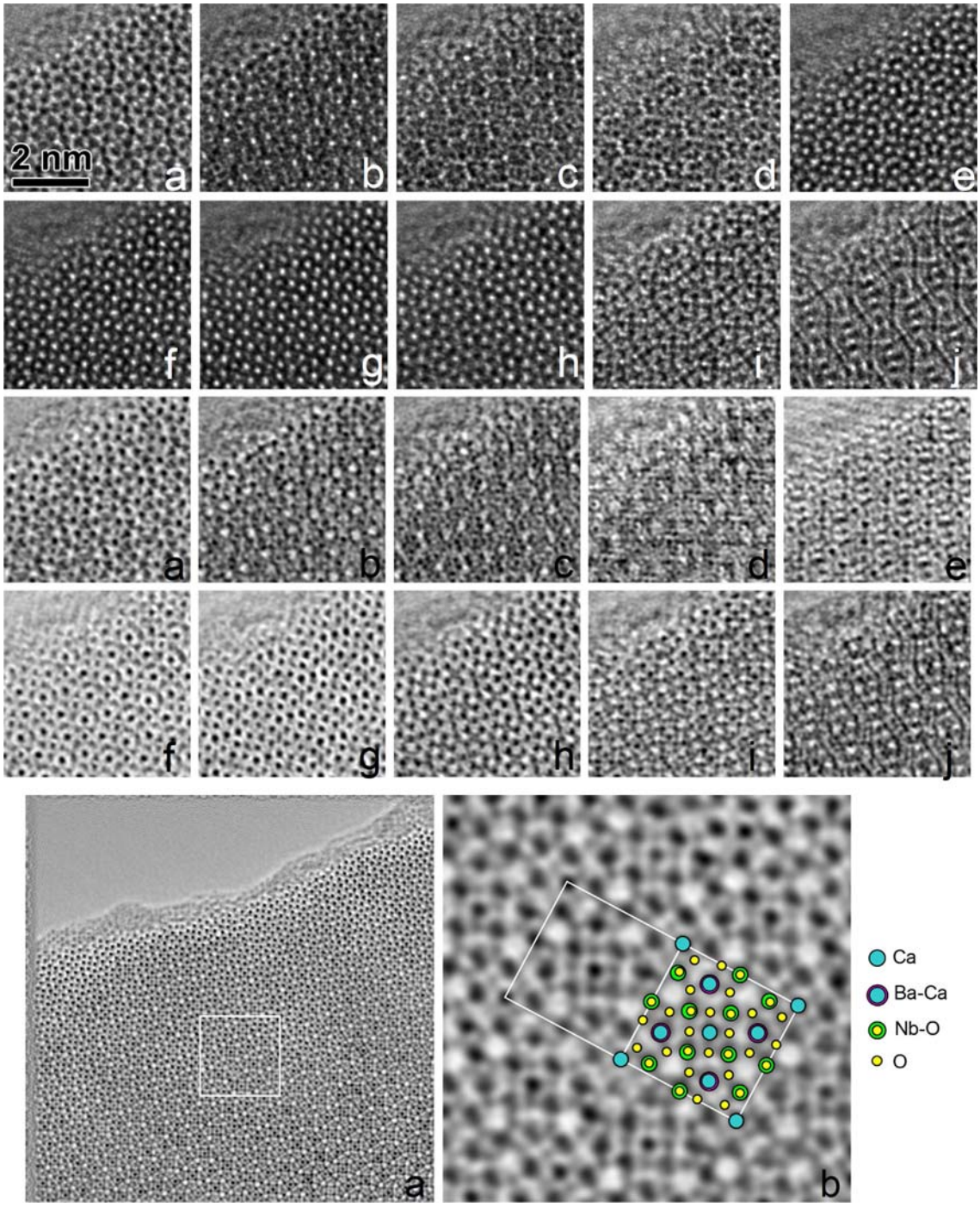

Fig. 9 Experimental images (top) and corresponding CTF corrected images (middle) of $Ca_{0.28}Ba_{0.72}Nb_2O_6$ (*P4bm*, $a = 12.45$, $c = 3.97$ Å) from 10 of the 20 images (even numbers, (A)–(J)) in the through-focus series. Bottom: Image reconstructed from the through-focus series with (A) the full view and (A) a magnified image from the marked area in (A), with the projected structural model superimposed. Reproduced from ref. Wan W., Hovmöller S., Zou X., Ultramicroscopy **2012**, 50–60 , with permission from Elsevier, copyright 2012.

The through-focus structure projection reconstruction is especially useful for beam-sensitive and disordered materials, because the signal to noise ratio can be greatly enhanced by averaging reconstructed images taken at different defocus values. Crystallographic symmetry can be applied on the reconstructed images by using crystallographic image processing[4,6] to further improve the images and obtain crystal structure factor amplitudes and phases required for crystal structure determination.

10.03.3.3 STEM for electron crystallography applications: Imaging modes and different types of image contrast

STEM imaging is very different to conventional TEM. We can regard the electron optics in a STEM as demagnifying the electron source such that it is imaged onto the specimen at atomic dimension.[93] So the angular dark field (ADF) image intensity can be straightforwardly interpreted as the convolution between an object function $O(\mathbf{r})$ and a point-spread function (PSF) $P(\mathbf{r})$ that is simply the intensity of the illuminating probe.[100]

$$I(\mathbf{r}) = |P(\mathbf{r})|^2 \otimes O(\mathbf{r}) \tag{24}$$

Therefore, the interference effects between spatially separated parts of the probe are no longer observed. In contrast to HRTEM, STEM is an incoherent imaging tool. As seen in Fig. 8, the resolution limit of the ADF (green arrow) is approximately twice that of the HRTEM image (red arrow) for the same objective lens and aperture. The improved resolution can be understood as follows. The illuminating beam in the STEM is a converging cone, and each Bragg reflection appears as a disk with the center at angles $2\theta_B$ according to $d_{hkl} = \frac{\lambda}{2\sin\theta_B} \approx \frac{\lambda}{2\theta_B}$, and with diameter determined by the diameter of the objective aperture. The diffraction disks overlap, in such case they interfere. Clearly the limiting resolution for incoherent imaging corresponds to the diameter of the disks just overlapping, whereas for coherent imaging constructive interference between the zero-order disc and two diffracted discs is required, that limits the resolution to one radius of the disc. In contrast to HRTEM, the transfer function for STEM is positive at all u values, so *atoms always appear bright in STEM*.

Back to Fig. 1 in Section 10.03.1, whereas TEM mode uses a parallel electron beam, and the images are essentially interference patterns of the scattered electrons formed by the objective lens, STEM mode uses a focused electron beam to scan over the specimen, and the images are formed by collecting transmitted electrons within a certain range of scattering angle using annular detectors. The segmentation of STEM detectors allows for the simultaneous imaging of bright- and dark-field signals, but also the selection of an angular range of scattered electrons, and thus, determine whether or not the contrast is rather coherent or incoherent.[93] High angle annular dark-field (HAADF) STEM provides a way of imaging Z-contrast by collecting incoherently scattered electrons with scattering angles >50 mrad being dominated by Rutherford scattering, which is frequently exploited for atomic resolution imaging. For annular dark-field (ADF) STEM, Bragg scattered electrons are used for image formation and the image contrast is determined by diffraction contrast.[101]

10.03.3.3.1 Crewe's Z-contrast

The atomic number dependence of the ADF signal has been investigated since a pioneering study by Crewe et al.,[102] and now it is known that this signal is proportional to Z^n, $4/3 \leq n \leq 2$ for the elastic scattering contribution. The larger the scattering angle, the closer n approaches the value 2, which is the classical Rutherford scattering result.

The formation mechanism of the Z-contrast is simply understood for a single atom. A scattering cross section for an isolated atom is straightforwardly computed from electron scattering factor tables, employing the Mott-Bethe formula (Eq. 5). Integrating $|f(Z,\theta)|^2$ over the annulus

$$\sigma_{el} = 2\pi \int_{\theta_0}^{\pi} |f(Z,\theta)|^2 \sin\theta d\theta \tag{25}$$

we can see that essentially the exponent n is not constant with Z for a given annulus geometry, here designated by θ_0, the detector inner collection angle (the outer angle is assumed to be large). In a general form,[103]

$$n = \frac{1}{\ln Z} \ln\left[\frac{\sigma(Z,q_0)}{\sigma(1,q_0)}\right] \tag{26}$$

The exponent n is a constant only for HAADF detectors, and approaches values in the range 1.9–2. The scattering vector q is related to θ via $q = (2/\lambda)\sin(\theta/2)$, giving $\sin\theta\, d\theta \equiv \lambda^2 q\, dq$ $(0 \leq q \leq 2/\lambda)$. For $\theta_0 \to 0$ detector inner collection angles, the scattering cross section can be expressed as

$$\sigma_{el} = \frac{\hbar^2}{\pi E_0^2 \beta^2} Z^{4/3} \propto Z^{4/3} \tag{27}$$

and it predicts a constant $n = 4/3$, also independent of Z.

The ratio of the ADF signal, I_{el}, to the (inelastic) energy loss signal, I_{inel}, was thus expected to be proportional to Z and independent of sample thickness, hence the term "Z-contrast."

$$\frac{\sigma_{inel}}{\sigma_{el}} = \frac{4}{Z} \ln \frac{\hbar^2}{\pi m_0 J R \lambda} \simeq \frac{26}{Z} \tag{28}$$

where J is the mean ionization energy of an atom, and R is the screening constant given by $R = a_0 Z^{-1/3}$. However, it quickly became clear that the ideas underpinning Crewe's $Z^{4/3}$-contrast method often failed when applied to typical materials. Studies of supported catalysts, which are typically small high-Z particles on low-Z supports, revealed strong diffraction contrast arising from Bragg reflections in the crystalline component phases, frequently masking any underlying Z-dependency.

10.03.3.3.2 Z^{2-x} contrast

HAADF–STEM is sensitive to variations in the Z number in the specimen (the contrast is approximately proportional to Z^2), making the images easily interpretable; on the other hand, it only utilizes a very small fraction of the incident electrons (those scattered to very high angles), producing insufficient signal under the low-electron-dose conditions required to image sensitive materials. While it was demonstrated that the image contrast benefits overall from the enhanced *Z*-dependence as well as from the suppression of direct diffraction effects, in practice few studies use the collection angles at which the exponent *n* approaches 1.9–2, and often have to deal with diffraction artefacts. Another problem of HAADF is that light atoms are only weakly or not at all visible, making it difficult to pinpoint their position and quantify them. This gets even more challenging when the light elements are positioned very close to heavier elements, e.g. O, N, C, B and Li when imaged together with heavier atoms like Si, Ga, Sr, Au etc. The Z^{2-x} contrast was interpreted in two ways: (1) incoherent imaging by elastically scattered electrons, by Nellist and Pennycook[94]; and (2) imaging by thermal diffuse scattering (TDS) by Watanabe.[104] An interested reader may wish to find more details in the original works as well as in ref. 94.

Establishing depth-sectioning in STEM, by changing the defocus of the probe inside specimens, was especially important for electron crystallography. Surprisingly the electron probe does not broaden as rapidly with sample thickness as originally thought,[105] enabling us to get depth-sensitive information about the specimen and empowering a 3D STEM imaging technique akin to confocal optical microscopy. In recent years, significant progress has been made in 3D STEM electron tomography, combining 2D projection images in multiple directions in order to reconstruct 3D structure for nanoparticles.[106,107] However, the number of investigations in which atomic positions in 3D have been directly measured is small. In addition to the many technical challenges of 3D STEM acquisition and reconstruction, one of the main problems is that 3D reconstructions at the atomic scale often correspond to a continuous 3D volume of intensity values, hampering the extraction of the exact coordinates for atoms inside the specimen. A breakthrough occurred when statistical algorithms were developed to translate HAADF-STEM images into counting results (number of atoms in each atomic column). The first 3D reconstruction at the atomic scale was done for a 3 nm Ag nanoparticle embedded in an Al matrix, and was based on only two HAADF-STEM images acquired along different zone-axes.[108] Discrete tomography was then used to combine the images into a 3D reconstruction with atomic resolution. It was assumed that all of the atoms were positioned on a face-centered-cubic grid without the presence of vacancies. This finding opened up a whole new range of tomography experiments that nowadays enable even grain boundary and point defect detection. Thus, **Fig. 10** shows an atomic scale reconstruction of an FePt nanoparticle revealing the presence of different ordered structures and different degrees of ordering.[109] The whole FePt nanoparticle contains 23,196 atoms.

Tomography can be also performed in spectroscopy modes (EELS and EDX), although atomic resolution remains far off due to the lower signal levels.[110]

Recent advances in aberration corrected microscopy have also enabled the direct visualization and quantification of truly atomic level phenomena, including exact location, distribution, segregation, or clustering of point defects. C_s-corrected STEM, using mainly a dark field detector, has been revealed to be the most advanced and indispensable technique to locate them. One example is the beam induced diffusion of single Ce and Mn dopants inside bulk wurtzite-type AlN single crystals, identifying correlated vacancy-dopant and interstitial-dopant kick-out mechanisms,[111–113] presented in **Fig. 11**. The beam induced dynamics of vacancies is also characteristic for light elements, e.g. oxygen vacancy ordering in a $LaCoO_3/SrTiO_3$ superlattice.[114] Extended reviews showing how aberration correctors are being applied to allow major insights into the structure, chemistry and behavior of oxides,[115] ordered nanoporous materials,[116] and nanomaterials[117] have been recently published.

10.03.3.3.3 ABF-STEM

ABF-STEM method is invented to overcome the weakness of HAADF for imaging light atoms. In the ABF image, the contrast of light atomic columns is related to forward elastic scattering, whereas the contrast of heavy atomic columns originates from both thermal diffuse scattering and elastic scattering contributions. Elastic scattering tends to forward-focus the electron probe when it is placed on columns of light elements. Thermal scattering tends to scatter the electron probe to high angles when it is placed on columns of heavy elements. However, the distribution of scattered electrons remains uniform when the probe is positioned between the columns. As a result, both light element and heavy-element columns reduce the electron intensity in the outer area of the bright-field detector as compared to its value when the probe is between columns. Thus, both light and heavy atomic columns appear as dark spots in ABF images, but since the intensity reduction for both of them is of comparable magnitude, light elements are generally more visible in the presence of much heavier elements as compared to HAADF-STEM. Findlay et al.[118] formulated an imaging theory of ABF-STEM explaining the variation of image contrast with thickness and defocus. ABF is sensitive to the thickness of specimens, and a contrast reversal is observed in over/underfocus conditions, since ABF automatically reintroduces the wave interference effects in the imaging. Thus, it is necessary in advance to estimate focus conditions with the help of simulation. Hydrogen[119] and lithium[120] atomic columns have been visualized for the first time by using the ABF method.

10.03.3.3.4 Integrated differential phase-contrast (iDPC)

More complex detector geometries are also becoming popular, particularly a segmented detector which allows a differential phase-contrast (DPC) mode.[121–123] Forming the difference signal between opposite segments provides a measure of beam deflection, which can be used to form an image of electric or magnetic fields. iDPC[124] is an extension of the DPC-STEM technique enabling direct imaging of the phase of the transmission function for non-magnetic samples and yielding an image that is directly interpretable as the (projected) electrostatic potential. The resulting contrast is now roughly proportional to Z, which improves drastically

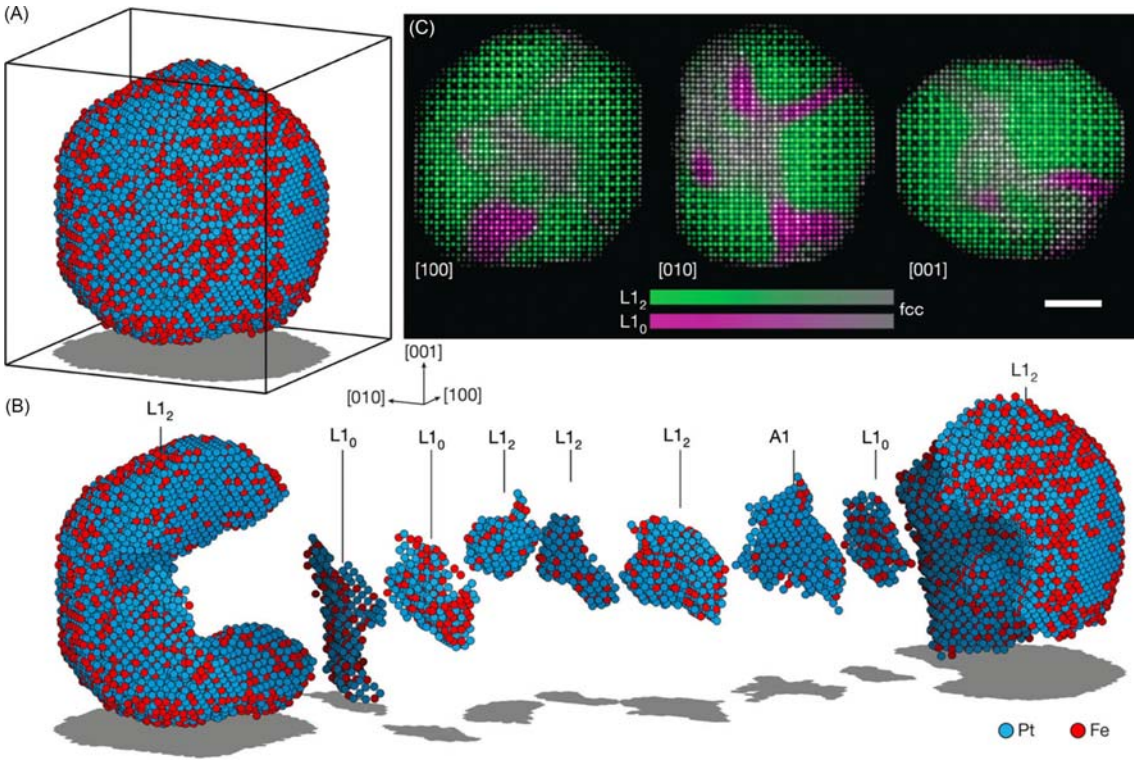

Fig. 10 3D determination of atomic coordinates, chemical species, and grain structure of an FePt nanoparticle. (A) Overview of the 3D positions of individual atomic species with Fe atoms in red and Pt atoms in blue. (B) The nanoparticle consists of two large $L1_2$ grains, three small L12 grains, three small L10 grains, and a Pt-rich A1 grain. (C) Multislice image. Reproduced from ref. Yang, Y.; Chen, C.-C.; Scott, M. C.; Ophus, C.; Xu, R.; Pryor, A.; Wu, L.; Sun, F.; Theis, W.; Zhou, J.; Eisenbach, M.; Kent, P. R. C.; Sabirianov, R. F.; Zeng, H.; Ercius, P.; Miao, J. *Nature* **2017**, *542*, 75–79, with permission from Springer Nature, copyright 2017.

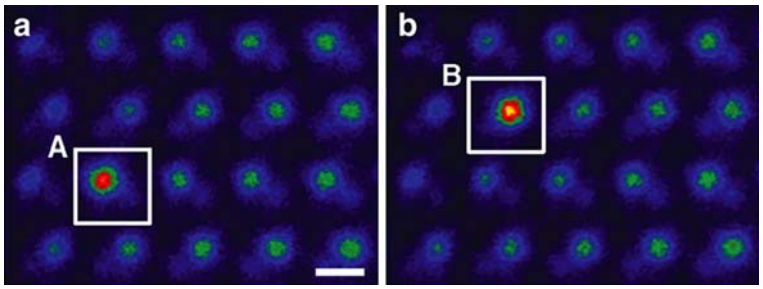

Fig. 11 Atomic-resolution STEM images of the beam induced Ce hopping from column A to B in AlN. Images are averages over (A) 19 frames before the jump and (B) 19 frames after the jump. Reproduced from ref. Ishikawa, R.; Lupini, A. R.; Findlay, S. D.; Taniguchi, T.; Pennycook, S. J. *Nano Lett.* **2014**, *14*, 1903–1908, with permission from the American Chemical Society, copyright 2014.

the detectability of light elements among heavy elements in one image. Even hydrogen atoms at α-Ti/γ-TiH metal-metal hydride interfaces and away from the interface can be resolved by the iDPC-STEM.[125] In the iDPC-STEM technique the signal to noise ratio is superior compared to ADF-STEM imaging and also to other phase contrast high resolution TEM imaging, as was recently demonstrated for imaging of dose-sensitive materials like zeolite and biomaterials. Very recently light - element aromatics inside ZSM-5 zeolite channels were imaged for the first time directly under low dose iDPC - STEM conditions (Fig. 12).[126]

10.03.3.4 How can 3D crystallographic information be obtained from 2D high resolution images?

Transmission electron microscopy images are only two-dimensional projections of 3D objects. Ideally, we need to know the positions of the atoms, their chemical nature, and the bonding between them in three dimensions. Starting from 2D high resolution images we may wish to follow one of three major routes to obtain 3D structure model.

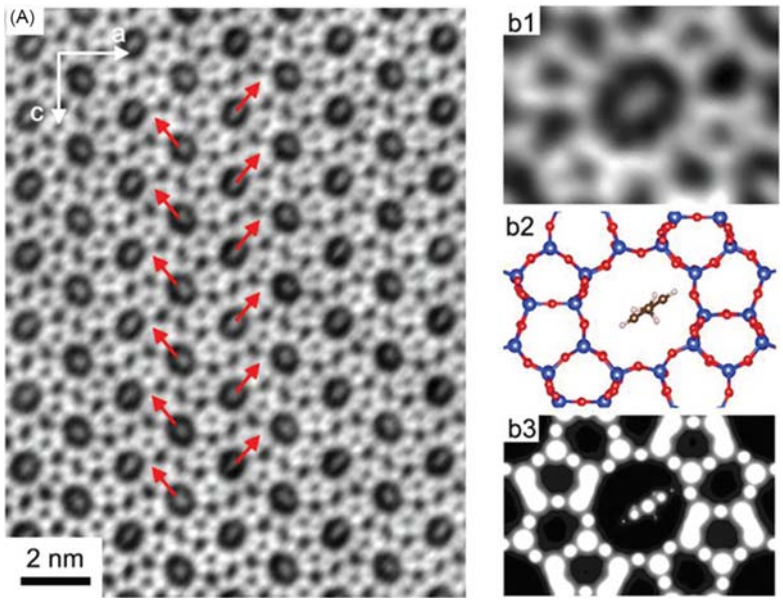

Fig. 12 (A) iDPC-STEM images of para-xylene (PX) filled ZSM-5 from the [010] projection. PX adsorption at the intersection of the straight and sinusoidal channels is most probable, where the C6-planes of PXs are nearly parallel to the straight channels and co-oriented to the long axis of elliptical Si10-ring, marked as the red arrows, (B) The corresponding (1) magnified image, (2) calculated structural model, and (3) electrostatic potential of the filled channels. Reproduced from ref. Shen, B.; Chen, X.; Cai, D.; Xiong, H.; Liu, X.; Meng, C.; Han, Y.; Wei, F. *Adv. Mater.* **2020**, *32*, 1906103, with permission from the John Wiley & Sons, Inc., copyright 2020.

The first route, model building, utilizes images along one or several projections. In order to build a feasible model, additional information, such as atomic arrangements from thermodynamics and/or data from NMR, adsorption, electron diffraction, and other methods, are needed. The expected HRTEM image is calculated considering the CTF. Since the specimen thickness and defocus are commonly unknown with the necessary accuracy, these two parameters are systematically varied and a matrix of images is calculated. Comparison with the measured image shows if the assumed atomic arrangement explains the electron microscope images. Model building requires prior-knowledge of the material, since there may be different 3D models matching a specific 2D image. Many successful examples of structure solution are based on the model building employing high resolution TEM or STEM images taken along one or several projections. In practical terms, learning about material structure is not limited by resolution in this case, but by the ability to process information in the context of atomic arrangements regardless of the technique. For example, a combination of X-ray diffraction, selected-area zonal electron diffraction, and HRTEM was found to be a powerful combination for the study mixed oxides at the atomic level long before the widespread use of aberration corrected microscopes.

A more general approach is 3D reconstruction based on images acquired along several different zone axes. An important advantage of images over diffraction is that the structure factor phase information, that is lost in diffraction, can be obtained directly from images (Eq. 23). **Fig. 13** illustrates the determination of structure factor amplitudes and phases from HRTEM image by crystallographic image processing CRISP.[6] By combining structure factors obtained from images of different projections, a 3D potential map can be reconstructed using the Eq. (29),

$$\varphi(x,y,z) = \sum_h \sum_k \sum_l F(hkl)\,\exp[-2\pi i(hx+ky+lz)] \tag{29}$$

From the 3D potential of the specimen, reconstructed from images taken along different zone axes, the atomic positions in the material can be obtained. In order to obtain the 3D structure, it is necessary to take images from many crystals with different orientations. One challenge to combine images from different orientations is to find a common origin for the unit cell.[56] Another challenge is beam damage to the sample. It is far from straightforward to acquire a large number of TEM images, since samples tend to degrade. Nevertheless, 3D reconstruction has been used to solve the structures of relatively beam-sensitive zeolites, for example the high-silica zeolite beta[28] and an intergrown zeolite ITQ-39.[127]

A third approach relies on exit wave reconstruction, accompanied by indirect correction for the lens aberrations via digital image processing. Interferometric and non-interferometric phase retrieval is possible. One approach requires interference of the object exit wave with a reference wave (which does not travel through the specimen). This is mainly used in off-axis and in-line holography.[128] A completely different approach is to determine the phase of the electron beams scattered by the object, and then computationally back-propagate this to the object plane – it is used in ptychography and its variants.[129] As we discussed in **Section 10.03.3.3**, the contrast in STEM mainly arises from overlapping, interfering diffraction discs. The fringes within the overlap between two interfering diffracted electron beams could be used to determine the phase difference between them. Using linked pairs of diffracted electron waves, it is possible to phase all the Bragg diffractions (if you knew the phase of the first one). This is ptychography, first

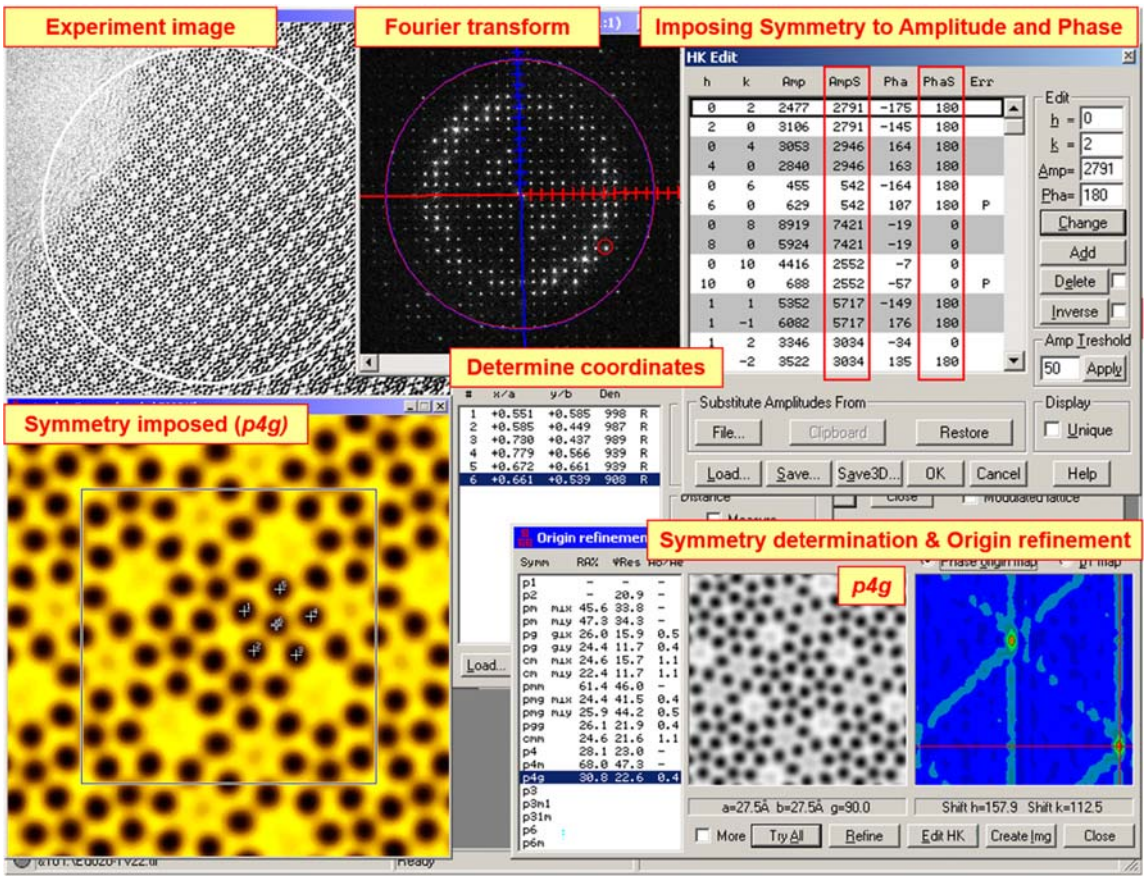

Fig. 13 Determination of structure factor amplitudes and phases from HRTEM image by crystallographic image processing using CRISP.

proposed in visible-light optics and later for electron microscopy by Hoppe.[130] Some books claim that once you can say the word correctly, you can practice it.[131] The truly remarkable feature of ptychography is that, for thin crystals, some frequency information recovery methods provide the phase of Bragg diffractions corresponding to d-spacings that are much finer than the probe width.[132,133] Although it is promising, numerically appealing and producing results, there are still challenges to be addressed regarding these methods. They involve sometimes iterative reconstruction schemes, which do not always converge, they are restricted to WPOA, and deal with ill-conditioned problems such as deconvolution.

10.03.3.5 Advantages of aberration correction for HRTEM and HRSTEM investigations

Reducing lens aberrations has been a goal of electron-optical designers for several decades, and it appears to have been finally reached.[98] Electromagnetic lenses are never perfect and exhibit a variety of defects, including spherical aberration, defocus, coma, astigmatism and higher order aberrations, leading to distortion of the image. Spherical aberration C_s is a resolution limiting aberration, equally important in HRTEM and STEM, and it describes the effect that electrons travelling far away from the optical axis are not focused into the same focal point as those propagating near the optical axis. The *spherical aberration cannot be compensated for in a round lens* (Scherzer's theorem). Thus, a multi-element aberration corrector is required. Real C_s correctors may be designed either as an octupole/quadrupole assembly or as a hexapole assembly.[134] For example, the concept of the hexapole corrector consisting of two hexapole elements and two lens doublets, which provide for a complete compensation of spherical aberration (of the imaging part) in the objective lens, was proposed by Rose for the first time.[135,136] As soon as spherical aberration in the objective lens is corrected (C_s drops by three orders of magnitude to a few microns compared to a value of about 1 mm without correction), the second largest lens defect, the chromatic aberration, C_c, comes into play. C_c arises from the spread of the initial speed of electrons (and, consequently, their energies) emitted from the electron gun, and can be compensated using a monochromator, which reduces the inherent energy spread in the electron beam from typically 0.7 eV to values smaller than 0.2 eV depending on the setting.

The reduction of aberrations not only increases the point-to-point resolution (which is expressed by Eq. 18), but it also leads to an improvement of the image quality in general. First, tilting the incident beam by up to 30 mrad was found to introduce negligible image shift, defocus, astigmatism or coma, so that the use of hollow-cone illumination is greatly facilitated. Second, the reduction of so-called delocalization effects. Due to a non-zero C_s value, electrons from one point of an object are not imaged into a single point but rather into a small disk smearing out the information. Reducing delocalization is crucial when studying e.g. interfaces. When

a crystal grain boundary is observed, lattice fringes appear across the boundary and this artificial contrast may result in misinterpretation of special interface structures. Last but not the least for electron crystallography, the size of the region which can be studied by nanodiffraction can be usefully reduced, due to decreased positional error of the selected-area aperture.[137,138] Against intuition, it is not meaningful to compensate C_s entirely to zero, since contrast is proportional to the sine of the wave-abberation function, and at $C_s = 0$ and $z = 0$, there is essentially no contrast at all for very low specimen thickness. However, enhanced contrast may be achieved under negative spherical aberration imaging conditions, $C_s < 0$.[139] The image signal obtained with C_s tuned to negative values is significantly more robust against noise caused by amorphous surface layers, resulting in a measurement precision for atomic positions that is a factor of 2–3 better than conventional HRTEM at an identical noise level. This provides extraordinary new opportunities to materials science.[140,141]

Aberration corrected microscopy brings us closer to the quantum world, but it also urges us to rethink some standard concepts of conventional TEM, for example, an "independent atom model", which neglects the effects of the bonding electrons, or an "ideally weak phase object."[142,143] As discussed before, WPOA is realized in a very thin sample consisting of atoms with low Z, which, owing to their weak electron scattering, induce only very weak phase shifts in the imaging electron-wave field, yielding a direct representation of the specimen scattering potential by the image contrast. Single-layer graphene can be considered, with respect to electron scattering, the weakest object so far available. Nitrogen-doped graphene, on the other hand, should have a scattering potential almost identical to that of regular graphene. However, recently Meyer et al.[144] revealed that the contrast difference between the C and N in HRTEM images may be non-negligible (**Fig. 14**). A density-functional theory was used to calculate the expected electron density around the nitrogen atom and to predict the atomic scattering potential for the electrons. By solving the Schrödinger equation for this potential, a local atomic-scale phase modulation in the electron wave was found, which was then observed as the contrast in an aberration-corrected transmission electron microscope. It is worth noting that the contrast of the N defect appears primarily due to a change in the electron distribution on the neighboring carbons, rather than on the nitrogen atom itself, hence, it is exclusively the charge redistribution due to chemical bonding that makes it possible to find nitrogen substitutions in graphene.

Finally, we make some remarks about the indirect benefits of aberration correction, caused mainly by advances in instrumentation arriving together with the aberration correction. Whereas in the past, there has been a tendency to either concentrate on imaging-based studies or spectroscopic studies, currently, the use of multiple simultaneously acquired signals is a growing feature of aberration-corrected microscopy. This can include the combination of imaging with EELS,[145] Energy-dispersive X-ray spectroscopy, cathodoluminescence, and secondary electrons, to provide a complete quantitative picture of the structure, chemistry and properties at the atomic or nanoscale. Aberration correction also facilitates the development of low voltage transmission electron microscopy using an electron beam with an energy in the range from 5 to 60 kV, which is invaluable for studies of soft materials, graphene, carbon nanotubes, fullerenes and other beam sensitive samples.[146] A final important benefit of aberration correction results from the fact that combined C_s/C_c correction can be used to improve image resolution while a wide objective lens polepiece gap allows additional space for high tilt holders, detectors, and other components around the sample.

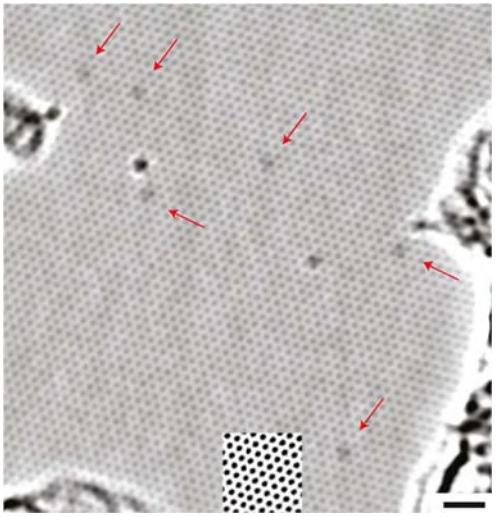

Fig. 14 Gaussian low-pass filtered image of nitrogen-doped graphene showing six nitrogen substitution defects marked by red arrows. The filter is needed to discern the N dopants against the much stronger signal of the single layer graphene lattice. The inset shows an unfiltered section of the image on the same contrast scale. Scale bar is 1 nm. Reproduced from ref. Meyer, J. C.; Kurasch, S.; Park, H. J.; Skakalova, V.; Künzel, D.; Groß, A.; Chuvilin, A.; Algara-Siller, G.; Roth, S.; Iwasaki, T.; Starke, U.; Smet, J. H.; Kaiser, U. *Nat. Mater.* **2011**, *10*, 209–215, with permission from the Springer Nature, copyright 2011.

10.03.4 Applications of electron crystallography for studies of inorganic and functional materials

In this section we show how electron crystallography, based both on imaging and diffraction, meets challenges in the structure determination of inorganic and functional materials. 3D ED is designed for the determination of structure from nanosized crystals. However, ideally ordered crystals are rare even at this scale and, when it comes to the structural analysis of nano-volumes, researchers often have to deal with features such as vacancies, dislocations, planar defects and others. In the past, deviations from ideal crystals have often been ignored or neglected, mostly due to insufficient ED data quality, and HRTEM was considered to be the most relevant way to study defects, except for maybe point defects, which can only be detected by HRTEM when they are in clusters or columns. Today, crystals with disorder can be handled by 3D ED. We will also address some of the problems that still confront the method, including light element detection and obtaining structural information from 2D materials, thin films and amorphous materials.

10.03.4.1 Ab initio structure determination of perfectly periodic crystals by 3D ED and imaging

With the development of 3D ED techniques, ab initio structure determination using nano- and submicron-sized crystals can be performed as easily as single crystal X-ray diffraction (SCXRD). ITQ-43 was the first example of a zeolite whose structure was determined ab initio by 3D ED.[147] Using ADT data collected at 100 K, the structure of ITQ-43 was solved by direct methods. The positions of all the Si and Ge atoms, and 13 out of 24 O atoms, were directly determined. The missing O atoms were located from difference Fourier maps or added manually according to the coordination geometry of Si and Ge. This structure determination revealed an extra-large 28-ring channel with an accessible pore size of 21.9 Å × 19.6 Å in their longest axes (**Fig. 15**A). The first coordination polymer structure to be solved using electron diffraction data was the ζ-phase of Pigment Red.[148] Using a stepwise tilt-series, ED patterns of the needle-shaped crystals were collected. They were used to obtain a structural model after extracting the intensities. A specific molecular packing of Pigment Red (**Fig. 15**B) was revealed. As the small pigment crystals were only available in a phase mixture, electron diffraction showed a unique advantage.

The enormous advantages of 3D ED for characterizing nanometer and sub-micrometer crystals have made it possible to determine the structures of inorganic compounds that remained unknown for decades. For example, the structure of zeolite ZSM-25[149] was solved using 3D ED data after the material was first synthesized 30 years ago. In addition to the structure, a 3D ED study by RED revealed a close structural relationship between several zeolites ZSM-25, rho (RHO) and Paulingite (PAU). This opened a new strategy for the targeted synthesis of new zeolites, where five new zeolite structures in the RHO family were synthesized with most of their structures determined by 3D ED (**Fig. 16**A).[149,150,152] Moreover, the structure of bismuth subgallate, which is a long-used active pharmaceutical ingredient, was solved using 3D ED data. The structure was previously believed to be a coordination complex where gallate coordinates to Bi^{3+} via its carboxylate group with hydroxide anions for charge balance. Surprisingly, the structure of bismuth subgallate, as determined from cRED data, is a one-dimensional coordination polymer. The gallate anions coordinate to Bi^{3+} via the phenolates rather than the carboxylate groups, and the carboxylic acid groups form hydrogen bonds with each other[151] (**Fig. 16**B).

Imaging is often synergetic to the electron diffraction. Thus, the structure of the complex zeolite IM-5 (*Cmcm*, $a = 14.33(7)$ Å, $b = 56.9(2)$ Å, $c = 20.32(7)$ Å), which remained unsolved for nearly 10 years, was determined by combining SAED, 3D reconstruction from HRTEM images along different zone axes, and powder X-ray diffraction. The unit cell and space group were determined from extinctions in the SAED patterns and the projection symmetries of HRTEM images. The phases and amplitudes of structure factors for 144 independent reflections were obtained from HRTEM images along the [100], [010], and [001] directions. All 24 unique Si positions could be determined from the 3D potential map calculated by inverse Fourier transformation of these 144

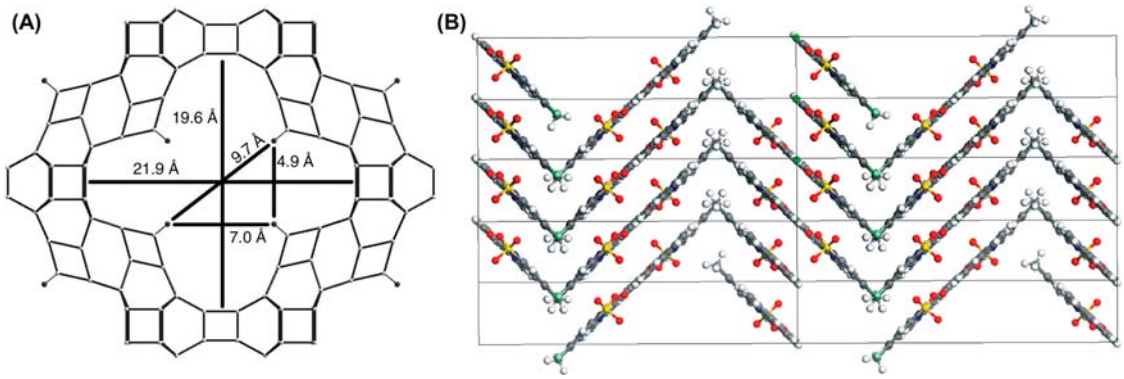

Fig. 15 Structural models for (A) ITQ-43,[147] and (B) ζ-phase Pigment Red[148] determined using 3D ED data. Reproduced from ref. Jiang, J.; Jorda, J. L.; Yu, J.; Baumes, L. A.; Mugnaioli, E.; Diaz-Cabanas, M. J.; Kolb, U.; Corma, A. *Science* **2011**, *333*, 1131–1134 and ref. Gorelik, T.; Schmidt, M. U.; Brüning, J.; Beko, S.; Kolb, U. *Cryst. Growth Des.* **2009**, *9*, 3898–3903, with permission from the American Association for the Advancement of Science, and the American Chemical Society, respectively, copyright 2011 and 2009.

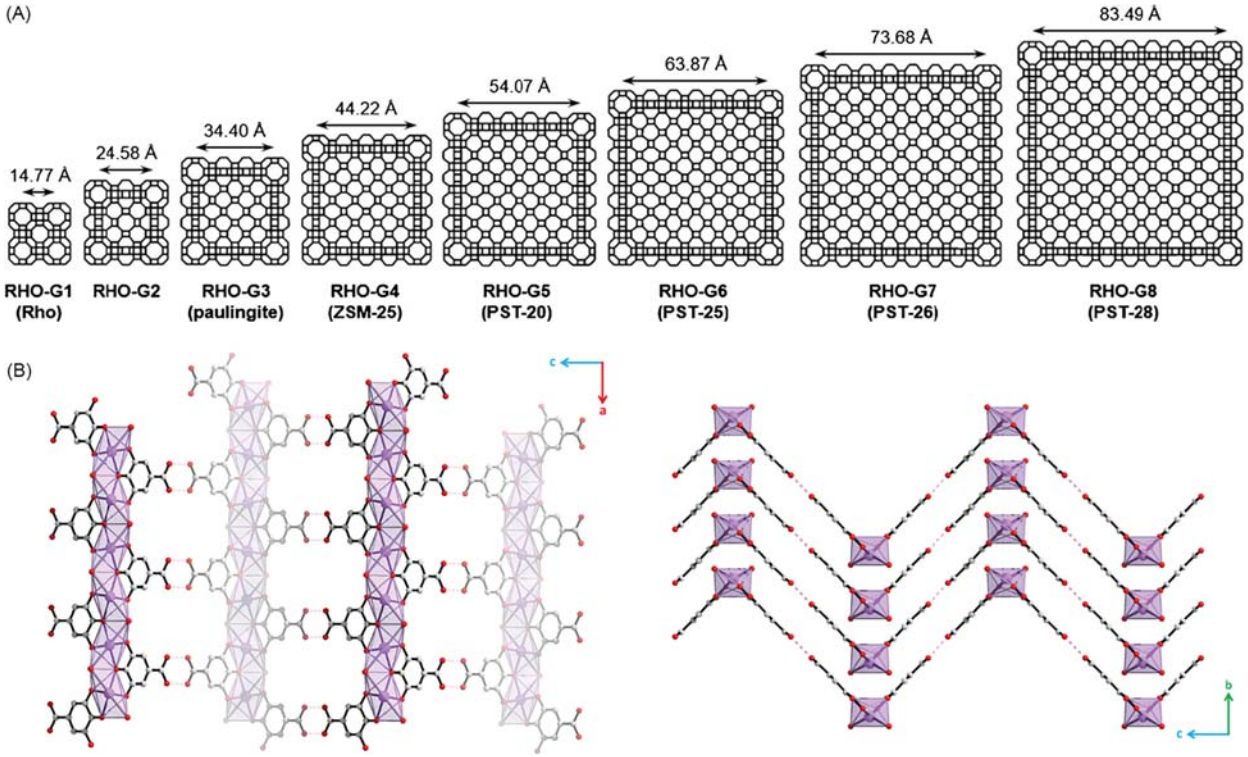

Fig. 16 (A) Framework representations of cross sections (*ca.* 12 Å thick) of RHO-G1 to RHO-G8 in the RHO family of embedded isoreticular zeolites.[150] (B) Structural model of bismuth subgallate viewed along the [010] and [100] directions.[151] Reproduced from ref. Shin, J.; Xu, H.; Seo, S.; Guo, P.; Min, J. G.; Cho, J.; Wright, P. A.; Zou, X.; Hong, S. B. *Angew. Chem. Int. Ed.* **2016**, *55*, 4928–4932 and ref. Wang, Y.; Takki, S.; Cheung, O.; Xu, H.; Wan, W.; Öhrström, L.; Inge, A. K. *Chem. Commun.* **2017**, *53*, 7018–7021, with permission from the John Wiley & Sons, Inc., and the Royal Society of Chemistry, respectively, copyright 2016 and 2017.

independent reflections (Fig. 17). Oxygen atoms were added between each Si-Si pair and further refined together with the Si positions by distance-least-squares.[153,154]

Prior knowledge of the crystal structure can be used to predict certain features in STEM[155] or HRTEM[156] images and thus distinguish between different material modifications, such as enantiomorphic structures. In Fig. 18, the two chiral tellurium (Te) structures are indistinguishable along the [010] direction, but when rotating the models from the [010] direction clockwise or anticlockwise by 30° around the spiral axis, curves in the right-handed structure bend to the right and curves in the left-handed structure bend to the left.[155] Thus, recording two images along the proper zone axes in a tilt series is sufficient to determine the handedness of a Te chiral crystal. Other methods, such as electron backscatter diffraction,[157] fringes in TEM images,[158] and electron vortex beams[159] have also been used for the determination of handedness. These methods, however, are more complex, and cannot be applied for local handedness determination at the atomic level.

10.03.4.2 Outside the realm of perfectly periodic crystals

10.03.4.2.1 Mixed occupancies and vacancies

Point defects in the lattice could appear in the form of substitutional atoms (mixed occupancies), interstitial atoms, or vacancies. Often, they can be revealed from difference Fourier maps, the same way as in the XRD analysis. If one crystallographic site is occupied by two different atoms, an accurate determination of the ratio between them maybe a challenge for 3D ED, particularly if the scattering powers of these two chemical species differs insignificantly. Proximity of the ED intensities to the kinematical limit plays a decisive role in such cases. One example, where the mixed occupancy refinement became possible, is the structure of a novel borosilicate zeolite EMM-26 determined from RED data (Fig. 19).[160] In addition to the framework structure, which consists of 2D intersecting 10 × 10-ring channels, notably, the occupancies of the Si and B atoms could be determined directly from the RED data. It was shown that the B atoms preferred to partially occupy three of the seven unique 4-coordinated positions, with occupancies of 0.12(4), 0.05(5), and 0.39(5), respectively.

In certain cases, reducing the multiple scattering contribution by using the precession technique, followed by a dynamical refinement,[52] may be very helpful. For example, an orthopyroxene $(Mg,Fe)SiO_3$ structure[11] contained two cationic sites M1 and M2 co-occupied by Fe^{2+} and Mg^{2+}. According to the XRD refinement, occupancies of Fe^{2+} at the M1 and M2 sites were 0.150(3) and 0.424(3), respectively. In contrast to the EMM-26 case[160] described above, kinematical refinement of the ED data leads to unreliable

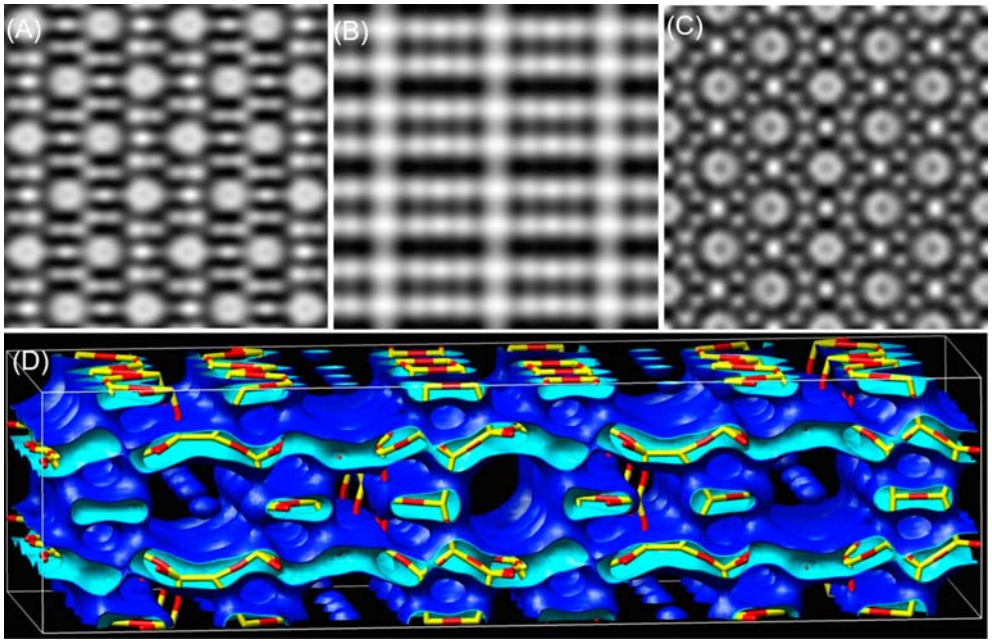

Fig. 17 3D potential map of a complex zeolite catalyst IM-5 obtained from HRTEM images taken along the three main crystallographic axes (*Cmcm*, $a = 14.33(7)$ Å, $b = 56.9(2)$ Å, $c = 20.32(7)$ Å). Top: Projected potential map along [100] (A), [010] (B) and [001] (C) directions. Bottom: The 3D electrostatic potential map generated from the HRTEM images. Reproduced from ref. Sun, J.; He, Z.; Hovmöller, S.; Zou, X.; Gramm, F.; Baerlocher, C.; McCusker, L.B. *Z. Für Krist. - Cryst. Mater.* **2010**, *225*, 77–85 with permission from the De Gruyter, copyright 2010.

occupancies. However, PEDT dynamical isotropic refinement resulted in occupancy estimates for Fe^{2+} at M2 of 0.425(4), and the occupancy of Fe^{2+} at M1 was found to be slightly higher than those in the reference – 0.176(4). An anisotropic dynamical refinement leads to an improved occupancy of Fe1 as well. Thus, the reliable refinement of individual occupancies may be non-trivial in 3D ED, since atomic occupancies tend to correlate with displacement parameters. Chemically reasonable restraints as well as additional compositional information obtained e.g., by spectroscopy methods, may be invaluable when dealing with this problem.

In molecular crystallography disorder may be also associated with a vacancy or an uncertainty in the position of a molecular fragment. One example of direct defect observation at atomic resolution is a low-dose HRTEM imaging study of UiO-66 nanocrystals.[161] Compared with the perfect structure of UiO-66 (Fig. 20A), it was found that the UiO-66 crystals contained a large number of missing linker defects. Viewing along the [110] direction of perfect UiO-66, the observed contrast characteristic of horizontally arranged BDC linkers is not present in Fig. 20B. Using electron crystallography, the space group was determined to be *I*4/*mmm* and the 3D electrostatic potential map of the defect was reconstructed from HRTEM images along three distinct projections. The reconstructed potential map revealed an 8-connected Zr_6 cluster, which differs from the 12-connected Zr_6 cluster in the perfect UiO-66 structure (Fig. 20C). Moreover, the reconstructed potential map also allows the identification of the terminal formate groups, which replace the missing BDC linkers.

10.03.4.2.2 Planar discontinuities: Stacking disorder and nano-twinning

Countless examples of materials with stacking disorder exist, ranging from close-packed metals, ice and diamond to zeolites, open-framework materials and pharmaceuticals.[162] Disorder arises because of the different ways layers in the structure can stack on top of one another, which can include rotations, translational displacements and mirror operations. A proper treatment of disorder relies on model building, e.g. the order-disorder approach for polytypic structures, and on the quantitative analysis of the diffuse scattering. Structural analysis of materials at the order–disorder borderline by means of 3D ED was reviewed in ref. 30.

One example of a material with stacking faults is zeolite beta,[28] which has a heavily faulted structure hindering its structure determination for more than 20 years. The structure is formed by epitaxial stacking of a topologically identical building layer. Depending on the shift of the neighboring layers, different polytypes of zeolite beta can be constructed (Fig. 21 A–C). First, the average unit cell dimensions and possible space groups were determined from a series of SAED patterns. Next, a high quality HRTEM image taken along the [100] zone-axis revealed 4-, 5-, 6- and 12-rings in this projection, as well as the typical pore stacking sequences. The pore stacking was identified to be of two types ABAB… and ABCABC…, with a shift of one-third of the intralayer pore spacing. Electron diffraction also showed diffuse streaks parallel to the c*-axis for reflections with $h \neq 3n$ or $k \neq 3n$ and sharp spots for reflections with $h = 3n$ and $k = 3n$ (Fig. 21 D), which agrees with the stacking sequences observed by HRTEM (Fig. 21 E). Finally, computer-assisted modelling was used to derive 3D models of polytypes A and B, based on prior knowledge of typical bond lengths and typical connectivity rules in zeolites. In addition, a hypothetical model of polytype C, with AA… stacking, was proposed.

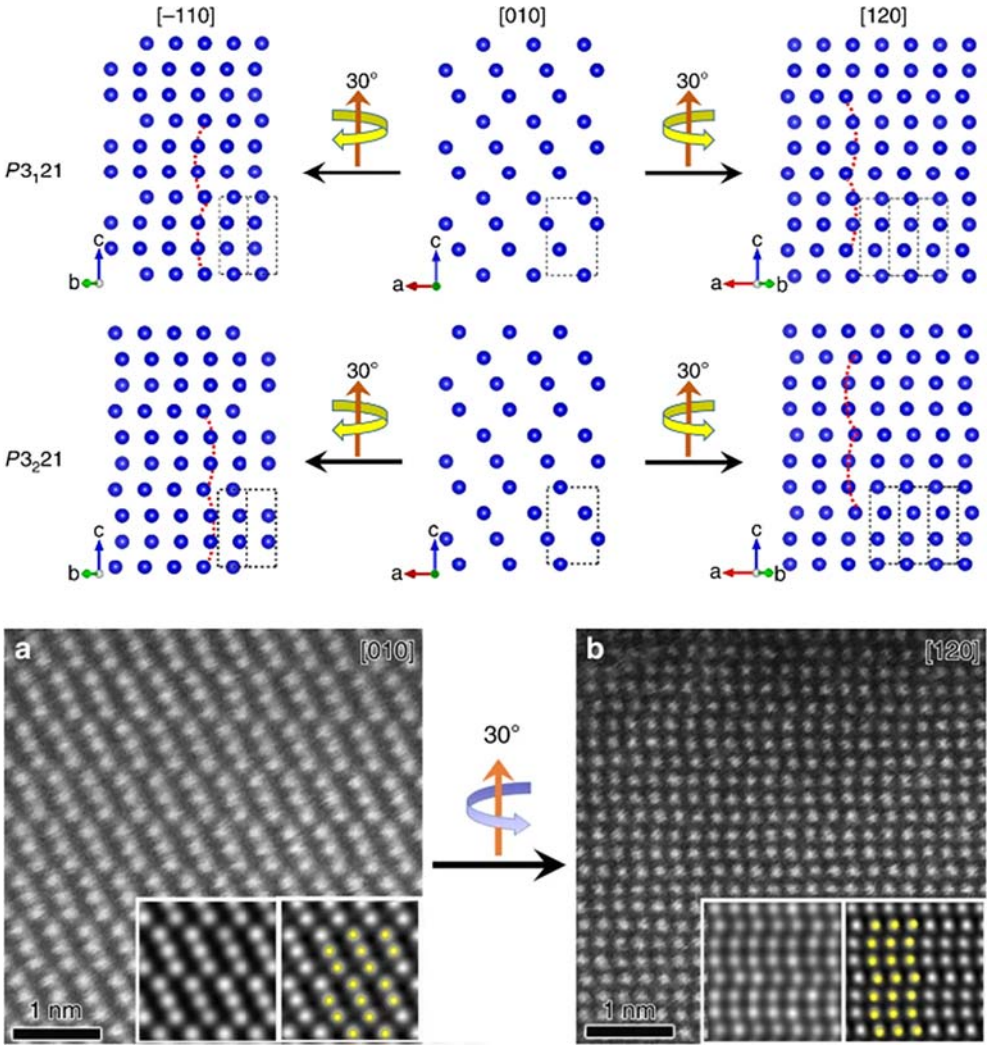

Fig. 18 Upper panel: projections of tellurium crystal structural models with right−/left-handedness along different orientations in a tilt series. Lower panel: STEM-ADF images of a Te crystal along (a) [010] and (b) [120] zone axes in a tilt-series (insets are simulated (left) and p1 symmetry-averaged images (right) overlaid with structural models, with yellow spheres representing Te atoms). Reproduced from ref. Dong, Z.; Ma, Y. *Nat. Commun.* **2020**, *11*, 1588, with permission from the Springer Nature, copyright 2020.

Interestingly, real materials with the framework of polytype C (framework code **BEC**) were later reported as a germanate FOS-5, a silicate and silicogermanate.[28]

Additional studies of local structural modulations, such as planar discontinuities, surface termination and pore connectivity in zeolites of the pentasil family have been reviewed by Zhang et al.[163] Another comprehensive review of stacking disorder in zeolites and open-frameworks has been prepared by Willhammar and Zou, and can be found in ref. 162.

When nano-twinning occurs, one simple option to overcome it, exclusively available in 3D ED but not in X-Ray diffraction, is to sample reflections from one single domain and perform a conventional structural analysis. For example, a 50 nm size beam was focused onto individual domains of twinned crystals for the structure solution of CAU-7, with composition Bi(BTB) (BTB = 1,3,5-benzenetrisbenzoate), which is a bismuth based catalytically active MOF.[164] The twinned CAU-7 crystal consists of three twin components and gives a pseudohexagonal symmetry. Based on the ADT data, the crystal symmetry was determined to be orthorhombic with $a = 32$ Å, $b = 28$ Å, $c = 4$ Å and extinction group (*Pb-a*). ADT datasets from two different single twin domains were merged together and 1158 independent reflections were obtained with a resolution of 1.15 Å. Structure solution was performed by simulated annealing and the resulting structure model was refined, using the Rietveld method, against PXRD data.

10.03.4.2.3 Superstructures and aperiodic structures

Electron crystallography has been applied to study materials with modulated structures such as $CeNbO_{4+\delta}$, which is a family of oxygen hyperstoichiometry materials with varying oxygen content ($CeNbO_4$, $CeNbO_{4.08}$, $CeNbO_{4.25}$, $CeNbO_{4.33}$).[165] Although

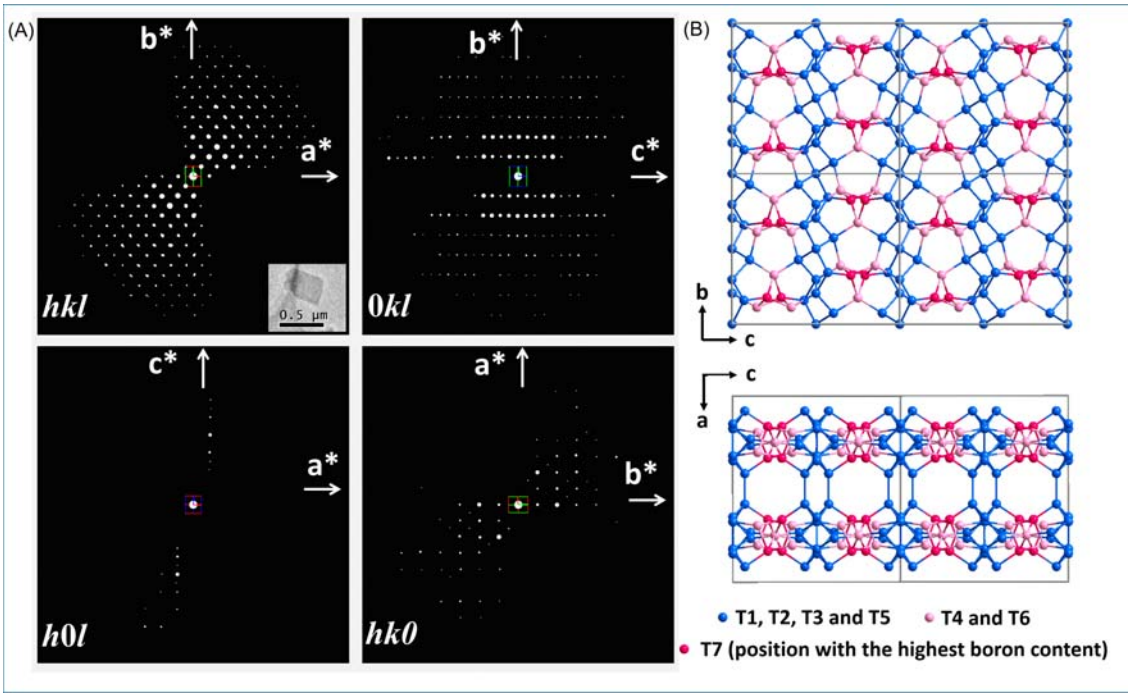

Fig. 19 (A) Reciprocal lattices reconstructed from RED data. (b) The structural model of EMM-26 viewed along the [100] and [010] directions. The Si-rich sites are shown in blue and B-rich sites in pink and magenta. Bridging O atoms have been omitted for clarity.[160] Reproduced from ref. Guo, P.; Strohmaier, K.; Vroman, H.; Afeworki, M.; Ravikovitch, P. I.; Paur, C. S.; Sun, J.; Burton, A.; Zou, X. *Inorg. Chem. Front.* **2016**, *3*, 1444–1448, with permission from the Royal Society of Chemistry, copyright, 2016.

their mixed oxide ionic conduction has been known for several decades, the transport mechanism remained elusive until the atomic structures of $CeNbO_{4.08}$ and $CeNbO_{4.33}$ were determined by 3D ED (Fig. 22A).[165] The 3D ED data was processed with an approximate supercell to determine the structure in (3 + 1)D superspace. Reflection conditions from the 3D reciprocal lattice reconstructed using the 3D ED data for $CeNbO_{4.08}$ indicated a superspace group of $X2/c(\alpha 0\gamma)0s$ and satellites up to order 7 were required. A (3 + 1)D structural model was constructed from the supercell. In addition to the parent structure of $CeNbO_4$, the modulated structure of $CeNbO_{4.08}$ was found to contain one additional oxygen site (O3) (Fig. 22B). The modulated structural model was refined against the 3D ED data with modulation functions up to order 7 and modulation of the atomic displacement parameters (ADPs) up to order 3 for Ce and 2 for Nb. A similar approach was applied to solve the modulated structure of $CeNbO_{4.33}$.

10.03.4.3 Detecting light elements by 3D ED and imaging

Electron diffraction can be used to locate low-Z atoms, such as H. By using dynamical refinement, localization of H atoms can be achieved by PED from single nano- to submicron-sized crystals. Cobalt aluminophosphate (CAP) is an example[91] of this. CAP has a general chemical formula of $Co_{1.13}Al_2P_4O_{20}H_{11.74}$, and consists of a regular stacking of $CoP_4O_{12}(OH)_2{\cdot}2H_2O$ and $AlO_5{\cdot}H_2O$ layers along the *b*-axis (Fig. 23). The cobalt site, Co(1), has a reduced occupancy, and there is an additional partially occupied, Co(2), site. The localization of fully occupied H positions was straightforward. However, identification of the remaining H positions was challenging due to their partial occupancy. Although electron potential maxima can be observed in the individual difference maps at each expected hydrogen position, they were very close to the noise level. To improve the data completeness and enhance the signals from the H atoms, the structural model of CAP was refined against merged PED data from six crystals. From the merged dataset, the standard deviation σ for the difference potential map is 0.144 e $Å^{-1}$, and the heights of the maxima of H atoms range from 3.34σ to 6.86σ. The highest noise maximum has a height of 2.34σ if the maxima at the position of cations (3.45σ) are neglected. Thus, based on the difference potential map, the H atoms were located and refined with distance restraints. The R value of the refinement decreased by 0.0088 with the addition of the H atoms.

Hydrogen[119] as well as lithium[120] atomic columns have been directly visualized for the first time using the ABF imaging method, which has been of utmost importance for understanding materials dedicated for hydrogen storage, such as YH_2, VH_2, and NbH_2. However, ABF imaging of H atoms is only possible for very thin specimens (< 10 nm), otherwise, the signal from the hydrogen atoms cannot be detected. Additionally, atom columns may appear white or black in the ABF image (see Section 10.03.3.3) hampering interpretation. Recently hydrogen atoms in titanium monohydride, at its interface with titanium as well as away from the interface, were imaged using the iDPC-STEM technique. iDPC visualizes the hydrogen columns with higher contrast

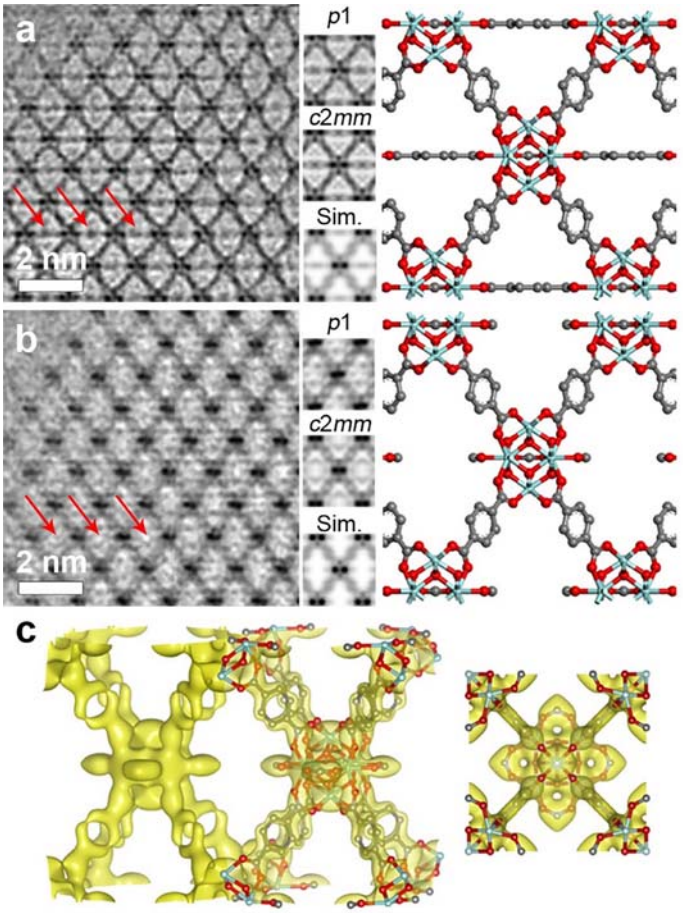

Fig. 20 CTF-corrected low-dose HRTEM images and structural models of (A) a perfect UiO-66 and (B) a UiO-66 with missing linker defects. The images are along the equivalent directions ([110] for the perfect UiO-66 in (A), and [100] for the UiO-66 with defects (B)). The red arrows indicate the missing BDC linkers. (C) Reconstructed electrostatic potential map of the UiO-66 with missing linker defect, showing an 8-connected node.[161] Reproduced from ref. Liu, L.; Chen, Z.; Wang, J.; Zhang, D.; Zhu, Y.; Ling, S.; Huang, K.-W.; Belmabkhout, Y.; Adil, K.; Zhang, Y.; Slater, B.; Eddaoudi, M.; Han, Y. *Nat. Chem.* **2019**, *11*, 622–628, with permission from the Springer Nature, copyright 2019.

and better localization as compared to ABF, whereas HAADF typically cannot image light and heavy elements simultaneously (Fig. 24). The iDPC contrast does not reverse as long as the probe is focused into the specimen, unlike ABF imaging.

10.03.4.4 2D materials and thin films

Dimensionally confined 2D materials such as graphene, BN, or transition metal dichalcogenides e.g., MoS_2, $TaSe_2$, TaS_2, have a 3D structure in reciprocal space, consisting of nearly infinite Bragg rods (Fig. 25). Each Bragg rod oscillates with intensity and phase determined by the atomic arrangement within and between each 2D layer. Using a simple kinematical model of diffraction, the structure of these Bragg rods can be mapped across a range of stacking geometries. Key structural parameters such as surface roughness, inter- and intralayer spacing, stacking order, and interlayer twist can be thus determined from ED data.[166,167]

Epitaxial thin film heterostructures are critical for integrating multi-functionality on a chip and creating smart structures for next generation devices. Accurate structure refinement for epitaxial thin films is a challenge in many aspects, whether by XRD or by 3D ED, due to the small amount of material deposited on the thicker substrate and the intricate epitaxial relationships. In contrast to multilayer 2D materials, the positions and integrated intensities of reflections can be extracted with good accuracy for oxide thin films, resulting in accurate lattice parameters,[168,169] even in the presence of strain[170] and twinning.[171] A structure refinement using 3D ED data may result in fairly good estimates (within $\sim$0.1 Å)[170] of the atomic positions. However, presently electron diffraction is still unable to map e.g. octahedral tilts or oxygen vacancies at perovskite interfaces.

10.03.4.5 Electron pair-distribution function analysis (ePDF) for amorphous materials

Poorly crystalline or amorphous materials typically do not produce diffraction data with sharp and well-resolved Bragg reflections, and therefore they cannot be studied using the classical approach. The structure of such materials is assessed using broad rings in

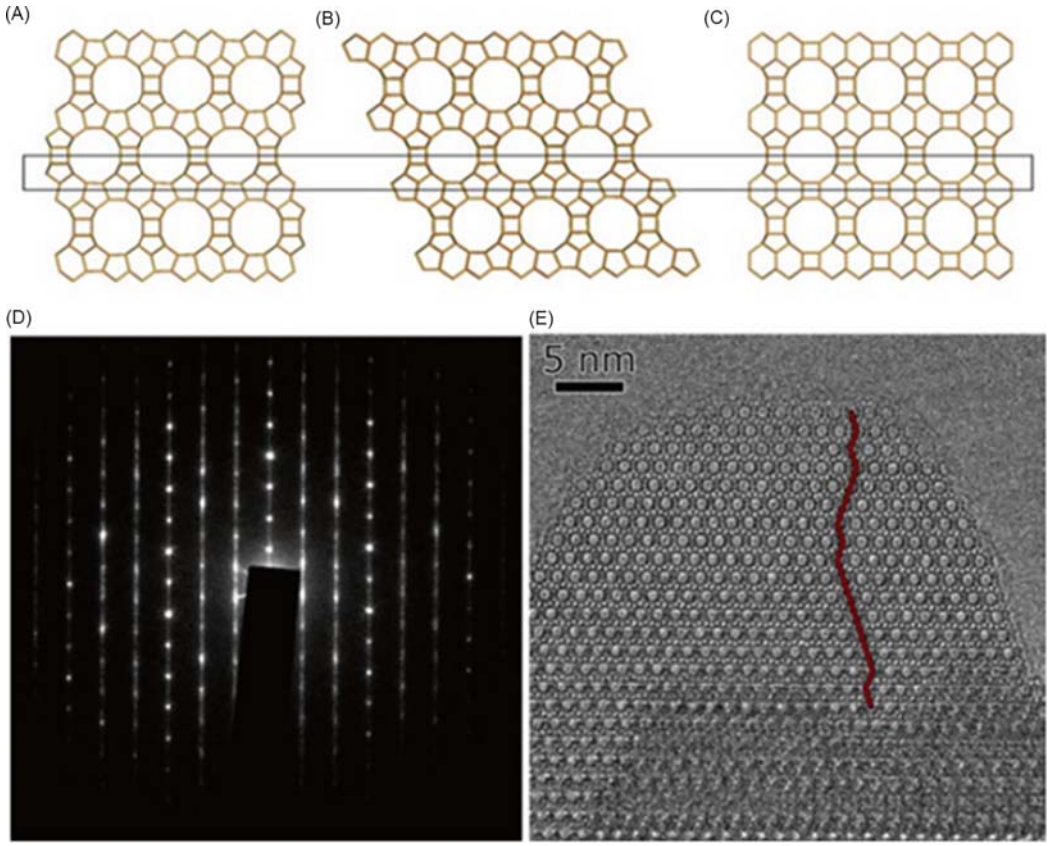

Fig. 21 The structure of zeolite beta viewed along [100] for polytypes (A) A, (B) B, and (C) C. (D) Selected-area electron diffraction pattern taken along the [100] zone-axis showing both streaks and sharp spots. (E) HRTEM image along [100] revealing an intergrowth between ABCABC and ABAB type stacking. Reproduced from ref. Willhammar, T.; Zou, X. *Zeolites in Sustainable Chemistry*. Xiao, F.-S.; Meng, X (eds.). Springer Berlin Heidelberg: Berlin, Heidelberg, 2016, pp. 151–186, with permission from the Springer, copyright 2016.

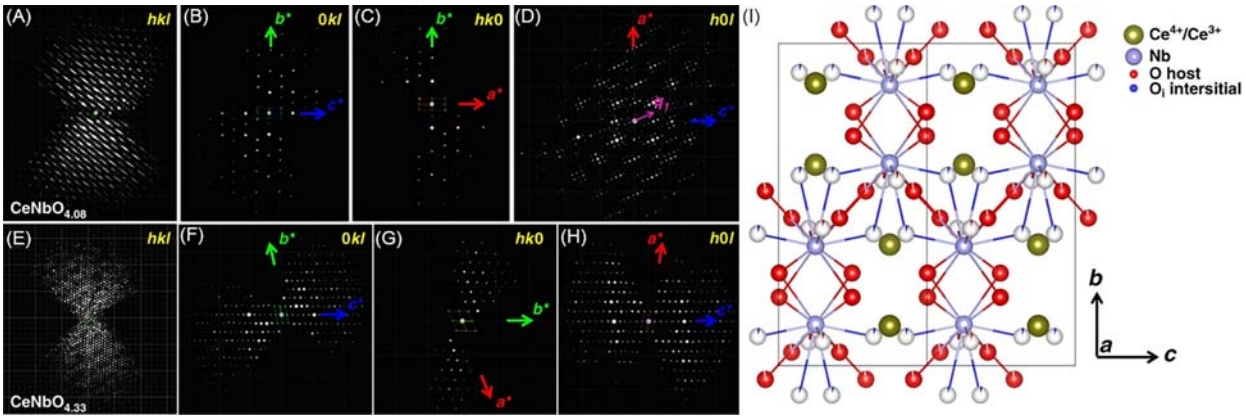

Fig. 22 3D reciprocal lattice reconstructed from the 3D ED data of $CeNbO_{4.08}$ (A) and $CeNbO_{4.33}$ (E). (B–D) Slices extracted from the reconstructed reciprocal lattice of $CeNbO_{4.08}$ showing (0*kl*), (*hk*0), and (*h*0*l*) planes, respectively. Reflection conditions: 0*klm*: $k + l = 2n$. *hk*0*m*: $h + k = 2n$, *h*0*lm*: $h + m = 2n$, $l + m = 2n$, *h*00*m*: $h + m = 2n$, 0 *k*00: $k = 2n$, 00 *lm*: $l + m = 2n$. (F–H) Slices cut from the reconstructed reciprocal lattice of $CeNbO_{4.33}$ showing the (0*kl*), (*hk*0), and (*h*0*l*) planes, respectively. Reflection conditions: no special systematic reflections appear forbidden. (i) Average structure, for the (3 + 1)D incommensurately modulated structure of $CeNbO_{4.08}$, along the $[100]_p$ direction. The interstitial O3 (blue atom) is located between Ce cations within the Ce cationic chain.[165] Reproduced from ref. Li, J.; Pan, F.; Geng, S.; Lin, C.; Palatinus, L.; Allix, M.; Kuang, X.; Lin, J.; Sun, J. *Nat. Commun.* **2020**, *11*, 4751, with permission from the Springer Nature, copyright, 2020.

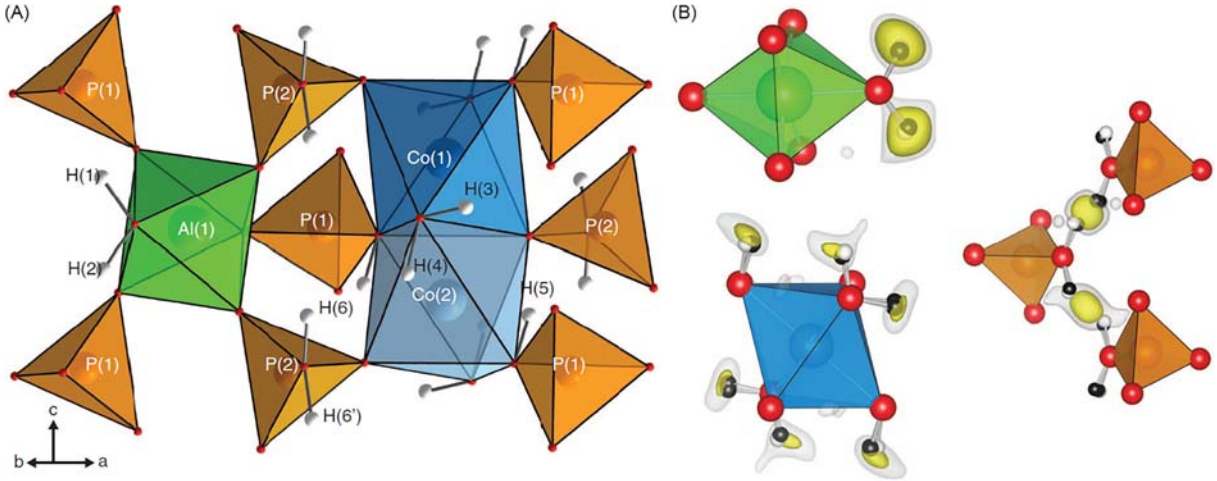

Fig. 23 (A) A view of the CAP structure along the [−2−10] direction. It shows the coordination environment of the $Al(1)O_6$, $Co(1)O_6$, and $Co(2)O_6$ octahedra, where the $Co(2)O_6$ octahedron is partially occupied. (B) Isosurface representation of the difference potential map of CAP, showing $AlO_5{\cdot}H_2O$, (B) $CoO_2(OH)_2{\cdot}2H_2O$, and (C) PO_3OH groups. The isosurface levels are contoured at $2\sigma[\Delta V(\mathbf{r})]$ (gray) and $3\sigma[\Delta V(\mathbf{r})]$ (yellow).[91] Green octahedra, Al atoms; blue octahedra, Co atoms; brown tetrahedra, P atoms; red spheres, O atoms. Reproduced from ref. Palatinus, L.; Brázda, P.; Boullay, P.; Perez, O.; Klementová, M.; Petit, S.; Eigner, V.; Zaarour, M.; Mintova, S. *Science* **2017**, *355*, 166–169, with permission from the American Association for the Advancement of Science, copyright, 2017.

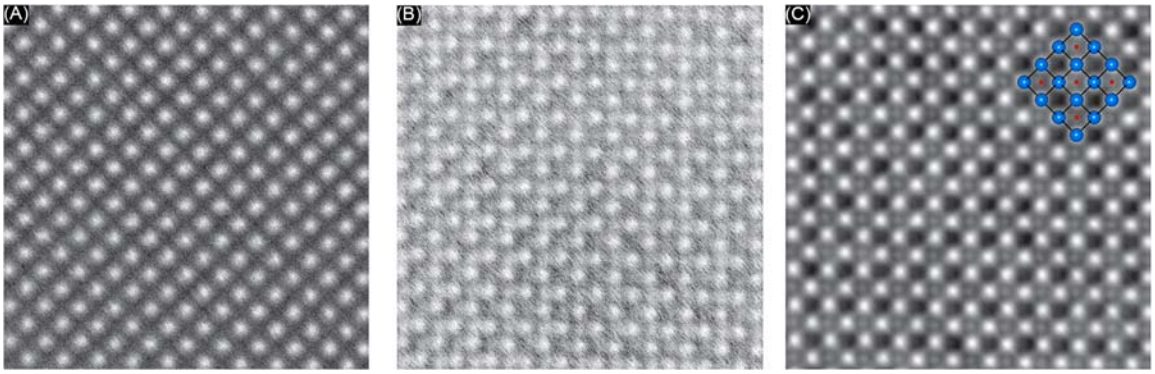

Fig. 24 Comparison of high-resolution images for γ-TiH, away from the α-Ti/γ-TiH interface. (A) HAADF. (B) Contrast-inverted ABF. (C) iDPC. Field of view is 3.13 × 3.13 nm. Reproduced with permission from ref. de Graaf, S.; Momand, J.; Mitterbauer, C.; Lazar, S.; Kooi, B. J. *Sci. Adv.* **2020**, *6*, eaay4312 the American Association for the Advancement of Science, Science Advances, copyright, 2020.

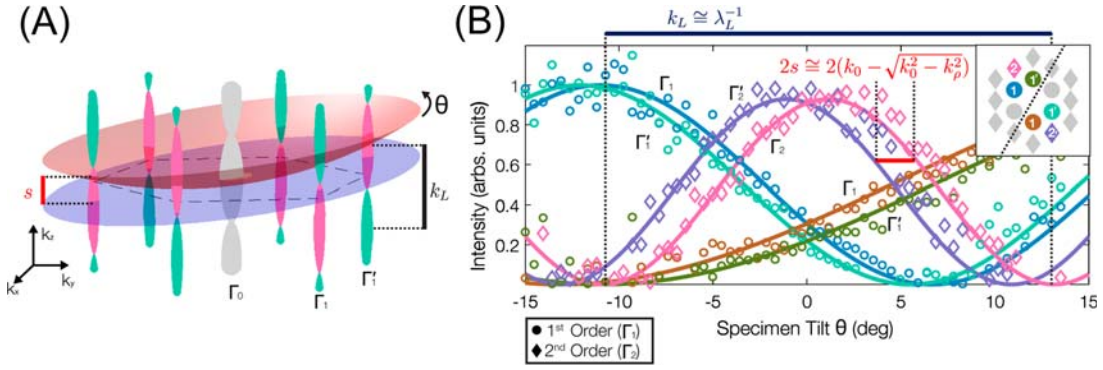

Fig. 25 (A) 3D reciprocal rod structure of bilayer graphene. (B) Kinematical (solid curves) and experimental (°, ◆) tilt patterns of bilayer graphene. For a typical TEM operating energy (blue, 200 keV), SAED is recorded for a nearly planar slice through the k-space origin; red surface exaggerates the curvature of Ewald sphere with low-energy electrons (0.3 keV). Tilting the specimen in the TEM column changes the beam's incident angle and effectively rocks the diffraction plane with respect to the Bragg rods, accessing out-of-plane information. Nontrivial Ewald sphere curvature separates analogous second-order Friedel pair tilt patterns (magenta and blue) with phase difference associated with the excitation errors. Reproduced from ref. Sung, S. H.; Schnitzer, N.; Brown, L.; Park, J.; Hovden, R. *Phys. Rev. Mater.* **2019**, *3*, 064003 with permission from the APS Physics, copyright, 2019.

SAED patterns instead of discrete Bragg reflections, with techniques like electron Pair Distribution Function (ePDF).[172] ePDF has been applied to study amorphous carbon, silicon and silicon carbide layers,[172] and later it was adopted for nanoparticles such as e.g. SnO_2,[173] anatase TiO_2,[172] and $NaYF_4$,[174] since it was shown that e-PDF matches well the equivalent X-Ray PDF. However, it was observed that, because of the strong dynamical effects present in ED, the height of the ePDF peaks could become strongly altered when compared to the theoretical calculated PDF peak heights. Although such dynamical effects do not affect the accuracy of ePDF peak positions, which correspond to interatomic distances, they do have an influence on the PDF peak height, and this could lead to wrong information on coordination numbers. In some cases, e.g. for $NaYF_4$,[174] reliable information on the coordination number (number of F atoms around Na/Y, 3) could be extracted with the help of precession diffraction, by comparing experimental and calculated total area around the ePDF peak at 2.36 Å (Na/Y- F bond length).

10.03.4.6 Orientation and secondary phases maps

Crystallography and diffraction experiments allow insight not only into the atomic arrangement in materials, but also the microstructure that the material exhibits, from grains and orientations, to secondary phases and interfaces.[175,176] By scanning an electron probe across a crystalline sample, one can generate spatially resolved diffraction maps. Both CBED patterns and Bragg spot patterns can be used, but the latter has the advantage of great simplicity in identifying the position of a diffracted beam as compared to the procedure of feature matching in the line patterns. It is worth noting that for orientation/phase mapping the structures of all the phases should be known in advance. The expected crystal structures can be used to prepare diffraction pattern templates for different orientations/phases. Calculating a correlation index between the experimental ED pattern and each template in a library then allows the best estimation of the phase/crystal orientation (ASTAR[177] and 3D-OMiTEM[178]). The technique has numerous applications for engineering materials, such as Al alloys and engineered steels; but one particularly relevant application is structural studies of oxide thin-films, where it plays a role in characterizing thermal/corrosion barriers or device materials.[175] These have the complexity of large numbers of small grains, often of different chemical nature. One example is CuO in the grain boundaries of Cu_2O thin films, which is acting as a photovoltaic device. For maximum conversion efficiency, the formation of CuO at the interface between Cu_2O and the n-type layer (Si) needs to be suppressed. TEM automated phase and orientation mapping is able to detect the nanometric CuO grains with very high precision (Fig. 26).[179]

10.03.4.7 Phase analysis and serial ED

The phase analysis of mixtures can also be realized by 3D ED, even in cases which present difficulties for powder X-ray diffraction (PXRD). Using RED, for example, four distinct phases were identified in a multiphase sample containing submicrometre-sized crystals. They were in the Ni-Se-O-Cl system and their structures were determined by RED (Fig. 27).[180] TEM observation found that the crystals were very small, and they showed different morphologies indicating a multiphase sample. RED data were then collected on individual crystals. The reconstructed 3D reciprocal lattices from crystals showed different unit cells, which is a clear indication that they have different structures. Further analyzing the data, the unit cell and space group for Phase 1 ($NiSeO_3$) was determined from the reconstructed 3D reciprocal lattice and 2D slices of the RED data. This information was used to search the crystal database and identify its structure. Phases 2–4 ($Ni_3Se_4O_{10}Cl_2$, $Ni_5Se_6O_{14}(OH)_2Cl_4$, and $Ni_5Se_4O_{12}C_{l2}$, respectively) were unknown compounds,

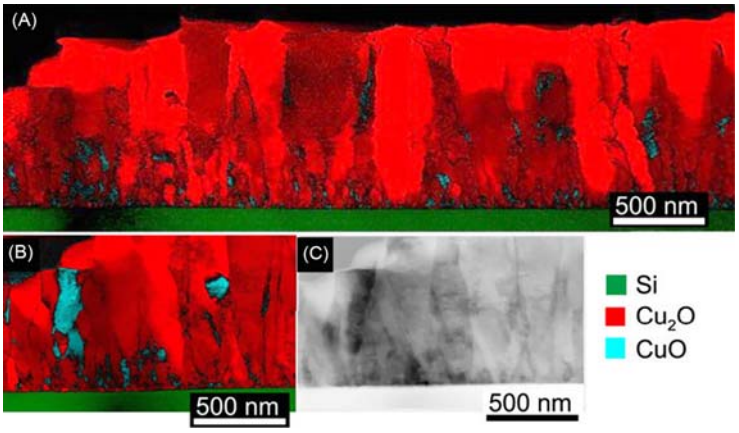

Fig. 26 TEM characterization of Cu_2O films. (A, B) Automatic crystal orientation/phase (ASTAR) mapping of the Cu_2O thin film cross section. The red color corresponds to the Cu_2O structure, the blue color represents the CuO structure, and the green color refers to the silicon substrate. (C) Reconstructed correlation gray scale index map related to (B). Reproduced from ref. Deuermeier, J.; Liu, H.; Rapenne, L.; Calmeiro, T.; Renou, G.; Martins, R.; Muñoz-Rojas, D.; Fortunato, E. *APL Mater.* **2018**, *6*, 096103 with permission from American Institute of Physics Publishing Group, copyright, 2018.

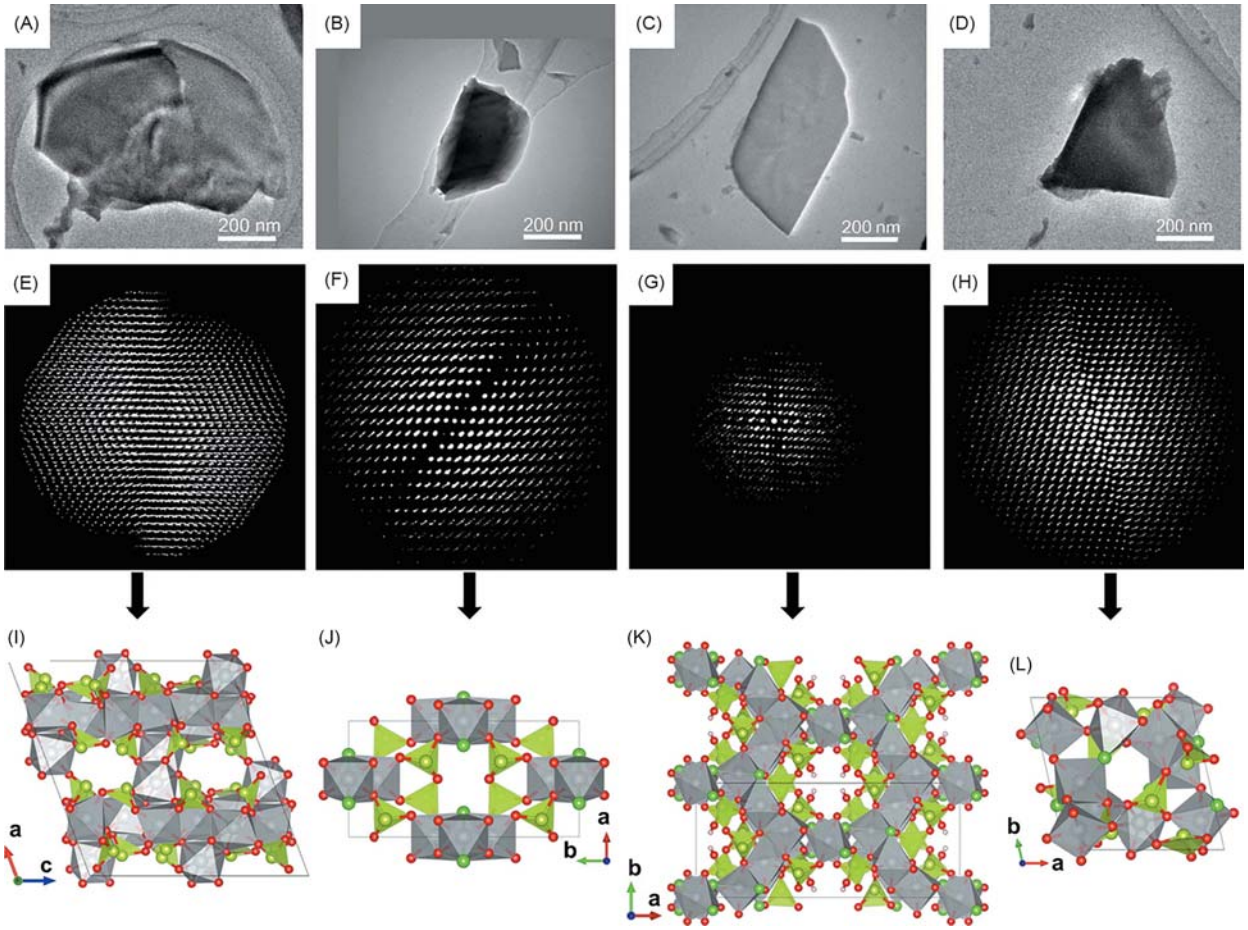

Fig. 27 TEM images of the (A) Phase 1, (B) Phase 2, (C) Phase 3 and (D) Phase 4 crystals used for RED data collection. The corresponding reconstructed 3D reciprocal lattices of (E) Phase 1, (F) Phase 2, (G) Phase 3 and (H) Phase 4. Structural models for (I) Phase 1, (J) Phase 2, (K) Phase 3 and (L) Phase 4 determined by RED. Gray octahedra; Ni, green-yellow trigonal pyramids; Se, red spheres; O atoms, green spheres; Cl atoms; brown spheres, H atoms.[180] Reproduced from ref. Yun, Y.; Wan, W.; Rabbani, F.; Su, J.; Xu, H.; Hovmöller, S.; Johnsson, M.; Zou, X. *J. Appl. Crystallogr.* **2014**, *47*, 2048–2054, with permission from the International Union of Crystallography, copyright, 2014.

whose structures were determined independently using the RED data. With the recent development of SerialRED, such procedures have largely been simplified. SerialRED has been used for phase analysis of e.g., a mixture of zeolites PST-20 and ZSM-25.[69]

10.03.5 Conclusions and future prospects

Electron crystallography is a well-developed technique with a rich history. However, there are still many possibilities for further advancement. Inorganic and materials chemistry greatly benefits from crystallography at the nanometer scale. The number of structures solved by 3D ED continues to grow. 3D ED can be also performed *in-situ* and offers a possibility to follow the nucleation and growth of a crystal, providing valuable structural details for catalysis. The true promise of 3D ED comes from its potential to determine the charge states in molecules. The mechanism by which electrons interact with crystals is different from that of X-rays. The structures studied by 3D ED are built on maps of electrostatic potential, rather than electron density maps as with X-ray crystallography. With adequate modelling of atomic scattering factors for electrons, 3D ED can tell us about the charge distribution at the atomic level, e.g., oxidation states of atoms in the crystal and more. Currently TEM remains the main working instrument for solving electron crystallography tasks. Progress in electron crystallography has arrived together with the development in the TEM equipment. Camera technology is quickly progressing and, alongside hybrid pixel detectors (e.g., Timepix and EIGER), the use of direct electron detectors for 3D ED is already starting. Automation of data collection has the outmost importance. Several protocols and software packages have already been developed, but many of them are commercial and/or closed source. Accessibility of modern TEMs to non-specialists is limited. Therefore, in the near future, users could either ship samples to the specialized TEM centers, and following sample loading, could collect 3D ED data remotely, similar to the way most X-ray synchrotron facilities operate, or purchase a dedicated electron diffractometer. In contrast to imaging, electron diffraction work does not rely to any substantial extent

on aberration correction, so that the key points for the future electron diffractometer are the stability of the goniometer, flexibility in the illumination conditions, and specific low-dose procedures for sample searching and data acquisition.

With an ever-growing family of inorganic crystals, it is vital to uncover their structures for the fundamental understanding of their physical and chemical properties. This chapter has highlighted several electron crystallography techniques for structure elucidation with inorganic materials. These includes electron diffraction techniques, which rely on the intensities of reflections to calculate and obtain the phase information for crystals, and high-resolution imaging techniques which allow direct observation of atoms in real space and are powerful for studies of local structure. As described in this chapter, using these techniques, structural information at the atomic level can be obtained from a focused area, typically in the range of nanometers. With future advances in the resolution of these techniques, greater structural detail for inorganic materials will become accessible, in order to shed the light on their unique properties.

References

1. Eggeman, A. S.; Midgley, P. A. In *Advances in Imaging and Electron Physics;* Hawkes, P. W., Ed., Elsevier, 2012; pp 1–63.
2. Sperling, R.; Amos, L. A.; Klug, A. *J. Mol. Biol.* **1975,** *92,* 541–558.
3. Hovmöller, S.; Zou, X.; Weirich, T. E. *Advances in Imaging and Electron Physics*, Elsevier, 2002; pp 257–289.
4. Zou, X.; Sundberg, M.; Larine, M.; Hovmöller, S. *Ultramicroscopy* **1996,** *62,* 103–121.
5. Hovmöller, S.; Zou, X. *Microsc. Res. Tech.* **1999,** *46,* 147–159.
6. Hovmöller, S. *Ultramicroscopy* **1992,** *41,* 121–135.
7. Kolb, U.; Gorelik, T.; Kübel, C.; Otten, M. T.; Hubert, D. *Ultramicroscopy* **2007,** *107,* 507–513.
8. Kolb, U.; Gorelik, T.; Otten, M. T. *Ultramicroscopy* **2008,** *108,* 763–772.
9. Kolb, U.; Krysiak, Y.; Plana-Ruiz, S. *Acta Crystallogr. Sect. B Struct. Sci. Cryst. Eng. Mater.* **2019,** *75,* 463–474.
10. Gemmi, M.; Oleynikov, P. *Z. Für Krist. - Cryst. Mater.* **2013,** *228,* 51–58.
11. Palatinus, L.; Corrêa, C. A.; Steciuk, G.; Jacob, D.; Roussel, P.; Boullay, P.; Klementová, M.; Gemmi, M.; Kopeček, J.; Domeneghetti, M. C.; Cámara, F.; Petříček, V. *Acta Crystallogr. Sect. B Struct. Sci. Cryst. Eng. Mater.* **2015,** *71,* 740–751.
12. Palatinus, L.; Brázda, P.; Jelínek, M.; Hrdá, J.; Steciuk, G.; Klementová, M. *Acta Crystallogr. Sect. B Struct. Sci. Cryst. Eng. Mater.* **2019,** *75,* 512–522.
13. Wan, W.; Sun, J.; Su, J.; Hovmoller, S.; Zou, X. *J. Appl. Crystallogr.* **2013,** *46,* 1863–1873.
14. Cichocka, M. O.; Ångström, J.; Wang, B.; Zou, X.; Smeets, S. *J. Appl. Crystallogr.* **2018,** *51,* 1652–1661.
15. Jones, C. G.; Martynowycz, M. W.; Hattne, J.; Fulton, T. J.; Stoltz, B. M.; Rodriguez, J. A.; Nelson, H. M.; Gonen, T. *ACS Cent. Sci.* **2018,** *4,* 1587–1592.
16. Nannenga, B. L. *Struct. Dyn.* **2020,** *7*, 014304.
17. Pinsker, Z. G. *Electron Diffraction*. Translated by Spink, J.A.; Feigl, E, Butterworths Scientific Publications, 1953.
18. Vainshtein, B. K. *Structure Analysis by Electron Diffraction*, Pergamon Press Ltd.: Oxford, 1964.
19. Zvyagin, B. B. *Electron-Diffraction Analysis of Clay Mineral Structures*, Springer: US, Boston, MA, 1967.
20. Nicolopoulos, S.; Gonzalez-Calbet, J. M.; Vallet-Regi, M.; Corma, A.; Corell, C.; Guil, J. M.; Perez-Pariente, J. *J. Am. Chem. Soc.* **1995,** *117,* 8947–8956.
21. Sinkler, W.; Marks, L. D.; Edwards, D. D.; Mason, T. O.; Poeppelmeier, K. R.; Hu, Z.; Jorgensen, J. D. *J. Solid State Chem.* **1998,** *136,* 145–149.
22. Sinkler, W.; Bengu, E.; Marks, L. D. *Acta Crystallogr. A* **1998,** *54,* 591–605.
23. Gjønnes, J.; Hansen, V.; Berg, B. S.; Runde, P.; Cheng, Y. F.; Gjønnes, K.; Dorset, D. L.; Gilmore, C. J. *Acta Crystallogr. A* **1998,** *54,* 306–319.
24. Weirich, T. E.; Zou, X. D.; Ramlau, R.; Simon, A.; Cascarano, G. L.; Giacovazzo, C.; Hovmöller, S. *Acta Crystallogr. A* **2000,** *56,* 29–35.
25. Gemmi, M.; Mugnaioli, E.; Gorelik, T. E.; Kolb, U.; Palatinus, L.; Boullay, P.; Hovmöller, S.; Abrahams, J. P. *ACS Cent. Sci.* **2019,** *5,* 1315–1329.
26. Huang, Z.; Grape, E. S.; Li, J.; Inge, A. K.; Zou, X. *Coord. Chem. Rev.* **2021,** *427*, 213583.
27. Willhammar, T.; Yun, Y.; Zou, X. *Adv. Funct. Mater.* **2014,** *24,* 182–199.
28. Willhammar, T.; Zou, X. In *Zeolites in Sustainable Chemistry;* Xiao, F.-S., Meng, X., Eds., Springer Berlin Heidelberg: Berlin, Heidelberg, 2016; pp 151–186.
29. Huang, Z.; Willhammar, T.; Zou, X. *Chem. Sci.* **2021,** *12,* 1206–1219.
30. Mugnaioli, E.; Gorelik, T. E. *Acta Crystallogr. Sect. B Struct. Sci. Cryst. Eng. Mater.* **2019,** *75,* 550–563.
31. Clabbers, M. T. B.; Xu, H. *Drug Discov. Today Technol.* **2020.** https://doi.org/10.1016/j.ddtec.2020.12.002.
32. Zuo, J. M.; Spence, J. C. H. *Advanced Transmission Electron Microscopy: Imaging and Diffraction in Nanoscience*, Springer-Verlag: New York, 2017.
33. Zou, X.; Hovmöller, S.; Oleynikov, P. *Electron Crystallography: Electron Microscopy and Electron Diffraction*, Oxford University Press: Oxford, New York, 2011.
34. Bethe, H. *Ann. Phys.* **1928,** *392,* 55–129.
35. Howie, A.; Whelan, M. J. *Proc R Soc Lond. Ser A* **1961,** *263,* 217–237.
36. Cowley, J. M.; Moodie, A. F.; IUCr. The scattering of electrons by atoms and crystals. I. A new theoretical approach. *Acta Crystallographica* **1957,** *10,* 609–619.
37. Goodman, P.; Moodie, A. F. *Acta Crystallogr. A* **1974,** *30,* 280–290.
38. Ishizuka, K.; Uyeda, N. *Acta Crystallogr. A* **1977,** *33,* 740–749.
39. van Dyck, D. *Phys. Status Solidi A* **1979,** *52,* 283–292.
40. Van Dyck, D.; Coene, W. *Ultramicroscopy* **1984,** *15,* 29–40.
41. Lobato, I.; Van Dyck, D. *Ultramicroscopy* **2012,** *119,* 63–71.
42. Peng, L.-M. In *Advances in Imaging and Electron Physics;* Hawkes, P. W., Ed., Elsevier, 1994; pp 205–351.
43. Peng, L.-M. *Micron* **1999,** *30,* 625–648.
44. Doyle, P. A.; Turner, P. S. *Acta Crystallogr. A* **1968,** *24,* 390–397.
45. Rez, D.; Rez, P.; Grant, I. *Acta Crystallogr. A* **1994,** *50,* 481–497.
46. Lobato, I.; Van Dyck, D. *Acta Crystallogr. Sect. Found. Adv.* **2014,** *70,* 636–649.
47. Bragg, W. H.; Bragg, W. L. *Proc R Soc Lond A* **1913,** *88,* 428–438.
48. Claffey, W. J.; Priore, R.; Parsons, D. F. *J. Appl. Crystallogr.* **1970,** *3,* 516–519.
49. Neumann, W.; Komrska, J.; Hofmeister, H.; Heydenreich, J. *Acta Crystallogr. A* **1988,** *44,* 890–897.
50. Peng, L.-M. *J. Electron Microsc. (Tokyo)* **2005,** *54,* 199–207.
51. Gemmi, M.; Lanza, A. E. *Acta Crystallogr. Sect. B Struct. Sci. Cryst. Eng. Mater.* **2019,** *75,* 495–504.
52. Vincent, R.; Midgley, P. A. *Ultramicroscopy* **1994,** *53,* 271–282.
53. Midgley, P. A.; Eggeman, A. S. *IUCrJ* **2015,** *2,* 126–136.
54. Palatinus, L.; Petříček, V.; Corrêa, C. A. *Acta Crystallogr. Sect. Found. Adv.* **2015,** *71,* 235–244.
55. Gemmi, M.; Nicolopoulos, S. *Ultramicroscopy* **2007,** *107,* 483–494.

56. Zou, X. D.; Mo, Z. M.; Hovmoller, S.; Li, X. Z.; Kuo, K. H. *Acta Crystallogr. A* **2003,** *59,* 526–539.
57. Dorset, D. L.; Hauptman, H. A. *Ultramicroscopy* **1976,** *1,* 195–201.
58. Dorset, D. L. *Acta Crystallogr. A* **1998,** *54,* 750–757.
59. Boullay, P.; Palatinus, L.; Barrier, N. *Inorg. Chem.* **2013,** *52,* 6127–6135.
60. Zhang, D.; Oleynikov, P.; Hovmöller, S.; Zou, X. *Z. Für Krist. - Cryst. Mater.* **2010,** *225,* 94–102.
61. Shi, D.; Nannenga, B. L.; Iadanza, M. G.; Gonen, T. *eLife* **2013,** *2*, e01345.
62. Nederlof, I.; van Genderen, E.; Li, Y.-W.; Abrahams, J. P. *Acta Crystallogr. D Biol. Crystallogr.* **2013,** *69,* 1223–1230.
63. Nannenga, B. L.; Shi, D.; Leslie, A. G. W.; Gonen, T. *Nat. Methods* **2014,** *11,* 927–930.
64. Plana-Ruiz, S.; Krysiak, Y.; Portillo, J.; Alig, E.; Estradé, S.; Peiró, F.; Kolb, U. *Ultramicroscopy* **2020,** *211*, 112951.
65. Gemmi, M.; La Placa, M. G. I.; Galanis, A. S.; Rauch, E. F.; Nicolopoulos, S. *J. Appl. Crystallogr.* **2015,** *48,* 718–727.
66. Smeets, S.; Wang, B.; Cichocka, M. O.; Ångström, J.; Wan, W. *Instamatic*, Zenodo, 2019.
67. Smeets, S.; Wan, W. *J. Appl. Crystallogr.* **2017,** *50,* 885–892.
68. Bücker, R.; Hogan-Lamarre, P.; Mehrabi, P.; Schulz, E. C.; Bultema, L. A.; Gevorkov, Y.; Brehm, W.; Yefanov, O.; Oberthür, D.; Kassier, G. H.; Dwayne Miller, R. J. *Nat. Commun.* **2020,** *11,* 996.
69. Wang, B.; Zou, X.; Smeets, S. *IUCrJ* **2019,** *6,* 854–867.
70. Kolb, U.; Mugnaioli, E.; Gorelik, T. E. *Cryst. Res. Technol.* **2011,** *46,* 542–554.
71. Kabsch, W. *Acta Crystallogr. D Biol. Crystallogr.* **2010,** *66,* 125–132.
72. Kabsch, W. *Acta Crystallogr. D Biol. Crystallogr.* **2010,** *66,* 133–144.
73. Winter, G.; Waterman, D. G.; Parkhurst, J. M.; Brewster, A. S.; Gildea, R. J.; Gerstel, M.; Fuentes-Montero, L.; Vollmar, M.; Michels-Clark, T.; Young, I. D.; Sauter, N. K.; Evans, G. *Acta Crystallogr. Sect. Struct. Biol.* **2018,** *74,* 85–97.
74. Clabbers, M. T. B.; Gruene, T.; Parkhurst, J. M.; Abrahams, J. P.; Waterman, D. G. *Acta Crystallogr. Sect. Struct. Biol.* **2018,** *74,* 506–518.
75. Battye, T. G. G.; Kontogiannis, L.; Johnson, O.; Powell, H. R.; Leslie, A. G. W. *Acta Crystallogr. D Biol. Crystallogr.* **2011,** *67,* 271–281.
76. Ge, M.; Yang, T.; Wang, Y.; Carraro, F.; Liang, W.; Doonan, C.; Falcaro, P.; Zheng, H.; Zou, X.; Huang, Z. *Faraday Discuss.* **2021.** https://doi.org/10.1039/D1FD00020A.
77. Shmueli, U. *International Tables for Crystallography Volume B, Reciprocal Space*, International Union Of Crystallography, 2006.
78. Hauptman, H. *Science* **1986,** *233,* 178–183.
79. Patterson, A. L. *Z. Für Krist. - Cryst. Mater.* **1935,** *90,* 517–542.
80. Brünger, A. T.; Karplus, M.; Petsko, G. A. *Acta Crystallogr. A* **1989,** *45,* 50–61.
81. Oszlányi, G.; Sütő, A. *Acta Crystallogr. A* **2005,** *61,* 147–152.
82. Oszlányi, G.; Sütő, A. *Acta Crystallogr. A* **2008,** *64,* 123–134.
83. Sheldrick, G. M. *Acta Crystallogr. A* **2008,** *64,* 112–122.
84. Sheldrick, G. M. *Acta Crystallogr. Sect. Found. Adv.* **2015,** *71,* 3–8.
85. Burla, M. C.; Caliandro, R.; Carrozzini, B.; Cascarano, G. L.; Cuocci, C.; Giacovazzo, C.; Mallamo, M.; Mazzone, A.; Polidori, G. *J. Appl. Crystallogr.* **2015,** *48,* 306–309.
86. Petříček, V.; Dušek, M.; Palatinus, L. *Z. Für Krist. - Cryst. Mater.* **2014,** *229,* 345–352.
87. Muller, P.; Herbst-Irmer, R.; Spek, A.; Schneider, T.; Sawaya, M. *Crystal Structure Refinement: A Crystallographer's Guide to SHELXL*, Oxford University Press: Oxford, New York, 2006.
88. Wang, Y.; Yang, T.; Xu, H.; Zou, X.; Wan, W. *J. Appl. Crystallogr.* **2018,** *51,* 1094–1101.
89. Huang, Z.; Ge, M.; Carraro, F.; Doonan, C. J.; Falcaro, P.; Zou, X. *Faraday Discuss.* **2020.** https://doi.org/10.1039/D0FD00015A.
90. Roslova, M.; Smeets, S.; Wang, B.; Thersleff, T.; Xu, H.; Zou, X. *J. Appl. Crystallogr.* **2020,** *53,* 1217–1224.
91. Palatinus, L.; Brázda, P.; Boullay, P.; Perez, O.; Klementová, M.; Petit, S.; Eigner, V.; Zaarour, M.; Mintova, S. *Science* **2017,** *355,* 166–169.
92. Zuo, J. M.; Spence, J. C. H. *Ultramicroscopy* **1991,** *35,* 185–196.
93. Carter, B.; Williams, D. B. *Transmission Electron Microscopy: Diffraction, Imaging, and Spectrometry*, Springer International Publishing, 2016.
94. Nellist, P. D.; Pennycook, S. J. In *Advances in Imaging and Electron Physics;* Hawkes, P. W., Ed., Elsevier, 2000; pp 147–203.
95. O'Keefe, M. A. *Ultramicroscopy* **1992,** *47,* 282–297.
96. Scherzer, O. *J. Appl. Phys.* **1949,** *20,* 20–29.
97. Stadelmann, P. A. *Ultramicroscopy* **1987,** *21,* 131–145.
98. Spence, J. C. H. *Mater. Sci. Eng. R Rep.* **1999,** *26,* 1–49.
99. Wan, W.; Hovmöller, S.; Zou, X. *Ultramicroscopy* **2012,** *115,* 50–60.
100. Aert, S. V.; Dyck, D. V.; den Dekker, A. J. *Opt. Express* **2006,** *14,* 3830–3839.
101. Tanaka, N., Ed.; *Scanning Transmission Electron Microscopy of Nanomaterials: Basics of Imaging and Analysis*, Imperial College Press: Hackensack, NJ, 2014.
102. Crewe, A. V.; Wall, J.; Langmore, J. *Science* **1970,** *168,* 1338–1340.
103. Treacy, M. M. J. *Microsc. Microanal.* **2011,** *17,* 847–858.
104. Watanabe, K.; Yamazaki, T.; Hashimoto, I.; Shiojiri, M. *Phys. Rev. B* **2001,** *64*, 115432.
105. Borisevich, A. Y.; Lupini, A. R.; Pennycook, S. J. *Proc. Natl. Acad. Sci.* **2006,** *103,* 3044–3048.
106. Bals, S.; Goris, B.; Backer, A. D.; Aert, S. V.; Tendeloo, G. V. *MRS Bull.* **2016,** *41,* 525–530.
107. Miao, J.; Ercius, P.; Billinge, S. J. L. *Science* **2016,** 353. https://doi.org/10.1126/science.aaf2157.
108. Van Aert, S.; Batenburg, K. J.; Rossell, M. D.; Erni, R.; Van Tendeloo, G. *Nature* **2011,** *470,* 374–377.
109. Yang, Y.; Chen, C.-C.; Scott, M. C.; Ophus, C.; Xu, R.; Pryor, A.; Wu, L.; Sun, F.; Theis, W.; Zhou, J.; Eisenbach, M.; Kent, P. R. C.; Sabirianov, R. F.; Zeng, H.; Ercius, P.; Miao, J. *Nature* **2017,** *542,* 75–79.
110. Collins, S. M.; Midgley, P. A. *Ultramicroscopy* **2017,** *180,* 133–141.
111. Pennycook, S. J.; Li, C.; Li, M.; Tang, C.; Okunishi, E.; Varela, M.; Kim, Y.-M.; Jang, J. H. *J. Anal. Sci. Technol.* **2018,** 9. https://doi.org/10.1186/s40543-018-0142-4.
112. Ishikawa, R.; Lupini, A. R.; Findlay, S. D.; Taniguchi, T.; Pennycook, S. J. *Nano Lett.* **2014,** *14,* 1903–1908.
113. Ishikawa, R.; Mishra, R.; Lupini, A. R.; Findlay, S. D.; Taniguchi, T.; Pantelides, S. T.; Pennycook, S. J. *Phys. Rev. Lett.* **2014,** *113.* https://doi.org/10.1103/PhysRevLett.113.155501.
114. Jang, J. H.; Kim, Y.-M.; He, Q.; Mishra, R.; Qiao, L.; Biegalski, M. D.; Lupini, A. R.; Pantelides, S. T.; Pennycook, S. J.; Kalinin, S. V.; Borisevich, A. Y. *ACS Nano* **2017,** *11,* 6942–6949.
115. MacLaren, I.; Ramasse, Q. M. *Int. Mater. Rev.* **2014,** *59,* 115–131.
116. Li, C.; Zhang, Q.; Mayoral, A. *ChemCatChem* **2020,** *12,* 1248–1269.
117. Tanaka, N. *Sci. Technol. Adv. Mater.* **2008,** *9*, 014111.
118. Findlay, S. D.; Shibata, N.; Sawada, H.; Okunishi, E.; Kondo, Y.; Ikuhara, Y. *Ultramicroscopy* **2010,** *110,* 903–923.
119. Ishikawa, R.; Okunishi, E.; Sawada, H.; Kondo, Y.; Hosokawa, F.; Abe, E. *Nat. Mater.* **2011,** *10,* 278–281.
120. Oshima, Y.; Sawada, H.; Hosokawa, F.; Okunishi, E.; Kaneyama, T.; Kondo, Y.; Niitaka, S.; Takagi, H.; Tanishiro, Y.; Takayanagi, K. *Microscopy* **2010,** *59,* 457–461.
121. Shibata, N.; Findlay, S. D.; Kohno, Y.; Sawada, H.; Kondo, Y.; Ikuhara, Y. *Nat. Phys.* **2012,** *8,* 611–615.
122. Müller, K.; Krause, F. F.; Béché, A.; Schowalter, M.; Galioit, V.; Löffler, S.; Verbeeck, J.; Zweck, J.; Schattschneider, P.; Rosenauer, A. *Nat. Commun.* **2014,** *5,* 5653.

123. Lazic, I.; Bosch, E. G. T.; Lazar, S. *Ultramicroscopy* **2016,** *160,* 265–280.
124. Yücelen, E.; Lazic, I.; Bosch, E. G. T. *Sci. Rep.* **2018,** *8,* 2676.
125. de Graaf, S.; Momand, J.; Mitterbauer, C.; Lazar, S.; Kooi, B. J. *Sci. Adv.* **2020,** *6,* eaay4312.
126. Shen, B.; Chen, X.; Cai, D.; Xiong, H.; Liu, X.; Meng, C.; Han, Y.; Wei, F. *Adv. Mater.* **2020,** *32,* 1906103.
127. Willhammar, T.; Sun, J.; Wan, W.; Oleynikov, P.; Zhang, D.; Zou, X.; Moliner, M.; Gonzalez, J.; Martínez, C.; Rey, F.; Corma, A. *Nat. Chem.* **2012,** *4,* 188–194.
128. Xu, W.; Jericho, M. H.; Meinertzhagen, I. A.; Kreuzer, H. J. *Proc. Natl. Acad. Sci.* **2001,** *98,* 11301–11305.
129. Hüe, F.; Rodenburg, J. M.; Maiden, A. M.; Sweeney, F.; Midgley, P. A. *Phys. Rev. B* **2010,** *82,* 121415.
130. Hoppe, W. *Acta Crystallogr. Sect. A* **1969,** *25,* 495–501.
131. Spence, J. In *Transmission electron microscopy diffraction, imaging, and spectrometry;* Carter, C. B., Williams, D. B., Eds., Springer International Publishing: Cham, 2016; pp 145–166.
132. McCallum, B. C.; Rodenburg, J. M. *Ultramicroscopy* **1992,** *45,* 371–380.
133. Chapman, H. N. *Ultramicroscopy* **1996,** *66,* 153–172.
134. Rose, H. H. *J. Electron Microsc. (Tokyo)* **2009,** *58,* 77–85.
135. Rose, H. H. *Optik* **1990,** *85,* 19–24.
136. Haider, M.; Uhlemann, S.; Schwan, E.; Rose, H.; Kabius, B.; Urban, K. *Nature* **1998,** *392,* 768–769.
137. Dwyer, C.; Kirkland, A. I.; Hartel, P.; Müller, H.; Haider, M. *Appl. Phys. Lett.* **2007,** *90*, 151104.
138. Yamasaki, J.; Sawada, H.; Tanaka, N. *Microscopy* **2005,** *54,* 123–126.
139. Urban, K. W.; Jia, C.-L.; Houben, L.; Lentzen, M.; Mi, S.-B.; Tillmann, K. *Philos. Trans. R. Soc. Math. Phys. Eng. Sci.* **2009,** *367,* 3735–3753.
140. Jia, C. L.; Mi, S. B.; Barthel, J.; Wang, D. W.; Dunin-Borkowski, R. E.; Urban, K. W.; Thust, A. *Nat. Mater.* **2014,** *13,* 1044–1049.
141. Jia, C.-L.; Mi, S.-B.; Urban, K.; Vrejoiu, I.; Alexe, M.; Hesse, D. *Nat. Mater.* **2008,** *7,* 57–61.
142. Urban, K. W. *Nat. Mater.* **2011,** *10,* 165–166.
143. Li, S.; Chang, Y.; Wang, Y.; Xu, Q.; Ge, B. *Micron* **2020,** *130,* 102813.
144. Meyer, J. C.; Kurasch, S.; Park, H. J.; Skakalova, V.; Künzel, D.; Groß, A.; Chuvilin, A.; Algara-Siller, G.; Roth, S.; Iwasaki, T.; Starke, U.; Smet, J. H.; Kaiser, U. *Nat. Mater.* **2011,** *10,* 209–215.
145. Scott, J.; Thomas, P. J.; MacKenzie, M.; McFadzean, S.; Wilbrink, J.; Craven, A. J.; Nicholson, W. A. P. *Ultramicroscopy* **2008,** *108,* 1586–1594.
146. Bacovský, J. *MethodsX* **2018,** *5,* 1033–1047.
147. Jiang, J.; Jorda, J. L.; Yu, J.; Baumes, L. A.; Mugnaioli, E.; Diaz-Cabanas, M. J.; Kolb, U.; Corma, A. *Science* **2011,** *333,* 1131–1134.
148. Gorelik, T.; Schmidt, M. U.; Brüning, J.; Beko, S.; Kolb, U. *Cryst. Growth Des.* **2009,** *9,* 3898–3903.
149. Guo, P.; Shin, J.; Greenaway, A. G.; Min, J. G.; Su, J.; Choi, H. J.; Liu, L.; Cox, P. A.; Hong, S. B.; Wright, P. A.; Zou, X. *Nature* **2015,** *524,* 74–78.
150. Shin, J.; Xu, H.; Seo, S.; Guo, P.; Min, J. G.; Cho, J.; Wright, P. A.; Zou, X.; Hong, S. B. *Angew. Chem. Int. Ed.* **2016,** *55,* 4928–4932.
151. Wang, Y.; Takki, S.; Cheung, O.; Xu, H.; Wan, W.; Öhrström, L.; Inge, A. K. *Chem. Commun.* **2017,** *53,* 7018–7021.
152. Lee, H.; Shin, J.; Choi, W.; Choi, H. J.; Yang, T.; Zou, X.; Hong, S. B. *Chem. Mater.* **2018,** *30,* 6619–6623.
153. Baerlocher, C.; Gramm, F.; Massüger, L.; McCusker, L. B.; He, Z.; Hovmöller, S.; Zou, X. *Science* **2007,** *315,* 1113–1116.
154. Sun, J.; He, Z.; Hovmöller, S.; Zou, X.; Gramm, F.; Baerlocher, C.; McCusker, L. B. *Z. Für Krist. - Cryst. Mater.* **2010,** *225,* 77–85.
155. Dong, Z.; Ma, Y. *Nat. Commun.* **2020,** *11,* 1588.
156. Ma, Y.; Oleynikov, P.; Terasaki, O. *Nat. Mater.* **2017,** *16,* 755–759.
157. Winkelmann, A.; Nolze, G. *Ultramicroscopy* **2015,** *149,* 58–63.
158. Ohsuna, T.; Liu, Z.; Che, S.; Terasaki, O. *Small* **2005,** *1,* 233–237.
159. Juchtmans, R.; Béché, A.; Abakumov, A.; Batuk, M.; Verbeeck, J. *Phys. Rev. B* **2015,** *91*, 094112.
160. Guo, P.; Strohmaier, K.; Vroman, H.; Afeworki, M.; Ravikovitch, P. I.; Paur, C. S.; Sun, J.; Burton, A.; Zou, X. *Inorg. Chem. Front.* **2016,** *3,* 1444–1448.
161. Liu, L.; Chen, Z.; Wang, J.; Zhang, D.; Zhu, Y.; Ling, S.; Huang, K.-W.; Belmabkhout, Y.; Adil, K.; Zhang, Y.; Slater, B.; Eddaoudi, M.; Han, Y. *Nat. Chem.* **2019,** *11,* 622–628.
162. Willhammar, T.; Zou, X. *Z. Für Krist. - Cryst. Mater.* **2013,** *228,* 11–27.
163. Zhang, Q.; Mayoral, A.; Li, J.; Ruan, J.; Alfredsson, V.; Ma, Y.; Yu, J.; Terasaki, O. *Angew. Chem. Int. Ed.* **2020,** *59,* 19403–19413.
164. Feyand, M.; Mugnaioli, E.; Vermoortele, F.; Bueken, B.; Dieterich, J. M.; Reimer, T.; Kolb, U.; de Vos, D.; Stock, N. *Angew. Chem. Int. Ed.* **2012,** *51,* 10373–10376.
165. Li, J.; Pan, F.; Geng, S.; Lin, C.; Palatinus, L.; Allix, M.; Kuang, X.; Lin, J.; Sun, J. *Nat. Commun.* **2020,** *11,* 4751.
166. Sung, S. H.; Schnitzer, N.; Brown, L.; Park, J.; Hovden, R. *Phys. Rev. Mater.* **2019,** *3*, 064003.
167. Meyer, J. C.; Geim, A. K.; Katsnelson, M. I.; Novoselov, K. S.; Booth, T. J.; Roth, S. *Nature* **2007,** *446,* 60–63.
168. Zhang, W.; Li, M.; Chen, A.; Li, L.; Zhu, Y.; Xia, Z.; Lu, P.; Boullay, P.; Wu, L.; Zhu, Y.; MacManus-Driscoll, J. L.; Jia, Q.; Zhou, H.; Narayan, J.; Zhang, X.; Wang, H.; Appl, A. C. S. *Mater. Interfaces* **2016,** *8,* 16845–16851.
169. Veis, M.; Minár, J.; Steciuk, G.; Palatinus, L.; Rinaldi, C.; Cantoni, M.; Kriegner, D.; Tikuisis, K. K.; Hamrle, J.; Zahradník, M.; Antos, R.; Železný, J.; Šmejkal, L.; Marti, X.; Wadley, P.; Campion, R. P.; Frontera, C.; Uhlířová, K.; Duchon, T.; Kuzel, P.; Novák, V.; Jungwirth, T.; Výborný, K. *Phys. Rev. B* **2018,** *97*, 125109.
170. Rotella, H.; Copie, O.; Steciuk, G.; Ouerdane, H.; Boullay, P.; Roussel, P.; Morales, M.; David, A.; Pautrat, A.; Mercey, B.; Lutterotti, L.; Chateigner, D.; Prellier, W. *J. Phys. Condens. Matter* **2015,** *27*, 175001.
171. Steciuk, G.; David, A.; Petrícek, V.; Palatinus, L.; Mercey, B.; Prellier, W.; Pautrat, A.; Boullay, P. *J. Appl. Crystallogr.* **2019,** *52,* 626–636.
172. Gorelik, T. E.; Neder, R.; Terban, M. W.; Lee, Z.; Mu, X.; Jung, C.; Jacob, T.; Kaiser, U. *Acta Crystallogr. Sect. B Struct. Sci. Cryst. Eng. Mater.* **2019,** *75,* 532–549.
173. Abeykoon, A. M. M.; Hu, H.; Wu, L.; Zhu, Y.; Billinge, S. J. L. *J. Appl. Crystallogr.* **2015,** *48,* 244–251.
174. Das, P. P.; Nicolopoulos, S.; Gemmi, M. *Acta Crystallogr. Sect. Found. Adv.* **2017,** *73,* C983.
175. Eggeman, A. S. *Acta Crystallogr. Sect. B Struct. Sci. Cryst. Eng. Mater.* **2019,** *75,* 475–484.
176. Wu, G.; Zhu, W.; He, Q.; Feng, Z.; Huang, T.; Zhang, L.; Schmidt, S.; Godfrey, A.; Huang, X. *Nano Mater. Sci.* **2020,** *2,* 50–57.
177. Rauch, E. F.; Duft, A. *Mater. Sci. Forum* **2005,** *495–497,* 197–202.
178. Liu, H. H.; Schmidt, S.; Poulsen, H. F.; Godfrey, A.; Liu, Z. Q.; Sharon, J. A.; Huang, X. *Science* **2011,** *332,* 833–834.
179. Deuermeier, J.; Liu, H.; Rapenne, L.; Calmeiro, T.; Renou, G.; Martins, R.; Muñoz-Rojas, D.; Fortunato, E. *APL Mater.* **2018,** *6*, 096103.
180. Yun, Y.; Wan, W.; Rabbani, F.; Su, J.; Xu, H.; Hovmöller, S.; Johnsson, M.; Zou, X. *J. Appl. Crystallogr.* **2014,** *47,* 2048–2054.

Всё для Победы! НАРОДНЫЙ ФРОНТ
https://pobeda.onf.ru/
LET'S HELP THE RUSSIA

10.04 Synchrotron diffraction studies on spin crossover materials

Lee T. Birchall and Helena J. Shepherd, School of Physical Sciences, University of Kent, Canterbury, United Kingdom

© 2023 Elsevier Ltd. All rights reserved.

10.04.1	**Introduction**	**86**
10.04.1.1	Ligand-field theory and the origin of thermal spin-crossover	87
10.04.1.2	Structure and properties of SCO complexes	87
10.04.1.3	Thermal SCO	88
10.04.1.4	Pressure-induced SCO	89
10.04.1.5	Light-induced excited spin state trapping (LIESST)	89
10.04.1.6	Types of SCO complex	89
10.04.2	**Synchrotron diffraction studies of SCO materials**	**90**
10.04.2.1	Mononuclear SCO materials	92
10.04.2.2	Multinuclear SCO complexes and frameworks	93
10.04.2.3	LIESST effect studies using synchrotron diffraction	97
10.04.2.4	Time-resolved synchrotron studies of SCO materials	98
10.04.2.5	X-ray induced excited spin state trapping	99
10.04.2.6	Charge density studies	99
10.04.2.7	Pressure-induced SCO	100
10.04.2.8	Pair distribution function	103
10.04.2.9	Synchrotron GIXRD and in-plane XRD studies	103
10.04.3	**Outlook**	**104**
References		**104**

Abstract

Spin crossover materials are able to switch reversibly between high spin and low spin states in response to external stimuli including temperature, pressure and light irradiation. The transition between spin states causes a change in color, magnetic and structural properties, leading to potential applications in sensing, display and actuation technologies. Observing the structural changes that occur during a transition is vital to elucidating the mechanism of the phenomenon. From identifying small structural changes to allowing the effects of extreme conditions to be probed *in-situ*, synchrotron facilities have been invaluable in the understanding of spin crossover systems. However, the sensitivity of these materials to such a diverse range of perturbations means that high-flux X-ray sources may themselves impact upon the spin state of the material. This chapter provides an overview of insights gained through synchrotron diffraction studies on spin crossover materials as well as some perspectives of these challenging experiments.

10.04.1 Introduction

The ability to economically produce materials with increasingly useful properties is a defining factor in the pace of virtually all areas of technological innovation. As growth increases exponentially, the materials we rely on to construct and power the latest electronic and mechanical devices must become more efficient, more reliable and less expensive. While refining the properties of traditional materials can fulfil these requirements to a point, eventually we must seek new 'smart' materials that can push the fundamental boundaries beyond those of existing systems. Molecular-based spin crossover (SCO) materials that show switchable functionality are one of these promising classes of 'smart' material. They can react to a stimulus with a detectable response, existing in two (or more) physically different states that can be selected at will depending upon the application in hand. While development of these useful properties for technological application is a major driving force, it is of course necessary to understand the fundamental aspects of the SCO phenomenon. In this respect, synchrotron diffraction studies have played an important role in rationalizing the relationship between structure and properties and thus allowing the development of ever more useful switchable systems.

This chapter begins with an introduction to the theoretical aspects of the SCO phenomenon and its origins, before looking at the effect of the process on the structure and properties of materials. We then survey several of the important diffraction-based studies that have been conducted on SCO materials at synchrotrons, with particular emphasis on studies that were only possible thanks to the unique equipment and expertise found at such large-scale central facilities. While not intending to be an exhaustive overview of all diffraction studies of SCO materials conducted using synchrotron radiation, we hope it serves to highlight the existing possibilities. We conclude with some discussion of the perspectives for structural studies of SCO materials at synchrotrons.

 https://doi.org/10.1016/B978-0-12-823144-9.00159-X

10.04.1.1 Ligand-field theory and the origin of thermal spin-crossover

An isolated transition metal atom or ion in a spherical field contains five degenerate 3*d* orbitals: d_{xy}, d_{xz}, d_{yz}, $d_{x^2}-y^2$, and d_{z^2}. However, in an octahedral ligand field, this degeneracy is broken, resulting in two sub-sets of degenerate orbitals. The d_{xy}, d_{xz}, and d_{yz} orbitals (t_{2g} subset) are stabilized, and the $d_{x^2}-y^2$, and d_{z^2} orbitals, (e_g subset) are destabilized with respect to the barycenter. The difference in energy between the t_{2g} and e_g sets is known as the octahedral crystal field splitting energy, variously represented by 10Dq or Δ_{oct}. The t_{2g} sub-set are largely non-bonding, while the e_g sub-set are antibonding with respect to the metal-ligand (M-L) bond.

The magnitude of Δ_{oct} is dependent on the transition metal and its oxidation state, the chemical nature of the ligands and the coordination geometry. For a given transition metal with a known charge, Δ_{oct} can be tuned by the selection of ligands, which can be rationalized based on the spectrochemical series.[1] Weak-field ligands generate a small Δ_{oct}. Electrons fill orbitals singly according to Hund's rule due to the spin pairing energy (Π) associated with repulsion between two electrons occupying the same orbital. When the ligand field is weak, the spin pairing energy may be greater than the crystal field splitting, $\Pi > \Delta_{oct}$. Thus, electrons will singly occupy the orbitals in the higher energy e_g sub-set before spin pairing electrons in the same orbitals within the t_{2g} sub-set. This configuration maximizes the spin multiplicity and is referred to as the high-spin (HS) state. Conversely, in the presence of strong-field ligands, a large Δ_{oct} results. When $\Delta_{oct} > \Pi$, electrons spin pair within the t_{2g} set before occupying the higher energy e_g sub-set. This results in a configuration with the minimum spin multiplicity and is referred to as the low-spin (LS) state. For complexes in the HS state, more electrons occupy the antibonding orbitals within the e_g sub-set than is the case for complexes in the LS state. This results in a weakening, and therefore lengthening, of the M-L bonds in the HS state compared to those in the LS state.

At intermediate fields, it is possible to observe a thermally-induced SCO process, which can be rationalized by inspection of the diagram shown in Fig. 1, where the nuclear coordinate represents the M-L bond length, $r_{M\text{-}L}$.[2] The minimum of the potential well representing the HS state is displaced horizontally as a result if the increased M-L bond length as discussed previously. When the energy difference between the lowest vibronic levels of HS and LS states (ΔE°_{HL}) is sufficiently small (on the order of thermal energy, k_BT), it is possible to populate the HS state at elevated temperature due to entropic differences of both electronic and vibrational origin between the two states.[3] When thermal SCO is observed in a complex, it is often the case that pressure and light-induced transitions will also be observed.

A more thorough description of ligand field considerations as they relate to SCO materials can be found elsewhere.[3] It is important to note that the LS state remains the quantum mechanical ground state at all temperatures, but at elevated temperature the HS state becomes the thermodynamically stable state. During a SCO from LS to HS on warming, the ligand field increases significantly.

10.04.1.2 Structure and properties of SCO complexes

The difference in bond lengths between the LS and HS states, Δr_{HL}, is significant and varies depending on the metal and its charge as well as the chemistry and geometry of the ligand system. Diffraction techniques can be used to determine the spin state of a SCO material through analysis of bond lengths.[4] The volume of the ML_6 octahedron can also be used as an indicator of spin-state and, being a measure of several different M-L bonds, is often more robust to differences in ligand. Typical values of Δr_{HL} for d^6 Fe^{2+} complexes are of the order of 10% and corresponding changes in volume (ΔV_{HL}) are c.a. 25%.[5] Unit cell parameters are also sensitive to SCO processes, with reductions of between 2% and 10% in the volume of the unit cell (typically toward the smaller end) on transition from HS to LS state. However, it is important to note that highly anisotropic distortion of the structure in these typically

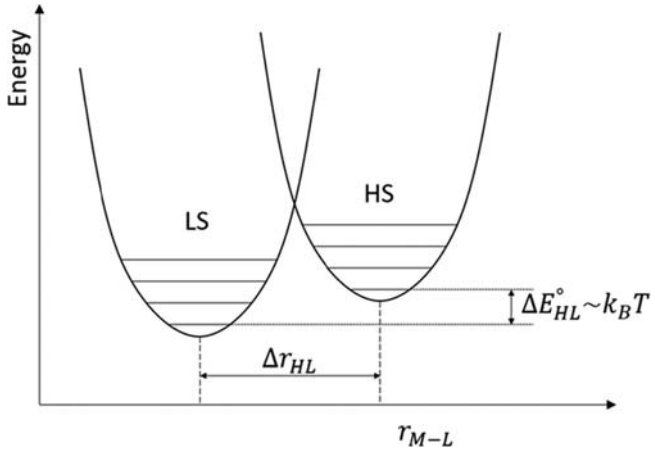

Fig. 1 Representation of the HS and LS potential wells for a SCO material. The nuclear coordinate is the M-L distance. Thermal SCO is possible when $\Delta E^{\circ}_{HL} \approx k_BT$.

low-symmetry systems is often observed, which can lead to significantly smaller changes in unit cell volume during SCO than that observed in individual unit cell parameters.[6]

Among the possible electronic configurations for the LS and HS states of d^4–d^7 first row transition metal complexes, six out of eight contain degenerate states, making them susceptible to Jahn-Teller distortions. Fe^{2+} (d^6) SCO complexes typically show the greatest change in distortion upon switching from the non-degenerate LS state to the degenerate HS state, not only due to the Jahn-Teller effect but also because they exhibit the largest change in bond lengths between the LS and HS states. Therefore, it is common for distortion parameters to be used in conjunction with bond lengths to confirm the spin-state of a material from structural measurements.[5] The Jahn-Teller effect is not the only source of distortion in SCO complexes. The nature and flexibility of the ligands can result in significant distortion from perfect octahedral symmetry, which can become even more significant when Jahn-Teller effects are also present. The choice of ligand system also impacts the way in which a Jahn-Teller distortion manifests and therefore it is most common and practical to compare distortions among SCO complexes that contain a similar set of ligands. The structural changes that occur during SCO are not only useful for determining the spin state, but have also shown potential for applications in actuator devices.[7,8]

The energy required to excite a complex from the ground state to an excited state is different depending on the spin state. The energy of these electronic transitions often falls within the visible region, and consequently, a color change is frequently observed in a sample undergoing SCO. In these cases, thermochromism can be a useful indicator for the presence of SCO, and curves can be plotted by following the color of the material as a function of the applied stimulus. Color change can also be a useful property to exploit for application, particularly in display and sensor devices.[9,10] However, in certain cases these color changes can be masked by charge-transfer transitions occurring in both spin states for certain combinations of metal ion and ligand.

During SCO, the number of unpaired electrons changes and hence these materials also show switchable magnetic properties. In the case of d^6 complexes such as the commonly studied Fe(II) ion, the HS state is paramagnetic while the LS state is diamagnetic, with a change in spin multiplicity, $\Delta S = 2$ upon SCO. Magnetic properties may be important for potential applications, but the type of application is dependent on the SCO material itself and the way it responds to a specific stimulus. Since the properties of SCO materials are related directly to structure, the structural characterization, analysis and understanding of structure-property relationships are imperative to have a chance at developing smart materials for specific applications.

10.04.1.3 Thermal SCO

Thermal SCO curves such as those shown in Fig. 2 are typically plotted using the mole fraction of complexes in the HS state (γ_{HS}) as a function of temperature.[2] From these results, the thermal equilibrium temperature ($T_{1/2}$) is extracted as the temperature where the ratio of LS/HS states is equal. The temperature range required to fully convert the SCO material from one spin state to another provides information as to how gradual or abrupt the transition is and therefore the extent of communication between active sites. SCO curves are frequently determined from magnetometry data, although they can also be calculated from structural parameters such as the ML_6 volume, or spectroscopic data.[11]

In solution, the SCO of an individual complex has no impact on the remaining complexes. However, in the solid-state, the proximity of neighboring SCO complexes is greatly increased, and numerous intermolecular interactions may be present between each complex. In such a case, changes in metal-ligand bond length and distortion of the complex during SCO can induce an internal pressure and elastic frustration within the lattice. This has an impact on complexes in close proximity to the switching center, but also can impact the spin state of complexes much further away in the crystal lattice. The degree to which the change in spin state of one complex affects those around it depend on crystal packing of the complexes and the strength of intermolecular interactions through which this elastic coupling is manifested. A high degree of cooperativity results in very abrupt transitions that can take place across a temperature interval of less than 1 K. Such materials may well have promising applications as barocaloric materials for solid-state cooling.[12] If the cooperativity is particularly high, the transition can also be accompanied by hysteresis, where the temperature of the transition on warming is higher than that on cooling, as shown in Fig. 2(a). The presence of this thermal hysteresis loop imparts a so-called *molecular memory* onto the material in so much as the spin state of the material will depend on its thermal history within the region of the hysteresis. This form of molecular bistability is less useful for solid-state cooling, but has raised the possibility of applications in memory storage devices, with each molecule capable of storing one binary digit with

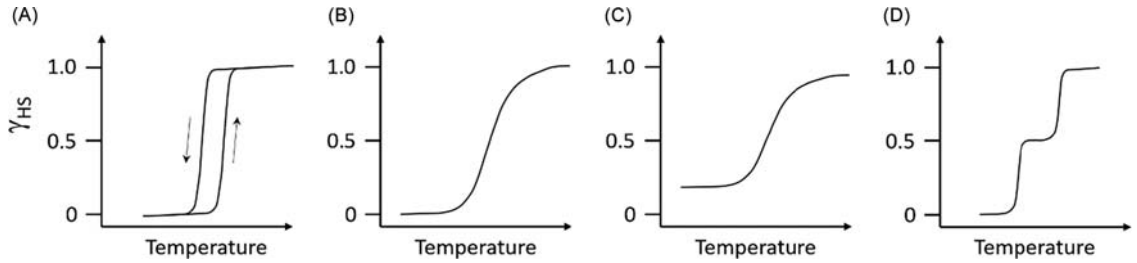

Fig. 2 Illustration of the variation of mole-fraction of the HS state (γ_{HS}) as a function of temperature during (a) an abrupt spin transition accompanied by hysteresis, (b) gradual, (c) incomplete and (d) stepped SCO.

the HS and LS states representing 0 and 1. However, the practicalities of manufacturing and addressing individual molecules while maintaining switching properties has meant that this potential application has yet to be realized.

Even in the solid-state, communication between SCO complexes can be relatively poor, resulting in little or no cooperativity. SCO materials that are weakly cooperative exhibit a gradual SCO that is dominated by thermal equilibrium and a slow change in the LS/HS ratio is observed (Fig. 2(b)). SCO materials with gradual transitions can usually be thermally cycled between spin states, in both heating and cooling modes, without causing a change in $T_{1/2}$. Therefore, SCO materials that show gradual transitions are particularly interesting for their potential in sensing applications.[13] In some materials the SCO process can be incomplete, with a residual HS component at low temperatures, as shown in Fig. 2(c). Stepped spin transitions have been observed, where a distinct plateau can be observed in the plot of γ_{HS} as a function of temperature (Fig. 2(d)). This will often be seen in materials with more than one crystallographically distinct SCO-active center, where each active site experiences slightly different packing effects and ligand field environments, leading to slightly different $T_{1/2}$ values at each site. Somewhat more counterintuitively, stepped SCO is also occasionally observed in materials that have a single unique SCO center, and the transition to the mixed spin intermediate phase (IP) is accompanied by symmetry breaking and long-range crystallographic ordering of HS and LS states.[14–16] Such materials increase the number of accessible states and thus see possible application as molecular logic gates.[17]

10.04.1.4 Pressure-induced SCO

The difference in volume between the HS and LS states, ΔV°_{HL}, results in a substantial pressure dependence of the spin state in SCO materials.[18] An increase in pressure destabilizes the larger HS state and so the LS state becomes favored as pressure increases, as shown in Fig. 3(a).[19] The difference in the zero-point energy between spin states, ΔE°_{HL}, decreases by $p\Delta V^{\circ}_{HL}$ when pressure is applied. The effect of pressure on a thermal spin transition can be approximated using the Clausius-Clapyron equation, which predicts a linear shift of the transition temperature, $T_{1/2}$ by up to 200 K GPa^{-1}. While there are many exceptions, it is common for relatively small applied pressures to cause a significant increase in $T_{1/2}$.[18]

10.04.1.5 Light-induced excited spin state trapping (LIESST)

It has been discussed that the LS state is the thermodynamic ground state for SCO materials at temperatures below $T_{1/2}$. It is however possible (for certain SCO systems) to populate a metastable high spin state at these temperatures using light irradiation, both in solution and the solid state.[20–23] This photoexcitation process proceeds through population of high-energy MLCT states and a series of rapid intersystem crossing events, which results in population of the HS state. At ambient temperatures, these metastable states have short lifetimes (sub-microsecond) as the energy barrier to HS → LS relaxation is thermally accessible. At lower temperatures, this is not the case, and relaxation takes place via a tunneling process, which can be very slow.[24] The result is to effectively trap the material in a metastable HS state with virtually infinite lifetimes at low temperatures. This process is known as light-induced excited spin state trapping (LIESST) and is illustrated in Fig. 4. On warming the material in the meta-stable HS state, relaxation back to the LS ground state occurs at a temperature known as T_{LIESST}, as shown in Fig. 4. Light-induced return to the LS ground state is also possible via a related mechanism using a different irradiation wavelength; this process is known as reverse-LIESST.

10.04.1.6 Types of SCO complex

There are many reported SCO-active materials, and they can be categorized in a variety of ways. Spin transitions are found in nature, including in the functioning of several haem derivatives and a number of geologically relevant materials.[25] While these systems are fascinating in their own right, we restrict the conversation here to synthetic, molecular-based materials developed since Cambi's work on such systems in the 1930s.[26] In this final introductory section, we describe some of the most commonly encountered materials that have been studied in detail at synchrotron facilities. We categorize them into discrete mononuclear complexes, multinuclear complexes and framework materials. A list of the complexes we describe in this chapter is given in Table 1.

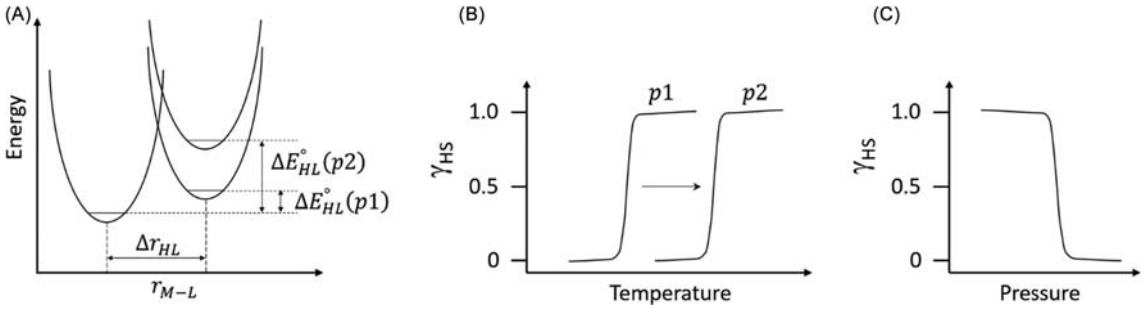

Fig. 3 Representation of the effect of pressure (p2 > p1) on (a) the HS and LS potential wells for a SCO material and (b) the temperature of the thermal spin transition. (c) Isothermal SCO curve illustrating variation of γ_{HS} as a function of pressure.

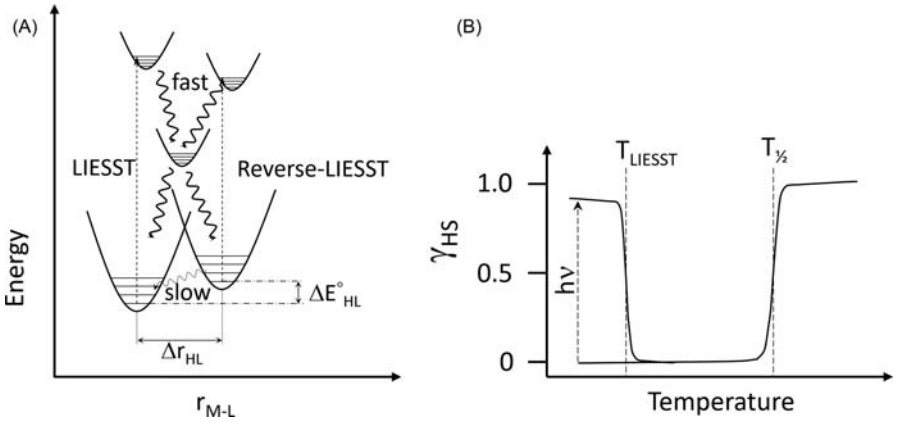

Fig. 4 (a) Schematic illustration of the LIESST and reverse-LIESST processes. Intersystem crossing and other relaxation processes are rapid. At very low temperatures quantum tunneling from the HS to the LS state is very slow, resulting in a trapping of the metastable HS state. (b) SCO curve including the LIESST effect and subsequent relaxation at the temperature, T_{LIESST}.

The most common type of spin crossover materials are mononuclear coordination complexes of Fe^{II}, although there are also many examples of other SCO-active ions. In the case of Fe^{II}, the appropriate ligand field for SCO is most often imparted by a N_6 coordination sphere, although some exceptions are known.[26] The variety in SCO behavior observed in different complexes is dictated not only by the ligand field exerted by the ligand set, but is also heavily influenced by the intermolecular interactions in the crystal structure. This is most clearly demonstrated by the fact that different polymorphs of the same SCO complex often show dramatically different types of SCO behavior.[67] Therefore, structural analysis from diffraction methods is essential in understanding how the SCO behavior is influenced by crystal packing effects. Through detailed and extensive structural analysis of many molecular SCO complexes and the supramolecular interactions that hold them together, it is hoped that it may one day be possible to design SCO materials with a given behavior using a crystal engineering approach.

Using ligands which are capable of bridging between metal centers can result in the formation of 1-dimensional chains, otherwise known as coordination polymers. The most commonly studied class of coordination polymer is the $[Fe^{II}(R\text{-trz})_3]A_2$ family of compounds (where R-trz = 4-substituted, 1,2,4-triazole, A = monovalent anion).[68] In these materials, chains are constructed through iron atoms triply bridged by triazole ligands. A huge variety of substituents have been introduced at the 4-position to tune the physical, chemical and SCO properties of these systems. Several materials in this family have high temperature spin transitions accompanied by wide hysteresis, and so there is particular emphasis on development of these systems for application.[68,69] Hofmann-type frameworks typically consist of 2-dimensional layers made up of square planar or near-linear metallo-ligands which bind the SCO metal centers such as Fe(II) equatorially through CN groups. In the axial positions of the ML_6 SCO octahedron, the nature of the ligand can determine whether the material will be a 2-D layered structure or a 3-D pillared structure if bridging axial ligands are used.[70] 2-D and 3-D Hoffman-type structures along with other types of metal-organic frameworks (MOFs) have the potential for guest-responsive SCO behavior.[71] Additionally, multi-dimensional structures can exhibit very interesting spin-crossover behavior due to presence of distinct metal centers. This can result in multi-step SCO which is desirable for memory storage applications. In-depth structural analysis is extremely important in understanding these complex processes as diffraction measurements allow for the determination of spin-state for the distinct metal centers and the order in which they undergo spin transitions.

10.04.2 Synchrotron diffraction studies of SCO materials

Complex analyses such as time-resolved diffraction and high-pressure measurements are carried out at synchrotron facilities due to the availability of equipment for generating complex sample environments and, crucially, the expertise to facilitate such experiments. But often synchrotron facilities are necessary for single-crystal and powder diffraction analysis, without complex experimental setups. This is the case when only small or weakly diffracting crystals can be grown[72] or when the need for multiple datasets (often as a function of temperature) demands rapid data collection. Some SCO materials are very difficult to grow suitable single crystals of at all and so synchrotron powder X-ray diffraction (PXRD) data can be used for structure solution.[73] Framework materials with significant void space and solvent content often require high flux X-ray sources to obtain suitable resolution for structure solution. Furthermore, due to the significant strain involved during cooperative spin transitions it is not uncommon for crystal quality to decay[74] to the extent that single-crystal data collection is impossible in a typical laboratory setting. In the next two sections we will discuss examples of structural studies of mononuclear and larger polynuclear SCO materials without complex sample environments using synchrotron radiation. We will then move on to discussing more elaborate experiments in subsequent sections.

Table 1 List of complexes discussed in this chapter and associated references.

Complex	*Number in Text*	*References*
$[Fe(5\text{-}Me\text{-}bpp)_2][BF_4]_2$ 5-Me-bpp = 2,6-*bis*-[5-methyl-1*H*-pyrazol-3-yl]pyridine	**1**	27
$[Fe(qsal\text{-}F)_2]NCS$ Hqsal-F = 5-F-N-quinolylsalicylaldimine	**2**	28
$[Fe(pybzim)_3](ClO_4)_2 \cdot H_2O$ pybzim = 2-(2′-pyridyl)benzimidazole	**3**	29
$[Fe(pic)_3]Cl_2$ pic = 2-picolylamine	**4**	30,31
$[Fe(ptp)_2](ClO_4)_2$ Hptp = (2-(pyrazol-1-yl)-6-(1H-tetrazol-5-yl)pyridine)	**5**	32
$[Fe^{III}(H\text{-}5\text{-}Br\text{-}thsa\text{-}Me)(5\text{-}Br\text{-}thsa\text{-}Me)] \cdot H_2O$ thsa = 5-bromosalicylaldehyde methylthiosemicarbazone	**6**	33
$[Fe(tame)_2]Br_2 \cdot MeOH$ tame = 1,1,1-tris(aminomethyl)ethane	**7**	34
$[Fe_4L_4](BF_4)_8 \cdot n(solvent)$ L = 1,3,5-tris(4-(1-methyl-2-imidazolecarboxaldehyde) phenyl)-benzene	**8**	35
$[Fe_4L_6](BF_4)_8$ L = ((E,E)- N,N′-([1,1′-biphenyl]-4,4′-diyl)bis[1-(1,3-thiazol-4-yl)methanimine])	**9**	36
$[Fe_8L_6] \cdot A \cdot Solvent$ L = hexakis(μ-5,10,15,20-tetrakis(4-(imidazol-4-y-lmethyleneamino)phenyl)porphyrin)	**10**	37
$[Fe(tbenpy)\{Au(CN)_2\}_2]\{2H_2O, DMF\}$ tbenpy = N1,N3,N5-tri(pyridin-4-yl)benzene-1,3,5-tricarboxamide	**11**	38
$[Fe(dpsme)Pt(CN)4] \cdot 2/3dpsme \cdot EtOH \cdot H2O$ dpsme = 4,4′-di(pyridylthio)methane	**12**	39
$[Fe(NCS)_2(bped)_2] \cdot 3EtOH$ bped = DL-1,2-bis(4′-pyridyl)-1,2-ethanediol	**13**	40
$[Fe(proptrz)_2M(CN)_4] \cdot 2H_2O$ proptrz = (E)-3-phenyl-N-(4H-1,2,4-triazol-4-yl)prop-2-yn-1-imine	**14**	41
$[Fe(dpyu)\{Pt(CN)_4\}] \cdot 9H_2O$ dpyu = 1,3-di(pyridin-4-yl)urea	**15**	42
$[Fe(NCS)_2(bpbd)_2]$ bpbd = 2,3-bis(4′-pyridyl)-2,3-butanediol	**16**	43
$[Fe(btzx)_3](ClO_4)_2$ btzx = 1,4-bis(tetrazol1-ylmethyl)benzene	**17**	44
$[Fe(pz)Pt(CN)_4]$ pz = pyrazine	**18**	45,46
$[Fe(phen)_2(NCSe)_2]$ Phen = 1,10-phenanthroline	**19**	47
trans-$[Fe(tzpy)_2(NCS)_2]$ tzpy = 3-(2-pyridyl)[1,2,3]triazolo[1,5-*a*]pyridine	**20**	48
$[Fe(n\text{-}Bu\text{-}im)_3(tren)](PF_6)_2$ (n-Bu-im)$_3$(tren) = n- butylimidazoltris(2-ethylamino) amine	**21**	49
$[Fe(tpa)(tcc)]PF_6$ tpa = tris(2-pyridylmethyl)amine; tcc = 3,4,5,6-tetrachlorocatecholate	**22**	50–53
$[Fe(H_4L)_2](ClO_4)_2 \cdot H_2O \cdot 2(CH_3)_2CO$ H_4L = 2,6-bis(5-(2-hydroxyphenyl)pyrazol-3-yl) pyridine	**23**	54
$[Fe(teec)_6](ClO_4)_2$ or $[Fe(teec)_6](BF_4)_2$ teec = chloroethyltetrazole	**24**	55,56
$[Fe(phen)_2(NCS)_2]$ phen = 1,10-phenanthroline	**25**	57

(Continued)

Table 1 List of complexes discussed in this chapter and associated references.—cont'd

Complex	*Number in Text*	*References*
$[Co(diox)_2(4\text{-CN-py})_2]\cdot$benzene diox = 3,5-di-t-butylsemiquinonate; 4-CN-py = 4-cyanopyridine	**25**	58,59
$Fe(btr)_2(NCS)_2\bullet H_2O$ btr = 4,4′-1,2,4- triazole	**27**	60
$[Fe^{II}(bapbpy)(NCS)_2]$ bapbpy = 6,6′-bis(2-aminopyridyl)-2,2′-bipyridine	**28**	15
$[\{Fe(bpp)(NCS)_2\}_2(4,4'\text{-bipy})]\bullet 2MeOH$ bpp = 2,6-bis(pyrazol-3-yl)pyridine; 4,4′-bipy = 4,4′-bipyridine	**29**	61
$[Fe(L)_2]2ClO_4$ L = 2,6-bis{3-methylpyrazol-1-yl}pyrazine	**30**	62
$[Fe^{II}(HB(tz)_3)_2]$ tz = 1,2,4-triazol-1-yl	**31**	63
[Fe(PM-PeA)$(NCSe)_2$] PM-PeA = N-(2′-pyridylmethylene)-4-(phenylethynyl) aniline	**32**	64
$[Fe(Htrz)_2(trz)](BF_4)$ trz = 1,2,4-triazole	**33**	65,66

10.04.2.1 Mononuclear SCO materials

Pask et al. used synchrotron data in the study of $[Fe(5\text{-Me-bpp})_2][BF_4]_2$ (**1**), which undergoes a spin transition with a relatively wide thermal hysteresis loop of 65 K. During the study they also synthesized and performed structural analysis of the Zn(II) and Cu(II) analogues, which are not SCO active.[27] Variable temperature synchrotron powder XRD was carried out on the materials investigated and allowed a complex series of phase transitions to be unraveled. The implications of these phase transitions on the SCO properties were elucidated from this detailed crystallographic study. Phonsri et al. reported $[Fe(qsal\text{-}X)_2]$NCS complexes (**2**) which were found to display stepped SCO behavior through magnetic measurements.[28] Single crystal diffraction measurements at a synchrotron facility revealed that two distinct Fe(III) centers are present within the crystal structure, one of which undergoes SCO before the other, resulting in the stepped SCO behavior. Members of the same group have successfully used synchrotron studies to investigate a number of interesting structural effects in Fe(III) SCO materials including the effect of crystallite size[75] and chemical modifications to the ligands.[76] The use of synchrotron facilities in these cases was vital due to weak diffraction from the small crystals obtained from synthesis.

Boča et al.[29] used of a range of techniques to obtain various thermodynamic and SCO related parameters for $[Fe(pybzim)_3](ClO_4)_2\cdot H_2O$ (**3**). One of the techniques involved monitoring the unit cell parameters of the structure at temperatures within the range of 50–250 K via powder diffraction. The crystal structure is triclinic and required the use of synchrotron radiation to obtain data of sufficient resolution across the temperature range to allow unit cell refinement. The SCO curves obtained from magnetic susceptibility measurements and synchrotron PXRD unit cell analyses were very comparable and identical $T_{1/2}$ values were obtained. Variable temperature synchrotron PXRD analysis was able to provide high-quality, high-resolution data that would have taken much longer to collect using home-lab PXRD diffractometers.

Solvated SCO materials are particularly interesting for investigating the role of intermolecular interactions on cooperativity. Investigation of a series of solvates allows small and systematic changes to the structure and properties of the material without altering the coordination environment around the metal center. Upon desolvation of single crystals, it is very common for the SCO properties to change substantially, and the desolvation process is frequently accompanied by deterioration in crystal quality such that powder diffraction is required. Hostettler et al.[30] synthesized a total of six alcohol solvates of $[Fe(pic)_3]Cl_2$ (**4**) to compare with the stepped transition shown by the ethanol solvate. By keeping the functional group of the molecules of solvation the same, it was expected that the resulting structures would be similar and have related SCO properties. The structures were in fact found to be either isostructural or polytypic, but the SCO properties varied significantly where abrupt, gradual, stepped, hysteretic SCO and a complete lack of SCO were all observed. Additionally, the structures varied in the crystallographic phase transitions that occurred upon cooling. While these results highlighted the difficulty of crystal engineering SCO materials with predictable properties through varying the solvent, they also demonstrate the need for in-depth variable temperature single crystal XRD measurements to begin to understand systems such as these. Synchrotron facilities provide an ideal platform to rapidly improve understanding in this area through rapid data collection of multiple comparable materials at a wider range of temperatures. Another case in which synchrotron structural data allowed vital insight into complex SCO behavior is the highly unusual case of $[Fe(ptp)_2](ClO_4)_2$ (**5**), which shows four very different SCO behaviors from the same material.[32] A series of single-crystal-to-single-crystal phase transitions follows

a solvent-loss process, allowing access to distinct SCO properties depending on the thermal history of the sample. The entire process can be followed using one unique crystal measured at multiple temperatures over several sequential thermal cycles.

As well as allowing for the collection of a greater number of datasets within a temperature range of interest on small crystals, the increased flux available at a synchrotron when compared to a typical laboratory X-ray source can reveal unexpected and very significant structural details that have a direct impact on the SCO behavior. This was clearly demonstrated in the case of the ethanol solvate of **4**,[31] which has a stepped SCO on cooling. It was long believed to be an example of a two-step SCO that did not show long-range ordering of HS and LS sites around the temperature in which the IP was observed. However, closer investigation of the diffraction pattern using synchrotron radiation showed the appearance and subsequent disappearance of weak supercell reflections as the crystal was cooled through the transition. Between 124 and 114 K, these supercell reflections revealed a unit cell doubling and resultant ordering of HS and LS sites within the crystal.[31] Symmetry-breaking phase transitions are not uncommon in SCO materials,[16] and thus the ability to observe weak supercell reflections as well as diffuse scatter (characteristic of shorter-range ordering) using high-flux sources is paramount to understanding the mechanisms of SCO in different materials. Later, Li et al.[33] synthesized a mononuclear Fe(III) SCO complex (**6**) that exhibited a hysteretic three-step SCO transition with multistability. Four unique states were identified as *I*: HS, *II*: 4HS:2LS, *III*: 2HS:4LS and *IV*: LS. Synchrotron based single-crystal X-ray diffraction (SCXRD) was used to probe the structures of each of the unique states by allowing the supercell reflections resulting from symmetry breaking to be observed.

The high flux X-ray beams available at synchrotrons vastly speed up data collection and can allow full SCO curves to be obtained based on structural information such as octahedral volumes, in a fraction of the time it would take in a laboratory setting. The increased speed is important when many temperature points are desired across a large temperature range. Ideally all measurements should be done sequentially without interruption as the thermal history of each crystal impacts its structure and properties. If small structural details are to be interpreted appropriately it is desirable to collect data on one high quality crystal across the entire temperature range. The high flux of a synchrotron source then becomes something of a problem if it causes sample damage to get worse over time. Chernyshov et al. recently investigated the effect of radiation damage on the SCO material $[Fe(tame)_2]Br_2 \cdot MeOH$ (**7**).[34] They showed that radiation damage accumulated progressively with increasing time and sample temperature. The result was an anisotropic expansion of the unit cell as dose increases, overwhelming the expected volume decrease expected during the HS → LS transition. The transition becomes more gradual and, using the same rationale that explains why increased pressures favor the LS state, the increase in cell volume is likely to favor the HS state. These preliminary results show clearly that while the use of synchrotrons can be a boon to many studies of SCO materials, the X-ray beam used to probe the material cannot necessarily be assumed entirely innocent. The use of multiple complimentary techniques in investigating SCO properties should allow the identification of these problems if and when they arise.[34]

10.04.2.2 Multinuclear SCO complexes and frameworks

One strategy to try to improve cooperativity in SCO materials is to link them together covalently into complexes with more than one SCO-active metal center.[70] From multinuclear complexes with a discrete number of different SCO sites in the same complex[77,78] to metal-organic frameworks (MOFs) with an effectively infinite 3D connectivity of many metal centers, this strategy has seen successes in creating cooperative SCO behavior.[71]

SCO cages are very interesting due to the delicate interplay between metal centers within the cages and the potential for ions or other guests to exist in the cavities and influence properties. Structural studies of macromolecular and MOF spin-crossover materials are often difficult due to the poor crystal quality and stability. This is particularly the case for structures that are held together or supported by the presence of solvent molecules. Li et al.[35] reported the synthesis and characterization of a large tetrahedral cage, **8**, Fig. 5(a), where the crystals suffered from rapid solvent loss. Even with the use of synchrotron radiation and after attempting many crystals, a resolution of 0.9 Å was achievable. The studies revealed that three crystallographically distinct cages were present in the structure, two of which contained one SCO active Fe^{II} center and three Fe^{II} centers in the HS state. The third cage contained three SCO active Fe centers and one Fe center in the HS state. It is likely that the SCO of one Fe center within each cage directly impacts on the ability of the other iron sites to undergo SCO due to steric and distortion effects. This also correlates well with the gradual and incomplete nature of the SCO curve obtained from thorough magnetic measurements. The structural studies also revealed that nothing was present within the central cavity of these cages. Having structural information such as this allows for informed design of new SCO cage systems.

Members of the same team later reported the synthesis and characterization of a different tetrahedral cage (**9**) Fig. 5(b), which showed gradual, incomplete SCO with hysteresis.[36] The crystal structure of this material was also very challenging to obtain, and a resolution of only 1.2 Å could be obtained at the synchrotron. The structure revealed that a BF_4^- anion was present within the cage cavity, and the potential for encapsulating other anions within SCO cages holds interesting possibilities. Again, the use of synchrotron radiation in the diffraction experiment allowed the structure of the cage to be obtained, where bond length and distortion analysis was used to determine which Fe centers participate in SCO. Struch et al. used a subcomponent self-assembly approach to design an octanuclear SCO cage complex (**10**) (Fig. 5(c)) that undergoes SCO in solution.[37] The crystals of the material were very susceptible to rapid solvent loss and a resolution of only 1.3 Å could be achieved using synchrotron radiation. However, the data quality was sufficient to verify the structure of the material and to confirm the large void space within the cage that explains the host-guest properties observed in the material.

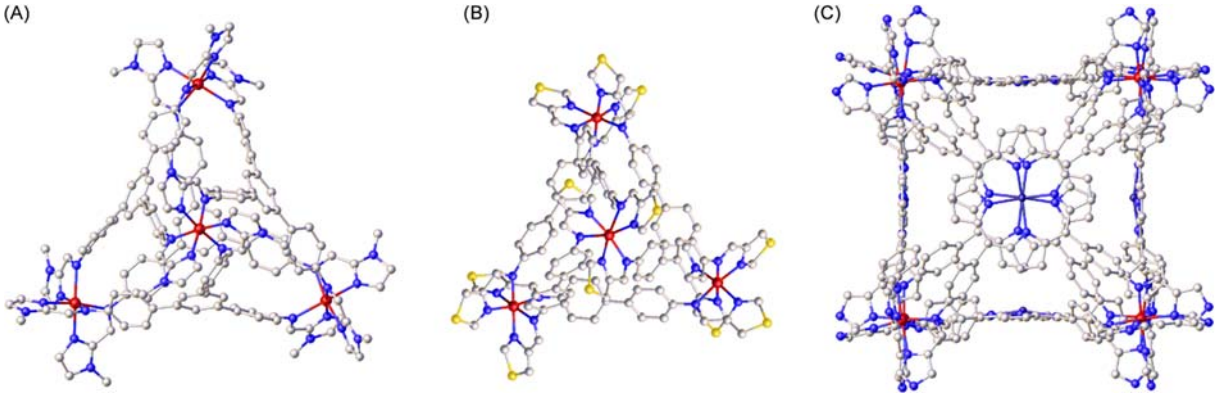

Fig. 5 Structures of SCO supramolecular cage structures (a) **8**,[35] (b) **9**,[36] and (c) **10**.[37] Color key: red—iron, blue—nitrogen, gray—carbon, yellow—Sulfur, purple—zinc. Anions, guest molecules and hydrogen atoms have been removed for clarity.

Variable temperature SCXRD is a powerful tool for understanding how the structures of SCO materials change during a transition and this information can lead to important structure-property relationships. This is particularly useful when characterizing new types of SCO materials and coordination environments. Ahmed et al.[38] recently used variable temperature synchrotron single crystal and powder diffraction studies to obtain structural information on a novel 3D Hoffman-type material (**11**) with a coordination environment of $Fe^{II}(py)_3(N \equiv C\cdots)_3$. In 3D Hoffman-type materials, the 2D layers are typically held together by organic 'pillar' ligands, however, this material showed that metallo-ligands like $[Au(CN)_2]^-$ can also act as 'pillars.' While this particular material did not show stepped SCO, Sciortino et al. reported a 3D pillared Hoffman-type MOF (**12**) which exhibits a three-step SCO with abrupt transitions and hysteresis (**Fig. 6**).[39] Variable temperature PXRD using synchrotron diffraction confirmed that the MOF remained as a single phase throughout the entire temperature range of the SCO. Furthermore, shifts in Bragg peaks occurred consistent with the transition temperatures determined through magnetic measurements and thermal hysteresis was also seen in the structure analysis. On cooling, the MOF undergoes a transition from a fully HS state to a 50:50 LS:HS state IP which involves a change in symmetry from monoclinic *P2/a* to triclinic $P\bar{1}$. This could be seen at low angles in the PXRD patterns as modulation peaks, which appear due to the Fe^{II} centers becoming inequivalent upon SCO. An additional structural change occurs upon further cooling of the material due to SCO from 50:50 LS:HS to a 75:25 LS:HS state. Despite the high resolution and low noise of data obtained through synchrotron diffraction, modulation peaks were not observed for the 75:25 LS:HS state in the PXRD data. Instead, some weak supercell reflections were found during SCXRD measurements at 130 K, which allowed the 75:25 LS:HS state to be modeled with three unique Fe^{II} centers are present in the structure. The final transition from the 75:25 LS:HS state to the fully LS state, resulted in the reemergence of monoclinic *P2/a* symmetry and the equivalence of all Fe^{II} centers restored.

The presence of guest molecules within MOF SCO materials can impact the SCO behavior significantly and there are several different ways in which the guests can be manipulated. For example, MOFs often grow with solvent molecules present within the pores and a change in SCO behavior can be observed upon solvent removal. While the quality of the crystal structure can diminish when the solvent leaves the structure, some materials do remain stable upon guest removal and allow for different guests

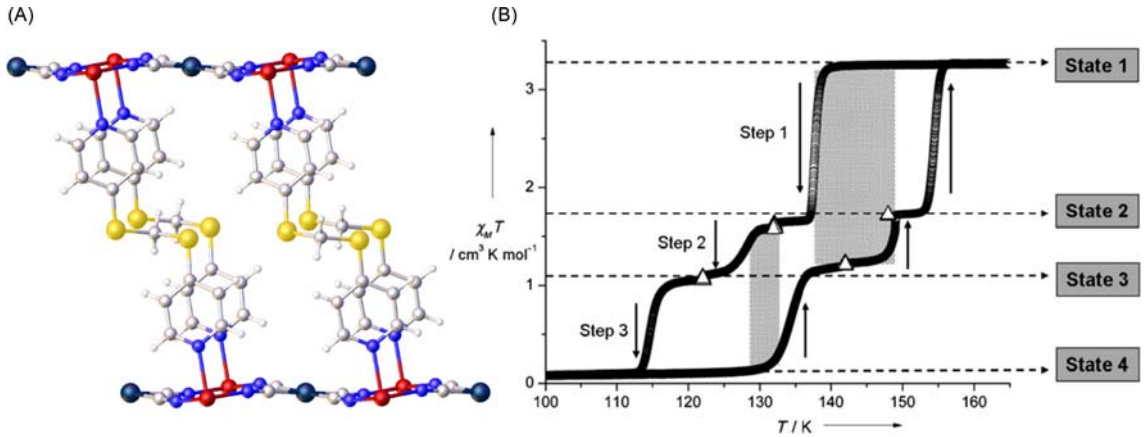

Fig. 6 (a) Structure of Hoffman-type SCO materials **12** and (b) magnetic properties of **12** as a function of temperature. Reproduced from Sciortino, N. F.; Scherl-Gruenwald, K. R.; Chastanet, G.; Halder, G. J.; Chapman, K. W.; Létard, J.-F.; Kepert, C. J. Hysteretic Three-Step Spin Crossover in a Thermo- and Photochromic 3D Pillared Hofmann-Type Metal-Organic Framework. *Angew. Chem.* **2012**, *124* (40), 10301–10305. doi:10.1002/ange.201204387.

to be introduced into the structure. Furthermore, some MOFs may have smaller pores which can accommodate gaseous guest molecules. Neville et al.[40] synthesized a porous SCO active interpenetrated MOF material (**13**) where ethanol molecules were present within the pores as determined by SCXRD. The desolvation of the framework was studied to understand its impact on the SCO properties and the structure of the material. Variable temperature SCXRD studies found that a single-crystal-to-single-crystal transformation occurs on the loss of ethanol from the pores, resulting in an increase in symmetry from orthorhombic *Pccn* to tetragonal *I*4/*mcm*. While SCXRD is useful to determine the overall symmetry of the material, variable temperature PXRD measurements using synchrotron diffraction were used to further study the overall crystallinity of the structure during the transition as well as investigating the structural transition further. These measurements provided a much more detailed look at the overall transition, allowing the emergence and increase of the tetragonal phase to be observed along with the decrease and disappearance of the orthorhombic phase across the temperature range. The variable temperature PXRD measurements also allowed the SCO of the solvated and desolvated structures to be analyzed. While the SCO behavior for this material was gradual, this analysis can be useful to follow unit cell parameters and determine how the SCO may propagate within the structure. Overall, for this material, the unit cell parameters changed gradually with temperature and no hysteresis was found to be present upon cycling of the temperature range. Furthermore, the loss of solvent was found to result in a decrease in cooperativity, likely due to decreased distortion of the Fe^{II} centers upon removal of ethanol.

The effect of the solvent within a MOF on the SCO behavior is unique to each material. This is evidenced when comparing the previous MOF, **13**, which loses cooperativity upon solvent loss, to the 2D Hoffman-type material reported by Zenere et al.[41], **14**, which exhibits improved cooperativity and more complete SCO upon guest removal. These 2D layered structures contain Hoffman-type layers using Pd or Pt equatorial metallo-ligands, with long ligands in the axial positions, which hold the 2D layers together through π–π stacking interactions. However, within the 2D layers, water molecules are present and participate in hydrogen bonding with the axial ligands. Analysis of the structure revealed that incomplete SCO occurred, resulting in a 50:50 LS:HS state. Structural analysis through SCXRD showed that loss of distortion due to HS $\rightarrow$ LS SCO in one Fe^{II} center, resulted in increased distortion of the adjacent Fe^{II} center, inhibiting it from undergoing a SCO. Investigation of the loss of water from the materials was difficult due to a large decrease in crystallinity upon dehydration, making SCXRD analysis impossible. Variable temperature PXRD analysis was instead used to study the dehydration of the materials. Despite the use of synchrotron radiation, the patterns of the dehydrated materials were poor quality due to broad peaks and peak overlap. However, the LS state of the dehydrated material containing Pd-based metallo-ligands was suitable for Rietveld refinement and revealed that the overall layered Hoffman-type structure remains intact upon dehydration. While the refinement was limited due to the data quality, the structural model indicates that improved interaction occurs between the axial ligands upon removal of the water molecules. This enhanced communication within the structure resulted in more cooperative SCO behavior where complete conversion to the LS state occurs abruptly and with hysteresis. The use of synchrotron-based diffraction in this study was absolutely vital in obtaining a structural model of the dehydrated material. These studies demonstrate how the presence of solvent molecules can frustrate the communication within MOFs and in-particular 2D Hoffman-type layered structures.

The impact of hydration and dehydration on SCO behavior was also studied by Mondal et al.[42] for a 3D Hoffman-type MOF structure, **15**. The 2D Hoffman-type layers were bridged by ligands that contain a urea functional group, which has a propensity to form hydrogen bonds, both as a donor and an acceptor. The as-synthesized MOF structure contains nine water molecules, where SCXRD studies showed that one water molecule participates in hydrogen bonding between the urea functional groups and the remaining eight water molecules remained unresolved in lattice void space. Similar to **14**,[41] the hydrated structure of **15** undergoes an incomplete SCO transition with small hysteresis, where complete SCO is likely inhibited partly due to interruption of host-host interactions by the hydrogen bonding water molecules. Unfortunately, upon dehydration, the crystallinity of the structure decreased such that even with synchrotron PXRD measurements, Rietveld refinement was not possible and structural information could not be obtained. Dehydration resulted in a two-step incomplete SCO where 33% of the Fe^{II} centers remain in the HS state, with $T_{1/2}$ shifting significantly to higher temperatures. Again, this is similar to **14** where the loss of water molecules resulted in improved lattice communication through uninterrupted host-host intermolecular interactions.[41] Variable temperature synchrotron PXRD was used by Mondal et al.[42] to further investigate the structural changes that occur in **15** during the transition. Their results showed that the material remains as a single-phase throughout the SCO temperature range studied and shifts in Bragg peaks were present, in-line with the transition temperatures determined through magnetic measurements. Rehydration of the material was also found to be possible and was confirmed using PXRD. Furthermore, the magnetic behavior of the material also reverted to that of the hydrated phase, showing reversibility through hydration and dehydration. These properties are very desirable for potential applications in sensing. The use of synchrotron PXRD does not always guarantee that structure solution will be possible, but for these materials and future iterations of these materials, it will be essential for understanding the magneto-structural properties during desolation and solvation, especially given the tendency for crystallinity to diminish upon solvent loss.

Synchrotron facilities are well equipped for investigations involving solvation and desolvation as demonstrated by the studies from Neville et al.[43] They reported the synthesis of a SCO MOF (**16**) that remains stable upon desolvation due to its rigid structure. This allowed for the removal of a solvent and subsequent re-solvation with a different solvent to analyze the effects on SCO behavior. SCXRD analysis on a home diffractometer was carried out on the various 'as-synthesized' solvates and 're-solvated' crystals. The solvents used varied from the aprotic solvents acetone and acetonitrile to the protic solvents methanol, ethanol and 1-propanol. Magnetic measurements of the solvates revealed a range of SCO behaviors and transition temperatures from gradual SCO for the aprotic solvates to more abrupt SCO with the protic solvates. The methanol and ethanol solvates even showed some hysteretic behavior and therefore these structures were studied in more detail to elucidate a possible cause for hysteresis.

SCXRD analysis of the different solvates showed that the structures were in the tetragonal *P*4/*ncc* space group, even at lower temperatures of 100 K for the methanol and ethanol solvates where they are in the LS state. However, PXRD analysis using synchrotron radiation was able to find that the symmetry for the LS methanol and ethanol solvates was in fact orthorhombic *Pccn*. Finding this subtle difference through the use of synchrotron diffraction was extremely important for understanding the structure-property relationships for these solvates. Knowing the correct space group, the SCXRD data at 100 K for these solvates were reprocessed, resulting in improved refinement of the crystal structures. Not only did the synchrotron PXRD allow the subtle phase transition to be observed, but it was also able to find that it occurs approximately 40 K above the SCO transition. Upon modeling the structures in the correct orthorhombic space group, it was found that the shape of the porous channels of the methanol and ethanol solvates changes during the HS → LS transition. These structural changes are likely the cause of the hysteresis observed in the SCO behavior for these solvates.

It is also particularly important to highlight the techniques that were used for the powder diffraction measurements in this study of **16**, as it demonstrates the complex experimental setups possible at synchrotron facilities. Starting with the methanol solvate, variable temperature PXRD measurements were conducted between 260 K → 90 K → 260 K, followed by heating to 375 K to allow for desolvation to occur. The next solvate was produced by using a stream of ethanol vapor while cooling down to 90 K, where again data were collected between 260 K → 90 K → 260 K. This process was repeated until all of the solvated structures had been analyzed by introducing the corresponding solvent vapor onto the powder. Synchrotron-based experimental setups such as this that allow for fast and efficient measurements of a variety of structures are invaluable to elucidating complex structure-property correlations in porous SCO materials.

Not all MOFs are porous however and can therefore crystallize without forming a solvate. Coronado et al.[44] synthesized a *co*-ordination polymer, **17**, in which adjacent metal centers were bridged via three ligands rather than a single rigid ligand typically used in the Hofmann-type MOFs described above. This resulted in 1-D cylinder-like MOF chains which crystallize in a close-packing arrangement, leading to a structure that contains void spaces between bridging ligands but no permanent channels. While such MOF structures may not be able to adsorb solvents, gaseous guests are significantly smaller and can still impact the SCO behavior of a material. During the study, gas adsorption studies were performed on the material using CO_2 and N_2 as the gases, both individually and as a mixture. They found that CO_2 was selectively adsorbed into the structure with a high uptake of 0.9 CO_2 molecules per void. Magnetic measurements showed that the adsorption of CO_2 resulted in a very similar SCO profile but with an increase in the transition temperature of around 9 K, as shown in **Fig. 7**(a). To rationalize the change in SCO transition temperature but similar behavior, variable temperature synchrotron PXRD studies were undertaken.[44] Rietveld refinement was conducted, modeling CO_2 molecules within the void created by the bridging ligands (**Fig. 7**(b)) and compared to refinements excluding these guests. These refinements show that by obtaining good quality data through synchrotron diffraction, various models can be tested to ensure that an appropriate model and interpretation are reached.

From the structure obtained for the material with adsorbed CO_2, it could be seen that the CO_2 molecules participate in O═C═O═$^{\delta-}\cdots\pi$ interactions. This interaction can be used to rationalize the slightly increased SCO transition temperature as it results in increased electron density within the ligand and therefore increased strength of the Fe-N bonds. Without the use of synchrotron diffraction, these important pieces of information would likely remain undiscovered. It is important to understand the role of any guest on the magneto-structural properties of a material and the equipment at synchrotron facilities make such measurements a lot quicker and easier to carry out. While gases may result in more subtle changes to the SCO properties of a material due to weaker interactions with the host, these studies can help us to further understand the factors affecting switching behavior. Furthermore,

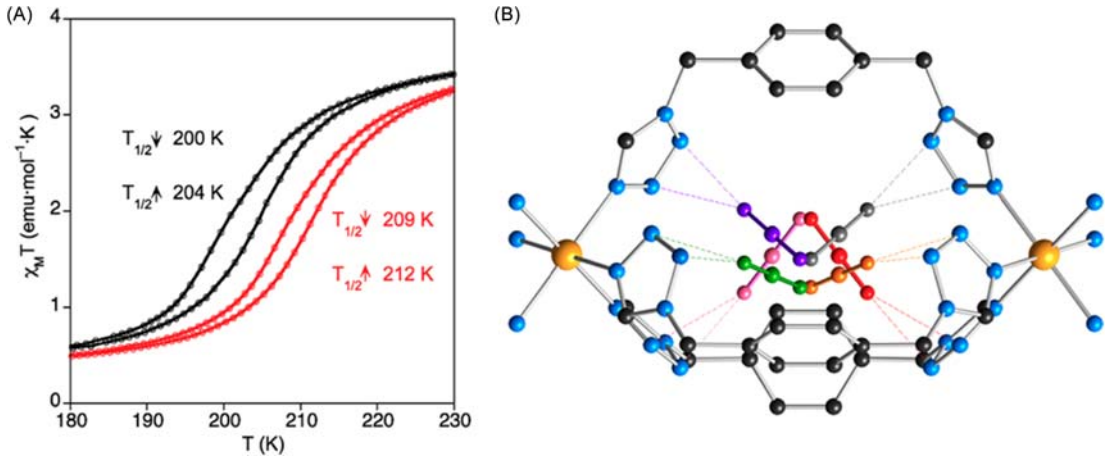

Fig. 7 (a) SCO curve of **17** before (black) and after (red) CO_2 adsorption. (b) Structure of **17** included adsorbed CO_2 molecules modeled in the void space between bridging ligands. Adapted from Coronado, E.; Giménez-Marqués, M.; Mínguez Espallargas, G.; Rey, F.; Vitórica-Yrezábal, I. J. Spin-Crossover Modification through Selective CO2 Sorption. *J. Am. Chem. Soc.* **2013**, *135* (43), 15986–15989. doi:10.1021/ja407135k.

there are potential applications in gas sensing, especially for this material where selective adsorption of CO_2 from a CO_2/N_2 mixture was observed.

Some MOF SCO materials have even been shown to exhibit guest responsive behavior toward both solvents and gaseous guests. Southon et al.[45] investigated the effects of adsorption of the gases; CO_2, O_2 and N_2 as well as the solvents; water, acetone, ethanol, methanol, acetonitrile and toluene, on the SCO properties of a 3D Hoffman-type MOF (**18**). Synchrotron PXRD analysis was carried out on the dihydrate MOF structure to understand the structural features of the SCO transition in more detail. It was found the structural change that occurs upon spin transition between the LS and HS states was discontinuous and therefore eliminated the presence of any intermediate phase. The dehydration of the material was also studied by synchrotron PXRD. Close examination of the data found some diffuse scatter during the dehydration process that was attributed to the formation of an intermediate characterized by tetragonal supercell reflections, which was suggested to be the monohydrate MOF structure. From the variable temperature synchrotron PXRD measurements carried out on the dihydrate and guest-free material, it was possible to calculate the LS:HS fractions at different temperatures using Rietveld refinement. This data was used to plot SCO curves based on the PXRD measurements, where the SCO curve for the dihydrate material was displaced to lower temperatures compared to measurements using other techniques such as magnetic susceptibility. However, this discrepancy was attributed to ethanol solvate impurities due to the washing process. These findings demonstrate the importance of using multiple techniques in addition to structural information to characterize the properties of SCO materials. In this study, gas adsorption isotherms were used to analyze the SCO properties of the MOF with gasses adsorbed. For the analysis of SCO properties of the various solvated MOF structures, magnetic susceptibility and optical reflectivity measurements were used and were in good agreement with each other. While it does not appear that variable temperature synchrotron PXRD measurements were carried out on the solvated MOF materials, synchrotron PXRD patterns were obtained at temperatures corresponding to the LS and HS states of the solvates. These measurements are important because subtle changes to the structure can be detected, for example, the patterns for the LS structures of the ethanol and acetonitrile solvates indicate an orthorhombic unit cell similar to the dihydrate rather than the tetragonal unit cell associated with the guest-free MOF.

10.04.2.3 LIESST effect studies using synchrotron diffraction

Many SCO materials have been shown to exhibit the LIESST effect, where switching from the LS state to a metastable HS state is possible for some SCO systems at low temperatures through irradiation with light. As the LIESST effect is typically observed at very low temperatures, structural studies in the home laboratory can be complicated due to the need to access sample temperatures below 80 K during data collection and the requirement for *in-situ* light irradiation at these low temperatures. Such specialist equipment does exist in a few home laboratories, and some of these were used to pioneer the structural study of LIESST effects in SCO materials.[79–82] Such capabilities are also increasingly common on small molecule beamlines at central facilities, and allow data collection on small crystals, something which is often required to ensure penetration of light into the whole crystal and so complete photoexcitation. Furthermore, the reduced collection times possible with synchrotron radiation can also allow for short-lived processes to be studied, providing an opportunity for detailed mechanistic insights.

An early synchrotron-based SCXRD study was conducted on the metastable HS state of $[Fe(phen)_2(NCSe)_2]$ (**19**) at both a second-generation and a third-generation synchrotron facility.[47] Interestingly, while the more modern facility was used to determine low temperature structures, it was not possible to determine room temperature structures of the thermal HS state using the same experimental setup due to radiation damage. Data for the room-temperature HS state were however able to be collected at the second-generation source, where the brilliance was orders of magnitude lower. This effect, as well as the possibility for X-ray-induced excited spin state trapping (*vide-infra*) show that despite the many benefits of using synchrotrons for diffraction studies of stimuli-responsive materials, problems may well arise, and experimentalists must be prepared for such difficulties. Sheu et al. used a low temperature vacuum camera in Weisenburg geometry to determine the metastable HS state in *trans*-$[Fe(tzpy)_2(NCS)_2]$ (**20**) at 40 K.[48] A pump-probe experiment was used to overcome difficulties caused by relaxation from the metastable HS state, which was observed even at these very low temperatures. The pump-probe illumination regime allowed damage to the crystal caused by continued laser irradiation to be minimized. Again, the need for experimental adaptations in response to problems related to both the SCO processes and external stimuli is clear; these are still not routine experiments.

Delgado et al.[49] investigated the LIESST behavior of $[Fe(n\text{-}Bu\text{-}im)_3(tren)](PF_6)_2$, (**21**), which was reported previously by Seredyuk et al.[83] This system was particularly interesting because it displayed significant differences in its SCO transition temperature and hysteresis width based on the scan rate used during the magnetic susceptibility measurements. Additionally, the structure of the LS state also varied depending on the cooling rate used, resulting in two possible LS structures, which were termed LS_1 and LS_2. The hysteresis widths of LS_1 and LS_2 were found to be 14 K and 41 K, respectively, which demonstrates that there are clear differences in the structural rearrangements associated with the SCO transitions. Given the differences in transition temperature, hysteresis, and structure between LS_1 and LS_2, it can also be expected that both the LS → HS excitation and the HS → LS relaxation during the LIESST process should differ. These differences in LIESST behavior were investigated using a variety of methods, but synchrotron-based SCXRD was vital in elucidating the subtle structural changes that occurred during the LIESST process.[49] Two different HS states, HS_1^{1irr} and HS_1^{2irr}, were generated by irradiating the LS_1 state at 25 K and 90 K, respectively. The HS_1^{1irr} photogenerated state did not differ too drastically from the LS_1 state. In contrast, the HS_1^{2irr} photogenerated state showed significant disorder and conformational change in the butyl groups of the ligand compared to the LS_1 state. Due to the rapid measurements available through synchrotron based SCXRD, the structural relaxation of the HS_1^{2irr} state to the LS_1 state was also able to be

investigated. The measurements revealed that the long relaxation times resulted from the kinetics of the rearrangement of the butyl chains, which is shown in Fig. 8.

In terms of the LS_2 state, it was found that the relaxation time was not significantly impacted by the irradiation and relaxation temperatures. A further experiment was also carried out as part of the study where the HS state was thermally quenched at low temperature and found to be structurally very similar to the HS_1^{2irr} state. Consequently, the relaxation time of the quenched HS structure was found to be very comparable to that of the HS_1^{2irr} relaxation time. Furthermore, some interesting and important observations were also noted during the study, where the relaxation time was found to vary slightly from crystal to crystal. When powder samples were measured, the nucleation time associated with the relaxation decreased. This demonstrates the dependence of kinetically controlled phenomena such as this on the size and quality of the crystals used.

The effects of particle size on SCO behavior, particularly cooperativity were later followed-up by members of the same team using synchrotron X-ray powder diffraction combined with mechanoelastic modeling to investigate nanoparticles of [Fe(*pz*)$Pt(CN)_4$] (**18**). They investigated the photoexcitation of these particles and subsequent relaxation processes in an effort to determine the mechanism by which the relaxations proceeds and to establish the particle size at which the phase nucleation and growth mechanisms responsible for cooperativity become evident.[46] It was shown that for large particles (above c.a. 200 nm) the relaxation and cooperativity mechanisms are comparable to that of the bulk. Below this size, inhomogeneities (likely associated with the increased contribution of surface effects) cause random relaxations, which in turn result in properties deviating significantly from the those of bulk materials.

10.04.2.4 Time-resolved synchrotron studies of SCO materials

The time structure of a synchrotron beam can be used to resolve sequential time-dependent dynamic aspects of the SCO process. Advances in detector technology that allow for time-gating may allow for further experimental flexibility and the possibility of conducting advanced experiments away from central facilities as these new technologies become more widely available. There have been several time-resolved spectroscopic studies of SCO systems,[84–87] particularly those focusing on the kinetics of recovery to the thermally stable LS state after excitation with light.[88,89] However, time-resolved structural studies are a more recent addition to the landscape. Collet and co-workers used a combination of synchrotron X-ray diffraction and optical spectroscopy to investigate

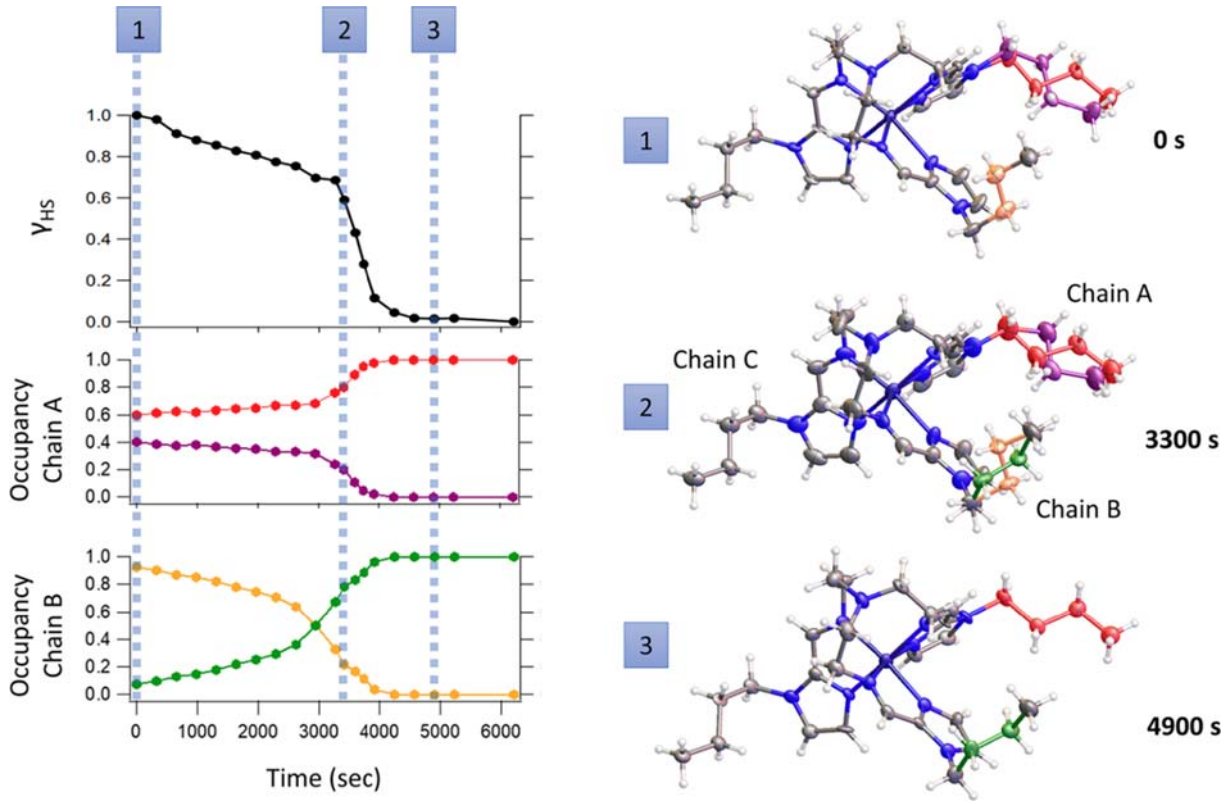

Fig. 8 Relaxation curve obtained by single-crystal X-ray diffraction using synchrotron radiation at 90 K after irradiation at the same temperature in **21**. Relative occupancies of butyl chains as a function of time is also shown, alongside the structure of the complex at three different time points. Reproduced from Delgado, T.; Tissot, A.; Guénée, L.; Hauser, A.; Valverde-Muñoz, F. J.; Seredyuk, M.; Real, J. A.; Pillet, S.; Bendeif, E. E.; Besnard, C. Very Long-Lived Photogenerated High-Spin Phase of a Multistable Spin-Crossover Molecular Material. *J. Am. Chem. Soc.* **2018**, *140* (40), 12870–12876. doi:10.1021/jacs.8b06042.

the out-of-equilibrium switching dynamics in the compound $[Fe(tpa)(tcc)]PF_6$ (**22**), with a time-resolution of 100 ps for the structural measurements.[50–53] The study revealed successive dynamic steps in this out-of-equilibrium process, triggered by a femto-second laser pulse that causes local pico-second switching, followed by nano-second volume expansion and subsequent thermal switching at the millisecond time scale, as shown schematically in Fig. 9. The findings are distinct from those observed when investigating long-lived metastable states at low temperatures as described above. These challenging structural investigations allow for multi-step processes to be understood in detail. Time-resolved powder diffraction studies have also been performed with several SCO systems and allows for further monitoring of photo-induced switching dynamics in real time.[90] A more detailed review on both the technical advances and application of time resolved diffraction to SCO materials can be found elsewhere.[91]

Apart from these studies with very high time resolution, more routine experiments with high flux sources can allow much more rapid data collection than in the home lab. As a consequence, relaxation processes that occur over longer timescales can also be monitored *in-situ* using synchrotron diffraction techniques. This was done by Craig et al., who investigated the structural relaxation of an Fe(II) complex (**23**) within the hysteresis loop using cell parameters over a period of c.a. 30 min.[54] Dova et al.[55,56] found that the results of powder diffraction experiments on $[Fe(teec)_6]^{2+}$ complexes (**24**) depended on the duration of the diffraction experiment and the length of time over which it had had to relax at a given temperature. This is an important consideration when planning variable temperature structural experiments for comparison with other techniques such as magnetometry in which the time required to collect a given data point may be significantly different. Using a synchrotron there is likely room for greater flexibility in this regard as the time for a given data collection can be decreased when compared to an experiment using a sealed tube for example.

10.04.2.5 X-ray induced excited spin state trapping

During an XAFS measurement using synchrotron facilities, it was observed that the incident X-ray beam used to probe the sample was able to switch the spin state of $[Fe(phen)_2(NCS)_2]$ (**25**) at low temperatures from the LS to HS state in an analogous manner to the LIESST effect.[57] Referred to as soft X-ray induced excited spin state trapping (SOXIESST), the equivalent process using hard X-rays (HAXIESST) was also later observed in the same compound.[92] While neither of these studies involved diffraction studies, it is clearly very important to be aware that high flux X-ray beams have the potential to affect the spin state of SCO materials at low temperatures. Synchrotron diffraction studies on a cobalt complex, $[Co(diox)_2(4\text{-CN-py})_2]\cdot$benzene (**26**) that exhibits valence tautomerism have revealed similar effects, where the LS $Co^{3+} \rightarrow$ HS Co^{2+} switching can be induced by X-rays below 60 K.[58,59] It was found that the mole fraction of the metastable HS Co^{2+} state increased when the flux of the incident X-ray beam was increased, as shown in Fig. 10.

10.04.2.6 Charge density studies

It is frequently seen that small changes to the ligands of SCO materials can have a huge impact on the switching properties, and thus understanding the electronic properties (e.g., σ-donor, π-acceptor capacity) of those ligands is of great importance to the development on new SCO materials. The way in which these and other electronic properties change during SCO has important implications for the mechanism of spin state switching. As a consequence, detailed charge density studies of SCO systems both in the LS ground state, as well as the light-induced metastable HS state at low temperatures have been of interest to the community.[60,93] One significant challenge of charge-density studies on switchable materials is the fact that mosaicity tends to increase as the crystal undergoes the dynamic SCO process in the solid state.[74] Furthermore, irradiation of crystals with lasers to reach the metastable HS state can lead to substantial deterioration of the crystal quality. A charge density study by Pillet et al. was conducted on $Fe(btr)_2(NCS)_2 \bullet H_2O$ (**27**), which shows an abrupt SCO with hysteresis as well as the LIESST effect at low temperatures.[60] The difference in distribution of the iron deformation density beautifully illustrates crystal field effects, as shown in Fig. 11. It was found that using synchrotron

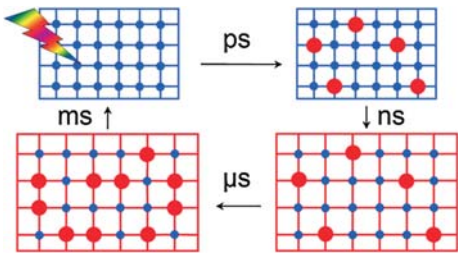

Fig. 9 Illustration of the dynamic processes that occur after irradiation of a LS material (blue circles) with an ultrafast laser pulse. HS sites are generated (red circles) within 1 ps. Lattice expansion and thermal stabilization occur on ns and μs timescales respectively. Recovery to thermal equilibrium occurs on the ms scale and the material returns to the ground state. Reproduced from Lorenc, M.; Hébert, J.; Moisan, N.; Trzop, E.; Servol, M.; Buron-Le Cointe, M.; Cailleau, H.; Boillot, M. L.; Pontecorvo, E.; Wulff, M.; Koshihara, S.; Collet, E. Successive Dynamical Steps of Photoinduced Switching of a Molecular Fe(III) Spin-Crossover Material by Time-Resolved x-Ray Diffraction. *Phys. Rev. Lett.* **2009**, *103* (2), 2–5. doi:10.1103/PhysRevLett.103.028301.

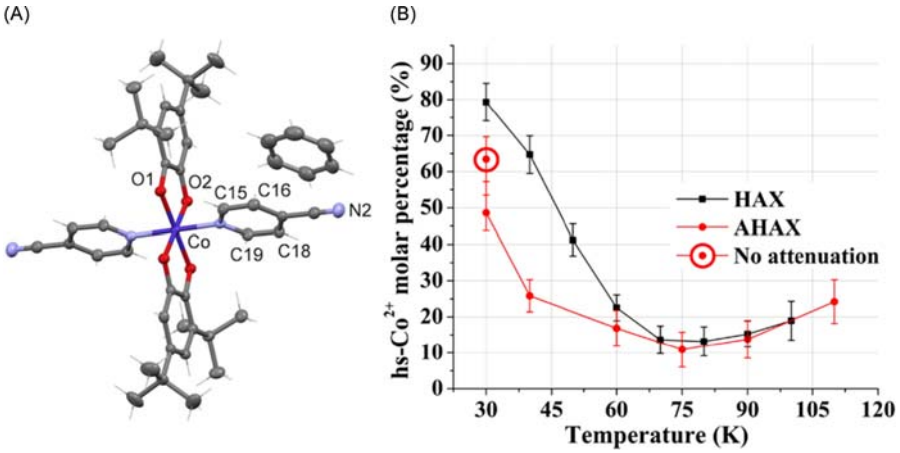

Fig. 10 (a) Structure of **26** and (b) Molar percentage of the metastable HS Co^{2+} state in **26** as a function of temperature under sample exposure to a non-attenuated X-ray beam (HAX) and to a 78% attenuated X-ray beam (AHAX). The encircled spot indicates the additional non attenuated data collection performed after AHAX experiment. Reproduced from Francisco, T. M.; Gee, W. J.; Shepherd, H. J.; Warren, M. R.; Shultz, D. A.; Raithby, P. R.; Pinheiro, C. B. Hard X-Ray-Induced Valence Tautomeric Interconversion in Cobalt-o-Dioxolene Complexes. *J. Phys. Chem. Lett.* **2017**, *8* (19), 4774–4778. doi:10.1021/acs.jpclett.7b01794.

radiation allowed the collection of diffraction data on metastable materials to higher resolution than is possible using a lab source.[94] This was shown to improve the deconvolution of thermal motion from the electron density and allowed the authors to evaluate 3*d* orbital populations as well as electronic properties of the ligands.

10.04.2.7 Pressure-induced SCO

The effect of pressure on SCO materials was described in the introduction and a wider review of high-pressure studies in the field is available.[18] The vast majority of high-pressure diffraction studies of SCO materials involve the use of a diamond anvil cell (DAC) to generate the pressure. The use of a DAC limits the angular resolution of accessible data, which is a significant problem for single crystal diffraction studies. Molecular-based SCO materials are typically low symmetry (often monoclinic or triclinic) and the lack of access to large regions of reciprocal space mean it is often difficult to achieve a complete dataset using equipment available in a standard diffraction lab. In addition, the sample chamber is relatively small, and the diamond windows of the cell can absorb X-rays, meaning that accurate determination of diffracted intensities from low-flux sources can be problematic. Synchrotron X-ray diffraction beamlines can be helpful in both regards: access to shorter wavelengths allows access to a higher proportion of reciprocal space given a hard limit on angular resolution and reduces absorption effects. Furthermore, the inherent high flux of the beam is ideal for measuring data on small crystals relatively quickly, allowing more data points to be recorded within a given time limit. That said, the relatively low pressures required to induce SCO at ambient temperature mean that diffraction data from samples under applied pressure is possible—although not routine—in a home laboratory.[95,96]

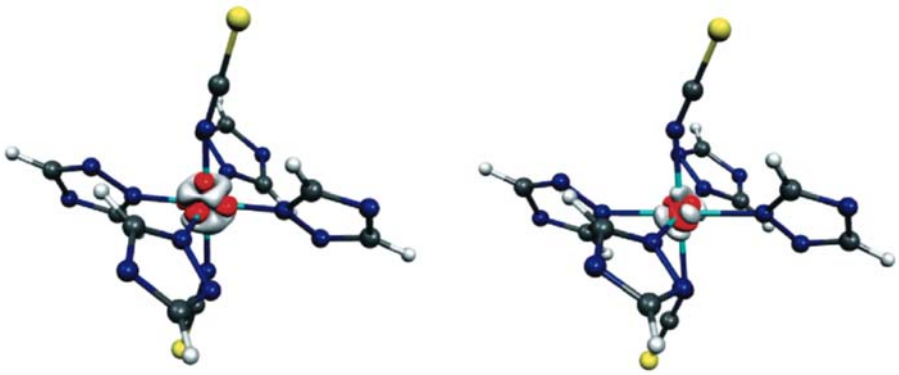

Fig. 11 Static deformation density of iron in the LS (left) and HS (right) states of **27** at 15 K (isosurface of 0.2 e Å-3, positive shown in gray, negative in red). Reproduced from Legrand, V.; Pillet, S.; Souhassou, M.; Lugan, N.; Lecomte, C. Extension of the Experimental Electron Density Analysis to Metastable States: A Case Example of the Spin Crossover Complex Fe(Btr)2(NCS)2·H2O. *J. Am. Chem. Soc.* **2006**, *128* (42), 13921–13931. doi:10.1021/ja064355f.

To the best of our knowledge, the first high-pressure synchrotron diffraction studies of molecular SCO materials reported on a pressure-induced stepped spin transition associated with structural symmetry breaking.[15] The molecular complex $[Fe^{II}(bapbpy)(NCS)_2]$ (**28**) has half a molecule in the asymmetric unit at ambient pressure. On application of a pressure of 4 kbar, a symmetry breaking phase transition results in a tripling in the volume of the unit cell, characterized by the appearance of supercell reflections in the diffraction pattern (Fig. 12). In this phase there is one LS molecule and half a HS molecule in the asymmetric unit, giving an IP with long-range order of -HS-LS-LS- centers throughout the crystal. On further compression to 11 kbar, a second pressure-induced spin transition occurs, also accompanied by a crystallographic phase transition to a state with 1 LS molecule in the asymmetric unit. Interestingly, this study also included measurement of the diffraction pattern using a combination of high pressure and low temperature simultaneously. This allowed the plotting of an experimental P-T phase diagram for the first-time using diffraction data from

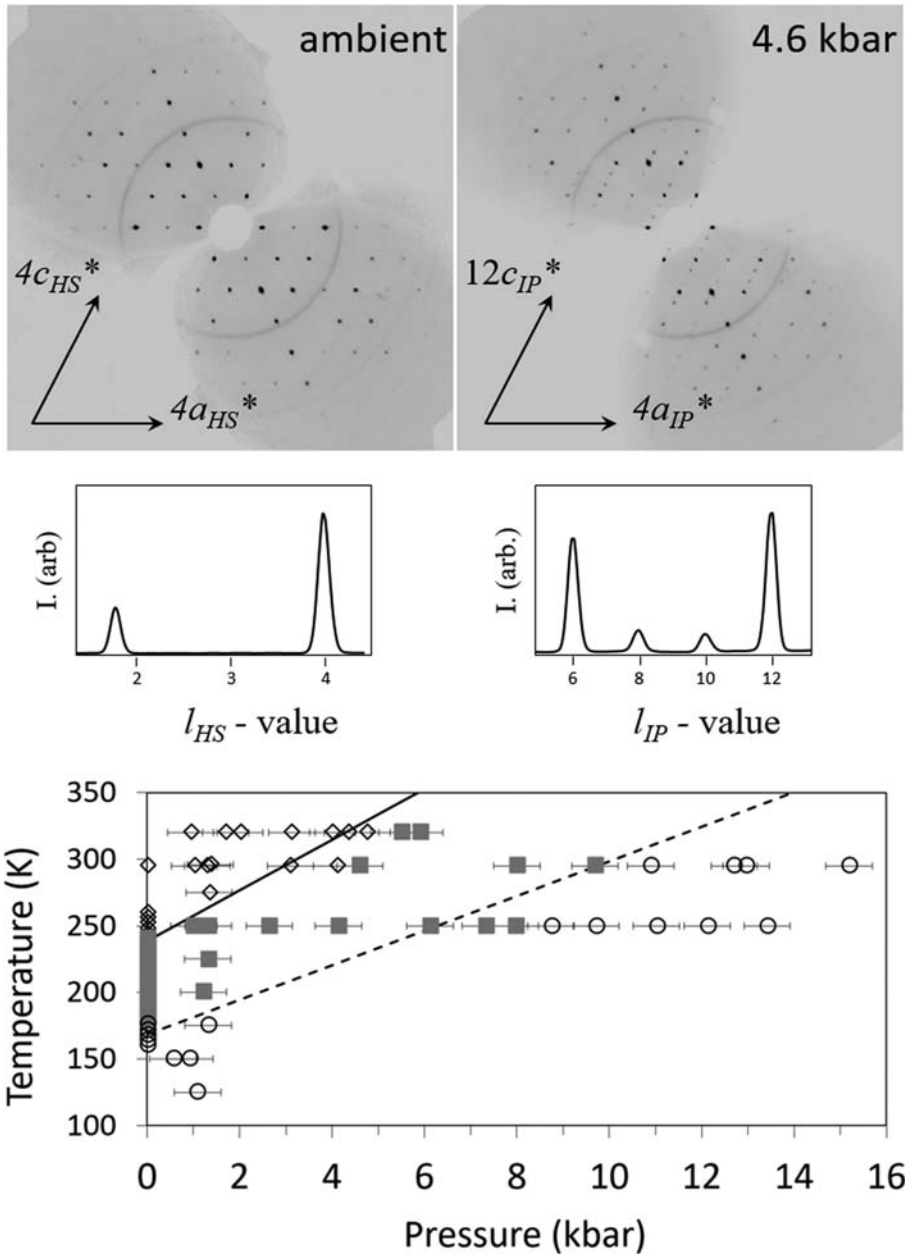

Fig. 12 Appearance of supercell reflections observed in **28** on increasing pressure to 4.6 kbar, characteristic of the pressure-induced formation of the intermediate mixed spin phase. Pressure-temperature phase diagram of the same compound derived from diffraction data. Reproduced from Shepherd, H. J.; Bonnet, S.; Guionneau, P.; Bedoui, S.; Garbarino, G.; Nicolazzi, W.; Bousseksou, A.; Molnár, G. Pressure-Induced Two-Step Spin Transition with Structural Symmetry Breaking: X-Ray Diffraction, Magnetic, and Raman Studies. *Phys. Rev. B: Condens. Matter Mater. Phys.* **2011**, *84* (14), 144107. doi:10.1103/PhysRevB.84.144107.

a sample enclosed in a DAC, which was mounted inside a large cryostat. These types of experiments are certainly beyond the capability of most well-equipped home laboratories.

The dinuclear complex [{Fe(bpp)$(NCS)_2$}$_2$(4,4′-bipy)]•2MeOH (**29**) was investigated using ambient temperature high pressure X-ray diffraction on I15 at Diamond Light Source.[61] A thermally inaccessible pressure-induced LS phase was reported and attributed to the decoupling of SCO from a crystallographic phase transition in this material. The use of synchrotron diffraction data allowed the determination of unit cell parameters at many pressures between ambient and 20 kbar. This enabled the fitting of an equation of state and hence the determination of elastic parameters for the material.

A mononuclear Fe^{II} complex (**30**) was also investigated at high pressure using a DAC.[62] The study allowed the rationalization of the unusual magnetic properties in this material, a result of an order-disorder crystallographic phase transition. The structural changes observed during the pressure-induced SCO were highly anisotropic, manifested by an increase of the *c*-axis under pressure, mitigated by significant compression of the *a*-axis. The importance of understanding elastic properties and anisotropy was articulated in a publication concerning the molecular material [Fe^{II}(HB$(tz)_3)_2$] (**31**), in which a wide range of complimentary techniques were used to determine a complete set of elastic moduli for a spin crossover solid.[63] This information is vital to the application of these systems in recently developed actuating applications.[97] From a high pressure single-crystal diffraction study using synchrotron radiation, important information was deduced about the pressure dependence of the lattice volume and the unit cell anisotropy. Crystal structure analysis at different pressures revealed that the pronounced anisotropy of the lattice compressibility is correlated with the difference in spacing between the molecules and the distribution of the stiffest C-H···N interactions in different crystallographic directions.

The high-pressure studies described above all concern single crystal diffraction experiments, where use of synchrotron radiation was important, but perhaps not essential to obtaining a result. By contrast, high quality powder diffraction data are much more difficult (if not impossible) to obtain at elevated pressures in the home laboratory. A powder diffraction study on the complex [Fe(PM-PeA)$(NCSe)_2$] (**32**) benefitted from the very low instrumental peak broadening offered by synchrotron radiation.[64] The (110) Bragg peaks of the HS and LS phases are clearly distinguishable thanks to the high resolution of the data, as shown in Fig. 13. The authors were also able to control temperature during data collection, providing experimental proof of the linear relationship of the transition pressure with increasing temperature. The quality of the data was sufficiently high to allow Rietveld refinement of cell parameters and HS/LS ratio within the sample across a range of temperatures and pressures. Remarkably, the large range of pressure over which both HS and LS phases were apparent allowed extraction of cell parameters for both spin states over a wide pressure range. This provided the opportunity to determine bulk moduli for each spin state independently from the same experiment. As the authors themselves highlight, the use of high-pressure powder diffraction using synchrotron radiation has a huge scope for further probing the structural properties of SCO materials and uncovering a better understanding of fundamental aspects of their behavior.

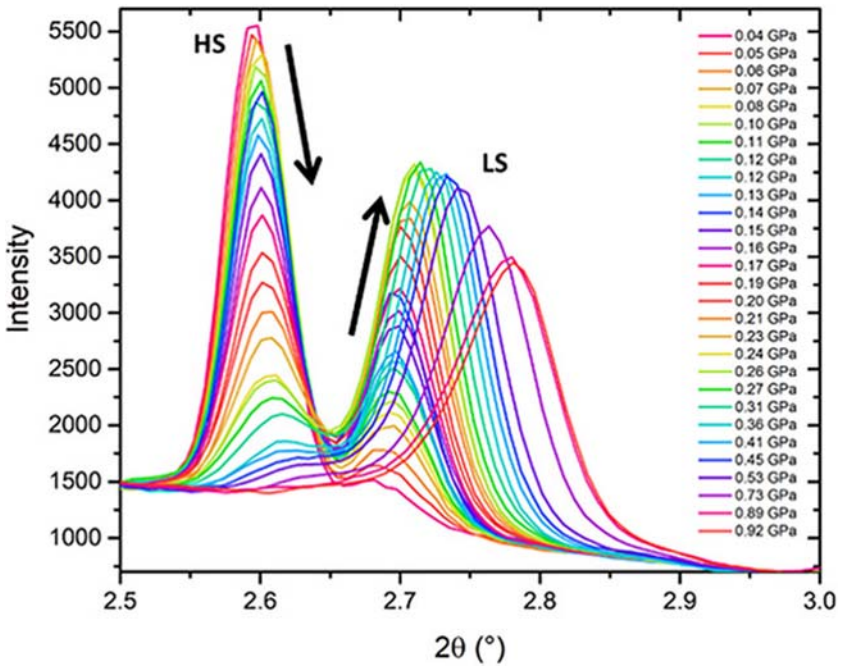

Fig. 13 Evolution of the intensity of the (110) peaks of the HS ans LS state as a function of temperature for **32**. Reproduced from Tailleur, E.; Marchivie, M.; Itié, J. P.; Rosa, P.; Daro, N.; Guionneau, P. Pressure-Induced Spin-Crossover Features at Variable Temperature Revealed by in Situ Synchrotron Powder X-Ray Diffraction. *Chem. A Eur. J.* **2018**, *24* (54), 14495–14499. doi:10.1002/chem.201802828.

10.04.2.8 Pair distribution function

Pair distribution function (PDF) experiments rely on analysis of very weak diffuse scattering data to characterize local as well as long-range order in amorphous materials or nanoparticles. To date there have only been a few reports of PDF studies on SCO materials, but they offer great promise in evaluating the materials at the length scales in which they may well find technological application. The first such study looked at coherent-domain size reduction effects in the coordination polymer $[Fe(Htrz)_2(trz)](BF_4)$ (**33**), in particles within the range of 50–10 nm.[65] The data indicated that within that range, domain size does not significantly affect the structure of the material. Some limitations of PDF analysis were highlighted by the authors, including the high degree of anisotropy in the crystallites in this 1D coordination polymer material, which cannot be accommodated in the PDF method. They also highlighted the importance of obtaining synchrotron data for these kinds of studies to allow more insight into small structural modifications caused by size-reduction. Data collected on the same compound at a synchrotron source[66] are shown in **Fig. 14** and provide confirmation of local coordination environment, proof for the 1D polymeric structure as well as information regarding packing of individual chains. Furthermore, data measured as a function of temperature clearly reveal the structural impacts of the SCO process. More detail can be found in an excellent recent review of diffraction techniques for the study of SCO materials.[66]

10.04.2.9 Synchrotron GIXRD and in-plane XRD studies

In order to use SCO materials for specific future applications, it is essential to understand how the SCO materials behave when in different environments, such as in contact with a surface or as a thin film. Furthermore, the preparation of application-based materials such as thin films can be done in various ways and these methods are still being developed and understood. Consequently, the structural characterization of these materials is very important to determine the success of the preparation technique and the overall structure. Several studies have used synchrotron-based diffraction techniques to characterize thin films of SCO materials.

Cavallini et al.[98] have used 2D grazing-incidence X-ray diffraction (2D-GIXRD) to analyze thin deposits which were prepared using lithographically controlled wetting (LCW) to deposit the SCO material onto a silicon surface. Tanaka et al.[99] prepared thin films using nanoparticle spin coating and used in-plane synchrotron XRD to characterize the thin films and to track the SCO of the films by looking at small peak shifts associated with SCO. Rubio-Giménez et al.[100] reported the manufacture of ultrathin films through a bottom-up layer-by-layer approach, using synchrotron-based 2D-GIXRD to analyze the overall crystallinity of the films and to understand how the structure was oriented in-relation to the substrate. Synchrotron facilities are also well equipped to perform other non-diffraction based experiments such as X-ray absorption spectroscopy (XAS), which Rubio-Giménez et al.[100] also utilized to further characterize their ultrathin films. Fourmental et al.[101] investigated the relationship between a SCO monolayer and

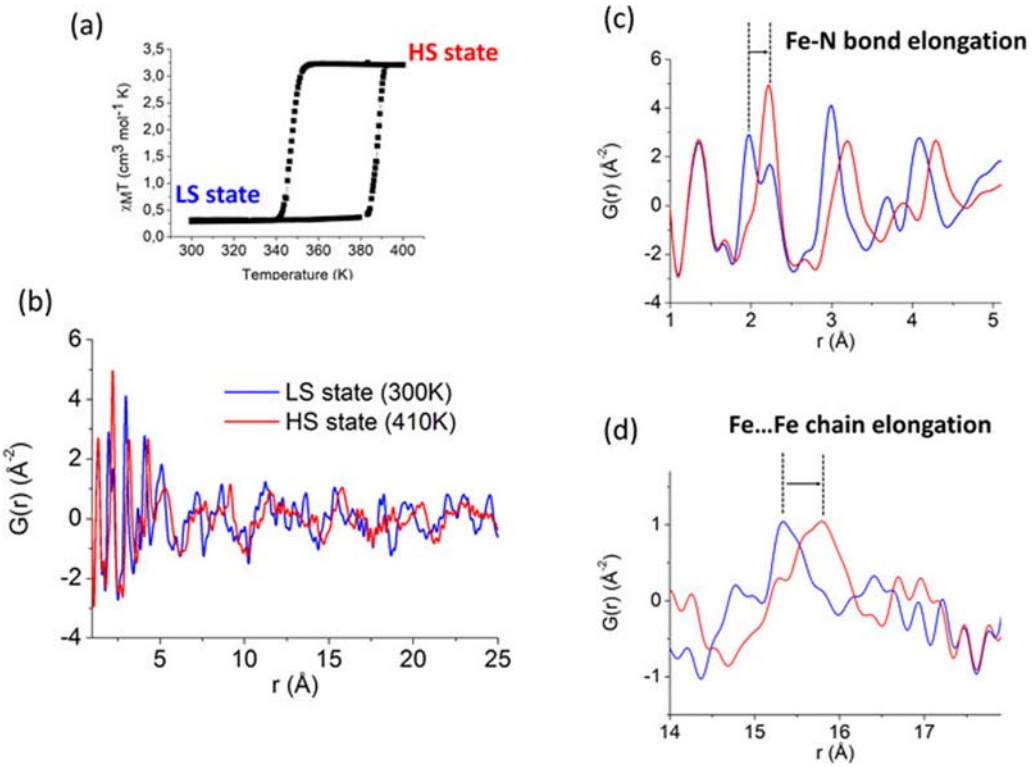

Fig. 14 (a) SCO behavior of **33** as a function of temperature. (b)–(d) PDF derived in the LS state (blue) and in the HS state (red). Reproduced from Pillet, S. Spin-Crossover Materials: Getting the Most from x-Ray Crystallography. *J. Appl. Phys.* **2021**, *129* (18), 181101. doi:10.1063/5.0047681.

a Au(111) substrate using synchrotron based 2D-GIXRD. The results were able to show that an epitaxial relationship existed between the monolayer and the substrate. This allowed for further modeling to understand how the epitaxial strain on the monolayer impacts the SCO properties. These studies demonstrate that synchrotron facilities are, and will be, very useful for the characterization of future SCO materials such as thin-films, not only using 2D-GIXRD but through additional experimental techniques available at synchrotron facilities such as XAS.

10.04.3 Outlook

The increased flux available at synchrotron sources provides a number of exciting opportunities for the study of SCO materials. As in the case of any type of crystalline material, synchrotrons continue to allow access to structural data from small and weakly diffracting materials that would otherwise be impossible to study using most lab-based diffraction equipment. Of more particular interest to the study of SCO materials, increasing the speed of data collection allows for multiple datasets to be recorded as a function of a particular stimulus (temperature, pressure, light irradiation etc.). This is of great importance to the understanding and eventual application of these materials in which properties are so intricately linked to structure.

Synchrotrons also offer a number of further benefits to the study of SCO materials beyond increased flux. The possibility to develop and exploit exotic experimental setups is much greater at central facilities, and the sensitivity of SCO materials to a wide range of stimuli presents many opportunities for investigating dynamic structural effects and elucidating mechanistic processes. Sample environments that can be routinely accessed at many synchrotron facilities include very low temperatures, *in-situ* light irradiation, high pressures and gas loading for example. The ability to tune the wavelength of the X-ray beam at a synchrotron source also increases data quality/quantity in cases where absorption effects or angular resolution are important to the final result, for example, in charge density or high-pressure experiments. The time structure of the synchrotron as well as advanced hardware and data processing routines allows for the possibility of time-resolved investigations of SCO materials. While X-ray free electron lasers (X-FELs)[102] and electron sources[103,104] have the potential to allow exceptional time and spatial resolution in structural studies of SCO materials, such experiments remain far from routine. The ability to reduce the size of the X-ray beam may allow for spatial mapping of an inhomogeneous sample, for example, domains of different spin states nucleating and propagating within a single crystal.

The increased flux from synchrotron facilities does however present some challenges (and of course further opportunities) for the investigation of SCO systems that are unlikely to be encountered using a more routine experimental setup. While in most laboratory settings the beam from a standard diffractometer acts merely as a probe of the existing structure, beams available at synchrotron sources have the potential to change the spin state of SCO materials. Examples of both X-ray-induced excited spin state trapping and radiation damage causing changes in the spin state have been observed. While both of these effects provide opportunities to investigate novel phenomena, the possibility of X-ray-induced effects may interfere with results of more standard structural experiments. The potential for such events should thus be evaluated and eliminated as a cause of unusual and unexpected behavior when performing synchrotron studies of SCO materials. This is particularly important as both synchrotron and indeed laboratory X-ray sources get brighter and thus the chances of observing such behavior increases.

References

1. *Absorption Spectra and Chemical Bonding in Complexes*, Elsevier, 1962. https://doi.org/10.1016/c2013-0-05287-5.
2. Gütlich, P.; Garcia, Y.; Goodwin, H. A. Spin Crossover Phenomena in Fe(ii) Complexes. *Chem. Soc. Rev.* **2000,** *29* (6), 419–427. https://doi.org/10.1039/b003504l.
3. Hauser, A. Ligand Field Theoretical Considerations. In *Spin Crossover in Transition Metal Compounds I*; *Topics in Current Chemistry*. 2004, vol. 233; pp 49–58. https://doi.org/10.1007/b13528.
4. Collet, E.; Guionneau, P. Structural Analysis of Spin-Crossover Materials: From Molecules to Materials. *C. R. Chim.* **2018,** *21* (12), 1133–1151. https://doi.org/10.1016/J.CRCI.2018.02.003.
5. Guionneau, P.; Marchivie, M.; Bravic, G.; Létard, J.-F.; Chasseau, D. Structural Aspects of Spin Crossover. Example of the [FeIILn(NCS)2] Complexes. In *Spin Crossover Transit. Met. Compd. II*; 2004, vol. 234; pp 97–128. https://doi.org/10.1007/b95414.
6. Shepherd, H. J.; Palamarciuc, T.; Rosa, P.; Guionneau, P.; Molnár, G.; Létard, J. F.; Bousseksou, A. Antagonism between Extreme Negative Linear Compression and Spin Crossover in [Fe(Dpp) 2(NCS) 2]·py. *Angew. Chem. Int. Ed.* **2012,** *51* (16), 3910–3914. https://doi.org/10.1002/anie.201108919.
7. Shepherd, H. J.; Gural'skiy, I. A.; Quintero, C. M.; Tricard, S.; Salmon, L.; Molnár, G.; Bousseksou, A. Molecular Actuators Driven by Cooperative Spin-State Switching. *Nat. Commun.* **2013,** *4,* 2607. https://doi.org/10.1038/ncomms3607.
8. Gural'skiy, I. A.; Quintero, C. M.; Costa, J. S.; Demont, P.; Molnar, G.; Salmon, L.; Shepherd, H. J.; Bousseksou, A. Spin Crossover Composite Materials for Electrothermomechanical Actuators. *J. Mater. Chem. C* **2014,** *2* (16), 2949–2955. https://doi.org/10.1039/c4tc00267a.
9. Boukheddaden, K.; Ritti, M. H.; Bouchez, G.; Sy, M.; Dîrtu, M. M.; Parlier, M.; Linares, J.; Garcia, Y. Quantitative Contact Pressure Sensor Based on Spin Crossover Mechanism for Civil Security Applications. *J. Phys. Chem. C* **2018,** *122* (14), 7597–7604. https://doi.org/10.1021/acs.jpcc.8b00778.
10. Molnár, G.; Rat, S.; Salmon, L.; Nicolazzi, W.; Bousseksou, A.; Molnár, G.; Rat, S.; Salmon, L.; Nicolazzi, W.; Bousseksou, A. Spin Crossover Nanomaterials: From Fundamental Concepts to Devices Stimuli-Responsive Materials. *Adv. Mater.* **2018,** *30* (5), 1703862. https://doi.org/10.1002/adma.201703862.
11. Murray, K. S. The Development of Spin-Crossover Research. In *Spin-Crossover Materials: Properties and Applications*, John Wiley and Sons, 2013; pp 1–54. https://doi.org/10.1002/9781118519301.ch1.
12. Sandeman, K. G. Research Update: The Mechanocaloric Potential of Spin Crossover Compounds. *APL Mater.* **2016,** *4* (11). https://doi.org/10.1063/1.4967282.
13. Linares, J.; Codjovi, E.; Garcia, Y. Pressure and Temperature Spin Crossover Sensors with Optical Detection. *Sensors* **2012,** *12,* 4479–4492. https://doi.org/10.3390/S120404479.

14. Griffin, M.; Shakespeare, S.; Shepherd, H. J.; Harding, C. J.; Létard, J. F.; Desplanches, C.; Goeta, A. E.; Howard, J. A. K.; Powell, A. K.; Mereacre, V.; Garcia, Y.; Naik, A. D.; Müller-Bunz, H.; Morgan, G. G. A Symmetry-Breaking Spin-State Transition in Iron(III). *Angew. Chem. Int. Ed.* **2011,** *50* (4), 896–900. https://doi.org/10.1002/anie.201005545.
15. Shepherd, H. J.; Bonnet, S.; Guionneau, P.; Bedoui, S.; Garbarino, G.; Nicolazzi, W.; Bousseksou, A.; Molnár, G. Pressure-Induced Two-Step Spin Transition with Structural Symmetry Breaking: X-Ray Diffraction, Magnetic, and Raman Studies. *Phys. Rev. B: Condens. Matter Mater. Phys.* **2011,** *84* (14), 144107. https://doi.org/10.1103/PhysRevB.84.144107.
16. Shatruk, M.; Phan, H.; Chrisostomo, B. A.; Suleimenova, A. Symmetry-Breaking Structural Phase Transitions in Spin Crossover Complexes. *Coord. Chem. Rev.* **2015,** *289–290* (1), 62–73. https://doi.org/10.1016/J.CCR.2014.09.018.
17. Clements, J. E.; Price, J. R.; Neville, S. M.; Kepert, C. J. Hysteretic Four-Step Spin Crossover within a Three-Dimensional Porous Hofmann-Like Material. *Angew. Chem. Int. Ed.* **2016,** *55* (48), 15105–15109. https://doi.org/10.1002/ANIE.201605418.
18. Gaspar, A. B.; Molnár, G.; Rotaru, A.; Shepherd, H. J. Pressure Effect Investigations on Spin-Crossover Coordination Compounds. *C. R. Chim.* **2018,** 1095–1120. https://doi.org/10.1016/j.crci.2018.07.010.
19. Ksenofontov, V.; Gaspar, A. B.; Gütlich, P. Pressure Effect Studies on Spin Crossover and Valence Tautomeric Systems. In *Spin Crossover in Transition Metal Compounds III*, Springer-Verlag: Berlin/Heidelberg, 2004; pp 23–64. https://doi.org/10.1007/b95421.
20. Lawthers, I.; McGarvey, J. J. Spin-State Relaxation Dynamics in Iron(III) Complexes: Photochemical Perturbation of the 2T .Dblharw. 6A Spin Equilibrium by Pulsed-Laser Irradiation in the Ligand-to-Metal Charge-Transfer Absorption Band. *J. Am. Chem. Soc.* **2002,** *106* (15), 4280–4282. https://doi.org/10.1021/JA00327A045.
21. McGravey, J. J.; Lawthers, I. Photochemically-Induced Perturbation of the 1A ⇌5T Equilibrium in Fe11 Complexes by Pulsed Laser Irradiation in the Metal-to-Ligand Charge-Transfer Absorption Band. *J. Chem. Soc. Chem. Commun.* **1982**, (16), 906–907. https://doi.org/10.1039/C39820000906.
22. Decurtins, S.; Gütlich, P.; Köhler, C. P.; Spiering, H.; Hauser, A. Light-Induced Excited Spin State Trapping in a Transition-Metal Complex: The Hexa-1-Propyltetrazole-Iron (II) Tetrafluoroborate Spin-Crossover System. *Chem. Phys. Lett.* **1984,** *105* (1), 1–4. https://doi.org/10.1016/0009-2614(84)80403-0.
23. Gutlich, P.; Decurtins, S.; Hasselbach, K. M.; Spiering, H.; Hauser, A. Light-Induced Excited-Spin-State Trapping in Iron(II) Spin-Crossover Systems. Optical Spectroscopic and Magnetic Susceptibility Study. *Inorg. Chem.* **1985,** *24* (14), 2174–2178. https://doi.org/10.1021/ic00208a013.
24. Hauser, A. Light-Induced Spin Crossover and the High-Spin{\textrightarrow}Low-Spin Relaxation. In *Spin Crossover in Transition Metal Compounds II*, Springer Berlin Heidelberg: Berlin, Heidelberg, 2004; pp 155–198. https://doi.org/10.1007/b95416.
25. Antonangeli, D.; Siebert, J.; Aracne, C. M.; Farber, D. L.; Bosak, A.; Hoesch, M.; Krisch, M.; Ryerson, F. J.; Fiquet, G.; Badro, J. Spin Crossover in Ferropericlase at High Pressure: A Seismologically Transparent Transition? *Science* **2011,** *331* (6013), 64–67 https://doi.org/10.1126/science.1198429.
26. Gütlich, P. Spin Crossover—Quo Vadis? *Eur. J. Inorg. Chem.* **2013**, (5–6), 581–591 https://doi.org/10.1002/EJIC.201300092.
27. Pask, C. M.; Greatorex, S.; Kulmaczewski, R.; Baldansuren, A.; McInnes, E. J. L.; Bamiduro, F.; Yamada, M.; Yoshinari, N.; Konno, T.; Halcrow, M. A. Elucidating the Structural Chemistry of a Hysteretic Iron(II) Spin-Crossover Compound from its Copper(II) and Zinc(II) Congeners. *Chem. A Eur. J.* **2020,** *26* (21), 4833–4841. https://doi.org/10.1002/chem.202000101.
28. Phonsri, W.; Harding, D. J.; Harding, P.; Murray, K. S.; Moubaraki, B.; Gass, I. A.; Cashion, J. D.; Jameson, G. N. L.; Adams, H. Stepped Spin Crossover in Fe(iii) Halogen Substituted Quinolylsalicylaldimine Complexes. *Dalton Trans.* **2014,** *43* (46), 17509–17518. https://doi.org/10.1039/c4dt01701c.
29. Boča, R.; Boča, M.; Ehrenberg, H.; Fuess, H.; Linert, W.; Renz, F.; Svoboda, I. Spin Crossover in Iron(II) Tris(2-(2′-Pyridyl)Benzimidazole) Complex Monitored by Variable Temperature Methods: Synchrotron Powder Diffraction, DSC, IR Spectra, Mössbauer Spectra, and Magnetic Susceptibility. *Chem. Phys.* **2003,** *293* (3), 375–395. https://doi.org/10.1016/S0301-0104(03)00375-6.
30. Hostettler, M.; Törnroos, K. W.; Chernyshov, D.; Vangdal, B.; Bürgi, H. B. Challenges in Engineering Spin Crossover: Structures and Magnetic Properties of Six Alcohol Solvates of Iron(II) Tris(2-Picolylamine) Dichloride. *Angew. Chem. Int. Ed.* **2004,** *43* (35), 4589–4594. https://doi.org/10.1002/anie.200460736.
31. Chernyshov, D.; Hostettler, M.; Törnroos, K. W.; Bürgi, H. B. Ordering Phenomena and Phase Transitions in a Spin-Crossover Compound—Uncovering the Nature of the Intermediate Phase of [Fe(2-Pic) 3]Cl2·EtOH. *Angew. Chem. Int. Ed.* **2003,** *42* (32), 3825–3830. https://doi.org/10.1002/anie.200351834.
32. Gentili, D.; Demitri, N.; Schäfer, B.; Liscio, F.; Bergenti, I.; Ruani, G.; Ruben, M.; Cavallini, M. Multi-Modal Sensing in Spin Crossover Compounds. *J. Mater. Chem. C* **2015,** *3* (30), 7836–7844. https://doi.org/10.1039/C5TC00845J.
33. Li, Z.-Y.; Ohtsu, H.; Kojima, T.; Dai, J.-W.; Yoshida, T.; Breedlove, B. K.; Zhang, W.-X.; Iguchi, H.; Sato, O.; Kawano, M.; Yamashita, M. Direct Observation of Ordered High-Spin-Low-Spin Intermediate States of an Iron(III) Three-Step Spin-Crossover Complex. *Angew. Chem.* **2016,** *128* (17), 5270–5275. https://doi.org/10.1002/ange.201511281.
34. Chernyshov, D.; Dyadkin, V.; Törnroos, K. W. Preliminary Observations of the Interplay of Radiation Damage with Spin Crossover. *Acta Crystallogr. Sect. B: Struct. Sci. Cryst. Eng. Mater.* **2022,** *78* (3), 392–396. https://doi.org/10.1107/s205252062200467x.
35. Li, L.; Saigo, N.; Zhang, Y.; Fanna, D. J.; Shepherd, N. D.; Clegg, J. K.; Zheng, R.; Hayami, S.; Lindoy, L. F.; Aldrich-Wright, J. R.; Li, C. G.; Reynolds, J. K.; Harman, D. G.; Li, F. A Large Spin-Crossover [Fe4L4]8+ Tetrahedral Cage. *J. Mater. Chem. C* **2015,** *3* (30), 7878–7882. https://doi.org/10.1039/c5tc00991j.
36. Li, L.; Craze, A. R.; Mustonen, O.; Zenno, H.; Whittaker, J. J.; Hayami, S.; Lindoy, L. F.; Marjo, C. E.; Clegg, J. K.; Aldrich-Wright, J. R.; Li, F. A Mixed-Spin Spin-Crossover Thiozolylimine [Fe4L6]8+ Cage. *Dalton Trans.* **2019,** *48* (27), 9935–9938. https://doi.org/10.1039/c9dt01947b.
37. Struch, N.; Bannwarth, C.; Ronson, T. K.; Lorenz, Y.; Mienert, B.; Wagner, N.; Engeser, M.; Bill, E.; Puttreddy, R.; Rissanen, K.; Beck, J.; Grimme, S.; Nitschke, J. R.; Lützen, A. An Octanuclear Metallosupramolecular Cage Designed to Exhibit Spin-Crossover Behavior. *Angew. Chem. Int. Ed.* **2017,** *56* (18), 4930–4935. https://doi.org/10.1002/ANIE.201700832.
38. Ahmed, M.; Xie, Z.; Thoonen, S.; Hua, C.; Kepert, C. J.; Price, J. R.; Neville, S. M. A New Spin Crossover Fellcoordination Environment in a Two-Fold Interpenetrated 3-D Hofmann-Type Framework Material. *Chem. Commun.* **2021,** *57* (1), 85–88. https://doi.org/10.1039/d0cc07326a.
39. Sciortino, N. F.; Scherl-Gruenwald, K. R.; Chastanet, G.; Halder, G. J.; Chapman, K. W.; Létard, J.-F.; Kepert, C. J. Hysteretic Three-Step Spin Crossover in a Thermo- and Photochromic 3D Pillared Hofmann-Type Metal-Organic Framework. *Angew. Chem.* **2012,** *124* (40), 10301–10305. https://doi.org/10.1002/ange.201204387.
40. Neville, S. M.; Halder, G. J.; Chapman, K. W.; Duriska, M. B.; Southon, P. D.; Cashion, J. D.; Létard, J. F.; Moubaraki, B.; Murray, K. S.; Kepert, C. J. Single-Crystal to Single-Crystal Structural Transformation and Photomagnetic Properties of a Porous Iron(II) Spin-Crossover Framework. *J. Am. Chem. Soc.* **2008,** *130* (9), 2869–2876. https://doi.org/10.1021/ja077958f.
41. Zenere, K. A.; Duyker, S. G.; Trzop, E.; Collet, E.; Chan, B.; Doheny, P. W.; Kepert, C. J.; Neville, S. M. Increasing Spin Crossover Cooperativity in 2D Hofmann-Type Materials with Guest Molecule Removal. *Chem. Sci.* **2018,** *9* (25), 5623–5629. https://doi.org/10.1039/c8sc01040d.
42. Mondal, D. J.; Roy, S.; Yadav, J.; Zeller, M.; Konar, S. Solvent-Induced Reversible Spin-Crossover in a 3D Hofmann-Type Coordination Polymer and Unusual Enhancement of the Lattice Cooperativity at the Desolvated State. *Inorg. Chem.* **2020,** *59* (18), 13024–13028. https://doi.org/10.1021/acs.inorgchem.0c02240.
43. Neville, S. M.; Halder, G. J.; Chapman, K. W.; Duriska, M. B.; Moubaraki, B.; Murray, K. S.; Kepert, C. J. Guest Tunable Structure and Spin Crossover Properties in a Nanoporous Coordination Framework Material. *J. Am. Chem. Soc.* **2009,** *131* (34), 12106–12108. https://doi.org/10.1021/ja905360g.
44. Coronado, E.; Giménez-Marqués, M.; Mínguez Espallargas, G.; Rey, F.; Vitórica-Yrezábal, I. J. Spin-Crossover Modification through Selective CO2 Sorption. *J. Am. Chem. Soc.* **2013,** *135* (43), 15986–15989. https://doi.org/10.1021/ja407135k.
45. Southon, P. D.; Liu, L.; Fellows, E. A.; Price, D. J.; Halder, G. J.; Chapman, K. W.; Moubaraki, B.; Murray, K. S.; Létard, J. F.; Kepert, C. J. Dynamic Interplay between Spin-Crossover and Host-Guest Function in a Nanoporous Metal-Organic Framework Material. *J. Am. Chem. Soc.* **2009,** *131* (31), 10998–11009. https://doi.org/10.1021/ja902187d.
46. Delgado, T.; Enachescu, C.; Tissot, A.; Hauser, A.; Guénée, L.; Besnard, C. Evidencing Size-Dependent Cooperative Effects on Spin Crossover Nanoparticles Following Their HS → LS Relaxation. *J. Mater. Chem. C* **2018,** *6* (46), 12698–12706. https://doi.org/10.1039/c8tc04315a.

47. MacLean, E. J.; McGrath, C. M.; O'Connor, C. J.; Sangregorio, C.; Seddon, J. M. W.; Sinn, E.; Sowrey, F. E.; Teat, S. J.; Terry, A. E.; Vaughan, G. B. M.; Young, N. A. Structural Study of the Thermal and Photochemical Spin States in the Spin Crossover Complex [Fe(Phen)2(NCSe)2]. *Chem. A Eur. J.* **2003,** *9* (21), 5314–5322. https://doi.org/10.1002/CHEM.200304865.
48. Sheu, C. F.; Chen, K.; Chen, S. M.; Wen, Y. S.; Lee, G. H.; Chen, J. M.; Lee, J. F.; Cheng, B. M.; Sheu, H. S.; Yasuda, N.; Ozawa, Y.; Toriumi, K.; Wang, Y. Structure and Electronic Configuration of an Iron(II) Complex in a LIESST State: A Pump and Probe Method. *Chem. A Eur. J.* **2009,** *15* (10), 2384–2393. https://doi.org/10.1002/chem.200802279.
49. Delgado, T.; Tissot, A.; Guénée, L.; Hauser, A.; Valverde-Muñoz, F. J.; Seredyuk, M.; Real, J. A.; Pillet, S.; Bendeif, E. E.; Besnard, C. Very Long-Lived Photogenerated High-Spin Phase of a Multistable Spin-Crossover Molecular Material. *J. Am. Chem. Soc.* **2018,** *140* (40), 12870–12876. https://doi.org/10.1021/jacs.8b06042.
50. Lorenc, M.; Hébert, J.; Moisan, N.; Trzop, E.; Servol, M.; Buron-Le Cointe, M.; Cailleau, H.; Boillot, M. L.; Pontecorvo, E.; Wulff, M.; Koshihara, S.; Collet, E. Successive Dynamical Steps of Photoinduced Switching of a Molecular Fe(III) Spin-Crossover Material by Time-Resolved x-Ray Diffraction. *Phys. Rev. Lett.* **2009,** *103* (2), 2–5. https://doi.org/10.1103/PhysRevLett.103.028301.
51. Cailleau, H.; Lorenc, M.; Guérin, L.; Servol, M.; Collet, E.; Buron-Le Cointe, M. Structural Dynamics of Photoinduced Molecular Switching in the Solid State. *Acta Crystallogr., Sect. A: Found. Crystallogr.* **2010,** *66* (2), 189–197. https://doi.org/10.1107/S0108767309051046.
52. Cailleau, H.; Lorenc, M.; Buron-Le Cointe, M.; Servol, M.; Cammarata, M.; Collet, E. Impacting Materials by Light and Seeing their Structural Dynamics. *Eur. Phys. J. Spec. Top.* **2013,** *222* (5), 1077–1092. https://doi.org/10.1140/epjst/e2013-01908-x.
53. Collet, E.; Lorenc, M.; Cammarata, M.; Guérin, L.; Servol, M.; Tissot, A.; Boillot, M. L.; Cailleau, H.; Buron-Le Cointe, M. 100 Picosecond Diffraction Catches Structural Transients of Laser-Pulse Triggered Switching in a Spin-Crossover Crystal. *Chem. A Eur. J.* **2012,** *18* (7), 2051–2055. https://doi.org/10.1002/CHEM.201103048.
54. Craig, G. A.; Costa, J. S.; Roubeau, O.; Teat, S. J.; Shepherd, H. J.; Lopes, M.; Molnár, G.; Bousseksou, A.; Aromi, G. High-Temperature Photo-Induced Switching and Pressure-Induced Transition in a Cooperative Molecular Spin-Crossover Material. *Dalton Trans.* **2014,** *43* (2), 729–737. https://doi.org/10.1039/C3DT52075G.
55. Dova, E.; Peschar, R.; Takata, M.; Nishibori, E.; Schenk, H.; Stassen, A. F.; Haasnoot, J. G. Low-Spin State Structure of [Fe(Chloroethyltetrazole)6](BF4)2 Obtained from Synchrotron Powder Diffraction Data. *Chem. A Eur. J.* **2005,** *11* (20), 5855–5865. https://doi.org/10.1002/CHEM.200500036.
56. Dova, E.; Peschar, R.; Sakata, M.; Kato, K.; Schenk, H. High-Spin- and Low-Spin-State Structures of $[Fe(Chloroethyltetrazole)_6](ClO4)_2$ from Synchrotron Powder Diffraction Data. *Chem. A Eur. J.* **2006,** *12* (19), 5043–5052. https://doi.org/10.1002/chem.200501594.
57. Collison, D.; Garner, C. D.; McGrath, C. M.; Mosselmans, J. F. W.; Roper, M. D.; Seddon, J. M. W.; Sinn, E.; Young, N. A. Soft X-Ray Induced Excited Spin State Trapping and Soft X-Ray Photochemistry at the Iron L2,3 Edge in $[Fe(Phen)_2(NCS)_2]$ and $[Fe(Phen)_2(NCSe)_2]$ (Phen = 1,10-Phenanthroline). *J. Chem. Soc. Dalton Trans.* **1997**, (22), 4371–4376. https://doi.org/10.1039/a703728g.
58. Francisco, T. M.; Gee, W. J.; Shepherd, H. J.; Warren, M. R.; Shultz, D. A.; Raithby, P. R.; Pinheiro, C. B. Hard X-Ray-Induced Valence Tautomeric Interconversion in Cobalt-o-Dioxolene Complexes. *J. Phys. Chem. Lett.* **2017,** *8* (19), 4774–4778. https://doi.org/10.1021/acs.jpclett.7b01794.
59. Leroy, L.; Francisco, T. M.; Shepherd, H. J.; Warren, M. R.; Saunders, L. K.; Shultz, D. A.; Raithby, P. R.; Pinheiro, C. B. Controlled Light and Temperature Induced Valence Tautomerism in a Cobalt-o-Dioxolene Complex. *Inorg. Chem.* **2021,** *60* (12), 8665–8671. https://doi.org/10.1021/acs.inorgchem.1c00638.
60. Legrand, V.; Pillet, S.; Souhassou, M.; Lugan, N.; Lecomte, C. Extension of the Experimental Electron Density Analysis to Metastable States: A Case Example of the Spin Crossover Complex $Fe(Btr)_2(NCS)_2 \cdot H_2O$. *J. Am. Chem. Soc.* **2006,** *128* (42), 13921–13931. https://doi.org/10.1021/ja064355f.
61. Shepherd, H. J.; Rosa, P.; Vendier, L.; Casati, N.; Létard, J. F.; Bousseksou, A.; Guionneau, P.; Molnár, G. High-Pressure Spin-Crossover in a Dinuclear Fe(ii) Complex. *Phys. Chem. Chem. Phys.* **2012,** *14* (15), 5265–5271. https://doi.org/10.1039/c2cp23940j.
62. Shepherd, H. J.; Tonge, G.; Hatcher, L. E.; Bryant, M. J.; Knichal, J. V.; Raithby, P. R.; Halcrow, M. A.; Kulmaczewski, R.; Gagnon, K. J.; Teat, S. J. A High Pressure Investigation of the Order-Disorder Phase Transition and Accompanying Spin Crossover in [FeL12](ClO4)2 (L1 = 2,6-Bis{3-Methylpyrazol-1-Yl}-Pyrazine). *Magnetochemistry* **2016,** *2* (1), 9. https://doi.org/10.3390/magnetochemistry2010009.
63. Mikolasek, M.; Manrique-Juarez, M. D.; Shepherd, H. J.; Ridier, K.; Rat, S.; Shalabaeva, V.; Bas, A. C.; Collings, I. E.; Mathieu, F.; Cacheux, J.; Leichle, T.; Nicu, L.; Nicolazzi, W.; Salmon, L.; Molnár, G.; Bousseksou, A. Complete Set of Elastic Moduli of a Spin-Crossover Solid: Spin-State Dependence and Mechanical Actuation. *J. Am. Chem. Soc.* **2018,** *140* (28), 8970–8979. https://doi.org/10.1021/jacs.8b05347.
64. Tailleur, E.; Marchivie, M.; Itié, J. P.; Rosa, P.; Daro, N.; Guionneau, P. Pressure-Induced Spin-Crossover Features at Variable Temperature Revealed by in Situ Synchrotron Powder X-Ray Diffraction. *Chem. A Eur. J.* **2018,** *24* (54), 14495–14499. https://doi.org/10.1002/chem.201802828.
65. Grosjean, A.; Négrier, P.; Bordet, P.; Etrillard, C.; Mondieig, D.; Pechev, S.; Lebraud, E.; Létard, J. F.; Guionneau, P. Crystal Structures and Spin Crossover in the Polymeric Material [Fe(Htrz)2(Trz)](BF4) Including Coherent-Domain Size Reduction Effects. *Eur. J. Inorg. Chem.* **2013,** *2* (5–6), 796–802. https://doi.org/10.1002/ejic.201201121.
66. Pillet, S. Spin-Crossover Materials: Getting the Most from x-Ray Crystallography. *J. Appl. Phys.* **2021,** *129* (18), 181101. https://doi.org/10.1063/5.0047681.
67. Tao, J.; Wei, R.-J.; Huang, R.-B.; Zheng, L.-S. Polymorphism in Spin-Crossover Systems. *Chem. Soc. Rev.* **2012,** *41* (2), 703–737. https://doi.org/10.1039/C1CS15136C.
68. Roubeau, O. Triazole-Based One-Dimensional Spin-Crossover Coordination Polymers. *Chem. A Eur. J.* **2012,** *18* (48), 15230–15244. https://doi.org/10.1002/chem.201201647.
69. Enríquez-Cabrera, A.; Ridier, K.; Salmon, L.; Routaboul, L.; Bousseksou, A. Complete and Versatile Post-Synthetic Modification on Iron-Triazole Spin Crossover Complexes: A Relevant Material Elaboration Method. *Eur. J. Inorg. Chem.* **2021,** *2021* (21), 2000–2016. https://doi.org/10.1002/EJIC.202100090.
70. Niel, V.; Martinez-Agudo, J. M.; Muñoz, M. C.; Gaspar, A. B.; Real, J. A. Cooperative Spin Crossover Behavior in Cyanide-Bridged Fe(II)-M(II) Bimetallic 3D Hofmann-Like Networks (M = Ni, Pd, and Pt). *Inorg. Chem.* **2001,** *40* (16), 3838–3839. https://doi.org/10.1021/ic010259y.
71. Garcia, Y.; Niel, V.; Muñoz, M. C.; Real, J. A. Spin Crossover in 1D, 2D and 3D Polymeric Fe(II) Networks. In *Spin Crossover in Transition Metal Compounds I*; 2004, vol. 233; pp 229–257. https://doi.org/10.1007/b95408.
72. McPherson, J. N.; Hogue, R. W.; Akogun, F. S.; Bondi, L.; Luis, E. T.; Price, J. R.; Garden, A. L.; Brooker, S.; Colbran, S. B. Predictable Substituent Control of CoIII/II Redox Potential and Spin Crossover in Bis(Dipyridylpyrrolide)Cobalt Complexes. *Inorg. Chem.* **2019,** *58* (3), 2218–2228. https://doi.org/10.1021/acs.inorgchem.8b03457.
73. Dova, E.; Stassen, A. F.; Driessen, R. A. J.; Sonneveld, E.; Goubitz, K.; Peschar, R.; Haasnoot, J. G.; Reedijk, J.; Schenk, H. Structure Determination of the [Fe(Teec)6](BF4)2 Metal Complex from Laboratory and Synchrotron X-Ray Powder Diffraction Data with Grid-Search Techniques. *Acta Crystallogr. Sect. B Struct. Sci.* **2001,** *57* (4), 531–538. https://doi.org/10.1107/S010876810100828X.
74. Lakhloufi, S.; Tailleur, E.; Guo, W.; Le Gac, F.; Marchivie, M.; Lemée-Cailleau, M.-H.; Chastanet, G.; Guionneau, P. Mosaicity of Spin-Crossover Crystals. *Crystal* **2018,** *8* (9), 363. https://doi.org/10.3390/CRYST8090363.
75. Phonsri, W.; Macedo, D. S.; Davies, C. G.; Jameson, G. N. L.; Moubaraki, B.; Murray, K. S. Heteroleptic Iron(III) Schiff Base Spin Crossover Complexes: Halogen Substitution, Solvent Loss and Crystallite Size Effects. *Dalton Trans.* **2017,** *46* (21), 7020–7029. https://doi.org/10.1039/C7DT00947J.
76. Phonsri, W.; Macedo, D. S.; Vignesh, K. R.; Rajaraman, G.; Davies, C. G.; Jameson, G. N. L.; Moubaraki, B.; Ward, J. S.; Kruger, P. E.; Chastanet, G.; Murray, K. S. Halogen Substitution Effects on N2O Schiff Base Ligands in Unprecedented Abrupt FeII Spin Crossover Complexes. *Chem. A Eur. J.* **2017,** *23* (29), 7052–7065. https://doi.org/10.1002/CHEM.201700232.
77. Bousseksou, A.; Molnár, G.; Real, J. A.; Tanaka, K. Spin Crossover and Photomagnetism in Dinuclear Iron(II) Compounds. *Coord. Chem. Rev.* **2007,** *251* (13–14), 1822–1833. https://doi.org/10.1016/J.CCR.2007.02.023.
78. Hogue, R. W.; Singh, S.; Brooker, S. Spin Crossover in Discrete Polynuclear Iron(Ii) Complexes. *Chem. Soc. Rev.* **2018,** 7303–7338. https://doi.org/10.1039/c7cs00835j.
79. Kusz, J.; Spiering, H.; Gütlich, P. X-Ray Study of the Light-Induced Metastable State of a Spin-Crossover Compound. *J. Appl. Cryst.* **2000,** *33* (2), 201–205. https://doi.org/10.1107/S0021889899014739.
80. Marchivie, M.; Guionneau, P.; Howard, J. A. K.; Chastanet, G.; Létard, J. F.; Goeta, A. E.; Chasseau, D. Structural Characterization of a Photoinduced Molecular Switch. *J. Am. Chem. Soc.* **2002,** *124* (2), 194–195. https://doi.org/10.1021/JA016980K.

81. Money, A. V.; Evans, I. R.; Halcrow, M. A.; Goeta, A. E.; Howard, J. A. K. Light Induced Excited High Spin-State Trapping in [FeL 2](BF 4) 2 (L = 2,6-Di(Pyrazol-1-Yl)Pyridine). *Chem. Commun.* **2003**, (1), 158–159. https://doi.org/10.1039/B210146G.
82. Pillet, S.; Bendeif, E. E.; Bonnet, S.; Shepherd, H. J.; Guionneau, P. Multimetastability, Phototrapping, and Thermal Trapping of a Metastable Commensurate Superstructure in a FeII Spin-Crossover Compound. *Phys. Rev. B: Condens. Matter Mater. Phys.* **2012,** *86* (6), 1–11. https://doi.org/10.1103/PhysRevB.86.064106.
83. Seredyuk, M.; Muñoz, M. C.; Castro, M.; Romero-Morcillo, T.; Gaspar, A. B.; Real, J. A. Unprecedented Multi-Stable Spin Crossover Molecular Material with Two Thermal Memory Channels. *Chem. A Eur. J.* **2013,** *19* (21), 6591–6596. https://doi.org/10.1002/chem.201300394.
84. Wolf, M. M. N.; Groß, R.; Schumann, C.; Wolny, J. A.; Schünemann, V.; Døssing, A.; Paulsen, H.; McGarvey, J. J.; Diller, R. Sub-Picosecond Time Resolved Infrared Spectroscopy of High-Spin State Formation in Fe(II) Spin Crossover Complexes. *Phys. Chem. Chem. Phys.* **2008,** *10* (29), 4264–4273. https://doi.org/10.1039/B802607F.
85. Smeigh, A. L.; Creelman, M.; Mathies, R. A.; Mccusker, J. K. Femtosecond Time-Resolved Optical and Raman Spectroscopy of Photoinduced Spin Crossover: Temporal Resolution of Low-to-High Spin Optical Switching. *J. Am. Chem. Soc.* **2008,** *130,* 14105–14107. https://doi.org/10.1021/ja805949s.
86. Gallé, G.; Etrillard, C.; Degert, J.; Guillaume, F.; Létard, J. F.; Freysz, E. Study of the Fast Photoswitching of Spin Crossover Nanoparticles Outside and Inside Their Thermal Hysteresis Loop. *Appl. Phys. Lett.* **2013,** *102* (6), 063302. https://doi.org/10.1063/1.4792527.
87. Wolny, J. A.; Diller, R.; Schünemann, V. Vibrational Spectroscopy of Mono- and Polynuclear Spin-Crossover Systems. *Eur. J. Inorg. Chem.* **2012**, (16), 2635–2648. https://doi.org/10.1002/ejic.201200059.
88. Enachescu, C.; Hauser, A.; Girerd, J. J.; Boillot, M. L. Photoexcitation and Relaxation Dynamics of Catecholato–Iron(III) Spin-Crossover Complexes. *ChemPhysChem* **2006,** *7* (5), 1127–1135. https://doi.org/10.1002/CPHC.200500671.
89. Galí, G.; Deldicque, D.; Degert, J.; Forestier, T.; Ĺtard, J. F.; Freysz, E. Room Temperature Study of the Optical Switching of a Spin Crossover Compound inside its Thermal Hysteresis Loop. *Appl. Phys. Lett.* **2010,** *96* (4), 041907. https://doi.org/10.1063/1.3294312.
90. Azzolina, G.; Collet, E.; Mariette, C.; Cammarata, M.; Trzop, E.; Sander, M.; Levantino, M.; Nakagawa, K.; Tokoro, H.; Ohkoshi, S. I.; Bertoni, R. Single Laser Shot Photoinduced Phase Transition of Rubidium Manganese Hexacyanoferrate Investigated by X-Ray Diffraction. *Eur. J. Inorg. Chem.* **2019.** https://doi.org/10.1002/EJIC.201801478.
91. Chergui, M.; Collet, E. Photoinduced Structural Dynamics of Molecular Systems Mapped by Time-Resolved X-Ray Methods. *Chem. Rev.* **2017,** *117,* 11025–11065. https://doi.org/10.1021/acs.chemrev.6b00831.
92. Vankó, G.; Renz, F.; Molnár, G.; Neisius, T.; Kárpáti, S. Hard-X-Ray-Induced Excited-Spin-State Trapping. *Angew. Chem. Int. Ed.* **2007,** *46* (28), 5306–5309. https://doi.org/10.1002/anie.200604432.
93. Lecomte, C.; Aubert, E.; Legrand, V.; Porcher, F.; Pillet, S.; Guillot, B.; Jelsch, C. Charge Density Research: From Inorganic and Molecular Materials to Proteins. *Z. Krist.* **2005,** *220* (4), 373–384. https://doi.org/10.1524/zkri.220.4.373.61623.
94. Pillet, S.; Legrand, V.; Weber, H. P.; Souhassou, M.; Létard, J. F.; Guionneau, P.; Lecomte, C. Out-of-Equilibrium Charge Density Distribution of Spin Crossover Complexes from Steady-State Photocrystallographic Measurements: Experimental Methodology and Results. *Z. Krist.* **2008,** *223* (4–5), 235–249. https://doi.org/10.1524/zkri.2008.0023.
95. Granier, T.; Gallois, B.; Gaultier, J.; Real, J. A.; Zarembowitch, J. High-Pressure Single-Crystal x-Ray Diffraction Study of Two Spin-Crossover Iron(II) Complexes: Fe(Phen) 2(NCS)2 and Fe(Btz)2(NCS)2. *Inorg. Chem.* **2002,** *32* (23), 5305–5312. https://doi.org/10.1021/IC00075A058.
96. Guionneau, P.; Marchivie, M.; Garcia, Y.; Howard, J. A. K.; Chasseau, D. Spin Crossover in [MnIII(Pyrol)3tren] Probed by High-Pressure and Low-Temperature x-Ray Diffraction. *Phys. Rev. B: Condens. Matter Mater. Phys.* **2005,** *72* (21). https://doi.org/10.1103/PHYSREVB.72.214408/FIGURES/1/THUMBNAIL.
97. Manrique-Juárez, M. D.; Rat, S.; Salmon, L.; Molnár, G.; Quintero, C. M.; Nicu, L.; Shepherd, H. J.; Bousseksou, A. Switchable Molecule-Based Materials for Micro- and Nanoscale Actuating Applications: Achievements and Prospects. *Coord. Chem. Rev.* **2016,** 395–408. https://doi.org/10.1016/j.ccr.2015.04.005.
98. Cavallini, M.; Bergenti, I.; Milita, S.; Kengne, J. C.; Gentili, D.; Ruani, G.; Salitros, I.; Meded, V.; Ruben, M. Thin Deposits and Patterning of Room-Temperature-Switchable One-Dimensional Spin-Crossover Compounds. *Langmuir* **2011,** *27* (7), 4076–4081. https://doi.org/10.1021/la104901m.
99. Tanaka, D.; Aketa, N.; Tanaka, H.; Tamaki, T.; Inose, T.; Akai, T.; Toyama, H.; Sakata, O.; Tajiri, H.; Ogawa, T. Thin Films of Spin-Crossover Coordination Polymers with Large Thermal Hysteresis Loops Prepared by Nanoparticle Spin Coating. *Chem. Commun.* **2014,** *50* (70), 10074–10077. https://doi.org/10.1039/c4cc04123b.
100. Rubio-Giménez, V.; Bartual-Murgui, C.; Galbiati, M.; Núñez-López, A.; Castells-Gil, J.; Quinard, B.; Seneor, P.; Otero, E.; Ohresser, P.; Cantarero, A.; Coronado, E.; Real, J. A.; Mattana, R.; Tatay, S.; Martí-Gastaldo, C. Effect of Nanostructuration on the Spin Crossover Transition in Crystalline Ultrathin Films. *Chem. Sci.* **2019,** *10* (14), 4038–4047. https://doi.org/10.1039/c8sc04935a.
101. Fourmental, C.; Mondal, S.; Banerjee, R.; Bellec, A.; Garreau, Y.; Coati, A.; Chacon, C.; Girard, Y.; Jérô Me Lagoute, J.; Rousset, S.; Boillot, M.-L.; Mallah, T.; Enachescu, C.; Barreteau, C.; Yannick, J.; Dappe, J.; Smogunov, A.; Narasimhan, S.; Repain, V. Importance of Epitaxial Strain at a Spin-Crossover Molecule – Metal Interface. *J. Phys. Chem. Lett* **2019,** *10,* 34. https://doi.org/10.1021/acs.jpclett.9b01303.
102. Lemke, H. T.; Kjær, K. S.; Hartsock, R.; Van Driel, T. B.; Chollet, M.; Glownia, J. M.; Song, S.; Zhu, D.; Pace, E.; Matar, S. F.; Nielsen, M. M.; Benfatto, M.; Gaffney, K. J.; Collet, E.; Cammarata, M. Coherent Structural Trapping through Wave Packet Dispersion during Photoinduced Spin State Switching. *Nat. Commun.* **2017,** *8* (1), 1–8. https://doi.org/10.1038/ncomms15342.
103. Jiang, Y.; Liu, L. C.; Müller-Werkmeister, H. M.; Lu, C.; Zhang, D.; Field, R. L.; Sarracini, A.; Moriena, G.; Collet, E.; Miller, R. J. D. Structural Dynamics upon Photoexcitation in a Spin Crossover Crystal Probed with Femtosecond Electron Diffraction. *Angew. Chem. Int. Ed.* **2017,** *56* (25), 7130–7134. https://doi.org/10.1002/ANIE.201702497.
104. Jiang, Y.; Liu, L. C.; Sarracini, A.; Krawczyk, K. M.; Wentzell, J. S.; Lu, C.; Field, R. L.; Matar, S. F.; Gawelda, W.; Müller-Werkmeister, H. M.; Miller, R. J. D. Direct Observation of Nuclear Reorganization Driven by Ultrafast Spin Transitions. *Nat. Commun.* **2020,** *11* (1), 1–8. https://doi.org/10.1038/s41467-020-15187-y.

10.05 EXAFS studies of inorganic catalytic materials

Lisa Allen[a,b], Miren Agote-Arán[a,b], Andrew M. Beale[a,b,c], Peixi Cong[a,b], Sofia Mediavilla-Madrigal[b,d], and Stephen W.T. Price[c], [a] Department of Chemistry, University College London, London, United Kingdom; [b] Rutherford Appleton Laboratory, Harwell Science and Innovation Campus, Research Complex at Harwell, Didcot, United Kingdom; [c] Rutherford Appleton Laboratory, Harwell Science and Innovation Campus, Finden Ltd., Didcot, United Kingdom; and [d] Cardiff Catalysis Institute, School of Chemistry, Cardiff University, Cardiff, United Kingdom

© 2023 Elsevier Ltd. All rights reserved.

10.05.1	**Introduction**	**109**
10.05.2	**Background**	**109**
10.05.2.1	X-ray absorption near edge structure (XANES)	110
10.05.2.2	Extended X-ray absorption fine structure (EXAFS)	111
10.05.2.3	XAFS data acquisition	112
10.05.2.3.1	Scanning mode	112
10.05.2.3.2	Energy dispersive EXAFS (EDE) mode	113
10.05.2.4	Data analysis	114
10.05.2.5	Sample environment	115
10.05.2.5.1	Cells for gas-solid reactions	115
10.05.2.5.2	Cells for electrochemical reactions	115
10.05.2.5.3	Cells for grazing incidence measurements	116
10.05.2.5.4	Cells for gas-liquid and gas-liquid-solid reactions	116
10.05.3	**Supported catalysts**	**116**
10.05.3.1	Catalysts for CO_2 hydrogenation	117
10.05.3.1.1	Supported catalysts measured at atmospheric pressure	117
10.05.3.1.2	Supported catalysts measured at elevated pressures	118
10.05.3.2	Palladium catalysts for emissions abatement	122
10.05.3.2.1	Rationalizing the effect of the preparation method on properties and performance	122
10.05.3.2.2	Active state of Pd revealed under in situ and operando conditions	123
10.05.3.3	Interrogation of bimetallic species	127
10.05.3.3.1	Catalyst self-assembly	127
10.05.3.3.2	Selective oxidation using bimetallic catalysts	127
10.05.3.3.3	Noble metal promotion of Cobalt reduction in Co Fischer-Tropsch catalysts	128
10.05.3.3.4	Selective hydrogenation using bimetallic single atom catalysts (SACs)	128
10.05.3.4	Using EXAFS to determine metal particle size and shape	130
10.05.3.5	Catalysis using ions of low nuclearity	130
10.05.3.6	EXAFS in combination with other techniques	132
10.05.3.6.1	Combined XAFS/vibrational spectroscopic study of catalyst synthesis and reaction	132
10.05.3.6.2	Combined XAFS/UV-vis study of catalyst synthesis and reaction	133
10.05.3.6.3	Combined XAFS/XRD	133
10.05.3.7	Catalysis in the liquid phase	133
10.05.3.8	XAFS and electrochemistry	134
10.05.3.8.1	Hydrogen evolution reaction (HER)	135
10.05.3.8.2	Oxygen evolution reaction (OER)	136
10.05.3.8.3	Oxygen reduction reaction (ORR)	137
10.05.3.8.4	CO_2 reduction reaction (CO_2RR)	138
10.05.4	**Obtaining more information on the state of the catalyst**	**139**
10.05.4.1	Imaging studies	139
10.05.4.2	Novel analysis methods for determining active species present	140
10.05.4.2.1	Post reaction data analysis methods	140
10.05.4.2.2	Modulation excitation methods	141
10.05.5	**Conclusions and future perspectives**	**141**
References		**143**

Abstract

Extended X-ray Absorption Fine Structure or EXAFS spectroscopy is commonly used to characterize inorganic materials and in particular, those used in heterogeneous catalysis. This chapter begins by introducing the EXAFS technique including a brief history of its development, the theory behind it, sample environments, data analysis routines and limitations. What then follows is the main body of the work where select examples are presented from literature which demonstrate the power of the technique to characterize catalytic active sites comprising single site (ions/atoms), clusters, nanoparticles and even bulk structures in attempt to show the scope of what is possible with the EXAFS technique as far as the determination of catalyst structure-activity relationships where thermal and electrocatalytic reactions are concerned. The chapter concludes with a summary of the current state of the art as well as an outlook of what is on the horizon as far as the technique is concerned.

10.05.1 Introduction

Improvement to a given system is often driven by the knowledge of how it functions. Although this may not be applicable to the British weather, the statement is certainly true for catalyst science. There are numerous examples of how techniques applied for real time (i.e., in situ and *operando*) catalyst characterization have enabled the identification of pertinent structure-activity relationships upon which improvements in catalyst performance can be based. Techniques can of course be classified in many ways but perhaps the most common is to delineate techniques into those that characterize the catalyst and those which characterize the adsorbates. X-ray absorption fine structure spectroscopy (XAFS) falls very much into the former classification and in this chapter, we highlight the benefits that this technique brings to this field with particular focus on the extended part of the spectrum more commonly referred to as Extended X-ray Absorption Fine Structure (EXAFS). EXAFS is well suited to the interrogation of catalytic materials since it provides qualitative and quantitative local structure information (i.e., coordination, bond distance and oxidation state) on active components present at 'catalytic concentrations' (typically $\sim$ % wt. loadings). Furthermore, the highly penetrating nature of the 'hard (i.e., >4 keV)' incident X-rays lends the technique to being employed in combination with a number of sample environments that enable high time ($<$s) and spatial resolution ($\sim$nm). At the time of writing this chapter there are thought to be 40 beamlines (mid-2022) capable of performing EXAFS measurements on catalytic samples, many of which now possess integrated gas delivery systems for intimate control of the sample environment. The beamlines have also been designed with modularity in mind and are therefore amenable to the housing of a range of reactor cells for studying (reacting) solids, liquids and gases and often in combined mode (e.g., with powder XRD, optical spectroscopies, thermal analysis, etc.). This renders it an underpinning technique for catalyst characterization such that it is now common to include EXAFS data in many of the prominent studies of the structure of catalytic materials. This chapter begins with an introduction to the theory, instrumentation and analysis methods used to record and interpret XAFS data before moving on to use exemplars to demonstrate the type of insight that can be obtained from these measurements. The Chapter concludes with a discussion of what the future holds for the technique particularly in light of the development of 4th generation synchrotron light sources offering greater brightness and coherence.

10.05.2 Background

X-ray absorption spectroscopy (XAS) or XAFS (the terms are used interchangeably) is an element specific analytic technique which is used for determining the local geometric and electronic structure of matter. In the field of catalysis, XAFS is a powerful tool for elucidating the nature and evolution of active species.[1]

The experiments require an intense and tunable source of X-rays since this is beneficial for signal quality, the volume of information that can be obtained and the breadth of materials that can be studied. Therefore, XAFS measurements are usually performed at synchrotron radiation sources and the history and development of this technique has occurred in parallel to that of synchrotrons.

The X-ray absorption phenomenon probes the transitions from a core electron of an atom to excited states. When the incident X-ray has energy I equal to the binding energy of a core electron of a given element, absorption of the radiation occurs; this results in the ejection of the core electron to a higher energy orbital or to the continuum, and the formation of a core hole.[2] The attenuation of X-ray intensity is proportional to the absorption characteristics of the material, the sample path length of the radiation and the incident intensity as shown in Eq. (1). After integration over the path length, the Beer Lambert equation, Eq. (2), can be obtained, Eq. (2):

$$\Delta \mathrm{I} = \mathrm{I}(E)\mathrm{I}_0\mathrm{d}x \tag{1}$$

$$\mathrm{I} = \mathrm{I}_0\mathrm{e}^{-\mu \mathrm{E}x} \tag{2}$$

wIe $\mu(E)$ is the absorption coefficient function of the photon energy, dx is the path length and I_0 incident X-ray intensity. $\mu(E)$ is proportional to the dipole transition probability between the initial and final state wavefunctions according to Fermi's Golden Rule.[3]

Following the absorption process, the atom is left in an excited state. This excited state has a limited lifespan known as the core-hole lifetime after which the system decays by emitting electrons (Auger effect) and photons (X-ray fluorescence). The details of the

emission phenomena are out of the scope of this chapter but it is of importance to point out that the intensity of fluorescence emission (released when electrons in the upper level fill the core-holes) is approximately proportional to the absorption coefficient.[2] The fluorescence detection is therefore systematically used in beamlines as an X-ray absorption measurement method (i.e., fluorescence detected XAFS). Naturally one can also use it to detect the photo- or secondary Auger electrons but as these tend to have a low mean free path due to being absorbed by the atmosphere, these detection methods tend to be used mainly in vacuo.[4]

In a typical XAFS measurement, spectra are collected by scanning the incident X-ray energy over a sample. The resulting absorption spectra exhibit a monotonic intensity decrease with increasing incident X-ray energy, this decrease is approximately proportional to $1/E$.[3] When the incoming photons reach an energy sufficient to excite an electron from a core level of an element, a rise in $\mu(E)$ occurs. This rise is known as the absorption edge and the energy of incident X-ray at which the edge occurs is known as E_{edge} or E_0. The absorption edges are named according to their associated electronic transitions. Thus, edges corresponding to transitions from the inner-most electronic shells—i.e., principal quantum—number (n) = 1—are termed K-edges, transitions from the second shell ($n = 2$) are known as L-edges, from third shell ($n = 3$) are denoted as M-edge and so on.[2]

At the E_{edge} the core electrons are excited to a vacant orbital; the kinetic energy (E_k) of the excited electron at the absorption edge is known as E_0 or inner potential. For any energy above E_{edge}, the core electron is excited to the continuum resulting in a photoelectron with kinetic energy given by Eq. (3):

$$\mathrm{E_k} = h\nu - \mathrm{E_{binding}} \tag{3}$$

where h is the Plank's constant, ν the frequency of the photoelectron and $E_{binding}$ is the minimum energy required for ejecting a core electron.

The photoelectron can be described as a spherical wave function with wave vector, k, as shown in Eq. (4). The photoelectron outgoing from an atom backscatters off the neighboring atoms; both the ongoing and backscattered waves interfere with each other and the resulting final wave function ($\Phi_j(k)$) is a sum of both (Eq. 5).[5]

$$k = \sqrt{\left(\frac{8\pi^2 m_e}{h^2}\right)(h\nu - E_0)} \tag{4}$$

$$\Phi_j(k) = \Phi_{outgoing} + \Phi_{backscattered} \tag{5}$$

where m_e is the electron mass.

The interference between the two waves can be constructive or destructive and determines the variation in $\mu(E)$ above $\mathrm{E_{edge}}$. This variation causes the characteristic oscillations of $\mu(E)$ in the XAFS spectra known as X-ray absorption fine structure (XAFS).[6]

Thus, an XAFS spectrum is typically divided into two regions: (1) the region that lies within the first 30–50 eV of the edge position is usually referred as X-ray Absorption Near Edge Structure (XANES), and (2) the spectral region beyond 50 eV above the absorption edge including the fine structure which is termed as Extended X-ray Absorption Fine Structure (EXAFS).

Both spectral regions give complementary information; XANES is sensitive to the coordination chemistry and formal oxidation state of the absorbing atom whereas EXAFS can be used to determine the distance, coordination number and the nature of the absorber's nearest neighboring atoms. An example of an X-ray absorption spectrum is shown in **Fig. 1** together with a schematic representation of the X-ray absorption and photoelectron scattering phenomena.

10.05.2.1 X-ray absorption near edge structure (XANES)

The absorption edge for a given element arises due to electronic transitions from the core level to higher unfilled or partially filled orbitals. These electronic transitions have to obey the dipole selection rule: changes in the orbital quantum number (l) has to be ± 1 (i.e., $s \rightarrow p$, or $p \rightarrow d$).[7] Thus, the edge absorption and XANES features will be strongly related to the availability of final states and therefore to the electronic structure of the element under study.

Transition metal oxides have unfilled $3d$ orbitals or bands near the Fermi level and a filled $3p$ band. A $1s \rightarrow 3d$ electronic transition is dipole forbidden ($\Delta l = 2$), nevertheless the transition is allowed in case of strong hybridization of the metal $3d$ levels with the oxygen $2p$; this results in a well-defined peak below the main absorption edge which is known as a pre-edge peak. The pd hybridization is markedly affected by the coordination environment. Hence, the features and intensity of the pre-edge peak give insights regarding the coordination symmetry of the absorbing atom.

The empty states or bands above the Fermi level in a compound are also sensitive to the atomic valence. This allows for the determination of the oxidation state through analysis of the absorption edge position.

Furthermore, XANES spectra can be used as fingerprint to identify the phases present in the sample provided that spectra of relevant reference compounds are also acquired or available. Quantitative analysis of different species is possible by linear combination fitting (LCF) analysis of known reference spectra or by principal component analysis (PCA).

As discussed later, the EXAFS region, arising mainly from single scattering effects, can be theoretically predicted and modelled through computational methods to refine the structural information of the absorbing atom. This is not however, the case for the XANES region. The near-edge features are governed by multiple scattering effects where the photoelectron is scattered several times by different neighboring atoms before returning to the absorbing atom. Multiple scattering effects are sensitive to small variations in structure and in principle, it should be possible to use XANES for the determination of an element's local environment. Although

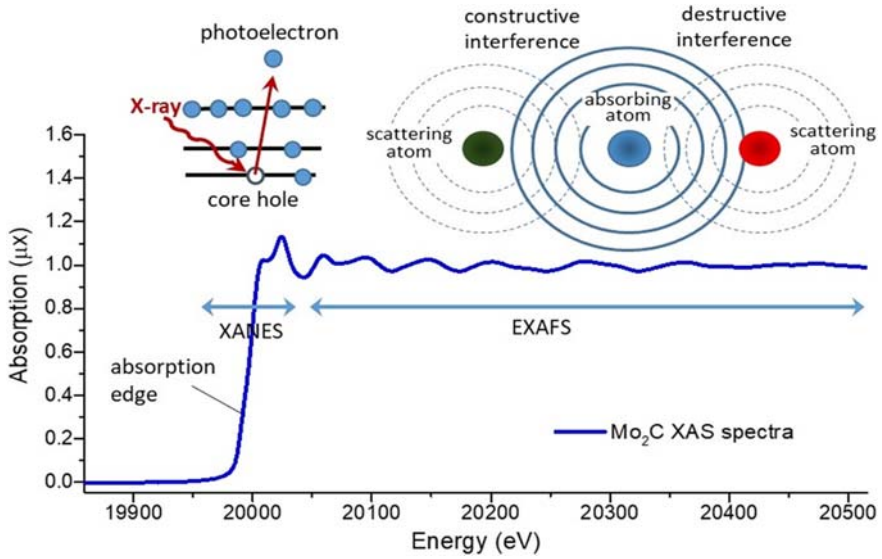

Fig. 1 XAFS spectrum of Mo_2C at the Mo—K edge where the edge position, XANES and EXAFS spectral regions are indicated. Above the spectra schematic representations of the fundamentals of X-ray absorption phenomena are depicted. These include the ejection of a core electron upon the absorption of X-rays (top left) and the scattering the photoelectron as a spherical wave (top right). The out-going wave is depicted in solid blue circles and the scattered in dashed ones.

there has been progress in the theoretical interpretation of XANES spectra, this is still not widely applied for detailed characterization as the analysis is more computationally demanding.[8]

10.05.2.2 Extended X-ray absorption fine structure (EXAFS)

As explained earlier in this section, the EXAFS spectrum arises from the interference of the ongoing and the backscattered photoelectron. This interference pattern is dependent on the number, distance and nature of the scattering atoms. Thus, the EXAFS contains information regarding the local structure of the absorbing atom that can be obtained by theoretical methods.

To extract the structural information from the EXAFS a mathematical expression is used which relates the photoelectron scattering effect with the structural parameters. A theoretical EXAFS is then modelled and fitted to the real spectra for the refinement of these parameters.

For the derivation this mathematical expression, the EXAFS is given as a function of wave vector, $\chi(k)$ defined as the normalized part of the absorption coefficient μ as shown in Eq. (6).

$$\chi(k) = (\mu - \mu_0)/\mu_0 \tag{6}$$

Where μ is the observed absorption coefficient, and μ_0 is the absorption observed in the absence of neighbor atoms and scattering effects (i.e., smooth background function representing the absorption of an isolated atom).[6]

The simplest and most used EXAFS equation, Eq. (7), was derived by Stern, Sayers, and Lytle and is based on the single-scattering plane wave approximation.[9]

$$\chi(k) = S_0^2 \sum_j \frac{N_j A_j}{r_i^2} e^{\left(-\frac{2r_j}{\lambda}\right)_e \left(-2\sigma_j^2 k^2\right)} sin\left[2kr_j + 2\Phi_j(k)\right] \tag{7}$$

where $S_0{}^2$ is the so-called amplitude reduction factor, λ is the photoelectron mean-free path, the sum over i runs over the different coordination shells around the absorbing atom, $A_j(k)$ is the backscattering amplitude function of the scattering atom, $\Phi_j(k)$ is the phase function of the couple absorber/scatterer (Eq. 5), N_i is the coordination number, r_i is the interatomic distance and σ_i is the Debye-Waller factor that quantifies the disorder of each i shell.[10,11]

In this approximation the photoelectron is viewed as a plane wave and it assumes that the atomic radii is much smaller than the inter-atomic distances. Therefore, the equation is valid only for k values above 3. This derivation also assumes that single scattering effects dominate (i.e., the photoelectron is only scattered once before returning to the absorbing atom).

$A_j(k)$ and $\phi_j(k)$ functions in Eq. (7) are tabulated or calculated ab initio by data processing software. Alternatively, they could be measured independently on model compounds. Then the structural parameters N_j, r_j and $\sigma_j{}^2$, can be determined in a least-squares approach where the difference between the experimental and the modelled function is minimized using least squares regression along the sampled experimental points.[6] The minimization routine can be done either in k-space, or in R-space, working on the Fourier transformed (FT) function. The FT of the EXAFS functions, a breakthrough for the technique when first used in early

1970, separates the contributions of the different coordination shells in R-space by transforming the data from frequency domain into a space domain.[9] Indeed this is nowadays typically how EXAFS data are displayed—the radial distribution (shown in Fig. 2) providing information on the number and distance of the nearest neighbors, typically limited to the first 3–4 Å from the absorber due to the r_i^2 term shown in Eq. (7). Two points of note are: (a) the contributions representing the absorber-scatter distances appear shorter than the Pauling ionic radii due to the phase-shift experienced by the photo-electron as it leaves the absorber and scatters off the near neighbors and (b) contributions shorter than those distances are not due to the structure but have been ascribed to electronic effects.[6]

10.05.2.3 XAFS data acquisition

10.05.2.3.1 Scanning mode

XAFS measurements can nowadays be performed at a number of synchrotron facilities around the world. Using B_{18} beamline at Diamond Light Source in Harwell, United Kingdom as an exemplar, the bending magnet beamline comprises fast scanning double crystal monochromators that select the energy of the incident beam E according to the Bragg's equation.[12] The most commonly used crystal planes are Si(111) and Si(311) with d values of 3.1356 and 1.6375 Å, respectively. These are used to tune the incident energy around the adsorption edge of interest (typically K and L edges). Spectra can be acquired in transmission mode by using three ion chambers measuring: the incident intensity (I_0), the intensity of the beam after passing through the sample (I_t) and the intensity of the beam after passing through a metal foil (I_{ref}). A metal foil corresponding to the element being measured is placed between I_t and I_{ref} and serves as reference for calibration of the data. In transmission mode the number of X-ray photons absorbed by core electrons to create a photoelectron and a core-hole is counted.

Transmission mode is widely used for XAFS collection as it results in best spectra quality. Nonetheless, such mode requires a sample thickness that ensures enough X-ray transmission and an absorption edge jump of ~ 1 (see Eq. 8). Catalytic materials usually comprise multiple elements; the total absorption coefficient μ of a sample can be calculated as follows:

$$\mu \approx \rho N \sum_i \frac{n_i}{N} \sigma_i \tag{8}$$

where ρN is the number density of the material as a whole, and ni/N number fraction of element I and Si the absorption cross section of at given energy. A good example illustrating the change in μ and its dependence on sample composition (loss or gain of atoms) was recently reported by Lomachenko et al. this work also demonstrating the high sensitivity of the technique.[13] Note energy-dependent cross-section data can be found in the following reference.[14]

It is not always possible to measure diluted samples (i.e., where the weight of the element of interest is present below 1%) in transmission mode and it can be particularly challenging in operando studies where the sample dimensions should also fulfil specific reaction conditions. When this is not feasible, catalysts can be interrogated instead in fluorescence mode. In this mode a multi-element solid state detector (typically comprised of Si or Ge) is placed at 90° relative to the X-ray beam path to detect the sample fluorescence radiation (I_f). As fluorescence photon flux is approximately proportional to the absorption coefficient of the element being proved, I_f detection allows for acquisition of XAFS spectra. The statement on the proportionality of fluorescence intensity to μ(E) is only valid in the limiting case of thin film or very dilute samples. For thick and concentrated samples, an energy-

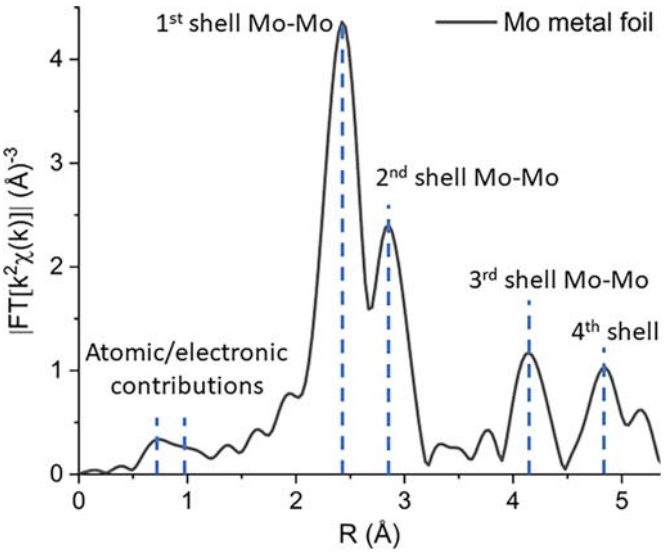

Fig. 2 Fourier Transform radial distribution function of a phase uncorrected metal foil recorded at the Mo K-edge illustrating the nearest neighbor contributions or shells of the hexagonal close packed (hcp) structure.

dependent reduction in intensity (i.e., fluorescence XAFS) termed self-absorption occurs.[15] The reduction in intensity depends on the depth that the incident X-ray beam can penetrate the sample. That is, as the oscillatory EXAFS signal hits its maximum, the penetration depth dwindles, and as the signal hits the minimum, the depth increases. This results in XAFS spectra whose intensities are suppressed affecting the reliability of the information that can be derived from them. For samples where it is not possible to prepare them in such a way so as to avoid self-absorption, there are algorithms to correct the subsequent data. For example the XAFS data reduction program Athena offers four different algorithms for correcting this self-absorption effect, namely Fluo, Booth, Troger, and Atoms algorithm.[5] While all four are suitable for EXAFS data correction, only the Fluo algorithm is suitable for XANES data.

Increasingly, XAFS studies are being performed in dedicated setups to perform experiments in situ or else under *operando* conditions by simultaneously recording XAFS spectra and reactor gas composition.[16] These setups, available at a number of beamlines typically utilize quartz capillaries <3 mm in radial diameter as a micro-reactor. Samples are plugged in the capillary and fixed with quartz wool.[17] The setup also comprises a gas delivery system for the micro-reactor which includes switching valves and mass flow controllers to adjust the reactant flow over the catalyst bed. The gas outlet is connected to an online gas analysis system (such as mass spectrometer, gas chromatograph or Fourier transform infra-red spectrometer). Additional features (heated lines, pressure controllers etc.) can be placed if the experiment requires. A hot air source is used to control the sample temperature up to 780 °C while the micro-reactor is located on a motorized stage which can be remotely adjusted to place the catalyst bed on the X-ray beam path. As an example, **Fig. 3** below depicts an experimental setup for operando XAFS measurements in transition and fluorescence mode.

10.05.2.3.2 Energy dispersive EXAFS (EDE) mode

An alternative way to collect data is in Energy Dispersive EXAFS (EDE) mode, where a fixed bent crystal monochromator is typically used to provide a focused X-ray beam containing all the energies required to make an XAFS measurement. The bent crystal monochromator can be employed in either the Laue (transmission) or Bragg (reflection) geometry using silicon (1 1 1, 2 0 0 or 3 1 1) monochromators with the latter being the most frequently used.[18,19] Whole spectra are collected on position sensitive detectors and since the technique is normally located on undulator beamlines, the high flux enables data acquisition in ms or faster. Since there are no moving parts, the beam is also considered to be very stable in terms of energy (0.01 eV) and position (150 nm). For the purpose of this chapter, it is worth highlighting how EDE has been successfully employed to study rapid changes (s – ms time resolution) in nanoparticle composition as a result of changes in gas composition/gas adsorption in three-way catalysts (TWC). Crucial to the understanding of the adsorbate-induced changes in the supported nanoparticles was the coupling of EDE with Diffuse Reflectance Fourier Transform Infra-Red Spectroscopy (DRIFTS) and online Mass Spectrometry to obtain simultaneous multi-technique characterization data recorded from the same reaction cell.[20] Studies have been used for example to understand the redox kinetics of supported Rh/Rh_2O_3 nanoparticles, understanding how these kinetics are affected by the nature and properties of the support and the formation of sub-structures and intercalation compounds in supported Pd systems (studied as powders or electrodes) as function of both time and space (reactor bed profile).[21] In addition, some of the best examples of studying complexes undergoing

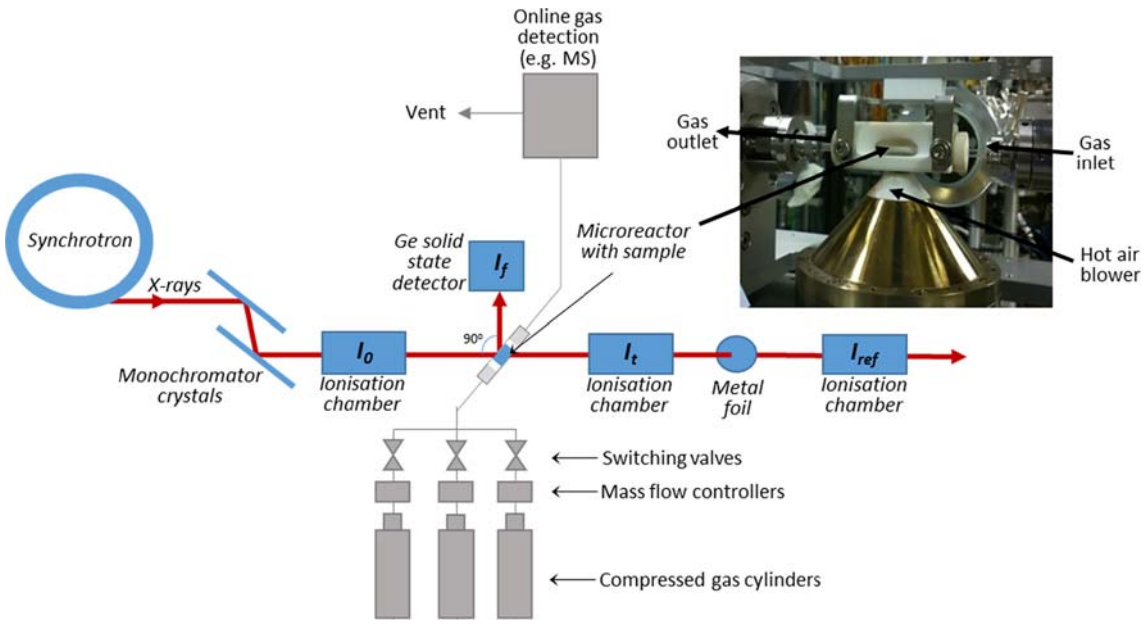

Fig. 3 Schematic representation of an operando setup for measuring XAFS in transmission mode (using three ionization chambers for the detection of I_o, I_t and I_{ref}) or in fluorescence mode (using a solid state detector perpendicular to the beam path for the detection of I_f). The schematic includes the gass delivery system (i.e., pressurized gas cylinders, switching valves and mass flow controllers), a micro-reactor, and an online gass detection system. A picture of the microreactor and gas blower for sample temperature control available in B_{18} beamline is included in the top right corner.

reactions (or deactivation) in the liquid phase involve the application of EDE and often in conjunction with UV-vis.[22,23] One should be mindful however that EDE delivers a very large energy dose to the system under study and which is concentrated into a small area.[24] This can lead to unwanted side-effects that are not always obvious to predict or understand.[24,25]

EDE for catalysis research is perhaps less popular than it used to be as the time resolution available on beamlines operating in scanning mode improves (many are now routinely operating at >1 Hz). Furthermore since there is no parallel collection of I_0 during data acquisition, normalization is more challenging and EXAFS data more difficult to extract.[18] The technique still offers big advantages in some fields of research, particularly high pressure physics and chemical imaging and with the possibility to obtain data with a time resolution in the microsecond or even faster this technique may still play a role in catalytic science.[26]

10.05.2.4 Data analysis

There are a number of programs for XAFS data processing but by far the most popular is the Demeter IFEFFIT software package comprising Athena and Artemis.[5,27] Recently, programs have been also developed for fast spectra processing to facilitate the handling of large datasets resulting from time resolved operando measurements.[28] The first stage in XAFS spectra processing comprises several steps such as: (1) deglitching, (2) background removal of fitting pre-edge, (3) normalization of the edge jump intensity, (4) determination of the edge position (E_0) using the maximum of the first derivative or the energy at half-step height, (5) calibration by assigning the E_0 of the metal foil spectra and correcting for the E_0 offset on the sample spectra, (6) isolation of the EXAFS by removing the contributions of the free atom absorption in the post edge by applying a spline function and, (7) Fourier transform of the EXAFS to obtain a radial distribution function which serves as guidance into the distance of the neighboring atom.

Once isolated, the raw $\chi(k)$ is often weighted by k^n (with $n = 1,2,3$) to compensate for the reduction in EXAFS amplitude in the high k range. The value of n can also be helpful in distinguishing different types of scatterer contributions (atoms, ions) since the backscattering amplitude determines the k response. An element of low nuclear charge (Z) will scatter mainly at low k-values, while heavy elements will scatter significantly at higher k-values. Furthermore, a window function such as the Hanning window or Kaiser-Bessel window is applied to the data to suppress signals with low values of k (the XANES region) as well as those regions possessing a high value of k (mostly noise).

With the EXAFS oscillations appropriately isolated the fitting the EXAFS formula (Eq. 7) can be performed allowing for the least squares refinement of the coordination number (N), interatomic distance (r), the Debye Waller factor (σ^2) and the shift in edge energy (E_0); the objective here is to reduce the difference between a theoretical structural model of the data and the data itself. This is determined by a measure of the goodness of fit between the two datasets. In the early stages of XAFS analysis, the common approach to determine the nature of the environment around the absorber relied on the comparison of obtained XAFS data with those for reference materials. This spectral comparison or fingerprinting had many disadvantages, chief among them being a possible lack of a suitable reference material to compare against and secondly an inability to differentiate subtle differences between samples/datasets which leaves the analysis subjective to bias. On the other hand, EXAFS scattering amplitude and phase shift can also be obtained from theoretical calculations. This approach allows analysis of EXAFS data from in situ, or under *operando* conditions else for the interrogation of meta-stable materials, where suitable standards are not available. Furthermore, this approach also provides a reliable way to account for multiple scattering contributions. Using the path expansion method used by FEFF (and the Demeter software package) as an example, the theoretical calculations accept inputs (i.e., the starting model) as a list of Cartesian coordinates of atoms. A list of scattering paths is enumerated from the starting model, first the single scattering paths, followed by the multiple scattering paths. These paths are sorted by increasing half-path length (i.e., the interatomic distance r_j) and given an important factor which represents the spectral weight of each path generated. Then the effective scattering amplitude and the effective phase shift are computed based on the muffin-tin potentials. Using the calculated terms (scattering amplitude and phase shift) and modelled terms (coordination number, interatomic distance, etc.), Eq. (7) are evaluated, and the result is compared to the data. The fitting software employs a Levenberg-Marquardt least-squares non-linear minimization algorithm. A residual function is computed from each data point between the model calculation and the observed data (for a k-space fit). For a fit that is evaluated in the R-space, the residual function is calculated with the difference between both the real and imaginary parts of the Fourier-transformed data and the model calculation. The modelled parameters are varied until the residual function is minimized (calculated spectra best match the observed one).

To evaluate the goodness of fit, fitting statistics such as R-factor R and reduced chi-square ${\chi_\nu}^2$ are introduced by the EXAFS analysis software. R-factor is often interpreted as percentage misfit and viewed as how close the fit overlaps with the data. The quality of the fit, on the other hand, is represented by ${\chi_\nu}^2$ and it measures the closeness of the fitted function to the data by the unused information content. This parameter allows one to compare the quality of fit produced by different models, such as the question that does the introduction of an extra fitting parameter improves the overall quality of the fit (not just considering how it improves the misfit). Small values for R and ${\chi_\nu}^2$ certainly contribute to a defensible fit. Nevertheless, the fitted parameters also must not take non-physical values, and the fitted model needs to be *chemically* meaningful e.g., bond distances cannot be shorter than the sum of the individual tabulated radii.[29]

Critical then to obtaining a meaningful analysis of the data is a good starting model since the technique does not provide Ab initio insights and furthermore, the least squares analysis procedure does not readily permit the exploring of large deviations in structural space. As can be seen in Eq. (7), this is further complicated by the strong correlation between the components that contribute to the amplitude of the EXAFS signal (N_j, and ${\sigma_j}^2$) and to a lesser extent the E_0 and r_j. Fitting can be performed on the isolated EXAFS in k-space or after FT. Only when fitting is performed in k-space are the original EXAFS data actually being fitted

and therefore can be readily deciphered in terms of the information contained in Eq. (7). Fitting in r-space in contrast offers no such guarantees and is more susceptible to analysis without structural meaning. In either case data fitting is concluded when there is a close match between raw and modelled data in both k- and r-space. It is generally understood that information contained in the EXAFS phase i.e., interatomic distances (r_j) can be determined with a higher accuracy and precision than the components that give rise to the amplitude (N_j, and σ_j^2). It is possible to derive multiple distances and coordination numbers although there is a maximum number (n_{ind}) of these independent parameters that can be analysed by fitting of the EXAFS equation which has been defined using the well-known Nyqvist theorem shown in Eq. (9)[30]:

$$n_{ind} = 2 + \frac{2\Delta k \Delta R}{\pi} \tag{9}$$

where Δk is the examined k-space range and ΔR the R-space range containing the optimized shells. The components that comprise Eq. (9) can also be used to determine the capability of EXAFS to resolve contributions from two different scattering contributions (Eq. 10), although in practice it is likely that this represents a best-case scenario, with the technique struggling to resolve similar distances that are less than 0.15 Å.[10,31]

$$\Delta R \geq \frac{\pi}{2\Delta k} \tag{10}$$

From our experience of EXAFS analysis is that the technique is largely tractable where the element of the local structure being probed has a $Z \geq$ Mn and where the that of the near neighbors $Z \geq 6$.[32] When the Z of the absorber is lower than this, poor scattering from the comparatively low energy outgoing photoelectron renders it very difficult to obtain reliable near neighbor distances and in particular the coordination numbers. The same 'effect' is observed for an increasing incident energy although this time due to a diminishing scattering cross-section of the nearest neighbor. Higher incident energies are required for probing higher Z elements and the higher nuclear charge leads to increased core-hole lifetime and a greater number of multi-electron excitations leading to signal broadening which also renders near neighbor information difficult to obtain.[33] Some elements, particularly those in the first group of the periodic table, are already plagued by multiple excitations rendering EXAFS data and local structure impossible to obtain without significant experimental efforts to correct for these effects.[34]

10.05.2.5 Sample environment

10.05.2.5.1 Cells for gas-solid reactions

The XAFS community has been highly active and innovative in the development of suitable sample environments to obtain 'meaningful' data on catalyst samples and were thus at the forefront of innovation in terms of studying samples under in situ and more latterly *operando* conditions. Gas cells are readily available for the study of pellets, disks, powders, coatings etc. often at elevated temperatures and pressures (50 bar) with many of these cells also permitting multi-technique sample interrogation.[35–37] Whilst for ex situ measurements, free-standing pellets are primarily used, the micro capillary reactor (internal diameters typically ranging between 0.5 mm and 3.0 mm) has become the sample cell of choice for the study of reacting gases mainly because it is more suitable for operando studies; although the acquired data is typically less clean (due to pinholes and capillary curvature) than that acquired from pellets there are fewer problems with gas diffusion (particularly dead volume) which allows for good correlation between changes in gas composition and the evolving spectra as well as such conditions being more akin to the industrial environment being mimicked as some of the exemplars below nicely illustrate.[38,39] Sample heating is usually achieved through unidirectional hot-air blowers in these setups although variants do exist where heating is achieved through either induction or else hot rods in close proximity to the sample, the former heating method allowing temperatures $>1200\ ^\circ C$ to be reached. Many EXAFS beamlines nowadays possess intricate gas delivery systems so that alongside sample temperature, gas composition switching can be controlled remotely and even pre-programmed with the data acquisition rendering complicated operando studies now widely available.[36] In that regards, developments in multi-tubular, 'high-throughput' reactors is particularly timely as this will allow for obtaining a large number of data under near identical conditions allowing more intimate evaluation and correlations to be made between the acquired data.[40]

Another advantage of the capillary cell is that it is typically available in both horizontal and vertical geometries and has therefore been successfully applied in imaging studies as well as more conventional single point measurements.[41,42]

10.05.2.5.2 Cells for electrochemical reactions

Similar considerations are made for in situ/*operando* electrochemical cells where again the design must maintain a balance between achieving high quality XAFS data with good (electrochemical) performance, for example minimizing any overpotential that can occur when deviating from an optimized electrochemical cell. Often in situ electrochemical cells require smooth electrolyte flow over a thin layer to minimize beam absorption and to prevent localized electrolyte heating/outgassing. This has been brought into sharper focus by more recent studies focusing on water splitting which necessitate operation at potentials where gas is evolved, and so the removal of this is required to maintain a stable beam path through electrolyte otherwise signal quality degrades at potentials where gas is evolved.[43]

Many designs are based on a modular thin layer configuration, with flexibility to change window material/thickness, reference, counter and working electrode contacts, and can accommodate a range of both aqueous and non-aqueous electrolytes.[44] The

advantageous configurations of these cells facilitate both the use of different collection modes e.g., transmission and fluorescence XAFS, and also the use of multiple synchrotron based techniques. For example, studies by Wise and Binninger used in situ electrochemical cells to study catalysts with XAFS in combination with XRD and SAXS respectively (albeit not with simultaneous data collection).[44,45] Similar cells may also be used for photoelectrochemical/photoelectrocatalytic systems such as for water splitting.

The thin layer design of many of these in situ electrochemical cells works well when looking at half cells, i.e., following the reaction at a single electrode. However, additional cell design considerations apply when looking at entire devices e.g., operating fuel cells. These can include the need for elevated temperatures and humidification of gas streams, awareness of the stability of the polymer electrolyte membrane found within fuel cells to prolonged beam exposure, compromises in flow plate design/thickness to enable beam penetration, interference with the XAFS signal of the electrode of interest by the catalyst on the other electrode in cell e.g., if anode and cathode have Pt catalysts then the XAFS signal will be a combination of both therefore a different (e.g., Pd based) catalyst may be used for the electrode not being studied. Recent studies on functional electrocatalytic devices include those on fuel cell studies and gas diffusion electrodes within Zn-air batteries.[46]

10.05.2.5.3 Cells for grazing incidence measurements

Electrochemical XAFS studies often require the characterization of catalyst layers or films be they contiguous or else a dispersion of nanoparticles necessitating a different approach to sample interrogation to obtain information on the physicochemical state of the surface.[47] This information can be obtained under Grazing Incidence conditions (GI) which the incident X-ray beam impinges on the sample at a shallow angle to study the sample surface, ideally $\sim 1^{\circ}$ so as to create an evanescent wave which probes only the first few nm in depth. Grazing incidence XAFS is capable of revealing intricate information on the state and morphology of supported nanoparticles even when they make comprise a tiny fraction of the total component to be measured.[48] Specialized dome reactor environments are available for such studies which, depending on the dome material, can reach temperatures and pressures in the order of a few 100 s of °C.[49] The comparatively low volume of active species can however make activity difficult to determine unless the catalytic reaction under study is simple. There have however been some very elegant studies combining GIXANES with advanced data interrogation methods to determine the evolution of the state of Cu and the structural change in the Cu_xPd_y clusters during propane oxidation.[50]

10.05.2.5.4 Cells for gas-liquid and gas-liquid-solid reactions

Studies in the liquid phase are rare due to inherent complexities of delivering reactants in this kinetic state as well as the sensitivity of the catalyst/solvent to the incident X-ray beam. For the study of supported catalysts, batch reactor cells have been developed in which the catalyst sample is retained at the bottom of the cell and which allows for interrogation in fluorescence mode (simultaneously with Attenuated Total Reflection-IR (ATR-IR)).[51] Although the data are somewhat noisy, it is still possible to determine the redox state of the catalyst and link this with product yields. If the reactants are volatile enough they can be delivered in the gas phase either via passing a carrier gas over a reservoir or else controlled injection dosing via heated transfer lines.[52] This has the advantages of improving the signal-to-noise in the data as well as allowing for real time monitoring of the catalyst performance ultimately allowing for a better understanding of structure activity relationships. When the catalyst and reactants/solvent are in the same kinetic state an entirely different approach is required and typically exploits stop-flow or continuous flow conditions. The former setup has been used commonly for studying the early stages (ms − s) of a catalytic reaction, often requiring energy dispersive methods and in combination with techniques like UV-vis spectroscopy.[22,53] The possibility to perform the same experiment many times renders the stop-flow approach attractive for studying the very initial stages of a catalytic reaction although these have fallen somewhat out of favor when compared to continuous flow setups which are better suited to mitigating the high energy load on the sample.[54] It is more difficult to obtain the sorts of initial kinetic data with continuous flow setups however.[53]

In order to demonstrate the power and possibilities of the EXAFS technique, we have selected a series of case studies which span the typical materials used and their catalytic application. Three of the sections are particularly detailed as they represent what we determine to be particularly vibrant and important areas of study currently. Each section begins with a preamble setting the scene before delving more deeply into the studies and learnings in the wider context of the research topic.

10.05.3 Supported catalysts

The material at the cornerstone of heterogeneous catalysis comprising nanoparticles of metals and metal oxides at weight concentrations $\leq 5\%$, on a high surface area oxide.[55] As discussed previously, such materials are prime candidates for interrogation using the EXAFS technique since the parameters of active site 'size' and redox state known to vary with catalytic performance can be readily examined often in real time. This combination of prominence of the material and the suitability of the technique to probe these parameters means that EXAFS has a long history and will continue to remain a very popular technique for catalyst characterization. With time, the availability of beamlines, infrastructure for sample preparation and sample mounting and software for data processing has resulted in EXAFS being available to an increasingly wider number of users.

As mentioned above, EXAFS has proven particularly powerful for characterizing the composition (i.e., metallic, oxidic, sulfidic) and to a latter extent the morphology of supported nanoparticles, clusters and atoms (ions) and can often be used to better understand nebula properties such as metal-support interactions (MSI) which can have a big influence on catalyst performance[56,57]. The MSI manifests itself in a number of ways for example, affecting the shape/morphology of the supported component, their electronic

state and the formation of an interfacial region between metal and support (in extreme cases leading to metal-support compounds such as mixed oxides or alloys) which has been proposed as the active zone in some high profile catalytic studies.[58] It has been used for example to determine when the Strong Metal Support Interaction (SMSI) occurs leading to alterations in catalytic performance.[59] Unfortunately direct interactions of reactants/intermediates involved in the catalytic process are not normally detectable. This is primarily because even when the supported metal nanoparticles are small (≤ 1 nm) it is difficult to unambiguously determine which adsorber has induced a change in an oxidation state; for example in Fischer-Tropsch Synthesis, a change in the oxidation state of cobalt nanoparticles could be due to adsorption of CO, H_2 (dissociated), water or else due to Co_2C formation.[60] We say 'not normally' since it is possible to pare back the experiment and dose with one gas at a time (i.e., CO) but identifying the intermediate structure only really becomes tractable when the metal species possess a low nuclearity, so for example, ions in porous materials.

10.05.3.1 Catalysts for CO_2 hydrogenation

CO_2 utilization has generated considerable interest over the last few decades. Anthropogenic Carbon emissions have grown exponentially, leading to severe environmental effects, such as the increment of the average global temperature and the acidification of the oceans. Technology for the capture and subsequent conversion of this greenhouse gas into higher value-added chemicals is currently under development. Copper-based catalysts are commonly used in such conversion reactions from lab to industrial scale. However, recent studies have shown that other (bi and multi)metallic formulations could further enhance the activity and selectivity of CO_2.[61] In this context, X-ray techniques have attracted widespread interest due to their ability to provide insights into even a single catalyst particle's or site's local coordination arrangement to determine its active and/or inactive phases. This remarkable feature allows to follow the changes in arrangement structure and link them to the catalytic activity performance of said catalysts under a variety of experimental conditions, which ultimately aims to improve catalytic efficiency by manipulating the composition of these catalysts and tailoring it to the process needs. This section gives an overview of several past studies which make use of such techniques to characterize metallic catalysts used for methanol synthesis on their own or in combination with other imaging methods.

10.05.3.1.1 Supported catalysts measured at atmospheric pressure

One of the earliest EXAFS studies on methanol synthesis catalysts was performed by the Haldor Topsøe Research group, where Grunwaldt et al. studied copper on zinc oxide/alumina catalysts (hereby denoted as Cu/ZnO) in situ, combining both X-ray diffraction (XRD) and X-ray absorption fine structure spectroscopy (XAFS) techniques to follow the evolution of the copper geometry and electronic structure during reduction and reaction.[62] Moreover, in situ quick-EXAFS (qEXAFS) measurements were performed to track dynamical changes in the catalysts.

During the temperature-programmed reduction of the CuO/ZnO precursor, qEXAFS were recorded above the Cu K-edge at different temperatures together with in situ XRD diffractograms after reduction. Simultaneously, reduction activity was monitored by on-line mass spectrometric analysis. The latter revealed that the catalyst starts to reduce at approximately 180 °C, as shown by the uptake of hydrogen and production of water. EXAFS spectra corroborated this; the magnitude of the peak attributed to the Cu−O ($\sim$2.0 Å) shell decreased with increasing reduction temperature, leading to its disappearance at 220 °C, while a new peak representing the first Cu−Cu shell developed at larger distances ($\sim$2.5 Å). Moreover, the shift to lower energies of the Cu edge and the disappearance of the distinct rising absorption edge intensity ascribed to oxidic Cu after reduction observed in raw qEXAFS data substantiated the formation of Cu metal nanoparticles at around 200 °C. After reduction at 220 °C, EXAFS and XRD data were collected and analyzed to obtain information regarding the phase identity and the particle/crystallite size of such phases present in Cu/ZnO. Spectral data were fitted to obtain coordination numbers and atomic distances. Subsequently, the copper nanoparticle size was estimated to be around 10–15 Å which explained the absence of diffraction lines for metallic copper in the XRD patterns.

Under reaction conditions, changes in structure and activity as a function of the gas mixture reduction potential and composition were studied cycling "dry" and "wet" syngas depending on the gas mixture's water content. Online mass spectrometry data showed that the activity of the catalyst diminished when tested under wet synthesis gas (more reducing conditions) but increased significantly when tested once more under dry gas (more oxidizing conditions). In addition, upon changing from dry to wet syngas, the Cu−Cu shell coordination number increased and largely reverted to its previous value when the change was reversed (see Fig. 4). This was, however, more difficult to observe in XRD as a result of the very broad peaks recorded consistent with small Cu nanoparticles being present in the sample. Additionally, the morphology for the wetting/nonwetting of the Cu particles on the Zn support was modelled based on the changes observed by EXAFS, where more oxidizing conditions resulted in the formation of more spherically shaped Cu particles, whilst upon increasing the reduction potential, more disk-like particles were formed with higher Cu surface area. As the system was tested under increasingly harsher (i.e., 600 °C) reducing conditions, surface Zn−Cu alloying and, subsequently, brass alloy formation was expected.

To confirm whether alloying occurs in the Cu/ZnO system, further analysis of the EXAFS data was performed. Data showed that the Cu−Cu bond length remained constant, very close in value to Cu−Cu distances in metallic copper. In contrast, coordination numbers were observed to vary considerably as the system was subjected to the evolving reaction conditions. As a result, the authors concluded that the data recorded did not indicate a compelling case for the formation of bulk alloy since the Cu−Zn bond length in the alloy is predicted to be marginally longer (based on Zn possessing a larger atomic radius). Fitting of the EXAFS spectra with models comprising Cu and/or Cu−Zn were performed to clarify the effect of the closest neighbors on different clusters and then compared to bulk samples with various neighboring shells, namely bulk copper and Cu−Zn alternating shells. Analysis of the first

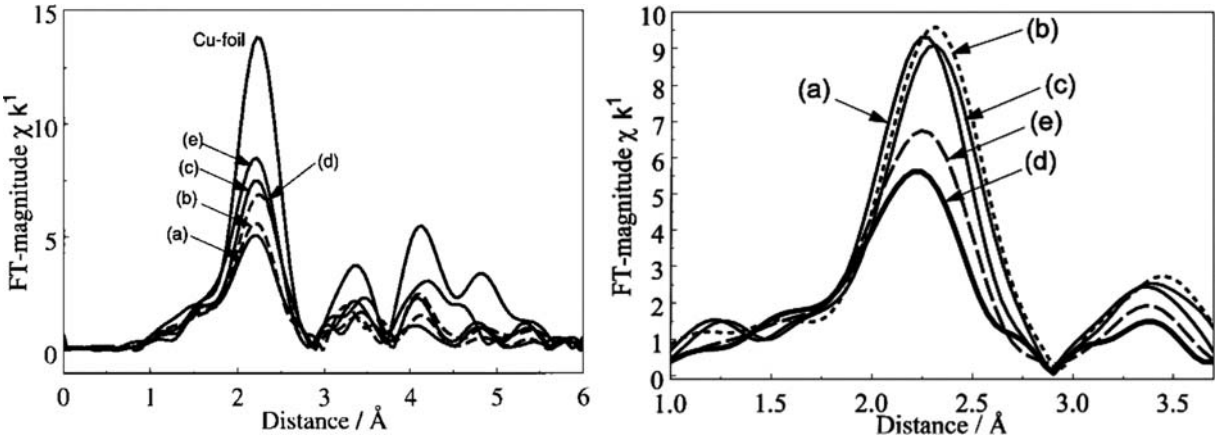

Fig. 4 (left) FT-RDF of the in situ EXAFS data at the Cu,K-edge of the Cu/ZnO catalysts, recorded: (a) in reduction gas; (b) after change to "dry" synthesis gas (1st cycle); (c) after change to "wet" synthesis gas (1st cycle); (d) after change to "dry" synthesis gas (2nd cycle); (e) after change to "wet" synthesis gas (2nd cycle). (right) FT-RDF at the Cu edge of (a) Cu/SiO_2, (b) Cu/ZnO, (c) $Cu_{68}Zn_{32}$, (d) Cu/ZnO (dry synthesis gas conditions at 220 °C, 1st cycle), and (e) Cu/ZnO (after reduction at 300 °C). Adapted with permission from Grunwaldt, J.D. et al. *J. Catal.* **2000** *194* (2), 452–460, Copyright 2000 Elsevier.

shell EXAFS contribution at the Cu K-edge and Zn edges was not able to differentiate between homonuclear and heteronuclear scattering since both atoms are next to each other in the periodic table and are therefore similar in size and possess similar X-ray scattering properties. Cu/SiO_2 was also reduced at high temperatures, and its FT radial distribution function (RDF) compared to the reduced Cu/ZnO. From this simple comparison it was clear that the main peak in the FT-RDF was shifted to larger distances in Cu/ZnO than for Cu/SiO_2 confirming alloy formation the former sample (Fig. 4). Comparing these spectra with the one recorded at reaction conditions did not reveal such a shift. Hence, the authors concluded that no substantial bulk alloying would likely occur at typical reaction temperatures (~220 °C). Lastly, the spectra collected at less harsh reduction conditions were compared to the spectra discussed before and FTIR results in the literature. Only the Cu–Cu coordination number was higher, and accordingly, larger Cu particle sizes were obtained as the reaction temperature was increased. Still, no peak shifts were observed in the FT-RDF, excluding one more time Zn-rich bulk alloy formation.

By utilizing combined techniques simultaneously, Grunwaldt and co-workers were able to obtain a more complete image of the catalyst structure as well as allowing them to establish meaningful structure-activity relationships. In particular, including in situ XAFS measurements in the experiment made the tracking of dynamical and structural changes possible since that would not otherwise be observed due to the limitation of the XRD technique to determine the presence of phases containing small particles with precision.

More recent studies on a similarly supported catalyst by H. Bahruji et al. also investigated the possibility of alloying after reduction by EXAFS data analysis.[63] Spectra of Pd/ZnO catalysts synthesized using different preparation methods were collected to study the changes in the Pd nanoparticles' nature in the system when subjected to different reduction temperatures. For those prepared by sol-immobilization and tested under mild reduction conditions (150 °C), no evidence of alloying with Zn was observed. The lower Pd–Pd coordination number seen in the Pd K-edge data, relative to that of bulk Pd actually suggests that Pd exists as small metallic nanoparticles. When the same system and a similar one synthesized by incipient wetness impregnation were treated at higher temperatures (400 °C), EXAFS data analysis demonstrated that alloying had occurred as the predominant contribution in the RDF, dominated by Pd–Pd scattering, appeared to shift to lower R-values at the same time a shoulder appeared at 2.85 Å; ergo instead of one peak due to Pd–Pd scattering, two peaks appeared which were assigned to a Pd–Zn scattering path (low R component), while the shoulder corresponded to a Pd–Pd path. These results indicated that Pd was present in two different environments; possibly a mixture of metallic Pd nanoparticles and as well as the presence of a β-PdZn alloy (also suggested by the XPS data). However, XRD data recorded separately to this, revealed only evidence for the β-PdZn alloy. When comparing results for the differing preparation methods, the coordination numbers for alloyed and non-alloyed Pd of the catalyst prepared using the impregnation method were greater and smaller, respectively, indicative of more extensive alloying in that system under harsh reduction conditions.

10.05.3.1.2 Supported catalysts measured at elevated pressures

The previous examples focused on in situ EXAFS experiments performed at atmospheric pressure but with time the capability to perform measurements at higher pressures has grown. The advantage is that it is now possible to observe any significant changes in the evolution of a catalyst structure in situ during for example CO_2 hydrogenation reactions, which are typically performed at elevated pressures, i.e., >20 bar gas, to effect a significant methanol yield; recent work has shown for example that 93% methanol yields can be obtained at 360 bar gas and operating temperatures ~260 °C.[64] Additionally, novel catalysts have been developed to

improve the efficiency of the reaction at an industrial scale, such as (Pd)In-based catalysts and where previous DFT studies indicated that the formation of oxygen sites on the In surface under reaction conditions was key in the activation and hydrogenation of CO_2.[65]

Snider et al. utilized in situ EXAFS under reaction conditions to discern the relationship between the In−Pd catalyst's properties and its catalytic performance.[66] EXAFS spectra of the In-Pd/SiO_2 catalyst samples synthesized by an impregnation method were collected after impregnation (i.e., catalyst synthesis), subsequent calcination, after reduction/activation in dilute hydrogen conditions and high-pressure reaction conditions (40 bar). Considering firstly the perspective from Pd, the FT-RDF of the catalysts after preparation (initial state) possessed a major peak at lower radial distances (2.01 Å) attributed to PdO (**Fig. 5**). The coordination numbers obtained from least squares fitting of the data structure among all samples are lower than that of bulk PdO, indicative of the materials' nanostructure. This phase, however, is wholly reduced as the reduction step takes place at mild temperatures (300 °C) and low pressures (5 bar). All catalysts share a similar feature corresponding to Pd bonded to either In or other Pd atoms since their *Z*-numbers differ by only 4 units and there is insufficient scattering contrast between them to allow deconvolution into two distinctive features. For the catalyst with higher In metal loading, the In contribution's distance (2.77 Å) was in agreement with In−Pd intermetallic compounds previously reported in the literature, while for those with lower In loading and higher Pd loading, this distance (2.75 Å) fell between that of metallic Pd (2.74 Å) and InPd alloy (2.81 Å). This implied that the In particles were not completely incorporated into the reduced phase. Upon switching to reaction conditions, i.e., mild temperatures and high pressures, spectra displayed again a complete reduction of the Pd phase. Simultaneously, the feature attributed to bonded Pd atoms shifted to higher atomic distances (2.76–2.77 Å) for all samples. Such increase coincided with the formation of the In−Pd alloy, whose atomic distance had been reported in past studies to be within the range of 2.76–2.80 Å in which the value obtained here (~2.77 Å) fits right over the lower bound. Smaller distances within this range (2.76–2.80 Å) are associated with more Pd-rich intermetallic phases or mixtures, suggesting that the samples tested consisted of some additional phases not observed here since XRD data were not recorded. Moreover, the shift to higher atomic distances (from 2.75 Å to 2.77 Å) showed that the incorporation of extra In particles into the intermetallic compound occurred under CO_2 hydrogenation conditions performed at higher pressure (40 bar). The coordination number among all the samples did, however, remain constant upon switching to reduction or reaction conditions and agreed with the nanoparticulate forms of the materials observed by other imaging techniques (i.e., TEM, etc.). It should be noted that even though the catalysts studied by Pd EXAFS differ in stoichiometry (In:Pd (2:1), (1:1) and (1:2)) and possessed different crystalline structures (i.e., (2:1) possessed primarily an In_3Pd_2 intermetallic structure, (1:1) a single InPd intermetallic one and (1:2) also a single InPd with some minor and more Pd-rich fcc structure), they seemed to be very much alike. This implied that the catalyst performance changes are induced by differences in the indium component rather than the palladium one. In situ In EXAFS data was thus collected under the same conditions described above.

Unlike with Pd, the In data revealed changes in the structure of the system (**Fig. 5**). After calcination, the peaks present in the FT as well as the fitting of the EXAFS data corresponded to those of indium oxide (In_2O_3), suggesting In was fully oxidized and in nanoparticulate form according to the coordination numbers obtained. Upon the introduction of hydrogen, the extent of reduction seems to vary among the different catalyst systems. As the Pd:In ratio was increased, the oxide peak contribution diminished while a new peak started to form at an atomic distance that closely matched that of the first In−Pd shell of a crystallographic PdIn alloy structure. Similar to the Pd case, this distance fell within the range enclosed by metallic Pd and In−Pd intermetallic compounds. With the subsequent co-introduction of CO_2 and increase in pressure to 40 bar, In was further reduced, leading to an intensity gain of the peak attributed to alloy formation relative to the oxide one. For those samples with lower Pd loading, it could be observed that they were composed of a mixture of oxide and intermetallic compounds, whilst the sample with the highest Pd loading only seemed to contain indium alloyed to palladium. The distance between the Pd and In for all bimetallic catalysts increased slightly (from 2.74–2.76 Å to 2.75–2.78 Å) upon switching to reaction conditions which was again in agreement with the values reported in the literature. This further proved that extra In would incorporate into the intermetallic compound under reaction conditions. Moreover, the In K-edge coordination numbers did not remain constant and thus provided some additional insights into the catalyst structure. Their values were smaller than those determined at the Pd K-edge, which the authors speculated to be caused by an enrichment of indium content at the surface.

In recent years and as *operando* X-ray capability has expanded, so has there been increasing examples of studies characterizing catalysts for methanol synthesis from CO_2 at high pressures. The studies allow researchers to correlate the evolution of catalyst nanoparticles during CO_2 hydrogenation with time on stream (TOS). A recent publication on this topic by Tsoukalou and coworkers, correlated the catalytic performance of as-prepared model monodispersed nanocrystalline In_2O_3 nanoparticles to morphology changes at both atomic and nanoscale levels during the reaction, studying the local environment surrounding In particles and the catalyst's crystallinity and phase composition respectively.[67] For this purpose, they performed a series of experiments differentiating three distinct catalytic regimes when the system was subjected to reaction conditions (300 °C, 20 bar), namely activation (TOS 0–50 min), stable performance (TOS 50–90 min), and deactivation (TOS 90 min onwards). They associated them with changes in particle properties measured by combined time-resolved *operando* XAFS and powder XRD. Data from XAFS-XRD experiments as well as GC spectra was collected quasi-simultaneously, as illustrated by **Fig. 6**. From changes in these data sets, it was possible to observe and determine how much the nanoparticles' chemical and structural characteristics evolve with TOS. More specifically, the local atomic structure was studied by analyzing FT-EXAFS spectra, which featured two peaks (centered at ca. 1.8 Å and 3.3 Å) at distances consistent with the In−O and the In−In shells. As with the previous study by Snider et al., the intensity of these peaks decreased as a function of time under reaction conditions, which was also made apparent by the changes in the shell coordination numbers (initially 5.5 for In−O and 4.5 for In−In) at the different stages of performance obtained by fitting. In the first stage, these peaks decreased slightly (CN decreased to 4.2 and 4.9, respectively), possibly due to the creation of oxygen

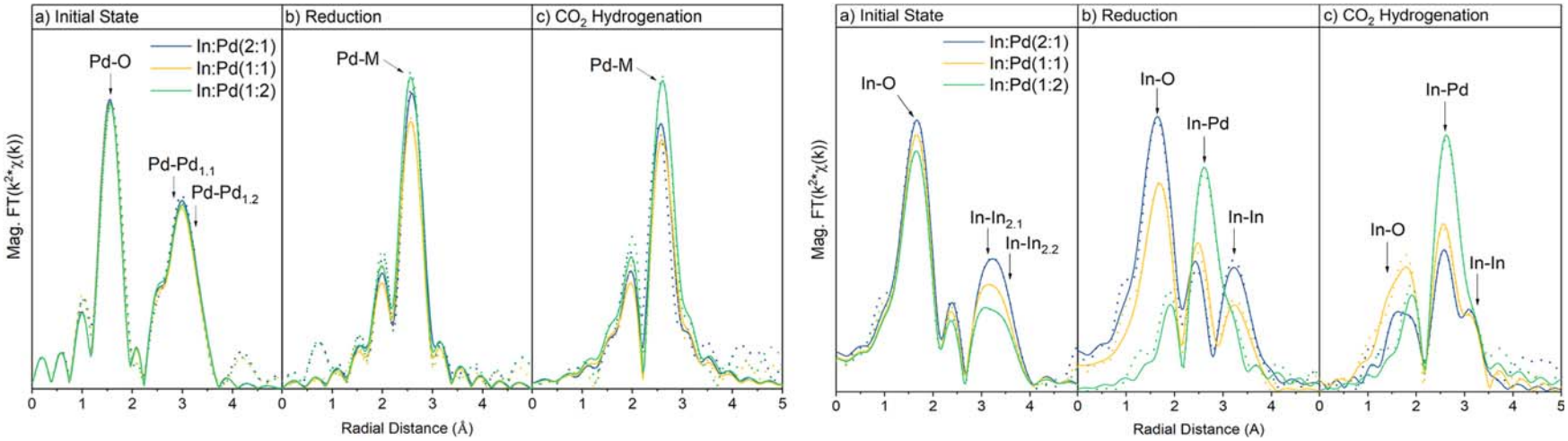

Fig. 5 In situ Pd K-edge EXAFS-FT (left) and In K-edge EXAFS-FT (right) collected on In–Pd/SiO_2 under: (a) initial conditions (25 °C, 1 bar, He), (b) reduction (300 °C, 5 bar, H_2), and (c) CO_2 hydrogenation (300 °C, 40 bar, 4/1 H_2/CO_2). In:Pd(2:1)/SiO_2 is shown in blue, In:Pd(1:1)/SiO_2 in yellow, and In:Pd(1:2)/SiO_2 in green. Dotted lines depict the experimental data, while the solid lines show the fit to the model. Adapted with permission from Snider, J. L.; Streibel, V.; Hubert, M. A.; Choksi, T. S.; Valle, E.; Upham, D. C. et al. ACS Catal. **2019**, *9* (4), 3399-3412, doi: 10.1021/acscatal.8b04848, Copyright 2019 American Chemical Society.

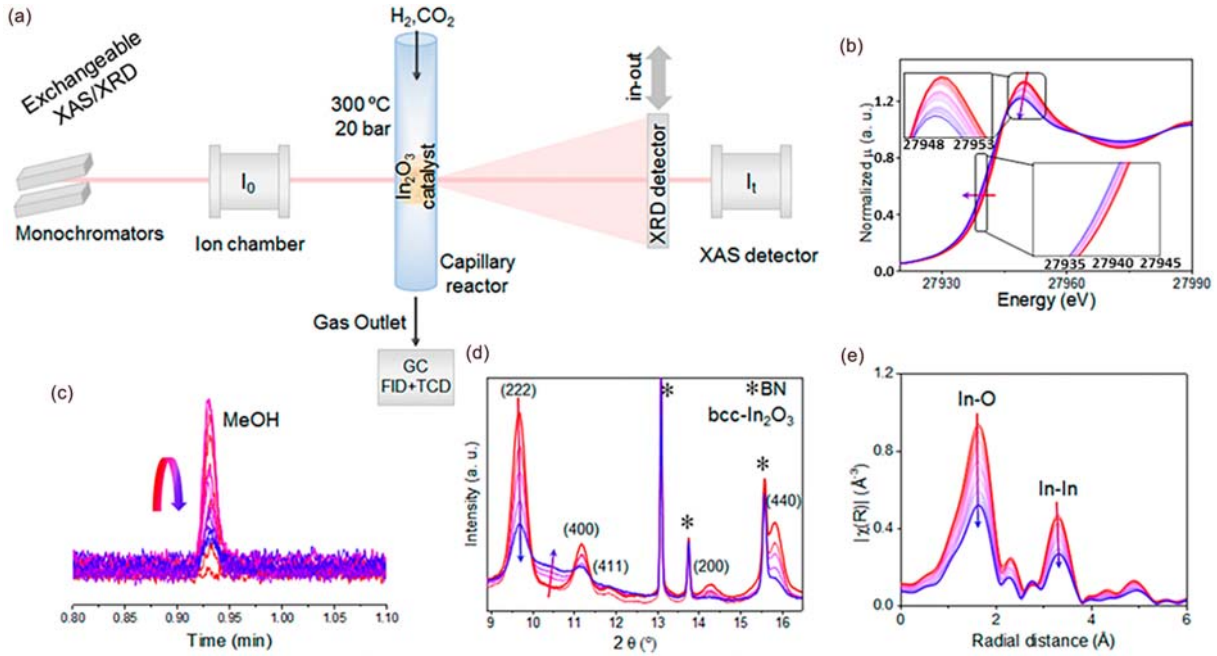

Fig. 6 (a) Schematic representation of the combined *operando* XAFS/XRD experiment at BM31 located in ESRF; (b) *operando* In K-edge XANES under reaction conditions; (c) a selection of gas chromatographs displaying the evolution of methanol produced with TOS; (d) XRD patterns indexing Bragg peaks of In_2O_3 and boron nitride; (e) FT-EXAFS spectra of the In_2O_3 NPs during reaction conditions. The arrows signal the direction of changes with TOS. Adapted with permission from Tsoukalou, A.; Abdala, P. M.; Stoian, D.; Huang, X.; Willinger, M.-G.; Fedorov, A. et al. Structural Evolution and Dynamics of an In_2O_3 Catalyst for CO_2 Hydrogenation to Methanol: An Operando XAS-XRD and In Situ TEM Study. J. Am. Chem. Soc. **2019**, *141* (34), 13497-13505, doi: 10.1021/jacs.9b04873, Copyright 2019 American Chemical Society.

vacancies. In contrast, the coordination numbers for both shells declined rapidly (down to 3.2 and 2.4, respectively) in the following stages, and a significant drop (CN as low as 1.7 and 1.3, respectively) was observed after 210 min. This phenomenon, which was ascribed to a reduction in the nanocrystallites' long-range order with TOS, occurred concurrently with the discovery of molten metallic In^0 by XANES analysis. Moreover, during the stable performance and deactivation stages, the applied model based on the In_2O_3 configuration used to fit the data did not match the spectra collected accurately. Still, when the contributions from metallic In shells (fitted at In−In distance of ca. 3.1 Å) were included, the fit's quality improved significantly. These results further underlined the importance of the presence of metallic In species as the catalyst begins to produce the desired methanol product. An additional reference XAFS-XRD experiment with metallic In powder was then performed to compare the local structure evolution of In in the molten state (melting point 156.6 °C) heating to 300 °C under a reductive atmosphere to avoid oxidation. Normalized and FT-EXAFS data showed a significant decrease in the intensity of the only peak present (In−In scattering contribution) when the temperature rises, leading to low In−In distances (2.9 Å), whilst In Bragg reflections due to crystalline In^0 disappeared in the XRD pattern. According to these conclusions, the authors suggested that the gradual formation of molten metallic indium may be partially correlated to the continuous decline in value of the In−In shell coordination number of the In_2O_3 crystal structure with TOS, proving that In^0 was present under CO_2 hydrogenation conditions.

Building on the activation/reaction study, the authors used XAFS-XRD to investigate regeneration of the deactivated catalyst bed via an oxidation under either air or CO_2. Passing CO_2 through the spent catalyst led to an increase in the intensity of the peaks assigned to the In−O and In−In shells, which yielded higher coordination numbers than the deactivated case (from 1.7 for In−O and 1.3 for In−In to 2.9 and 2, respectively). Upon switching the gas flow from CO_2 to air, the catalyst seemed to further regenerate based on the further rise in the coordination numbers' values (up to 3.8 and 3.1, respectively). However, these were significantly smaller in value than those calculated for as-prepared calcined In_2O_3 nanoparticles, thus indicating that the oxidative regeneration treatments performed were not able to fully re-oxidize the deactivated catalyst. XRD data analysis also revealed differences in the crystalline phases of the spent catalyst when subjected to CO_2 oxidation. The profile featured one narrow and a wider reflection attributed to bcc (body-centered cubic)-In_2O_3. Based on the broadness of these reflections, the crystallite size could be calculated for the former (ca. 6.5 nm) but not for the sharp component due to the instrument's inability to precisely probe large crystallites ($\geq$70 nm). This result suggested that despite having subjected the catalyst to oxidation, this did not lead to the complete recovery of the original size but the formation of larger In_2O_3 crystallites. In addition, very small partially reduced In_2O_3 nanocrystals were also preserved throughout, as shown by the presence of small, broad peaks overlapping with the sharp ones under all the different conditions tested.

Within the next few years, *operando* X-ray studies combined with other advanced imaging methods are likely to become an essential component in catalyst characterization. When applied simultaneously to monitor the evolution of a catalyst with TOS, it is

possible to obtain information about such catalysts under more realistic sample environments and more effectively examine the impact that atomic to nanoscale changes have on their activity.

10.05.3.2 Palladium catalysts for emissions abatement

The abatement of emissions from vehicles has never been so critical, and there is a great drive towards reducing pollution and reaching carbon neutrality across the world. The successful removal of harmful emissions such as NOx and particulate matter (PM) from diesel and gasoline powered engines using oxidation/reduction catalytic systems and in particular the application of the three-way catalyst (TWC) has already been well documented elsewhere.[68,69] However, as we enter a new era of energy conversion processes, the use of natural gas, where the main component is CH_4, is a promising alternative, long term option for the automotive industry as we move away from refined crude oil. CH_4 has a high energy mass density, and when used as an alternative fuel source, shows a reduction in released pollutants such as particulate matter and carbon dioxide (CO_2) and has the potential for a circular economy via biogas/biomethane.[70] As such recent focus has switched towards abatement technologies for CH_4 and CO removal and this has seen dramatic improvements in performance over the past few decades thanks to catalysis.[68,71]

Supported Pd catalysts in particular have shown excellent activity for the oxidation of CH_4 and CO, even within the same system (i.e., the same supported catalyst shows high efficacy for the amelioration of both) and where it is particularly remarkable that Pd can already activate the highly stable C−H bond of CH_4 below 500 °C.[72,73] However, the rationale behind this performance is still up for debate, with multiple active phases being reported, such as PdO, metallic Pd and mixed phase PdO_x being most prevalent in the literature.[74] X-ray characterization techniques, such as XAFS, are well suited for the study of these catalytic systems as the active Pd species are present at concentrations $< 1\%$ wt and ideally $< 0.5\%$. XAFS is perhaps the most appropriate technique to characterize the Pd species particularly under in situ/*operando* conditions, where the evolution of the evolving local environment in real time is necessary in order to correlate with catalytic performance. The value of this insight for this particular system beyond mechanistic insight allowing for eventual rational design concerns improved utilization of resources (atom efficiency), catalyst lifetime and resistance to poisoning. In this section, several studies that utilize XAFS to study supported Pd catalysts are reviewed, where in situ and *operando* studies that take advantage of the extended X-ray absorption fine structure (EXAFS) component are able to give insightful knowledge regarding the transformations of Pd during synthesis and catalysis.

10.05.3.2.1 Rationalizing the effect of the preparation method on properties and performance

The chosen synthetic method and conditions for a supported metal catalyst can have a great effect on the nanoparticles key traits, such as (nanoparticle) morphology, activity and stability. Therefore, it is critical to understand the effect of different preparation methods in order to obtain favorable structural sites towards reactions such as methane oxidation. In a recent effort, Dann et al. studied two 3% Pd/γ-Al_2O_3 catalysts prepared by incipient wetness impregnation using two different Pd precursor solutions: $Pd(NH_3)_4(OH)_2$ and $Pd(NO_3)_2$. The two catalysts were given the shorthand Pd/γ-Al_2O_3-ex(NH_3) and Pd/γ-Al_2O_3-ex(NO_3) respectively.[75] The calcination step of their synthesis was monitored by in situ XAFS and *operando* diffuse reflectance infrared Fourier-transform spectroscopy (DRIFTS) with mass spectroscopy (MS), in order to understand the local coordination environment of Pd in the bulk and the surface phenomena in tandem.

Post-calcination ex situ analysis from transmission electron microscopy (TEM), X-ray diffraction (XRD), Raman spectroscopy and Fourier-transform extended X-rays absorption fine structure (FT-EXAFS) indicated that the Pd/γ-Al_2O_3-ex(NH_3) catalyst had a smaller mean Pd nanoparticle size, 1.1–3.1 nm, compared to the $Pd(NO_3)_2$ precursor catalyst, 2.7–4.4 nm, and also had a lower light-off temperature (T_{50}, 380 °C compared to 390 °C) for methane conversion. Prior to calcination under in situ conditions, the room temperature FT-EXAFS spectra were also analyzed. The k^2-weighted EXAFS spectrum of the ammonia precursor catalyst was comparable to that of the precursor solution. A fitting model was used to determine that the coordination about the Pd center of the catalyst was consistent with a $[Pd(NH_3)_4]^{2+}$ complex being present. In contrast, the Pd/γ-Al_2O_3-ex(NO_3) catalyst required additional scattering paths from PdO, such as the second shell Pd−Pd scattering path, to fit the EXAFS data, where a tetrahedral PdO structure was observed.

During the DRIFTS experiment, assessment of the Pd/γ-Al_2O_3-ex(NH_3) catalyst versus the precursor solid showed a retention of the unique H−N−H vibrational modes, at 1490 cm^{-1} and 1345 cm^{-1}, up until 225 °C is reached, where gaseous N_2O was detected by the MS at the reactor outlet. This was attributed to the oxidation of surface NH_3 species, leaving behind N═O adsorbed to the γ-Al_2O_3 surface. Between 360 °C and 400 °C, gaseous NO is seen in the outlet. The Pd/γ-Al_2O_3-ex(NO_3) catalyst was compared with γ-Al_2O_3 treated with HNO_3, where both samples possessed broad asymmetric O−N−O stretching bands at 1320 and 1300 cm^{-1}, from room temperature to 100 °C. However, a narrowing and shift in the O−N−O stretching band of the Pd/γ-Al_2O_3-ex(NO_3) catalyst from 1300 cm^{-1} to 1270 cm^{-1} was observed between 100 °C and 200 °C, suggesting a bidentate nitrate coordination to a Pd(2+) metal center, seemingly consistent with the formation of a tetrahedral PdO_4 species observed in the EXAFS data, and γ-Al_2O_3 respectively.

The nucleation of PdO nanoparticles during calcination was followed by in situ FT-EXAFS spectra, Fig. 7, where the amplitude of the PdO second shell Pd−Pd scattering pattern at 3 Å was followed and the coordination number determined. An increase in this feature suggests an increase in Pd neighbors and therefore a growth of PdO nanoparticles. The Pd/γ-Al_2O_3-ex(NH_3) catalyst remains constant until the temperature reaches 200–360 °C, where the scattering intensity at 3 Å decreased due to the dampening effect of the Debye-Waller factor at high temperatures. This indicated there was no change in the local structure of Pd during the calcination from room temperature to 360 °C. After this temperature, the second shell Pd−Pd scattering feature appears and begins to increase

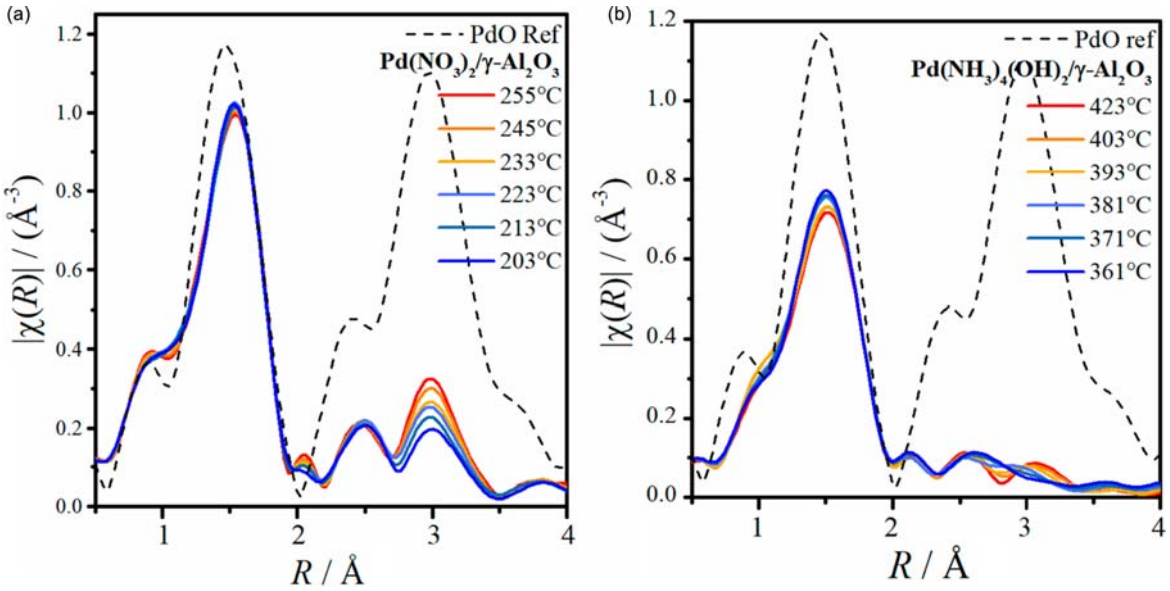

Fig. 7 In situ FT-EXAFS spectra of the calcination process of (a) the Pd/γ-Al_2O_3-ex(NO_3) catalyst and (b) the Pd/γ-Al_2O_3-ex(NH_3) catalyst, showing that both molecular precursors produce PdO nanoparticles during calcination, however the $Pd(NH_3)_4(OH)_2$ precursor triggers PdO formation at 360 °C compared to the $Pd(NO_3)_2$ precursor at 200 °C, as shown by the growth of the second shell Pd—Pd scattering pattern at 3 Å. Furthermore, the reduction in amplitude of the same scattering pattern for the Pd/γ-Al_2O_3-ex(NH_3) catalyst, with dampening effects taken into account and subsequent reduction in the calculation of coordination number, suggested smaller PdO nanoparticles were synthesized by the $Pd(NH_3)_4(OH)_2$ precursor.

in intensity as the temperature rises. From 360 °C to 500 °C, the coordination number for second shell Pd—Pd increases from 0.8 to 1.1. The Pd/γ-Al_2O_3-ex(NO_3) catalyst also stays stable for a time, until 200 °C is reached, where an increase in the second shell Pd—Pd is observed continuously and coordination number also increases from 1.4 to 2.2. A shift in the Pd—Pd distance was not observed during PdO growth, suggesting there was not a significant change in the local geometry of Pd, where an evolution from bridging nitrates to tetrahedral PdO must have taken place.

The combination of EXAFS, DRIFTS and supporting ex situ techniques have shown that the formation of PdO nanoparticles initiates at higher temperatures, 360 °C versus 200 °C, in the calcination step and produces smaller PdO nanoparticles, ~2.1 versus 3.5 nm, when using the $Pd(NH_3)_4(OH)_2$ precursor compared to the $Pd(NO_3)_2$ precursor. This was credited to the stabilizing effect of the initial tetrahedral ammonia complex and later on, the stabilizing effect of the N═O species (from oxidized NH_3), allowing for the controlled aggregation of PdO to occur. Moreover, a lower light-off temperature for methane oxidation was observed for the Pd/γ-Al_2O_3-ex(NH_3) catalyst compared to the Pd/γ-Al_2O_3-ex(NO_3) catalyst, which was assigned to the improvement in dispersion and smaller nanoparticles.

10.05.3.2.2 Active state of Pd revealed under in situ and operando conditions

10.05.3.2.2.1 Effect of changing the CH_4 and O_2 ratio and concentrations

The use of in situ spectroscopic techniques has been invaluable in understanding the phase transformation and subsequent activity of supported Pd catalysts towards CH_4 oxidation. Nilsson et al. investigated two supported Pd catalysts, 2% Pd/γ-Al_2O_3 and 2% Pd/CeO_2 using energy dispersive X-ray absorption spectroscopy (ED-XAFS) under *operando* conditions.[76] For the interests of this chapter, only the Pd/γ-Al_2O_3 catalyst will be discussed as EXAFS analysis could not be performed on the Pd/CeO_2 catalyst due to lower data quality (sample is too absorbing). In this study, the oxidation of CH_4 at low temperatures (≤500 °C) was investigated by exposing the catalyst to rich-lean cycling experiments, where rich refers to a gas stream of 0.1% CH_4 in He and lean refers to 0.1% CH_4 and 1.5% oxygen (O_2) in He. Cycling was conducted at 400, 350 and 300 °C to assess the effect of temperature. The authors also performed a modulation excitation stimulation (MES) experiment (see **Section 10.05.3.2.2.2** for further details) so as to be sensitive to very small changes in the Pd XAFS spectra during exposure to either rich or lean gas streams.

By following the outlet gas and the XANES white line or rising absorption edge intensity, key features and variations of the Pd chemical state were revealed. During the lean period, the outlet concentration of CH_4 initially drops for the Pd catalyst at all temperatures, which is almost matched by an increase in the rising absorption intensity. This was followed by a short increase in CH_4 concentration, then finally a steady state of CH_4 oxidation is reached. It was suggested that the introduction of O_2 rapidly oxidized reduced Pd, producing surface oxygen active sites on Pd responsible for CH_4 oxidation initially. When these sites are depleted, the CH_4 concentration rises until the oxidation of Pd is sufficient to maintain a steady state and produce sustainable PdO as the active site. During the rich period, the white line intensity decreases and there is an increase in CH_4 as O_2 is removed from the system,

indicative of PdO sites being depleted. After this, activation of CH_4 can still occur, however an increase in H_2 and CO suggests partial oxidation is preferred over metallic Pd.

Local structural information about the Pd species for Pd/γ-Al_2O_3 was determined by EXAFS analysis at the end of each CH_4 rich/lean period. The FT-EXAFS spectra after the CH_4 rich period at 350 °C featured two peaks at 1.7 Å and 2.5 Å, indicative of metallic Pd with a single Pd neighbor. The bond distance for the first Pd−Pd scattering shell was found to be 2.70 Å, shorter than that of bulk Pd at 2.75 Å but consistent with the presence of small particles. After the CH_4 lean period at 350 °C, there is distinct change in the R-space spectrum consistent with the formation of PdO, further confirmed by least squares data fitting showing a comparable Pd−O bond distance to that of bulk PdO. The evolution of the FT-EXAFS over time at 350 °C was assessed, switching between CH_4 rich and lean conditions. When O_2 is introduced to the a consecutive reduction in metallic Pd−Pd scattering contributions and an evolution consistent with Pd−O was observed, in agreement with the white line intensity.

MS data at the point of O_2 introduction shows three key stages happening in rapid succession: an initial decrease in CH_4 concentration, a sudden slight increase in CH_4 concentration and finally followed by steady state conversion of CH_4. By combining this and other work, these observations were explained as: an increase in CH_4 conversion due to the increase in O_2 concentration in the feed and subsequent surface oxide species being formed, followed by a decrease in CH_4 conversion due to the surface oxide being depleted, until finally the relatively slow bulk oxidation ("secondary" oxidation) of Pd to PdO is reached after a time under lean conditions, where steady state CH_4 conversion is reached.

Furthermore, complete CH_4 oxidation (i.e., the formation of CO_2 and H_2O instead of CO and H_2) is observed with the presence of O_2 in the gas feed. When O_2 is removed, the reverse is observed (i.e., reformation of the metallic Pd nanoparticles and an increase in incomplete CH_4 oxidation). Interestingly, examination of the FT-EXAFS spectra after the CH_4 lean period at 300 °C, found a strong metallic Pd−Pd scattering contribution in the spectrum alongside Pd−O, with calculated bond distances of 2.71(2) and 2.00(2) Å respectively. Both bond distances are reduced compared to the bulk crystal structure counterparts by ∼0.011 and 0.04 Å, likely due to a reduction in surface area as nanoparticles. Comparing this to the 350 °C scenario, this suggests that Pd is not fully oxidized at 300 °C at the end of the CH_4 lean period.

Further investigation by the same research group was conducted to understand how the O_2 concentration in the feed affects the chemical state of Pd and subsequent activity towards CH_4 oxidation.[77] In a similar setup, a 5% Pd/γ-Al_2O_3 catalyst was exposed to rich/lean cycling experiments at 360 °C, where comparing three different O_2 concentrations, 0.15%, 0.25% and 1.5%, was investigated. The CH_4 conversion and Pd oxidation trends were similar to the previous work, except for slight variations for the two lowest O_2 concentrations, where O_2 became a rate limiting reactant and the slower, "secondary" oxidation process was not observed. From this, they concluded that the CH_4 oxidation activity for the catalysts under 0.15% and 0.25% O_2 concentrations is derived from the oxygen surface coverage of Pd. Whereas under 1.5% O_2, more bulk PdO can be formed and is proposed to be the most active phase showing the highest conversion.

Further quantification of the varying extent of oxidation was conducted by fittings of the FT-EXAFS data. Average Pd−O coordination numbers during the lean period of 0.6, 0.8 and 1.4 were derived for 0.15%, 0.25% and 1.5% O_2 concentrations, respectively. By also considering the bulk coordination number of Pd−O to be 4, the calculated coordination numbers give rise to an approximate PdO formation of 15%, 20% and 40% respectively. Complete oxidation of Pd was not observed by XANES or EXAFS during any of the O_2 experiments and it was assumed a mixture of oxidized and metallic Pd co-existed in the CH_4 lean period. A model was suggested to explain the two oxidation regimes of Pd nanoparticles in these experiments. Under lower O_2 concentration conditions, Fig. 8, only rapid oxidation was observed, corresponding to surface oxidation of larger particles and/or partial oxidation

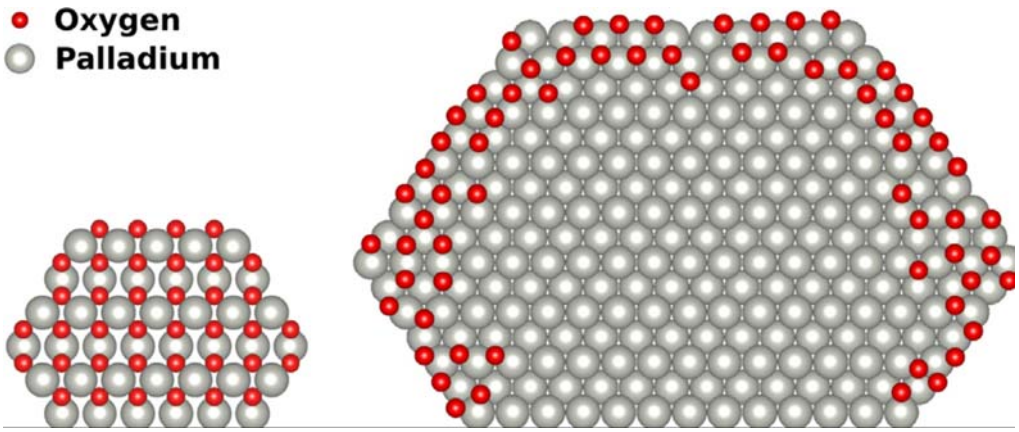

Fig. 8 Graphical representation of the oxidation of supported Pd nanoparticles under reduced O_2 concentrations, 0.15% and 0.25%, showing that different nanoparticle sizes are likely to be oxidized at different extents. Smaller nanoparticles (left) can be completely oxidized, whereas larger nanoparticles (right) can only reach surface/sub-surface oxidation, where a metallic core remains. Adapted with permission from Nilsson, J.; Carlsson, P.-A.; Martin, N. M.; Adams, E. C.; Agostini, G.; Grönbeck, H. et al. Methane Oxidation Over Pd/Al_2O_3 Under Rich/Lean Cycling Followed by Operando XAFS and Modulation Excitation Spectroscopy. *J. Catal.* 2017, 356, 237–245, doi: 10.1016/j.jcat.2017.10.018, Copyright 2017 Elsevier.

of smaller nanoparticles. Increasing the O_2 concentration to 1.5% introduced the second regime, where oxygen could diffuse into the bulk of the larger nanoparticles, which increased the fraction of PdO and is a slower process.

10.05.3.2.2.2 Effect of co-fed exhaust gases on Pd speciation and activity

Understanding the effect of a mixture of pollutants in exhaust gases is vital in understanding the behavior of a catalyst under increasingly realistic conditions. Marchionni et al. investigated the effect of CO on the oxidation of CH_4 over a 1.4% Pd/γ-Al_2O_3 catalyst, using a multi-technique approach.[73] *Operando* high-energy X-ray diffraction (HEXRD), XAFS and in situ DRIFTS were employed separately, but using the same reactor cell and same experimental conditions (outlined below) for each individual technique, to combine the power of each technique. The first MES experiment consisted of the alternate, periodic admittance of 0.25% CH_4 and then 1% O_2 separately in 60 s intervals at 320 °C, balanced in argon, where a full modulation period lasted 120 s. A second experiment was also set up with a similar fashion to study the effect of CO, where the periodic admittance of 0.25% CH_4 *and* 1% CO were alternated with 1% O_2, each with 60 s intervals.

Data from HEXRD during ME was similar to that of the static XRD experiments, where reflections due to γ-Al_2O_3 dominated the data pattern, although some small intensity differences at 2.33, 2.74, 3.15 and 5.32 $Å^{-1}$, corresponding to the periodic reduction and oxidation of Pd were observed. The enhanced sensitivity afforded by the ME or phase-sensitive detection (PSD) technique allowed the authors to observe two different PdO contributions to be isolated; an initial, fast-forming component due to the formation of an amorphous Pd oxide, denoted as PdO_a and a slower-forming, more crystalline oxide phase denoted as PdO_c. The addition of CO in the gas stream showed different behavior as a reductant compared to CH_4, where an asymmetric peak shift was observed from 2.771 $Å^{-1}$ at $\varphi^{PSD} = 60°$ to 2.706 $Å^{-1}$ at $\varphi^{PSD} = 210°$, indicating a lattice expansion (ca. 2.4%) within Pd and reduction of PdO to Pd was faster with CO present.

In agreement with HEXRD data, XANES shows Pd oxidation in the presence of O_2 only, but in the CH_4 gas feed, there are variations in the reduction of Pd i.e., it remains partially oxidized. The gas feed with $CH_4/CO/O_2$ shows similar variations, but a small shift to higher energy of the first white-line peak at 24370 eV and broadening in the edge-jump energy suggested the formation of a Pd carbide (PdC) phase. Analysis of the FT-EXAFS data was able to shed more insight on possible PdC formation although indirectly. The insertion of carbon into the Pd lattice should increase the first Pd—Pd bond distance in metallic Pd by 1.1–1.2%, and in this work the distance increased from 2.73 Å to 2.76 Å. This insertion is likely to happen via CO dissociation across the Pd surface and subsequent atomic carbon storage within the nanoparticles, as confirmed by DRIFTS. Simultaneously to this, the Pd—Pd coordination number increased to 9 with the introduction of CO, indicative of the reduction of the outer PdO_c layer. It should be noted that no carbide species were found in the CH_4 gas feed, suggesting there is an alternative pathway to CH_4 activation that does not involve carbon insertion.

DRIFTS was used to understand the surface chemistry under reaction conditions, which greatly complements the structure information given by the X-ray methods. In summary, it was suggested that CO is a possible intermediate species in the oxidation of CH_4 to CO_2. When CO was added alongside CH_4 in the gas mixture, additional CO adsorption sites could be resolved and the coverage of CO across Pd increased compared to CH_4 alone. By combining the knowledge found via this multi-technique approach, the authors concluded that the active site for the complete oxidation of CH_4 was partially oxidized Pd, however a secondary pathway of CH_4 decomposition across metallic Pd was also observed. With the presence of CO and CH_4 in the gas mixture, CO adsorbed immediately and indiscriminately on metallic Pd, indicative of the PdC species found by HEXRD and EXAFS. This phenomenon acted as the inhibitory step in CH_4 oxidation and this work demonstrates the need for catalysts to complete oxidize CO before the abatement of CH_4 can be obtained.

Despite the successes of Pd-based catalysts for CH_4 oxidation, the effect of steam-induced sintering has not been fully realized, and steam is often devoid from the experimental conditions, despite its presence (5–10%) when the catalyst is applied practically.[78] There is a great need to develop and understand catalytic systems that are resistant to this sintering, which is often a main deactivation pathway. Petrov et al. designed a 1% Pd-based mordenite zeolite catalyst with sodium-exchanged sites (herein denoted as Pd/Na-MOR) that exhibits resistance to the effects of steam.[79] Two catalysts were used as a reference: the original 1% Pd-based mordenite (Pd/H-MOR) and a 1% Pd-based mordenite with back-exchanged ammonium nitrate (Pd/H-MOR-BE).

Each catalyst was subjected to a reaction mixture of 1% CH_4, 4% O_2, 0 or 5% H_2O balanced in N_2 and heated from room temperature to 500 °C. The two reference catalysts (Pd/H-MOR and Pd/H-MOR-BE) showed similar T_{50} values for the oxidation of CH_4 with steam, 435 °C and 440 °C respectively and without steam, 400 °C for both. In comparison, the as-synthesized Pd/Na-MOR catalyst showed lower T_{50} values of 375 °C and 340 °C respectively. The stability of each catalyst after 65 h under this regime was also examined, with cycles of 10 min. of lean operation and 3 s of rich operation. The three reference catalysts all began to deactivate after around 4 h, whereas the Pd/Na-MOR catalyst showed the best stability, with around 80% methane conversion after the entire 65 h on stream. Ex situ scanning transmission electron microscopy (STEM) images showed there were small variations, 1.4, 2.4 and 3 nm, in mean Pd diameter between samples due to changes in acid site availability for Pd/H-MOR, Pd/H-MOR-BE and Pd/Na-MOR respectively. The microscopy images of the spent catalyst (16 h on stream) show significant sintering of Pd for the two reference catalysts, both showing large size variations of Pd from 3 nm to 50 nm and an increase of mean Pd diameter to 14 nm and 11 nm respectively. In contrast, Pd/Na-MOR did not show any significant sintering, with a mean Pd diameter of 4.4 nm and 4.6 nm for 16 h and 65 h on stream.

The Pd/H-MOR and Pd/Na-MOR catalysts were exposed to the wet reaction conditions at 400 °C for 90 min. The in situ FT-EXAFS spectra obtained throughout the experiment showed a gradual increase in the first shell metallic Pd—Pd scattering and in both second shell Pd—Pd scattering paths of PdO for the Pd/H-MOR catalyst over time. Calculation of the fraction of reduced versus

oxidized Pd at the end of the experiment was determined by the fractional coordination numbers. For Pd/H-MOR, the first shell Pd−O scattering of PdO and the first shell metallic Pd−Pd scattering were found to have a coordination number of 3 and 2.8, respectively. Firstly, this corresponds to approximately 75% oxidized Pd. Secondly, the 25% reduced Pd component with a coordination number of 2.8 indicates that this reduced Pd is organized in large particles with an average coordination number of 11. In comparison, Pd/Na-MOR showed no significant coordination number changes and remained in the PdO state throughout with a first shell Pd−O coordination number of 3.9, similar to that of bulk PdO.

The redox properties of the Pd/H-MOR and Pd/Na-MOR catalysts were assessed using a rich-lean cycling experiment via simultaneous *operando* XAFS, Fig. 9, where O_2 was removed from the gas feed and re-introduced later. Application of LCF to the XANES revealed the fraction of Pd(2+) and Pd(0) within the nanoparticles, and in the first few seconds of oxygen removal, both catalysts were completely reduced to Pd(0). During this time, metallic Pd continued to oxidize methane via steam reforming (i.e., $CH_4 + 2\ H_2O \rightarrow CO_2 + 4\ H_2$). Upon re-introduction with oxygen, both catalysts show a similar trend to the previous studies: a rapid oxidation to PdO followed by a slow increase in this component over time to reach a steady Pd^{2+} fraction. It was observed that the Pd/Na-MOR catalyst contained PdO only at the start of the experiment, and that this did not change significantly after removal and re-introduction of oxygen according to both LCF and in the FT-EXAFS spectra (Pd−O scattering paths could be meaningfully fitted, with a coordination number of 3.9). Removal of oxygen introduces the formation of metallic Pd, with a maximum coordination number of 10.4, and re-introduction of oxygen increases PdO coordination to 3.6 but a small remainder of metallic coordination of 1.2 is observed. In contrast, the Pd/H-MOR catalyst has a lower PdO contribution after rich-lean cycling, and a metallic Pd−Pd coordination number of 4.9 is observed even after re-oxidation. Additionally, the rate at which re-oxidation occurred was almost 4× faster for Pd/Na-MOR. The authors ascribed the enhanced performance of the Pd/Na-MOR catalyst to the effects of strong acid sites within the zeolite constraining the Pd, even during cycling gas conditions and under steam and despite the presence

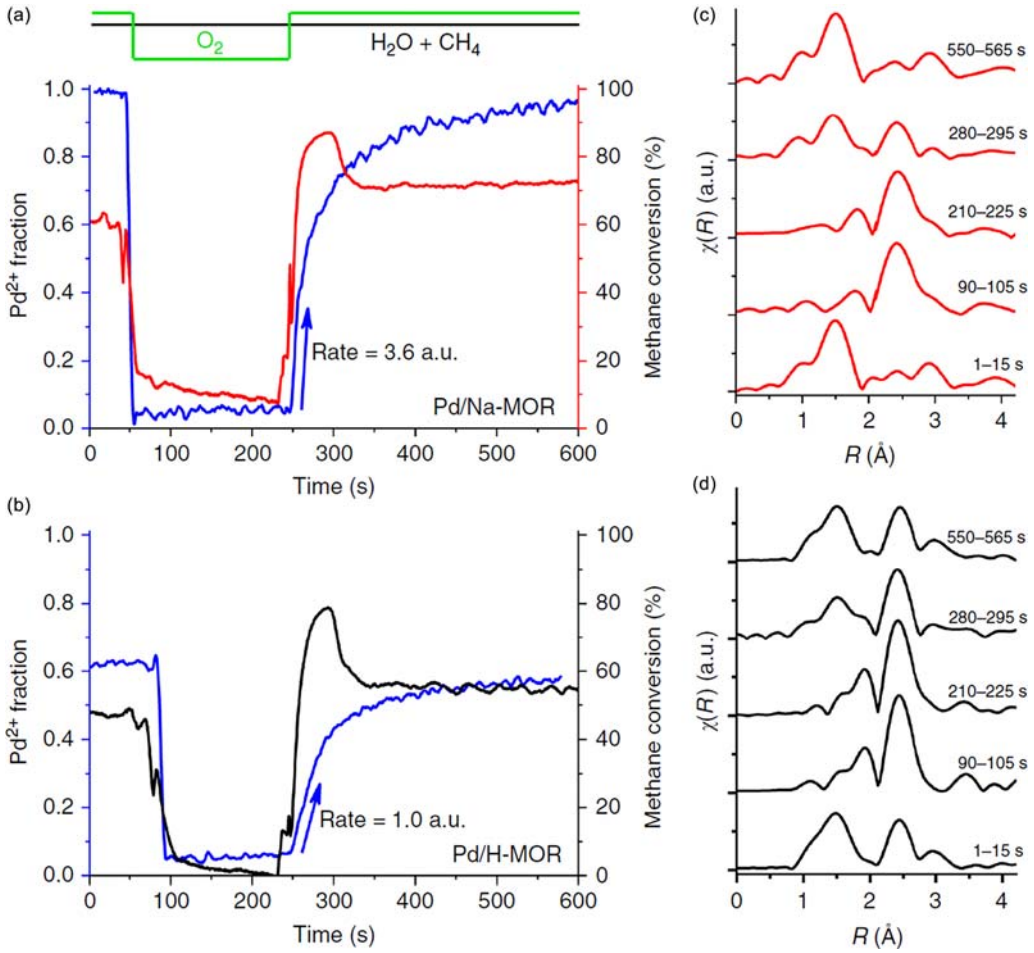

Fig. 9 *Operando* EXAFS experiments under 1% CH_4, 4% O_2 and 5% H_2O gas feed at 350 °C with O_2 removal/addition (green and black lines, top left). Graphs (a) and (b) show the fraction of oxidized Pd in Pd/Na-MOR and Pd/H-MOR, the corresponding catalytic activity towards CH_4 oxidation during O_2 removal and addition and the arbitrary rate of re-oxidation. Graphs (c) and (d) show the simultaneous and averaged in situ Pd K-edge FT-EXAFS spectra of Pd/Na-MOR and Pd/H-MOR. From Petrov, A. W.; Ferri, D.; Krumeich, F.; Nachtegaal, M.; van Bokhoven J. A.; Kröcher, O. (2018) Stable Complete Methane Oxidation Over Palladium Based Zeolite Catalysts. *Nat. Commun.* **2018**, *9* (1), 2545

of Na. The improved catalytic performance of this catalyst is twofold: the Pd is able to remain as small, immobile nanoparticles with a large active surface area that are more reactive towards e.g., oxygen, meaning redox reactions can occur quickly and the active PdO form with oxygen vacancies can be sustained, therefore CH_4 oxidation is sustained.

10.05.3.3 Interrogation of bimetallic species

Supported bimetallic catalysts can prove to be advantageous by improving traits such as stability and activity of the nanoparticles compared to their monometallic counterparts.[80] Some of the best known examples of this includes the Fe or Co alloyed with noble metals (NM) used in Fischer-Tropsch catalysts and Pt alloys used in emission control.[81] However, there are a number of catalytic process that have been shown to work better when alloys are formed.[80]

10.05.3.3.1 Catalyst self-assembly

Although on paper less exciting, catalyst self-assembly is an important subject worthy of much greater attention as we seek to maximize returns on catalyst material(s) and their performance. In that regards XAFS can be a very informative technique when it comes to understanding catalyst formation or 'activation' particularly where nanoparticles are concerned. An elegant example of this concerns the work of Nashner et al. who performed detailed in situ characterization of the microstructural evolution using XAFS and STEM to study the nucleation and growth of a nearly homogeneous population of carbon-supported bimetallic nanoclusters from $PtRu_5C(CO)_{16}$ clusters whilst heating in H_2.[82] In the first instance XANES data was examined for the Pt L_3-edge during the reduction process and thus at different stages during the nucleation and growth of the $PtRu_5$ clusters; the edge energy progressively shifts during the heating cycle to a limiting value consistent with a metallic state. The intensity of the peak centered between 2 Å and 3 Å in the FT of the Pt L_3 and Ru K-edge EXAFS data resulting from Ru-M and Pt-M bonding interactions, generally increases with the annealing temperature. In addition to the metal contribution, the Pt and Ru data also show significant structure below 1.5 Å in spectra measured below 423 K (although these contributions decline dramatically above this temperature). These latter low-*r* peaks result from interactions occurring between the metals and low-*Z* elements (i.e., C). This conclusion was confirmed by analyzing this region using suitable models for these bonding interactions (i.e., PtO_2 and RuO_2).

Disappearance of the low-*Z* contributions at $T > 423$ K suggested disintegration of the initial nanoclusters and subsequently saw the formation of metal nearest neighbors at shorter bond distances (i.e., 2.6–2.8 Å). Initial metal nearest neighbor distances were observed to be slightly longer than those seen in the final nanoparticle structure and suggested the formation of an intermediate state with a large static disorder (i.e., large σ^2 for the metal bonds). Analysis of the EXAFS data revealed a retention of 1–2 M-CO bonds in the structure; the large degree of static disorder was proposed to be due to the retention of bonding of the initial CO ligands. The gradual increasing observation of Pt—Pt, Pt—Ru, and Ru—Ru bond distances reflect nucleation of metal aggregates as the structures evolve into the final close-packed nanoparticle from the cluster precursor. The authors proposed that the increase in a significant number of Pt—Pt contributions during the nucleation stage indicates the formation of an initial, compact (Pt-rich) structure. An increasing Ru content was observed in the EXAFS data with continued high-temperature annealing which suggested structure inversion (Pt atoms were proposed to exchange with Ru surface atoms to form a surface Pt shell) and the formation of core-segregated Pt atoms. The authors estimate that over 50% of the metals occupy surface (i.e., low coordination) sites in these nanoparticles.

Perhaps the two key findings from this study concerned: (a) the observation that transport-dependent nucleation and growth of nanometer-sized alloy particles is mediated by the molecular precursor. In particular, the breaking of bonds between the surface atoms and CO ligands appears to control the rate of formation of the final metallic state of the nanocluster; (b) that reconstruction and distribution of the metal components evolves during both nucleation and growth of nanoscopic metal crystals. These observations highlight clearly why research and development of catalytic materials needs to pay close heed to the 'activation' i.e., application of heat etc. as it has a big impact on the final structure and therefore the catalytic properties.

10.05.3.3.2 Selective oxidation using bimetallic catalysts

As mentioned previously, the oxidation of CO has been extensively studied under various conditions and with various metals. Gibson et al. studied a $AuPd/\gamma\text{-}Al_2O_3$ catalyst via a combined XAFS and DRIFTS *operando* experiment, where the oxidation of CO was examined during heating and cooling to/from 350 °C.[83] In this work, the Pd K-edge and Au L_3-edge spectra were collected separately with a fresh catalyst each time and DRIFTS was utilized simultaneously with the outlet monitored by MS. The mean particle size was derived ex situ by TEM and found to be 4.1 nm; additionally, energy dispersive X-ray (EDX) analysis showed the supported nanoparticles to contain a mixture of Au and Pd. The Pd K-edge XANES spectra collected during the experiment revealed that the initial PdO was reduced to metallic Pd by 152 °C and from 263 °C onwards, after CO oxidation light-off, re-oxidation appeared to occur. Upon cooling, the catalyst reverts back to the metallic Pd phase and remains reduced, even in the presence of O_2 in the gas feed. Only small changes were seen in the Au L_3-edge XANES spectra, but alloying could be inferred by the reduction of the rising absorption edge at 11923 eV, which was credited to Pd filling the Au d-band via electron transfer.

Analysis of the FT-EXAFS spectra revealed key structural information regarding the catalyst during the reaction. At room temperature, the Pd FT data was fitted using three PdO scattering paths, one metallic Pd path and one Pd—Au path. On heating the catalyst, the PdO contributions disappeared at 150 °C and the calculated coordination numbers of metallic Pd and Pd—Au increase from 5 to 7 and 2 to 4 respectively, correlating with the XANES. At 263 °C, a contribution from a low z-number element is observed which was suggested to be the re-oxidation to PdO from the XANES, however no PdO contributions were observed in the FT-EXAFS.

Instead, this new scattering path was possibly due to adsorbed oxygen/carbon, or the formation of a PdC phase. During cooling, as the concentration of CO_2 reduces in the outlet, the low z-number element path also started to decrease and diminish, but the coordination numbers of metallic Pd and Pd−Au remain constant throughout, again suggesting the reduced Pd state is stable within this temperature range.

Furthermore, AuPd restructuring was observed in the FT-EXAFS during heating. At 205 °C, the metallic Pd−Pd coordination number decreased as Pd−Au increases, implying that a segregation process occurs, where the Pd transfers to the surface of the nanoparticle. The increase of the Au−Au coordination number from 6 to 8 during heating of the implies a concurrent Au core formation. The catalyst begins the experiment as an AuPd alloy, but during the 150–200 °C heating period, the nanoparticles transform into a stable core-shell structure with a gradient between the metals. Scrutiny of the DRIFTS data confirms much of the behavior found from EXAFS but adds some additional surface information. At room temperature, the strong preference of CO adsorption on Pd suggests that the surface begins as Pd-rich, and the low activity suggests that the interface between Au and Pd blocks the typical edge and step sites required for low temperature CO oxidation. In addition, CO adsorption on Au(0) is observed up until 95 °C and during cooling, only metallic Pd−CO adsorption sites are seen, providing further evidence of a core-shell structure. Overall, by combining both spectroscopic techniques alongside MS, a detailed picture of the restructuring of this AuPd catalyst could be observed in real-time.

10.05.3.3.3 Noble metal promotion of Cobalt reduction in Co Fischer-Tropsch catalysts

Fischer–Tropsch (FT) catalysts comprising Co typically contain NM promoters in the process, to facilitate Co reducibility at lower reduction temperatures leading to Co FT catalysts with higher site density, dispersion, and activity; the rising costs of NMs, renders their efficient use increasingly critical to achieve favorable economics for the Co FT processes. Reduction of Co oxide to the active Co metal occurs in two steps i.e., (1) reduction of Co_3O_4 to CoO, and (2) the reduction of CoO to Co metal. Ru and Pt facilitate both steps of this reduction process whereas Ag, Pt, Re and Ru have been found to only promote the latter step. NMs promote dissociative H_2 adsorption producing H atoms, which can combine with O atoms/ions and Co metal reduction at much lower temperatures thus avoiding high rates of metal atom/crystallite migration and sintering.[84] In a study by Mehrbod et al. the researchers investigated how NMs (Pt, Re, Ru and Ag) promoted reducibility of Co species supported on γ-alumina which is known to be able to stabilize smaller metallic Co particle sizes because of the relatively strong metal-support interaction. In this study, they compared the direct decomposition and reducibility of the impregnated $Co(NO_3)_2$ salt vs. the reduction of Co_3O_4 formed after calcination of the $Co(NO_3)_2$ salt.[85]

TPR-XANES of the Pt-25%Co/Al_2O_3 calcined catalyst saw that between RTP and around 300 °C, Co_3O_4 converts to CoO with conversion to metallic Co observed at ~400 °C. In contrast, with the uncalcined catalysts, CoO_X decomposition products are first formed that are then oxidized to a spinel (e.g., Co_3O_4) via the effect of NOx species. CoO formation occurred at the lower temperature of 240 °C, and the maximum amount of CoO was detected at 295 °C for the Pt-promoted catalyst, whereas higher temperatures are required for other uncalcined catalysts, including: unpromoted (400 °C), Ru (335 °C), Re (379 °C) and Ag (361 °C) promoted catalysts. Moreover, the temperature range for spectra representing CoO was relatively narrow for Pt ($\Delta \sim 50$ °C), whereas it was wider for unpromoted ($\Delta = 130$ °C), as well as Ru ($\Delta = 112$ °C), Ag ($\Delta = 126$ °C), and Re ($\Delta = 140$ °C) promoted catalysts. A wider range for CoO spectra were also observed for uncalcined 12%Co/TiO_2 and Re-12%Co/TiO_2.

CoO to Co^0 conversion was accompanied with different final extents of reduction by 560 °C. The trend in temperature to achieve 50% Co metallic formation was: air calcined Pt-Co/Al_2O_3 (383 °C) < uncalcined Pt-Co/Al_2O_3 (428 °C) < uncalcined Ru-Co/Al_2O_3 (462 °C) < uncalcined Re-Co/Al_2O_3 (546 °C). For the Ag-promoted and unpromoted catalysts the metallic cobalt is less than 20% for both catalysts, even at 560 °C. Importantly the authors determined that the addition of Pt improved the extent of reduction, which increased from 37% to 65%. EXAFS analysis was used to determine differences in Co^0 particle size with the un-promoted and uncalcined Re, Ru and Ag promoted catalysts exhibiting lower coordination numbers than that of the platinum promoted catalyst, suggesting the existence of smaller Co crystallites.

Importantly the authors also examined the effect of catalyst formulation on activity, particularly CO conversion. For the uncalcined and the unpromoted calcined catalyst CO conversion was typically ~45% initially, although this was observed to decrease with time particularly for the unpromoted calcined catalyst. When Pt was added, the initial CO conversion increases by ~10% and was explained in terms of a higher Co^0 active site density of the Pt-promoted catalyst.

10.05.3.3.4 Selective hydrogenation using bimetallic single atom catalysts (SACs)

The term single-atom catalyst has gained in the last ~10 years, traction as an area for intensive investigation.[86] More recently this research has expanded to include the finessing of the single atoms by alloying using a second metal.[87] The current interest with single atom catalysts is the achievement of catalytic sites with low nuclearity on a support. For a long time 'single-sites' for catalytic processes were thought to be easier to rationalize via isomorphous incorporation of metal ions into microporous and mesoporous frameworks.[88] EXAFS was particularly informative for identifying changes in the oxidation and coordination states of the ions as they underwent activation or when employed in a catalytic reaction.[89] One could rightly point out that in the microporous materials, the metal substituents are present as ions which is indeed true (as proven by EXAFS). However, one would also expect single atoms, when present on a catalyst surface would also retain an ionic character in order to be able to stick to the surface. If they are present in their reduced form then they are unlikely to be atomic, rather clustered. So to us it seems SAC is a misnomer as is single atom bimetallic catalyst although that term is perhaps more moot. One particular compelling example of the power of EXAFS to characterize the properties of single sites concerns the work of Barrett et al. who used acetonitrile as a probe molecule to determine

the Lewis acid properties of the substituent Co(2+) ions in an aluminophosphate framework—normally such an interaction would be difficult to see since acetonitrile comprises (CH_3CN) atoms that are weak X-ray scatters.[90] However, a large second shell scattering contribution from the ligand can be seen due to strong forward multiple scattering of the EXAFS signal along a linear bond. Multiple scattering is not limited to situations where there is a linear bond but in many cases can be (and is) ignored in data fitting in favor of fitting of additional shells with single path scattering.[91] This demonstration study and others showed nicely how detailed structural information can be gleaned when fitting multiple coordination shells and accounting for multiple scattering events in the EXAFS analysis.[92] On the other hand it shows if multiple scattering is not accounted for in a multi-shell fit, the EXAFS models may well be incorrect.

Selective hydrogenation reactions are an important class of catalytic reactions used in both bulk and fine chemical synthesis.[93] Acetylene hydrogenation is a particularly important bulk chemical reaction typically performed using Pd-based catalysts although enhancing the selectivity to ethylene is challenging. In a recent study by Pei et al. catalysts were prepared using only parts per million levels of Pd addition added to a primary metal, in this case Cu, thereby creating a Pd SAC supported on silica gel and tested it for the semi-hydrogenation of acetylene under conditions approximate to the front-end hydrogenation process (i.e., high H_2:acetylene concentrations).[94] Their results showed that the Cu-alloyed Pd SAC could attain ~85% ethylene selectivity with 100% acetylene conversion; far better than when alloying was attempted with Ag or Au. Due to the low Pd content of the catalysts XAFS was used to analyze the chemical environment of Pd. A visual comparison of the EXAFS oscillations from the Pd K-edge in the $CuPd/SiO_2$ bimetallic catalysts were different from that of the Pd foil hinting at the close proximity of Cu to the Pd present. These observations were also borne out in the R space (**Fig. 10**) plots which showed that the distance in the first shell was shorter than that of the Pd foil and the supported Pd catalyst, suggesting the formation of CuPd alloy. Formal fitting of the data also allowed of both Pd−O and Pd−Pd in the Pd/SiO_2 catalyst whereas for the bimetallic catalysts with relatively high Pd content ($CuPd_{0.015}/SiO_2$), both Pd−Cu and Pd−Pd bonding was determined but with lower loading, ($CuPd_{0.006}/SiO_2$) only Pd−Cu bonds existed in the catalyst, indicating complete isolation of Pd atoms by Cu. These data are also consistent with XANES spectra at the Pd K-edge of the $CuPd_{0.006}/SiO_2$, $CuPd_{0.015}/SiO_2$, and $CuPd_{0.006}/SiO_2$ catalysts with that of Pd foil. After reduction at 250 °C, the adsorption edge for the $Pd_{0.006}/SiO_2$ catalyst was at 24355.8 eV, which was higher than that of Pd foil (24,350.0 eV): that is, part of the Pd was in an oxidized state. The adsorption edges for the $CuPd_{0.015}/SiO_2$ and $CuPd_{0.006}/SiO_2$ catalysts were at 24348.0 and 24,348.1 eV, indicating that palladium in these two catalysts was slightly negatively charged.[94]

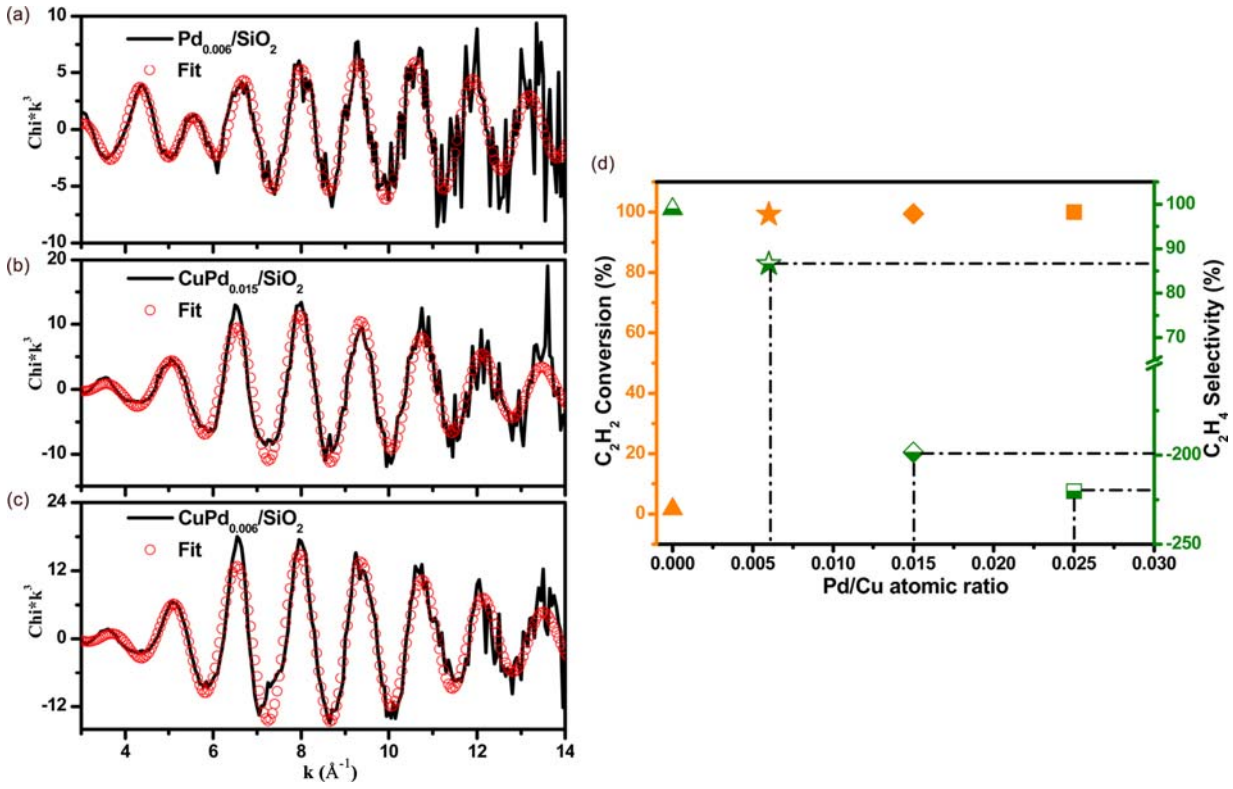

Fig. 10 k^3-weighted EXAFS spectra in k space for: (a) $Pd_{0.006}/SiO_2$, (b) $Pd_{0.015}/SiO_2$ and (c) $CuPd_{0.006}/SiO_2$ and (d) acetylene conversion (shown in orange) and ethylene selectivity (shown in green) at 160 °C as a function of the Pd/Cu atomic ratio. Adapted with permission from Pei, G. X.; Liu, X. Y.; Yang, X.; Zhang, L.; Wang, A.; Li, L. et al. Performance of Cu-Alloyed Pd Single-Atom Catalyst for Semihydrogenation of Acetylene under Simulated Front-End Conditions. *ACS Catal.* **2017**, *7* (2), 1491–1500, doi: 10.1021/acscatal.6b03293, Copyright 2017 American Chemical Society.

To better understand the relationship between the structures of the catalysts and the catalytic performances, the influence of the Pd/Cu atomic ratios on the conversion and selectivity of the catalysts at 160 °C was determined and is also summarized in Fig. 10. This study showed that, over the $CuPd/SiO_2$ catalysts, the conversion of acetylene could reach 100%. As indicated by the XAFS results, decreasing Pd/Cu atomic ratios led to better Pd dispersion which correlated with increased selectivity to ethylene increased greatly. The ethylene selectivity over the Cu-alloyed Pd SAC was higher than that of the Au-alloyed Pd SAC ($AuPd_{0.025}/SiO_2$), over which the selectivity decreased obviously with increasing reaction temperature.

10.05.3.4 Using EXAFS to determine metal particle size and shape

EXAFS lends itself very well to the characterization of nano-structured metallic species which often represent the species of interest in supported catalysts. There exists many theoretical/hypothetical studies which show for example that the coordination number derived from a first shell analysis can be correlated with the particle size and when considering higher shells, even particle shape.[95] This has been demonstrated conclusively for cubic close-packed (ccp) metals and to some extent for hexagonal close-packed (hcp) and body-centered cubic (bcc). In practice this analysis is limited to particle diameters <3 nm ($\sim$561 atoms) since larger nanostructures containing many hundreds of atoms are less easy to 'resolve' based on coordination number alone (i.e., a difference of particle size between 1 nm and 2 nm represents a coordination number difference of 2 units whereas between 3 nm and 4 nm, this is 0.2 units) due to inherent practical limitations of extracting reliable coordination numbers (estimated to be $\sim$10%). This type of analysis makes a number of assumptions; (a) that the particle size distribution in the sample is narrow, (b) that the static disorder (Debye-Waller factor) does not change (i.e., due to structural disorder or vibrational anharmonicity) with particle size and (c) for higher shell analysis, necessary to extract morphological information, multiple scattering effects are also negligible. There is experimental evidence that these assumptions generally for particle sizes >1 nm. Generally, for estimations of size, particles are also assumed to be spherical although it has been shown from a ratio analysis of higher shell coordination numbers that it is possible to determine structural deviations from this. It should also be noted that increasing thermal disorder, particularly when performing in situ or *operando* experiments can lead to sometimes dramatic reductions in FT intensities and thereby coordination numbers to rend the study of coordination number extraction and the evolving properties of nano-particles difficult. This though is quite often due to the reaction temperature exceeding both or either of the Tamman and Huttig temperatures which lead to increasing atomic disorder.[96]

Although somewhat debatable it is hard to argue a case for a more suitable structural technique for the characterization of bimetallic (and even beyond that i.e., trimetallic systems) systems other than EXAFS. Numerous models exist that allow for very detailed structural information pertaining to the structure and distribution of the compositional elements to be extracted although it does require local structure input from both edges. Some data analysis programs even allow for dual edge refinement to allow very detailed structural insight to be obtained. The extent of alloying or perhaps the extent to which a random alloy is created can often be inferred from the change in the shape/frequency of the EXAFS oscillations as the number of interactions increases. This is particularly true when one of the elements exceeds $Z > 78$ (Pt) and is referred to as the Generalized Ramsauer Townsend effect caused by a 'pi phase flip' in the backscattering amplitude from 6 Å.[97] Meanwhile differentiating between elements where $\Delta Z < 3$ does not appear possible rendering detailed structural analysis of bimetallic formation either impossible or very difficult. Even when $\Delta Z > 3$, there can be problems obtaining the original EXAFS data if the absorption edges overlap.

Metal particle size and morphology insight is difficult to obtain from EXAFS data alone. The most comprehensive analysis typically combines the benefits of a volume averaged technique such as EXAFS with number averaged techniques such as TEM and where such data is easier to glean. It can be that there is a mismatch between the information derived from these two techniques and this can often be understood in terms of a severe particle size distribution.[98] This normally manifests itself in terms of a smaller particle size estimate derived from EXAFS and suggests that there are many particles, clusters or even single atoms/ions that many TEM instruments are unable to resolve. This is obviously a problem when studying heterogeneous catalysts as it makes it difficult to differentiate/identify the species primarily responsible for a catalytic activity and or selectivity. When comparing more than one volume averaged technique, in this case XRD vs. EXAFS there has been a compelling case made for the latter providing the most true representation of the real particle size/morphology.[99] It should be remarked at this stage that it is also possible to extract information on particle size from simulation of the XANES data although this normally requires accurate models (i.e., size and morphology) to begin with so cannot be used directly to determine this information.[100]

Particle size and morphological information of other heteronuclear systems such as oxides had generally proved more difficult for two reasons. Firstly, the near neighbor typically used to extract size information is now the heteroatom which is typically of lower Z than the absorber, scattering X-rays less efficiently than the absorber rending a greater error in the determined coordination number. Secondly there is a wider availability of heteronuclear structures, often of lower symmetry than the cubic cells seen for the metals which can mean a wider of variety of bond distances (static disorder) contributing to a signal and these are often difficult to disentangle particularly with increasing R.

10.05.3.5 Catalysis using ions of low nuclearity

The study of the catalytic properties of metal ions in porous materials such as zeolites and zeotypes has been a cornerstone of the application of the EXAFS technique since time immemorial. Perhaps the largest number of recent studies concern catalysts for methane activation (oxidative and non-oxidative), the selective catalytic reduction of NOx and selective oxidation.[101] Much

discussion from these studies has focused on the nuclearity of active species with proposals put forward for the presence of mononuclear, dinuclear, polynuclear and in some instances bulk oxides being the most important for high yields of the desired products. It should be noted that EXAFS is not particularly brilliant for unambiguously differentiating or identifying the extent of nuclearity in these catalysts. For example, Cu-containing zeolites (ZSM-5 & MOR) have shown to be active for methane to methanol conversion yet there are only very small differences in the second shell intensity attributable to Cu−Cu scattering (see **Fig. 11**) which have been attributed to bi- and tri-nuclear Cu species in Cu-ZSM-5 and Cu-MOR respectively.[102] Only after computer simulations were performed was it possible for Grunder et al. to determine that the greater performance of Cu-MOR could attributed to the presence of a tri-nuclear species—the MOR topology being particularly accommodating for such a novel species. The challenge with identifying such species unambiguously is the presence of an EXAFS contribution for the zeolite framework at a similar position. Correlations have also been made in Fe-containing systems with the presence of mononuclear and dinuclear species being implicated in obtaining improved methanol yields in the presence of H_2O_2 when reactions are carried out under elevated (pressure) conditions.[103]

As can be seen from the above studies, EXAFS is rarely used alone to positively identify the presence of active species. This problem is further compounded by the tendency of porous materials to possess a number of adsorption or cationic sites, often with slightly different local structure environments.[104] Indeed the local structure might even be the same but the composition of the structure sufficiently different to effect different reactivity. Using Mo containing catalysts for the non-oxidative dehydroaromatization of methane into benzene as an example. These systems have been studied for nigh on 30 years as they continue to show promise for CH_4 conversion to H_2, C_6H_6 and possibly high quality nano-structured carbon.[105] The problem with this technology has been very quick deactivation (< 1 h time on stream) which has proven very difficult to mitigate despite recent research efforts.

In many ways the study of Mo-containing zeolites is an X-ray spectroscopists dream. The K-absorption edge of Mo is bang on 20.000 keV, and is sufficiently penetrating that sample preparation is comparatively facile (when compared to studying transition metals in the first row) ensuring that as long as the experimenter follows good sample prep, high quality spectra are almost assured. Furthermore, Mo is known to exhibit a range of oxidation states particularly +6, +5, +4 and 0 often when in the solid oxide state, this involves species with mixed oxidation states as Mo is known to form a number of oxides and sub-oxides.[106] XANES has been shown generally to be a pretty good way at differentiating between Mo oxidation and coordination states of the oxides although there is less evidence for the efficacy of this for samples of lower nuclearity. EXAFS of Mo containing compounds on the other hand is more challenging as the Mo environments tend to be asymmetric; notably contains a short (1.68 Å) Mo═O bond as well as one very long Mo−O component at 2.3 Å rendering least squares fitting of the M−O shells challenging.[107] The possible formation of carbides and oxy-carbides is even more challenging to confirm not least due to a lack of suitable references.

The work published in 2016 by the various groups all used XAFS in one way shape or form to identify the nature of the Mo containing species and the key results from these studies can be summarized as follows. The work of Lezcano-Gonzalez et al. showed using in situ/operando valence-to-core emission spectroscopy (subsequently confirmed by EXAFS in the work of Agote-Aran et al.), that molybdenum oxy-carbide species form after an initial induction period but that these go on to carburize to form active Mo_2C-like species that migrate from the zeolite pores onto the surface.[17,108] Vollmer et al. also observed similar behavior but actually proposed that low-levels of NMR-detected molybdenum oxy-carbide were in fact the species responsible for the methane-to-benzene reaction.[109] In contrast Kosinov et al. using Mo K-edge XANES observed similar behavior although interpreted reduction of Mo showed some weight loading dependency and that in fact the active species were thought to be Mo (IV) species that remained attached to the zeolite framework.[110] On the one hand then it is comforting to know that the behavior of these Mo species is consistent across the studies suggesting that reduced Mo species in some form are responsible for methane activation/benzene formation. More recent work again using XAFS as a core technique, has also resulted in the conclusion that Mo_2C-type species (EXAFS bond lengths) seem to be prevalent in active catalysts.[111] It is important to not at this stage that the presence of Mo_2C vs. MoO_2 is really only possible when considering the Mo−NN (Nearest Neighbor) bond lengths and which can be seen in the work of Agote-Aran et al., these clearly lengthen with time.[17] Extrapolation of the K-edge position using references also

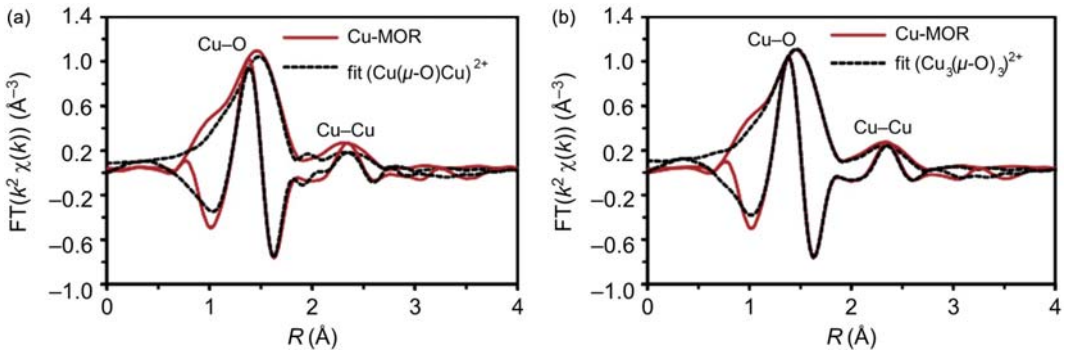

Fig. 11 Comparison of the k^2-weighted Fourier transformed EXAFS at the Cu K-edge of the Cu-MOR zeolite activated in O_2 at 450 °C with EXAFS simulation of an intrazeolite (a) binuclear $[Cu(\mu\text{-}O)Cu]^{2+}$, (b) trinuclear $[Cu_3(\mu\text{-}O)_3]^{2+}$ complexes. From Grundner, S.; Markovits, M. A. C.; Li, G.; Tromp, M.; Pidko, E. A.; Hensen, E. J. M. et al. Single-site Trinuclear Copper Oxygen Clusters in Mordenite for Selective Conversion of Methane to Methanol. *Nat. Commun.* **2015**, *6* (1), 7546. doi: 10.1038/ncomms8546.

enables one to determine that the oxidation state of Mo in Mo_2C is a rather unusual +2 although it is important to note that this approach may not be entirely tractable as the change in ligand type will affect the nature of the chemical bond and therefore an unknown effect on the position of the edge (i.e., the extrapolation to determine the Mo oxidation state does not take this into account and what was observed in these studies may be a coincidence). However, these studies also highlight an additional challenge, namely the difficulty to discriminate between different Mo species and their possible roles. It is remarkable that close examination of the XANES and a detailed EXAFS analysis of 4% Mo-ZSM-5 suggests an almost exclusive formation of Td. Mo^{6+} and not the trace of even a hint of the presence of multiple Mo species although there is compelling evidence from other characterization techniques that Mo may also be present as Al_2MoO_4 due to interaction/reaction with Al leached from the framework of ZSM-5. This is perhaps best illustrated in the recent work by Caballero et al. using TPR which indicated the possible presence of multiple Mo species.[112]

So the question is, what has been learnt from these studies about the system and the possibility of XAFS to discriminate/identify active sites for this reaction? On one hand these data show that XAFS is very powerful and capable of studying the best-performing catalysts operating at real conditions (operando). These studies alongside others have identified that molybdenum carbide species are present at times when benzene yields are high. This is not totally unsurprising since bulk Mo_2C also shows activity for this reaction albeit low due to a vanishingly small surface area although this can be mitigated by nano-sizing and dispersion.[113] The results from XAFS studies suggest that the most active species are only Mo_2C-like but it is really only with computational studies are we able to get a better feeling for their structure and properties and even if it were possible to identify an active structure in silico, it will continue to remain a challenge to differentiate between (likely) multiple species that differ only subtly in nature using XAFS.[114] Furthermore it is nigh on impossible to identify and characterize active species that are present in low concentrations using conventional curve fitting methods and this is where alternative, more sensitive analysis methods are employed such as multivariate curve resolution (MCR) or machine learning (ML) methods which are discussed later.

10.05.3.6 EXAFS in combination with other techniques

It is well established that one technique is never enough to understand the salient features of a heterogeneous catalyst. Indeed there are many studies that show that a deep understanding of catalyst materials involves a plethora of techniques.[115] Modern-day EXAFS studies have the advantage that they can be readily performed in capillary reactors with sieve fractions and under plug-flow conditions, time-resolved and under operando conditions rendering such studies key if not totally decisive.[39,116] A combination of the use of narrow capillaries and the availability of both fiber-optic optical spectroscopies (i.e., UV-vis/Raman) and a plethora of X-ray detectors renders the use of combined techniques commonplace.[117] Perhaps the most successful combination of techniques to date were in fact the first exemplars; the first combination of EXAFS and optical techniques (IR) and the combination of EXAFS and XRD.[118,119] The first example of EXAFS and transmission IR used supported wafers and has largely been superseded by combined EXAFS and DRIFTS measurements as this allows for the examination of packed beds and which has been shown to be particularly beneficial when probing rapid catalyst response with changes in gas composition.[120] There have been many studies of supported catalysts studied under conditions akin to those seen in automotive exhaust systems with phenomena such as rapid changes in redox and the formation of intermediate carbides and nitrides thought to be key intermediates in the process.[121] Rapid data acquisition with ms time resolution was primarily the preserve of the energy-dispersive (white beam) mode of EXAFS until recently. Coincidentally one of the first successful demonstrations of XAFS and XRD used an energy-resolving detector to acquire the PXRD data.[119] Again these have been very much superseded by the application of a bank of detectors and more recently 2D area detectors which offer better sensitivity and data resolution. Nowadays, the versatility of modern day analytical techniques has resulted in a number of 'multi-modal' combined spectroscopic/scattering studies on catalyst synthesis or reaction studies.[122–124]

10.05.3.6.1 Combined XAFS/vibrational spectroscopic study of catalyst synthesis and reaction

Although there are many successful demonstrations of the benefits of XAFS and IR (see **Section 10.05.3.3.1** for a case study), there are far fewer studies exploiting the benefits of combining XAFS and Raman, although quite a few beamlines offer the capacity to perform such measurements. The crystallization mechanism of ZnAlPO-34 zeotypes from a synthesis gel has demonstrated the successful confluence of XAFS and Raman (also in combination with Small and Wide Angle X-ray Scattering) to observe the correlation with simultaneous changes in the local structure of Zn (becomes less disordered) and the conformation of the templating agent (Raman observing that the TEAOH template molecules adopted a tg.tg confirmation as formation of the crystalline CHA framework occurs) leading to the conclusion that self-assembly occurs via a disordered gel to ordered crystal transformation.[124] The work by Kongmark et al. also showed how Raman/XRD could determine the formation of Bi_2O_3 layers preceded the coordination change from Td to Oh Mo^{6+} as the active catalyst γ-Bi_2MoO_6 forms from its synthetic components. Beyond self-assembly, Beale et al. applied Raman spectroscopy in combination with Uv-vis spectroscopy and EDE to observe, under operando conditions, coking and Mo sintering in SiO_2/γ-Al_2O_3 supported catalysts used in propane dehydrogenation.[123] The lack of additional studies is likely due to a combination of challenges of measuring certain samples (i.e., sample fluorescence/instability) as well as the requirement in some places to connect the source laser shutter to the hutch interlock in order to provide safeguarding against scattered radiation.

10.05.3.6.2 Combined XAFS/UV-vis study of catalyst synthesis and reaction

UV-vis spectroscopy is also very amenable to combining with XAFS since the probes used are very straightforward to apply either external to or within the plug-flow reactor itself, with the technique providing complementary information on oxidation and coordination states. It has been successfully demonstrated to differentiate between the darkening of the catalyst being due to coking or reduction of Mo-based catalysts for dehydrogenation (using EDE) and oxidative dehydrogenation reactions (scanning XAFS) as well as to differentiate between changes in Co oxidation state in CoAlPO-34 zeotypes. It is also one of the few successful technique combinations applied to examine the reactivity of homogeneous catalytic systems.

There are far fewer studies of catalytic materials in the liquid phase and for a good number of practical reasons. The handling of liquids is technically more challenging and the comparatively (with respect to gas) dense liquid medium attenuates strongly the spectroscopic response of the catalyst. For homogeneous catalysts this issue is further compounded by the comparatively low concentrations used. Using what is known as a stopped-flow cell in which reactants and catalyst are mixed and measured simultaneously during reactions over minutes with a time resolution of milliseconds. Much of these initial studies were able to determine the mechanisms of deactivation, for example the formation of increasingly polymeric Pd species during allylic amination, with the (P—P ligand)Pd(allyl) complex reacting to then form a (P—P ligand)Pd^0-complex forming dimers, trimers and bigger clusters, eventually precipitating as palladium black under true catalytic conditions.[22]

The incident X-ray beam is also known to induce sample instabilities. Indeed the same stopped-flow setup has been used to observe the formation of beam-induced Cu nanoparticles from Cu-amino acid complexes with both XANES and UV-vis being able to discriminate color changes based on X-ray beam induced reduction to Cu^+ or Cu^0.[24] The energy supplied by the focused white beam from the synchrotron can be considerable and this can lead to localized heating as well as photolysis and the generation of free electrons and radical species either from the compounds being investigated, else the surroundings (often H_2O). However, these problems are not insurmountable, but they do require more careful consideration than your typical gas-phase heterogeneous catalysis experiment.

10.05.3.6.3 Combined XAFS/XRD

As a technique combination for catalyst characterization, combined XAFS/XRD has the greatest tradition since the first reports appeared from Germany and the United Kingdom in the early 1990s. Some good examples demonstrating the power of this technique combination includes HRPD and EXAFS to identify Cu active site location and interaction in zeolite SSZ-13 during the standard SCR reaction, the tracking of metallic Cu nanostructure evolution from a $CuFe_2O_4$ spinel and more recently with the advent of simultaneous measurements, the kinetics of Co microstructure evolution or Pt/Pt-O core shell structures in the cathode catalysts present in polymer electrolyte fuel cells under transient potential operations.[125] In this latter example the authors demonstrated that congruent data could be obtained with a time resolution of 20 ms.

XRD can also be combined with multi-edge XAFS to elucidate possible synergistic effects in bimetallic systems.[126] This is demonstrated recently by a study on a Ni—Fe catalyst for CO_2 methanation reaction. Relative to the monometallic Ni catalyst the bimetallic nanoparticles exhibited higher fractions of Ni reduction during the H_2 activation period, while both EXAFS and XRD analysis indicates alloy formation. Oxidation of the Fe was observed immediately upon CO_2 activation, while the Ni remained reduced. An increase in temperature to 450 °C resulted in leaching and sintering of the FeOx to the nanoparticle surface. The dynamic of the Fe species was investigated further with modulation excitation XAFS (information on modulation excitation spectroscopy is provided in later section). With the aid of theoretical calculation, the author was able to demonstrate the redox cycle of the Fe that is likely located at the surface of the metal particles, and its promotional effect for CO_2 dissociation during the methanation reaction.

Indeed, there are several reports of catalysts comprising supported nanoparticles measured under reaction conditions i.e., reducing or oxidizing conditions where combined XAFS/XRD has provided a more comprehensive understanding of the structure and properties of the nanoparticles. Some further selected examples include the observation that small (<1.5 nm) nanoparticles comprising mixed $Pd^{0/2+}$ being particularly active for methane oxidation on Pd/CeO_2, the observation of the metallic Cu phase with water gas shift activity in Cu/CeO_2 catalysts and the observation of α-MoO_3 sublimation in α-MoO_3/Fe_2MoO_4 catalysts during oxidative dehydrogenation of methanol to formaldehyde (**Fig. 12**).[127–129]

10.05.3.7 Catalysis in the liquid phase

There has been a long desire to perform in situ XAFS studies to elucidate the structure-active relationship on active solid materials that catalyze liquid phase reactions in a fashion similar to those experiments on gas phase systems. However, as stated previously, the monitoring of catalyst in liquid present a unique set of technical challenges that are not limited to higher X-ray attenuation of the liquid medium and the challenge for handling possible corrosive chemicals placed under harsh conditions. As such the number of studies performed in the liquid phase number considerably less than those performed in the gas-phase. Below we discuss some specific studies that demonstrate what is possible here although we note that there are other examples discussed earlier in this chapter. Furthermore, we do not discuss electrocatalysis at this stage as we have allocated a subsequent section to cover this topic of growing importance in more detail.

One of the earliest studies employed a flow cell with Kapton windows and XAFS fluorescence detection and was performed by Sankar et al. The experiment on the petrochemical significant cyclohexene epoxidation with H_2O_2 using the mesoporous catalyst Ti-incorporated MCM-41 was able to resolve changes in local structural (they observed an increase in the local site disorder) to the

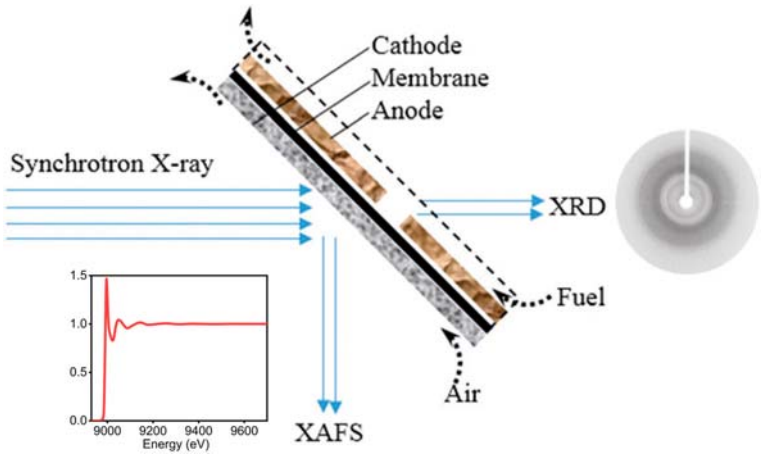

Fig. 12 Setup for recording combined in situ XAFS/XRD data from an electrochemical cell during charge/discharge. Note the XAFS data is recorded in fluorescence mode whilst the XRD is recorded in transmission. From Qin, H.; Lin, L.; Jia, J.; Ni, H.; He, Y.; Wang, J. et al. Synchrotron Radiation In Situ X-Ray Absorption Fine Structure and In Situ X-Ray Diffraction Analysis of a High-Performance Cobalt Catalyst Towards the Oxygen Reduction Reaction. *Phys. Chem. Chem. Phys.* **2017**, *19* (45), 30749–30755, doi: 10.1039/C7CP05888H.

active Ti ions during catalytic epoxidation.[130] The time resolution only allowed for acquiring data at different stages of the catalyst lifetime (i.e., before and during catalytic reaction). Furthermore the group had to develop their own cell to perform such experiments. Nowadays, many beamlines offer purposely constructed specialized sample cells to perform in situ or under operando liquid phase experiments under flow conditions. These cells are often comprised of special X-ray windows to allow the measurement to be performed in transmission geometry at elevated temperature and/or high pressure.[22,54,131] Using an in situ cell, Lee et al. were able to monitor the structural evolution of a Pd/C catalyst for selective aerobic oxidation of cinnamyl alcohol under reaction flow. XANES reveals a rapid reduction of the Pd catalyst 40 min into the reaction, and the EXAFS analysis confirms the PdO present in the fresh catalyst was indeed reduced to the metallic state at the end. They demonstrated that the rate of cinnamyl alcohol oxidation can be correlated directly to this Pd reduction.[132] The same researchers also showed how insights (state of the active Pd species) into a liquid phase reaction can be obtained by performing experiments in the gas-phase using a volatile substrate.[52] Kawai et al. revealed that the Ni_2P/SiO_2 catalyst for hydrodesulfurization remained stable at reaction conditions when placed under realistic high pressure (3 MPa) and high temperature (613 K) with the measurements made possible by the use of a low-volume cell with cubic boron nitride windows.[133] With the aid of the difference spectra technique, the author was able to isolate subtle changes in the EXAFS spectra and assign it to a surface N—S bond. We et al. conducted operando multi-edge monitoring of Pt/C and Pt-Re/C catalysts for glycerol aqueous-phase reforming and were able to observe growth in particle size.

10.05.3.8 XAFS and electrochemistry

The field of electrocatalysis is developing at pace, with advances in characterization techniques, software and theory aiding our understanding of the complex processes that occur at the active site, with XAFS having proven to be one of the most useful tools for this purpose. This has in recent years been motivated by an increased awareness of our impact on the environment and the need to develop green, sustainable energy processes (both storage and generation) and chemical synthesis methods directing the development of novel electrocatalytic materials.

XAFS can be used to study separate cathode/anode reactions in half-cells, or within fully functional devices, with the electrode/electrolyte interface probed to provide insight into working mechanisms and dynamic processes, such as the oxygen evolution reaction (OER), oxygen reduction reaction (ORR), hydrogen evolution reaction (HER) or CO_2 reduction reaction (CO_2RR). All of these environments are complex three-phase systems, with a solid electrocatalyst (often nanoparticulate) and both gaseous and liquid reagents/products. The electrolyte composition and pH can change under reaction conditions, as can the catalyst composition, oxidation state, crystallographic structure, strain, morphology, surface characteristics, defects, etc., highlighting the need for in situ/operando characterization to elucidate the structure-activity relationships.

Recent reviews covering the use of XAFS for studying electrochemical systems and devices include those of Russell 2004 for low temperature fuel cells, studies of specific reactions such as Fabbri 2017 and Varsha 2020 for water splitting (HER/OER), as well as more recent reviews covering the broader field such as Lassalle-Kaiser 2017, Wang 2019, Timoshenko 2020 and Li 2020, as well as looking at approaches to achieve surface sensitivity, Huang 2021.[35,43,134]

The study of electrocatalytic reactions requires specialized electrochemical cells, needing to accommodate the working, counter and reference electrodes, static/flowing liquid electrolyte, being capable of maintaining the correct potential and minimizing any internal resistance, whilst providing the shortest path possible through the highly absorbing electrolyte for the X-rays to reach the solid-liquid interface of the electrode at which the electrocatalytic reaction occurs.[44,135] When studying gaseous evolution

reactions this is complicated further by increased noise caused by the gas bubbles forming and the need to prevent these from collecting at the electrode and altering the beam path.

Further challenges for in situ/*operando* XAFS of electrocatalytic systems relate to the timescales involved, with conventional XAFS measurements taking 10–15 min scan. The electrochemical processes being studied can be faster than the conventional measurement time, and therefore instead of providing a clear spectrum of an intermediate/transition state, the XAFS spectrum would instead be an average. It should be noted however that much useful kinetic information may still be obtained from steady state measurements. Whilst the development of quick scanning monochromators (QEXAFS) and energy-dispersive (ED) EXAFS measurements facilitate significantly faster measurements, they tend to come with a decrease in the signal-noise ratio, or in the case of ED an increase in flux. This increased flux (or even the prolonged exposure of a conventional scan) can result in beam damage to the electrolyte, the electrode (such as the polymer binder) and in the case of PEMFCs, even damage the Nafion membrane.

Efforts to reduce and replace the use of rare and expensive noble metals for catalysts (e.g., platinum group metals—PGM) with cheaper and more abundant ones. With the former improvements have been made by reducing nanoparticle size, alloying the noble metals, and developing core@shell materials all of which focus on increasing the proportion of the active metal at the surface whilst minimizing the amount of inactive/inaccessible atoms in the core of the nanoparticles. Replacement of the use of noble metals with more abundant ones such as transition metals instead focuses on achieving increases in efficiency (thermodynamic, kinetic) and can be achieved through binary, ternary and higher combinations of these metals as well as through manipulation of the support material.

Many in situ and *operando* electrochemical experimental setups are optimized for use with hard X-rays (>5 keV) to probe the K and L edges of heavier metals, and success has been had using tender X-rays (2–3 keV) however challenges remain in the soft X-ray regime (<2 keV) to probe the edges of lighter elements (C, N, O) with adaptations to vacuum being required.

10.05.3.8.1 Hydrogen evolution reaction (HER)

Electrochemical generation of hydrogen is an important enabling technology for the production of sustainable fuels, since it can act as an energy carrier. Sustainable hydrogen production from water electrolysis has received much attention, and recently molybdenum sulfides (MoS_x) have been shown to catalyst HER in molecular, nanoparticulate and amorphous forms, in acidic media. Lassalle-Kaiser investigated the structure of MoS_x catalysts using in situ XAFS at both Mo and S edges, probing both the metal centers and sulfur ligands under functional conditions (see **Fig. 13**).[136]

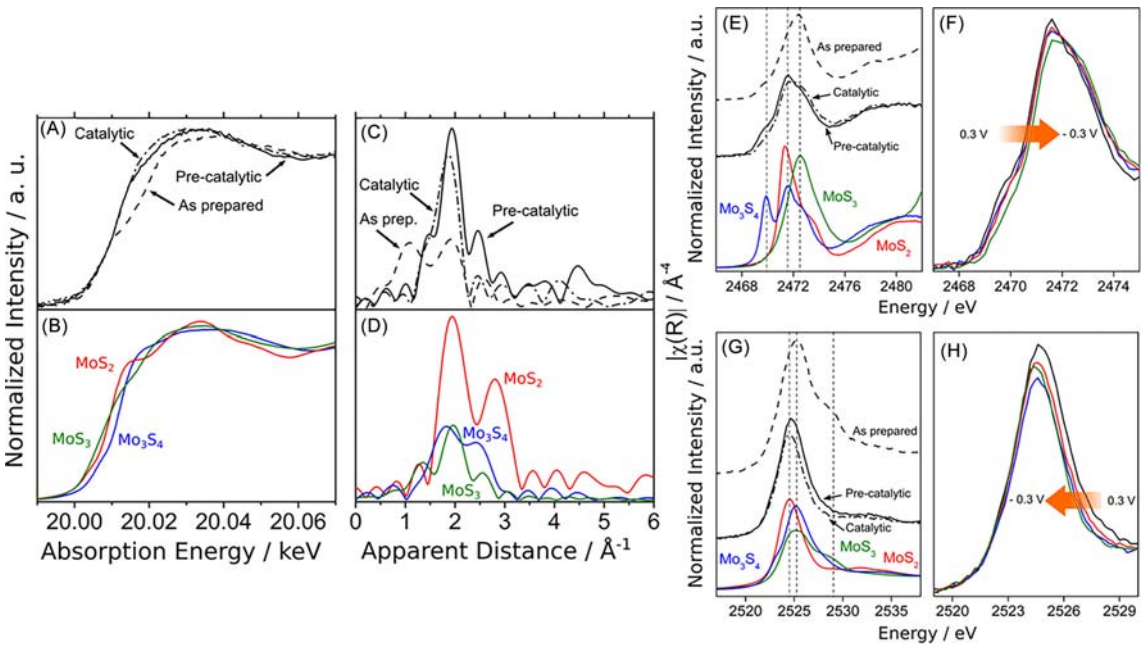

Fig. 13 (a) Mo K-edge XANES spectra of the MoS_x film as prepared and in the precatalytic and catalytic states. (b) Mo K-edge XANES spectra of Mo_3S_4, MoS_2 and MoS_3. (c) Mo K-edge Fourier transform EXAFS (k^3-weighted) of the MoS_x film as prepared and in the precatalytic and catalytic states. (d) Mo K-edge Fourier transform EXAFS (k^3-weighted) of Mo_3S_4, MoS_2, and MoS_3. Sulfur K-edge spectra of (e) the MoS_x film as prepared, in the precatalytic and catalytic states, together with Mo_3S_4, MoS_2 and MoS_3 reference spectra, and (f) the MoS_x film poised at 0.3 (black), 0.1 (blue), −0.1 (red), and −0.3 V (green) in nitric acid at pH = 2. (g) Molybdenum L_3-edge spectra of the MoS_x film as prepared, in the precatalytic and catalytic states, together with Mo_3S_4, MoS_2, and MoS_3 and (h) the MoS_x film poised at 0.3 (black), 0.1 (blue), −0.1 (red), and −0.3 V (green) in nitric acid. From Lassalle-Kaiser, B.; Merki, D.; Vrubel, H.; Gul, S.; Yachandra, V. K.; Hu, X. et al. Evidence From In Situ X-Ray Absorption Spectroscopy for the Involvement of Terminal Disulfide in the Reduction of Protons by an Amorphous Molybdenum Sulfide Electrocatalyst. *J. Am. Chem. Soc.* **2015**, *137* (1), 314–321, doi: 10.1021/ja510328m.

Through comparison with model compounds, they were able to determine the presence of terminal disulfides, and demonstrate how these are involved in the reduction of protons. In situ XAFS shows the surface of the pre-catalytic film becomes hydrolyzed at 0.3 V (pH = 2), by loss of Mo−O interactions. Whilst this had been observed by XPS, the detection by XAFS revealed that this extended to the bulk of the material. Fitting of 6 Mo−S interactions at $R = 2.40$ Å and 1 Mo − Mo interaction at $R = 2.74$ Å indicate the MoS_3 structure, however additional Mo $L_{2,3}$-edge and S K-edge XAFS fits reveal characteristics of Mo_3S_4 and suggest a fraction of trinuclear Mo_3S_x units are present. Significantly, this composition differs from the as-prepared material, and reveals that the catalyst is reduced once it is immersed in acidic media, forming an amorphous Mo^{4+}, S^{2+} material. The XANES features at the S K and Mo $L_{2,3}$-edge therefore suggest that a fraction of MoS_3 and/or Mo_3S_4 is still present, even though MoS_2 would seem the best fit, with the authors proposing that the MoS_3 disulfide ligands at the surface are converted to MoS_2.

On reduction of the applied potential to −0.3 V (catalytic conditions) there is a reduction in the Mo−Mo interaction at ca. $R = 2.75$ Å with an accompanying increase in the Mo−S distance signifying further conversion of MoS_3 to MoS_2 causing the disappearance of the bridging disulfide units. The S oxidation state is observed to increase slightly which is attributed to the presence of terminal disulfide units. The subtle changes in the XAFS strongly suggest that these chemical changes are occurring only at the surface, i.e., the solid-liquid interface, and the authors proposed H_+ is able to bond to these terminal disulfides, oxidizing to Mo^{4+}, before reacting with an additional proton to generate H_2 and reducing the surface back to Mo^{3+}. Whilst the role of these terminal disulfides had been previously proposed, using in situ XAFS this was the first study to experimentally observe it, contributing to further mechanistic insights, notably the reductive breaking of the S−S bond being the limiting step (Fig. 14).

10.05.3.8.2 Oxygen evolution reaction (OER)

The OER is affected by higher potential losses than the HER, and so development of stable catalysts that operate at low overpotentials is crucial. One class of materials that have received much attention for OER in acidic media are iridium-based oxides, with the relative importance of crystalline IrO_2 vs hydrous IrO_x being debated, along with determination of the oxidation state of Ir under operating conditions, the role of metallic Ir and of mixed metal oxides such as Ir−Ru.

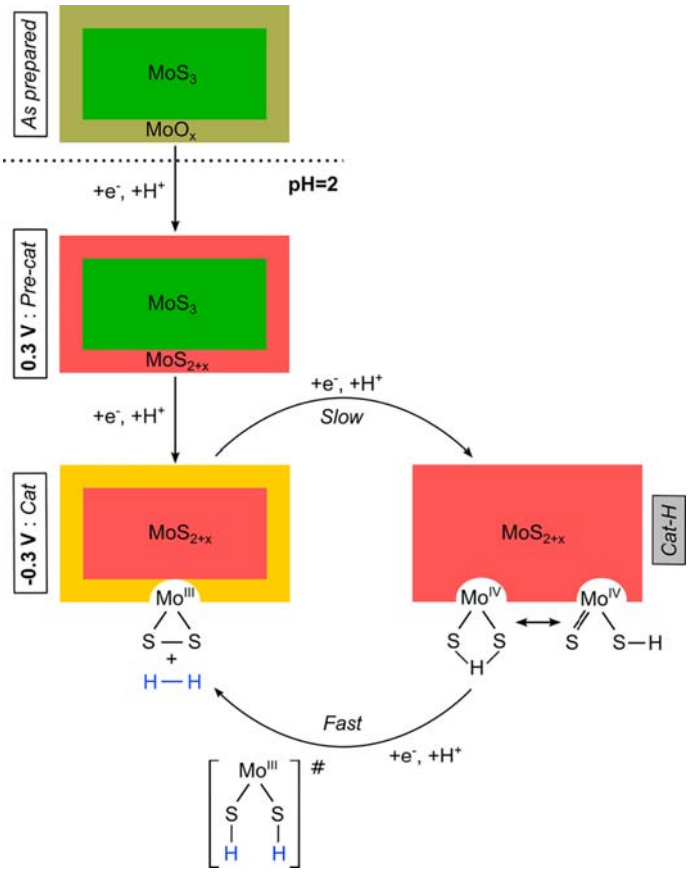

Fig. 14 Proposed changes and catalytic cycle for the MoS_x film as prepared and at pH = 2 under pre-catalytic and catalytic conditions. The Cat-H species is putative and has not been observed experimentally. From Lassalle-Kaiser, B.; Merki, D.; Vrubel, H.; Gul, S.; Yachandra, V. K.; Hu, X. et al. Evidence From In Situ X-ray Absorption Spectroscopy for the Involvement of Terminal Disulfide in the Reduction of Protons by an Amorphous Molybdenum Sulfide Electrocatalyst. *J. Am. Chem. Soc.* **2015**, *137* (1), 314–321. doi: 10.1021/ja510328m.

Cheng 2019 reported on a nanorod IrO_x-TiO_2 on Ti mesh (ITOT) for acidic OER that demonstrated improvements in activity and high cyclic stability over IrRu based catalysts. The first shell bond length of Ir−O (∼1.7 Å) has been linked to the oxidation state, with longer bonds equating to lower oxidation states.[137] The ITOT catalyst was prepared with and without a calcination step prior to study. EXAFS fitting of the ITOT catalyst calculated the Ir−O bond to be 1.73 Å indicating a lower oxidation state then Ir^{4+}. In acidic media, the potential was varied from 1.05–2.2 V with a final hold at open circuit potential (OCP), whilst recording the XAFS spectra in situ. This revealed the Ir−O bond to shorten as the potential increased in uncalcined samples (indicating increasing oxidation state), whilst a calcination step resulted in no bond-length change as a function of the applied potential (Fig. 15). Further, the bond lengths and valence state of the uncalcined sample was shown to return to its initial state. This was corroborated by the XANES spectra, and showed that Ir valency increased beyond Ir^{4+} at the highest potentials for the uncalcined sample. The uncalcined sample exhibited higher OER activity, excellent durability during a 100 h, 10 mA cm^{-2} chronopotentiometry test and better cycling stability (OER) onset potential of 1.428 V with excellent stability, increasing marginally to just 1.461 V after 700 cycles. The Ir^{3+} and the mixed-valent $Ir^{3+/4+}$ hydrated amorphous oxyhydroxides which caused the high surface concentration of OH were directly observed by in situ XAFS, as was the controllable aspect of their nature; the formation of these beneficial mixed oxidation states was attributed to the role of the TiO_2 support. It was also found that a small proportion of metallic Ir in the core of the nanorods is beneficial for charge transfer, corroborated by similar in situ EXAFS studies on iridate pyrochlores by Burnett 2020 who proposed a single-site band model where there is involvement of electrons from the conduction band of metallic particles and not just the oxidized surface sites.[138] Further. this dynamic and controllable change of the Ir oxidation state as revealed by in situ XAFS, contributed to the development of a proposed mechanism for OER on Ir-catalysts in acidic media.

10.05.3.8.3 Oxygen reduction reaction (ORR)

Carbon has long been used as a support material for ORR catalysts due to its high conductivity, low cost and chemical stability, whilst recent efforts to reduce the amount of Pt in ORR electrocatalysts have included the development of Pt−Sn alloys. However, there are still challenges faced from the corrosion of the carbon support when operating at higher current densities. To this end, Su 2020 among others has investigated graphene as an alternative to carbon, due to the improved corrosion resistance and both mass/charge transfer properties.[139]

The Pt_3Sn/G catalyst was shown to have a more positive onset potential, improved ORR activity at 0.85 V than commercial Pt/C catalysts, and also greater stability during accelerated durability testing of 5000 cycles (both more stable nanoparticle size when compared with commercial Pt/C, and also smaller decrease in current density during linear sweep voltammetry). EXAFS measurements at both Pt L_3 and Sn K edges revealed the catalyst to be alloyed, resulting in increased occupancy of the Pt 5d bands through

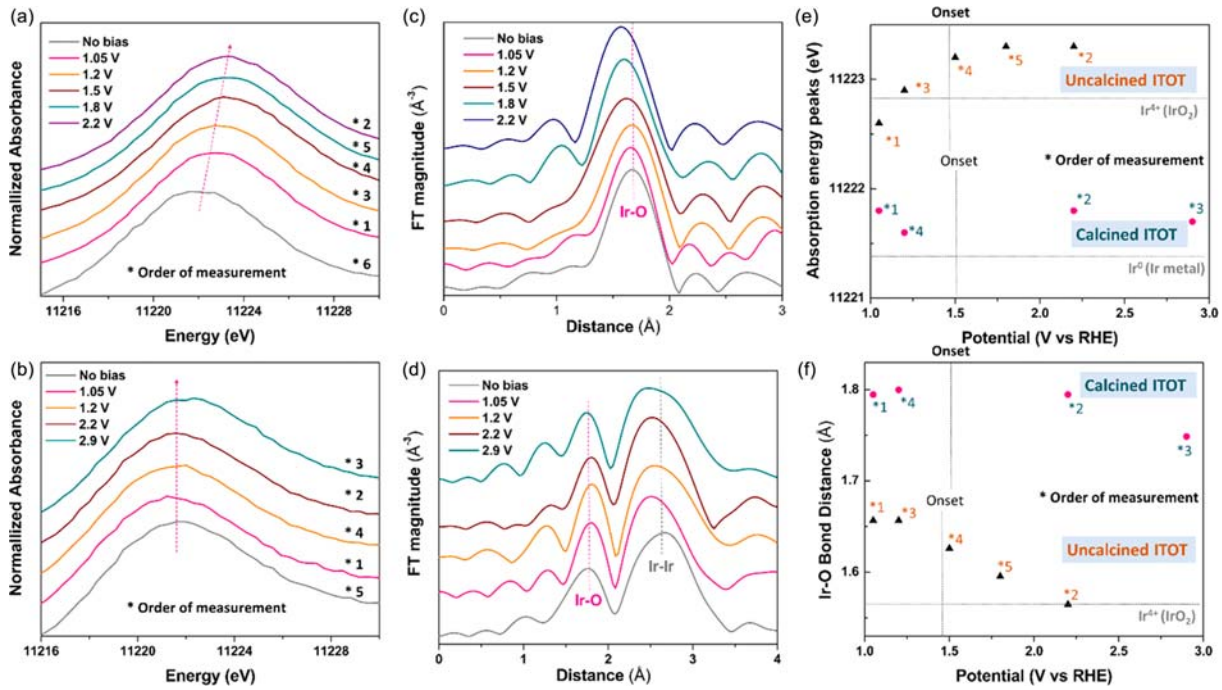

Fig. 15 In situ XAFS analysis of the ITOT catalysts. (a and b) In situ XANES absorption edge of the uncalcined ITOT (a) and calcined ITOT (b) catalysts at different applied potentials. (c and d) In situ Fourier transformed EXAFS spectra of the uncalcined ITOT (c) and calcined ITOT (d) catalysts with the k weight of 2 at the applied potentials. (e) The XANES absorption energy peak positions of the uncalcined and calcined samples at different applied potentials. (f) The EXAFS-determined Ir−O bond distance of the uncalcined and calcined samples as a function of the applied potentials. From Cheng, J.; Yang, J.; Kitano, S.; Juhasz, G.; Higashi, M.; Sadakiyo, M. et al. Impact of Ir-Valence Control and Surface Nanostructure on Oxygen Evolution Reaction over a Highly Efficient Ir–TiO_2 Nanorod Catalyst. *ACS Catal.* **2019**, *9* (8), 6974–6986. doi: 10.1021/acscatal.9b01438.

hybridization with the Sn 5d bands, and revealing the Sn to be present as partially reduced SnO_2 (see Fig. 16). The authors propose that this hybridization may be the cause of the observed catalytic enhancement, leading to increased O_2 adsorption and a weakened O—O double bond. In situ QEXAFS of the catalyst during cyclic voltammetry (CV) in acidic media tracked the white-line intensity of the Pt. A decrease in intensity with increasing potential was observed, which then returned to the starting intensity as the CV was swept back to the start potential (Fig. 16). Fitting of the EXAFS showed the recoverable nature of the Pt—O, Pt—Pt and Pt—Sn bonds during the CV test, indicating that the electrode surface is stable to cycling, and helping to understand the reaction mechanism of proton electroreduction and hydrogen adsorption on the electrocatalyst surface.

10.05.3.8.4 CO_2 reduction reaction (CO_2RR)

CO_2 can be selectively reduced to hydrocarbons using CuO_x catalysts. Lin 2020 developed an operando time-resolved XAFS approach to determine the active state of the catalyst. By switching the potential (redox-shuttle), the authors were able to achieve a fixed $Cu^{0/1+}$ oxidation state ratio (1-to-1) to selectively produce C_2H_5OH, demonstrating how electrocatalysis can be used to utilize captured CO_2 for the synthesis of useful/feedstock chemicals.[140]

Whilst conventional XAFS measurements enabled observation of the catalyst under steady-state conditions, the operando approach employed by Lin achieved temporal resolution of 5–60 s/spectrum, which could be compared/combined with the electrochemical data (chronoamperometry and redox-shuttle approaches), in order to reveal the active state of the Cu catalysts during each approach, and to correlate this to the product selectivity. Through fitting of the EXAFS, the redox-shuttle approach was found to maintain an even mixture of Cu oxidation states (ca. 50% each Cu^0 and Cu^{1+}), whereas the chronoamperometric approach resulted in an increasing proportion of metallic Cu and a corresponding decrease in Cu^{1+}. The chemical nature of the CuO_x catalyst was found to reach a steady state under redox-shuttling, and that this delicate balance of oxidation states was responsible for the selectivity to C_2H_5OH. Further, these findings indicated that differing surface compositions of Cu^0/Cu^{1+} may result in differing product selectivity, for example a Cu^0-dominated surface having higher selectivity towards CO (Fig. 17).

The application of in situ and *operando* XAFS to study electrocatalytic reactions has been shown to help reveal the active state of the electrocatalysts, and to provide insight into reaction mechanisms. Recent developments in time-resolved approaches enable the study of these dynamic systems on relevant timescales, and not just under steady state conditions. The insights gained from these studies help motivate future work in both the design and engineering of catalyst structure and composition, as well as further technique development.

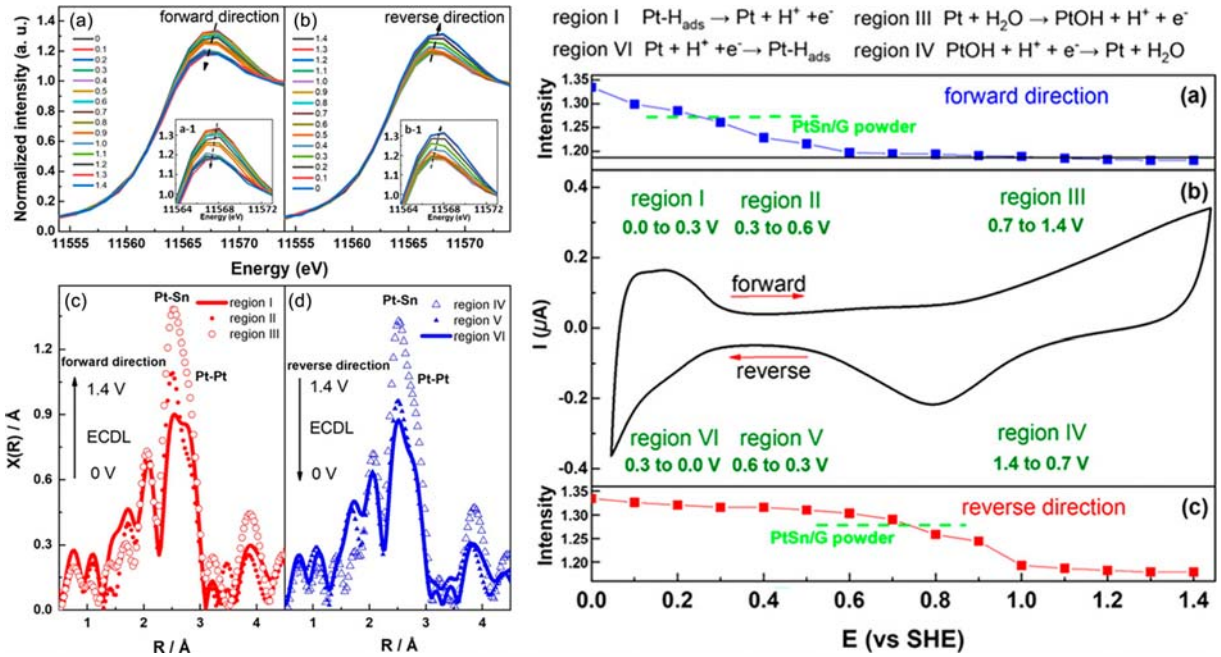

Fig. 16 (left) In situ Pt L_3-edge XANES spectra and *R*-space (k^3-weighted QEXAFS spectra) of Pt_3Sn/G catalysts under the CV test of (a) and (c) in the forward direction, as well as (b) and (d) in the reverse direction. Insets in (a) and (b) are the enlarged rising absorption edge regions. (right) Peak intensity of the white line of the in situ Pt L_3-edge XAFS spectra for Pt_3Sn/G catalysts under the CV test. The proposed reaction mechanisms associated with the corresponding CV voltages are shown at the top. Adapted with permission from Su, B.-J.; Wang, K.-W.; Tseng, C.-J.; Pao, C.-W.; Chen, J.-L.; Lu, K.-T. et al. High Durability of Pt_3Sn/Graphene Electrocatalysts toward the Oxygen Reduction Reaction Studied with In Situ QEXAFS. *ACS Appl. Mat. Interf.* **2020**, *12* (22), 24710–24716, doi: 10.1021/acsami.0c02415, Copyright 2020 American Chemical Society.

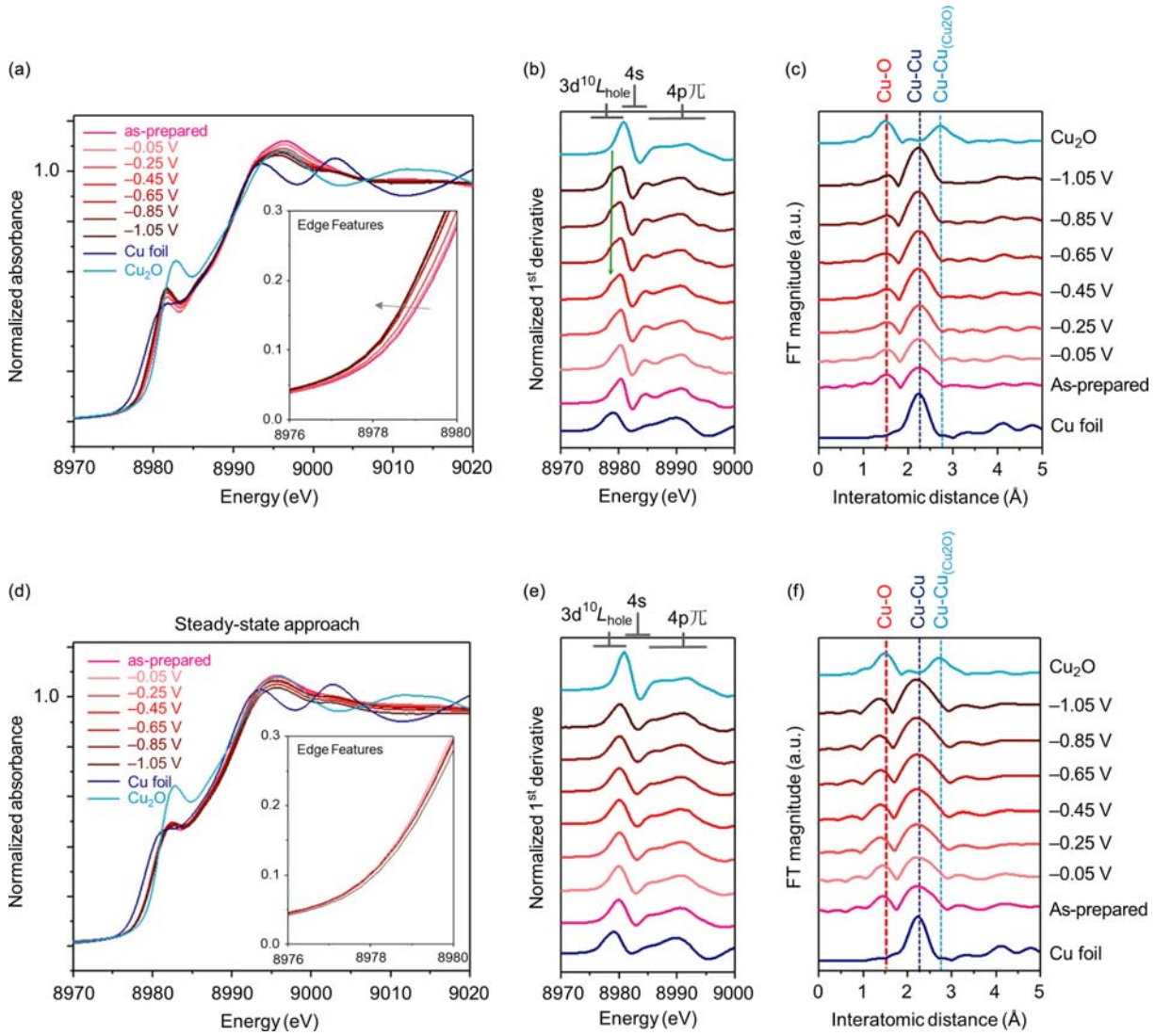

Fig. 17 (a) Potential dependence of operando Cu K edge XANES spectra without phase-correction of the CuO_x under CO_2RR in 0.5 M CO_2-saturated $KHCO_3$ using chronoamperometry (CA) and the corresponding 1st derivative spectra (b). In (c) potential dependence of operando EXAFS spectra of the CuO_x under eCO_2RR in 0.5 M CO_2-saturated $KHCO_3$ using CA. In (d) the potential dependence of operando Cu K edge XANES spectra without phase-correction of the CuO_x under CO_2RR in 0.5 M CO_2-saturated $KHCO_3$ using redox shuttling and the corresponding 1st derivative spectra (e). (f) Potential dependence of operando EXAFS spectra of the CuO_x under eCO_2RR in 0.5 M CO_2-saturated $KHCO_3$ using redox shuttling. From Lin, S.-C.; Chang, C.-C.; Chiu, S.-Y.; Pai, H.-T.; Liao, T.-Y.; Hsu, C.-S. et al. Operando Time-Resolved X-Ray Absorption Spectroscopy Reveals the Chemical Nature Enabling Highly Selective CO_2 Reduction. *Nat. Commun.* **2020**, *11* (1), 3525, doi: 10.1038/s41467-020-17231-3.

10.05.4 Obtaining more information on the state of the catalyst

10.05.4.1 Imaging studies

In addition to the understanding that one technique is not enough to fully characterize an active catalyst, so it is also true that the measurement of only one part of a catalyst sample may not allow for the identification of the species responsible for desired performance. Ideally, in most studies, focused beams are located in the middle of the hot zone in a reactor bed. This can be a particular problem If the catalytic reaction is carried out at low space velocities (i.e., conversion of methane) as it may transpire that what is actually being measured by the characterization techniques is the behavior of the catalyst in response to the product stream which can be more reactive than the initial reactant. In addition, variation at the micro and nano-scale heterogeneities in the sample composition or preparation process can occur. As a result, there has been a push towards bed reactor and single particle profiling/imaging to put these variations in composition into context of catalytic performance. The porosity and morphology of reactor beds and catalyst particles have been studied already for a number of years using simple absorption contrast tomography although in recent times there has been a push to perform what is now commonly referred to as chemical imaging i.e., where instead of an absorption contrast image derived based on Eq. (1), a full spectrum per measured pixel is obtained. XANES imaging has been

successfully performed on a number of occasions to profile a range of catalysts and often under reaction conditions and with a spatial resolution reaching nm and temporal resolution that is sub-second, see Meirer et al. and references therein for a more comprehensive appreciation of this topic.[141–143] The application of EXAFS imaging is comparatively limited mainly because so many datasets have to be obtained, it involves acquisition times lasting many hours. There is at least one example by Tada et al. who used an X-ray μ-beam (1000 nm (h) × 800 nm (v)) to characterize a single particle of mean size 750 nm of $NiO_x/Ce_2Zr_2O_y$ ($0 \leq x \leq 1$, $7 \leq y \leq 8$) at the Ni K-edge (μ-XANES and μ-EXAFS) in 2D. They identified from the refined coordination numbers and bond lengths of the first and second shells, the presence of NiO species in the inactive catalyst used for methane reforming to syn gas with each map taking 3 h to acquire.[144] Furthermore in this study, the measurements were made ex situ and the samples that were pre-reduced suffered from partial reoxidation and illustrates an additional challenge for EXAFS imaging regarding the availability of suitable cells to perform such experiments under in situ or *operando* conditions. Standard capillary or plug-flow reactor cells for example, need to possess very small internal diameters (400 μm) in addition to some modification to the sample composition in order to avoid self-absorption effects leading to shadowing of the XAFS signal.[41,145] This is less of an issue when using micro-reactors that are also amenable to interrogation using transmission electron microscopy (TEM) although the data acquired do not possess depth contrast and there are challenges with collecting data under operando conditions (reactant bypass).[141,146] For the time being, the acquisition of spatially resolved data may be best realized by spot EXAFS data acquisition from regions of interest in data profiled by XRF or XANES mapping/tomography.

10.05.4.2 Novel analysis methods for determining active species present

10.05.4.2.1 Post reaction data analysis methods

In an ideal world, an in situ or *operando* EXAFS experiment will allow for the identification of the active species responsible for catalytic performance and ideally, if the time resolution is high enough, the intermediates in a reaction thereby allowing a better understanding of a catalytic mechanism. This premise is complicated by two main problems. Firstly that many of the heterogeneous catalysts prepared by conventional preparation methods often contain a wide variety of species which may (active) or may not (spectator species) contribute to a catalysts desired performance. Even when observing species in real time and with high time resolution it is not always possible to identify those that are responsible for the catalytic performance. Modelling of EXAFS data for example is typically performed on the basis that only one component (the active) is present despite complementary characterization data often revealing evidence to the contrary. There are also two ways to solve this problem which can be classified as bottom-up or top-down. The former requires that more time and effort be expended in catalyst design or synthesis i.e., the control of the nanoparticle size, morphology and composition although it should be noted that when using micelle-based methods for catalyst nanoparticle delivery it can sometimes be difficult to effect the same metal support interactions obtained with more conventional methods. The latter approach requires a deeper delve into the data using principal component analysis (PCA) else the application of machine learning (ML) methods. For a more comprehensive overview of the application of such methods the reader is encouraged to consult the review of Timoshenko and Frenkel.[147]

A common form of ML methods used for the study of XAFS data utilize neural networks (NN). The NN is a series of algorithms that tries to recognize underlying relationships in a set of data in a process akin to the way the human brain operates. In recent times these have been successfully applied for the study of XANES and EXAFS spectra to obtain coordination numbers and distances from monometallic and bimetallic nanoparticles and the metal component of oxide clusters. Although very powerful, a successful application of NN-based methods requires a large number of training data sets typically in the tens to hundreds of thousands. Although much progress has been made in creating and curating XAFS spectral databases, they tend to contain well characterized crystalline reference compounds and are therefore not broad enough to tackle the breadth of (possible) local environments encountered in heterogeneous catalyst (i.e., nanoparticles). Ab initio simulations of XAFS data are therefore often the only viable approach for constructing such data sets although automated procedures for selection of active learning training examples for a particular problem may be helpful.[148] This renders the generation of training data to be the most time-consuming part of these methods since the accuracy of NN predictions depends on the quality (and quantity) of the inputs. The output should also be validated using sets of experimental data for well-defined model samples and performed on a case-by-case basis. Where relevant experimental spectra are unavailable to minimize bias the NN should be ideally 'supervised' to predict structures that can be present in real catalytic materials and particularly the active states observed in situ or under *operando* conditions. Supervised machine learning (SML) approaches have been successfully applied to characterize, for example, the NP size, shape and interatomic distance and other structurally relevant parameters affecting the XAFS spectra. For example, in the work by Timoshenko et al. the CNs for the first four coordination shells were used to determine the average size and shape for experimentally investigated NPs.[149] Not only were the XAFS obtained NPs sizes in agreement with TEM results, preformed Pt NPs, synthesized via inverse-micelle encapsulation were determined to be more spherical, while NPs prepared via support impregnation were found to be flatter. The same group has also shown how subtlety in the asymmetric shapes of RDF peaks, can be used to obtain information on the average density of atom packing, which is different for face-centered cubic (fcc) and body-centered cubic (bcc) structures on Fe undergoing a phase change.[150]

In situ changes in NP shape, increase in disorder, interactions with adsorbates, and so on, that are difficult to tackle with supervised ML methods and therefore require unsupervised ML methods which employ data clustering and dimensionality reduction to help determine the presence of uncommon/unknown components.[147] Cluster analysis attempts to find a few spectra that could represent the whole data set and has found particular use to map the distribution of similar species in imaging studies.[151] This then allows for performing a more detailed analysis of these representative spectra whilst still providing a complete description

of the sample. Perhaps a more powerful and more widely applied approach is principal component analysis (PCA). This is used to determine the orthogonal vectors that account for the largest discrepancies between spectra in the data set and to identify the components that contribute most significantly to ideally a large number of acquired spectra. If the spectra for the pure compounds are known, the spectra for the unknown components can be reconstructed using target transformation.[152] PCA-XANES has been used on a number of occasions in time-resolved in situ studies of catalysts.[153] Alternative approaches to this which are more commonly referred to as blind signal separation (BSS) methods include independent component analysis (ICA), non-negative matrix factorization (NNMF) and multivariate-curve resolution with alternating least-squares (MCR-ALS), with perhaps the latter the most popular BSS method for XANES data analysis.[147,154–156] It should be noted however that MCR-ALS yields only the corresponding XAFS spectra for pure components, without any reference to oxidation/coordination states and hence for interpretation of the obtained spectra, it is necessary to compare them with the spectra of reference materials. It is important to note then that the PCA and BSS methods are most advantageous for determining the speciation over conventional LCF, when the structure of the investigated material differs significantly from the structure of well-defined bulk reference materials.

One of the pitfalls of conventional EXAFS analysis is when two or more scattering paths have similar path lengths, and their EXAFS signal can interfere with each other destructively and mask the intensity in the Fourier transform (FT). This is often the case for higher coordination shell contribution. Furthermore, since FT–EXAFS is the delocalization of χ in k–space and complete localization in R-space, the loss of resolution in the original data space means information on elemental speciation of the backscattering atom is lost in the magnitude of the FT transformed signal. The wavelet transform (WT) analysis offers a way to distinguish overlapping EXAFS scatters paths by providing resolution in both k and R space.[157] The 3D contour generated from the EXAFS data can be compared to a reference compound or theoretical calculation, and information on the local environment around the absorber atom can be obtained directly without fitting the EXAFS data. WT-EXAFS has recently been employed for the structural characterization of the active Cu species in Cu-ion-exchanged chabazite catalysts for selective catalytic reduction (NH_3-SCR) of NO_x.[158] The analysis has been successfully applied to identify Cu−Cu second shell scattering path and provides direct evidence for the formation of Cu- pairs in the NH_3-SCR reaction.

10.05.4.2.2 Modulation excitation methods

An alternative strategy for improving the sensitivity of X-ray absorption spectroscopy involves the modulated excitation approach in which the sample is excited with multiple periodic external simulation (typically a change in the concentration of a reactant, temperature or voltage jump) with the subsequent spectra Fourier filtered using the same frequency as the excitation. Although similar to a difference spectrum, the resultant demodulated spectrum has been shown to contain a more marked signal (for EXAFS the signal is stronger at higher k values) because it only contains the response from the component changing with a particular frequency. The approach allows for distinguishing between multiple intermediate species and the order in which they appear based on the difference in the phase delay. It has been successfully demonstrated for determining the presence of precious metal Me^0 core-MeO shell nanoparticles when oscillating between reducing $H_2/CH_4/CO$ and oxidizing (O_2 containing) atmospheres.[159] Importantly the application of this technique allows for the separation and detailed EXAFS analysis of the components in a mixed spectra (i.e., comprising both Pd and PdO) which is not possible from the time-resolved data which also contains a mixture of both phases (Fig. 18). Furthermore it has also been shown by Konig et al. that this method can be used to improve the fitting of the EXAFS data, particularly the detection of oxidic surfaces on Ru nanoparticles as well as the potential-induced changes in coordinating ligand environment in Fe/N/C-catalysts to determine the more ORR-active form.[160] Critical for the performing of valid studies is the confirmation, typically by online MS analysis/a potentiostat of the reversibility of the system under study and hence thus far the most successful demonstrators of this approach have involved systems with simple gas mixtures known to be robust to fast gas switching and temperature excursions.

The application of these advanced experimental and data analyses methods has really only become more commonplace in the last ~10 years but their application is already enabling catalysis researchers to delve deeper into the data and to extract more meaningful structure-activity relationships. It should be noted however that neither advanced data analysis or experimental modulation is an assured way of differentiating between active species and spectators that may dominate any spectroscopic signal. There may well also be a case for combining the methodologies i.e., to perform ML analysis on data acquired through modulation experiments.

10.05.5 Conclusions and future perspectives

EXAFS as a technique has gone from strength to strength in the last 25 years or so—from a technique that was essentially niche to one that is now commonly used for catalyst characterization. This can be traced to a combination of factors including, a greater number of beamlines, a quicker rate of data acquisition (spectra are now typically acquired in minutes), a greater availability of sample environments and the availability of resources to perform and help with the data analysis. Modern software available at some synchrotrons even has the capability to perform real time data processing i.e., isolating the EXAFS and providing an FT as the spectra are acquired.[161] EXAFS spectroscopy will continue to be an essential tool for studying and characterizing catalysts for a long time yet. This is down to a combination of the suitability of the nature of heterogeneous catalysts as well as the versatility of the technique to yield valuable information ex situ and in situ or under *operando* conditions, often in combination with other X-ray or optical spectroscopy techniques. There will always be a need to create innovative catalysts in order to develop and realize

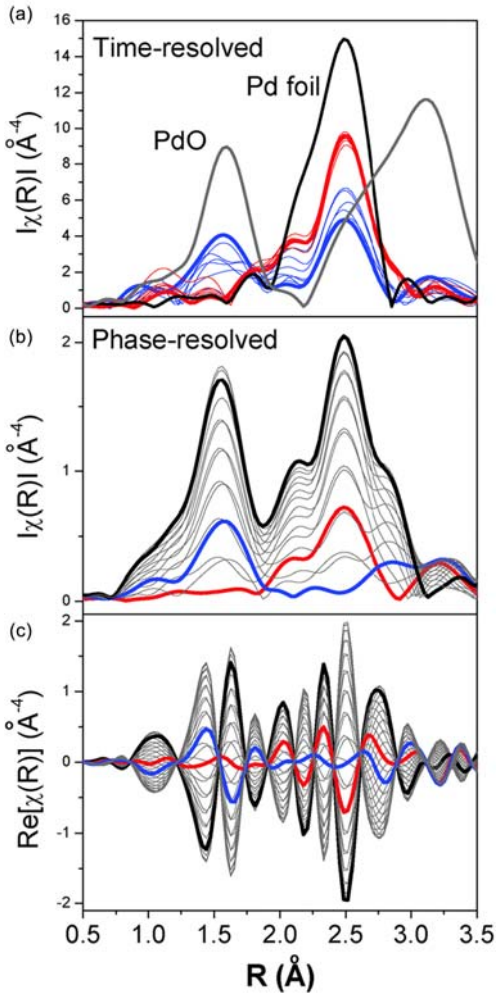

Fig. 18 ME-EXAFS & FT results at the Pd K-edge obtained on 1.6 wt% Pd/Al_2O_3 during a 1 vol% O_2/He to 1 vol% H_2/He modulation experiment. (a) k^3-weighted FT-EXAFS spectra of bulk PdO (grey), Pd foil (black) and averaged time-resolved spectra recorded in 1 vol% O_2/He (blue) and in 1 vol% H_2/He (red); (b) phase-resolved FT-EXAFS spectra ($0° < \varphi^{PSD} < 360°$); (c) real part of the phase-resolved FT-EXAFS spectra in (b). In (b) and (c) the spectra at $\varphi^{PSD} = 160°$ (black line), $\varphi^{PSD} = 230°$ (red line) and $\varphi^{PSD} = 250°$ (blue line) are highlighted. From Chiarello G. L.; Ferri D. Modulated Excitation Extended X-Ray Absorption Fine Structure Spectroscopy. *Phys. Chem. Chem. Phys.* **2015**, *17* (16), 10579–10591, doi: 10.1039/C5CP00609K.

more sustainable processes and the insight provided by techniques like EXAFS underpins their development at all stages of the development process (i.e., from concept, to design, to application and to, where necessary, improvement and scale-up).[162]

We are currently at the beginning of the 4th generation light source era which is an exciting time for the EXAFS technique. The increased brightness this generation will offer, often coupled with more sensitive and better performing detectors will allow for collecting data in scanning mode with time resolutions regularly in the ms and theoretically even faster. This may well allow for better resolution of reaction steps and therefore a greater possibility to understand reaction mechanisms particularly when combined with advanced analytical methods such as MES. Careful consideration of data handling is needed however if the advantages of the increased volume can be exploited to maximum benefit. As highlighted earlier, capability (i.e., ML and MCR methods) is being developed that will allow users to extract the most value/information from their data. The impact of increased brightness (although one notes that the gain in brightness is perhaps of the order of $\sim$3 times unlike coherent scattering which gains by orders of magnitude) on the sample and the data quality should be carefully tensioned against the risk that this benefit might actually cause the changes in the sample observed in an experiment.[163]

Lab-based XAFS spectroscopy has recently undergone a renaissance and will again serve to complement the work done at SR sources. Whether they offer sufficient k-range to enable EXAFS analysis is unclear yet they will offer possibilities for performing long duration experiments during catalyst start-up or deactivation which generally aren't tractable at SR sources. This may of course change with the development of Table-Top synchrotrons which are making progress but are yet to be widely available.[164]

As far as Free Electron Lasers (FELS) are concerned, these offer the ultimate in time-resolution (femto-seconds able to observe bond breaking and formation) although challenges remain recording EXAFS data and particularly with the sample environment i.e.,

manipulation, delivery and interrogation which is performed very differently to the more conventional XAFS spectroscopy covered herein.[165] Interestingly the development of infrastructure for the study of metalloenzymes using such FEL-XAFS may mean that homogeneous catalysis experiments are more tractable in the near future than heterogeneous catalysis ones.[166]

References

1. Iwasawa, Y.; Kiyotaka, A.; Tada, M. *XAFS Techniques for Catalysts, Nanomaterials, and Surfaces*, Springer, 2017. https://doi.org/10.1007/978-3-319-43866-5.
2. Teo, B. K. *EXAFS: Basic Principles and Data Analysis*, Springer: Berlin, Heidelberg, 1986. https://doi.org/10.1007/978-3-642-50031-2.
3. Dirac, P. A. M.; Bohr, N. H. D. The Quantum Theory of the Emission and Absorption of Radiation. *Proc. R. Soc. Lond. Ser. A* **1927,** *114* (767), 243–265. https://doi.org/10.1098/rspa.1927.0039; Fermi, E. *Nuclear Physics*, University of Chicago Press, 1950.
4. Smith, J. W.; Saykally, R. J. Soft X-Ray Absorption Spectroscopy of Liquids and Solutions. *Chem. Rev.* **2017,** *117* (23), 13909–13934. https://doi.org/10.1021/acs.chemrev.7b00213.
5. Ravel, B.; Newville, M. ATHENA, ARTEMIS, HEPHAESTUS: Data Analysis for X-Ray Absorption Spectroscopy Using IFEFFIT. *J. Synchrotron Radiat.* **2005,** *12,* 537–541. https://doi.org/10.1107/s0909049505012719.
6. Koningsberger, D. C.; Mojet, B. L.; van Dorssen, G. E.; Ramaker, D. E. XAFS Spectroscopy; Fundamental Principles and Data Analysis. *Top. Catal.* **2000,** *10* (3–4), 143–155. https://doi.org/10.1023/A:1019105310221.
7. Rehr, J. J.; Ankudinov, A. L. Progress in the Theory and Interpretation of XANES. *Coord. Chem. Rev.* **2005,** *249* (1), 131–140. https://doi.org/10.1016/j.ccr.2004.02.014; Groot, F. M. F. D. XANES Spectra of Transition Metal Compounds. *J. Phys.* **2009,** *190*, 012004. https://doi.org/10.1088/1742-6596/190/1/012004.
8. Joly, Y.; Grenier, S. Theory of X-Ray Absorption Near Edge Structure. In *X-Ray Absorption and X-Ray Emission Spectroscopy*, John Wiley & Sons, 2016; pp 73–97. https://doi.org/10.1002/9781118844243.ch4; Davies, C. J.; Mayer, A.; Gabb, J.; Walls, J. M.; Degirmenci, V.; Thompson, P. B. J.; Cibin, G.; Golunski, S.; Kondrat, S. A. Operando Potassium K-Edge X-Ray Absorption Spectroscopy: Investigating Potassium Catalysts during Soot Oxidation. *Phys. Chem. Chem. Phys.* **2020,** *22* (34), 18976–18988. https://doi.org/10.1039/D0CP01227K.
9. Stern, E. A.; Sayers, D. E.; Lytle, F. W. Extended X-Ray-Absorption Fine-Structure Technique. III. Determination of Physical Parameters. *Phys. Rev. B* **1975,** *11* (12), 4836–4846. https://doi.org/10.1103/PhysRevB.11.4836.
10. Lee, P. A.; Citrin, P. H.; Eisenberger, P.; Kincaid, B. M. Extended X-Ray Absorption Fine Structure—Its Strengths and Limitations as a Structural Tool. *Rev. Mod. Phys.* **1981,** *53* (4), 769–806. https://doi.org/10.1103/RevModPhys.53.769.
11. Lee, P. A.; Pendry, J. B. Theory of Extended X-Ray Absorption Fine Structure. *Phys. Rev. B* **1975,** *11* (8), 2795–2811. https://doi.org/10.1103/PhysRevB.11.2795.
12. Diaz-Moreno, S.; Amboage, M.; Basham, M.; Boada, R.; Bricknell, N. E.; Cibin, G.; Cobb, T. M.; Filik, J.; Freeman, A.; Geraki, K.; et al. The Spectroscopy Village at Diamond Light Source. *J. Synchrotron Radiat.* **2018,** *25,* 998–1009. https://doi.org/10.1107/S1600577518006173.
13. Lomachenko, K. A.; Molokova, A. Y.; Atzori, C.; Mathon, O. Quantification of Adsorbates by X-Ray Absorption Spectroscopy: Getting TGA-Like Information for Free. *J. Phys. Chem. C* **2022,** *126* (11), 5175–5179. https://doi.org/10.1021/acs.jpcc.2c00226.
14. McMaster, W. H.; Kerr Del Grande, N.; Mallett, J. H.; Hubbell, J. H. Compilation of X-Ray Cross Sections UCRL-50174, Sections I, II Revision 1, III, IV. *At. Data Nucl. Data Tables* **1970,** *8* (4), 443–444. https://doi.org/10.1016/S0092-640X(70)80026-2.
15. Tröger, L.; Arvanitis, D.; Baberschke, K.; Michaelis, H.; Grimm, U.; Zschech, E. Full Correction of the Self-Absorption in Soft-Fluorescence Extended X-Ray-Absorption Fine Structure. *Phys. Rev. B* **1992,** *46* (6), 3283–3289. https://doi.org/10.1103/PhysRevB.46.3283.
16. Whiting, G. T.; Meirer, F.; Weckhuysen, B. M. Operando EXAFS and XANES of catalytic solids and related materials. In *XAFS Techniques for Catalysts, Nanomaterials, and Surfaces;* Iwasawa, Y., Asakura, K., Tada, M., Eds., Springer International Publishing, 2017; pp 167–191.
17. Agote-Aran, M.; Kroner, A. B.; Islam, H. U.; Slawinski, W. A.; Wragg, D. S.; Lezcano-Gonzalez, I.; Beale, A. M. Determination of Molybdenum Species Evolution during Non-Oxidative Dehydroaromatization of Methane and its Implications for Catalytic Performance. *ChemCatChem* **2019,** *11* (1), 473–480. https://doi.org/10.1002/cctc.201801299.
18. Newton, M. A.; Dent, A. J. *Energy-Dispersive EXAFS: Principles and Application in Heterogeneous Catalysis*, John Wiley & Sons, Inc., 2013.
19. Iwasawa, Y.; Suzuki, A.; Nomura, M. Time-Resolved Energy-Dispersive XAFS for in-Situ Characterization of Nano-Structures and Catalysts. *Phys. Scripta* **2005,** *T115,* 59–65. https://doi.org/10.1238/Physica.Topical.115a00059.
20. Newton, M. A.; Jyoti, B.; Dent, A. J.; Fiddy, S. G.; Evans, J. Synchronous, Time Resolved, Diffuse Reflectance FT-IR, Energy Dispersive EXAFS (EDE) and Mass Spectrometric Investigation of the Behaviour of rh Catalysts during NO Reduction by CO. *Chem. Commun.* **2004,** *21,* 2382–2383. https://doi.org/10.1039/b405694a.
21. Kroner, A. B.; Newton, M. A.; Tromp, M.; Russell, A. E.; Dent, A. J.; Evans, J. Time-Resolved, In Situ DRIFTS/EDE/MS Studies on Alumina Supported Rh Catalysts: Effects of Ceriation on the Rh Catalysts in the Process of CO Oxidation. *Catal. Struct. React.* **2017,** *3* (1–2), 13–23. https://doi.org/10.1080/2055074X.2016.1266762; Dann, E. K.; Gibson, E. K.; Catlow, C. R. A.; Celorrio, V.; Collier, P.; Eralp, T.; Amboage, M.; Hardacre, C.; Stere, C.; Kroner, A.; et al. Combined Spatially Resolved Operando Spectroscopy: New Insights into Kinetic Oscillations of CO Oxidation on Pd/γ-Al_2O_3. *J. Catal.* **2019,** *373,* 201–208. https://doi.org/10.1016/j.jcat.2019.03.037.
22. Tromp, M.; Sietsma, J. R. A.; van Bokhoven, J. A.; van Strijdonck, G. P. F.; van Haaren, R. J.; van der Eerden, A. M. J.; van Leeuwen, P.; Koningsberger, D. C. Deactivation Processes of Homogeneous Pd Catalysts Using in Situ Time Resolved Spectroscopic Techniques. *Chem. Commun.* **2003,** *1,* 128–129. https://doi.org/10.1039/b206758g.
23. Olivo, G.; Barbieri, A.; Dantignana, V.; Sessa, F.; Migliorati, V.; Monte, M.; Pascarelli, S.; Narayanan, T.; Lanzalunga, O.; Di Stefano, S.; et al. Following a Chemical Reaction on the Millisecond Time Scale by Simultaneous X-Ray and UV/Vis Spectroscopy. *J. Phys. Chem. Lett.* **2017,** *8* (13), 2958–2963. https://doi.org/10.1021/acs.jpclett.7b01133.
24. Mesu, J. G.; Beale, A. M.; de Groot, F. M. F.; Weckhuysen, B. M. Probing the Influence of X-Rays on Aqueous Copper Solutions Using Time-Resolved In Situ Combined Video/X-Ray Absorption Near-Edge/Ultraviolet – Visible Spectroscopy. *J. Phys. Chem. B.* **2006,** *110* (35), 17671–17677. https://doi.org/10.1021/jp062618m.
25. Martis, V.; Nikitenko, S.; Sen, S.; Sankar, G.; van Beek, W.; Filinchuk, Y.; Snigireva, I.; Bras, W. Effects of X-Rays on Crystal Nucleation in Lithium Disilicate. *Cryst. Growth Des.* **2011,** *11* (7), 2858–2865. https://doi.org/10.1021/cg200004y.
26. Pascarelli, S.; Mathon, O.; Munoz, M.; Mairs, T.; Susini, J. Energy-Dispersive Absorption Spectroscopy for Hard-X-Ray Micro-XAS Applications. *J. Synchrotron Radiat.* **2006,** *13,* 351–358. https://doi.org/10.1107/s0909049506026938; Sanchez, D. F.; Simionovici, A. S.; Lemelle, L.; Cuartero, V.; Mathon, O.; Pascarelli, S.; Bonnin, A.; Shapiro, R.; Konhauser, K.; Grolimund, D.; et al. 2D/3D Microanalysis by Energy Dispersive X-Ray Absorption Spectroscopy Tomography. *Sci. Rep.* **2017,** *7.* https://doi.org/10.1038/s41598-017-16345-x.
27. Newville, M. IFEFFIT: Interactive XAFS Analysis and FEFF Fitting. *J. Synchrotron Radiat.* **2001,** *8,* 322–324. https://doi.org/10.1107/s0909049500016964.
28. Clark, A. H.; Imbao, J.; Frahm, R.; Nachtegaal, M. ProQEXAFS: A Highly Optimized Parallelized Rapid Processing Software for QEXAFS Data. *J. Synchrotron Radiat.* **2020,** *27* (2), 551–557. https://doi.org/10.1107/S1600577519017053.
29. Shannon, R. Revised Effective Ionic Radii and Systematic Studies of Interatomic Distances in Halides and Chalcogenides. *Acta Crystallogr. A* **1976,** *32* (5), 751–767. https://doi.org/10.1107/S0567739476001551.
30. Stern, E. A. Number of Relevant Independent Points in X-Ray-Absorption Fine-Structure Spectra. *Phys. Rev. B* **1993,** *48* (13), 9825–9827. https://doi.org/10.1103/PhysRevB.48.9825.
31. Penner-Hahn, J. E. X-Ray Absorption Spectroscopy. *eLS* **2005.** https://doi.org/10.1038/npg.els.0002984.

32. Bordiga, S.; Bonino, F.; Damin, A.; Lamberti, C. Reactivity of Ti(IV) Species Hosted in TS-1 Towards H_2O_2-H_2O Solutions Investigated by Ab Initio Cluster and Periodic Approaches Combined with Experimental XANES and EXAFS Data: A Review and New Highlights. *Phys. Chem. Chem. Phys.* **2007,** *9* (35), 4854–4878. https://doi.org/10.1039/b706637f; Bordiga, S.; Coluccia, S.; Lamberti, C.; Marchese, L.; Zecchina, A.; Boscherini, F.; Buffa, F.; Genoni, F.; Leofanti, G.; Petrini, G.; et al. XAFS Study of Ti-Silicalite—Structure of Framework Ti(IV) in the Presence and Absence of Reactive Molecules (H_2O, NH_3) and Comparison with UltraViolet-Visible and IR Results. *J. Phys. Chem.* **1994,** *98* (15), 4125–4132. https://doi.org/10.1021/j100066a036; Nenu, C. N.; Groppo, E.; Lamberti, C.; Beale, A. M.; Visser, T.; Zecchina, A.; Weckhuysen, B. M. Dichloromethane as a Selective Modifying Agent to Create a Family of Highly Reactive Chromium Polymerization Sites. *Angew. Chem. Int. Ed.* **2007,** *46* (9), 1465–1468. https://doi.org/10.1002/anie.200602593; Di Vece, M.; van der Eerden, A. M. J.; Grandjean, D.; Westerwaal, R. J.; Lohstroh, W.; Nikitenko, S. G.; Kelly, J. J.; Koningsberger, D. C. Structure of the Mg_2Ni Switchable Mirror: An EXAFS Investigation. *Mater. Chem. Phys.* **2005,** *91* (1), 1–9. https://doi.org/10.1016/j.matchemphys.2004.09.008; Jalilehvand, F.; Spangberg, D.; Lindqvist-Reis, P.; Hermansson, K.; Persson, I.; Sandstrom, M. Hydration of the Calcium Ion. An EXAFS, Large-Angle X-Ray Scattering, and Molecular Dynamics Simulation Study. *J. Am. Chem. Soc.* **2001,** *123* (3), 431–441. https://doi.org/10.1021/ja001533a.
33. Kaito, T.; Mitsumoto, H.; Sugawara, S.; Shinohara, K.; Uehara, H.; Ariga, H.; Takakusagi, S.; Hatakeyama, Y.; Nishikawa, K.; Asakura, K. K-Edge X-Ray Absorption Fine Structure Analysis of Pt/Au Core–Shell Electrocatalyst: Evidence for Short Pt–Pt Distance. *J. Phys. Chem. C* **2014,** *118* (16), 8481–8490. https://doi.org/10.1021/jp501607f.
34. Kodre, A.; Aron, I.; Gomilek, J. P.; Miheli, A. Atomic Absorption Background in EXAFS of Rb in InterAlkaline Alloys. *Physica Scripta* **2005,** *218.* https://doi.org/10.1238/physica.topical.115a00218.
35. Russell, A. E.; Rose, A. X-Ray Absorption Spectroscopy of Low Temperature Fuel Cell Catalysts. *Chem. Rev.* **2004,** *104* (10), 4613–4635. https://doi.org/10.1021/cr020708r; Timoshenko, J.; Cuenya, B. R. In Situ/Operando Electrocatalyst Characterization by X-Ray Absorption Spectroscopy. *Chem. Rev.* **2021,** *121* (2), 882–961. https://doi.org/10.1021/acs.chemrev.0c00396.
36. van Beek, W.; Safonova, O. V.; Wiker, G.; Emerich, H. SNBL, a Dedicated Beamline for Combined In Situ X-Ray Diffraction, X-Ray Absorption and Raman Scattering Experiments. *Phase Transit.* **2011,** *84* (8), 726–732. https://doi.org/10.1080/01411594.2010.549944.
37. Tinnemans, S. J.; Mesu, J. G.; Kervinen, K.; Visser, T.; Nijhuis, T. A.; Beale, A. M.; Keller, D. E.; van der Eerden, A. M. J.; Weckhuysen, B. M. Combining Operando Techniques in One Spectroscopic-Reaction Cell: New Opportunities for Elucidating the Active Site and Related Reaction Mechanism in Catalysis. *Catal. Today* **2006,** *113* (1–2), 3–15. https://doi.org/10.1016/j.cattod.2005.11.076.
38. Clausen, B. S.; Topsoe, H.; Frahm, R. Application of combined X-ray diffraction and absorption techniques for in situ catalyst characterization. In *Advances in Catalysis;* Eley, D. D., Haag, W. O., Gates, B., Knozinger, H., Eds.; vol. 42; Elsevier, 1998; pp 315–344; Jacques, S. D. M.; Leynaud, O.; Strusevich, D.; Stukas, P.; Barnes, P.; Sankar, G.; Sheehy, M.; O'Brien, M. G.; Iglesias-Juez, A.; Beale, A. M. Recent Progress in the Use of in Situ X-Ray Methods for the Study of Heterogeneous Catalysts in Packed-Bed Capillary Reactors. *Catal. Today* **2009,** *145* (3–4), 204–212. https://doi.org/10.1016/j.cattod.2009.02.012.
39. Grunwaldt, J. D.; Caravati, M.; Hannemann, S.; Baiker, A. X-Ray Absorption Spectroscopy under Reaction Conditions: Suitability of Different Reaction Cells for Combined Catalyst Characterization and Time-Resolved Studies. *Phys. Chem. Chem. Phys.* **2004,** *6* (11), 3037–3047. https://doi.org/10.1039/b403071k.
40. Bare, S. R.; Kelly, S. D.; Ravel, B.; Greenlay, N.; King, L.; Mickelson, G. E. Characterizing Industrial Catalysts Using In Situ XAFS under Identical Conditions. *Phys. Chem. Chem. Phys.* **2010,** *12* (27), 7702–7711. https://doi.org/10.1039/b926621f.
41. Price, S. W. T.; Martin, D. J.; Parsons, A. D.; Slawinski, W. A.; Vamvakeros, A.; Keylock, S. J.; Beale, A. M.; Mosselmans, J. F. W. Chemical Imaging of Fischer-Tropsch Catalysts under Operating Conditions. *Sci. Adv.* **2017,** *3* (3). https://doi.org/10.1126/sciadv.1602838.
42. Gonzalez-Jimenez, I. D.; Cats, K.; Davidian, T.; Ruitenbeek, M.; Meirer, F.; Liu, Y.; Nelson, J.; Andrews, J. C.; Pianetta, P.; de Groot, F. M. F.; et al. Hard X-Ray Nano-tomography of Catalytic Solids at Work. *Angew. Chem. Int. Ed.* **2012,** *51* (48), 11986–11990. https://doi.org/10.1002/anie.201204930.
43. Fabbri, E.; Abbott, D. F.; Nachtegaal, M.; Schmidt, T. J. Operando X-Ray Absorption Spectroscopy: A Powerful Tool toward Water Splitting Catalyst Development. *Curr. Opin. Electrochem.* **2017,** *5* (1), 20–26. https://doi.org/10.1016/j.coelec.2017.08.009.
44. Wise, A. M.; Richardson, P. W.; Price, S. W. T.; Chouchelamane, G.; Calvillo, L.; Hendra, P. J.; Toney, M. F.; Russell, A. E. Inhibitive Effect of Pt on pd-Hydride Formation of pd@Pt Core-Shell Electrocatalysts: An In Situ EXAFS and XRD Study. *Electrochim. Acta* **2018,** *262,* 27–38. https://doi.org/10.1016/j.electacta.2017.12.161.
45. Binninger, T.; Fabbri, E.; Patru, A.; Garganourakis, M.; Han, J.; Abbott, D. F.; Sereda, O.; Kötz, R.; Menzel, A.; Nachtegaal, M.; et al. Electrochemical Flow-Cell Setup for In Situ X-Ray Investigations. *J. Electrochem. Soc.* **2016,** *163* (10), H906–H912. https://doi.org/10.1149/2.0201610jes.
46. Marini, E.; Oliveira De Souza, D.; Aquilanti, G.; Liebert, M.; Rossi, F.; Bozzini, B. Operando XAS of a Bifunctional Gas Diffusion Electrode for Zn-Air Batteries under Realistic Application Conditions. *Applied Sciences* **2021,** *11* (24). https://doi.org/10.3390/app112411672.
47. Farmand, M.; Landers, A. T.; Lin, J. C.; Feaster, J. T.; Beeman, J. W.; Ye, Y.; Clark, E. L.; Higgins, D.; Yano, J.; Davis, R. C.; et al. Electrochemical Flow Cell Enabling Operando Probing of Electrocatalyst Surfaces by X-Ray Spectroscopy and Diffraction. *Phys. Chem. Chem. Phys.* **2019,** *21* (10), 5402–5408. https://doi.org/10.1039/C8CP07423B.
48. Tyo, E. C.; Yin, C.; Di Vece, M.; Qian, Q.; Kwon, G.; Lee, S.; Lee, B.; Debartolo, J. E.; Seifert, S.; Winans, R. E.; et al. Oxidative Dehydrogenation of Cyclohexane on Cobalt Oxide (Co_3O_4) Nanoparticles: The Effect of Particle Size on Activity and Selectivity. *ACS Catalysis* **2012,** *2* (11), 2409–2423. https://doi.org/10.1021/cs300479a.
49. Lee, S.; Lee, B.; Seifert, S.; Vajda, S.; Winans, R. E. Simultaneous Measurement of X-Ray Small Angle Scattering, Absorption and Reactivity: A Continuous Flow Catalysis Reactor. *Nucl. Instrum. Methods Phys. Res. Sect. A* **2011,** *649* (1), 200–203. https://doi.org/10.1016/j.nima.2010.12.172.
50. Liu, Y.; Halder, A.; Seifert, S.; Marcella, N.; Vajda, S.; Frenkel, A. I. Probing Active Sites in CuxPdy Cluster Catalysts by Machine-Learning-Assisted X-Ray Absorption Spectroscopy. *ACS Appl. Mater. Interfaces* **2021,** *13* (45), 53363–53374. https://doi.org/10.1021/acsami.1c06714.
51. Makosch, M.; Kartusch, C.; Sá, J.; Duarte, R. B.; van Bokhoven, J. A.; Kvashnina, K.; Glatzel, P.; Fernandes, D. L. A.; Nachtegaal, M.; Kleymenov, E.; et al. HERFD XAS/ATR-FTIR Batch Reactor Cell. *Phys. Chem. Chem. Phys.* **2012,** *14* (7), 2164–2170. https://doi.org/10.1039/C1CP21933B.
52. Lee, A. F.; Ellis, C. V.; Naughton, J. N.; Newton, M. A.; Parlett, C. M. A.; Wilson, K. Reaction-Driven Surface Restructuring and Selectivity Control in Allylic Alcohol Catalytic Aerobic Oxidation over Pd. *J. Am. Chem. Soc.* **2011,** *133* (15), 5724–5727. https://doi.org/10.1021/ja200684f.
53. Zhang, K.; Liu, R.; Irving, T.; Auld, D. S. A Versatile Rapid-Mixing and Flow Device for X-Ray Absorption Spectroscopy. *J. Synchrotron Radiat.* **2004,** *11* (2), 204–208. https://doi.org/10.1107/S0909049503028474.
54. Fovanna, T.; Alxneit, I.; Clark, A. H.; Checchia, S.; Di Michiel, M.; Kröcher, O.; Nachtegaal, M.; Ferri, D. Reduction of PdO/Al_2O_3 in Liquid Cyclohexane Followed In Situ by ATR-IR, High-Energy XRD, and XAS. *J. Phys. Chem. C* **2021,** *125* (30), 16473–16482. https://doi.org/10.1021/acs.jpcc.1c01882.
55. de Jong, K. P. *General Aspects*, John Wiley & Sons, Inc, 2009. https://doi.org/10.1002/9783527626854.ch1.
56. Carrier, X.; Marceau, E.; Carabineiro, H.; Rodríguez-González, V.; Che, M. EXAFS Spectroscopy as a Tool to Probe Metal–Support Interaction and Surface Molecular Structures in Oxide-Supported Catalysts: Application to Al_2O_3-Supported Ni(ii) Complexes and ZrO_2-Supported Tungstates. *Phys. Chem. Chem. Phys.* **2009,** *11* (35), 7527–7539. https://doi.org/10.1039/B822969D.
57. Kikkawa, S.; Teramura, K.; Asakura, H.; Hosokawa, S.; Tanaka, T. In Situ Time-Resolved XAS Study on Metal-Support-Interaction-Induced Morphology Change of PtO_2 Nanoparticles Supported on γ-Al_2O_3 under H_2 Reduction. *Catal. Today* **2022.** https://doi.org/10.1016/j.cattod.2022.02.012.
58. Green Isabel, X.; Tang, W.; Neurock, M.; Yates John, T. Spectroscopic Observation of Dual Catalytic Sites during Oxidation of CO on an Au/TiO_2 Catalyst. *Science* **2011,** *333* (6043), 736–739. https://doi.org/10.1126/science.1207272; Li, Y.; Kottwitz, M.; Vincent, J. L.; Enright, M. J.; Liu, Z.; Zhang, L.; Huang, J.; Senanayake, S. D.; Yang, W.-C. D.; Crozier, P. A.; et al. Dynamic Structure of Active Sites in Ceria-Supported Pt Catalysts for the Water Gas Shift Reaction. *Nat. Commun.* **2021,** *12* (1), 914. https://doi.org/10.1038/s41467-021-21132-4.
59. Tauster, S. J.; Fung, S. C.; Baker, R. T. K.; Horsley, J. A. Strong Interactions in Supported-Metal Catalysts. *Science* **1981,** *211* (4487), 1121–1125. https://doi.org/10.1126/science.211.4487.1121.

60. Rochet, A.; Moizan, V.; Diehl, F.; Pichon, C.; Briois, V. Quick-XAS and Raman Operando Characterisation of a Cobalt Alumina-Supported Catalyst under Realistic Fischer–Tropsch Reaction Conditions. *Catal. Today* **2013,** *205,* 94–100. https://doi.org/10.1016/j.cattod.2012.08.021; Nayak, C.; Jain, P.; Vinod, C. P.; Jha, S. N.; Bhattacharyya, D. Operando X-Ray Absorption Spectroscopy Study of the Fischer-Tropsch Reaction with a co Catalyst. *J. Synchrotron Radiat.* **2019,** *26* (1), 137–144. https://doi.org/10.1107/S1600577518015588.
61. Jiang, X.; Nie, X.; Guo, X.; Song, C.; Chen, J. G. Recent Advances in Carbon Dioxide Hydrogenation to Methanol Via Heterogeneous Catalysis. *Chem. Rev.* **2020,** *120* (15), 7984–8034. https://doi.org/10.1021/acs.chemrev.9b00723.
62. Grunwaldt, J. D.; Molenbroek, A. M.; Topsoe, N. Y.; Topsoe, H.; Clausen, B. S. In Situ Investigations of Structural Changes in Cu/ZnO Catalysts. *J. Catal.* **2000,** *194* (2), 452–460. https://doi.org/10.1006/jcat.2000.2930.
63. Bahruji, H.; Bowker, M.; Hutchings, G.; Dimitratos, N.; Wells, P.; Gibson, E.; Jones, W.; Brookes, C.; Morgan, D.; Lalev, G. Pd/ZnO Catalysts for Direct CO_2 Hydrogenation to Methanol. *J. Catal.* **2016,** *343,* 133–146. https://doi.org/10.1016/j.jcat.2016.03.017.
64. Stangeland, K.; Li, H.; Yu, Z. Thermodynamic Analysis of Chemical and Phase Equilibria in CO_2 Hydrogenation to Methanol, Dimethyl Ether, and Higher Alcohols. *Ind. Eng. Chem. Res.* **2018,** *57* (11), 4081–4094. https://doi.org/10.1021/acs.iecr.7b04866; Bansode, A.; Urakawa, A. Towards Full One-Pass Conversion of Carbon Dioxide to Methanol and Methanol-Derived Products. *J. Catal.* **2014,** *309,* 66–70. https://doi.org/10.1016/j.jcat.2013.09.005.
65. Ye, J.; Liu, C.; Mei, D.; Ge, Q. Active Oxygen Vacancy Site for Methanol Synthesis from CO_2 Hydrogenation on In_2O_3(110): A DFT Study. *ACS Catal.* **2013,** *3* (6), 1296–1306. https://doi.org/10.1021/cs400132a.
66. Snider, J. L.; Streibel, V.; Hubert, M. A.; Choksi, T. S.; Valle, E.; Upham, D. C.; Schumann, J.; Duyar, M. S.; Gallo, A.; Abild-Pedersen, F.; et al. Revealing the Synergy between Oxide and Alloy Phases on the Performance of Bimetallic In–Pd Catalysts for CO_2 Hydrogenation to Methanol. *ACS Catal.* **2019,** *9* (4), 3399–3412. https://doi.org/10.1021/acscatal.8b04848.
67. Tsoukalou, A.; Abdala, P. M.; Stoian, D.; Huang, X.; Willinger, M.-G.; Fedorov, A.; Müller, C. R. Structural Evolution and Dynamics of an In_2O_3 Catalyst for CO_2 Hydrogenation to Methanol: An Operando XAS-XRD and In Situ TEM Study. *J. Am. Chem. Soc.* **2019,** *141* (34), 13497–13505. https://doi.org/10.1021/jacs.9b04873.
68. Farrauto, R. J.; Deeba, M.; Alerasool, S. Gasoline Automobile Catalysis and its Historical Journey to Cleaner Air. *Nat. Catal.* **2019,** *2* (7), 603–613. https://doi.org/10.1038/s41929-019-0312-9.
69. Twigg, M. V. Catalytic Control of Emissions From Cars. *Catal. Today* **2011,** *163* (1), 33–41. https://doi.org/10.1016/j.cattod.2010.12.044; Huang, C.; Shan, W.; Lian, Z.; Zhang, Y.; He, H. Recent Advances in Three-Way Catalysts of Natural Gas Vehicles. *Cat. Sci. Technol.* **2020,** *10* (19), 6407–6419. https://doi.org/10.1039/D0CY01320J.
70. Korakianitis, T.; Namasivayam, A. M.; Crookes, R. J. Natural-Gas Fueled Spark-Ignition (SI) and Compression-Ignition (CI) Engine Performance and Emissions. *Prog. Energy Combust. Sci.* **2011,** *37* (1), 89–112. https://doi.org/10.1016/j.pecs.2010.04.002; Prussi, M.; Padella, M.; Conton, M.; Postma, E. D.; Lonza, L. Review of Technologies for Biomethane Production and Assessment of Eu Transport Share in 2030. *J. Clean. Prod.* **2019,** *222,* 565–572. https://doi.org/10.1016/j.jclepro.2019.02.271; D'Adamo, I.; Falcone, P. M.; Huisingh, D.; Morone, P. A Circular Economy Model Based on Biomethane: What Are the Opportunities for the Municipality of Rome and beyond? *Renew. Energy* **2021,** *163,* 1660–1672 https://doi.org/10.1016/j.renene.2020.10.072.
71. Winkler, S. L.; Anderson, J. E.; Garza, L.; Ruona, W. C.; Vogt, R.; Wallington, T. J. Vehicle Criteria Pollutant (PM, NOx, CO, HCs) Emissions: How Low Should we Go? *NPJ Clim. Atmos. Sci.* **2018,** *1* (1), 26 https://doi.org/10.1038/s41612-018-0037-5.
72. Ferri, D.; Elsener, M.; Kröcher, O. Methane Oxidation over a Honeycomb Pd-Only Three-Way Catalyst under Static and Periodic Operation. *Appl. Catal. Environ.* **2018,** *220,* 67–77. https://doi.org/10.1016/j.apcatb.2017.07.070; Lampert, J. K.; Kazi, M. S.; Farrauto, R. J. Palladium Catalyst Performance for Methane Emissions Abatement from Lean Burn Natural Gas Vehicles. *Appl. Catal. Environ.* **1997,** *14* (3), 211–223. https://doi.org/10.1016/S0926-3373(97)00024-6; Chen, J.; Zhong, J.; Wu, Y.; Hu, W.; Qu, P.; Xiao, X.; Zhang, G.; Liu, X.; Jiao, Y.; Zhong, L.; et al. Particle Size Effects in Stoichiometric Methane Combustion: Structure–Activity Relationship of Pd Catalyst Supported on Gamma-Alumina. *ACS Catal.* **2020,** *10* (18), 10339–10349. https://doi.org/10.1021/acscatal.0c03111.
73. Marchionni, V.; Nachtegaal, M.; Ferri, D. Influence of CO on Dry CH_4 Oxidation on Pd/Al_2O_3 by Operando Spectroscopy: A Multitechnique Modulated Excitation Study. *ACS Catal.* **2020,** *10* (8), 4791–4804. https://doi.org/10.1021/acscatal.9b05541.
74. Jiang, D.; Khivantsev, K.; Wang, Y. Low-Temperature Methane Oxidation for Efficient Emission Control in Natural Gas Vehicles: Pd and Beyond. *ACS Catal.* **2020,** *10* (23), 14304–14314. https://doi.org/10.1021/acscatal.0c03338; Ciuparu, D.; Lyubovsky, M. R.; Altman, E.; Pfefferle, L. D.; Datye, A. Catalytic Combustion of Methane over Palladium Based Catalysts. *Catal. Rev.* **2002,** *44* (4), 593–649. https://doi.org/10.1081/CR-120015482.
75. Dann, E. K.; Gibson, E. K.; Catlow, R. A.; Collier, P.; Eralp Erden, T.; Gianolio, D.; Hardacre, C.; Kroner, A.; Raj, A.; Goguet, A.; et al. Combined In Situ XAFS/DRIFTS Studies of the Evolution of Nanoparticle Structures from Molecular Precursors. *Chem. Mater.* **2017,** *29* (17), 7515–7523. https://doi.org/10.1021/acs.chemmater.7b02552.
76. Nilsson, J.; Carlsson, P.-A.; Fouladvand, S.; Martin, N. M.; Gustafson, J.; Newton, M. A.; Lundgren, E.; Grönbeck, H.; Skoglundh, M. Chemistry of Supported Palladium Nanoparticles during Methane Oxidation. *ACS Catal.* **2015,** *5* (4), 2481–2489. https://doi.org/10.1021/cs502036d.
77. Nilsson, J.; Carlsson, P.-A.; Martin, N. M.; Adams, E. C.; Agostini, G.; Grönbeck, H.; Skoglundh, M. Methane Oxidation over Pd/Al_2O_3 under Rich/Lean Cycling Followed by Operando XAFS and Modulation Excitation Spectroscopy. *J. Catal.* **2017,** *356,* 237–245. https://doi.org/10.1016/j.jcat.2017.10.018.
78. Gholami, R.; Alyani, M.; Smith, K. J. Deactivation of Pd Catalysts by Water during Low Temperature Methane Oxidation Relevant to Natural Gas Vehicle Converters. *Catalysts* **2015,** *5* (2). https://doi.org/10.3390/catal5020561; Gélin, P.; Urfels, L.; Primet, M.; Tena, E. Complete Oxidation of Methane at Low Temperature over Pt and Pd Catalysts for the Abatement of Lean-Burn Natural Gas Fuelled Vehicles Emissions: Influence of Water and Sulphur Containing Compounds. *Catal. Today* **2003,** *83* (1), 45–57. https://doi.org/10.1016/S0920-5861(03)00215-3.
79. Petrov, A. W.; Ferri, D.; Krumeich, F.; Nachtegaal, M.; van Bokhoven, J. A.; Kröcher, O. Stable Complete Methane Oxidation over Palladium Based Zeolite Catalysts. *Nat. Commun.* **2018,** *9* (1), 2545. https://doi.org/10.1038/s41467-018-04748-x.
80. Sankar, M.; Dimitratos, N.; Miedziak, P. J.; Wells, P. P.; Kiely, C. J.; Hutchings, G. J. Designing Bimetallic Catalysts for a Green and Sustainable Future. *Chem. Soc. Rev.* **2012,** *41* (24), 8099–8139. https://doi.org/10.1039/C2CS35296F.
81. Ponec, V. Alloy Catalysts: The Concepts. *Appl. Catal. Gen.* **2001,** *222* (1), 31–45. https://doi.org/10.1016/S0926-860X(01)00828-6.
82. Nashner, M. S.; Frenkel, A. I.; Adler, D. L.; Shapley, J. R.; Nuzzo, R. G. Structural Characterization of Carbon-Supported Platinum—Ruthenium Nanoparticles from the Molecular Cluster Precursor PtRu5C(CO)16. *J. Am. Chem. Soc.* **1997,** *119* (33), 7760–7771. https://doi.org/10.1021/ja971039f.
83. Gibson, E. K.; Beale, A. M.; Catlow, C. R. A.; Chutia, A.; Gianolio, D.; Gould, A.; Kroner, A.; Mohammed, K. M. H.; Perdjon, M.; Rogers, S. M.; et al. Restructuring of AuPd Nanoparticles Studied by a Combined XAFS/DRIFTS Approach. *Chem. Mater.* **2015,** *27* (10), 3714–3720. https://doi.org/10.1021/acs.chemmater.5b00866.
84. Cook, K. M.; Poudyal, S.; Miller, J. T.; Bartholomew, C. H.; Hecker, W. C. Reducibility of Alumina-Supported Cobalt Fischer–Tropsch Catalysts: Effects of Noble Metal Type, Distribution, Retention, Chemical State, Bonding, and Influence on Cobalt Crystallite Size. *Appl. Catal. Gen.* **2012,** *449,* 69–80. https://doi.org/10.1016/j.apcata.2012.09.032.
85. Mehrbod, M.; Martinelli, M.; Castro, J. D.; Alhraki, N.; Cronauer, D. C.; Kropf, A. J.; Marshall, C. L.; Jacobs, G. Fischer-Tropsch Synthesis: Direct Cobalt Nitrate Reduction of Promoted Co/Al_2O_3 Catalysts. *Catal. Today* **2021,** *369,* 129–143. https://doi.org/10.1016/j.cattod.2020.03.033.
86. Fu, Q.; Saltsburg, H.; Flytzani-Stephanopoulos, M. Active Nonmetallic Au and Pt Species on Ceria-Based Water-Gas Shift Catalysts. *Science* **2003,** *301* (5635), 935–938. https://doi.org/10.1126/science.1085721; Mitchell, S.; Pérez-Ramírez, J. Single Atom Catalysis: A Decade of Stunning Progress and the Promise for a Bright Future. *Nat. Commun.* **2020,** *11* (1), 4302. https://doi.org/10.1038/s41467-020-18182-5.
87. Hannagan, R. T.; Giannakakis, G.; Flytzani-Stephanopoulos, M.; Sykes, E. C. H. Single-Atom Alloy Catalysis. *Chem. Rev.* **2020,** *120* (21), 12044–12088. https://doi.org/10.1021/acs.chemrev.0c00078.
88. Thomas, J. M.; Raja, R.; Lewis, D. W. Single-Site Heterogeneous Catalysts. *Angew. Chem. Int. Ed.* **2005,** *44* (40), 6456–6482. https://doi.org/10.1002/anie.200462473; Van Velthoven, N.; Waitschat, S.; Chavan, S. M.; Liu, P.; Smolders, S.; Vercammen, J.; Bueken, B.; Bals, S.; Lillerud, K. P.; Stock, N.; et al. Single-Site Metal–Organic Framework Catalysts for the Oxidative Coupling of Arenes Via C–H/C–H Activation. *Chem. Sci.* **2019,** *10* (12), 3616–3622. https://doi.org/10.1039/C8SC05510F.

89. Thomas, J. M.; Sankar, G. The Role of Synchrotron-Based Studies in the Elucidation and Design of Active Sites in Titanium – Silica Epoxidation Catalysts. *Acc. Chem. Res.* **2001,** *34* (7), 571–581. https://doi.org/10.1021/ar010003w.
90. Barrett, P. A.; Sankar, G.; Jones, R. H.; Catlow, C. R. A.; Thomas, J. M. Interaction of Acetonitrile with Cobalt-Containing Aluminophosphates: An X-Ray Absorption Investigation. *J. Phys. Chem. B.* **1997,** *101* (46), 9555–9562. https://doi.org/10.1021/jp970701r.
91. Ravel, B. Quantitative EXAFS analysis. In *X-Ray Absorption and X-Ray Emission Spectroscopy*, Wiley, 2016; pp 281–302. https://doi.org/10.1002/9781118844243.ch11.
92. Kervinen, K.; Bruijnincx, P. C. A.; Beale, A. M.; Mesu, J. G.; van Koten, G.; Klein Gebbink, R. J. M.; Weckhuysen, B. M. Zeolite Framework Stabilized Copper Complex Inspired by the 2-His-1-Carboxylate Facial Triad Motif Yielding Oxidation Catalysts. *J. Am. Chem. Soc.* **2006,** *128* (10), 3208–3217. https://doi.org/10.1021/ja0567992.
93. Zaarour, M.; Cazemier, J.; Ruiz-Martínez, J. Recent Developments in the Control of Selectivity in Hydrogenation Reactions by Confined Metal Functionalities. *Cat. Sci. Technol.* **2020,** *10* (24), 8140–8172. https://doi.org/10.1039/D0CY01709D.
94. Pei, G. X.; Liu, X. Y.; Yang, X.; Zhang, L.; Wang, A.; Li, L.; Wang, H.; Wang, X.; Zhang, T. Performance of Cu-Alloyed Pd Single-Atom Catalyst for Semihydrogenation of Acetylene under Simulated Front-End Conditions. *ACS Catal.* **2017,** *7* (2), 1491–1500. https://doi.org/10.1021/acscatal.6b03293.
95. Greegor, R. B.; Lytle, F. W. Morphology of Supported Metal Clusters: Determination by EXAFS and Chemisorption. *J. Catal.* **1980,** *63* (2), 476–486. https://doi.org/10.1016/0021-9517(80)90102-5; Benfield, R. E. Mean Coordination Numbers and the Non-metal–Metal Transition in Clusters. *J. Chem. Soc. Faraday Trans.* **1992,** *88* (8), 1107–1110. https://doi.org/10.1039/FT9928801107; Jentys, A. Estimation of Mean Size and Shape of Small Metal Particles by EXAFS. *Phys. Chem. Chem. Phys.* **1999,** *1* (17), 4059–4063. https://doi.org/10.1039/A904654B; Frenkel, A. Solving the 3D Structure of Metal Nanoparticles. *Z. Kristallog.* **2007,** *222* (11), 605–611. https://doi.org/10.1524/zkri.2007.222.11.605; Beale, A. M.; Weckhuysen, B. M. EXAFS as a Tool to Interrogate the Size and Shape of Mono and Bimetallic Catalyst Nanoparticles. *Phys. Chem. Chem. Phys.* **2010,** *12* (21), 5562–5574. https://doi.org/10.1039/B925206A.
96. Dai, Y.; Lu, P.; Cao, Z.; Campbell, C. T.; Xia, Y. The Physical Chemistry and Materials Science behind Sinter-Resistant Catalysts. *Chem. Soc. Rev.* **2018,** *47* (12), 4314–4331. https://doi.org/10.1039/C7CS00650K.
97. McKale, A. G.; Veal, B. W.; Paulikas, A. P.; Chan, S. K.; Knapp, G. S. Generalized Ramsauer-Townsend Effect in Extended x-Ray-Absorption Fine Structure. *Phys. Rev. B* **1988,** *38* (15), 10919–10921. https://doi.org/10.1103/PhysRevB.38.10919.
98. Rogers, S. M.; Catlow, C. R. A.; Chan-Thaw, C. E.; Chutia, A.; Jian, N.; Palmer, R. E.; Perdjon, M.; Thetford, A.; Dimitratos, N.; Villa, A.; et al. Tandem Site- and Size-Controlled Pd Nanoparticles for the Directed Hydrogenation of Furfural. *ACS Catal.* **2017,** *7* (4), 2266–2274. https://doi.org/10.1021/acscatal.6b03190.
99. Calvin, S.; Luo, S. X.; Caragianis-Broadbridge, C.; McGuinness, J. K.; Anderson, E.; Lehman, A.; Wee, K. H.; Morrison, S. A.; Kurihara, L. K. Comparison of Extended x-Ray Absorption Fine Structure and Scherrer Analysis of x-Ray Diffraction as Methods for Determining Mean Sizes of Polydisperse Nanoparticles. *Appl. Phys. Lett.* **2005,** *87* (23), 233102. https://doi.org/10.1063/1.2137872.
100. Dai, Y.; Gorey, T. J.; Anderson, S. L.; Lee, S.; Lee, S.; Seifert, S.; Winans, R. E. Inherent Size Effects on XANES of Nanometer Metal Clusters: Size-Selected Platinum Clusters on Silica. *J. Phys. Chem. C* **2017,** *121* (1), 361–374. https://doi.org/10.1021/acs.jpcc.6b10167.
101. Beale, A. M.; Gao, F.; Lezcano-Gonzalez, I.; Peden, C. H. F.; Szanyi, J. Recent Advances in Automotive Catalysis for NOx Emission Control by Small-Pore Microporous Materials. *Chem. Soc. Rev.* **2015,** *44* (20), 7371–7405. https://doi.org/10.1039/C5CS00108K; Park, M. B.; Park, E. D.; Ahn, W.-S. Recent Progress in Direct Conversion of Methane to Methanol Over Copper-Exchanged Zeolites. *Front. Chem.* **2019,** *7*. https://doi.org/10.3389/fchem.2019.00514.
102. Groothaert, M. H.; van Bokhoven, J. A.; Battiston, A. A.; Weckhuysen, B. M.; Schoonheydt, R. A. Bis(μ-Oxo)Dicopper in Cu-ZSM-5 and its Role in the Decomposition of NO: A Combined In Situ XAFS, UV – Vis – Near-IR, and Kinetic Study. *J. Am. Chem. Soc.* **2003,** *125* (25), 7629–7640. https://doi.org/10.1021/ja029684w; Alayon, E. M.; Nachtegaal, M.; Ranocchiari, M.; van Bokhoven, J. A. Catalytic Conversion of Methane to Methanol over Cu–Mordenite. *Chem. Commun.* **2012,** *48* (3), 404–406. https://doi.org/10.1039/C1CC15840F; Grundner, S.; Markovits, M. A. C.; Li, G.; Tromp, M.; Pidko, E. A.; Hensen, E. J. M.; Jentys, A.; Sanchez-Sanchez, M.; Lercher, J. A. Single-Site Trinuclear Copper Oxygen Clusters in Mordenite for Selective Conversion of Methane to Methanol. *Nat. Commun.* **2015,** *6* (1), 7546. https://doi.org/10.1038/ncomms8546.
103. Hammond, C.; Forde, M. M.; Ab Rahim, M. H.; Thetford, A.; He, Q.; Jenkins, R. L.; Dimitratos, N.; Lopez-Sanchez, J. A.; Dummer, N. F.; Murphy, D. M.; et al. Direct Catalytic Conversion of Methane to Methanol in an Aqueous Medium by Using Copper-Promoted Fe-ZSM-5. *Angew. Chem. Int. Ed.* **2012,** *51* (21), 5129–5133. https://doi.org/10.1002/anie.201108706; Hammond, C.; Dimitratos, N.; Jenkins, R. L.; Lopez-Sanchez, J. A.; Kondrat, S. A.; Hasbiab Rahim, M.; Forde, M. M.; Thetford, A.; Taylor, S. H.; Hagen, H.; et al. Elucidation and Evolution of the Active Component within Cu/Fe/ZSM-5 for Catalytic Methane Oxidation: From Synthesis to Catalysis. *ACS Catal.* **2013,** *3* (4), 689–699. https://doi.org/10.1021/cs3007999; Yu, T.; Li, Z.; Jones, W.; Liu, Y.; He, Q.; Song, W.; Du, P.; Yang, B.; An, H.; Farmer, D. M.; et al. Identifying Key Mononuclear Fe Species for Low-Temperature Methane Oxidation. *Chem. Sci.* **2021,** *12* (9), 3152–3160. https://doi.org/10.1039/D0SC06067D.
104. Deka, U.; Lezcano-Gonzalez, I.; Weckhuysen, B. M.; Beale, A. M. Local Environment and Nature of cu Active Sites in Zeolite-Based Catalysts for the Selective Catalytic Reduction of NOx. *ACS Catal.* **2013,** *3* (3), 413–427. https://doi.org/10.1021/cs300794s.
105. Menon, U.; Rahman, M.; Khatib, S. J. A Critical Literature Review of the Advances in Methane Dehydroaromatization over Multifunctional Metal-Promoted Zeolite Catalysts. *Appl. Catal. Gen.* **2020,** *608*, 117870. https://doi.org/10.1016/j.apcata.2020.117870.
106. Ressler, T.; Jentoft, R. E.; Wienold, J.; Günter, M. M.; Timpe, O. In Situ XAS and XRD Studies on the Formation of Mo Suboxides during Reduction of MoO_3. *J. Phys. Chem. B.* **2000,** *104* (27), 6360–6370. https://doi.org/10.1021/jp000690t.
107. Brookes, C.; Bowker, M.; Gibson, E. K.; Gianolio, D.; Mohammed, K. M. H.; Parry, S.; Rogers, S. M.; Silverwood, I. P.; Wells, P. P. In Situ Spectroscopic Investigations of $MoOx/Fe_2O_3$ Catalysts for the Selective Oxidation of Methanol. *Cat. Sci. Technol.* **2016,** *6* (3), 722–730. https://doi.org/10.1039/C5CY01175B.
108. Lezcano-González, I.; Oord, R.; Rovezzi, M.; Glatzel, P.; Botchway, S. W.; Weckhuysen, B. M.; Beale, A. M. Molybdenum Speciation and its Impact on Catalytic Activity during Methane Dehydroaromatization in Zeolite ZSM-5 as Revealed by Operando X-Ray Methods. *Angew. Chem. Int. Ed.* **2016,** *55* (17), 5215–5219. https://doi.org/10.1002/anie.201601357.
109. Vollmer, I.; van der Linden, B.; Ould-Chikh, S.; Aguilar-Tapia, A.; Yarulina, I.; Abou-Hamad, E.; Sneider, Y. G.; Olivos Suarez, A. I.; Hazemann, J.-L.; Kapteijn, F.; et al. On the Dynamic Nature of Mo Sites for Methane Dehydroaromatization. *Chem. Sci.* **2018,** *9* (21), 4801–4807. https://doi.org/10.1039/C8SC01263F.
110. Kosinov, N.; Hensen, E. J. M. Reactivity, Selectivity, and Stability of Zeolite-Based Catalysts for Methane Dehydroaromatization. *Adv. Mater.* **2020,** *32* (44), 2002565. https://doi.org/10.1002/adma.202002565.
111. Rahman, M.; Infantes-Molina, A.; Boubnov, A.; Bare, S. R.; Stavitski, E.; Sridhar, A.; Khatib, S. J. Increasing the Catalytic Stability by Optimizing the Formation of Zeolite-Supported Mo Carbide Species Ex Situ for Methane Dehydroaromatization. *J. Catal.* **2019,** *375,* 314–328. https://doi.org/10.1016/j.jcat.2019.06.002.
112. López-Martín, Á.; Platero, F.; Colón, G.; Caballero, A. Elucidating the Nature of Mo Species on ZSM-5 and its Role in the Methane Aromatization Reaction. *React. Chem. Eng.* **2021,** *6* (7), 1265–1276. https://doi.org/10.1039/D1RE00044F.
113. Kanitkar, S.; Abedin, M. A.; Bhattar, S.; Spivey, J. J. Methane Dehydroaromatization over Molybdenum Supported on Sulfated Zirconia Catalysts. *Appl. Catal. Gen.* **2019,** *575,* 25–37. https://doi.org/10.1016/j.apcata.2019.01.013.
114. Gao, J.; Zheng, Y.; Fitzgerald, G. B.; de Joannis, J.; Tang, Y.; Wachs, I. E.; Podkolzin, S. G. Structure of Mo2Cx and Mo4Cx Molybdenum Carbide Nanoparticles and their Anchoring Sites on ZSM-5 Zeolites. *J. Phys. Chem. C* **2014,** *118* (9), 4670–4679. https://doi.org/10.1021/jp4106053.
115. Beale, A. M.; O'Brien, M. G.; Weckhuysen, B. M. *Techniques Coupling for Catalyst Characterisation*, John Wiley & Sons, Inc, 2012. https://doi.org/10.1002/9783527645329.ch23; Kubacka, A.; Iglesias-Juez, A.; Martínez-Arias, A.; Di Michiel, M.; Newton, M. A.; Fernández-García, M. Surface and Bulk Approach to Time-Resolved Characterization of Heterogeneous Catalysts. *ChemCatChem* **2012,** *4* (6), 725–737. https://doi.org/10.1002/cctc.201200131.
116. Tsakoumis, N. E.; York, A. P. E.; Chen, D.; Rønning, M. Catalyst Characterisation Techniques and Reaction Cells Operating at Realistic Conditions; towards Acquisition of Kinetically Relevant Information. *Cat. Sci. Technol.* **2015,** *5* (11), 4859–4883. https://doi.org/10.1039/C5CY00269A.
117. Bentrup, U. Combining In Situ Characterization Methods in One Set-up: Looking with More Eyes into the Intricate Chemistry of the Synthesis and Working of Heterogeneous Catalysts. *Chem. Soc. Rev.* **2010,** *39* (12), 4718–4730. https://doi.org/10.1039/B919711G.

118. Young, N. A. Is Nickel Dibromide Bent in a Nitrogen Matrix? A Combined Simultaneous Fourier-Transform Infrared and X-Ray Absorption Fine Structure Matrix Isolation Study. *J. Chem. Soc.* **1996,** *2,* 249–251. https://doi.org/10.1039/DT9960000249; Clausen, B. S.; Steffensen, G.; Fabius, B.; Villadsen, J.; Feidenhans'l, R.; Topsøe, H. In Situ Cell for Combined XRD and on-Line Catalysis Tests: Studies of Cu-Based Water Gas Shift and Methanol Catalysts. *J. Catal.* **1991,** *132* (2), 524–535. https://doi.org/10.1016/0021-9517(91)90168-4.
119. Couves, J. W.; Thomas, J. M.; Waller, D.; Jones, R. H.; Dent, A. J.; Derbyshire, G. E.; Greaves, G. N. Tracing the Conversion of Aurichalcite to a Copper Catalyst by Combined X-Ray Absorption and Diffraction. *Nature* **1991,** *354* (6353), 465–468. https://doi.org/10.1038/354465a0.
120. Newton, M. A.; van Beek, W. Combining Synchrotron-Based X-Ray Techniques with Vibrational Spectroscopies for the In Situ Study of Heterogeneous Catalysts: A View from a Bridge. *Chem. Soc. Rev.* **2010,** *39* (12), 4845–4863. https://doi.org/10.1039/B919689G.
121. Dann, E. K.; Gibson, E. K.; Blackmore, R. H.; Catlow, C. R. A.; Collier, P.; Chutia, A.; Erden, T. E.; Hardacre, C.; Kroner, A.; Nachtegaal, M.; et al. Structural Selectivity of Supported Pd Nanoparticles for Catalytic NH_3 Oxidation Resolved Using Combined Operando Spectroscopy. *Nat. Catal.* **2019,** *2* (2), 157–163. https://doi.org/10.1038/s41929-018-0213-3; Newton, M. A.; Belver-Coldeira, C.; Martínez-Arias, A.; Fernández-García, M. Dynamic In Situ Observation of Rapid Size and Shape Change of Supported Pd Nanoparticles during CO/NO Cycling. *Nat. Mater.* **2007,** *6* (7), 528–532. https://doi.org/10.1038/nmat1924.
122. Bentrup, U.; Radnik, J.; Armbruster, U.; Martin, A.; Leiterer, J.; Emmerling, F.; Brückner, A. Linking Simultaneous in Situ WAXS/SAXS/Raman with Raman/ATR/UV–vis Spectroscopy: Comprehensive Insight into the Synthesis of Molybdate Catalyst Precursors. *Top. Catal.* **2009,** *52* (10), 1350–1359. https://doi.org/10.1007/s11244-009-9309-y.
123. Beale, A. M.; van der Eerden, A. M. J.; Kervinen, K.; Newton, M. A.; Weckhuysen, B. M. Adding a Third Dimension to Operando Spectroscopy: A Combined UV-vis, Raman and XAFS Setup to Study Heterogeneous Catalysts under Working Conditions. *Chem. Commun.* **2005,** *24,* 3015–3017. https://doi.org/10.1039/B504027B.
124. Beale, A. M.; O'Brien, M. G.; Kasunič, M.; Golobič, A.; Sanchez-Sanchez, M.; Lobo, A. J. W.; Lewis, D. W.; Wragg, D. S.; Nikitenko, S.; Bras, W.; et al. Probing ZnAPO-34 Self-Assembly Using Simultaneous Multiple In Situ Techniques. *J. Phys. Chem. C* **2011,** *115* (14), 6331–6340. https://doi.org/10.1021/jp200043b.
125. Deka, U.; Juhin, A.; Eilertsen, E. A.; Emerich, H.; Green, M. A.; Korhonen, S. T.; Weckhuysen, B. M.; Beale, A. M. Confirmation of Isolated Cu^{2+} Ions in SSZ-13 Zeolite as Active Sites in NH_3-Selective Catalytic Reduction. *J. Phys. Chem. C* **2012,** *116* (7), 4809–4818. https://doi.org/10.1021/jp212450d; Frenkel, A. I.; Wang, Q.; Marinkovic, N.; Chen, J. G.; Barrio, L.; Si, R.; Cámara, A. L.; Estrella, A. M.; Rodriguez, J. A.; Hanson, J. C. Combining X-Ray Absorption and X-Ray Diffraction Techniques for In Situ Studies of Chemical Transformations in Heterogeneous Catalysis: Advantages and Limitations. *J. Phys. Chem. C* **2011,** *115* (36), 17884–17890. https://doi.org/10.1021/jp205204e; Sekizawa, O.; Uruga, T.; Higashi, K.; Kaneko, T.; Yoshida, Y.; Sakata, T.; Iwasawa, Y. Simultaneous Operando Time-Resolved XAFS–XRD Measurements of a Pt/C Cathode Catalyst in Polymer Electrolyte Fuel Cell under Transient Potential Operations. *ACS Sustain. Chem. Eng.* **2017,** *5* (5), 3631–3636. https://doi.org/10.1021/acssuschemeng.7b00052; Qin, H.; Lin, L.; Jia, J.; Ni, H.; He, Y.; Wang, J.; Li, A.; Ji, Z.; Liu, J. Synchrotron Radiation In Situ X-Ray Absorption Fine Structure and In Situ X-Ray Diffraction Analysis of a High-Performance Cobalt Catalyst towards the Oxygen Reduction Reaction. *Phys. Chem. Chem. Phys.* **2017,** *19* (45), 30749–30755. https://doi.org/10.1039/C7CP05888H.
126. Serrer, M.-A.; Gaur, A.; Jelic, J.; Weber, S.; Fritsch, C.; Clark, A. H.; Saraçi, E.; Studt, F.; Grunwaldt, J.-D. Structural Dynamics in Ni–Fe Catalysts during CO_2 Methanation—Role of iron Oxide Clusters. *Cat. Sci. Technol.* **2020,** *10* (22), 7542–7554. https://doi.org/10.1039/D0CY01396J.
127. Gaur, A.; Schumann, M.; Raun, K. V.; Stehle, M.; Beato, P.; Jensen, A. D.; Grunwaldt, J.-D.; Høj, M. Operando XAS/XRD and Raman Spectroscopic Study of Structural Changes of the Iron Molybdate Catalyst during Selective Oxidation of Methanol. *ChemCatChem* **2019,** *11* (19), 4871–4883. https://doi.org/10.1002/cctc.201901025.
128. Danielis, M.; Betancourt, L. E.; Orozco, I.; Divins, N. J.; Llorca, J.; Rodríguez, J. A.; Senanayake, S. D.; Colussi, S.; Trovarelli, A. Methane Oxidation Activity and Nanoscale Characterization of Pd/CeO_2 Catalysts Prepared by Dry Milling pd Acetate and Ceria. *Appl. Catal. Environ.* **2021,** *282*, 119567. https://doi.org/10.1016/j.apcatb.2020.119567.
129. Wang, X.; Rodriguez, J. A.; Hanson, J. C.; Gamarra, D.; Martínez-Arias, A.; Fernández-García, M. Ceria-Based Catalysts for the Production of H_2 through the Water-Gas-Shift Reaction: Time-Resolved XRD and XAFS Studies. *Top. Catal.* **2008,** *49* (1), 81. https://doi.org/10.1007/s11244-008-9071-6.
130. Sankar, G.; Rey, F.; Thomas, J. M.; Greaves, G. N.; Corma, A.; Dobson, B. R.; Dent, A. J. Probing Active Sites in Solid Catalysts for the Liquid-Phase Epoxidation of Alkenes. *J. Chem. Soc. Chem. Commun.* **1994,** *19,* 2279–2280. https://doi.org/10.1039/C39940002279.
131. Guilera, G.; Newton, M. A.; Polli, C.; Pascarelli, S.; Guinó, M.; Hii, K. K. In Situ Investigation of the Oxidative Addition in Homogeneous Pd Catalysts by Synchronised Time Resolved UV-Vis/EXAFS. *Chem. Commun.* **2006,** *41,* 4306–4308. https://doi.org/10.1039/B606772G.
132. Lee, A. F.; Wilson, K. Structure–Reactivity Correlations in the Selective Aerobic Oxidation of Cinnamyl Alcohol: In Situ XAFS. *Green Chem.* **2004,** *6* (1), 37–42. https://doi.org/10.1039/B310505A.
133. Kawai, T.; Bando, K. K.; Lee, Y. K.; Oyama, S. T.; Chun, W. J.; Asakura, K. EXAFS Measurements of a Working Catalyst in the Liquid Phase: An In Situ Study of a Ni_2P Hydrodesulfurization Catalyst. *J. Catal.* **2006,** *241* (1), 20–24. https://doi.org/10.1016/j.jcat.2006.03.024.
134. Varsha, V. M.; Nageswaran, G. Operando X-Ray Spectroscopic Techniques: A Focus on Hydrogen and Oxygen Evolution Reactions. *Front. Chem.* **2020,** *8.* https://doi.org/10.3389/fchem.2020.00023; Lassalle-Kaiser, B.; Gul, S.; Kern, J.; Yachandra, V. K.; Yano, J. In Situ/Operando Studies of Electrocatalysts Using Hard X-Ray Spectroscopy. *J. Electron Spectros. Relat. Phenomena* **2017,** *221,* 18–27. https://doi.org/10.1016/j.elspec.2017.05.001; Wang, M.; Árnadóttir, L.; Xu, Z. J.; Feng, Z. In Situ X-Ray Absorption Spectroscopy Studies of Nanoscale Electrocatalysts. *Nano-Micro Letters* **2019,** *11* (1), 47. https://doi.org/10.1007/s40820-019-0277-x; Li, J.; Gong, J. Operando Characterization Techniques for Electrocatalysis. *Energ. Environ. Sci.* **2020,** *13* (11), 3748–3779. https://doi.org/10.1039/D0EE01706J.
135. Khare, R.; Jentys, A.; Lercher, J. A. Development of Photochemical and Electrochemical Cells for Operando X-Ray Absorption Spectroscopy during Photocatalytic and Electrocatalytic Reactions. *Phys. Chem. Chem. Phys.* **2020,** *22* (34), 18891–18901. https://doi.org/10.1039/D0CP00654H.
136. Lassalle-Kaiser, B.; Merki, D.; Vrubel, H.; Gul, S.; Yachandra, V. K.; Hu, X.; Yano, J. Evidence from In Situ X-Ray Absorption Spectroscopy for the Involvement of Terminal Disulfide in the Reduction of Protons by an Amorphous Molybdenum Sulfide Electrocatalyst. *J. Am. Chem. Soc.* **2015,** *137* (1), 314–321. https://doi.org/10.1021/ja510328m.
137. Cheng, J.; Yang, J.; Kitano, S.; Juhasz, G.; Higashi, M.; Sadakiyo, M.; Kato, K.; Yoshioka, S.; Sugiyama, T.; Yamauchi, M.; et al. Impact of Ir-Valence Control and Surface Nanostructure on Oxygen Evolution Reaction over a Highly Efficient Ir–TiO_2 Nanorod Catalyst. *ACS Catal.* **2019,** *9* (8), 6974–6986. https://doi.org/10.1021/acscatal.9b01438.
138. Burnett, D. L.; Petrucco, E.; Russell, A. E.; Kashtiban, R. J.; Sharman, J. D. B.; Walton, R. I. In Situ XAFS of Acid-Resilient Iridate Pyrochlore Oxygen Evolution Electrocatalysts under Operating Conditions. *Phys. Chem. Chem. Phys.* **2020,** *22* (34), 18770–18773. https://doi.org/10.1039/D0CP01378A.
139. Su, B.-J.; Wang, K.-W.; Tseng, C.-J.; Pao, C.-W.; Chen, J.-L.; Lu, K.-T.; Chen, J.-M. High Durability of Pt3Sn/Graphene Electrocatalysts toward the Oxygen Reduction Reaction Studied with In Situ QEXAFS. *ACS Appl. Mater. Interfaces* **2020,** *12* (22), 24710–24716. https://doi.org/10.1021/acsami.0c02415.
140. Lin, S.-C.; Chang, C.-C.; Chiu, S.-Y.; Pai, H.-T.; Liao, T.-Y.; Hsu, C.-S.; Chiang, W.-H.; Tsai, M.-K.; Chen, H. M. Operando Time-Resolved X-Ray Absorption Spectroscopy Reveals the Chemical Nature Enabling Highly Selective CO_2 Reduction. *Nat. Commun.* **2020,** *11* (1), 3525. https://doi.org/10.1038/s41467-020-17231-3.
141. Meirer, F.; Weckhuysen, B. M. Spatial and Temporal Exploration of Heterogeneous Catalysts with Synchrotron Radiation. *Nat. Rev. Mat.* **2018,** *3* (9), 324–340. https://doi.org/10.1038/s41578-018-0044-5.
142. Pattammattel, A.; Tappero, R.; Ge, M.; Chu, Y. S.; Huang, X.; Gao, Y.; Yan, H. High-Sensitivity Nanoscale Chemical Imaging with Hard x-Ray Nano-XANES. *Sci. Adv.* **2020,** *6* (37), eabb3615. https://doi.org/10.1126/sciadv.abb3615.
143. Alizadehfanaloo, S.; Garrevoet, J.; Seyrich, M.; Murzin, V.; Becher, J.; Doronkin, D. E.; Sheppard, T. L.; Grunwaldt, J.-D.; Schroer, C. G.; Schropp, A. Tracking Dynamic Structural Changes in Catalysis by Rapid 2D-XANES Microscopy. *J. Synchrotron Radiat.* **2021,** *28* (5), 1518–1527. https://doi.org/10.1107/S1600577521007074.
144. Tada, M.; Ishiguro, N.; Uruga, T.; Tanida, H.; Terada, Y.; Nagamatsu, S.-I.; Iwasawa, Y.; Ohkoshi, S.-I. μ-XAFS of a Single Particle of a Practical NiOx/Ce2Zr2Oy Catalyst. *Phys. Chem. Chem. Phys.* **2011,** *13* (33), 14910–14913. https://doi.org/10.1039/C1CP20895K.

145. Ruiz-Martínez, J.; Beale, A. M.; Deka, U.; O'Brien, M. G.; Quinn, P. D.; Mosselmans, J. F. W.; Weckhuysen, B. M. Correlating Metal Poisoning with Zeolite Deactivation in an Individual Catalyst Particle by Chemical and Phase-Sensitive X-Ray Microscopy. *Angew. Chem. Int. Ed.* **2013,** *52* (23), 5983–5987. https://doi.org/10.1002/anie.201210030.
146. Grunwaldt, J.-D.; Wagner, J. B.; Dunin-Borkowski, R. E. Imaging Catalysts at Work: A Hierarchical Approach from the Macro- to the Meso- and Nano-Scale. *ChemCatChem* **2013,** *5* (1), 62–80. https://doi.org/10.1002/cctc.201200356.
147. Timoshenko, J.; Frenkel, A. I. "Inverting" X-Ray Absorption Spectra of Catalysts by Machine Learning in Search for Activity Descriptors. *ACS Catal.* **2019,** *9* (11), 10192–10211. https://doi.org/10.1021/acscatal.9b03599.
148. Ueno, T.; Hino, H.; Hashimoto, A.; Takeichi, Y.; Sawada, M.; Ono, K. Adaptive Design of an X-Ray Magnetic Circular Dichroism Spectroscopy Experiment with Gaussian Process Modelling. *NPJ Comput. Mat.* **2018,** *4* (1), 4. https://doi.org/10.1038/s41524-017-0057-4; Martini, A.; Bugaev, A. L.; Guda, S. A.; Guda, A. A.; Priola, E.; Borfecchia, E.; Smolders, S.; Janssens, K.; De Vos, D.; Soldatov, A. V. Revisiting the Extended X-Ray Absorption Fine Structure Fitting Procedure through a Machine Learning-Based Approach. *Chem. A Eur. J.* **2021,** *125* (32), 7080–7091. https://doi.org/10.1021/acs.jpca.1c03746.
149. Timoshenko, J.; Lu, D.; Lin, Y.; Frenkel, A. I. Supervised Machine-Learning-Based Determination of Three-Dimensional Structure of Metallic Nanoparticles. *J. Phys. Chem. Lett.* **2017,** *8* (20), 5091–5098. https://doi.org/10.1021/acs.jpclett.7b02364.
150. Timoshenko, J.; Anspoks, A.; Cintins, A.; Kuzmin, A.; Purans, J.; Frenkel, A. I. Neural Network Approach for Characterizing Structural Transformations by X-Ray Absorption Fine Structure Spectroscopy. *Phys. Rev. Lett.* **2018,** *120* (22), 225502. https://doi.org/10.1103/PhysRevLett.120.225502.
151. Swann, E.; Sun, B.; Cleland, D. M.; Barnard, A. S. Representing Molecular and Materials Data for Unsupervised Machine Learning. *Mol. Simul.* **2018,** *44* (11), 905–920. https://doi.org/10.1080/08927022.2018.1450982; Price, S. W. T.; Ignatyev, K.; Geraki, K.; Basham, M.; Filik, J.; Vo, N. T.; Witte, P. T.; Beale, A. M.; Mosselmans, J. F. W. Chemical Imaging of Single Catalyst Particles with Scanning μ-XANES-CT and μ-XRF-CT. *Phys. Chem. Chem. Phys.* **2015,** *17* (1), 521–529. https://doi.org/10.1039/C4CP04488F.
152. Ressler, T.; Wong, J.; Roos, J.; Smith, I. L. Quantitative Speciation of Mn-Bearing Particulates Emitted from Autos Burning (Methylcyclopentadienyl)Manganese Tricarbonyl-Added Gasolines Using XANES Spectroscopy. *Environ. Sci. Tech.* **2000,** *34* (6), 950–958.
153. Fernandez-Garcia, M.; Marquez Alvarez, C.; Haller, G. L. XANES-TPR Study of Cu-Pd Bimetallic Catalysts: Application of Factor Analysis. *J. Phys. Chem.* **1995,** *99* (33), 12565–12569. https://doi.org/10.1021/j100033a032; Blanco-Brieva, G.; Capel-Sanchez, M. C.; Campos-Martín, J. M.; Fierro, J. L. G.; Lede, E. J.; Adrini, L.; Requejo, F. G. Titanium K-Edge XANES Analysis to Unravel the Local Structure of Alkene Epoxidation Titanium-Polysiloxane Homogeneous Catalysts. *Adv. Synth. Catal.* **2003,** *345* (12), 1314–1320. https://doi.org/10.1002/adsc.200303119.
154. Moya-Cancino, J. G.; Honkanen, A.-P.; van der Eerden, A. M. J.; Schaink, H.; Folkertsma, L.; Ghiasi, M.; Longo, A.; Meirer, F.; de Groot, F. M. F.; Huotari, S.; et al. Elucidating the K-Edge X-Ray Absorption Near-Edge Structure of Cobalt Carbide. *ChemCatChem* **2019,** *11* (13), 3042–3045. https://doi.org/10.1002/cctc.201900434.
155. Rochet, A.; Baubet, B.; Moizan, V.; Pichon, C.; Briois, V. Co-K and Mo-K Edges Quick-XAS Study of the Sulphidation Properties of Mo/Al_2O_3 and $CoMo/Al_2O_3$ Catalysts. *C. R. Chim.* **2016,** *19* (10), 1337–1351. https://doi.org/10.1016/j.crci.2016.01.009.
156. Voronov, A.; Urakawa, A.; Beek, W. V.; Tsakoumis, N. E.; Emerich, H.; Rønning, M. Multivariate Curve Resolution Applied to In Situ X-Ray Absorption Spectroscopy Data: An Efficient Tool for Data Processing and Analysis. *Anal. Chim. Acta* **2014,** *840,* 20–27. https://doi.org/10.1016/j.aca.2014.06.050.
157. Funke, H.; Scheinost, A. C.; Chukalina, M. Wavelet Analysis of Extended x-Ray Absorption Fine Structure Data. *Phys. Rev. B* **2005,** *71* (9), 094110. https://doi.org/10.1103/PhysRevB.71.094110.
158. Negri, C.; Selleri, T.; Borfecchia, E.; Martini, A.; Lomachenko, K. A.; Janssens, T. V. W.; Cutini, M.; Bordiga, S.; Berlier, G. Structure and Reactivity of Oxygen-Bridged Diamino Dicopper(II) Complexes in Cu-Ion-Exchanged Chabazite Catalyst for NH_3-Mediated Selective Catalytic Reduction. *J. Am. Chem. Soc.* **2020,** *142* (37), 15884–15896. https://doi.org/10.1021/jacs.0c06270.
159. Chiarello, G. L.; Ferri, D. Modulated Excitation Extended X-Ray Absorption Fine Structure Spectroscopy. *Phys. Chem. Chem. Phys.* **2015,** *17* (16), 10579–10591. https://doi.org/10.1039/C5CP00609K.
160. König, C. F. J.; van Bokhoven, J. A.; Schildhauer, T. J.; Nachtegaal, M. Quantitative Analysis of Modulated Excitation X-Ray Absorption Spectra: Enhanced Precision of EXAFS Fitting. *J. Phys. Chem. C* **2012,** *116* (37), 19857–19866. https://doi.org/10.1021/jp306022k; Ebner, K.; Clark, A. H.; Saveleva, V. A.; Smolentsev, G.; Chen, J.; Ni, L.; Li, J.; Zitolo, A.; Jaouen, F.; Kramm, U. I.; et al. Time-Resolved Potential-Induced Changes in Fe/N/C-Catalysts Studied by in Situ Modulation Excitation X-Ray Absorption Spectroscopy. *Adv. Energy Mat.* **2022,** *12* (14), 2103699. https://doi.org/10.1002/aenm.202103699.
161. Diamond (2022) https://www.diamond.ac.uk/Instruments/Spectroscopy/B18.html (Accessed 01/02/2022).
162. García-Serna, J.; Piñero-Hernanz, R.; Durán-Martín, D. Inspirational Perspectives and Principles on the Use of Catalysts to Create Sustainability. *Catal. Today* **2022,** *387,* 237–243. https://doi.org/10.1016/j.cattod.2021.11.021.
163. Dimper, R.; Reichert, H.; Raimondi, P.; Ortiz, L. S.; Sette, F.; Susini, A. J. *ESRF Upgrade Programme Phase II (2015–2022),* Technical Design Study, 2015.
164. Petersen, C. R.; Moselund, P. M.; Huot, L.; Hooper, L.; Bang, O. Towards a Table-Top Synchrotron Based on Supercontinuum Generation. *Infrared Phys. Technol.* **2018,** *91,* 182–186. https://doi.org/10.1016/j.infrared.2018.04.008; Holburg, J.; Müller, M.; Mann, K.; Wild, P.; Eusterhues, K.; Thieme, J. High-Resolution Table-Top NEXAFS Spectroscopy. *Anal. Chem.* **2022,** *94* (8), 3510–3516. https://doi.org/10.1021/acs.analchem.1c04374.
165. Buades, B.; Moonshiram, D.; Sidiropoulos, T. P. H.; León, I.; Schmidt, P.; Pi, I.; Di Palo, N.; Cousin, S. L.; Picón, A.; Koppens, F.; et al. Dispersive Soft x-Ray Absorption Fine-Structure Spectroscopy in Graphite with an Attosecond Pulse. *Optica* **2018,** *5* (5), 502–506. https://doi.org/10.1364/OPTICA.5.000502.
166. Chatterjee, R.; Weninger, C.; Loukianov, A.; Gul, S.; Fuller, F. D.; Cheah, M. H.; Fransson, T.; Pham, C. C.; Nelson, S.; Song, S.; et al. XANES and EXAFS of Dilute Solutions of Transition Metals at XFELsThis Article Will Form Part of a Virtual Special Issue on X-Ray Free-electron Lasers. *J. Synchrotron Radiat.* **2019,** *26* (5), 1716–1724. https://doi.org/10.1107/S1600577519007550; Bergmann, U.; Kern, J.; Schoenlein, R. W.; Wernet, P.; Yachandra, V. K.; Yano, J. Using X-Ray Free-electron Lasers for Spectroscopy of Molecular Catalysts and Metalloenzymes. *Nat. Rev. Phys.* **2021,** *3* (4), 264–282. https://doi.org/10.1038/s42254-021-00289-3.

10.06 Coherent x-ray diffraction studies of inorganic crystalline nanomaterials

Wonsuk Cha[a], **Sungwook Choi**[b], **and Hyunjung Kim**[b], [a] X-ray Science Division, Argonne National Laboratory, Argonne, IL, United States; and [b] Department of Physics, Sogang University, Seoul, Korea

© 2023 Elsevier Ltd. All rights reserved.

10.06.1	**Introduction to coherent X-rays**	**149**
10.06.1.1	Source of X-rays	149
10.06.1.1.1	Coherent X-rays	150
10.06.1.2	Applications of coherent X-rays	151
10.06.2	**Introduction to coherent X-ray diffraction imaging in Bragg geometry (BCDI)**	**152**
10.06.2.1	Fundamentals of coherent X-ray diffraction imaging	153
10.06.2.2	Bragg coherent X-ray diffraction imaging (BCDI)	155
10.06.2.2.1	Resolution	157
10.06.2.2.2	Sensitivity to lattice displacement	157
10.06.2.2.3	Strain tensor	160
10.06.2.3	In-situ/operando capabilities	160
10.06.3	**BCDI studies of catalytic materials**	**165**
10.06.3.1	Sample environments for in-situ/operando studies	166
10.06.3.2	Active site determination using BCDI	166
10.06.3.3	Strain and defect evolution during catalysis	168
10.06.4	**Crystal growth and dissolution studied via BCDI**	**170**
10.06.5	**BCDI studies of energy storage materials**	**174**
10.06.5.1	Strain energy landscape in Lithium-ion battery cathode nanoparticles	174
10.06.5.2	Dislocation dynamics during battery cycling	177
10.06.6	**Ultrafast dynamics using BCDI**	**179**
10.06.7	**Future prospects for BCDI at fourth-generation synchrotron sources**	**183**
References		**183**

Abstract

Nanomaterials have been used in many applications because of their enhanced surface-to-volume ratio. They show remarkably different properties when compared to their bulk state and many efforts have been made to enhance the efficiency of nanomaterials. Strain engineering is a growing research field, since strain can alter the properties of materials. Therefore, it is essential to understand the relationship between the structure, including strain, and properties of nanomaterials. There is demand for new characterization tools to image nanomaterials under realistic operating conditions at high resolution, so that nanomaterial efficiency can be improved and new types of nanomaterial can be designed.

Bragg coherent X-ray diffraction imaging (BCDI) has emerged as a powerful technique for three-dimensional imaging of nanocrystals at high resolution. BCDI can be used to map the internal lattice displacement field distribution in various crystalline nanomaterials, such as metals and metal oxides, because of its unique sensitivity to the lattice. BCDI, combined with in-situ or operando approaches, is a powerful tool to address scientific questions on nanomaterials and it has opened new areas of scientific research. This chapter introduces state-of-the-art BCDI techniques and reviews recent research on catalysis and energy-related materials, from among many applications to inorganic nanomaterials.

10.06.1 Introduction to coherent X-rays

10.06.1.1 Source of X-rays

Since X-rays were discovered in 1895 by Wilhelm Röntgen,[1] a tremendous amount of structure determination of materials and new techniques has been achieved. Because of the short wavelength and penetration depth in materials, it is useful to investigate structures and properties of materials nondestructively, for example, determining the internal structure and chemical composition of materials. In the early days, X-ray physics, including the discovery of X-rays, was the most influential research area of basic science. Later, X-rays were applied widely in physics, chemistry, biology, and medicine.[2]

The Coolidge tube has been used as a standard X-ray tube for many decades. This X-ray source consists of an evacuated glass tube with a tungsten filament and a water-cooled metal block anode. Electrons emitted by the filament are accelerated toward the metal anode and then impinge on the anode. This process produces X-rays and the X-ray flux is limited by cooling efficiency. In order to

overcome this limitation, the rotating anode was developed in the 1960s. Rotating the metal anode dissipates the heat over a much larger volume than the Coolidge tube, allowing the total power to be increased.[3]

Synchrotron sources provide much brighter X-rays than laboratory-based sources, as shown in Fig. 1. To compare the X-ray flux from different sources, a measure called brilliance or brightness is defined as the number of photons/s·mrad^2·mm^2·0.1% bandwidth, considering the number of photons per unit time, the collimation of the beam, the source area, and the spectral distribution of X-rays.[3] Synchrotrons typically consist of an accelerator, a storage ring, and beamlines. Electrons are accelerated to a velocity close to the speed of light in the accelerator and traveling along the storage ring. Synchrotron radiation is produced along a direction tangential to the orbit of electrons when the electron's trajectory is changed by an external magnetic force. This happens in either bending magnets, which are essential to keep the electrons in a closed-loop, or insertion devices, such as wigglers and undulators, which are installed in straight sections of the storage ring. The beamlines utilize X-rays generated by either the bending magnets or the insertion devices. First generation synchrotron radiation sources used parasitic radiation from accelerators mainly designed for high-energy physics, for example, Synchrotron Ultraviolet Radiation Facility (SURF-I) in the USA and Deutsches Elektronen-Synchrotron (DESY) in Germany. Synchrotrons designed primarily to produce synchrotron radiation are called second-generation. The Synchrotron Radiation Source (SRS) in the UK was the first second-generation synchrotron source. Rings making extensive use of insertion devices are called third-generation sources. In the insertion device, e.g., undulators, electrons, following a sinusoidal trajectory, produce X-ray beams with higher flux. The European Synchrotron Radiation Facility (ESRF) in France, Advanced Photon Source (APS) in the USA, and SPring-8 in Japan were the first group of third-generation synchrotron sources. Fourth-generation synchrotrons, also called diffraction limited storage rings (DLSR), are multi-bend achromat storage rings with very small X-ray emittances. MAX-IV in Sweden is the first one of this type and many synchrotrons are starting to operate or preparing to upgrade to fourth generation magnet lattices.

X-ray free-electron lasers (XFELs), with long straight sections containing undulators, generate extremely bright X-rays with very short pulse widths (a few tens of femtoseconds) and an almost fully coherent beam.

In addition, compact light sources and compact X-ray free-electron lasers are available, which are based on the interaction of a high power laser with the electrons. This process forces the electrons to wiggle and hence induces X-ray emission.[2,4]

10.06.1.1.1 Coherent X-rays

In the X-ray regime, the use of the coherence became practical starting with third-generation synchrotrons. Undulators, consisting of arrays of alternating magnets, generate coherent X-rays in the following way. As electrons traverse through this section, the magnetic

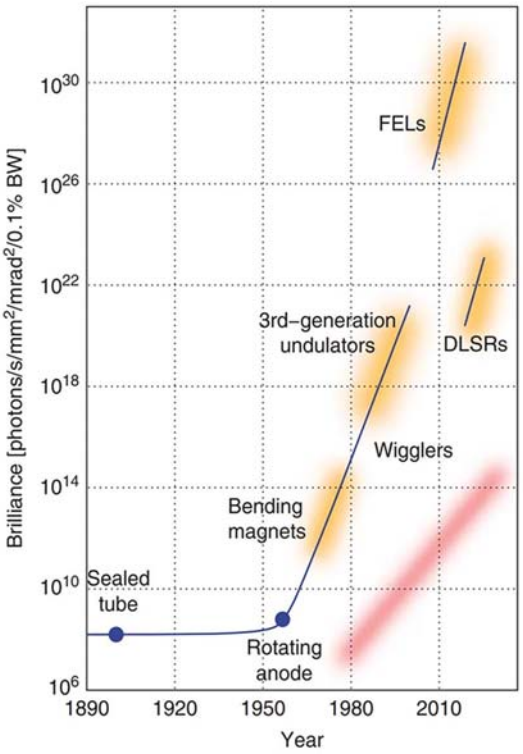

Fig. 1 Historical graph of the brilliance of X-ray sources. DLSR denotes diffraction limited storage rings and FELs denotes free electron lasers. Reproduced from Willmott, P. *An Introduction to Synchrotron Radiation: Techniques and Applications*. John Wiley: Chichester, West Sussex, UK, 2019, with permission from John Wiley & Sons, Ltd.

field that alternates from up and down forces electrons to be on oscillating paths in a horizontal plane. Radiation produced at each oscillation is in phase, and thus added coherently.[3]

Regarding the coherence of X-rays, one can define the degree of coherence with the longitudinal and transverse coherence with the assumption of a plane wave in the following way. As shown in Fig. 2A, X-rays of slightly different wavelengths, but within the allowed bandwidth passed by the monochromator, become out of phase with one another as they propagate. The distance for X-rays to be out of phase is defined as longitudinal coherence length (L_L);

$$L_L = \frac{1}{2}\frac{\lambda^2}{\Delta\lambda}$$

where λ is the wavelength. Therefore, for the synchrotron X-rays, the longitudinal coherence length is determined by the quality of the monochromator. A typical Si (111) double crystal monochromator has a $\sim 10^4$ spectral resolution ($\lambda/\Delta\lambda$), which results in a $\sim$0.5 μm longitudinal coherence length for X-rays of wavelength 1 Å.[2,3]

As shown in Fig. 2B, X-rays traveling along slightly different directions can interfere with each other even though they have the same wavelength. If one observes two waves relatively far from the source, one wave gets out of phase with the other at a certain distance and they are in phase again the same distance away. This distance is defined as transverse coherence length (L_T);

$$L_T = \frac{\lambda}{2}\frac{R}{D}$$

where R is the distance between the observation point and the source and D the lateral dimension of the source.[2,3] Typical horizontal and vertical source sizes at a third-generation source, e.g., the Advanced Photon Source are about 275 μm and 10 μm, respectively[5] and measurements are performed about 50 m away from the source, so that the transverse coherence lengths in the horizontal and vertical directions for X-rays of 1 Å wavelength are approximately 9 μm and 250 μm, respectively. X-rays produced by free-electron lasers are almost fully coherent in the lateral direction.[6,7] However, the longitudinal coherence length is still determined by the monochromaticity of the beam.[8] The coherent volume can be determined by multiplying two transverse coherence lengths and the longitudinal coherence length.

10.06.1.2 Applications of coherent X-rays

The first observation of a coherent X-ray effect on scattering in the hard X-ray regime was reported by Sutton et al.[9] in the early 1990s at the second-generation synchrotron, National Synchrotron Light Source (NSLS) in the USA. Coherent X-ray illumination of ordered crystalline Cu_3Au created a speckle patterns in the vicinity of a (001) Bragg peak. The speckles are diffracted from randomly arranged antiphase domains in the entire illuminated volume. This observation opened up possibilities for new characterization techniques using coherent X-rays.

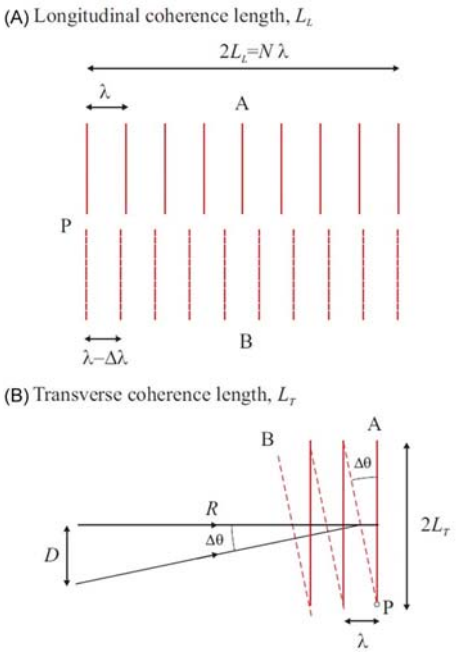

Fig. 2 Definition of coherence lengths. (A) longitudinal coherence length (B) transverse coherence length. Reproduced from Als-Nielsen, J.; McMorrow, D. *Elements of Modern X-Ray Physics*. Wiley: Hoboken, 2011, with permission from John Wiley & Sons, Ltd.

Fig. 3 illustrates the different measurement regimes for a plane wave incident on a sample, depending on the sample to detection plane distance.[10] In the contact regime, absorption is the dominant part of phase contrast and this enables phase-contrast imaging, which has been used in biology to differentiate between different kinds of soft tissue. In the near field regime, phase difference arises in the scattering due to inhomogeneous refractive indexes through the material. In the Fresnel regime, amplitude distribution changes rapidly depending on the distance from the sample because of substantial interference. Therefore, edge-enhanced phase contrast can be obtained. One can obtain multiple images of the object at different orientations and reconstruct them into a three-dimensional image. This technique is called computational tomography. As the detector moves further away from the sample into the Fraunhofer regime, interference patterns from speckle patterns provide information on the shape and internal structure of the object.[11] Our discussion will focus on X-ray characterization techniques in the Fraunhofer regime.

The unique feature of the coherent X-ray forms interference patterns in the scattered waves from different parts of the object, whereas incoherent illumination gives an ensemble average of diffracted waves from each part of the material.[11] The left and right sides of Fig. 4 compare the results from coherent (left) and incoherent (right) illumination in a small-angle X-ray scattering study of colloids. This measurement was carried out with XFEL. The coherent scattering from the colloidal suspension gives rise to a grainy structure on concentric ring patterns, characteristics of well-defined speckle patterns. An averaged pattern of 50 coherent illuminations shows only smooth concentric ring patterns, which is the signature of diffraction from incoherently illuminated spherical particles with well-defined diameter.[12]

Taking intensity-intensity correlation of the speckle patterns at a fixed wave vector, one can get the dynamic structure factor, i.e., S(q, t). This technique is called X-ray photon correlation spectroscopy,[9,11] which enables measuring the dynamics of domain fluctuation of antiferromagnetic domains,[13] thermal fluctuation of ferroelectric nanodomains,[14] capillary waves on the surface of thin polymer films,[15] critical phenomena in complex fluids,[16] dynamics of nanoparticles in entangled polymer melts,[17] and atomic diffusion in intermetallic alloys.[18]

Another approach to utilize coherent X-rays is to retrieve the phase to get an image of the object. Using a phase retrieval algorithm with the coherent X-ray diffraction patterns, one can obtain the electron density and phase information. This technique is lensless coherent X-ray diffraction imaging.[11] This chapter focuses on the application of coherent X-ray diffraction imaging, mainly in Bragg geometry.

10.06.2 Introduction to coherent X-ray diffraction imaging in Bragg geometry (BCDI)

Nanomaterials can possess remarkably different properties from their bulk state, due to a considerable fraction of their volume being close to the external surface and their large interface area.[19] In nanomaterials, it is important to measure and understand strain, defined as the spatial derivative of the displacement of the material from an ideal lattice, as small strains can lead to deviations from the bulk properties. Because of the enhanced role of surfaces in nanomaterials, engineering the strain in them may be

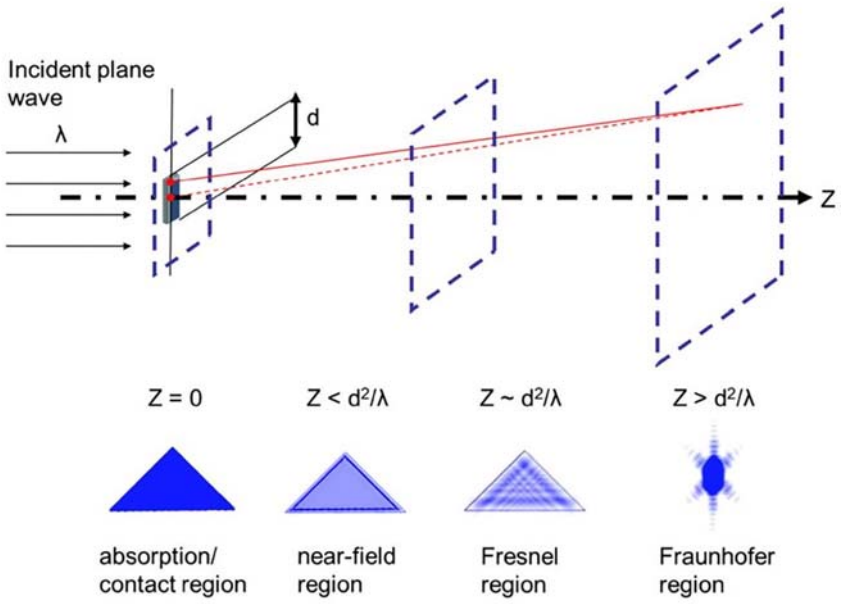

Fig. 3 Dependence on the propagation distance between the sample and the detection planes for an incident plane-wave. It illustrates the absorption, near-field, Fresnel and Fraunhofer regions. Reproduced from Abbey, B. From Grain Boundaries to Single Defects: A Review of Coherent Methods for Materials Imaging in the X-Ray Sciences. *JOM* **2013**, *65*(9), 1183–1201, doi: 10.1007/s11837-013-0702-4, with permission from Springer Nature.

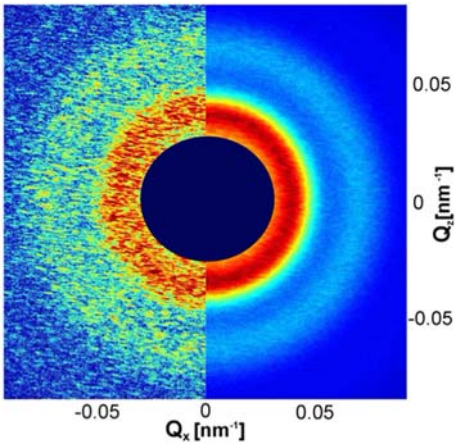

Fig. 4 X-ray diffraction pattern from the colloidal sample with XFEL. A single shot coherent pattern (left half) is compared to the scattering ring obtained from a sum of 50 successive shots (right half). The middle circular shadow is the beam stop preventing the direct beam at the detector. Reproduced from Lee, S.; Roseker, W.; Gutt, C.; Fischer, B.; Conrad, H.; Lehmkühler, F.; Steinke, I.; Zhu, D.; Lemke, H.; Cammarata, M.; Fritz, D. M.; Wochner, P.; Castro-Colin, M.; Hruszkewycz, S. O.; Fuoss, P. H.; Stephenson, G. B.; Grübel, G.; Robert, A. Single Shot Speckle and Coherence Analysis of the Hard X-Ray Free Electron Laser LCLS. *Opt. Express* **2013**, *21*(21), 24647, doi: 10.1364/OE.21.024647, with permission from *OPTICAL SOC AMER*.

a promising technology for controlling their properties. The mechanisms of strain relaxation and dislocation dynamics in nanomaterials are not fully understood. Quantitative and qualitative studies to address scientific questions on nanomaterials require a new characterization tool for three-dimensional strain distribution measurements at high resolution, and with high strain sensitivity,[19,20] in whole particles.

Electron microscopy has been widely used to examine nanomaterials. In particular, transmission electron microscopy (TEM) reveals the strain in individual nanomaterials quantitatively. TEM can also map nanomaterials at nearly atomic resolution by direct imaging. However, the relatively strong interaction of electrons with condensed materials limits the penetration depth to a few nanometers. Atom probe tomography (APT) can be useful for information beyond a cubic nanometer scale. However, destruction of the sample occurs during the APT process.[19–21]

Characterization of nanomaterials by hard X-rays is based on the fundamental advantage of utilizing a weakly interacting probe with an extremely short wavelength. The large penetrating power of hard X-rays also has benefits for in-situ/operando studies with temperature, various gas environments, and extreme pressure, etc. The benefits of nanoscale imaging with hard X-rays include direct and nondestructive imaging based on structural changes, such as strain gradients, dislocations, and grain boundaries. Depending on the geometry and sensitivity, one can get images containing a variety of information using X-ray microscopy techniques: the chemical states and coordination number of transition metal elements with transmission microscopy, the element distribution in the materials with fluorescence microscopy, and strain distributions with Bragg diffraction microscopy. High-resolution X-ray microscopy uses X-ray focusing optics. Kirkpatrick-Baez mirrors, Fresnel zone plates, multilayer Laue lenses, and compound refractive lenses have been commonly used to focus X-ray beams down to about 10 nm.[22] Up to now, the smallest spot size in the hard X-ray regime is 5 nm, which was achieved using a multilayer Laue lens.[23] In the case of X-ray microscopy, high resolution imaging depends upon the focusing optics. However, fabricating X-ray optics capable of generating tiny X-ray spots in challenging.[24,25]

10.06.2.1 Fundamentals of coherent X-ray diffraction imaging

Coherent X-ray diffraction imaging (CDI) is a lensless technique and generally refers to methods that use computational algorithms to invert coherent X-ray diffraction (CXD) patterns into an image of the sample in real space. This technique exploits the brilliance of modern third-generation synchrotrons and X-ray free-electron lasers to image nanomaterials at very high spatial resolution. The basic principle of CDI measurement is coherent illumination of a sample, which is smaller than the coherent volume of the beam. Coherent X-rays scattered from different regions of the sample interfere constructively or destructively and reach a detector with a fixed relative phase to each other. It is how this technique can image the local structure of nanomaterials at very high resolution without lenses. The X-ray beam itself shows a point-to-point correlation in phase that is preserved throughout the interaction within the sample. Because CDI does not require a lens, in principle, the spatial resolution of CDI is only limited by the wavelength of X-ray. Therefore, the samples can be mounted within an in-situ sample environment cell without interfering with X-ray optics.[19,24–26]

X-ray diffraction in the far-field is directly related to the Fourier transform of the density of the object. Therefore, one can perform an inverse Fourier transform on the diffraction pattern, if you have both amplitude and phase, to obtain an image of the sample in real space. However, intensity is measured when one records diffraction patterns from an object, and the phase information is

missing, so that it is not possible to reconstruct an image of the object by performing an inverse Fourier transformation of the diffraction pattern.[20,26,27]

However, one can obtain an image of the sample once the missing phases are retrieved. This idea is based on the initial observation by Sayre[28] regarding direct structure determination for centrosymmetric structures. To retrieve phases, iterative algorithms were proposed by Gerchberg and Saxton for electron microscopy.[29] The algorithm iterates between real and reciprocal space by Fourier transformation and inverse Fourier transformation. Because of two intensity measurements in both real and reciprocal spaces in electron microscopy, the measured modulus values are used as constraints and the moduli from the Fourier transforms in both spaces are replaced with measured values. However, for CDI, there is only one intensity measurement in reciprocal space. It means that we need to use as much prior information about the object as possible to aid phase retrieval. The "error reduction" and "hybrid input-output" algorithms proposed by Fienup[30] have been widely used for phase retrieval from CXD patterns. Typically, the iterative calculation starts from a randomly selected phase with the measured amplitude. The guess of the object is obtained using a Fourier transform with constraints in real space applied. For example, non-negative density and a volume, called support, which defines the space being occupied by the guess and limits the size of the object. The support determines how the density distribution of the object is modified at each iteration. In practice, improper support often causes the reconstruction of an incorrect image of the object. Marchesini et al.[31] developed a new method called shrinkwrap, allowing the size and the shape of the support to be changed during each iteration. Each generated real space image is inverse Fourier-transformed to reciprocal space. The calculated amplitude from the Fourier transform is replaced with the amplitude from the measurement. These steps are repeated until a correct solution is obtained.[32] Various algorithms are available for phase retrieval. Among these algorithms, a combination of error reduction and hybrid input-output is effective in convergence and calculation speed. Chen et al.[33] introduced a guided hybrid input-output algorithm combining hybrid input-output with optimization to improve the reliability of a reconstructed image. In this algorithm, multiple sequences of phase retrieval are performed with slightly different initial phase values for each sequence. The images are combined together periodically during iterative calculations to converge to a single solution. Another method to improve image quality is to correct for imperfections in the coherence of the X-ray beam.[34] It appears as reduced visibility of interference in the CXD patterns and non-uniform density distribution in the reconstructed image. Considering the partial coherence effect on the phase retrieval process improves image interpretability, removes artifacts, and minimizes failure of phase retrieval.[20,24,27,35] Recently, there have been many efforts to utilize machine learning reconstruction methods[36,37] to estimate the image of the object rapidly and to improve the accuracy of iterative phase retrieval.

Typically, CDI is performed in two different geometries, transmission and Bragg, as shown in **Fig. 5**A and B, respectively. In the former case, the scattered X-rays near the direct beam are collected with the detector sitting downstream of the sample. Whereas in the latter, the sample and the detector are oriented to capture scattering in the vicinity of a Bragg peak from the sample. The former is useful for examining disordered samples, whereas crystalline samples can be measured with both.[24,38] The first CDI was demonstrated with non-crystalline specimens by Miao et al. in 1999.[39] CXD patterns of an array of Au nanoparticles on a silicon nitride membrane were successfully converted to an image in real space, at a spatial resolution of about 75 nm. Many kinds of metal nanoparticles have been explored at a spatial resolution of a few nanometers, for example, individual Au nanoparticles at about 5 nm[40] and a Ag nanocube at about 3 nm.[41] In addition, various types of biological samples have been studied, such as a dried yeast cell,[42] a dried human chromosome,[43] unstained single virus,[44] and a hydrated yeast cell.[45] Element-sensitive imaging is also available by obtaining CXD patterns above and below the absorption edge of a specific element inside the specimen.[46]

Bragg geometry provides essential advantages when compared to transmission geometry. When the intensity distribution is recorded around a Bragg peak, the retrieved phase information can be converted to a lattice displacement.[19,47] Since the part satisfying the Bragg condition within the object only contributes to CXD patterns, the external shape of the reconstructed image is not necessarily the same as the crystal boundary. Therefore, the result from imaging, i.e., the Bragg electron density, can sensitively detect the grain boundary, defects, etc.[48,49] Experimentally, objects with different crystallographic orientations under X-ray illumination lead to diffraction patterns distributed azimuthally around Debye-Scherrer rings. Therefore, an isolated CXD pattern can be obtained during measurements.[50] Three-dimensional images can be obtained readily by taking a rocking curve without being obscured by the direct beam.[49]

Au nanocrystals were reconstructed from CXD patterns in Bragg geometry as the first demonstration.[21,32,49] The three-dimensional deformation field distribution in a Pb nanocrystal on a Si substrate was imaged at a spatial resolution of about 40 nm.[47] Further studies were carried out for nano- and micro-scale crystals, for example, Au nanocrystals,[48,51,52] Ag nanocubes,[53] Pt nanocrystals,[54–57] Pd nanocrystals, $BaTiO_3$ nanoparticles,[24,58] ZnO microcrystals,[59,60] zeolite microcrystals,[61,62] energy-related materials like battery materials,[63–66] quantum materials such as nanodiamond,[67] and SiC crystals.[68]

CDI in grazing incidence reflection geometry, as shown in **Fig. 5**C, has been demonstrated. This mode enables the volumetric investigation of materials buried on a substrate or mounted on an opaque substrate using X-rays.[38,69] Another type of CDI is ptychography, which allows imaging of samples that are larger than the coherent lengths. Scanning the sample across the coherent X-ray beam is used to create an image of an extended field of view at high resolution.[24,70] Further applications include studies of nano structures,[71] ferroelectric thin films,[72] ferrimagnetic thin films,[73] multilayered semiconductor devices,[74,75] and biological samples.[76]

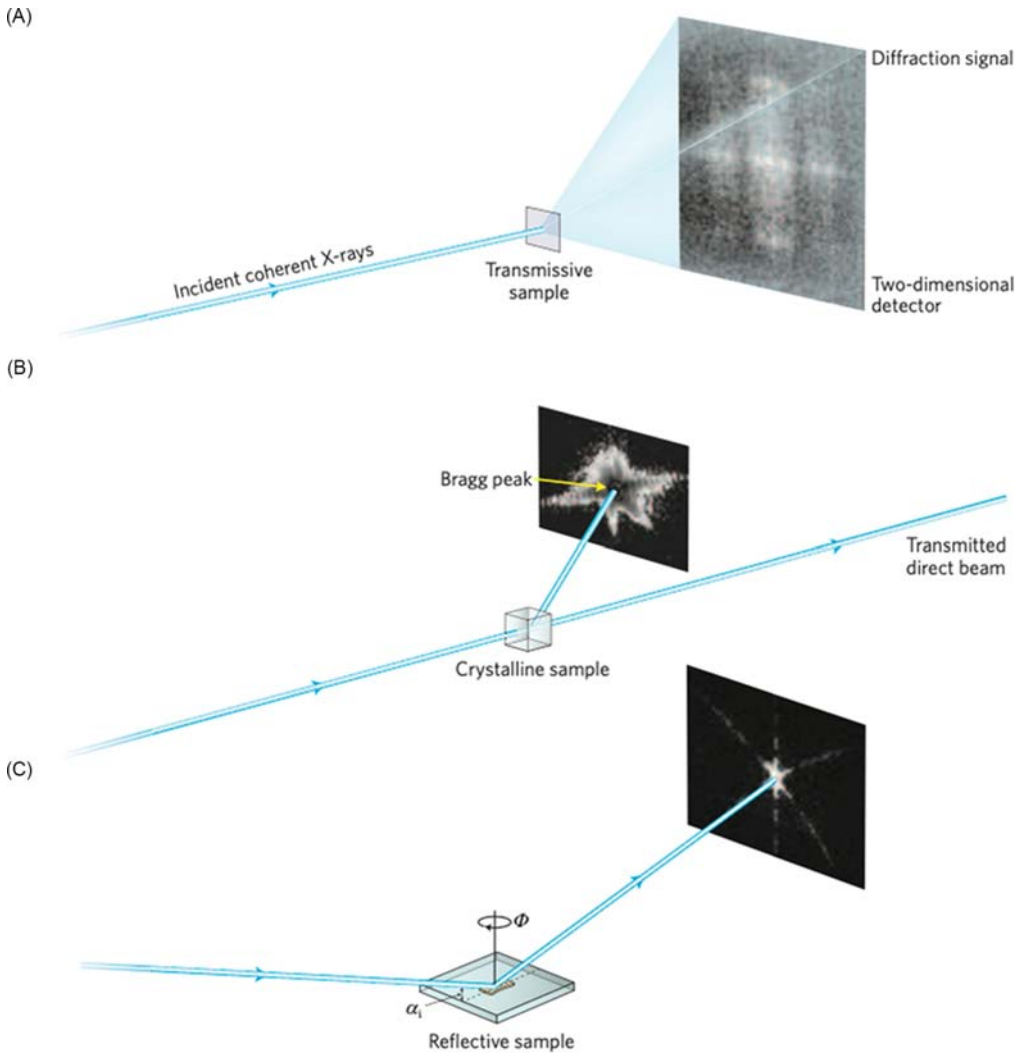

Fig. 5 Geometries for CDI. (A) Transmission geometry, (B) Bragg geometry, (C) grazing incidence reflection geometry. Reproduced from, Mancuso, A. P.; Williams, G. J. High-Resolution Surface Structures. *Nat. Photon* **2012**, *6*(9), 574–575, with permission from NATURE RESEARCH.

10.06.2.2 Bragg coherent X-ray diffraction imaging (BCDI)

When a crystal is illuminated using X-rays with coherence lengths larger than the dimensions of the crystal, CXD can be obtained with additional interference fringes on a Bragg peak. Fig. 6 shows a typical CXD pattern at the Au (11-1) Bragg peak. This CXD pattern shows two characteristic features.[49] One is the radial flares arising from the facets of the crystal. Another is the fringes along the flares. The fringes are interference from the two facets that are parallel to each other.

In the kinematic approximation, the intensity distribution in the vicinity of a Bragg peak is given by the square magnitude of a complex amplitude expressed as a function of wavevector transfer $\mathbf{q}$,

$$A(\mathbf{q}) = \int \rho(\mathbf{r}) e^{i\mathbf{q}\cdot\mathbf{r}} d\mathbf{r}$$

where $\rho(\mathbf{r})$ is the density distribution inside the finite-sized crystal. This density inside the crystal can be written as the product of a function describing the shape of the crystal, $s(\mathbf{r})$ and the lattice of the crystal. When the atoms in the crystal sit on an ideal lattice, the density distribution can be expressed as a set of delta functions,

$$\rho(\mathbf{r}) = s(\mathbf{r}) \sum_{\mathbf{R}} \delta(\mathbf{r} - \mathbf{R})$$

where $\mathbf{R}$ is the lattice vector. The Fourier transform of the lattice function in real space is the reciprocal lattice function and the Fourier transform of the shape function is overlaid around every reciprocal lattice point. Therefore, the local symmetry can be observed in the intensity distributions around Bragg peaks.[21,49,77]

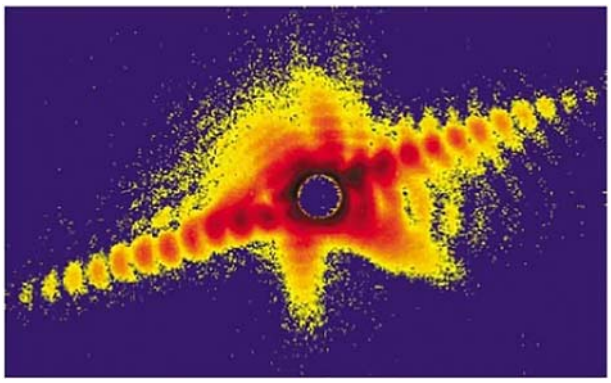

Fig. 6 CXD pattern at Au (11-1) Bragg peak. Reproduced from, Robinson, I. K.; Vartanyants, I. A.; Williams, G. J.; Pfeifer, M. A.; Pitney, J. A. Reconstruction of the Shapes of Gold Nanocrystals Using Coherent X-Ray Diffraction. *Phys. Rev. Lett.* **2001**, *87*(19), 195505, with permission from *AMER PHYSICAL SOC*.

Fig. 7 shows the calculated three-dimensional CXD patterns depending on the shape and the orientation of ideal crystals.[61] The direction of fringes is related to facets parallel to each other and the spacing of fringes reflects the dimension of the crystal along the corresponding direction.

When the crystal is strained, atoms in the crystal deviate from their ideal lattice points. The density distribution of the strained crystal can be rewritten as

$$\rho(\mathbf{r}) = s(r)\sum_{R}\delta(\mathbf{r}-\mathbf{R}-\mathbf{u}(\mathbf{r}))$$

where $\mathbf{u}(\mathbf{r})$ represents the displacement of atoms inside the crystal. Thus, the amplitude can be expressed by

$$A(\mathbf{q}) = \int \rho(\mathbf{r}) e^{i\mathbf{q}\cdot\mathbf{r}} e^{i\mathbf{q}\cdot\mathbf{u}(\mathbf{r})} d\mathbf{r}$$

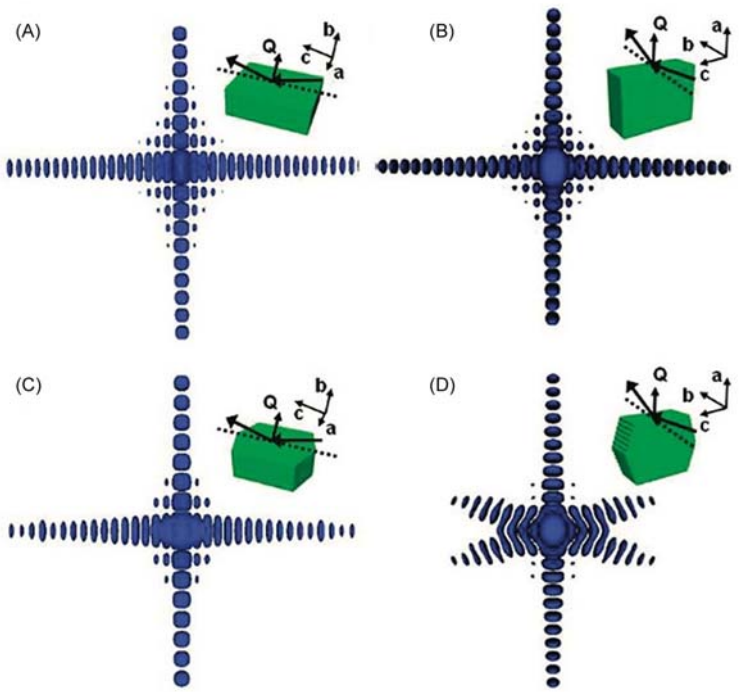

Fig. 7 Calculated three-dimensional CXD patterns depending on the orientation of an object. A rectangular parallelepiped with (A) the **b**-axis parallel to wavevector transfer **Q** and (B) the **a**-axis parallel to **Q.** A hexagonal parallelepiped with (C) the **b**-axis parallel to **Q** and (D) the **a**-axis parallel to **Q**. Reproduced from, Cha, W.; Song, S.; Jeong, N. C.; Harder, R.; Yoon, K. B.; Robinson, I. K.; Kim, H. Exploration of Crystal Strains Using Coherent X-Ray Diffraction. *New J. Phys.* **2010**, *12*(3), 035022, with permission from *IOP PUBLISHING LTD*.

and the deviation from local symmetry is observed in the CXD pattern of the vicinity of Bragg peaks.[21,49,77]

Fig. 8 shows simulated CXD patterns (lower panel) for a rectangular parallelepiped crystal with different strain states represented by parabolic phase distributions (upper panel).[61] The ideal case retains the local symmetry in the CXD pattern, whereas the introduced parabolic phase distribution in the crystal induces asymmetric CXD patterns. The latter distorts even the central Bragg peak. Therefore, the strain states of crystals can be identified from CXD patterns.

Fig. 9 displays CXD patterns measured around the (11-1) Bragg peak of a Au microcrystal.[21] The strongest flare is close to the direction normal to the substrate, which is the same as the (111) direction of the crystal. This intensity enhancement along the direction of the crystal facets is well-known and is the origin of crystal truncation rods. The fringe spacing is related to the distance between parallel facets, i.e., the crystal size, with a relationship of $2\pi/\Delta q_{\text{fringe}}$. Therefore, the general shape and size of a crystal can be estimated before reconstructing a three-dimensional image in real space.

Fig. 10 shows two-dimensional slices through a three-dimensional reconstructed electron density at the distance (z) from the center ($z = 0$) image of the Au nanocrystal shown in Fig. 9.[20] Iterative calculations with error reduction and hybrid input-output algorithms enabled the reconstruction of a three-dimensional image even though randomly selected phase values were used as a starting point. As a result, the three-dimensional images have higher contrast than the two-dimensional projected image reported in the previous work.[49]

10.06.2.2.1 Resolution

The highest atomic resolution imaging has been achieved typically using scanning force microscopy and transmission electron microscopy. However, these techniques require special sample treatment processes for the measurements and are not suitable for mapping the internal structure of whole nanocrystals in three-dimensions. As CDI is a lensless imaging technique, the achievable resolution is not limited by optics. In principle, the wavelength of the X-rays is the only variable determining the image resolution. However, atomic resolution has not yet been achieved with CDI. In practice, the resolution is determined by the scattering angle at which the diffraction data becomes unusable due to poor signal to noise ratio. Therefore nanomaterials with higher scattering cross-sections can be imaged with higher resolution using the same experimental conditions. The typical spatial resolution of three-dimensional images from BCDI measurement is about 10 nm along a preferred direction. Up to date, the best-reported resolution for three-dimensional BCDI is 4 nm.[78] This limited resolution is due to low coherent X-ray flux. One can expect an improvement in resolution with the higher coherent flux from next generation X-ray sources.

10.06.2.2.2 Sensitivity to lattice displacement

In the CXD pattern, the asymmetric intensity distribution can be decomposed into symmetric and asymmetric parts. The former is related to the average electron density, and the latter is associated with the local displacement of atoms from the ideal lattice. Fig. 11 shows a strained region as a block displaced from the ideal crystal structure by a vector $\mathbf{u}(\mathbf{r})$. In the figure, the wave vectors reflected from the strained part and the regular area of the material are illustrated. Because of the path length difference between the waves, the phase of the scattering from the strained part is shifted relative to the other. The total phase shift, φ, is given by.

$\varphi = \mathbf{k}_f \cdot \mathbf{u} - \mathbf{k}_i \cdot \mathbf{u} = \mathbf{Q} \cdot \mathbf{u}$.where $\mathbf{k}_i$ and $\mathbf{k}_f$ are the incoming and outgoing wave vectors, respectively, and $\mathbf{Q}$ is total wavevector transfer. When $\mathbf{Q}$ is set to a Bragg condition, all the unit cell corners scatter in phase if the crystal does not have any deformation. Therefore, the deformed region in the final image has a complex density with the same amplitude as the rest of the crystal but different phases, φ $(\mathbf{r})$. Hence, a three-dimensional real space map of the internal lattice displacement field projected onto $\mathbf{Q}$

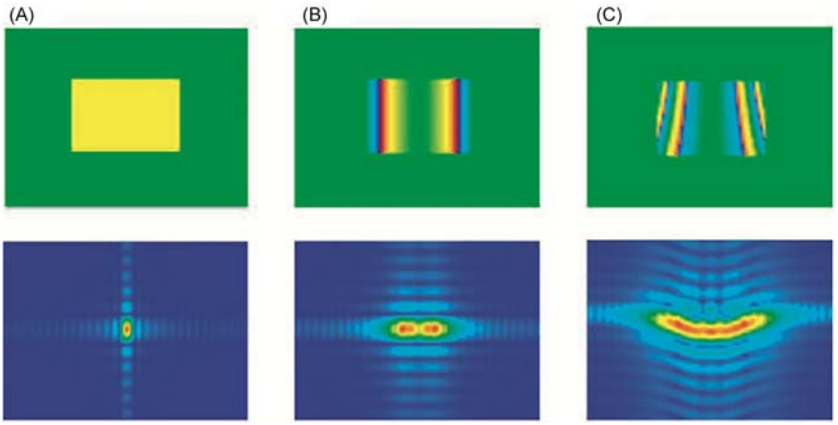

Fig. 8 Simulated rectangular parallelepiped objects with internal phase structure (upper panel) and corresponding calculated CXD patterns (lower panel). (A) Unstrained, (B) with parabolic phase with a single wrap of the phase, and (C) with parabolic phase two full wraps of phase between the center and each end. Reproduced from, Cha, W.; Song, S.; Jeong, N. C.; Harder, R.; Yoon, K. B.; Robinson, I. K.; Kim, H. Exploration of Crystal Strains Using Coherent X-Ray Diffraction. *New J. Phys.* **2010**, *12*(3), 035022, with permission from IOP PUBLISHING LTD.

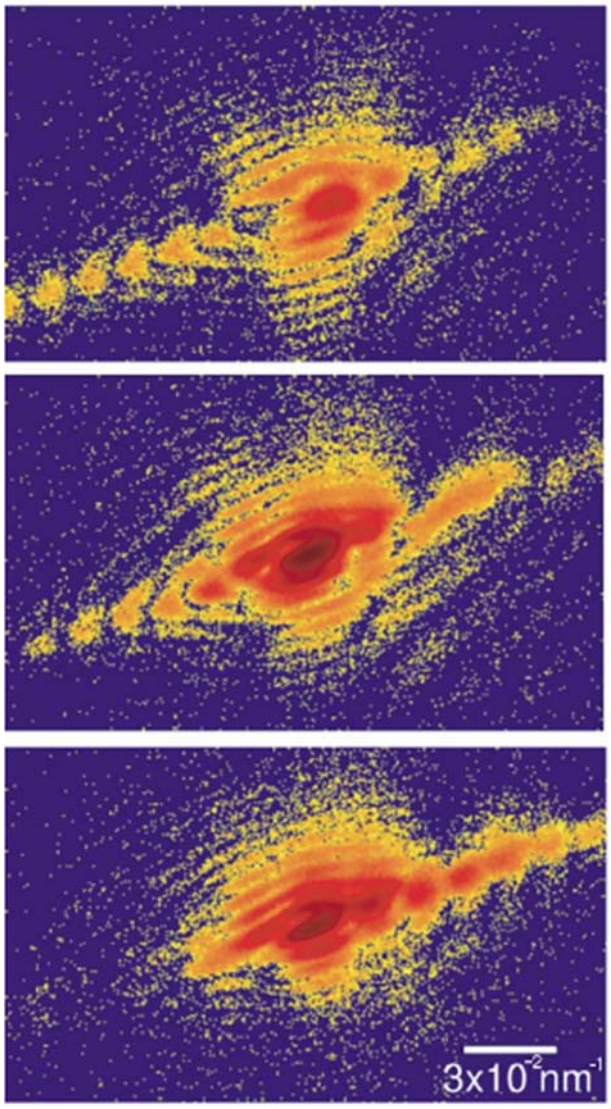

Fig. 9 Two-dimensional slices through the three-dimensional CXD pattern from a Au nanocrystal at (11-1) Bragg peak. Reproduced from, Williams, G. J.; Pfeifer, M. A.; Vartanyants, I. A.; Robinson, I. K. Three-Dimensional Imaging of Microstructure in Au Nanocrystals. *Phys. Rev. Lett.* **2003**, *90*(17), 175501. with permission from AMER PHYSICAL SOC.

can be obtained at each position. A 2π phase shift indicates a change of one lattice plane. The sensitivity to lattice distortion is a few picometers or better.[19]

Pfeifer et al.[47] demonstrated that the lattice displacement distribution in an individual Pb nanocrystal could be obtained from retrieved phases. Three-dimensional CXD patterns around the (111) Bragg peak for Pb were successfully inverted to obtain a three-dimensional image in real space, as shown in Fig. 12. The distribution of electron density shows the shape of the crystal and the phases are interpreted as a lattice distortion projected along the wavevector transfer **Q**. The electron density is constant without defects. A local deformation is sensitively observed in the phase distribution. In this case, a significant phase deviation is observed with a maximum of 1.1 rad at the bottom of the crystal, indicating a maximum displacement of $(1.1/2\pi)$ times the (111) lattice spacing, i.e., 0.5 Å. The deformation field distribution was attributed to contact forces at the interface with the substrate.[19,47]

The refractive index of a material should be considered when retrieving phases. The refractive index of a material in the X-ray regime is

$$n = 1 - \delta + i\beta$$

where δ is of order $\sim 10^{-6}$ and the imaginary part β is even smaller than δ so that the refraction effect was not considered in the CXD imaging. However, it can be important when the sample is optically thick. The refractive index in the X-ray regime is smaller in materials than in vacuum, so X-rays have a longer wavelength when they travel through a material than through vacuum. This leads

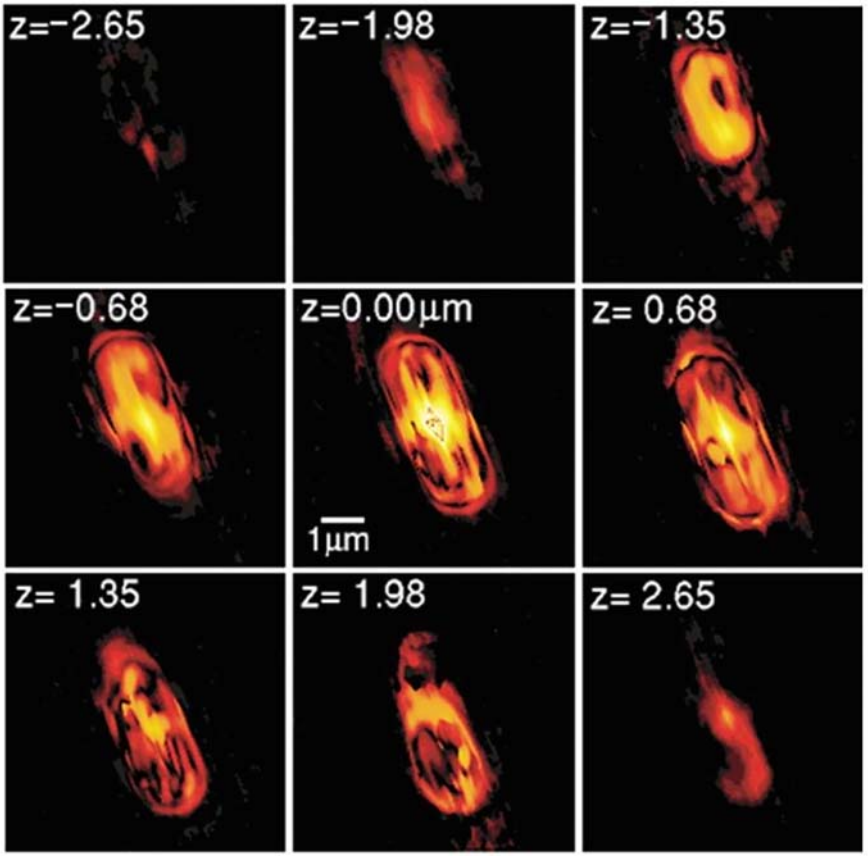

Fig. 10 Two-dimensional slices of three-dimensional reconstructed density at the distance (z in micrometer) from the center (z = 0). Reproduced from, Williams, G. J.; Pfeifer, M. A.; Vartanyants, I. A.; Robinson, I. K. Three-Dimensional Imaging of Microstructure in Au Nanocrystals. *Phys. Rev. Lett.* **2003**, *90*(17), 175,501. with permission from AMER PHYSICAL SOC.

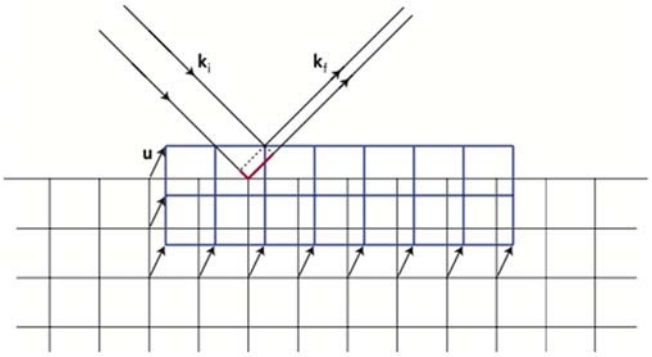

Fig. 11 Phase shift originated from the distorted region (in blue) by assuming a displacement **u** from the ideal lattice. (Ref. [19]) See the text for the detail explanation of the geometry. Reproduced from Robinson, I.; Harder, R. Coherent X-Ray Diffraction Imaging of Strain at the Nanoscale. *Nat. Mater.* **2009** *8*(4), 291–298, with permission from NATURE RESEARCH.

to a phase shift proportional to the optical path length of the X-rays through the material. A 750 nm-sized Pb crystal is large enough to show a significant phase shift due to this refractive index effect. Fig. 13A shows the calculated phase shift due to refraction based on the three-dimensional reconstruction shown in Fig. 12. The maximum phase shift reaches 0.76 rad, a significant fraction of the experimentally observed value of − 1.4 rad due to lattice displacements in the Pb crystal. Once phase shift due to the refraction effect are taken into account, more distinct lattice distortion in the Pb crystal is observed near the surface, as shown in Fig. 13(bottom).[19,26,79]

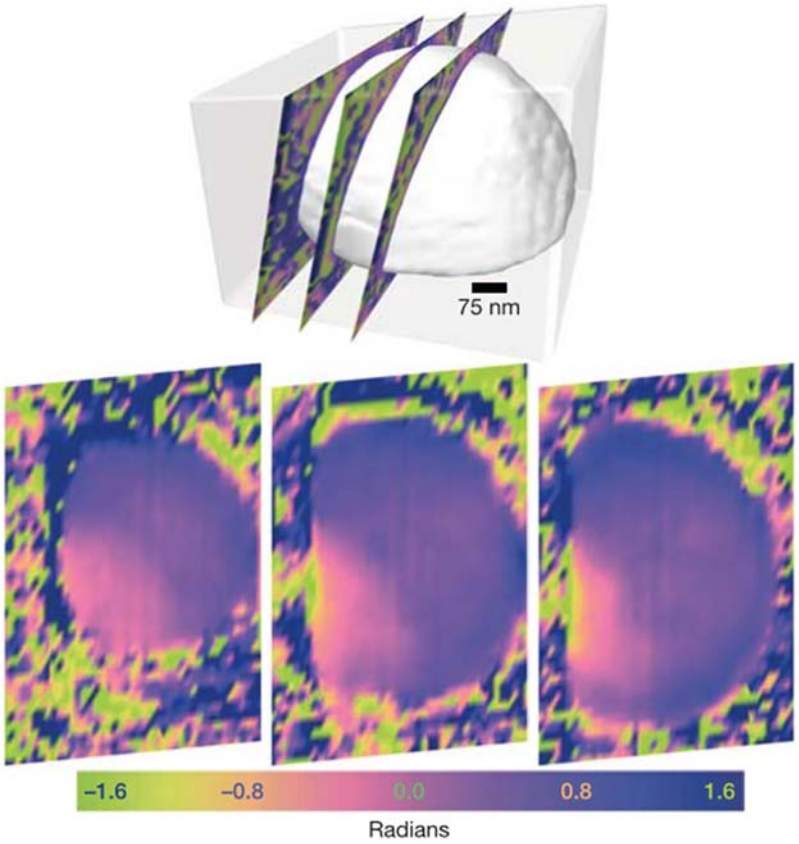

Fig. 12 Three-dimensional map of phases inside a Pb nanocrystal. It can be interpreted as a lattice deformation distribution. Reproduced from, Pfeifer, M. A.; Williams, G. J.; Vartanyants, I. A.; Harder, R.; Robinson, I. K. Three-Dimensional Mapping of a Deformation Field inside a Nanocrystal. *Nature* **2006**, *442*(7098), 63–66, with permission from NATURE RESEARCH.

10.06.2.2.3 Strain tensor

BCDI using a single Bragg peak measurement reveals the lattice displacement in the direction of measured wavevector transfer. Therefore, BCDI using multiple Bragg peaks from the same crystal can provide a complete three-dimensional lattice displacement field distribution, which can be turned into the full strain tensor by differentiation. BCDI measurements of three or more Bragg peaks, with linearly independent Miller indices, are required to reconstruct the full three-dimensional strain tensor for the crystal.[59,80] Newton et al.[59] demonstrated this approach on a rod-shaped ZnO microcrystal synthesized on a Si substrate by chemical vapor deposition. Three-dimensional CXD patterns on multiple Bragg peaks, such as (011), (0-11), (101), (-101), (-111), and (1-11), were collected. Each diffraction pattern was inverted to obtain three-dimensional images in real space. They are aligned with each other and then combined to construct the three-dimensional lattice displacement field distribution. All three orthogonal components of the lattice displacement vector calculate the full component of the strain tensor shown in **Fig. 14**.

Typically, BCDI measurements make use of a CXD pattern from a single nanocrystal, which satisfies the Bragg condition, from among several arbitrarily oriented nanocrystals. Orienting the sample and positioning the detector for the measurement of other Bragg peaks requires good knowledge of the crystallographic orientation of the sample. Combining Laue diffraction with BCDI eliminates this requirement. A polychromatic X-ray beam is used to collect Laue patterns from the sample, which can then be used to calculate its crystallographic orientation. Once the orientation is determined, one can orient the sample and the detector for the desired Bragg condition and then record CXD patterns on the sample with a monochromatic X-ray beam that follows the same path as the polychromatic beam.[81] This approach can be used to study adjunct grains in the nanocrystals at a grain boundary.

10.06.2.3 In-situ/operando capabilities

Watari et al.[51] demonstrated the possibility of in-situ BCDI on Au nanocrystals. They measured CXD patterns on a single Au nanocrystal at the (1–11) Bragg peak. During the measurement, gas-phase thiol was dosed to form a self-assembled monolayer (SAM). They found that physical contact between the Au nanocrystal surface and a thiol monolayer caused a small strain at the crystal surface. To resolve very small surface strain changes, they adopted difference Fourier map (DFM) analysis, which is a method widely used in protein crystallography. From the DFM results of the images before and after thiol dosing, they observed a facet dependence

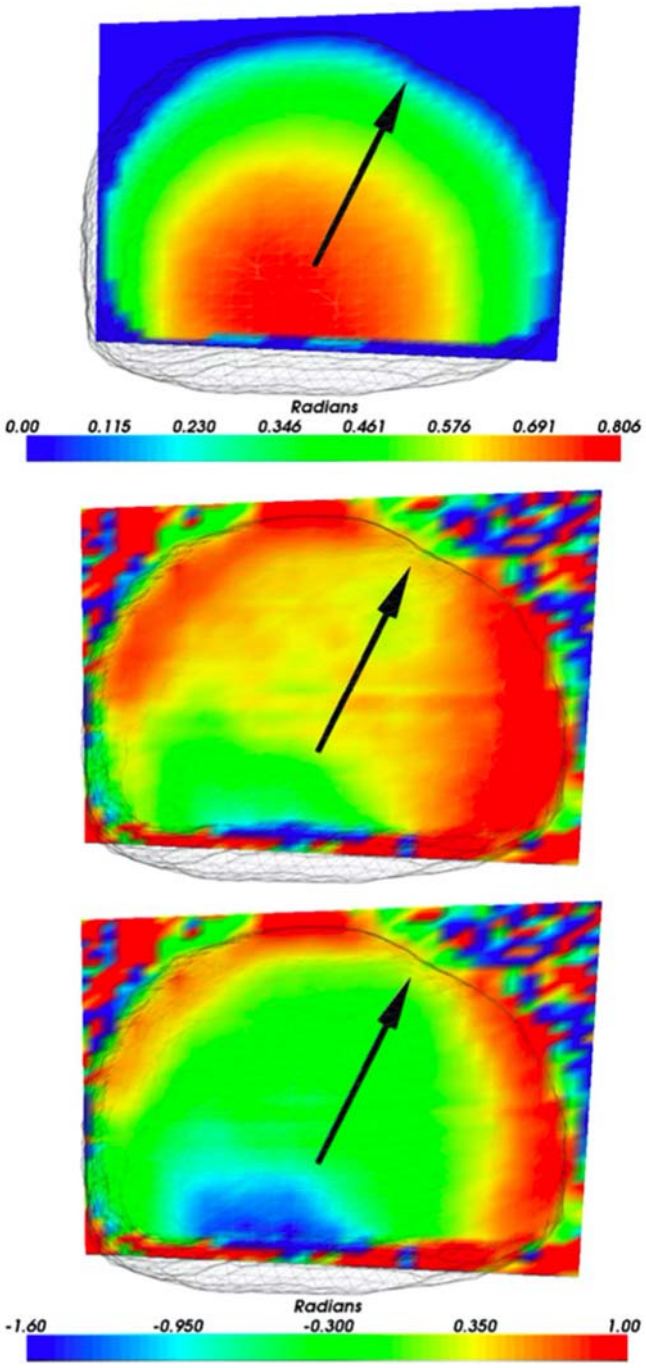

Fig. 13 Phase map before and after correction for refraction. (Top) Calculated phase due to refraction, (Middle) phase distribution before the correction, and (Bottom) phase distribution after the correction. Reproduced from, Harder, R.; Pfeifer, M. A.; Williams, G. J.; Vartaniants, I. A.; Robinson, I. K. Orientation Variation of Surface Strain. *Phys. Rev. B* **2007**, *76*(11), 115425, with permission from AMER PHYSICAL SOC.

of the surface strain induced by the thiol molecule. The facet dependence of the surface strain was compared to simulations using finite element analysis (FEA). From the FEA results, they found compressive stresses on the flat surface and tensile stresses on the curved surface of the nanocrystal. For the nanocrystal measured, flat facets correspond to the Au {111} surface families, and curved facets correspond to another crystallographic orientation. Overall, this study indicates that the local strain field can be measured for nanocrystals in-situ.

A practical scientific application of in-situ BCDI was reported by Cha et al.[62] They observed temperature-dependent internal deformation of ZSM-5 zeolite crystals. Fig. 15A shows CXD patterns for a ZSM-5 microcrystal collected at room temperature. The data shows an Airy ring pattern around a (200) Bragg peak and facet-dependent directional fringe patterns. Surprisingly,

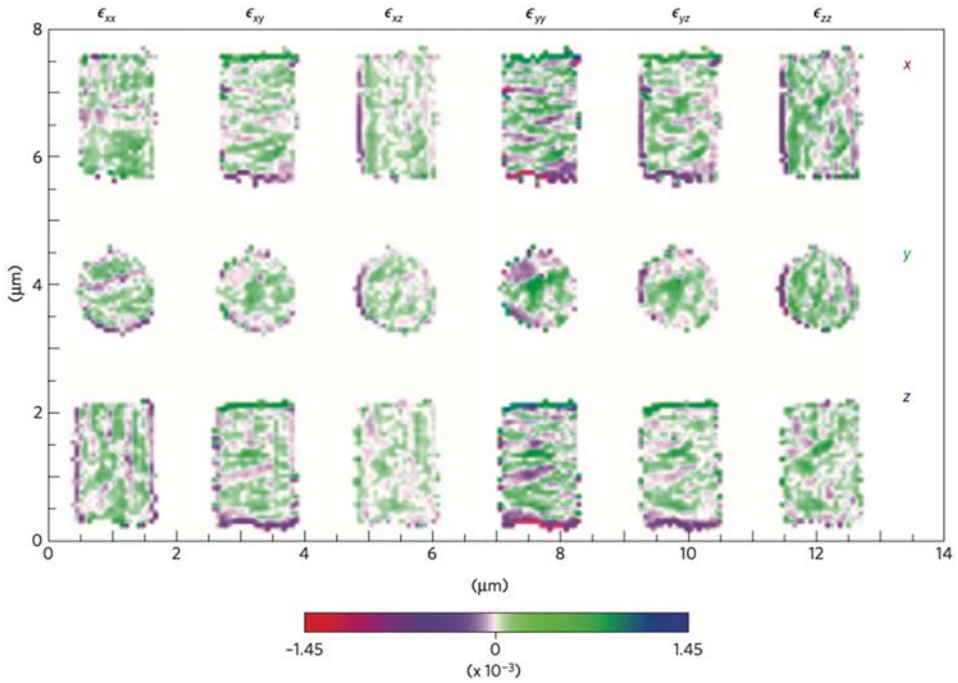

Fig. 14 Two-dimensional slices of three-dimensional strain tensor components of a ZnO nanorod measured on multiple Bragg peaks. Reproduced from, Newton, M. C.; Leake, S. J.; Harder, R.; Robinson, I. K. Three-Dimensional Imaging of Strain in a Single ZnO Nanorod. *Nat. Mater.* **2010**, *9*(2), 120–124, with permission from NATURE RESEARCH.

this diffraction pattern was distorted at 200 °C. The direction of fringe patterns was changed and even the center of the Bragg peak became a triangular shape, as displayed in Fig. 15B. This change is not due to either the shape of the sample or the crystallographic axes of the crystal. In addition, it is not seen in the diffraction patterns at 90° rotation shown in the insets of Fig. 15A and B. Fig. 15C shows the 2D slices through the center of the retrieved 3D images as a function of measurement temperature depending on calcination conditions. The triangular deformation appears in ZSM-5 microcrystals calcined at 450 °C for 12 h or less. However, ZSM-5 microcrystals calcined at 550 °C do not show such changes. This was explained using a core-shell model with different thermal expansion behaviors originated from the organic residue at the core of the ZSM-5. An organic template is used for the synthesis and removed by calcination at high temperatures. In this study, they found that ZSM-5 crystals calcined at 450 °C possess a minute amount of organic residue in the core of the crystal, independent of calcination time. This residue leads to positive thermal expansion, whereas the organic free shell of the crystal shows intrinsic negative thermal expansion.

Another unique finding from BCDI is the dislocation inside grains in a film. Yau et al.[82] imaged grain growth in Au thin films using BCDI. Because of texture in the film, an isolated CXD pattern was obtained. The samples were 200 nm thick Au polycrystalline films on substrates, which had been heated to 400 °C. The Au grain in the pristine state showed high surface curvature and a dislocation site at the corner indicated by a white arrow in Fig. 16A. Lower Bragg electron density is observed at the dislocation site. On increasing the temperature, the grain grows and faceting of the grain occurred. The important feature was non-uniform growth. In the vicinity of the dislocation site, there was more rapid growth. The authors suggested that the correlation between rapid grain growth and the dislocation implies grain boundary movement to dislocation within the grain. To display changes of the grains during the growth process more clearly, they used cross-correlation matrix calculation between displacement fields for different times. Fig. 16B shows the correlation matrix of the displacement field from the reconstructed image during growth. From this result, they deduced that significant growth occurred at 400 °C, which is close to one-half of the melting point for Au. At this temperature, the annihilation of the dislocation was observed. On maintaining the high temperature, the grain stagnated and kept its internal displacement field. They also imaged the coherent twin boundary (CTB) dynamics during the growth. Because twin domains have different crystallographic orientations, a CXD measurement at a fixed Bragg peak does not show both of the domains. Therefore, both twin domains can't be simultaneously imaged by BCDI.[48] For this reason, the different stacking order of the CTB appeared as missing electron density. Fig. 16C shows the imaging results for the CTB in the grain. They tracked the twin boundary of Au grains on B-doped diamond substrates that were not pre-annealed. At room temperature, pristine grains were separated with seven or eight segments. With increasing temperature, some sections became larger and sharper, whereas the others were smaller. These intragrain dynamics were slightly different at each temperature step.

Cherukara et al.[83] also employed BCDI to image single grains and visualize the strain state of an individual Cu grain in a free-standing polycrystalline Cu thin film following tensile loading. The Cu thin film was deposited on a MgO substrate and placed on a tension rig mounted on the center of a diffractometer after the film was removed from the substrate. CXD patterns were collected at

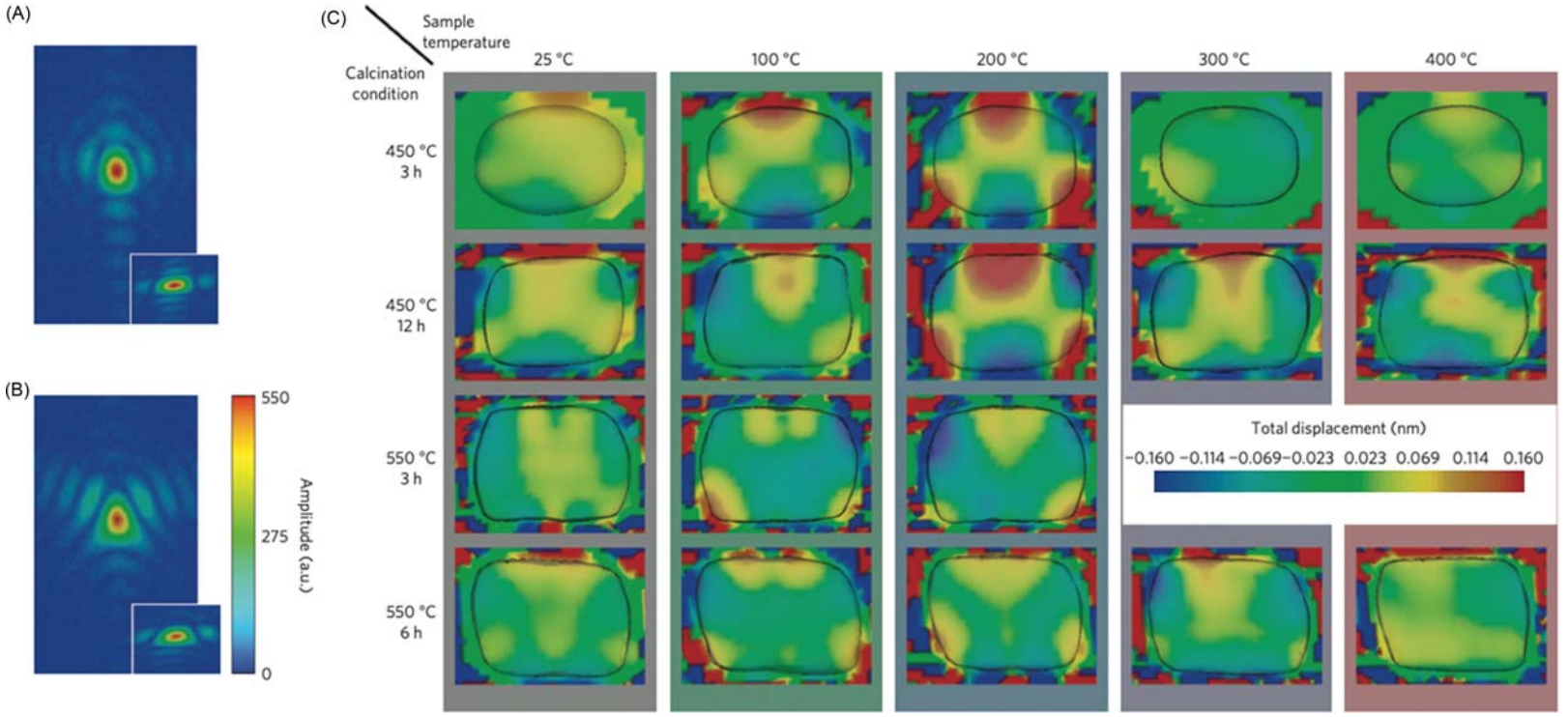

Fig. 15 CXD patterns and internal displacement distribution for a ZSM-5 zeolite crystal. (A) A typical CXD pattern of an unstrained ZSM-5 zeolite crystal measured at room temperature, (B) A triangular CXD pattern on a ZSM-5 zeolite crystal at 200 °C. (C) The calcination temperature and time dependence shown in 2D slices through the 3D reconstructions as a function of temperature. Reproduced from, Cha, W.; Jeong, N. C.; Song, S.; Park, H.; Thanh Pham, T. C.; Harder, R.; Lim, B.; Xiong, G.; Ahn, D.; McNulty, I.; Kim, J.; Yoon, K. B.; Robinson, I. K.; Kim, H. Core–Shell Strain Structure of Zeolite Microcrystals. *Nat. Mater.* **2013**, *12*(8), 729–734, with permission from NATURE RESEARCH.

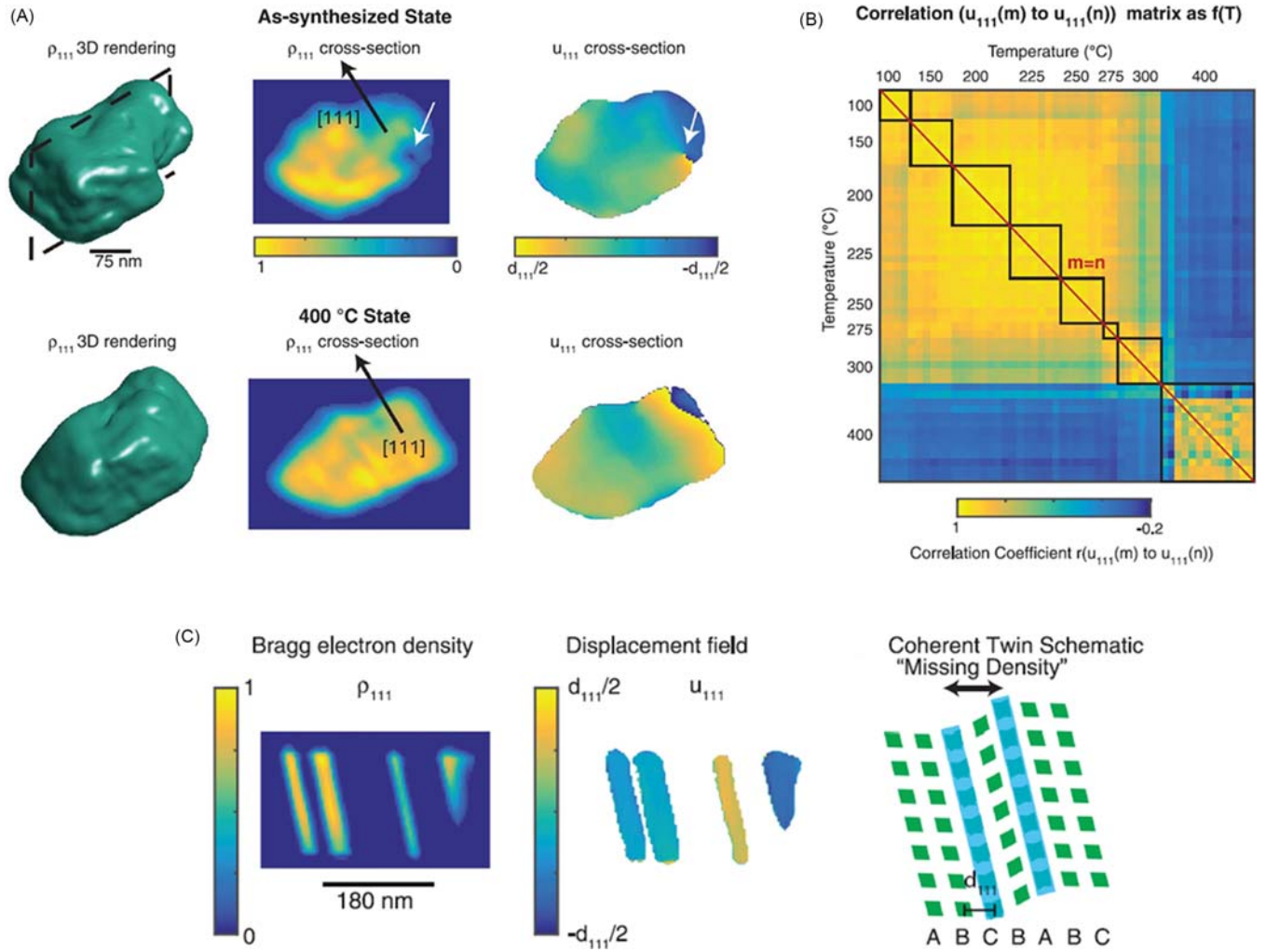

Fig. 16 Grain growth and grain boundary dynamics during heating of Au polycrystalline film. (A) 3D rendering, cross-section of Au electron density, and displacement cross-section of Au grain at as-synthesized state (first row) and at 400 °C (second row), (B) Correlation matrix of the displacement as a function of temperatures, (C) A. Bragg electron density, B. displacement field from 2D slice through coherent twin boundaries in a Au grain and C. schematic diagram explaining a missing density at the twin boundary. Reproduced from, Yau, A.; Cha, W.; Kanan, M. W.; Stephenson, G. B.; Ulvestad, A. Bragg Coherent Diffractive Imaging of Single-Grain Defect Dynamics in Polycrystalline Films. *Science* **2017**, *356*(6339), 739–742, with permission from AMER ASSOC ADVANCEMENT SCIENCE.

the Cu (111) Bragg peak on an isolated Cu grain until distorted patterns appeared due to the applied external load on the sample. Fig. 17 displays reconstructed images of the Cu grain. A cylindrical region of low Bragg electron density is observed as marked with a white circle in Fig. 17A. The corresponding lattice displacement map in Fig. 17B shows a circular shape of empty region with negative maximum value of the displacement next to the positive maximum, which is a signature of a defect. The strain distribution projected along the wave vector transfer exhibits a discontinuity along a plane normal to the axis of the defect, as seen in Fig. 17C. To understand the origin of the observation, they carried out molecular dynamics (MD) simulations using an atomistic model. Low Bragg electron density and variation in lattice displacement are caused by a screw dislocation formed inside the grain. Interestingly, this screw dislocation was not split into partials even though splitting of the screw dislocation is energetically favorable. They also confirmed that interaction between grains in the thin film prevents the dissociation of the dislocation into partials.

Many efforts have been made to improve the in-situ and operando capabilities of BCDI. Cha et al.[84] demonstrated a new approach to reconstruct a three-dimensional image of Bragg electron density and lattice displacement field distribution for a nanocrystal using CXD patterns recorded using an X-ray energy scan. This method eliminates the need to rotate the sample the 3D imaging. Hence, this would enable a new nanoscale strain imaging on nanomaterials in realistic environments. This method also prevents vibration caused by motorized stages so that the BCDI can be used for three-dimensional strain imaging during mechanical deformation. Simultaneous measurements at two Bragg conditions were demonstrated by Lauraux et al.[85] They oriented a sample and positioned two detectors to capture CXD patterns around two Bragg peaks simultaneously. Because BCDI with a single Bragg peak reveals the lattice displacements projected along with a wave vector transfer, dislocations are often invisible when the Burger's vector of the dislocation is perpendicular to the wavevector transfer. Simultaneous measurements at multiple Bragg conditions bring advantages for in-situ and operando BCDI experiments revealing lattice distortions along different wavevector transfer directions.

10.06.3 BCDI studies of catalytic materials

Many modern products and chemical processes rely upon catalysts. Recently, the development and design of catalysts have been highlighted not only for the efficient production of chemicals but also for environmentally friendly production. Elucidating the catalytic process at a molecular scale is one of the most important topics in inorganic chemistry. X-ray-based techniques have been widely used for studying catalysts to understand surface structure and chemical state. Surface-sensitive characterization methods include surface X-ray diffraction, crystal truncation rod measurements, and X-ray photoelectron spectroscopy.

Nanoparticles are widely used as catalysts because of their high surface area to volume ratios. The three-dimensional morphology as well as the structural response of nanoscale catalysts is important since it determines catalytic activity and efficiency because the shape of the catalysts is highly related to surface atomic structure. For this reason, in-situ nanoscale imaging of the catalysts has been achieved by many techniques during catalytic reactions over the past decade. For example, Altantzis[86] et al. studied facet evolution during the oxidation/reduction process of the Pt nanocrystal using in-situ electron tomography. They found an increase of high index facets and a decrease of the low index facet such as {100} or {111} in an oxidizing atmosphere.

BCDI has emerged as a powerful platform for in-situ/operando measurements on catalysts, energy-storage materials, nanocrystals in electronics, and photonics. The strengths of CDI for in-situ/operando studies are that vacuum conditions are not needed and the sample requirements are less demanding than those for electron microscopy. Various measurement conditions can be changed such as temperature, gas atmosphere, electric bias, high-pressure, and liquid flow. In this section, we show BCDI studies of catalysts focusing on different scientific questions.

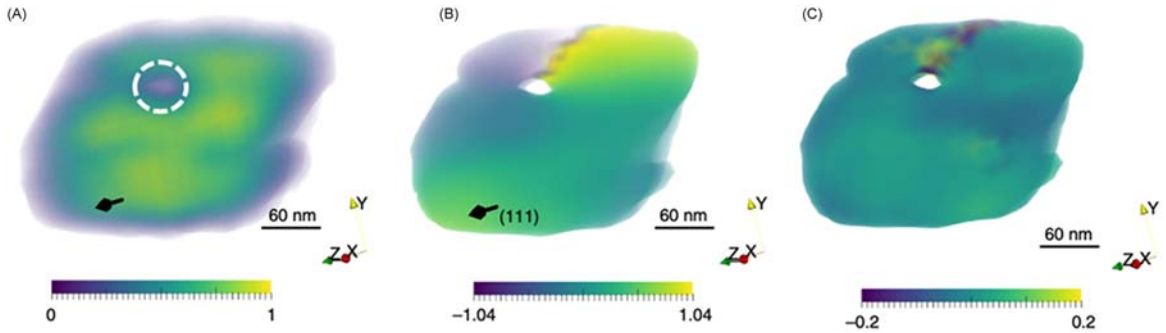

Fig. 17 Reconstructed image of a Cu grain. (A) Electron density map showing a cylindrical region of low amplitude in a white circle. Color indicates amplitude., (B) volume rendering of displacement, and (C) 3D rendering of strain in the grain projected along the (111) direction. Reproduced from, Cherukara, M. J.; Pokharel, R.; O'Leary, T. S.; Baldwin, J. K.; Maxey, E.; Cha, W.; Maser, J.; Harder, R. J.; Fensin, S. J.; Sandberg, R. L. Three-Dimensional X-Ray Diffraction Imaging of Dislocations in Polycrystalline Metals under Tensile Loading. *Nat. Commun.* **2018**, *9*(1), 3776, with permission from NATURE RESEARCH.

10.06.3.1 Sample environments for in-situ/operando studies

In-situ catalysis studies using BCDI have been performed in gas and liquid flow. Fig. 18 shows examples of sample cells for liquid and gas flow. In Fig. 18A, a schematic of the in-situ BCDI experiment using a liquid cell is shown for a catalytic process.[87] This in-situ sample cell for BCDI experiments has advantages compared to the in-situ TEM cell[88] shown in Fig. 18B. Because vacuum conditions are required for the electron beam, the in-situ TEM cell must have an extremely compact size that can be a major difficulty for the investigation of real working systems. Fig. 18C shows a typical gas cell for in-situ BCDI.[89] Since most of the catalytic reactions in the gas phase occur at high temperatures (>400 °C), these cells consist of a heater stage, cooling system, and gas flow systems. By attaching an external mass spectrometry system[52] to the reactor, gas effluent can be simultaneously analyzed to determine the conversion ratio of the catalytic reaction. Fig. 18D is a schematic process for the in-situ BCDI experiment with a gas environment. The catalytic process at each gas stage is built using an external gas flow control system. Kim. et al.[54] studied catalysis using a Pt nanoparticle in the gas cell. In their study, H_2 (1% balanced in N_2) was used to clean Pt surfaces. 20% oxygen concentration balanced in N_2 flows for the adsorption of the oxygen atom. The adsorbed oxygen atoms reacted with CH_4 during the third stage of gas flow. By using discrete gas flows, every reaction process can be measured.

10.06.3.2 Active site determination using BCDI

To date, a number of studies using BCDI have been highlighted as nanoscale imaging of catalytic phenomena. In the studies of catalytic materials, identification of the active sites is fundamental to improve catalytic efficiency and to elucidate the relationship of the size/morphology of the catalysts.[54] Early examples of BCDI for resolving an active site during catalytic reaction include the study of Ulvestad et al.[87] Strain development was observed during ascorbic acid decomposition reaction on an Au nanoparticle. They used an in-situ liquid cell for reactant flow over the Au nanoparticles, as shown in Fig. 18A. Using a Mylar film over the liquid flow systems, they measured CXD patterns on Au nanoparticles successively for several hours. Fig. 19A shows the displacement field

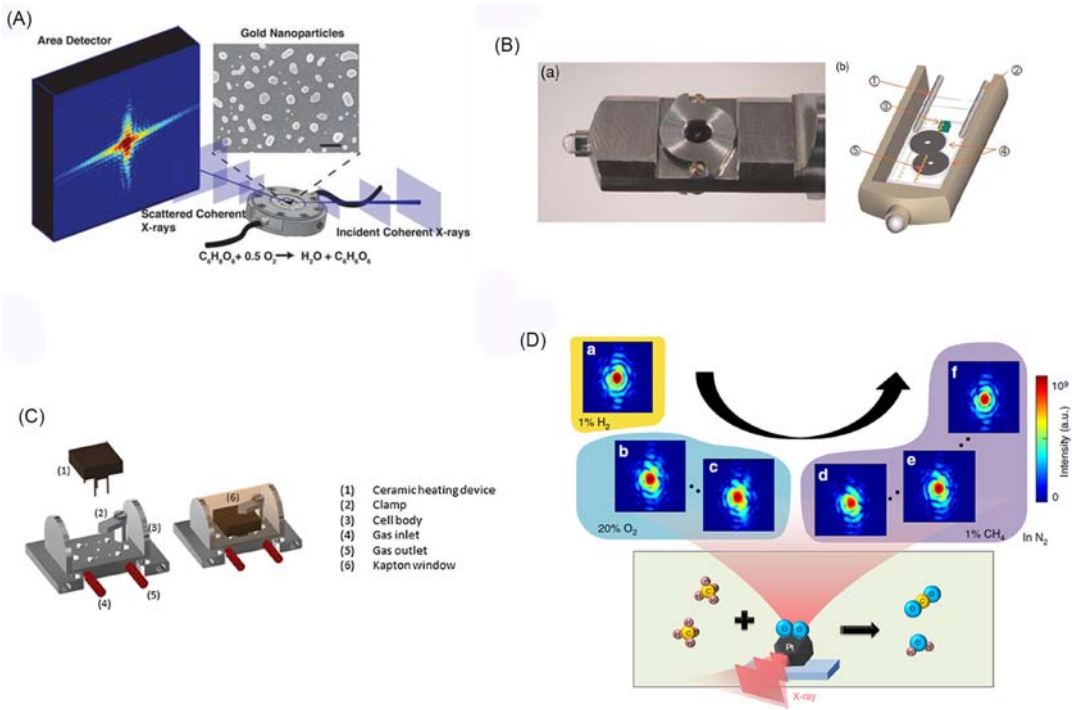

Fig. 18 In-situ experiment setup for BCDI and TEM. (A) Schematic of an in-situ BCDI study under liquid flow, (B) in-situ sample cell for TEM, (C) a sample cell with heating stage with gas flow and (D) schematic of an in-situ BCDI experiment with gas flow. Reproduced from Ulvestad, A.; Sasikumar, K.; Kim, J. W.; Harder, R.; Maxey, E.; Clark, J. N.; Narayanan, B.; Deshmukh, S. A.; Ferrier, N.; Mulvaney, P.; Sankaranarayanan, S. K. R. S.; Shpyrko, O. G. In Situ 3D Imaging of Catalysis Induced Strain in Gold Nanoparticles. *J. Phys. Chem. Lett.* **2016**, *7*(15), 3008–3013, with permission from AMER CHEMICAL SOC. Reproduced from Yaguchi, T.; Suzuki, M.; Watabe, A.; Nagakubo, Y.; Ueda, K.; Kamino, T. Development of a High Temperature-Atmospheric Pressure Environmental Cell for High-Resolution TEM. *J. Electron Microscopy* **2011**, *60*(3), 217–225,with permission from OXFORD UNIV PRESS. Reproduced from Rochet, A.; Suzana, A. F.; Passos, A. R.; Kalile, T.; Berenguer, F.; Santilli, C. V.; Pulcinelli, S. H.; Meneau, F. In Situ Reactor to Image Catalysts at Work in Three-Dimensions by Bragg Coherent X-Ray Diffraction. *Catal. Today* **2019**, *336*, 169–173, with permission from ELSEVIER. Reproduced from Kim, D.; Chung, M.; Carnis, J.; Kim, S.; Yun, K.; Kang, J.; Cha, W.; Cherukara, M. J.; Maxey, E.; Harder, R.; Sasikumar, K.; K. R. S. Sankaranarayanan, S.; Zozulya, A.; Sprung, M.; Riu, D.; Kim, H. Active Site Localization of Methane Oxidation on Pt Nanocrystals. *Nat. Commun.* **2018**, *9*(1), 3422, with permission from NATURE RESEARCH.

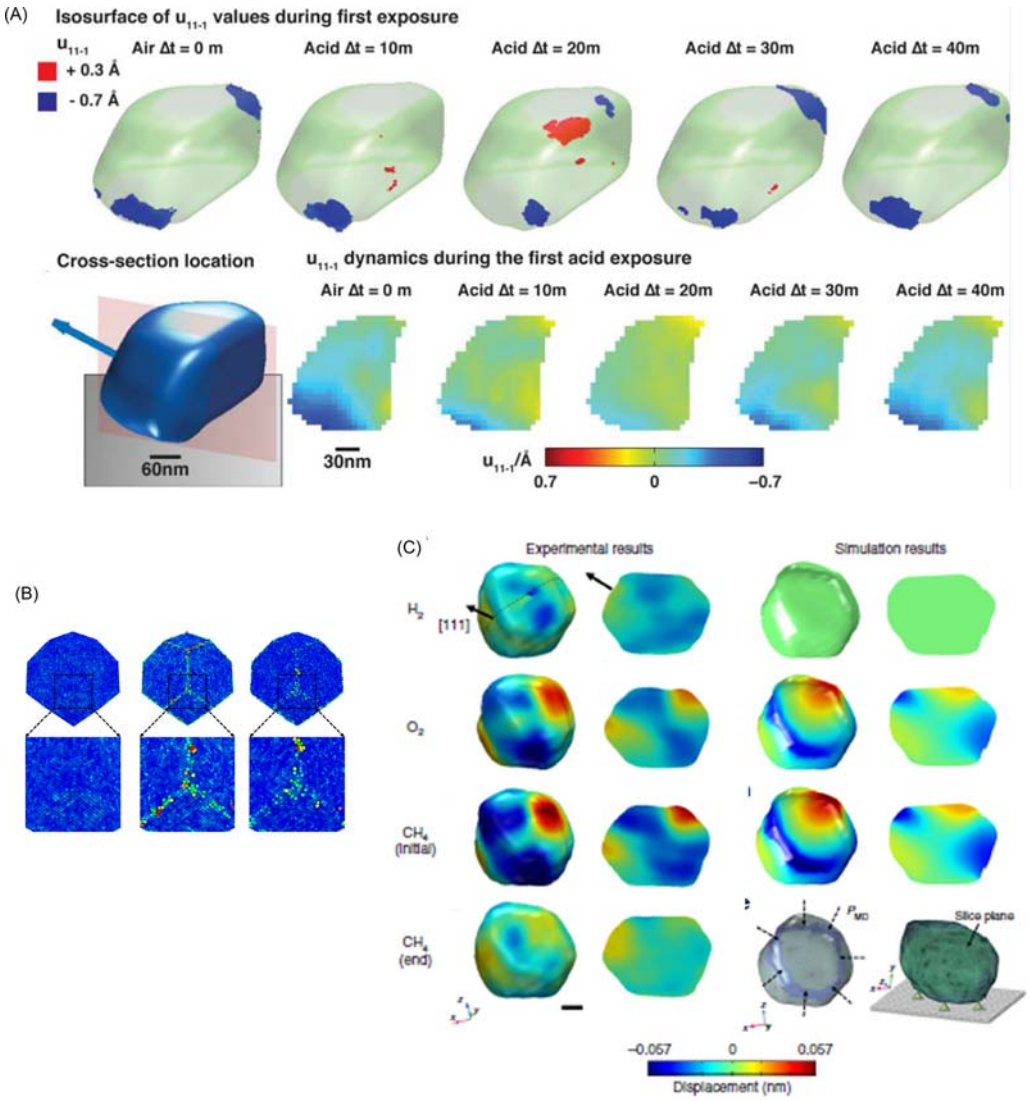

Fig. 19 Active site identification using BCDI for Au and Pt nanocrystal with MD/FEM simulation results. (A) Displacement dynamics in a Au crystal during ascorbic acid exposure, (B) reactive MD simulation of Pt catalytic activity, and (C) displacement distribution by BCDI and FEA depending on catalysis reaction steps. Reproduced from Ulvestad, A.; Sasikumar, K.; Kim, J. W.; Harder, R.; Maxey, E.; Clark, J. N.; Narayanan, B.; Deshmukh, S. A.; Ferrier, N.; Mulvaney, P.; Sankaranarayanan, S. K. R. S.; Shpyrko, O. G. In Situ 3D Imaging of Catalysis Induced Strain in Gold Nanoparticles. *J. Phys. Chem. Lett.* **2016**, *7*(15), 3008–3013, with permission from AMER CHEMICAL SOC. Reproduced from Kim, D.; Chung, M.; Carnis, J.; Kim, S.; Yun, K.; Kang, J.; Cha, W.; Cherukara, M. J.; Maxey, E.; Harder, R.; Sasikumar, K.; K. R. S. Sankaranarayanan, S.; Zozulya, A.; Sprung, M.; Riu, D.; Kim, H. Active Site Localization of Methane Oxidation on Pt Nanocrystals. *Nat. Commun.* **2018**, *9*(1), 3422, with permission from NATURE RESEARCH.

distribution of Au nanoparticles during ascorbic acid flow. In this figure, the highly deformed region in the nanoparticle is highlighted. They found an intense distribution of displacement field at the corner of the nanoparticle as a result of the catalytic reaction. Because of the under-coordination of the near edge atoms, these corner sites act as the preferential site of the catalytic reaction. This observation was investigated by MD simulations using the ReaxFF system and FEA. They verified that nanoparticle edge sites are more catalytically active, and there is more lattice distortion as a result of the absorption of the molecules.

Another study of active site determination during a catalytic reaction was conducted by Kim et. at.[54] They measured CXD patterns on a single truncated octahedral Pt nanoparticle during successive gas flows. Experimental procedures were explained in an earlier section (see Fig. 18D). From the MD simulation shown in Fig. 19B, they found that more O atoms adsorbed at the edges of the nanoparticles than on the surfaces, and compressive forces arise when dissociated O atoms are adsorbed at the Pt edges. The observed increase in compression at the sites is enhanced by CH_4 decomposition. After the catalytic reaction, the strain is released. The adsorption/desorption of dissociated O atoms is favored at low coordination number Pt atoms, in particular, at the edges and corners of the nanoparticle. Using this information, FEA was performed to estimate displacement field changes during each gas stage. Fig. 19C shows the measured displacement field distribution (left) and compares it to that calculated by FEA simulations

(right). From this result, they verify structural deformation at the active site of the Pt catalysts during the oxidation and CH_4 catalysis.

10.06.3.3 Strain and defect evolution during catalysis

Lattice strain and defect dynamics are important aspects of the catalytic process. Because surface strain and defects have a considerable impact on catalytic efficiency, there have been many efforts to measure and control both strain and defects.[90] However, previous studies using traditional measurement techniques, such as powder diffraction, have only focused on the ensemble-averaged quantities because of difficulty measuring the local properties of nanoscale catalysts. BCDI has the advantage of measuring local surface/internal strain and defect dynamics during the catalytic reaction. Kim et al.[55] show that intense strain develops around the defects during a methane oxidation reaction. Absorbed oxygen molecules at particular locations on a Pt nanoparticle induce an intense strain field. This strain is released after the CH_4 oxidation reaction is completed. Strain dynamics related to the defects of the Pt nanoparticle during the catalytic process are consistent with the calculated strain energy shown in **Fig. 20**A. They also found that the Bragg electron density changes at the defects during the catalytic reaction. A loss of the Bragg electron density is observed at the defects where the initially strained part, which turns out to be more catalytically active. The existence of the initial strain field makes a difference in the strain energy during the reaction. However, Pt nanoparticles without initial tensile strain exhibit no loss of the Bragg electron density, which means that dislocations and/or stacking faults are not created. The dislocation/defect dynamics are investigated by the loss of the electron density and strain energy increment over the dislocation cost.

Fernández et al.[57] studied strain evolution in high-index faceted tetrahexahedral Pt nanocrystals during a CO oxidation reaction. They measured CXD patterns at the Pt (002) Bragg peak under various gas flows with different gas ratios. They observed the strain evolution and tilt of the Pt lattice for each gas flow. The oxidation of Pt nanoparticles induces a maximum tensile strain of 0.09% along the out-of-plane direction. They explained that the tensile strains arise from the formation of an oxide layer due to O_2 flows that can cause insufficient thermal coupling between substrate/Pt nanoparticles or lattice mismatch between Pt and PtO. After oxidation of the Pt nanoparticle, CO gas mixtures were flowed. A decrease in the strain field was observed from the reduction of the Pt oxide layer. Passos et al.[52] researched the catalytic hysteresis during the CO oxidation process using shape-controlled Au nanoparticles with two kinds of morphologies, i.e., cuboctahedral and cubic. They found different catalytic activity hysteresis for the two types of Au nanoparticles. Cuboctahedral particles were more active during the heating cycle (inverse hysteresis), but the cubic nanoparticles were more active during the cooling cycle (normal hysteresis). These findings demonstrate that catalytic nanoparticle morphology can affect the catalytic hysteresis properties. Strain dynamics during CO conversion have an inverse hysteresis feature, as shown in **Fig. 20**B. The strain pattern in the cuboctahedral particle on cooling matches the strain pattern at 100 °C. The strain energy landscape in **Fig. 20**C shows a hysteresis behavior for the cuboctahedral particle, with irreversible loss of the elastic energy after a catalytic cycle via strain evolution. On the other hand, the cubic nanoparticle shows no evolutions in strain energy during the CO conversion cycle. This difference is compatible with the observed inverse/normal hysteresis feature for the two morphologies of Au nanoparticles.

The dependence of strain development on the atomic arrangements, i.e., the crystallographic orientations, has been investigated by BCDI measurements. Abuin et al.[91] studied Pt nanoparticles with twin boundaries and high index facets during CO oxidation. Imaging results were confirmed by atomic force microscopy (AFM) measurements. In **Fig. 21**A, the surface strain distributions for pristine and Ar/CO exposed states are shown. The curved surface of the nanoparticle shows a more strained region than the flat Pt terrace. After CO flows, there was a shift of the strain distribution to tensile strain. In particular, the shift of the surface strain was larger than bulk, implying that CO adsorption on the Pt surface induces overall surface lattice expansion and there was an elastic response of the bulk strain field. They also focused on the morphological changes during CO oxidation catalysis. During the process, a high index terminated surface in the vicinity of the Pt (111) low index facet expanded laterally, as shown in **Fig. 21**B. With these changes, the overall step was flattened. Choi et al.[56] studied the strain field evolution in Pt nanoparticles during hydrogen peroxide decomposition. The measurements were performed, during exposure to 35% hydrogen peroxide, at two different Bragg peaks, e.g., Pt (200) and Pt (1-11), to observe the crystallographic orientation sensitivity of the response related to the catalytic activity. Strain field evolution of a Pt nanoparticle at (1-11) was more than at (200). **Fig. 21**C shows the strain distribution near the surface and at the center of Pt, each nanoparticle in the pristine state and after 12 min of H_2O_2 exposure. Strain field evolution inside the crystal is observed in the Pt (1-11) case, but in the Pt (200) case there are no significant changes except at the surface. A density functional theory (DFT) calculation provides the explanation for this finding. From the DFT calculation, the displacement fields for the top-layer at both (111) and (200) Pt surfaces were calculated. The distortion of the atoms at the Pt (111) surface was larger than the Pt (200) case. This difference was reflected in the BCDI results with the elastic response of the inside of the Pt nanoparticles.

For industrial applications, alloy nanoparticles are highlighted for both efficiency and economic feasibility. For these bimetallic alloys, compositional segregation has been reported in the oxidizing or reducing atmospheres. Because compositional redistribution in alloy catalysts affects their catalytic activity, it is crucial to measure this elemental segregation. Since segregation occurs during reactions, in-situ studies are helpful to understand the complete process. Kawaguchi et al.[92] studied bimetallic Pt-Rh alloy catalysts in the reducing environment associated with hydrogen evolution. They measured internal changes of the strain field with different gas flows at two different temperatures (550 °C and 700 °C) as shown in **Fig. 22**. At lower temperatures, oxidizing (5% O_2 balanced in He) gas flows cause no effect, but reducing (3.8% H_2 balanced in He) gas flows induces an internal strain field and deforms the shape of nanoparticles. They explained that the evolution of the internal strain field could be interpreted as the compositional strain induced by the segregation of Rh. However, the deformation of the Pt-Rh nanoparticle at 700 °C was much smaller than the one at

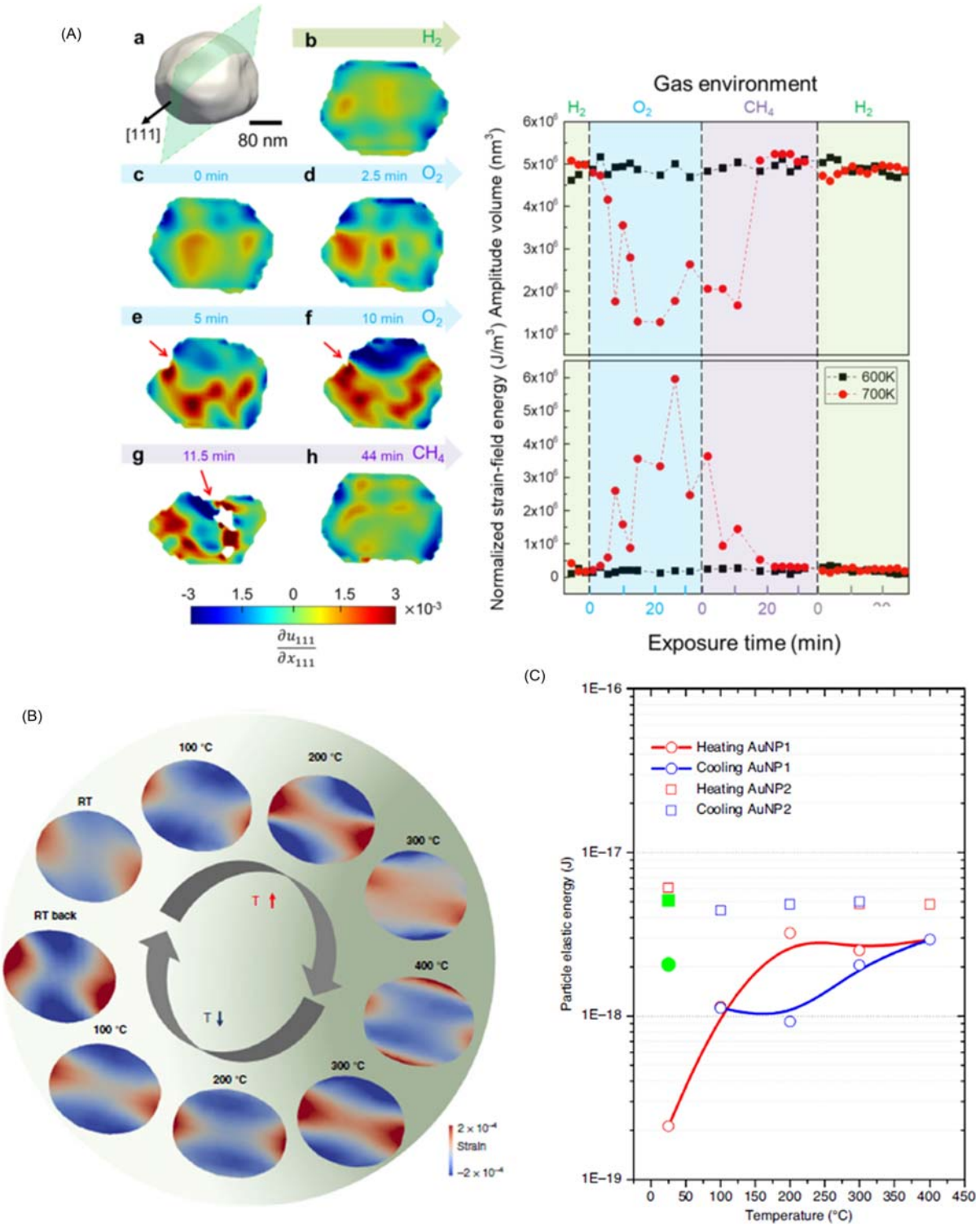

Fig. 20 Strain dynamics and strain energy landscape for Pt and Au nanocrystals during catalytic reactions. (A) Strain field distribution and normalized strain field energy of a Pt nanocrystal as a function of exposure time and various gas flows. (B) 2D slices of strain distribution through the center of 3D reconstructions of a Au cuboctahedron crystal during CO oxidation reaction. (C) Elastic energy landscape of Au nanocrystals under catalytic reaction conditions with increasing/decreasing temperature. Reproduced from, Kim, D.; Chung, M.; Kim, S.; Yun, K.; Cha, W.; Harder, R.; Kim, H. Defect Dynamics at a Single Pt Nanoparticle during Catalytic Oxidation. *Nano Lett.* **2019**, *19*(8), 5044–5052, with permission from AMER CHEMICAL SOC. Reproduced from Passos, A. R.; Rochet, A.; Manente, L. M.; Suzana, A. F.; Harder, R.; Cha, W.; Meneau, F. Three-Dimensional Strain Dynamics Govern the Hysteresis in Heterogeneous Catalysis. *Nat. Commun.* **2020**, *11*(1), 4733, with permission from NATURE RESEARCH.

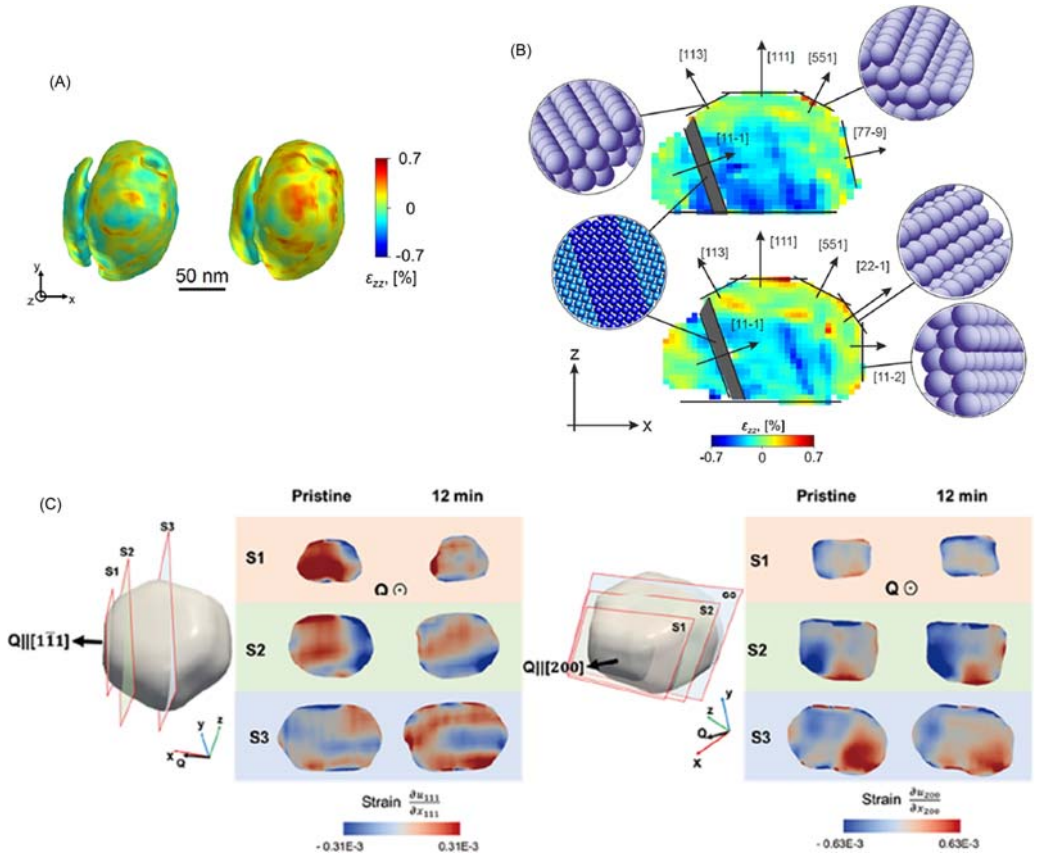

Fig. 21 Strain distribution in Pt nanocrystals. (A) Surface strain distribution of a Pt nanocrystal under Ar and Ar/CO flows. (B) 2D slices of out-of-plane strain component through the center of the 3D reconstructions under Ar and Ar/CO flows. (C) Strain distribution, taken at Pt (1-11) (left) and Pt (200) (right) Bragg conditions, near the surface and at the center of Pt nanocrystals in pristine state and after H_2O_2 exposure for 12 min. Reproduced from Abuin, M.; Kim, Y. Y.; Runge, H.; Kulkarni, S.; Maier, S.; Dzhigaev, D.; Lazarev, S.; Gelisio, L.; Seitz, C.; Richard, M.-I.; Zhou, T.; Vonk, V.; Keller, T. F.; Vartanyants, I. A.; Stierle, A. Coherent X-Ray Imaging of CO-Adsorption-Induced Structural Changes in Pt Nanoparticles: Implications for Catalysis. *ACS Appl. Nano Mater.* **2019**, *2*(8), 4818–4824, with permission from AMER CHEMICAL SOC. Reproduced from Choi, S.; Chung, M.; Kim, D.; Kim, S.; Yun, K.; Cha, W.; Harder, R.; Kawaguchi, T.; Liu, Y.; Ulvestad, A.; You, H.; Song, M. K.; Kim, H. In Situ Strain Evolution on Pt Nanoparticles during Hydrogen Peroxide Decomposition. *Nano Lett.* **2020**, *20*(12), 8541–8548, with permission from AMER CHEMICAL SOC.

a lower temperature. Because of the faster diffusion of Rh at 700 °C, compositional heterogeneity was relieved on a short timescale. Using the strain field evolution, they deduced the Rh composition near the surface of the nanoparticle. They found an increase of Rh under reducing conditions due to Rh segregation. Interestingly, there were overall changes in the Rh composition for the whole nanoparticle. It means that Rh atoms of the neighboring Rh islands can migrate to the larger particle measured. At 700 °C, this migration effect can occur in He flows because the equilibrium oxygen partial pressure of RhO_x is high. This study shows that internal compositional changes in a single alloy nanoparticle can be measured by BCDI without using a spectroscopic method. This approach can be applied to more complex oxide nanoparticles, such as fuel-cell materials.

10.06.4 Crystal growth and dissolution studied via BCDI

The next examples are BCDI studies of crystal growth and dissolution. Elucidating growth and dissolution mechanisms is difficult because these processes involve the interplay of many crystallographic characteristics such as defects, dislocations, crystal orientation, and grain boundaries. BCDI can identify these crystallographic properties during real-time growth and dissolution. The first BCDI study of crystal growth and dissolution was done by Clark et al.[93] They studied $CaCO_3$ nanoparticles made by precipitation. CXD patterns at the (104) Bragg peak were collected during the growth and dissolution processes. For the crystal growth, they added droplets of $CaCl_2$ solution to precipitate $CaCO_3$. They observed the formation of {104} facets of the $CaCO_3$ nanoparticle with adding droplets. In contrast, the dissolution of the nanoparticle was measured during the deposition of dilute acetic acid. Fig. 23 shows that the morphology and surface displacement field changed during the crystal growth and dissolution processes. The morphology of the $CaCO_3$ nanoparticle was rhombohedral as confirmed by SEM. With precursor solution exposure, the size of the nanoparticle became larger and the facets were rounded. Interestingly, there was a difference in the growth ratio. The facets that were directly

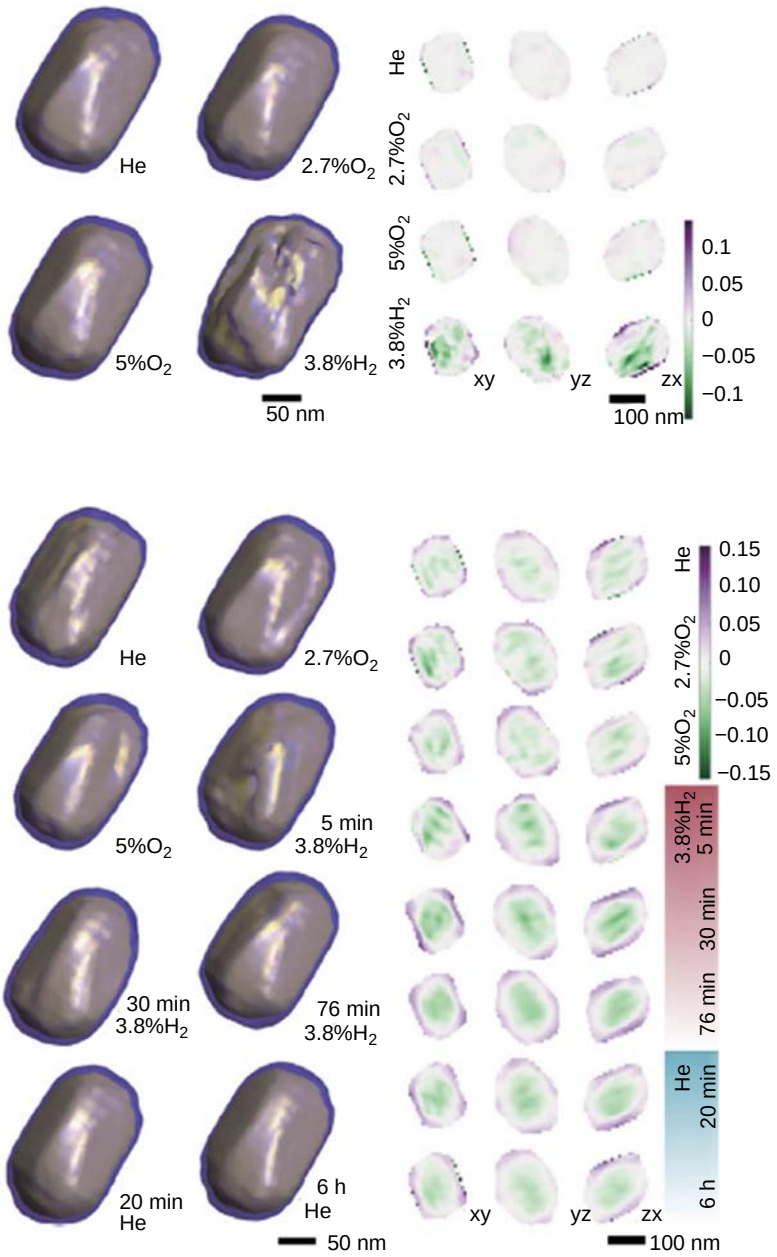

Fig. 22 Alloying and dealloying process in Pt-Rh. 3D reconstruction and Rh composition difference calculated from the compositional strain of Pt-Rh nanocrystal at 550 °C (top) and 700 °C (bottom). Reproduced from Kawaguchi, T.; Keller, T. F.; Runge, H.; Gelisio, L.; Seitz, C.; Kim, Y. Y.; Maxey, E. R.; Cha, W.; Ulvestad, A.; Hruszkewycz, S. O.; Harder, R.; Vartanyants, I. A.; Stierle, A.; You, H. Gas-Induced Segregation in Pt-Rh Alloy Nanoparticles Observed by In Situ Bragg Coherent Diffraction Imaging. *Phys. Rev. Lett.* **2019**, *123*(24), with permission from AMER PHYSICAL SOC.

exposed to the precursor solution were growing relatively fast. However, the contact to a substrate remained unchanged. From the perspective of the surface displacement field, the overall intensity of the displacement was maintained during the crystal growth and the surface displacement field remained maximum with respect to the internal displacement field attributed from the crystal growth front. During the dissolution process, the overall size of the crystal decreased. Strikingly, some sites intensely retreated during the early dissolution step. From the surface displacement field, they found that these sites were correlated with levels of deformation and strain. After the dissolution stage, the remaining displacement field was smaller than at any other stage, suggesting that highly strained regions were more easily dissolved. Another important finding from the study was dislocation propagation during crystal growth and dissolution. There was a hollow density point in the Bragg electron density, with a phase shift of 2π that is a representative phase field at the planer dislocation core. Considering this, the type of dislocation in this study is a screw dislocation. They modeled the displacement field near the screw dislocation and compared it with the BCDI results. They tracked the core sites of the dislocations during the growth/dissolution process. Initially, the dislocations were mainly found near the surface of the

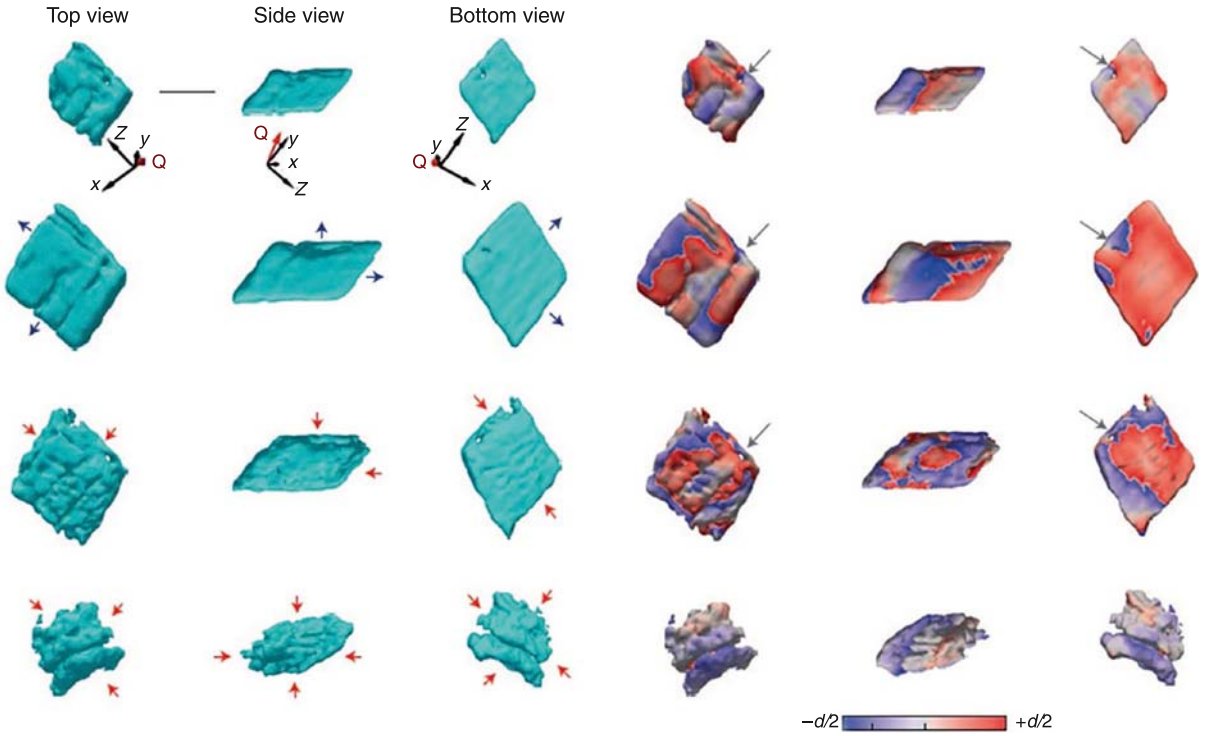

Fig. 23 Dislocation evolution during crystal growth and dissolution for a $CaCO_3$ nanocrystal. Three-dimensional rendering of reconstructed electron density (left) and lattice displacement projected along wavevector transfer **Q** in the pristine (first row), growth (second row), and dissolution (other rows) states. Reproduced from Clark, J. N.; Ihli, J.; Schenk, A. S.; Kim, Y.-Y.; Kulak, A. N.; Campbell, J. M.; Nisbet, G.; Meldrum, F. C.; Robinson, I. K. Three-Dimensional Imaging of Dislocation Propagation during Crystal Growth and Dissolution. *Nat. Mater.* **2015**, *14*(8), 780–784, with permission from NATURE RESEARCH.

nanoparticle. During growth, rapidly growing surfaces had higher dislocation densities than the unexposed facet of the nanoparticle. This finding indicates that dislocation dynamics during growth can affect the transport of the growth materials. For the dissolution process, etch-pits on the surface seen as missing density during dissolution were associated with the near-surface dislocation sites.

Yuan et al.[94] studied Fe_3O_4 nanoparticles during their dissolution. Using dilute HCl solution, they converted Fe_3O_4 nanoparticles into Fe_2O_3 nanoparticles with a stoichiometric change of the Fe(II)/Fe(III) ratio. Release of Fe^{2+} from the Fe_3O_4 nanoparticle contracts the lattice. Using this effect, they resolved non-stoichiometry-induced strain and defect dynamics. They imaged Fe_3O_4 nanoparticles with two morphologies, pyramidal and octahedral. Fig. 24A and B show morphological changes and surface displacement fields during crystal dissolution for pyramidal and octahedral Fe_3O_4 nanoparticles, respectively. Both crystals showed surface roughening with the CXD pattern weakening. A loss of total volume is shown in the figure. For both nanoparticles, some regions were apparently dissolved during oxidation. The authors suggest that the volume reduction was induced by a localized transformation from Fe_3O_4 to the amorphous or Fe_2O_3 phase. Some facets were not dissolved. They proposed that these facets were embedded surfaces at the twin dislocation boundary, which were protected against the acid solution. However, the evolution of the strain was different for the two morphologies. For the pyramid-type nanoparticle, there was an increase in strain after acid exposure. Both tensile and compressive strains had increased after 4–9 min of reaction and decreased slightly by 14 min. The authors determined that the compressive strain was related to lattice contraction due to the leaching of Fe(II) from the Fe_3O_4 crystal and that this also changes the local amplitude of the Bragg electron density. For the view of the overall lattice spacing, there was 0.04% contraction of the (311) Bragg peak accompanied by an increase in its FWHM. The strain dynamics for the octahedron-shaped crystal were more dramatic. Both tensile and compressive strains increased more rapidly than for the pyramid shape nanocrystal. Dislocations developed during the dissolution process. At the middle of the nanocrystal, there was an opposite sign crossing of strain signs. This dislocation loop disappeared at 3 min.

Other studies of crystal dissolution were reported by Cha et al.[95] They examined selective dissolution in Au-Ag alloy nanocrystals prepared by a dewetting procedure from Au-Ag thin films on glassy carbon rods. By applying a HNO_3 solution to the alloy nanoparticles, they dissolved Ag from the alloy. They found that the selective dissolution of Ag from the Au-Ag alloy nanocrystals induced surface roughening. This process generates missing Bragg electron densities. In SEM images, a pit-like feature emerged after the dissolution of Ag. For the lattice spacing, the overall lattice constant was decreased by about 0.21% because Ag has a larger lattice constant than Au. The surface changes in the Au-Ag alloy nanocrystals during dealloying altered the lattice displacement field distribution at the surface, as shown in Fig. 25. After exposure to 7 M HNO_3 for 30 s, the magnitude of the lattice displacement at the

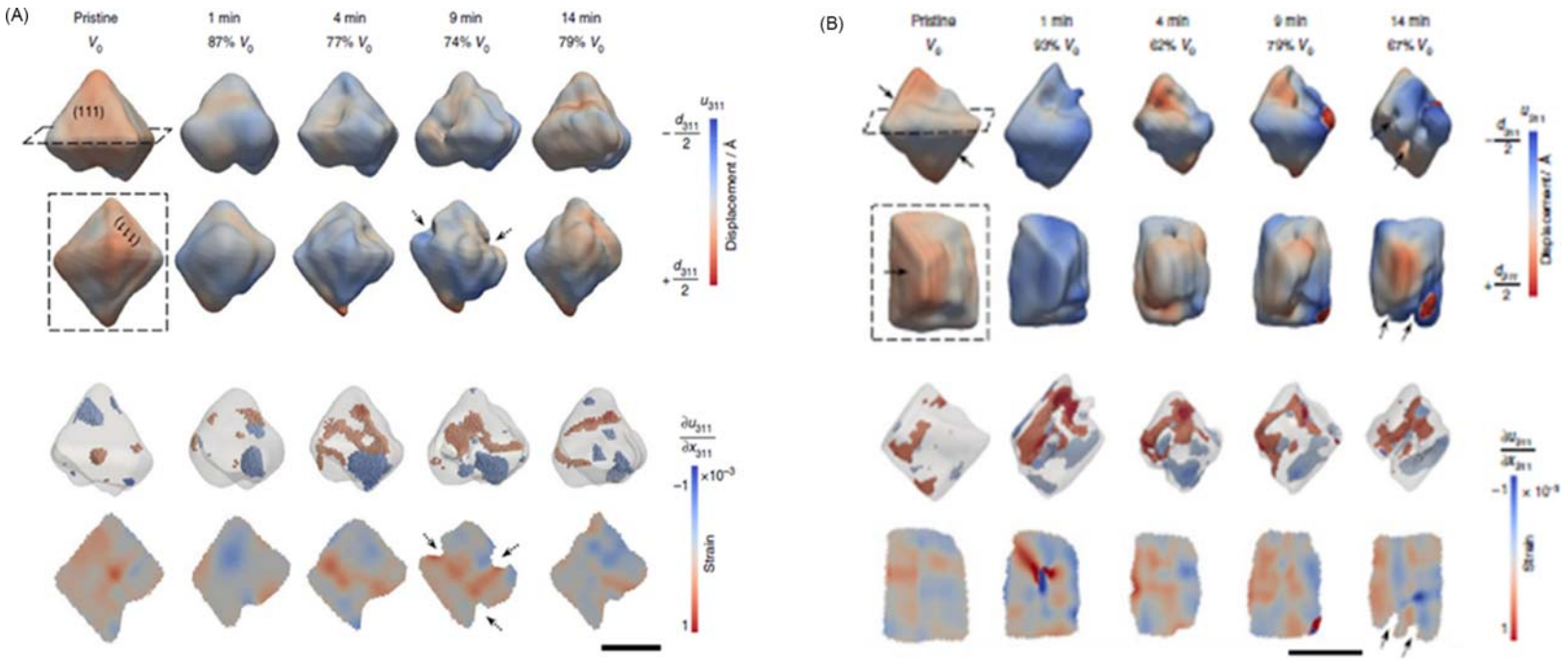

Fig. 24 Lattice displacement field (top) and strain (bottom) distribution of Fe_3O_4 nanocrystals during dissolution processes. (A) Three- and two-dimensional views of a pyramidal Fe_3O_4 nanocrystal. (B) Similar views of an octahedral Fe_3O_4 nanocrystal. Reproduced from Yuan, K.; Lee, S. S.; Cha, W.; Ulvestad, A.; Kim, H.; Abdilla, B.; Sturchio, N. C.; Fenter, P. Oxidation Induced Strain and Defects in Magnetite Crystals. *Nat. Commun.* **2019**, *10*(1), 703, with permission from NATURE RESEARCH.

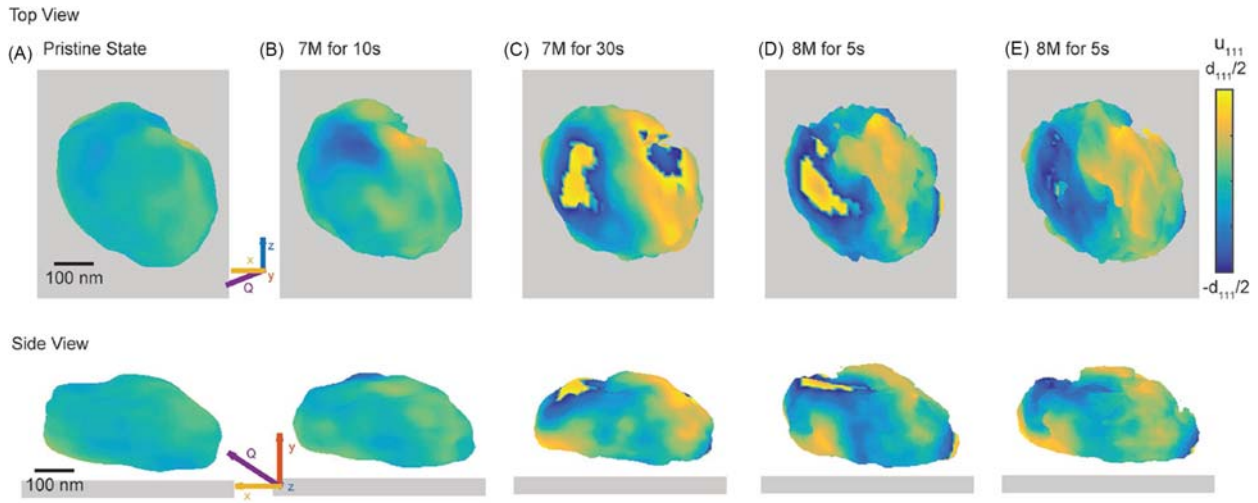

Fig. 25 BCDI results for a Au-Ag alloy during dissolution. Top and side view of 3D reconstruction colored with lattice displacement field for a single Au-Ag nanocrystal during a dealloying process. Reproduced from Cha, W.; Liu, Y.; You, H.; Stephenson, G. B.; Ulvestad, A. Dealloying in Individual Nanoparticles and Thin Film Grains: A Bragg Coherent Diffractive Imaging Study. *Adv. Funct. Mater.* **2017**, *27*(25), 1700331, with permission from WILEY-V C H VERLAG GMBH.

surface increased. Successive acid exposures with a higher concentration (8 M) for 5 s induced the propagation of an intense displacement field to the interior of the nanocrystals. This implies the formation of a pore structure inside the nanocrystal. In addition, they also imaged the dealloying process for grains in the thin film. Similar to the single nanoparticle, dealloying grains in the thin film also led to a decrease of Bragg electron density with a pit-like surface. Strain development with corresponding Bragg electron density loss was also observed in the alloy thin film.

10.06.5 BCDI studies of energy storage materials

Energy storage materials play a crucial role in mobile devices, transportation, and energy storage systems. Electrical/chemical energy storage mechanisms are intimately related to structural features that limit the movement of ions, such as Li^{+}, in the materials. That is because ion transport is affected by the lattice of the host material. Measuring lattice strain and lattice dislocation is fundamental to understand how energy storage materials work and why they degrade during charge/discharge cycles. Studies of strain evolution and dislocation dynamics, during the operation of Li-ion based battery materials, have been conducted along with simultaneous electrochemical measurements. Next-generation energy storage materials, such as hydrogen fuel cells and all-solid-state batteries, have been studied. In this section, BCDI studies of energy storage materials are discussed.

10.06.5.1 Strain energy landscape in Lithium-ion battery cathode nanoparticles

The first BCDI study of a Li-ion battery material was carried out by Ulvestad et al.[96] They examined the internal strain field in a $LiNi_{0.5}Mn_{1.5}O_{4-\delta}$ (LNMO) cathode nanoparticle. They imaged both 400 nm and 700 nm-sized nanoparticles with ex-situ and in-situ coin cell environments. Fig. 26A shows reconstructed images of these nanoparticles indicating a different mean strain field in the outer shell and inside the nanoparticle. They observed that the different strain fields originated from different states of lithiation. The strain in the 400 nm-sized nanoparticles is more homogeneous than the larger one shown in Fig. 26B. The authors concluded that larger particles were more inhomogeneously lithiated. Although it was impossible to separate from other possible origins, such as a size effect, they found that strain field analysis of Li-ion battery cathode nanoparticles can give insight into the structural changes associated with the lithiation and delithiation process in a single nanoparticle. They also found that there was a difference in the mean strain values for the inner-core and the outer-shell. They suggested that inhomogeneous core-shell strain fields might be connected to the presence of Mn^{3+} at the surface, produced during a high-temperature calcination procedure. Because Mn^{3+} has a $3d^4$ electron configuration, a Jahn-Teller effect can distort the lattice producing a small strain field.

Using an operando coin-cell environment, Ulvestad et al.[63] studied LNMO cathode nanoparticles during charging and discharging cycles. They measured the strain field evolution in them. Fig. 27A illustrates the strain evolution during discharge from 4.7 V open-circuit voltage (OCV) to 3.5 V OCV, corresponding to Li-ion insertion into the lattice. During the discharge cycle, lattice strain increased until 4.5 V OCV and the strain field was homogeneous at the fully discharged state. They concluded that the intense strain fields observed for intermediate states originated from phase separation and co-existence during the lithiation. Moreover, the strain state for the fully lithiated material was more homogeneous than for the pristine material (4.7 V, OCV). This indicates that all unit cells were almost equivalent at the fully discharged state. They also measured strain dynamics

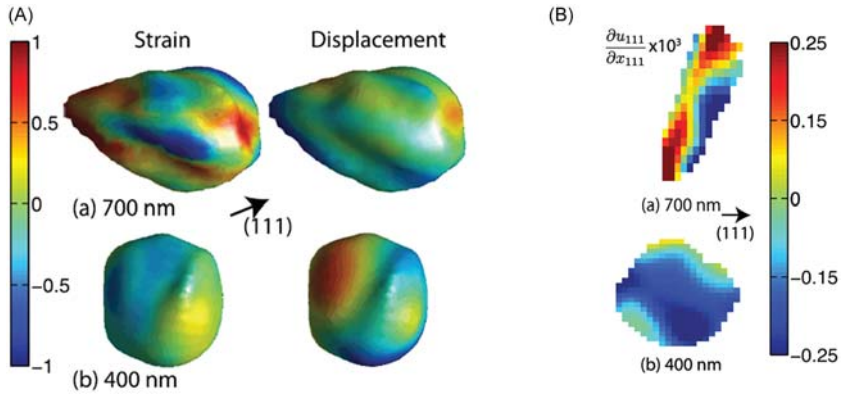

Fig. 26 Surface/internal strain imaging of 700 nm- and 400 nm-sized cathode nanoparticles of Li-ion battery. (A) Three-dimensional rendering of strain and lattice displacement, (B) Two-dimensional section of strain distribution inside nanoparticles. Reproduced from Ulvestad, A.; Cho, H. M.; Harder, R.; Kim, J. W.; Dietze, S. H.; Fohtung, E.; Meng, Y. S.; Shpyrko, O. G. Nanoscale Strain Mapping in Battery Nanostructures. *Appl. Phys. Lett.* **2014**, *104*(7), 073108, with permission from AMER INST PHYSICS.

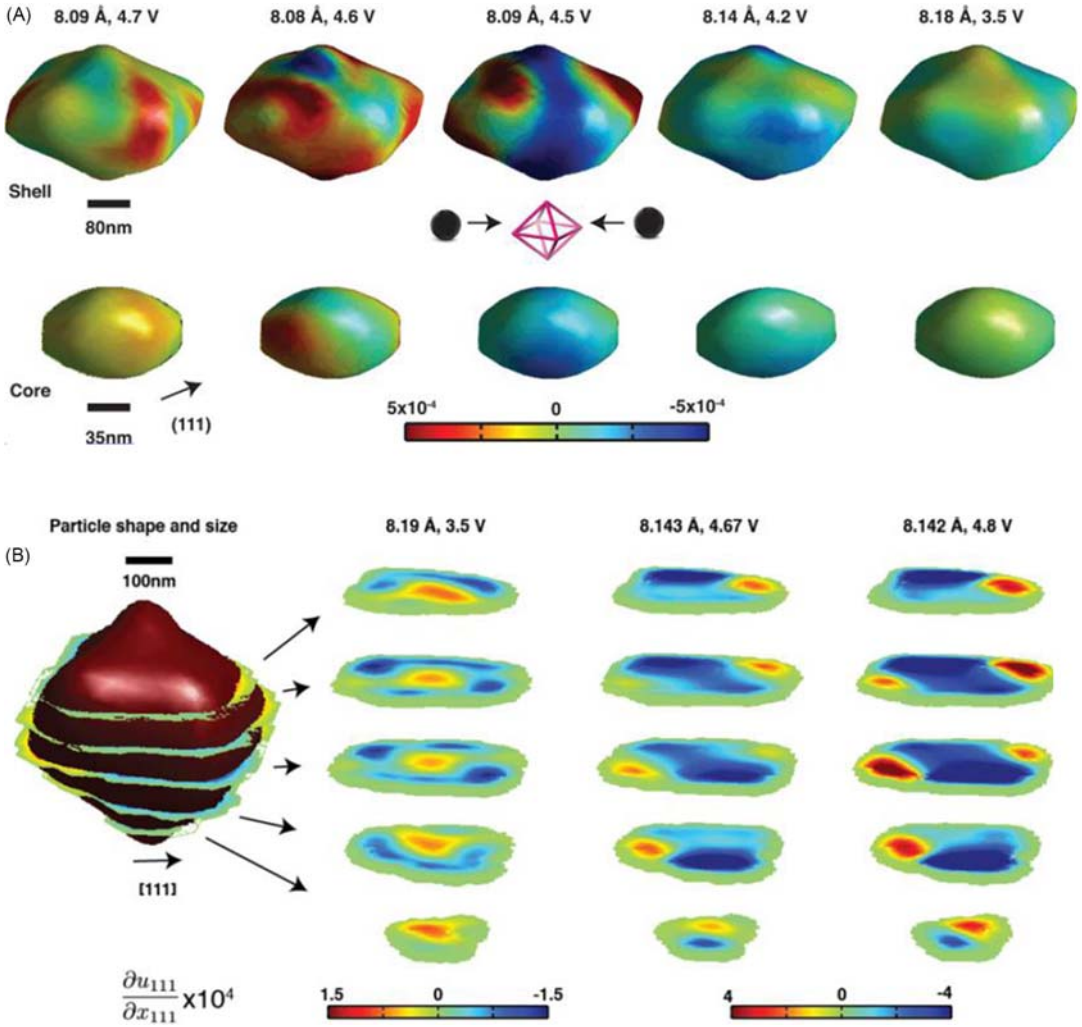

Fig. 27 Strain dynamics in LNMO cathode nanoparticles during charging and discharging cycles. (A) Three-dimensional iso-surface rendering with strain as a function of OCV, (B) Two-dimensional cross-sections of strain distribution through a particle during charging. Reproduced from Ulvestad, A.; Singer, A.; Cho, H.-M.; Clark, J. N.; Harder, R.; Maser, J.; Meng, Y. S.; Shpyrko, O. G. Single Particle Nanomechanics in Operando Batteries via Lensless Strain Mapping. *Nano Lett.* **2014**, *14*(9), 5123–5127, with permission from AMER CHEMICAL SOC.

during the charging cycle. The strain field in the cathode nanoparticle decreased gradually during delithiation. Fig. 27B shows the changes in strain distributions during the charging cycle. At the beginning of the cycle, there was only a geometrical compressive strain at the edge of the nanoparticle. However, as the nanoparticle is being charged, and overall strain decreases, a stripe pattern in strain emerges. To interpret the stripe strain features, the authors introduced a free energy model of the nonuniform binary solution. Based on the free energy model, they suggested that the stripe strain feature resulted from elastic energy relaxation at the particle boundaries. They also estimated 50 nm for the diffuse width of the stripe boundary, which provides an estimate for the minimum size for coexistence of two phases from the reconstructed images. This indicates that particles with dimensions less than 50 nm cannot include separated phases but can only contain one phase. To show the overall strain evolution during charging and discharging cycles, they calculated the elastic energy for a single cathode nanoparticle. The elastic energy during the charging and discharging cycles looked quite different. Although the OCV of the sample was the same, there was an energy barrier between the two processes. It might originate from other lattice distortions, such as cracks and dislocation nucleation.

During a charge and discharge cycle, some nanoparticles can become disconnected from conduction pathways, such as functional electrodes and the conductive matrix around cathode nanoparticles. Disconnection in a real battery system can occur due to various factors, including surface chemical changes, physical misconnection, and particle cracking or movement. Because of the difficulties associated with identifying the connectivity of a single nanoparticle, it was almost impossible to measure disconnection events associated with a single nanoparticle. Ulvestad et al.[97] reported the elastic energy evolution during a disconnection event in LNMO cathode nanoparticles. Fig. 28 shows the change in lattice constant for a single cathode nanoparticle and the OCV of a coin cell during charge and discharge cycles. As the system is fully discharged, the lattice constant increases as Li moves into the particle. However, a decrease in the lattice constant is not observed for the charge cycles. They concluded that there was a disconnection event about 8 h after starting the charge and discharge cycle. The changes in the lattice constant were not entirely dependent on OCV. There was a tiny response to the bias of the system that implies the formation of the surface layer, which might be associated with a disconnection event. Before the disconnection event at 6 h, there is a large surface/internal strain in the cathode nanoparticle. Compressive and tensile strain can originate from an inhomogeneous Li distribution, with Li poor and Li rich states, respectively. The formation of a region with poor Li conductivity could lead to an inhomogeneous strain distribution. After disconnection events, there was a release of internal strain due to Li rearrangement within the cathode nanoparticle. Only surface strain remained after the disconnection event, which originated from trapped Li in an electrolyte layer. To quantify the disconnection

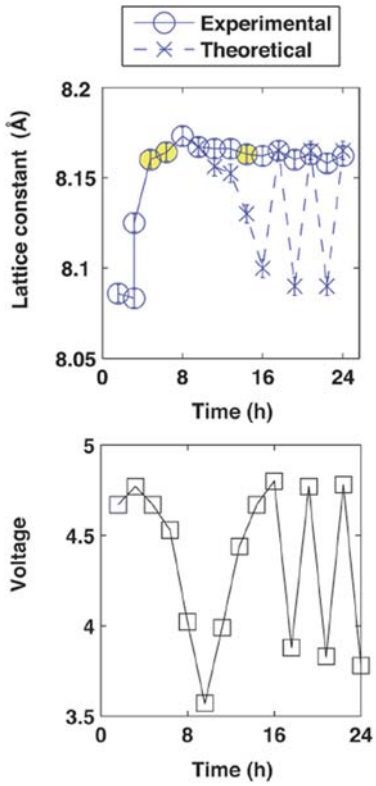

Fig. 28 Changes in lattice constant for LNMO cathode nanoparticles. Variation of lattice constant (top) and potential (bottom) during charge and discharge cycles. Reproduced from, Ulvestad, A.; Clark, J. N.; Singer, A.; Vine, D.; Cho, H. M.; Harder, R.; Meng, Y. S.; Shpyrko, O. G. In Situ Strain Evolution during a Disconnection Event in a Battery Nanoparticle. *Phys. Chem. Chem. Phys.* **2015**, *17*(16), 10551–10555, with permission from ROYAL SOC CHEMISTRY.

event, via the strain distribution, the elastic energy was calculated. Initially, the strain energy is relatively low, however, the strain energy increases due to the structural transformation. Then the strain energy drops to a similar value on complete discharge.[63]

10.06.5.2 Dislocation dynamics during battery cycling

The Li distribution in a nanoparticle can be deduced from the tensile and compressive strains. Using an elastic energy calculation, one can examine phase coexistence during battery cycling. Moreover, discontinuous changes of elastic energy along the voltage bias provide supposition of the plastic deformation, i.e., dislocations. In this section, operando imaging of dislocations, by BCDI, in cathode nanoparticles will be reviewed.

Dislocations are important in energy storage materials, because ion transport is affected by the unique strain field and electric field around dislocation points. For this reason, the existence of dislocations can affect the battery performance. As mentioned above, BCDI is an important tool for imaging lattice displacements in 3D. Ulvestad et al.[64] studied dislocation dynamics in LNMO cathode nanoparticles under operating conditions. They found that there was a strain field at the pristine LNMO nanoparticle. With the angular fitting of the displacement field in the vicinity of the dislocation core, they verified that there were edge dislocations in the LNMO nanoparticle. The dislocation was stable at room temperature without OCV changes. On charging, the dislocation line moved as a function of electrical bias. Fig. 29 shows the dislocation dynamics during the charging process. The line indicates the three-dimensional distribution of dislocation cores. The preferential direction of dislocation movement was out of the nanoparticle. They deduced Poisson's ratio for the nanoparticle during the charging process by the angular fitting of the displacement field near the dislocation core. Poisson's ratio for the LNMO nanoparticle decreased on delithiation. Poisson's ratio became negative at 4.5 V OCV. The negative Poisson' ratio, i.e., auxetic properties, indicates that on stretching, the material expands both parallel and perpendicular to the direction of the applied force. They claimed that the auxetic behavior of the LNMO nanoparticles arose from a hinge-like structure in LNMO unit cell. They suggested a mechanism of the hinge structure in the cathode nanoparticle. The hinge structure moves more easily with the lithiation process and consequently derived negative Poisson's ratio. They showed the formation of a lithium-rich phase in the vicinity of the dislocation core. They found that the new phase nucleated, during charging, near dislocations. The tensile strained region, due to the higher Li content, near the dislocation. These findings confirmed the role of the dislocation core as a nucleation point during the phase transformation of an ionic crystal.

Singer et al.[65] observed the creation and nucleation of dislocations during battery operation. They imaged $Li_{1.2}Ni_{0.133}Mn_{0.533}Co_{0.133}O_2$ nanoparticles, which is a Li-rich layered oxide (LRLO) cathode material, during a charging cycle. In reconstructed images, singularity points in phase are created while the cathode nanoparticle is being charged. The discontinuity in the phase around this

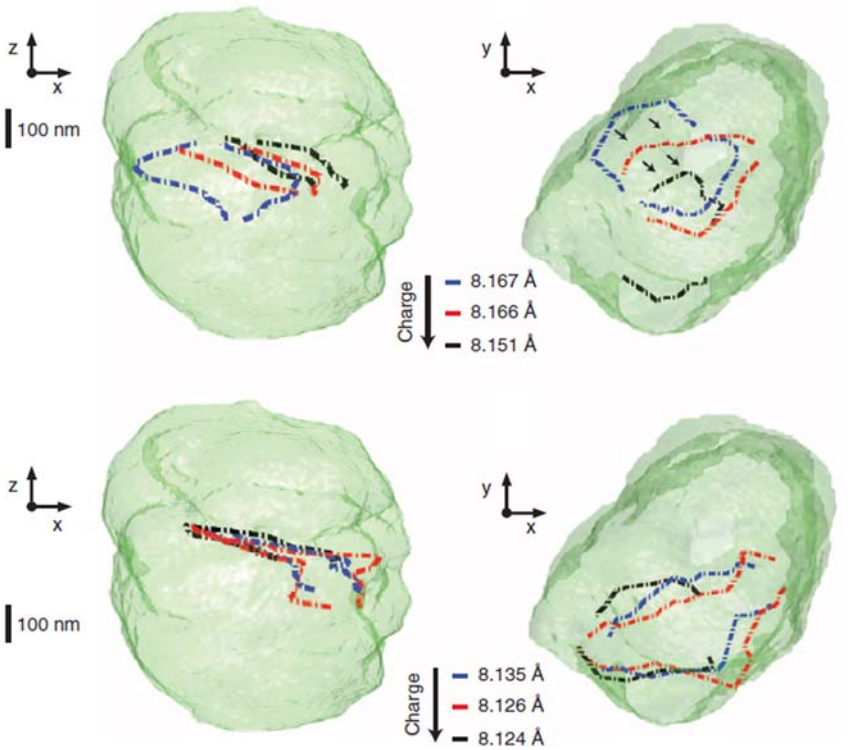

Fig. 29 The evolution of near dislocation displacement field in a single LNMO cathode nanoparticle during charging. Reproduced from Ulvestad, A.; Singer, A.; Clark, J. N.; Cho, H. M.; Kim, J. W.; Harder, R.; Maser, J.; Meng, Y. S.; Shpyrko, O. G. Topological Defect Dynamics in Operando Battery Nanoparticles. *Science* **2015**, *348*(6241), 1344–1347, with permission from AMER ASSOC ADVANCEMENT SCIENCE.

singularity is a signature of dislocations. In this case, the imperfection shows line dislocations with the Burgers vector perpendicular to the layers. At 4.3 V the first formation of an extra half-plane dislocation occurred and, on further charging, more dislocations emerged and finally formed a dislocation network as shown in Fig. 30A. During charging, the dislocations moved slightly. Above 4.4 V, the distortion in the CXD patterns was too great to reconstruct the three-dimensional image of the nanoparticle as well as the strain field distribution inside the nanoparticle. This nanoparticle also exhibits evolution of lattice displacement and strain during the charge cycle as displayed in Fig. 30B. A continuous lattice displacement field at 4.0 V changes slightly and the inhomogeneity of strain increases up to 4.2 V. At 4.3 V, plastic deformation occurs via the nucleation of dislocations. Both compressive and tensile strain is observed around the singularity points, indicating the formation of an extra half-plane. Further charging to 4.4 V induces additional dislocations and movement of dislocations appeared at 4.3 V. In classical layered oxide materials such as $LiNi_{0.80}Co_{0.15}Al_{0.05}O_2$ (NCA), the number of dislocations was less than for the LRLO material. In two different NCA nanoparticles, either one or zero dislocations were formed during delithiation on charging to 4.8 V. This difference between LRLO and classical layered oxides was confirmed by ensemble-averaged measurements using X-ray powder diffraction. In the LRLO material, strain increased monotonically with delithiation, whereas elastic energy for the NCA nanoparticle peaked at 4.2 V and decreased on further charging. The authors suggested that different diffusion velocities were responsible for the difference. In LRLO, diffusion drops on charging and the formation of a Li-depleted region at the nanoparticle boundary. For this reason, there was a large concentration difference that created the dislocation network. However, in the classical layered oxide, the diffusion ratio was high enough that

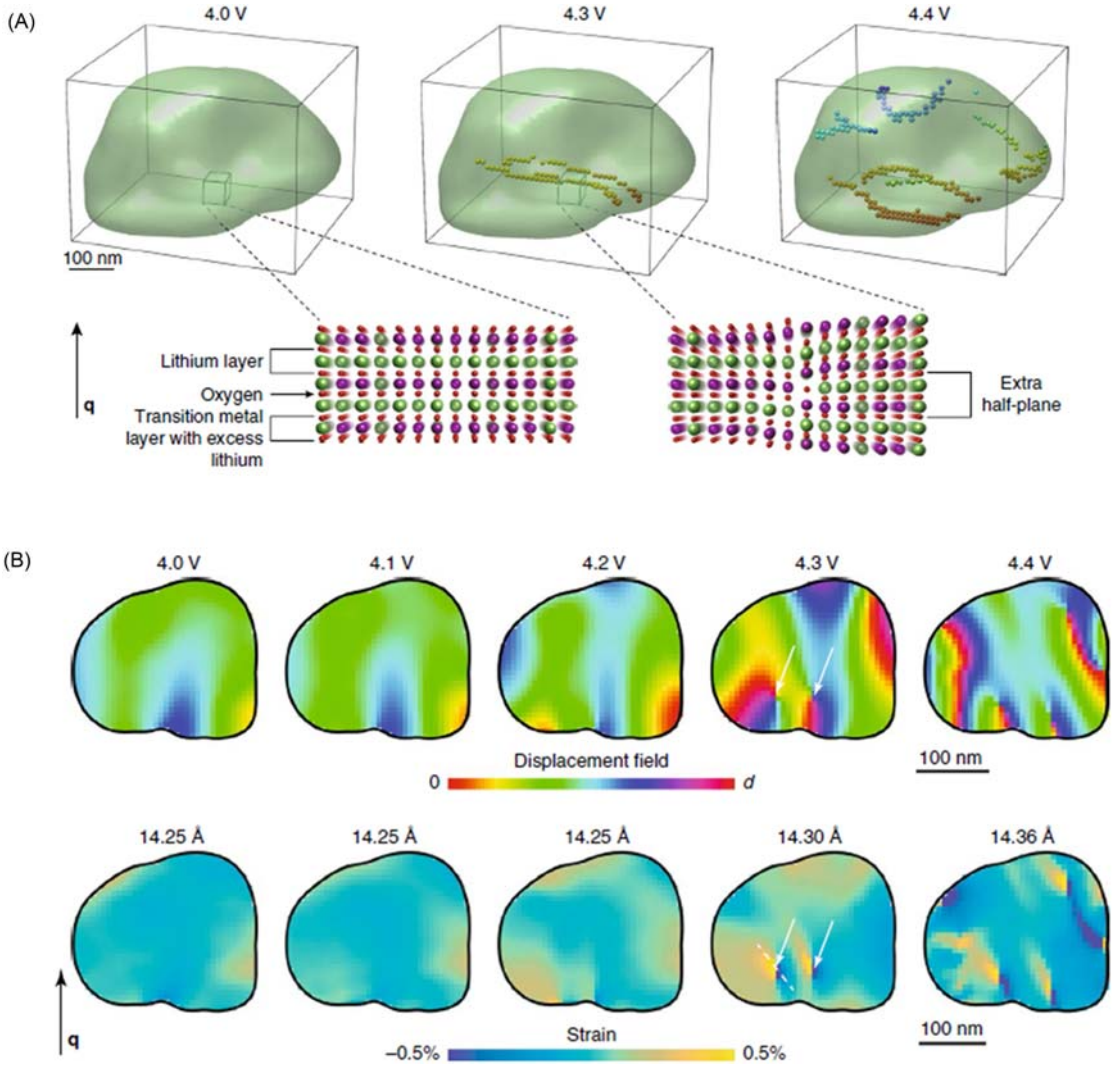

Fig. 30 Dislocation and strain dynamics in cathode nanoparticles of layered oxide materials. (A) Creation of a dislocation network during battery operation. (B) Slice of the displacement field and strain during charging. Reproduced from Singer, A.; Zhang, M.; Hy, S.; Cela, D.; Fang, C.; Wynn, T. A.; Qiu, B.; Xia, Y.; Liu, Z.; Ulvestad, A.; Hua, N.; Wingert, J.; Liu, H.; Sprung, M.; Zozulya, A. V.; Maxey, E.; Harder, R.; Meng, Y. S.; Shpyrko, O. G. Nucleation of Dislocations and Their Dynamics in Layered Oxide Cathode Materials during Battery Charging. *Nat. Energy* **2018**, *3*(8), 641–647, with permission from NATURE RESEARCH.

there were few or no dislocations. They found that dislocation formation and nucleation can lead to voltage fade in a battery. Edge dislocations in a nanoparticle can perturb the oxygen layer stacking sequence. The ABCABC sequence of the LRLO can change to an ABCBCABC sequence. This perturbed layer arrangement is energetically unfavorable, leading to an increased total Gibbs free energy for the nanoparticle. This dislocation induced thermodynamically unfavorable state leads to "voltage fade" that reduces the overall energy density of the battery. The degraded LRLO nanoparticle can recover its storage capacity by recovering its original layered structure. On successive cycling, dislocations can disappear if they move out to the boundary. High-temperature annealing of the nanoparticle can release dislocations inside the nanoparticles by rearranging their superstructure. The authors observed that charge storage and the CXD patterns recovered after annealing at 150 °C.

Wang et al.[98] conducted CDI on Li-rich layered battery materials ($Li_{1.2}Ni_{0.13}Co_{0.13}Mn_{0.54}O_2$). They compared the results from full-field transmission X-ray microscopy, X-ray powder diffraction, and X-ray absorption spectroscopy to characterize larger scale properties of the materials. By combining these X-ray characterization techniques, they obtained both chemical state maps and atomic-scale structural changes.

10.06.6 Ultrafast dynamics using BCDI

In this section, BCDI experiments using XFELs will be discussed. Because of the ultrashort, fully coherent, and extremely intense X-ray pulses, XFELs have become a key source for probing ultrafast phenomena in materials. Using the X-ray pump-probe (XPP) method, the first study of a single nanoparticle was reported by Clack et al.[99] By combining the XPP technique with BCDI, they measured ultrafast lattice vibration excited by a laser pulse, i.e., coherent acoustic phonon propagation in a single gold nanoparticle. Fig. 31A shows a schematic of the ultrafast BCDI experiment. A Ti-sapphire laser of 800 nm wavelength with a 50 fs pulse width was used as an optical pump and focused coherent X-rays with an 80 fs pulse length served as an X-ray probe. After adjusting the spatial overlap and relative timing between the pump and the probe, they measured coherent acoustic phonons generated from the optical laser pump. The lattice vibrations appeared in the CXD patterns. Before time-zero, the diffraction pattern is highly symmetric because of the homogeneous lattice distribution of the Au nanocrystal. The well-defined fringe patterns indicate that the nanocrystal has a well-faceted shape. After the generation of the coherent phonons, the CXD patterns became asymmetric, which was attributed to strain inhomogeneity in the nanocrystal. Note that the overall expansion or contraction of the nanoparticle cannot distort the diffraction pattern. The distortion of the CXD patterns indicates the presence of a strain gradient in the nanocrystal, however, a change in the overall lattice constant shifts the position of the diffraction peak. The angular deviation of the Au (111) Bragg peak is plotted along with the time delay for two different nanocrystals. There was a harmonic expansion and contraction in the Bragg peak position. Immediately after the optical pump's arrival, there was an expansion of the lattice. Because of the finite size of the nanoparticle in comparison to the penetration depth of the pump laser, there was only an electron meditated effect on the lattice. For this reason, they suggested a two-temperature model to explain energy transfer to the lattice through electron-phonon coupling. They fitted the oscillation of the Bragg peak position with two oscillation models. Both nanocrystals had two oscillation components with about 100 ps and about 250 ps periods, which varied slightly with the size of the nanocrystals. The oscillation of the whole lattice agreed well with MD simulations and previous results from ultrafast X-ray diffraction on an ensemble of nanoparticles or thin film. They found another lattice oscillation mode from the BCDI results. Since the local strain gradient in the nanocrystal does not shift the Bragg peak, only imaging of the displacement field can identify those local modes. Fig. 31B shows slices of the reconstructed image and displacement field in the nanocrystal after the arrival of the laser pump. In these results, homogeneous changes of the lattice, such as a breathing mode, vanished leaving only inhomogeneous components. To emphasize the

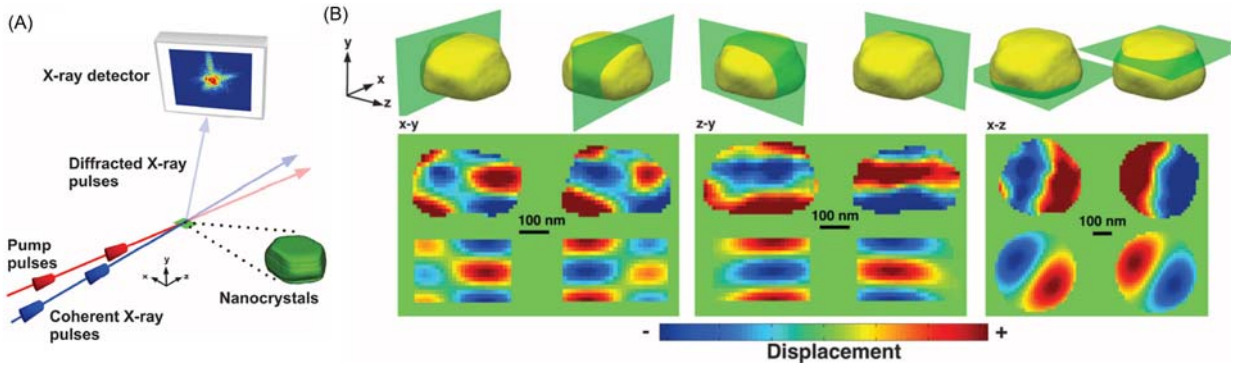

Fig. 31 Ultrafast time-resolved BCDI for a Au nanocrystal. (A) Schematic diagram of the experimental setup (B) Visualization of the propagation of lattice vibrational modes in a nanoparticle from the experiment (middle) and simulation (bottom) at each cross-section displayed at the top. Reproduced from Clark, J. N.; Beitra, L.; Xiong, G.; Higginbotham, A.; Fritz, D. M.; Lemke, H. T.; Zhu, D.; Chollet, M.; Williams, G. J.; Messerschmidt, M.; Abbey, B.; Harder, R. J.; Korsunsky, A. M.; Wark, J. S.; Robinson, I. K. Ultrafast Three-Dimensional Imaging of Lattice Dynamics in Individual Gold Nanocrystals. *Science* **2013**, *341*(6141), 56–59, with permission from AMER ASSOC ADVANCEMENT SCIENCE.

lattice displacement that was provoked by the pump, they subtracted the initial displacement field from the after time-zero data sets. They found that there was an intersection of the expansion region and contraction region as delay time increased. This oscillatory change of the local strain field implied that the presence of the shear vibration mode is a higher vibration mode than breathing mode. In Fig. 31B, they compared the measured displacement field with the MD simulation result for a cylinder-shaped object with a radius of 200 nm and a height of 220 nm, similar to the dimension of the measured Au nanocrystals. Using the great sensitivity of BCDI to local displacements (picometers), they visualized the propagation of lattice vibration modes in a nanoparticle.

Cherukara et al.[100] studied various lattice deformation modes in ZnO nanorods with an X-ray pump-probe technique and BCDI. Because ZnO has a novel piezoelectric property, resolving their dynamical response is important for its applications in actuators and sensing devices. They used a third-generation synchrotron source. To induce lattice deformations in the ZnO nanorod, they used an optical laser with a wavelength of 1064 nm and an incident laser fluence of 1.16 mJ/cm^2. CXD patterns were collected at the (100) Bragg peak of the ZnO. From the collective motion of the diffraction patterns, they resolved overall lattice vibration modes, i.e., breathing and rotation modes. After the arrival of the laser pump, there were peak shifts both perpendicular and parallel to the wavevector transfer. They concluded that overall pattern shift along the direction parallel to wavevector transfer arose from the breathing mode of the lattice, which gives uniform volumetric changes of the lattice. In contrast, the shift of the pattern along the other directions originated from a homogeneous rotational deformation of the lattice. They deduced the frequency of each homogeneous deformation mode by Fourier transformation of the time-varying peak shift value. The frequency of the breathing modes was 230 MHz, corresponding to the lattice expansion and contraction along the long axis of the ZnO crystal. In addition, two other frequencies were observed at 77 and 383 MHz, which are related to lattice deformations in the lateral plane. Using FEA, they simulated these two homogeneous deformation modes and compared them with the results. The simulated frequency of the breathing mode was calculated from the averaged displacement projected along [100]. The calculated breathing mode was about 260 MHz, which matches well with the measured value. The rotational deformation frequency was simulated using eigenmode analysis. They considered the first two main rotational deformations with frequencies of about 290 MHz and 200 MHz, respectively. This observation agrees well with the frequency about 230 MHz. However, other deformation modes cannot be resolved from the peak shift of the CXD patterns. From the viewpoint of the CXD pattern, these inhomogeneous strain gradients show as a distortion of the CXD patterns. Applying phase retrieval algorithms for BCDI, deformation of the CXD patterns can be used to create an image of the three-dimension displacement field distribution. Fig. 32 shows the inhomogeneous deformation with increasing time delay. Two axial and radial slices are shown and compared with the results from the FEA simulation. In both slices, the propagation of the inhomogeneous strain was observed. These complex deformation modes were the products of the interplay between different axial, radial, and torsional deformation modes. They decomposed complex deformations into several inhomogeneous components. Using FEA and the decomposed deformation modes, they obtained the generated electric potential of the ZnO nanorod, which is closely related to their application for energy harvesting.

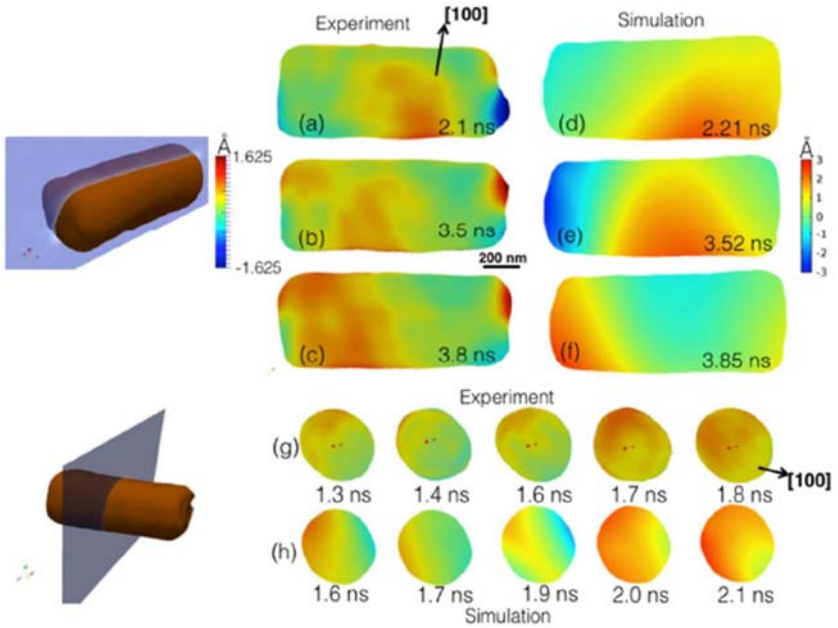

Fig. 32 Inhomogeneous deformation from imaged displacement field and predicted field from FEA simulation for a ZnO nanorod. Reproduced from Cherukara, M. J.; Sasikumar, K.; Cha, W.; Narayanan, B.; Leake, S. J.; Dufresne, E. M.; Peterka, T.; McNulty, I.; Wen, H.; Sankaranarayanan, S. K. R. S.; Harder, R. J. Ultrafast Three-Dimensional X-Ray Imaging of Deformation Modes in ZnO Nanocrystals. *Nano Lett.* **2017**, *17*(2), 1102–1108, with permission from AMER CHEMICAL SOC.

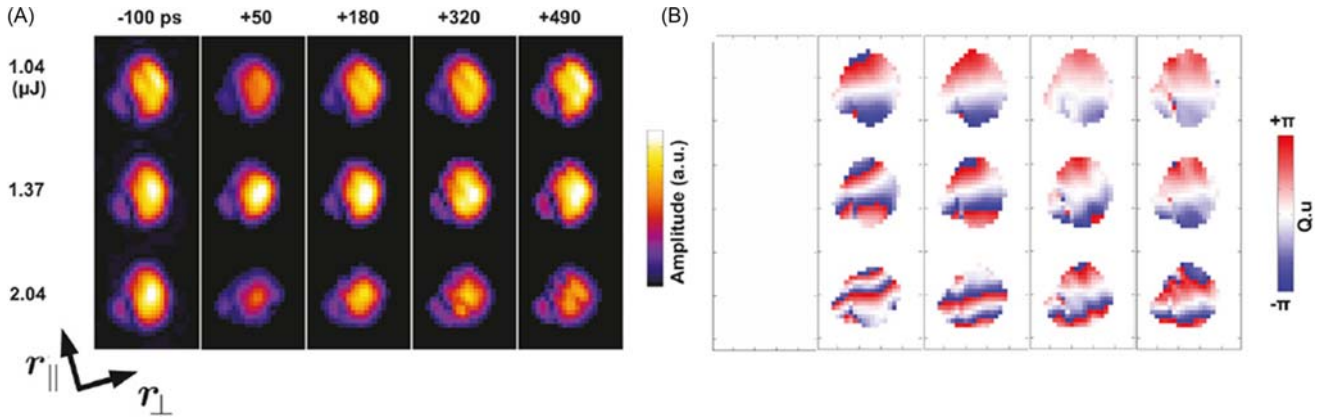

Fig. 33 Real-space retrieved images of a nanocrystal undergoing transient melting. (A) Recovered real-space images for selected times (horizontally) and as a function of pulse energy (vertically). Significant morphology changes are apparent for the highest pulse energy, consistent with a loss of crystallinity attributed to surface melting. The most dramatic changes occur at the point where the greatest nonlinearity occurs (+50 ps). (B) Recovered images of the phase (modulo 2π or 1 lattice spacing) after subtraction of the −100-ps time. The phase shows the projected displacement as a function of time (horizontally) and pulse energy (vertically). (Scale bar, 200 nm.). Reproduced from, Clark, J. N.; Beitra, L.; Xiong, G.; Fritz, D. M.; Lemke, H. T.; Zhu, D.; Chollet, M.; Williams, G. J.; Messerschmidt, M. M.; Abbey, B.; Harder, R. J.; Korsunsky, A. M.; Wark, J. S.; Reis, D. A.; Robinson, I. K. Imaging Transient Melting of a Nanocrystal Using an X-Ray Laser. *Proc. Nat. Acad. Sci.* **2015**, *112* (24), 7444–7448. with permission from NATL ACAD SCIENCES.

Clark et al.[101] showed direct evidence for the ultrafast melting of a nanoparticle. Because of the small size of the nanoparticle, they exhibit different melting behavior when compared with the bulk. Since the amplitude in BCDI is directly related to the electron density, Bragg electron density can be changed by phase transformation and the presence of dislocations or other defects. They measured the melting of the gold nanoparticles using ultrafast BCDI at an XFEL. They used an optical pump laser with wavelength 800 nm and pulse energy from 1 to 2 μJ. At the lowest pump energy, a shift of the diffraction patterns was observed, indicating overall changes in the lattice spacing. However, at the highest pumping power, the diffraction pattern was distorted. They suggested that the distortion in the CXD pattern originated from transient size changes of the nanoparticle due to melting rather than an inhomogeneous strain field. They observed that oscillatory behavior of the peak shift was displayed with peak intensity. With the highest pulse energy, there was the most prominent periodic intensity loss attributed to transient melting and recrystallization. From the oscillation of the CXD patterns, they found several pieces of evidence for transient melting of the nanoparticle, non-linearity of the peak shift and peak broadening, and softening of the longitudinal acoustic phonon. To separate the effects of size and inhomogeneous strain on the peak broadening, they imaged gold nanoparticles with a time delay. **Fig. 33**A and B show the Bragg electron density and local lattice displacement for the nanoparticle with different pulse energies and delay times, respectively. The left void region in the nanoparticle is a twined region that does not satisfy the Bragg condition. For the lowest pump energy, the morphology of the nanoparticle changed little with delay time. However, with 2 uJ pulse energy, large morphology and size changes are observed, especially at 50 ps time delay. At this point, the nanoparticle had the smallest core size with the largest halo size and low Bragg electron density, indicating the presence of a crystalline core surrounded by an ordered liquid halo. After 50 ps, there was a slight restoration of the shape at the halo near the core site. From the corrugated phase features for the highest pulse energy shown in **Fig. 33**, non-uniform surface melting was inferred.

In addition to the ultrafast time structure arising from ultrashort X-ray pulses, full spatial coherence and the high flux of X-rays are used in work by Kang et al.[102] They employed an XFEL to obtain in-situ visualization of the catalytic process in ZSM-5 zeolite nanocrystals. They measured two-dimensional CXD patterns with a single shot from the XFEL. Two successive gas flow conditions, i.e., the flow of C_3H_6 and NO with O_2, were used to implement the catalytic process. Since the ZSM-5 microcrystal was exchanged with Cu(II), catalytic activity was at the Cu site. Adsorption and de-adsorption of C_3H_6 during NO_x deoxygenation induced strain dynamics in the zeolite microcrystal. They observed the strain evolution of the two-dimensional CXD patterns during the C_3H_6 adsorption and NO_x deoxygenation catalysis process. The time resolution of each measurement was 0.5 s. During the C_3H_6 absorption process, there was a significant change in the CXD patterns and the mean value of the lattice constant. When NO with O_2 is inserted, i.e., NO_x deoxygenation catalysis starts, a higher distortion is observed. The distortions disappeared after the catalytic process finished. The internal lattice displacement was very inhomogeneous during the catalytic reaction. **Fig. 34** shows the DFT

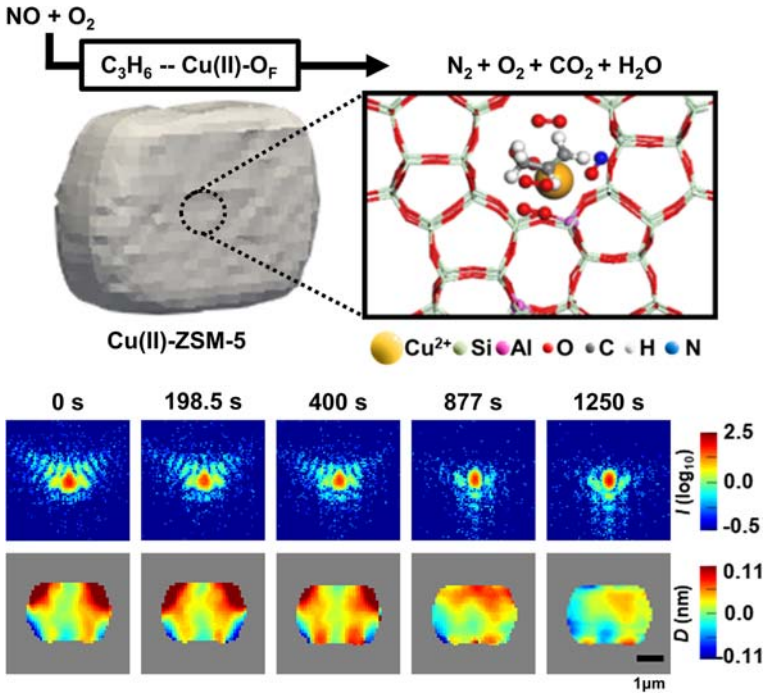

Fig. 34 (Top) DFT result of the relevant locations of the reactants (NO, O_2, and C_3H_6) in a nanopore of the Cu-ZSM-5 catalysts and (bottom) the CXD patterns (first row) and displacements (second row) from the imaging of the CXD patterns during the NOx deoxygenation. For details see reference Kang, J.; Carnis, J.; Kim, D.; Chung, M.; Kim, J.; Yun, K.; An, G.; Cha, W.; Harder, R.; Song, S.; Sikorski, M.; Robert, A.; Thanh, N. H.; Lee, H.; Choi, Y. N.; Huang, X.; Chu, Y. S.; Clark, J. N.; Song, M. K.; Yoon, K. B.; Robinson, I. K.; Kim, H. Time-Resolved in Situ Visualization of the Structural Response of Zeolites during Catalysis. *Nat. Commun.* **2020**, *11*(1), 5901.

result of the relevant locations of the reactants (NO, O_2, and C_3H_6) in a nanopore of the Cu-ZSM-5 catalysts and the CXD patterns (first row) and displacements (second row) from the imaging of the CXD patterns during the NOx deoxygenation. The authors suggested that this inhomogeneous strain field distribution arose from the inhomogeneous distribution of Cu(II) in the ZSM-5, which was confirmed by X-ray fluorescence microscopy. There was a ring-like region with a high density of Cu in the microcrystal. The strain field associated with this inhomogeneous Cu distribution was simulated using FEA and DFT. They were able to observe these changes with at least 100 times higher temporal resolution than with a typical synchrotron due to the high coherent flux available from the XFEL.

10.06.7 Future prospects for BCDI at fourth-generation synchrotron sources

Recent developments in accelerator technology have opened new opportunities to provide higher brightness and coherence in the X-ray beams from fourth-generation synchrotron sources. The key component of these new machines is their multi-bend achromat lattice, which decreases the bending angle for each of the dipole bending magnets. Tighter focusing by multipole magnets between the dipole bend magnets keeps the X-ray beam compact and with much lower emittance than current third-generation sources. Indeed, orders of magnitude improvement in X-ray brightness is expected at the new synchrotron X-ray sources. Simultaneously, low emittance provides orders of magnitude higher coherent X-ray flux.[5,103] Up to now, two new fourth-generation synchrotron X-ray sources, MAX IV[104] in Sweden and Sirius[105] in Brazil, are in operation, and a upgraded ESRF-BES[106] in France has started to operate in 2020. More such synchrotron sources are planned as either new builds or upgrades, e.g., APS-U[5] in the USA and SPring-8-II[107] in Japan.

The highest achieved spatial resolution for CDI is currently 3 nm for an Ag nanocube in two-dimension[41] and 4 nm for an Au nanocrystal in three-dimension.[78] With higher coherent flux will improve the spatial resolution of BCDI.[24,78] Atomic resolution imaging would require about one year of measurement time with the brilliance and coherent flux of a third-generation synchrotron source. However, upgraded X-ray sources will deliver a couple of orders of magnitude more coherent photons to the sample.[108]

References

1. Röntgen, W. K. A New Form Of Radiation. *Science* **1896,** *3* (72), 726–729. https://doi.org/10.1126/science.3.72.726.
2. Willmott, P. *An Introduction to Synchrotron Radiation: Techniques and Applications,* 2nd ed.; John Wiley: Chichester, West Sussex, UK, 2019.
3. Als-Nielsen, J.; McMorrow, D. *Elements of Modern X-Ray Physics,* 2nd ed.; Wiley: Hoboken, 2011.
4. Graves, W.; Chen, J.; Fromme, P.; Holl, M.; Hong, K.-H.; Kirian, R.; Limborg-Deprey, C.; Malin, L.; Moncton, D.; Nanni, E.; Schmidt, K.; Spence, J.; Underhill, M.; Weierstall, U.; Zatsepin, N.; Zhang, C. ASU Compact XFEL. *Proceedings of the 38th International Free-Electron Laser Conference*, *FEL2017;* 2018; pp 225–228. https://doi.org/10.18429/JACOW-FEL2017-TUB03.
5. Borland, M.; Abliz, M.; Arnold, N.; Berenc, T.; Blednykh, A.; Byrd, J.; Calvey, J.; Carter, J.; Carwardine, J.; Cease, H.; Conway, Z.; Decker, G.; Dooling, J.; Emery, L.; Fuerst, J.; Harkay, K.; Jain, A.; Jaski, M.; Kallakuri, P.; Kelly, M.; Kim, S.-H.; Lill, R.; Lindberg, R.; Liu, J.; Liu, Z.; Nudell, J.; Preissner, C.; Sajaev, V.; Sereno, N.; Sun, X.; Sun, Y.; Veseli, S.; Wang, J.; Wienands, U.; Xiao, A.; Yao, C. The Upgrade of the Advanced Photon Source. *Proc. IPAC'18;* 2018; pp 2872–2877. https://doi.org/10.18429/JACOW-IPAC2018-THXGBD1. *IPAC2018*.
6. Robert, A.; Curtis, R.; Flath, D.; Gray, A.; Sikorski, M.; Song, S.; Srinivasan, V.; Stefanescu, D. The X-Ray Correlation Spectroscopy Instrument at the Linac Coherent Light Source. *J. Phys.: Conf. Ser.* **2013,** *425* (00), 212009. https://doi.org/10.1088/1742-6596/425/21/212009.
7. Yun, K.; Kim, S.; Kim, D.; Chung, M.; Jo, W.; Hwang, H.; Nam, D.; Kim, S.; Kim, J.; Park, S.-Y.; Kim, K. S.; Song, C.; Lee, S.; Kim, H. Coherence and Pulse Duration Characterization of the PAL-XFEL in the Hard X-Ray Regime. *Sci. Rep.* **2019,** *9* (1), 3300. https://doi.org/10.1038/s41598-019-39765-3.
8. Gutt, C.; Wochner, P.; Fischer, B.; Conrad, H.; Castro-Colin, M.; Lee, S.; Lehmkühler, F.; Steinke, I.; Sprung, M.; Roseker, W.; Zhu, D.; Lemke, H.; Bogle, S.; Fuoss, P. H.; Stephenson, G. B.; Cammarata, M.; Fritz, D. M.; Robert, A.; Grübel, G. Single Shot Spatial and Temporal Coherence Properties of the SLAC Linac Coherent Light Source in the Hard X-Ray Regime. *Phys. Rev. Lett.* **2012,** *108* (2), 024801. https://doi.org/10.1103/PhysRevLett.108.024801.
9. Sutton, M.; Mochrie, S. G. J.; Greytak, T.; Nagler, S. E.; Berman, L. E.; Held, G. A.; Stephenson, G. B. Observation of Speckle by Diffraction with Coherent X-Rays. *Nature* **1991,** *352* (6336), 608–610. https://doi.org/10.1038/352608a0.
10. Abbey, B. From Grain Boundaries to Single Defects: A Review of Coherent Methods for Materials Imaging in the X-Ray Sciences. *JOM* **2013,** *65* (9), 1183–1201. https://doi.org/10.1007/s11837-013-0702-4.
11. van der Veen, F.; Pfeiffer, F. Coherent X-Ray Scattering. *J. Phys.: Condens. Matter.* **2004,** *16* (28), 5003–5030. https://doi.org/10.1088/0953-8984/16/28/020.
12. Lee, S.; Roseker, W.; Gutt, C.; Fischer, B.; Conrad, H.; Lehmkühler, F.; Steinke, I.; Zhu, D.; Lemke, H.; Cammarata, M.; Fritz, D. M.; Wochner, P.; Castro-Colin, M.; Hruszkewycz, S. O.; Fuoss, P. H.; Stephenson, G. B.; Grübel, G.; Robert, A. Single Shot Speckle and Coherence Analysis of the Hard X-Ray Free Electron Laser LCLS. *Opt. Express* **2013,** *21* (21), 24647. https://doi.org/10.1364/OE.21.024647.
13. Shpyrko, O. G.; Isaacs, E. D.; Logan, J. M.; Feng, Y.; Aeppli, G.; Jaramillo, R.; Kim, H. C.; Rosenbaum, T. F.; Zschack, P.; Sprung, M.; Narayanan, S.; Sandy, A. R. Direct Measurement of Antiferromagnetic Domain Fluctuations. *Nature* **2007,** *447* (7140), 68–71. https://doi.org/10.1038/nature05776.
14. Zhang, Q.; Dufresne, E. M.; Chen, P.; Park, J.; Cosgriff, M. P.; Yusuf, M.; Dong, Y.; Fong, D. D.; Zhou, H.; Cai, Z.; Harder, R. J.; Callori, S. J.; Dawber, M.; Evans, P. G.; Sandy, A. R. Thermal Fluctuations of Ferroelectric Nanodomains in a Ferroelectric-Dielectric PbTiO 3/SrTiO 3 Superlattice. *Phys. Rev. Lett.* **2017,** *118* (9), 097601. https://doi.org/10.1103/PhysRevLett.118.097601.
15. Kim, H.; Rühm, A.; Lurio, L. B.; Basu, J. K.; Lal, J.; Lumma, D.; Mochrie, S. G. J.; Sinha, S. K. Surface Dynamics of Polymer Films. *Phys. Rev. Lett.* **2003,** *90* (6), 068302. https://doi.org/10.1103/PhysRevLett.90.068302.
16. Sheyfer, D.; Zhang, Q.; Lal, J.; Loeffler, T.; Dufresne, E. M.; Sandy, A. R.; Narayanan, S.; Sankaranarayanan, S. K. R. S.; Szczygiel, R.; Maj, P.; Soderholm, L.; Antonio, M. R.; Stephenson, G. B. Nanoscale Critical Phenomena in a Complex Fluid Studied by X-Ray Photon Correlation Spectroscopy. *Phys. Rev. Lett.* **2020,** *125* (12), 125504. https://doi.org/10.1103/PhysRevLett.125.125504.
17. Carnis, J.; Cha, W.; Wingert, J.; Kang, J.; Jiang, Z.; Song, S.; Sikorski, M.; Robert, A.; Gutt, C.; Chen, S.-W.; Dai, Y.; Ma, Y.; Guo, H.; Lurio, L. B.; Shpyrko, O.; Narayanan, S.; Cui, M.; Kosif, I.; Emrick, T.; Russell, T. P.; Lee, H. C.; Yu, C.-J.; Grübel, G.; Sinha, S. K.; Kim, H. Demonstration of Feasibility of X-Ray Free Electron Laser Studies of Dynamics of Nanoparticles in Entangled Polymer Melts. *Sci. Rep.* **2015,** *4* (1), 6017. https://doi.org/10.1038/srep06017.

18. Leitner, M.; Sepiol, B.; Stadler, L.-M.; Pfau, B.; Vogl, G. Atomic Diffusion Studied with Coherent X-Rays. *Nat. Mater.* **2009,** *8* (9), 717–720. https://doi.org/10.1038/nmat2506.
19. Robinson, I.; Harder, R. Coherent X-Ray Diffraction Imaging of Strain at the Nanoscale. *Nat. Mater.* **2009,** *8* (4), 291–298. https://doi.org/10.1038/nmat2400.
20. Karpov, D.; Fohtung, E. Bragg Coherent Diffractive Imaging of Strain at the Nanoscale. *J. Appl. Phys.* **2019,** *125* (12), 121101. https://doi.org/10.1063/1.5054294.
21. Williams, G. J.; Pfeifer, M. A.; Vartanyants, I. A.; Robinson, I. K. Three-Dimensional Imaging of Microstructure in Au Nanocrystals. *Phys. Rev. Lett.* **2003,** *90* (17), 175501. https://doi.org/10.1103/PhysRevLett.90.175501.
22. Salditt, T., Egner, A., Luke, D. R., Eds.; Nanoscale Photonic Imaging; *Topics in Applied Physics*vol. 134; Springer International Publishing: Cham, 2020. https://doi.org/10.1007/978-3-030-34413-9.
23. Kang, H. C.; Maser, J.; Stephenson, G. B.; Liu, C.; Conley, R.; Macrander, A. T.; Vogt, S. Nanometer Linear Focusing of Hard X Rays by a Multilayer Laue Lens. *Phys. Rev. Lett.* **2006,** *96* (12), 127401. https://doi.org/10.1103/PhysRevLett.96.127401.
24. Harder, R.; Robinson, I. K. Coherent X-Ray Diffraction Imaging of Morphology and Strain in Nanomaterials. *JOM* **2013,** *65* (9), 1202–1207. https://doi.org/10.1007/s11837-013-0682-4.
25. Holt, M.; Harder, R.; Winarski, R.; Rose, V. Nanoscale Hard X-Ray Microscopy Methods for Materials Studies. *Annu. Rev. Mat. Res.* **2013,** *43* (1), 183–211. https://doi.org/10.1146/annurev-matsci-071312-121654.
26. Kim, D.; Choi, S.; Yun, K.; Kang, J.; Kim, J.; Kim, S.; Kim, H. Nanoscale Strain Imaging Using Coherent X-Ray Light Sources. *J. Korean Phys. Soc.* **2018,** *73* (6), 793–804. https://doi.org/10.3938/jkps.73.793.
27. Marchesini, S. Invited Article: A Unified Evaluation of Iterative Projection Algorithms for Phase Retrieval. *Rev. Sci. Instrum.* **2007,** *78* (1), 011301. https://doi.org/10.1063/1.2403783.
28. Sayre, D. Some Implications of a Theorem Due to Shannon. *Acta Crystallogr.* **1952,** *5* (6), 843. https://doi.org/10.1107/S0365110X52002276.
29. Gerchberg, R. W.; Saxton, W. O. A Practical Algorithm for the Determination of Phase from Image and Diffraction Plane Pictures. *Optik* **1972,** *35,* 237–246.
30. Fienup, J. R. Reconstruction of an Object from the Modulus of Its Fourier Transform. *Opt. Lett.* **1978,** *3* (1), 27. https://doi.org/10.1364/OL.3.000027.
31. Marchesini, S.; He, H.; Chapman, H. N.; Hau-Riege, S. P.; Noy, A.; Howells, M. R.; Weierstall, U.; Spence, J. C. H. X-Ray Image Reconstruction from a Diffraction Pattern Alone. *Phys. Rev. B* **2003,** *68* (14), 140101. https://doi.org/10.1103/PhysRevB.68.140101.
32. Williams, G. J.; Pfeifer, M. A.; Vartanyants, I. A.; Robinson, I. K. Internal Structure in Small Au Crystals Resolved by Three-Dimensional Inversion of Coherent x-Ray Diffraction. *Phys. Rev. B* **2006,** *73* (9), 094112. https://doi.org/10.1103/PhysRevB.73.094112.
33. Chen, C.-C.; Miao, J.; Wang, C. W.; Lee, T. K. Application of Optimization Technique to Noncrystalline X-Ray Diffraction Microscopy: Guided Hybrid Input-Output Method. *Phys. Rev. B* **2007,** *76* (6), 064113. https://doi.org/10.1103/PhysRevB.76.064113.
34. Clark, J. N.; Huang, X.; Harder, R.; Robinson, I. K. High-Resolution Three-Dimensional Partially Coherent Diffraction Imaging. *Nat. Commun.* **2012,** *3* (1), 993. https://doi.org/10.1038/ncomms1994.
35. Fienup, J. R. Phase Retrieval Algorithms: A Comparison. *Appl. Optics* **1982,** *21* (15), 2758–2769. https://doi.org/10.1364/AO.21.002758.
36. Wu, L.; Juhas, P.; Yoo, S.; Robinson, I. Complex Imaging of Phase Domains by Deep Neural Networks. *IUCrJ* **2021,** *8* (1), 12–21. https://doi.org/10.1107/S2052252520013780.
37. Scheinker, A.; Pokharel, R. Adaptive 3D Convolutional Neural Network-Based Reconstruction Method for 3D Coherent Diffraction Imaging. *J. Appl. Phys.* **2020,** *128* (18), 184901. https://doi.org/10.1063/5.0014725.
38. Mancuso, A. P.; Williams, G. J. High-Resolution Surface Structures. *Nat. Photon* **2012,** *6* (9), 574–575. https://doi.org/10.1038/nphoton.2012.209.
39. Miao, J.; Charalambous, P.; Kirz, J.; Sayre, D. Extending the Methodology of X-Ray Crystallography to Allow Imaging of Micrometre-Sized Non-Crystalline Specimens. *Nature* **1999,** *400* (6742), 342–344. https://doi.org/10.1038/22498.
40. Schroer, C. G.; Boye, P.; Feldkamp, J. M.; Patommel, J.; Schropp, A.; Schwab, A.; Stephan, S.; Burghammer, M.; Schöder, S.; Riekel, C. Coherent X-Ray Diffraction Imaging with Nanofocused Illumination. *Phys. Rev. Lett.* **2008,** *101* (9), 090801. https://doi.org/10.1103/PhysRevLett.101.090801.
41. Takahashi, Y.; Nishino, Y.; Tsutsumi, R.; Kubo, H.; Furukawa, H.; Mimura, H.; Matsuyama, S.; Zettsu, N.; Matsubara, E.; Ishikawa, T.; Yamauchi, K. High-Resolution Diffraction Microscopy Using the Plane-Wave Field of a Nearly Diffraction Limited Focused x-Ray Beam. *Phys. Rev. B* **2009,** *80* (5), 054103. https://doi.org/10.1103/PhysRevB.80.054103.
42. Shapiro, D.; Thibault, P.; Beetz, T.; Elser, V.; Howells, M.; Jacobsen, C.; Kirz, J.; Lima, E.; Miao, H.; Neiman, A. M.; Sayre, D. Biological Imaging by Soft X-Ray Diffraction Microscopy. *Proc. Natl. Acad. Sci. U. S. A.* **2005,** *102* (43), 15343–15346. https://doi.org/10.1073/pnas.0503305102.
43. Nishino, Y.; Takahashi, Y.; Imamoto, N.; Ishikawa, T.; Maeshima, K. Three-Dimensional Visualization of a Human Chromosome Using Coherent X-Ray Diffraction. *Phys. Rev. Lett.* **2009,** *102* (1), 018101. https://doi.org/10.1103/PhysRevLett.102.018101.
44. Song, C.; Jiang, H.; Mancuso, A.; Amirbekian, B.; Peng, L.; Sun, R.; Shah, S. S.; Zhou, Z. H.; Ishikawa, T.; Miao, J. Quantitative Imaging of Single, Unstained Viruses with Coherent X Rays. *Phys. Rev. Lett.* **2008,** *101* (15), 158101. https://doi.org/10.1103/PhysRevLett.101.158101.
45. Nam, D.; Park, J.; Gallagher-Jones, M.; Kim, S.; Kim, S.; Kohmura, Y.; Naitow, H.; Kunishima, N.; Yoshida, T.; Ishikawa, T.; Song, C. Imaging Fully Hydrated Whole Cells by Coherent X-Ray Diffraction Microscopy. *Phys. Rev. Lett.* **2013,** *110* (9), 098103. https://doi.org/10.1103/PhysRevLett.110.098103.
46. Song, C.; Bergstrom, R.; Ramunno-Johnson, D.; Jiang, H.; Paterson, D.; de Jonge, M. D.; McNulty, I.; Lee, J.; Wang, K. L.; Miao, J. Nanoscale Imaging of Buried Structures with Elemental Specificity Using Resonant X-Ray Diffraction Microscopy. *Phys. Rev. Lett.* **2008,** *100* (2), 025504. https://doi.org/10.1103/PhysRevLett.100.025504.
47. Pfeifer, M. A.; Williams, G. J.; Vartanyants, I. A.; Harder, R.; Robinson, I. K. Three-Dimensional Mapping of a Deformation Field inside a Nanocrystal. *Nature* **2006,** *442* (7098), 63–66. https://doi.org/10.1038/nature04867.
48. Ulvestad, A.; Clark, J. N.; Harder, R.; Robinson, I. K.; Shpyrko, O. G. 3D Imaging of Twin Domain Defects in Gold Nanoparticles. *Nano Lett.* **2015,** *15* (6), 4066–4070. https://doi.org/10.1021/acs.nanolett.5b01104.
49. Robinson, I. K.; Vartanyants, I. A.; Williams, G. J.; Pfeifer, M. A.; Pitney, J. A. Reconstruction of the Shapes of Gold Nanocrystals Using Coherent X-Ray Diffraction. *Phys. Rev. Lett.* **2001,** *87* (19), 195505. https://doi.org/10.1103/PhysRevLett.87.195505.
50. Yau, A.; Harder, R. J.; Kanan, M. W.; Ulvestad, A. Imaging the Hydrogen Absorption Dynamics of Individual Grains in Polycrystalline Palladium Thin Films in 3D. *ACS Nano* **2017,** *11* (11), 10945–10954. https://doi.org/10.1021/acsnano.7b04735.
51. Watari, M.; McKendry, R. A.; Vögtli, M.; Aeppli, G.; Soh, Y.-A.; Shi, X.; Xiong, G.; Huang, X.; Harder, R.; Robinson, I. K. Differential Stress Induced by Thiol Adsorption on Facetted Nanocrystals. *Nat. Mater.* **2011,** *10* (11), 862–866. https://doi.org/10.1038/nmat3124.
52. Passos, A. R.; Rochet, A.; Manente, L. M.; Suzana, A. F.; Harder, R.; Cha, W.; Meneau, F. Three-Dimensional Strain Dynamics Govern the Hysteresis in Heterogeneous Catalysis. *Nat. Commun.* **2020,** *11* (1), 4733. https://doi.org/10.1038/s41467-020-18622-2.
53. Harder, R.; Liang, M.; Sun, Y.; Xia, Y.; Robinson, I. K. Imaging of Complex Density in Silver Nanocubes by Coherent X-Ray Diffraction. *New J. Phys.* **2010,** *12* (3), 035019. https://doi.org/10.1088/1367-2630/12/3/035019.
54. Kim, D.; Chung, M.; Carnis, J.; Kim, S.; Yun, K.; Kang, J.; Cha, W.; Cherukara, M. J.; Maxey, E.; Harder, R.; Sasikumar, K.; Sankaranarayanan, K. R. S.; Zozulya, A.; Sprung, M.; Riu, D.; Kim, H. Active Site Localization of Methane Oxidation on Pt Nanocrystals. *Nat. Commun.* **2018,** *9* (1), 3422. https://doi.org/10.1038/s41467-018-05464-2.
55. Kim, D.; Chung, M.; Kim, S.; Yun, K.; Cha, W.; Harder, R.; Kim, H. Defect Dynamics at a Single Pt Nanoparticle during Catalytic Oxidation. *Nano Lett.* **2019,** *19* (8), 5044–5052. https://doi.org/10.1021/acs.nanolett.9b01332.
56. Choi, S.; Chung, M.; Kim, D.; Kim, S.; Yun, K.; Cha, W.; Harder, R.; Kawaguchi, T.; Liu, Y.; Ulvestad, A.; You, H.; Song, M. K.; Kim, H. In Situ Strain Evolution on Pt Nanoparticles during Hydrogen Peroxide Decomposition. *Nano Lett.* **2020,** *20* (12), 8541–8548. https://doi.org/10.1021/acs.nanolett.0c03005.

57. Fernández, S.; Gao, L.; Philipp Hofmann, J.; Carnis, J.; Labat, S.; Chahine, A. G.; van Hoof, A. J. F.; (Tiny) Verhoeven, M. W. G. M.; Schülli, T. U.; Hensen, E. J. M.; Thomas, O.; Richard, M.-I. In Situ Structural Evolution of Single Particle Model Catalysts under Ambient Pressure Reaction Conditions. *Nanoscale* **2019,** *11* (1), 331–338. https://doi.org/10.1039/C8NR08414A.
58. Diao, J.; Shi, X.; Assefa, T. A.; Wu, L.; Suzana, A. F.; Nunes, D. S.; Batey, D.; Cipiccia, S.; Rau, C.; Harder, R. J.; Cha, W.; Robinson, I. K. Evolution of Ferroelastic Domain Walls during Phase Transitions in Barium Titanate Nanoparticles. *Phys. Rev. Mater.* **2020,** *4* (10), 106001. https://doi.org/10.1103/PhysRevMaterials.4.106001.
59. Newton, M. C.; Leake, S. J.; Harder, R.; Robinson, I. K. Three-Dimensional Imaging of Strain in a Single ZnO Nanorod. *Nat. Mater.* **2010,** *9* (2), 120–124. https://doi.org/10.1038/nmat2607.
60. Leake, S. J.; Harder, R.; Robinson, I. K. Coherent Diffractive Imaging of Solid State Reactions in Zinc Oxide Crystals. *New J. Phys.* **2011,** *13* (11), 113009. https://doi.org/10.1088/1367-2630/13/11/113009.
61. Cha, W.; Song, S.; Jeong, N. C.; Harder, R.; Yoon, K. B.; Robinson, I. K.; Kim, H. Exploration of Crystal Strains Using Coherent X-Ray Diffraction. *New J. Phys.* **2010,** *12* (3), 035022. https://doi.org/10.1088/1367-2630/12/3/035022.
62. Cha, W.; Jeong, N. C.; Song, S.; Park, H.; Thanh Pham, T. C.; Harder, R.; Lim, B.; Xiong, G.; Ahn, D.; McNulty, I.; Kim, J.; Yoon, K. B.; Robinson, I. K.; Kim, H. Core–Shell Strain Structure of Zeolite Microcrystals. *Nat. Mater.* **2013,** *12* (8), 729–734. https://doi.org/10.1038/nmat3698.
63. Ulvestad, A.; Singer, A.; Cho, H.-M.; Clark, J. N.; Harder, R.; Maser, J.; Meng, Y. S.; Shpyrko, O. G. Single Particle Nanomechanics in Operando Batteries via Lensless Strain Mapping. *Nano Lett.* **2014,** *14* (9), 5123–5127. https://doi.org/10.1021/nl501858u.
64. Ulvestad, A.; Singer, A.; Clark, J. N.; Cho, H. M.; Kim, J. W.; Harder, R.; Maser, J.; Meng, Y. S.; Shpyrko, O. G. Topological Defect Dynamics in Operando Battery Nanoparticles. *Science* **2015,** *348* (6241), 1344–1347. https://doi.org/10.1126/science.aaa1313.
65. Singer, A.; Zhang, M.; Hy, S.; Cela, D.; Fang, C.; Wynn, T. A.; Qiu, B.; Xia, Y.; Liu, Z.; Ulvestad, A.; Hua, N.; Wingert, J.; Liu, H.; Sprung, M.; Zozulya, A. V.; Maxey, E.; Harder, R.; Meng, Y. S.; Shpyrko, O. G. Nucleation of Dislocations and Their Dynamics in Layered Oxide Cathode Materials during Battery Charging. *Nat. Energy* **2018,** *3* (8), 641–647. https://doi.org/10.1038/s41560-018-0184-2.
66. Assefa, T. A.; Suzana, A. F.; Wu, L.; Koch, R. J.; Li, L.; Cha, W.; Harder, R. J.; Bozin, E. S.; Wang, F.; Robinson, I. K. Imaging the Phase Transformation in Single Particles of the Lithium Titanate Anode for Lithium-Ion Batteries. *ACS Appl. Energy Mater.* **2021,** *4* (1), 111–118. https://doi.org/10.1021/acsaem.0c02010.
67. Hruszkewycz, S. O.; Cha, W.; Andrich, P.; Anderson, C. P.; Ulvestad, A.; Harder, R.; Fuoss, P. H.; Awschalom, D. D.; Heremans, F. J. In Situ Study of Annealing-Induced Strain Relaxation in Diamond Nanoparticles Using Bragg Coherent Diffraction Imaging. *APL Mater.* **2017,** *5* (2), 026105. https://doi.org/10.1063/1.4974865.
68. Hruszkewycz, S. O.; Maddali, S.; Anderson, C. P.; Cha, W.; Miao, K. C.; Highland, M. J.; Ulvestad, A.; Awschalom, D. D.; Heremans, F. J. Strain Annealing of SiC Nanoparticles Revealed through Bragg Coherent Diffraction Imaging for Quantum Technologies. *Phys. Rev. Mater.* **2018,** *2* (8), 086001. https://doi.org/10.1103/PhysRevMaterials.2.086001.
69. Sun, T.; Jiang, Z.; Strzalka, J.; Ocola, L.; Wang, J. Three-Dimensional Coherent X-Ray Surface Scattering Imaging Near Total External Reflection. *Nat. Photon.* **2012,** *6* (9), 586–590. https://doi.org/10.1038/nphoton.2012.178.
70. Pfeiffer, F. X-Ray Ptychography. *Nat. Photon.* **2018,** *12* (1), 9–17. https://doi.org/10.1038/s41566-017-0072-5.
71. Rodenburg, J. M.; Hurst, A. C.; Cullis, A. G.; Dobson, B. R.; Pfeiffer, F.; Bunk, O.; David, C.; Jefimovs, K.; Johnson, I. Hard-X-Ray Lensless Imaging of Extended Objects. *Phys. Rev. Lett.* **2007,** *98* (3), 034801. https://doi.org/10.1103/PhysRevLett.98.034801.
72. Hruszkewycz, S. O.; Highland, M. J.; Holt, M. V.; Kim, D.; Folkman, C. M.; Thompson, C.; Tripathi, A.; Stephenson, G. B.; Hong, S.; Fuoss, P. H. Imaging Local Polarization in Ferroelectric Thin Films by Coherent X-Ray Bragg Projection Ptychography. *Phys. Rev. Lett.* **2013,** *110* (17), 177601. https://doi.org/10.1103/PhysRevLett.110.177601.
73. Tripathi, A.; Mohanty, J.; Dietze, S. H.; Shpyrko, O. G.; Shipton, E.; Fullerton, E. E.; Kim, S. S.; McNulty, I. Dichroic Coherent Diffractive Imaging. *Proc. Natl. Acad. Sci.* **2011,** *108* (33), 13393–13398. https://doi.org/10.1073/pnas.1104304108.
74. Hruszkewycz, S. O.; Holt, M. V.; Murray, C. E.; Bruley, J.; Holt, J.; Tripathi, A.; Shpyrko, O. G.; McNulty, I.; Highland, M. J.; Fuoss, P. H. Quantitative Nanoscale Imaging of Lattice Distortions in Epitaxial Semiconductor Heterostructures Using Nanofocused X-Ray Bragg Projection Ptychography. *Nano Lett.* **2012,** *12* (10), 5148–5154. https://doi.org/10.1021/nl303201w.
75. Hruszkewycz, S. O.; Allain, M.; Holt, M. V.; Murray, C. E.; Holt, J. R.; Fuoss, P. H.; Chamard, V. High-Resolution Three-Dimensional Structural Microscopy by Single-Angle Bragg Ptychography. *Nat. Mater.* **2017,** *16* (2), 244–251. https://doi.org/10.1038/nmat4798.
76. Deng, J.; Lo, Y. H.; Gallagher-Jones, M.; Chen, S.; Pryor, A., Jr.; Jin, Q.; Hong, Y. P.; Nashed, Y. S. G.; Vogt, S.; Miao, J.; Jacobsen, C. Correlative 3D X-Ray Fluorescence and Ptychographic Tomography of Frozen-Hydrated Green Algae. *Sci. Adv.* **2018,** *19*.
77. Robinson, I. K.; Vartanyants, I. A. Use of Coherent X-Ray Diffraction to Map Strain Fields in Nanocrystals. *Appl. Surf. Sci.* **2001,** *182,* 186–191.
78. Cherukara, M. J.; Cha, W.; Harder, R. J. Anisotropic Nano-Scale Resolution in 3D Bragg Coherent Diffraction Imaging. *Appl. Phys. Lett.* **2018,** *113* (20), 203101. https://doi.org/10.1063/1.5055235.
79. Harder, R.; Pfeifer, M. A.; Williams, G. J.; Vartaniants, I. A.; Robinson, I. K. Orientation Variation of Surface Strain. *Phys. Rev. B* **2007,** *76* (11), 115425. https://doi.org/10.1103/PhysRevB.76.115425.
80. Hofmann, F.; Phillips, N. W.; Harder, R. J.; Liu, W.; Clark, J. N.; Robinson, I. K.; Abbey, B. Micro-Beam Laue Alignment of Multi-Reflection Bragg Coherent Diffraction Imaging Measurements. *J. Synchrotron Radiat.* **2017,** *24* (5), 1048–1055. https://doi.org/10.1107/S1600577517009183.
81. Pateras, A.; Harder, R.; Cha, W.; Gigax, J. G.; Baldwin, J. K.; Tischler, J.; Xu, R.; Liu, W.; Erdmann, M. J.; Kalt, R.; Sandberg, R. L.; Fensin, S.; Pokharel, R. Combining Laue Diffraction with Bragg Coherent Diffraction Imaging at 34-ID-C. *J. Synchrotron Radiat.* **2020,** *27* (5), 1430–1437. https://doi.org/10.1107/S1600577520009844.
82. Yau, A.; Cha, W.; Kanan, M. W.; Stephenson, G. B.; Ulvestad, A. Bragg Coherent Diffractive Imaging of Single-Grain Defect Dynamics in Polycrystalline Films. *Science* **2017,** *356* (6339), 739–742. https://doi.org/10.1126/science.aam6168.
83. Cherukara, M. J.; Pokharel, R.; O'Leary, T. S.; Baldwin, J. K.; Maxey, E.; Cha, W.; Maser, J.; Harder, R. J.; Fensin, S. J.; Sandberg, R. L. Three-Dimensional X-Ray Diffraction Imaging of Dislocations in Polycrystalline Metals under Tensile Loading. *Nat. Commun.* **2018,** *9* (1), 3776. https://doi.org/10.1038/s41467-018-06166-5.
84. Cha, W.; Ulvestad, A.; Allain, M.; Chamard, V.; Harder, R.; Leake, S. J.; Maser, J.; Fuoss, P. H.; Hruszkewycz, S. O. Three Dimensional Variable-Wavelength X-Ray Bragg Coherent Diffraction Imaging. *Phys. Rev. Lett.* **2016,** *117* (22), 225501. https://doi.org/10.1103/PhysRevLett.117.225501.
85. Lauraux, F.; Labat, S.; Yehya, S.; Richard, M.-I.; Leake, S. J.; Zhou, T.; Micha, J.-S.; Robach, O.; Kovalenko, O.; Rabkin, E.; Schülli, T. U.; Thomas, O.; Cornelius, T. W. Simultaneous Multi-Bragg Peak Coherent X-Ray Diffraction Imaging. *Crystals* **2021,** *11* (3), 312. https://doi.org/10.3390/cryst11030312.
86. Altantzis, T.; Lobato, I.; De Backer, A.; Béché, A.; Zhang, Y.; Basak, S.; Porcu, M.; Xu, Q.; Sánchez-Iglesias, A.; Liz-Marzán, L. M.; Van Tendeloo, G.; Van Aert, S.; Bals, S. Three-Dimensional Quantification of the Facet Evolution of Pt Nanoparticles in a Variable Gaseous Environment. *Nano Lett.* **2019,** *19* (1), 477–481. https://doi.org/10.1021/acs.nanolett.8b04303.
87. Ulvestad, A.; Sasikumar, K.; Kim, J. W.; Harder, R.; Maxey, E.; Clark, J. N.; Narayanan, B.; Deshmukh, S. A.; Ferrier, N.; Mulvaney, P.; Sankaranarayanan, S. K. R. S.; Shpyrko, O. G. In Situ 3D Imaging of Catalysis Induced Strain in Gold Nanoparticles. *J. Phys. Chem. Lett.* **2016,** *7* (15), 3008–3013. https://doi.org/10.1021/acs.jpclett.6b01038.
88. Yaguchi, T.; Suzuki, M.; Watabe, A.; Nagakubo, Y.; Ueda, K.; Kamino, T. Development of a High Temperature-Atmospheric Pressure Environmental Cell for High-Resolution TEM. *J. Electron Microsc.* **2011,** *60* (3), 217–225. https://doi.org/10.1093/jmicro/dfr011.
89. Rochet, A.; Suzana, A. F.; Passos, A. R.; Kalile, T.; Berenguer, F.; Santilli, C. V.; Pulcinelli, S. H.; Meneau, F. In Situ Reactor to Image Catalysts at Work in Three-Dimensions by Bragg Coherent X-Ray Diffraction. *Catal. Today* **2019,** *336,* 169–173. https://doi.org/10.1016/j.cattod.2018.12.020.
90. Strasser, P.; Koh, S.; Anniyev, T.; Greeley, J.; More, K.; Yu, C.; Liu, Z.; Kaya, S.; Nordlund, D.; Ogasawara, H.; Toney, M. F.; Nilsson, A. Lattice-Strain Control of the Activity in Dealloyed Core–Shell Fuel Cell Catalysts. *Nat. Chem.* **2010,** *2* (6), 454–460. https://doi.org/10.1038/nchem.623.

91. Abuin, M.; Kim, Y. Y.; Runge, H.; Kulkarni, S.; Maier, S.; Dzhigaev, D.; Lazarev, S.; Gelisio, L.; Seitz, C.; Richard, M.-I.; Zhou, T.; Vonk, V.; Keller, T. F.; Vartanyants, I. A.; Stierle, A. Coherent X-Ray Imaging of CO-Adsorption-Induced Structural Changes in Pt Nanoparticles: Implications for Catalysis. *ACS Appl. Nano Mater.* **2019,** *2* (8), 4818–4824. https://doi.org/10.1021/acsanm.9b00764.
92. Kawaguchi, T.; Keller, T. F.; Runge, H.; Gelisio, L.; Seitz, C.; Kim, Y. Y.; Maxey, E. R.; Cha, W.; Ulvestad, A.; Hruszkewycz, S. O.; Harder, R.; Vartanyants, I. A.; Stierle, A.; You, H. Gas-Induced Segregation in Pt-Rh Alloy Nanoparticles Observed by *In Situ* Bragg Coherent Diffraction Imaging. *Phys. Rev. Lett.* **2019,** *123* (24), 246001. https://doi.org/10.1103/PhysRevLett.123.246001.
93. Clark, J. N.; Ihli, J.; Schenk, A. S.; Kim, Y.-Y.; Kulak, A. N.; Campbell, J. M.; Nisbet, G.; Meldrum, F. C.; Robinson, I. K. Three-Dimensional Imaging of Dislocation Propagation during Crystal Growth and Dissolution. *Nat. Mater.* **2015,** *14* (8), 780–784. https://doi.org/10.1038/nmat4320.
94. Yuan, K.; Lee, S. S.; Cha, W.; Ulvestad, A.; Kim, H.; Abdilla, B.; Sturchio, N. C.; Fenter, P. Oxidation Induced Strain and Defects in Magnetite Crystals. *Nat. Commun.* **2019,** *10* (1), 703. https://doi.org/10.1038/s41467-019-08470-0.
95. Cha, W.; Liu, Y.; You, H.; Stephenson, G. B.; Ulvestad, A. Dealloying in Individual Nanoparticles and Thin Film Grains: A Bragg Coherent Diffractive Imaging Study. *Adv. Funct. Mater.* **2017,** *27* (25), 1700331. https://doi.org/10.1002/adfm.201700331.
96. Ulvestad, A.; Cho, H. M.; Harder, R.; Kim, J. W.; Dietze, S. H.; Fohtung, E.; Meng, Y. S.; Shpyrko, O. G. Nanoscale Strain Mapping in Battery Nanostructures. *Appl. Phys. Lett.* **2014,** *104* (7), 073108. https://doi.org/10.1063/1.4866030.
97. Ulvestad, A.; Clark, J. N.; Singer, A.; Vine, D.; Cho, H. M.; Harder, R.; Meng, Y. S.; Shpyrko, O. G. In Situ Strain Evolution during a Disconnection Event in a Battery Nanoparticle. *Phys. Chem. Chem. Phys.* **2015,** *17* (16), 10551–10555. https://doi.org/10.1039/C5CP00372E.
98. Wang, L.; Dai, A.; Wang, J.; Xu, W.; Lee, S.; Cha, W.; Harder, R.; Liu, T.; Ren, Y.; Yin, G.; Zuo, P.; Wang, J.; Lu, J. Structural Distortion Induced by Manganese Activation in Lithium-Rich Layered Cathode. *J. Am. Chem. Soc.* **2020.** https://doi.org/10.1021/jacs.0c05498. jacs.0c05498.
99. Clark, J. N.; Beitra, L.; Xiong, G.; Higginbotham, A.; Fritz, D. M.; Lemke, H. T.; Zhu, D.; Chollet, M.; Williams, G. J.; Messerschmidt, M.; Abbey, B.; Harder, R. J.; Korsunsky, A. M.; Wark, J. S.; Robinson, I. K. Ultrafast Three-Dimensional Imaging of Lattice Dynamics in Individual Gold Nanocrystals. *Science* **2013,** *341* (6141), 56–59. https://doi.org/10.1126/science.1236034.
100. Cherukara, M. J.; Sasikumar, K.; Cha, W.; Narayanan, B.; Leake, S. J.; Dufresne, E. M.; Peterka, T.; McNulty, I.; Wen, H.; Sankaranarayanan, S. K. R. S.; Harder, R. J. Ultrafast Three-Dimensional X-Ray Imaging of Deformation Modes in ZnO Nanocrystals. *Nano Lett.* **2017,** *17* (2), 1102–1108. https://doi.org/10.1021/acs.nanolett.6b04652.
101. Clark, J. N.; Beitra, L.; Xiong, G.; Fritz, D. M.; Lemke, H. T.; Zhu, D.; Chollet, M.; Williams, G. J.; Messerschmidt, M. M.; Abbey, B.; Harder, R. J.; Korsunsky, A. M.; Wark, J. S.; Reis, D. A.; Robinson, I. K. Imaging Transient Melting of a Nanocrystal Using an X-Ray Laser. *Proc. Natl. Acad. Sci.* **2015,** *112* (24), 7444–7448. https://doi.org/10.1073/pnas.1417678112.
102. Kang, J.; Carnis, J.; Kim, D.; Chung, M.; Kim, J.; Yun, K.; An, G.; Cha, W.; Harder, R.; Song, S.; Sikorski, M.; Robert, A.; Thanh, N. H.; Lee, H.; Choi, Y. N.; Huang, X.; Chu, Y. S.; Clark, J. N.; Song, M. K.; Yoon, K. B.; Robinson, I. K.; Kim, H. Time-Resolved in Situ Visualization of the Structural Response of Zeolites During Catalysis. *Nat. Commun.* **2020,** *11* (1), 5901. https://doi.org/10.1038/s41467-020-19728-3.
103. Eriksson, M.; van der Veen, J. F.; Quitmann, C. Diffraction-Limited Storage Rings – a Window to the Science of Tomorrow. *J. Synchrotron Radiat.* **2014,** *21* (5), 837–842. https://doi.org/10.1107/S1600577514019286.
104. Tavares, P. F.; Leemann, S. C.; Sjöström, M.; Andersson, Å. The MAX IV Storage Ring Project. *J. Synchrotron Radiat.* **2014,** *21* (5), 862–877. https://doi.org/10.1107/S1600577514011503.
105. Liu, L.; Milas, N.; Mukai, A. H. C.; Resende, X. R.; de Sá, F. H. The Sirius Project. *J. Synchrotron Radiat.* **2014,** *21* (5), 904–911. https://doi.org/10.1107/S1600577514011928.
106. Raimondi, P. ESRF-EBS: The Extremely Brilliant Source Project. *Synchrotron Radiation News* **2016,** *29* (6), 8–15. https://doi.org/10.1080/08940886.2016.1244462.
107. Tanaka, H.; Ishikawa, T.; Goto, S.; Takano, S.; Watanabe, T.; Yabashi, M. SPring-8 Upgrade Project. *Proceedings of the 7th International Particle Accelerator Conference, IPAC2016;* 2016; pp 2867–2870**.** https://doi.org/10.18429/JACoW-IPAC2016-WEPOW019.
108. Dietze, S. H.; Shpyrko, O. G. Coherent Diffractive Imaging: Towards Achieving Atomic Resolution. *J. Synchrotron Radiat.* **2015,** *22* (6), 1498–1508. https://doi.org/10.1107/S1600577515017336.

Всё для Победы!
НАРОДНЫЙ ФРОНТ
https://pobeda.onf.ru/
LET'S HELP THE RUSSIA

10.07 Panoramic (in beam) studies of materials synthesis

Mercouri G. Kanatzidis and Rebecca McClain, Department of Chemistry, Northwestern University, Evanston, IL, United States

© 2023 Elsevier Ltd. All rights reserved.

10.07.1	Introduction	187
10.07.2	Experimental techniques and analytical methods	188
10.07.3	Oxides	191
10.07.4	Chalcogenides	192
10.07.5	Other compositions	197
10.07.6	Conclusion and outlook	197
References		198

Abstract

As the interest in rational synthesis for solid-state materials accelerates, there is an urgent need to understand the design principles concealed within these reactions. In situ material synthesis provides such an avenue to not only uncover these assembling rules, but also for finding new materials even in seemingly familiar phase spaces. Historically, this technique was largely employed for crystallization observations. However, as described in this chapter, the increased accessibility of in-house diffractometer setups—and consequent decreased requirement for synchrotron or spallation sources—enables the science community to apply this powerful technique to their chemical class of interest (e.g. oxides, chalcogenides). As detailed in the chapter, all in situ material synthesis measurements yield novel information that build toward an overall understanding of the driving force for reaction progressions and assembly rules. These advances, along with technological improvements, point the way toward more wide-ranging studies to fully flesh out the design principles that can be applied to larger families of materials, as well as combinatorial studies with complementary probes or calculations that can guide or confirm these design principles to enable rational design of complex solid-state materials.

10.07.1 Introduction

The current technological revolution demands new materials with higher efficiencies and new capabilities. To that point, there have been many research thrusts centered on material design correlated with targeted properties,[1–4] and recently there has been a push to utilize machine learning to design materials ab initio.[5–7] However, the synthetic insight needed to realize these compounds does not yet exist for most systems. This is due to the historically ex situ nature of traditional solid-state synthesis, in which only indirect information about the reaction pathways is obtainable. In situ techniques can address this dearth of insight as they are powerful tools for the direct observation of changes in long- or short-range order over the course of a reaction. Depending on the technique(s) employed, information gleaned may include crystallization kinetics and/or processes (e.g. such as those effecting particle size or morphology), nucleation kinetics and/or processes, changes in coordination environments, or observation of transient phases, including competitive product or polymorph formation.[8–13] With the ability to uncover transient phases, in situ approaches neatly address both the themes of materials discovery and synthetic insight toward the rational design of materials.

Traditionally, syntheses of inorganic materials have been determined through heuristic means, with knowledge of only the inputs (starting materials) and outputs (final products). Using this approach, the observer does not gain intuition for the reaction progression leading to products. The observer is not privy to information on when the product(s) begin to grow or, moreover, if transient phases form that do not remain on completion of the reaction. Previously, product crystal growth was monitored by quenching mid-reaction. These ex situ studies can be conducted in laboratory conditions and may also reveal previously unknown transient phases, such as polymorphs or intermediate phases. However, these studies are performed under the assumption that quenching does not alter the reaction or crystal growth process. In contrast, in situ studies enable continuous monitoring of the reactions with minimal or no alteration to reaction conditions.

Using in situ powder X-ray diffraction, all crystalline phases, even transient ones, may be observed in snapshots from simultaneously collected diffraction data. This "panoramic" view of phase evolution not only illuminates the reaction progression, but also unveils possible metastable phases. The realization of metastable phases has been sought through methods such as *chimie douce*,[14] "turning down the heat,"[15] flux syntheses,[16–20] and metathesis reactions,[21,22] as they widen the accessible compositional space. As more panoramic syntheses are conducted in increasingly broader compositional space, reaction progressions can be systematically cataloged to build understanding of syntheses. Comparisons can be drawn within similar reaction types to determine patterns in ordering principles and those ordering principles will then subsequently be tested, as illustrated in Fig. 1. Ultimately, these ordering principles combine to formulate synthetic design principles akin to retrosynthesis used by organic chemists. The experimental

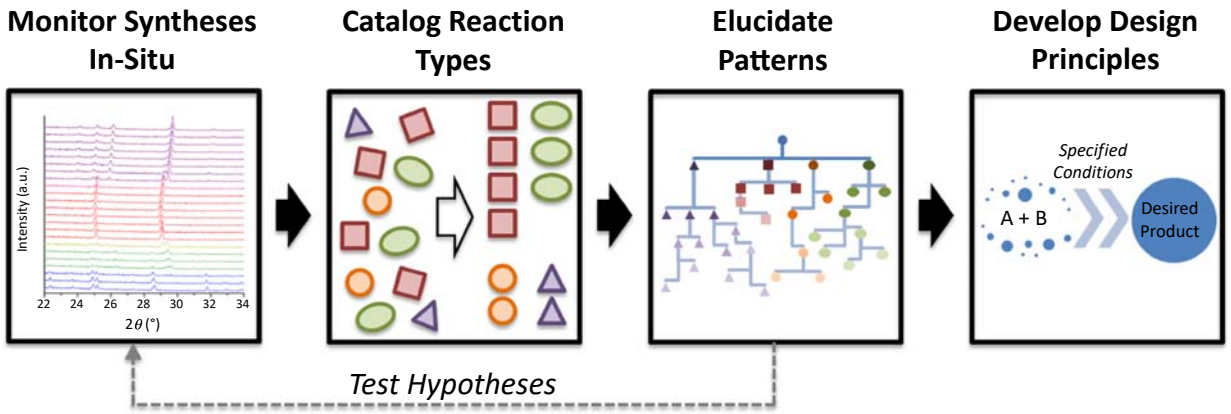

Fig. 1 In situ panoramic synthesis: a route to rational synthesis of inorganic extended solids.

synthesis design strategies compliment of this the ongoing in silico materials design efforts however a lot of new information will need to be generate and added before theory and experiment can converge to a single coherent synthesis science.[23]

This chapter will focus on in situ X-ray or neutron diffraction, as other panoramic methods have been summarized elsewhere.[8,24,25] Historically, this panoramic technique was primarily used for hydrothermal syntheses of molecular sieves, such as zeolites. Early studies sought to exploit control of product particle size, crystal growth rate, structural transformations, porosity, and/or morphology.[26,27] Later studies shifted to enlightening the pathways to these materials.[13,26,28] As studies of panoramic syntheses continue to proliferate, systematic alterations to the synthetic conditions should be applied for optimal comparison across similar reaction types. Known syntheses can then be probed by altering parameters to evaluate the phase and energetic landscape. Such parameterization can include the effects of (1) starting materials, whether that be their ratio[29] or composition,[30] (2) heating conditions, or (3) use of non-reactive fluxes.[31]

In the following sections, we explore and summarize the panoramic syntheses that have been reported to date. The experimental and analytical requirements are detailed, followed by a discussion of the in situ diffraction studies reported for oxides, chalcogenides, heteroanions as well as intermetallics and pnictogens, which have been grouped according to these chemical classes. These works highlight the utility of panoramic synthesis to derive the chemistry that drives compound formation in these diverse systems, showcasing this technique as a pathway toward materials by design.

10.07.2 Experimental techniques and analytical methods

Pivotal to the success of this technique is the spatial and temporal resolution of the instrument's detector and optics. The spatial resolution of the detector is crucial for distinguishing Bragg peaks, particularly when using high energy X-ray sources. The spatial resolution of the optics is also important: the radiation source should be focused on a small area of the sample, particularly when working with reaction vessels such as capillaries. High temporal resolution data collection is desired to accurately capture phase evolution and glean insight into the kinetics of a reaction. Overall, the data collection rate for two-dimensional detectors, such as image plates, pixel array detectors, and charge-coupled devices (CCDs), are higher than that of strip or point detectors. Near-simultaneous data collection[32,33] is coming to fruition with the continually improved detector technologies.

Panoramic syntheses can be conducted using in-house radiation sources as well as synchrotron or spallation sources.[34] In-house in situ experiments have been conducted using both angular[10,29,30,35] and energy dispersive[10,36,37] X-ray diffractometers coupled with a furnace attachment. Angular dispersive X-ray diffraction (ADXRD) is the most common detection method for in-house X-ray diffractometers. In ADXRD, a monochromatic energy beam irradiates the sample and a diffractogram is measured at multiple scattering angles. Energy dispersive XRD (EDXRD), on the other hand, uses a fixed scattering angle and irradiates the sample using a broad energy range. The fixed scattering angle enables a faster acquisition time relative to ADXRD. When working with highly attenuating samples, such as heavy metals, or when thick sample vessels must be penetrated such as with hydrothermal reactions, the in-house radiation source needs to be of sufficiently high energy to penetrate the sample. Commonly, molybdenum and silver radiation are used in place of copper radiation. In cases where the samples are too attenuating for these sources, radiation from particle accelerators can be employed. Neutrons, from reactors or spallation sources, are usually intrinsically more penetrating than X-rays, due to their weak interaction with mater, and synchrotrons can provide high fluxes of X-rays at energies greater than those readily available from laboratory tubes sources, providing greater penetrating power.[34]

While powder diffraction data for materials under non-ambient conditions have been recorded since the earliest days of X-ray and neutron diffraction, panoramic synthesis requires more specialized equipment.[38,39] Depending on the reaction type, a specific, specialized reaction cell is required. To date, hydrothermal, bulk solid-state, gas-flow, flux, and self-propagating high-temperature syntheses have been conducted in situ. Capillary reactors have been coupled with X-ray sources for hydrothermal, solid-state, flux,

and gas-flow syntheses.[10,40] The capillary reactors use a furnace, resistive coil heater, or hot air blower. Designs for X-ray furnaces are widely available in the literature (Fig. 2)[41,42]; in addition, furnaces are commercially available as attachments for in-house diffractometers. Resistive coil heaters, such as those designed by Chupas and coworkers, can be used with flow cells or furnaces, depending on if the starting materials are placed in the cell's capillary or sealed in an inner capillary (Figs. 3 and 4).[40] Other X-ray diffraction panoramic syntheses were conducted, on flat sample holders or on layers mounted on a resistive strip heater, to monitor gas-flow or self-propagating high-temperature syntheses.[43–47] Hydrothermal reaction cells have been developed as pressure cells or flow cells, as shown in a representative schematic in Fig. 5.[13,24,28,34,37,48–51]

While in situ diffraction techniques detect the phase evolution of crystalline materials, changes in local order or the growth and identity of amorphous phases are inaccessible with these techniques. Therefore, complementary in situ probes are crucial when evaluating local order and the amorphous phases that may also inform the guiding synthetic principles of a reaction.[10,23,34] Spectroscopic techniques, like Raman or infrared spectroscopy, can indicate functional groups or bonding schemes present in a reaction. Simultaneous scattering techniques, such as small-angle X-ray scattering, can distinguish between amorphous and crystalline nanostructure. Absorption techniques, such as X-ray absorption spectroscopy, can determine the local coordination or electronic structure. Simultaneous collection of these complementary in situ probes is optimal as it guarantees the reaction conditions are exactly matched.

Beyond these, other experimental approaches deserve mention due to their value when preparing for, or trying to understand, an in situ study. They include co-refinements using in situ neutron and X-ray diffraction data, where the different dependence of scattering power on atomic number for these two techniques can enable the distribution of elements over the available crystallographic sites to be determined even in complex materials. X-ray scattering techniques, such as Pair Distribution Function, can also be paired with diffraction techniques to elucidate changes in local structure. Thermal analyses such as differential thermal analyses (DTA) and differential scanning calorimetry (DSC) indicate when an exothermic or endothermic event occurs. These events may indicate phase formation, phase transition, or melting/crystallization. DSC also enables the calculation of reaction enthalpies for these events, which provides insight into the driving energetics of the reaction. Knowledge of the temperatures for the events also proves advantageous, as it indicates noteworthy temperature points for further study. This is particularly useful for in situ diffraction setups that do not have continuous collection, but stepwise collection.

Conducting successful panoramic syntheses involves surmounting many challenges including sample size effects, adverse reactions (such as reactions with the container and incongruent evaporation), poor signal-to-noise ratio, and sample movement. For X-ray diffraction, very small samples are investigated. Therefore, obtaining data from a representative portion of the reaction mixture may be difficult and the results may be difficult to reproduce. In contrast, neutron diffraction is not similarly limited. This is because neutron sources produce large, relatively weak neutron beams, so the sample volume required for neutron diffraction is inherently large and better reflects the behavior of a bulk reaction mixture. The selection of the sample vessel must also be thoughtfully considered, as reactions between the reaction mixture and vessel are possible. For example, the attack of glass capillaries by alkali binaries[54] has been observed, and the attack of silica-containing capillaries by some oxides would be expected. Carbon coating the capillary can mitigate these problems. Care must be taken not only when preparing the vessel, but also the reaction mixture. When using fluxes or highly attenuating samples, signal-to-noise ratios may suffer,[55] and dilution should be considered. Glassy carbon and ground fused silica are amorphous and have been used as diluents. Test runs should be done ex situ prior to the in situ experiment to ensure that there is no reaction between the reaction materials and the diluent. Finally, when measuring highly mobile samples such as reactions using fluxes or those going to the melt, one must be careful to ensure the reaction mixture does not move outside the beam during data collection.[56] When possible, the sample vessel should be oriented vertically or the sample should be rastered for full data collection.

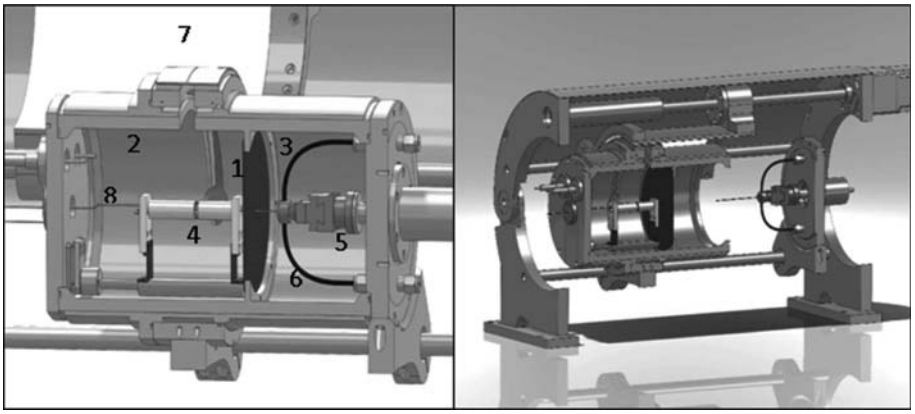

Fig. 2 Left: cross-sectional view of the imaging-plate holder and vacuum chamber. The main components of the experimental station are: (1) thermal barrier; (2) hot zone; (3) cold zone; (4) heating element; (5) sample alignment stage; (6) gas-flow system; (7) the detector system which consists of a translating curved holder that supports the imaging plate; (8) thermocouple. Right: cross-sectional view of the open chamber.[41]

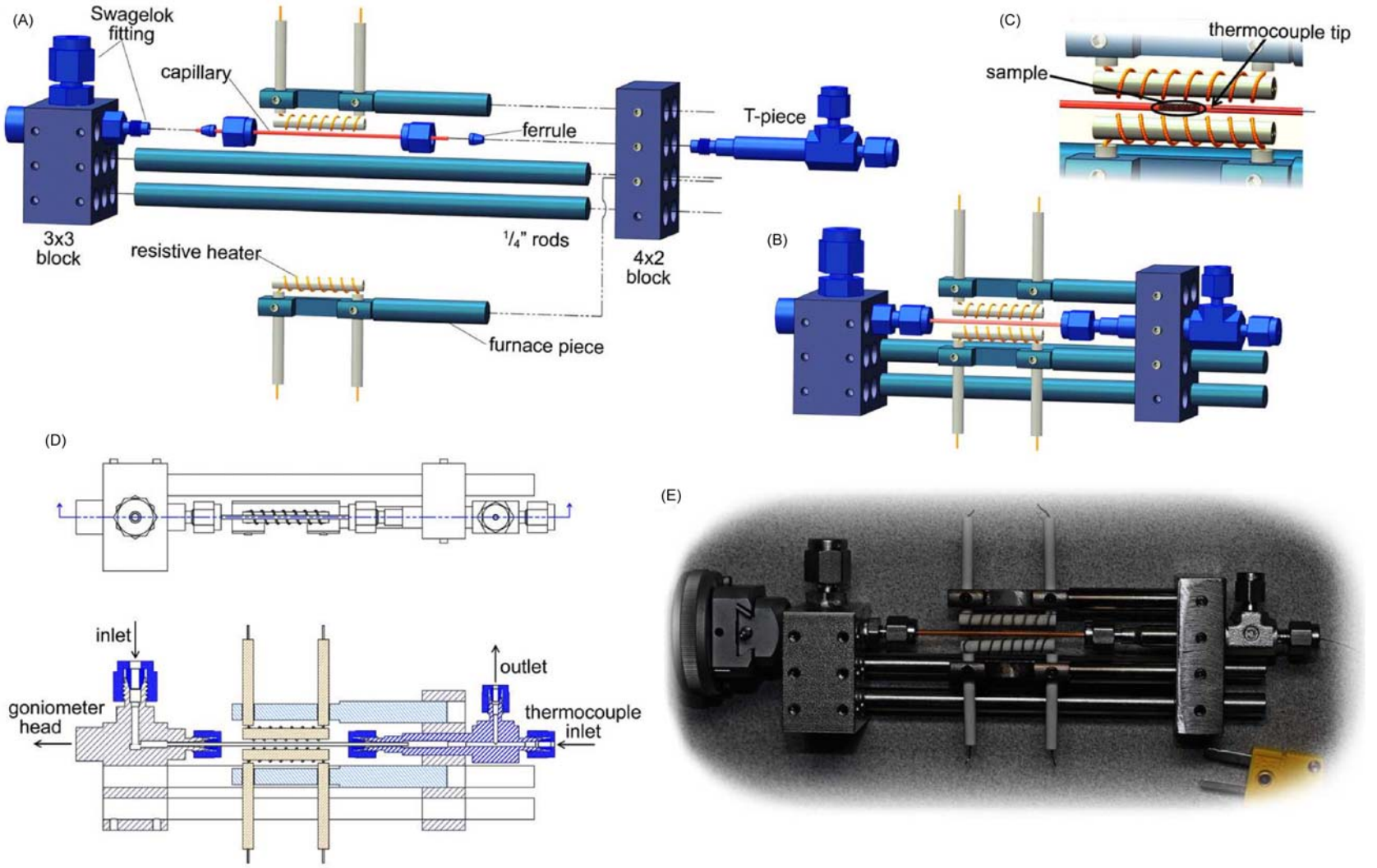

Fig. 3 (A) An "exploded" representation of the flow-cell/furnace components, indicating how they fit together; (B) the fully assembled flow-cell/furnace; (C) an expanded view of the sample region, indicating the relative position of the sample and thermocouple tip within the furnace hot zone; (D) a top view of the flow-cell/furnace, with a corresponding cross section through the sample plane showing the gas/fluid path; (E) a photograph of the flow-cell/furnace mounted in a goniometer head. Heat shields have been omitted for clarity.[40]

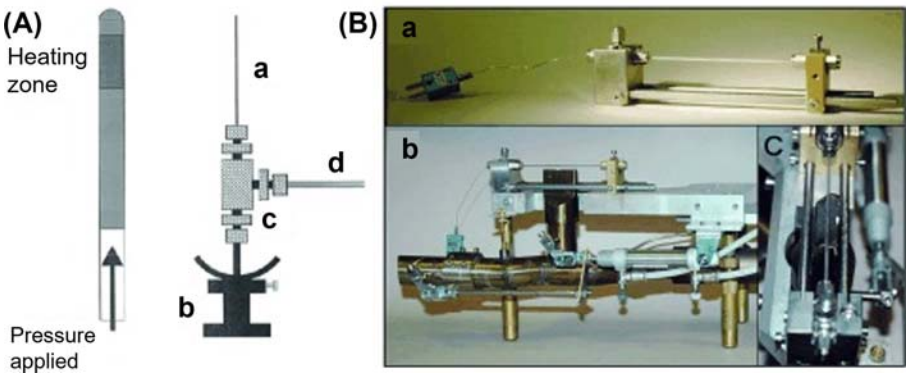

Fig. 4 (A) First published in situ capillary setup by Norby et al.[52] Capillary mounted on goniometer. (a) Capillary, measuring 0.5–1 mm; (b) goniometer head; (c) Swagelok T-piece; and (d) pressure tube. (B) In situ capillary setup by Becker et al.[53] capable of reaching supercritical conditions for H_2O and other solvents.[10]

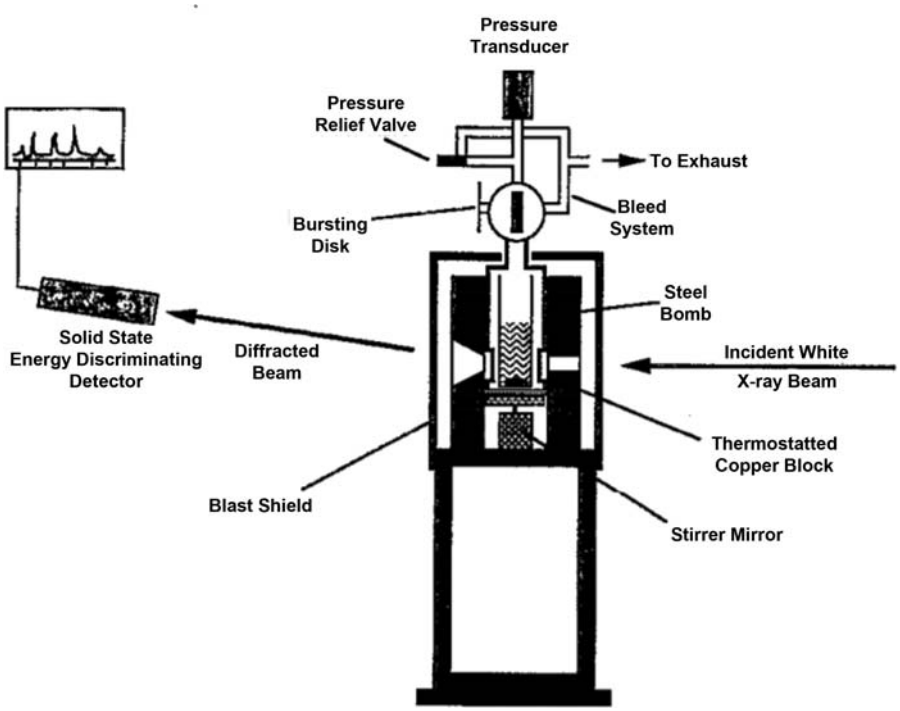

Fig. 5 Schematic of pressure cell developed for hydrothermal in situ reactions.[37]

10.07.3 Oxides

In situ studies of oxide syntheses first became prominent in hydrothermal and solvothermal systems.[24,28,51,57] These studies tried to understand the crystallization mechanisms of mesoporous silicates and zeolites. In these early studies, the formation pathway was observed with the desire to understand the crystallization timescale or product morphology. In situ studies were then applied to solid-phase (e.g. powder) and flux reactions. These early studies were primarily explorative, designed to unveil the reaction pathway and enable our understanding of solid-state synthesis.

Bieringer and coworkers has been prolific in their in situ work with solid oxides. Their earlier studies observed the formation pathway for a number of bixbyites.[44–46,58,59] They also noted intermediate defect phases in the AVO_3 (A = Sc, In),[44] $ScVO_4$,[45] and $YPrO_{3+\delta}$[58,59] formation reactions and high temperature phase transformations in the $Sc_{(1-x)}Lu_xVO_3$ ($0.0 \leq x \leq 1.0$) reduction reactions.[46] Their diffraction work, using co-refinement of X-ray and neutron data, provides a foundation for the preparation of metastable bixbyite and thermodynamically stable perovskite and bixbyite structures. They also begin to catalog oxygen defects in the $YPrO_{3+\delta}$ system with an eye toward oxygen defect control. In these studies, they follow the unit cell parameter evolution during oxygen uptake and loss in $YPrO_{3+\delta}$ and also reported, for the first time, a cation site splitting upon oxygenation in this system.[58,59]

During their investigations of oxide syntheses, Bieringer and coworkers also observed an unexplained transient phase in their $BaCe_{1-x}M_xO_{3-x}$ (M = La, In) reactions.[60] Using a combination of in situ X-ray and neutron diffraction, as well as the complementary probes thermogravimetric analysis and X-ray photoelectron spectroscopy, they confirmed that the materials were reacting with the platinum heater to form the double perovskite, Ba_2CePtO_6. This finding is surprising as their reaction conditions, ranging 950–1300 °C, are regarded low for a reaction with platinum.[60] Through further exploration, they found that oxygen atmosphere is required for formation and the double perovskite does not form in dynamic vacuum.

Bieringer and coworkers also discovered intermediate phases during the reduction and oxidation of $InVO_4$.[43] The previously unknown $InVO_3$ was revealed as a transient phase during the reduction of $InVO_4$ and, with the synthetic details provided by in situ materials synthesis, $InVO_3$ was synthesized.[43] The in situ diffraction data shows that $InVO_3$ begins to form at 500 °C and disappears by 800 °C, where it decomposes to In_2O_3 and V_2O_3. Normally, for compounds in the AVO_3 series (A = rare earth metals), reaction temperatures over 1000 °C are employed. The in situ observation of this series enabled the discovery and subsequent bulk synthesis of $InVO_3$.

In situ diffraction, using neutrons, was also employed to study reactions forming $La_4Mo_2O_{11}$ and $Ce_4Mo_2O_{11}$.[55] Initially, zur Loye and coworkers set out to better understand single crystal growth in a flux. However, the in situ study uncovered several transient phases, which they were able to isolate using the conditions laid out by the in situ reaction. In these studies, zur Loye and coworkers also observed different transient phases based on reagent-to-flux ratio while maintaining the same final product, thereby incidentally investigating the directing effects of the starting materials on transient phase formation.[55] They found that higher ratios of flux led to improved dissolution of starting materials and, consequently, increased interaction of cations and the reducing agent to form reduce metastable phases.[55]

Similar to zur Loye's work, O'Hare and coworkers altered the flux identity during the synthesis of the N = 3 Aurivillius phase, $Bi_5Ti_3Fe_{0.5}Cr_{0.5}O_{15}$.[56] They showed that the nature of the flux influences the composition of the intermediate phases. The studies showed that certain intermediates (β*-Bi_2O_3 and $Bi_4Ti_3O_{12}$) are necessary for the successful formation of the product phase, while others form adventitiously. This work also discovered a new metastable phase, Ti-stabilized β*-Bi_2O_3, with the composition $Bi_{7.68}Ti_{0.32}O_{12.16}$.[56]

Building on the groundwork laid by other researchers who have explored how reaction parameter(s) influence the outcome, Neilson and coworkers conducted a thorough exploration and consequential mapping of $YMnO_3$ formation during metathesis based syntheses. They began their work with ex situ experiments investigating the effect of precursor on product selectivity in the reaction $YCl_3 + Mn_2O_3 + A_2CO_3$ (A = Li, Na, K).[61] They found that lithium carbonate directed the product to the orthorhombic perovskite $YMnO_3$ at temperatures between 550 °C and 850 °C, and that sodium carbonate led to pyrochlore $Y_2Mn_2O_7$ at 650 °C. No apparent selectivity was observed for K_2CO_3.[61] This was also seen by data mining and computational studies across all anion types.[62] They then built on this knowledge and focused on the formation of orthorhombic $YMnO_3$, by monitoring the lithium carbonate reaction in situ.

When exploring perovskite $YMnO_3$ formation, Neilson and coworkers further studied material effects, by investigating the reaction pathway for $Mn_2O_3 + 2.2YCl_3 \cdot 6H_2O + 3Li_2CO_3$ in oxygen and helium atmospheres.[63] The reaction first progresses by the reactivity of YCl_3 to form YOCl, followed by the formation of $LiMnO_2$, and ultimately the melting of LiCl and YMnO3 formation. Under an O_2 atmosphere, the reaction follows a direct route, while under He, $LiMnO_2$ is not formed and Mn_2O_3 reacts to form the spinel Mn_3O_4. It was also observed that the two atmospheres led to different rates of orthorhombic and hexagonal $YMnO_3$ polymorph growth. The over-oxidized orthorhombic phase, unsurprisingly, grows faster in an O_2 atmosphere, while the growth rates are about equal under He. Neilson and coworkers thereby discovered that both the identity of the carbonate, in the assisted metathesis reaction, and the atmosphere determine product identity.[63] The analysis of the crystalline intermediates led to two hypotheses for the reaction pathway leading to $YMnO_3$ formation: (1) $Y_2O_3 + Mn_2O_3$ in LiCl flux or (2) YOCl + $LiMnO_2$. In situ studies of these two pathways showed that both led to the target $YMnO_3$, but the ternary metathesis reaction (reaction 2) proceeds to the final product faster than the flux reaction (reaction 1). The faster conversion in reaction 2 can be rationalized since both starting materials adopt layered structures that facilitate increased diffusion when compared to the structurally dense oxides involved in reaction 1. Their work to date has examined three methods for forming $YMnO_3$: assisted metathesis (using YCl_3), ternary metathesis (using YOCl), and LiCl flux. They also conducted many ex situ reactions with YCl_3 under O_2 at various temperatures to determine the distribution of $YMnO_3$ structure types. Neilson and coworkers further built on their work, demonstrating that both the structure of the $LiMnO_2$ precursor and the reaction temperature influence the proportions of hexagonal and orthorhombic $YMnO_3$ in the product.[64] They achieved selectivity in their reactions, specifically the concentration of defects in the $YMnO_3$ products, as well as tuning the spinel intermediate composition.[64]

10.07.4 Chalcogenides

Chalcogenide phase spaces have been underexplored using in situ studies. However, more panoramic syntheses have been conducted recently, with increasing complexity as the field evolves from simply exploring systems for materials discovery to more pointed targets, such as the effect of precursors.[29,30,32,65] These studies have uncovered structural intermediates providing insights into the reaction pathway, proposed a tolerance factor for whether a material's cations order or disorder on a given site, and demonstrated that the phase providing the highest change in Gibbs energy in the shortest time forms first. Overwhelmingly, these in situ diffraction studies show that there are significant opportunities for new insights and discoveries in chalcogenide systems. Here we organize

the discussion of these studies by their intended or actual outcomes, from simple exploratory materials discovery, to systematic investigations of precursors and the mechanistic principles that underlie reactions.

Early studies in the chalcogenide phase space sought to reveal and capitalize on the opportunity for materials discovery using panoramic synthesis.[32,33] These studies explored previously well-investigated systems by varying the ratios between precursors to tease out new materials. For example, Haynes et al. targeted a previously discovered $Cs_2SnP_2Se_6$ composition and explored the phase space by reacting increasing amounts of tin with an alkali metal flux (nominally Cs_2Se_2) and a glassy phosphoselenide (PSe_2).[33] As shown in Fig. 6A and B, a plethora of transient intermediates appear over the course of this single reaction and six new compounds were discovered. Haynes et al. isolated three of the new compounds using information gleaned from the in situ studies. The formation temperature was identified for each compound as well as indications if the compound would be rich or poor in specific elements based on the compositions of concurrent phases.

Sometimes in situ studies lead to surprising discoveries. A study by Bhutani et al. sought to combine panoramic synthesis with predictive computational calculations to target the first ternary in the Ba−Ru−S phase space.[35] Two reactions were conducted with nominal compositions matching those of the predicted compounds $BaRu_2S_2$ and $BaRuS_3$, to determine if they formed as a transient intermediate. No ternary was found; however, a high temperature polymorph of BaS_2 was discovered and formed in both reactions.

Shoemaker et al. also demonstrated the opportunities that in situ studies provide for materials discovery while monitoring the effect of precursor ratios on phase formation in the K−Cu−S and K−Sn−S composition spaces.[32] Their work investigated the reactions $M + x\ K_2S_3$ and $M + x\ K_2S_5$, where M is Cu or Sn and x equals 1 or 5. For the Cu: K_2S_3 reactions, increasing the ratio from 1:1 to 1:5 did not alter the fundamental reaction progression. For both reactions, KCu_3S_2 forms first, followed by the appearance of a new phase, $K_3Cu_4S_4$, then subsequently their dissolution and, ultimately, $K_3Cu_8S_6$ formation (Fig. 6A and B). However, the higher flux ratio shortens the temperature range over which KCu_3S_2 and $K_3Cu_4S_4$ appear, and reintroduces KCu_3S_2 upon cooling. Moreover, when the flux was exchanged for one with a longer sulfur chain and lower melting point (K_2S_5), the only ternary formed was KCu_4S_3, which has little structural resemblance to those formed in the previous experiment with K_2S_3. Increasing the amount of K_2S_5 flux did not alter the temperature range over which the ternary appears, as observed in the previous experiment, but it did suppress the crystallization of KCu_4S_3 and, instead, yielded a K−Cu−S glass.

The panoramic view of the K−Sn−S compositional space yielded three new ternaries and the study, in total, led to the discovery of four new ternaries.[32] The reaction of $Sn + K_2S_3$ produced two new compounds: $K_4Sn_2S_6$ and $K_6Sn_2S_7$. The former was isolated using the "recipe" suggested by the in situ conditions, while the structure of the latter was determined by analogy with the known phase, $Rb_6Sn_2S_7$. With an increase in the amount of flux, no crystalline ternaries formed over the course of the reaction and the final product was a glass, as also seen in the $Cu + 5\ K_2S_5$ reaction. When increasing the polysulfide chain from K_2S_3 to K_2S_5, another new ternary forms from the melt upon heating. The new phase, $K_5Sn_2S_8$, notably contains a S_4^{2-} polysulfide chain along with S^{2-} units. Upon further heating, $K_5Sn_2S_8$ disappears and both $K_4Sn_2S_6$ and $K_2Sn_2S_5$ form. The two phases disappear at higher temperatures and reform upon cooling. Increasing the flux ratio does not greatly alter the reaction progression, except $K_2Sn_2S_5$ does not form.

While solid-state synthesis from elemental powders has been widely adopted, there is a lost opportunity to explore how alternative precursors can change kinetic barriers. Jiang et al. systematically exchanged the elemental precursors in the synthesis of Fe_2SiS_4 for the respective binaries to observe the alternate intermediate states and kinetic consequences that arise from these substitutions.[30] Starting with the elements, they showed that the formation and subsequent peritectic decomposition of FeS_2 was key for Fe_2SiS_4 formation as shown in Fig. 7A, therefore FeS_2 was used, instead of the elements Fe and S, in the subsequent experiment, as illustrated in Fig. 7B. This substitution confirmed that the FeS_2 peritectic is critical to the sulfidation of silicon and therefore for final product formation. This work demonstrated a stark difference between the kinetics for iron and silicon sulfidation, as iron readily fully sulfidized and silicon sulfidation only occurred upon FeS_2 decomposition. Armed with knowledge of silicon's slow reaction kinetics relative to iron, two syntheses using silicon containing binary precursors were executed: 2FeS: SiS_2 and Fe_3Si: Fe_5Si_3: 16S, as shown in Fig. 7C and D. Both reactions successfully circumvented the FeS_2 peritectic and initiated Fe_2SiS_4 formation at lower temperatures than the previous reactions (previously >743 °C, 682 °C for the binary sulfides, and 586 °C for the silicides). For the binary sulfides, a very different reaction progression took place, as shown by the slow reaction between $Fe_{1-x}S$ and SiS_2, thereby producing Fe_2SiS_4, in Fig. 7C. The synthesis using iron silicides is hypothesized to expedite the reaction, as it mitigates intrinsic diffusion limitations by employing precursors that mix iron and silicon on the atomic scale. Here, the rapid iron sulfidation kinetics were an asset, as the favorable dealloying of the iron silicide to form iron sulfides left a silicon network that was better able to form SiS_2, rather than crystalline silicon. Therefore, this reaction demonstrated more facile Si−S bond formation by breaking Si−Si bonds through the pre-reacting of iron and silicon to form iron silicides. This study demonstrated that the reaction follows the pathway that reaches the most immediate local maximum fraction, as opposed to the global maximum. Pre-reacting Si helps avoid slow steps, such as the FeS_2 peritectic decomposition. Changing the initial bonding in precursors can be used to engineer reaction pathways. The Fe−Si−S system approaches the same equilibrium state via different paths through phase space as the precursors are changed.

Neilson and coworkers looked at the formation of $CuSe_2$ using metathesis reactions, and examined the directing effects of atmosphere, annealing, and temperature.[65] They also tested intermediate phases as starting materials to see their effect on final product identity.[65]

Neilson and coworkers ground Na_2Se_2 and $CuCl_2$ (1) in humid air and (2) under dry conditions. Grinding led to the formation of NaCl, Se, and poorly crystallized phases, thus they annealed the mixture at 100 °C under vacuum. A pyrite polymorph of $CuSe_2$ was observed to form, which is usually a high-pressure phase and metastable under ambient conditions. When analyzing the second reaction, they did not observe product formation by PXRD until the sample was exposed to atmosphere—which yield a diffraction

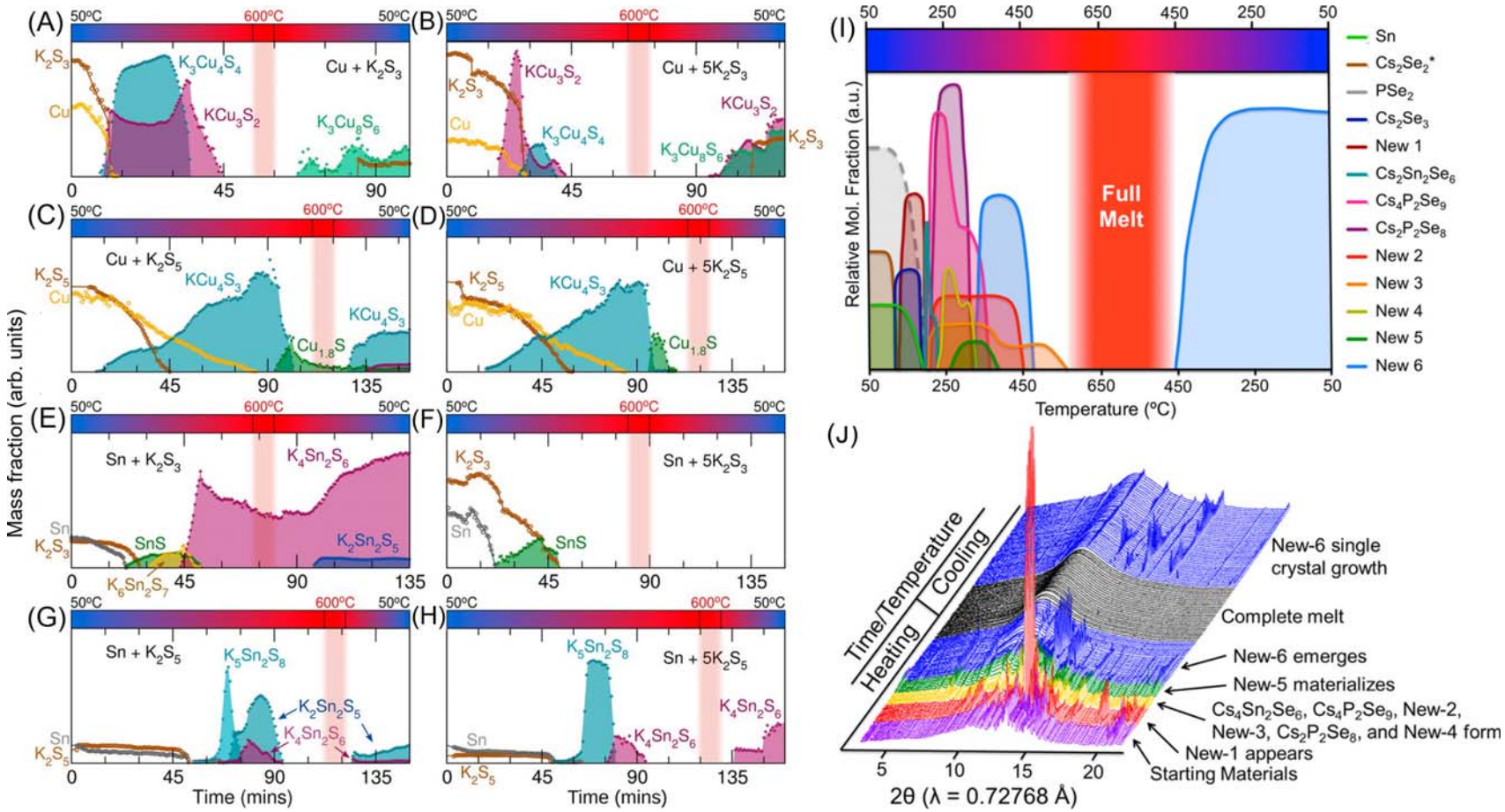

Fig. 6 Reaction maps of panoramic reactions, illustrating the opportunities for materials discovery by panoramic synthesis.[32,33] (A–D) Reactions in the K–Cu–S phase space.[32] Specifically, (A) and (B) show the reactions of Cu with K_2S_3 in a 1:1 and 1:5 stoichiometry, respectively. Similarly, (C) and (D) show the reactions of Cu with K_2S_5 in a 1:1 and 1:5 stoichiometry, respectively. (E–H) Reactions in the K–Sn–S phase space, where (E) and (F) use K_2S_3 and (G) and (H) use K_2S_5 in a 1:1 and 1:5 stoichiometry, respectively.[32] (I) Reaction map and (J) diffraction overlay for the reaction $2\ Cs_2Se_2 + Sn + 4PSe_2$.[33]

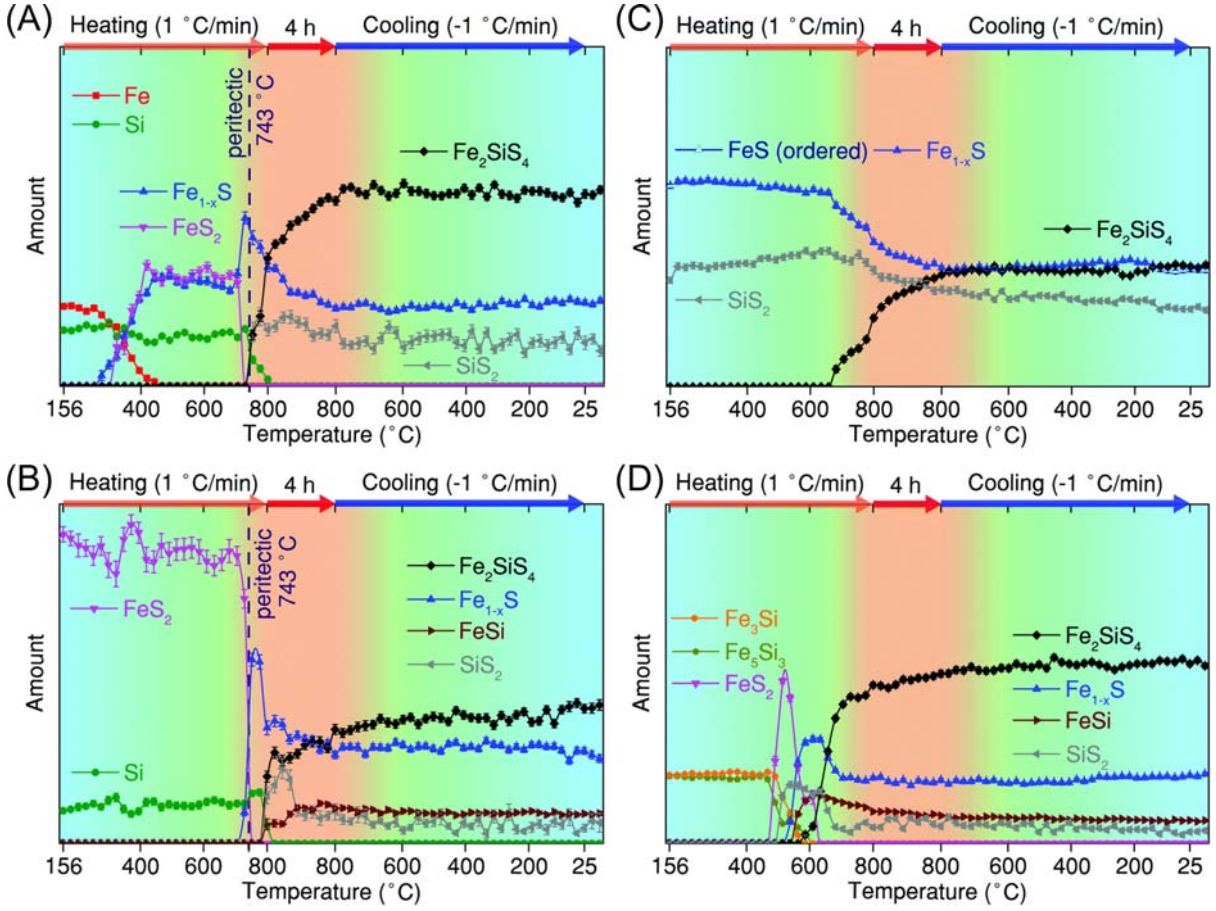

Fig. 7 Reaction pathways to form Fe_2SiS_4 from reactions (A) 2Fe: Si: 4S, (B) $2FeS_2$: Si, (C) 2FeS: SiS_2, and (D) Fe_3Si: Fe_5Si_3: 16S.[30]

pattern for NaCl, indicating that humidity plays a role in product crystallization. When increasing the temperature to 300 °C for reaction 2, bulk phase pure marcasite $CuSe_2$ formed. Without exposure to humidity, a higher temperature is needed to overcome the larger activation barrier for NaCl formation whose subsequent energy release drives the formation of the most-stable product, m-$CuSe_2$. The air exposed sample was studied in situ up to 370 °C. This revealed intermediate and decomposition products. Marcasite begins to form at *ca.* 110 °C along with p-$CuSe_2$. The pyrite phase starts to disappear at 175 °C, while the marcasite phase fraction increases. At greater than 245 °C, a two-step decomposition to CuSe and Cu_2Se was observed.

These findings illustrate the potential importance of partial hydration, by exposure to humidity. The moisture apparently enhanced sodium and chloride mobility, and led to NaCl formation. The subsequent gradual enthalpy release from NaCl formation upon grinding enabled the reaction to proceed to the intermediate phases, CuSe and Se. Partial solvation directed the reaction to the pyrite polymorph of $CuSe_2$ rather than marcasite. The former is usually a high-pressure phase and is metastable under ambient conditions.

To investigate the bounds of pyrite formation, the authors parameterized anneal time and precursor identities. With regards to time, the authors increased the reaction time for the humidity exposed reaction from 24 h to 6 weeks and discovered that a mixture of marcasite and pyrite $CuSe_2$ were present. This finding illustrates that there is no thermodynamic preference for the pyrite polymorph and that it is a kinetic product. With insight into the intermediate phases preceding pyrite $CuSe_2$ formation, the authors reacted CuSe + Se in stoichiometric amounts to determine if pyrite formation without the metathesis pathway were possible. They observed that, post grinding and annealing, the reaction produced only a small amount of pyrite along with unreacted precursors. On increasing the annealing time, equal amounts of the two polymorphs formed and, on further increasing it, the fraction of the marcasite polymorph eventually surpassed that of the pyrite. This study also used complementary probes to investigate the nature of intermediate products. The energetics of the two reactions ($Na_2Se_2 + CuCl_2$, with and without moisture) differ greatly, as shown by differential scanning calorimetry. The reaction involving humidity exposure during grinding is associated with a small endotherm, indicating that the energy associated with NaCl formation has already been released and that a small activation barrier must be overcome to form pyrite from CuSe and Se. In contract, the reaction where the precursors had been ground in dry conditions showed a large exotherm, ostensibly from NaCl formation. This gives credence to the authors' hypothesis that NaCl formation in the humidity-exposed reaction serves to facilitate CuSe and Se formation. Poorly ordered phases coexist with the crystalline phases in the reaction. An investigation of the local structure, using pair distribution function (PDF) methods, showed minimal

changes to the local atomic distances for the humidity-exposed reaction mixture at low reaction temperatures, despite many changes in the PXRD such as the formation of NaCl, CuSe, and Se growth and reaction, as well as $CuSe_2$ formation and growth. This suggests that there are close structural relationships between the poorly ordered phases and the intermediate crystalline phases CuSe, Se, and the product p-$CuSe_2$. Other studies have been able to identify explicitly structurally related intermediate phases pertaining to product formation.[29,66]

The identification and investigation of structural intermediates gives insight into reaction mechanisms, and provides an additional stepping stone to reaction-by-design. Neilson and coworkers' studies of metathesis reactions include investigations of structurally important intermediate phases. In their study of the reaction $Na_2S_2 + FeCl_2$, they discovered that the metathesis reaction did not proceed through the expected simple salt exchange.[67] Rather, their in situ studies painted a more complex picture. A combined study using variable temperature X-ray diffraction (both in-house and synchrotron) and differential scanning calorimetry (DSC) showed that the pathway involves extensive redox chemistry.[67] Rather than direct formation of FeS_2 and NaCl, the intermediates $NaFeS_2$ and S_8 were observed via synchrotron XRD. The presence of broad peaks, indexed to $NaFeS_2$, showed that iron was oxidized from Fe^{2+} to Fe^{3+} before further oxidation of S^{2-} to S_2^{2-} found in FeS_2. Correspondingly, the presence of elemental sulfur demonstrates that sulfur disproportionates from $[S_2]^{2-}$ to S^0 and S^{2-}, giving elemental sulfur and $NaFeS_2$ as reaction products. As the reaction progresses, sulfur comproportionates to give the final product: $3S^{2-} + 2Fe^{3+} + S^0 \rightarrow 2FeS_2$. The lack of any signal in the DSC at the melting or decomposition temperatures for Na_2S_2 and $FeCl_2$ precludes the formation of Fe^{3+} and S^{2-} during melting or decomposition and instead suggested a reaction to form these species.

In order to balance the reaction with $NaFeS_2$ as an intermediate phase, chlorine or chloride must be present in the intermediate phases. Ex situ experiments showed no chlorine gas present, therefore the reaction likely proceeds through the formation of NaCl and attack on the $FeCl_2$ by the disproportionated sulfur to yield products of $(2 - x)$ NaCl + $Na_{1-0.5x}FeS_{2-x}Cl_x + xS$. The incorporation of chloride into $NaFeS_2$ is supported by the poor crystallinity of the $NaFeS_2$ phase in addition to a larger lattice parameters when compared to previous reports for this compound. The heat released from NaCl formation does not drive the reaction. However, the formation of the intermediate and pyrite does drive it; which is contrary to expectations for a metathesis reaction. Instead, the heat released during NaCl formation is either spread over a large temperature range or released adiabatically (heat does not leave the system).[22] Next the comproportionation of sulfur involves the reaction of elemental sulfur and $NaFeS_2$, $3S^{2-} + 2Fe^{3+} + S^0 \rightarrow 2FeS_2$, thus terminating the reaction. Rather than simple salt exchange, this metathesis reaction follows a complex mechanism starting with disproportionation, followed by the formation of a low-density intermediate phase, and culminating in anionic comproportionation and atomic rearrangement into pyrite. Cursory studies of the analogous cobalt system showed that metathesis reactions proceeded in a similar fashion. Na_2CoS_2 was formed as an intermediate when reacting $CoCl_2$ and Na_2S_2.

A similar study conducted by McClain et al. built upon the previous chalcogenide in situ work and encompassed three important features: (1) materials discovery in well-investigated systems, (2) investigations with different precursors, and (3) the discovery of a structural intermediate. Furthermore, a design principle was proposed that extends beyond the investigated system.[29] McClain et al. selected the K–Bi–Q (Q = S, Se) phase space for investigation, as the A–Pn–Q (A = alkali metal; Pn = Sb, Bi) compositional space contains a plethora of isostructural analogues or shared structural motifs, thereby potentially permitting any observations to be applied beyond the K–Bi–Q system under investigation. Additionally, some of these materials are of interest for thermoelectric and optical applications.[29] Using K_2Q and Bi_2Q_3 (Q = S, Se), McClain et al. targeted the known ternaries $KBiQ_2$, which crystallize with a rocksalt structure. In situ reactions with the ratio 1.5 $K_2S + Bi_2S_3$ successfully formed $KBiS_2$ and also revealed that K_3BiS_3 formed as an intermediate phase.[29] An isostructural analogue, K_3BiSe_3, forms during the reaction of 1.5 $K_2Se + Bi_2Se_3$ to give rocksalt $KBiSe_2$. The presence of this ternary in both reaction systems suggests that it is mechanistically important for $KBiQ_2$ formation. The K_3BiQ_3 structural intermediate can be considered as a critical transitional point for the formation of $KBiQ_2$, as illustrated in Fig. 8. Upon modifying the precursor ratios to 1:1, two additional compounds were discovered: β-$KBiS_2$ and β-$KBiSe_2$. These cation-ordered materials have an α-$NaFeO_2$ structure, and they are closely related to the cation-disordered rocksalt material α-$KBiS_2$. The panoramic syntheses reveal that the α-$KBiQ_2$ polymorphs are present as high temperature phases during the formation of β-$KBiQ_2$. Density functional theory (DFT) calculations corroborate that these cation-ordered β-$KBiQ_2$ polymorphs are thermodynamically more stable at low temperatures than α-$KBiQ_2$. This study highlights the power of panoramic synthesis to uncover new phases in a well-known system, while tuning precursor ratios, and unveiling a structural intermediate that underlies the formation of the target compounds.

In the context of the broader $APnQ_2$ materials family (A = alkali metal; Pn = Sb, Bi), this work also provides a missing link that enabled the identification of a tolerance factor governing phase formation in this system. The ability of $KBiQ_2$ to form both disordered and ordered phases, while $NaBiQ_2$ and $RbBiQ_2$ crystallize in the rocksalt and α-$NaFeO_2$ structure types, respectively, suggests that there is a site-sharing tolerance requirement for the six-coordinate cations: $\left(\frac{r^+}{r^{3+}}\right)$ should be 1.33 or less in order to form a cation-disordered rocksalt structure. For ratios higher than 1.33, the cation-ordered phase forms. Inspection of the antimony analogues shows a similar cation radii tolerance requirement for metal site sharing: $NaSbS_2$ crystallizes in both the rocksalt and $KSbS_2$ structure types, while $KSbS_2$ only forms a cation-ordered structure. The six-coordinate cation ratio $(\frac{Na^+}{Sb^{3+}})$ is 1.3, which is in alignment with that found for the bismuth ternaries.[29] This pioneering study proposes a new design principle for a chalcogenide system.

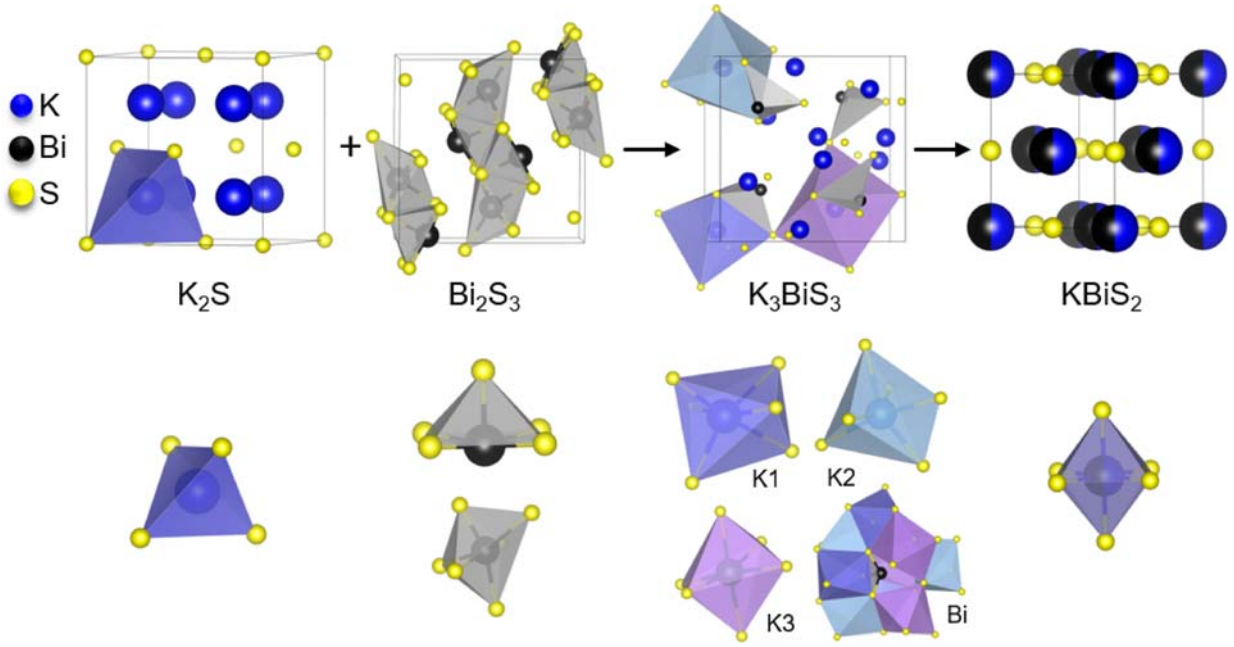

Fig. 8 Reaction progression of the starting materials K_2S and Bi_2S_3 to form $KBiS_2$.[29]

10.07.5 Other compositions

These in situ capabilities have also been applied to novel systems such as reactions in intermetallic and pnictogen systems. Latturner and coworkers explored Ba/Yb/Mg/Si compositions in a Mg/Al flux using neutron diffraction.[68] Notably, they observed that shorter dwell times changed the final product's identity. Their panoramic experiments showed not only formation of the previously reported $Ba_2Yb_{0.9}Mg_{11.1}Si_7$, $Ba_5Yb_2Mg_{17}Si_{12}$, and $Ba_{20}Yb_5Mg_{61}Si_{43}$, but also a new compound, $Ba_6Yb_{1.84}Mg_{18.16}Si_{13}$, which crystallizes in the $Zr_6Ni_{20}P_{13}$ structure type. They observed many competing products and therefore monitored the temperature dependence of phase transformation as well as dwell time. With a combination of quenching experiments in the furnace and in situ panoramic neutron powder diffraction studies they were able to determine the reaction parameters that favor particular products. From this work they learned that in this system the crystallization of products from the metal flux does not involve precipitation followed by interconversion to different phases. Instead the rate of cooling across the supersaturated metastable zone is most important. For example, under slow-cooling conditions, the $Ba_5Yb_2Mg_{17}Si_{12}$ precipitates from the flux at 800 °C and a faster cooling rate leads to the formation of $Ba_{20}Yb_5Mg_{61}Si_{43}$ in the flux at 640 °C.

Recently, Zaikina and co-workers reported in situ panoramic synthetic investigations in the Na—Zn—Sb system, and discovered two new compositionally similar but structurally different ternary antimonides with new structure types.[54] They employed a hydride route to obtain $NaZn_4Sb_3$ and HT-$Na_{1-x}Zn_{4-y}Sb_3$ during in situ high-temperature powder X-ray diffraction experiments. HT-$Na_{1-x}Zn_{4-y}Sb_3$ only formed within a narrow temperature range and under Na/Zn depleted reaction conditions.

Neilson and coworkers investigated the formation of Mn_3N_2 by metathesis.[69] They studied the reaction of $MnCl_2$ with Mg_2NCl or Mg_3N_2 to form Mn_3N_2. They used metathesis to circumvent the need for high temperatures or pressures to increase the chemical potential of nitrogen. Their in situ work uncovered that the reaction proceeds at low temperatures via interdiffusion, forming a previously unknown solid-solution intermediate with the composition of $Mg_xMn_{1-x}Cl_2$. This Mg/MnCl salt is a medium for cation diffusion.[69]

10.07.6 Conclusion and outlook

Historically, in situ studies of materials synthesis had specialized use in crystallization rate observations. With the advent of more commercially available diffractometer setups, thereby no longer necessitating synchrotrons for certain systems, the synthesis science community will be able to access and use this powerful technique more routinely. As demonstrated in the studies discussed in this chapter, panoramic synthesis has immense potential for materials discovery and unveiling the assembling principles for solid-state materials. Give that this approach to materials discovery and reaction path identification is in its infancy, there is a lot of room for exploration. By more routinely pairing in situ panoramic materials syntheses with computational insight, to not only select productive phase spaces, but also rationalize the observed trends and progressions, work focusing on rational design may quickly advance.[4,35] At present, computational and text mining studies have already been used to investigate precursor choice on anthropogenic biases,[70] switchability,[62] and synthesis recipe.[71] Cataloging failed reactions is also of interest.[72] Rapid progress continues to

be made in computationally-driven predictive syntheses of inorganic materials, but it too is in its infancy.[23] Other steps include extending parameters to other synthetic variables, such as pressure.[73]

References

1. Jain, A.; Ong, S. P.; Hautier, G.; Chen, W.; Richards, W. D.; Dacek, S.; Cholia, S.; Gunter, D.; Skinner, D.; Ceder, G.; Persson, K. A. Commentary: The Materials Project: A Materials Genome Approach to Accelerating Materials Innovation. *APL Mater.* **2013,** *1* (1), 011002.
2. de Pablo, J. J.; Jackson, N. E.; Webb, M. A.; Chen, L.-Q.; Moore, J. E.; Morgan, D.; Jacobs, R.; Pollock, T.; Schlom, D. G.; Toberer, E. S. New Frontiers for the Materials Genome Initiative. *Npj Comput. Mater.* **2019,** *5* (1), 41.
3. Oganov, A. R.; Pickard, C. J.; Zhu, Q.; Needs, R. J. Structure Prediction Drives Materials Discovery. *Nat. Rev. Mater.* **2019,** *4* (5), 331–348.
4. Butler, K. T.; Frost, J. M.; Skelton, J. M.; Svane, K. L.; Walsh, A. Computational Materials Design of Crystalline Solids. *Chem. Soc. Rev.* **2016,** *45* (22), 6138–6146.
5. Butler, K. T.; Davies, D. W.; Cartwright, H.; Isayev, O.; Walsh, A. Machine Learning for Molecular and Materials Science. *Nature* **2018,** *559* (7715), 547–555.
6. Liu, Y.; Zhao, T.; Ju, W.; Shi, S. Materials Discovery and Design Using Machine Learning. *J. Materiomics* **2017,** *3* (3), 159–177.
7. Gubernatis, J. E.; Lookman, T. Machine Learning in Materials Design and Discovery: Examples from the Present and Suggestions for the Future. *Phys. Rev. Mater.* **2018,** *2* (12), 120301.
8. Pienack, N.; Bensch, W. In-Situ Monitoring of the Formation of Crystalline Solids. *Angew. Chem. Int. Ed. Engl.* **2011,** *50* (9), 2014–2034.
9. Stock, N.; Biswas, S. Synthesis of Metal-Organic Frameworks (MOFs): Routes to Various MOF Topologies, Morphologies, and Composites. *Chem. Rev.* **2012,** *112* (2), 933–969.
10. Jensen, K. M.; Tyrsted, C.; Bremholm, M.; Iversen, B. B. In Situ Studies of Solvothermal Synthesis of Energy Materials. *ChemSusChem* **2014,** *7* (6), 1594–1611.
11. Hansen, T. C.; Kohlmann, H. Chemical Reactions Followed by In Situ Neutron Powder Diffraction. *Z. Anorg. Allg. Chem.* **2014,** *640* (15), 3044–3063.
12. Van Vleet, M. J.; Weng, T.; Li, X.; Schmidt, J. R. In Situ, Time-Resolved, and Mechanistic Studies of Metal–Organic Framework Nucleation and Growth. *Chem. Rev.* **2018,** *118* (7), 3681–3721.
13. Walton, R. I.; Smith, R. I.; O'Hare, D. Following the Hydrothermal Crystallisation of Zeolites Using Time-Resolved In Situ Powder Neutron Diffraction. *Micropor. Mesopor. Mater.* **2001,** *48* (1–3), 79–88.
14. Gopalakrishnan, J. Chimie Douce Approaches to the Synthesis of Metastable Oxide Materials. *Chem. Mater.* **1995,** *7* (7), 1265–1275.
15. Stein, A.; Keller, S. W.; Mallouk, T. E. Turning Down the Heat: Design and Mechanism in Solid-State Synthesis. *Science* **1993,** *259* (5101), 1558–1564.
16. Kanatzidis, M. G. New Directions in Synthetic Solid State Chemistry: Chalcophosphate Salt Fluxes for Discovery of New Multinary Solids. *Curr. Opin. Solid State Mater. Sci.* **1997,** *2* (2), 139–149.
17. Bugaris, D. E.; zur Loye, H.-C. Materials Discovery by Flux Crystal Growth: Quaternary and Higher Order Oxides. *Angew. Chem. Int. Ed.* **2012,** *51* (16), 3780–3811.
18. Kanatzidis, M. G. Discovery-Synthesis, Design, and Prediction of Chalcogenide Phases. *Inorg. Chem.* **2017,** *56* (6), 3158–3173.
19. Boltersdorf, J.; King, N.; Maggard, P. A. Flux-Mediated Crystal Growth of Metal Oxides: Synthetic Tunability of Particle Morphologies, Sizes, and Surface Features for Photocatalysis Research. *CrstEngComm* **2015,** *17* (11), 2225–2241.
20. Kanatzidis, M. G.; Pöttgen, R.; Jeitschko, W. The Metal Flux: A Preparative Tool for the Exploration of Intermetallic Compounds. *Angew. Chem. Int. Ed.* **2005,** *44* (43), 6996–7023.
21. Parkin, I. Solid State Metathesis Reaction for Metal Borides, Silicides, Pnictides and Chalcogenides: Ionic or Elemental Pathways. *Chem. Soc. Rev.* **1996,** *25* (3), 199–207.
22. Martinolich, A. J.; Neilson, J. R. Toward Reaction-by-Design: Achieving Kinetic Control of Solid State Chemistry with Metathesis. *Chem. Mater.* **2017,** *29* (2), 479–489.
23. Alberi, K.; Nardelli, M. B.; Zakutayev, A.; Mitas, L.; Curtarolo, S.; Jain, A.; Fornari, M.; Marzari, N.; Takeuchi, I.; Green, M. L. The 2019 Materials by Design Roadmap. *J. Phys. D Appl. Phys.* **2018,** *52* (1), 013001.
24. Cheetham, A. K.; Mellot, C. F. In Situ Studies of the Sol – Gel Synthesis of Materials. *Chem. Mater.* **1997,** *9* (11), 2269–2279.
25. Francis, R. J.; O'Hare, D. The Kinetics and Mechanisms of the Crystallisation of Microporous Materials. *J. Chem. Soc. Dalton Trans.* **1998**, (19), 3133–3148.
26. Munn, J.; Barnes, P.; Häusermann, D.; Axon, S. A.; Klinowski, J. In-Situ Studies of the Hydrothermal Synthesis of Zeolites Using Synchrotron Energy-Dispersive X-Ray Diffraction. *Phase Transit.* **1992,** *39* (1–4), 129–134.
27. Polak, E.; Munn, J.; Barnes, P.; Tarling, S.; Ritter, C. Time-Resolved Neutron Diffraction Analyses of Hydrothermal Syntheses Using a Novel Autoclave Cell. *J. Appl. Cryst.* **1990,** *23* (4), 258–262.
28. Walton, R. I.; Millange, F.; O'Hare, D.; Davies, A. T.; Sankar, G.; Catlow, C. R. A. An In Situ Energy-Dispersive X-Ray Diffraction Study of the Hydrothermal Crystallization of Zeolite A. 1. Influence of Reaction Conditions and Transformation into Sodalite. *J. Phys. Chem. B* **2001,** *105* (1), 83–90.
29. McClain, R.; Malliakas, C. D.; Shen, J.; He, J.; Wolverton, C.; González, G. B.; Kanatzidis, M. G. Mechanistic Insight of $KBiQ_2$ (Q = S, Se) Using Panoramic Synthesis Towards Synthesis-by-Design. *Chem. Sci.* **2021,** *12,* 1378–1391.
30. Jiang, Z.; Ramanathan, A.; Shoemaker, D. P. In Situ Identification of Kinetic Factors that Expedite Inorganic Crystal Formation and Discovery. *J. Mater. Chem. C* **2017,** *5* (23), 5709–5717.
31. Geselbracht, M. J.; Noailles, L. D.; Ngo, L. T.; Pikul, J. H.; Walton, R. I.; Cowell, E. S.; Millange, F.; O'Hare, D. Probing Molten Salt Flux Reactions Using Time-Resolved In Situ High-Temperature Powder X-Ray Diffraction: A New Synthesis Route to the Mixed-Valence $NaTi_2O_4$. *Chem. Mater.* **2004,** *16* (6), 1153–1159.
32. Shoemaker, D. P.; Hu, Y. J.; Chung, D. Y.; Halder, G. J.; Chupas, P. J.; Soderholm, L.; Mitchell, J. F.; Kanatzidis, M. G. In Situ Studies of a Platform for Metastable Inorganic Crystal Growth and Materials Discovery. *Proc. Natl. Acad. Sci. U. S. A.* **2014,** *111* (30), 10922–10927.
33. Haynes, A. S.; Stoumpos, C. C.; Chen, H.; Chica, D.; Kanatzidis, M. G. Panoramic Synthesis as an Effective Materials Discovery Tool: The System Cs/Sn/P/Se as a Test Case. *J. Am. Chem. Soc.* **2017,** *139* (31), 10814–10821.
34. Walton, R. I.; O'Hare, D. Watching Solids Crystallise Using Powder Diffraction. *Chem. Commun.* **2000,** *23,* 2283–2291.
35. Bhutani, A.; Schiller, J. A.; Zuo, J. L.; Eckstein, J. N.; Greene, L. H.; Chaudhuri, S.; Shoemaker, D. P. Combined Computational and In Situ Experimental Search for Phases in an Open Ternary System, Ba–Ru–S. *Chem. Mater.* **2017,** *29* (14), 5841–5849.
36. Jiang, Z.; Sharma, J.; Okasinski, J. S.; Chen, H.; Shoemaker, D. P. In Situ Energy-Dispersive X-ray Diffraction of Local Phase Dynamics During Solvothermal Growth of Cu_4O_3. *J. Appl. Cryst.* **2021,** *54* (1), 42–53.
37. Evans, J. S. O.; Francis, R. J.; O'Hare, D.; Price, S. J.; Clark, S. M.; Flaherty, J.; Gordon, J.; Nield, A.; Tang, C. C. An Apparatus for the Study of the Kinetics and Mechanism of Hydrothermal Reactions by In Situ Energy Dispersive X-Ray Diffraction. *Rev. Sci. Instrum.* **1995,** *66* (3), 2442–2445.
38. Westgren, A. Rontgen Spectrographic Investigation of Iron and Steel. *Iron Steel Inst. (British)* **1921,** *103,* 303.
39. Delapalme, A.; Raison, P.; Lander, G. H.; Rebizant, J.; Schweiss, P.; Kanellakopulos, B. Studies of $U(C_5H_5)_3Cl$: II-Temperature Dependence of the Molecular Configurations. *Z. Kristallogr. Cryst. Mater.* **1994,** *209* (9), 727–732.
40. Chupas, P. J.; Chapman, K. W.; Kurtz, C.; Hanson, J. C.; Lee, P. L.; Grey, C. P. A Versatile Sample-Environment Cell for Non-ambient X-Ray Scattering Experiments. *J. Appl. Cryst.* **2008,** *41* (4), 822–824.
41. Riello, P.; Lausi, A.; Macleod, J.; Plaisier, J. R.; Zerauschek, G.; Fornasiero, P. In Situ Reaction Furnace for Real-Time XRD Studies. *J. Synchrotron Radiat.* **2013,** *20* (1), 194–196.

42. Misture, S. T. Large-Volume Atmosphere-Controlled High-Temperature x-Ray Diffraction Furnace. *Meas. Sci. Technol.* **2003,** *14* (7), 1091–1098.
43. Lundgren, R. J.; Cranswick, L. M.; Bieringer, M. In Situ X-Ray Powder Diffraction, Synthesis, and Magnetic Properties of $InVO_3$. *J. Solid State Chem.* **2006,** *179* (12), 3599–3606.
44. Shafi, S. P.; Lundgren, R. J.; Cranswick, L. M. D.; Bieringer, M. Formation, Structure and Magnetism of the Metastable Defect Fluorite Phases $AVO_{3.5+x}$ (A = In, Sc). *J. Solid State Chem.* **2007,** *180* (12), 3333–3340.
45. Shafi, S. P.; Kotyk, M. W.; Cranswick, L. M. D.; Michaelis, V. K.; Kroeker, S.; Bieringer, M. In Situ Powder X-Ray Diffraction, Synthesis, and Magnetic Properties of the Defect Zircon Structure $ScVO_{4-x}$. *Inorg. Chem.* **2009,** *48* (22), 10553–10559.
46. Lundgren, R. J.; Cranswick, L. M. D.; Bieringer, M. Phase Stability, Structural Evolution and Magnetic Properties of $Sc_{1-x}Lu_xVO_3$ ($0.0 \leq x \leq 1.0$). *Chem. Mater.* **2007,** *19* (16), 3945–3955.
47. Gauthier, V.; Bernard, F.; Gaffet, E.; Josse, C.; Larpin, J. P. In-Situ Time Resolved X-Ray Diffraction Study of the Formation of the Nanocrystalline $NbAl_3$ Phase by Mechanically Activated Self-Propagating High-Temperature Synthesis Reaction. *Mater. Sci. Eng. A* **1999,** *272* (2), 334–341.
48. Moorhouse, S. J.; Vranješ, N.; Jupe, A.; Drakopoulos, M.; O'Hare, D. The Oxford-Diamond in Situ Cell for Studying Chemical Reactions Using Time-Resolved X-Ray Diffraction. *Rev. Sci. Instrum.* **2012,** *83* (8), 084101.
49. Xia, F.; Brugger, J.; Qian, G.; Ngothai, Y.; O'Neill, B.; Zhao, J.; Pullen, S.; Olsen, S.; Pring, A. Single-Pass Flow-through Reaction Cell for High-Temperature and High-Pressure In Situ Neutron Diffraction Studies of Hydrothermal Crystallization Processes. *J. Appl. Cryst.* **2012,** *45* (2), 166–173.
50. Ok, K. M.; O'Hare, D.; Smith, R. I.; Chowdhury, M.; Fikremariam, H. New Large Volume Hydrothermal Reaction Cell for Studying Chemical Processes under Supercritical Hydrothermal Conditions Using Time-Resolved In Situ Neutron Diffraction. *Rev. Sci. Instrum.* **2010,** *81* (12), 125107.
51. Walton, R. I.; Millange, F.; Smith, R. I.; Hansen, T. C.; O'Hare, D. Real Time Observation of the Hydrothermal Crystallization of Barium Titanate Using In Situ Neutron Powder Diffraction. *J. Am. Chem. Soc.* **2001,** *123* (50), 12547–12555.
52. Norby, P. Hydrothermal Conversion of Zeolites: An In Situ Synchrotron X-Ray Powder Diffraction Study. *J. Am. Chem. Soc.* **1997,** *119* (22), 5215–5221.
53. Becker, J.; Bremholm, M.; Tyrsted, C.; Pauw, B.; Jensen, K. M. O.; Eltzholt, J.; Christensen, M.; Iversen, B. B. Experimental Setup for In Situ X-Ray SAXS/WAXS/PDF Studies of the Formation and Growth of Nanoparticles in Near- and Supercritical Fluids. *J. Appl. Cryst.* **2010,** *43* (4), 729–736.
54. Gvozdetskyi, V.; Owens-Baird, B.; Hong, S.; Cox, T.; Bhaskar, G.; Harmer, C.; Sun, Y.; Zhang, F.; Wang, C.-Z.; Ho, K.-M.; Zaikina, J. V. From $NaZn_4Sb_3$ to HT-$Na_{1-x}Zn_{4-y}Sb_3$: Panoramic Hydride Synthesis, Structural Diversity, and Thermoelectric Properties. *Chem. Mater.* **2019,** *31* (21), 8695–8707.
55. Abeysinghe, D.; Huq, A.; Yeon, J.; Smith, M. D.; zur Loye, H.-C. In Situ Neutron Diffraction Studies of the Flux Crystal Growth of the Reduced Molybdates $La_4Mo_2O_{11}$ and $Ce_4Mo_2O_{11}$: Revealing Unexpected Mixed-Valent Transient Intermediates and Determining the Sequence of Events during Crystal Growth. *Chem. Mater.* **2018,** *30* (3), 1187–1197.
56. Moorhouse, S. J.; Wu, Y.; Buckley, H. C.; O'Hare, D. Time-Resolved In Situ Powder X-Ray Diffraction Reveals the Mechanisms of Molten Salt Synthesis. *Chem. Commun.* **2016,** *52* (96), 13865–13868.
57. O'Brien, S.; Francis, R. J.; Fogg, A.; O'Hare, D.; Okazaki, N.; Kuroda, K. Time-Resolved In Situ X-Ray Powder Diffraction Study of the Formation of Mesoporous Silicates. *Chem. Mater.* **1999,** *11* (7), 1822–1832.
58. Lussier, J. A.; Devitt, G.; Szkop, K. M.; Bieringer, M. Oxygen trapping and cation site-splitting in $Y_{2-x}Pr_xO_{3+\delta}$ ($0.0 \leq x < 2.0$ and $\delta \leq 1.0$). *J. Solid State Chem.* **2016,** *242,* 126–132.
59. Lussier, J. A.; Szkop, K. M.; Sharma, A. Z.; Wiebe, C. R.; Bieringer, M. Order/Disorder and In Situ Oxide Defect Control in the Bixbyite Phase $YPrO_{3+\delta}$ ($0 \leq \delta < 0.5$). *Inorg. Chem.* **2016,** *55* (5), 2381–2389.
60. Lussier, J. A.; Shafi, S. P.; Donaberger, R. L.; Bieringer, M. Platinum Uptake and Ba_2CePtO_6 Formation During in Situ $BaCe_{1-x}M_xO_{3-\delta}$ (M = La, In) Formation. *Inorg. Chem.* **2014,** *53* (16), 8809–8815.
61. Todd, P. K.; Neilson, J. R. Selective Formation of Yttrium Manganese Oxides through Kinetically Competent Assisted Metathesis Reactions. *J. Am. Chem. Soc.* **2019,** *141* (3), 1191–1195.
62. He, T.; Sun, W.; Huo, H.; Kononova, O.; Rong, Z.; Tshitoyan, V.; Botari, T.; Ceder, G. Similarity of Precursors in Solid-State Synthesis as Text-Mined from Scientific Literature. *Chem. Mater.* **2020,** *32,* 7861–7873.
63. Todd, P. K.; Smith, A. M. M.; Neilson, J. R. Yttrium Manganese Oxide Phase Stability and Selectivity Using Lithium Carbonate Assisted Metathesis Reactions. *Inorg. Chem.* **2019,** *58* (22), 15166–15174.
64. Todd, P. K.; Wustrow, A.; McAuliffe, R. D.; McDermott, M. J.; Tran, G. T.; McBride, B. C.; Boeding, E. D.; O'Nolan, D.; Liu, C.-H.; Dwaraknath, S. S.; Chapman, K. W.; Billinge, S. J. L.; Persson, K. A.; Huq, A.; Veith, G. M.; Neilson, J. R. Defect-Accommodating Intermediates Yield Selective Low-Temperature Synthesis of $YMnO_3$ Polymorphs. *Inorg. Chem.* **2020,** *59* (18), 13639–13650.
65. Martinolich, A. J.; Kurzman, J. A.; Neilson, J. R. Polymorph Selectivity of Superconducting $CuSe_2$ Through Kinetic Control of Solid-State Metathesis. *J. Am. Chem. Soc.* **2015,** *137* (11), 3827–3833.
66. Martinolich, A. J.; Kurzman, J. A.; Neilson, J. R. Circumventing Diffusion in Kinetically Controlled Solid-State Metathesis Reactions. *J. Am. Chem. Soc.* **2016,** *138* (34), 11031–11037.
67. Martinolich, A. J.; Neilson, J. R. Pyrite Formation Via Kinetic Intermediates Through Low-Temperature Solid-State Metathesis. *J. Am. Chem. Soc.* **2014,** *136* (44), 15654–15659.
68. Vasquez, G.; Huq, A.; Latturner, S. E. In Situ Neutron Diffraction Studies of the Metal Flux Growth of Ba/Yb/Mg/Si Intermetallics. *Inorg. Chem.* **2019,** *58* (12), 8111–8119.
69. Rognerud, E. G.; Rom, C. L.; Todd, P. K.; Singstock, N. R.; Bartel, C. J.; Holder, A. M.; Neilson, J. R. Kinetically Controlled Low-Temperature Solid-State Metathesis of Manganese Nitride Mn_3N_2. *Chem. Mater.* **2019,** *31* (18), 7248–7254.
70. Jia, X.; Lynch, A.; Huang, Y.; Danielson, M.; Lang'at, I.; Milder, A.; Ruby, A. E.; Wang, H.; Friedler, S. A.; Norquist, A. J.; Schrier, J. Anthropogenic Biases in Chemical Reaction Data Hinder Exploratory Inorganic Synthesis. *Nature* **2019,** *573* (7773), 251–255.
71. Kononova, O.; Huo, H.; He, T.; Rong, Z.; Botari, T.; Sun, W.; Tshitoyan, V.; Ceder, G. Text-Mined Dataset of Inorganic Materials Synthesis Recipes. *Sci. Data* **2019,** *6* (1), 203.
72. Raccuglia, P.; Elbert, K. C.; Adler, P. D. F.; Falk, C.; Wenny, M. B.; Mollo, A.; Zeller, M.; Friedler, S. A.; Schrier, J.; Norquist, A. J. Machine-Learning-Assisted Materials Discovery Using Failed Experiments. *Nature* **2016,** *533* (7601), 73–76.
73. Phelan, W. A.; Zahn, J.; Kennedy, Z.; McQueen, T. M. Pushing Boundaries: High Pressure, Supercritical Optical Floating Zone Materials Discovery. *J. Solid State Chem.* **2019,** *270,* 705–709.

10.08 X-ray diffraction methods for high-pressure solid-state synthesis

Scott D. Thiel[a], Alexandra D. Tamerius[b], and James P.S. Walsh[a], [a] Department of Chemistry, University of Massachusetts Amherst, Amherst, MA, United States; and [b] Department of Chemistry and Physical Sciences, Marian University, Indianapolis, IN, United States

© 2023 Elsevier Ltd. All rights reserved.

10.08.1	**Introduction**	**201**
10.08.1.1	Review of some fundamental concepts in solid-state synthesis	202
10.08.1.1.1	Atomic diffusion requires very high temperatures	202
10.08.1.1.2	Stable heating relies on sophisticated apparatus	203
10.08.1.1.3	Reactant interfaces dictate product yield	203
10.08.1.1.4	Phase stability is very sensitive to temperature	204
10.08.1.1.5	Chemical isolation of the reactants is critical	204
10.08.1.2	Additional considerations for synthesis at high pressures	204
10.08.1.2.1	Diffusion rates are greatly diminished under pressure	204
10.08.1.2.2	Sample homogeneity is difficult to control	205
10.08.1.2.3	Encapsulation materials must be chemically inert	205
10.08.1.2.4	Pressure must be measured alongside temperature	205
10.08.1.2.5	Anisotropy of the pressure field can be important	205
10.08.2	**High-pressure apparatus for chemical synthesis with in situ X-ray diffraction**	**206**
10.08.2.1	Paris–Edinburgh press	206
10.08.2.1.1	Overview of the Paris–Edinburgh press (PEP)	206
10.08.2.1.2	Using the PEP for chemical synthesis	207
10.08.2.1.3	In situ X-ray diffraction in the PEP	207
10.08.2.1.4	Advantages and disadvantages of the PEP	208
10.08.2.1.5	Example syntheses with the PEP	208
10.08.2.2	Diamond anvil cell	209
10.08.2.2.1	Overview of the diamond anvil cell (DAC)	209
10.08.2.2.2	Using the DAC for chemical synthesis	211
10.08.2.2.3	In situ X-ray diffraction in the DAC	212
10.08.2.2.4	Advantages and disadvantages of the DAC	213
10.08.2.2.5	Examples of synthesis with the DAC	213
10.08.2.3	Multi-anvil press	214
10.08.2.3.1	Overview of the multi-anvil press (MAP)	214
10.08.2.3.2	Using the MAP for chemical synthesis	215
10.08.2.3.3	In situ X-ray diffraction in the MAP	216
10.08.2.3.4	Advantages and disadvantages of the MAP	216
10.08.2.3.5	Examples of synthesis with the MAP	216
10.08.3	**Conclusion**	**217**
Acknowledgment		**218**
References		**218**

Abstract

This chapter provides a comprehensive overview of modern high pressure solid-state synthesis methods, with a specific focus on their integration with in situ X-ray diffraction methods. Fundamental concepts in solid-state synthesis are re-examined within the context of synthesis at high pressures, and additional considerations specific to high pressure are introduced. We examine three common apparatuses for achieving high pressures: the Paris–Edinburgh press, the diamond anvil cell, and the multi-anvil press. We present the advantages and disadvantages of each method in the context of high-pressure synthesis, using illustrative examples from the literature. We hope that this chapter will provide the curious solid-state chemist with the foundational understanding required to begin their foray into world of high-pressure synthesis.

10.08.1 Introduction

High pressure has a profoundly fundamental impact on chemistry. Elemental properties that we take for granted such as atomic radius, electronegativity, and electronic configuration can all be drastically altered by extreme compression,[1,2] leading to unexpected new chemistry such as the formation of electrides, stable oxides of noble gases, and ionic bonding in helium.[3–6] In addition to refining our foundational understanding of chemistry, these exotic new phases open the door to next-generation materials with unprecedented and perhaps even unimagined properties.

The range of pressures accessible within our universe is vast, covering ~50 orders of magnitude.[7–11] For practical reasons, we have so far disproportionately explored chemistry close to 1 atm, which is roughly in the middle of this scale. Although special to the inhabitants of planet Earth, this pressure is somewhat arbitrary. It is also a rather low pressure from the standpoint of chemistry, being many orders of magnitude below the pressures at which chemistry gives way to nuclear synthesis. These intermediate pressures, which remain remarkably unexplored, present a tantalizing opportunity for chemical and materials discovery.

The theme of *exploration* appears frequently in reviews of high-pressure science,[12–14] and for good reason: pressure transports us to a new space where undiscovered solid-state compounds can become thermodynamically accessible. Stated another way, it generates a new potential energy surface (PES)—energy as a function of some subset of physical variables—where new thermodynamic minima arise (Fig. 1). If a system is given sufficient energy to overcome its local energy barriers, and if the new minimum has a lower free energy than the reactants, then the new phase becomes synthetically accessible. The driving force is no different to that which drives traditional solid-state chemistry, but the destinations are new. The source of the dramatic changes to the PES are related to the response of orbital energies to extreme compression,[1,2,15] and the phases lurking in these new minima can reveal characteristics that contrast with the chemical intuition we have formed from our study of ambient pressure phases. This makes these phases extremely promising for materials discovery, since novel chemical properties often translate into novel material properties.

Diamond is perhaps one of the most famous examples of an exotic high-pressure material. Under sufficient compression (above ~5 GPa), the diamond allotrope of carbon becomes lower in energy than graphite, and with enough heat energy to overcome the barrier in the PES, pressurized graphite can be transformed into diamond. The sp^3-bonded network in diamond is drastically different to the sp^2-bonded sheets in graphite, and this difference in bonding is reflected in the stark contrast in the properties of these two phases. Diamond is an extremely hard material with optical transparency, low electrical conductivity, and high thermal conductivity, while graphite is a soft layered material with poor optical transparency in the bulk, good electrical conductivity, and high thermal conductivity.

Since the energy barrier for the transformation remains high at low pressures, diamonds formed at high pressure are stable against decomposition after the pressure is removed, allowing them to be recovered to ambient conditions. A feature of recoverable high-pressure materials is that they exist within local minima in the PES. Such phases are referred to as metastable, which is a term that distinguishes them from the thermodynamic ground state yet emphasizes their stability against decomposition. Incidentally, the metastability of diamond—an optically transparent phase with unrivalled hardness and bulk modulus—has been critical to the advancement of high-pressure science (Section 10.08.2.2).[16,17]

Although high-pressure methods have been available for decades,[16,18] when it comes to chemical synthesis the added complexity of these experiments has historically made them much less efficient and far more expensive than traditional low-pressure solid-state methods. Part of this is because the apparatus used to access high-pressure and high-temperature conditions have historically been something of a black box, with the sample only being examined after recovery back to ambient pressures

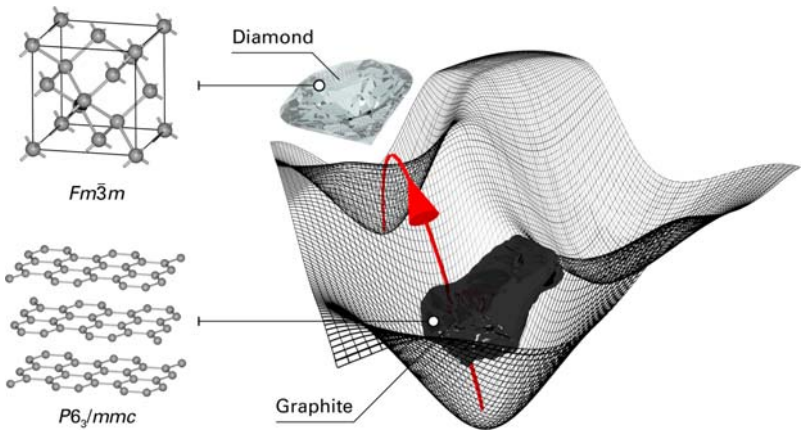

Fig. 1 Artistic illustration of a two-dimensional potential energy surface in the carbon system. The ground state allotrope of carbon under ambient pressure is the graphite structure, which exists in the global enthalpy minimum. The diamond structure is a higher energy structure existing in its own local minimum— i.e. diamond is a metastable allotrope under ambient conditions. It is locally stable, but cannot be accessed through traditional heating approaches. Under high pressures, the PES is transformed such that diamond becomes the global minimum and can be accessed with heating.

and temperatures. These samples offer little to no information on the chemistry that occurred throughout the reaction, especially in the all-too-common cases where the high-pressure phases are not quenchable (i.e. they do not persist once pressure is removed).

The recent development and proliferation of synchrotron-based in situ techniques at high pressure is rapidly changing this picture, and many modern beamlines allow for the real-time analysis of samples under extreme conditions of both pressure and temperature.[19–27] In this chapter, we will focus on X-ray diffraction, showing how this has been successfully integrated with methods that access pressures up to hundreds of gigapascals and thousands of degrees. Our main goal is to provide the synthetic solid-state chemist with a working understanding of the current capabilities for materials synthesis under these extreme conditions. We will begin by introducing some of the fundamental concepts in solid-state synthesis to provide a familiar basis for understanding the strengths and limitations of modern high-pressure methods. We will then describe the common high-pressure methods available at synchrotron facilities by recasting them as advanced synthetic chemistry reaction vessels. Finally, we will provide illustrative examples from the recent literature that focus on the discovery of exciting new materials. Our ultimate goal is to inspire solid-state researchers to explore high pressure as a synthetic variable in their own work.

10.08.1.1 Review of some fundamental concepts in solid-state synthesis

Although extreme pressure demands a significant departure from traditional solid-state methods in terms of the experimental setup required, the fundamental aspects that dictate the efficiency of synthesis remain unchanged. In this section, we will briefly outline some of the universal requirements for solid-state synthesis. This will provide a basis for appreciating the nuances of synthesis at high pressures (Section 10.08.1.2).

10.08.1.1.1 Atomic diffusion requires very high temperatures

One of the main features of solid-state synthesis that distinguishes it from other chemical synthesis methods is the need for very high temperatures, routinely on the order of hundreds or even thousands of degrees. This requirement arises from the very high densities present in the solid state, where most atoms have a high coordination number. Unlike solution-based chemical reactions, where the reactants can rapidly mix and react to form products, solid-state reactions often rely on the diffusion of atoms through dense solids. This is a much slower process than liquid diffusion, and usually serves as the rate-limiting step in solid-state reactions.[28]

In order for a solid-state reaction to proceed, energy is required to break bonds and to relocate the atoms to their new positions in the product phase. The diffusion of atoms through a lattice can be represented by the isotropic diffusion coefficient (D), which contains terms describing the geometric (γ), entropic (S), and enthalpic (H) factors for diffusion of atoms within a material (Eq. 1). The geometric and entropic components can be combined into a single term, D_0, and the $-\Delta H$ term can be relabeled as the activation energy (Q). Recasting the equation then highlights the fundamentally Arrhenius behavior of diffusion (Eq. 2).

$$D = \gamma e^{\frac{\Delta S}{R}} e^{\frac{-\Delta H}{RT}} \tag{1}$$

$$D = D_0 e^{\frac{-Q}{RT}} \tag{2}$$

If a reaction relies on the diffusion of atoms—as a great deal of solid-state reactions do—then the activation energy of diffusion usually serves as the main rate-limiting step, and the most straightforward way to overcome this barrier is to raise the temperature. The Boltzmann distribution tells us that while low energy states are the most densely occupied, there will always be some occupation of higher energy states so that even at low temperatures it may be possible for an atom to overcome the activation energy required for diffusion. At higher temperatures, there will be an even greater occupation of these high-energy states, leading to an increased probability for an atom to diffuse to another site. Thus, higher temperatures lead to increased rates of diffusion. Another generality that can be derived is that the temperatures needed for solid-state reactions are often closely related to the melting point of the reactants.[29] That is, the energy required to melt a solid depends upon the energy required to break the chemical bonds in the solid matrix.

One of the structural factors that directly impacts diffusion rates is the availability of interstitial sites. For example, smaller atoms can readily diffuse by hopping between the interstitial sites in a parent lattice consisting of larger atoms. One famous example of this is the diffusion of carbon atoms in iron lattices to form steels. This process, which is referred to as carburization, occurs when iron is heated in the presence of carbon. The energy barrier for the diffusion of carbon into iron is relatively low, primarily due to the small size of carbon atoms.[30] Other common examples of solids that exhibit comparatively fast diffusion rates are intercalated battery materials, where ions such as lithium can readily diffuse in and out of a host material.[31,32]

In contrast, if the bonding interaction between the interstitial atoms and the parent lattice are strong, then this can lead to a reduced rate of diffusion through the solid. In such cases, or when the atoms are too large to squeeze past each other, the predominant diffusion mechanism can involve the local migration of vacancies that leads to a net diffusion of atoms within the structure. This mechanism is often slower than interstitial diffusion and depends on factors such as the number of vacancies in the structure as well as the vacancy formation energy.

There is a special class of solid-state transformations that can occur with little to no atomic diffusion at all. These are known as diffusionless transformations. They are also sometimes called martensitic or displacive transformations, although these terms

technically refer to more specific cases of diffusionless transformations. While it may be a stretch to call these transformations chemical reactions, they nevertheless lead to significant changes in crystal structure and by extension the bulk properties of the material.[33]

10.08.1.1.2 Stable heating relies on sophisticated apparatus

As a rule of thumb, a temperature greater than 2/3 the melting point of the least refractory (i.e. lowest melting point) reactant is required for synthesis to proceed. There are a number of methods for heating samples to very high temperatures, but the most common is resistive heating. In this method, a large electrical current is driven through a conductor with a high electrical resistance, leading to a well-defined and sustained heat output. Resistive heating methods allow for the achievement of very precise temperatures that are stable over indefinite periods of time. With appropriately shaped heating elements, an approximately uniform temperature can be applied to the entire volume of the sample being heated. Commercial laboratory furnaces can achieve temperatures of around 1200–1700 °C,[34,35] while more specialized equipment can reach temperatures as high as 2200 °C under vacuum,[36] and 3000 °C under argon.[37]

More specialist techniques for heating include laser heating and arc melting, which are able to access very high temperatures. Laser heating transfers heat to materials through the absorption of photons, with an advantage being the ability to heat materials without physical contact. Laser heating will usually only directly heat the surface of materials, and so for materials with a low thermal diffusivity this can result in unavoidable temperature gradients throughout the sample. Still, laser heating provides access to much higher temperatures than would otherwise be achievable with laboratory-sized furnaces, with standard setups being able to access ~5000 K.[38]

Similar to laser heating, arc furnaces also rapidly heat materials to extreme temperatures without physical contact.[39] However, instead of photons, arc furnaces pass a large electrical current across a gap between the sample and an electrode, which is usually made of graphite or tungsten. The sample has to be electrically conductive for this method to work. The plasma created by the arc is capable of reaching extreme temperatures and can be used to heat a large amount of material. Industrial arc furnaces with multi-ton capacity can achieve around 1800 °C, while smaller laboratory-scale furnaces can achieve around 3000 °C. Extreme temperatures are particularly advantageous for accessing and accurately measuring the melting points of highly refractory materials.[40,41]

One advantage of pushing the reaction temperature above the melting point of one or more reactants is that the liquid component can then act as a solvent, or "flux." Fluxes can greatly improve diffusion rates and can even promote access to kinetic products in the solid state.[42–46] Elements with relatively low melting points such as bismuth, tin, and indium, or low melting point salts, are commonly used as fluxes. They can either participate in the reaction itself (self-flux), or serve only as a solvent for the reactants (inert-flux).[47] Some uses of flux are more esoteric such as the case of using iron as a flux to reduce the pressure required to form diamond.[48,49]

It is important to note that the complete melting of the precursor phases may not be required, and that sufficient diffusion of atoms can occur while the reactants are still primarily crystalline solids. Although the required reaction times may increase as the diffusion rates decrease at lower temperature, one benefit of maintaining the crystallinity of both the reactants and products is that it allows us to monitor progression of the reaction via in situ X-ray diffraction.

Synthesis from the melt or even the gas phase is not always the most desirable approach for accessing solid-state compounds. Indeed, there are many cases where the goals and requirements of the reaction are not compatible with performing the reaction at such high temperatures, and so the reaction must be carried out fully in the solid state. For example, the target product may be a metastable phase, in which case the reaction temperature needs to be limited, since a high thermal energy could promote the thermodynamic phase rather than the target metastable phase. An example of this is $Ni_{31}Si_{12}$, which only forms below ~1000 °C. Upon heating above 1000 °C, $Ni_{31}Si_{12}$ gives way to $Ni_{25}Si_9$.

10.08.1.1.3 Reactant interfaces dictate product yield

An important consequence of performing reactions at temperatures below the melt is that reactions are confined to the interface between the reactants. This limitation can be overcome by maximizing the interfaces, thereby maximizing the volume over which the reaction can occur. Although the reactions are still highly localized, a faster overall reaction with a higher yield can be achieved. The most common way to increase reactant interfaces is to prepare well-mixed powders with very small particle sizes. A standard approach to this is ball milling, which uses hard spheres to mechanically grind samples through repeated impacts.[50] While ball milling produces a distribution of particle sizes, very narrow ranges of particle sizes can be obtained through subsequent mechanical sieving techniques. The final product is a well-mixed precursor powder with enhanced material interfaces compared to the coarser starting powders.

When a high yield of the final product is required, but diffusion rates are particularly slow, it is possible to iterate between high-temperature reactions and ambient temperature mechanical mixing steps to maximize reaction interfaces and circumvent the bottleneck of low diffusion rates. In some cases, the mechanical and thermal energy from the work of milling and mixing may inadvertently be sufficient to induce chemistry between the reactants, or may weld smaller particles into larger particles. Although this can be exploited as a method for synthesis,[51] it is usually unwanted in cases where the goal is to create fine powders of the elements. However, it is worth noting that in some cases these unwanted phases can be annealed out during heating. Indeed, another method for overcoming the challenges of slow diffusion at low temperature is to rapidly heat starting materials to extreme temperatures (typically using an arc melt furnace) over the course of a few seconds, to achieve well mixed material from a molten liquid or even a precursor compound. This precursor is then annealed at a much lower temperature for a long period of time on the order of hours or weeks to obtain the desired phase.

10.08.1.1.4 Phase stability is very sensitive to temperature

Precise control of temperature can be critical in the solid state, with reaction products sometimes differing significantly as a result of only a few degrees difference in the reaction temperature. A simple illustrative example of this is the Ni–Si system, which can form multiple high temperature phases. The stability fields of these high-temperature phases in some cases differ by less than 100 °C, defining very narrow stability regions, and requiring very precise and stable temperatures to target them.

Temperature can also be critical for controlling crystal growth processes. For example, in the semiconductor industry, single-crystal silicon is produced using either the Czochralski or floating zone method, where the temperature is finely controlled within degrees to allow the polycrystalline sample to melt and form a single crystal. Failure to control temperature precisely can lead to changes of crystal growth direction and the adoption of impurities from surroundings, rendering regions of the silicon unusable.[52]

Solid-state chemists have developed several ways to harness the sensitivity of crystallization to temperature to access desired materials by deliberately introducing temperature gradients within a sample. So-called zone furnaces are one way that solid-state chemists can use temperature gradients to their advantage by heating different parts of a sample to different temperatures. This technique can be used to melt polycrystalline material at the hotter end, leading to monocrystalline growth in the cooler end. Other uses of zone furnaces include zone refining and zone leveling, which leverage the difference in the diffusion of an impurity at the solid–liquid boundary to control the presence of impurities in the crystallizing melt. Zone refining concentrates the impurity in one location to purify the rest of the material, while zone leveling evenly distributes a solute throughout the purified material. This technique is common for transistor and diode semiconductors made from gallium and silicon power and detector devices.[53–55] Thus, temperature can also be used to control the chemical composition of a melt, allowing us to control purity. More exotic uses of temperature gradients include the incorporation of volatile phases such as iodine, which enables vapor transport from the hot end to the cool end of the reaction vessel.[56]

10.08.1.1.5 Chemical isolation of the reactants is critical

As with all chemical reactions, the formation of side products is an impediment to both yield and purity. The high temperatures involved in solid-state synthesis tends to increase the reactivity of all species present, including those that constitute the reaction vessels, the atmosphere, and any experimental probes present. Care must therefore be taken to isolate the reaction from reactive surroundings as much as possible. Common ways of achieving this include the use of inert atmospheres such as argon gas or vacuum, or the selection of relatively unreactive vessel materials such as alumina or graphite crucibles, sealed silica (quartz) glass ampules, or welded niobium or tantalum tubes. Fully or partially evacuated quartz ampules serve the additional benefit of leading to much lower pressures generated within the vessel when heating to high temperatures, minimizing the risk of the vessel breaking due to high internal gas/vapor pressures. Materials can even be combined to reap multiple benefits. For example, niobium or tantalum foils or carbon coatings can be used as protective linings inside a quartz ampule, retaining the benefits of a high vacuum in cases where the quartz may otherwise interfere with the reaction. In many cases, air-sensitive samples are prepared entirely under an inert atmosphere before being sealed in ampules.

At elevated temperatures, the inertness of any material is pushed to its limits. For example, the Czochralski process for growing silicon single crystals typically uses a quartz vessel, selected for its chemical inertness. However, the quartz still leaches small amounts of oxygen into the molten silicon.[57] Although the amount of oxygen is small (30–40 ppm)[58] and is negligible for most purposes, it is nevertheless present. In cases where higher purity silicon is necessary, such as for high-performance transistors and other silicon components, the float zone method is used. Here, the need for a vessel is removed entirely, and the sample is suspended by its own surface tension.[55,59] Another example of impurities arising from presumed inert vessels is the leaching of trace amounts of sodium present in borosilicate glass into a reaction solution or melt.[60,61]

10.08.1.2 Additional considerations for synthesis at high pressures

The vast range of techniques that solid-state chemists have developed under ambient pressure reflects the advanced level of control that can be exerted over many aspects of chemical synthesis. As we will see in the following sections, such control is much more difficult to achieve in high-pressure solid-state synthesis, in large part due to the many complicating factors arising from the high-pressure instrumentation itself. Rather than view this as a negative, we should instead view it as an opportunity for solid-state chemists to join the challenge in developing techniques that bridge this gap, so that chemists will be able to exert a similarly high degree of control over chemical space under extreme pressures. As we will see, in situ X-ray diffraction is playing a vital role in assessing the efficiency of synthesis with high-pressure methods.

10.08.1.2.1 Diffusion rates are greatly diminished under pressure

One major difference observed in high-pressure reactions is that diffusion rates are decreased significantly regardless of the diffusion mechanism.[29,62–69] This means that high-pressure reactions in a given system will generally need to be performed at higher temperatures than they otherwise would in order to recover the diffusion rates present under ambient pressures. The requirement for stable high temperatures leads to a number of complications, not only in terms of the instrumentation required to heat the sample in a reliable and measurable way, but also with respect to the selection of materials for the reaction vessels (often referred to as sample assemblies by the high-pressure community), which must maintain their structural and chemical integrity under extreme pressure and temperature conditions. This is without even considering the requirements for in situ diffraction, which is contingent on having a path of high X-ray transmission on both sides of the sample.

One important point is that diffusionless structural transformations will be unaffected by the diminished diffusion rates. Thus, one consequence of slower diffusion rates at high pressure could be an increased preference for diffusionless structural changes, even though an entirely different structure may be thermodynamically more stable. In this way, pressure may offer a direct pathway toward kinetic products. A number of elements and compounds have been shown to undergo diffusionless transitions at ambient temperatures and high pressures (Xe,[70] Li,[71] Fe,[72] RuO_2,[73] $MgFe_2O_4$[74]).

10.08.1.2.2 Sample homogeneity is difficult to control

Homogeneity is another aspect whose importance is magnified by high pressure. Because the nature of high-pressure experiments requires small sample sizes, it is important for the samples to be well mixed so that the overall target composition is achieved. While a particle size of 5 μm might be sufficiently small for traditional ceramic methods, a single particle of this size would be only an order of magnitude smaller than the sample space in a high-pressure diamond anvil cell experiment. Further, since the decreased diffusion leads to reactions that are even more localized, a high degree of homogeneity of the reactant mixture is needed to ensure reactions are as complete as possible, and to provide sufficiently pure product for analysis. This is very difficult to achieve in high-pressure reactions because the sample cannot be as readily removed and reground as in traditional methods.

10.08.1.2.3 Encapsulation materials must be chemically inert

Similar to ambient pressure chemistry, chemical isolation within high-pressure experiments is achieved primarily through the careful design of the high-pressure assembly such that only chemically inert materials are in direct contact with the sample. The selected materials must also maintain their integrity over the pressure and temperature range of the experiment. Fortunately, these properties tend to go hand-in-hand. Various materials find use across high-pressure methods, but magnesium oxide, diamond, and boron nitride are especially common, being selected for their high melting points and demonstrable chemical inertness up to moderate temperatures and pressures.[75–78] For air-sensitive samples, oxygen and moisture can be eliminated by assembling and sealing the highpressure assembly inside a glove box.

10.08.1.2.4 Pressure must be measured alongside temperature

High-pressure experiments rely on the ability to precisely monitor the pressure experienced by the sample. In theory, if the exact instrument dimensions, input forces, and material responses of all components were known, then the pressure could be calculated anywhere in the high-pressure assembly. In reality, these values are rarely known to a sufficient precision to be used in this way, and we instead use other methods for determining the pressure.[79] Furthermore, when synthesizing novel materials, the pressure-dependent response of the new material is likely to be unknown even if that of the rest of the system was known precisely.

If a material possesses properties that can be readily measured while under pressure, and if those properties have already been calibrated against pressure, then the material can be used as a *pressure calibrant*. As an example, gold is an excellent pressure calibrant because its crystallographic lattice parameters as a function of pressure are well known. This relationship between pressure and volume is an example of an equation of state.[80] All that is required to determine the pressure that a sample of gold is experiencing is the measurement of a single lattice parameter (the *a* cell length of fcc-Au), which can be measured to a high precision using X-ray diffraction. Any inert material with a well known equation of state that compresses without any distortions or phase transitions can be used as a pressure calibrant using X-ray diffraction. Some common examples include gold, platinum, aluminum, NaCl, and LiF.[81–84]

Another property that can be used for pressure calibration is fluorescence, since fluorescence lines will generally shift under applied pressures. This has the advantage that less sophisticated equipment is required to measure optical emissions versus diffraction. Ruby ($Cr:Al_2O_3$) and Sm:YAG ($Sm:Y_3Al_5O_{12}$)[85] are popular calibrants used in this way. In theory, any property that is well studied and changes consistently and significantly over a given pressure range can be used to calibrate pressure. For example, the superconducting transition temperature (T_c) of Pb is used as an internal pressure calibrant in high-pressure magnetometery experiments.[86]

10.08.1.2.5 Anisotropy of the pressure field can be important

Another important consideration for high-pressure experiments is the *uniformity* of the pressure applied to the sample. Just as non-uniformities in temperature can have a critical influence on chemical reactions, so too can differences in pressure.[87] For example, bismuth undergoes several phase transitions between 0 and 5 GPa, meaning that multiple allotropes might exist within the same sample space if the pressure gradient is sufficiently broad.[88,89] We must also worry about nonuniformities that arise from the fact that pressure is a vector rather than a scalar quantity. In particular, unequal pressure along various directions can result in non-uniform stresses on the crystal lattice. This is particularly prevalent in layered compounds.[90–92] These non-uniform stresses on the crystal lattice can also significantly influence material properties. For example, Skyrmion ordering within MnSi has been shown to depend very sensitively on the direction of compression relative to an external magnetic field.[93] Another particularly exciting area is the impact of strain on electronic structure and bonding. In the $IrTe_2$ topological semimetal, uniaxial strain alters the relative bond strengths parallel and perpendicular of the compression axis, enabling a pressure tuning of the electronic structure and a potential stabilization of the superconducting state.[94]

Although non-uniform stresses are clearly an important synthetic parameter to explore, we typically avoid such complications at the outset and design experiments that subject samples to as uniform a pressure as possible. The condition where a pressure transmitting medium is free of frictional or internal stresses is termed hydrostatic. It is important to note that hydrostatic does not mean

that the pressure is the same at every point in the medium, but that at every point the pressure is the same in all directions. To illustrate this point, a column of water at rest will have a higher local pressure at the bottom than at the top, but the pressure at any point will be equal in all directions. This distinction is generally unimportant for high pressure chemistry since the pressures achieved are far greater than the pressure gradients introduced by hydrostatics, but we should be careful when using the term.

Whether or not the pressure experienced by a sample is hydrostatic depends on the ability of the pressure transmitting medium to remain a compressible fluid. A good pressure transmitting medium will ideally remain a compressible fluid at the pressures used in the experiment. In practice, all pressure transmitting media have a pressure limit above which they cannot behave truly hydrostatically.[95] This limit has been quantified for many commonly used substances, usually through the measurement of lattice strains experienced by a single crystal as a function of pressure.[96,97] The term *quasi-hydrostatic* is often used to indicate that a pressure transmitting medium is effectively hydrostatic, with its deviation from ideal hydrostaticity being on the order of uncertainty in the measurement.

10.08.2 High-pressure apparatus for chemical synthesis with in situ X-ray diffraction

Having provided an overview of the most important factors influencing the efficiency and reproducibility of solid-state reactivity, we are now ready to introduce high-pressure methods in the context of chemical synthesis. It is important to realize that high-pressure methods have a rich history of development over the last century or so, and that we owe a great deal to the pioneering work of the many scientists who led us here through trial, error, and innovation.[16,18,98] It is also important to realize that these techniques are constantly evolving, and that the methods we will introduce here are simply the latest generation.

The challenge of achieving high static pressures in the laboratory reduces to a relatively simple principle: apply the largest manageable force over the smallest manageable area. Here, the word manageable encapsulates safety, achievability, and affordability, all of which are important considerations to the experimentalist. When designed and set up properly, a high-pressure device can exploit the relationship $P = F/A$ to apply a moderate force (F) over an exceedingly small area (A) to generate an extreme pressure (P). For example, a force of 10 N over an area of 1 cm^2 leads to a pressure of 100 kPa (approximately atmospheric pressure). The same force on a much smaller area of 100 μm^2 leads to 100 GPa—the pressure roughly 1500 miles below the earth's surface.[99] The requirement of a small area over which to direct the forces leads naturally to very small sample sizes in laboratory-scale high-pressure experiments. Currently this scale is on the order of 100–1000 μm, although even smaller samples may be used in extreme cases.[100]

The first successful high-pressure experiments were performed in 1914 by Percy Bridgman, who is credited with the invention of the Bridgman seal. While compressing various materials, Bridgman noticed that the compressed material had the tendency to flow or creep around the edges of the compressing pistons. To combat this, Bridgman designed a series of seals around the piston made from materials with varying compressibility. For example, a harder material like steel can be used on the load-side, while a softer material like rubber is used on the sample-side. When compressed, the apparatus directs pressure along these seals, causing them to deform and in turn apply pressure both inwards against the walls of the sample container, and outwards against the piston. The arrangement of these seals ensures that the pressure of the innermost seal always exceeds that of the pressure medium in the sample chamber, preventing the pressure medium from leaking out of the sample chamber. This approach allowed Bridgman to readily achieve pressures up to 2 GPa,[101] and his work would become the basis for all modern opposed-anvil type apparatuses. We will discuss two opposed-anvil devices: the Paris–Edinburgh press and the diamond anvil cell.

Another major advancement in the field of high pressure science came with the invention of the multi-anvil apparatus. Designed by Tracy Hall in the 1950s, this apparatus relies on the arrangement of more than two anvils directing force toward the sample.[18] Multi-anvil devices are capable of taking large volumes of sample to very high pressures, and as such they are often simply referred to as "large volume presses." However, this term can encapsulate a number of fundamentally different devices. In this chapter, we will focus primarily on the Kawai-type multi-anvil apparatus, which has proven to be a highly versatile reaction vessel for the solid-state chemist.

The diamond anvil cell, the Paris–Edinburgh press, and the Kawai-type multi-anvil apparatus have all been integrated with in situ X-ray diffraction. Furthermore, all three of these techniques allow for in situ temperature control of the sample space, making them ideal platforms for solid-state chemical synthesis.

10.08.2.1 Paris–Edinburgh press

10.08.2.1.1 Overview of the Paris–Edinburgh press (PEP)

A schematic of a typical Paris–Edinburgh press is shown in Fig. 2A.[102,103] To generate pressure, two opposing anvils made of tungsten carbide or steel are driven toward each other using a single hydraulic ram to compress a sample with a volume on the order of 1–10 mm^3. The components that encapsulate the sample are known collectively as the sample assembly, and a typical assembly is shown in Fig. 2B. Assemblies undergo significant plastic deformation during the experiment and are not intended to be reusable. The anvils, on the other hand, can be used over and over as long as they are not severely damaged by the compression (minor cracks and chips are typically not problematic).

The sample is immediately surrounded by the sample sleeve, which is usually made from boron nitride or magnesium oxide, although any material that maintains structural integrity under compression and heating while also being chemically compatible

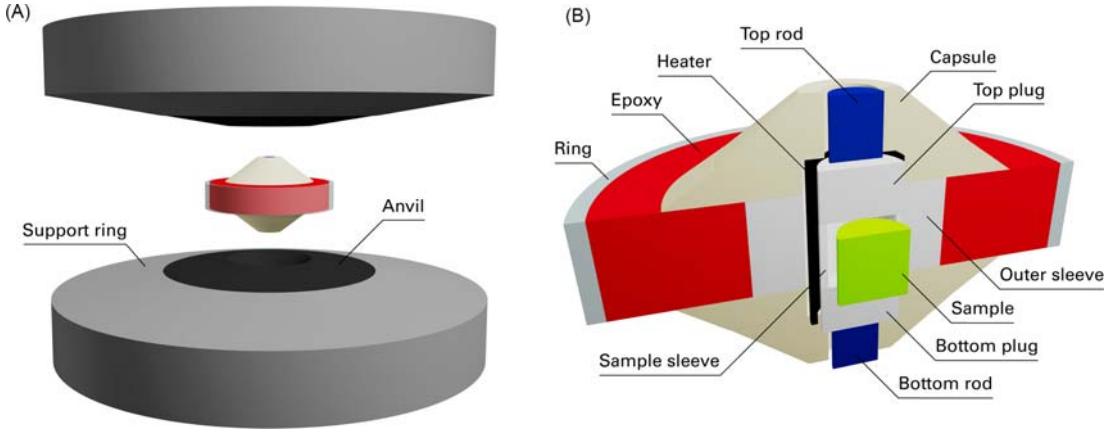

Fig. 2 (A) Schematic showing the axial arrangement of the Paris–Edinburgh press anvils and sample assembly. The anvils are usually made from tungsten carbide, and are set into steel support rings. Each anvil has a recess at its center that accommodates the sample assembly. (B) Cut-out schematic of the PEP sample assembly. The sample sleeve is typically made from h-BN or MgO. Top and bottom plugs, as well as the outer sleeve, are made from MgO. The standard capsule material is zirconia. Tantalum rods offer additional compressive support along the compression axis. Lateral support is provided by a ring of cured boron epoxy and an outer lexan ring.

with the sample (i.e. it does not react with the sample) can be used for this purpose. The sleeve is designed in such a way that it will fully encapsulate the sample throughout compression. If the sleeve fractures, then it becomes possible for the reactants to diffuse out of the central chamber and mix with other parts of the assembly. This is obviously undesirable, and for certain reactants it becomes necessary to use specially designed sample sleeves that are more resistant to such failure. For example, if a liquid melt is expected to form under high temperatures, then a double cup (a set of two interlocking cups) will offer better sample containment. Leaking of the sample out of the sample space leads to a rapid decrease in pressure and ultimately the complete failure of the assembly. Such failures are universal across all high-pressure techniques, and are often referred to as "blow-outs." It is perhaps obvious that when a blow-out occurs the experiment is over. Whether the instrument itself is damaged depends on the severity of the failure and the nature of the energy release, but complete anvil fracture is always a possibility. Thus, a properly balanced construction of the assembly and careful consideration of the interaction of its components with the sample is critical for successful reactions in any high-pressure setup.

There have been innumerable modifications made to the PEP by experimental groups seeking to push the experimental capabilities to new limits. For example, although the Paris–Edinburgh press typically uses tungsten carbide anvils, it is possible to achieve even higher pressures by using sintered diamond anvils. In addition to the higher pressures achieved, the X-ray transparency (low absorption) of diamond also enhances the physically accessible scattering range during X-ray measurements.[104]

10.08.2.1.2 Using the PEP for chemical synthesis

In order to perform chemical synthesis, a reliable method for heating to high temperatures is required. Similar to ambient pressure furnace reactions, resistive heating is the go-to method for achieving high temperatures within the PEP. The sample space is surrounded by a cylindrical heating element, leading to a uniform heating of the sample (Fig. 2B). Graphite is commonly used for the heating element, which is beneficial for diffraction studies since the low-Z of carbon makes it highly transparent to X-rays. However, under high pressures graphite has a tendency to transform into diamond, which is not electrically conductive and therefore diminishes the heat output. Lanthanum chromite ($LaCrO_3$) and rhenium are popular alternatives to graphite when very high temperatures and pressures are required, although windows must be machined into these heaters to allow X-rays to pass through the sample to allow in situ diffraction. The Paris–Edinburgh press is often pressure-calibrated for a given assembly and anvil design, allowing for a reliable targeting of sample pressure using only the measurement of the hydraulic load being applied by the press. Calibration is performed by using X-ray diffraction to monitor the lattice parameters of a calibrant with a known pressure-volume curve. When X-rays are not available, the volume collapse associated with known phase transitions can also be used to anchor a calibration curve. In some cases, when a highly accurate measure of pressure is required, one or more calibrants can be measured alongside the sample itself.

10.08.2.1.3 In situ X-ray diffraction in the PEP

When using tungsten carbide anvils, which are opaque to X-rays, the only access to the sample is along the radial direction. The standard X-ray Diffraction (XRD) setup is shown in Fig. 3, with the incoming X-ray beam perpendicular to the compression direction. The shape of the anvils dictates the range of scattering in the vertical direction, while the radial aperture is determined by the support columns ($\sim 70^\circ$ for four-column presses, $\sim 140^\circ$ for two-column presses). X-ray photons are absorbed by the assembly materials on both sides of the sample, which necessitates a high-flux X-ray source and/or long exposure times. Soller slits can be used to selectively reject scattered photons from everywhere except the sample space, leading to much cleaner diffraction.[105]

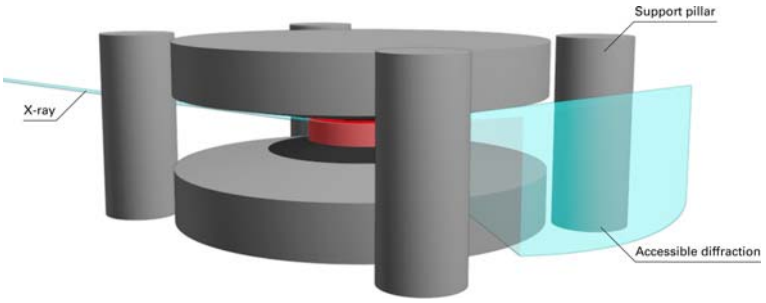

Fig. 3 X-ray diffraction configuration in the Paris–Edinburgh press. The X-rays are delivered perpendicular to the compression axis. The range of accessible diffraction is determined by the conical angle of the anvils (vertical access) and the support pillars of the press itself (horizontal access). Illustrated here is the accessible diffraction in a four-column press.

10.08.2.1.4 Advantages and disadvantages of the PEP

The primary advantage of the Paris–Edinburgh press is the relatively large sample space it offers compared to other high-pressure devices. Larger sample sizes mitigate some of the technical difficulties encountered with high-pressure experiments. For example, a major practical benefit to the beginner is that the scale of the assembly is "only" millimeters rather than micrometers, which makes the sample preparation much more manageable. Another benefit to the larger sample size is a much greater control over sample composition, since the sample dimensions are still much larger than particle sizes encountered in mechanically-mixed samples. Another advantage of the large sample size is that it enables the study of bulk liquids at high pressure.[106]

The footprint of a Paris–Edinburgh press is around 0.5 m × 0.5 m × 0.5 m. This puts it in the range of typical benchtop instrumentation, making it straightforward to house in existing laboratories. Its small form factor also makes it relatively portable, allowing it to be moved between laboratories and beamlines. Indeed, the original driving force for the invention of the PEP was to create an instrument that minimizes both size and weight while still allowing for high pressures and large sample volumes.[102]

The combination of a simple design with few moving parts and a "large" sample scale makes the Paris–Edinburgh press an ideal entry point into high-pressure synthesis. It is much more forgiving of slight imperfections and misalignment in the sample preparation compared with other high-pressure techniques (see below), making it a robust method for accessing high pressures and temperatures.

The trade-off for large sample sizes and experimental stability is that the Paris–Edinburgh press is limited to lower pressures compared to other high-pressure devices (recall that pressure is inversely related to area), with an upper limit of around 7 GPa for standard configurations. Of course, depending on the reaction being pursued, this may be a sufficiently high pressure. It should also be noted that advances are constantly being made to this press type, and we can expect even higher pressures in novel configurations (e.g. polycrystalline diamond (PCD) anvils may soon become commonplace).

10.08.2.1.5 Example syntheses with the PEP

In situ X-ray diffraction integrated with the PEP was used to study the breakdown of magnetite (Fe_3O_4) into Fe_4O_5 and Fe_2O_3 above 9.5–11.0 GPa and at temperatures of 973–1673 K.[107] The sample assembly contained magnetite powder enclosed within a hexagonal boron nitride (h-BN) capsule, with a graphite heater surrounding the h-BN capsule. A small hole was bored into the side of the h-BN capsule and packed with a mixture of NaCl:Au (10:1). This mixture served as both a pressure and temperature calibrant, since the equations of state for both phases are known as a function of P and T. That is, only one P,T condition will be consistent with both densities determined from XRD. This obviated the need for a thermocouple to measure the sample temperature, allowing for a greater sample volume. Sintered diamond anvils were used instead of the more common tungsten carbide anvils, permitting pressures up to 17 GPa. Soller slits were used to filter the measured diffraction such that scattering from outside the sample space was rejected,[108] leading to excellent quality diffraction patterns free of scattering contributions from the assembly.

The growth of diamond from an Fe—Ni—C melt was studied at pressures up to 6 GPa and temperatures of up to 1600 K using in situ X-ray diffraction in the PEP.[109] The sample space of the PEP was loaded with the Fe—Ni alloy and high-purity synthetic graphite in a 1:4 ratio. The mixture was surrounded by h-BN and then by a graphite heater, with platinum also being placed within the assembly as a pressure calibrant. Diamond crystallization from the melt was monitored using energy-dispersive X-ray diffraction at a fixed Bragg angle of 10°. The pressure and temperature were monitored using the equations of state of h-BN and Pt, whose volumes were determined simultaneously through diffraction. The kinetics of the transformation were tracked through monitoring the integral of the (111) reflection of diamond. The Avrami equation[110] was used to determine the rate of transformation between graphite and diamond, revealing that the process is diffusion-controlled with a constant nucleation rate. Such detailed kinetic analysis would not have been possible without the in situ analysis enabled by X-ray diffraction.

Carbon nanothreads, which are polymeric chains of sp^3-bonded carbon atoms with "diamond-like" cores, can be synthesized under high pressures through the compression of benzene and derivative monomer species so that they react mechanochemically. Studies have shown that nanothreads form under pressure in such a way that they align along the compression axis, leading to a route for the synthesis of single crystals with extended long-range order.[111] The PEP was shown to allow for the scalable synthesis of single crystals of furan nanothreads at ~1 GPa.[112] In these experiments, the samples were recoverable and could be studied with

ex situ methods. It is notable that heating was not required in these samples since the molecular monomers are in close proximity in the precursor crystals, such that long-range diffusion is not a prerequisite for the synthesis.

10.08.2.2 Diamond anvil cell

10.08.2.2.1 Overview of the diamond anvil cell (DAC)

The diamond anvil cell (DAC) is perhaps the most widely used and versatile of the high pressure techniques on account of its modularity and small form factor.[113,114] It is also the device that can reach the highest pressures under static compression. A schematic of a diamond anvil cell is shown in Fig. 4. The primary purpose of the cell body is to drive together two identical single-crystal diamond anvils to generate very high pressures in samples held between them. The anvils are typically around 0.25 carat in size, and are polished into a shape known as a modified brilliant cut. The brilliant cut has a set of faces known as pavilion faces that converge to meet at a point known as the culet. In high pressure experiments, the culet is polished into a flat face with a well-defined diameter, typically in the range of 100–1000 μm. The very small area of the culet face is what allows for the generation of extremely high pressures.

DACs are hand-held devices with a very small footprint of around 5 cm × 5 cm × 5 cm, making it relatively simple to integrate them with other methods designed around sample holders of similar dimensions, such as diffraction and optical spectroscopy. The major benefit of using superhard diamond for the anvils is the extreme pressures that can be reached, with pressures surpassing 500 GPa now being possible (albeit in the hands of highly-skilled experimentalists). Another benefit to using diamond is its transparency to a wide range of wavelengths, allowing them to offer a window into the sample space across a variety of techniques.

A highly uniaxial compression is required so that the anvils maintain perfect alignment throughout the experiment. This is typically achieved using either a "piston–cylinder" or "pin" cell design. In the piston–cylinder design, the cell is machined in such a way that one part (the piston) has an outer diameter slightly smaller than the inner diameter of the other part (the cylinder). This enforces both a precise lateral alignment of the culet faces during compression, as well as a strictly uniaxial compression of the sample. In the pin design, one side of the cell has a number of pins that align with holes on the other side of the cell. As with the piston–cylinder design, the pins ensure that the cell can only close in a precise geometry. Although both designs remain popular, the piston–cylinder design is considered superior in terms of enforcing a uniaxial compression, and is universally favored for megabar (100 GPa) pressures and higher.

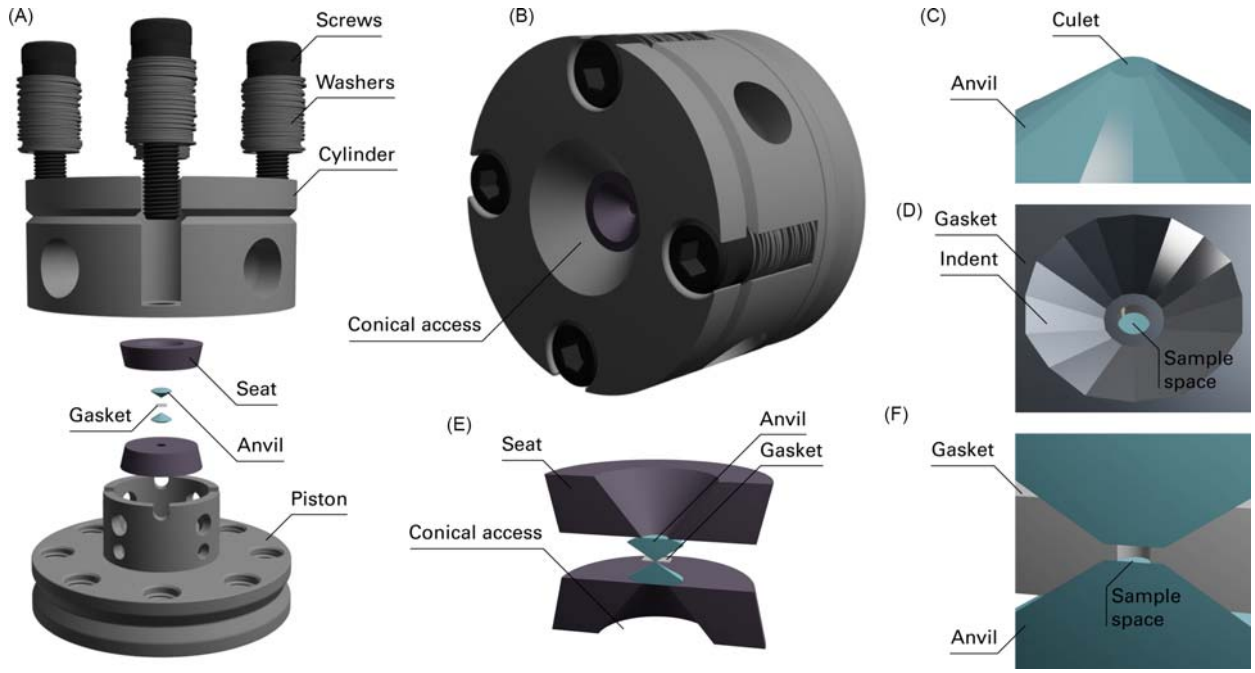

Fig. 4 (A) Exploded view of a piston–cylinder "symmetric" type DAC. Each anvil is set onto a seat, which is in turn set onto each side of the cell. The screws pass through the cylinder side and engage with threads in the piston side. Once fully tightened, turns of the screw drive the cell together. Belleville washers dampen the force applied to the anvils. (B) View of a "closed-up" cell, showing the wide conical access machined into the cylinder side (the same access is machined into the piston side). (C) Close-up view of a diamond anvil, showing the flat face polished at the culet—the meeting point of the pavilion faces. (D) An indented and drilled gasket, showing the impression of the pavilion faces. The sample hole is usually 1/2 to 2/3 the diameter of the culet. (E) Cut-out schematic showing the conical access provided by the seats when the diamonds are engaged. (F) Close-up cut-out side view of the sample space between diamond anvils in a closed cell.

The diamonds do not sit directly in the cell, but are instead set onto seats (also sometimes known as backing plates). The materials used for seats are selected primarily for their strength, since they transmit very high loads to the diamond anvils. Depending on the experiment, they may also need to be maintain their structural integrity at high temperatures without deforming. For example, Al_2O_3 seats may be preferred to tungsten carbide seats, which use cobalt as a binder to hold the WC grains together and therefore soften under temperatures approaching the melting point of cobalt. In other cases, the seats may need to be made from materials with a high X-ray transparency; this allows experimentalists to maximize the measurable range of diffraction without sacrificing anvil support by using seats with a wider conical access.

The anvils are secured in place on the seats using an epoxy adhesive. It is important to note that the epoxy is not placed *between* the anvil and the seat as an adhesive layer, but rather placed *around* the anvil and the seat to prevent movement of the anvil during handling. Indeed, the cement offers little to no support during the experiment itself. The seats are set into each side of the cell and their lateral positions are finely adjusted by set screws so that the two anvils are aligned precisely when the cell is closed. Precise alignment of the anvils is known as centering the cell, and is a critical step. Poor alignment is a major cause of anvil failure leading to blow-outs during experiments.

Although the sample can be directly compressed by the two anvils without the use of a gasket material, this leads to a highly anisotropic stress, which is usually not desired. Instead, a gasket material is placed between the diamonds and the sample is loaded into a hole made in the center of the gasket. Holes can be drilled using mechanical drill bits, electrical discharge machining (EDM) drills, or laser drilling methods. EDM drills and laser drills are the most common methods used for the small sample holes required in modern experiments, which are on the order of 500 μm or less.

The diameter of the gasket hole is smaller than that of the culet so that the sample space is effectively a cylinder with diamond as the ceiling and floor of the space and the gasket material as the surrounding walls. The gasket material is selected based on the target pressure, with strong metals being favored for the highest pressures (steel, rhenium, and tungsten are common). As the anvils are driven together, the gasket is deformed and flows along the path of least resistance. Most of the gasket mass flows away from the anvils, but some of it will flow inward toward the sample space, reducing its volume and increasing the pressure within. This flow will continue with further increase in the anvil load up to the point that the pressure in the sample space is so high that the gasket material can no longer flow inwards and the sample hole diameter begins to increase. At this point, the experiment should be halted to prevent the inevitable blow-out when the sample hole reaches the edge of the culet.

If the sample space contained only the sample surrounded by air, then the compression would lead to only a very small increase in pressure as the gas is compressed into a smaller volume. This pressure would be far too low to prevent the gasket flowing inwards, and the sample hole would quickly be reduced until it closed entirely around the sample. To avoid this, the sample is surrounded by a pressure transmitting medium.

The pressure transmitting medium should be a solid or a liquid so that its compressibility is relatively low compared to a gas. It should also ideally be hydrostatic so that it can redistribute pressure evenly as the sample hole collapses (see earlier discussion on hydrostaticity). Although many liquids and condensed gases exhibit hydrostaticity at low pressures, they all have a threshold pressure at which this is no longer the case.[96] Simple solvent mixtures such as 16:3:1 methanol:ethanol:water have been shown to display reasonable hydrostaticity, and are convenient pressure transmitting media that can be readily loaded on the benchtop. However, noble gases such as helium, neon, and argon are preferred where hydrostaticity to very high pressures is required, such as during single crystal diffraction experiments.[115–118] Although the gases are loaded as liquids, they are much more compressible than other media, and so the initial sample space is often drilled to be much larger to offset the significant decrease in the volume of the sample space during compression.

Pressure monitoring within a DAC can be achieved in a number of ways. The most common way is to include a pressure calibrant within the sample space. A pressure calibrant is any material where a given property has been calibrated against pressure in a separate set of experiments. Within DACs, the optical fluorescence of ruby ($Cr:Al_2O_3$) is a widely used calibrant.[16,119] Ruby is excited with green/blue light and strongly fluoresces in the red, which is convenient because the entire visible spectrum of light readily transmits through diamond. The wavelength of the R_1 and R_2 fluorescence lines have been well characterized as a function of both pressure and temperature.[16,120–122] Measuring the emission profile of the ruby allows the pressure in the sample space to be calculated simply by measuring the shift in wavelength of these two features in the spectrum during compression (**Fig. 5**).[123–125] Spectrometers designed specifically for these measurements are a common feature in high-pressure laboratories, being relatively robust and simple to use, as well as having a small footprint.

Another common approach for pressure determination in the DAC is to monitor the density of a standard material that has already been calibrated against pressure.[79] Solid noble metals like gold and platinum are favored for this purpose due to: (1) their moderately high compressibility, which leads to a smooth change in density over a large pressure range; (2) their high-symmetry cubic crystal structures, which concentrates their diffraction intensities into a relatively small number of intense peaks; and (3) the lack of any phase transitions under pressure, which avoids complications caused by discontinuities in density. Small grains of the standard can either be loaded alongside the sample within the sample space, much like ruby spheres are loaded alongside the sample, or they can mixed intimately with the sample in the case of measurements on powders.

During in situ diffraction experiments, the pressure medium itself can also act as a reliable pressure calibrant, albeit to a lower precision than can be obtained using standards surrounded by a quasi-hydrostatic pressure medium as described above. KBr and MgO are examples of pressure media for which an equation of state is known and can be used to allow for a reasonable pressure determination.[27,119] Refractory oxides are particularly useful as pressure transmitting media because they also act as thermal insulators, which can be important in laser heating experiments (see below).

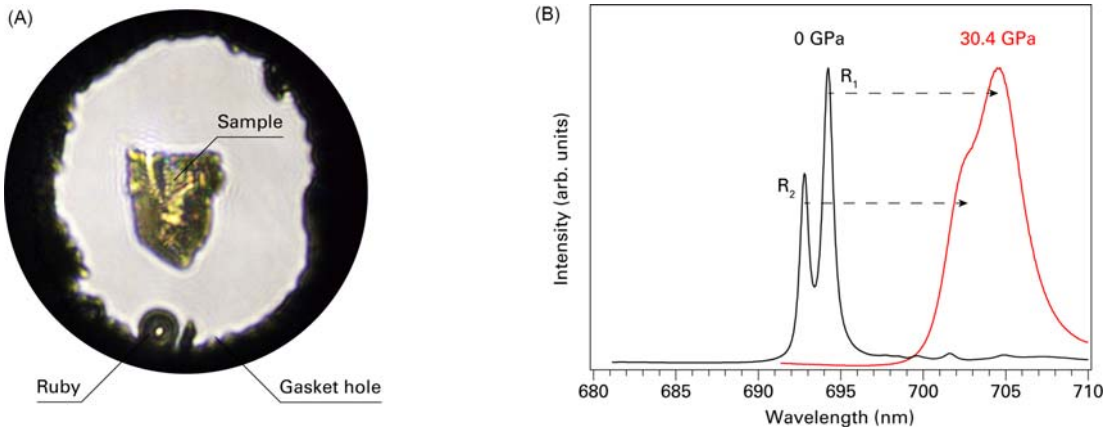

Fig. 5 (A) Photograph of a sample space viewed along the compression axis (through the diamonds) of a diamond anvil cell. A small ruby sphere is loaded alongside the sample, close to the gasket. (B) Comparison of the ruby fluorescence signal recorded at two different pressures, illustrating the shift of the signal to larger wavelengths as a function of compression. At low pressures, the R_1 and R_2 fluorescence lines are sharp and well resolved. At higher pressures, non-hydrostaticity broadens the features, making them more difficult to resolve.

A method of pressure determination that is unique to the diamond anvil cell is the measurement of the Raman spectrum of the diamond anvil itself.[126,127] In this technique, the laser light is focused at the culet, and the high frequency edge of the Raman band is analyzed. This feature has been shown to exhibit a predictable shift with pressure, making it a very useful method for determining pressure in cases where optical access to the sample is degraded (e.g. lensing effects caused by anvil deformation at high pressure can make fluorescence methods intractable).

10.08.2.2.2 Using the DAC for chemical synthesis

The temperature of the sample in the DAC can be controlled using either resistive heating or laser heating, and both methods are widely used. Resistive heating methods operate on the same principle as that used in furnaces, albeit on a smaller scale. Mo, Pt, PtRh, and NiCr are commonly used for the wire in heating elements, and are typically hand wound around a refractory material such as alumina. These heating elements are placed inside the cell and surround the anvils and seats (Fig. 6). They are able to achieve a highly uniform heat distribution throughout the sample space, but are generally limited to temperatures below the oxidation temperature of the wire component. This can be offset to some degree by flowing a reducing gas over the element (e.g. 5 wt% H_2 in Ar), or by encapsulating it completely to prevent oxygen exposure. Tungsten-based elements are able to reach $\sim$1200 °C. This approach is known as external resistive heating, so named because the source of heat is outside the sample space. An alternative approach is to place the heating element within the sample space itself—an emerging technique known as internal resistive heating.[128] In cases of extreme temperatures in the heater, the entire cell can become hot, making it susceptible to oxidation. The steel

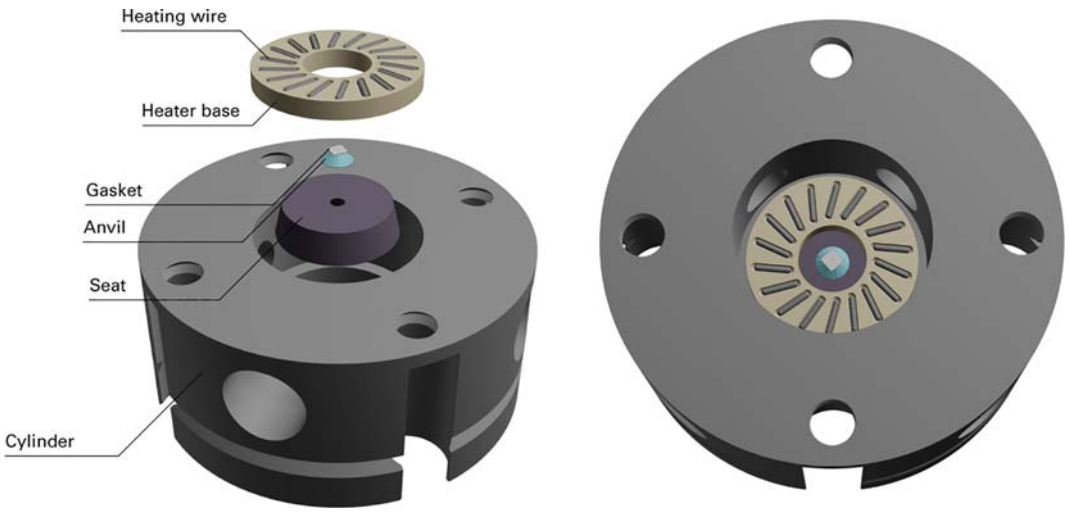

Fig. 6 Illustration of a typical external resistive heater used in a diamond anvil cell. The heater base is machined out of a non-conductive material such as pyrophyllite, and contains precisely spaced holes and guides to wrap the heating element wire through. Typical wire materials include platinum, or platinum–rhenium alloys. The assembled heating element is placed inside the DAC and surrounds the anvils and gasket.

components and diamond anvils can be protected by placing the entire DAC assembly in a vacuum can, or by flowing a large volume of reducing gas over it.

Laser heating methods are capable of reaching up to ~5000 K using infrared lasers focused on the sample through one or both sides of the DAC.[129] A prerequisite quality of the sample is that it must optically couple to the laser light for efficient heating to take place. This can make the heating of insulating materials more tricky. However, there are advanced methods that allow the laser heating of optically transparent wide-band-gap materials using CO_2 lasers.[130]

Although laser heating leads to higher temperatures, they also produce highly localized temperatures over only a few tens of microns.[131] This is non-ideal in cases where whole-sample heating is desired. However, in XRD studies where the X-rays are highly focused, it is possible to collect diffraction data entirely within the "hot spot." The localized nature of the heating also has the benefit that it allows for multiple separate heating experiments to be performed within a single diamond anvil cell.

Since diamond is one of the most thermally conductive materials, laser heating necessitates thermal insulation between the sample and the diamond anvils to ensure that: (1) the diamond does not act as a thermal sink preventing samples from reaching high temperatures; (2) damage to the anvils by graphitization at elevated temperatures is avoided; and (3) carbon from diamond cannot react with the sample.[132] Magnesium oxide is commonly used as a thermal insulator during laser heating.[133,134] Although we have considered laser heating alongside X-ray diffraction, it has also been integrated with a wide range of other methods including Raman spectroscopy,[135–138] Brillouin scattering,[138–140] X-ray absorption spectroscopy,[141–145] inelastic X-ray scattering,[146] and Mössbauer spectroscopy.[147] Many of these methods offer highly complementary information to XRD.

10.08.2.2.3 In situ X-ray diffraction in the DAC

Although the uniaxial compression geometry in the diamond anvil cell makes this device similar to the Paris–Edinburgh press in terms of the load configuration, the transparency of the anvils to X-rays lead to a different standard setup for diffraction. While the PEP is limited to only the radial geometry, in the DAC the diffraction can be collected either through the anvils along the compression axis (axial), or it can be collected by aligning the beam perpendicular to the compression axis (radial). These geometries are illustrated in Fig. 7.

Since diamond is transparent to X-rays, while common gasket materials are not, the axial configuration is the most common diffraction geometry in DACs. In cases where the radial geometry is desired, X-ray transparent gasket materials such as beryllium can be used. For example, the radial diffraction direction is crucial for deformation studies.[148] The diffraction angles available for radial diffraction can be improved by using panoramic DACs, which have large cutouts in the radial direction.[149,150]

The conical access in diamond anvil cells is typically 70–90 degrees for diffraction experiments in the axial geometry. Although larger conical apertures are available in specialist cells, they greatly reduce the stability at high pressures. It is also worth noting that the larger the conical access machined into the seat, the less support provided to the anvils, and the lower the maximum pressures that can be achieved before anvil failure. Much wider angles can be accessed in the radial direction, although maximum achievable pressures are limited by the reduced stability of the cell as a whole.

The wide conical aperture available in both configurations makes angle-resolved diffraction straightforward, and allows for the near real-time collection of data up to a high resolution during in situ heating provided that the source is brilliant enough. This technique has been implemented on a number of synchrotron beamlines, with PXRD data being possible with exposure times on the order of a few seconds. Upcoming advances in synchrotron capabilities are expected to further decrease the time required to collect high fidelity diffraction data, potentially opening a door to time-resolved kinetic studies in the solid state.

Single crystal X-ray diffraction experiments in the DAC are more complicated than PXRD studies for a number of reasons. Since only portions of the Ewald sphere are accessible in high-pressure vessels, it is crucial to load crystals in an orientation that maximizes the number of unique reflections that can be harvested. This is particularly important in the case of low symmetry materials. Another

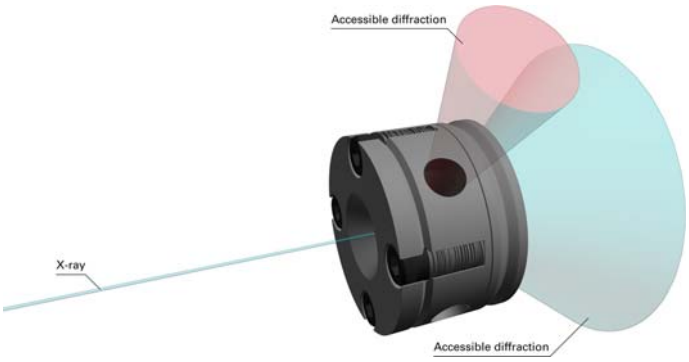

Fig. 7 Illustration of the accessible diffraction in the DAC. Accessible diffraction along the axial direction is shown in blue, and is the most common geometry. The range of accessible diffraction is determined by the conical access machined into the two sides of the cell. Accessible diffraction along the direction perpendicular to the incoming radiation is shown in red. The perpendicular access is usually restricted compared that of the axial geometry. The choice of gasket material is critical for the perpendicular geometry, with beryllium being a common choice for many experiments due to its low absorption over many wavelengths.

challenge is that single crystals can sometimes fragment under pressure, usually during a phase transition that has a significant effect on volume, resulting in a breakdown of the single crystal domain into multiple domains. This makes single crystal X-ray diffraction less viable, but other methods such as multi-grain analysis can be used instead.

A further complication is the corrections required to obtain accurate reflection intensities needed for reliable crystal structure solution and refinement. In the axial geometry, two classes of reflection can be harvested: (A) reflections collected when the incoming and outgoing beam only traveled through diamond, the pressure transmitting medium (PTM), and the sample itself; and (B) reflections that also passed through the seats and/or the gasket. Class A reflections are more desirable than Class B reflections since the absorption corrections are more straightforward—the dimensions of the diamond are usually known to a high precision, allowing for a reliable calculation of path length for correction for any arbitrary reflection, while the absorption from the sample itself and the pressure transmitting medium can be corrected with empirical methods.

Class B reflections can still be corrected and used in refinements, but the absorption effects are much more severe. This is particularly problematic since higher angle reflections are typically weaker due to diminished scattering power of all elements at high resolutions. For single crystal diffraction studies, it is therefore important that the Class A reflections approach or surpass the desired resolution. Absorption corrections in the diamond anvil cell can be performed using the ABSORB program, which can numerically correct the diamond absorption, as well as absorption from the PTM and the gasket, given that the dimensions and absorption values are well known.[151] Outside of cell design, the achievable resolution is controlled by the energy of the incident wavelength, with higher energy being preferred. Higher energy X-rays (hard X-rays) are also preferred in general because their absorption by diamond is less.[152]

10.08.2.2.4 Advantages and disadvantages of the DAC

A major benefit of the DAC is its very small footprint, which makes it much more mobile than hydraulic press based devices. Moreover, their small size greatly facilitate their integration with other techniques, especially given the transparency of diamond to a wide range of wavelengths. The ability to handle (and even ship) the cell while at pressure, along with the high-pressure stability of diamond, allows samples to be held at pressure indefinitely.

The lowest X-ray absorption is seen for materials containing predominantly light elements such as Be, B, C, or N. Since diamonds are made of carbon, diamond anvil cells are the go-to technique for high-pressure single crystal X-ray diffraction measurements, where accurate measurements of reflection intensities is critical. Furthermore, diamond anvil cells are light enough to be easily mounted on a single crystal goniometer, allowing the sample to be rotated over many orientations with respect to the beam and detectors,[153] which is not currently feasible with hydraulic presses.

Another benefit of the DAC is its very high degree of modularity, which allows for a plethora of modifications to enable complex high pressure experiments. For example, the DAC may be outfitted with a gas membrane for smooth pressure control or pressure modulation. Piezo-driven motors or oil hydraulics can also be used in place of screws.[154] Electrodes may be added to the surface of the diamond to probe electrical conductivity in situ. This approach has recently led to the discovery of record-breaking superconducting transition temperatures in high-pressure phases.[155,156]

Modifications can also be made to the diamond itself. For example, conical holes can be drilled into the rear side of the diamond anvils to minimize the path length of radiation travelling through the diamond. These so-called perforated diamond anvils enable experiments at wavelengths that are readily absorbed by diamond (e.g. soft X-rays).[157] Another possible modification to diamond anvils are the integration of complex circuits to probe magnetic susceptibility or other electromagnetic properties. These circuits are usually deposited into the surface of the diamond using a combination of sputtering methods, lithography, and chemical vapor deposition.[158,159] Other materials have been explored to replace the steel components of diamond anvil cells, such as plastics and CuBe, but each have their own benefits and limitations. CuBe is frequently use as a non-magnetic alternative to steel for investigating the magnetic properties of high-pressure materials.[113]

The main disadvantage of the DAC is that the extremely small size of the culets—which is a prerequisite for high pressures—significantly reduces the maximum sample sizes, especially at very high pressures. This restriction not only increases the severity of the issues caused by poor diffusion under high pressure (**Section 10.08.1.2**), but also significantly increases the difficulty of sample preparation. Thus, special care must be taken during synthesis experiments to ensure that homogenized starting materials are used.

Another challenge in DACs is the non-hydrostaticity of the pressure medium, which is unavoidable at extreme pressures and can introduce significant pressure gradients and anisotropic stress fields within the sample. This effect can be mitigated to some degree through thermal annealing, or by performing highly localized experiments using radiation focused to a few tens of microns, which limits the pressure gradient across the probed region. Working with X-ray radiation focused to this degree currently requires access to synchrotron facilities. Fortunately, access for general users is only improving.[160]

10.08.2.2.5 Examples of synthesis with the DAC

In addition to breaking records for the highest static pressures on earth, DACs have recently been in the spotlight for shattering records in high temperature superconductivity.[156,161] In one study, a lanthanum hydride compound was synthesized above 175 GPa using pulsed laser heating. The choice of pulsed laser heating rather than continuous wave is related to the observed stability field of the target phase, where obtaining a phase-pure sample requires careful control of the temperature to between 1000–1800K to avoid the formation of byproduct phases. *In situ* X-ray diffraction was used to monitor the expansion of the lanthanum sublattice after the heating (the much lighter hydrogen atoms could not be detected with XRD). Aided by density functional theory calculations, the new phase was identified as LaH_{10} in the clathrate structure—a well known structure type observed in

solid-state materials under ambient pressure. It was shown that LaH_{10} can be synthesized by two different methods. The first method combined gaseous hydrogen with lanthanum metal, while the second combined ammonia borane with lanthanum metal. The major advantage of using ammonia borane was the formation of insulating cubic boron nitride, which greatly improved the stability of the subsequent resistivity measurements by strengthening the pressure transmitting medium.[155]

One of the most powerful features of high-pressure as a synthetic technique is that it can encourage reactions between elements that would otherwise not react under ambient pressure. The DAC has been the authors' method of choice for exploring new reactivity at high-pressure, and it has enabled us to discover a number of new phases. We highlight here three cases in particular where we were able to synthesize the first intermetallic phases within a given transition metal–bismuth binary system. In the Cu–Bi system, we were able to use in situ X-ray diffraction in the DAC to map out the pressure–temperature phase stability of two metastable high-pressure phases, CuBi and $Cu_{11}Bi_7$, up to ~5 GPa experimentally.[162] The resolution of the stability field lines was made possible by the large number of *P*,*T* data points that could be collected with rapid in situ methods. In another study, $FeBi_2$, the first compound in the iron–bismuth system, was synthesized with laser heating in the DAC to 1400 K at pressures above 30 GPa.[14] The DAC was a vital tool for this discovery, since few other high-pressure methods can easily reach such high pressures, at least not in standard configurations. In a third study, we reported the formation of Cu_3Pb and examined its pressure-dependent formation and stability by examining subtle structural changes in the product and reactants as a function of pressure.[164] We are particularly excited about further advances in rapid X-ray diffraction to further understand the formation and deformation of high-pressure materials.

In some cases, high pressure has been shown to enable the mechanochemical synthesis of novel materials without the need for heating. One exciting area is the synthesis of carbon nanothreads from the slow and cold (unheated) compression of monomeric precursors such as benzene.[111] When brought into close proximity through extreme compression, the benzene monomers can undergo reactions to form sp^3-bonded carbon nanothreads. The diamond-like nature of the carbon in these materials could make them useful in applications requiring high directional strength. The DAC was recently used to study the pressure-induced polymerization of furan to form nanothreads.[112] Because furan is a liquid under standard conditions, the sample loading is not straightforward. For single crystal studies, the furan sample was loaded as a liquid and then pressurized until single crystals began to grow. By then backing off the pressure, the crystals could be re-melted into the liquid until only a few crystals remained. Pressure was then increased slowly to the point where these crystals could grow into large single crystals. This method relies on optical access to the sample so that the experimentalist can monitor what is happening in the sample space, and would not be possible with other techniques.

10.08.2.3 Multi-anvil press

10.08.2.3.1 Overview of the multi-anvil press (MAP)

Multi-anvil systems are so named because they generate pressures using four, six, or eight inner anvils arranged in tetrahedral, cubic, or octahedral geometries, respectively. This is in contrast to the two opposed-anvil methods introduced above (PEP and DAC). The tetrahedral arrangement was developed first,[18,165] but has since given way to the more popular cubic and octahedral geometries.[18,166] We will focus our discussion on the octahedral geometry, and in particular the Kawai-type geometry.

Kawai-type multi-anvil systems involve six first-stage outer anvils arranged in a cubic geometry that apply load to eight second-stage inner anvils arranged in an octahedral geometry. The eight inner anvils lie within the cubic space of the outer anvils, and each have one corner truncated to a triangular face. These triangular faces are oriented inward to form an octahedral cavity at the center of the eight cubes. This octahedral cavity houses the octahedral sample assembly. A typical sample assembly is shown in **Fig. 8**. The eight cube second-stage anvils are known as the Kawai-type assembly after the apparatus in which it originally appeared.[167] Within the assembly itself is a sample pellet enclosed within a sample sleeve typically made of either boron nitride or magnesium oxide. In heating experiments, the sample sleeve is placed within a cylindrical resistive heater, just as for the assemblies used in the PEP.

The ends of the cylindrical heater are typically plugged with aluminum oxide, magnesium oxide, zirconium oxide, and type C thermocouple wires (**Fig. 8**). The filled cylindrical heater is then placed within in a ceramic octahedron—typically made of spinel or magnesium oxide—and held in place using zirconium oxide cement. This assembly is placed in the space at the center of the eight inner anvil cubes, and the entire Kawai assembly is placed within the cube shaped cavity of the six outer anvils. During compression, the octahedron is compressed uniformly as the eight second-stage anvils are pushed together. Pyrophyllite is added between the inner anvil cubes to act as a gasket material.

The six outer anvils do not need to be six independently driven anvils. An alternative is to have an arrangement of steel wedges that together provide the six faces of the first-stage anvils within which the second-stage anvils are housed. One such arrangement, known as the Walker geometry, is shown in **Fig. 9**. The cubic cavity in the center of the six wedges is oriented with its [111] direction parallel to the compression axis, so that three wedges are above the Kawai assembly and three are below. One advantage of this geometry is that a single uniaxial compression force from the hydraulics can be used to compress the guide blocks holding the wedges, distributing the force evenly to the second-stage anvils and thereby all eight sides of the octahedral assembly. (In reality, the compression of the cubes is not fully isotropic, and this can be a limitation to this approach at very high pressures when the applied pressure to the octahedron becomes significantly axial.) Modifications to the Walker module simplify the experimental preparation by combining the wedges into two guide blocks each containing three wedges and having these remain seated in the press.[168] Guide blocks have become part of the standard configuration for Kawai type multi anvil experiments (up to ~25 GPa), as they increase reliability and stability at moderate pressures.

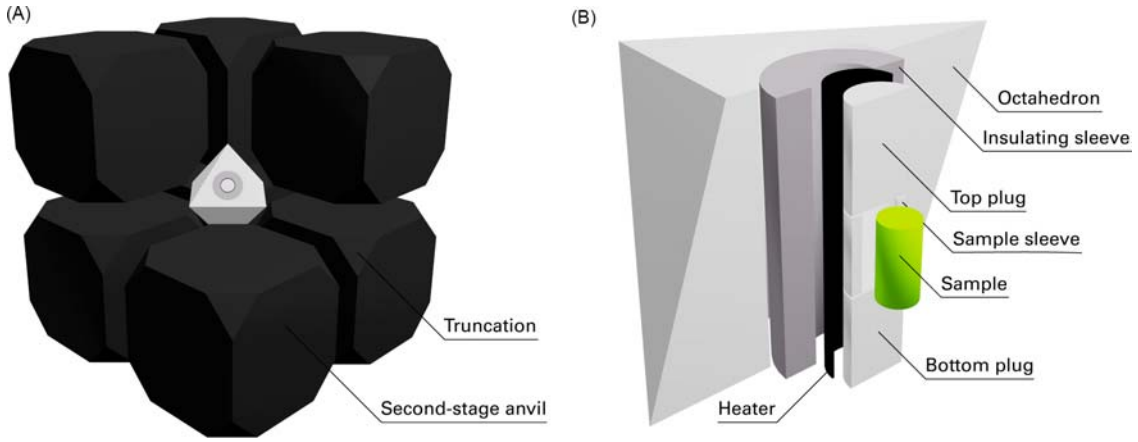

Fig. 8 (A) Illustration of a Kawai assembly. Eight second-stage anvils, typically made from tungsten carbide, are arranged to form a cube. The corners of the cubes are truncated to form an octahedral space at the center of the cubes. One of the anvils is not shown so that the octahedral sample assembly can be seen. Pyrophyllite (not shown) is added to the space between the anvils to act as a gasketing material. (B) Cut-out view of the sample octahedron. The sample is surrounded by a sample sleeve, usually made of MgO or h-BN. Top and bottom plugs are usually made from MgO. The sample is surrounded by a heater, which makes electrical contact to the truncated edges of two of the second-stage anvils. The heater is surrounded by an insulating sleeve and then the sample octahedron. The octahedron is usually made from magnesium oxide, but it can also be made from zirconia. If a highly insulating material is chosen for the octahedron (e.g. zirconia), the insulating sleeve may not be required.

10.08.2.3.2 Using the MAP for chemical synthesis

The Kawai-type MAP is capable of reaching ~25 GPa in standard configurations.[169] To reach higher pressures, it is necessary to use smaller assemblies and smaller truncations on the second-stage anvils. With such modifications, pressures up to ~65 GPa can be reached.[169] The downside is that sample sizes are reduced with higher target pressures, and the experiments are generally more prone to failure. Assembly sizes are denoted by numbers that represent in millimeters both the edge length of the octahedron and the edge length of the triangular face on the truncated second-stage cubes (Fig. 8). The 14/8 assembly, which has an octahedron

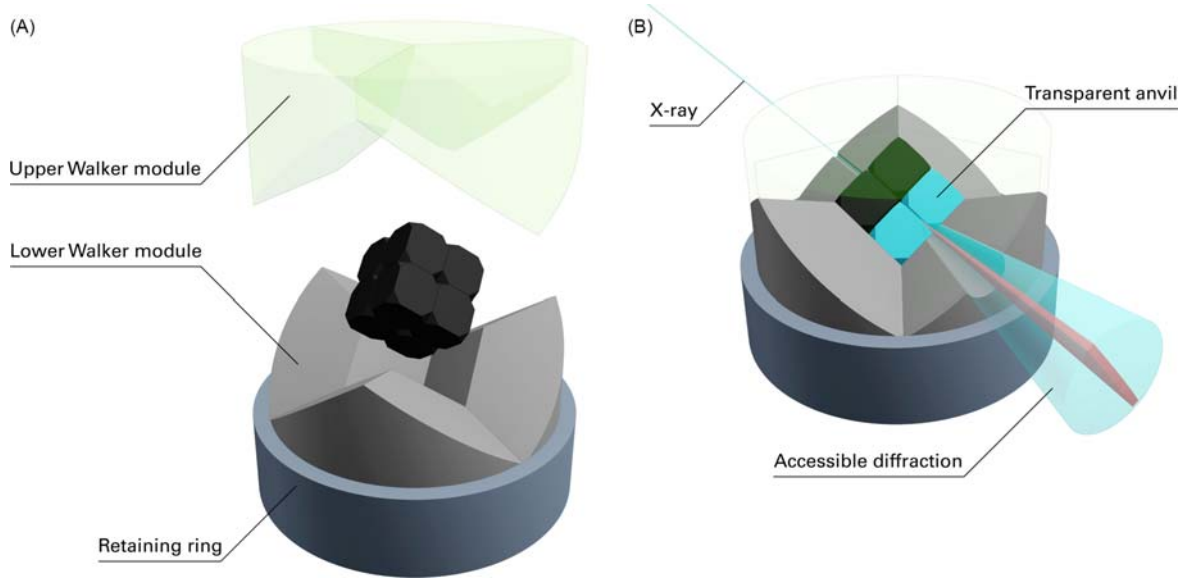

Fig. 9 (A) Illustration of the use of a Walker module as the first-stage anvils. A total of six wedges— three above and three below—form a cubic cavity within which the second-stage anvil assembly is placed. The orientation of the cube is such that the [111] direction is parallel to the compression axis. A uniaxial force from the press drives the upper and lower module together, leading to a near-isotropic collapse of the octahedral space at the center of the second-stage anvils. (B) Modifications made to the Walker module to allow for in situ X-ray diffraction. A narrow channel is machined into the wedges on the upstream side of the module to accommodate the incident X-rays. A conical access is machined into the wedges on the downstream side of the module. Two common ranges of accessible diffraction are illustrated. When fully opaque material (e.g. tungsten carbide) is used for all eight of the Kawai assembly cubes, only the photons that pass through the narrow gap between the cubes can be collected (shown in red). In the case that the two cubes on the downstream side are transparent to X-rays (e.g. PCD anvils, shown in blue), then the accessible diffraction is instead determined by the conical aperture in the wedges (shown in blue).

edge length of 14 mm and an anvil truncation edge length of 8 mm, is a widely used standard that can hold samples of up to ~25 mm^3, and can reach pressures of ~15 GPa. This volume is much larger than could be achieved in a diamond anvil cell, even at the lowest pressures, and this upper pressure limit is much higher than can be achieved in a standard PEP. Thus, the MAP occupies a sweet spot for solid-state chemists targeting the synthesis of large volumes of sample.

As with the Paris–Edinburgh press, samples in the multi-anvil press must be heated with resistive methods. Heaters are made from the same variety of materials as listed earlier for the PEP (graphite, rhenium, $LaCrO_3$). As mentioned earlier, for chemical synthesis above 10 GPa, graphite is usually not used since it can transform into diamond, which is an electrical insulator. The temperature of these reactions is typically measured directly using a type C thermocouple within the pressure assembly. For synthesis reactions, the thermocouple must be isolated from the sample mixture to prevent unwanted reactions with the metals in the thermocouple itself.

Pressure and temperature can both be controlled precisely in the MAP, and it can remain stable for many hours under high pressure and high temperature conditions. This allows for the prescription of well-defined heating and compression profiles, making it ideal for solid-state synthesis. Increasing and decreasing pressure is slower in MAP experiments than other high-pressure methods since it relies on the speed at which the hydraulics operate in the press itself. A 1000-ton presses takes an hour or so to compress, and are usually decompressed over a similar timescale (although it is possible to relieve the pressure much more quickly if desired, at the risk of inducing a blowout in the sample).

10.08.2.3.3 In situ X-ray diffraction in the MAP

Unlike the Paris–Edinburgh press and the diamond anvil cell, the Kawai-type apparatus is not naturally suited to X-ray diffraction owing the inner and outer anvils obstructing the majority of the Ewald sphere. The standard material used for the second-stage anvils is tungsten carbide, which is opaque to X-rays. In these experiments, the only path to and from the sample is along the narrow spacing between the second-stage anvils. Since this is only a very small solid angle, it is not possible to perform angle-resolved diffraction. Instead, energy-resolved diffraction is performed by irradiating the sample with a white beam and using a point detector that measures a range of wavelengths to record the diffraction pattern in momentum space. In general, the space in between the anvils during compression is typically sufficient to offer an unobstructed path through the sample from both sides as long as the second stage assembly is not fully compressed (at high loads this gap may close fully). The downside to this method is that data collection is very slow, and the signal to noise is poor.

An alternative approach is to use second-stage anvils made from polycrystalline diamond (PCD) supported in boron epoxy in place of tungsten carbide. Although the major benefit of this approach is that anvils made of polycrystalline diamond are able to achieve higher pressures as a result of their superior bulk hardness,[170–172] a simultaneous advantage is that the lower X-ray absorption of PCD anvils allows for diffracted intensities to be measured *through* the anvils.[173,174] Although it is possible to use PCD for all of the anvils and thereby achieve very high pressures, this is expensive–only one or two of the downstream-facing anvils need to be replaced to enable angle-resolved methods (**Fig. 9**). Although PCD anvils enable angle-resolved diffraction, very high flux beams are still required owing the sample thickness. Even with high-brilliance synchrotron sources, a highly absorbing sample can still prove problematic, and can necessitate the use of smaller sample sizes.[175]

10.08.2.3.4 Advantages and disadvantages of the MAP

A major advantage of the multi-anvil press is the comparatively large sample size (up to ~25 mm^3). For the solid-state chemist, the benefit of the larger sample size is the ease of sample preparation compared to DACs and the ability to prepare bulk samples for recovery and further study using other experiments. Indeed, large single crystals have been quenched from MAP reactions, enabling much more detailed structural studies than would be possible in situ.[162,176,177] Flux reactions, which use molten materials as a solvent, can also be performed in the MAP.[178] Special care must be taken to ensure that the flux does not leak out of the sample space, such as through the use of a double cup sample setup. X-ray imaging is particularly useful for monitoring the melt in these experiments.

An advantage of the MAP compared to the PEP is a more isotropic compression, which allows for a much higher maximum pressure. The Kawai-type MAP can use single-piece guide blocks for the first-stage anvils, which has the benefit of an increased stability. However, it should be noted that under very high pressures this leads to a non-uniformity of the compression. There are other MAP techniques that are able to maintain isotropic compression to higher pressures, such as the DIA-type, which uses additional independently drivable anvils to allow for modification of the stress field applied to the second-stage anvils.[179]

One consequence of the larger sample sizes is that they require a much larger applied force—on the order of hundreds of tons—which necessitates a large hydraulic press and inherently limits the highest achievable pressures. The higher applied loads also increase the time required to successfully achieve pressure, with compression runs sometimes taking hours. Another challenge of the multi-anvil press is that the assemblies can be more intricate and complex than the Paris– Edinburgh press, especially when smaller assemblies are used.

10.08.2.3.5 Examples of synthesis with the MAP

In the earth sciences, the MAP has long been used for the high-pressure synthesis of metastable phases, which is not surprising given that many of the high-pressure techniques that exist today originated in some way or another from the field of mineral physics. One important area of research in planetary sciences is the deep-earth water cycle.[180] In order to understand the role that water plays in mantle composition and rheology, it is critical to determine the amount of water that can be hosted in the high-pressure phases that

constitute the upper mantle. This in turn relies on a detailed understanding of crystal structure, and in particular the ability of a given structure to host water. Because the high-pressure phases that constitute the upper and lower mantle are not found naturally in the earth's crust, they must be chemically synthesized in the lab. MAP synthesis allows mineral physicists to synthesize high-pressure minerals in significant quantities, often as large single crystals. Moreover, the chemical composition can be controlled so that end-members, or specific mineral compositions relevant to the mantle, can be synthesized.

Wadsleyite, β-$(Mg, Fe)_2SiO_4$, a high-pressure polymorph of olivine, (α-$(Mg, Fe)_2SiO_4$), has long been studied as a potential water host in the earth's mantle.[181,182] Large single crystals of wadsleyite can be synthesized using high pressures, and can be recovered to ambient pressures. Recently, crystals on the order of 0.5–1.0 mm were obtained from a MAP synthesis at 16 GPa and 1850 K.[183] The isolation of pristine single crystals of metastable high-pressure phases unlocks techniques that would otherwise be impossible, such as single crystal neutron diffraction studies to locate the exact positions and relative occupancies of bound –OH and OH_2 moieties.[184]

Another hydrous magnesium silicate mineral implicated in the deep earth water cycle, "phase D" ($MgSi_2H_2O_6$), has also been synthesized and characterized using the MAP.[185,186] In a recent MAP synthesis,[187] single crystals were grown from a heated mixture of $Mg(OH)_2$ and silica gel ($SiO_2 \cdot H_2O$) loaded into a 10/3.5 assembly and pressurized to 19 GPa. The reactants were sealed inside chemically inert gold cylindrical capsules with dimensions of 1.5 mm length and 1.2 mm outer diameter. The sealed capsules were critical to prevent the loss of water, and therefore maintain a precise elemental composition. The sample space was heated using a $LaCrO_3$ heater, with a type C thermocouple embedded close to the sample space. This allowed for the accurate cycling of temperature between 900 and 1100 °C over the course of 30 min, leading to the growth of large single crystals. A key aspect of this synthesis is that the sample homogeneity must be maintained throughout the synthesis, since chemical gradients are known to lead to complicated mineral assemblages not representative of the loaded chemical stoichiometries.[188,189] To achieve this, the entire 600-ton press was rotated 180° onto its head every 7 min.[190]

The Kawai-type MAP was used to map out the pressure–temperature phase stability of Mg^2C using in situ X-ray diffraction. A mixture of magnesium powder and glassy carbon was compressed to 18 GPa and heated using rhenium furnaces to temperatures of 1550 K. Laser-cut rhenium heaters were used to allow for in situ XRD measurements while heating. By monitoring the crystalline phases present at various *PT* conditions, an accurate determination of the stability field could be constructed. The antifluorite structure ($Fm\bar{3}m$), of Mg_2C is metastable, and had previously been synthesized and recovered to ambient pressures. However, the optimum pathway for synthesis was not known. This work revealed that thermal quenching at high pressures is critical for recovering a high yield of this phase.

10.08.3 Conclusion

We have reviewed some of the state-of-the-art high-pressure methods available to the solid-state chemist. Each technique was described in the context of achievable pressure and temperature conditions in the sample space, the complexity and scale of sample preparation, and the ease with which they can be integrated with in situ techniques, in particular X-ray diffraction. For the synthetic solid-state chemist, the ideal reaction vessel would have the following features: (1) A sufficiently large sample volume to allow for the targeting of exact stoichiometries, as well as the synthesis of large enough quantities for ex situ bulk properties measurements; (2) The ability to uniformly heat the entire sample space to the high temperatures required to induce chemical reactivity, and to hold these temperatures over long timescales (i.e. days); and (3) A very wide pressure range allowing the experimentalist to examine any arbitrary pressure over a range of hundreds of gigapascals using the same equipment.

No single device currently possesses all three features, since (1) and (3) are seemingly incompatible, but two out of three can be achieved depending on the priorities of the experimentalist. The press methods (Paris–Edinburgh press and multi-anvil press) cover (1) and (2), and are an ideal choice when the desired pressures are below 7 GPa and 25 GPa, respectively. The diamond anvil cell method covers (2) and (3), and is the best option when a wide range of pressures are required (up to and beyond 25 GPa), or when in situ methods are crucial. Recent advances in the development of sintered polycrystalline diamond anvils are poised to extend the upper pressure limits in hydraulic press devices, which will blur the current distinctions made based on achievable pressures.

All three methods have been fully integrated with X-ray diffraction, and at synchrotrons a near real-time collection of diffraction data is now possible. This provides synthetic chemists with a direct method for determining which crystalline phases are present at high-*PT* conditions, as well as their quantitative ratio. This information is critical for the optimization of reaction conditions targeting novel phases. In terms of reciprocal space coverage and resolution, the DAC is far superior to either the PEP or MAP, and is the go-to method when the highest quality diffraction data are required. The DAC is also the method of choice for single crystal X-ray diffraction, being suitable for HP-SCXRD up to pressures of hundreds of gigapascals provided that the pressure medium is sufficiently hydrostatic, and also that the sample crystal does not undergo significant distortions under extreme pressures.

In closing, the field of high pressure science has never been more accessible to the solid-state chemist. In particular, with the advent of high-pressure in situ X-ray diffraction methods, and in particular their integration with beamlines serving the general user community, high-pressure synthesis is no longer a "black box" technique where only recoverable samples can be studied. Metastable phases that do not survive decompression can now be examined under the conditions at which they form, and their synthesis can be optimized through the real-time mapping of phase boundaries as a function of varying pressures and temperatures. The

incredible agility with which the solid-state chemist can now navigate high-pressure phase space is unprecedented, and is sure to lead us through a new frontier in materials discovery.

Acknowledgment

We thank Chung-Jui (Raymond) Yu for assistance with 3D illustrations.

References

1. Dong, X.; Oganov, A. R.; Qian, G.; Zhou, X.-F.; Zhu, Q.; Wang, H.-T. *How do chemical properties of the atoms change under pressure.* arXiv:1503.00230, 2015.
2. Rahm, M.; Cammi, R.; Ashcroft, N. W.; Hoffmann, R. Squeezing All Elements in the Periodic Table: Electron Configuration and Electronegativity of the Atoms under Compression. *J. Am. Chem. Soc.* **2019,** *141,* 10253–10271.
3. Liu, Z.; Botana, J.; Hermann, A.; Valdez, S.; Zurek, E.; Yan, D.; Lin, H. Q.; Miao, M. S. Reactivity of He with Ionic Compounds under High Pressure. *Nat. Commun.* **2018,** *9,* 1–10.
4. Dong, X.; et al. A Stable Compound of Helium and Sodium at High Pressure. *Nat. Chem.* **2017,** *9,* 440–445.
5. Gao, H.; Sun, J.; Pickard, C. J.; Needs, R. J. Prediction of Pressure-Induced Stabilization of Noble-Gas-Atom Compounds with Alkali Oxides and Alkali Sulfides. *Phys. Rev. Mater.* **2019,** *3,* 1–7.
6. Miao, M. S. Caesium in High Oxidation States and as a p-Block Element. *Nat. Chem.* **2013,** *5,* 846–852.
7. Burkert, V. D.; Elouadrhiri, L.; Girod, F. X. The Pressure Distribution inside the Proton. *Nature* **2018,** *557,* 396–399.
8. Özel, F.; Freire, P. Masses, Radii, and the Equation of State of Neutron Stars. *Annu. Rev. Astron. Astrophys.* **2016,** *54,* 401–440.
9. Dziewonski, A. M.; Anderson, D. L. Preliminary Reference Earth Model. *Phys. Earth Planet. In.* **1981,** *25,* 297–356.
10. Dubrovinsky, L.; Dubrovinskaia, N.; Prakapenka, V. B.; Abakumov, A. M. Implementation of Micro-Ball Nanodiamond Anvils for High-Pressure Studies above 6 Mbar. *Nat. Commun.* **2012,** *3,* 1163.
11. Thompson, W.; Hanrahan, S. Characteristics of a Cryogenic Extreme Highvacuum Chamber. *J. Vac. Sci. Technol.* **1977,** *14,* 643–645.
12. Miao, M.; Sun, Y.; Zurek, E.; Lin, H. Chemistry under High Pressure. *Nat. Rev. Chem.* **2020,** *4,* 508–527.
13. Boeri, L.; Hennig, R. G.; Hirschfeld, P. J.; Profeta, G.; Sanna, A.; Zurek, E.; Pickett, W. E.; Amsler, M.; Dias, R.; Eremets, M.; et al. The 2021 Room-Temperature Superconductivity Roadmap. *J. Phys. Condens. Matter* **2022,** *34,* 183002.
14. Walsh, J. P.; Freedman, D. E. High-Pressure Synthesis: A New Frontier in the Search for Next-Generation Intermetallic Compounds. *Acc. Chem. Res.* **2018,** *51,* 1315–1323.
15. Matveychuk, Y. V.; Bartashevich, E. V.; Skalyova, K. K.; Tsirelson, V. G. Quantum Electronic Pressure and Crystal Compressibility for Magnesium Diboride under Simulated Compression. *Mater. Today Commun.* **2021,** *26,* 101952.
16. Piermarini, G. J. High Pressure X-Ray Crystallography With the Diamond Cell at NIST/NBS. *J. Res. Natl. Inst. Stand. Technol.* **2001,** *106,* 889–920.
17. Block, S.; Piermarini, G. The Diamond Cell Stimulates Highpressure Research. *Phys. Today* **1976,** *29,* 44–55.
18. Liebermann, R. C. Multi-Anvil, High Pressure Apparatus: A Half-Century of Development and Progress. *High Pressure Res.* **2011,** *31,* 493–532.
19. Nataf, L.; Baudelet, F.; Polian, A.; Jonane, I.; Anspoks, A.; Kuzmin, A.; Irifune, T. Recent Progress in High Pressure X-Ray Absorption Spectroscopy Studies at the ODE Beamline. *High Pressure Res.* **2020,** *40,* 82–87.
20. Paszkowicz, W. High-Pressure Powder X-Ray Diffraction at the Turn of the Century. *Nucl. Instrum. Methods Phys. Res., Sect. B* **2002,** *198,* 142–182.
21. Kagi, H. Outline of the High-Pressure and High-Temperature Material Science Station for Deep Earth and Planetary Sciences. *Nihon Kessho Gakkaishi* **2008,** *50,* 35–39.
22. Stan, C. V.; Beavers, C. M.; Kunz, M.; Tamura, N. X-Ray Diffraction under Extreme Conditions at the Advanced Light Source. *Quantum. Beam Sci.* **2018,** *2,* 4.
23. Fei, Y.; Wang, Y. High-Pressure and High-Temperature Powder Diffraction. *Rev. Mineral. Geochem.* **2000,** *41,* 521–557.
24. Shen, G.; Wang, Y. High-Pressure Apparatus Integrated with Synchrotron Radiation. *Rev. Mineral. Geochem.* **2014,** *78,* 745–777.
25. Frenkel, A. I.; Rodriguez, J. A.; Chen, J. G. Synchrotron Techniques for In Situ Catalytic Studies: Capabilities, Challenges, and Opportunities. *Acs Catal.* **2012,** *2,* 2269–2280.
26. Neuville, D. R.; Hennet, L.; Florian, P.; de Ligny, D. In Situ High-Temperature Experiments. *Rev. Mineral. Geochem.* **2014,** *78,* 779–800.
27. Salamat, A.; Fischer, R. A.; Briggs, R.; McMahon, M. I.; Petitgirard, S. In Situ Synchrotron X-Ray Diffraction in the Laser-Heated Diamond Anvil Cell: Melting Phenomena and Synthesis of New Materials. *Coord. Chem. Rev.* **2014,** *277,* 15–30.
28. Bamford, C., Tipper, C., Eds.; Reactions in the Solid State; *Comprehensive Chemical Kinetics*vol. 22; Elsevier, 1980; pp 247–282.
29. Tiwari, G. P.; Mehrotra, R. S.; Iijima, Y. Solid State Diffusion and Bulk Properties. *Diffus. Processes Adv. Technol. Mater.* **2005,** 69–111.
30. Kuera, J.; Stránsk, K. Diffusion in Iron, Iron Solid Solutions and Steels. *Mater. Sci. Eng. A* **1982,** *52,* 1–38.
31. Liu, M.; Rong, Z.; Malik, R.; Canepa, P.; Jain, A.; Ceder, G.; Persson, K. A. Spinel Compounds as Multivalent Battery Cathodes: A Systematic Evaluation Based on Ab Initio Calculations. *Energ. Environ. Sci.* **2015,** *8,* 964–974.
32. Kang, K.; Ceder, G. Factors That Affect Li Mobility in Layered Lithium Transition Metal Oxide. *Phys. Rev. B* **2006,** *74,* 094105.
33. Christian, J. *The Theory of Transformations in Metals and Alloys*; vol. 21; Elsevier, 2002; pp 1–22.
34. Thermo Scientific Furnaces. tech. rep. BRFURNACE0418; Thermo Fischer Scientific Inc., 2017
35. High Temperature Muffle furnace, https://www.thomassci.com/scientific-supplies/High-Temperature-Muffle-Furnace, 2021.
36. High Temperature Vacuum Furnace. https://brofurnaces.com/vacuum-furnace/high-temp-vacuum-furnace.html, 2021.
37. 3000C Top Loading Graphite Furnace. https://mrf-furnaces.com/products/3000ctop-loading-graphite-furnace/, 2019.
38. Von Allmen, M.; Blatter, A. *Laser-Beam Interactions with Materials*, Springer, 1995; pp 41–67.
39. Bhat, G. New Developments in Plasma Arc Melting. *J. Vac. Sci. Technol.* **1972,** *9,* 1344–1350.
40. Langstaff, D.; Gunn, M.; Greaves, G. N.; Marsing, A.; Kargl, F. Aerodynamic Levitator Furnace for Measuring Thermophysical Properties of Refractory Liquids. *Rev. Sci. Instrum.* **2013,** *84*, 124901.
41. Kapush, D.; Ushakov, S.; Navrotsky, A.; Hong, Q.-J.; Liu, H.; van deWalle, A. A Combined Experimental and Theoretical Study of Enthalpy of Phase Transition and Fusion of Yttria above 2000 C Using Drop-N-Catch Calorimetry and First-Principles Calculation. *Acta Mater.* **2017,** *124,* 204–209.
42. Jangg, G.; Kieffer, R. *Preparation of Transition Metal Borides From the Auxiliary Metal Bath.* tech. rep, Technische Hochschule: Vienna, 1973.
43. Champagne, B.; Dallaire, S.; Adnot, A. Production of TiB_2 in an Auxiliary Iron Bath. *J. Less-Common Met.* **1984,** *98,* 21–25.
44. Nakano, K.; Hayashi, H.; Imura, T. Single Crystal Growth of IVa-Diborides from Metal Solutions. *J. Cryst. Growth* **1974,** *24,* 679–682.
45. Higashi, I.; Takahashi, Y.; Atoda, T. Crystal Growth of Borides and Carbides of Transition Metals from Molten Aluminum Solutions. *J. Cryst. Growth* **1976,** *33,* 207–211.
46. Lundström, T. Preparation and Crystal Growth of Non-oxidic Refractories from Molten Metallic Solutions. *J. Less-Common Met.* **1984,** *100,* 215–228.
47. Kanatzidis, M. G.; Pöttgen, R.; Jeitschko, W. The Metal Flux: A Preparative Tool for the Exploration of Intermetallic Compounds. *Angew. Chem. Int. Ed.* **2005,** *44,* 6996–7023.
48. Hazen, R. M.; Hazen, R. M. *The Diamond Makers*, Cambridge University Press, 1999.

49. Elwell, D. *Man-Made Gemstones*, E. Horwood, 1979.
50. Lynch, A.; Rowland, C. *The History of Grinding*, Society for Mining, Metallurgy, and Exploration: Littleton, CO, 2005.
51. Suryanarayana, C. Mechanical Alloying and Milling. *Prog. Mater. Sci.* **2001,** *46,* 1–184.
52. Doi, T., Miranescu, I. D., Kurokawa, S., Eds.; *Advances in CMP Polishing Technologies*, Elsevier, 2012; pp 15–111. Chapter 3.
53. Goldsmith, N.; Mayer, A.; Vieland, L. The Preparation of High Purity Gallium. *J. Less-Common Met.* **1962,** *4,* 564–571.
54. Williams, R. *Gallium Arsenide Processing Techniques*, Dedham, MA: Artech House, 1984.
55. Ferrazza, F. *Practical Handbook of Photovoltaics*, Elsevier, 2012; pp 79–97.
56. Laing, C. C.; Shen, J.; Chica, D. G.; Cuthriell, S. A.; Schaller, R. D.; Wolverton, C.; Kanatzidis, M. G. Photoluminescent $Re_6Q_8I_2$ (Q = S, Se) Semiconducting Cluster Compounds. *Chem. Mater.* **2021,** *33,* 5780–5789.
57. Maeda, S.; Abe, K.; Kato, M.; Nakanishi, H.; Hoshikawa, K.; Terashima, K. Oxygen Concentration in Czochralski Silicon Crystals Depending on Silicon Monoxide Evaporation from Boron Doped Silicon Melts. *J. Cryst. Growth* **1998,** *192,* 117–124.
58. Seidl, A.; Marten, R.; Müller, G. Oxygen Distribution in Czochralski Silicon Melts Measured by an Electrochemical Oxygen Sensor. *Mater. Sci. Eng. B* **1996,** *36,* 46–49.
59. Borghesi, A.; Pivac, B.; Sassella, A.; Stella, A. Oxygen Precipitation in Silicon. *J. Appl. Phys.* **1995,** *77,* 4169–4244.
60. Kinoshita, M.; Harada, M.; Sato, Y.; Hariguchi, Y. Percolation Phenomenon for Dissolution of Sodium Borosilicate Glasses in Aqueous Solutions. *J. Am. Ceram. Soc.* **1991,** *74,* 783–787.
61. Kerisit, S.; Du, J. Monte Carlo Simulation of Borosilicate Glass Dissolution Using Molecular Dynamics-Generated Glass Structures. *J. Non Cryst. Solids* **2019,** *522*, 119601.
62. Karato, S. Pressure Dependence of Diffusion in Ionic Solids. *Phys. Earth Planet. In.* **1981,** *25,* 38–51.
63. Shewmon, P. *Diffusion in Solids*, McGraw-Hill: Materials Science and Engineering Series, 1963.
64. Murch, G.; Murch, G. *Atomic Diffusion Theory in Highly Defective Solids* In: *Diffusion and Defect Monograph Series*, Trans Tech SA, 1980.
65. Manning, J. *Diffusion Kinetics for Atoms in Crystals*, Van Nostrand, 1968.
66. Mehrer, H. *Diffusion in Solids: Fundamentals, Methods, Materials, Diffusion-Controlled Processes* In: *Springer Series in Solid-State Sciences*, Springer Berlin Heidelberg, 2007.
67. Aziz, M. J. Pressure and Stress Effects on Diffusion in Si. *Defect Diffus. Forum* **1998,** *153-155,* 1–10.
68. Chernyshev, A. P. Effect of Hydrostatic Pressure on Self-Diffusion in Metal Nanoparticles. *Physica E* **2009,** *41,* 1738–1740.
69. Ott, A.; Nordén-Ott, A. Effect of Hydrostatic Pressure on Self-Diffusion in Single Crystals of Indium. *J. Appl. Phys.* **1971,** *42,* 3745–3749.
70. Cynn, H.; Yoo, C.; Baer, B.; Iota-Herbei, V.; McMahan, A.; Nicol, M.; Carlson, S. Martensitic fcc-to-hcp Transformation Observed in Xenon at High Pressure. *Phys. Rev. Lett.* **2001,** *86,* 4552.
71. Schaeffer, A. M.; Cai, W.; Olejnik, E.; Molaison, J. J.; Sinogeikin, S.; Dos Santos, A. M.; Deemyad, S. Boundaries for Martensitic Transition of ^{7}Li under Pressure. *Nat. Commun.* **2015,** *6,* 1–6.
72. Giles, P.; Longenbach, M.; Marder, A. High-Pressure α ε Martensitic Transformation in Iron. *J. Appl. Phys.* **1971,** *42,* 4290–4295.
73. Haines, J.; Léger, J. Phase Transitions in Ruthenium Dioxide up to 40 GPa: Mechanism for the Rutile-to-Fluorite Phase Transformation and a Model for the High-Pressure Behavior of Stishovite SiO_2. *Phys. Rev. B* **1993,** *48,* 13344.
74. Wang, Z.; Lazor, P.; Saxena, S.; ONeill, H. S. C. High Pressure Raman Spectroscopy of Ferrite $MgFe_2O_4$. *Mater. Res. Bull.* **2002,** *37,* 1589–1602.
75. Coppari, F.; Smith, R.; Eggert, J.; Wang, J.; Rygg, J.; Lazicki, A.; Hawreliak, J.; Collins, G.; Duffy, T. Experimental Evidence for a Phase Transition in Magnesium Oxide at Exoplanet Pressures. *Nat. Geosci.* **2013,** *6,* 926–929.
76. McWilliams, R. S.; Spaulding, D. K.; Eggert, J. H.; Celliers, P. M.; Hicks, D. G.; Smith, R. F.; Collins, G. W.; Jeanloz, R. Phase Transformations and Metallization of Magnesium Oxide at High Pressure and Temperature. *Science* **2012,** *338,* 1330–1333.
77. Soubiran, F.; Militzer, B. Anharmonicity and Phase Diagram of Magnesium Oxide in the Megabar Regime. *Phys. Rev. Lett.* **2020,** *125*, 175701.
78. Taniguchi, T. Materials Science Research of Boron Nitride Obtained at High Pressure and High Temperature. *J. Cerma. Soc. Jpn.* **2020,** *128,* 620–626.
79. Angel, R. J.; Allan, D. R.; Miletich, R.; Finger, L. W. The Use of Quartz as an Internal Pressure Standard in High-Pressure Crystallography. *J. Appl. Cryst.* **1997,** *30,* 461–466.
80. Heinz, D. L.; Jeanloz, R. The Equation of State of the Gold Calibration Standard. *J. Appl. Phys.* **1984,** *55,* 885–893.
81. Mao, H.; Wu, Y.; Chen, L.; Shu, J.; Hemley, R. Pressure Calibration to 304 GPa on the Basis of X-Ray Diffraction Measurements of Pt, Fe and Csl. *High-Pressure Sci. Technol.* **1990,** *5,* 773–775.
82. Decker, D. L. Equation of State of NaCl and its Use as a Pressure Gauge in High-Pressure Research. *J. Appl. Phys.* **1965,** *36,* 157–161.
83. Ming, L.; Manghnani, M.; Balogh, J.; Qadri, S.; Skelton, E.; Jamieson, J. Gold as a Reliable Internal Pressure Calibrant at High Temperatures. *J. Appl. Phys.* **1983,** *54,* 4390–4397.
84. Dong, H.; Dorfman, S. M.; Holl, C. M.; Meng, Y.; Prakapenka, V. B.; He, D.; Duffy, T. S. Compression of Lithium Fluoride to 92 GPa. *High Pressure Res.* **2014,** *34,* 39–48.
85. Trots, D. M.; Kurnosov, A.; Ballaran, T. B.; Tkachev, S.; Zhuravlev, K.; Prakapenka, V.; Berkowski, M.; Frost, D. J. The Sm: YAG Primary Fluorescence Pressure Scale. *J. Geophys. Res. Solid Earth* **2013,** *118,* 5805–5813.
86. Eiling, A.; Schilling, J. Pressure and Temperature Dependence of Electrical Resistivity of pb and Sn from 1-300K and 0-10 GPa-Use as Continuous Resistive Pressure Monitor Accurate over Wide Temperature Range; Superconductivity under Pressure in Pb, Sn and In. *J. Phys. F* **1981,** *11,* 623.
87. Ma, Y.; Selvi, E.; Levitas, V. I.; Hashemi, J. Effect of Shear Strain on the α–ε Phase Transition of Iron: A New Approach in the Rotational Diamond Anvil Cell. *J. Phys. Condens. Matter* **2006,** *18,* S1075.
88. Bridgman, P. *Collected Experimental Papers, Volume V*, Harvard University Press, 2013; pp 2953–2966.
89. Bundy, F. P. Phase Diagram of Bismuth to 130 000 kg/cm^2, 500°C. *Phys. Rev.* **1958,** *110,* 314–318.
90. Beck, H.; Limmer, A.; Denner, W.; Schulz, H. Influence of High Hydrostatic Pressure on the Crystal Structure of BaFCl in the Pressure Range up to 6.5 GPa. *Acta Crystallogr., Sect. B: Struct. Sci.* **1983,** *39,* 401–404.
91. Shen, Y. R.; Englisch, U.; Chudinovskikh, L.; Porsch, F.; Haberkorn, R.; Beck, H. P.; Holzapfel, W. B. A Structural Study on the PbFCl-Type Compounds MFCl (M = Ba, Sr and Ca) and BaFBr under High Pressure. *J. Phys. Condens. Matter* **1994,** *6,* 3197–3206.
92. Shalimov, A.; Bak-Misiuk, J.; Kaniewski, J.; Misiuk, A.; Domagala, J.; Kowalczyk, E. Strain State of InAlAs/InP Layers Subjected to High Pressure Treatment. *Phys. Status Solidi C* **2005,** *2,* 1948–1952.
93. Chacon, A.; Bauer, A.; Adams, T.; Rucker, F.; Brandl, G.; Georgii, R.; Garst, M.; Pfleiderer, C. Uniaxial Pressure Dependence of Magnetic Order in MnSi. *Phys. Rev. Lett.* **2015,** *115,* 267202.
94. Yan, X.; Dong, H.; Li, Y.; Lin, C.; Park, C.; He, D.; Yang, W. Phase Transition Induced Strain in ZnO under High Pressure. *Sci. Rep.* **2016,** *6,* 1–6.
95. Piermarini, G.; Block, S.; Barnett, J. Hydrostatic Limits in Liquids and Solids to 100 Kbar. *J. Appl. Phys.* **1973,** *44,* 5377–5382.
96. Angel, R. J.; Bujak, M.; Zhao, J.; Gatta, G. D.; Jacobsen, S. D. Effective Hydrostatic Limits of Pressure Media for High-Pressure Crystallographic Studies. *J. Appl. Cryst.* **2007,** *40,* 26–32.
97. Zhao, J.; Ross, N. L. Non-hydrostatic Behavior of KBr as a Pressure Medium in Diamond Anvil Cells up to 5.63 GPa. *J. Phys. Condens. Matter* **2015,** *27*, 185402.
98. Jacobs, R. B. X-Ray Diffraction of Substances under High Pressures. *Phys. Rev.* **1938,** *54,* 325.
99. Zeidler, A.; Crichton, W. A. Materials under Pressure. *MRS Bulletin* **2017,** *42,* 710–713.
100. Dewaele, A.; Loubeyre, P.; Occelli, F.; Marie, O.; Mezouar, M. Toroidal Diamond Anvil Cell for Detailed Measurements Under Extreme Static Pressures. *Nat. Commun.* **2018,** *9,* 1–9.
101. Bridgman, P. W. The Technique of High Pressure Experimenting. *Proc. Am. Acad. Arts Sci.* **1914,** *49,* 627–643.

102. Besson, J.; Hamel, G.; Grima, T.; Nelmes, R.; Loveday, J.; Hull, S.; Häusermann, D. A Large Volume Pressure Cell for High Temperatures. *High Pressure Res.* **1992,** *8,* 625–630.
103. Klotz, S.; Hamel, G.; Frelat, J. A New Type of Compact Large-Capacity Press for Neutron and X-Ray Scattering. *High Pressure Res.* **2004,** *24,* 219–223.
104. Morard, G.; Mezouar, M.; Rey, N.; Poloni, R.; Merlen, A.; Le Floch, S.; Toulemonde, P.; Pascarelli, S.; San-Miguel, A.; Sanloup, C.; Fiquet, G. Optimization of Paris-Edinburgh Press Cell Assemblies for In Situ Monochromatic X-Ray Diffraction and X-Ray Absorption. *High Pressure Res.* **2007,** *27,* 223–233.
105. Yu, T.; Prescher, C.; Ryu, Y. J.; Shi, F.; Greenberg, E.; Prakapenka, V.; Eng, P.; Stubbs, J.; Kono, Y.; Shen, G.; et al. A Paris-Edinburgh Cell for High-Pressure and High-Temperature Structure Studies on Silicate Liquids Using Monochromatic Synchrotron Radiation. *Minerals* **2019,** *9,* 715.
106. Kono, Y.; Kenney-Benson, C.; Hummer, D.; Ohfuji, H.; Park, C.; Shen, G.; Wang, Y.; Kavner, A.; Manning, C. E. Ultralow Viscosity of Carbonate Melts at High Pressures. *Nat. Commun.* **2014,** *5,* 1–8.
107. Woodland, A. B.; Frost, D. J.; Trots, D. M.; Klimm, K.; Mezouar, M. In Situ Observation of the Breakdown of Magnetite (Fe_3O_4) to Fe_4O_5 and Hematite at High Pressures and Temperatures. *Am. Mineral.* **2012,** *97,* 1808–1811.
108. Morard, G.; Mezouar, M.; Bauchau, S.; Álvarez-Murga, M.; Hodeau, J.-L.; Garbarino, G. High Efficiency Multichannel Collimator for Structural Studies of Liquids and Low-Z Materials at High Pressures and Temperatures. *Rev. Sci. Instrum.* **2011,** *82*, 023904.
109. Solozhenko, V. L.; Turkevich, V. Z.; Kurakevych, O. O.; Crichton, W. A.; Mezouar, M. Kinetics of Diamond Crystallization from the Melt of the Fe-Ni- C System. *J. Phys. Chem. B.* **2002,** *106,* 6634–6637.
110. Avrami, M. Kinetics of Phase Change. I General Theory. *J. Chem. Phys.* **1939,** *7,* 1103–1112.
111. Li, X.; Baldini, M.; Wang, T.; Chen, B.; Xu, E.-S.; Vermilyea, B.; Crespi, V. H.; Hoffmann, R.; Molaison, J. J.; Tulk, C. A.; et al. Mechanochemical Synthesis of Carbon Nanothread Single Crystals. *J. Am. Chem. Soc.* **2017,** *139,* 16343–16349.
112. Huss, S.; Wu, S.; Chen, B.; Wang, T.; Gerthoffer, M. C.; Ryan, D. J.; Smith, S. E.; Crespi, V. H.; Badding, J. V.; Elacqua, E. Scalable Synthesis of Crystalline One-Dimensional Carbon Nanothreads through Modest-Pressure Polymerization of Furan. *ACS Nano* **2021,** *15,* 4134–4143.
113. Miletich, R.; Allan, D.; Kuhs, W. Reviews in Mineralogy and Geochemistry. *Rev. Mineral. Geochem.* **2000,** *41,* 445–519.
114. Occelli, F.; Loubeyre, P.; LeToullec, R. Properties of Diamond under Hydrostatic Pressures up to 140 GPa. *Nat. Mater.* **2003,** *2,* 151–154.
115. Klotz, S.; Chervin, J.-C.; Munsch, P.; Marchand, G. L. Hydrostatic Limits of 11 Pressure Transmitting Media. *J. Phys. D Appl. Phys.* **2009,** *42*, 075413.
116. Sasaki, S.; Kato, S.; Kume, T.; Shimizu, H.; Okada, T.; Aoyama, S.; Kusuyama, F.; Murata, K. Elastic Properties of New Pressure-Transmitting Medium Daphne 7474 under High Pressure. *Jpn. J. Appl. Phys.* **2010,** *49*, 106702.
117. Tateiwa, N.; Haga, Y. Appropriate Pressure-Transmitting Media for Cryogenic Experiment in the Diamond Anvil Cell up to 10 GPa. *J. Phys.: Conf. Ser.* **2010,** *215*, 012178.
118. Liebenberg, D. A New Hydrostatic Medium for Diamond Anvil Cells to 300 kbar Pressure. *Phys. Lett. A* **1979,** *73,* 74–76.
119. Jayaraman, A. Ultrahigh Pressures. *Rev. Sci. Instrum.* **1986,** *57,* 1013–1031.
120. Chervin, J.; Canny, B.; Mancinelli, M. Ruby-Spheres as Pressure Gauge for Optically Transparent High Pressure Cells. *Int. J. High Pressure Res.* **2001,** *21,* 305–314.
121. Chijioke, A. D.; Nellis, W.; Soldatov, A.; Silvera, I. F. The Ruby Pressure Standard to 150GPa. *J. Appl. Phys.* **2005,** *98*, 114905.
122. Forman, R. A.; Piermarini, G. J.; Barnett, J. D.; Block, S. Pressure Measurement Made by the Utilization of Ruby Sharp-Line Luminescence. *Science* **1972,** *176,* 284–285.
123. Iizuka, R.; Kagi, H.; Komatsu, K. Comparing Ruby Fluorescence Spectra at High Pressure in between Methanol-Ethanol Pressure Transmitting Medium and its Deuteride. *J. Phys.: Conf. Ser.* **2010,** *215*, 012177.
124. Nakano, K.; Akahama, Y.; Ohishi, Y.; Kawamura, H. Ruby Scale at Low Temperatures Calibrated by the NaCl Gauge: Wavelength Shift of Ruby R1 Fluorescence Line at High Pressure and Low Temperature. *Jpn. J. Appl. Phys.* **2000,** *39,* 1249–1251.
125. Syassen, K. Ruby under Pressure. *High Pressure Res.* **2008,** *28,* 75–126.
126. Hanfland, M.; Syassen, K. A Raman Study of Diamond Anvils under Stress. *J. Appl. Phys.* **1985,** *57,* 2752–2756.
127. Akahama, Y.; Kawamura, H. Pressure Calibration of Diamond Anvil Raman Gauge to 310 GPa. *J. Appl. Phys.* **2006,** *100*, 043516.
128. Heinen, B. J.; Drewitt, J. W.; Walter, M. J.; Clapham, C.; Qin, F.; Kleppe, A. K.; Lord, O. T. Internal Resistive Heating of Non-metallic Samples to 3000 K and $>$ 60 GPa in the Diamond Anvil Cell. *Rev. Sci. Instrum.* **2021,** *92*, 063904.
129. Meng, Y.; Shen, G.; Mao, H. Double-Sided Laser Heating System at HPCAT for In Situ X-Ray Diffraction at High Pressures and High Temperatures. *J. Phys. Condens. Matter* **2006,** *18,* S1097.
130. Smith, D.; Smith, J. S.; Childs, C.; Rod, E.; Hrubiak, R.; Shen, G.; Salamat, A. A CO_2 Laser Heating System for In Situ High Pressure-Temperature Experiments at HPCAT. *Rev. Sci. Instrum.* **2018,** *89*, 083901.
131. Campbell, A. J. Measurement of Temperature Distributions across Laser Heated Samples by Multispectral Imaging Radiometry. *Rev. Sci. Instrum.* **2008,** *79*, 015108.
132. Aprilis, G.; et al. Comparative Study of the Influence of Pulsed and Continuous Wave Laser Heating on the Mobilization of Carbon and its Chemical Reaction with Iron in a Diamond Anvil Cell. *J. Appl. Phys.* **2019,** *125*, 095901.
133. Fedotenko, T.; Dubrovinsky, L.; Aprilis, G.; Koemets, E.; Snigirev, A.; Snigireva, I.; Barannikov, A.; Ershov, P.; Cova, F.; Hanfland, M.; Dubrovinskaia, N. Laser Heating Setup for Diamond Anvil Cells for In Situ Synchrotron and in House High and Ultra-High Pressure Studies. *Rev. Sci. Instrum.* **2019,** *90*, 104501.
134. Patel, N. N.; Sunder, M.; Sharma, S. M. Laser Heated Diamond Anvil Cell Facility for High Temperature High Pressure Research: Application to Material Synthesis and Melting Studies. *Indian J. Phys.* **2018,** *92,* 1259–1269.
135. Zhou, Q.; Ma, Y.; Cui, Q.; Cui, T.; Zhang, J.; Xie, Y.; Yang, K.; Zou, G. Raman Scattering System for a Laser Heated Diamond Anvil Cell. *Rev. Sci. Instrum.* **2004,** *75,* 2432–2434.
136. Goncharov, A. F.; Crowhurst, J. C. Pulsed Laser Raman Spectroscopy in the Laser-Heated Diamond Anvil Cell. *Rev. Sci. Instrum.* **2005,** *76*, 063905.
137. Zinin, P. V.; Prakapenka, V. B.; Burgess, K.; Odake, S.; Chigarev, N.; Sharma, S. K. Combined Laser Ultrasonics, Laser Heating, and Raman Scattering in Diamond Anvil Cell System. *Rev. Sci. Instrum.* **2016,** *87*, 123908.
138. Zhang, J. S.; Bass, J. D.; Zhu, G. Single-Crystal Brillouin Spectroscopy with CO_2 Laser Heating and Variable Q. *Rev. Sci. Instrum.* **2015,** *86*, 063905.
139. Kurnosov, A.; Marquardt, H.; Dubrovinsky, L.; Potapkin, V. A Waveguide-Based Flexible CO_2-Laser Heating System for Diamond-Anvil Cell Applications. *C. R. Geosci.* **2019,** *351,* 280–285.
140. Li, F.; Cui, Q.; He, Z.; Cui, T.; Gao, C.; Zhou, Q.; Zou, G. Brillouin Scattering Spectroscopy for a Laser Heated Diamond Anvil Cell. *Appl. Phys. Lett.* **2006,** *88*, 203507.
141. Boehler, R.; Musshoff, H. G.; Ditz, R.; Aquilanti, G.; Trapananti, A. Portable Laser-Heating Stand for Synchrotron Applications. *Rev. Sci. Instrum.* **2009,** *80*, 045103.
142. Kantor, I.; Marini, C.; Mathon, O.; Pascarelli, S. A Laser Heating Facility for Energy-Dispersive X-Ray Absorption Spectroscopy. *Rev. Sci. Instrum.* **2018,** *89*, 013111.
143. Boccato, S.; Sanson, A.; Kantor, I.; Mathon, O.; Dyadkin, V.; Chernyshov, D.; Carnera, A.; Pascarelli, S. Thermal and Magnetic Anomalies of α-Iron: An Exploration by Extended X-Ray Absorption Fine Structure Spectroscopy and Synchrotron X-Ray Diffraction. *J. Phys. Condens. Matter* **2016,** *28*, 355401.
144. Boccato, S.; Torchio, R.; D'Angelo, P.; Trapananti, A.; Kantor, I.; Recoules, V.; Anzellini, S.; Morard, G.; Irifune, T.; Pascarelli, S. Compression of Liquid Ni and Co under Extreme Conditions Explored by X-Ray Absorption Spectroscopy. *Phys. Rev. B* **2019,** *100*, 180101.
145. Boccato, S.; Torchio, R.; Kantor, I.; Morard, G.; Anzellini, S.; Giampaoli, R.; Briggs, R.; Smareglia, A.; Irifune, T.; Pascarelli, S. The Melting Curve of Nickel Up to 100 GPa Explored by XAS. *J. Geophys. Res. Solid Earth* **2017,** *122,* 9921–9930.
146. Sakamaki, T.; Ohtani, E.; Fukui, H.; Kamada, S.; Takahashi, S.; Sakairi, T.; Takahata, A.; Sakai, T.; Tsutsui, S.; Ishikawa, D.; Shiraishi, R.; Seto, Y.; Tsuchiya, T.; Baron, A. Q. R. Constraints on Earth's Inner Core Composition Inferred from Measurements of the Sound Velocity of hcp-Iron in Extreme Conditions. *Sci. Adv.* **2016,** *2*, e1500802.

147. Kupenko, I.; Dubrovinsky, L.; Dubrovinskaia, N.; McCammon, C.; Glazyrin, K.; Bykova, E.; Ballaran, T. B.; Sinmyo, R.; Chumakov, A. I.; Potapkin, V.; Kantor, A.; Rüffer, R.; Hanfland, M.; Crichton, W.; Merlini, M. Portable Double-Sided Laser-Heating System for Mössbauer Spectroscopy and X-Ray Diffraction Experiments at Synchrotron Facilities with Diamond Anvil Cells. *Rev. Sci. Instrum.* **2012,** *83*, 124501.
148. Brennan, M. C.; Fischer, R. A.; Couper, S.; Miyagi, L.; Antonangeli, D.; Morard, G. High-Pressure Deformation of Iron–Nickel–Silicon Alloys and Implications for Earths Inner Core. *J. Geophys. Res. Solid Earth* **2021,** *126*. e2020JB021077.
149. Boehler, R.; Guthrie, M.; Molaison, J. J.; dos Santos, A. M.; Sinogeikin, S.; Machida, S.-I.; Pradhan, N.; Tulk, C. A. Large-Volume Diamond Cells for Neutron Diffraction Above 90 GPa. *High Pressure Res.* **2013,** *33,* 546–554.
150. Mao, H.; Xu, J.; Struzhkin, V.; Shu, J.; Hemley, R.; Sturhahn, W.; Hu, M.; Alp, E.; Vocadlo, L.; Alfè, D.; et al. Phonon Density of States of Iron up to 153 Gigapascals. *Science* **2001,** *292,* 914–916.
151. Angel, R. Absorption Corrections for Diamond-Anvil Pressure Cells Implemented in the Software Package Absorb6.0. *J. Appl. Cryst.* **2004,** *37,* 486–492.
152. Moore, M. Imaging Diamond with X-Rays. *J. Phys. Condens. Matter* **2009,** *21*, 364217.
153. Allan, D.; Miletich, R.; Angel, R. A Diamond-Anvil Cell for Single-Crystal X-Ray Diffraction Studies to Pressures in Excess of 10 GPa. *Rev. Sci. Instrum.* **1996,** *67,* 840–842.
154. Kantor, I.; Prakapenka, V.; Kantor, A.; Dera, P.; Kurnosov, A.; Sinogeikin, S.; Dubrovinskaia, N.; Dubrovinsky, L. BX90: A New Diamond Anvil Cell Design for X-Ray Diffraction and Optical Measurements. *Rev. Sci. Instrum.* **2012,** *83*, 125102.
155. Somayazulu, M.; Ahart, M.; Mishra, A. K.; Geballe, Z. M.; Baldini, M.; Meng, Y.; Struzhkin, V. V.; Hemley, R. J. Evidence for Superconductivity above 260 K in Lanthanum Superhydride at Megabar Pressures. *Phys. Rev. Lett.* **2019,** *122*, 027001.
156. Snider, E.; Dasenbrock-Gammon, N.; McBride, R.; Debessai, M.; Vindana, H.; Vencatasamy, K.; Lawler, K. V.; Salamat, A.; Dias, R. P. Room-Temperature Superconductivity in a Carbonaceous Sulfur Hydride. *Nature* **2020,** *586,* 373–377.
157. Dadashev, A.; Pasternak, M.; Rozenberg, G. K.; Taylor, R. Applications of Perforated Diamond Anvils for Very High-Pressure Research. *Rev. Sci. Instrum.* **2001,** *72,* 2633–2637.
158. Samudrala, G. K.; Moore, S. L.; Vohra, Y. K. Fabrication of Diamond Based Sensors for Use in Extreme Environments. *Materials* **2015,** *8,* 2054–2061.
159. Matsumoto, R.; Sasama, Y.; Fujioka, M.; Irifune, T.; Tanaka, M.; Yamaguchi, T.; Takeya, H.; Takano, Y. Note: Novel Diamond Anvil Cell for Electrical Measurements Using Boron-Doped Metallic Diamond Electrodes. *Rev. Sci. Instrum.* **2016,** *87*, 076103.
160. Shen, G.; Mao, H. K. High-Pressure Studies with X-Rays Using Diamond Anvil Cells. *Rep. Prog. Phys.* **2016,** *80*, 016101.
161. Drozdov, A. P.; Eremets, M. I.; Troyan, I. A.; Ksenofontov, V.; Shylin, S. I. Conventional Superconductivity at 203 Kelvin at High Pressures in the Sulfur Hydride System. *Nature* **2015,** *525,* 73–76.
162. Clarke, S. M.; Walsh, J. P. S.; Amsler, M.; Malliakas, C. D.; Yu, T.; Goedecker, S.; Wang, Y.; Wolverton, C.; Freedman, D. E. Discovery of a Superconducting Cu–Bi Intermetallic Compound by High-Pressure Synthesis. *Angew. Chem. Int. Ed.* **2016,** *55,* 13446–13449.
163. Walsh, J. P. S.; Clarke, S. M.; Meng, Y.; Jacobsen, S. D.; Freedman, D. N. Discovery of $FeBi_2$. *ACS Cent. Sci.* **2016,** *2,* 867–871, 11.
164. Tamerius, A. D.; Clarke, S. M.; Gu, M.; Walsh, J. P. S.; Marco, E.; Meng, Y.; Hendon, C. H.; Rondinelli, J. M.; Jacobsen, S. D.; Freedman, D. N. Discovery of Cu_3Pb. *Angew. Chem.* **2018,** *130,* 12991–12995, 39.
165. Hall, H. T. Some High-Pressure, High-Temperature Apparatus Design Considerations: Equipment for Use at 100 000 Atmospheres and 3000°C. *Rev. Sci. Instrum.* **1958,** *29,* 267–275.
166. Hall, H. T. High Pressure Apparatus: Ram-in-Tie-Bar Multianvil Presses. *Rev. Phys. Chem. Jpn.* **1967,** *37,* 63–71.
167. Kawai, N.; Endo, S. The Generation of Ultrahigh Hydrostatic Pressures by a Split Sphere Apparatus. *Rev. Sci. Instrum.* **1970,** *41,* 1178–1181.
168. Huppertz, H. Multianvil High-Pressure/High-Temperature Synthesis in Solid State Chemistry. *Zeitschrift für Kristallographie-Crystalline Materials* **2004,** *219,* 330–338.
169. Ishii, T.; Liu, Z.; Katsura, T. A Breakthrough in Pressure Generation by a Kawai-Type Multi-Anvil Apparatus with Tungsten Carbide Anvils. *Engineering* **2019,** *5,* 434–440.
170. Yamazaki, D.; Ito, E.; Yoshino, T.; Tsujino, N.; Yoneda, A.; Guo, X.; Xu, F.; Higo, Y.; Funakoshi, K. Over 1Mbar Generation in the Kawai-Type Multianvil Apparatus and Its Application to Compression of $(Mg_{0.92}Fe_{0.08})SiO_3$ Perovskite and Stishovite. *Phys. Earth Planet. In.* **2014,** *228,* 262–267. High-Pressure Research in Earth Science: Crust, Mantle, and Core.
171. Yamazaki, D.; Ito, E.; Yoshino, T.; Tsujino, N.; Yoneda, A.; Gomi, H.; Vazhakuttiyakam, J.; Sakurai, M.; Zhang, Y.; Higo, Y.; Tange, Y. High-Pressure Generation in the Kawai-Type Multianvil Apparatus Equipped With Tungsten-Carbide Anvils and Sintered-Diamond Anvils, and X-Ray Observation on $CaSnO_3$ and (Mg, Fe)SiO_3. *C. R. Geosci.* **2019,** *351,* 253–259. High-Pressure Mineral Physics Seminar(HPMPS-9, Saint-Malo, France, 2428 September 2017).
172. Ishii, T.; Shi, L.; Huang, R.; Tsujino, N.; Druzhbin, D.; Myhill, R.; Li, Y.; Wang, L.; Yamamoto, T.; Miyajima, N.; Kawazoe, T.; Nishiyama, N.; Higo, Y.; Tange, Y.; Katsura, T. Generation of Pressures over 40 GPa Using Kawai-Type Multi-Anvil Press with Tungsten Carbide Anvils. *Rev. Sci. Instrum.* **2016,** *87*, 024501.
173. Wang, Y.; Rivers, M.; Sutton, S.; Nishiyama, N.; Uchida, T.; Sanehira, T. The Large-Volume High-Pressure Facility at GSECARS: A Swiss-Army-Knife Approach to Synchrotron-Based Experimental Studies. *Phys. Earth Planet. In.* **2009,** *174,* 270–281. Advances in High Pressure Mineral Physics: From Deep Mantle to the Core.
174. Wang, Y. In *High-Pressure Crystallography;* Boldyreva, E., Dera, P., Eds., Springer Netherlands: Dordrecht, 2010; pp 81–96.
175. Duffy, T. S. Synchrotron Facilities and the Study of the Earth's Deep Interior. *Rep. Prog. Phys.* **2005,** *68,* 1811–1859.
176. Liu, Z.; Fei, H.; Chen, L.; McCammon, C.; Wang, L.; Liu, R.; Wang, F.; Liu, B.; Katsura, T. Bridgmanite Is Nearly Dry at the Top of the Lower Mantle. *Earth Planet. Sci. Lett.* **2021,** *570*, 117088.
177. Kurnosov, A.; Marquardt, H.; Frost, D. J.; Ballaran, T. B.; Ziberna, L. Evidence for a Fe^{3+}-rich Pyrolitic Lower Mantle from (Al, Fe)-Bearing Bridgmanite Elasticity Data. *Nature* **2017,** *543,* 543–546.
178. Dobson, D. P.; Jacobsen, S. D. The Flux Growth of Magnesium Silicate Perovskite Single Crystals. *Am. Mineral.* **2004,** *89,* 807–811.
179. Wang, Y.; Durham, W. B.; Getting, I. C.; Weidner, D. J. The Deformation-DIA: A New Apparatus for High Temperature Triaxial Deformation to Pressures up to 15 GPa. *Rev. Sci. Instrum.* **2003,** *74,* 3002–3011.
180. Ringwood, A. E. The Chemical Composition and Origin of the Earth. *Adv. Earth Science* **1966,** *65,* 287.
181. Smyth, J. R. Beta-Mg_2SiO_4; a Potential Host for Water in the Mantle? *Am. Mineral.* **1987,** *72,* 1051–1055.
182. Smyth, J. R. Hydrogen in High Pressure Silicate and Oxide Mineral Structures. *Rev. Mineral. Geochem.* **2006,** *62,* 85–115.
183. Kawazoe, T.; Buchen, J.; Marquardt, H. Synthesis of Large Wadsleyite Single Crystals by Solid-State Recrystallization. *Am. Mineral.* **2015,** *100,* 2336–2339.
184. Jacobsen, S. D. Effect of Water on the Equation of State of Nominally Anhydrous Minerals. *Rev. Mineral. Geochem.* **2006,** *62,* 321–342.
185. Frost, D. J.; Fei, Y. Stability of Phase D at High Pressure and High Temperature. *J. Geophys. Res. Solid Earth* **1998,** *103,* 7463–7474.
186. Yang, H.; Prewitt, C. T.; Frost, D. J. Crystal Structure of the Dense Hydrous Magnesium Silicate, Phase D. *Am. Mineral.* **1997,** *82,* 651–654.
187. Rosa, A. D.; Mezouar, M.; Garbarino, G.; Bouvier, P.; Ghosh, S.; Rohrbach, A.; Sanchez-Valle, C. Single-Crystal Equation of State of Phase D to Lower Mantle Pressures and the Effect of Hydration on the Buoyancy of Deep Subducted Slabs. *J. Geophys. Res. Solid Earth* **2013,** *118,* 6124–6133.
188. Tracy, R. J. *Characterization of Metamorphism through Mineral Equilibria*, De Gruyter, 2018; pp 354–398.
189. Lanari, P.; Engi, M. Local Bulk Composition Effects on Metamorphic Mineral Assemblages. *Rev. Mineral. Geochem.* **2017,** *83,* 55–102.
190. Schmidt, M. W.; Ulmer, P. A Rocking Multianvil: Elimination of Chemical Segregation in Fluid-Saturated High-Pressure Experiments. *Geochim. Cosmochim. Acta* **2004,** *68,* 1889–1899.

10.09 Local structure determination using total scattering data

Simon J.L. Billinge[a,b], Sandra H. Skjaervoe[a], Maxwell W. Terban[c], Songsheng Tao[a], Long Yang[a], Yevgeny Rakita[a], and Benjamin A. Frandsen[d], [a] Department of Applied Physics and Applied Mathematics, Columbia University, New York, NY, United States; [b] Condensed Matter Physics and Materials Science Department, Brookhaven National Laboratory, Upton, NY, United States; [c] Max Planck Institute for Solid State Research, Heisenbergstraße, Stuttgart, Germany; and [d] Department of Physics and Astronomy, Brigham Young University, Provo, UT, United States

© 2023 Elsevier Ltd. All rights reserved.

10.09.1	**Introduction**	**222**
10.09.1.1	Total scattering measurements	224
10.09.1.2	Formal description of the PDF	224
10.09.2	**Structural phase transitions**	**224**
10.09.3	**Battery electrode materials under cycling**	**225**
10.09.4	**Semiconductor nanoparticles**	**226**
10.09.5	**Inorganic molecular cluster structures**	**228**
10.09.6	**Soft inorganic structures: Halide perovskites**	**229**
10.09.7	**Metal-organic frameworks and host-guest systems**	**230**
10.09.8	**Layered materials**	**231**
10.09.9	**Polycrystalline thin films**	**233**
10.09.10	**Amorphous systems**	**237**
10.09.11	**Nucleation of crystallites**	**238**
10.09.12	**Magnetic crystals**	**240**
10.09.13	**Future development**	**241**
Acknowledgments		**242**
References		**242**

Abstract

"This article describes the application of total scattering and atomic pair distribution function (PDF) studies to the study of local and intermediate range structure in complex materials. We give a brief introduction to the methods, and then survey a sampling of different applications of them in various inorganic chemistry applications, including energy materials, nanoparticles, layered materials, metal organic frameworks and host-guest systems, polycrystalline thin films, atomic clusters, hybrid-perovskites. We also discuss studies of local magnetism and amorphous materials."

10.09.1 Introduction

Atomic structure plays an important role in determining the properties of materials, and it is widely appreciated that a detailed knowledge of structure is needed to better understand or predict the properties. For crystalline materials, a starting point is the crystal structure, obtained using crystallographic methods that exploit the diffractive nature of crystals to short wavelength radiation. This is the periodically averaged view of the material structure and, whilst enormously valuable, is an idealization of the real situation. We are increasingly learning to appreciate the often significant roles in a material's functionality played by various imperfections or deviations from these idealized models, not to mention the countless materials that do not play by the same rules of periodicity such as nano- and amorphous materials. Thus, further insights are often required, beyond the perfectly-ordered, model structures (Fig. 1A and B). In this article we describe the atomic pair distribution function (PDF) analysis of total scattering powder diffraction data as an approach to gain insight into the real structure of materials. What we mean by real structure is the atomic arrangement taking into account defects, structural relaxations around those defects, morphology, structural coherence and so on. We can delve deeper by using total scattering methods.

Total scattering measurements are very similar to conventional diffraction measurements. What makes them" total" is that they take into account all the information in the scattering pattern, even the diffuse signals in-between (and underneath) the Bragg peaks. This includes the diffraction intensities coming from the periodic structure giving rise to Bragg peaks (the global, or average, structure, Fig. 1B), elastic diffuse scattering (the static local structure, Fig. 1C), and inelastic diffuse scattering from moving atoms that contain information about dynamics[1] (Fig. 1E). To harvest the structural information as completely as possible, measurements require as wide a range of reciprocal space as possible (corresponding to smaller *d*-spacing resolution), which require shorter wavelengths and higher fluxes of X-rays, neutrons, or electrons. The techniques have come into their own with increases in short wavelength flux at neutron spallation sources and X-ray synchrotrons (Fig. 1A) and improvements in transmission electron microscopes,

 https://doi.org/10.1016/B978-0-12-823144-9.00040-6

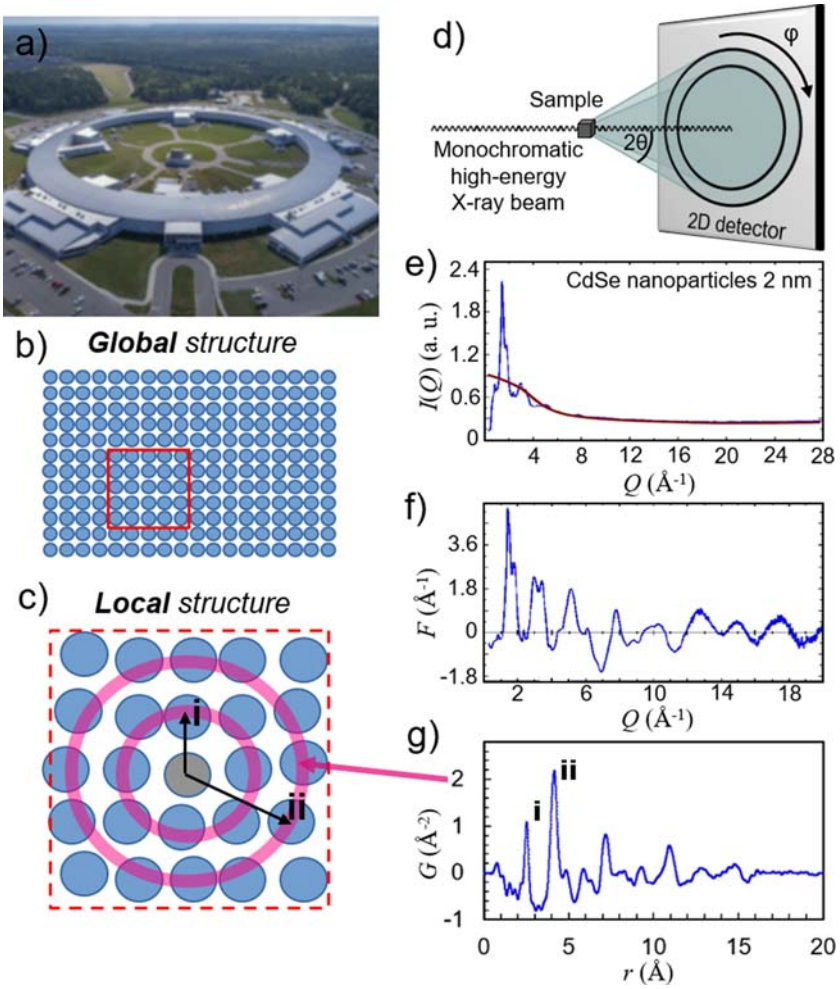

Fig. 1 (A) Aerial photo of NSLS II at Brookhaven National laboratory on Long Island, NY, a state-of-the-art X-ray synchrotron facility. (B) Sketch of a highly crystalline global structure, the way one might imagine it looks like with assessment by conventional Bragg diffraction analysis, as this probes only the periodic component of the structure. (C) Close up of an excerpt of the structure sketch above, where the atoms are now randomly displaced out of the high-symmetry positions. This might not lead to a global lowering of the symmetry, since the displacements cancel out, but locally, it can have great implications. (D) Sketch of the experimental setup showing monochromatic X-rays with high energy scattering off the sample to form bright rings for angles 2θ (2theta), where the Bragg condition is fulfilled. (E) An example of a measured scattering intensity $I(Q)$, here for a sample of CdSe nanoparticles where the red line highlights the diffuse scattering, (F) the corrected reduced scattering function $F(Q)$ and (G) the pair distribution function $G(r)$. The pink arrow pointing to the circles in panel (C) illustrates the link between the coordination environment around each atom and the peaks of the PDF. (A) Photo by Brookhaven National Laboratory, (E and F) reprinted with permission from Billinge, SJL. The Rise of the X-Ray Atomic Pair Distribution Function Method: A Series of Fortunate Events. *Philos. Trans. R. Soc. A Math. Phys. Eng. Sci.* **2019** *377*(2147), 20180413.

which allow weak diffuse signals to be more accurately measured. Finally, with the advent of powerful computers and advanced software, the somewhat computationally intensive analysis has become straightforward and user-friendly, leading to a massive growth in the application of these methods.[2]

A practical, powerful, and often intuitive way to analyze total scattering data is to Fourier transform the reciprocal space scattering function $S(Q)$ to real space to obtain the PDF, $G(r)$. The PDF is basically a histogram of inter-atomic distances, spatially and temporally averaged over the entire sample (Fig. 1C and G). The peak positions indicate that pairs of atoms are separated by said distance; the intensity reflects the number of pairs and scattering power of constituent atoms, and the width represents the variation of a specific pair distance due to thermal motion or disorder. Processes such as atomic relaxation, displacement, or dynamic correlation affect the PDF peaks differently, leading to splitting, changes in shape, sharpening and so on. The information found in the low-r region of the PDF is directly related to the short- and mid-range local arrangements of atoms, regardless of the long-range order. Assessing this information requires that we approach the data analysis a bit differently than for crystallographic structure solution from reciprocal space. A crystallographer's goal is to determine the periodic arrangement of atomic motifs, which requires using the highest possible symmetry that fits the diffraction pattern.[3] In a PDF analysis, we are often interested in

determining how the local structure can deviate from these high-symmetry descriptions, or even determining some details of the local structure in cases where we cannot so readily determine an 'average' model.[1]

When analyzing the PDF, we often start by evaluating the data in a model-independent way. Our ability to understand intuitively what the PDF peaks mean enables us to learn a lot about a material by simply looking at the peaks. Using intuition about bonds and structural degrees of freedom we can build a structural model to fit the data that goes beyond the global crystal symmetry. These models can be as small as a single molecule or cluster, a crystallographic unit cell, or larger depending on how many degrees of freedom one wants to allow. Since local chemical bonding is imperative for the mechanisms that cause symmetry to break, the inorganic chemist's real-space bonding perspective is of great advantage when it comes to PDF analysis. In this article we will explore a number of different situations which serve to exemplify the kind of chemical and structural scenarios where total scattering and PDF can add significant value, as well as giving hints at how the PDF analysis was done to extract the information. More details can be obtained by reading the original papers referenced. A slightly technical reference book for the technique is Ref. 1 and a more gentle introduction to the method can be found in Ref. 4 For visual clarification of the formalisms of total scattering, see Ref. 5. For more about the implications of using neutrons for obtaining the PDF, see Ref. 6.

10.09.1.1 Total scattering measurements

Total scattering measurements are typically performed on powder samples, just like in an in-house powder diffractometer. When doing a total scattering measurement we are obtaining the scattered intensity in a large portion of the reciprocal space, and we typically need synchrotron X-rays or spallation neutrons with high enough intensity to achieve that. Anyone can apply for beamtime to perform specific experiments for free by submitting an application to the facilities' websites. The facilities are divided into several beamlines, all with their own specialized expertise, experimental setups, and sample environments. Reaching out to the beamline scientist in advance of a proposal will increase the chances of a proposal being accepted, since one is better equipped to tailor the proposal to the specific beamline's expertise and interests.

10.09.1.2 Formal description of the PDF

The coherent signal that is scattered out of the sample is referred to as the scattering intensity $I(Q)$, derived in 1915 by Pieter Debye,[7]

$$I_{coh}(Q) = \sum_i \sum_j f_i(Q) f_j(Q) \frac{\sin\left(Qr_{ij}\right)}{Qr_{ij}} \tag{1}$$

where $f_i(Q)$ and $f_j(Q)$ are form factors for the atoms i and j separated by r_{ij} and Q is the reciprocal space distance. The acquisition of the scattering intensity can be done rapidly using a 2D detector, where the scattering from the sample forms bright rings where the Bragg condition is fulfilled.

In order to get the pair distribution function $G(r)$ from the data we first need to integrate over the azimuthal angle (**Fig. 1**D) of the 2D pattern, obtaining the 1D function $I(Q)$, illustrated in the top panel of **Fig. 1**E). The next step is removing contributions from parasitic scattering, such as background, Compton scattering, absorption and fluorescence, resulting in the coherent intensity, $I_{coh}(Q)$, that can be converted to the total scattering structure function $S(Q)$ according to

$$S(Q) = \frac{1}{N\langle f\rangle^2}\left[I_{coh}(Q) + \langle f\rangle^2 - \langle f^2\rangle\right] \tag{2}$$

where N is the number of scatterers and f is the atomic form factor. The final step is to Fourier transform the reduced scattering function $F(Q) = Q[S(Q) - 1]$ (**Fig. 1**F), which gives the pair distribution function $G(r)$ (**Fig. 1**G), defined as.[1]

$$G(r) = 4\pi r[\rho(r) - \rho_0], \tag{3}$$

where $\rho(r)$ is the atomic pair density and ρ_0 is the average number density.

While these steps are somewhat advanced, there are several tools available that simplify the process, such a PDFgetX3,[8] PDFgetN,[9] PDFgetN3,[10] GSAS-II,[11] TOPAS,[12] GudrunX and GudrunN.[13] The analysis of $G(r)$ can finally be done using easy-to-use software, such as PDFgui[14] and TOPAS.[12]

10.09.2 Structural phase transitions

Many of the materials we use undergo structural phase transitions that bring about the very properties we use them for. A good example is that of ferroelectric materials: dielectric crystalline materials that form a switchable spontaneous electric polarization below a critical temperature, while no polarization can be measured above. These materials have applications in capacitors, data storage and sensors, among many others.

The changes in the long-range symmetry of the crystal brought about by the phase transition can be seen crystallographically. The local point of view, however, is often overlooked. In some cases this has led to incomplete and incoherent descriptions of a material's properties.

A "classic" example of this is the ferroelectric $BaTiO_3$, which goes through a series of phase transitions where the electric polarization changes direction as the symmetry is lowered. At high temperatures, the structure has cubic symmetry and no electric polarization. On cooling, the symmetry of the average structure breaks to tetragonal, then to orthorhombic, and finally to rhombohedral, all three accompanied by the emergence of an electric polarization in the direction of the long-axis of the respective crystal structure. The change in symmetry and polarization direction were therefore believed to be due to a collective displacement of the Ti atoms inside the octahedra in the direction defined by the distortion of the unit cell. However, PDF analysis revealed that the Ti atoms were always, in all phases at all temperatures, displaced along the body diagonal of the cell, in the direction defined by the rhombohedral distortion seen at low temperatures. The crystallographic symmetry is therefore merely the average over different sets of local disordered rhombohedral displacements.[15–17] This was among the first examples showing how understanding of the local structure can resolve conflicts between the average symmetry and physical properties, which can sometimes appear to be contradictory. For $BaTiO_3$ it meant that one could understand one of the reasons for its significantly lower polarization compared to its close relative $PbTiO_3$. PDFs have since been used to study phase transitions in a wide range of different materials. We mention in particular the confirmation of polar nanodomains in "relaxor" ferroelectrics[18–21] and other related oxide perovskites,[22,23] local structural symmetry breaking at metal-insulator transitions,[24–26] the link between structure and emergence of superconductivity,[27,28] the unusual symmetry breaking in the structurally softer halide perovskites,[29,30] and the interplay between the magnetic ordering and incommensurate structural symmetry breaking in a hexagonal manganite.[31]

In a recent study, the PDF technique was used to reconcile decades of seemingly anomalous observations across the structural phase transitions in the scientifically and technologically interesting multiferroic hexagonal manganite, $YMnO_3$ (Fig. 2A). The high temperature transition at 1250 K was already known to cause a symmetry breaking from the non-polar $P6_3/mmc$ to the polar $P6_3cm$, although any measurable polarization could not be found until a temperature several hundred degrees lower. Attempts at describing the mechanism of the phase transition with Bragg diffraction proved inconclusive. The most glaring anomaly was that the atomic positions, as extracted from Rietveld analysis, seemed to make discontinuous jumps across the transition[32]—a sign pointing to a first-order transition—even though this was inconsistent with the smoothly evolving lattice constants[32] and heat capacity measurements.[33] In order to reconcile these apparent anomalies, Skjærvø et al.[34] performed high-temperature neutron PDF measurements on a powder sample for temperatures ranging from room temperature to above the transition. Neutrons allowed the signal from the Y and Mn to be distinguished, as Mn has a negative scattering length. The PDF analysis showed that the structure went through an order-disorder transition, evidenced by the lack of qualitative changes in the low-r data across the transition (Fig. 2B). Had the local symmetry breaking been consistent with the long-range order, the PDF would change qualitatively across the transition, as demonstrated in the lower panel of Fig. 2B. In other words, the local bonding environment stayed the same across the transition, leading to the conclusion that any loss in symmetry must be due to disordering. Instead of the discontinuous jumps in atomic positions observed for the average structure data, the PDF fits gave continuously changing values (Fig. 2C) that were far away from those associated with the high-symmetry phase. Interestingly, the study further suggested that this order-disorder mechanism was of a type not previously known, with the primary order parameter being able to rotate continuously over all angles upon approaching the transition from below. The discovery of this mechanism reconciled the anomalous diffraction data and macroscopic measurements.

10.09.3 Battery electrode materials under cycling

The efficiency of an electrochemical device such as a fuel cell or a battery depends heavily on the atomic composition, structure, and morphology of the materials making up the various components of the device - anode, cathode, electrolyte, and separators. Optimization relies on our ability to both understand the materials individually as well as their interaction with the other components as the device operates. Studies to probe the structure and morphology can be done on the individual components post-operation (*ex situ*), under relevant physical conditions in the beam (*in situ*), or even studying changes to the material directly in the beam in an operating device such as a cycling battery (*operando*).

Electrochemical processes cause dramatic structural changes in materials. To fully understand these changes we often need several scattering techniques. Conventional diffraction can tell us the changes in overall symmetry, order, crystallite size and phase composition; small-angle scattering can tell us about the particle size distribution, morphology, and texture. PDF is the ideal choice if we want to uncover details of short range effects and how they deviate from the global symmetry.[35] PDF has been used *ex situ* for studying Li intercalation in silicon anode materials[36]; atomic defects in Fe particles[37] and structural robustness of the cathode material[38] in conversion type cathodes made from Fe fluorides, oxides and oxyfluorides; *operando* local accommodation of sodium in phosphorous anodes[39] and of Li in Li-Fe-S cathodes.[40] PDF has also been used to study *operando* the local atomic changes in noble metal transition metal nanocatalysts during oxygen reduction reactions.[41] More recently, the development of 3D δ-PDF has proven useful for model independent studies of local structural changes by subtracting the Bragg signal. Being restricted to single crystals, the method was successfully applied to understand the ordering of sodium along the different crystallographic axes of the sodium-intercalated compound V_2O_5.[42]

In a study of Li accommodation in Li-Fe-S cathodes,[40] PDF was combined with X-ray absorption spectroscopy and first-principles calculations to shed light on the formation of phases in the Li-Fe-S composition space during repeated charge-discharge cycles of the cathode. The study revealed a complex picture of intermediate phases during both charging and discharging,

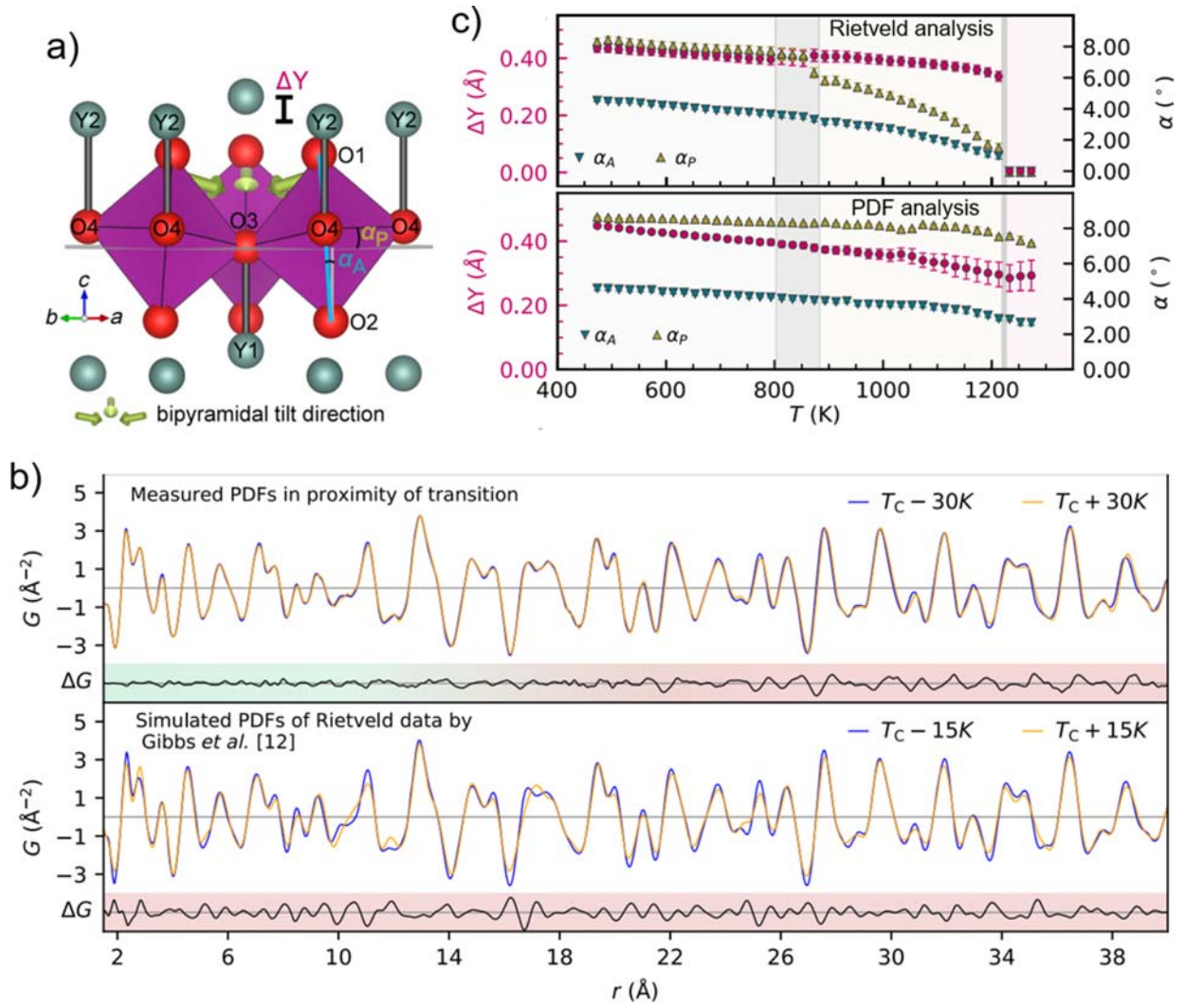

Fig. 2 (A) An excerpt of the hexagonal manganite structure in its polar ground state with $P6_3cm$ symmetry. Yttrium in green-blue, oxygen in red and manganese in trigonal bipyramidal polyhedra in purple. The excerpt emphasizes the connection between the corrugation δY of the Y atoms along c (distance in the c direction between Y1 and Y2) and the tilting of the Mn-O polyhedra, defined through the two tilt parameters α_A and α_P. Green arrows indicate the directions of the polyhedral tilts. In the average structure at high temperature $\delta Y = \alpha_A = \alpha_P = 0$. (B) Comparison of experimental (top) and simulated (bottom) PDFs for temperatures bracketing the structural transition at T_C. The simulated PDFs are calculated using the average structure information from previously reported Rietveld refinements[32] across the transition. Corresponding difference curves are shown underneath. The shaded green and red areas behind the difference curve indicate, respectively, regions of low and high difference. (C) Comparison of resulting fitting parameters δY, α_A and α_P from Rietveld analysis of the reciprocal space data (top) and PDF analysis of the real space data (bottom). The Rietveld fitting was done with the polar ground state model below T_C (indicated by the gray vertical line at 1223 K), and the high-symmetry non-polar model above, as inferred from the Bragg reflections. The PDF data was fitted with the polar ground state model over the entire temperature range. Reproduced from Skjærvø, S.H.; Meier, Q.N.; Feygenson, M.; Spaldin, N.A.; Billinge, S.J.L.; Bozin, E.S.; Selbach, S.M. Unconventional Continuous Structural Disorder at the Order-Disorder Phase Transition in the Hexagonal Manganites. *Phys. Rev. X* **2019**, *9*(3), 031001.

resembling mechanisms of intercalation rather than pure conversion, as shown in Fig. 3. Most interestingly, the initial structure of FeS_2 with octahedrally coordinated iron was never recovered during the cycling. Since the gradual evolution through partially lithiated intermediates for the most part do not lead to any changes in the long-range ordering of the material, the effects would not have been observable with conventional diffraction, thereby illustrating clearly the need for PDF in describing the structure.

10.09.4 Semiconductor nanoparticles

In recent years the characterization of atomic structure in nanoparticles has become one of the main uses of PDF. Quantum dots (QDs), for example, CdSe nanoparticles (CdSe NPs) of a few nm diameter, are among the most important and the most studied of

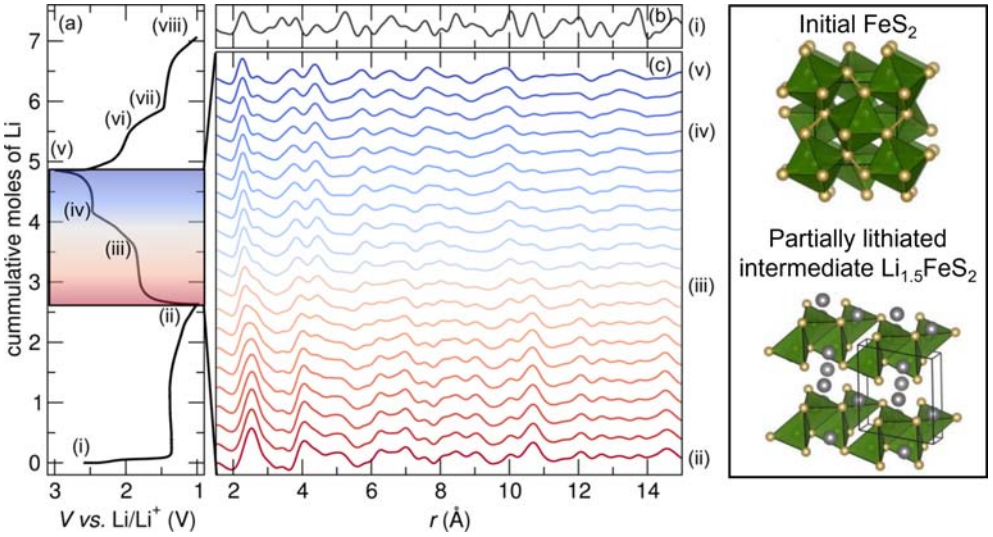

Fig. 3 The effect of electrochemical cycling on the local structure during the first 1.5 cycles of *operando* electrochemistry. (A) Amount of Li accumulated in the material as a function of voltage. (B) PDF of the as-prepared FeS_2 before cycling (see top right for structure). (C) PDFs showing the evolution of the local structure. The local structure evolves through partially lithiated phases where Fe is tetrahedrally coordinated (see bottom right image for example). The tetrahedral coordination differs significantly from the octahedral coordination in the original FeS_2 structure, which is never recovered during the cycling. Reproduced from. Butala, M.M.; Mayo, M.; Doan-Nguyen, V.V.T.; Lumley, M.A.; Göbel, C.; Wiaderek, K.M.; Borkiewicz, O.J.; Chapman, K.W.; Chupas, P.J.; Balasubramanian, M.; Laurita, G.; Britto, S.; Morris, A.J.; Grey, C.P.; Seshadri, R. Local Structure Evolution and Modes of Charge Storage in Secondary Li-FeS_2 Cells. *Chem. Mater.* **2017**, *29*(7), 3070–3082.

these. Unlike bulk materials, small nanoparticles do not give rise to sharp X-ray or neutron Bragg peaks, but instead, only broad, diffuse scattering features. The PDF method can add significant value in helping us to interpret these.[43,44] QDs have unique opto-electronic properties coming from the size and internal structure of their inorganic cores as well as the nature of the passivating ligand shell and it is important to understand factors such as defects, surface relaxations and internal strains, as well as the average internal arrangement of atoms in the core. There are many excellent studies of QD structures using PDF.[45–50]

Surprising progress can be made by taking simple modeling approaches. This requires some creativity in designing models and modeling approaches, and the best way of doing this is highly dependent on the system in question. For example, in the case of CdSe quantum dots, there is particular interest in the relationship between size and structure.[45,46] Bulk CdSe generally takes the wurtzite crystal structure. A cutout of the structure is illustrated in Fig. 4 along with its sister structure zinc blende. In the wurtzite structure, the anions sit in a hexagonal closed packed (hcp) structure, while the cations are in the tetrahedral sites in the structure. In the closely related zinc blende structure, on the other hand, the anions form a cubic closed packed (ccp) structure with the cations in the tetrahedral sites. The difference between the hcp and ccp structures can be understood in terms of atom layering: the atomic layers in the wurtzite (hcp) structure can be described as an ABABAB stacking, while the layer stacking in the zinc blende (ccp) structure is ABCABC. Layered structures like CdSe are prone to stacking faults, where the layering does not follow either ABABAB or ABCABC though the whole structure, but may have other sequences. PDF was able to show that stacking faults were important in CdSe NPs and to characterize the stacking fault density.[45,46] In this modeling, which used the program PDFgui, a strategy was used where a bulk crystal structure was used for the starting model which was modified to explain the finite size of the particles by attenuating the PDF peaks with increasing r using a particular functional form, called the characteristic function, that encodes the particle size and shape. The PDF was also able to show that a spontaneous size-dependent compressive strain appeared in the QDs as they got very small, both a small reduction in the average Cd-Se bond length, and a small broadening of the PDF peak associated with that bond indicated a heterogeneous strain (different bond lengths in different parts of the sample).[46] To learn more about factors such as defects, surface relaxations and differences in bond lengths between the center and edge of the nanoparticles, it is necessary to build explicit cut-out models of the nanoparticles and modify them as desired. This is not possible with PDFgui but can be done with other programs such as diffpy-CMI[51] and DISCUS.[52,53]

Beyond QDs, PDF studies are also numerous on metallic nanoparticles.[54–62] To make the study of such systems easier, Banerjee et al.[60] recently demonstrated that a high throughput data-mining approach could be used to screen large numbers of models (thousands) from different families of cluster motifs, which will make PDF studies on metallic nanoparticles more straightforward in the future. The *cluster-mining* capability will be deployed on the PDFitc.com[63] cloud platform in the future.

When clusters are sufficiently small they can have unique (atomically precise) structures and it makes sense to attempt to solve the structure exactly. This was done on 102-atom gold clusters using the techniques of protein crystallography.[64] However, nanoparticle structures have also been solved *ab initio* from PDF.[65–67] Single particle electron microscopy approaches also look promising in this regard.[68] We expect PDF studies of discrete nanoparticles to remain an important area of research for the foreseeable future.

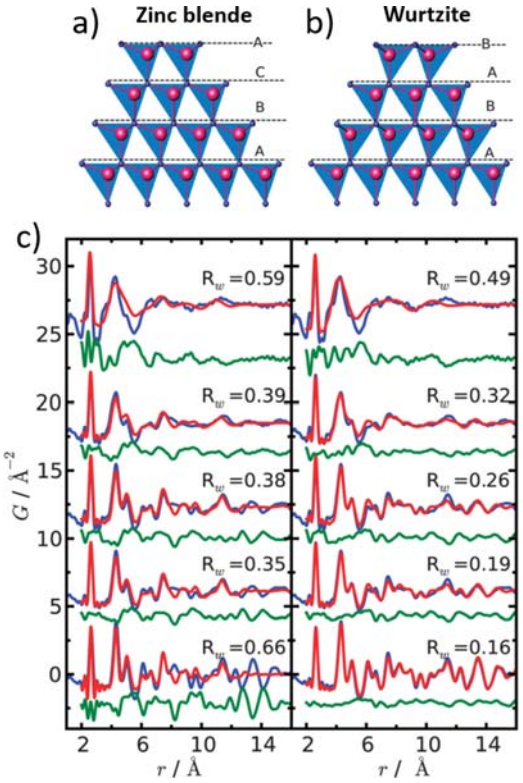

Fig. 4 Layer stacking sequences of the two closely related zinc blende (A) and wurtzite (B) structures, with A, B and C denoting the difference in the stacking type. (C) Measured PDF for CdSe nanoparticles of various sizes, with small nanoparticles of 13 nm at the top and bulk-sized particles at the bottom. The fitting residual R_w is given next to the curves. The wurtzite structure gives consistently better fit than then zinc blende structure, even for the smallest particles, as seen from the R_w values. Reproduced from Yang, X.; Masadeh, A.S.; McBride, J.R.; Bozin, E.S.; Rosenthal, S.J.; Billinge, S.J.L. Confirmation of Disordered Structure of Ultrasmall CdSe Nanoparticles From X-ray Atomic Pair Distribution Function Analysis. *Phys. Chem. Chem. Phys.* **2013**, *15*(22), 8480–8486.

10.09.5 Inorganic molecular cluster structures

Materials consisting of even smaller building blocks than the nanoparticles in the previous sections can exhibit extraordinary electronic properties beyond those found for the bulk version. Such ultra-small building blocks have been named clusters or superatoms.[69,70] The cobalt chalcogenides have been successfully built into diatomic and triatomic superatom molecules,[71] which have attracted considerable attention because of their potential applications in solar cells,[72] electrocatalysis,[73] and lithium-ion batteries.[74]

In a recent work,[75] a new solution-phase chemical approach was developed to dissociate the capping ligands from the molecular cluster $Co_6Se_8(PEt_3)_6$ using elemental Se as a phosphine scavenger. The high surface-to-volume ratio of the resulting Co-Se microspheres (CoSe-MS) make them promising materials for electrochemical devices, such as Na and Li ion batteries.

The structures of the CoSe-MS clusters are good candidates for study with X-ray PDF. However, due to the large phase space of possible cobalt selenium structures, manual fitting to a wide range of models would be a tedious job. To simplify this type of job, Yang et al.[76] recently developed the *structure-mining* approach to find the best-fit candidate structures from PDF data in a highly automated way. This approach (available on *PDF in the cloud* (PDFitc), https://pdfitc.org, see **Fig. 5**[63]) fetches, from structural databases, all the structures meeting the experimenter's search criteria, and performs structure refinements on them without human intervention.

In the study of the Co-Se nanoclusters, the *structure-mining* searched for all the structures containing Co and Se with any stoichiometry, returning the nanocrystalline Co_3Se_4 (NC-Co_3Se_4) as the best fit (**Fig. 6**A inset). A closer inspection of the fit (**Fig. 6**A) suggested that even though this single-phase model fit the PDF peaks well in the high-*r* region, additional unfitted signal was evident in the difference curve in the low-*r* region. The authors improved the model by invoking a second phase with a significantly shorter structural coherence, as shown in **Fig. 6**B, indicating that the material consists of short-range-ordered (SRO) and longer-range-ordered (LRO) Co_3Se_4 nanoclusters.

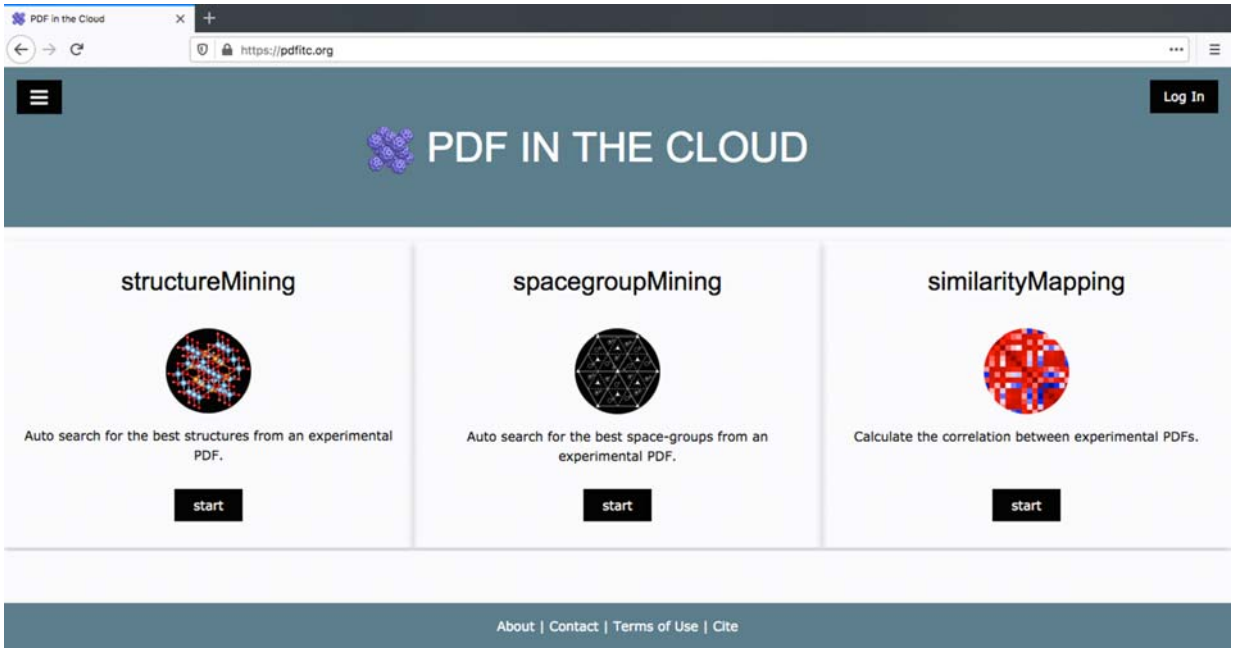

Fig. 5 The home web page of PDFitc. Reproduced from Yang, L.; Culbertson, E.A.; Thomas, N.K.; Vuong,H.T.; Kjær, E.T.S.; Jensen, K. M. Ø.; Tucker, M.G.; Billinge, S.J.L. A Cloud Platform for Atomic Pair Distribution Function Analysis: PDFitc. *Acta Crystallogr. A* **2021,** *77*(1), 2–6, with permission of the International Union of Crystallography.

10.09.6 Soft inorganic structures: Halide perovskites

Unlike regular (oxide) perovskites, Halide Perovskites (HaP) are ABX_3 structures with X being a halide, and A and B being mono- and di-valent cations, respectively. In recent years HaP, those with A as methylammonium (CH_3NH_3, or MA), formamidinium or Cs, B being Pb or Sn, and X being Br or I, have caught the attention of the scientific community due to their outstanding opto-electronic performance in photovoltaics, LED, and radiation detection applications.[77–79] Structural imperfections, which normally inhibit carrier mobilities and introduce recombination pathways for photo-generated carriers are, surprisingly, found to have only a benign effect on HaPs with a small impact on device performance. This is in sharp contrast to the detrimental effects of analogous imperfections in classical semi-conductors, such as Si or GaAs.[80,81] Evidence for self-healing,[82] low formation energy with respect to their binaries[83] and low mechanical stiffness,[84] and thermodynamic theory and modeling of point defects[85,86] suggested that the structure is dynamic in nature. This has indeed been experimentally corroborated by studies using PDF,[30,87,88] Raman[89] and IR[90] spectroscopies.

Generally, materials with a soft backbone will have a higher tendency to possess multiple local distortions, which will tend to average out into a high-symmetry representation due to the same reason. Because PDF measures the instantaneous structure, it is capable of studying the local broken symmetries even when they are fluctuating as dynamic disorder.[30,88]

For example, $MAPbI_3$ grown from solution was observed in conventional diffraction to have a perfect cubic perovskite-like structure above 330 K, but with a highly dynamic MA group.[91,92] A closer look at the total scattering revealed a picture that is much less symmetric at short-range.[30] **Fig. 7** shows that the calculated structural distortions, which are coupled to the MA^+ motion, result in anharmonic shallow double well-potentials, which are directly observed using PDF. By fitting different symmetry models to the PDF, over different ranges of r, the local and long-range structure could be differentiated. The long-range structure is clearly well fit with the cubic model, while the short/mid-range structure was best fit by tetragonal models with a preference towards the non-centrosymmetric one.[30]

Combining the real space PDF analysis with a reciprocal space analysis via the Debye Scattering Equation (DSE),[1] results in an accurate way to study nanoscale structural domains. The DSE approach extracts nanostructural information by detailed modeling of high-Q resolution diffraction peak line shapes, which complements the low-Q resolution, high r-resolution, PDF measures of the local structure. This combined approach was used with great success in the HaP to reveal nanoscale microstructure.[93] For $CsPbX_3$ nanocrystals, Bertolotti et al. used a joint DSE/PDF approach to show that the nanocrystals form orthorhombic sub-domains (occurring both in the room and high-temperature phases) hinged through a two-dimensional (2D) or three-dimensional (3D) network of twin boundaries across which the coherence of the Pb sub-lattice is preserved throughout the whole nanocrystal as shown in **Fig. 8**. The density of these twin boundaries determines the size of the sub-domains and results in an apparent higher-symmetry structure on average in the high-temperature modification.

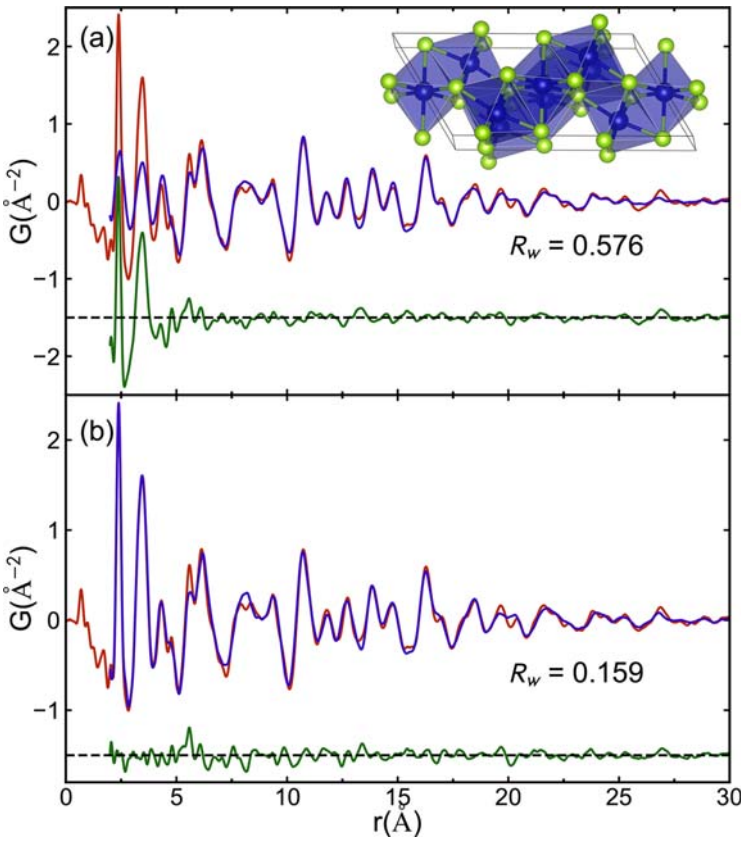

Fig. 6 Measured X-ray PDF from the CoSe-MS (light red curve) with (A) the best-fit calculated PDF (purple) for the NC-Co_3Se_4 model. The model was fit over a range of $5 < r < 30$ Å but the plot shows the calculated curve extended to low-*r*. (B) The best-fit calculated PDF (purple) for the two-phase (SRO + LRO NC-Co_3Se_4) model. The fit was performed over a range of $2 < r < 30$ Å. The difference curves are shown offset below (green). R_w is the goodness of fit. The inset in (A) is the NC-Co_3Se_4 structure, where Co atoms are in blue, Se atoms are in green and octahedra are emphasized in shaded blue. Adapted with permission from Aydt, A.P.; Qie, B.; Pinkard, A.; Yang, L.; Cheng, Q.; Billinge S.J.L.; Yang, Y.; Roy, X. Microporous Battery Electrodes From Molecular Cluster Precursors. *ACS Appl. Mater. Interfaces* **2019**, *11*(12), 11292–11297, Copyright 2019 American Chemical Society.

10.09.7 Metal-organic frameworks and host-guest systems

The term metal–organic framework (MOF) arose in the 1990s for a subclass of coordination compounds, typically considered to require crystallinity and ordered microporosity, although, this definition overlooks various types of structural disorder that are commonly observed in these materials.

The distinct sub-components comprising the frameworks, metal-ion or cluster nodes connected by organic linkers, result in non-typical structural degrees of freedom that can enable a rich diversity of defects and disorder in their formation. These can include the orientation and coordination of inorganic nodes, flexibility of the organic linker conformations, and the possibility for occupancy disorder.[94] Such properties are implicated for example in the phenomenon of breathing modes,[95] interaction with adsorbed chemical species,[96] negative thermal expansion,[97] and even amorphization.[98,99]

Local structure studies of amorphous MOFs are difficult, and the number of well-characterized states is relatively limited. The first detailed structural investigation was presented by Bennet et al.[98] on the structure of amorphized zeolitic imidazolate framework (*a*-ZIF) obtained by heating ZIF-4 up to 300 °C. The composition of the *a*-ZIF state could be constrained by the observation that it could be further transformed into a dense crystalline phase ZIF-zni on heating to 400 °C. While little information could be gleaned from the amorphous diffraction halo, both neutron and X-ray PDF measurements showed that the local structures of ZIF-4, *a*-ZIF, and ZIF-zni were nearly identical up to approximately 6 Å, Fig. 9A and B, confirming the maintenance of tetrahedral coordination of Zn and bridging by imidazolate ions. A direct analogy to amorphous silica, where Zn replaces Si and imidazolate ions replace O, allowed for reverse Monte Carlo (RMC) refinements to be adapted, showing that *a*-ZIF forms with a continuous random network topology as shown in Fig. 9C and D.

Products from different amorphization pathways have been further investigated with a focus on potential applications in sensors or encapsulation, for example, storage of radioactive agents[100] or even drug delivery.[101] PDF analysis has become a hallmark in the local structure characterization of these states. In cases where no crystalline analogue is formed, the confirmation of microporosity as well as successful incorporation and immobilization of reactive node species can be made by combination with theoretical

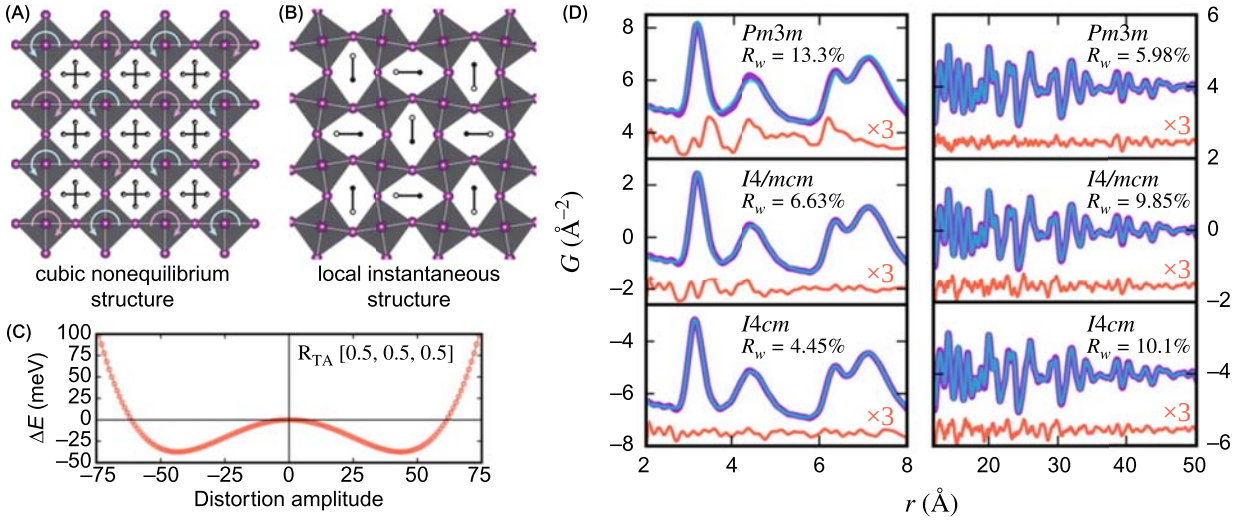

Fig. 7 Local symmetry breaking in $MAPbI_3$ at 350 K. (A and B) Distortions from cubic symmetry and coupling to motion of the MA^+ ion. (C) DFT-based lattice dynamic calculations show that the energy minimum at the *R* point for 350 K is displaced to give a double-well potential that causes local symmetry breaking. (D) Comparison of the experimental PDF (purple) to cubic ($Pm\bar{3}m$), centrosymmetric (*I4/mcm*), and noncentrosymmetric (*I4cm*) tetragonal models (blue) shows a superior fit for the low-symmetry models at low *r* (2–8 Å). At high *r* (12–50 Å), however, the models perform oppositely, with the high-symmetry cubic structure giving the best agreement to the data. The residuals (orange) are scaled for clarity. Reproduced from. Beecher, A.N.; Semonin, O.E.; Skelton, J.M.; Frost, J.M.; Terban, M.W.; Zhai, H.; Alatas, A.; Owen, J.S.; Walsh, A.; Billinge, S.J.L. Direct Observation of Dynamic Symmetry Breaking above Room Temperature in Methylammonium Lead Iodide Perovskite. *ACS Energy Lett.* **2016,** 1(4), 880–887.

calculations.[102] The survival of the chemical configuration, coordination, and porosity into a molten state has also been observed, leading to further investigations into liquid MOFs.[103–105] On the other hand, the nucleation of ordered frameworks and intermediate species from solution has also been studied *in situ*[106,107] (see **Section 10.09.11** for more details on *in situ* studies on nucleation phenomena).

MOFs can also be susceptible to varying types of static disorder[108,109] and diverging stimulus-response effects occurring independent from the crystallographic symmetry. For example, octahedral M_6O_8 nodes with M = Zr and Hf have been observed to undergo distortions on heating.[110] While no changes in the overall crystallographic nature of the framework could be observed from the Bragg reflections in Zr- and Hf-based analogues of MOFs NU-1000 and UiO-66, the distortions could be confirmed in real space, indicated by a splitting of the peak associated with the M-M pair distances. Similar distortions have been observed due to chemical interactions through adsorption or bridging of guest species.[111] This indicates that the node structures, like their linker counterparts, are not immune to external (or internal) stimuli and further suggests the ability to tune local electronic properties and possibly catalytic performance.

Interactions with guest species are fundamental to the application of MOFs for gas storage and separations. In particular, various MOFs have been identified as potential catalysts for remediation and neutralization of toxic gas agents[112]. To optimize and implement these technologies requires efficient catalytic function and high cyclability, and therefore understanding of the reaction mechanism and associated structural effects on the framework. Rapid data collection and complex sample environments available at specialized synchrotron beamlines now allow for holistic investigations of the average and local structure under multivariable conditions. This has recently been used to study the uptake and neutralization of dimethyl methylphosphonate (DMMP) within the MOF UiO-67 [$Zr_6(\mu_3\text{-}O)_4(\mu_3\text{-}OH)_4(BPDC)_6$; BPDC: biphenyl-4,4′-dicarboxylate][113] (**Fig. 10**). DMMP acts as a simulant for the nerve agent sarin, which can be taken up, bound, and detoxified by the framework. *In situ* total scattering experiments were performed with controlled temperature and gas-feed composition to study the guest and host structure during framework activation, loading, and re-activation. To test the mechanism of adsorption and neutralization, models for different mechanistic steps were prepared through periodic DFT relaxations of a crystallographic cell with one linker replaced by different binding interactions between DMMP or methyl methylphosphonate (MMPA) and the Zr_6 cluster. Possible signals could then be predicted through calculation of dPDFs associated with DMMP-DMMP or DMMP-cluster pairs, **Fig. 10**A–H. Signals corresponding to adsorbed DMMP and its interaction with the framework could be extracted from experimental dPDF analysis, **Fig. 10**I. Distinct binding signals arise from P-Zr pair correlations during gas loading, and the distances agree well with bidentate bound MMPA, confirming the reaction mechanism.

10.09.8 Layered materials

Many materials form distinct layered motifs, which can succumb to a variety of two-dimensional defects in their formation. The effects of so-called *turbostratic* disorder, where the order between the orientations of separate layers is reduced or lost completely,

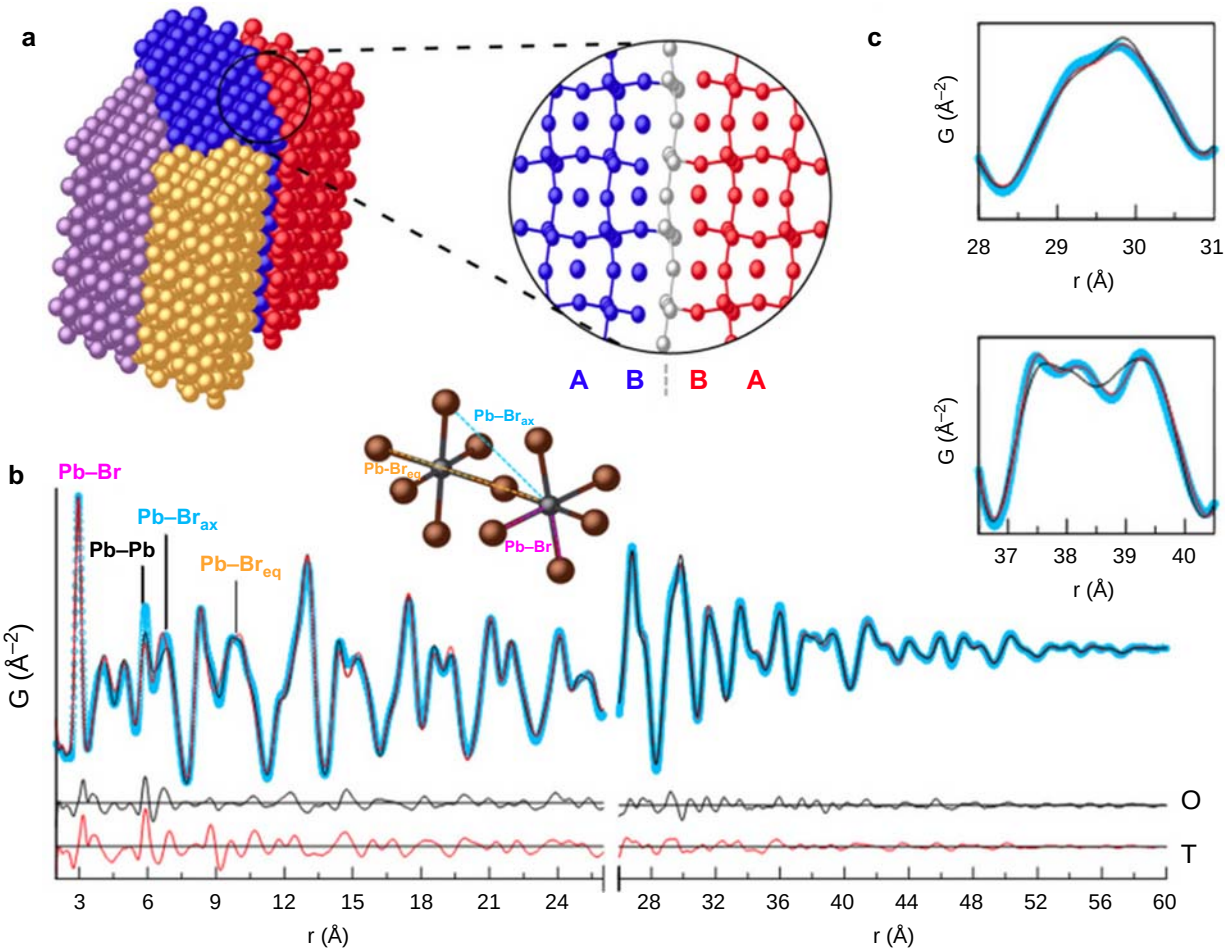

Fig. 8 (A) Atomistic representation of nanotwins within a $CsPbX_3$ nanocrystal; the twin boundary highlighted in the circle shows the discontinuity of the halides lattice and the coherence of the Pb sublattice, (B) and an inset (C) are $G(r)$ fits of RT $CsPbBr_3$ QDs: the black (red) solid lines show the residuals of the orthorhombic (tetragonal) model(s) in the low and medium r sections. The proposed orthorhombic structure fits significantly better ($R_w = 12.9\%$) than the tetragonal structure ($R_w = 18.5\%$). In the 26–70 Å range, however, a tetragonal structure is preferred ($R_w = 10.9\%$ vs. 12.4%). The assignment of the marked peaks (Pb–Br, Pb$\cdots$Br$_{ax}$, and Pb$\cdots$Br$_{eq}$) is sketched in the inset (Pb, black; Br, brown). Interestingly, inter-octahedral Pb–Pb peaks in (B) are much narrower than expected, whereas Pb–Br peaks are broader, indicating a more ordered arrangement of the Pb network and the discontinuity of halide sub-lattice at the twin boundaries. Reproduced from Bertolotti, F.; Protesescu, L.; Kovalenko, M.V.; Yakunin, S.; Cervellino, A.; Billinge, S.J.L.; Terban, M.W.; Pedersen, J.S.; Masciocchi, N.; Guagliardi, A. Coherent Nanotwins and Dynamic Disorder in Cesium Lead Halide Perovskite Nanocrystals. *ACS Nano* **2017**, *11*(4), 3819–3831.

was described by Warren.[114] Yet, this and other types of disorder involving random distributions of different preferred local interlayer interactions continue to plague crystal structure investigations today, and can be aided greatly by local structure information for materials as diverse as water ice,[115] covalent–organic frameworks,[116] and honeycomb structures formed by edge sharing $M^{n+}O_{6/2}^{(6-n)-}$ octahedra condensed into sixfold rings.[117,118]

PDF analysis has been successful in determining the structure of many layered materials for which structure solution or refinement by reciprocal-space methods is not feasible. This has been shown for example in cases with very high stacking fault density, extensive disorder, and for layered nanomaterials. Examples and applications include CdSe quantum dots[45,46] (see **Section 10.09.4** for details), vanadium oxide nanosheets for potassium-ion storage,[119] carbon nitride[120] and cobalt-based[121] photocatalysts for hydrogen/oxygen evolution, and nanocrystalline zirconium phosphonate-phosphate structures as ion exchangers for nuclear fuel remediation.[122] Others include layered double hydroxide nanosheets,[123] exfoliated-restacked metal dichalcogenides,[124] and transition metal-carbide MXenes.[125] Improvements in refinement algorithms and posterior analysis of large models can be expected to aid in the modeling and interpretation of such systems.[126]

PDF analysis was used to aid the detailed structure solution of the layered double oxide hydroxide $H_3LiIr_2O_6$. This material is attracting considerable attention as a potential pH sensor material and for its topological quantum spin liquid behavior. The structure was solved by Bette et al.[117] through a tedious process involving a careful indexing of the observable peaks in the high-resolution diffraction patterns, assessment of possible stacking transitions from known structure analogues, calculation of diffraction patterns from those possible stacking patterns, and Rietveld refinement of the diffraction data with constrained models

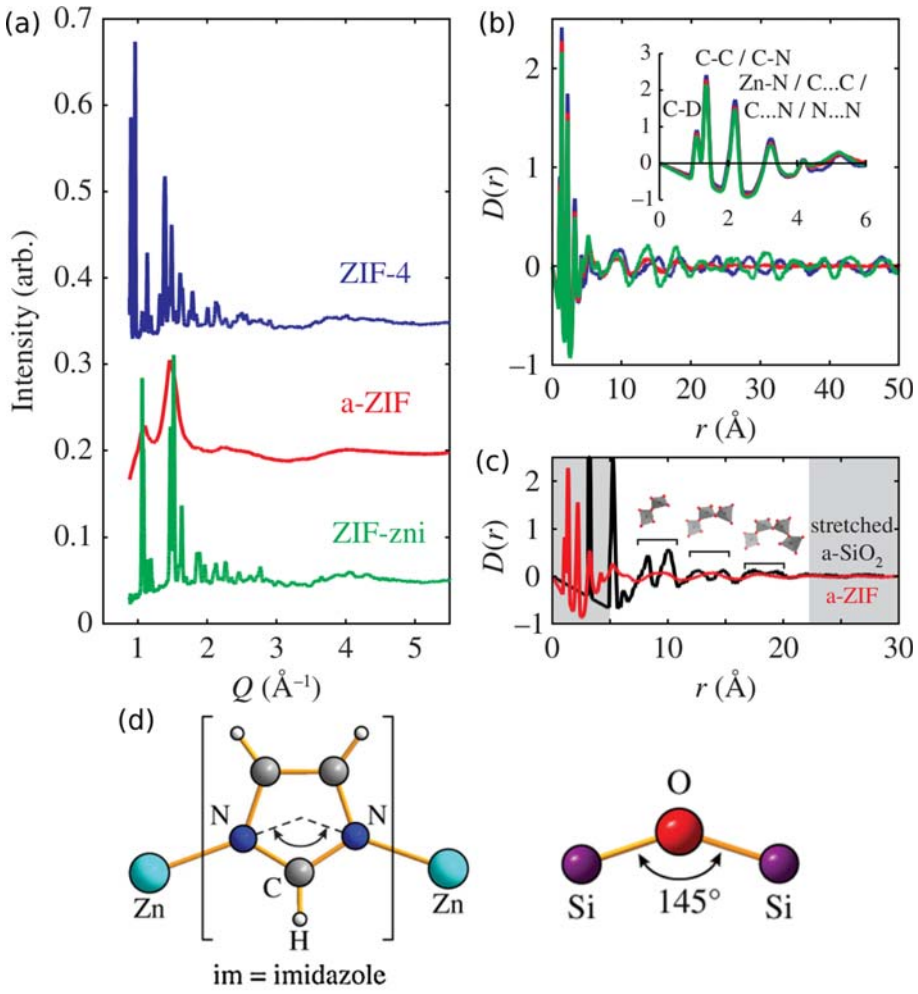

Fig. 9 (A) Neutron total scattering $S(Q)$ at low Q for the desolvated ZIF-4 framework at 300 °C (top), amorphized a-ZIF product at 320 °C (middle), and recrystallized ZIF-zni at 400 °C (bottom). (B) The differential correlation functions $D(r)$, which are related to the $G(r)$, for the three phases. The inset highlights how the local structure of the three phases is practically identical. (C) Overlay of the $D(r)$ functions for a-ZIF and a-SiO_2, where the latter data set has been stretched in r such that the peaks that represent analogous Zn–Zn and Si–Si distances in the two materials overlap. (D) Representations of the Zn-im-Zn and Si-O-Si linkages in tetrahedral ZIF and silicate networks respectively. Reproduced from Bennett, T.D.; Goodwin, A.L.; Dove M.T.; Keen, D.A.; Tucker, M.G.; Barney, E.R.; Soper, A.K.; Bithell, E.G.; Tan, J.-C.; Cheetham, A.K. Structure and Properties of An amorphous Metal–Organic Framework. *Phys. Rev. Lett.* **2010**, *104*(11), 115503.

using a simulated annealing approach that helps to avoid local minima. Before the Rietveld analysis, PDF analysis was used to decide on the appropriate restraints of specific pair bond distances, and afterward, to check the agreement between the local structure and the expected stacking sequences, as depicted in Fig. 11.

10.09.9 Polycrystalline thin films

Historically, PDF was applied to bulk powders or bulk amorphous materials. In 2015 it was shown that signals could be extracted from thin films of polycrystalline or nanocrystalline films.[127] The signal from the film is very small compared to that of the substrate making these measurements challenging. However, the advent of high flux, high energy synchrotron sources, large area 2D detectors that are efficient even at these high energies,[128] and more advanced data reduction algorithms[8] allow the extraction of very dilute signals.[129] This opened the door to extracting PDFs from thin films (tfPDF) even in normal incidence, as shown in Fig. 12.

Using this approach, it was possible to measure quantitatively reliable PDFs from polycrystalline and amorphous films of a few hundred nanometer thickness on substrates that were even millimeters thick.[127] The PDF extracted from a transparent conducting layer of indium tin oxide of 70 nm on a 4 mm glass slide substrate could even be successfully modeled.[130] Similarly, titania films synthesized under microwave electromagnetic radiation were shown to vary in amorphous and crystalline phase content, nanoparticle size, and film thickness as a function of synthesis temperature and microwave power.[131] This approach is obviously useful if

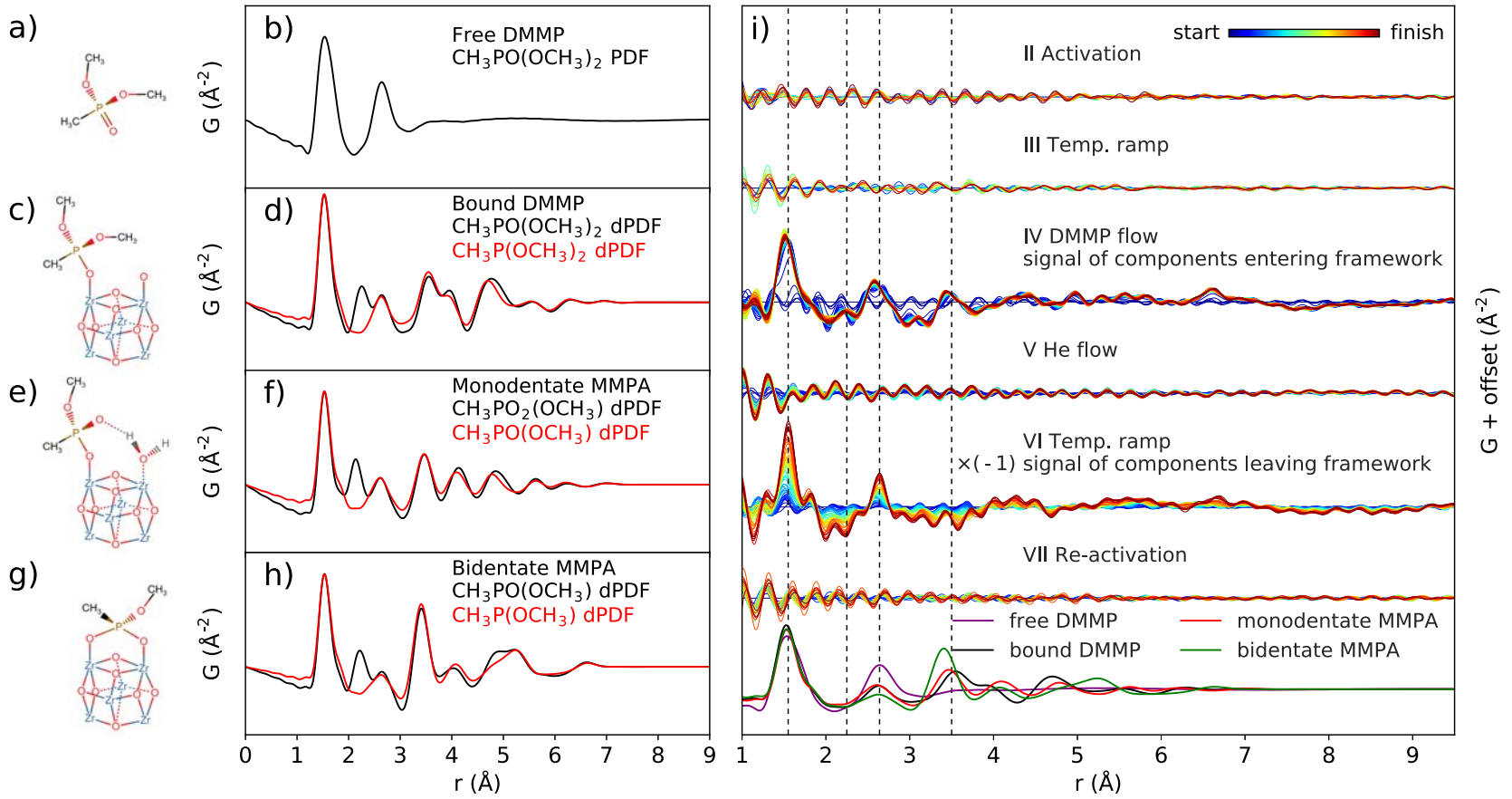

Fig. 10 Schematic representations of the structures and corresponding simulated PDFs for an isolated DMMP molecule (A and B), bound DMMP (C and D), monodentate MMPA (E and F), and bidentate bound MMPA (G and H). Red curves show the difference PDFs (dPDFs) representing DMMP + DMMP-cluster pair distances with bridging oxygen considered as part of the cluster (black curves with bridging oxygen as part of DMMP). Models for simulated PDFs were obtained from DFT relaxation. (I) Experimental dPDFs for all the different steps of the process with the blue curve representing the start of a given step, and with each step offset for comparison. The simulated PDF for an isolated molecule of DMMP and the dPDFs of DMMP and MMPA binding states are plotted for reference at the bottom. Reproduced from Terban, M.W.; Ghose, S.J.; Plonka, A.M.; Troya, D.; Juhás, P.; Dinnebier, R.E.; Mahle, J.J.; Gordon, W.O.; Frenkel, A.I. Atomic Resolution Tracking of Nerve-Agent Simulant Decomposition and Host Metal–Organic Framework Response in Real Space. *Commun. Chem.* **2021,** *4*(2).

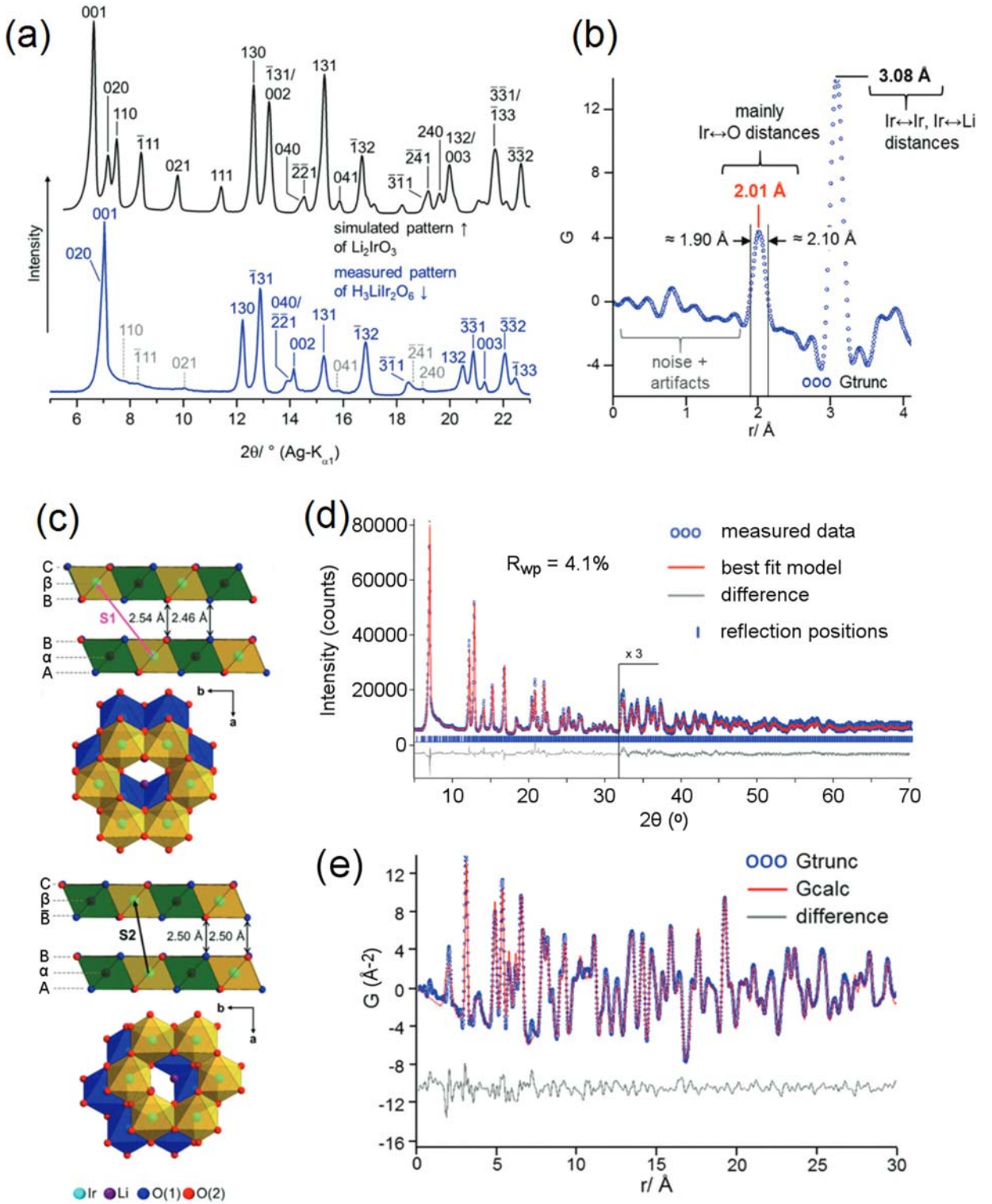

Fig. 11 (A) Comparison of a simulated X-ray powder diffraction pattern from predicted structure (black) and experimental pattern of $HsLiIr_2O_6$. (B) Excerpt of the measured PDF highlighting the constraints chosen for neighbor bond distances. (C) Examples of two different stacking patterns of two layers of the structure with stacking vectors used to describe the faulting scenarios. (D) The final Rietveld refinement obtained by unconstrained simulated annealing, which resulted in stacking vectors matching closely to that expected from structure considerations. (E) Measured PDF fitted using a 12-layer stacking supercell model obtained by global optimization. Reproduced from Bette, S.; Takayama, T.; Kitagawa, K.; Takano, R.; Takagi, H.; Dinnebier, R.E. Solution of the Heavily Stacking Faulted Crystal Structure of the Honeycomb Iridate $H_3LiIr_2O_3$. *Dalton Trans.* **2017**, *46*, 15216–15227.

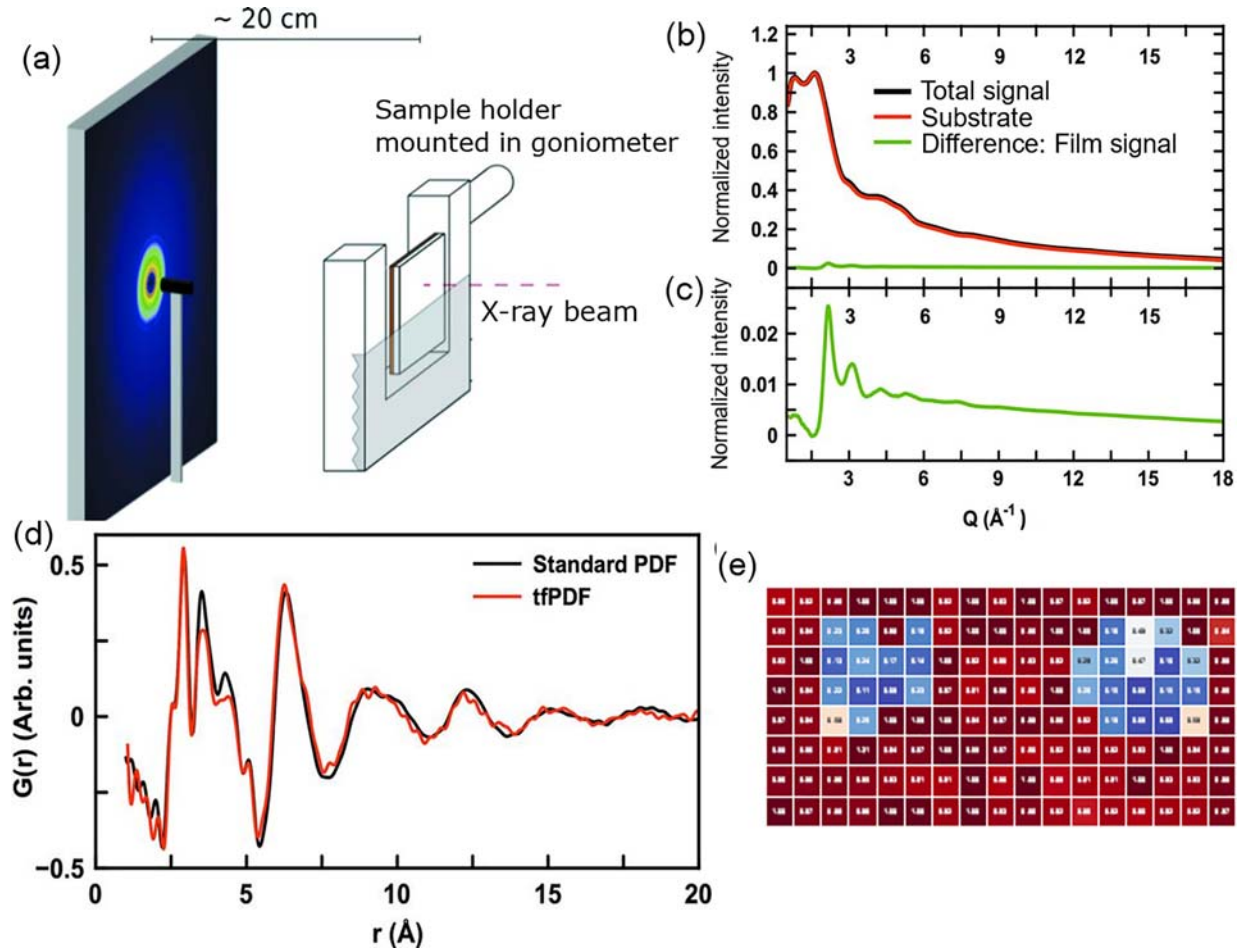

Fig. 12 (A) Setup used for tfPDF measurements. The X-ray beam hits the substrate before the film. (B) Normalized data collected for sample 1A (black) and the clean substrate (red), and difference between the two (green), also shown on an expanded scale in (C). (D) Comparison between the tfPDF for sample 1A and a powder sample of similar composition, where the data were obtained for a sample measured in a standard capillary. (E) The distribution of nanoparticles on a chip extracted from tfPDFs. The pixels containing nanoparticles are indicated in blue. Reproduced from Jensen, K. M. Ø.; Blichfeld, A.B.; Bauers, S.R.; Wood, S.R.; Dooryhée, E.; Johnson, D.C.; Iversen, B.B.; Billinge, S.J.L. Demonstration of thin film pair distribution function analysis (tfPDF) for the study of local structure in amorphous and crystalline thin films. *IUCrJ* **2015**, 2(5), 481–489.

your nano-sample happens to be in thin film geometry, but it also opens the door to doing spatially resolved measurements where films are heterogeneous. The ability to study thin films in this spatially resolved manner opens the door to "lab-on-a-chip" experiments, such as the case of dots of nanoparticles that can be written onto a substrate using an ink-jet printing device that writes using nanoparticle inks.[132] This is illustrated in Fig. 12E which shows a pixelation of one such chip. The dots containing nanoparticles are indicated in blue. However, in each of the pixels in the image we have a full and quantitative PDF that contains all the structural information about the nanoparticles that are deposited in that dot.

In cases where the signal from the film is very weak, it may be necessary to carry out a measurement in grazing incidence. This approach increases the signal from the film relative to the substrate, because the incident beam does not penetrate deeply into the substrate, whilst making a large footprint on the surface of the film.[133] This was used, for example, to show that thin Indium Gallium oxide films had distinct structures when compared to bulk material made using a gel method.[134] Grazing incidence thin film measurements are experimentally challenging, because the critical angle of high energy X-rays is very small for most films, and very stable and precise diffractometers are required, coupled with very stable X-ray optics. Such beamlines are becoming available, and it is expected that the importance of these grazing incidence thin film PDF measurements[133,135,136] will grow in the future.

A potential drawback for many thin film measurements is that the particles in the (polycrystalline) films take on a preferred crystallographic orientation (texture). For example, they may have more or less fiber texture with a preferred crystallographic direction lying perpendicular to the surface. This makes quantitative PDF analysis impossible unless steps are taken to mitigate this. Fortunately, approaches are emerging that will allow the PDF of textured samples to be studied.[137]

10.09.10 Amorphous systems

The first applications of the PDF technique was for the structural study of amorphous materials and liquids for which reciprocal space diffraction techniques are inadequate. Still, the PDF was far from adequate, since only low-energy X-rays were available back then. The limited Q range reduces the real-space resolution and increases the effects of termination ripples in the Fourier transformation of the data, which can affect the most precious signal at low *r*. This meant that the only quantities that could be reliably deduced were the average distance to the nearest neighbors and the coordination number (from the *radial distribution functions*, RDF).[138,139] With the modern development of high-energy radiation sources and 2D detectors, the complex structural details in the signal became accessible, uncovering the details of *e.g.*, anisotropy and the formation of crystalline clusters. Modern PDF measurements can allow, for example, a more accurate representation of the shape of the first peak, medium-order structural interpretation using higher order peaks, and structural contributions from additional phases can be isolated using differential PDF methods.[1]

The structure of amorphous systems may evolve over time, which is evidenced by observation of excess specific heat released by the breaking and reforming of bonds.[140] For example, X-ray PDF was used to explore the relaxation mechanism of metallic glasses during annealing at temperatures just below the glass transition temperature. Through a series of studies that started in the early 1980s (Refs. 141,142), and more recently and accurately in 2007[143], the structural relaxation mechanism of Zr-Cu-Ni-Al-Ti metallic glasses was probed with PDF. The PDF (see **Fig. 13**) showed that the evolution of the amorphous phase into the crystalline form involved the elimination of areas with both higher- and lower-than-average densities,[143] rather than, the previously assumed, elimination of "free volume" (*i.e.*, higher-than-average density) in the structure.[140]

When the sample is heterogeneous, it is important to study the spatial (as well as temporal) changes across the sample. This is possible with X-rays, but also with electron diffraction carried out in an electron microscope. Electron beams can routinely be focused to resolutions of a few Å allowing for nanometer-scale mapping of local structure in glasses. Although electron-diffraction based PDF (ePDF) was introduced already in the 1960s,[144], it has only caught the eye of the community in the last decade due to recent improvements in the fabrication of very thin samples, microscopy hardware (*e.g.*, lenses, detectors) and software-analysis tools,[1] yielding sufficiently accurate PDFs that can be used for structural fitting.[145] The advent of faster data acquisition and analysis methods allows the ePDF measurements to be carried out in a spatially resolved way, resulting in a full PDF at each location in the thin sample with spatial resolutions at the nanoscale.

Recent studies used ePDF in a 4D-STEM mode scan to create local-structure maps that classified differences in local structure in metallic glasses[146,147] and organic polymer composite materials.[148] A more recent study by Rakita et al.[149] showed a generic concept for mapping structural heterogeneity in complex material systems, using structural features from ePDF in the form of scalar quantities of interest (QoI). From a focused ion beam (FIB) lift-out of a hot-rolled amorphous $Zr_{65}Cu_{17.5}Ni_{10}Al_{7.5}$ bulk metallic glass (BMG) capped with a crystalline Ni composite, electron diffraction images were collected with a 3 nm spatial resolution and reduced to 1D PDFs. The reduced 1D PDF plots, were then used to extract local-order structural quantities of interest (QoI), such as the average inter-atomic pair distance using the first PDF peak-maximum position, and the atomic-number weighted distribution of inter-atomic bond lengths at the first coordination by extracting the PDF peak width. Recording the value of each QoI as a function of position resulted in a structure-oriented microscopy, and with a positional resolution of just a few nm, scanning nanostructure electron microscopy (SNEM) maps, as shown in **Fig. 14**, could be generated. After the BMG was distinguished from the surrounding Ni, the 2D QoI-based SNEM maps (panel F) reflect, with ~5 nm spatial accuracy, variations in local order,

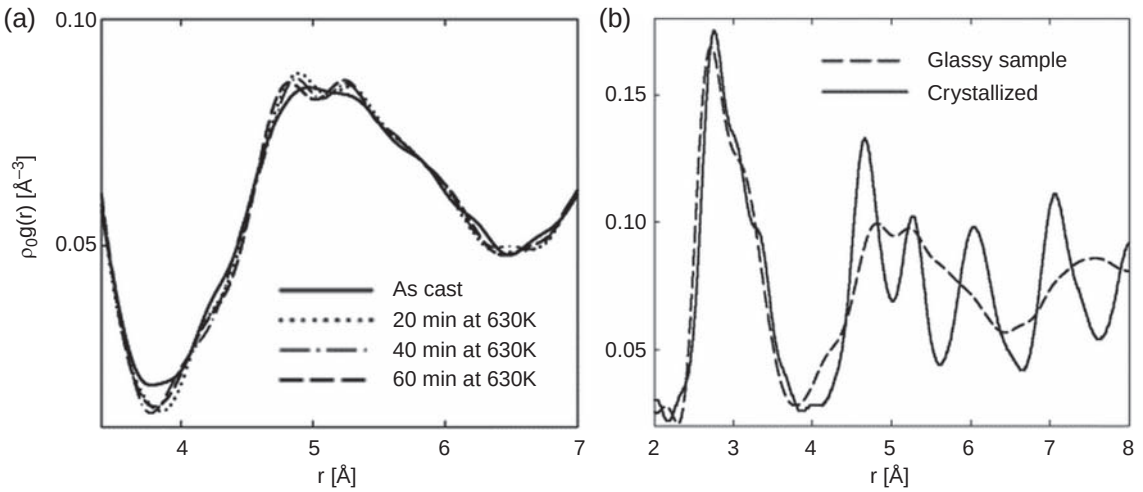

Fig. 13 PDF of bulk metallic glass $Zr_{52.5}Cu_{17.9}Ni_{14.6}Al_{10.0}Ti_{5.0}$ (at.%) annealed under its glass transition temperature (630 K): (A) changes in PDF in the range of the second atomic shell after annealing for varying times. (B) Comparison between a sample annealed for 60 min and a crystallized sample. Reproduced from Dmowski, W.; Fan, C.; Morrison, M.L.; Liaw, P.K.; Egami, T. Structural Changes in Bulk Metallic Glass after Annealing Below the Glass-Transition Temperature. *Mater. Sci. Eng. A* **2007**, *471*(1), 125–129.

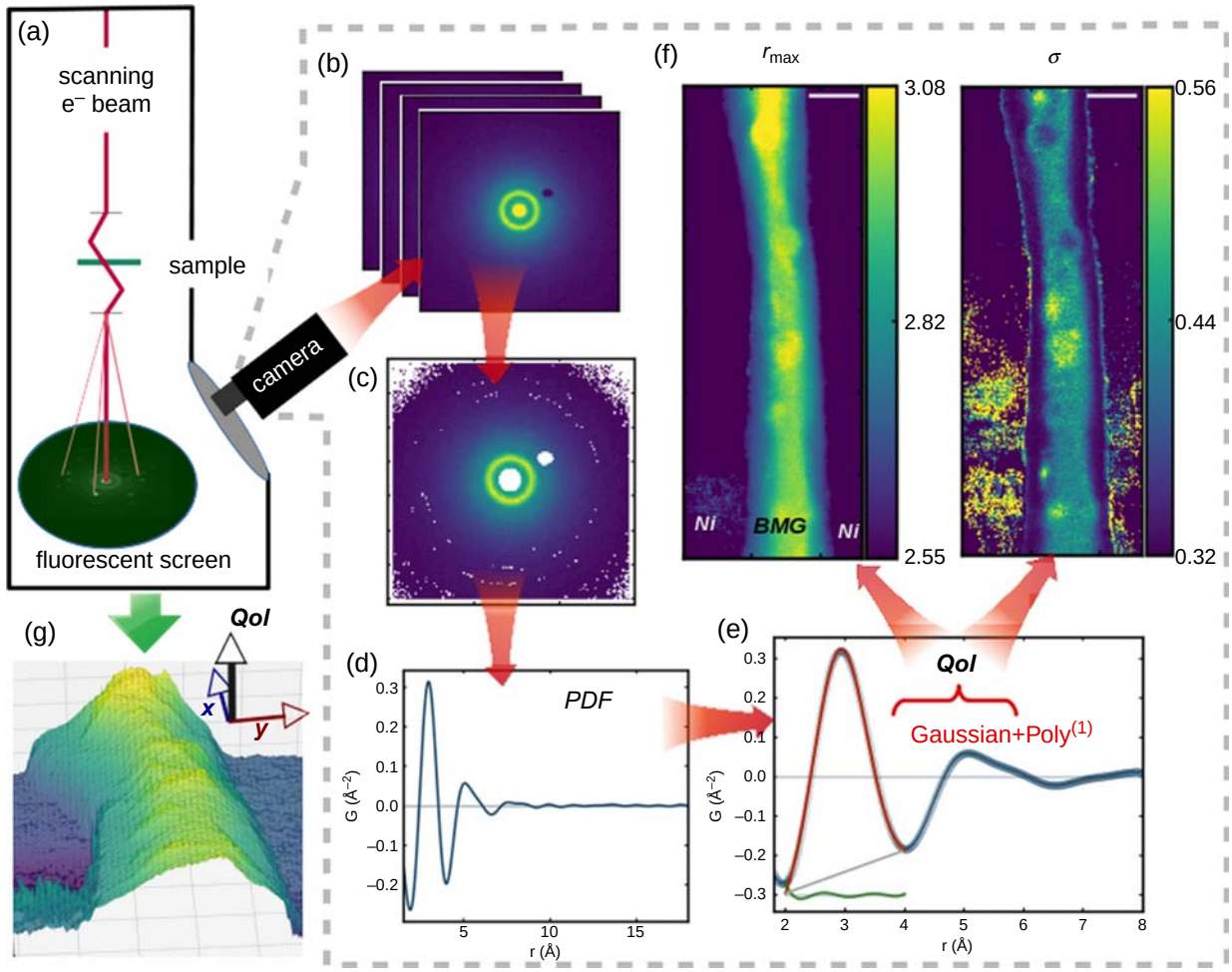

Fig. 14 An overview summary of SNEM experimental data collection, data reduction, extraction of a quantity of interest (QoI), and visualization. (A) Schema of the electron-microscopy and the recording of diffraction patterns: patterns were collected using an external fast camera that recorded the diffraction data on a fluorescent screen detector. (B) An example of a recorded diffraction pattern gained from the amorphous part of the BMG. (C) Extraction of the virtual dark field using a manual annular mask for the direct beam and an automatic mask for the damaged pixels. (D) Derived PDF from the diffraction pattern. (E) Example of an extraction of a QoI—here a Gaussian + first order polynomial, where blue curve is data, red is fit, and green is the difference between fit and data. (F) Maps of the QoI r_{max}, which is the maximum of the first peak, and σ, which is the peak width. The maps in (F) show structural heterogeneity in the BMG, where r_{max}, reflects the average pair distances and σ reflects the distribution of the existing pairs within the first coordination shell. The scale bars in (F) refer to 100 nm. (G) A 3D representation of a QoI map that summarizes the concept behind SNEM; this specific example shows a 3D r_{max} QoI SNEM map shown in (F). Reproduced from Y. Rakita, J. L. Hart, P. Pratim Das, S. Nicolopoulos, S. Shahrezaei, S. N. Mathaudhu, M. L. Taheri, and S. J. L. Billing (2021) Studying heterogeneities at the nanoscale with scanning nanostructure electron microscopy (SNEM). https://arxiv.org/abs/2110.03589.

composition, and local structure. The r_{max} map, which represents the average pair-distance, yields information about the Zr contribution, as also evident from an EELS map from the same region.[149] From the map of the width, σ, of the first PDF peak, sharper and narrower peaks were observed coincident with Zr-rich areas (brighter yellow in r_{max} map), suggesting variations in the number of different chemical species in the two regions. However, the PDF contains more than just chemical information, allowing in principle differentiation between random solid solution, segregated, relaxed, or intermetallic regions[150]. These examples emphasize the potential of PDF for investigating the spatial or temporal heterogeneity of the local structure in materials at a nanometer length scale (Fig. 14).

10.09.11 Nucleation of crystallites

Crystal growth can happen via self-assembly of smaller units referred to as crystallization centers, such as monomers, molecular clusters, or nanocrystals.[151] The crystallization centers can appear spontaneously in a medium (primary nucleation) - often in a super-saturated medium at a given temperature or pressure,[152] for instance when ice crystals nucleate in water below the freezing

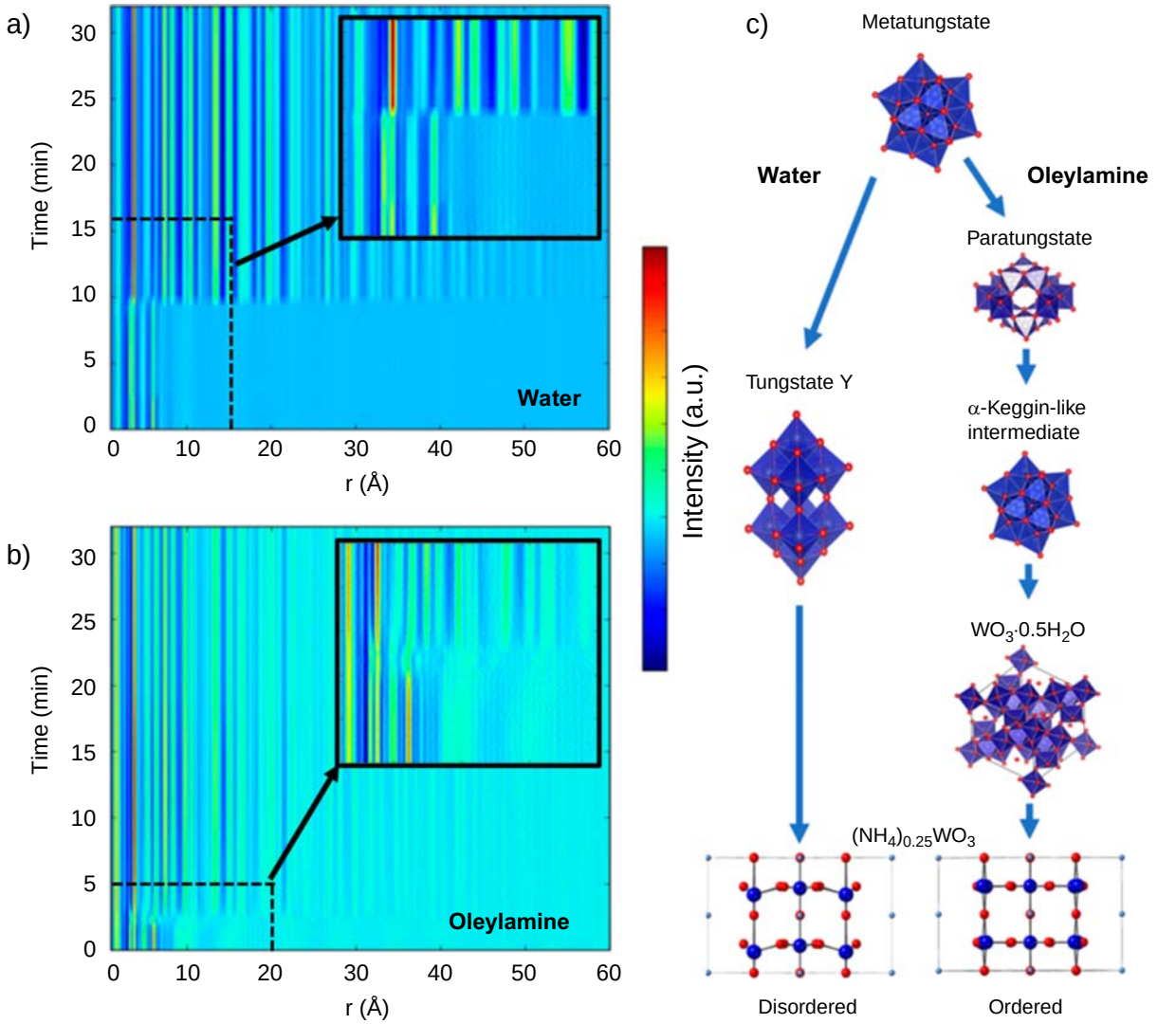

Fig. 15 Time-resolved PDFs obtained during the synthesis of the hexagonal tungsten bronze $(NH_4)_{0.25}WO_3$ nanoparticles in water (A) and in oleylamine (B). The insets show the region just before crystallization. (C) The suggested formation pathway of nucleation in water and oleylamine, based on the time-resolved PDFs. In both solutions, the process starts with the initial dissolution of the crystalline metatungstate precursor. In water, the pathway goes via the formation of α-Keggin-structured clusters, which upon heating enter an equilibrium with a Tungstate Y cluster $W_{10}O_{32}$, from which the tungsten bronze crystallize into 70 nm nanoparticles with a disordered WO_3 structure. In oleylamine, the metatungstate also dissolves to form α-Keggin-structured clusters, which then quickly transform into an amorphous phase similar to the paratungstate cluster. Then, moments before crystallization, the amorphous phase breaks up and another α-Keggin-like structure is observed. Crystallization happens in two steps; first nanoparticles with a cubic pyrochlore structure $WO_3 \cdot 0.5H_2O$ form, secondly they undergo a phase change into the hexagonal tungsten oxide bronze structure, as seen in the synthesis in water, however with no clear structural disorder on the tungsten sites. Reproduced from Juelsholt, M.; Christiansen, T.L.; Jensen, K.M.Ø. Mechanisms for Tungsten Oxide Nanoparticle Formation in Solvothermal Synthesis: From Polyoxometalates to Crystalline Materials. *J. Phys. Chem. C* **2019**, *123*(8), 5110–5119.

temperature. They can also be introduced intentionally or accidentally to a system (secondary nucleation). The key goal of any synthesis is to have control of the morphology, composition, and structure of the product. Controlling nucleation can guide the consequently grown phase, and therefore the nucleation processes are not only interesting in and of themselves. They are widely utilized in controlling the synthesis of new and better materials, for a wide range of applications where functional materials are used, *e.g.*, batteries, fuel cells, solar cells, electronics, sensors, catalysts, and for medical imaging. Examples of synthesis processes that utilize nucleation are sol-gel, molten-salt, precipitation, and solvo-/hydrothermal synthesis.

Nuclei are clustered species in a bulk medium that possess a unique structural order that is different from the surrounding bulk. These clusters do not span over long distances, which infers that understanding nucleation requires a probe that can follow the evolution at the short- to mid- to long-range order. Knowing already that PDF is a probe for local order, it has been widely used for tracing and reconstructing the structures of nuclei. PDF has been used to study nucleation during the sol-gel synthesis of SiO_2-TiO_2 aerogels,[153] during the reduction-precipitation synthesis of Pt nanoparticles[154] and during the molten-salt synthesis

of MgO in $NaNO_3$.[155] But the vast majority of scattering measurements on nucleation processes have examined the particularly promising process of hydrothermal or solvothermal synthesis. The development of *in situ* setups has enabled studies of solvo-/hydrothermal synthesis, a very widely used method to synthesize materials at both elevated pressures and temperatures inside thick-walled closed containers. The *in situ* setups bypass the use of a container, whose walls cannot be penetrated by X-rays, by using capillaries with pressure supplied at each end. PDF has been used to determine the evolution of the structure from precursor to product for a wide range of materials, including SnO_2[156] and CeO_2[157] nanoparticles, Y-stabilized ZrO_2,[158] Li-Fe-Mn-phosphate cathode materials,[159,160] nanoparticles of maghemite,[161] WO_3,[162,163] $ZnWO_4$[164] and MnO_2,[165] lepidocrocite-type layered titanates,[166] Pd-Pt core-shell nanoparticles,[167] ZIF-8[106] and UiO-66 metal-organic framework materials,[107] zeolites,[168] hierarchical and microporous aluminophosphate,[169] Sr-Ba niobates[170] and $ZnAl_2O_4$ nanocrystals.[171]

In the study by Juelsholt et al.,[162] for example, the mechanisms for the formation of tungsten oxide nanoparticles from the initial precursor to the final crystalline particles were elucidated. Monitoring the nucleation process both in water and in the solvent oleylamine, the authors could deconstruct the nucleation mechanisms of the WO_3 particles. Despite the formation of the same Keggin-cluster in both precursor solutions, and its similarity to the end product, they found that the reaction route in water went through fewer steps leading to a disordered WO_3 structure, while the oleylamine route went through more steps but gave a well-ordered WO_3 structure.

10.09.12 Magnetic crystals

PDF can also be applied to studies of magnetic structure using magnetic PDF (mPDF) analysis.[172,173] Just like the atomic PDF, the mPDF provides a real-space map of pairwise correlations between magnetic moments, although it is more complex than the atomic PDF because it involves orientational correlations (*e.g.*, ferromagnetic versus antiferromagnetic alignment) as well as spatial correlations between moments. mPDF analysis must be done using neutrons, which scatter from magnetic moments relatively strongly, whereas the magnetic scattering cross section for X-rays is too small to make mPDF analysis possible with current methodologies. Here, we briefly introduce mPDF analysis of neutron data and provide an example of its application to the antiferromagnetic oxide $NaMnO_2$.

The most common way to obtain the mPDF is to measure it simultaneously with the atomic PDF in a standard neutron PDF experiment on a magnetic material. The total PDF pattern obtained from the usual data reduction protocols is the sum of the atomic PDF and the mPDF. The mPDF is typically isolated either by (1) modeling the atomic PDF and subtracting it from the total PDF signal; or (2) collecting a PDF pattern at a temperature where the magnetic correlations are negligible and subtracting it from the PDF patterns with non-negligible magnetic contributions. The general approach to obtaining the mPDF is outlined schematically in Fig. 16. Whether the magnetic structure is of primary interest or merely a curiosity (or annoyance!) in the data, the ability to recognize and model the mPDF is valuable for performing a complete and reliable PDF analysis of any system of interest.

The inorganic material α-$NaMnO_2$ provides a useful example of combined atomic and magnetic PDF analysis.[174] This compound is the end member for the Na_xMnO_2 system, which has been investigated as a potential battery electrode material. $NaMnO_2$ is also magnetic, with the spins on the Mn^{3+} ions exhibiting long-range antiferromagnetic order below $T_N = 45$ K, and short-range antiferromagnetic correlations persisting to significantly higher temperatures. The interesting aspect of this material from a magnetic point of view is that the Mn^{3+} spins form networks of isosceles triangles in the crystallographic structure, making $NaMnO_2$ a geometrically frustrated antiferromagnet. As illustrated in Fig. 17C, one side of the triangle (r_1) is shorter than the other two, so the strong antiferromagnetic interactions lead to oppositely aligned spins on either end of r_1. However, the two isosceles legs (r_2 and r_3) are equal in length. Consequently, whether the spin on the lower vertex is up or down, the spin alignment along one leg will be antiferromagnetic (favored) while the other will be ferromagnetic (disfavored), thus frustrating the system. How the system selects a unique, long-range ordered magnetic ground state below 45 K despite the degeneracy between the two isosceles legs remained a mystery for a long time.

This mystery was resolved through a combined atomic and magnetic PDF analysis of $NaMnO_2$, which revealed that a short-range structural distortion breaks the isosceles symmetry locally and promotes short-range antiferromagnetic correlations along the shorter isosceles leg (see Fig. 17C). The magnetic correlations grow in magnitude and spatial extent as the temperature is lowered and eventually transition to genuine long-range magnetic order, even while the structural distortion exists only on short length scales. Representative PDF patterns collected at 5 K (with long-range magnetic order) and 50 K (with short-range magnetic order) are shown in Fig. 17A and B. The black curve is the experimental total PDF, with the best-fit total PDF overlaid as the red curve. The gray and blue curves (offset vertically and multiplied by two for clarity) represent the mPDF data and fit, respectively. The small overall fit residual (lower green curve) indicates a good fit to the total PDF. At 50 K, the mPDF pattern is strongly damped at high r, indicating a finite magnetic correlation length, and the overall magnitude is smaller due to increased thermal fluctuations of the magnetization.

By tracking the behavior of the local structural distortion and the magnetic correlations as a function of temperature across the magnetic transition, this work established a novel coupling between magnetism and a short-range structural distortion to relieve the magnetic frustration. More generally, this example highlights the power of combined atomic and magnetic PDF analysis in magnetic materials. Such an approach will be valuable for numerous other systems with coupling between the magnetic and structural properties.

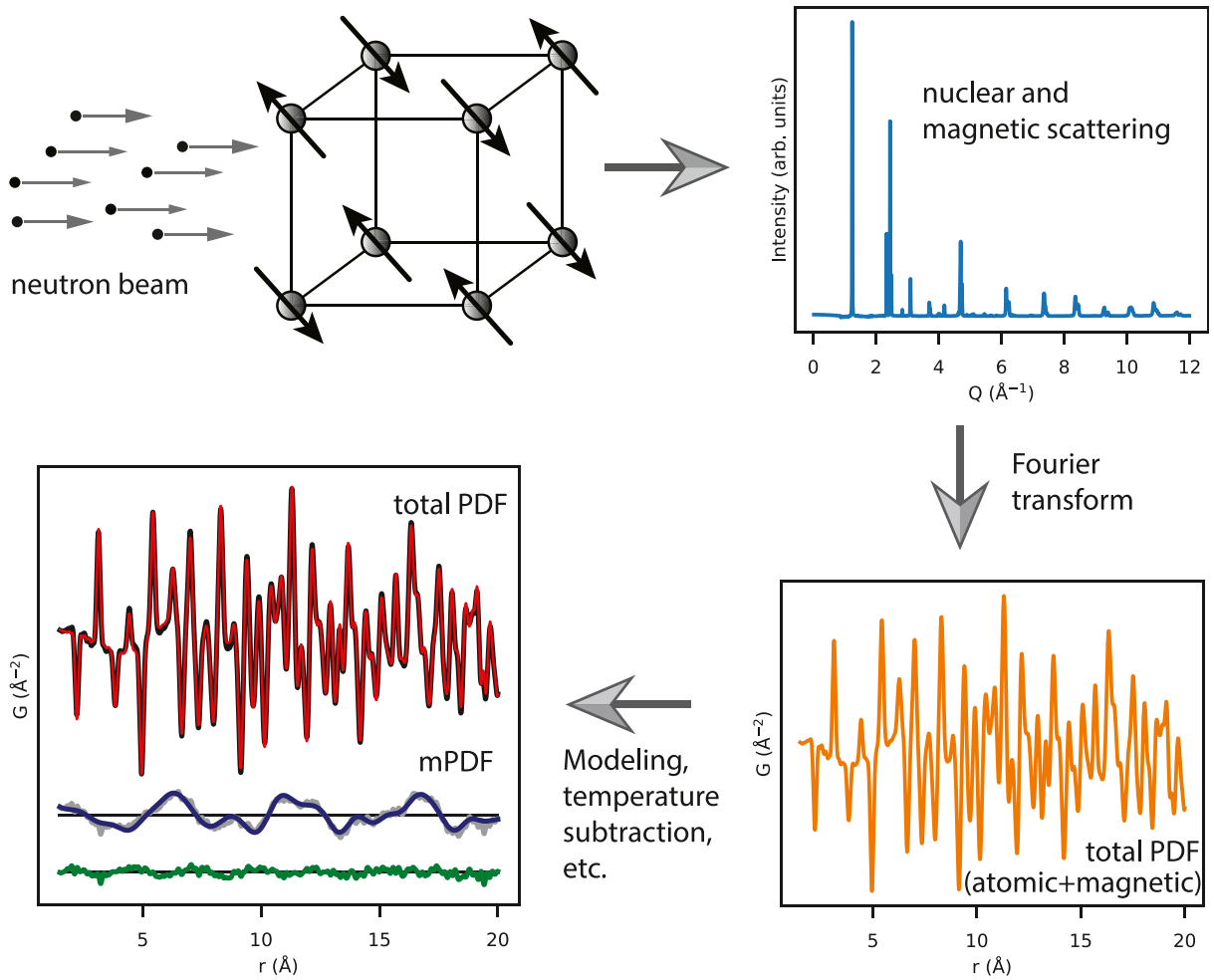

Fig. 16 Schematic illustration of how the mPDF can be obtained for a typical neutron PDF experiment. After fitting a structural model to the PDF, which contains both the structural and magnetic signal, the magnetic part of the signal cannot be adequately fitted and will be left in the difference curve.

10.09.13 Future development

Here, we point out some promising directions in PDF analysis that address emerging challenges in materials science.

One reason why the conventional powder diffraction and PDF techniques have become popular in the scientific community is that reliable, trustworthy, and easy-to-use data analysis and modeling programs have become available. For example, in the PDF context, GUI (graphical user interface) programs such as xPDFsuite[175] and PDFgui,[14] have been very popular.[2] In the future, especially in view of "big-data" and cloud-computing, we would expect more web-based PDF analysis platforms, such as "PDF in the cloud" (PDFitc),[63] to help users analyze and interpret their PDF data in a more convenient manner, and to build knowledge of materials. In principle, these platforms can become single-button analyzers for PDF making materials characterization more straightforward by sharing community expertise.

In the wake of the implementation of new data tools such as materials databases, machine learning, and high-throughput methods,[176] new approaches to PDF analysis have recently been created, such as automated structure-mining based conventional modeling approaches[60,76] and machine learning to suggest the space group of novel nanomaterials.[177]

Most PDF work is performed using synchrotron X-rays or spallation neutrons, with only some using electrons. Better utilization of these precious resources is made possible by greater automation of experiments, with the community further pushing in the direction of *autonomation*, meaning that an *in situ* experiment is evolving in time with input parameters being determined by a mathematical decision algorithm based on results from previous measurements. This is particularly important when we seek to explore an input parameter space that is high dimensional (many control parameters) in a smart way.[178,179] At the time of writing these efforts are yet to be demonstrated for PDF, but with improvements in infrastructure for automation and automated data reduction in a streaming context,[180–182] this is just around the corner.

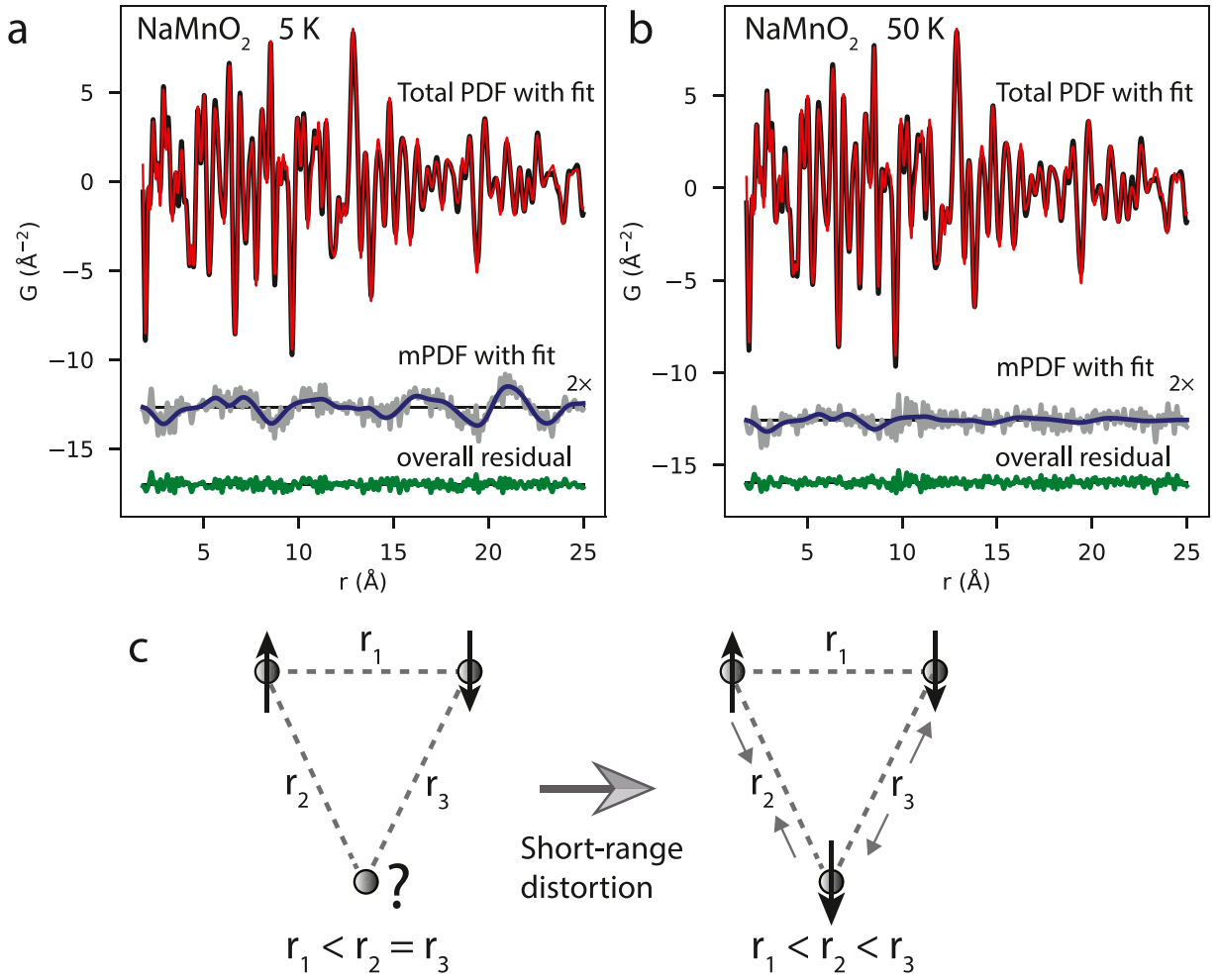

Fig. 17 Joint atomic and magnetic PDF analysis of $NaMnO_2$ at 5 K (A) and 50 K (B). Black and red curves are the total PDF data and the total PDF fit, respectively. The mPDF data (gray curves) reveal long-range antiferromagnetic correlations at 5 K and short-range correlations at 50 K, and they are well described by the fits (blue curves). (C) Triangular motif of Mn^{3+} spins in $NaMnO_2$. The triangles are isosceles in the average structure (left), resulting in magnetic frustration. The PDF analysis shows that a short-range structural distortion lifts this degeneracy locally, relieving the magnetic frustration and allowing a unique magnetic ground state to be selected.

With the growth of *in situ* PDF experimentation,[113,183–185] the coupling of computed tomography with PDF[186,187] and spatial resolution that can get down to 10–100 um with X-rays[186,187] and 10–100 nm with electrons,[146–148] advances in reaction evolution and phase transition evolution studies with high spatial resolution will start to have significant impacts in our understanding of material processing. Integration with automation can unlock the capability to trace boundaries in structural evolution at the nanoscale, especially at early stages where long-range order is absent. Also, introducing floating liquid phase cells in a TEM[188] and integrating it with electron-PDF analysis can unlock the possibility to investigate nucleation reactions at the nanoscale.

Acknowledgments

S.H·S, Y.S.R., L.Y. and S.T. were supported by the U.S. National Science Foundation through grant DMREF-1922234. S.J.L.B was supported by the U.S. Department of Energy, Office of Science, Office of Basic Energy Sciences (DOE-BES) under contract No. DE-SC0012704. M.W.T. gratefully acknowledges support from BASF. Soham Banerjee and Robert Koch are acknowledged for valuable discussions.

References

1. Egami, T.; Billinge, S. J. L. *Underneath the Bragg Peaks: Structural Analysis of Complex Materials*, 2nd ed.; Elsevier: Amsterdam, 2012.
2. Billinge, S. J. L. The Rise of the X-Ray Atomic Pair Distribution Function Method: A Series of Fortunate Events. *Philos. Trans. R. Soc. A Math. Phys. Eng. Sci.* **2019,** *377* (2147), 20180413.

3. Aroyo, M. I. *International Tables for Crystallography, Volume A, Space-group Symmetry,* 6th ed.; Wiley, 2017.
4. Billinge, S. J. L.; Banerjee, S.; Bozin, E. S.; Jensen, K. M.Ø.; Frandsen, B. A.; Terban, M. W.; Koch, R. J. *PDF to the People: An Atomic Pair Distribution Function Analysis Primer*. unpublished, 2021.
5. Peterson, P. F.; Olds, D.; McDonnell, M. T.; Page, K. Illustrated Formalisms for Total Scattering Data: A Guide for New Practitioners. *J. Appl. Cryst.* **2021,** *54* (1), 317–332. Number: 1 Publisher: International Union of Crystallography.
6. Olds, D.; Saunders, C. N.; Peters, M.; Proffen, T.; Neuefeind, J.; Page, K. Precise Implications for Real-Space Pair Distribution Function Modeling of Effects Intrinsic to Modern Time-of-Flight Neutron Diffractometers. *Acta Crystallogr. A* **2018,** *74* (4), 293–307.
7. Debye, P. Dispersion of Rontgen Rays. *Ann. Phys.* **1915,** *351,* 809–823.
8. Juhás, P.; Davis, T.; Farrow, C. L.; Billinge, S. J. L. PDFgetX3: A Rapid and Highly Automatable Program for Processing Powder Diffraction Data Into Total Scattering Pair Distribution Functions. *J. Appl. Cryst.* **2013,** *46* (2), 560–566.
9. P.F. Peterson, M. Gutmann, TH. Proffen, and S.J.L. Billinge. PDFgetN: A User-friendly Program to Extract the Total Scattering Structure Factor and the Pair Distribution Function From Neutron Powder Diffraction Data. J. Appl. Cryst., 33(4): 1192, 2000. Publisher: Wiley-Blackwell.
10. Juhás, P.; Louwen, J. N.; van Eijck, L.; Vogt, E. T. C.; Billinge, S. J. L. PDFgetN3: Atomic Pair Distribution Functions From Neutron Powder Diffraction Data Using Ad Hoc Corrections. *J. Appl. Cryst.* **2018,** *51* (5), 1492–1497. Publisher: International Union of Crystallography.
11. Toby, B. H.; Von Dreele, R. B. GSAS-II: The Genesis of a Modern Open-Source All Purpose Crystallography Software Package. *J. Appl. Cryst.* **2013,** *46* (2), 544–549. Publisher: International Union of Crystallography.
12. Coelho, A. A. *TOPAS Academic: General Profile and Structure Analysis Software for Powder Diffraction Data*, Bruker AXS, 2004.
13. Soper, A. *GudrunN and GudrunX: Programs for Correcting Raw Neutron and X-ray Diffraction Data to Differential Scattering Cross Section*. undefined, 2011.
14. Farrow, C. L.; Juhás, P.; Liu, J. W.; Bryndin, D.; Bozin, E. S.; Bloch, J.; Proffen, T.; Billinge, S. J. L. PDFfit2 and PDFgui: Computer Programs for Studying Nanostructure in Crystals. *J. Phys. Condens. Matter* **2007,** *19* (33), 335219.
15. Kwei, G. H.; Lawson, A. C.; Billinge, S. J. L.; Cheong, S. W. Structures of the Ferroelectric Phases of Barium Titanate. *J. Phys. Chem.* **1993,** *97* (10), 2368–2377.
16. Kwei, G. H.; Billinge, S. J. L.; Cheong, S.-W.; Saxton, J. G. Pair-Distribution Functions of Ferroelectric Perovskites: Direct Observation of Structural Ground States. *Ferroelectrics* **1995,** *164* (1), 57–73.
17. Senn, M. S.; Keen, D. A.; Lucas, T. C. A.; Hriljac, J. A.; Goodwin, A. L. Emergence of Long-Range Order in $BaTiO_3$ FROM LOCAL SYMMETRY-BREAKING Distortions. *Phys. Rev. Lett.* **2016,** *116* (20), 207602.
18. Westphal, V.; Kleemann, W.; Glinchuk, M. D. Diffuse Phase Transitions and Random-Field-Induced Domain States of the "Relaxor" Ferroelectric $PbMg_{1/3}Nb_{2/3}O_3$. *Phys. Rev. Lett.* **1992,** *68* (6), 847–850.
19. Jeong, I.-K.; Darling, T. W.; Lee, J. K.; Proffen, T.; Heffner, R. H.; Park, J. S.; Hong, K. S.; Dmowski, W.; Egami, T. Direct Observation of the Formation of Polar Nanoregions in $Pb(Mg_{1/3}Nb_{2/3})O_3$ Using Neutron Pair Distribution Function Analysis. *Phys. Rev. Lett.* **2005,** *94* (14), 147602.
20. Jeong, I.-K.; Lee, J. K. Local Structure and Medium-Range Ordering in Relaxor ferroelectric $Pb(Zn_{1/3}Nb_{2/3})O_3$ Studied Using Neutron Pair Distribution Function Analysis. *Appl. Phys. Lett.* **2006,** *88* (26), 262905.
21. Jeong, I.-K.; Lee, J. K.; Heffner, R. H. Local Structural View on the Polarization Rotation in Relaxor Ferroelectric $(1\text{-}x)Pb(Zn_{1/3}Nb_{2/3})O_3 - xPbTiO_3$. *Appl. Phys. Lett.* **2008,** *92* (17), 172911.
22. Goodwin, A. L.; Redfern, S. A. T.; Dove, M. T.; Keen, D. A.; Tucker, M. G. Ferroelectric Nanoscale Domains and the 905 K Phase Transition in $SrSnO_3$: A Neutron Total-Scattering Study. *Phys. Rev. B* **2007,** *76* (17), 174114.
23. Widenmeyer, M.; Checchia, S.; Xiao, X.; Scavini, M.; Weidenkaff, A. Effects of Nanodomains on Local and Long-Range Phase Transitions in Perovskite-Type $Eu_{0.8}Ca_{0.2}TiO_{3-\delta}$. *Nanomaterials* **2020,** *10* (4).
24. Billinge, S. J. L.; DiFrancesco, R. G.; Kwei, G. H.; Neumeier, J. J.; Thompson, J. D. Direct Observation of Lattice Polaron Formation in the Local Structure of $La_{1-x}Ca_xMnO_3$. *Phys. Rev. Lett.* **1996,** *77* (4), 715–718.
25. Li, B.; Louca, D.; Yano, S.; Marshall, L. G.; Zhou, J.; Goodenough, J. B. Insulating Pockets in Metallic $LaNiO_3$. *Adv. Electron. Mater.* **2016,** *2* (2), 1500261.
26. Yang, L.; Koch, R. J.; Zheng, H.; Mitchell, J. F.; Yin, W.; Tucker, M. G.; Billinge, S. J. L.; Bozin, E. S. Two-Orbital Degeneracy Lifted Local Precursor to a Metal-Insulator Transition in $MgTi_2O_4$. *Phys. Rev. B* **2020,** *102* (23), 235128.
27. Bozin, E. S.; Chatterji, T.; Billinge, S. J. L. Local Structure of ReO_3 at Ambient Pressure From Neutron Total-Scattering Study. *Phys. Rev. B* **2012,** *86* (9), 094110.
28. Bozin, E. S.; Zhong, R.; Knox, K. R.; Gu, G.; Hill, J. P.; Tranquada, J. M.; Billinge, S. J. L. Reconciliation of Local and Long-Range Tilt Correlations in Underdoped $La_{2-x}Ba_xCuO_4$ ($0 \leq x \leq 0.155$). *Phys. Rev. B* **2015,** *91* (5), 054521.
29. Chupas, P. J.; Chaudhuri, S.; Hanson, J. C.; Qiu, X.; Lee, P. L.; Shastri, S. D.; Billinge, S. J. L.; Grey, C. P. Probing Local and Long-Range Structure Simultaneously: An In Situ Study of the High-Temperature Phase Transition of α-AlF_3. *J. Am. Chem. Soc.* **2004,** *126* (15), 4756–4757.
30. Beecher, A. N.; Semonin, O. E.; Skelton, J. M.; Frost, J. M.; Terban, M. W.; Zhai, H.; Alatas, A.; Owen, J. S.; Walsh, A.; Billinge, S. J. L. Direct Observation of Dynamic Symmetry Breaking above Room Temperature in Methylammonium Lead Iodide Perovskite. *ACS Energy Lett.* **2016,** *1* (4), 880–887.
31. Tong, P.; Louca, D.; Lee, N.; Cheong, S.-W. Oxygen Displacements and Magnetoelectric coupling in $LuMnO_3$. *Phys. Rev. B* **2012,** *86* (9), 094419.
32. Gibbs, A. S.; Knight, K. S.; Lightfoot, P. High-temperature phase transitions of hexagonal $YMnO_3$. *Phys. Rev. B* **2011,** *83* (9), 094111.
33. Nénert, G.; Pollet, M.; Marinel, S.; Blake, G. R.; Meetsma, A.; Palstra, T. T. M. Experimental Evidence for An Intermediate Phase in the Multiferroic YMnO3. *J. Phys. Condens. Matter* **2007,** *19* (46), 466212.
34. Skjærvø, S. H.; Meier, Q. N.; Feygenson, M.; Spaldin, N. A.; Billinge, S. J. L.; Bozin, E. S.; Selbach, S. M. Unconventional Continuous Structural Disorder at the Order-Disorder Phase Transition in the Hexagonal Manganites. *Phys. Rev. X* **2019,** *9* (3), 031001.
35. Ren, Y.; Zuo, X. Synchrotron X-Ray and Neutron Diffraction, Total Scattering, and Small-Angle Scattering Techniques for Rechargeable Battery Research. *Small Methods* **2018,** *2* (8), 1800064.
36. Key, B.; Morcrette, M.; Tarascon, J.-M.; Grey, C. P. Pair Distribution Function Analysis and Solid State NMR Studies of Silicon Electrodes for Lithium Ion Batteries: Understanding the (De)Lithiation Mechanisms. *J. Am. Chem. Soc.* **2011,** *133* (3), 503–512.
37. Wiaderek, K. M.; Borkiewicz, O. J.; Pereira, N.; Ilavsky, J.; Amatucci, G. G.; Chupas, P. J.; Chapman, K. W. Mesoscale Effects in Electrochemical Conversion: Coupling of Chemistry to Atomic- and Nanoscale Structure in Iron-Based Electrodes. *J. Am. Chem. Soc.* **2014,** *136* (17), 6211–6214.
38. Dambournet, D.; Chapman, K. W.; Duttine, M.; Borkiewicz, O.; Chupas, P. J.; Groult, H. Lithium Insertion Mechanism in Iron-Based Oxyfluorides With Anionic Vacancies Probed by PDF Analysis. *ChemistryOpen* **2015,** *4* (4), 443–447.
39. Sottmann, J.; Di Michiel, M.; Fjellvåg, H.; Malavasi, L.; Margadonna, S.; Vajeeston, P.; Vaughan, G. B. M.; Wragg, D. S. Chemical Structures of Specific Sodium Ion Battery Components Determined by Operando Pair Distribution Function and X-ray Diffraction Computed Tomography. *Angew. Chem. Int. Ed.* **2017,** *56* (38), 11385–11389.
40. Butala, M. M.; Mayo, M.; Doan-Nguyen, V. V. T.; Lumley, M. A.; Göbel, C.; Wiaderek, K. M.; Borkiewicz, O. J.; Chapman, K. W.; Chupas, P. J.; Balasubramanian, M.; Laurita, G.; Britto, S.; Morris, A. J.; Grey, C. P.; Seshadri, R. Local Structure Evolution and Modes of Charge Storage in Secondary Li-FeS_2 Cells. *Chem. Mater.* **2017,** *29* (7), 3070–3082.
41. Petkov, V.; Prasai, B.; Shan, S.; Yang, R.; Wu, J.; Cronk, H.; Luo, J.; Zhong, C.-J. Structural Dynamics and Activity of Nanocatalysts inside Fuel Cells by in Operando Atomic Pair Distribution Studies. *Nanoscale* **2016,** *8* (20), 10749–10767.
42. Krogstad, M. J.; Rosenkranz, S.; Wozniak, J. M.; Jennings, G.; Ruff, J. P. C.; Vaughey, J. T.; Osborn, R. Reciprocal Space Imaging of Ionic Correlations in Intercalation Compounds. *Nat. Mater.* **2020,** *19* (1), 63–68.

43. Murray, C. B.; Norris, D. J.; Bawendi, M. G. Synthesis and Characterization of Nearly Monodisperse CdE (E = Sulfur, Selenium, Tellurium) Semiconductor Nanocrystallites. *J. Am. Chem. Soc.* **1993,** *115* (19), 8706–8715.
44. Alivisatos, A. P. Semiconductor Clusters, Nanocrystals, and Quantum Dots. *Science* **1996,** *271* (5251), 933–937.
45. Masadeh, A. S.; Bozin, E. S.; Farrow, C. L.; Paglia, G.; Juhás, P.; Karkamkar, A.; Kanatzidis, M. G.; Billinge, S. J. L. Quantitative Size-Dependent Structure and Strain Determination of CdSe Nanoparticles Using Atomic Pair Distribution Function Analysis. *Phys. Rev. B* **2007,** *76,* 115413.
46. Yang, X.; Masadeh, A. S.; McBride, J. R.; Bozin, E. S.; Rosenthal, S. J.; Billinge, S. J. L. Confirmation of Disordered Structure of Ultrasmall CdSe Nanoparticles From X-ray Atomic Pair Distribution Function Analysis. *Phys. Chem. Chem. Phys.* **2013,** *15* (22), 8480–8486.
47. Neder, R. B.; Korsunskiy, V. I. Structure of Nanoparticles From Powder Diffraction Data Using the Pair Distribution Function. *J. Phys. Condens. Matter* **2005,** *17* (5), S125–S134. Publisher: IOP Publishing.
48. Christiansen, T. L.; Cooper, S. R.; Jensen, K. M.Ø. There's no Place Like Real-Space: Elucidating Size-Dependent Atomic Structure of Nanomaterials Using Pair Distribution Function Analysis. *Nanoscale Adv.* **2020,** *2* (6), 2234–2254. Publisher: RSC.
49. Owen, J.; Brus, L. Chemical Synthesis and Luminescence Applications of Colloidal Semiconductor Quantum Dots. *J. Am. Chem. Soc.* **2017,** *139* (32), 10939–10943. Publisher: American Chemical Society.
50. Harrell, S. M.; McBride, J. R.; Rosenthal, S. J. Synthesis of Ultrasmall and Magic-Sized CdSe Nanocrystals. *Chem. Mater.* **2013,** *25* (8), 1199–1210. Publisher: American Chemical Society.
51. Juhás, P.; Farrow, C.; Yang, X.; Knox, K.; Billinge, S. Complex Modeling: A Strategy and Software Program for Combining Multiple Information Sources to Solve Ill Posed Structure and Nanostructure Inverse Problems. *Acta Crystallogr. A* **2015,** *71* (6), 562–568.
52. Proffen, T.; Neder, R. B. DISCUS: A Program for Diffuse Scattering and Defect-Structure Simulation. *J. Appl. Cryst.* **1997,** *30* (2), 171–175.
53. Page, K.; Hood, T. C.; Proffen, T.; Neder, R. B. Building and Refining Complete Nanoparticle Structures With Total Scattering Data. *J. Appl. Cryst.* **2011,** *44* (2), 327–336.
54. Poulain, A.; Sobczak, I.; Ziolek, M. Size of Au-Nanoparticles Supported on Mesostructural Cellular Foams Studied by the Pair Distribution Function Technique. *Cryst. Growth Des.* **2016,** *16* (10), 5985–5993.
55. Wu, J.; Shan, S.; Petkov, V.; Prasai, B.; Cronk, H.; Joseph, P.; Luo, J.; Zhong, C.-J. Composition–Structure–Activity Relationships for Palladium-Alloyed Nanocatalysts in Oxygen Reduction Reaction: An *Ex-Situ*/*In-Situ* High Energy X-Ray Diffraction Study. *ACS Catal.* **2015,** *5* (9), 5317–5327.
56. Fleury, B.; Cortes-Huerto, R.; Taché, O.; Testard, F.; Menguy, N.; Spalla, O. Gold Nanoparticle Internal Structure and Symmetry Probed by Unified Small-Angle X-Ray Scattering and X-Ray Diffraction Coupled With Molecular Dynamics Analysis. *Nano Lett.* **2015,** *15* (9), 6088–6094.
57. Kumara, C.; Zuo, X.; Ilavsky, J.; Chapman, K. W.; Cullen, D. A.; Dass, A. Super-Stable, Highly Monodisperse Plasmonic Faradaurate-500 Nanocrystals With 500 Gold Atoms: Au∼500(SR)∼120. *J. Am. Chem. Soc.* **2014,** *136* (20), 7410–7417.
58. Page, K.; Proffen, T.; Terrones, H.; Terrones, M.; Lee, L.; Yang, Y.; Stemmer, S.; Seshadri, R.; Cheetham, A. K. Direct Observation of the Structure of Gold Nanoparticles by Total Scattering Powder Neutron Diffraction. *Chem. Phys. Lett.* **2004,** *393* (4), 385–388.
59. Petkov, V.; Shastri, S. D. Element-Specific Structure of Materials With Intrinsic Disorder by High-Energy Resonant X-ray Diffraction And Differential Atomic Pair-Distribution Functions: A study of PtPd Nanosized Catalysts. *Phys. Rev. B* **2010,** *81* (16), 165428.
60. Banerjee, S.; Liu, C.-H.; Jensen, K. M.Ø.; Juhás, P.; Lee, J. D.; Tofanelli, M.; Ackerson, C. J.; Murray, C. B.; Billinge, S. J. L. Cluster-Mining: An Approach for Determining Core Structures of Metallic Nanoparticles from Atomic Pair Distribution Function Data. *Acta Crystallogr. A* **2020,** *76* (1), 24–31.
61. Petkov, V.; Shastri, S.; Kim, J.-W.; Shan, S.; Luo, J.; Wu, J.; Zhong, C.-J. Application of Differential Resonant High-Energy X-Ray Diffraction to Three-Dimensional Structure Studies of Nanosized Materials: A Case Study of Pt–Pd Nanoalloy Catalysts. *Acta Crystallogr. A* **2018,** *74* (5), 553–566.
62. Banerjee, S.; Liu, C.-H.; Lee, J. D.; Kovyakh, A.; Grasmik, V.; Prymak, O.; Koenigsmann, C.; Liu, H.; Wang, L.; Abeykoon, A. M. M.; Wong, S. S.; Epple, M.; Murray, C. B.; Billinge, S. J. L. Improved Models for Metallic Nanoparticle Cores From Atomic Pair Distribution Function (PDF) Analysis. *J. Phys. Chem. C* **2018,** *122* (51), 29498–29506. Publisher: American Chemical Society.
63. Yang, L.; Culbertson, E. A.; Thomas, N. K.; Vuong, H. T.; Kjær, E. T. S.; Jensen, K. M.Ø.; Tucker, M. G.; Billinge, S. J. L. A Cloud Platform for Atomic Pair Distribution Function Analysis: PDFitc. *Acta Crystallogr. A* **2021,** *77* (1), 2–6.
64. Jadzinsky, P. D.; Calero, G.; Ackerson, C. J.; Bushnell, D. A.; Kornberg, R. D. Structure of a Thiol Monolayer-Protected Gold Nanoparticle at 1.1 Å Resolution. *Science* **2007,** *318* (5849), 430–433.
65. Juhás, P.; Cherba, D. M.; Duxbury, P. M.; Punch, W. F.; Billinge, S. J. L. *Ab Initio* Determination of Solid-State Nanostructure. *Nature* **2006,** *440* (7084), 655–658.
66. Young, C. A.; Goodwin, A. L. Applications of Pair Distribution Function Methods to Contemporary Problems in Materials Chemistry. *J. Mater. Chem.* **2011,** *21* (18), 6464.
67. Beecher, A. N.; Yang, X.; Palmer, J. H.; LaGrassa, A. L.; Juhás, P.; Billinge, S. J. L.; Owen, J. S. Atomic Structures and Gram Scale Synthesis of Three Tetrahedral Quantum Dots. *J. Am. Chem. Soc.* **2014,** *136* (30), 10645–10653.
68. Miao, J.; Ercius, P.; Billinge, S. J. L. Atomic Electron Tomography: 3D Structures Without Crystals. *Science* **2016,** *353* (6306).
69. Castleman, A. W.; Khanna, S. N. Clusters, Superatoms, and Building Blocks of New Materials. *J. Phys. Chem. C* **2009,** *113* (7), 2664–2675.
70. Reber, A. C.; Khanna, S. N. Superatoms: Electronic and Geometric Effects on Reactivity. *Acc. Chem. Res.* **2017,** *50* (2), 255–263.
71. Champsaur, A. M.; Velian, A.; Paley, D. W.; Choi, B.; Roy, X.; Steigerwald, M. L.; Nuckolls, C. Building Diatomic and Triatomic Superatom Molecules. *Nano Lett.* **2016,** *16* (8), 5273–5277.
72. Wang, M.; Anghel, A. M.; Marsan, B.; Cevey Ha, N.-L.; Pootrakulchote, N.; Zakeeruddin, S. M.; Grätzel, M. CoS Supersedes Pt as Efficient Electrocatalyst for Triiodide Reduction in Dye-Sensitized Solar Cells. *J. Am. Chem. Soc.* **2009,** *131* (44), 15976–15977.
73. Sun, Y.; Liu, C.; Grauer, D. C.; Yano, J.; Long, J. R.; Yang, P.; Chang, C. J. Electrodeposited Cobalt-Sulfide Catalyst for Electrochemical and Photoelectrochemical Hydrogen Generation from Water. *J. Am. Chem. Soc.* **2013,** *135* (47), 17699–17702.
74. Wang, Q.; Jiao, L.; Han, Y.; Hongmei, D.; Peng, W.; Huan, Q.; Song, D.; Si, Y.; Wang, Y.; Yuan, H. CoS_2 Hollow Spheres: Fabrication and Their Application in Lithium-Ion Batteries. *J. Phys. Chem. C* **2011,** *115* (16), 8300–8304.
75. Aydt, A. P.; Qie, B.; Pinkard, A.; Yang, L.; Cheng, Q.; Billinge, S. J. L.; Yang, Y.; Roy, X. Microporous Battery Electrodes From Molecular Cluster Precursors. *ACS Appl. Mater. Interfaces* **2019,** *11* (12), 11292–11297.
76. Yang, L.; Juhás, P.; Terban, M. W.; Tucker, M. G.; Billinge, S. J. L. Structure-Mining: Screening Structure Models by Automated Fitting to the Atomic Pair Distribution Function over Large Numbers of Models. *Acta Crystallogr. A* **2020,** *76* (3), 395–409.
77. Arya, S.; Mahajan, P.; Gupta, R.; Srivastava, R.; Tailor, N. K.; Satapathi, S.; Radhakrishnan Sumathi, R.; Datt, R.; Gupta, V. A Comprehensive Review on Synthesis and Applications of Single Crystal Perovskite Halides. *Prog. Solid State Chem.* **2020,** *60,* 100286.
78. Chouhan, L.; Ghimire, S.; Subrahmanyam, C.; Miyasaka, T.; Biju, V. Synthesis, Optoelectronic Properties and Applications of Halide Perovskites. *Chem. Soc. Rev.* **2020,** *49* (10), 2869–2885.
79. Choi, J. J.; Yang, X.; Norman, Z. M.; Billinge, S. J. L.; Owen, J. S. Structure of Methylammonium Lead Iodide Within Mesoporous Titanium Dioxide: Active Material in High-Performance Perovskite Solar Cells. *Nano Lett.* **2014,** *14* (1), 127–133.
80. Brenner, T. M.; Egger, D. A.; Kronik, L.; Hodes, G.; Cahen, D. Hybrid Organic—Inorganic Perovskites: Low-Cost Semiconductors With Intriguing Charge-Transport Properties. *Nat. Rev. Mater.* **2016,** *1* (1), 1–16.
81. Kim, G.-W.; Petrozza, A. Defect Tolerance and Intolerance in Metal-Halide Perovskites. *Adv. Energy Mater.* **2020,** *10* (37), 2001959.
82. Ceratti, D. R.; Rakita, Y.; Cremonesi, L.; Tenne, R.; Kalchenko, V.; Elbaum, M.; Oron, D.; Potenza, M. A. C.; Hodes, G.; Cahen, D. Self-Healing Inside $APbBr_3$ Halide Perovskite Crystals. *Adv. Mater.* **2018,** *30* (10), 1706273.
83. Ciccioli, A.; Latini, A. Thermodynamics and the Intrinsic Stability of Lead Halide Perovskites $CH_3NH_3PbX_3$. *J. Phys. Chem. Lett.* **2018,** *9* (13), 3756–3765.

84. Rakita, Y.; Cohen, S. R.; Kedem, N. K.; Hodes, G.; Cahen, D. Mechanical Properties of $APbX_3$ (A = Cs or CH_3NH_3; X = I or Br) Perovskite Single Crystals. *MRS Commun.* **2015,** *5* (4), 623–629.
85. Rakita, Y.; Lubomirsky, I.; Cahen, D. When Defects Become 'Dynamic': Halide Perovskites: A New Window on Materials? *Mater. Horiz.* **2019,** *6* (7), 1297–1305.
86. Cohen, A. V.; Egger, D. A.; Rappe, A. M.; Kronik, L. Breakdown of the Static Picture of Defect Energetics in Halide Perovskites: The Case of the Br Vacancy in $CsPbBr_3$. *J. Phys. Chem. Lett.* **2019,** *10* (16), 4490–4498.
87. Worhatch, R. J.; Kim, H. J.; Swainson, I. P.; Yonkeu, A. L.; Billinge, S. J. L. Study of Local Structure in Selected Organic-Inorganic Perovskites in the $Pm\bar{3}m$ Phase. *Chem. Mater.* **2008,** *20* (4), 1272–1277.
88. Lee, J.-W.; Seo, S.; Nandi, P.; Jung, H. S.; Park, N.-G.; Shin, H. Dynamic Structural Property of Organic-Inorganic Metal Halide Perovskite. *iScience* **2021,** *24* (1), 101959.
89. Yaffe, O.; Guo, Y.; Tan, L. Z.; Egger, D. A.; Hull, T.; Stoumpos, C. C.; Zheng, F.; Heinz, T. F.; Kronik, L.; Kanatzidis, M. G.; Owen, J. S.; Rappe, A. M.; Pimenta, M. A.; Brus, L. E. Local Polar Fluctuations in Lead Halide Perovskite Crystals. *Phys. Rev. Lett.* **2017,** *118* (13), 136001.
90. Pérez-Osorio, M. A.; Milot, R. L.; Filip, M. R.; Patel, J. B.; Herz, L. M.; Johnston, M. B.; Giustino, F. Vibrational Properties of the Organic–Inorganic Halide Perovskite $CH_3NH_3PbI_3$ from Theory and Experiment: Factor Group Analysis, First-Principles Calculations, and Low-Temperature Infrared Spectra. *J. Phys. Chem. C* **2015,** *119* (46), 25703–25718.
91. Baikie, T.; Barrow, N. S.; Fang, Y.; Keenan, P. J.; Slater, P. R.; Piltz, R. O.; Gutmann, M.; Mhaisalkar, S. G.; White, T. J. A Combined Single Crystal Neutron/X-Ray Diffraction and Solid-State Nuclear Magnetic Resonance Study of the Hybrid Perovskites $CH_3NH_3PbX_3$ (X = I, Br and Cl). *J. Mater. Chem. A* **2015,** *3* (17).
92. Whitfield, P. S.; Herron, N.; Guise, W. E.; Page, K.; Cheng, Y. Q.; Milas, I.; Crawford, M. K. Structures, Phase Transitions and Tricritical Behavior of the Hybrid Perovskite Methyl Ammonium Lead Iodide. *Sci. Rep.* **2016,** *6* (1), 35685.
93. Bertolotti, F.; Protesescu, L.; Kovalenko, M. V.; Yakunin, S.; Cervellino, A.; Billinge, S. J. L.; Terban, M. W.; Pedersen, J. S.; Masciocchi, N.; Guagliardi, A. Coherent Nanotwins and Dynamic Disorder in Cesium Lead Halide Perovskite Nanocrystals. *ACS Nano* **2017,** *11* (4), 3819–3831.
94. Cheetham, A. K.; Bennett, T. D.; Coudert, F.-X.; Goodwin, A. L. Defects and Disorder in Metal Organic Frameworks. *Dalton Trans.* **2016,** *45,* 4113–4126.
95. Schneemann, A.; Bon, V.; Schwedler, I.; Senkovska, I.; Kaskel, S.; Fischer, R. A. Flexible Metal–Organic Frameworks. *Chem. Soc. Rev.* **2014,** *43,* 6062–6096.
96. Chapman, K. W.; Chupas, P. J.; Kepert, C. J. Selective Recovery of Dynamic Guest Structure, in a Nanoporous Prussian Blue through In Situ X-Ray Diffraction: A Differential Pair Distribution Function Analysis. *J. Am. Chem. Soc.* **2005,** *127* (32), 11232–11233.
97. Burtch, N. C.; Baxter, S. J.; Heinen, J.; Bird, A.; Schneemann, A.; Dubbeldam, D.; Wilkinson, A. P. Negative Thermal Expansion Design Strategies in a Diverse Series of Metal–Organic Frameworks. *Adv. Funct. Mater.* **2019,** *29* (28), 1904669.
98. Bennett, T. D.; Goodwin, A. L.; Dove, M. T.; Keen, D. A.; Tucker, M. G.; Barney, E. R.; Soper, A. K.; Bithell, E. G.; Tan, J.-C.; Cheetham, A. K. Structure and Properties of An amorphous Metal–Organic Framework. *Phys. Rev. Lett.* **2010,** *104* (11), 115503.
99. Keen, D. A.; Bennett, T. D. Structural Investigations of Amorphous Metal–Organic Frameworks Formed Via Different Routes. *Phys. Chem. Chem. Phys.* **2018,** *20,* 7857–7861.
100. Bennett, T. D.; Saines, P. J.; Keen, D. A.; Tan, J.-C.; Cheetham, A. K. Ball-Milling-Induced Amorphization of Zeolitic Imidazolate Frameworks (ZIFs) for the Irreversible Trapping of Iodine. *Chem. A Eur. J.* **2013,** *19* (22), 7049–7055.
101. Orellana-Tavra, C.; Baxter, E. F.; Tian, T.; Bennett, T. D.; Slater, N. K. H.; Cheetham, A. K.; Fairen-Jimenez, D. Amorphous Metal–Organic Frameworks for Drug Delivery. *Chem. Commun.* **2015,** *51,* 13878–13881.
102. Nguyen, A. I.; Van Allsburg, K. M.; Terban, M. W.; Bajdich, M.; Oktawiec, J.; Ziegler, M. S.; Dombrowski, J. P.; Lakshmi, K. V.; Drisdell, W. S.; Yano, J.; Billinge, S. J. L.; Tilley, T. D. Stabilization of Reactive Co_4O_4 Cubane Oxygen-Evolution Catalysts Within Porous Frameworks. *PNAS* **2019,** *116* (24), 11630–11639.
103. Gaillac, R.; Pullumbi, P.; Beyer, K. A.; Chapman, K. W.; Keen, D. A.; Bennett, T. D.; Coudert, F.-X. Liquid Metal–Organic Frameworks. *Nat. Mater.* **2017,** *16* (11), 1149–1154.
104. Longley, L.; Collins, S. M.; Li, S.; Smales, G. J.; Erucar, I.; Qiao, A.; Hou, J.; Doherty, C. M.; Thornton, A. W.; Hill, A. J.; Yu, X.; Terrill, N. J.; Smith, A. J.; Cohen, S. M.; Midgley, P. A.; Keen, D. A.; Telfer, S. G.; Bennett, T. D. Flux Melting of Metal–Organic Frameworks. *Chem. Sci.* **2019,** *10,* 3592–3601.
105. Liu, M.; McGillicuddy, R. D.; Vuong, H.; Tao, S.; Slavney, A. H.; Gonzalez, M. I.; Billinge, S. J. L.; Mason, J. A. Network-Forming Liquids From Metal–Bis(acetamide) Frameworks With Low Melting Temperatures. *J. Am. Chem. Soc.* **2021,** *143* (7), 2801–2811.
106. Terban, M. W.; Banerjee, D.; Ghose, S.; Medasani, B.; Shukla, A.; Legg, B. A.; Zhou, Y.; Zhu, Z.; Sushko, M. L.; De Yoreo, J. J.; Liu, J.; Thallapally, P. K.; Billinge, S. J. L. Early Stage Structural Development of Prototypical Zeolitic Imidazolate Framework (ZIF) in Solution. *Nanoscale* **2018,** *10,* 4291–4300.
107. Xu, H.; Sommer, S.; Broge, N. L. N.; Gao, J.; Brummerstedt, B. The Chemistry of Nucleation: In Situ Pair Distribution Function Analysis of Secondary Building Units During UiO-66 mof Formation. *Chem. Eur. J.* **2019,** *25* (8), 2051–2058.
108. Collings, I. E.; Tucker, M. G.; Keen, D. A.; Goodwin, A. L. Static Disorder and Local Structure in Zinc(II) Isonicotinate, a Quartzlike Metal–Organic Framework. *Z. Krist.* **2012,** *227,* 313–320.
109. Koschnick, C.; Stäglich, R.; Scholz, T.; Terban, M. W.; von Mankowski, A.; Savasci, G.; Binder, F.; Schökel, A.; Etter, M.; Nuss, J.; Siegel, R.; Germann, L. S.; Ochsenfeld, C.; Dinnebier, R. E.; Senker, J.; Lotsch, B. V. Understanding disorder and linker deficiency in porphyrinic zirconium-based metal–organic frameworks by resolving the Zr_8O_6 cluster conundrum in PCN-221. *Nat. Commun.* **2021,** *12,* 3099.
110. Platero-Prats, A. E.; Mavrandonakis, A.; Gallington, L. C.; Liu, Y.; Hupp, J. T.; Farha, O. K.; Cramer, C. J.; Chapman, K. W. Structural Transitions of the Metal–Oxide Nodes Within Metal–Organic Frameworks: On the Local Structures of NU-1000 and UiO-66. *J. Am. Chem. Soc.* **2016,** *138* (12), 4178–4185.
111. Platero-Prats, A. E.; League, A. B.; Bernales, V.; Ye, J.; Gallington, L. C.; Vjunov, A.; Schweitzer, N. M.; Li, Z.; Zheng, J.; Mehdi, B. L.; Stevens, A. J.; Dohnalkova, A.; Balasubramanian, M.; Farha, O. K.; Hupp, J. T.; Browning, N. D.; Fulton, J. L.; Camaioni, D. M.; Lercher, J. A.; Truhlar, D. G.; Gagliardi, L.; Cramer, C. J.; Chapman, K. W. Bridging Zirconia Nodes Within a Metal–Organic Framework via Catalytic Ni-Hydroxo Clusters to Form Heterobimetallic Nanowires. *J. Am. Chem. Soc.* **2017,** *139* (30), 10410–10418.
112. Islamoglu, T.; Chen, Z.; Wasson, M. C.; Buru, C. T.; Kirlikovali, K. O.; Afrin, U.; Mian, M. R.; Farha, O. K. Metal–Organic Frameworks Against Toxic Chemicals. *Chem. Rev.* **2020,** *120* (16).
113. Terban, M. W.; Ghose, S. K.; Plonka, A. M.; Troya, D.; Juhás, P.; Dinnebier, R. E.; Mahle, J. J.; Gordon, W. O.; Frenkel, A. I. Atomic Resolution Tracking of Nerve-Agent Simulant Decomposition and Host Metal–Organic Framework Response in Real Space. *Commun. Chem.* **2021,** *4* (2).
114. Warren, B. E. X-Ray Diffraction in Random Layer Lattices. *Phys. Rev.* **1941,** *59,* 693–698.
115. Playford, H. Y.; Whale, T. F.; Murray, B. J.; Tucker, M. G.; Salzmann, C. G. Analysis of Stacking Disorder in Ice I Using Pair Distribution Functions. *J. Appl. Cryst.* **2018,** *51* (4), 1211–1220.
116. Pütz, A. M.; Terban, M. W.; Bette, S.; Haase, F.; Dinnebier, R. E.; Lotsch, B. V. Total Scattering Reveals the Hidden Stacking Disorder in a 2D Covalent Organic Framework. *Chem. Sci.* **2020,** *11,* 12647–12654.
117. Bette, S.; Takayama, T.; Kitagawa, K.; Takano, R.; Takagi, H.; Dinnebier, R. E. Solution of the Heavily Stacking Faulted Crystal Structure of the Honeycomb Iridate $H_3LiIr_2O_3$. *Dalton Trans.* **2017,** *46,* 15216–15227.
118. Bette, S.; Takayama, T.; Duppel, V.; Poulain, A.; Takagi, H.; Dinnebier, R. E. Crystal Structure and Stacking Faults in the Layered Honeycomb, Delafossite-Type Materials $Ag_3LiIr_2O_6$ and $Ag_3LiRu_2O_6$. *Dalton Trans.* **2019,** *48,* 9250–9259.
119. Charles, D. S.; Feygenson, M.; Page, K.; Neuefeind, J.; Xu, W.; Tenga, X. Structural Water Engaged Disordered Vanadium Oxide Nanosheets for High Capacity Aqueous Potassium-Ion Storage. *Nat. Commun.* **2017,** *8,* 15520.
120. Schlomberg, H.; Kröger, J.; Savasci, G.; Terban, M. W.; Bette, S.; Moudrakovski, I.; Duppel, V.; Podjaski, F.; Siegel, R.; Senker, J.; Dinnebier, R. E.; Ochsenfeld, C.; Lotsch, B. V. Structural Insights Into Poly(heptazine imides): A Light-Storing Carbon Nitride Material for dark Photocatalysis. *Chem. Mater.* **2019,** *31,* 7478–7486.

121. Farrow, C. L.; Bediako, D. K.; Surendranath, Y.; Nocera, D. G.; Billinge, S. J. L. Intermediate-Range Structure of Self-Assembled Cobalt-Based Oxygen Evolving Catalysts. *J. Am. Chem. Soc.* **2013,** *135,* 6403–6406.
122. Terban, M. W.; Shi, C.; Silbernagel, R.; Clearfield, A.; Billinge, S. J. L. Local Environment of Terbium(III) Ions in Layered Nanocrystalline Zirconium(IV) Phosphonate–Phosphate Ion Exchange Materials. *Inorg. Chem.* **2017,** *56* (15), 8837–8846.
123. Funnell, N. P.; Wang, Q.; Connor, L.; Tucker, M. G.; O'Hare, D.; Goodwin, A. L. Structural Characterisation of a Layered Double Hydroxide Nanosheet. *Nanoscale* **2014,** *6,* 8032–8036.
124. Petkov, V.; Billinge, S. J. L.; Heising, J.; Kanatzidis, M. G. Application of Atomic Pair Distribution Function Analysis to Materials With Intrinsic Disorder. Three-dimensional Structure of Exfoliated-Restacked WS_2: Not Just a Random Turbostratic Assembly of Layers. *J. Am. Chem. Soc.* **2000,** *122,* 11571.
125. Shi, C.; Beidaghi, M.; Naguib, M.; Mashtalir, O.; Gogotsi, Y.; Billinge, S. J. L. Structure of Nanocrystalline Ti_3C_2 MXene Using Atomic Pair Distribution Function. *Phys. Rev. Lett.* **2014,** *112,* 125501.
126. Metz, P. C.; Koch, R.; Misture, S. T. Differential Evolution and Markov Chain Monte Carlo Analyses of Layer Disorder in Nanosheet Ensembles Using Total Scattering. *J. Appl. Cryst.* **2018,** *51,* 1437–1444.
127. Jensen, K. M.Ø.; Blichfeld, A. B.; Bauers, S. R.; Wood, S. R.; Dooryhée, E.; Johnson, D. C.; Iversen, B. B.; Billinge, S. J. L. Demonstration of Thin Film Pair Distribution Function Analysis (tfPDF) for the Study of Local Structure in Amorphous and Crystalline Thin Films. *IUCrJ* **2015,** *2* (5), 481–489.
128. Chupas, P. J.; Chapman, K. W.; Lee, P. L. Applications of an Amorphous Silicon-Based Area Detector for High-Resolution, High-Sensitivity and Fast Time-Resolved Pair Distribution Function Measurements. *J. Appl. Cryst.* **2007,** *40* (3), 463–470.
129. Terban, M. W.; Johnson, M.; Di Michiel, M.; Billinge, S. J. L. Detection and Characterization of Nanoparticles in Suspension at Low Concentrations Using the X-Ray Total Scattering Pair Distribution Function Technique. *Nanoscale* **2015,** *7* (12), 5480–5487.
130. Private communication.
131. Nakamura, N.; Terban, M. W.; Billinge, S. J. L.; Reeja-Jayan, B. Unlocking the Structure of Mixed Amorphous-Crystalline Ceramic Oxide Films Synthesized Under Low Temperature Electromagnetic Excitation. *J. Mater. Chem. A* **2017,** *5* (35), 18434–18441.
132. Hitt, J. L.; Li, Y. C.; Tao, S.; Yan, Z.; Gao, Y.; Billinge, S. J. L.; Mallouk, T. E.; et al. *Nat. Commun.* **2021,** *12* (1), 1114.
133. Dippel, A.-C.; Roelsgaard, M.; Boettger, U.; Schneller, T.; Gutowski, O.; Ruett, U. Local Atomic Structure of Thin and Ultrathin Films Via Rapid High-Energy X-Ray Total Scattering at Grazing Incidence. *IUCrJ* **2019,** *6* (2), 290–298.
134. Wood, S. R.; Woods, K. N.; Plassmeyer, P. N.; Marsh, D. A.; Johnson, D. W.; Page, C. J.; Jensen, K. M.Ø.; Johnson, D. C. Same Precursor, Two Different Products: Comparing the Structural Evolution of In–Ga–O "Gel-Derived" Powders and Solution-Cast Films Using Pair Distribution Function Analysis. *J. Am. Chem. Soc.* **2017,** *139* (15), 5607–5613. PMID: 28328207.
135. Roelsgaard, M.; Dippel, A.-C.; Borup, K. A.; Nielsen, I. G.; Broge, N. L. N.; Roh, J. T.; Gutowski, O.; Iversen, B. B. Time-Resolved Grazing-Incidence Pair Distribution Functions During Deposition by Radio-Frequency Magnetron Sputtering. *IUCrJ* **2019,** *6* (2), 299–304.
136. Dippel, A.-C.; Gutowski, O.; Klemeyer, L.; Boettger, U.; Berg, F.; Schneller, T.; Hardtdegen, A.; Aussen, S.; Hoffmann-Eifert, S.; Zimmermann, M. V. Evolution of Short-Range Order in Chemically and Physically Grown Thin Film Bilayer Structures for Electronic Applications. *Nanoscale* **2020,** *12* (24), 13103–13112.
137. Gong, Z.; Billinge, S. J. L. Atomic Pair Distribution Functions (PDFs) From Textured Polycrystalline Samples: Fundamentals. *arXiv* **2018**, 1805.10342 [cond-mat].
138. Warren, B. E.; Krutter, H.; Morningstar, O. Fourier Analysis of X-ray Patterns of Vitreous SiO_2 and B_2O_2. *J. Am. Ceram. Soc.* **1936,** *19* (1 – 12), 202–206.
139. Konnert, J. H.; Karle, J. The Computation of Radial Distribution Functions for Glassy Materials. *Acta Crystallogr., Sect. A: Cryst. Phys., Diffr., Theor. Gen. Crystallogr.* **1973,** *29* (6), 702–710.
140. Cohen, M. H.; Turnbull, D. Molecular Transport in Liquids and Glasses. *J. Chem. Phys.* **1959,** *31* (5), 1164–1169.
141. Egami, T. Structural Relaxation in Amorphous $Fe_{40}Ni_{40}P_{14}B6$ Studied by Energy Dispersive X-Ray Diffraction. *J. Mater. Sci.* **1978,** *13* (12), 2587–2599.
142. Srolovitz, D.; Egami, T.; Vitek, V. Radial Distribution Function and Structural Relaxation in Amorphous Solids. *Phys. Rev. B* **1981,** *24* (12), 6936–6944.
143. Dmowski, W.; Fan, C.; Morrison, M. L.; Liaw, P. K.; Egami, T. Structural Changes in Bulk Metallic Glass after Annealing Below the Glass-Transition Temperature. *Mater. Sci. Eng. A* **2007,** *471* (1), 125–129.
144. Kakinoki, J.; Komura, Y.; Ino, T. Electron Diffraction Study of Evaporated Carbon Films. *Acta Crystallogr.* **1960,** *13* (3), 171–179.
145. Milinda Abeykoon, A. M.; Malliakas, C. D.; Juhás, P.; Bozin, E. S.; Kanatzidis, M. G.; Billinge, S. J. L. Quantitative Nanostructure Characterization Using Atomic Pair Distribution Functions Obtained From Laboratory Electron Microscopes. *Z. Krist.* **2012,** *227* (5), 248–256.
146. Mu, X.; Di Wang, T. F.; Kübel, C. Radial Distribution Function Imaging by STEM Diffraction: Phase Mapping and Analysis of Heterogeneous Nanostructured Glasses. *Ultramicroscopy* **2016,** *168,* 1–6.
147. Liu, S. Y.; Cao, Q. P.; Mu, X.; Xu, T. D.; Wang, D.; Ståhl, K.; Wang, X. D.; Zhang, D. X.; Kübel, C.; Jiang, J. Z. Tracing Intermediate Phases During Crystallization in a Ni–Zr Metallic Glass. *Acta Mater.* **2020,** *186,* 396–404.
148. Xiaoke, M.; Mazilkin, A.; Sprau, C.; Colsmann, A.; Kübel, C. Mapping Structure and Morphology of Amorphous Organic Thin Films by 4D-STEM Pair Distribution Function Analysis. *Microscopy* **2019,** *68* (4), 301–309.
149. Rakita, Y.; Hart, J. L.; Pratim Das, P.; Nicolopoulos, S.; Shahrezaei, S.; Mathaudhu, S. N.; Taheri, M. L.; Billing, S. J. L. *Studying heterogeneities at the nanoscale with scanning nanostructure electron microscopy (SNEM). Preprint at,* 2021. https://arxiv.org/abs/2110.03589.
150. George, E. P.; Raabe, D.; Ritchie, R. O. High-Entropy Alloys. *Nat. Rev. Mater.* **2019,** *4* (8), 515–534.
151. De Yoreo, J. J.; Gilbert, P. U. P. A.; Sommerdijk, N. A. J. M.; Penn, R. L.; Whitelam, S.; Joester, D.; Zhang, H.; Rimer, J. D.; Navrotsky, A.; Banfield, J. F.; Wallace, A. F.; Michel, F. M.; Meldrum, F. C.; Cölfen, H.; Dove, P. M. Crystallization by Particle Attachment in Synthetic, Biogenic, and Geologic Environments. *Science* **2015,** *349* (6247).
152. Dhanaraj, G., Byrappa, K., Prasad, V., Dudley, M., Eds.; *Springer Handbook of Crystal Growth. Springer Handbooks*, Springer-Verlag: Berlin Heidelberg, 2010.
153. Indrea, E.; Peter, A.; Silipas, D. T.; Dreve, S.; Suciu, R.-C.; Rosu, M. C.; Danciu, V.; Cosoveanu, V. Structural Characterisation of Binary SiO_2/TiO_2 Nanoparticle Aerogels by X-Ray Scattering. *J. Phys. Conf. Ser.* **2009,** *182,* 012066.
154. Chupas, P. J.; Chapman, K. W.; Jennings, G.; Lee, P. L.; Grey, C. P. Watching Nanoparticles Grow: The Mechanism and Kinetics for the Formation of TiO_2-Supported Platinum Nanoparticles. *J. Am. Chem. Soc.* **2007,** *129* (45), 13822–13824.
155. Rekhtina, M.; Pozzo, A. D.; Stoian, D.; Armutlulu, A.; Donat, F.; Blanco, M. V.; Wang, Z.-J.; Willinger, M.-G.; Fedorov, A.; Abdala, P. M.; Müller, C. R. Effect of Molten Sodium Nitrate on the Decomposition Pathways of Hydrated Magnesium Hydroxycarbonate to Magnesium Oxide Probed by In Situ Total Scattering. *Nanoscale* **2020,** *12* (31), 16462–16473.
156. Jensen, K. M.Ø.; Christensen, M.; Juhás, P.; Tyrsted, C.; Bøjesen, E. D.; Lock, N.; Billinge, S. J. L.; Iversen, B. B. Revealing the Mechanisms Behind SnO_2 Nanoparticle Formation and Growth During Hydrothermal Synthesis: An In Situ Total Scattering Study. *J. Am. Chem. Soc.* **2012,** *134* (15), 6785–6792.
157. Tyrsted, C.; Jensen, K. M.Ø.; Bøjesen, E. D.; Lock, N.; Christensen, M.; Billinge, S. J. L.; Iversen, B. B. Understanding the Formation and Evolution of Ceria Nanoparticles Under Hydrothermal Conditions. *Angew. Chem. Int. Ed.* **2012,** *51* (36), 9030–9033.
158. Tyrsted, C.; Pauw, B. R.; Jensen, K. M.Ø.; Becker, J.; Christensen, M.; Iversen, B. B. Watching Nanoparticles Form: An In Situ (Small-/Wide-Angle X-ray Scattering/Total Scattering) Study of the Growth of Yttria-Stabilised Zirconia in Supercritical Fluids. *Chem. Eur. J.* **2012,** *18* (18)), 5759–5766.
159. Jensen, K. M.Ø.; Christensen, M.; Gunnlaugsson, H. P.; Lock, N.; Bpjesen, E. D.; Proffen, T.; Iversen, B. B. Defects in Hydrothermally Synthesized $LiFePO_4$ and $LiFei_{1-x}Mn_xPO_4$ Cathode Materials. *Chem. Mater.* **2013,** *25* (11), 2282–2290.
160. Jensen, K. M.Ø.; Tyrsted, C.; Bremholm, M.; Iversen, B. B. In Situ Studies of Solvothermal Synthesis of Energy Materials. *ChemSusChem* **2014,** *7* (6), 1594–1611.
161. Jensen, K. M.Ø.; Andersen, H. L.; Tyrsted, C.; Bøjesen, E. D.; Dippel, A. C.; Lock, N.; Billinge, S. J. L.; Iversen, B. B.; Christensen, M. Mechanisms for Iron Oxide Formation Under Hydrothermal Conditions: An In Situ Total Scattering Study. *ACS Nano* **2014,** *8* (10), 10704–10714.

162. Juelsholt, M.; Christiansen, T. L.; Jensen, K. M.Ø. Mechanisms for Tungsten Oxide Nanoparticle Formation in Solvothermal Synthesis: From Polyoxometalates to Crystalline Materials. *J. Phys. Chem. C* **2019,** *123* (8), 5110–5119.
163. Saha, D.; Jensen, K. M.Ø.; Tyrsted, C.; Bpjesen, E. D.; Mamakhel, A. H.; Dippel, A.-C.; Christensen, M.; Iversen, B. B. In Situ Total X-Ray Scattering Study of WO_3 Nanoparticle Formation Under Hydrothermal Conditions. *Angew. Chem. Int. Ed.* **2014,** *53* (14), 3667–3670.
164. Bøjesen, E. D.; Jensen, K. M.Ø.; Tyrsted, C.; Mamakhel, A.; Andersen, H. L.; Reardon, H.; Chevalier, J.; Dippel, A.-C.; Iversen, B. B. The Chemistry of $ZnWO_4$ Nanoparticle Formation. *Chem. Sci.* **2016,** *7* (10), 6394–6406.
165. Birgisson, S.; Saha, D.; Iversen, B. B. Formation Mechanisms of Nanocrystalline MnO_2 Polymorphs Under Hydrothermal Conditions. *Cryst. Growth Des.* **2018,** *18* (2), 827–838.
166. Tominaka, S.; Yamada, H.; Hiroi, S.; Kawaguchi, S. I.; Ohara, K. Lepidocrocite-Type Titanate Formation From Isostructural Prestructures under Hydrothermal Reactions: Observation by Synchrotron X-Ray Total Scattering Analyses. *ACS Omega* **2018,** *3* (8), 8874–8881.
167. Broge, N. L. N.; Pedersen, F. S.; Sommer, S.; Iversen, B. B. Formation Mechanism of Epitaxial Palladium-Platinum Core-Shell Nanocatalysts in a One-Step Supercritical Synthesis. *Adv. Funct. Mater.* **2019,** *29* (31), 1902214.
168. Yamada, H.; Tominaka, S.; Ohara, K.; Liu, Z.; Okubo, T.; Wakihara, T. Structural Evolution of Amorphous Precursors toward Crystalline Zeolites Visualized by an In Situ X-Ray Pair Distribution Function Approach. *J. Phys. Chem. C* **2019,** *123* (46), 28419–28426.
169. Potter, M. E.; Light, M. E.; Irving, D. J. M.; Oakley, A. E.; Chapman, S.; Chater, P.; Cutts, G.; Watts, A.; Wharmby, M.; Vandegehuchte, B. D.; Schreiber, M. W.; Raja, R. Exploring the Origins of Crystallisation Kinetics in Hierarchical Materials Using In Situ X-Ray Diffraction and Pair Distribution Function Analysis. *Phys. Chem. Chem. Phys.* **2020,** *22* (34), 18860–18867.
170. Grendal, O. G.; Nylund, I.-E.; Blichfeld, A. B.; Tominaka, S.; Ohara, K.; Selbach, S. M.; Grande, T.; Einarsrud, M.-A. Controlled Growth of $Sr_xBai_{1-x}Nb_2O_6$ Hopper- and Cube-Shaped Nanostructures by Hydrothermal Synthesis. *Chem.* **2020,** *26* (42), 9348–9355.
171. Sommer, S.; Bpjesen, E. D.; Reardon, H.; Iversen, B. B. Atomic Scale Design of Spinel $ZnAl_2O_4$ Nanocrystal Synthesis. *Cryst. Growth Des.* **2020,** *20* (3), 1789–1799.
172. Frandsen, B. A.; Yang, X.; Billinge, S. J. L. Magnetic Pair Distribution Function Analysis of Local Magnetic Correlations. *Acta Crystallogr. A* **2014,** *70* (1), 3–11.
173. Frandsen, B. A.; Billinge, S. J. L. Magnetic Structure Determination From the Magnetic Pair Distribution Function (mPDF): Ground State of MnO. *Acta Crystallogr. A* **2015,** *71* (3), 325–334.
174. Frandsen, B. A.; Bozin, E. S.; Aza, E.; Martínez, A. F.; Feygenson, M.; Page, K.; Lappas, A. Nanoscale Degeneracy Lifting in a Geometrically Frustrated Antiferromagnet. *Phys. Rev. B* **2020,** *101*, 024423.
175. Yang, X.; Juhas, P.; Farrow, C. L.; Billinge, S. J. L. *xPDFsuite: An end-to-end software solution for high throughput pair distribution function transformation, visualization and analysis,* 2015. *Preprint on.* https://arxiv.org/abs/1402.3163.
176. Himanen, L.; Geurts, A.; Foster, A. S.; Rinke, P. Data-Driven Materials Science: Status, Challenges, and Perspectives. *Adv. Sci.* **2019,** *6* (21), 1900808.
177. Liu, C.-H.; Tao, Y.; Hsu, D.; Du, Q.; Billinge, S. J. L. Using a Machine Learning Approach to Determine the Space Group of a Structure From the Atomic Pair Distribution Function. *Acta Crystallogr. A* **2019,** *75* (4), 633–643.
178. Kusne, A. G.; Yu, H.; Wu, C.; Zhang, H.; Hattrick-Simpers, J.; DeCost, B.; Sarker, S.; Oses, C.; Toher, C.; Curtarolo, S.; Davydov, A. V.; Agarwal, R.; Bendersky, L. A.; Li, M.; Mehta, A.; Takeuchi, I. On-the-Fly Closed-Loop Materials Discovery via Bayesian Active Learning. *Nat. Commun.* **2020,** *11* (1), 5966.
179. Rakita, Y.; O'Nolan, D.; McAuliffe, R. D.; Veith, G. M.; Chupas, P. J.; Billinge, S. J. L.; Chapman, K. W. Active Reaction Control of Cu Redox State Based on Real-Time Feedback From In Situ Synchrotron Measurements. *J. Am. Chem. Soc.* **2020,** *142* (44), 18758–18762.
180. Bluesky Project (n.d.). https://blueskyproject.io/.
181. Tao, S. *PDFstream: The Configs Analysis Toolbox for the Study on Pair Distribution Function (PDF).* https://github.com/xpdAcq/pdfstream, 2021.
182. Anon, Christopher Right. SHED. unpublished, 2021.
183. Nakamura, N.; Laisuo, S.; Bai, J.; Ghose, S.; Reeja-Jayan, B. In Situ Synchrotron Pair Distribution Function Analysis to Monitor Synthetic Pathways Under Electromagnetic Excitation. *J. Mater. Chem. A* **2020,** *8* (31), 15909–15918.
184. Xu, H.; Sommer, S.; Broge, N. L. N.; Gao, J.; Iversen, B. B. The Chemistry of Nucleation: In Situ Pair Distribution Function Analysis of Secondary Building Units During UiO-66 MOF Formation. *Chem.* **2019,** *25* (8), 2051–2058.
185. Morandeau, A. E.; White, C. E. In Situ X-ray Pair Distribution Function Analysis of Accelerated Carbonation of a Synthetic Calcium–Silicate–Hydrate Gel. *J. Mater. Chem. A* **2015,** *3* (16), 8597–8605.
186. Jacques, S. D. M.; Di Michiel, M.; Kimber, S. A. J.; Yang, X.; Cernik, R. J.; Beale, A. M.; Billinge, S. J. L. Pair Distribution Function Computed Tomography. *Nat. Commun.* **2013,** *4* (1), 2536.
187. Jensen, K. M.Ø.; Yang, X.; Laveda, J. V.; Zeier, W. G.; See, K. A.; Di Michiel, M.; Melot, B. C.; Corr, S. A.; Billinge, S. J. L. X-Ray Diffraction Computed Tomography for Structural Analysis of Electrode Materials in Batteries. *J. Electrochem. Soc.* **2015,** *162* (7), A1310.
188. De Yoreo, J. J. In-Situ Liquid Phase TEM Observations of Nucleation and Growth Processes. *Prog. Cryst. Growth Charact. Mater.* **2016,** *62* (2), 69–88.

10.10 In situ scattering studies of material formation during wet-chemical syntheses

Susanne L. Skjærvø[*], **Mikkel Juelsholt**[*], **and Kirsten M.Ø. Jensen,** Department of Chemistry, University of Copenhagen, Copenhagen, Denmark

© 2023 Elsevier Ltd. All rights reserved.

10.10.1	**Why do we need in situ studies?**	**248**
10.10.2	**Peering into the black box: Development of experimental setups for wet-chemical synthesis studies**	**249**
10.10.3	**Chemical insight from in situ powder diffraction studies**	**252**
10.10.3.1	Identifying complex reaction pathways	253
10.10.3.2	Understanding phase transformations: Kinetic analyses of material formation	253
10.10.3.3	Nanoparticle growth	255
10.10.3.4	Changes in crystal structure during material formation	257
10.10.3.5	Mapping of synthesis parameters	258
10.10.4	**Chemical insights from total scattering experiments**	**259**
10.10.4.1	PDF studies of particle nucleation	260
10.10.4.2	Challenges and limitations for in situ total scattering experiments	262
10.10.5	**Nanoparticle size and shape: Information from Small-Angle X-ray scattering**	**262**
10.10.6	**Combination of techniques: Spectroscopy and scattering**	**265**
10.10.7	**Summary and outlook**	**266**
References		**267**

Abstract

Time-resolved in situ X-ray and neutron scattering can provide unique insight into material formation processes. Here, the use of such experiments for studies of wet-chemical material synthesis is described. We focus especially on techniques that can provide atomic structural information, i.e., powder diffraction and total scattering, and also describe how the combination with other techniques (small angle scattering and X-ray spectroscopy) can be used. Through examples, we illustrate the different kinds of information that can be obtained. This includes knowledge of crystallization kinetics and activations energies, insight into particle and crystallite growth mechanisms, and structural understanding of nucleation processes.

10.10.1 Why do we need in situ studies?

Over the last decades, the field of inorganic material discovery and "materials by design" have rapidly grown. The development of new, advanced functional materials is at the heart of our current technological revolutions into e.g., green energy, and experimental and computational mapping of materials structure/property relations are now accelerating the discovery of materials for new applications. However, realization of these ideas requires that we as chemists can synthesize materials with desired structures and characteristics.[1] At this point, much of the development of material synthesis methods relies on "trial-and-error" experiments, where large parameter spaces are explored to optimize the synthesis of a given material. The shortcomings of this approach are obvious and make it difficult to advance the concepts developed in "materials by design." Instead, we must reach a stage, where synthesis methods can be rationally designed, and where the outcome of a synthesis can be predicted. This development relies on an understanding of the chemical mechanisms that control material nucleation and growth, i.e., the fundamental processes that dictate which atomic structure and nanostructure may form in a synthesis.[2,3]

In this context, time-resolved in situ studies can play a large role.[1,4] Using e.g., neutron or synchrotron X-ray radiation, it is possible to follow material synthesis from precursor species to the final product and obtain structural insight into the process to understand how materials form. In this article, we will use selected examples to illustrate how such experiments can be applied to investigate processes in material formation. We will focus mainly on diffraction methods for characterizing atomic structure in inorganic materials, i.e., powder diffraction experiments and total scattering experiments with Pair Distribution Function (PDF) analysis. We will furthermore discuss how the combination with other important in situ techniques, such as small angle scattering and X-ray spectroscopy can aid in understanding the fundamental chemical processes that take place during material formation.

[*]These authors contributed equally to the work.

The literature of in situ X-ray and neutron studies of inorganic material formation is vast, and several reviews have over the years been written on the subject.[5–9] Here, we will focus on the use of time-resolved in situ experiments for studies of wet-chemical syntheses, and we will use examples to illustrate the kind of information that can be obtained. The development of wet-chemical synthesis methods for e.g., nanoparticle preparation makes an excellent case for the application of time-resolved in situ studies. Wet-chemical methods can provide environmentally friendly and simple routes to e.g., small, uniform nanoparticles, and a range of different types of materials can be prepared. The presence of a solvent reduces the need for high reaction temperatures and other harsh reaction drivers, and a very large parameter space is available, which in many cases makes it possible to tune reactions to obtain products with given characteristics.[10–12] However, their formation mechanisms are in many cases unknown. The presence of a solvent introduces new and potentially complicated ways for reactants in a synthesis to reassemble into the product structure. This ultimately leads to challenges in understanding how reactions can be controlled and eventually designed to form the products desired. This is the key challenge that most time-resolved in situ studies aim to solve by following the entire pathway from precursors over various intermediate phases to the products.

When considering which types of wet-chemical synthesis methods have been studied with time-resolved in situ techniques, studies involving hydro- and solvothermal reactions historically account for a very large fraction. The reason for this is the inherently mysterious nature of these reactions, involving closed reaction vessels which are heated for a considerable amount of time, producing autogenous pressure inside, before the products can be revealed. Another commonly studied method is the sol-gel method where an amorphous gel is converted to the crystalline product.[13] Other wet-chemical methods such as precipitation syntheses involving unpressurized heating, mixing of aqueous chemicals, etc. are often somewhat easier to follow ex situ; with the use of transparent reaction vessels any visual changes to the reaction mixture can be easily seen, and the use of septa makes the withdrawal of aliquots during the reaction a simple procedure. However, in situ studies of such reactions can provide extensive knowledge into fundamental nucleation and growth processes.[14,15]

In this article, we first briefly describe some of the experimental setups that have been developed for X-ray and neutron scattering studies of material formation over the past 30 years, since the first in situ study of a solvothermal synthesis was done. We will then introduce how powder diffraction methods (using X-rays or neutrons) can be applied for studies of crystallite formation and growth, highlighting in particular identification of reaction routes through crystalline intermediates, studies of crystallite growth, and studies of reaction kinetics. We subsequently introduce the possibilities X-ray and neutron total scattering provide for in situ studies of material formation, giving new insight into nucleation processes, as structural information from e.g., nanoscale clusters and ionic complexes can be obtained. Finally, the combination with other techniques such as small angle scattering and X-ray spectroscopy methods is considered. We have generally tried to focus on how different types of information can be extracted from various experiments. Many review papers have been written on the development of in situ diffraction and scattering studies,[5–7,9,16–20] and we refer to them and the references therein for further reading.

10.10.2 Peering into the black box: Development of experimental setups for wet-chemical synthesis studies

The field of in situ studies owes much of its growth to the development of high flux neutron sources and, especially, 3rd generation synchrotron X-ray sources in the 1990s. One of the first in situ studies of an evolving wet-chemical reaction was published in 1990 by Polak et al.[21] Using neutrons, the hydrothermal syntheses of tobermorite, zeolite-A and sodalite were followed. Traditionally, hydrothermal synthesis is done in autoclaves, i.e., thick and sealed metal vessels, which are built to keep the autogenous pressure forming when heating the aqueous precursors inside. The setup by Polak et al. (listed among other setups since used in **Table 1**) included an aluminum autoclave, penetrable by neutrons, and the study was successful in determining a quite complex phase evolution over the course of a 20 h reaction with a time resolution of 5 min. By following Bragg peak intensities, it was possible to map how crystalline precursor species were consumed during the reaction while the product formed.

Two years later, the same group published the first in situ XRD study of a solvothermal reaction, investigating the hydrothermal formation of zeolites.[40] The setup involved a steel autoclave which is difficult to penetrate with X-rays, but due developments in producing high-intensity X-rays with synchrotrons at the time, an adequate diffracted X-ray signal could be detected. Importantly, the experiments were done using Energy-Dispersive (ED) X-ray diffraction experiments, where a white X-ray beam consisting of a wide range of energies is shined onto the sample. Scattering intensities are then measured as a function of photon energy at a fixed diffraction angle. This setup meant that a time-resolution of just a few seconds could be achieved, as seen for the synthesis of VPI-5 in **Fig. 1**. The energy-dispersive detection of X-rays simplified the design of the reactor (**Fig. 1**, right), as the diffracted signal could be detected within a much smaller angular range compared to angular-dispersive techniques. However, the solid-state detectors of the time had a fairly low energy-resolution, making it hard to distinguish closely spaced diffraction peaks.

After these pioneering experiments, studies of wet-chemical reactions using energy-dispersive X-ray diffraction quickly gained attention. Several large-volume reactors for solvothermal reactions were developed for ED-XRD,[42] as listed in **Table 1**. For example, the O'Hare group developed several innovative large-volume in situ reaction cells, such as the Oxford-Diamond In Situ Cell (ODISC) of 2012.[42] The cell could be assembled in three different configurations; for solid-state reactions at low and high temperature (up to 1200 °C) and hydrothermal reactions.

Generally, the combination of a large-volume in situ reaction cell with energy-dispersive X-ray diffraction offered a way of understanding the mechanisms at play inside the industrially important autoclave reaction vessels. The ED-XRD methods provides many opportunities for designing in situ cells, as only a narrow angular window for the outgoing beam is necessary. The high flux of

Table 1 Overview of selected in situ hydro−/solvothermal cells. Year of publication, measurement type it was optimized for, internal reaction volume, main pressure-holding materials, heating method, maximum working temperature, pressurization method and maximum working pressure for each specific cell.

First author	*Year*	*Meas. type*[a]	*Volume (mL)*	*Pressure vessel materials*	*Heating method*	*Max. temp. (°C)*	*Pressurization method*[b]	*Max. pres. (bar)*
Polak[15]	1990	AD-ND	15	Al	Furnace	195	Autogenous	10
He[16]	1992	ED-XRD		Steel	Oil/water bath	200	Autogenous	N/A
Norby[22]	1994	AD-XRD	<< 1	Capillary + glue	Resistance heater (plate)	N/A	Autogenous	N/A
Evans[23]	1995	TOF-ND	18	Steel	Circulating oil element	230	Autogenous	30
Norby[24]	1997	AD-XRD	<<1	Capillary + steel + Vespel ferrules	Hot air	260	Gas	60
Walton[25]	1999	TOF-ND	100	Ti-Zr	Resistance heater (blocks)	250	Autogenous	20
O'Neill[26]	2006	AD-ND	42 (flow)	Steel	Resistance heater (blocks)	300	Gas	100
Beale[17]	2006	AD-XRD	N/A	N/A	N/A	N/A	N/A	N/A
Jensen[27]	2007	AD-XRD	30	Steel + borosilicate windows	N/A	>100	Gas	>100
Nikitenko[28]	2008	AD-XRD	N/A	N/A	N/A	N/A	N/A	N/A
Bremholm[29,30]	2008	AD-XRD	<<1	Capillary + steel + graphite ferrules	Hot air	450	HPLC pump	300
Becker.[29,30]	2008	AD-XRD	<5 (flow)	Capillary + steel + graphite ferrules	Hot air	450	HPLC pump	300
Ok[31]	2010	TOF-ND AD-ND	185	Inconel 718	Resistance heater (cup)	450	Autogenous	400
Xia[32]	2010	AD-ND	320 (flow)	Ti-Zr	Tabular heaters insulated by ceramic blocks	300	Gas	85
Xia[33]	2010	AD-ND	320	Ti-Zr	Tabular heaters insulated by ceramic blocks	300	Gas	90
Moorhouse[34]	2012	ED-XRD	25	Steel	IR lamps	–	Autogenous	–
Xia[35]	2012	AD-ND	65 (flow)	Steel	Vacuum furnace	400	HPLC pump	460
Yoko[36]	2016	AD-XRD	<5 (flow)	Steel	Preheated aqueous precursors	>430	HPLC pump	>300
Skjærvø[37]	2017	AD-XRD	<<1	Capillary + steel + graphite ferrules	Hot air	>400	HPLC pump	>250
Heidenreich[38]	2017	AD-XRD	11	Aluminum + borosilicate	Resistive heater (mantle)	180	Autogenous	17
Fujita[39]	2017	AD-XRD	–	Capillary + steel + ferrules	Hot air	>400	HPLC pump	>300

The list is not exhaustive.

[a] *AD*, angle-dispersive; *ED*, energy-dispersive; *ND*, neutron diffraction; *TOF*, time-of-flight; *XRD*, X-ray diffraction.

[b] *HPLC*, high-pressure liquid chromatography.

a white X-ray beam is furthermore very useful for time-resolved in situ experiments. The large-cell reaction vessels used for such experiments are often very close in design to those used in standard laboratory work, meaning that results and knowledge from in situ experiments can quickly be compared to other syntheses as done in the lab. Using such experiments, important insights have been gained into e.g. the formation of zeolites[40,41,43,44] and other porous materials.[34,45,46] The formation of a range of important metal oxide materials has also been studied.[31,47–55]

The ED-XRD method comes with some inherent drawbacks. The Bragg peak widths are determined by the energy resolution of the detector applied and the dispersion in the fixed 2θ diffraction angle.[56] This highly limits the Q-space resolution available, and closely spaced reflections in the diffraction pattern cannot be distinguished. ED-XRD thus falls short for reactions with multiple, less crystalline or low-symmetry phases due to peak convolution. Today, Energy-dispersive XRD is quite rarely used, and beamlines offering the possibility are getting sparse,[57] and in situ X-ray diffraction experiments are generally done using angular resolved methods.

Compared to ED-XRD, angular resolved X-ray diffraction experiments puts more restraints on the design of reaction cells for in situ studies, as a wider opening angle for detection of the outgoing beam is required. The X-ray flux may furthermore be limited compared to ED-XRD, as the beam is monochromatized. However, angular dispersive diffraction allows data analysis with e.g., Rietveld or PDF methods, which is much more challenging for ED-XRD experiments. In the 1990s, quartz capillary reactors for angular-dispersive in situ studies of solvothermal reactions were introduced by Norby et al.[58,59] The design drew inspiration from plug flow reactors and an operando catalysis cell by Topsøe et al.[60] having a small reaction volume which could easily transmit X-rays, enabling angular-dispersive X-ray diffraction of a high time-resolution. A sketch of the capillary cell, involving external pressurization by gas and heating with a hot-air blower, is shown in Fig. 2. The cell offered wide temperature and pressure ranges, and several

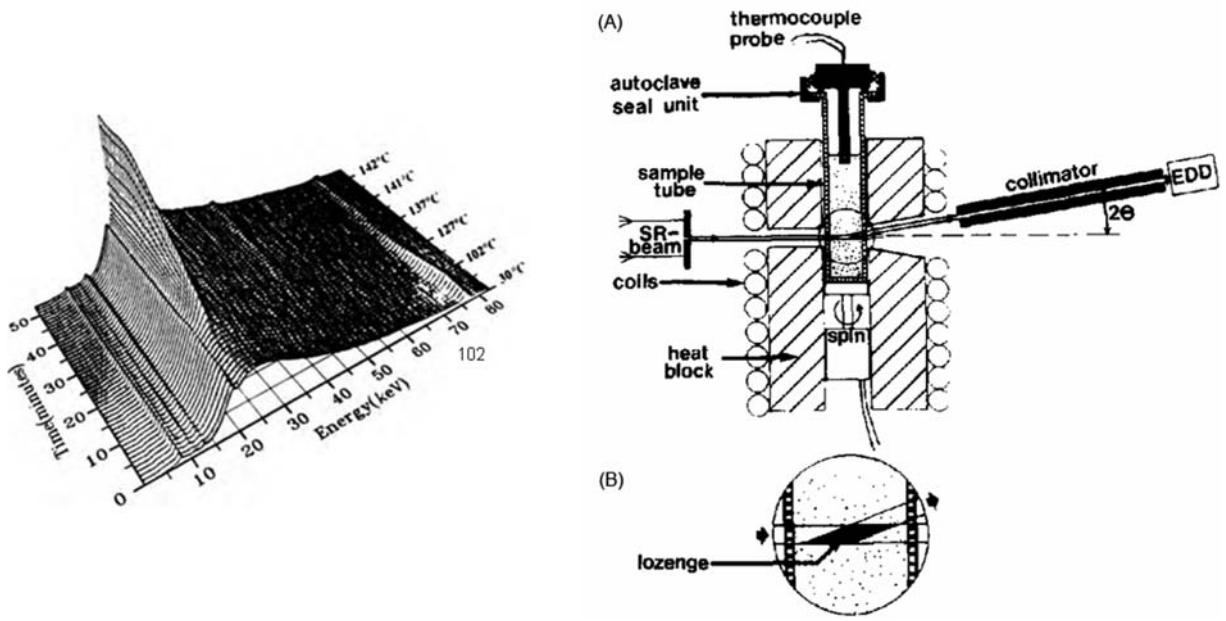

Fig. 1 Left: ED-XRD data obtained during the early stages of the hydrothermal synthesis of VPI-5. Right: The experimental setup, a steel autoclave with a small incoming and outgoing window, allowing ED-XRD data to be obtained.[41] Reprinted from He, H.; Barnes, P.; Munn, J.; Turrillas, X.; Klinowski, J: Autoclave Synthesis and Thermal Transformations of the Aluminophosphate Molecular Sieve VPI-5: An In Situ X-Ray Diffraction Study. *Chem. Phys. Lett.* **1992**, *196* (3–4), 267–273, with permission from Elsevier.

types of syntheses were studied with this setup, including hydrothermal synthesis of zeolites,[22,61] aluminophosphates[24,62] and reactions in the MgO-$MgCl_2$-H_2O systems.[63,64]

Since then, capillary cells and angular dispersive X-ray diffraction experiments have been widely used and developed by several other research groups.[65–67] Such cells can be applied for studies of a range of different reactions, as well as for different characterization methods from scattering to spectroscopy, where high quality data can be obtained. For example, Becker et al. presented the first in situ small-volume reaction cell which could be applied for hydrothermal synthesis under supercritical conditions.[29] By closing the capillary in both ends using graphite ferrules and stabilizing it with a steel frame, pressures up to 300 bar could be obtained using a high-pressure liquid chromatography (HPLC) pump. Heating was achieved by hot air, and the design principles were further used for making small-volume flow reactors. The setup and versions of it was used to study the formation of various functional oxides in sub- and supercritical water.[30,37,68–82] Other groups have developed similar reaction cells for the study of hydrothermal and solvothermal reactions,[23,25–28,32,33,36,39,83–85] with a sketch given in **Fig. 3**. Many different capillary materials have been applied, including single-crystal sapphire,[35] quartz,[38] as well as thin steel tubes.[86,87] Generally, the material chosen should be able to withstand synthesis temperature and pressure, as well as the chemical conditions present during the solvothermal process. Heating can be done using e.g., a jet of hot air, [29] resistive heating,[88,89] microwave heating,[90,91] or other methods.[35,38,86,87]

While small capillary type reaction cells allows collection of time-resolved, high quality X-ray data for e.g., Rietveld refinement, whole powder pattern analysis or PDF analysis, the experimental conditions in the small cell cannot always be directly compared to laboratory (or industrial) scale synthesis. However, if applying high energy X-rays (>50 keV), reaction cells closer in design to those used for laboratory scale synthesis can be used. In the case of high energy X-rays, a Q-range sufficient for e.g., Rietveld refinement can be covered with a quite narrow angular opening, giving more opportunities for cell design. Such large-volumes cells have been used e.g. for hydrothermal and supercritical synthesis of different oxide materials[54,92] including AlOOH,[93] Fe_3O_4[94] and TiO_2[95], as well as for MOF formation.[96,97]

Several setups for in situ neutron diffraction have also been developed since the first experiments in the 1990s. Compared to X-rays, neutrons interact weakly with matter. This makes them suited for experiments applying special sample environments such as autoclaves, as it allows for the use of e.g., thicker reactor walls.[98–104] The interaction between neutrons and matter furthermore gives interesting opportunities for setup design. An example is the ISIS/Oxford cell,[99] which was constructed using a Zr/Ti alloy whose composition results in an average neutron scattering length of zero. When using such a cell, the only diffraction signal thus originates from the sample itself. This cell has been used, for example, for the synthesis of $BaTiO_3$[105] and zeolites,[106] and can be applied for both neutron time-of-flight experiments, or monochromatic neutron diffraction experiments. The Zr/Ti alloy cannot withstand harsh reaction conditions, and the so-called CAU-Oxford-ISIS cell was therefore developed from Inconel steel.[101] This cell has been used to study synthesis in supercritical water under batch conditions.[31] The use of time-of-flight neutron experiments made it possible to design the cell such that only a small window for the outgoing beam was needed.

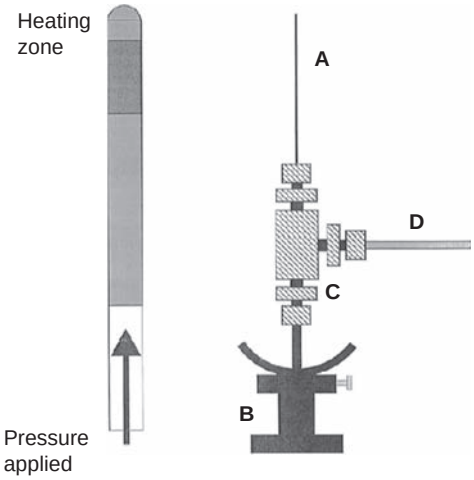

Fig. 2 The Norby-cell,[59] consisting of a quartz glass capillary mounted on a goniometer head with a Swagelok T-piece through Vespel® ferrules. Pressure could be externally applied through the connected tubing. Reprinted with permission from Norby, P. Hydrothermal Conversion of Zeolites: An in Situ Synchrotron X-ray Powder Diffraction Study. *J. Am. Chem: Soc.* **1997**, *119*, 5215–5221. Copyright (2021) American Chemical Society.

Table 1 gives an overview of some of the reactor setups for in situ studies developed over the past 30 years for wet-chemical synthesis (and in particular solvothermal synthesis) of materials. The type of setup required, as well as its complexity, is obviously very dependent on the reaction of interest, and on the experimental method to be used. While in situ studies of solvothermal and hydrothermal synthesis require setups that can widthstand either autogenous or applied solvent pressure, material formation in solvents below the boiling point can sometimes be done with simpler setups, e.g., in closed or open capillaries. High time resolution can be obtained with e.g., flow-cells taking advantage of steady-state reactions.[107–110] Microfluidic setups are now being more and more widely used for studies of soft matter,[111] and may also appear more commonly in materials chemistry in the future.[112]

The development of reaction cells is often driven by research groups with an interest in specific reactions and synthesis methods, but more and more synchrotron beamlines and neutron instruments are now also developing user-available sample environments for such studies. With this development, in situ studies of chemical reactions are likely to become much more widely applied in the future.

10.10.3 Chemical insight from in situ powder diffraction studies

Powder diffraction, using either neutrons (PND) or X-rays (PXRD), give insight into the atomic structure of crystalline materials. In situ studies with PXRD or PND can thus provide information on e.g., the appearance of crystalline intermediates, allowing to map complex reaction pathways, and identify any structural changes that may take place during material formation, relating to, for

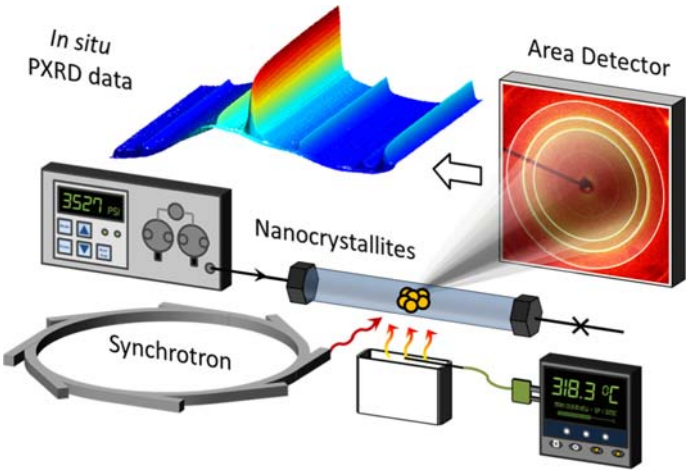

Fig. 3 A capillary cell used for in situ angular resolved X-ray diffraction of sub- and supercritical solvothermal synthesis.[32] The capillary is pressurized using a HPLC pump and heated with a jet of hot air. Reprinted with permission from Andersen, H. L.; Christensen, M. In Situ Powder X-Ray Diffraction Study of Magnetic $CoFe_2O_4$ Nanocrystallite Synthesis. *Nanoscale* **2015**, *7* (8), 3481–3490.

example, defects in the crystal structure. The Bragg peak widths reflect the crystallite size, and in situ diffraction experiments can therefore also provide insight into crystallite growth during a material formation. Dependent on both the data quality and the experimental method, information can be extracted from e.g., Rietveld refinement or Whole Powder Pattern Modelling.[9] The following sections give examples of in situ powder diffraction experiments, showing the types of knowledge that can be obtained on formation pathways, reaction kinetics and crystallite growth.

10.10.3.1 Identifying complex reaction pathways

The key strength of powder diffraction is the ability to identify and analyze the structure of crystalline phases, and when performed in situ it can thus uncover even the most complex reaction schemes involving several intermediate crystalline phases.[33,50,99,113–119] For instance, using a small-volume capillary cell and angular synchrotron powder X-ray diffraction, Skjærvø et al. studied the hydrothermal synthesis of $NaNbO_3$ from a Nb_2O_5 precursor in a NaOH solution.[84] The in situ data (**Fig. 4**) showed that even a well-known oxide like $NaNbO_3$ forms hydrothermally via a reaction path involving at least four crystalline intermediate phases. The data were obtained with an unprecedented time-resolution of 0.1 s/frame, recording a total of seven phases in less than 5 s, which were found to vary for different temperatures and NaOH concentrations. Only two of the intermediate phases had been previously identified through ex situ studies, indicating that the remaining intermediate phases might not be stable at ambient conditions and therefore not possible to identify ex situ. Using Rietveld refinement and analysis of peak width, the in situ data also allowed following the crystallite size of both the crystalline intermediate $Na_2Nb_2O_6 \cdot H_2O$ and the final $NaNbO_3$ nanoparticles, showing how the size of the intermediate crystallites decreased as $NaNbO_3$ nanoparticles grew.

Reactions in molten salt have also been shown through in situ powder diffraction to give complex reaction schemes with several intermediate phases.[120] By using the large-volume ODISC cell, Moorhouse et al. showed how the $n = 4$ Aurivillius phase $Bi_5Ti_3Fe_{0.5}Cr_{0.5}O_{15}$ forms in molten Na_2SO_4 at 950 °C.[92] As seen in **Fig. 5**, several metastable intermediate phases preceded the formation of the product, giving the following phase progression: α-Bi_2O_3 → δ-Bi_2O_3, $Bi_{12}TiO_{20}$ → $Bi_4Ti_3O_{12}$ → $Bi_5Ti_3Fe_{0.5}Cr_{0.5}O_{15}$. In this study, both angular-resolved and energy resolved X-ray diffraction was used, where the angular-resolved data proved most useful for Rietveld refinement.

10.10.3.2 Understanding phase transformations: Kinetic analyses of material formation

In addition to revealing the phases that are present, in situ studies can also provide important information about *how* these phases transform from one to the other. Understanding whether nucleation is homogeneous or heterogeneous (or something else), and how crystallite growth processes occur is important for targeting specific products, but in the absence of in situ studies, literature has often assumed the simplest mechanisms. This can for instance be a direct precipitation from a dissolved precursor, but as seen from the complex reaction pathways described in the previous section, this may not be true. Ex situ studies have provided many valuable insights, but as intermediate phases may not always be stable at ambient conditions, they are not always able to reveal the true reaction mechanism.

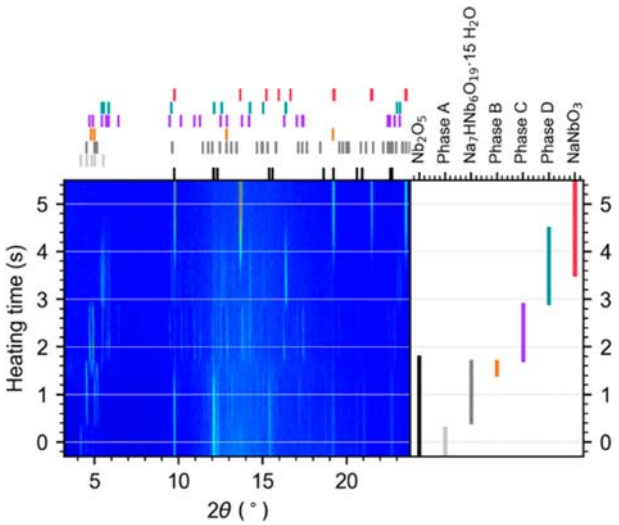

Fig. 4 2D contour plot of the reaction scheme in the Na—Nb—O system during hydrothermal synthesis from Nb_2O_5 powder in 9 M NaOH, including a schematic showing the phase development. Supercritical conditions (423 °C and 250 bar) were approached through rapid heating.[84] Reprinted with permission from Skjærvø, S. L.; Wells, K. H.; Sommer, S.; Vu, T.-D.; Tolchard, J. R.; van Beek, W.; Grande, T.; Iversen, B. B.; Einarsrud, M.-A.: Rationalization of Hydrothermal Synthesis of $NaNbO_3$ by Rapid in Situ Time-Resolved Synchrotron X-ray Diffraction. *Crystal Growth & Design* **2018**, *18* (2), 770–774. Copyright (2021) American Chemical Society.

Using crystallization curves obtained from in situ powder diffraction data, different kinetic models can be used to analyze crystallization pathways and extract semi-quantitative information. This includes analysis using the Johnson-Mehl-Avrami model; originally developed for solid state transformations but now widely used for wet-chemical methods as well.[5,9] In this approach, the extent of reaction is described through the Avrami–Erofe'ev expression, $\alpha(t) = 1 - \exp(-[k_g(t - t_0)]^m)$. Here, k_g is a rate constant for crystal growth, t_0 the induction time for crystallization, and m the Avrami constant. The rate of crystallization of a certain phase can be determined by following the extent of crystallization as function of time. This can done by considering the time-dependent behaviors of the scale factor refined in Rietveld analysis,[121] or by simply following the evolution of normalized integrated intensity of specific Bragg peaks.[119] The Avrami constant can make it possible to distinguish between different types of reactions, e.g., diffusion controlled; phase boundary controlled, or controlled through nucleation and growth. If experiments are done at different temperatures, the temperature-dependent rate constants k can be used to determine activation energies using the Arrhenius equation. The Avrami-Erofe'ev approach has been used for in situ studies of e.g., solvothermal reactions.[91,116,117,122–126] Such analyses can, for example, be used to determine how changes in parameters, e.g., temperature, pH, or addition of additives, changes the mechanisms for crystallization.[127,128]

The Avrami-Erofe'ev expression was originally developed for solid state synthesis, and it thus has some limitations for the studies of wet-chemical reactions. For example, the Avrami-Erofe'ev models do not separate nucleation and growth regimes. In studies of zeolite crystallization, Gualtieri therefore proposed an extended model, where crystallization curves were modelled as:[61]

$$\alpha(t) = \frac{1}{1 + \exp\left(-\frac{t-a}{b}\right)}\left[1 - \exp\left(-k_g t\right)^n\right]$$

Here, α is again the extent of crystallization, and t is time. The constants a and b relate to the nucleation rate, while k_g is the rate constant for crystal growth. The parameter n relates to the dimension of crystal growth and can be used to extract information on anisotropic growth. This approach has been applied for obtaining activation energies for both nucleation and growth for a range of materials.[129–134]

Yeung et al. used kinetic models to gain insight into the formation of metal-organic-frameworks, MOFs. During the solvothermal synthesis of MOFs, different product phases can crystallize from similar reaction mixtures, and in order to understand why, Yeung et al. studied the solvothermal formation of lithium *meso*-tartrate MOFs in water/ethanol mixtures with in situ PXRD.[97] The experiments were done using angular resolved X-ray diffraction employing high energy, monochromatic X-rays and a large-volume reactor, mimicking real-laboratory conditions. From the in situ PXRD data obtained, it was possible to identify the interconversion between three different *meso*-tartrate phases; the kinetic phases $Li_2(meso\text{-}C_6H_4O_6)(H_2O)_{0.5}$ (phase 1); $Li_2(meso\text{-}C_6H_4O_6)$ (phase 2a) and the thermodynamically stable $Li_2(meso\text{-}C_6H_4O_6)$ (phase 2b). Using the in situ X-ray diffraction data, the authors used kinetic models to determine rate constants and activation energies for the different reaction steps. The authors used the Avrami-Erofe'ev and Gualtieri expressions to determine nucleation rate constants and crystal growth rate constants. They determined, for example, that the growth of phase 2a was surface reaction limited, rather than diffusion limited. When analyzing the formation of phase 2b from 2a, the authors found that neither the conventional Avrami-Erofe'ev or Gualtieri models fitted well to the crystallization curve. They

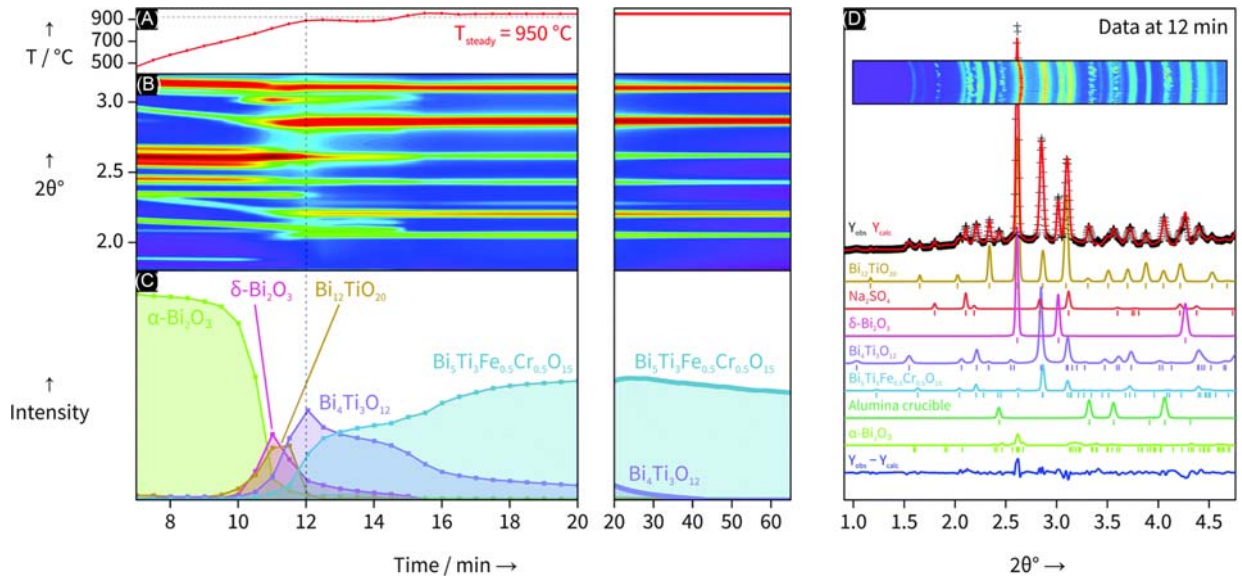

Fig. 5 Overview of the formation of $Bi_5Ti_3Fe_{0.5}Cr_{0.5}O_{15}$ in molten Na_2SO_4 at 950 °C, showing (A) reaction temperature, (B) PXRD heat-map and (C) areas under different phase patterns. The dotted line shows the position of the example refinement at 12 min which is decomposed into the present phases in (D).[92] Reprinted with permission from Moorhouse, S. J.; Wu, Y.; Buckley, H. C.; O'Hare, D. Time-Resolved In Situ Powder X-ray Diffraction Reveals the Mechanisms of Molten Salt Synthesis. *Chem. Commun.* **2016**, *52*, 13865–13865.

therefore proposed a modified Gualtieri model, allowing a cross-over between the nucleation and growth regimes in the reaction. This modification allows kinetic studies of successive transformations, as seen in many in situ studies. Using these models, the authors were thus able to extract rate constants and activation energies for all reaction steps and map the energy landscape of the reaction as illustrated in Fig. 6. Even though phase 2b was the thermodynamically stable product, Yeung et al. showed that a higher temperature is needed to form this product instead of 2a due to the need for overcoming a substantially higher activation energy. The different reaction rates could be explained by the structural relationships between the products and the reactants, as larger changes in conformation result in higher activation energies.

In some syntheses, a crystalline phase will be present in the synthesis mixture before heating, or a crystalline intermediate may form.[70,71,117,123,135,136] In such cases, the transformation mechanism to the final crystal structure can be investigated using similar models as presented above. The presence of intermediates can also have a large influence on the morphology of the resulting final product. In a study by Mi et al. it was investigated how the occurrence of intermediate phases in the formation of $Bi_{2-x}Sb_xTe_3$ can direct the growth and thus affect the resulting product morphology.[137] Using a small capillary cell and angular resolved studies, the synthesis of these ternary materials was studied using in situ PXRD. With precursors of $BiCl_3$, $SbCl_3$ and $K_2TeO_3 \cdot 3H_2O$ dissolved in water with addition of a reducing agent and a complexing agent, the authors observed how the reaction pathway was highly dependent on the material composition. While Bi_2Te_3 formed directly from solution without the presence of any intermediate structures, the authors found that an increasing amount of Sb would increase the activation energy (determined through Avrami-Erofe'ev analysis), resulting in a slower reaction. With Sb present, an intermediate phase of elemental Te nanorods therefore formed. The authors treated the PXRD data with Rietveld refinement, making it possible to extract a wealth of structural information. Importantly, the morphology of the crystallites was analyzed through modelling of the anisotropic broadening of Bragg peaks. This analysis showed that the intermediate Te phase directed the morphology of the final $BiSbTe_3$ product, forming strings of nanoplatelets instead of the free nanoplatelets which would form in absence of Sb (Fig. 7).

Song et al. studied the formation of a related material; $Bi_2Se_xTe_{3-x}$ hexagonal nanoplatelets, which was found to occur through oriented attachment.[66] By using a small-volume reaction cell they were able to follow the solvothermal formation from solid precursors in ethylene glycol, allowing investigations of crystallization curves, lattice parameters, and crystal size evolution under a variety of synthesis conditions. Kinetic analysis of the growth curves detected three formation steps; precursor dissolution followed by $Bi_2Se_xTe_{3-x}$ nucleation, rapid growth through oriented attachment and finally a slow epitaxial growth, as seen from Fig. 8. For binary compositions ($x = 0$ or 3) in particular, the fast oriented attachment growth was pronounced, while this step was inhibited for ternary compositions, leading to a less efficient growth. They found that the reason the ternary compositions could form partially through oriented attachment despite the lattice mismatch was the adjustment possibilities facilitated by the van der Waals gap between covalently bonded quintuple layers. Again, the combination of detailed Rietveld refinement of synchrotron X-ray data with kinetic modelling allowed extensive quantitative information to be extracted.

10.10.3.3 Nanoparticle growth

Bragg peak broadening relates to crystallite growth, and growth curves can readily be obtained from in situ powder diffraction data through analysis of peak widths though e.g., Rietveld refinement. This has been widely used in in situ studies in nanomaterial formation, where the influence of synthesis parameters on crystallite growth thus easily can be evaluated.[30,68,71,73,75,82,88,93,135,138–141] As

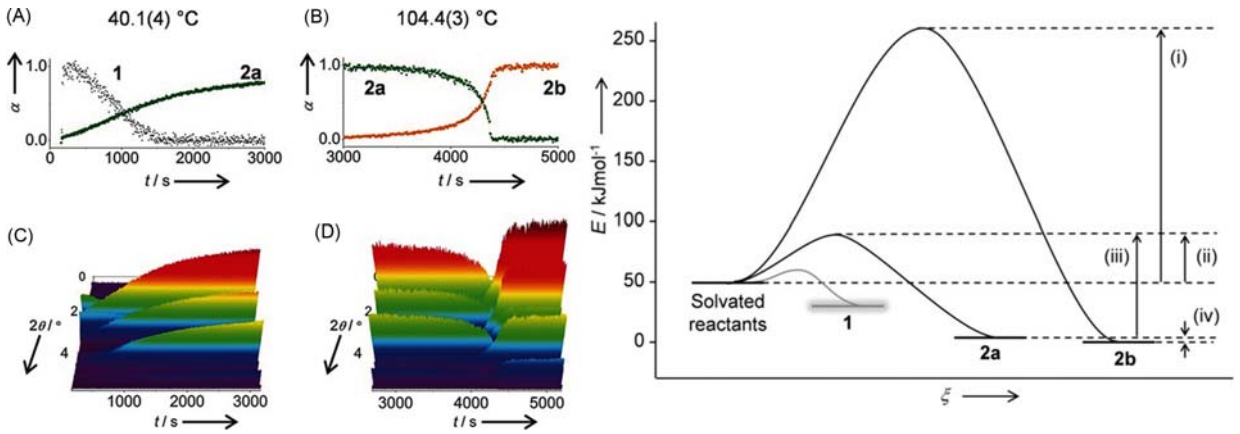

Fig. 6 Left: Conversions between lithium tartrate MOFs, shown through the extent of crystallization as a function of reaction time (A and B). XRD data are shown in (C and D). The hydrated phase 1 (grey points) is converted into the metastable 2a (green points), followed by conversion of 2a into the thermodynamic product 2b (orange points). Right: Relative reaction energy profile plotting energy (E) against reaction progress (ξ) for the formation of lithium meso-tartrate MOFs.[97] Reprinted with permission from Yeung, H. H. M.; Wu, Y.; Henke, S.; Cheetham, A. K.; O'Hare, D.; Walton, R. I.: In Situ Observation Of Successive Crystallizations and Metastable Intermediates in the Formation of Metal-Organic Frameworks. *Angew. Chem. Int. Ed.* **2016**, *55* (6), 2012–2016.

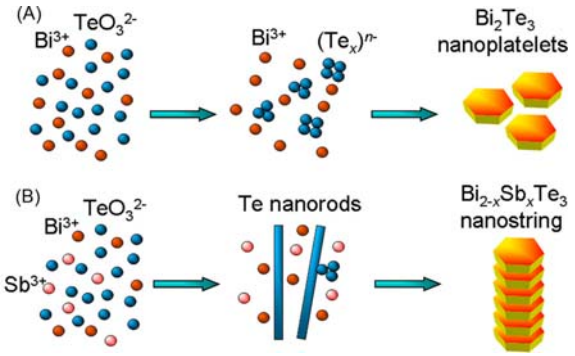

Fig. 7 Schematic illustration of the formation mechanisms of Bi_{2-x} Sb_x Te_3 (A) with or (B) without the intermediate formation of elemental Te nanorods.[137] Reprinted with permission from Mi, J.-L.; Nørby, P.; Bremholm, M.; Iversen, B. B.: Insight Into Nucleation and Growth of Bi_2–x$SbxTe_3$ (x = 0–2) Nanoplatelets in Hydrothermal Synthesis. *Chem. Mater.* **2017**, *29* (12), 5070–5079. Copyright (2021) American Chemical Society.

illustrated for the example of $Bi_{2-x}Sb_xTe_3$ above, analysis of the *hkl*-dependent broadening can furthermore reveal anisotropic crystallite sizes, and provide information on growth mechanisms.[30,68,72,126,142] Equally, dissolution or amorphization of crystalline nanoparticles or domains can also be followed from width analysis.[72,84]

In most Rietveld analyses, the peak profile is fitted using analytical functions. However, it is also possible to obtain a more physical analysis of strain and size effects through "whole powder pattern modelling" (WPPM), where peak profiles are described directly in terms of physical models of the microstructure and lattice defects in the sample.[143] Such analysis allows, for example, information on crystallite size distributions during the formation of crystallites to be obtained.[144] This has been used in several in situ studies,[65,145] e.g., in investigations of the formation of $CoFe_2O_4$ nanoparticles. Here, Andersen and Christensen used in situ PXRD to study the effect of synthesis parameters such as temperature and hydroxide concentration, as illustrated in Fig. 9.[32] The authors observed that while the final crystallite size was almost independent of temperature and pH value, the crystallite size distribution was heavily influenced by pH, with higher base concentrations giving narrower particle size distributions. As the properties of many nanomaterials are very size dependent, characterizing the size distribution is crucial in order to fully map material properties.

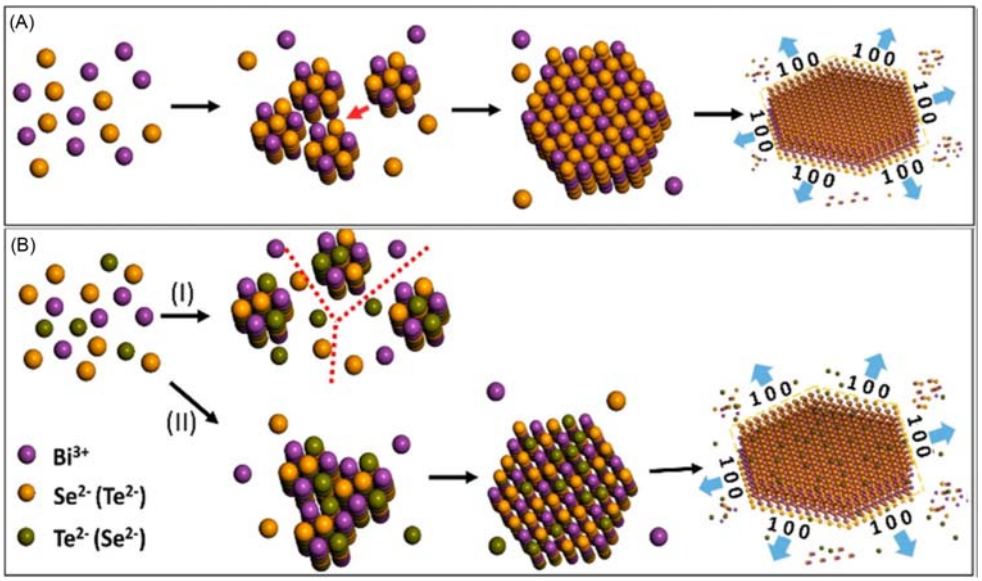

Fig. 8 Sketch of the growth steps for bismuth chalcogenide nanoplatelets. (A) Growth mechanism for the binary compounds, showing oriented attachment for the rapid growth step and then epitaxial growth for the slow growth step. (B) For ternary compounds, the possibility of oriented attachment is decreased due to different composition of the nuclei.[66] Reprinted with permission from Song, J.; Xia, F.; Zhao, M.; Zhong, Y. L.; Li, W.; Loh, K. P.; Caruso, R. A.; Bao, Q. Solvothermal Growth of Bismuth Chalcogenide Nanoplatelets by the Oriented Attachment Mechanism: An In Situ PXRD Study. *Chem. Mater.* **2015**, *27* (9), 3471–3482. Copyright (2021) American Chemical Society.

10.10.3.4 Changes in crystal structure during material formation

Modelling of high quality in situ powder diffraction allows detailed crystallographic information to be obtained during material formation. This includes, for example, analysis of unit cell parameters, strain and the presence of defects in the crystal structure.[146–149]

Strain in crystal lattices is reflected in the Bragg peak broadening, and as for crystallite size, it is thus possible to follow the evolution of lattice microstrain during material formation. For example, CeO_2 nanocrystals are known to exhibit line dislocations.[144,150] Using peak broadening analysis, it has been shown possible to follow a decrease in dislocation density as nanocrystals grow and order under solvothermal conditions.[144] A similar investigation has been made on the evolution of twin fault probabilities in ZnO nanocrystals.[151]

Rietveld refinement also allows analysis of the presence of e.g., point defects in materials. In studies of the synthesis of $LiFePO_4$, analysis of in situ PXRD data allowed investigations of the defect chemistry of the material.[69] From Rietveld analyses of angular-resolved PXRD data recorded on a second timescale, both the evolution of unit cell and defects in the structure could be followed. Large changes in the unit cell parameters were observed during the synthesis, which could be related to defects, and a large amount of Fe was observed on the Li site in the initially formed particles. The data showed that the defect concentration decreases with increasing synthesis time and temperature.

Phase transformations from one crystalline phase to another often results in strain and structural changes.[73] This was investigated for Li_2TiO_3 nanoparticles formed from a suspension of TiO_2 in an aqueous solution of LiOH.[126] Here, Rietveld refinement of the time resolved data showed that as Li-ions were inserted into the TiO_2 nanoparticles, the parameters of the tetragonal unit cell changed anisotropically towards those of the cubic Li_2TiO_3 phase. Combined with Avrami-Erofe'ev analysis of the reaction mechanism, this study gave much insight into the topotactic phase transformation.

In situ X-ray powder diffraction has recently been used for studies of high entropy alloys (HEAs); a relatively new type of material, where five or more elements form a homogeneous alloy. Broge et al studied a solvothermal synthesis of Pt–Ir–Pd–Rh–Ru

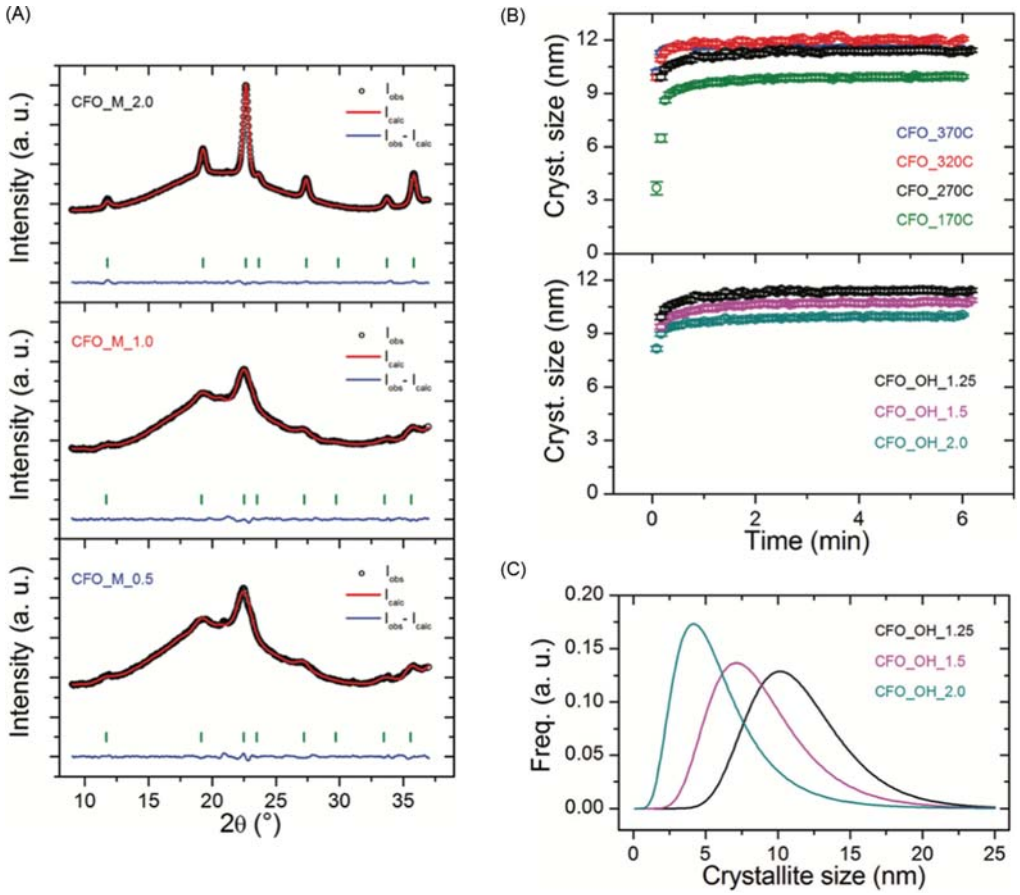

Fig. 9 (A) X-ray diffraction data and Rietveld refinement of data obtained during the synthesis of $CoFe_2O_4$ nanoparticles under different conditions. (B) Growth curves obtained from Rietveld refinement. The data show that neither the reaction temperature (top) or the amount of added NaOH (bottom) significantly affect the refined average crystallite size. (C) WPPM analysis of the same data allow size distributions to be obtained, showing a large influence of the NaOH concentration.[32] Reprinted with permission from Andersen, H. L.; Christensen, M. In Situ Powder X-Ray Diffraction Study of Magnetic $CoFe_2O_4$ Nanocrystallite Synthesis. *Nanoscale* **2015**, *7* (8), 3481–3490.

HEA nanoparticles, using a capillary cell and high resolution angular resolved powder X-ray diffraction.[152] The in situ data (Fig. 10) revealed nucleation of a single *fcc* phase, whose unit cell parameter decreased from 3.96 Å to 3.84 Å during crystallization and crystallite growth. The observation of initial particles with a larger unit cell parameter than that expected from the alloy showed that metals with larger atomic radii (Pt or Pd) were overrepresented in the initially formed particles. Further analysis of the growth (from Bragg-peak broadening) and of the synthesis of mono-metallic nanoparticles showed that the high entropy alloy nanoparticles form from an initial Pd core that autocatalyzes the reduction of the other metals, primarily on the (111) facets of the growing nanocrystals.

10.10.3.5 Mapping of synthesis parameters

In situ characterization is also very useful for gaining information about how different parameters affect the resulting products in less time compared to ex situ studies.[128,153] Rather than covering a large parameter space though extensive syntheses studies and ex situ characterization, the influence of e.g., reaction time and temperature on the resulting product can quickly be covered through much fewer in situ experiments, and more information can be obtained. For instance, Bremholm et al.[94] (Fig. 11) showed that magnetite nanoparticles can be formed in large quantities using a continuous flow supercritical water reactor in a matter of minutes, while controlling the size distribution simply by varying the pressure, temperature and residence time in the heating zone. Through minute-long experiments at four different temperatures, crystallite and particle size could be determined from PXRD and SAXS respectively, as a function of residence time in the heating zone, meaning that other crystallite/particle sizes than the resulting ones can be easily targeted by adjusting the residence time.

Broge et al. used an extensive in situ PXRD study to map the redox properties of a number of common solvents.[154] By dissolving simple transition metal salts (Cu(II), Ni(II), Co(II), Fe(III), Mn(II), Cr(III)) in five common solvents (water, ethanol, ethylene glycol, glycerol, and 10% hydrogen peroxide solution) and follow the formation of metallic and metal oxide phases using in situ powder diffraction, new insights into the solvent properties were obtained. While the studies provided knowledge on the

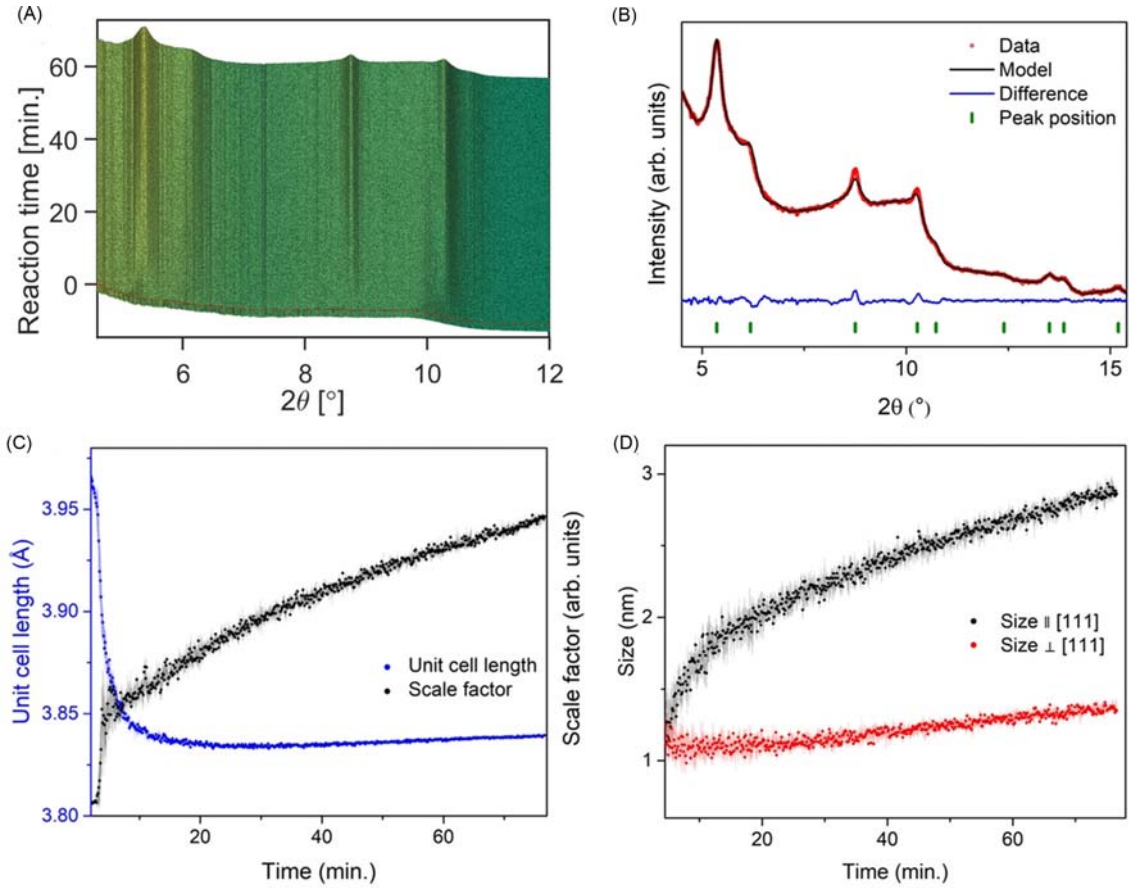

Fig. 10 (A) In situ XRD data obtained during the synthesis of HEA nanoparticles. (B) Representative Rietveld refinement of an in situ dataset. (C) Refined unit cell parameter and scale factor, plotted as a function of synthesis time. (D) Crystallite growth along and perpendicular to the (111) direction, obtained from Rietveld refinements.[152] Reprinted with permission from Broge, N. L. N.; Bondesgaard, M.; Søndergaard-Pedersen, F.; Roelsgaard, M.; Iversen, B. B. Autocatalytic Formation of High Entropy Alloy Nanoparticles. *Angew. Chem. Int. Ed.* **2020**, *7132*, 22104–22108.

formation of a range of metal and metal oxide compounds that are interesting in their own right, such systematic studies also give access to knowledge, which can be used in the design of other solvothermal syntheses.

10.10.4 Chemical insights from total scattering experiments

There is no doubt that in situ powder diffraction can offer invaluable information about the formation of many different products via many different syntheses, but even so, some things are still left in the dark by this technique. As powder diffraction relies on Bragg peaks, and is only sensitive to materials that possess long-range order, the atomic structure of amorphous and highly disordered structures cannot be characterized with conventional Bragg diffraction methods. The use of such techniques therefore limits the information that can be obtained on e.g., particle nucleation, i.e., the synthesis stages before crystalline materials have formed.[3] Here, total scattering methods with Pair Distribution Function (PDF) analysis can provide much needed information.[155–157] The PDF is obtained as the Fourier transform of total scattering data, i.e., data collected over a wide range of Q-space, where Bragg diffraction and diffuse scattering are treated equally. The PDF represents a histogram of all interatomic distances in the sample, regardless if the sample is crystalline, nanostructured or amorphous, and in situ PDF studies can thus provide unique insight into atomic rearrangements during the full material formation process, from e.g., solutions of precursor species to the final crystalline product.

The use of PDF analysis for structural characterization has over the last decades rapidly increased thanks to the development of high energy synchrotron sources, computational tools, software, and textbooks.[157] Now, PDF is also used more and more widely for in situ studies, and over the last years, many PDF studies on the formation of metal or metal oxides nanoparticles under solvothermal conditions have been done in order to investigate material formation[158–163] and the relation between precursor species and crystal structures.[139,140,146,164–174] Studies investigating MOFs[175], zeolites[176,177] and geopolymers,[178–181] have also been done. Synchrotron radiation is most commonly applied, although studies of reactions with slower kinetics such as geopolymer formation[182,183] have been done using neutrons.

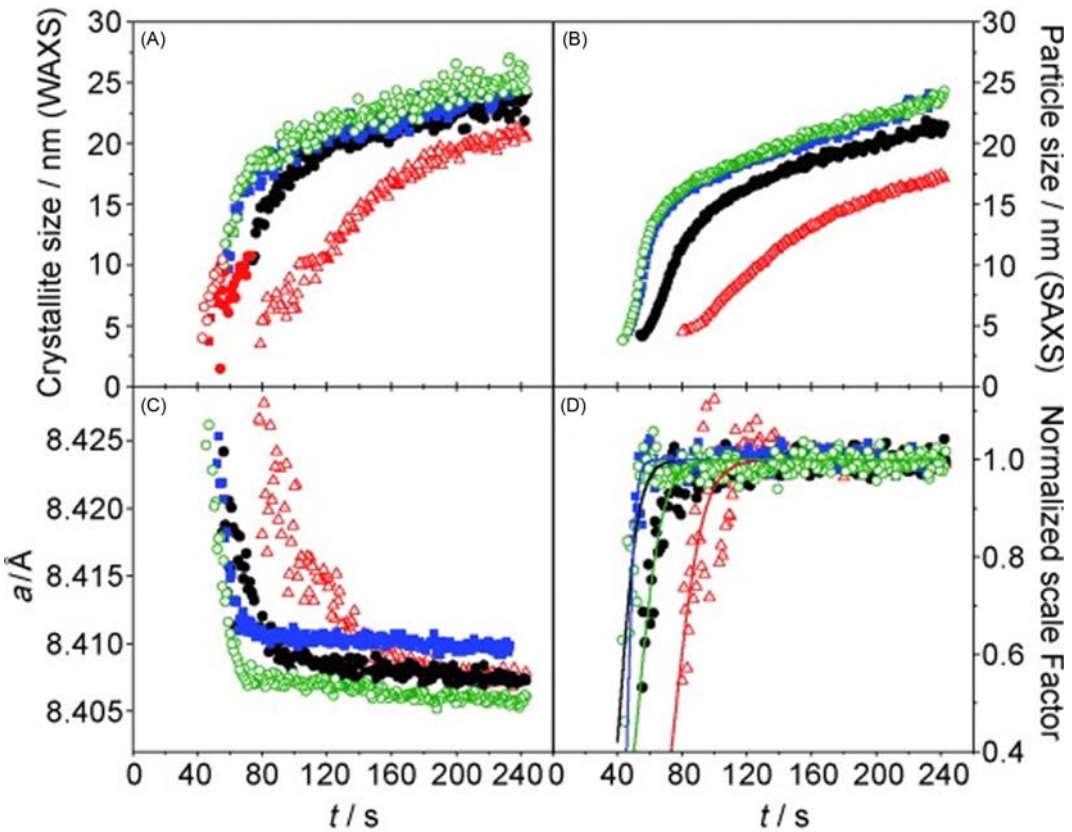

Fig. 11 Results from modelling of WAXS and SAXS data obtained during the formation of magnetite nanoparticles in a hydrothermal synthesis using a pulsed-flow reactor.[94] Results are shown for syntheses at 309 °C (red triangles), 337 °C (black dots), 367 °C (blue squares), and 395 °C (green circles). Evolution of crystallite (A) and particle sizes (B) determined by WAXS and SAXS, respectively. (C) Evolution of the unit cell parameter (A) and (D) evolution of the refined normalized WAXS scale factor, showing extent of crystallization. Reprinted with permission from Bremholm, M.; Felicissimo, M.; Iversen, B. B. Time-Resolved In Situ Synchrotron X-ray Study and Large-Scale Production of Magnetite Nanoparticles in Supercritical Water. *Angew. Chem. Int. Ed.* **2009**, *48* (26), 4788–4791.

10.10.4.1 PDF studies of particle nucleation

In situ X-ray PDF has, for example, been used to study the solvothermal synthesis of tungsten oxide.[166,184] Tungsten oxides show very rich structural chemistry, and several different polymorphs exist and can form in seemingly similar syntheses. By studying the formation pathway, it may be possible to deduce why a given polymorph forms over another by linking to the structural changes that take place from precursor clusters to the final material. For example, the formation of a hexagonal tungsten oxide was studied in water and oleylamine during a solvothermal synthesis.[184] While it was clear from previous studies that the solvent change affect the crystallite size, the influence of the solvent on the reaction mechanisms itself was unknown, and was investigated with in situ PDF, as illustrated in Fig. 12. The starting material used in the synthesis was ammonium meta-tungstate hydrate, $(NH_4)_6[H_2W_{12}O_{40}]\cdot xH_2O$. It is well-known that in an aqueous solution this polyoxometalate salt adopts the so-called α-Keggin cluster structure. This was confirmed by PDF, as the experimental data could be well-described by a Keggin cluster model. The PDF obtained from the solution of ammonium meta-tungstate hydrate in oleylamine showed very similar features, and this PDF could also be fitted with the Keggin structure. Upon heating, however, the α-Keggin clusters turned into different polyoxometalates, depending on the solvent. In water the α-Keggin cluster was converted to the Tungstate Y cluster, which eventually led to the formation of crystalline hexagonal tungsten oxide nanoparticles. In oleylamine, however, an equilibrium was established between the Keggin-clusters and a paratungstate cluster. Shortly before nucleation, this paratungstate cluster rearranged into a short-lived intermediate that had an atomic structure that resembled a fragment of the original α-Keggin cluster. This led to the formation of nanoparticles of crystalline pyrochlore $WO_3\cdot 0.5H_2O$, which eventually transformed to the hexagonal WO_3 structure. The entire reaction is summarized in Fig. 12G. The different solvent thus completely changes not only the growth of the particles, as often discussed in literature, but also the formation mechanisms itself, as it directs the structural evolution of the precursor cluster. The formation of the paratungstate cluster appear to be responsible for the formation of the pyrochlore phase. Through in situ total scattering and PDF, it was thus possible to gain important insights into the chemistry occurring up to the crystallization process.

In situ PDF has also been used to gain knowledge of the formation of maghemite nanoparticles.[146] Here, the formation mechanism of γ-Fe_2O_3 during a hydrothermal synthesis from aqueous solutions of ammonium iron(III) citrate was investigated, and again, the possibility to extract structural information both before and after nucleation of crystalline particles was used to elucidate reaction mechanisms. Fig. 13A and B shows the local range of the time-resolved PDFs obtained during the reaction, as well as selected PDFs from the process. Modelling showed that the starting structure in the solution was a $[Fe(H_2cit)H_2O]_n$ complex, with corner-sharing $[FeO_6]$-octahedra. This complex is characterized by a Fe−O PDF peak at ca. 2 Å and a Fe−Fe peak at ca. 3.75 Å. When the reaction is initiated by heating, this peak disappears, while the Fe−O peak remains, although it shifts to a slightly higher *r*-value. At the same time, a Fe−Fe peak appears at ca. 3.5 Å. This agrees well with the distance between two edge-sharing $[FeO_6]$ octahedra, as found in the final spinel maghemite structure. Soon after, a new peak appears at ca. 3.8 Å, corresponding to the distance between tetrahedrally coordinated and octahedrally coordinated iron in the spinel structure. Initially the Fe_O−Fe_O

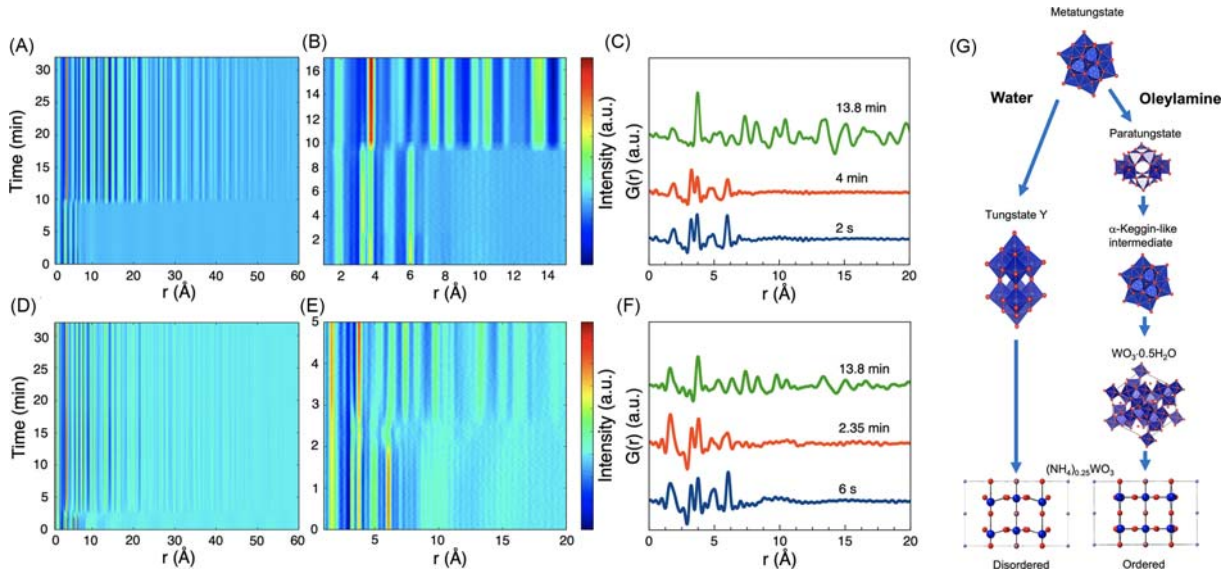

Fig. 12 (A) PDFs obtained during the synthesis of tungsten oxide nanoparticles in water. (B) The PDF range 1–15 Å showing the local structure just before crystallization. (C) PDFs obtained after 2 s, 4 and 13.8 min from the tungsten oxide synthesis in water. (D) PDFs obtained during the synthesis of tungsten oxide nanoparticles in oleylamine. (E) The PDF range 1–15 Å showing the local structure just before crystallization. (F) PDFs obtained from the synthesis in oleylamine, after 6 s, 4 min and 13.8 min. (G) The formation pathway for the solvothermal synthesis of hexagonal tungsten bronze nanoparticles in water and oleylamine. Reprinted with permission from Juelsholt, M.; Lindahl Christiansen, T.; Jensen, K. M. Ø. Mechanisms for Tungsten Oxide Nanoparticle Formation in Solvothermal Synthesis: From Polyoxometalates to Crystalline Materials. *J. Phys. Chem. C* **2019**, *123*, 5110–5119. Copyright 2019 American Chemical Society.

peak is more intense than the Fe_O—Fe_T peak, but as the reaction proceeds, this ratio is reversed. This indicates that as the small, iron oxide clusters of octahedra and tetrahedra grows to form nanoparticles, the condensation mainly occurs through tetrahedrally coordinated Fe, as illustrated in Fig. 13C. Further analysis showed that during the growth of the nanoparticles (from 1 to 8 nm), the tetrahedrally coordinated sites in the spinel structure were occupied, and based on the PDF refinements it was determined that in the beginning of the crystallite growth, the tetrahedral site was only 65% occupied. As the particles grew from 1–2 nm to 8 nm, the tetrahedral occupancy increased at the same rate as the nanoparticles growth. Generally, it was shown that the largest structural changes take place before clear Bragg peaks were seen in the data, i.e., before crystalline material had formed. This underpins the need for structural analysis of prenucleation clusters for understanding material formation processes.

The two examples of in situ PDF studies given above both concerned 3D structures with strong bonding in all directions. Several other in situ PDF studies have been performed on related materials, such as metal and metal oxide nanoparticles.[139,140,146,164–174] PDF has also been successfully applied to study the assembly of materials with weaker and more directional dependent bonding. Tominaka et al.[174] studied the formation of layered lepidocrocite-type titanate nanoparticles, whose structure consists of layers of $[TiO_6]$-octahedra spaced by tetramethyl ammonium hydroxide. The nanoparticles were synthesized hydrothermally from a solution

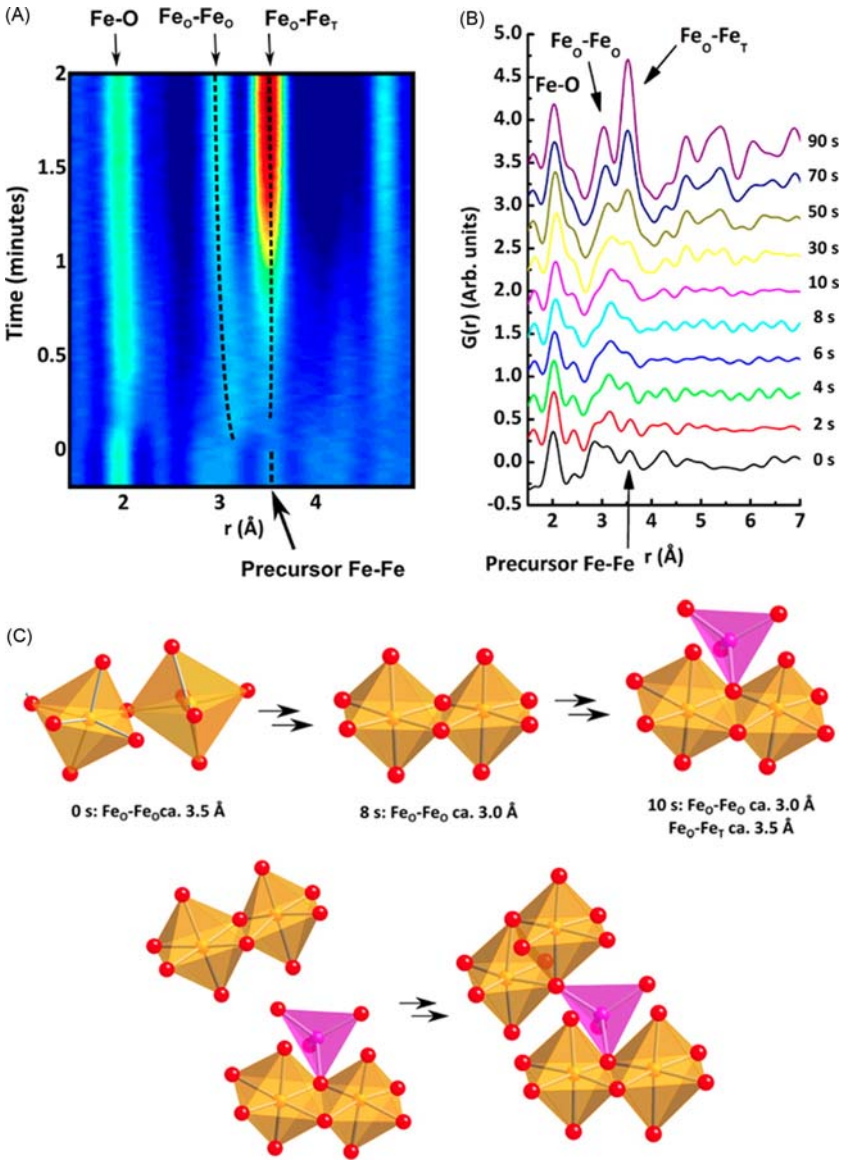

Fig. 13 (A) Time-resolved PDFs (1–5 Å) obtained from the synthesis of maghemite nanoparticles. (B) Individual PDFs at selected times. Important interatomic distances are indicated. (C) Suggested formation mechanism for maghemite. Adapted and reprinted with permission from Jensen, K. M. Ø.; Andersen, H. L.; Tyrsted, C.; Bøjesen, E. D.; Dippel, A.-C.; Lock, N.; Billinge, S. J. L.; Iversen, B. B.; Christensen, M.: Mechanisms for Iron Oxide Formation under Hydrothermal Conditions: An in Situ Total Scattering Study. *ACS Nano* **2014**, *8*, 10704–10714. Copyright (2021) American Chemical Society.

of tetramethyl ammonium hydroxide and titanium isopropoxide. From the in situ PDF data, it was observed that the starting solution contained < 1 nm platelets with atomic structure closely related to the titanium oxide layers in the crystalline titanate structure. As heat was applied, the platelets grew in size in two dimensions, and started stacking in the third to form the lepidocrocite-like structure.

In situ PDF has also been applied for studies of the formation of metal organic frameworks (MOFs), specifically UiO-66,[175] where Hu et al. established the formation mechanism illustrated in Fig. 14. The first step in the reaction is the formation of a hexanuclear Zr cluster when $ZrCl_4$ is mixed with N,N′-dimethylformamide and hydrochloric acid. Upon addition of the organic ligand the hexanuclear Zr clusters assemble to form large multinuclear clusters, which then assemble to form the MOF crystal.

10.10.4.2 Challenges and limitations for in situ total scattering experiments

There are some general considerations and limitations that are common for all in situ PDF experiments, compared to e.g., powder diffraction experiments. Firstly, PDF analysis requires a Q-range up to at least ca. 15 $Å^{-1}$ or higher, and high energy and high flux X-rays or neutrons are thus required. A limited Q-range will broaden the PDF peaks and introduce termination ripples in the PDF, which in severe cases can be mistaken for real PDF-peaks representing interatomic distances. Due to thermal vibration of atoms, and in the case of X-rays, the Q-dependence of the form factor f(Q), the intensity of the scattered signal decreases at higher momentum transfers, and obtaining high quality data at the highest Q-values thus generally require longer measurements than data for powder diffraction analysis.[185] During time-resolved in situ experiments, a compromise between time-resolution and PDF quality must therefore be found. Often, the Q_{max} is between 15 and 20 $Å^{-1}$ for in situ total scattering experiments. This can be good enough for e.g., identifying the atomic species present, but puts a limit on how much information about their structure can be extracted compared to other types of PDF experiments, where Q_{max} values up to 30 $Å^{-1}$ are sometimes used.

In many in situ studies of wet-chemical syntheses, the majority fraction of the scattered signal is not from the structures of interest, but rather from the sample environment, from the solvent, a material support, etc. This signal must be subtracted from the data before PDF analysis of the material of interest, i.e., the precursor clusters or the final nanoparticles. It is therefore important to ensure that the scattered signal from this material is significant and will be of high enough quality for PDF analysis. For example, precursor concentrations on the millimolar scale or less are often used for lab-scale wet chemical synthesis. This makes in situ PDF studies challenging, as the background signal will completely dominate scattering data collected from such experiments. In many in situ PDF experiments, precursor concentrations in the range 0.1–5 M are needed depending on the scattering power of the material, which can limit the type of reactions that can currently be studied with PDF. High quality background measurements are furthermore imperative. If background measurements are not done or not of high enough quality, the background can hide all the information about the reacting species. It is therefore crucial to obtain a good background measurement for each experiment that is performed. Sometimes, the addition of a reactant to the solvent can change the solvent structure[184,186] and a complete background subtraction can be impossible. Despite these limitations, in situ PDF experiments are becoming more and more widespread, and are likely to continue to do so in the future.

10.10.5 Nanoparticle size and shape: Information from Small-Angle X-ray scattering

Both diffraction and total scattering techniques are powerful tools for the study of materials and they can be used to extract information on atomic structural changes. As discussed above, knowledge of crystallite size and shape can also be obtained from these techniques, either from Bragg-peak width, or from the extent of PDF peaks. However, more information on nanoparticle size, shape

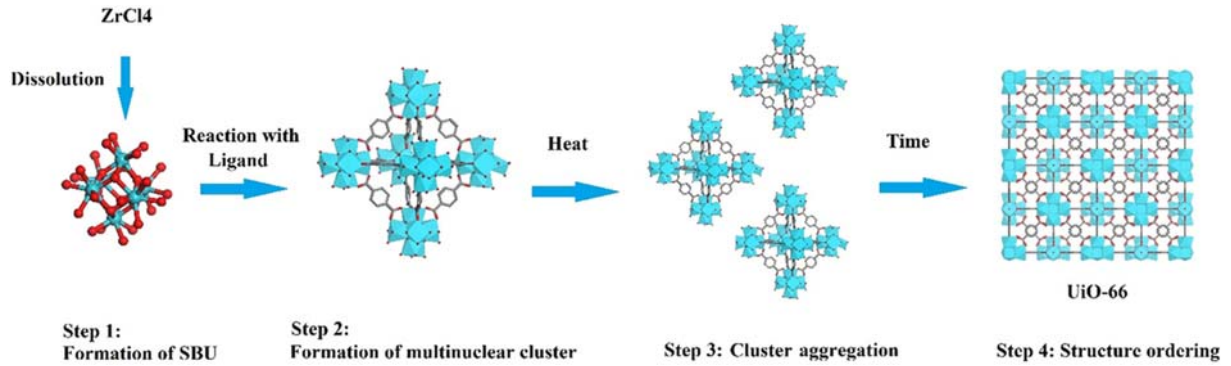

Fig. 14 The steps for forming the MOF UiO-66, as determined from in situ PDF experiments. A hexanuclear Zr cluster firstly forms. Upon addition of ligands, the hexanuclear Zr clusters assemble into larger units. These units then assemble into the MOF crystal structure.[175] Reprinted with permission from Xu, H.; Sommer, S.; Broge, N. L. N.; Gao, J.; Iversen, B. B.: The Chemistry of Nucleation: In Situ Pair Distribution Function Analysis of Secondary Building Units During UiO-66 MOF Formation. *Chem. Eur. J.* **2019**, *25* (8), 2051–2058.

and dispersity can often be obtained from in situ small angle scattering (SAS) experiments.[187] While the sizes that can be obtained from both diffraction and total scattering experiments relate to domains with atomic order, small-angle scattering allows particle sizes to be obtained, regardless of the existence of order. Small angle scattering data are furthermore quite sensitive to particle dispersity and particle morphology.

In situ SAXS experiments are quite widespread for studies of nanoparticle growth,[188–191] e.g., in studies of colloidal syntheses.[109,192–194] For example, Polte et al. have used SAXS (in combination with other techniques) to study the formation of gold nanoparticles in a classical citrate synthesis method, often employed in the formation of metallic nanoparticles.[195] Apart from studying the formation of nanoparticles of different sizes and shapes, in situ small angle scattering is also very suited to study the formation of nanoparticle "superlattices," where nanoparticles order in lattices, giving rise to Bragg-peaks in the low Q-range. This is illustrated in **Fig. 15** where Abécassis et al. used small-angle X-ray scattering to follow the formation of gold nanoparticles and their assembly into super-lattice structures.[196] As particles form, a signal characteristic of a spherical form factor appears. Soon after Bragg peaks appear from the formation of a cubic closed packed structure of nanoparticles.

The combination of powder diffraction (here often referred to as wide-angle (X-ray) scattering, WAXS), and small angle scattering can provide much insight into e.g., nanomaterial formation on all relevant length scales, i.e., from atomic structure to particle shape and size.[46,94,141,142,187,197–199] For example, Cravillon et al. used in situ SAXS/WAXS experiments to follow the nucleation and growth of nanocrystals of the MOF ZIF-8, consisting of divalent cations (Zn^{2+}) in a framework built from imidazolate ions.[200] During the synthesis of ZIF-8, measurements of SAXS and WAXS data were done simultaneously using two different X-ray detectors; close to the sample (WAXS) and far from the sample (SAXS). Examples of such data are shown in **Fig. 16**. From these data, the authors could show that amorphous clusters in the size-range 1.1 nm existed already before heating was initiated, i.e., they form spontaneously when mixing the precursors for MOF formation. From SAXS/WAXS analysis, the authors showed that the nanocrystalline ZIF-8 phase formed at the expense of these clusters, i.e., they must be a precursor phase or prenucleation cluster for the MOF. The data furthermore showed that the first ZIF-particles may be amorphous.

SAS experiments may also give structural insight to length scales larger than the nanometer scale.[45,201–203] For example, Xia et al. used a combination of SAXS and WAXS to follow the formation of mesoporous anatase beads for electrodes in dye-sensitized solar cells during solvothermal synthesis.[65] Here, they studied both the initial formation of anatase from an amorphous precursor, and the subsequent formation of a mesoporous network. The WAXS (PXRD) data allowed Rietveld refinements, from where crystallization curves could be extracted and analyzed with Avrami-Erove'ev kinetic models. The WAXS data were also analyzed using the WPPM method, so that crystallite size distributions could be obtained. The WAXS data thus provided extensive insights into the crystallization mechanisms, showing that initially, the amorphous titanium oxide dissolves, making the local solution supersaturated with respect to anatase and triggers initial nucleation. This lead the anatase particles to grow and their crystallite size increased with time. At this stage, new nucleation also took place, leading to anatase nanoparticles with a broad size distribution. In situ SAXS experiments were used to complement the WAXS information on crystallization, and analysis of SAXS data provided knowledge on the mesostructure of the product. The SAXS data showed formation of large pore structures between the beads during the course of the solvothermal process. Here, the SAXS/WAXS experiments were not done simultaneously, but nevertheless, the high reproducibility of the synthesis made it possible to relate SAXS and WAXS results.

Baumgartner et al. have used the combination of SAXS and WAXS to gain new fundamental insight into nucleation processes.[15] Classical nucleation theories have in recent decades been challenged by the new knowledge obtained in part from in situ studies,[3] and here, the authors were interested in establishing how nucleation takes place at the nanometer scale within an amorphous precursor. With millisecond time resolution, they studied the crystallization of iron oxide, i.e., magnetite (Fe_3O_4) nanoparticles, using aqueous solutions of $FeCl_3$ and $FeCl_2$ in NaOH as precursors. The experiments were done using fast millifluidic stop-flow reactors, and the experiments were done at room temperature. Such experiments allow studying the very early timepoints after

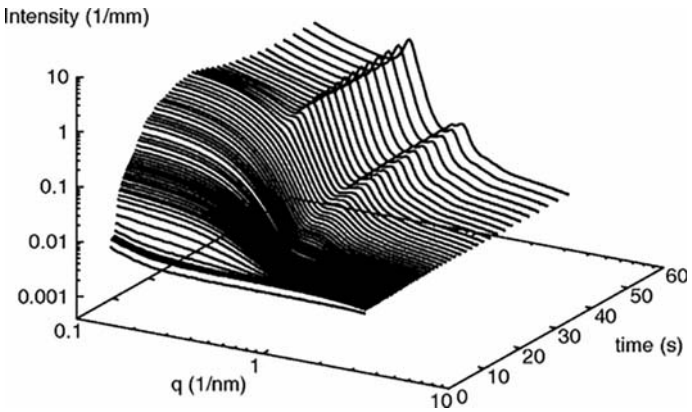

Fig. 15 In situ SAXS data obtained during the formation of gold nanoparticles and subsequent assembly into a ccp-structured nanoparticle superlattice.[196] Reprinted with permission from Abécassis, B.; Testard, F.; Spalla, O., Gold Nanoparticle Superlattice Crystallization Probed In Situ. *Phys. Rev. Lett.* **2008**, *100* (11), 115504.

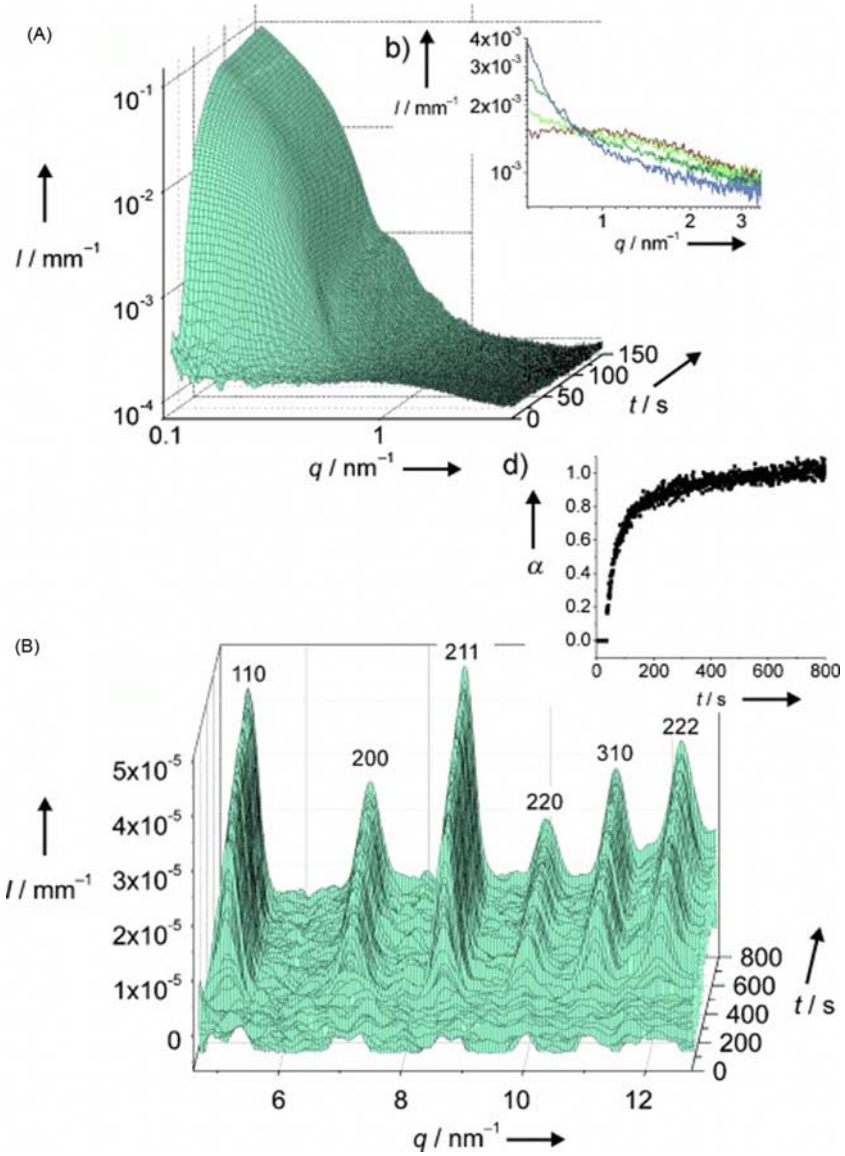

Fig. 16 SAXS (A and B) and WAXS (C) data obtained during the formation of ZIF-8 nanoparticles. The extent of crystallization obtained from the WAXS data is shown in (D).[200] Reprinted with permission from Cravillon, J.; Schroder, C. A.; Nayuk, R.; Gummel, J.; Huber, K.; Wiebcke, M., Fast Nucleation and Growth of ZIF-8 Nanocrystals Monitored by Time-Resolved In Situ Small-Angle and Wide-Angle X-Ray Scattering. *Angew. Chem. Int. Ed.* **2011**, *50* (35), 8067–8071.

mixing of reactants. The authors observed that as soon as reactant mixing had happened, aggregates of sub-nanometer amorphous particles had formed, most likely as iron(oxyhydr)oxide. At this point of the reaction, no crystalline particles were observed in the WAXS data. The amorphous particles grew to ca. 3 nm before any Bragg peaks appeared, and after crystallization, the growth rate significantly decreased. The growth rate abruptly decayed because the crystals had depleted the amorphous particles and grew by transfer from the ions in solution. Using their data, the authors could determine kinetic and thermodynamic parameters for the reaction. They highlighted that when crystallization takes place from small, viscous and/or insoluble nucleation precursors, both the thermodynamic properties and the size of transient precursor are important for the resulting product and must therefore be taken into account in the development of new nucleation theories.

The combination of small angle scattering and diffraction experiments thus provide complementary insight into nucleation, crystallization and growth processes. By further complementing such experiments with total scattering and PDF analysis, much new information can be obtained. For example, with PDF analysis, it may be possible to obtain atomic structural information on the small, amorphous precursor clusters described in the examples from both Cravillon and Baumgartner above. Combined, simultaneous small angle scattering and PDF experiments are still very scarce, mainly due to the challenges in collecting such

datasets at the same time. However, this kind of experiments, and the combination of e.g., SAXS and X-ray PDF for in situ investigations, is likely to rise in the coming years.

10.10.6 Combination of techniques: Spectroscopy and scattering

X-ray spectroscopy (XAS) techniques such as XANES (X-ray absorption near edge spectroscopy) and EXAFS (Extended X-ray absorption fine structure) have for decades been used to study chemical processes in situ, including studies of material formation.[17,204] From XAS data, detailed information on the chemical state of specific elements can be obtained. A XANES spectrum is sensitive to the oxidation state of the absorbing atom, and the chemical bonding to it, and XANES measurements can therefore provide a "fingerprint" of chemical information. With EXAFS, it is possible to extract quantitative information about the local atomic environment of the absorbing atom such as coordination number, type, and length of the chemical bonds to surrounding atoms.

By combining XAS and diffraction methods, insight into both local (electronic) structure, oxidation, and long-range structure can be obtained.[48,53,205–208] XAS methods do not rely on long-range order, and chemical information can be obtained from both solids, liquids and solutions. As an early example of the use of combined XRD and EXAFS for studies of solvothermal reactions, Michailovski et al. investigated the formation of MoO_3 nanorods from a solid, yellow molybdic acid $MoO_3 \cdot 2H_2O$ precursor material in solutions of acetic acid.[209] X-ray diffraction and EXAFS data were collected from individual experiments, with the X-ray diffraction data done using energy-dispersive measurements, allowing use of an autoclave-like setup. Importantly, the XAS experiments were done to investigate both the liquid phase and the solid/liquid interface by positioning the cell so that the X-ray beam probed different parts of the reaction medium.[210] From the EXAFS data of the liquid phase, the authors found that molybdenum species were only seen in solution after heating the autoclave to ca. 90 °C, indicating dissolution of the molybdic acid. A continuous change of the molybdenum coordination from $MoO_3 \cdot 2H_2O$ to MoO_3 followed, without the appearance of any intermediate phases. The reaction started as soon as the first soluble Mo species were detected and accelerated at higher temperature as the concentration of Mo species in solution increased. The observations from EXAFS thus strongly suggested a solution-based mechanism for material formation. This was complemented by ED-XRD, which showed the smooth transition from the crystalline precursor to the final MoO_3 nanorods with no intermediate phases present.

X-ray scattering methods only give limited options for distinguishing elements that are close to each other in the periodic table, or to investigate e.g., the inclusion of minority dopants into a host structure. Here, the element sensitivity of XAS techniques can provide new insight. For example, Hirsch et al.[211] have studied the formation of Ni-doped MoO_3 nanorods, using a combination of X-ray diffraction and XAS techniques. When Ni precursor is added to the starting reaction solution, it is apparent from in situ XANES and ex situ EXAFS measurements at the Ni K-edge and Mo K-edge that the nuclei already form with the desired chemical composition, i.e. the dopant is incorporated before the formation of crystalline material. Tyrsted et al. used combined XRD, PDF and EXAFS to follow the formation of yttrium-stabilized cubic zirconia, YSZ.[164] Nanoparticles of YSZ with 8% added Y were synthesized in a solvothermal reaction from metal nitrates dissolved in methanol, and the solvothermal material formation was followed in a small-volume capillary cell using X-ray total scattering for PDF analysis, as well as separate in situ XRD/EXAFS experiments. In situ PDF revealed a complex multistep sequence of atomic reorganizations (**Fig. 17**): Before nanoparticle nucleation, the precursor formed a polymeric species whose structure was incompatible with the final product. Instead of direct nucleation into the final nanocrystalline particles, a highly disordered intermediate precipitate formed with a local bonding environment similar to the product, although lacking the correct topology. During further solvothermal treatment nucleation and growth of ordered domains within the amorphous disordered structure took place. The X-ray PDF experiments, however, did not allow distinguishing between Y and Zr. Instead, by using separate in situ EXAFS experiments investigating the Y and Zr edge, it was shown that similar structural changes appeared around Zr and Y during the material formation (**Fig. 17**). This indicated that Y is incorporated in both the polymeric precursor species and the disordered intermediate structure before the final nanoparticle formation. It is likely that successful doping of materials relies on this process, i.e., that the dopant takes part in the nucleation process in a similar way to the host material.

The combination of X-ray scattering and spectroscopy methods can also provide much insight into the role of reduction and oxidation in material synthesis. For example, Ramamoorthy et al. combined SAXS, PDF, and XANES for extensive studies of prenucleation clusters for gold nanoparticles, showing that the synthesis did not follow classical nucleation theory.[212] Combined, the XANES, PDF and SAXS gave extensive insight into the nature of the prenucleation clusters. The data showed that during the initial stages of the synthesis, a prenucleation structure of $[Au_xCl_yOY_z]_n$ formed. These clusters, containing Au(I) and Au(III) species were ca. 1 nm in size, and PDF analysis showed that they contained an Au—Au correlation at ca. 3.4 Å. A burst nucleation led to fast growth of Au(0) nuclei of ca. 1.9 nm, which was followed by slower growth, where consumption of less reactive species resulted in particles of ca. 2.5 nm. The combination of chemical and structural insight from the three techniques can thus provide extensive insights into important chemical reactions, and this kind of knowledge can aid in understanding how tailor-made material synthesis routes can be designed in the future.

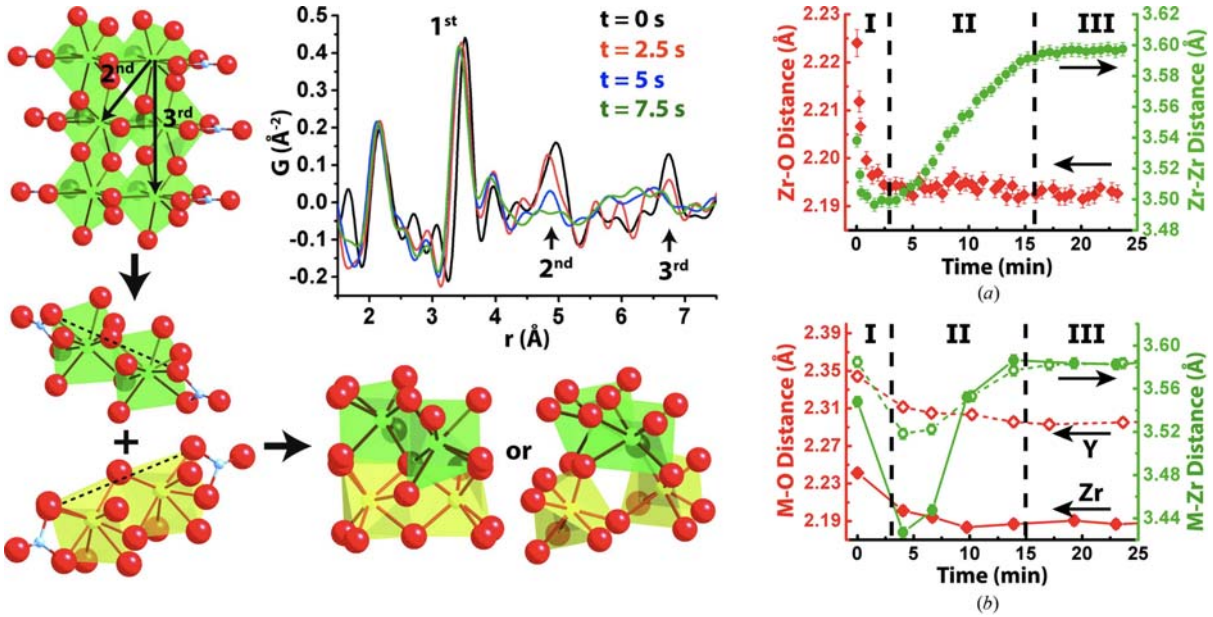

Fig. 17 Investigations of the formation of yttria-stabilized cubic zirconia, YSZ. Left: The initial structural changes as observed from PDF, showing that a polymeric precursor species transform into an amorphous matrix, eventually forming nanocrystalline YSZ. Right: By comparing changes in interatomic distances obtained from PDF (top) and Y and Zr EXAFS (bottom), it was shown that similar structural changes take place for Y and Zr during the material formation.[164] Reprinted from Tyrsted, C.; Lock, N.; Jensen, K. M. Ø.; Christensen, M.; Bøjesen, E. D.; Emerich, H.; Vaughan, G.; Billinge, S. J. L.; Iversen, B. B., Evolution of Atomic Structure During Nanoparticle Formation. *IUCrJ* **2014**, *1* (3), 165–171.

10.10.7 Summary and outlook

X-ray and neutron scattering are indispensable tools for gaining insights into material formation, and a range of different techniques can be used. With powder diffraction, the appearance and changes in crystalline phases can be studied, and through e.g., Rietveld refinement or WPPM analysis, information about both atomic and nanoscale structure can be extracted. This makes it possible to obtain detailed knowledge of e.g., crystallization kinetics, crystal growth, phase transformations, and any structural changes that may take place during material formation relating to e.g., defect chemistry and strain evolution.

While diffraction-based methods can provide much information into structures appearing after crystallization, the atomic scale structural changes that take place before this stage, i.e., during nucleation, are more challenging to study. Here, total scattering with PDF analysis can provide information. The ability to track the atomic structure from the sub-nanometer sized starting species to crystalline nanoparticles in a single experiment ensures that no important reaction step or intermediate is overlooked. While the high data quality required for PDF analysis can be a challenge in the design of in situ experiments, the use of in situ PDF, often combined with powder diffraction experiments, is likely to expand in the coming years with further developments of experimental setups, software and data analysis methods.

Small angle scattering methods are widely used to obtain information about nanoparticle formation and growth, as well as assembly into larger meso-scale structures. Small angle scattering is sensitive to particle size, shape and dispersity, and when combined with wide angle scattering experiments (powder diffraction or total scattering), complementary information on both nanostructure and atomic structure can be obtained. Simultaneous SAXS/WAXS experiments are thus very useful for obtaining fundamental knowledge on e.g., nucleation processes. The combination of e.g., powder diffraction or PDF analysis with X-ray spectroscopy methods such as XANES and EXAFS methods can also give important complementary information. For example, the "chemical fingerprint" obtained from XANES can aid in understanding reduction or oxidation processes taking place during synthesis. With EXAFS, knowledge of the local structure around specific elements can provide insight into the role of dopants during material formation, or help distinguishing between elements that are close to each-other in the periodic table. More and more synchrotron beamlines are now designed for, for example, combined SAXS/WAXS or XRD/XAS experiments. With the improvement in options for position-resolved studies, computed tomography (ct) studies may also provide new information on e.g., the spatial extent of crystallization.

The development of in situ studies has been driven by the advancement of X-ray and neutron sources since the 1990s. Now, dedicated beamlines and instruments for fast time-resolved studies exist at large scale facilities around the world. The continued development of e.g., new neutron sources with large increases in flux can give new possibilities for the use of neutrons for nucleation studies. The new XFEL sources being built around the world can also provide completely new options for experiments with extremely high time resolution for tracking structural changes. So far, XFEL studies of structural changes in materials are limited,[213] but formation studies, and studies of e.g., nucleation are likely to appear in the future.

Advancements in data analysis methods can also come to play a large role in the further development of in situ studies. As in any data-driven field, methods from data science and machine learning are likely to be more widely used for analysis for the increasingly large datasets that are obtained from time-resolved studies.[214] For example, machine learning methods have already been applied for e.g., component analysis[208,215–218] and in identifying symmetry and structural motifs in PDFs.[219,220]

Over the past 30 years, in situ studies have thus contributed much insight into material formation. However, the field is likely to grow much further in the future. While many studies historically have focused on obtaining knowledge on specific material systems, which could be used to optimize certain synthesis procedures, much attention is now given to studies of more fundamental processes, such as the development of non-classical nucleation theory.[221,222] One of the great unanswered questions in inorganic chemistry is why a specific structure forms under some given synthesis conditions.[1] Our missing ability to predict the outcome of a synthesis in inorganic materials chemistry can be put in stark contrast to molecular chemistry, where detailed knowledge of reaction mechanisms exists, making it possible to design synthesis pathways, and to a large extent predict their outcome. Detailed studies of complex nucleation processes, and development of new nucleation theories, may aid in getting to the next level of synthetic insight. With all the recent developments in sources and computational methods, as well as this wide interest in material synthesis, we see a bright light for in situ studies in the future.

References

1. Soderholm, L.; Mitchell, J. F. Perspective: Toward "Synthesis by Design": Exploring Atomic Correlations During Inorganic Materials Synthesis. *APL Materials* **2016,** *4* (5), 053212.
2. Sumpter, B. G.; Vasudevan, R. K.; Potok, T.; Kalinin, S. V. A Bridge for Accelerating Materials by Design. *Npj Comput. Mater.* **2015,** *1*, 15008.
3. Bøjesen, E. D.; Iversen, B. B. The Chemistry of Nucleation. *CrstEngComm* **2016,** *18* (43), 8332–8353.
4. Shoemaker, D. P.; Hu, Y.-J.; Young Chung, D.; Halder, G. J.; Chupas, P. J.; Soderholm, L.; Mitchell, J. F.; Kanatzidis, M. G. In Situ Studies of a Platform for Metastable Inorganic Crystal Growth and Materials Discovery. *Proc. Natl. Acad. Sci. U. S. A.* **2014,** *111* (30), 10922–10927.
5. Walton, R. I.; O'Hare, D. Watching Solids Crystallise Using In Situ Powder Diffraction. *Chem. Commun.* **2000**, (23), 2283–2291.
6. Hansen, T. C.; Kohlmann, H. Chemical Reactions Followed by In Situ Neutron Powder Diffraction. *Z. Anorg. Allg. Chem.* **2014,** *640* (15), 3044–3063.
7. Wu, S.; Li, M.; Sun, Y. In Situ Synchrotron X-Ray Characterization Shining Light on the Nucleation and Growth Kinetics of Colloidal Nanoparticles. *Angew. Chem. Int. Ed.* **2019,** *58* (27), 8987–8995.
8. Isnard, O. A Review of In Situ and/or Time Resolved Neutron Scattering. *C. R. Phys.* **2007,** *8* (7), 789–805.
9. Jensen, K. M.Ø.; Tyrsted, C.; Bremholm, M.; Iversen, B. B. In Situ Studies of Solvothermal Synthesis of Energy Materials. *ChemSusChem* **2014,** *7* (6), 1594–1611.
10. Hiley, C. I.; Walton, R. I. Controlling the Crystallisation of Oxide Materials by Solvothermal Chemistry: Tuning Composition, Substitution and Morphology of Functional Solids. *CrstEngComm* **2016,** *18* (40), 7656–7670.
11. Walton, R. I. Subcritical Solvothermal Synthesis of Condensed Inorganic Materials. *Chem. Soc. Rev.* **2002,** *31* (4), 230–238.
12. Nikam, A. V.; Prasad, B. L. V.; Kulkarni, A. A. Wet Chemical Synthesis of Metal Oxide Nanoparticles: A Review. *CrstEngComm* **2018,** *20* (35), 5091–5107.
13. Cheetham, A. K.; Mellot, C. F. In Situ Studies of the Sol-Gel Synthesis of Materials. *Chem. Mater.* **1997,** *9* (11), 2269–2279.
14. Gebauer, D.; Cölfen, H. Prenucleation Clusters and Non-classical Nucleation. *Nano Today* **2011,** *6* (6), 564–584.
15. Baumgartner, J.; Ramamoorthy, R. K.; Freitas, A. P.; Neouze, M.-A.; Bennet, M.; Faivre, D.; Carriere, D. Self-Confined Nucleation of Iron Oxide Nanoparticles in a Nanostructured Amorphous Precursor. *Nano Lett.* **2020,** *20* (7), 5001–5007.
16. Norby, P.; Schwarz, U. Powder Diffraction Under Non-ambient Conditions. In *Powder Diffraction: Theory and Practice;* Billinge, S. J. L., Dinnebier, R., Eds.; 2008; pp 439–463.
17. Pienack, N.; Bensch, W. In-Situ Monitoring of the Formation of Crystalline Solids. *Angew. Chem. Int. Ed.* **2011,** *50* (9), 2014–2034.
18. Majuste, D.; Ciminelli, V. S. T.; Eng, P. J.; Osseo-Asare, K. Applications of In Situ Synchrotron XRD in Hydrometallurgy: Literature Review and Investigation of Chalcopyrite Dissolution. *Hydrometallurgy* **2013,** *131–132,* 54–66.
19. Sun, Y. Watching Nanoparticle Kinetics in Liquid. *Mater. Today* **2012,** *15* (4), 140–147.
20. Sun, Y.; Ren, Y. In Situ Synchrotron X-Ray Techniques for Real-Time Probing of Colloidal Nanoparticle Synthesis. *Part. Part. Syst. Char.* **2013,** *30* (5), 399–419.
21. Polak, E.; Munn, J.; Barnes, P.; Tarling, S. E.; Ritter, C. Time-Resolved Neutron Diffraction Analyses of Hydrothermal Syntheses Using a Novel Autoclave Cell. *J. Appl. Cryst.* **1990,** *23* (4), 258–262.
22. Gualtieri, A. F.; Norby, P.; Artioli, G.; Hanson, J. C. Kinetic Study of Hydroxysodalite Formation from Natural Kaolinites by Time-Resolved Synchrotron Powder Diffraction. *Microporous Mater.* **1997,** *9* (3–4), 189–201.
23. Grendal, O. G.; Nylund, I. E.; Blichfeld, A. B.; Tominaka, S.; Ohara, K.; Selbach, S. M.; Grande, T.; Einarsrud, M.-A. Controlled Growth of $Sr_xBa_{1-x}Nb_2O_6$ Hopper- and Cube-Shaped Nanostructures by Hydrothermal Synthesis. *Chem. A Eur. J.* **2020,** *26,* 9348–9355.
24. Christensen, A. N.; Norby, P.; Hanson, J. C. In-Situ Investigation of Magnesium Aluminophosphate Synthesis by Synchrotron X-Ray Powder Diffraction. *Acta Chem. Scand.* **1997,** *51,* 249–258.
25. Liu, H.; Grendal, O. G.; Skjærvø, S. L.; Dalod, A. R. M.; van Beek, W.; Sekkat, A.; Einarsrud, M.-A.; Muñoz-Rojas, D. Reaction Pathway of the Hydrothermal Synthesis of $AgCuO_2$ from In Situ Time-Resolved X-Ray Diffraction. *Cryst. Growth Des.* **2020,** *20* (7), 4264–4272.
26. Fujita, T.; Kasai, H.; Nishibori, E. Hydrothermal Reactor for In-Situ Synchrotron Radiation Powder Diffraction at SPring-8 BL02B2 for Quantitative Design for Nanoparticle. *J. Supercrit. Fluids* **2019,** *147,* 172–178.
27. Fujita, T.; Kasai, H.; Nishibori, E. Ion Product Scale for Phase and Size Selective Crystal Growth of Zirconia Nanoparticles. *Cryst. Growth Des.* **2020,** *20* (8), 5589–5595.
28. Yoko, A.; Akizuki, M.; Hirao, N.; Kohara, S.; Kumar, M.; Umezawa, N.; Ohno, T.; Oshima, Y. In Situ X-Ray Diffraction for Millisecond-Order Dynamics of $BaZrO_3$ Nanoparticle Formation in Supercritical Water. *J. Supercrit. Fluids* **2016,** *107,* 746–752.
29. Becker, J.; Bremholm, M.; Tyrsted, C.; Pauw, B.; Jensen, K. M. O.; Eltzholt, J.; Christensen, M.; Iversen, B. B. Experimental Setup for In Situ X-Ray SAXS/WAXS/PDF Studies of the Formation and Growth of Nanoparticles in Near- and Supercritical Fluids. *J. Appl. Cryst.* **2010,** *43* (4), 729–736.
30. Mi, J.-L.; Christensen, M.; Tyrsted, C.; Jensen, K. M.Ø.; Becker, J.; Hald, P.; Iversen, B. B. Formation and Growth of Bi_2Te_3 in Biomolecule-Assisted Near-Critical Water: In Situ Synchrotron Radiation Study. *J. Phys. Chem. C* **2010,** *114* (28), 12133–12138.
31. Ok, K. M.; Lee, D. W.; Smith, R. I.; O'Hare, D. Time-Resolved In Situ Neutron Diffraction Under Supercritical Hydrothermal Conditions: A Study of the Synthesis of $KTiOPO_4$. *J. Am. Chem. Soc.* **2012,** *134* (43), 17889–17891.
32. Andersen, H. L.; Christensen, M. In Situ Powder X-Ray Diffraction Study of Magnetic $CoFe_2O_4$ Nanocrystallite Synthesis. *Nanoscale* **2015,** *7* (8), 3481–3490.
33. Granados-Miralles, C.; Saura-Múzquiz, M.; Bøjesen, E. D.; Jensen, K. M.Ø.; Andersen, H. L.; Christensen, M. Unraveling Structural and Magnetic Information during growth of Nanocrystalline $SrFe1_2O19$. *J. Mater. Chem. C* **2016,** *4* (46), 10903–10913.

34. Beale, A. M.; van der Eerden, A. M. J.; Jacques, S. D. M.; Leynaud, O.; O'Brien, M. G.; Meneau, F.; Nikitenko, S.; Bras, W.; Weckhuysen, B. M. A Combined SAXS/WAXS/XAFS Setup Capable of Observing Concurrent Changes Across the Nano-to-Micrometer Size Range in Inorganic Solid Crystallization Processes. *J. Am. Chem. Soc.* **2006,** *128* (38), 12386–12387.
35. Shen, X.-F.; Ding, Y.-S.; Hanson, J. C.; Aindow, M.; Suib, S. L. In Situ Synthesis of Mixed-Valent Manganese Oxide Nanocrystals: An In Situ Synchrotron X-Ray Diffraction Study. *J. Am. Chem. Soc.* **2006,** *128* (14), 4570–4571.
36. Marshall, K. P.; Blichfeld, A. B.; Skjærvø, S. L.; Grendal, O. G.; van Beek, W.; Selbach, S. M.; Grande, T.; Einarsrud, M.-A.; Fast, A. Low-Temperature Synthesis Method for Hexagonal $YMnO_3$: Kinetics, Purity, Size and Shape as Studied by in Situ X-Ray Diffraction. *Chem. A Eur. J.* **2020,** *26,* 1–9.
37. Nørby, P.; Roelsgaard, M.; Søndergaard, M.; Iversen, B. B. Hydrothermal Synthesis of $CoSb_2O_4$: In Situ Powder X-Ray Diffraction, Crystal Structure, and Electrochemical Properties. *Cryst. Growth Des.* **2016,** *16* (2), 834–841.
38. Francis, R. J.; O'Brien, S.; Fogg, A. M.; Halasyamani, P. S.; O'Hare, D.; Loiseau, T.; Ferey, G. Time-Resolved In-Situ Energy and Angular Dispersive X-Ray Diffraction Studies of the Formation of the Microporous Gallophosphate ULM-5 Under Hydrothermal Conditions. *J. Am. Chem. Soc.* **1999,** *121* (5), 1002–1015.
39. Grendal, O. G.; Blichfeld, A. B.; Skjærvø, S. L.; van Beek, W.; Selbach, S. M.; Grande, T.; Einarsrud, M.-A. Facile Low Temperature Hydrothermal Synthesis of $BaTiO_3$ Nanoparticles Studied by In Situ X-Ray Diffraction. *Crystals* **2018,** *8* (6), 253.
40. Munn, J.; Barnes, P.; Axon, S. A.; Klinowski, J. In-Situ Studies of the Hydrothermal Synthesis of Zeolites Using Synchrotron Energy-Dispersive X-Ray Diffraction. *Phase Transit.* **1992,** *39* (1–4), 129–134.
41. He, H.; Barnes, P.; Munn, J.; Turrillas, X.; Klinowski, J. Autoclave Synthesis and Thermal Transformations of the Aluminophosphate Molecular Sieve VPI-5: An In Situ X-Ray Diffraction Study. *Chem. Phys. Lett.* **1992,** *196* (3–4), 267–273.
42. Moorhouse, S. J.; Vranje, N.; Jupe, A.; Drakopoulos, M.; O'Hare, D. The Oxford-Diamond In Situ Cell for Studying Chemical Reactions Using Time-Resolved X-Ray Diffraction. *Rev. Sci. Instrum.* **2012,** *83* (8).
43. Cahill, C. L.; Benning, L. G.; Barnes, H. L.; Parise, J. B. In Situ Time-Resolved X-Ray Diffraction of Iron Sulfides During Hydrothermal Pyrite Growth. *Chem. Geol.* **2000,** *167* (1–2), 53–63.
44. Walton, R. I.; Smith, R. I.; O'Hare, D. Following the Hydrothermal Crystallisation of Zeolites Using Time-Resolved In Situ Powder Neutron Diffraction. *Microporous Mesoporous Mater.* **2001,** *48* (1–3), 79–88.
45. Grandjean, D.; Beale, A. M.; Petukhov, A. V.; Weckhuysen, B. M. Unraveling the Crystallization Mechanism of CoAPO-5 Molecular Sieves under Hydrothermal Conditions. *J. Am. Chem. Soc.* **2005,** *127,* 14454–14465.
46. Beale, A. M.; O'Brien, M. G.; Kasunič, M.; Golobič, A.; Sanchez-Sanchez, M.; Lobo, A. J. W.; Lewis, D. W.; Wragg, D. S.; Nikitenko, S.; Bras, W.; Weckhuysen, B. M. Probing ZnAPO-34 Self-Assembly Using Simultaneous Multiple In Situ Techniques. *J. Phys. Chem. C* **2011,** *115* (14), 6331–6340.
47. Walton, R. I.; Norquist, A.; Smith, R. I.; O'Hare, D. Recent Results from the In Situ Study of Hydrothermal Crystallisations Using Time-Resolved X-Ray and Neutron Diffraction Methods. *Faraday Discuss.* **2002,** *122,* 331–341.
48. Kiebach, R.; Pienack, N.; Bensch, W.; Grunwaldt, J.-D.; Michailovski, A.; Baiker, A.; Fox, T.; Zhou, Y.; Patzke, G. R. Hydrothermal Formation of W/Mo-Oxides: A Multi-disciplinary Study of Growth and Shape. *Chem. Mater.* **2008,** *20* (9), 3022–3033.
49. Engelke, L.; Schaefer, M.; Schur, M.; Bensch, W. In Situ X-Ray Diffraction Studies of the Crystallization of Layered Manganese Thioantimonates(III) Under Hydrothermal Conditions. *Chem. Mater.* **2001,** *13,* 1383–1390.
50. Engelke, L.; Schaefer, M.; Porsch, F.; Bensch, W. In-Situ Energy-Dispersive X-Ray Diffraction Studies of Crystal Growth and Compound Conversion Under Solvothermal Conditions. *Eur. J. Inorg. Chem.* **2003**, (3), 506–513.
51. Zhou, Y.; Pienack, N.; Bensch, W.; Patzke, G. R. The Interplay of Crystallization Kinetics and Morphology in Nanostructured W/Mo Oxide Formation: An In Situ Diffraction Study. *Small* **2009,** *5* (17), 1978–1983.
52. Zhou, Y.; Antonova, E.; Bensch, W.; Patzke, G. R. In Situ X-Ray Diffraction Study of the Hydrothermal Crystallization of Hierarchical Bi_2WO_6 Nanostructures. *Nanoscale* **2010,** *2* (11), 2412–2417.
53. Zhou, Y.; Antonova, E.; Lin, Y.; Grunwaldt, J.-D.; Bensch, W.; Patzke, G. R. In Situ X-Ray Absorption Spectroscopy/Energy-Dispersive X-Ray Diffraction Studies on the Hydrothermal Formation of $Bi_2W_{1-x}Mo_xO_6$ Nanomaterials. *Eur. J. Inorg. Chem.* **2012,** *2012* (5), 783–789.
54. Cook, D. S.; Wu, Y.; Lienau, K.; Moré, R.; Kashtiban, R. J.; Magdysyuk, O. V.; Patzke, G. R.; Walton, R. I. Time-Resolved Powder X-Ray Diffraction of the Solvothermal Crystallization of Cobalt Gallate Spinel Photocatalyst Reveals Transient Layered Double Hydroxides. *Chem. Mater.* **2017,** *29* (12), 5053–5057.
55. Reith, L.; Lienau, K.; Cook, D. S.; Moré, R.; Walton, R. I.; Patzke, G. R. Monitoring the Hydrothermal Growth of Cobalt Spinel Water Oxidation Catalysts: From Preparative History to Catalytic Activity. *Chem. A Eur. J.* **2018,** *24* (69), 18424–18435.
56. Billinge, S. J. L.; Dinnebier, R. E. *Powder Diffraction: Theory and Practice*, RSC Publishing: Cambridge, 2008.
57. Marschilok, A. C.; Bruck, A. M.; Abraham, A.; Stackhouse, C. A.; Takeuchi, K. J.; Takeuchi, E. S.; Croft, M.; Gallaway, J. W. Energy Dispersive X-Ray Diffraction (EDXRD) for Operando Materials Characterization Within Batteries. *Phys. Chem. Chem. Phys.* **2020,** *22* (37), 20972–20989.
58. Norby, P.; Nørlund Christensen, A.; Hanson, J. C. In Situ Studies of Zeolite Syntheses Using Powder Diffraction Methods. Crystallization of "Instant Zeolite A" Powder and Synthesis of CoAPO-5. *Stud. Surf. Sci. Catal.* **1994,** *84,* 179–186.
59. Norby, P. Hydrothermal Conversion of Zeolites: An In Situ Synchrotron X-Ray Powder Diffraction Study. *J. Am. Chem. Soc.* **1997,** *119,* 5215–5221.
60. Topsøe, H. Developments in Operando Studies and In Situ Characterization of Heterogeneous Catalysts. *J. Catal.* **2003,** *216,* 155–164.
61. Gualtieri, A. F.; Norby, P.; Artioli, G.; Hanson, J. C. Kinetics of Formation of Zeolite Na-A [LTA] From Natural Kaolinites. *Phys. Chem. Minerals* **1997,** *24,* 191–199.
62. Norby, P.; Hanson, J. C. Hydrothermal Synthesis of the Microporous Aluminophosphate CoAPO-5; In Situ Time-Resolved Synchrotron X-Ray Powder Diffraction Studies. *Catal. Today* **1998,** *39* (4), 301–309.
63. Christensen, A. N.; Norby, P.; Hanson, J. C. Chemical Rections in the System MgO-$MgCl_2$-H_2O Followed by Time-Resolved Synchrotron X-Ray Powder Diffraction. *J. Solid State Chem.* **1995,** *114,* 556–559.
64. Nørlund Christensen, A.; Norby, P.; Hanson, J. C. Time-Resolved Synchrotron X-Ray Powder Diffraction Study on Samples from the System MgO-MgCl2-H_2O. *Acta Chem. Scand.* **1995,** *49,* 331–334.
65. Xia, F.; Chen, D.; Scarlett, N. V. Y.; Madsen, I. C.; Lau, D.; Leoni, M.; Ilavsky, J.; Brand, H. E. A.; Caruso, R. A. Understanding Solvothermal Crystallization of Mesoporous Anatase Beads by In Situ Synchrotron PXRD and SAXS. *Chem. Mater.* **2014,** *26* (15), 4563–4571.
66. Song, J.; Xia, F.; Zhao, M.; Zhong, Y. L.; Li, W.; Loh, K. P.; Caruso, R. A.; Bao, Q. Solvothermal Growth of Bismuth Chalcogenide Nanoplatelets by the Oriented Attachment Mechanism: An In Situ PXRD Study. *Chem. Mater.* **2015,** *27* (9), 3471–3482.
67. Li, W.; Chen, D.; Xia, F.; Tan, J. Z. Y.; Song, J.; Song, W.-G.; Caruso, R. A. Flowerlike WS_2 and WS_2 Microspheres: One-Pot Synthesis, Formation Mechanism and Application in Heavy Metal Ion Sequestration. *Chem. Commun.* **2016,** *52* (24), 4481–4484.
68. Tyrsted, C.; Becker, J.; Hald, P.; Bremholm, M.; Pedersen, J. S.; Chevalier, J.; Cerenius, Y.; Iversen, S. B.; Iversen, B. B. In-Situ Synchrotron Radiation Study of Formation and Growth of Crystalline CexZr1-xO_2 Nanoparticles Synthesized in Supercritical Water. *Chem. Mater.* **2010,** *22* (5), 1814–1820.
69. Jensen, K. M.Ø.; Christensen, M.; Tyrsted, C.; Iversen, B. B. Real-Time Synchrotron Powder X-Ray Diffraction Study of the Antisite Defect Formation During Sub- and Supercritical Synthesis of $LiFePO_4$ and $LiFe_{1-x}Mn_xPO_4$ Nanoparticles. *J. Appl. Cryst.* **2011,** *44* (2), 287–294.
70. Laumann, A.; Jensen, K. M.Ø.; Tyrsted, C.; Bremholm, M.; Fehr, K. T.; Holzapfel, M.; Iversen, B. B.; Jensen, K. M.Ø.; Tyrsted, C.; Bremholm, M.; Fehr, K. T.; Holzapfel, M.; Iversen, B. B. In-Situ Synchrotron X-Ray Diffraction Study of the Formation of Cubic Li_2TiO_3 Under Hydrothermal Conditions. *Eur. J. Inorg. Chem.* **2011,** *2011* (14), 2221–2226.

71. Mi, J.-L.; Jensen, T. N.; Christensen, M.; Tyrsted, C.; Jørgensen, J.-E.; Iversen, B. B. High-Temperature and High-Pressure Aqueous Solution Formation, growth, Crystal Structure, and Magnetic Properties of $BiFeO_3$ Nanocrystals. *Chem. Mater.* **2011,** *23* (5), 1158–1165.
72. Jensen, K. M.Ø.; Christensen, M.; Tyrsted, C.; Bremholm, M.; Iversen, B. B. Structure, Size, and Morphology Control of Nanocrystalline Lithium Cobalt Oxide. *Cryst. Growth Des.* **2011,** *11* (3), 753–758.
73. Mi, J.-L.; Clausen, C.; Bremholm, M.; Lock, N.; Jensen, K. M.Ø.; Christensen, M.; Iversen, B. B. Rapid Hydrothermal Preparation of Rutile TiO_2 Nanoparticles by Simultaneous Transformation of Primary Brookite and Anatase: An In Situ Synchrotron PXRD Study. *Cryst. Growth Des.* **2012,** *12* (12), 6092–6097.
74. Mamakhel, A. H.; Tyrsted, C.; Bøjesen, E. D.; Hald, P.; Iversen, B. B. Direct Formation of Crystalline Phase Pure Rutile TiO_2 Nanostructures by a Facile Hydrothermal Method. *Cryst. Growth Des.* **2013,** *13* (11), 4730–4734.
75. Nørby, P.; Jensen, K. M.Ø.; Lock, N.; Christensen, M.; Iversen, B. B. In Situ Synchrotron Powder X-Ray Diffraction Study of Formation and growth of Yttrium and Ytterbium Aluminum Garnet Nanoparticles in Sub- and Supercritical Water. *RSC Adv.* **2013,** *3* (35), 15368–15374.
76. Philippot, G.; Jensen, K. M.Ø.; Christensen, M.; Elissalde, C.; Maglione, M.; Iversen, B. B.; Aymonier, C. Coupling In Situ Synchrotron Radiation with Ex Situ Spectroscopy Characterizations to Study the Formation of $Ba_{1-x}Sr_xTiO_3$ Nanoparticles in Supercritical Fluids. *J. Supercrit. Fluids* **2014,** *87,* 111–117.
77. Bøjesen, E. D.; Jensen, K. M.Ø.; Tyrsted, C.; Lock, N.; Christensen, M.; Iversen, B. B. In Situ Powder Diffraction Study of the Hydrothermal Synthesis of ZnO Nanoparticles. *Cryst. Growth Des.* **2014,** *14* (6), 2803–2810.
78. Nørby, P.; Johnsen, S.; Iversen, B. B. In Situ X-Ray Diffraction Study of the Formation, Growth, and Phase Transition of Colloidal $Cu_{2-x}S$ Nanocrystals. *ACS Nano* **2014,** *8* (5), 4295–4303.
79. Houlberg, K.; Bøjesen, E. D.; Tyrsted, C.; Mamakhel, A. H.; Wang, X.; Su, R.; Besenbacher, F.; Iversen, B. B. Hydrothermal Synthesis and In Situ Powder X-Ray Diffraction Study of Bismuth-Substituted Ceria Nanoparticles. *Cryst. Growth Des.* **2015,** *15* (8), 3628–3636.
80. Andersen, H. L.; Bøjesen, E. D.; Birgisson, S.; Christensen, M.; Iversen, B. B. Pitfalls and Reproducibility of In Situ Synchrotron Powder X-Ray Diffraction Studies of Solvothermal Nanoparticle Formation. *J. Appl. Cryst.* **2018,** *51* (2), 526–540.
81. Sommer, S.; Bøjesen, E. D.; Reardon, H.; Iversen, B. B. Atomic Scale Design of Spinel $ZnAl_2O_4$ Nanocrystal Synthesis. *Cryst. Growth Des.* **2020,** *20* (3), 1789–1799.
82. Lock, N.; Christensen, M.; Jensen, K. M.Ø.; Iversen, B. B. Rapid One-Step Low-Temperature Synthesis of Nanocrystalline γ-Al_2O_3. *Angew. Chem. Int. Ed.* **2011,** *50* (31), 7045–7047.
83. Skjærvø, S. L.; Sommer, S.; Nørby, P.; Bøjesen, E. D.; Grande, T.; Iversen, B. B.; Einarsrud, M.-A. Formation Mechanism and Growth of $MNbO_3$, M=K, Na by In Situ X-Ray Diffraction. *J. Am. Ceram. Soc.* **2017,** *100* (9), 3835–3842.
84. Skjærvø, S. L.; Wells, K. H.; Sommer, S.; Vu, T.-D.; Tolchard, J. R.; van Beek, W.; Grande, T.; Iversen, B. B.; Einarsrud, M.-A. Rationalization of Hydrothermal Synthesis of $NaNbO_3$ by Rapid In Situ Time-Resolved Synchrotron X-Ray Diffraction. *Cryst. Growth Des.* **2018,** *18* (2), 770–774.
85. Skjærvø, S. L.; Wells, K. H.; Beek, W.v.; Grande, T.; Einarsrud, M.-A. Kinetics during Hydrothermal Synthesis of Nanosized $KNa_{1-x}NbO_3$. *CrstEngComm* **2018,** *20,* 6795–6802.
86. Norby, P. In-Situ XRD as a Tool to Understanding Zeolite Crystallization. *Curr. Opin. Colloid Interface Sci.* **2006,** *11* (2–3), 118–125.
87. Bremholm, M.; Jensen, H.; Iversen, S. B.; Iversen, B. B. Reactor Design for In Situ X-Ray Scattering Studies of Nanoparticle Formation in Supercritical Water Syntheses. *J. Supercrit. Fluids* **2008,** *44* (3), 385–390.
88. Jensen, T. R.; Nielsen, T. K.; Filinchuk, Y.; Jorgensen, J. E.; Cerenius, Y.; Gray, E. M.; Webb, C. J. Versatile In Situ Powder X-Ray Diffraction Cells for Solid-Gas Investigations. *J. Appl. Cryst.* **2010,** *43,* 1456–1463.
89. Chupas, P. J.; Chapman, K. W.; Kurtz, C.; Hanson, J. C.; Lee, P. L.; Grey, C. P. A Versatile Sample-Environment Cell for Non-ambient X-Ray Scattering Experiments. *J. Appl. Cryst.* **2008,** *41,* 822–824.
90. Reinsch, H.; Stock, N. Formation and Characterisation of Mn-MIL-100. *CrstEngComm* **2013,** *15* (3), 544–550.
91. Feyand, M.; Nather, C.; Rothkirch, A.; Stock, N. Systematic and In Situ Energy Dispersive X-Ray Diffraction Investigations on the Formation of Lanthanide Phosphonatobutanesulfonates: Ln(O3P-C4H8-SO3)(H2O) (Ln = La-Gd). *Inorg. Chem.* **2010,** *49* (23), 11158–11163.
92. Moorhouse, S. J.; Wu, Y.; Buckley, H. C.; O'Hare, D. Time-Resolved In Situ Powder X-Ray Diffraction Reveals the Mechanisms of Molten Salt Synthesis. *Chem. Commun.* **2016,** *52,* 13865.
93. Lock, N.; Bremholm, M.; Christensen, M.; Almer, J.; Chen, Y.-S.; Iversen, B. B. In Situ High-Energy Synchrotron Radiation Study of Boehmite Formation, Growth, and Phase Transformation to Alumina in Sub- and Supercritical Water. *Chem. A Eur. J.* **2009,** *15* (48), 13381–13390.
94. Bremholm, M.; Felicissimo, M.; Iversen, B. B. Time-Resolved In Situ Synchrotron X-Ray Study and Large-Scale Production of Magnetite Nanoparticles in Supercritical Water. *Angew. Chem. Int. Ed.* **2009,** *48* (26), 4788–4791.
95. Eltzholtz, J.; Tyrsted, C.; Jensen, K. M.Ø.; Bremholm, M.; Christensen, M.; Becker-Christensen, J.; Iversen, B. B. Pulsed Supercritical Synthesis of Anatase TiO_2 Nanoparticles in a Water–Isopropanol Mixture Studied by In Situ Powder X-Ray Diffraction. *Nanoscale* **2013,** *5* (6), 2372–2378.
96. Breeze, M. I.; Clarkson, G. J.; Millange, F.; O'Hare, D.; Walton, R. I. Crystal Growth Exchange of Coordinated Solvent during Crystallization of a Metal-Organic Framework Observed by In Situ High-Energy X-Ray Diffraction. *Angew. Chem. Int. Ed.* **2016,** *55,* 4992–4996.
97. Yeung, H. H. M.; Wu, Y.; Henke, S.; Cheetham, A. K.; O'Hare, D.; Walton, R. I. In Situ Observation of Successive Crystallizations and Metastable Intermediates in the Formation of Metal-Organic Frameworks. *Angew. Chem. Int. Ed.* **2016,** *55* (6), 2012–2016.
98. Evans, J. S. O.; Francis, R. J.; O'Hare, D.; Price, S. J.; Clark, S. M. An Apparatus for the Study of the Kinetics and Mechanism of Hydrothermal Reactions by In Situ Energy Dispersive X-Ray Diffraction. *Rev. Sci. Instrum.* **1995,** *66* (3), 2442–2445.
99. Walton, R. I.; Francis, R. J.; Halasyamani, P. S.; O'Hare, D.; Smith, R. I.; Done, R.; Humphreys, R. J. Novel Apparatus for the In Situ Study of Hydrothermal Crystallizations Using Time-Resolved Neutron Diffraction. *Rev. Sci. Instrum.* **1999,** *70* (8), 3391–3396.
100. O'Neill, B.; Tenailleau, C.; Nogthai, Y.; Studer, A.; Brugger, J.; Pring, A. A Flow-through Hydrothermal Cell for In Situ Neutron Diffraction Studies of Phase Transformations. *Physica B Condens. Matter* **2006,** *385–386,* 942–945.
101. Ok, K. M.; O'Hare, D.; Smith, R. I.; Chowdhury, M.; Fikremariam, H. New Large Volume Hydrothermal Reaction Cell for Studying Chemical Processes Under Supercritical Hydrothermal Conditions Using Time-Resolved In Situ Neutron Diffraction. *Rev. Sci. Instrum.* **2010,** *81* (12), 125107.
102. Xia, F.; Qian, G.; Brugger, J.; Studer, A.; Olsen, S.; Pring, A. A Large Volume Cell for In Situ Neutron Diffraction Studies of Hydrothermal Crystallizations. *Rev. Sci. Instrum.* **2010,** *81* (10), 105107.
103. Xia, F.; Ngothai, Y.; Peak, J.; Tenailleau, C.; Etschmann, B.; Qian, G.; Brugger, J.; Studer, A.; Olsen, S.; Pring, A. A Thermosyphon-Driven Hydrothermal Flow-through Cell for In Situ and Time-Resolved Neutron Diffraction Studies. *J. Appl. Cryst.* **2010,** *43* (3), 511–519.
104. Xia, F.; Brugger, J.; Qian, G.; Ngothai, Y.; O'Neill, B.; Zhao, J.; Pullen, S.; Olsen, S.; Pring, A. Single-Pass Flow-through Reaction Cell for High-Temperature and High-Pressure In Situ Neutron Diffraction Studies of Hydrothermal Crystallization Processes. *J. Appl. Cryst.* **2012,** *45,* 166–173.
105. Walton, R. I.; Millange, F.; Smith, R. I.; Hansen, T. C.; O'Hare, D. Real Time Observation of the Hydrothermal Crystallization of Barium Titanate Using In Situ Neutron Powder Diffraction. *J. Am. Chem. Soc.* **2001,** *123* (50), 12547–12555.
106. Walton, R. I.; Millange, F.; O'Hare, D.; Davies, A. T.; Sankar, G.; Catlow, C. R. A. An In Situ Energy-Dispersive X-Ray Diffraction Study of the Hydrothermal Crystallization of Zeolite A. 1. Influence of Reaction Conditions and Transformation into Sodalite. *J. Phys. Chem. B* **2001,** *105* (1), 83–90.
107. Ibsen, C. J. S.; Birkedal, H. Influence of Poly(Acrylic Acid) on Apatite Formation Studied by In Situ X-Ray Diffraction Using an X-Ray Scattering Reaction Cell With High-Precision Temperature Control. *J. Appl. Cryst.* **2012,** *45* (5), 976–981.
108. Lindén, M.; Schunk, S. A.; Schüth, F. In Situ X-Ray Diffraction Study of the Initial Stages of Formation of MCM-41 in a Tubular Reactor. *Angew. Chem. Int. Ed.* **1998,** *37* (6), 821–823.

109. Polte, J.; Erler, R.; Thünemann, A. F.; Sokolov, S.; Ahner, T. T.; Rademann, K.; Emmerling, F.; Kraehnert, R. Nucleation and Growth of Gold Nanoparticles Studied Via In Situ Small Angle X-Ray Scattering at Millisecond Time Resolution. *ACS Nano* **2010,** *4* (2), 1076–1082.
110. Taddei, M.; Casati, N.; Steitz, D. A.; Dümbgen, K. C.; van Bokhoven, J. A.; Ranocchiari, M. In Situ High-Resolution Powder X-Ray Diffraction Study of UiO-66 Under Synthesis Conditions in a Continuous-Flow Microwave Reactor. *CrstEngComm* **2017,** *19* (23), 3206–3214.
111. Ghazal, A.; Lafleur, J. P.; Mortensen, K.; Kutter, J. P.; Arleth, L.; Jensen, G. V. Recent Advances in X-Ray Compatible Microfluidics for Applications in Soft Materials and Life Sciences. *Lab Chip* **2016,** *16* (22), 4263–4295.
112. Karim, A. M.; Al Hasan, N.; Ivanov, S.; Siefert, S.; Kelly, R. T.; Hallfors, N. G.; Benavidez, A.; Kovarik, L.; Jenkins, A.; Winans, R. E.; Datye, A. K. Synthesis of 1 Nm Pd Nanoparticles in a Microfluidic Reactor: Insights from In Situ X-Ray Absorption Fine Structure Spectroscopy and Small-Angle X-Ray Scattering. *J. Phys. Chem. C* **2015,** *119* (23), 13257–13267.
113. Modeshia, D. R.; Darton, R. J.; Ashbrook, S. E.; Walton, R. I. Control of Polymorphism in $NaNbO_3$ by Hydrothermal Synthesis. *Chem. Commun.* **2009**, (1), 68–70.
114. Beale, A. M.; Reilly, L. M.; Sankar, G. Watching the Crystallisation of Complex Oxides by In Situ X-Ray Techniques. *Appl. Catal., A* **2007,** *325* (2), 290–295.
115. Feyand, M.; Hubner, A.; Rothkirch, A.; Wragg, D. S.; Stock, N. Copper Phosphonatoethanesulfonates: Temperature Dependent In Situ Energy Dispersive X-Ray Diffraction Study and Influence of the pH on the Crystal Structures. *Inorg. Chem.* **2012,** *51* (22), 12540–12547.
116. Pienack, N.; Nather, C.; Bensch, W. Solvothermal Syntheses of Two New Thiostannates and an In-Situ Energy Dispersive X-Ray Scattering Study of Their Formation. *Eur. J. Inorg. Chem.* **2009**, (7), 937–946.
117. Du, Y.; Ok, K. M.; O'Hare, D. A Kinetic Study of the Phase Conversion of Layered Cobalt Hydroxides. *J. Mater. Chem.* **2008,** *18* (37), 4450–4459.
118. Feyand, M.; Koppen, M.; Friedrichs, G.; Stock, N. Bismuth tri- and Tetraarylcarboxylates: Crystal Structures, In Situ X-Ray Diffraction, Intermediates and Luminescence. *Chem. A Eur. J.* **2013,** *19* (37), 12537–12546.
119. Millange, F.; Medina, M. I.; Guillou, N.; Ferey, G.; Golden, K. M.; Walton, R. I. Time-Resolved In Situ Diffraction Study of the Solvothermal Crystallization of Some Prototypical Metal-Organic Frameworks. *Angew. Chem. Int. Ed.* **2010,** *49* (4), 763–766.
120. Geselbracht, M. J.; Noailles, L. D.; Ngo, L. T.; Pikul, J. H.; Walton, R. I.; Cowell, E. S.; Millange, F.; O'Hare, D. Probing Molten Salt Flux Reactions Using Time-Resolved In Situ High-Temperature Powder X-Ray Diffraction: A New Synthesis Route to the Mixed-Valence $NaTi_2O_4$. *Chem. Mater.* **2004,** *16* (6), 1153–1159.
121. Chen, J.; Bai, J.; Chen, H.; Graetz, J. In Situ Hydrothermal Synthesis of $LiFePO_4$ Studied by Synchrotron X-Ray Diffraction. *J. Phys. Chem. Lett.* **2011,** *2* (15), 1874–1878.
122. Norquist, A. J.; O'Hare, D. Kinetic and Mechanistic Investigations of Hydrothermal Transformations in Zinc Phosphates. *J. Am. Chem. Soc.* **2004,** *126* (21), 6673–6679.
123. Williams, G. R.; Norquist, A. J.; O'Hare, D. Incorporation of Li into MnOOH: An In Situ X-Ray and Neutron Diffraction Study. *Chem. Mater.* **2006,** *18* (16), 3801–3807.
124. Mitchell, S.; Biswick, T.; Jones, W.; Williams, G.; O'Hare, D. A Synchrotron Radiation Study of the Hydrothermal Synthesis of Layered Double Hydroxides from MgO and Al_2O_3 Slurries. *Green Chem.* **2007,** *9* (4), 373–378.
125. Kiebach, R.; Pienack, N.; Ordolff, M. E.; Studt, F.; Bensch, W. Combined In Situ EDXRD/EXAFS Investigation of the Crystal growth of [Co(C6H18N4)][Sb2S4] Under Solvothermal Conditions: Two Different Reaction Pathways Leading to the Same Product. *Chem. Mater.* **2006,** *18* (5), 1196–1205.
126. Laumann, A.; Jensen, K. M.Ø.; Tyrsted, C.; Bremholm, M.; Fehr, K. T.; Holzapfel, M.; Iversen, B. B. In-Situ Synchrotron X-Ray Diffraction Study of the Formation of Cubic Li(2) TiO(3) under Hydrothermal Conditions. *Eur. J. Inorg. Chem.* **2011**, (14), 2221–2226.
127. Oh, S.-J.; Lim, S.-J.; You, T.-S.; Ok, K. M. From a Metastable Layer to a Stable Ring: A Kinetic Study for Transformation Reactions of $Li_2Mo_3TeO_{12}$ to Polyoxometalates. *Chem. A Eur. J.* **2018,** *24* (26), 6712–6716.
128. Lin, M.-Y.; Chen, Y.-H.; Lee, J.-J.; Sheu, H.-S. Reaction Pathways of Iron-Sulfide Mineral Formation: An In Situ X-Ray Diffraction Study. *Eur. J. Mineral.* **2018,** *30,* 77–84.
129. Cravillon, J.; Schroder, C. A.; Bux, H.; Rothkirch, A.; Caro, J.; Wiebcke, M. Formate Modulated Solvothermal Synthesis of ZIF-8 Investigated Using Time-Resolved In Situ X-Ray Diffraction and Scanning Electron Microscopy. *CrstEngComm* **2012,** *14* (2), 492–498.
130. Millange, F.; El Osta, R.; Medina, M. E.; Walton, R. I. A Time-Resolved Diffraction Study of a Window of Stability in the Synthesis of a Copper Carboxylate Metal-Organic Framework. *CrstEngComm* **2011,** *13* (1), 103–108.
131. Antonova, E.; Seidlhofer, B.; Wang, J.; Hinz, M.; Bensch, W. Controlling Nucleation and Crystal Growth of a Distinct Polyoxovanadate Cluster: An In Situ Energy Dispersive X-Ray Diffraction Study Under Solvothermal Conditions. *Chem. A Eur. J.* **2012,** *18* (48), 15316–15322.
132. El Osta, R.; Frigoli, M.; Marrot, J.; Medina, M. E.; Walton, R. I.; Millange, F. Synthesis, Structure, and Crystallization Study of a Layered Lithium Thiophene-Dicarboxylate. *Cryst. Growth Des.* **2012,** *12* (3), 1531–1537.
133. El Osta, R.; Feyand, M.; Stock, N.; Millange, F.; Walton, R. I. Crystallisation Kinetics of Metal Organic Frameworks From In Situ Time-Resolved X-Ray Diffraction. *Powder Diffr.* **2013,** *28,* S256–S275.
134. Latroche, M.; Surble, S.; Serre, C.; Mellot-Draznieks, C.; Llewellyn, P. L.; Lee, J. H.; Chang, J. S.; Jhung, S. H.; Ferey, G. Hydrogen Storage in the Giant-Pore Metal-Organic Frameworks MIL-100 and MIL-101. *Angew. Chem. Int. Ed.* **2006,** *45* (48), 8227–8231.
135. Zhao, H. Y.; Chupas, P. J.; Chapman, K. W. Fast Time-Resolved Pair Distribution Function Studies of Supported Gold Nanoparticle Formation. *Z. Kristallogr* **2012,** *227* (5), 268–271.
136. Matsui, K.; Kikuma, J.; Tsunashima, M.; Ishikawa, T.; Matsuno, S. Y.; Ogawa, A.; Sato, M. In Situ Time-Resolved X-Ray Diffraction of Tobermorite Formation in Autoclaved Aerated Concrete: Influence of Silica Source Reactivity and Al Addition. *Cem. Concr. Res.* **2011,** *41* (5), 510–519.
137. Mi, J.-L.; Nørby, P.; Bremholm, M.; Iversen, B. B. Insight into Nucleation and Growth of $Bi_{2-x}Sb_xTe_3$ (x = 0–2) Nanoplatelets in Hydrothermal Synthesis. *Chem. Mater.* **2017,** *29* (12), 5070–5079.
138. Bremholm M, Becker-Christensen J, and Iversen BB (2009) High-pressure, high-temperature formation of phase-pure monoclinic zirconia nanocrystals studied by time-resolved in situ synchrotron X-ray diffraction. Adv. Mater. 21 (35), 3572–3575.
139. Tyrsted, C.; Jensen, K. M.Ø.; Bøjesen, D. B.; Lock, N.; Christensen, M.; Billinge, S. J. L.; Iversen, B. B. Understanding the Formation and Evolution of Ceria Nanoparticles Under Hydrothermal Conditions. *Angew. Chem. Int. Ed.* **2012,** *51.*
140. Jensen, K. M.Ø.; Christensen, M.; Juhas, P.; Tyrsted, C.; Bojesen, E. D.; Lock, N.; Billinge, S. J. L.; Iversen, B. B. Revealing the Mechanisms behind SnO_2 Nanoparticle Formation and Growth during Hydrothermal Synthesis: An In Situ Total Scattering Study. *J. Am. Chem. Soc.* **2012,** *134* (15), 6785–6792.
141. Tyrsted, C.; Pauw, B. R.; Jensen, K. M.Ø.; Becker, J.; Christensen, M.; Iversen, B. B. Watching Nanoparticles Form: An In Situ (Small-/Wide-Angle X-Ray Scattering/Total Scattering) Study of the Growth of Yttria-Stabilised Zirconia in Supercritical Fluids. *Chem. A Eur. J.* **2012,** *18* (18), 5759–5766.
142. Jensen, G. V.; Bremholm, M.; Lock, N.; Deen, G. R.; Jensen, T. R.; Iversen, B. B.; Niederberger, M.; Pedersen, J. S.; Birkedal, H. Anisotropic Crystal Growth Kinetics of Anatase TiO_2 Nanoparticles Synthesized in a Nonaqueous Medium. *Chem. Mater.* **2010,** *22* (22), 6044–6055.
143. Scardi, P.; Leoni, M. Line Profile Analysis: Pattern Modelling Versus Profile Fitting. *J. Appl. Cryst.* **2006,** *39,* 24–31.
144. Leoni, M.; Scardi, P. Nanocrystalline Domain Size Distributions From Powder Diffraction Data. *J. Appl. Cryst.* **2004,** *37,* 629–634.
145. Andersen, H. L.; Jensen, K. M.Ø.; Tyrsted, C.; Bøjesen, E. D.; Christensen, M. Size and Size Distribution Control of γ-Fe_2O_3 Nanocrystallites: An In Situ Study. *Cryst. Growth Des.* **2014,** *14* (3), 1307–1313.
146. Jensen, K. M.Ø.; Andersen, H. L.; Tyrsted, C.; Bøjesen, E. D.; Dippel, A.-C.; Lock, N.; Billinge, S. J. L.; Iversen, B. B.; Christensen, M. Mechanisms for Iron Oxide Formation Under Hydrothermal Conditions: An In Situ Total Scattering Study. *ACS Nano* **2014,** *8* (10), 10704–10714.
147. Jørgensen, J.-E.; Jensen, T. R.; Hanson, J. C. Hydrothermal Synthesis of Nanocrystalline ZnSe: An In Situ Synchrotron Radiation X-Ray Powder Diffraction Study. *J. Solid State Chem.* **2008,** *181* (8), 1925–1929.
148. Jørgensen, J.-E.; Mosegaard, L.; Thomsen, L. E.; Jensen, T. R.; Hanson, J. C. Formation of γ-Fe_2O_3 Nanoparticles and Vacancy Ordering: An In Situ X-Ray Powder Diffraction Study. *J. Solid State Chem.* **2006,** *180* (1), 180–185.

149. Zhang, N.; Zhang, X.; Shi, E.; Zhao, S.; Jiang, K.; Wang, D.; Wang, P.; Guo, S.; He, P.; Zhou, H. In Situ X-Ray Diffraction and Thermal Analysis of $LiNi_{0.8}Co_{0.15}Al_{0.05}O_2$ Synthesized Via co-Precipitation Method. *J. Energy Chem.* **2018,** *27* (6), 1655–1660.
150. Leoni, M.; Di Maggio, R.; Polizzi, S.; Scardi, P. X-Ray Diffraction Methodology for the Microstructural Analysis of Nanocrystalline Powders: Application to Cerium Oxide. *J. Am. Ceram. Soc.* **2004,** *87* (6), 1133–1140.
151. Ozgur, U.; Alivov, Y. I.; Liu, C.; Teke, A.; Reshchikov, M. A.; Dogan, S.; Avrutin, V.; Cho, S. J.; Morkoc, H. A Comprehensive Review of ZnO Materials and Devices. *J. Appl. Phys.* **2005,** *98* (4), 041301.
152. Broge, N. L. N.; Bondesgaard, M.; Søndergaard-Pedersen, F.; Roelsgaard, M.; Iversen, B. B. Autocatalytic Formation of High Entropy Alloy Nanoparticles. *Angew. Chem.* **2020,** *7132,* 22104–22108.
153. Ortatatlı, Ş.; Ternieden, J.; Weidenthaler, C. Low Temperature Formation of Ruddlesden–Popper-Type Layered $La_2CoO_{4\pm\delta}$ Perovskite Monitored Via In Situ X-Ray Powder Diffraction. *Eur. J. Inorg. Chem.* **2018,** *2018* (48), 5238–5245.
154. Broge, N. L. N.; Søndergaard-Pedersen, F.; Roelsgaard, M.; Hassing-Hansen, X.; Iversen, B. B. Mapping the Redox Chemistry of Common Solvents in Solvothermal Synthesis Through In Situ X-Ray Diffraction. *Nanoscale* **2020,** *12* (15), 8511–8518.
155. Billinge, S. J. L.; Levin, I. The Problem with Determining Atomic Structure at the Nanoscale. *Science* **2007,** *316* (5824), 561–565.
156. Christiansen, T. L.; Cooper, S. R.; Jensen, K. M.Ø. There's no Place Like Real-Space: Elucidating Size-Dependent Atomic Structure of Nanomaterials Using Pair Distribution Function Analysis. *Nanoscale Adv.* **2020,** *2* (6), 2234–2254.
157. Billinge, S. J. L.; Kanatzidis, M. G. Beyond Crystallography: The Study of Disorder, Nanocrystallinity and Crystallographically Challenged Materials With Pair Distribution Functions. *Chem. Commun.* **2004,** *4* (7), 749–760.
158. Chupas, P. J.; Chapman, K. W.; Jennings, G.; Lee, P. L.; Grey, C. P. Watching Nanoparticles Grow: The Mechanism and Kinetics for the Formation of TiO_2-Supported Platinum Nanoparticles. *J. Am. Chem. Soc.* **2007,** *129* (45), 13822–13824.
159. Henkelis, S. E.; Morris, S. A.; Mazur, M.; Wheatley, P. S.; McHugh, L. N.; Morris, R. E. Monitoring the Assembly–Disassembly–Organisation–Reassembly Process of Germanosilicate UTL through In Situ Pair Distribution Function Analysis. *J. Mater. Chem. A* **2018,** *6* (35), 17011–17018.
160. Peys, A.; White, C. E.; Rahier, H.; Blanpain, B.; Pontikes, Y. Alkali-Activation of CaO-FeO_x-SiO_2 Slag: Formation Mechanism From In-Situ X-Ray Total Scattering. *Cem. Concr. Res.* **2019,** *122,* 179–188.
161. Roelsgaard, M.; Dippel, A.-C.; Borup, K. A.; Nielsen, I. G.; Broge, N. L. N.; Roh, J. T.; Gutowski, O.; Iversen, B. B. Time-Resolved Grazing-Incidence Pair Distribution Functions during Deposition by Radio-Frequency Magnetron Sputtering. *IUCrJ* **2019,** *6* (2), 299–304.
162. Nakamura, N.; Su, L.; Bai, J.; Ghose, S.; Reeja-Jayan, B. In Situ Synchrotron Pair Distribution Function Analysis to Monitor Synthetic Pathways Under Electromagnetic Excitation. *J. Mater. Chem. A* **2020,** *8* (31), 15909–15918.
163. Potter, M. E.; Light, M. E.; Irving, D. J. M.; Oakley, A. E.; Chapman, S.; Chater, P.; Cutts, G.; Watts, A.; Wharmby, M.; Vandegehuchte, B. D.; Schreiber, M. W.; Raja, R. Exploring the Origins of Crystallisation Kinetics in Hierarchical Materials Using: In Situ X-Ray Diffraction and Pair Distribution Function Analysis. *Phys. Chem. Chem. Phys.* **2020,** *22* (34), 18860–18867.
164. Tyrsted, C.; Lock, N.; Jensen, K. M.Ø.; Christensen, M.; Bøjesen, E. D.; Emerich, H.; Vaughan, G.; Billinge, S. J. L.; Iversen, B. B.; Bøjesen, E. D.; Emerich, H.; Vaughan, G.; Billinge, S. J. L.; Iversen, B. B. Evolution of Atomic Structure During Nanoparticle Formation. *IUCrJ* **2014,** *1* (3), 165–171.
165. Saha, D.; Bøjesen, E. D.; Jensen, K. M.Ø.; Dippel, A.-C.; Iversen, B. B. Formation Mechanisms of Pt and Pt_3Gd Nanoparticles under Solvothermal Conditions: An In Situ Total X-Ray Scattering Study. *J. Phys. Chem. C* **2015,** *119* (23), 13357–13362.
166. Saha, D.; Jensen, K. M.Ø.; Tyrsted, C.; Bøjesen, E. D.; Mamakhel, H.; Dippel, A.-C.; Christensen, M.; Iversen, B. B. In Situ Total X-Ray Scattering Study of WO_3 Nanoparticle Formation Under Hydrothermal Conditions. *Angew. Chem. Int. Ed.* **2014,** *53,* 3667–3670.
167. Mi, J.-L.; Jensen, K. M.Ø.; Tyrsted, C.; Bremholm, M.; Iversen, B. B. In Situ Total X-Ray Scattering Study of the Formation Mechanism and Structural Defects in Anatase TiO_2 Nanoparticles under Hydrothermal Conditions. *CrstEngComm* **2015,** *17* (36), 6868–6877.
168. Bøjesen, E. D.; Jensen, K. M.Ø.; Tyrsted, C.; Mamakhel, A. H.; Andersen, H. L.; Reardon, H.; Chevalier, J.; Dippel, A.-C.; Iversen, B. B. The Chemistry of $ZnWO_4$ Nanoparticle Formation. *Chem. Sci.* **2016,** *7* (10), 6394–6406.
169. Dippel, A.-C.; Jensen, K. M.Ø.; Tyrsted, C.; Bremholm, M.; Bøjesen, E. D.; Saha, D.; Birgisson, S.; Christensen, M.; Billinge, S. J. L.; Iversen, B. B. Towards Atomistic Understanding of Polymorphism in the Solvothermal Synthesis of ZrO_2 Nanoparticles. *Acta Cryst. A* **2016,** *72* (6), 645–650.
170. Birgisson, S.; Saha, D.; Iversen, B. B. Formation Mechanisms of Nanocrystalline MnO_2 Polymorphs Under Hydrothermal Conditions. *Cryst. Growth Des.* **2018,** *18* (2), 827–838.
171. Broge, N. L. N.; Søndergaard-Pedersen, F.; Sommer, S.; Iversen, B. B. Formation Mechanism of Epitaxial Palladium–Platinum Core–Shell Nanocatalysts in a One-Step Supercritical Synthesis. *Adv. Funct. Mater.* **2019,** *29* (31), 1902214.
172. Sommer, S.; Gjerlevsen Nielsen, I.; Brummerstedt Iversen, B. Group 13 Precursor Structures and Their Effect on Oxide Nanocrystal Formation. *Chem. A Eur. J.* **2020,** *26* (5), 1022–1026.
173. Saha, D.; Bøjesen, E. D.; Mamakhel, A. H.; Iversen, B. B. Why Does Bi_2WO_6 Visible-Light Photocatalyst Always Form as Nanoplatelets? *Inorg. Chem.* **2020,** *59* (13), 9364–9373.
174. Tominaka, S.; Yamada, H.; Hiroi, S.; Kawaguchi, S. I.; Ohara, K. Lepidocrocite-Type Titanate Formation From Isostructural Prestructures Under Hydrothermal Reactions: Observation by Synchrotron X-Ray Total Scattering Analyses. *ACS Omega* **2018,** *3* (8), 8874–8881.
175. Xu, H.; Sommer, S.; Broge, N. L. N.; Gao, J.; Iversen, B. B. The Chemistry of Nucleation: In Situ Pair Distribution Function Analysis of Secondary Building Units During UiO-66 MOF Formation. *Chem. A Eur. J.* **2019,** *25* (8), 2051–2058.
176. Yamada, H.; Tominaka, S.; Ohara, K.; Liu, Z.; Okubo, T.; Wakihara, T. Structural Evolution of Amorphous Precursors Toward Crystalline Zeolites Visualized by an In Situ X-Ray Pair Distribution Function Approach. *J. Phys. Chem. C* **2019,** *123* (46), 28419–28426.
177. Terban, M. W.; Banerjee, D.; Ghose, S.; Medasani, B.; Shukla, A.; Legg, B. A.; Zhou, Y.; Zhu, Z.; Sushko, M. L.; De Yoreo, J. J.; Liu, J.; Thallapally, P. K.; Billinge, S. J. L. Early Stage Structural Development of Prototypical Zeolitic Imidazolate Framework (ZIF) in Solution. *Nanoscale* **2018,** *10* (9), 4291–4300.
178. White, C. E.; Page, K.; Henson, N. J.; Provis, J. L. In Situ Synchrotron X-Ray Pair Distribution Function Analysis of the Early Stages of Gel Formation in Metakaolin-Based Geopolymers. *Appl. Clay Sci.* **2013,** *73,* 17–25.
179. White, C. E.; Provis, J. L.; Bloomer, B.; Henson, N. J.; Page, K. In Situ X-Ray Pair Distribution Function Analysis of Geopolymer Gel Nanostructure Formation Kinetics. *Phys. Chem. Chem. Phys.* **2013,** *15* (22), 8573–8582.
180. Morandeau, A. E.; White, C. E. In Situ X-Ray Pair Distribution Function Analysis of Accelerated Carbonation of a Synthetic Calcium–Silicate–Hydrate Gel. *J. Mater. Chem. A* **2015,** *3* (16), 8597–8605.
181. Garg, N.; White, C. E. Mechanism of Zinc Oxide Retardation in Alkali-Activated Materials: An In Situ X-Ray Pair Distribution Function Investigation. *J. Mater. Chem. A* **2017,** *5* (23), 11794–11804.
182. White, C. E.; Provis, J. L.; Llobet, A.; Proffen, T.; van Deventer, J. S. J. Evolution of Local Structure in Geopolymer Gels: An In Situ Neutron Pair Distribution Function Analysis. *J. Am. Ceram. Soc.* **2011,** *94* (10), 3532–3539.
183. Kupwade-Patil, K.; Boul, P. J.; Rasner, D. K.; Everett, S. M.; Proffen, T.; Page, K.; Ma, D.; Olds, D.; Thaemlitz, C. J.; Büyüköztürk, O. Retarder Effect on Hydrating Oil Well Cements Investigated Using In Situ Neutron/X-Ray Pair Distribution Function Analysis. *Cem. Concr. Res.* **2019,** *126* (105920), 1–13.
184. Juelsholt, M.; Lindahl Christiansen, T.; Jensen, K. M.Ø. Mechanisms for Tungsten Oxide Nanoparticle Formation in Solvothermal Synthesis: From Polyoxometalates to Crystalline Materials. *J. Phys. Chem. C* **2019,** *123* (8), 5110–5119.
185. Egami, T.; Billinge, S. J. L. *Underneath the Bragg Peaks: Structural Analysis of Complex Materials;,* 1st ed.; vol. 16; Pergamon, 2003; pp 1–404.

186. Zobel, M.; Neder, R. B.; Kimber, S. A. J. Universal Solvent Restructuring Induced by Colloidal Nanoparticles. *Science* **2015,** *347* (6219), 292–294.
187. Li, T.; Senesi, A. J.; Lee, B. Small Angle X-Ray Scattering for Nanoparticle Research. *Chem. Rev.* **2016,** *116* (18), 11128–11180.
188. Tobler, D. J.; Shaw, S.; Benning, L. G. Quantification of Initial Steps of Nucleation and Growth of Silica Nanoparticles: An In-Situ SAXS and DLS Study. *Geochim. Cosmochim. Acta* **2009,** *73* (18), 5377–5393.
189. Tobler, D. J.; Benning, L. G. In Situ and Time Resolved Nucleation and Growth of Silica Nanoparticles Forming Under Simulated Geothermal Conditions. *Geochim. Cosmochim. Acta* **2013,** *114,* 156–168.
190. Baccile, N.; Teixeira, C. V.; Amenitsch, H.; Villain, F.; Lindén, M.; Babonneau, F. Time-Resolved In Situ Raman and Small-Angle X-Ray Diffraction Experiments: From Silica-Precursor Hydrolysis to Development of Mesoscopic Order in SBA-3 Surfactant-Templated Silica. *Chem. Mater.* **2008,** *20* (3), 1161–1172.
191. Caetano, B. L.; Meneau, F.; Santilli, C. V.; Pulcinelli, S. H.; Magnani, M.; Briois, V. Mechanisms of SnO_2 Nanoparticles Formation and Growth in Acid Ethanol Solution Derived from SAXS and Combined Raman–XAS Time-Resolved Studies. *Chem. Mater.* **2014,** *26* (23), 6777–6785.
192. Garcia, P. R. A. F.; Prymak, O.; Grasmik, V.; Pappert, K.; Wlysses, W.; Otubo, L.; Epple, M.; Oliveira, C. L. P. An In Situ SAXS Investigation of the Formation of Silver Nanoparticles and Bimetallic Silver–Gold Nanoparticles in Controlled Wet-Chemical Reduction Synthesis. *Nanoscale Adv.* **2020,** *2* (1), 225–238.
193. Abécassis, B.; Testard, F.; Kong, Q.; Francois, B.; Spalla, O. Influence of Monomer Feeding on a Fast Gold Nanoparticles Synthesis: Time-Resolved XANES and SAXS Experiments. *Langmuir* **2010,** *26* (17), 13847–13854.
194. Harada, M.; Tamura, N.; Takenaka, M. Nucleation and growth of Metal Nanoparticles During Photoreduction Using In Situ Time-Resolved SAXS Analysis. *J. Phys. Chem. C* **2011,** *115* (29), 14081–14092.
195. Polte, J.; Ahner, T. T.; Delissen, F.; Sokolov, S.; Emmerling, F.; Thünemann, A. F.; Kraehnert, R. Mechanism of Gold Nanoparticle Formation in the Classical Citrate Synthesis Method Derived From Coupled In Situ XANES and SAXS Evaluation. *J. Am. Chem. Soc.* **2010,** *132* (4), 1296–1301.
196. Abécassis, B.; Testard, F.; Spalla, O. Gold Nanoparticle Superlattice Crystallization Probed In Situ. *Phys. Rev. Lett.* **2008,** *100* (11), 115504.
197. Nikitenko, S.; Beale, A. M.; van der Eerden, A. M. J.; Jacques, S. D. M.; Leynaud, O.; O'Brien, M. G.; Detollenaere, D.; Kaptein, R.; Weckhuysen, B. M.; Bras, W. Implementation of a Combined SAXS/WAXS/QEXAFS Set-up for Time-Resolved In Situ Experiments. *J. Syncrotron Radiat.* **2008,** *15* (6), 632–640.
198. Hummer, D. R.; Heaney, P. J.; Post, J. E. In Situ Observations of Particle Size Evolution during the Hydrothermal Crystallization of TiO_2: A Time-Resolved Synchrotron SAXS and WAXS Study. *J. Cryst. Growth* **2012,** *344* (1), 51–58.
199. Kabelitz, A.; Guilherme, A.; Joester, M.; Reinholz, U.; Radtke, M.; Bienert, R.; Schulz, K.; Schmack, R.; Kraehnert, R.; Emmerling, F. Time-Resolved In Situ Studies on the Formation Mechanism of Iron Oxide Nanoparticles Using Combined Fast-XANES and SAXS. *CrstEngComm* **2015,** *17* (44), 8463–8470.
200. Cravillon, J.; Schroder, C. A.; Nayuk, R.; Gummel, J.; Huber, K.; Wiebcke, M. Fast Nucleation and Growth of ZIF-8 Nanocrystals Monitored by Time-Resolved In Situ Small-Angle and Wide-Angle X-Ray Scattering. *Angew. Chem. Int. Ed.* **2011,** *50* (35), 8067–8071.
201. Hornfeck, W.; Menke, D.; Forthaus, M.; Subatzus, S.; Franke, M.; Schöpe, H. J.; Palberg, T.; Perlich, J.; Herlach, D. Nucleation and Crystal growth in a Suspension of Charged Colloidal Silica Spheres with Bi-Modal Size Distribution Studied by Time-Resolved Ultra-Small-Angle X-Ray Scattering. *J. Chem. Phys.* **2014,** *141* (21), 214906.
202. O'Brien, M. G.; Beale, A. M.; Kuipers, B. W. M.; Erné, B. H.; Lewis, D. W.; Catlow, C. R. A. Role of Germanium on the Nucleation and Growth of Zeolite a From Clear Solutions as Studied by In Situ Small-Angle X-Ray Scattering, Wide-Angle X-Ray Scattering, and Dynamic Light Scattering. *J. Phys. Chem. C* **2009,** *113* (43), 18614–18622.
203. White, C. E.; Olds, D. P.; Hartl, M.; Hjelm, R. P.; Page, K. Evolution of the Pore Structure during the Early Stages of the Alkali-Activation Reaction: An In Situ Small-Angle Neutron Scattering Investigation. *J. Appl. Cryst.* **2017,** *50* (1), 61–75.
204. Koziej, D. Revealing Complexity of Nanoparticle Synthesis in Solution by In Situ Hard X-Ray Spectroscopy—Today and Beyond. *Chem. Mater.* **2016,** *28* (8), 2478–2490.
205. Kränzlin, N.; Staniuk, M.; Heiligtag, F. J.; Luo, L.; Emerich, H.; van Beek, W.; Niederberger, M.; Koziej, D. Rationale for the Crystallization of Titania Polymorphs in Solution. *Nanoscale* **2014,** *6* (24), 14716–14723.
206. Staniuk, M.; Hirsch, O.; Kränzlin, N.; Böhlen, R.; van Beek, W.; Abdala, P. M.; Koziej, D.; Krä, N.; Bö, R.; van Beek, W.; Abdala, P. M.; Koziej, D. Puzzling Mechanism behind a Simple Synthesis of Cobalt and Cobalt Oxide Nanoparticles: In Situ Synchrotron X-Ray Absorption and Diffraction Studies. *Chem. Mater.* **2014,** *26* (6), 2086–2094.
207. Beale, A. M.; Sankar, G. In Situ Characterization of Iron Phosphate and Bismuth Molybdate Catalysts Prepared by Hydrothermal Methods: An EDXRD and Combined XRD/XAS Study. *Nuclear Instruments and Methods in Physics Research, Section B* **2003,** *199,* 504–508.
208. Li, W.; Borkiewicz, O. J.; Saubanère, M.; Doublet, M.-L.; Flahaut, D.; Chupas, P. J.; Chapman, K. W.; Dambournet, D. Atomic Structure of 2 Nm Size Metallic Cobalt Prepared by Electrochemical Conversion: An In Situ Pair Distribution Function Study. *J. Phys. Chem. C* **2018,** *122* (42), 23861–23866.
209. Michailovski, A.; Grunwaldt, J.-D.; Baiker, A.; Kiebach, R.; Bensch, W.; Patzke, G. R. Studying the Solvothermal Formation of MoO_3 Fibers by Complementary In Situ EXAFS/EDXRD Techniques. *Angew. Chem. Int. Ed.* **2005,** *44* (35), 5643–5647.
210. Grunwaldt, J. D.; Ramin, M.; Rohr, M.; Michailovski, A.; Patzke, G. R.; Baiker, A. High Pressure In Situ X-Ray Absorption Spectroscopy Cell for Studying Simultaneously the Liquid Phase and the Solid/Liquid Interface. *Rev. Sci. Instrum.* **2005,** *76* (5), 054104.
211. Hirsch, O.; Zeng, G.; Luo, L.; Staniuk, M.; Abdala, P. M.; van Beek, W.; Rechberger, F.; Süess, M. J.; Niederberger, M.; Koziej, D. Aliovalent Ni in MoO_2 Lattice—Probing the Structure and Valence of Ni and Its Implication on the Electrochemical Performance. *Chem. Mater.* **2014,** *26* (15), 4505–4513.
212. Ramamoorthy, R. K.; Yildirim, E.; Barba, E.; Roblin, P.; Vargas, J. A.; Lacroix, L.-M.; Rodriguez-Ruiz, I.; Decorse, P.; Petkov, V.; Teychené, S.; Viau, G. The Role of Pre-Nucleation Clusters in the Crystallization of Gold Nanoparticles. *Nanoscale* **2020,** *12* (30), 16173–16188.
213. Vester, P.; Christensen, M.; Biasin, E.; Mariager, S. O.; Newby, G.; Khakhulin, D.; Zontone, F.; Wulff, M.; Feidenhans'l, R.; Nielsen, M. M.; Haldrup, K. X-Ray Tracking of Structural Changes during a Subnanosecond Solid-Solid Phase Transition in Cobalt Nanoparticles. *Phys. Rev. B* **2019,** *100* (24), 245425.
214. Bordallo, H. N.; Lioma, C.; Taylor, J.; Argyriou, D. N. Is Artificial Intelligence Magic Dust for Big-Science Facilities? *IUCrJ* **2020,** *7* (1), 1–2.
215. Geddes, H. S.; Blade, H.; McCabe, J. F.; Hughes, L. P.; Goodwin, A. L. Structural Characterisation of Amorphous Solid Dispersions Via Metropolis Matrix Factorisation of Pair Distribution Function Data. *Chem. Commun.* **2019,** *55* (89), 13346–13349.
216. Chapman, K. W.; Lapidus, S. H.; Chupas, P. J. Applications of Principal Component Analysis to Pair Distribution Function Data. *J. Appl. Cryst.* **2015,** *48* (6), 1619–1626.
217. Cole, J. M.; Cheng, X.; Payne, M. C. Modeling Pair Distribution Functions of Rare-Earth Phosphate Glasses Using Principal Component Analysis. *Inorg. Chem.* **2016,** *55* (21), 10870–10880.
218. Olds, D.; Peterson, P. F.; Crawford, M. K.; Neilson, J. R.; Wang, H.-W.; Whitfield, P. S.; Page, K. Combinatorial Appraisal of Transition States for In Situ Pair Distribution Function Analysis. *J. Appl. Cryst.* **2017,** *50* (6), 1744–1753.
219. Liu, C.-H.; Tao, Y.; Hsu, D.; Du, Q.; Billinge, S. J. L. Using a Machine Learning Approach to Determine the Space Group of a Structure From the Atomic Pair Distribution Function. *Acta Cryst. A* **2019,** *75* (4), 633–643.
220. Gu, R.; Banerjee, S.; Du, Q.; Billinge, S. J. L. Algorithm for Distance List Extraction From Pair Distribution Functions. *Acta Cryst. A* **2019,** *75* (5), 658–668.
221. Myerson, A. S.; Trout, B. L. Nucleation From Solution. *Science* **2013,** *341* (6148), 855–856.
222. Gebauer, D.; Kellermeier, M.; Gale, J. D.; Bergström, L.; Cölfen, H. Pre-Nucleation Clusters as Solute Precursors in Crystallisation. *Chem. Soc. Rev.* **2014,** *43* (7), 2348–2371.

Всё для Победы! НАРОДНЫЙ ФРОНТ
https://pobeda.onf.ru/
LET'S HELP THE RUSSIA
Z

10.11 Time resolved structural studies in molecular materials

Katarzyna Natalia Jarzembska and Radosław Kamiński, Department of Chemistry, University of Warsaw, Warsaw, Poland

© 2023 Elsevier Ltd. All rights reserved.

10.11.1	**Introduction**	**275**
10.11.1.1	Interaction of light and matter	275
10.11.1.2	Importance of solid-state studies	276
10.11.1.3	Research possibilities with X-ray diffraction methods	276
10.11.1.4	Short history of photocrystallography	276
10.11.1.5	Brief description of the chapter content	277
10.11.2	**Methods**	**277**
10.11.2.1	Data collection	278
10.11.2.1.1	Monochromatic method	278
10.11.2.1.2	Laue method	279
10.11.2.1.3	XFEL prospects	283
10.11.2.2	Data processing and analysis	283
10.11.2.2.1	Laue data processing for macromolecular crystals	283
10.11.2.2.2	Laue data processing for small-molecule crystals	284
10.11.2.2.3	Photodifference maps	286
10.11.2.2.4	Structure-model refinement	287
10.11.3	**Examples of time-resolved studies**	**288**
10.11.3.1	Macromolecular TR photocrystallography	288
10.11.3.2	TR studies of small organic molecules	290
10.11.3.3	TR studies of coordination compounds	292
10.11.3.3.1	$Pt(pop)_2(popH)_2 \cdot N(Et)_4$ cage complex	292
10.11.3.3.2	$Rh_2(dimen)_4 \cdot (PF_6)_2$ cage complex	293
10.11.3.3.3	$([3,5\text{-}(CF_3)_2pz]Cu)_3$ trimer complex	295
10.11.3.3.4	$Rh_2(\mu\text{-}pnp)_2(pnp)_2 \cdot (B(Ph)_4)_2$ 'half-cage' complex	296
10.11.3.3.5	$Cu(dppe)(dmp) \cdot PF_6$ and $Cu(phen)(P(Ph)_3)_2 \cdot BF_4$ photoactive complexes	298
10.11.3.3.6	$Fe(tpa)(tcc) \cdot PF_6$ spin-crossover complex	300
10.11.3.3.7	$Ag_2Cu_2(dpi)_4$ multicenter complex	301
10.11.3.3.8	$Cu_4(PhCO_2)_4$ carboxylate complex	302
10.11.3.3.9	In-house time-resolved photocrystallographic studies	304
10.11.4	**Summary and prospects**	**305**
Acknowledgments		**305**
References		**305**

Glossary

Asymmetric unit (ASU) The smallest closed part of the crystal unit cell (e.g. some symmetry-independent molecular fragment, a set of atoms) from which, by application of all symmetry operations of the space group, the whole crystal structure can be reproduced. [Definition follows the IUCr Online Dictionary of Crystallography.]

Crystal A material characterized by a sharp diffraction pattern (reciprocal-space definition), or alternatively, a solid built of atoms, ions and/or molecules, which, on average, form a long-range-ordered arrangement (real-space definition). [Both definitions follow the IUCr Online Dictionary of Crystallography.]

Density functional theory (DFT) A quantum mechanical approach based on two Hohenberg-Kohn theorems. The first one demonstrates that electron density, which depends only on three spatial coordinates, determines all the ground-state properties of a many-electron system (a promising alternative to a many-parameter-dependent wavefunction). The second theorem introduces the so-called density functional (e.g. energy function dependent directly on electron density) and proves that the ground-state electron density minimizes the energy functional. The exact form of this functional is though ultimately unknown. Much work has been devoted to finding approximate functionals for specific applications. DFT methods are usually much faster than the ab initio quantum chemistry techniques used to compute various molecular properties of studied systems.

Diffractometer An automated machine consisting of a (X-ray) source, a device for positioning and rotating samples (e.g. single crystals) called a goniometer or goniostat, and a light or particle-sensitive detector used to measure the intensity of the

diffracted (X-ray) beam. A diffractometer can be installed in a laboratory (in such case the X-ray source is small and compact), or can be a part of a synchrotron beamline.

Electron density A quantitative measure of the probability of an electron being found in a very small (infinitesimal) volume around a particular point in 3-dimentional space. It can be roughly expressed as the derivative of probability versus volume ($\varrho = \mathrm{d}P/\mathrm{d}V$), similarly to the definition of a matter density.

Ewald sphere A concept introduced to crystallography by Peter Ewald to facilitate the interpretation of diffraction conditions. It is a reciprocal-space sphere centered on a crystal with the radius equal to $1/\lambda$ (λ – radiation wavelength). When the reciprocal-space vector (anchored at the intersection of the direction of the primary beam interacting with the crystal and the sphere) intersects the sphere, the diffraction condition if fulfilled in the direction given by the point of intersection and the sphere origin.

Excited state A state of a quantum system which is not the one of the lowest energy (ground state). For atomic and molecular systems, it is possible, under certain conditions, for the system to migrate in-between various states. The respective state changes are called transitions. In photochemistry and photophysics, a transition from the ground state to any excited state is frequently associated with light absorption. Conversely, transition from excited state to the ground (or lower-in-energy excited) state may be associated with light emission. An electronic transition associated with some significant change of electron density distribution in-between molecular fragments is called a charge transfer.

Free-electron laser (FEL) A device in which the light pulse is generated via very long pass of ('free') electron bunch through a set of undulators. When the generated light is in the X-ray regime, such device is called an X-ray free-electron laser (XFEL). The generated light is called laser light due to its high coherence and intensity, even though the principle idea of the device is somewhat different than that behind a classical laser (amplification of radiation is achieved by interference effects occurring in undulator devices along the electron-bunch travel path).

Laser An optical device which produces a coherent and intense light beam by a process called "light amplification by stimulated emission of radiation." General working idea of the laser is to amplify the electromagnetic radiation via multiple interference effects occurring in the so-called optical cavity, in which stimulated emission in the initially pumped (with some external perturbation, e.g. flashlamp pulse) gain medium takes place.

Light-emitting diode (LED) A semiconductor device that emits light when the current is allowed to flow through it. Electrons and electron holes travel across the material and later recombine, bringing the system into the emissive state producing light (entire process is called electroluminescence). LEDs produced using organic materials are called organic light-emitting diodes (OLEDs).

Luminescence Light emission from a material that is in an excited state. Emission from a singlet excited state is called fluorescence and it is usually very rapid (in the order of ns) since the transitions to singlet (usually) ground states are allowed. In turn, emission from triplet excited states is called phosphorescence, and, due to the forbidden nature of triplet-to-singlet transitions, it is rather slow (luminescence lifetime from μs to seconds). In some cases, materials do not exhibit visible luminescence due to various deactivation processes taking place called non-radiative decay or quenching. The luminescence lifetime is defined as an average time between sample excitation and its return (decay) to the ground state. Stokes shift refers to the lower energy of the emission maximum when compared to the respective absorption energy, which usually indicates different geometrical properties of the respective ground and excited states.[188]

Molecular mechanics (MM) A set of methods for molecular modelling used where the application of ab initio or DFT approaches is hardly possible due to the size of the analyzed system (a very long or practically 'infinite' computing time is needed). In the case of MM, the energy of the system is modelled using so-called force fields, the parameters of which are based on experimental observations and some theoretical predictions (from more advanced theoretical methods or experiments). The combination of molecular mechanics with quantum mechanical (QM) methods leads to a set of methods called QM/MM (quantum-mechanics/molecular mechanics), in which a small part of a large system (e.g. single molecule) is treated more accurately i.e. with high-level method (e.g. DFT) while the remainder (e.g. solvent or crystal environment) is treated approximately using force-fields.

Reflection A spot recorded on a detector indicating the direction and intensity of the diffracted beam (i.e. the secondary beam of light or particles arising when the crystal is exposed to the primary beam and diffraction phenomenon takes place). A reflection can be described as a vector in the so-called reciprocal space (mathematically it is a dual space to the real space, it can be expressed with three basis vectors – $\mathbf{a}^*$, $\mathbf{b}^*$ and $\mathbf{c}^*$) with three numbers called indices (usually h, k and l). Reciprocal-space vector with components h, k and l ($\mathbf{h} = h\mathbf{a}^* + h\mathbf{b}^* + h\mathbf{c}^*$) associated with the reflection, indicate its direction in space (in turn, its intensity is expressed by a structure factor).

Structure factor A quantity representing the X-ray scattering power of the whole crystal. It is computed for a single reflection and is defined as a Fourier transform of the electron density of a single unit cell ($F(hkl) = \int \varrho(xyz)\, e^{2\pi\mathrm{i}(hx+ky+lz)}\, \mathrm{d}x\mathrm{d}y\mathrm{d}z$), thus it is a complex function. As with any complex number, it can be expressed as a modulus and a phase ($F = |F| e^{\mathrm{i}\varphi}$, φ – phase). For mosaic crystals (i.e. composed of slightly rotated domains; the most common case for real crystals) the intensity of a given X-ray reflection is proportional to the square modulus of the structure factor ($I \propto |F|^2$). Consequently, initially only the structure factor moduli are directly accessible from the diffraction experiment. Procedures for finding structure-factor phases for all the reflections are called structure-solution methods. After both the moduli and phases are known, one can determine the

electron density of the crystal by computing the inverse Fourier transform. [Definition follows the IUCr Online Dictionary of Crystallography.]

Synchrotron A cyclic particle accelerator, in which the particles (most frequently electrons) travel along a fixed closed-loop trajectory. This trajectory is maintained by the application of a magnetic field which varies during the acceleration process (it is 'synchronized' to the particles' energy). Charged particles travelling along the curved path emit electromagnetic radiation. In the case of electrons accelerated to very high speeds (almost the speed of light) the generated radiation is in the X-ray region. A typical X-ray synchrotron facility consists of several components: a linear accelerator (so-called linac), a booster (a true synchrotron) and a storage ring. The first two components accelerate electrons to their final speed, which later are injected (with the use of magnetic fields) into the storage ring, where their energy is kept approximately constant. Electrons are produced and travel as packets (called bunches). Storage rings contain several components: magnetic lenses, bending magnets and insertion devices. Bending magnets and insertion devices are used to produce X-ray radiation by changing the path of electron bunches. Insertion devices are of two types: wigglers and undulators. The bending magnet curves the electron path with a constant magnetic field and produces less intense and broad X-ray radiation. Wigglers and undulators are sets of small magnets which change the direction of electron more (undulator) or less (wiggler) frequently along a specified distance (e.g. 2 m) allowing for interference effects to sum up all electromagnetic field contributions for a single X-ray pulse. X-ray radiation coming from the undulator is currently the most intense X-ray radiation produced at a synchrotron facility. Every electron bunch travelling through the insertion device produces an X-ray pulse of specified spatial and time structure. A set of consecutive X-ray pulses is called a synchrotron train.

Thermochromism Material color changing due to temperature variation. This definition is extended to other processes, for instance, luminescence thermochromism is an effect where a different color of light is emitted by a given sample for different temperatures.

Unit cell The parallelepiped built on the crystallographic basis vectors of the direct lattice (**a**, **b** and **c**). Imprecisely, yet intuitively, together with the atoms inside it, the unit cell can be regarded as the smallest part of a crystal, out of which the entire crystal can be reconstructed by application of translations along lattice vectors. [Definition follows the IUCr Online Dictionary of Crystallography.]

Abstract

The following chapter provides a comprehensive overview of time-resolved photocrystallography studies, and related experimental and methodological progress. Particular emphasis is put on research dedicated to transition-metal coordination compounds. The introduction of synchrotron radiation has led to a major breakthrough in experimental capabilities in the field. Also, for small-molecule time-resolved photocrystallography the application of the polychromatic Laue method appeared essential. Thus, beamlines used for ultrafast (ca. 100 ps time resolution) experiments employing the Laue method are described in detail. Similarly, data processing techniques are outlined paying particular attention to advances in the Laue method: new X-ray diffraction signal evaluation methods, orientation matrix search and structural refinements based on intensity ratios. Examples described in this chapter comprise a set of complexes where significant structural changes were observed with atomic resolution. These include photoactive compounds in which inner part of the molecule undergoes bond shortening (e.g. cage of 'half-cage' complexes with metallophilic Pt···Pt or Rh···Rh interactions), compounds forming excimers in the solid state upon irradiation (pyrazolate copper complex), photoactive model complexes of relevance to solar-energy applications (copper ionic complexes), and finally, spin cross-over systems (iron complex). In addition, some selected examples of time-resolved studies with macromolecules and purely organic molecules are presented for comparison. Comments on recent results and future prospects concerning the application of X-ray free electron laser sources and laboratory diffractometers are provided.

10.11.1 Introduction

10.11.1.1 Interaction of light and matter

Interaction of light and matter is an intriguing and important phenomenon, which has fascinated humans for ages. However, despite real breakthroughs toward understanding its theoretical principles, the description of real-world systems remains a very challenging task. This is due to their complexity, which makes theoretical predictions often inaccurate or even not feasible. Some examples of light and matter interactions of great relevance are the *cis-trans* isomerization of retinene,[1,2] light-to-energy conversion in solar cells,[3] or light-induced biological transformations in proteins.[4,5] The common point of the above mentioned processes is the conversion of light energy into some sort of other action, such as charge transfer. This can further trigger transformations in which molecules change their geometry, function, emit photons of different energy, etc. Therefore, it is of high importance to study these phenomena, trace structural changes, gain information on the light-induced transient species in order to understand the nature of the examined transformations, their origins and their mechanisms. This will allow us to comprehensively control optical properties of such materials at the molecular level and further apply that knowledge to generate materials with

particular properties across all the size scales, from molecules to bulk materials, relevant for specific applications. Despite numerous efforts, this very challenging target continuous to remain far from being achieved.

10.11.1.2 Importance of solid-state studies

Considering light and matter interactions of technological relevance, it is worth stressing that solid-state photoactive materials are now of great, and constantly increasing, significance. Their applications range from sensors, optoelectronic devices and ultra-high capacity data storage media, to environmental and biomedical applications. Nevertheless, although methods for studying light-induced effects in solution are currently rather well-developed, solid-state investigations of this kind are much more demanding, thus less established. Therefore, considerable effort should be dedicated to studies of materials in their technologically-applicable solid-state form. In this respect, single crystals are unique, as they are characterized by a well-defined three-dimensional structure. This property makes them excellent model systems to mimic real-world situations, and also to supplement studies on solutions, or model the inter-surface environment. Furthermore, light-induced processes cause the earlier-mentioned structural distortions due to new bond formation, atom oxidation state changes, etc., which in the case of single crystals can be explored via X-ray diffraction techniques – the only method providing a full three-dimensional experimental picture of crystals. The tracing of processes triggered by light irradiation in crystals by means of X-ray diffraction methods is known as photocrystallography, a term coined in 2003 by Philip Coppens,[6] one of the pioneers in the field.

10.11.1.3 Research possibilities with X-ray diffraction methods

Crystal-structure determination using diffraction methods is now a routine procedure in chemistry and solid-state physics. These techniques allow determination of atom positions in a crystal with high precision and accuracy, and as a consequence provide information on interactions between various species present in the examined crystal structure. In addition, high-quality high-resolution measurements facilitate the modelling of the electron density distribution in a given crystal, which enables experimental determination of the nature of interactions occurring in its lattice.[7,8] Crystal architecture and interactions stabilizing the crystal lattice are, in turn, reflected in the macroscopic properties of the system. Furthermore, application of X-ray diffraction methods to samples excited using some source of UV–Vis light (e.g. laser, light-emitting diode (LED), Xe lamp or even sunlight) opens up the possibilities of tracking light-induced structural changes (e.g. chemical reactions) taking place in the solid state, and studying metastable states or short-lived excited states in crystals. It should be stressed that studies of very short-lived excited state species (with lifetimes of microseconds and shorter) are very challenging, technically advanced and require novel methods of data handling and analysis.[9–13]

10.11.1.4 Short history of photocrystallography

Photocrystallography is still a relatively immature field of science. The pioneering works were published by G. M. J. Schmidt and colleagues from the Weizmann Research Institute in Israel in the middle of the 20th century. The first experiments that they conducted concerned simple chemical reactions that occur in crystals when exposed to light.[9,14–16] Since in the 1950s and 1960s lasers were not available, such transformations were performed mainly with the use of sunlight as an excitation source. Despite numerous experimental difficulties, it was possible to find relationships linking the crystal structure of the analyzed compound with the reactions it may undergo in the solid state. At the beginning, these were studies of the [2 + 2] photodimerizations.[17] Over time, thanks to the introduction of new light sources (mainly lasers), research possibilities have been extended to polymerization reactions in crystals,[18,19] isomerizations,[20–22] [4 + 4] photodimerization reactions,[23] analysis of reaction kinetics in crystals,[24] cyclisation reactions[25–28] and many others.

Along with the development of lasers (strong and short excitation pulses of coherent light with a desired and well-defined wavelength), technical progress in the field of X-ray sources cannot be overestimated. Indeed, the use of synchrotron radiation, including X-ray free-electron laser (XFEL) radiation, for the study of single crystals has at least two significant advantages. These are:

(i) the high intensity of the X-ray beam coming from the synchrotron;
(ii) the possibility of generating very short X-ray pulses.

These features allowed for an extraordinary expansion of research capabilities, which revolutionized the field of photocrystallography. The first one allows studies of very small crystals, which are better penetrated by the laser light, and facilitates detection of subtle structural changes caused by light excitation. The second one enables time-resolved (TR) studies, which are extremely important for investigations of short-lived excited state species (e.g. with lifetimes from ms down to even ps), or monitoring the course of fast light-induced processes (indicated by structural changes – e.g. atom shifts or molecular fragment rotations) in crystals. The combination of laser excitation sources, synchrotron radiation and low-temperature technology made it feasible to study important transformations both in macromolecular systems and small-molecule crystals. In this context, the impressive early achievements of J. Hajdu, K. Moffat, J. R. Helliwell and co-workers concerning studies of biologically important photochemical processes taking place in protein crystals should be mentioned.[13,29,30] In turn, regarding small-molecule X-ray photocrystallography, the results published by the groups of P. R. Raithby, Y. Ohashi, E. Collet and P. Coppens, dealing with chemical reactions, photoswitchable systems and investigations of short-lived excited states in crystals, deserve particular attention.[9,11,12,22,31–33]

10.11.1.5 Brief description of the chapter content

The following chapter is dedicated to time-resolved X-ray photocrystallographic studies conducted on crystals of coordination compounds. The chapter will provide a useful basis for understanding various photocrystallographic methods and constitutes a valuable source of information on what has already been done in the field as well as on the current research possibilities. The latest trends in small-molecule TR photocrystallography are described along with data processing and analysis methods, including the advantages of using synchrotron radiation in studies of this kind and new prospects related to XFELs. Literature example studies are presented.

10.11.2 Methods

The exact method of performing a photocrystallographic experiment largely depends on the nature of the sample under consideration, as well as on the speed of processes taking place in a given crystal (e.g. the progress of a chemical reaction, excited-state lifetimes). Basically, the methods used are selected in a way to fit the crystallographic experiment to the timescale of the observed transformation, or vice versa. This can be achieved in various ways, as for example by conducting an experiment at low temperature in order to slow down the processes and supposedly 'freeze' the studied metastable states.[34] In many cases, the lifetime of the excited states under such conditions is on the order of hours or days, which makes a standard crystallographic experiment sufficient to determine their structure. In the case of short-lived excited states or rapid chemical processes, the measurement time needs to be shortened so as to facilitate observation of the ongoing processes in real time. Naturally, it is much more difficult to prepare and conduct the latter experiment, but much more interesting cognitively.

One can think of four main ways of performing photocrystallographic measurements (Fig. 1). In the first approach the crystal is irradiated for some time, and then, assuming that the lifetime of the excited (or metastable) molecules in the crystal is sufficiently long (or 'infinite'), a diffraction measurement is performed (Fig. 1A). This is known as the static (or steady-state) method. In turn, when the lifetime of the excited state is relatively short and cannot be easily extended by e.g. reduced temperature, the quasi-static (or quasi-steady-state), or more preferably stroboscopic method is used. In this case, the crystal is exposed to light irradiation (repetitive laser pulses with a defined time separation) in order to achieve a time-averaged saturation of the crystal with the excited species (i.e. a certain limit degree of conversion), and then an X-ray diffraction measurement is carried out while continuing the crystal irradiation. In the quasi-static approach the sample is measured in a standard way using the continuous X-ray beam (Fig. 1B), while in the stroboscopic method short X-ray pulses are generated and applied to the sample (e.g. using a rotating shutter) (Fig. 1C).[35] Hatcher & Raithby[33] describe quasi-static and stroboscopic methods together, since, despite the character of an X-ray beam, they are quite similar. In the extreme case, the diffraction of single X-ray pulses on the examined crystal, synchronized with the pulses of the excitation laser light, is recorded (single-pulse diffraction). This is the so-called pump-probe method (Fig. 1D). The sample is

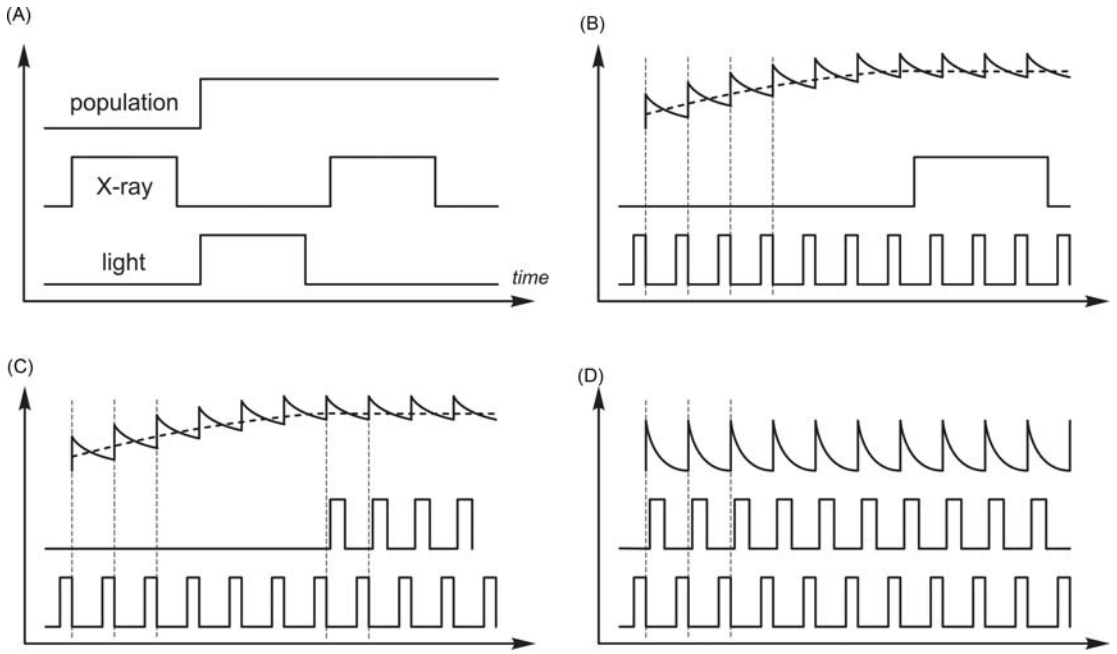

Fig. 1 Schematic representation of various types of photocrystallographic experiments: (A) static method, (B) quasi-static method, (C) stroboscopic method, (D) pump-probe method. Dashed line in (B) and (C) refers to average population. Modified and extended figure from Hatcher, L. E.; Raithby, P. R. Dynamic Single-Crystal Diffraction Studies Using Synchrotron Radiation. *Coord. Chem. Rev.* ***2014, 277–278, 69–79.***

excited (or 'pumped') with a laser pulse, and then (with a strictly defined delay) it is 'probed' with an X-ray pulse. This technique enables structural studies of molecular species with very short life times. A temporal resolution of up to about 100 ps is available using synchrotron sources (or even shorter in the case of XFELs). It should be noted that with the quasi-static and stroboscopic methods there is some risk of registering a diffraction signal from a number of different states simultaneously, due to a rather long 'probing' X-ray pulse. The pump-probe method is more selective as long as the sampling is done with sufficiently short (single) X-ray pulses. Finally, it is stressed that in all methods, except the static approach, the main assumption made concerns the reversibility of the light-induced process. It is presumed that after every light-pulse is applied to the sample, the system gets excited and then it relaxes back to the initial state. This allows measuring the same state multiple times (applying sufficient time-delay between successive laser pulses), thus increasing the resultant signal-to-noise ratio.

While the static, or in some cases, quasi-static experiments can be successfully carried out with a classic X-ray diffractometer, the stroboscopic and pump-probe methods are practically not feasible under laboratory conditions (the complexity of instrumentation increases drastically in such cases). So far, the only published examples of the use of the stroboscopic method to determine structural changes in a crystal with a resolution of several dozens of μs using a laboratory X-ray diffractometer are the studies carried out by Coppens and co-workers.[36,37] It is also worth mentioning here the latest results of D. Schaniel, S. Pillet and collaborators, who collected time-resolved data using a continuous beam and a special fast-gated detector.[38] However, when it becomes necessary to reduce the time of sample exposure to X-ray radiation to a few μs, and further ns or even ps, synchrotron, or possibly XFEL, sources become indispensable, because they provide sufficiently high X-ray radiation intensity in such a short time scale. All issues raised here with regard to TR methods will be discussed further in this chapter.

10.11.2.1 Data collection

The common feature of all synchrotron beamlines dedicated to time-resolved photocrystallographic experiments (apart from standard hardware shared by most beamlines) is the equipment allowing laser beam delivery to the sample. This is realized differently depending on the experiment, and the beamline. On beamlines with TR capabilities, this is usually done using special optical setups located either inside the X-ray hutch, or in a special 'laser' hutch from which the laser beam is delivered through fiber optics, or a set of mirrors, and appropriately conditioned (light pulses are stretched or compressed, polarization is changed etc.) before reaching the sample (Fig. 2).[6,34,35,39–43] It is noted that some of these solutions can also be applied when using laboratory diffractometers. Apart from that, the fundamental experimental differences result from the used X-ray radiation – whether it is mono- or polychromatic.

10.11.2.1.1 Monochromatic method

Simple photocrystallographic experiments using monochromatic X-ray radiation can be carried out practically on any beamline allowing for single crystal diffraction studies. The only necessary element here is the ability to deliver the laser light to the sample. Such solutions are available, for example, at the beamlines 15-ID-B ChemMatCARS at APS (Advanced Photon Source, Chicago,

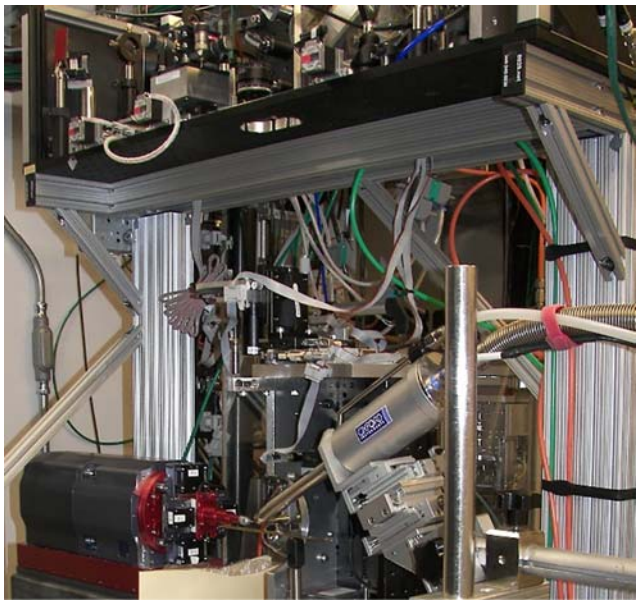

Fig. 2 Final part of the optical system used at the 14-ID-B BioCARS beamline (APS) (laser beam is delivered through the vacuum pipe from the second 'laser' hutch and appropriately conditioned). In the middle of the picture one can see focusing optics tube (a sample is mounted at the end of the red-color goniometer and exposed to cold nitrogen flow from the low-temperature device).

USA),[42] I19 at DLS (Diamond Light Source, Oxfordshire, United Kingdom),[44] P24 at DESY (Deutsches Elektronen-Synchrotron, Hamburg, Germany), BM01 at ESRF (European Synchrotron Radiation Facility, Grenoble, France), CRISTAL at SOLEIL (Paris, France), BL02B1 at SPring-8 (Hyogo, Japan).[45] It should be emphasized, however, that time-resolved studies are more demanding. To perform such experiments appropriately, short X-ray pulses must be generated and synchronized with the laser pulses. The structure of the synchrotron beam itself facilitates studies with picosecond resolution, as each electron bunch in the storage ring generates a single X-ray pulse of 20–150 ps duration. The generation of the desired short beam fragment, or the isolation of a single pulse from the primary beam, constitutes one of the biggest challenges. Both of these options can be realized by means of an appropriately constructed fast rotating shutter, i.e. the so-called chopper (**Fig. 3**),[46] or by a set of these (see later). By adjusting the rotation frequency, X-ray pulses of various duration can be isolated and further synchronized with laser pulses.[35] It should be noted here, however, that choppers used in majority of such experiments, do not isolate individual pulses from the synchrotron train, but rather 'cut-out' parts, the so-called bursts composed of multiple single pulses.[35] Such bursts had primarily been used in the stroboscopic method, until appropriate procedures to isolating single pulses were developed (see later). Nonetheless, for simplicity these bursts are often referred to as pulses, but one should keep in mind the difference.

In photocrystallographic experiments, a synchrotron beam interacts with a laser-light-excited crystal. The laser-irradiated sample consists of both ground- and excited-state molecules, since the excitation is almost always partial. The respective detector readouts (called diffraction frames) contain information about the so-called light-ON structure. The reference ground-state structure, called the light-OFF structure, is obtained using the same (or a similar) data collection strategy, however, without crystal exposure to the laser-light. Consequently, two sets of data, i.e. light-ON and light-OFF frame sets, are obtained. They can be further analyzed using various methods. More on data handling will be presented in the part dedicated to data processing. Here, the use of gating PAD detectors (pixel array detectors) will be discussed. These detectors are able to accumulate the signal and are sufficiently fast to register the light-ON and light-OFF frames separately without using shutters (**Fig. 4**A). After accumulating a sufficiently large number of individual measurements, the detector readout and the frames (both light-ON and light-OFF) are saved to disk. Experiments conducted with a PILATUS detector[47] indicate that the reflections recorded with the laser (the excitation line was 400 nm) are shifted on the detector in relation to those observed without irradiation.[48] For example, **Fig. 4**B shows the reflection shifts for α-perylene films of different thickness. It is worth mentioning that a similar idea was applied to the XPAD detector in a study of the influence of a static electric field on the crystal structure.[49] Finally, it is noted that a few stroboscopic experiments using a rotating chopper, or a gated PAD detector, have been performed on a laboratory diffractometer. They are described at the end of the chapter and treated separately.

10.11.2.1.2 Laue method

Despite the high intensity of synchrotron radiation, monochromatization significantly weakens the beam. Thus, in order to maintain high beam intensity, polychromatic radiation can be utilized (naturally it contains more photons in the single pulse, as it is characterized by a certain wavelength range, instead of a strictly selected wavelength). Application of a polychromatic X-ray beam constitutes the so-called Laue method, which dates back to the first diffraction experiment performed with the use of X-rays.[50,51] Naturally, this procedure has its drawbacks, such as much more complex further processing of the collected data (due to the unknown X-ray wavelength diffracted at a given angle resulting in the recorded reflection). However, the benefit that incomparably stronger signals are obtained in a much shorter time cannot be overestimated. Shorter exposure time also translates into diminished deterioration of the sample (most often it is the high-intensity laser light that degrades the crystal). Another advantage is that the crystal does not need to be rotated when measuring a single frame (all the reflections are captured between two limiting Ewald spheres), which is the case in a monochromatic experiment. A comparison of diffraction frames recorded using the

Fig. 3 Realization of a fast chopper used to produce X-ray pulses. Thin chopper slots are visible at the perimeter of the steel disk. The performance of this chopper was tested at the 15-ID-B ChemMatCARS beamline (APS). Reproduced with permission of the International Union of Crystallography from Gembicky, M.; Oss, D.; Fuchs, R.; Coppens, P. A Fast Mechanical Shutter for Submicrosecond Time-Resolved Synchrotron Experiments. *J. Synchrotron Rad.* ***2005, 12, 665–669***.

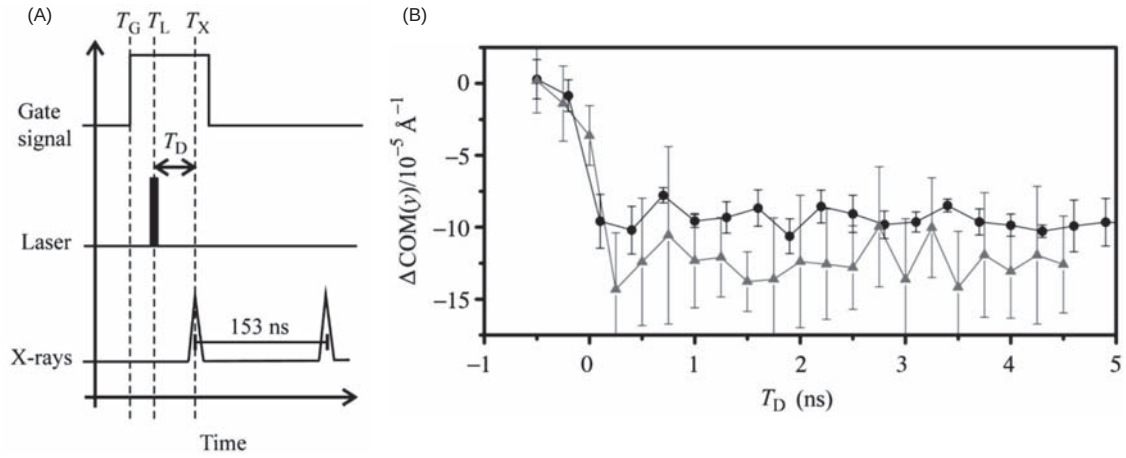

Fig. 4 (A) Scheme showing the gating of a PAD detector and its synchronization to the X-ray and laser pulses (timing scheme is the same as in the APS standard operating mode – consecutive synchrotron-train pulses are separated by 154 ns). (B) Reflection 001 center-of-gravity shift versus pump-probe time delay for two α-perylene thin films (circles – 700 nm thickness, triangles – 500 nm). Reproduced with permission of the International Union of Ejdrup, T.; Lemke, H. T.; Haldrup, K.; Nielsen, T. N.; Arms, D. A.; Walko, D. A.; Miceli, A.; Landahl, E. C.; Dufresne, E. M.; Nielsen, M. M. Picosecond Time-Resolved Laser Pump/X-Ray Probe Experiments Using a Gated Single-Photon-Counting Area Detector. *J. Synchrotron Rad.* ***2009, 16, 387–390.***

monochromatic and polychromatic methods is presented below (Fig. 5). Considerable differences in the exposure time should be noted, which strongly support the use of polychromatic radiation for time-resolved studies.[11,13]

There are only a few synchrotron lines in the world adapted to perform time-resolved polychromatic experiments with a time resolution of about 100 ps. Major beamlines dedicated to such measurements on single crystals are located at ESRF in France (ID09 beamline, formerly ID09B),[39] APS in the USA (14-ID-B BioCARS beamline)[40] and KEK (高エネルギー加速器研究機構, i.e. The High Energy Accelerator Research Organization) in Japan (NW14A beamline).[52] All these beamlines are located on high-energy storage rings: 6.0 GeV for ESRF (note the recently finished upgrade to so-called Extremely Brilliant Source), 7.0 GeV for APS (upgrade is planned for 2022) and 6.5 GeV for KEK (Photon Factory Advanced Ring – PF-AR). A very important and detailed study of the 14-ID-B BioCARS beamline was published in 2011 by Graber et al.[40] The following description will therefore briefly summarize this article, including comments regarding other beamlines.

Each beamline designed for TR experiments is located along an undulator section of the synchrotron ring, because this insertion device produces X-rays with much greater intensity than a bending magnet. X-rays from an undulator also exhibit better spatial and spectral characteristics. In the case of the ID09 and 14-ID-B BioCARS beamlines, the undulator allows limiting the spectrum of the generated X-rays. An X-ray beam spanning a narrow range of energies is called a 'pink' beam, in contrast to the parent 'white' beam with a wide spectral range. Example curves showing the dependence of X-ray intensity versus wavelength (the so-called λ-curves) are presented in Fig. 6.

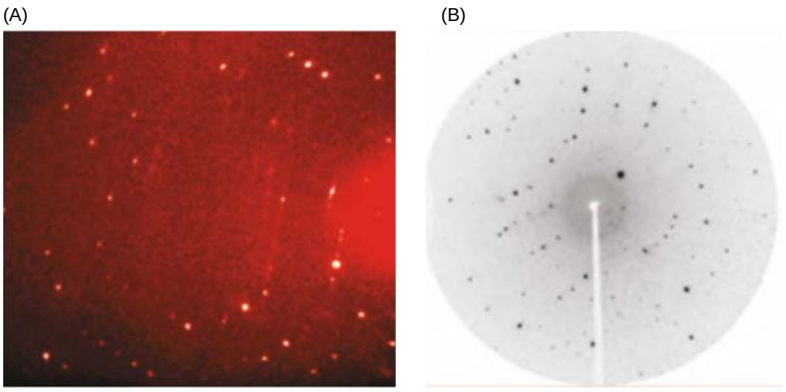

Fig. 5 (A) X-ray diffraction frame recorded with a monochromatic X-ray beam (1 μs exposure time) at 15-ID-B ChemMatCARS beamline (APS). (B) X-ray diffraction frame recorded with a polychromatic X-ray pulse (ca. 80 ps = $8 \cdot 10^{-5}$ μs) at 14-ID-B BioCARS beamline (APS). Reproduced with permission from Coppens, P. Molecular Excited-State Structure by Time-Resolved Pump-Probe X-Ray Diffraction. What Is New and What Are the Prospects for Further Progress? *J. Phys. Chem. Lett.* ***2011, 2, 616–621.*** Copyright (2011) American Chemical Society.

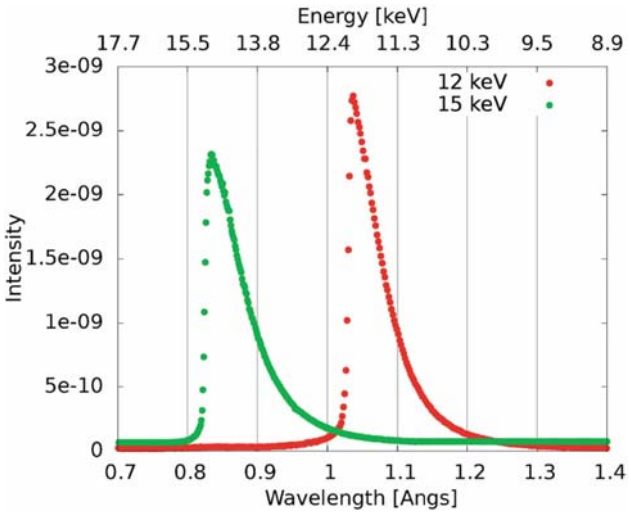

Fig. 6 Example λ-curves showing the X-ray intensity versus wavelength for two selected energy settings at the 14-ID-B BioCARS beamline (APS) used in Laue experiments. Note the higher harmonics are removed with the use of beryllium filters. Reproduced with permission of the International Union of Crystallography from Coppens, P.; Fournier, B. New Methods in Time-Resolved Laue Pump-Probe Crystallography at Synchrotron Sources. *J. Synchrotron Rad.* **2015**, *22*, 280–287.

Depending on the electron bunches (and their configuration), which are injected into the storage ring of the synchrotron, different X-ray pulses can be generated. For example, at the APS synchrotron (data from the official website: https://ops.aps.anl.gov/SRparameters/SRparameters.html), the standard configuration with 24 uniformly-spaced single electron bunches results in a train of pulses of 33.5 ps duration separated by 153 ns. In turn, the so-called hybrid mode generates intense pulses of about 50 ps duration separated by symmetrical 1.59 μs gaps from the series of weaker pulses. All beamlines are adapted to operate in various configurations in order to maximize the use of the available measurement time (called beamtime).

The polychromatic beam from the synchrotron pulse train is definitely too strong for any research (even the "pink" beam), not to mention the impossibility of its control and the isolation of single pulses. In order to weaken the beam, a rotating water-cooled high-heat-load shutter[53] is used. The resulting fragment of the beam (burst) is subjected to further processing using a millisecond shutter and finally a single pulse is separated by a fast-rotating triangular shutter designed by the Forschungszentrum Jülich in Germany (so-called Jülich chopper) (**Fig. 7**).[54] The timing diagram for extracting a single pulse from the entire beam is shown in **Fig. 8**.

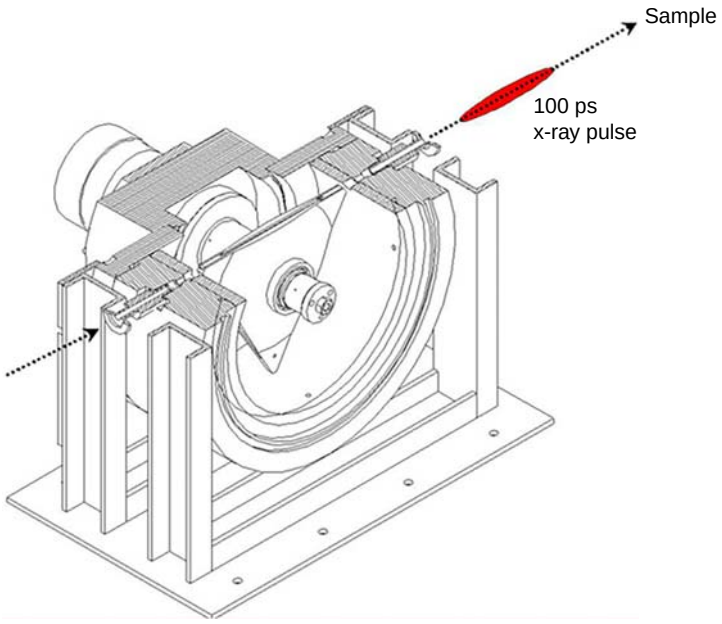

Fig. 7 Schematic of a triangular pulse selector manufactured by the Forschungszentrum Jülich (so-called Jülich chopper).[39,54] The chopper rotates in vacuum and is cooled down by black-body radiation. A 100 ps X-ray spatial distribution is additionally depicted in red. Graphic taken from the official ESRF website: www.esrf.eu.

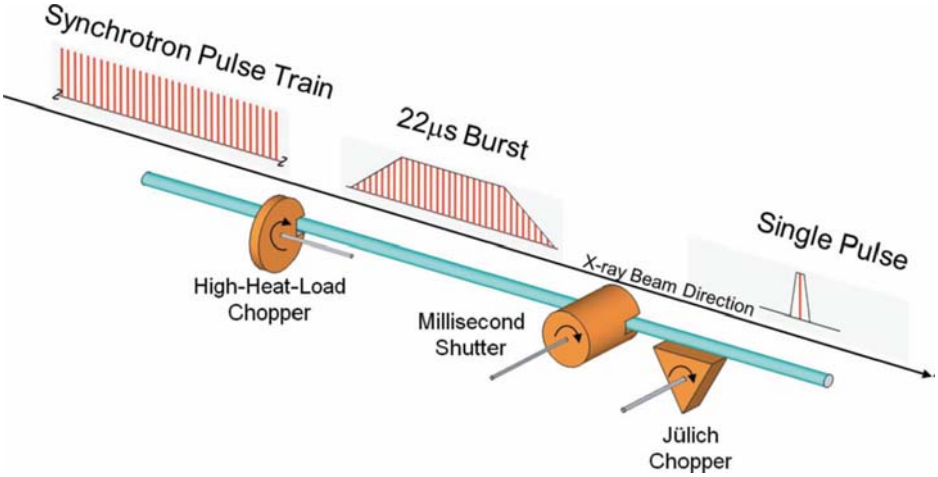

Fig. 8 Scheme showing single pulse isolation at the 14-ID-B BioCARS beamline (APS) via a set of choppers and shutters. Reproduced with permission of the International Union of Crystallography from *J. Synchrotron Rad.* **2011**, *18*, 658. Graber, T.; Anderson, S.; Brewer, H.; Chen, Y.-S.; Cho, H.; Dashdorj, N.; Henning, R. W.; Kosheleva, I.; Macha, G.; Meron, M.; Pahl, R.; Ren, Z.; Ruan, S.; Schotte, F.; Šrajer, V.; Viccaro, P. J.; Westferro, F.; Anfinrud, P.; Moffat, K. BioCARS: A Synchrotron Resource for Time-Resolved X-Ray Science. *J. Synchrotron Rad.* ***2011, 18, 658–670.***

Very similar solutions had been implemented at the ID09 beamline of the ESRF synchrotron, which was the prototype for the 14-ID-B BioCARS beamline. On the NW14A beamline, the attenuation of the beam is performed by the use of a graphite absorber.[52] The difference between the beamlines is mainly the spatial control of the X-ray beam with Kirkpatrick-Beatz (14-ID-B BioCARS),[40] toroidal (ID09),[39] or cylindrical (NM14A) mirrors.[52] An example of a toroidal mirror installed at the ID09 beamline is shown in Fig. 9. It is worth noting here that each beamline is additionally equipped with a monochromator, which, if necessary, allows the use of a monochromatic radiation. However, as already mentioned, in this case the achieved beam intensity is significantly lower, which results in longer exposure times while recording single frames.

In time-resolved photocrystallographic experiments, synchronization of X-ray and laser pulses is essential. Depending on the laser used, different technical solutions are utilized to guide the laser beam to the sample. For example, at the ID09 beamline,

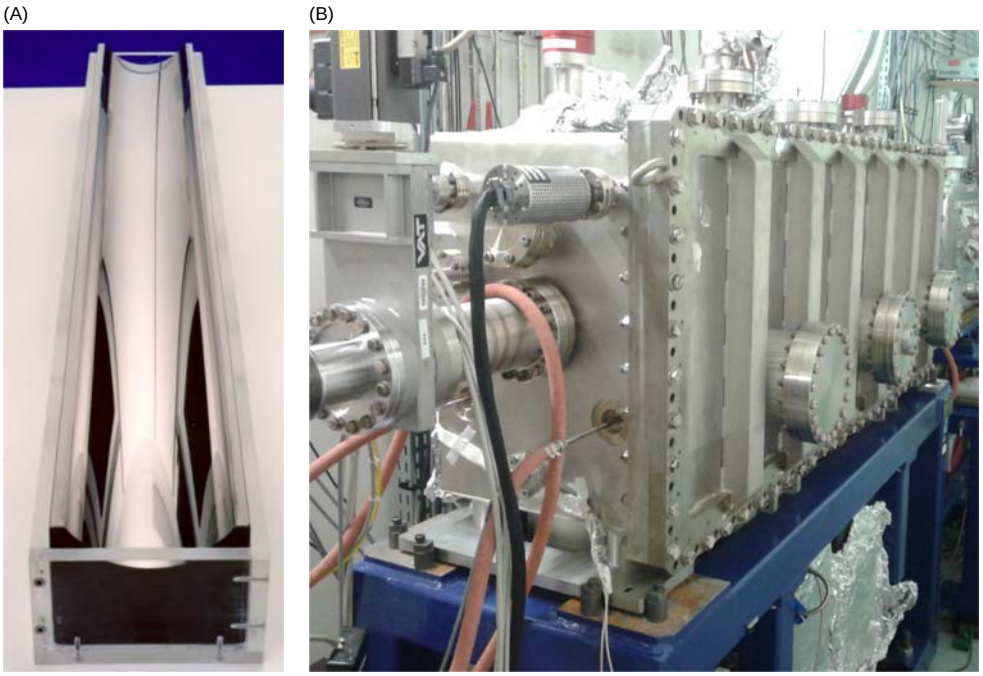

Fig. 9 Photos of the toroidal mirror used at the ID09 beamline (ESRF): (A) mirror before mounting in the vacuum chamber. [Photo taken from the official ESRF website: www.esrf.eu.] (B) Vacuum chamber with the toroidal mirror mounted inside. The mirror is installed on channels with a Ga/In alloy to minimize vibrations. The control of the mirror curvature is accomplished with a stepper motor gently pushing its middle part from the bottom.

all lasers are located in the same experimental hutch, while at the 14-ID-B BioCARS and NM14A beamlines, the femto- and picosecond lasers are placed in separate, specially adapted, rooms. The synchronization of pulses is controlled electronically, which is perfectly sufficient in the case of the currently available time scale.[55] The operation of all the shutters and the frequency of the lasers are adjusted to the frequency of circulation of the electron packets in the accumulation ring. The use of FPGA (field-programmable gate array) modules allows for pulse synchronization with a 10 ps accuracy.

Each of the aforementioned beamlines is equipped with a CCD (charge-coupled device) detector with a sufficiently large surface area. This allows the recording of fairly high resolution data, in many cases corresponding to atomic resolution (about 0.6 $Å^{-1}$), which enables structure determination of excited states with lifetimes as short as 100 ps. None of these beamlines is, however, equipped with a PAD detector yet. Therefore, at present it is hardly possible to perform pump-probe synchrotron experiments without the isolation of X-ray pulses.

The TR data collected for small-molecule crystals using the Laue method is essentially different from that obtained for macromolecules, and that from monochromatic experiments, where standard data processing methods can be used. The experimental procedure requires measuring light-ON and light-OFF data together.[12,56,57] Due to the low signal-to-noise ratio, single measurements are performed a number of times. A method developed specifically for small-molecule crystals employs the intensity ratios (described later in this chapter) and uses a measuring sequence in which successive pairs of light-ON and light-OFF frames are recorded several times (and only then the orientation of the sample is changed).[56,57] Optimization of this method facilitated collection of good quality data, examples of which will be presented and discussed later in the chapter.

10.11.2.1.3 XFEL prospects

Great research opportunities for TR photocrystallographic experiments have appeared along with the invention and availability of X-ray free-electron lasers. Major X-ray sources of this type are LCLS (Linac Coherent Light Source) in the USA,[58] SACLA (Spring-8 Angstrom Compact free electron Laser) in Japan,[59] FERMI (Free Electron laser Radiation for Multidisciplinary Investigations) in Italy,[60] PAL-XFEL (Pohang Accelerator Laboratory X-ray Free Electron Laser) in South Korea,[61] European XFEL (European X-ray Free Electron Laser) in Germany,[62] and SwissFEL (Swiss X-ray Free Electron Laser) in Switzerland.[63] While the X-rays generated in a synchrotron are polychromatic (such a beam can be further monochromatized along with some loss of its intensity), XFELs provide a very intense and virtually monochromatic beam (e.g. $\Delta E/E \leq 10^{-4}$, which is less than 0.01%, in the case of the European XFEL; the exception is the SwissFEL laser, where the beam is spectrally wider, up to about 2%[64]). Moreover, the XFEL generates pulses of femtosecond duration, which makes it possible to study ultrafast processes. Of course, this entails the need for comprehensive development of the desired research equipment, as well as data processing and analysis methods. In addition to modern electronic solutions, such as dedicated novel detection systems, advanced tailor-made laser systems for sample excitation are indispensable.

10.11.2.2 Data processing and analysis

Diffraction data processing provides a way to determine structure factors from the data recorded on the detector surface. A photocrystallographic experiment is, in particular, designed in a way to obtain structure factors for a crystal exposed to light (light-ON structure). There are two cases that should be distinguished here: static data and time-resolved data. Until now, static data has been measured using the monochromatic method (some proteins are an exception). This allows the use of standard tools for data indexing (finding the crystal orientation matrix and unit-cell dimensions), integration (e.g. using profile-fitting methods) and scaling. For time-resolved measurements, monochromatic data can be processed in a standard way. However, more sophisticated approaches are needed to handle polychromatic experimental data. Furthermore, diffraction data processing for large-molecule crystals (e.g. proteins; large lattice parameters) and small-molecule crystals (small lattice parameters) should be discussed separately, as the character of the respective diffraction patterns requires different treatment. Since the degree of excitation of molecules in a crystal usually amounts to only a few percent, it is important to develop data processing methods that will allow the extraction of this weak signal from the collected data.

10.11.2.2.1 Laue data processing for macromolecular crystals

Diffraction data from sufficiently large molecules (e.g. proteins) is characterized by dense diffraction patterns, i.e. many reflections are recorded on a single frame (**Fig. 10**). This is due to the considerable size of the respective unit cell and it is further enhanced by the use of polychromatic radiation. As a result, a typical diffraction pattern of this kind contains numerous reflections arranged on ellipses (**Fig. 10**).

The number of reflections and the presence of elliptical patterns constituted the basis for concepts behind some specific procedures. It is worth noting that the unit cell dimensions of the crystal are determined prior to the TR Laue experiment. Therefore, only the crystal orientation remains unknown. Various methods of determining the crystal orientation are currently available, the most interesting of which take advantage of diffraction pattern analysis.[65] It can be proved that reflections lying at the intersection of ellipses usually have low indices. Thus, the proper crystal orientation can be achieved by testing different possible indices for such reflections against the previously determined unit cell parameters. Such procedures work very well, even for single frames.

Once the crystal orientation is found, protein data can be integrated in the same way it is done for monochromatic data. The most common method here is the profile-fitting approach.[66,67] The main difference concerns data scaling. As the data is polychromatic, the number of corrections is much greater. The total scale factor for the integrated reflection intensities includes the following

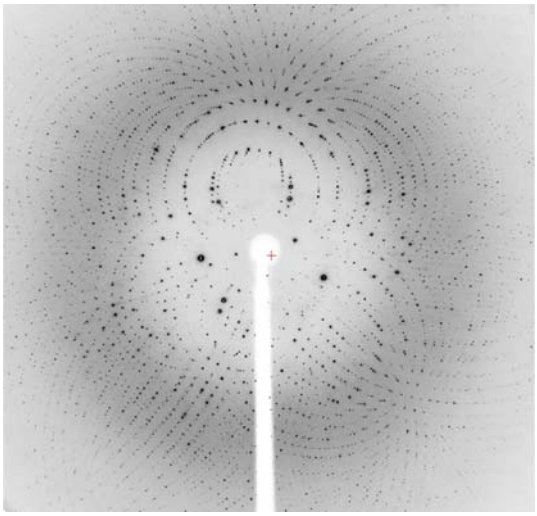

Fig. 10 An example protein X-ray Laue diffraction frame. Reproduced from the official 14-ID-B BioCARS beamline website: biocars.uchicago.edu.

components: Lorentz factor, polarization factor, isotropic and anisotropic scale factors and thermal vibration factors, absorption factor, X-ray crystal damage factors, corrections to account for the heterogeneity and non-linearity of the detector, and finally the factor responsible for the normalization of the radiation intensity versus wavelength. Together with the absorption correction, the last factor is the most important one. A popular approach is to model it with Chebyshev polynomials.[68] The methods for protein data processing are implemented in a number of programs, such as Daresbury *LAUE* software suite[65,69] or *LAUEVIEW* & *PRECOGNITION*.[70]

To date, most monochromatic TR macromolecular data has been collected at XFEL sources. In this case, a very large number of detector readouts for different orientations of various crystals is obtained (an example of the implementation of the measurement method and the experimental results are presented and discussed later). Such data is often extremely large, and therefore requires considerable computing power to process it. Moreover, due to the very short duration of an X-ray pulse and the fact that each successive crystal is measured with a different X-ray pulse, it is not possible to record the full integrated intensity of a given reflection. It turns out, however, that appropriate scaling of such combined data allows the reconstruction of a set of reflections with satisfactory quality for further analysis. The most frequently used programs here are *CHEETAH*[71] and *CRYSTFEL*.[72]

10.11.2.2.2 Laue data processing for small-molecule crystals

In the case of polychromatic data from small molecule crystals, the observed number of reflections on a single diffraction frame is much smaller (due to smaller unit-cell dimensions) than for macromolecular crystals (**Fig. 5**B). Naturally, the number of diffraction spots is still greater than for the monochromatic method. However, the recorded diffraction images can be considered 'sparse'. This makes it difficult, or simply impossible in many cases, to determine the crystal orientation matrix using the methods employed for macromolecular Laue diffraction data treatment. The basic problem is the lack of knowledge about the wavelength from which a given reflection originates. The difficulty of determining the orientation matrix for small-molecule crystals initially hampered the development of the field. However, ingenious algorithms supported by sufficiently high computing power made it possible to solve this problem in an effective manner.[73] Such a method of searching for an orientation matrix requires knowledge about reflection intensities. Therefore, the first step is devoted to signal detection and integration. This is the reverse of the standard methodology. Until now, several orientation-matrix-less methods have been developed and described in the literature, out of which the one described below was used for TR photocrystallographic studies of small molecules. The method involves searching for a signal by looking at a single pixel on the detector on the successive measurement frames (**Fig. 11**) and, by applying statistical assumptions or tools to check whether it contains signal.[74] Most of the frames include only background information. The methods for signal searching in such one-dimensional data can vary. The simplest algorithm assumes that a certain percentage of all pixels contain a signal. For example, the highest intensity pixels, which roughly constitute about 30% of all pixels, are considered to carry information about the signal. The rest is set to background. More advanced procedures involve statistical analysis of a pixels' intensity distribution. In one such approach, the one-dimensional input data set is broken down into background and signal regions by minimizing the background skewness (i.e., the third statistical moment). Indeed, the presence of a signal increases the skewness through the presence of pixels of significantly greater intensity.[75] This method stems from early developments used for two- or three-dimensional X-ray or neutron diffraction data.[76–79] Another approach is to apply the condition that the variance of the set of intensities is equal to the mean (a condition imposed by assuming the Poisson distribution).[80] In the case of redundant measurements for light-ON and light-OFF frames, the non-parametric Kruskal-Wallis test can be used in order to select pixels containing the signal.[10,74] The total signal from a single reflection registered on a given frame is composed of such individual pixels, and on

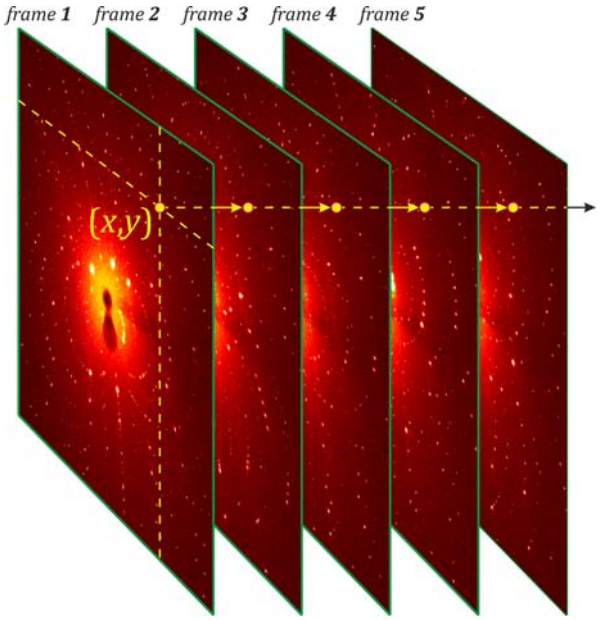

Fig. 11 Idea behind the pixel-based integration method. A selected pixel on the area detector is marked and analyzed versus frame index. Reproduced with permission of the International Union of Crystallography from supporting information of Szarejko, D.; Kamiński, R.; Łaski, P.; Jarzembska, K. N. Seed-Skewness Algorithm for X-Ray Diffraction Signal Detection in the Time-Resolved Synchrotron Laue Photocrystallography. *J. Synchrotron Rad.* ***2020, 27, 405–413.***

this basis the integration masks are created, which define the measured spot areas (Fig. 12). It is worth noting here that this method also allows for very good background estimation, due to the multitude of pixels with no signal.

The actual intensity values measured in the neighboring pixels are not independent. Since the applied statistical methods for individual pixels do not take this into account, in many cases very small (e.g. 1 pixel), or very irregular, signals are observed. In order to reduce such specific noise, signals found with too few pixels are rejected, whereas larger signals are smoothed using the so-called morphological operations known from image processing methods.[81] It should be emphasized, however, that this approach is largely based on our general intuition about data quality, not on actual physical premises. Therefore, models describing the nature of the observed diffraction signals, which will allow for a better understanding of the sources of errors and noise in this type of data, are desired[82] (currently these methods are better developed for monochromatic sources).

The next step in the data processing involves finding the crystal orientation. As the wavelength at which individual reflections are registered is not known, the reciprocal vectors describing every measured reflection, **h** vectors, are normalized[73]:

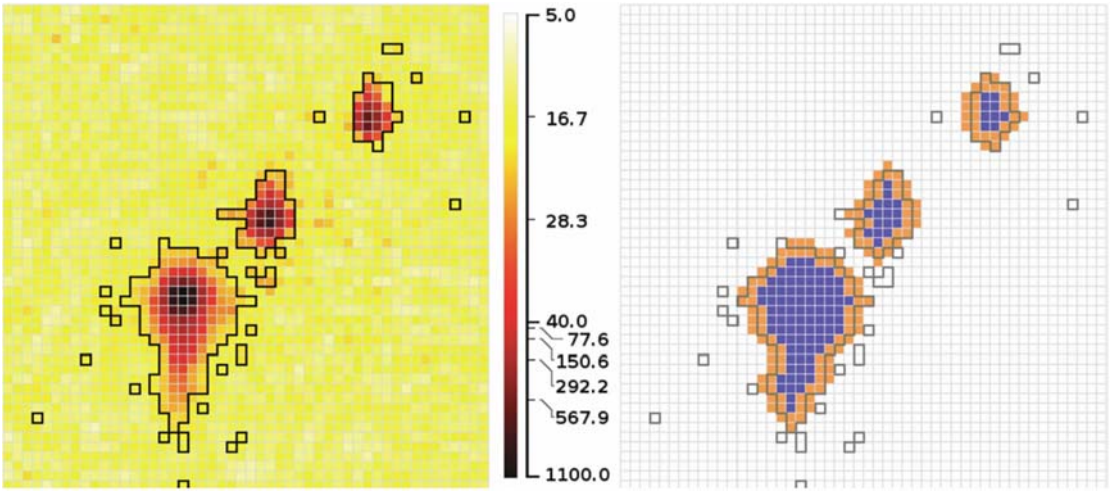

Fig. 12 Raw (left) and filtered (right) diffraction signals determined from Laue data. Reproduced with permission of the International Union of Crystallography from Kalinowski, J. A.; Fournier, B.; Makal, A.; Coppens, P. The LaueUtil Toolkit for Laue Photocrystallography. II. Spot Finding and Integration. *J. Synchrotron Rad.* ***2012, 19, 637–646.***

$$\underset{\sim}{\mathbf{h}} = \frac{\mathbf{h}}{\|\mathbf{h}\|}. \tag{1}$$

where $\|\mathbf{h}\|$ denotes norm (or length) of a given $\mathbf{h}$ vector. The vectors computed in this way are arranged in reciprocal space on the unit sphere (Fig. 13). Such a sphere can also be generated for the known reference ground-state crystal structure (determined in a standard way using e.g. a laboratory diffractometer). In the orientation-matrix search procedure these two data sets are compared. It is assumed that if a reflection is strong in a monochromatic experiment, it should also be strong in the Laue data. Therefore, the two spheres are overlapped in a search for the best match between as many strong reflections as possible. Whenever such a match fulfills a set criterion for its significance, the respective potential orientation matrix is added to the list. The best orientation matrix is determined on the basis of the highest number of occurrences of a given configuration of Euler angles in the mentioned list generated by the algorithm. This method requires a large amount of data, thus a single frame is certainly not sufficient to index the signals. Moreover, the knowledge of the ground-state crystal structure is indispensable here (not just the shape of the unit cell). Both the described integration and indexing methods were implemented in the *LAUEUTIL* package.[73,74] A recent somewhat similar algorithm, called *PINKINDEXER*,[83] uses the known unit-cell parameters and is based on mapping all possible rotations of candidate reciprocal-lattice points onto line fragments of the reciprocal space which correspond to Bragg peaks of unknown wavelength. The analysis of such mappings allows determination of the orientation matrix. This algorithm is very effective in indexing data from both synchrotron and XFEL sources. Its disadvantage, however, is a relatively long execution time. Finally, it is noted that data indexing using the above-described methods is very much dependent on the quality of the description for the experimental setup (mathematically expressed as an instrument model). In the case of the Laue method, it is possible to refine the instrument model similarly as it is done for monochromatic data,[84] but proceeding in a space of normalized reciprocal vectors.[85] This approach has recently been shown to work very well and, with such a refined instrument model, the indexing procedure for various Laue patterns from small-molecule crystals is notably more effective.

10.11.2.2.3 Photodifference maps

The extracted reflection intensities are primarily used to construct, so-called, photodifference maps, which indicate atomic shifts occurring upon excitation, prior to the actual structure refinement. In order to understand how these maps are computed, the basic principles of crystallography are recalled. It is known that the electron density distribution in a crystal can be calculated via the inverse Fourier transform of a set of structure factors. In order to perform such a mathematical operation, one must know both the structure factor magnitudes and phases. The magnitudes are obviously extracted directly from an X-ray diffraction experiment, whereas the phases are found at the structure-solution stage. A discrete set of structure factors (for reflections, $\mathbf{h}$'s), F's and their phases, φ's, gives rise to the electron density at a given point $\mathbf{r}$ according to the well-known formula:

$$\varrho(\mathbf{r}) = \frac{1}{V}\sum_{\mathbf{h}} |F(\mathbf{h})| e^{\mathrm{i}\varphi(\mathbf{h})} e^{-2\pi \mathrm{i}\mathbf{h}\cdot\mathbf{r}}, \tag{2}$$

where V is the unit-cell volume while the summation is over all available reflections. Generally, such a procedure can be performed for various sets of structure factors. During standard crystal-structure determination, structure factors calculated on the basis of the constructed structural model (F_c's, subscript "c" stands for calculated) are customary compared with the respective values obtained experimentally (F_o's, subscript "o" stands for observed). In such case there is obviously only one set of phases, namely the calculated ones (φ_c's), thus the formula for the so-called residual density map $\Delta\rho_{res}$ is as follows:

Fig. 13 Visualization of normalized reciprocal vectors for experimental (left) and theoretical (right) data. In the experimental data, the effect of data incompleteness is obvious. Reproduced with permission of the International Union of Crystallography from Kalinowski, J. A.; Makal, A.; Coppens, P. The LaueUtil Toolkit for Laue Photocrystallography: I. Rapid Orientation Matrix Determination for Intermediate Size Unit-Cell Laue Data. *J. Appl. Cryst.* ***2011, 44, 1182–1189.***

$$\Delta\varrho_{\mathrm{res}}(\mathbf{r}) = \frac{1}{V}\sum_{\mathbf{h}}(|F_{\mathrm{o}}(\mathbf{h})| - |F_{\mathrm{c}}(\mathbf{h})|)e^{\mathrm{i}\varphi_{\mathrm{c}}(\mathbf{h})}e^{-2\pi\mathrm{i}\mathbf{h}\cdot\mathbf{r}}. \tag{3}$$

By analogy, any two sets of structure factors, for example the ones for the respective light-ON and light-OFF structures, can be subtracted one from another yielding what we call a photodifference map $\Delta\rho_{\mathrm{phd}}$:

$$\Delta\varrho_{\mathrm{phd}}(\mathbf{r}) = \frac{1}{V}\sum_{\mathbf{h}}\left(|F^{\mathrm{ON}}(\mathbf{h})|e^{\mathrm{i}\varphi^{\mathrm{ON}}(\mathbf{h})} - |F^{\mathrm{OFF}}(\mathbf{h})|e^{\mathrm{i}\varphi^{\mathrm{OFF}}(\mathbf{h})}\right)e^{-2\pi\mathrm{i}\mathbf{h}\cdot\mathbf{r}} = \frac{1}{V}\sum_{\mathbf{h}}\left(|F^{\mathrm{ON}}(\mathbf{h})| - |F^{\mathrm{OFF}}(\mathbf{h})|\right)e^{\mathrm{i}\varphi^{\mathrm{OFF}}(\mathbf{h})}e^{-2\pi\mathrm{i}\mathbf{h}\cdot\mathbf{r}}, \tag{4}$$

where in the second expression it is assumed that $\varphi^{\mathrm{ON}} = \varphi^{\mathrm{OFF}}$, which is a common approach in TR studies (a close resemblance of the ground and excited-state structures validates this assumption due to the low population of excited-state species; see further examples). As discussed later in the text, the photodifference map provides a first indication of the structural changes occurring upon excitation. Positive peaks are observed at places where the excited-state atoms shifted in space; negative peaks indicate both charge flow and the increase of thermal vibrations of atoms, and are usually present at the ground-state atomic positions.

In the context of the Laue method, a significant achievement was to realize that determination of the light-ON and light-OFF crystal structures separately is not required. It turned out that a simple ratio of such intensities is perfectly sufficient[86]:

$$R(\mathbf{h}) = \frac{I^{\mathrm{ON}}(\mathbf{h})}{I^{\mathrm{OFF}}(\mathbf{h})}. \tag{5}$$

Obviously, this quantity does not contain full information about the crystal structure itself, but the picture becomes much more complete when combined with the reference monochromatic data collected at the temperature corresponding to that of the time-resolved measurement. It is assumed that the parameters of the crystal lattice do not change significantly during excitation and that the necessary corrections for the intensity of the corresponding reflections are the same for both the light-OFF and light-ON structures of the crystal. This seems reasonable, considering the fact that usually only a few percent of the molecules in a crystal get excited. Consequently, when using intensity ratios, effects from absorption, extinction, polarization, etc., which depend on the wavelength of X-rays, and otherwise would be problematic for polychromatic radiation, can be neglected. In turn, considering ratios as independent of the X-ray wavelength, the absolute structure factors for the light-OFF structure determined with high accuracy and precision using the monochromatic method (e.g. at another synchrotron beamline or using a laboratory diffractometer) can be multiplied by the square-roots of ratios determined experimentally (we recall that diffraction intensities are proportional to squares of structure factor moduli) in order to estimate structure factors for the light-ON crystal structure ($F_{\mathrm{e}}{}^{\mathrm{ON}}$, subscript "e" stands for estimated) as follows:

$$F_{\mathrm{e}}^{\mathrm{ON}}(\mathbf{h}) = \sqrt{R(\mathbf{h})}\cdot F_{\mathrm{o}}^{\mathrm{mOFF}}(\mathbf{h}), \tag{6}$$

where $F_{\mathrm{o}}^{\mathrm{mOFF}}$ are the observed structure factors for the light-OFF reference crystal determined by the monochromatic method. Assuming that the phases of individual structure factors do not change under the influence of excitation (thus they can be calculated from the model obtained on the basis of monochromatic data) the inverse Fourier transformation of the differences of these structure factors can be performed, yielding a photodifference electron density map defined as follows:

$$\Delta\varrho_{\mathrm{phd}} = \frac{1}{V}\sum_{\mathbf{h}}\left(|F_{\mathrm{e}}^{\mathrm{ON}}(\mathbf{h})| - |F_{\mathrm{o}}^{\mathrm{mOFF}}(\mathbf{h})|\right)e^{\mathrm{i}\varphi_{\mathrm{c}}^{\mathrm{mOFF}}(\mathbf{h})}e^{-2\pi\mathrm{i}\mathbf{h}\cdot\mathbf{r}} = \frac{1}{V}\sum_{\mathbf{h}}\left(\sqrt{R(\mathbf{h})} - 1\right)|F_{\mathrm{o}}^{\mathrm{mOFF}}(\mathbf{h})|e^{\mathrm{i}\varphi_{\mathrm{c}}^{\mathrm{mOFF}}(\mathbf{h})}e^{-2\pi\mathrm{i}\mathbf{h}\cdot\mathbf{r}}. \tag{7}$$

10.11.2.2.4 Structure-model refinement

The photodifference map constitutes a qualitative description of what happens when the crystal is excited by laser light, thus it constitutes a kind of signpost. However, it is possible to go a step further and fit a structural model to the measured data, similarly to what is done in classical crystallography. This becomes feasible when the collected data are of relatively high resolution and sufficient completeness. In this case, a refinement on the earlier-introduced intensity ratios R's is applied, i.e. the following function is minimized:

$$S_R = \sum_{\mathbf{h}} w(\mathbf{h})(|R_{\mathrm{o}}(\mathbf{h})| - |R_{\mathrm{c}}(\mathbf{h})|)^2. \tag{8}$$

Intensity ratios are often expressed as relative changes, called response ratios:

$$\eta(\mathbf{h}) = \frac{I^{\mathrm{ON}}(\mathbf{h}) - I^{\mathrm{OFF}}(\mathbf{h})}{I^{\mathrm{OFF}}(\mathbf{h})} = R(\mathbf{h}) - 1, \tag{9}$$

thus the refinement of a structural model based on the intensity ratios is termed a response-ratio refinement. The practical aspects of such a refinement are described in detail in the literature,[87] while the procedure itself has been implemented in the *LASER* program.[88] This program is based on a very early version of *JANA*,[89] which is an excellent tool to refine modulated and complicated crystal structures, later modified to accommodate response-ratio refinement techniques for TR photocrystallography.[90] The idea of refining the perturbed crystal-structure model against intensity ratios, rather than against structure factors themselves, was present in the early literature. Initial developments focused on the crystal-structure analysis of simple inorganic solids, such as TiO_2[91] or

$LiNbO_3$,[92] perturbed by a static electric field. Later, these methods were applied to organic molecules.[93,94] Nowadays, the field takes advantage of notable methodology and instrument development to facilitate description of a crystals' behavior in electric field at the atomic level.[49,95–97] It should be stressed that, when using the intensity ratio method, the main focus of the refinement is structural changes, which is a clear benefit of this approach when compared to a classical structure refinement against structure factors. As has been already pointed out, the ratio values can be independent of the structure factors for the reference structure, for instance, when using polychromatic radiation and measuring sets of successive light-OFF/light-ON frames.

The current version of the *LASER* program not only allows the determination of structural changes (i.e. geometrical parameters for the excited-state structure), but also population parameters for the excited molecules in a given crystal. It also enables simple estimation of the laser-light-induced temperature increase via the introduction of a so-called temperature scale factor. It is worth noting that the structure factors for the modelled structure can be calculated in two ways, depending on whether the excitation of particles in the crystal occurs randomly throughout its entire volume (random distribution model), or whether domains of excited-state molecules appear in the sample (cluster formation model). Appropriate models lead to different expressions for the whole crystal structure factor.[87] In the random distribution model, the expression for the structure factor for the light-ON structure takes the form:

$$F^{\mathrm{ON}} = (1-P)F^{\mathrm{GS}} + PF^{\mathrm{ES}}, \tag{10}$$

while in the cluster formation model:

$$\left|F^{\mathrm{ON}}\right|^2 = (1-P)\left|F^{\mathrm{GS}}\right|^2 + P\left|F^{\mathrm{ES}}\right|^2. \tag{11}$$

In both cases, F^{GS} and F^{ES} denote the structure factors for the ground and excited molecules, respectively, while the population parameter P stands for the fraction of excited molecules. These formulas are similar to the analogous expressions for the structure factor of a disordered crystal and a twin crystal, respectively.

Up to now, it has been found that the random distribution model seems to be more appropriate for describing the excitation in small-molecule molecular crystals. *LASER* can be used to refine both models versus monochromatic or polychromatic data. In the case of monochromatic data, typical discrepancy indicators for the light-ON and light-OFF structures can be used. For example, the discrepancy factor based on the structure factors looks as follows (note that the factor is referred to as $\underline{R}$ to distinguish it from ratios, R's):

$$\underline{R}[F] = \frac{\sum_{\mathbf{h}} ||F_{\mathrm{o}}(\mathbf{h})| - |F_{\mathrm{c}}(\mathbf{h})||}{\sum_{\mathbf{h}} |F_{\mathrm{o}}(\mathbf{h})|}. \tag{12}$$

In the case of refinement on polychromatic data, however, one must use discrepancy factors based on the ratio values. For this purpose, such factors were introduced in the literature and described in detail.[98,99] For instance, in analogy to the R-factor based on structure factors, the R-factor based on ratios can be defined as follows:

$$\underline{R}[R] = \frac{\sum_{\mathbf{h}} ||R_{\mathrm{o}}(\mathbf{h})| - |R_{\mathrm{c}}(\mathbf{h})||}{\sum_{\mathbf{h}} |R_{\mathrm{o}}(\mathbf{h})|}. \tag{13}$$

It turns out that they perform very well for the evaluation of models obtained after the refinement of the excited state structure. It is also worth noting that by assuming certain model properties for the observed errors in a statistical sense (including the absence of systematic errors and the normal distribution of random errors), theoretical values of such discrepancy indicators can be calculated.[100]

In the case of macromolecules, structural models are refined in a similar way as for 'classical' protein crystallography. The most famous tailor-made programs for this type of analysis are the *PHENIX*[101] and *REFMAC*[102] packages. In photocrystallographic studies of proteins, the experimental results are often supplemented with theoretical modelling, which allows for verification of the models for structural changes by calculating the entire dynamics of the process (e.g. reaction paths). The use of the so-called QM/MM (quantum-mechanics/molecular mechanics) approach, which combines quantum computational methods with classical force field approach, is most common here.

10.11.3 Examples of time-resolved studies

10.11.3.1 Macromolecular TR photocrystallography

Synchrotron radiation is a natural choice in the case of structural investigations of protein crystals and other complex biological systems. Bearing this in mind, it is not surprising that historically time-resolved photocrystallography experiments were first dedicated and developed for macromolecules.[11,13,33] Therefore, examples of such studies will be presented here to sketch the first steps in the field and show experimental possibilities. Time-resolved laser-pump/X-ray-probe experiments are technically extremely difficult regarding achieving sufficient space- and time-resolution. Nevertheless, in the case of proteins, many interesting processes can be tracked even at lower resolution (e.g. movements of whole molecules). In addition, macromolecular crystals are less dense (higher solvent content, higher molecular lability) than small-molecule crystals. Therefore, dynamic changes in such crystals are less limited by the environment, and therefore occur more easily.

One of the first examples of TR X-ray diffraction studies is the work on glycogen phosphorylase.[103,104] The attachment of the ligand molecule, maltoheptaose, to glycogen phosphorylase was monitored using pairs of monochromatic and Laue experiments. These were not really photocrystallographic studies, but such an approach introduced a time scale to macromolecular crystallography, which was already a significant achievement itself. A more important example was a study of the myoglobin complex with carbon monoxide, CO.[105] Here, protein crystals were cooled to 40 K and then TR Laue experiments were performed. Photolysis (i.e. light-triggered bond dissociation), leading to dissociation of CO from myoglobin, was induced by a continuous 633 nm He–Ne laser radiation, while subsequent structural changes were probed by a polychromatic X-ray beam. The data analysis indicated that the CO molecule moves away by about 2.5 Å (Fig. 14) from the initial position, which is consistent with the molecular dynamics modelling results.[106]

More recent examples of macromolecular photocrystallography include studies on photoactive yellow protein (PYP).[107] Time-resolved diffraction data was in this case collected by the Laue method at the 14-ID-B BioCARS and ID09 beamlines at room temperature. Protein crystals were excited either with a neodymium or a dye laser (laser pulses of 5–7 ns duration). Crystals were probed by X-ray pulses at 30 different time delays, ranging from 10 ns to 30 ms, to investigate accurately the structure evolution. For different data sets, the excitation degree ranged from 6 up to 34%. Fig. 15 shows the photodifference maps for different pump-probe delay times. It can be seen that the light-induced transformations take place in the chromophore binding pocket (the chromophore is a molecule, or a part of a molecule, in which light absorption takes place). Careful data analysis, using a singular-value decomposition method,[108] allowed determination of a chromophore time evolution practically with an atomic resolution. Recently, these

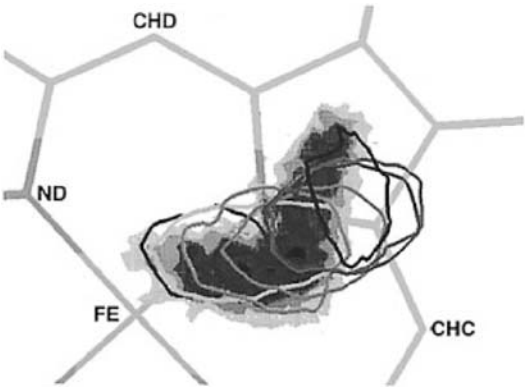

Fig. 14 Spatial map showing CO ligand migration inside a protein crystal after laser photolysis. Reproduced with permission from Teng, T.-Y.; Šrajer, V.; Moffat, K. Initial Trajectory of Carbon Monoxide after Photodissociation from Myoglobin at Cryogenic Temperatures. *Biochemistry* ***1997, 36, 12087–12100.*** Copyright (1997) American Chemical Society.

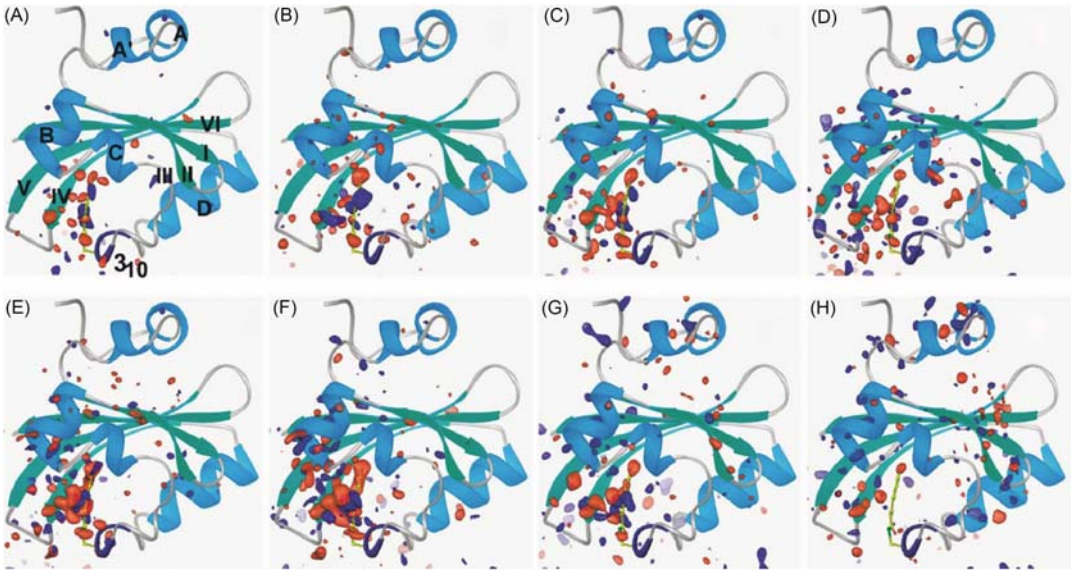

Fig. 15 Photodifference maps for the PYP protein. Letters indicate successive steps in the system time evolution (red surfaces – negative values, blue – positive). Reproduced with permission from Anderson, S.; Srajer, V.; Pahl, R.; Rajagopal, S.; Schotte, F.; Anfinrud, P.; Wulff, M.; Moffat, K. Chromophore Conformation and the Evolution of Tertiary Structural Changes in Photoactive Yellow Protein. *Structure* ***2004, 12, 1039–1045.***

studies have been extended to measurements using XFELs, which opened access to processes taking place on a time-scale shorter than 100 ps.[109]

The application of XFELs for photocrystallographic purposes is worth discussing here. In typical experiments of this kind, using XFEL sources and macromolecular samples, a jet of microcrystals is subjected to consecutive laser and X-ray pulses. An example experiment is shown in Fig. 16A.[110] The XFEL beam is so intense that it often destroys a crystal irretrievably, thus the described experimental approach is also called "serial crystallography" or "diffract and destroy." The loss of the crystal, however, is not a major problem. Since a highly monochromatic beam is used, indexing of the obtained data becomes relatively easy. Diffraction patterns can be measured separately for successive crystals in the stream and, on this basis, the changes occurring in the crystal structure during excitation can be reproduced. A study dedicated to tracing light-induced structure evolution in bacteriorhodopsin crystals (a photosensitive membrane protein, the so-called proton pump) is a good example of the technique.[111] Using this method, it was possible to track subtle changes in the hydrogen bond in the macromolecule, i.e. a transfer of a single proton (Fig. 16B). These studies show how protons are transported across the cell membrane against the concentration gradient.

10.11.3.2 TR studies of small organic molecules

Prior to discussing inorganic examples, it is also worth citing some of the few TR photocrystallographic studies devoted to purely organic small-molecule systems. A study of a co-crystal formed by tetrathiafulvalene and *p*-chloranil is an illustrative example.[112] The analyzed system is a typical one-dimensional organic material. It shows a phase transition from the 'neutral' (N) to 'ionic' (I) state when the temperature is decreased. The two phases differ in the degree of charge transfer between the co-crystal components. The system can be also transformed from the ionic to the neutral state and vice versa via exposure to light. The second-type of neutral phase (N′), obtained photochemically, is characterized by an even lower estimated charge transfer between the components than that recorded for the 'neutral' state N. This phase was consequently called 'over-neutral'. TR X-ray diffraction

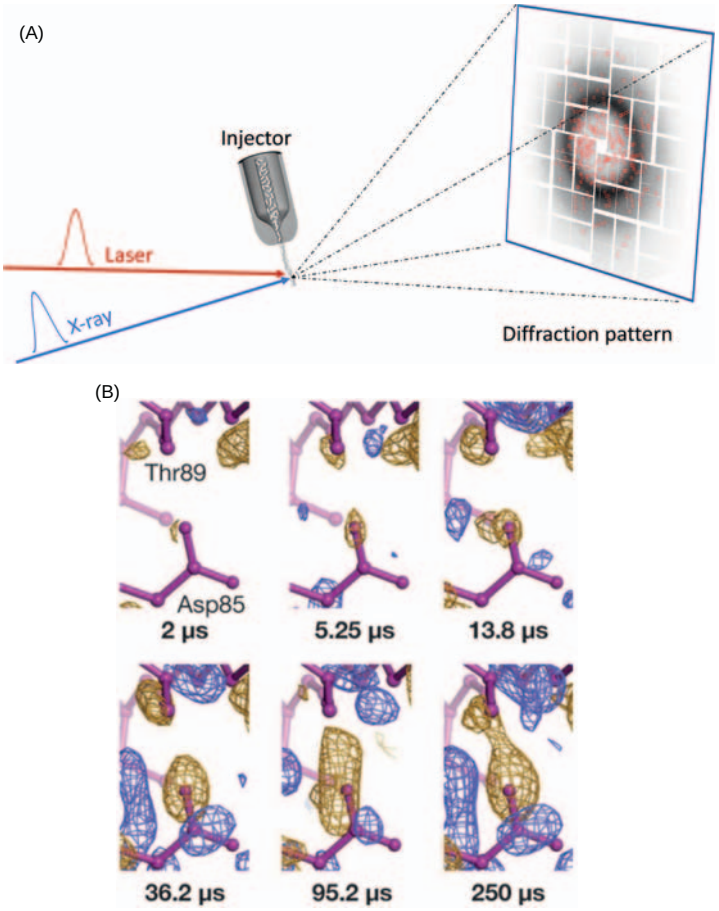

Fig. 16 (A) A serial pump-probe microcrystallography experiment as realized on an XFEL source. (B) Photodifference maps showing hydrogen transfer in the active site of the bacteriorhodopsin protein[111] (purple surfaces – positive values, yellow – negative, maps contoured at 3.5 σ level). Experiments were performed on the BL3 beamline at the SACLA XFEL. [*Open access* version provided by the Digital Object Repository at Paul Sherrer Institute (DORA PSI).] Reproduced with permission from Pandey, S.; Poudyal, I.; Malla, T. N. Pump-Probe Time-Resolved Serial Femtosecond Crystallography at X-Ray Free Electron Lasers. *Crystals* ***2020, 10(7), 628.***

experiments were carried out at 90 K on the NM14A beamline using monochromatic, 0.56366 Å, radiation. The phase transition was induced with a femtosecond laser set to 800 nm and the experiments were conducted at different pump-probe time delays. The resultant photodifference maps are presented in Fig. 17. During the formation of the N′ phase, one of the components remains essentially passive, while the chlorine atoms are visibly active – their shifts on both sides of the molecule are synchronized. After some time, the system returns to its initial state. A more detailed analysis indicates that the N′ phase is metastable with a lifetime of a few hundred ps.

A second example is the study of a [2+2] photocycloaddition reaction in α-styrylpyrylium triflate salt crystals.[113] This process is reversible at room temperature, while the compound changes color during the reaction, so it is also a promising material for applications in holographic data storage devices. The TR measurements were carried out at the ID09 beamline, with a grazing incidence geometry. For this purpose, crystals with thickness not exceeding 500 nm were grown on a metal surface by recrystallization of the compound from hexanol. Monochromatic 16.5 keV X-ray radiation was used in the experiment (ca. 50 ps X-ray pulses). The sample was excited with a Ti:Sapphire laser set to different wavelengths (520, 550 and 574 nm) with a constant pulse duration of 100 fs. The electron density distribution maps determined for the initial and final molecular state are shown in Fig. 18A and B. The reaction was monitored with a resolution of 20 ps, which was an outstanding achievement. Fig. 18C shows changes in the intensity of the 012 reflection over time, indicating the time-scale of the ongoing dimerization reaction and its reverse process. This is one of the few cases where the course of the reaction has been traced using X-ray diffraction at this short a timescale. Although it is not the subject of this chapter, it is also worth mentioning here the recent advanced femtosecond electron diffraction studies of some small-

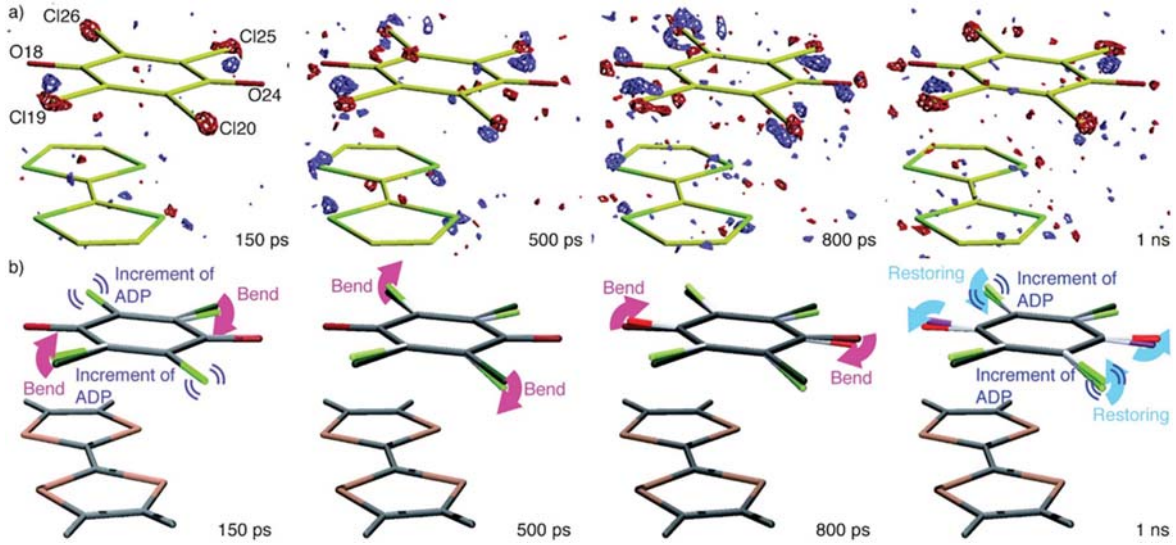

Fig. 17 Photodifference maps for a tetrathiafulvalene-*p*-chloranil crystal plotted for different delay times after the laser excitation. Bottom panels show the direction of atomic shifts (purple surfaces – positive values, red – negative, contours at 0.1 e·Å^{-3}). Reproduced with permission from Hoshino, M.; Nozawa, S.; Sato, T.; Tomita, A.; Adachi, S.-I.; Koshihara, S.-Y. Time-Resolved X-Ray Crystal Structure Analysis for Elucidating the Hidden 'over-Neutralized' Phase of TTF-CA. *RSC Adv.* ***2013, 3, 16313–16317.***

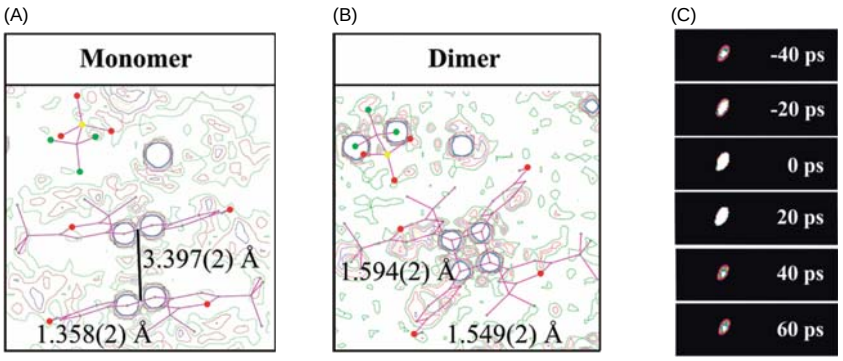

Fig. 18 Reconstructed electron density maps before (A) and after (B) light-induced dimerization reaction for the α-styrylpyrylium triflate. (C) Time evolution of the 012 reflection. Reproduced with permission from Hallmann, J.; Morgenroth, W.; Paulmann, C.; Davaasambuu, J.; Kong, Q.; Wulff, M.; Techert, S., Time-Resolved X-Ray Diffraction of the Photochromic α-Styrylpyrylium Trifluoromethanesulfonate Crystal Films Reveals Ultrafast Structural Switching. *J. Am. Chem. Soc.* ***2009, 131, 15018–15025.*** Copyright (2009) American Chemical Society.

molecule crystal samples.[114,115] These include, for example, investigations of a ring-closing cyclization reaction in dithienylethene molecular switches,[116,117] light-induced electron transfer in a platinum complex $Me_4P[Pt(dmit_2)]_2$ (dmit = 1,3-dithiol-2-thione-4,5-dithiolate),[118] and photoexcitation occurring in a charge-transfer co-crystal of tetrathiafulvalene with *p*-chloranil.[119] It is believed that, thanks to XFELs providing femtosecond pulses, it will be also possible to extend the capabilities of X-ray TR photocrystallography.

10.11.3.3 TR studies of coordination compounds

Finally, and most importantly regarding the subject of the current chapter, the application of the above-described time-resolved photocrystallographic methods to a number of transition-metal coordination compounds in a crystal state is presented and discussed. Systems have usually been chosen for such studies based on their photochemical properties (lifetimes of excited states, large Stokes shifts etc.) and related theoretical simulations (e.g. providing estimates of atomic shifts upon excitation), which indicate a high probability of significant light-induced structural changes. Various chemical systems containing platinum, rhodium, copper, silver or iron centers have been examined. Since TR X-ray diffraction experiments are very demanding and data processing and results' interpretation is usually rather challenging, the number of available research papers is limited. In this chapter, successful literature studies of this kind, dedicated to inorganic materials, are presented. The compounds under consideration are shown in Fig. 19. The set includes cage-like complexes where the inner part of the molecule undergoes bond shortening (Fig. 19A, B, and D), compounds forming excimers in the solid state upon irradiation (Fig. 19C), photoactive model complexes of interest for solar-energy applications (Fig. 19E, F, H, and I), and finally, spin cross-over systems (Fig. 19G). The achievements are discussed nearly chronologically, with an emphasis on advances in the experimental methods and theoretical tools used to determine the light-induced structural distortions and transformations. A summary of the experimental conditions used in the quoted studies, along with some key results, is gathered in Table 1.

10.11.3.3.1 $Pt(pop)_2(popH)_2 \cdot N(Et)_4$ cage complex

The first example of a fully successful time-resolved photocrystallographic study on small molecule crystals is work on the $Pt(pop)_2(popH)_2 \cdot N(Et)_4$ (pop = pyrophosphate, $H_2P_5O_5^{2-}$) complex (Fig. 19A).[120] The anion of this compound is characterized by a cage-like shape with the Pt⋯Pt interaction, formed in its inner part, stabilizing such a molecular structure. Additionally, two out of four pyrophosphate ligands are protonated. Interestingly, the corresponding crystal structure has never been published in the CSD (Fig. 19A is based on a similar IPUNUC structure). During excitation with 355 nm light, generated by a Nd:YAG laser, the system transforms from singlet to a first triplet excited state, in which, as indicated by theoretical calculations, the Pt⋯Pt distance gets shortened due to the electronic transition from the antibonding to the bonding molecular orbital located between the platinum centers. This excited state, giving rise to phosphorescence, has a lifetime of approximately 50 μs at 17 K.[131,132] Thanks to the sample's properties, a stroboscopic method could be applied. This early experiment was realized at the X3 line on the NSLS synchrotron (National Synchrotron Light Source, decommissioned in 2014), according to the previously described procedures.[35] At this beamline, monochromatic X-ray pulses ($\lambda_{X\text{-}ray} = 0.643$ Å) with a duration of 33 μs were generated by means of a fast chopper.

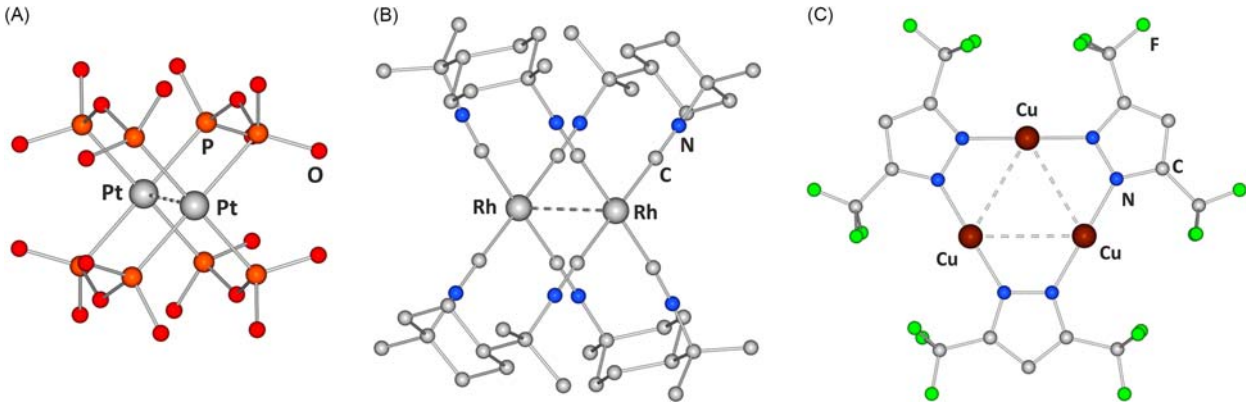

Fig. 19 Transition-metal coordination compounds studied to date using time-resolved X-ray synchrotron diffraction techniques: (A) $Pt(pop)_2(popH)_2 \cdot N(Et)_4$ (pop = pyrophosphate, $H_2P_5O_5^{2-}$)[120] (note: only anion shown), (B) $Rh_2(dimen)_4 \cdot (PF_6)_2$ (dimen = 1,8-diisocyano-*p*-menthane)[121] (note: only cation shown), (C) $([3,5\text{-}(CF_3)_2pz]Cu)_3$ (pz = pyrazolate),[122] (D) $Rh_2(\mu\text{-}pnp)_2(pnp)_2 \cdot (B(Ph)_4)_2$ (pnp = $MeN(P(OMe)_2)_2$)[57,123] (note: only cation shown), (E) $Cu(dppe)(dmp) \cdot PF_6$ (dppe = 1,2-bis(diphenylphosphino)ethane, dmp = 2,9-dimethyl-1,10-phenanthroline)[124] (note: only one cation from ASU shown), (F) $Cu(phen)(P(Ph)_3)_2 \cdot BF_4$ (phen = 1,10-phenanthroline)[125] (note: only one cation from ASU shown), (G) $Fe(tpa)(tcc) \cdot PF_6$ (tpa = tris(2-pyridylmethyl)amine, tcc = 3,4,5,6-tetrachlorocatecholate),[126] (H) $Ag_2Cu_2(dpi)_4$ (dpi = diphenylphosphino-3-methylindole)[127] (note: phenyl rings are omitted for clarity), (I) $Cu_4(PhCO_2)_4$[128] (note: only one molecule from ASU shown). In all cases hydrogen atoms are omitted for clarity, while any disorder is removed.

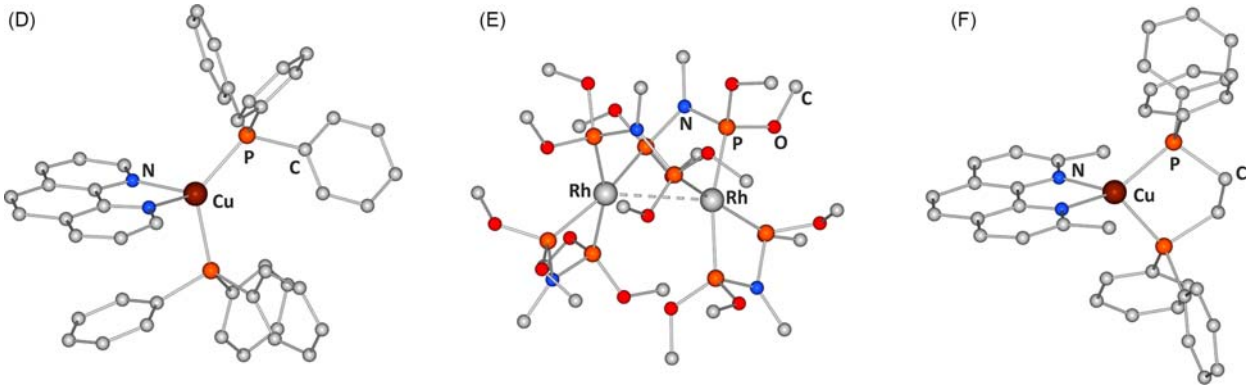

Fig. 19 (*continued*).

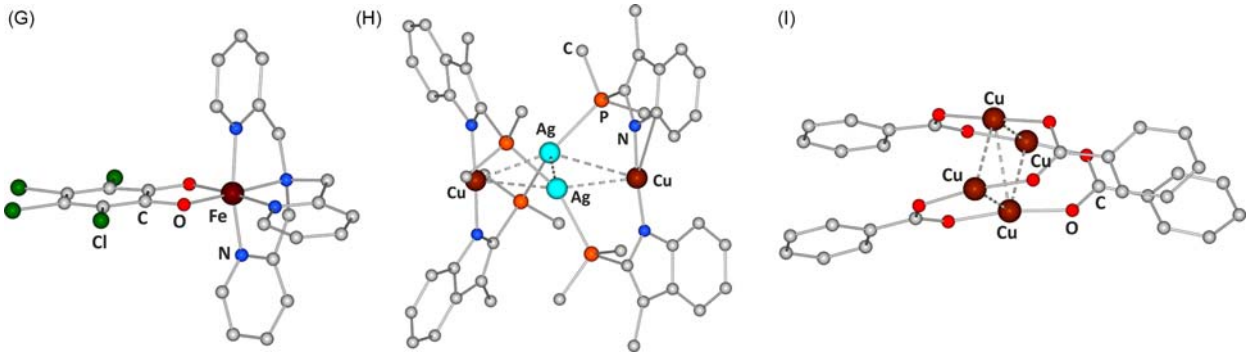

Fig. 19 (*continued*).

This allowed sufficient saturation of the studied system, and thus, the experimental observation of the excited-state structure. Fig. 20 shows the resultant photodifference map along with a refined model of the excited structure. It appears that the bond between platinum atoms is indeed shortened by as much as 0.28(9) Å (subsequent independent studies suggested the value of 0.24(3) Å[133]), which is very consistent with the values determined by other methods[134–136] (including e.g. the EXAFS technique yielding the value of 0.31(5) Å in solution). Such good agreement between the results obtained from different experiments confirmed the correctness of the applied methodology (especially in the context of the estimated population of excited states reaching only approximately 2%), and opened up possibilities for the direct determination and examination of short-lived excited state structures.

10.11.3.3.2 $Rh_2(dimen)_4 \cdot (PF_6)_2$ cage complex

A study of the $Rh_2(dimen)_4 \cdot (PF_6)_2$ (dimen = 1,8-diisocyano-*p*-menthane) complex (Fig. 19B) constitutes a similar case to the one described above. It was examined with the same technique, but on a newer beamline, i.e. 15-ID-B ChemMatCARS. Crystals of this complex were found to be luminescent. The emission has a maximum around 600 nm, and the estimated lifetime of the excited state is 11.7 μs at 23 K, when excited with the 440 nm laser light. These findings suggested that the structural changes occurring during the course of the photophysical cycle (i.e. successive system excitation and relaxation) would be rather significant (notable wavelength difference between the excitation line and the emission maximum, relatively long emission-decay lifetime indicates phosphorescence, thus the triplet nature of the excited state). Furthermore, for this complex both the emission maximum and lifetimes appeared to be invariant in the 355–532 nm excitation range. Consequently, the sample, kept at a temperature of 17 K, was excited either with 532 or 355 nm laser pulses at 12 kHz repetition frequency. The X-ray chopper yielded a 9.5 μs opening time, which was clearly shorter than the lifetime of the excited state. Refinement of the excited-state structure revealed a shortening of the Rh⋯Rh distance, despite the fact that a rather stiff structural model was applied (only 5 parameters were refined – Rh atoms positional parameters, population and temperature scale factor). The determined Rh⋯Rh distance amounted to 4.496(1) and 3.64(5) Å for the ground and excited-state, respectively, indicating the overall bond shortening of 0.86(5) Å. The nature of the electronic transition leading to the bond shortening is explained again by the promotion of an electron from an antibonding to a bonding Rh⋯Rh orbital. Such a large contraction of the metal-metal bond is further attributed by the authors to the shallowness of the Rh⋯Rh potential well in this particular complex (thus, even a small shift from its minimum causes significant structural distortions). Qualitative comparison of the experimental and theoretical results shows concurrent trends in structural changes. The theoretically-derived (VWNBLYP density functional with triple-ζ basis functions used to model the Rh atoms and double-ζ for other atoms; ZORA approximation included) Rh⋯Rh distance change confirms the significant bond shortening upon

Table 1 Summary of TR experiments in which structural changes were determined or estimated.

Complex	*TR method*	*X-ray radiation*	*Laser pulses*	*Exp. temp.*	*Lifetime(s)*	*Population(s)*	*Reference(s)*
$Pt(pop)_2(popH)_2 \cdot N(Et)_4$	stroboscopic[a]	monochromatic, $\lambda_{X\text{-}ray} = 0.643$ Å, 33 μs	Nd:YAG, $\lambda = 355$ nm	17 K	50 μs (514 nm, 17 K), $\lambda_{ex} = 370$ nm[b]	2%	120
$Rh_2(dimen)_4 \cdot (PF_6)_2$	stroboscopic[c]	monochromatic, $\lambda_{X\text{-}ray} = 0.49594$ Å, 9.5 μs	Nd vanadate, $\lambda = 355$ & 532 nm	23 K	11.7 μs (690 nm, 23 K), $\lambda_{ex} = 440$ nm	1.9–2.5%	121
$([3,5\text{-}(CF_3)_2pz]Cu)_3$	stroboscopic[c]	monochromatic, $\lambda_{X\text{-}ray} = 0.49594$ Å, 18 μs	Nd vanadate, $\lambda = 355$ nm	17 K	53 μs (17 K)[d]	–[e]	122
$Rh_2(\mu\text{-}pnp)_2(pnp)_2 \cdot (B(Ph)_4)_2$	pump-probe[f]	polychromatic, $E_{X\text{-}ray} = 12$ & 15 keV ($\Delta E/E = 8\%$), 100 ps	Ti:Sapphire, $\lambda = 390$ nm, 35 ps	225 K	35.3 μs (718 nm, 10 K), 46.5 μs (790 ns, 10 K), $\lambda_{ex} = 337$ nm	6.6% (12 keV), 4.7% (15 keV)	57,123
$Cu(dppe)(dmp) \cdot PF_6$	stroboscopic[c]	monochromatic, $\lambda_{X\text{-}ray} = 0.49594$ Å, 40 μs	Nd:YAG, $\lambda = 355$ nm, 50 ns	17 K	87.5 & 551.7 μs (17 K), $\lambda_{ex} = 366$ nm	7–10%	124,129
$Cu(phen)(P(Ph)_3)_2 \cdot BF_4$	pump-probe[f]	polychromatic, $E_{X\text{-}ray} = 15$ keV ($\Delta E/E = 8\%$), 100 ps	Nd:YAG, $\lambda = 420$ nm, 4 ns, $\tau = 2$ ns (90 K); Ti:Sapphire, $\lambda = 390$ nm, 35 ps, $\tau = 100$ ps (180 K)	90 & 180 K	10 & 102 μs (90 K), 8 & 72 (180 K), $\lambda_{ex} = 366$ nm	–[e]	125
$Fe(tpa)(tcc) \cdot PF_6$	pump-probe[f]	monochromatic, $E_{X\text{-}ray} = 15$ keV, 100 ps	$\tau = 500$ ps &50 μs[g]	–[e]	–[e]	1.5–2% (500 ps), 10.5(16)% (50 μs)	126
$Ag_2Cu_2(dpi)_4$	pump-probe[f]	polychromatic, $E_{X\text{-}ray} = 15$ keV ($\Delta E/E = 8\%$), 80 ps	Ti:Sapphire, $\lambda = 390$ nm, $\tau = 100$ ps	90 K	0.16(1) & 0.98(1) μs (90 K), $\lambda_{ex} = 390$ nm	0.8%	127
$Cu_4(PhCO_2)_4$	pump-probe[f]	polychromatic, $E_{X\text{-}ray} = 15$ keV ($\Delta E/E = 8\%$), 80 ps	Nd:YAG, $\lambda = 355$ nm (90 K), Ti:Sapphire, $\lambda = 360$ nm (225 K)	90 & 225 K	15.3(3) & 111.0(6) μs (547 nm, 90 K), 2.13(2) & 10.16(4) μs (668 nm, 250 K), $\lambda_{ex} = 355$ nm[d]	–[h]	128

Experimental conditions from the literature are provided (e.g. X-ray or laser pulse duration, experiment temperature, laser type etc.). Symbols used: $\lambda_{X\text{-}ray}$ – X-ray radiation wavelength, λ – laser wavelength, τ - delay between X-ray and laser pulses, λ_{ex} = laser excitation wavelength used to determine lifetimes.

[a]Data collected at the X3 beamline (NSLS).

[b]Emission maximum and excitation wavelengths according to Sperline et al.[130] According to Markert et al.[131] multi-temperature data was measured with a Xe lamp as an excitation source.

[c]Data collected at the 15-ID-B ChemMatCARS beamline (APS).

[d]Only selected lifetimes are presented (see text or the original publication for more information).

[e]Not provided.

[f]Data collected at the 14-ID BioCARS beamline (APS).

[g]Laser type and wavelength were not given in the paper, but in the optical experiments presented in the same paper 600 nm excitation was used.

[h]Not determined.

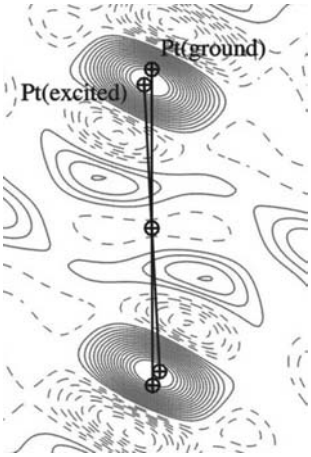

Fig. 20 Photodifference map for the $Pt(pop)_2(popH)_2 \cdot N(Et)_4$ complex superimposed onto the refined model for the excited-state structure (solid lines – positive values, dashed – negative, contours at ± 0.1 e $Å^{-3}$; molecule is located on an inversion center),[120] Pt⋯Pt interaction shortening is clearly visible. Reproduced with permission of the International Union of Crystallography from Kim, C. D.; Pillet, S.; Wu, G.; Fullagar, W. K.; Coppens, P., Excited-State Structure by Time-Resolved X-Ray Diffraction. *Acta Cryst. Sect. A* ***2002, 58, 133–137***.

excitation, however, the overall effect seems to be notably overestimated here (from 4.647 to 3.107 Å, yielding a total shortening of 1.54 Å). Such an outcome is to a great extent caused by running computations for isolated molecules, thus not taking into account crystal environment confining effects (further studies for a similar complex show that indeed this is the case[57]; see further in the text). Finally, the refined population of the excited states appeared to be comparable between two successive experiments. In the case of using the 532 nm excitation wavelength it amounted to about 2.5%, whereas for 355 nm to 1.9%. It should be noted here that such low population factors significantly limit the complexity of possible structural models which can be applied for the excited states. Furthermore, the population could not be increased by using a higher laser power, due to crystal deterioration under such conditions.

10.11.3.3.3 ([3,5-$(CF_3)_2$pz]Cu)$_3$ trimer complex

A study of ([3,5-$(CF_3)_2$pz]Cu)$_3$ (pz = pyrazolate) shows that the excitation does not have to be limited to a single molecule in the solid, as some molecules can be coupled upon irradiation leading to more complex excited species. In this case, a short-lived intermolecular excimer (i.e. excited dimer) is formed in the crystal structure. Multi-center copper(I) complexes with pyrazolates are known to exhibit strong emission with microsecond lifetimes and fulfill the criteria required for excimer formation, i.e. they are arranged in stacks in the solid state which facilitates molecular coupling.[137,138] The studied molecule is a classical example of this class of compounds being a triangular flat species (**Fig. 19**C). The crystal, on excitation with 366 nm laser light at 17 K, shows emission with a maximum at 590 nm. When excited with 337 nm light pulses, its emission maximum is located more to the red, i.e. at 660 nm. In both cases the determined phosphorescence lifetime is the same and equals 53(1) μs. Since the lifetime of the phosphorescent state at 17 K equals 53(1) μs the stroboscopic TR method was applied to determine transient species. The experiment was conducted again at the 15-ID-B ChemMatCARS beamline with a Nd-vanadate laser of 12 kHz repetition rate and a wavelength of 355 nm as the excitation source. An chopper provided X-ray probe pulses ($\lambda_{X\text{-ray}} = 0.49594$ Å) of about 18 μs duration, which is shorter than the lifetime of the phosphorescent state under study. The collected data allowed the refinement of a variety of structural parameters for the excited state, namely the excited-state population, positional parameters of the copper atoms and orientations of pyrazolate ligands treated as rigid bodies. The most interesting result here is that the intermolecular Cu⋯Cu distances shortened from 4.018(1) to 3.46(1) Å. This is accompanied by the contraction of the inter-planar distance between pairs of the neighboring molecules by 0.65 Å (from 3.952(1) to 3.33(1) Å) indicating the formation of excimers in the solid state (**Fig. 21**). Obviously, this effect is concurrent with the elongation of the inter-planar distance at the other side of the molecules from 3.610(1) to 3.91(1) Å (i.e. the stacks undergo dimerization rather than compression). It is worth stressing that the geometry of a single molecule itself is not much changed (the triangular molecules only slightly tilt by about 1°). Clearly, the biggest changes are associated with the longer Cu⋯Cu contacts formed between separated molecules, not the distances between the copper atoms within one molecule. The findings suggest a complex nature for the metal⋯metal interactions in such stacks, which involve cooperative effects, as supported by further studies of closed-shell transition-metal clusters.[139] Theoretical computations performed and presented in this paper for a molecular dimer indicate that the HOMO and HOMO − 1 orbitals of the ground state in such a system do not participate in the excimer formation. On the other hand, the LUMO seems to link two molecules, which indicates that the intermetallic electron transition occurs prior to the excimer formation. Regrettably in this case no further and more elaborate theoretical considerations were conducted.

Although this study was largely dedicated to the excited state observed at 17 K, it is worth mentioning that this complex exhibits quite complex spectroscopic behavior. For instance, once the temperature is increased to 77 K the emission lifetime reaches 77(1)

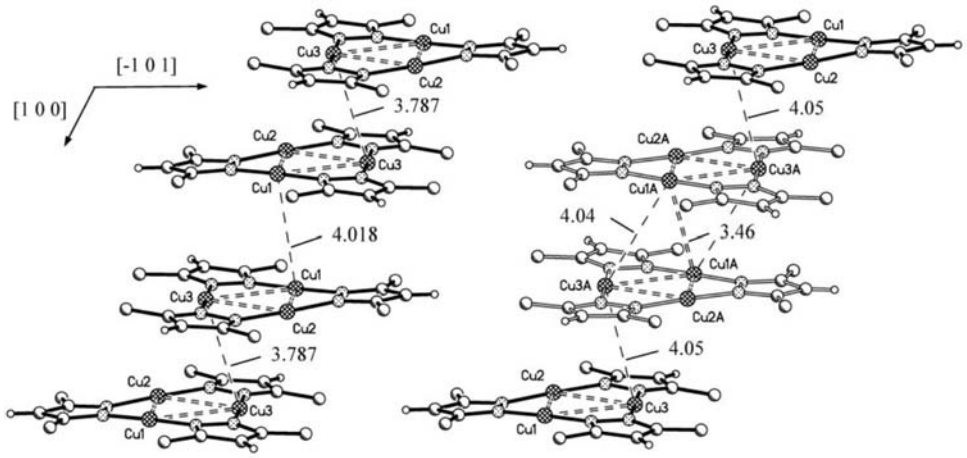

Fig. 21 Crystal structure of the $([3,5\text{-}(CF_3)_2pz]Cu)_3$ complex before (left) and after (right) light exposure. Dashed double lines denote intramolecular Cu···Cu distances within the formed excimer (right only). Reproduced with permission from Vorontsov, I. I.; Kovalevsky, A. Y.; Chen, Y.-S.; Graber, T.; Gembicky, M.; Novozhilova, I. V.; Omary, M. A.; Coppens, P., Shedding Light on the Structure of a Photoinduced Transient Excimer by Time-Resolved Diffraction. *Phys. Rev. Lett.* ***2005, 94, 193003***.

μs, but it decreases on further temperature rise, dropping to 41(1) μs at room temperature. Furthermore, the crystal emission color changes from green through yellow to orange when the sample is warmed up from 77 K to room temperature. Interestingly, at low temperatures from 4 to 77 K, the green emission is composed of two bands (ca. 515 and 570 nm). Therefore, various processes take place at different temperatures leading to distinct dominant excited states, which is certainly related to the character of the molecule under study, as well as, the crystal architecture it forms, which enables formation of a variety of excited states. It is also worth stressing that emission thermochromism (i.e. emission color change along with temperature variation) in certain classes of copper(I) complexes is a known and actively-studied behavior.[128,140,141]

10.11.3.3.4 $Rh_2(\mu\text{-pnp})_2(pnp)_2\cdot(B(Ph)_4)_2$ 'half-cage' complex

The first successful application of the TR Laue method was a study of the dinuclear rhodium(I) complex, $Rh_2(\mu\text{-pnp})_2(pnp)_2\cdot(B(Ph)_4)_2$ (pnp = $MeN(P(OMe)_2)_2$) (Fig. 19D).[57,123] This complex has two terminal ligands and two bridging ones linking the Rh centers. Additionally, the Rh atoms interact with each other forming a metallophilic bond. Such rhodium complexes attracted early attention due to their potential for photocatalysis or energy conversion.[142–144] The system under consideration exists as two polymorphs in the crystalline state, α and β.[145,146] The former polymorph can be obtained from a methanol-acetone solution and has one molecule in the asymmetric unit (ASU), whereas the latter crystallizes from methanol-DCM mixtures and it has two molecules in the ASU. The α-form was chosen as a model subject for TR Laue diffraction. The photochemical properties of this system are temperature-dependent. The α-form excited with 337 nm laser-light shows a single 730 nm emission band at 10 K, which quickly diminishes on increasing the temperature and disappears above 50 K. The 730 nm emission intensity decrease is accompanied by the growth of a 780 nm emission band (Fig. 22). Both of these bands are ascribed to phosphorescence. Blakely et al.[145] estimated the luminescence decay lifetimes for the sample excited with 337 nm laser pulses at 10 K based on time

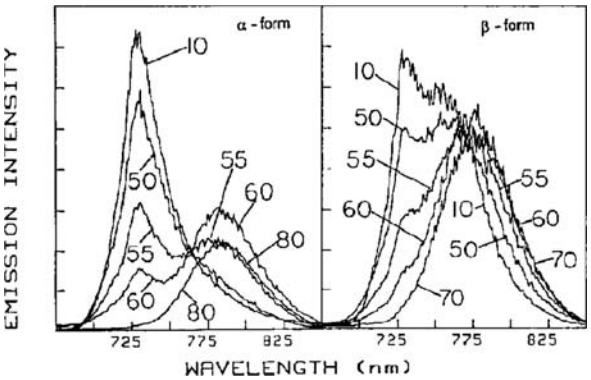

Fig. 22 Temperature-dependent emission spectra (excitation wavelength of 337 nm) from the two crystal forms of the $Rh_2(\mu\text{-pnp})_2(pnp)_2\cdot(B(Ph)_4)_2$ complex. Reproduced with permission from Blakley, R. L.; Yin, Y.; Lloyd, C.; Mague, J. T.; McPherson, G. L. Photophysics of a Flexible Ligand Bridged Rhodium(I) Dimer: An Excited State Conformational Change in a Crystalline Solid. *Chem. Phys. Lett.* ***1989, 157, 398–402***.

evolution of two emission wavelengths, i.e. 718 nm (close to the low-temperature emission band maximum) and 790 nm (around the high-temperature emission band maximum). They amounted to 35.3(2) μs and 46.5(3) μs, respectively. The presence of two bands and their behavior has been attributed to the thermally-activated transformation between the available excited-states.

The TR Laue experiment was performed at the 14-ID BioCARS beamline with a Ti:Sapphire laser system set to a 390 nm excitation wavelength and a 100 ps pump-probe delay. Thanks to such a fast TR experiment, it was possible to successfully conduct the measurement at 225 K despite the observed excited-state lifetime shortening. This relatively high temperature was crucial in this case since at lower temperature Laue diffraction spots were significantly broadened due to induced strain. It should be emphasized that this was the very first TR Laue experiment performed for a small-molecule crystal. It required the development of novel data collection and processing strategies. X-ray diffraction data at two undulator settings (yielding 12 and 15 keV X-ray beam energies) were collected as sets of interspersed light-ON and light-OFF diffraction frames. Further data processing followed the previously-described protocol based on the intensity ratios. This yielded six data sets, which were used to construct photodifference maps and, later, to refine an excited-state structural model.

The generated photodifference map is shown in **Fig. 23**A. It indicates the displacement of both Rh atoms, one more to the side (Rh1) and the second one toward the first one (Rh2). This suggests both a shortening of the Rh⋯Rh distance and a molecular rotation in the crystal structure upon excitation with the laser pulse. More details of structure became available from the response-ratio refinement. These are presented in **Fig. 23**B. According to these results, the rhodium atoms are shifted by 0.139(7) and 0.134(5) Å, for Rh1 and Rh2, respectively. This yields a total bond shortening of 0.136(8) Å. Furthermore, it was shown that the rest of the molecule follows the rhodium atoms, as other essential distances, such as Rh – P, are hardly changed. It is worth noting the rigid-body rotations determined for the terminal ligands. The refined parameters do not exceed 2.5°, while the changes are more pronounced for the ligand attached to the Rh1 atom than for the one bound to the Rh2 atom. This is in accordance with the overall molecule rotation as evidenced by the sideways shift of the Rh1 atom. The refined excited-state population reached 6.6% for the measurements with an X-ray beam of 12 keV, and 4.7% for 15 keV. Such a comparison shows that the results are reproducible within the error limit, despite the application of a different X-ray energy range.

Finally, a comparison of experimental results with theory was an important aspect of the study. As evidenced by quantum computations, the mechanism of structural deformation for the molecule is related to charge transfer from anti-bonding orbitals to higher bonding orbitals in the center of the molecule.[57] This so-called cluster-centered transition leads to the experimentally observed shortening of the Rh⋯Rh distance. However, similar to the earlier described examples, the geometries obtained from optimizations performed on isolated-molecules reflect to some extent trends observed in experimentally-derived geometry changes upon light-excitation, but there is significant quantitative discrepancy between these results. The Rh⋯Rh distance shortening was found to be in the range from 0.329 to 0.639 Å, dependent on the level of theory used, which is clearly overestimated with respect to the experimental outcome. Inclusion of crystal confining effects by application of the simple QM/MM approach was found to be a very good compromise.[147] The computations performed using the ADF program at the DFT(BP86)/TZP level of theory indicated shortening of the Rh⋯Rh distance by 0.157 Å, which is in almost quantitative agreement with the experimental results. It is thus

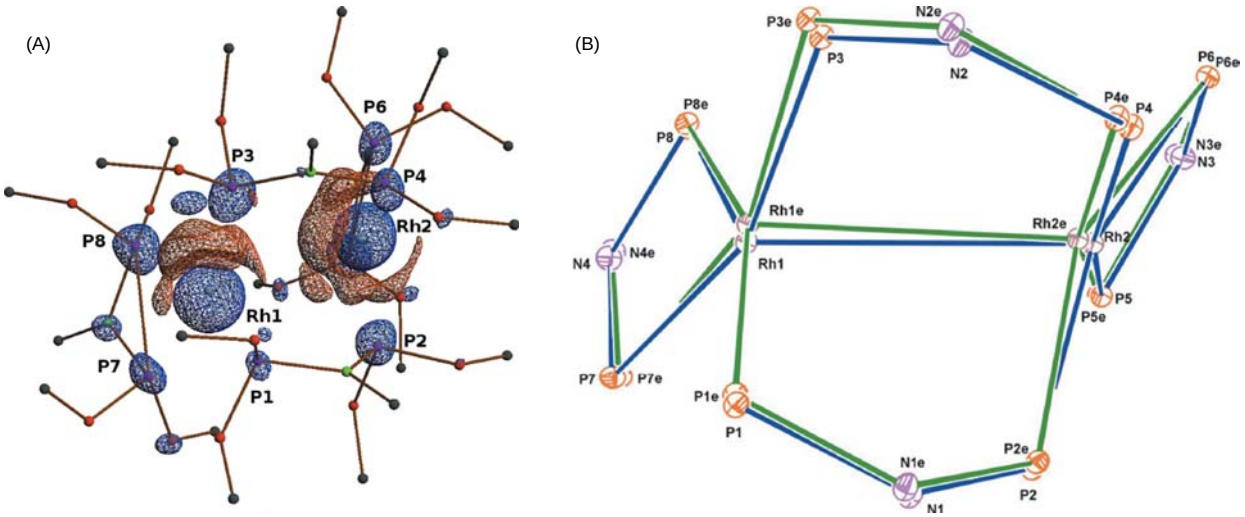

Fig. 23 (A) Photodifference map of the $Rh_2(\mu\text{-PNP})_2(PNP)_2^{2+}$ cation (red surfaces – positive values, blue – negative, isosurfaces at ± 0.25 e Å^{-1}; atom colors: gray—rhodium, green—nitrogen, violet—phosphorus, black—carbon, red—oxygen).[57] (B) Refined structural model for the light-induced crystal (blue lines – ground state, green – excited state; atom colors: pink—rhodium, pink—nitrogen, orange—phosphorus).[57,123] Reproduced with permission of the International Union of Crystallography from Makal, A.; Trzop, E.; Sokolow, J.; Kalinowski, J.; Benedict, J.; Coppens, P. The Development of Laue Techniques for Single-Pulse Diffraction of Chemical Complexes: Time-Resolved Laue Diffraction on a Binuclear Rhodium Metal-Organic Complex. *Acta Cryst. Sect. A* ***2011, 67, 319–326.***

clear that even in this case, in which the most significant structural changes are limited to the central part of the molecule, crystal packing effects indeed play an important role and cannot be neglected.

10.11.3.3.5 Cu(dppe)(dmp)·PF_6 and Cu(phen)$(P(Ph)_3)_2$·BF_4 photoactive complexes

Two copper(I) complexes (Fig. 19E and F) described in this chapter are examples of compounds having potential for solar-energy[148,149] or organic light-emitting diode (OLEDs)[150] applications. Copper-based compounds of this kind have been considered as potential cheap and more abundant alternatives to ruthenium or osmium photoactive complexes.[151] Therefore, numerous copper(I) complexes with chelating ligands, such as 1,10-phenanthroline (phen), have been extensively investigated with various techniques.[152–154] The studies of McMillin and co-workers provided many seminal contributions on the subject.[155–161] As far as spectroscopy is concerned, the reported lifetimes of emissive states in such complexes range from ns to several μs.[162,163] Consequently, a great deal of effort in molecule design was devoted to increasing the lifetimes of such species. In this respect, the replacement of one or two phenanthroline ligands by phosphine ligands provides the desired effect. Studies in this direction are still very active. Recent examples include the introduction of rigid phosphine ligands in order to obtain better properties for the construction of OLEDs.[164] It is also worth mentioning that for such complexes the electronic transition responsible for forming emissive states is always MLCT in character (metal-to-ligand charge transfer).[124,165]

The study of Cu(dppe)(dmp)·PF_6, was conducted using the stroboscopic method,[124,129] whereas Cu(phen)$(P(Ph)_3)_2$·BF_4, was successfully examined using the Laue method.[125] Furthermore, the study of the first complex may be considered as a benchmark case, to which newer results can be compared. Both complexes have similar molecular structures. Copper in a + 1 oxidation state is connected either to 1,10-phenanthroline or 2,9-dimethyl-1,10-phenanthroline (dmp), and coordinated by two $P(Ph)_3$ or a single chelating 1,2-bis(diphenylphosphino)ethane (dppe) ligand in the case of the Cu(dppe)$(dmp)^+$ and Cu(phen)$(P(Ph)_3)_2^+$ cations, respectively. PF_6^- or BF_4^- species serve as counter ions, and are considered passive during excitation. Both compounds are air-stable and no sign of copper oxidation over the time has been observed for these solids. Interestingly, two symmetry-independent molecules makeup the ASU of the crystal structures. The photophysical properties of these complexes are also similar, such as the bi-exponential character of phosphorescence decay. For Cu(dppe)(dmp)·PF_6 87.5 and 551.7 μs lifetimes were determined at 17 K with a rather broad emission maximum at around 660 nm. For Cu(phen)$(P(Ph)_3)_2$·BF_4 at 90 K, the respective lifetimes were ca. 10 and 102 μs (at 180 K the lifetimes are reduced to about 8 and 72 μs). The bi-exponential nature of emission decay is attributed to the coexistence of two chemically identical, yet structurally slightly different symmetry-independent cations in the crystal structures.

A stroboscopic experiment for the first complex was accomplished at the 15-ID-B ChemMatCARS beamline. The X-ray pulses ($\lambda_{X\text{-}ray} = 0.49594$ Å) were of ca. 40 μs duration which, at the experiment temperature of 17 K, was perfectly suitable to study excited states due to their longer lifetime. The excitation radiation was obtained with the Nd:YAG laser set to 355 nm with 50 ns pulses. The resulting photodifference maps for both symmetry-independent molecules are shown in Fig. 24. Quite large electron density peaks are present near both the copper and phosphorus atoms, clearly shifting upon laser-light excitation. The maps provided a good starting point for response-ratio refinements. Due to the complexity of the structure, a limited set of excited-state structural parameters were used in this step. For both ground and excited-state models, the ligands were set as rigid bodies, whereas copper atoms were refined freely. A high excited-state population was achieved, ca. 7–10%, a value considerably higher than those determined in the previous studies. The largest structural changes were observed for copper atoms, which shift by 0.26(2) and 0.28(2) Å in the case of Cu1 and Cu2, respectively. The superposition of the refined ground and excited-state geometries for two symmetry-independent molecules is illustrated in Fig. 25. It is clear that the two molecules distort in a different way. For example, the 2nd molecule (i.e. that with the Cu2 atom) does not flatten upon excitation, whereas the 1st molecule undergoes modest flattening. This was ascribed to crystal environment effects. Furthermore, it was evident that the Cu–P distances elongate (0.028(5) Å on

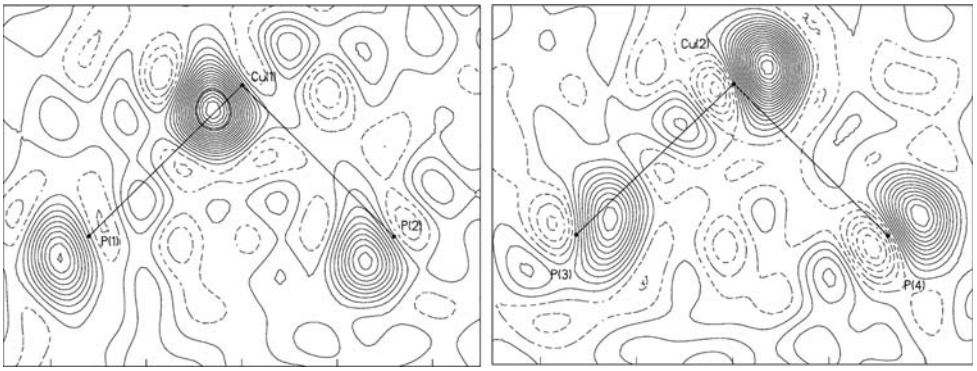

Fig. 24 Photodifference maps for the Cu(dppe)(dmp)·PF_6 complex around both copper atoms (Cu1 – left, Cu2 – right; solid lines – positive values, dashed – negative, contours at ±0.4 e·Å^{-3}). Reproduced with permission from Vorontsov, I. I.; Graber, T.; Kovalevsky, A. Y.; Novozhilova, I. V.; Gembicky, M.; Chen, Y.-S.; Coppens, P. Capturing and Analyzing the Excited-State Structure of a Cu(I) Phenanthroline Complex by Time-Resolved Diffraction and Theoretical Calculations. *J. Am. Chem. Soc.* ***2009, 131, 6566–6573.*** Copyright (2009) American Chemical Society.

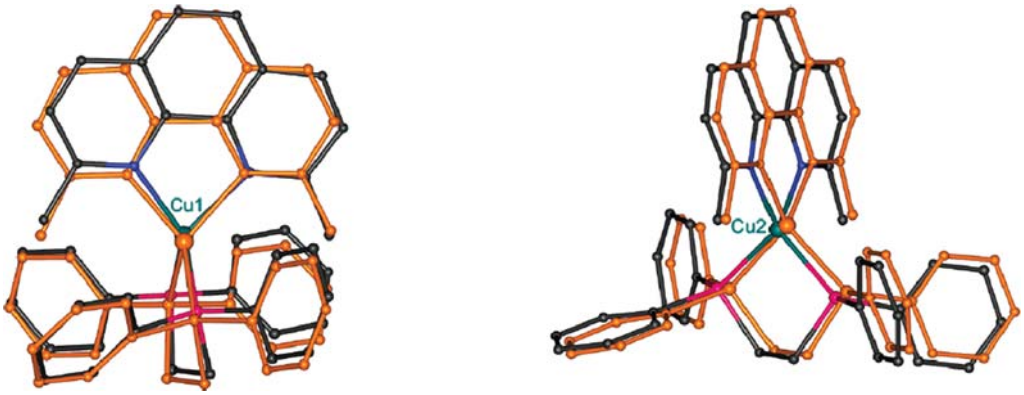

Fig. 25 Refined models for triplet excited states of Cu(dppe)(dmp)·PF_6 in the solid state (1st molecule – left, 2nd – right; ground state – gray lines, excited – orange). Both molecules are shown with different orientation to emphasize structural changes under light irradiation. Reproduced with permission from Vorontsov, I. I.; Graber, T.; Kovalevsky, A. Y.; Novozhilova, I. V.; Gembicky, M.; Chen, Y.-S.; Coppens, P. Capturing and Analyzing the Excited-State Structure of a Cu(I) Phenanthroline Complex by Time-Resolved Diffraction and Theoretical Calculations. *J. Am. Chem. Soc.* ***2009, 131, 6566–6573.*** Copyright (2009) American Chemical Society.

average), while in the case of Cu–N distances the experimental errors were too large to draw definitive conclusions regarding any changes.

A much more elaborate study was conducted for the second, more chemically labile (phosphine ligand replaced the bridging dppe moiety) complex. In this case, the Laue technique was used and the data collected at the 14-ID BioCARS beamline. Two sets of data were collected at two different temperatures – 90 and 180 K. In both cases, 100 ps X-ray pulses were used with the maximum energy of the pink-beam set to 15 keV. The 180 K data was collected using a Ti:Sapphire laser set to 390 nm (with 35 ps pulses) and a 100 ps pump-probe delay. For the 90 K data, a Nd:YAG laser with a 420 nm excitation wavelength and a 2 ns pump-probe delay was employed (the longer delay than that applied at 180 K caused more significant spot broadening upon excitation). The photodifference maps for both temperatures are shown in Fig. 26. Clearly, similar features appear at both

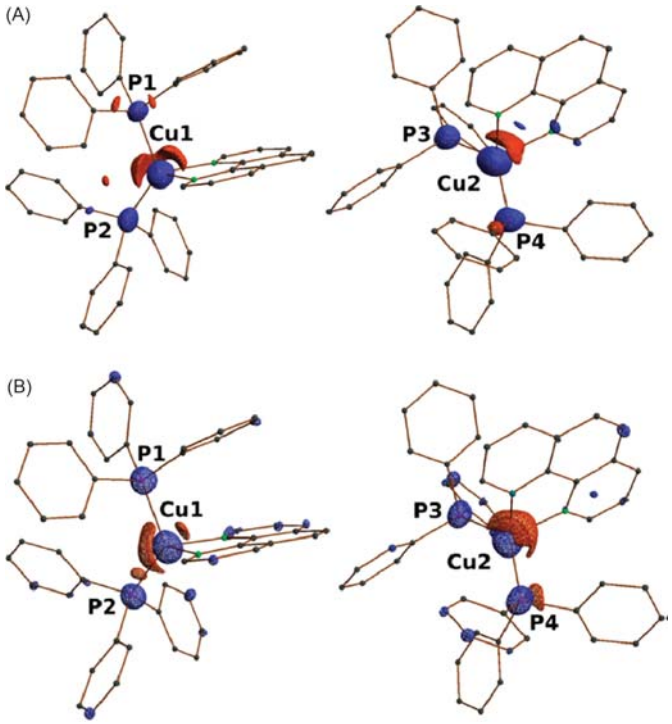

Fig. 26 Photodifference maps for Cu(phen)$(P(Ph)_3)_2$·BF_4 at two temperatures: (A) 180 K and (B) 90 K (red surfaces – positive values, blue – negative, isosurfaces at ± 0.25 e·$Å^{-3}$). Reproduced with permission from Makal, A.; Benedict, J.; Trzop, E.; Sokolow, J.; Fournier, B.; Chen, Y.; Kalinowski, J. A.; Graber, T.; Henning, R.; Coppens, P. Restricted Photochemistry in the Molecular Solid State: Structural Changes on Photoexcitation of Cu(I) Phenanthroline Metal-to-Ligand Charge Transfer (MLCT) Complexes by Time-Resolved Diffraction. *J. Phys. Chem. A* ***2012, 116, 3359–3365.*** Copyright (2012) American Chemical Society.]

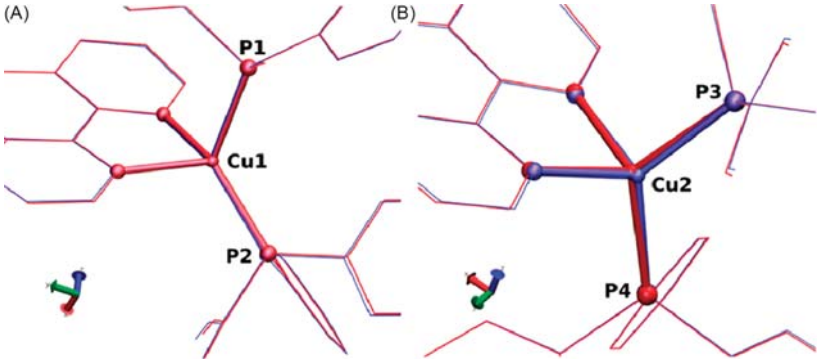

Fig. 27 Refined structural models for the triplet excited states of both molecules in the $Cu(phen)(P(Ph)_3)_2 \cdot BF_4$ crystal (1st molecule – left, 2nd – right; ground state – blue, excited state – red). Reproduced with permission from Makal, A.; Benedict, J.; Trzop, E.; Sokolow, J.; Fournier, B.; Chen, Y.; Kalinowski, J. A.; Graber, T.; Henning, R.; Coppens, P. Restricted Photochemistry in the Molecular Solid State: Structural Changes on Photoexcitation of Cu(I) Phenanthroline Metal-to-Ligand Charge Transfer (MLCT) Complexes by Time-Resolved Diffraction. *J. Phys. Chem. A* ***2012, 116, 3359–3365.*** Copyright (2012) American Chemical Society.

temperatures. Additionally, in both cases the symmetry-independent molecules behave differently. The Cu1 atom shifts roughly in the P–Cu–P plane moving away from the phenanthroline ligand, whereas the Cu2 atom shifts toward it. In this chapter, the 90 K data set will be further discussed. Based on the response-ratio-refined geometry, it was found that the Cu–P bonds in both molecules behave differently. For the 1st molecule, the respective bond length changes are equal to $+0.029(12)$ Å and $-0.016(16)$ Å, while for the 2nd molecule: $+0.038(14)$ and $-0.017(14)$ Å. The changes and the differences are very small, but at the same time they are well reproduced theoretically, using a QM/MM approach, which includes the crystal environment model. The differences between the molecules are also reflected in the absolute shifts of the copper atoms. They amount to 0.037(5) and 0.094(5) Å for the Cu1 and Cu2 atoms, correspondingly. This indicates that the 2nd molecule has more space, thus can undergo a greater distortion (as can be seen in Fig. 27). These shifts are much smaller than the ones observed for the other complex. Subsequent studies allowed assignment of individual molecules to emission lifetimes. It has been estimated that the more restrained molecule exhibits a shorter excited-state lifetime.[166]

10.11.3.3.6 Fe(tpa)(tcc)·PF_6 spin-crossover complex

The current example, $Fe(tpa)(tcc) \cdot PF_6$ (tpa = tris(2-pyridylmethyl)amine, tcc = 3,4,5,6-tetrachlorocatecholate) (Fig. 19G), is a particularly interesting system, being a representative of the so-called spin-crossover compounds. In such materials, the metallic center can be switched from its low-spin (LS) to high-spin (HS) state upon external perturbation, such as light or temperature. This process is often accompanied by significant deformation of, for instance, the metal coordination sphere. Despite many studies on such materials, in which magnetic, optical and static photocrystallographic results are presented, the investigation of what is happening to molecules directly after laser light perturbation is not well developed. Recent studies on the subject have been performed by E. Collet and co-workers.[32,167–170] The compound presented here is the only example for which structural changes

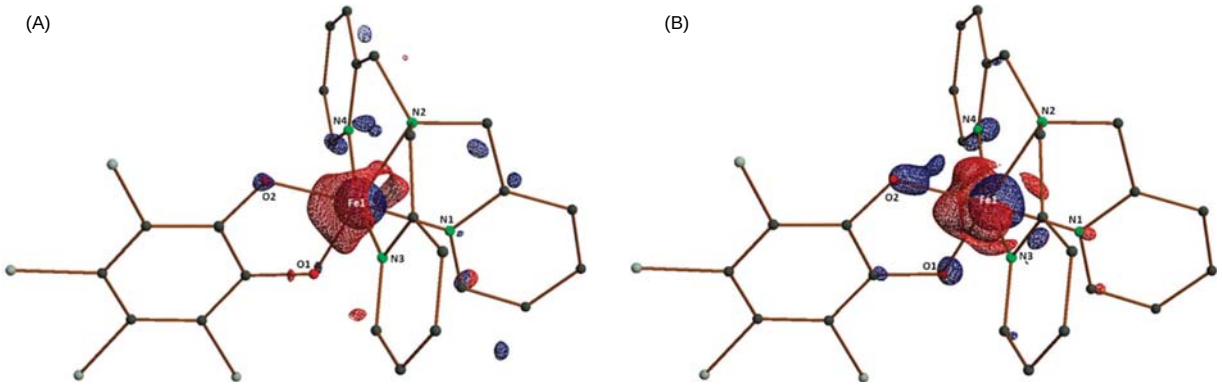

Fig. 28 Photodifference maps for the monoclinic form of $Fe(tpa)(tcc) \cdot PF_6$ (red surfaces – positive values, blue – negative): (A) after 500 ps (isosurfaces at ± 0.14 e Å^{-3}) and (B) 50 μs (isosurfaces at ± 0.46 e Å^{-3}). Central atom—iron; atom colors: black—carbon, white—hydrogen, green—nitrogen, red—oxygen. Reproduced with permission from Collet, E.; Moisan, N.; Baldé, C.; Bertoni, R.; Trzop, E.; Laulhé, C.; Lorenc, M.; Servol, M.; Cailleau, H.; Tissot, A.; Boillot, M.-L.; Graber, T.; Henning, R.; Coppens, P.; Cointea, M. B.-L. Ultrafast Spin-State Photoswitching in a Crystal and slower Consecutive Processes Investigated by Femtosecond Optical Spectroscopy and Picosecond X-Ray Diffraction. *Phys. Chem. Chem. Phys.* ***2012, 14, 6192–6199.***

were fully determined using TR X-ray diffraction. Although the experiment was performed on a synchrotron beamline capable of using polychromatic radiation, i.e. at 14-ID-B BioCARS, a monochromator was used. This has advantages in this particular case, since the researchers wanted to study not only structural changes occurring in the crystal at a given time point, but also the evolution of unit-cell parameters. Such information is readily available when using a monochromatic beam, whereas it is not that straightforward when polychromatic radiation is employed. Otherwise, the experiment was very similar to those where the Laue method was employed. The sample, in the form of the monoclinic polymorph, was exposed to the laser beam (presumably of 600 nm wavelength; this information is missing in the paper, however, it was stated that this wavelength is most suitable to induce spin-crossover switching in the examined complex). In the TR experiment two pump-probe delay times were used, namely 500 ps and 50 μs. It appeared that only the latter one allowed for full refinement and a quantitative determination of the structural changes in this molecule. On the other hand, in both cases data were of sufficient quality to generate the photodifference maps shown in Fig. 28. Clearly, for both delay times, the same characteristic feature around the iron is observed, which suggests this atom moves toward the tetrachlorocatecholate fragment upon excitation. The peaks are more pronounced for the 50 μs delay data set, which is related to the larger total population of the excited state found during the refinement. The population factors amounted to 1.5–2% and 10.5(16)% for the 500 ps and 50 μs data sets, respectively. It should be noted that for the 500 ps delay time, the population was estimated by varying the respective parameters manually until the $\underline{R}[R]$ factor (see Eq. 13 above) was minimized. The higher population obtained when probing after the longer time delay agrees well with optical studies performed in the same paper. It can be explained by the observation that conversion to the HS state can be stimulated by an increase in sample temperature and/or an increase of the sample's volume (which geometrically favors high-spin states). In turn, the temperature response of the crystal lattice (e.g. its expansion) to the laser pulse is homogenized over the crystal after 50 μs, thus after that time the heating results in thermal population of the HS state (which is not the case of 500 ps data). As far as the 50 μs data set is concerned, the refinement shows that the iron atom shifts by 0.17(2) Å. In addition, despite some larger standard deviations, the Fe–N bonds clearly elongate, which is consistent with the geometrical features characteristic of iron centers in their HS spin state. Overall, the study shows quantitatively that such spin-crossover systems can indeed be switched on a very short time-scale, and this can be observed with atomic resolution using TR X-ray techniques.

10.11.3.3.7 $Ag_2Cu_2(dpi)_4$ multicenter complex

The last but one example, in which the Laue method was applied, is the tetranuclear silver(I)-copper(I), $Ag_2Cu_2(dpi)_4$, complex (dpi = 2-diphenylphoshino-3-methylindole)[127] (Fig. 19H). This system appeared to be particularly promising as a model case for successful time-resolved photocrystallographic studies. First of all, crystals of $Ag_2Cu_2(dpi)_4$ were of very good quality, did not contain solvent species (the compound may be crystallized with[171] and without solvent moieties[127]), and they diffract well. Importantly, they show orange-red phosphorescence (emission maximum at 650 nm; 1 μs lifetime) when excited with 355–390 nm laser light, which indicates a large Stokes shift. The emissive state was assigned as a short-lived triplet. Even based on such information, one may expect that structural changes upon irradiation should be significant (large Stokes shift, triplet nature

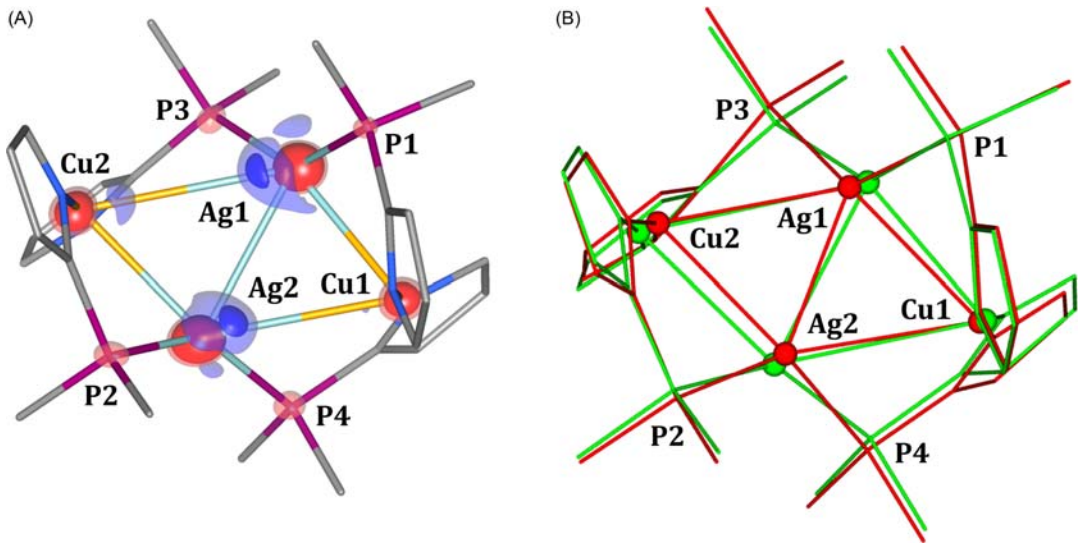

Fig. 29 (A) Photodifference map for the $Ag_2Cu_2(dpi)_4$ complex (blue surfaces – positive values, red – negative, solid isosurfaces at ± 0.55 e Å^{-3}, semi-transparent at ± 0.35 e Å^{-3}). (B) Refined excited-state model shown in comparison with the ground state (green – ground state, red – excited state). In both panels some parts of the molecule are removed for clarity). Reproduced with permission from Jarzembska, K. N.; Kamiński, R.; Fournier, B.; Trzop, E.; Sokolow, J. D.; Henning, R.; Chen, Y.; Coppens, P. Shedding Light on the Photochemistry of Coinage-Metal Phosphorescent Materials: A Time-Resolved Laue Diffraction Study of an AgI-CuI Tetranuclear Complex. *Inorg. Chem.* ***2014, 53, 10594–10601.*** Copyright (2014) American Chemical Society.

of the excited state) and detectable thanks to the heavy metal centers rich in electrons comprising the core of the molecule and the μs emission lifetime.

The time-resolved experiment was conducted at the 14-ID BioCARS beamline at 90 K with the use of 15 keV pink-beam X-rays. Single crystals were excited with the 390 nm light from the Ti:Sapphire laser (pulse duration of about 38 ps), and probed with 100 ps X-ray pulses applying a delay of 100 ps. The excellent quality photodifference map obtained after data processing is shown in Fig. 29A. It can be seen that formation of the lowest-energy excited triplet state involves shifts in all metal centers, both silver and copper. The observed signal showing atomic movements is notably asymmetric. The differences are especially visible for copper atoms (larger peak near Cu2 atom, smaller near Cu1 one). This can be explained by the unequal intermolecular interactions in the crystal on both sides of the molecule. As the X-ray diffraction signal intensity depends on the electron density, it is obviously stronger for the silver center than for the copper. Quantitative information on geometry changes was obtained via response-ratio refinement. Fig. 29B presents an overlay of the ground-state structure of the complex core and the analogous fragment of the refined triplet-state structure. This comparison shows the core contraction and that the molecule becomes more symmetric. It appears that the Ag···Ag distance significantly shortens upon excitation, namely by 0.38(3) Å, while the metal-metal bond length (2.66(3) Å) becomes comparable to the shortest argentophilic interactions ever reported in the literature.[172] In order to explain the nature of the electronic transition and get independent insight into expected structural changes and their amplitudes, theoretical calculations were performed. It turns out that the excitation follows the LMCT (ligand-to-metal charge transfer) mechanism, which results in an electron density shift from ligands to a silver-silver bonding orbital. Assignment of oxidation states indicate that the formally silver(I) in the ground-state becomes silver(0) in the excited state. This transfer of electron density reduces the metallic centers' repulsion, thus the argentophilic interaction is shortened and strengthened. Furthermore, the QM/MM approach again reflects the experimental results well. In this particular case, such modelling yielded a Ag···Ag contact shortening of 0.345 Å and provided a very comparable picture for the asymmetry of the structural distortions upon excitation. Calculations on isolated-molecules resulted in significantly overestimated structural changes (e.g. Ag···Ag contact shortening by 0.534 Å), while the optimized ground singlet and excited triplet states were naturally symmetric. This example is also important because the refined average population of excited states in the crystal reaches only about 1%, which shows that the presented measurement method is extremely sensitive.

The above-described study provided experimental insights into the nature of the observed luminescent properties and the structural consequences of light-induced excitation. Furthermore, these findings constituted a starting point for further interesting considerations of the relationships between structure and spectroscopic properties for $Ag_2Cu_2(dpi)_4$ crystals, including high-pressure investigations.[173]

10.11.3.3.8 $Cu_4(PhCO_2)_4$ carboxylate complex

Experimental results on structural changes upon irradiation are indispensable for verifying the performance of theoretical methods and/or providing insights when quantum computations do not deliver clear answers. The latter was an important issue in the work dedicated to $Cu_4(PhCO_2)_4$ and its hexanuclear analog.[128,174] Here we focus on $Cu_4(PhCO_2)_4$, crystals (Fig. 19I) of which show

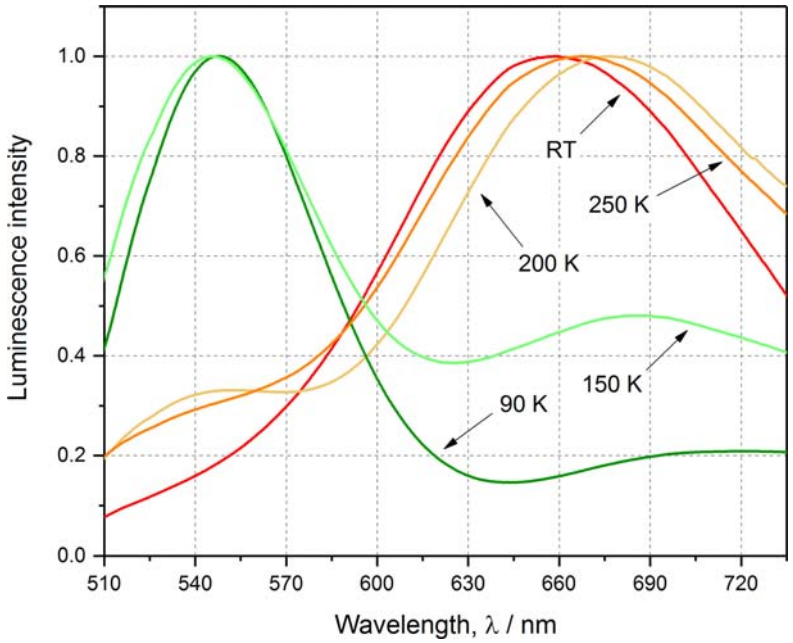

Fig. 30 Emission spectra for $Cu_4(PhCO_2)_4$ single crystals collected at different temperatures. Reproduced with permission from Jarzembska, K. N.; Hapka, M.; Kamiński, R.; Bury, W.; Kutniewska, S. E.; Szarejko, D.; Szczęśniak, M. M. On the Nature of Luminescence Thermochromism of Multinuclear Copper(I) Benzoate Complexes in the Crystalline State. *Crystals* **2019, 9, 36.**

luminescence thermochromism (Fig. 30). The red emission band observed at room temperature (ca. 680 nm) gradually diminishes on temperature reduction while, simultaneously, the higher-energy green emission band (ca. 546 nm) appears. The luminescence decay, in both cases, is well-represented by a bi-exponential function, where the microsecond decay times indicate phosphorescence. Luminescence thermochromism has already been observed for multi-center copper compounds, but mainly for cubane-type-core complexes containing halogen atoms and organic ligands in their structure. The $Cu_4I_4(py)_4$ (py = pyridine) system serves a good example. This complex also exhibits two emission bands. The low-energy emission is attributed to the triplet excited state localized on the cluster core (^{3}CC, cluster-centered), while the high-energy emission band is associated with charge transfer from the halogen substituent to the ligand (^{3}XLCT halide-to-ligand charge transfer).[175] Most probably, the behavior of $Cu_4(PhCO_2)_4$ crystals results from the existence of two emissive excited states, but surely of a different nature. To address this problem, both theoretical modelling and TR photocrystallography were employed.

An analysis of the one-particle transition-density matrix (1-TDM)[176–178] indicated that within the 10 lowest-energy electronic transitions there is a group of excitations centered on the complex core with a distinct MLCT contribution and also a second group with predominant $\pi \rightarrow \pi^*$ character. To model the possible structural changes accompanying the excitation of a complex molecule, the two lowest-energy triplet states were optimized, namely the first triplet state T_1 and the subsequent triplet T_2. It appears that these states are of notable ^{3}CC nature thus, in both cases, a significant contraction of the complex copper core is observed. The changes in the Cu⋯Cu distances are greater for T_1, while for T_2 the Cu–O bonds are noticeably affected and get elongated. Convergence was not achieved for the $\pi \rightarrow \pi^*$ transitions, where mainly deformations of the organic ligands are anticipated. Energetic analysis of transitions from both triplet states to the ground state showed that T_1 is most likely responsible for the low-energy red emission band. In turn, T_2 could be associated with the green emission. At this point, in order to get some independent information on the excitation nature, TR photocrystallographic experiments were conducted at the 14-ID-B BioCARS beamline on single-crystal samples at two different temperatures: 90 K (green emission prevails) and 225 K (solely the low-energy band is present). Regrettably, full refinement of the excited-state structure was not possible due to the relatively low data completeness, and perhaps quite low excited-state population. Nevertheless, the presence of negative peaks on the photodifference map (Fig. 31) at the original copper atoms' positions suggests that these atoms shift upon excitation. In the case of both photodifference maps, i.e. at 90 K and 225 K, the respective patterns for the symmetry-independent molecules look almost identical, despite the fact that different single-crystal samples were used, two different lasers, and also different reference monochromatic X-ray diffraction data sets. This indicates high reproducibility for the experimental results, and also suggests that, most likely, the same excited states had been captured in both experiments. Comparing the ns pump-probe delay with the μs decay times of the sample's emission, this explanation seems to be most reasonable. The time between the probe and the pump pulses could have been shorter than the time needed for conversion of the populated excited state to the final emissive electronic state. Therefore, in both experiments either the singlet excited state was probed, or the higher energy triplet state, which is associated with the green emission (if the latter is the case, T_2 will be in fact the high-energy emissive state). Since the crystal structure of $Cu_4(PhCO_2)_4$ contains two molecules in the ASU, a more accurate analysis of the photodifference maps indicates that the core of the B molecule undergoes greater deformation upon laser irradiation (as suggested by the large peak at the Cu7 atom) than it is the case for the A molecule (Fig. 31). This is most likely related to the observation that in the B molecule the shorter diagonal of the copper core is longer than that in the A species, thus it is subjected to greater contraction during excitation. This is also supported by results from QM/MM calculations for state T_1.

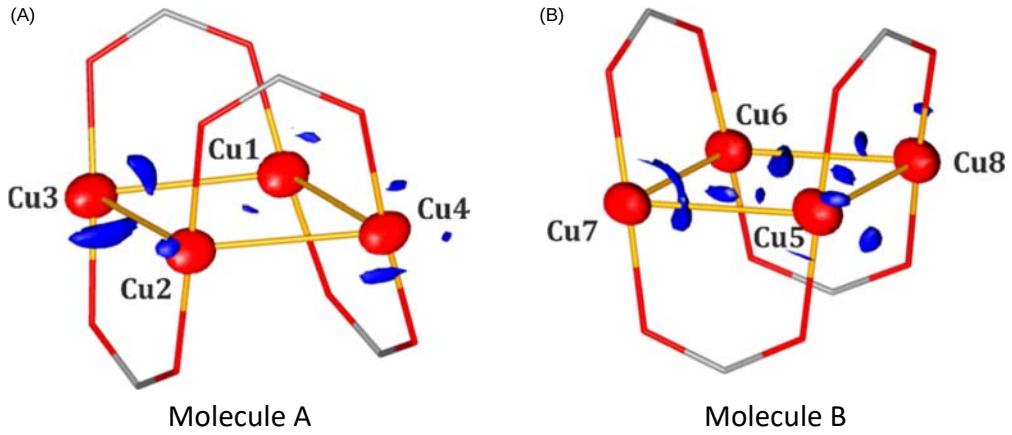

Fig. 31 Photodifference maps for the two $Cu_4(PhCO_2)_4$ symmetry-independent molecules in the ASU based on 90 K data (blue surfaces – positive values, red – negative, isosurfaces at −2.0/+0.9 e Å^{-3}). Reproduced with permission from Jarzembska, K. N.; Hapka, M.; Kamiński, R.; Bury, W.; Kutniewska, S. E.; Szarejko, D.; Szczęśniak, M. M. On the Nature of Luminescence Thermochromism of Multinuclear Copper(I) Benzoate Complexes in the Crystalline State. *Crystals* **2019, 9, 36.**

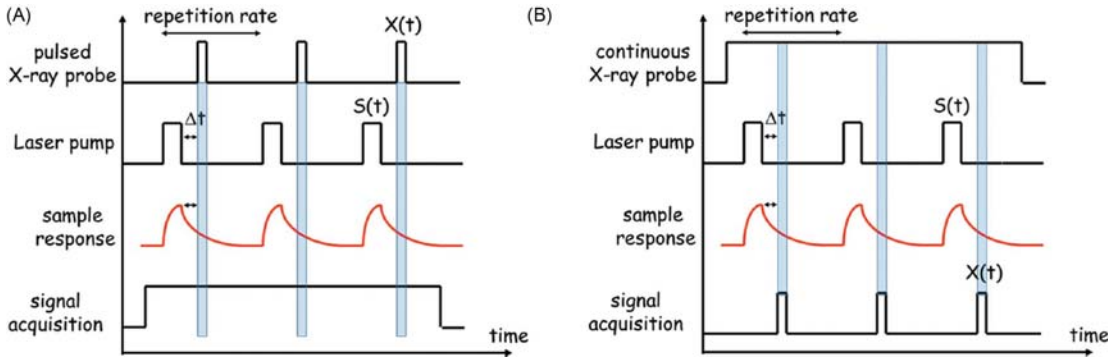

Fig. 32 Comparison of pump-probe experiments with an intrinsically pulsed X-ray source (A) and a fast-gated detector (B). Reproduced with permission of the International Union of Crystallography from Casaretto, N.; Schaniel, D.; Alle, P.; Wenger, E.; Parois, P.; Fournier, B.; Bendeif, E.-E.; Palin, C.; Pillet, S. In-House Time-Resolved Photocrystallography on the Millisecond Timescale Using a Gated X-Ray Hybrid Pixel Area Detector. *Acta Cryst. Sect. B* ***2017, 73, 696–707.***

10.11.3.3.9 In-house time-resolved photocrystallographic studies

The term in-house TR studies includes TR photocrystallographic experiments performed on a laboratory diffractometer. To date, only a handful of attempts of this kind have been reported, since the techniques are still under intensive development. The experiments presented here can be classified as two types. The first group is based on the same principles as the synchrotron studies, which intrinsically give access to X-ray pulses (Fig. 32A). Obviously, for the laboratory diffractometer with a continuous X-ray beam one must 'slice' the beam to generate pulses; this can be achieved with a rotating chopper.[37,179] The second approach relies on a gated detector allowing time-limited signal acquisition, while the sample is constantly exposed to X-rays[180] (Fig. 32B).

The second approach will be discussed first, since it is much more convenient when using a laboratory source. Given the overall readout time of the XPAD detector employed in the published experiments of this type,[181] the achieved time resolution was of the order of milliseconds. This was sufficient to study the time evolution of the reflection intensity from sodium nitroprusside, $Na_2[Fe(CN)_5NO]\cdot 2H_2O$, single crystals, as a proof of principle for the method. Molecules of this complex can form several linkage isomer states. In the ground state, the NO ligand is linear and binds to the iron core via the nitrogen atom (Fe − NO), whereas in the closest metastable state it is side-bound (i.e. both N and O atoms coordinate to the Fe center). According to the transient absorption spectroscopy measurements, when the molecule is excited (or switched) at 150 K it undergoes ligand reorganization, but after 100 ms it reverts completely to the ground state. Using TR photocrystallography, it was, among other things, possible to trace the evolution of selected reflections in terms of their shape, intensity and position (Fig. 33). This method, being relatively simple

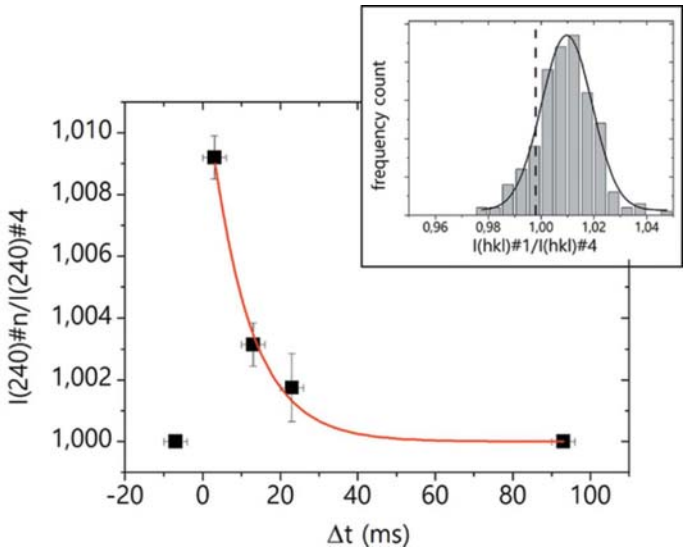

Fig. 33 Normalized intensity of the (240) reflection as a function of time. The inset shows the histogram of the normalized intensity distribution for this reflection. Positive shift of the distribution indicates molecular photoswitching. Reproduced with permission of the International Union of Crystallography from Casaretto, N.; Schaniel, D.; Alle, P.; Wenger, E.; Parois, P.; Fournier, B.; Bendeif, E.-E.; Palin, C.; Pillet, S. In-House Time-Resolved Photocrystallography on the Millisecond Timescale Using a Gated X-Ray Hybrid Pixel Area Detector. *Acta Cryst. Sect. B* ***2017, 73, 696–707.***

and very convenient to apply, will likely serve as a useful tool to study the photophysics and photochemistry of crystal samples in laboratories. Current developments focus on enhancing the method's precision and time resolution.

Access to a shorter timescale was made possible by application of a rotating chopper 'slicing' the continuous X-ray beam from the conventional source (a rotating generator was used to maximize the beam intensity). In the following experiments, the chopper was placed between the end of the X-ray tube collimator and the sample. It appeared that the chopper rotating at a high speed caused some severe disturbance to the cryostream used to cool the sample down. To eliminate this issue, a special enclosure was designed.[37] The rotating chopper was then synchronized with the laser pulses of the Nd:YAG nanosecond laser. At best, the setup was capable of chopping of the X-ray beam at 50 kHz frequently yielding 10 μs wide X-ray pulses with 10 μs intervals.[179,182] It was also possible to control the time resolution and spacing between X-ray pulses by using various chopper disks so as to fit the sample requirements. For instance, a study of the organic molecule, 1,4-dibromo-2,5-bis(octyloxy)benzene,[36] was carried out with very wide X-ray pulses of 325 μs, since the phosphorescence lifetime of this crystal sample was also determined to be 325 μs when excited with 355 nm light at 90 K. The data collection and processing strategies were similar to those applied in the case of TR Laue data (collection of both light-ON and light-OFF frames, computing intensity ratios, etc.). The main result from this study was that the refined excited-state structure showed elongation of the intermolecular Br⋯Br distances (from 3.290 to 3.380 Å) and C–Br bonds from 1.886(1) to 1.904(1) Å.

The second study of this kind was an investigation of the earlier mentioned Cu(dppe)(dmp)·PF_6 complex.[183,184] In this case, the experiment time-resolution was significantly greater – 30 μs, and X-ray pulses were coupled with 7 ns excitation laser pulses (355 nm). The copper atom shifts in the solid state were determined to be 0.042(6) and 0.072(5) Å, for the Cu1 and Cu2 atoms, respectively. These values differ from the ones reported previously using the stroboscopic method,[124] though they somewhat represent the same trend (shift of Cu2 seems to be slightly larger than that of Cu1). On the other hand, the magnitudes of the shifts are closer to those of the other copper(I) complex studied with the Laue technique.[125] It is therefore an open discussion as to how the complex behaves under light excitation.

10.11.4 Summary and prospects

Time-resolved photocrystallography is currently at the forefront of materials science research. It is a very dynamically developing field, including advances in instrumentation and data analysis tools, which open up wide possibilities for the investigation of photochemical and photophysical processes with atomic resolution. Knowledge about structural changes is not only of fundamental importance, it also provides useful information for the future design of new functional materials or photoactive drugs. It should be noted that the majority of the examples presented in this chapter were single snap shots of processes occurring in crystals after they had been exposed to the light pulse. Many of these processes can be incredibly complex and may involve many stages and multiple excited states, all different in nature and properties. A good example here is the so-called thermally-activated delayed fluorescence (TADF), in which the system goes back to the fluorescent state after staying a certain time in a supposedly more stable phosphorescent state. This process is triggered by temperature, thus showing the importance of higher-temperature studies, as well as the need to record a full 'molecular movie' at various time points throughout the reaction or photochemical cycle. To facilitate such studies, the development of new X-ray sources, namely upgrades of existing synchrotrons (4th generation start to emerge now) and further improvements to X-ray free-electron lasers, and new detector designs, are the most important issues. The latter are becoming faster and larger, and can now record significant amounts of high-quality data at different time delays with reference to the excitation light pulse almost simultaneously. This incredible increase of data collection speed is pivotal for recording real 'molecular movie'. Fast-readout and gated detectors such as PILATUS, XPAD or Timepix[185] are starting to be implemented in time-resolved studies with great success, as well as new data collection strategies – currently implemented in serial macromolecular crystallography.[186,187] In parallel, new data processing and analysis algorithms are being developed. Most importantly, these include new methods for polychromatic, XFEL data, and in-house X-ray diffraction data treatment. It is believed that, through many of these advances, TR photocrystallography will provide increasingly better temporal resolution and become a research tool complementary to ultrafast optical spectroscopy studies.

Acknowledgments

K.N.J. and R.K. acknowledge the SONATA BIS (2020/38/E/ST4/00400) and SONATA (2016/21/D/ST4/03753) grants of the National Science Centre in Poland for financial support, respectively.

References

1. Dowling, J. E.; Wald, G. The Biological Function of Vitamin-A Acid. *Nutr. Rev.* **1981,** *39*, 135–138.
2. Wald, G. The Molecular Basis of Visual Excitation. *Nature* **1968,** *219* (5156), 800–807.
3. Grätzel, M. Recent Advances in Sensitized Mesoscopic Solar Cells. *Acc. Chem. Res.* **2009,** *42*, 1788–1798.
4. Sancar, A. Structure and Function of DNA Photolyase and Cryptochrome Blue-Light Photoreceptors. *Chem. Rev.* **2003,** *103*, 2203–2238.

5. Conrad, K. S.; Manahan, C. C.; Crane, B. R. Photochemistry of Flavoprotein Light Sensors. *Nat. Chem. Biol.* **2014,** *10,* 801–809.
6. Coppens, P. What Can Time-Resolved Diffraction Tell us about Transient Species?: Excited-State Structure Determination at Atomic Resolution. *Chem. Commun.* **2003,** *12,* 1317–1320.
7. Gatti, C.; Macchi, P. *Modern Charge-Density Analysis*, Springer: Netherlands, 2012.
8. Coppens, P. *X-Ray Charge Densities and Chemical Bonding*, Oxford University Press: International Union of Crystallography, 1997.
9. Coppens, P. The Dramatic Development of X-Ray Photocrystallography over the Past Six Decades. *Struct. Dyn.* **2017,** *4*, 032102.
10. Coppens, P.; Fournier, B. New Methods in Time-Resolved Laue Pump-Probe Crystallography at Synchrotron Sources. *J. Synchrotron Rad.* **2015,** *22,* 280–287.
11. Coppens, P. Molecular Excited-State Structure by Time-Resolved Pump-Probe X-Ray Diffraction. What Is New and What Are the Prospects for Further Progress? *J. Phys. Chem. Lett.* **2011,** *2,* 616–621.
12. Coppens, P.; Benedict, J. B.; Messerschmidt, M.; Novozhilova, I.; Graber, T.; Chen, Y.-S.; Vorontsov, I.; Scheins, S.; Zheng, S.-L. Time-Resolved Synchrotron Diffraction and Theoretical Studies of Very Short-Lived Photo-Induced Molecular Species. *Acta Cryst. Sect. A* **2010,** *66,* 179–188.
13. Ren, Z.; Bourgeois, D.; Helliwell, J. R.; Moffat, K.; Šrajer, V.; Stoddard, B. L. Laue Crystallography: Coming of Age. *J. Synchrotron Rad.* **1999,** *6,* 891–917.
14. Cohen, M. D.; Schmidt, G. M. J. Topochemistry. Part I. A Survey. *J. Chem. Soc.* **1964,** 1996–2000.
15. Cohen, M. D.; Schmidt, G. M. J.; Sonntag, F. I. Topochemistry. Part II. The Photochemistry of Trans-Cinnamic Acids. *J. Chem. Soc.* **1964,** 2000–2013.
16. Schmidt, G. M. J.; Topochemistry. Part III. The Crystal Chemistry of some Trans-Cinnamic Acids. *J. Chem. Soc.* **1964,** 2014–2021.
17. Schmidt, G. M. J. Photodimerization in the Solid State. *Pure Appl. Chem.* **1971,** *27,* 647–678.
18. Wegner, G. Solid-State Polymerization Mechanisms. *Pure Appl. Chem.* **1977,** *49,* 443–454.
19. Hasegawa, M. Photopolymerization of Diolefin Crystals. *Chem. Rev.* **1983,** *83,* 507–518.
20. Zheng, S.-L.; Messerschmidt, M.; Coppens, P. Single-Crystal-to-Single-Crystal E to Z Isomerization of Tiglic Acid in a Supramolecular Framework. *Acta Cryst. Sect. B* **2007,** *63,* 644–649.
21. Zheng, S.-L.; Pham, O.; Vande Velde, C. M. L.; Gembicky, M.; Coppens, P. Competitive Isomerization and Dimerization in Co-Crystals of 1,1,6,6-Tetrahexaphenyl-2,4-Diyne-1,6-Diol and Sorbic Acid: A New Look at Stereochemical Requirements for [2+2] Dimerization. *Chem. Commun.* **2008,** 2538–2540.
22. Hatcher, L. E.; Raithby, P. R. Solid-State Photochemistry of Molecular Photo-Switchable Species: The Role of Photocrystallographic Techniques. *Acta Cryst. Sect. C* **2013,** *69,* 1448–1456.
23. Trzop, E.; Turowska-Tyrk, I. Monitoring Structural Transformations in Crystals. 12. Course of an Intramolecular [4+4] Photocycloaddition in a Crystal. *Acta Cryst. Sect. B* **2008,** *64,* 375–382.
24. Benedict, J. B.; Coppens, P. Kinetics of the Single-Crystal to Single-Crystal Two-Photon Photo-Dimerization of α-Trans Cinnamic Acid to α-Truxillic Acid. *J. Phys. Chem. A* **2009,** *113,* 3116–3120.
25. Harada, J.; Nakajima, R.; Ogawa, K. X-Ray Diffraction Analysis of Photochromic Reaction of Fulgides: Crystalline State Reaction Induced by Two-Photon Excitation. *J. Am. Chem. Soc.* **2008,** *130,* 7085–7091.
26. Brayshaw, S. K.; Schiffers, S.; Stevenson, A. J.; Teat, S. J.; Warren, M. R.; Bennett, R. D.; Sazanovich, I. V.; Buckley, A. R.; Weinstein, J. A.; Raithby, P. R. Highly Efficient Visible-Light Driven Photochromism: Developments towards a Solid-State Molecular Switch Operating through a Triplet-Sensitised Pathway. *Chem. Eur. J.* **2011,** *17,* 4385–4395.
27. Cox, J. M.; Walton, I. M.; Patel, D. G. D.; Xu, M.; Chen, Y.-S.; Benedict, J. B. The Temperature Dependent Photoswitching of a Classic Diarylethene Monitored by In Situ X-Ray Diffraction. *J. Phys. Chem. A* **2015,** *119,* 884–888.
28. Konieczny, K.; Bąkowicz, J.; Turowska-Tyrk, I. Structural Transformations in Crystals Induced by Radiation and Pressure. Part 3. The Pressure-Induced Structural Changes Versus the Rate of the Norrish-Yang Reaction in Crystals. *J. Photochem. Photobiol. A* **2016,** *325,* 111–115.
29. Hajdu, J.; Johnson, L. N. Progress with Laue Diffraction Studies on Protein and Virus Crystals. *Biochemistry* **1990,** *29,* 1669–1678.
30. Campbell, J. W.; Clifton, I. J.; Elder, M.; Machin, P. A.; Zurek, S.; Helliwell, J. R.; Habash, J.; Hajdu, J.; Harding, M. M. White beam Laue diffraction: Data processing developments and results for single crystal data. In *Biophysics and Synchrotron Radiation;* Bianconi, A., Castellano, A. C., Eds.; vol. 2; Springer: Berlin, Heidelberg, 1987; pp 52–60.
31. Ohashi, Y. Real-Time In Situ Observation of Chemical Reactions. *Acta Cryst. Sect. A* **1998,** *54,* 842–849.
32. Cailleau, H.; Lorenc, M.; Guérin, L.; Servol, M.; Collet, E.; Cointe, M. B.-L. Structural Dynamics of Photoinduced Molecular Switching in the Solid State. *Acta Cryst. Sect. A* **2010,** *66,* 189–197.
33. Hatcher, L. E.; Raithby, P. R. Dynamic Single-Crystal Diffraction Studies Using Synchrotron Radiation. *Coord. Chem. Rev.* **2014,** *277-278,* 69–79.
34. Brayshaw, S. K.; Knight, J. W.; Raithby, P. R.; Savarese, T. L.; Schiffers, S.; Teat, S. J.; Warren, J. E.; Warren, M. R. Photocrystallography - Design and Methodology for the Use of a Light-Emitting Diode Device. *J. Appl. Cryst.* **2010,** *43,* 337–340.
35. Fullagar, W. K.; Wu, G.; Kim, C.; Ribaud, L.; Sagerman, G.; Coppens, P. Instrumentation for Photocrystallographic Experiments of Transient Species. *J. Synchrotron Rad.* **2000,** *7,* 229–235.
36. Basuroy, K.; Chen, Y.; Sarkar, S.; Benedict, J.; Coppens, P. Exploring the Structural Changes on Excitation of a Luminescent Organic Bromine-Substituted Complex by in-House Time-Resolved Pump-Probe Diffraction. *Struct. Dyn.* **2017,** *4*, 024501.
37. Kamiński, R.; Benedict, J. B.; Nottingham, G.; Coppens, P. An Optical Chopper for Generation of Short X-Ray Pulses to Allow in-House Time-Resolved Photocrystallography. *J. Appl. Cryst.* **2014,** *47,* 1765–1768.
38. Casaretto, N.; Schaniel, D.; Alle, P.; Wenger, E.; Parois, P.; Fournier, B.; Bendeif, E.-E.; Palin, C.; Pillet, S. In-House Time-Resolved Photocrystallography on the Millisecond Timescale Using a Gated X-Ray Hybrid Pixel Area Detector. *Acta Cryst. Sect. B* **2017,** *73,* 696–707.
39. Wulff, M.; Plech, A.; Eybert, L.; Randler, R.; Schotte, F.; Anfinrud, P. Realisation of Sub-Nanosecond Pump and Probe Experiments at the ESRF. *Farad. Discuss.* **2002,** *122,* 13–26.
40. Graber, T.; Anderson, S.; Brewer, H.; Chen, Y.-S.; Cho, H.; Dashdorj, N.; Henning, R. W.; Kosheleva, I.; Macha, G.; Meron, M.; Pahl, R.; Ren, Z.; Ruan, S.; Schotte, F.; Šrajer, V.; Viccaro, P. J.; Westferro, F.; Anfinrud, P.; Moffat, K. BioCARS: A Synchrotron Resource for Time-Resolved X-Ray Science. *J. Synchrotron Rad.* **2011,** *18,* 658–670.
41. Kamiński, R.; Jarzembska, K. N.; Kutyła, S. E.; Kamiński, M. A Portable Light-Delivery Device for In Situ Photocrystallographic Experiments at Home Laboratory. *J. Appl. Cryst.* **2016,** *49,* 1383–1387.
42. Chen, Y.-S.; Brewer, H.; Meron, M.; Viccaro, J. Advanced Crystallographic Program at ChemMatCARS at Advanced Photon Source. *Acta Cryst. Sect. A* **2014,** *70,* C1727.
43. Yufit, D. S. In Situ Laser Irradiation Setup for a Bruker Three-Circle Goniometer. *J. Appl. Cryst.* **2017,** *50,* 1556–1558.
44. Nowell, H.; Barnett, S. A.; Christensen, K. E.; Teat, S. J.; Allan, D. R. I19, the Small-Molecule Single-Crystal Diffraction Beamline at Diamond Light Source. *J. Synchrotron Rad.* **2012,** *19,* 435–441.
45. Noda, Y.; Ohshima, K.; Toraya, H.; Tanaka, K.; Terauchi, H.; Maeta, H.; Konishi, H. First Results from the Crystal Structure Analysis Beamline at SPring-8. *J. Synchrotron Rad.* **1998,** *5,* 485–487.
46. Gembicky, M.; Oss, D.; Fuchs, R.; Coppens, P. A Fast Mechanical Shutter for Submicrosecond Time-Resolved Synchrotron Experiments. *J. Synchrotron Rad.* **2005,** *12,* 665–669.
47. Brönnimann, C.; Trüb, P. Hybrid pixel photon counting X-ray detectors for synchrotron radiation. In *Synchrotron Light Sources and Free-Electron Lasers;* Jaeschke, E. J., Khan, S., Schneider, J. R., Hastings, J. B., Eds., Springer: Cham, 2018; pp 995–1027.
48. Ejdrup, T.; Lemke, H. T.; Haldrup, K.; Nielsen, T. N.; Arms, D. A.; Walko, D. A.; Miceli, A.; Landahl, E. C.; Dufresne, E. M.; Nielsen, M. M. Picosecond Time-Resolved Laser Pump/X-Ray Probe Experiments Using a Gated Single-Photon-Counting Area Detector. *J. Synchrotron Rad.* **2009,** *16,* 387–390.

49. Fertey, P.; Alle, P.; Wenger, E.; Dinkespiler, B.; Cambon, O.; Haines, J.; Hustache, S.; Medjoubi, K.; Picca, F.; Dawiec, A.; Breugnon, P.; Delpierre, P.; Mazzolif, C.; Lecomte, C. Diffraction Studies under In Situ Electric Field Using a Large-Area Hybrid Pixel XPAD Detector. *J. Appl. Cryst.* **2013,** *46,* 1151–1161.
50. Friedrich, W.; Knipping, P.; Laue, M. Interferenz-Erscheinungen bei Röntgenstrahlen. *Verl. der Kgl. Bayer. Akad. der Wiss.* **1912,** *42,* 303–322.
51. Friedrich, W.; Knipping, P.; Laue, M. Interferenzerscheinungen bei Röntgenstrahlen. *Ann. Phys.* **1913,** *346,* 971–988.
52. Nozawa, S.; Adachi, S.-I.; Takahashi, J.-I.; Tazaki, R.; Guérin, L.; Daimon, M.; Tomita, A.; Sato, T.; Chollet, M.; Collet, E.; Cailleau, H.; Yamamoto, S.; Tsuchiya, K.; Shioya, T.; Sasaki, H.; Mori, T.; Ichiyanagi, K.; Sawa, H.; Kawata, H.; Koshihara, S.-Y. Developing 100 Ps-Resolved X-Ray Structural Analysis Capabilities on Beamline NW14A at the Photon Factory Advanced Ring. *J. Synchrotron Rad.* **2007,** *14,* 313–319.
53. Gembicky, M.; Adachi, S.-I.; Coppens, P. A kHz Heat-Load Shutter for White-Beam Experiments at Synchrotron Sources. *J. Synchrotron Rad.* **2007,** *14,* 295–296.
54. Cammarata, M.; Ewald, F.; Eybert, L.; Reichenbach, W.; Wulff, M.; Anfinrud, P.; Schotte, F.; Kong, Q.; Lindenau, B.; Rabiger, J.; Polachowski, S. Chopper System for Single Pulse Experiments with Synchrotron Radiation. *Rev. Sci. Instrum.* **2009,** *80,* 015101–015111.
55. Harmand, M.; Coffee, R.; Chollet, M. R. B. M.; French, D.; Zhu, D.; Fritz, D. M.; Lemke, H. T.; Medvedev, N.; Ziaja, B.; Toleikis, S.; Cammarata, M. Achieving Few-Femtosecond Time-Sorting at Hard X-Ray Free-Electron Lasers. *Nat. Photon.* **2013,** *7,* 215–218.
56. Kamiński, R.; Graber, T.; Benedict, J. B.; Henning, R.; Chen, Y.-S.; Scheins, S.; Messerschmidt, M.; Coppens, P. Optimizing the Accuracy and Precision of the Single-Pulse Laue Technique for Synchrotron Photo-Crystallography. *J. Synchrotron Rad.* **2010,** *17,* 479–485.
57. Makal, A.; Trzop, E.; Sokolow, J.; Kalinowski, J.; Benedict, J.; Coppens, P. The Development of Laue Techniques for Single-Pulse Diffraction of Chemical Complexes: Time-Resolved Laue Diffraction on a Binuclear Rhodium Metal-Organic Complex. *Acta Cryst. Sect. A* **2011,** *67,* 319–326.
58. Schoenlein, R. W.; Boutet, S.; Minitti, M. P.; Dunne, A. M. The Linac Coherent Light Source: Recent Developments and Future Plans. *Appl. Sci.* **2017,** *7,* 850.
59. Yabashi, M.; Tanaka, H.; Tono, K.; Ishikawa, T. Status of the SACLA Facility. *Appl. Sci.* **2017,** *7,* 604.
60. Giannessi, L.; Masciovecchio, C. FERMI: Present and Future Challenges. *Appl. Sci.* **2017,** *7,* 640.
61. Ko, I. S.; Kang, H.-S.; Heo, H.; Kim, C.; Kim, G.; Min, C.-K.; Yang, H.; Baek, S. Y.; Choi, H.-J.; Mun, G.; Park, B. R.; Suh, Y. J.; Shin, D. C.; Hu, J.; Hong, J.; Jung, S.; Kim, S.-H.; Kim, K.; Na, D.; Park, S. S.; Park, Y. J.; Jung, Y. G.; Jeong, S. H.; Lee, H. G.; Lee, S.; Lee, S.; Oh, B.; Suh, H. S.; Han, J.-H.; Kim, M. H.; Jung, N.-S.; Kim, Y.-C.; Lee, M.-S.; Lee, B.-H.; Sung, C.-W.; Mok, I.-S.; Yang, J.-M.; Parc, Y. W.; Lee, W.-W.; Lee, C.-S.; Shin, H.; Kim, J. H.; Kim, Y.; Lee, J. H.; Park, S.-Y.; Kim, J.; Park, J.; Eom, I.; Rah, S.; Kim, S.; Nam, K. H.; Park, J.; Park, J.; Kim, S.; Kwon, S.; An, R.; Park, S. H.; Kim, K. S.; Hyun, H.; Kim, S. N.; Kim, S.; Yu, C.-J.; Kim, B.-S.; Kang, T.-H.; Kim, K.-W.; Kim, S.-H.; Lee, H.-S.; Lee, H.-S.; Park, K.-H.; Koo, T.-Y.; Kim, D.-E.; Lee, K. B. Construction and Commissioning of PAL-XFEL Facility. *Appl. Sci.* **2017,** *7,* 479.
62. Tschenscher, T.; Bressler, C.; Grünert, J.; Madsen, A.; Mancuso, A.; Meyer, M.; Scherz, A.; Sinn, H.; Zastrau, U. Photon Beam Transport and Scientific Instruments at the European XFEL. *Appl. Sci.* **2017,** *7,* 592.
63. Milne, C. J.; Schietinger, T.; Aiba, M.; Alarcon, A.; Alex, J.; Anghel, A.; Arsov, V.; Beard, C.; Beaud, P.; Bettoni, S.; Bopp, M.; Brands, H.; Brönnimann, M.; Brunnenkant, I.; Calvi, M.; Citterio, A.; Craievich, P.; Csatari Divall, M.; Dällenbach, M.; D'Amico, M.; Dax, A.; Deng, Y.; Dietrich, A.; Dinapoli, R.; Divall, E.; Dordevic, S.; Ebner, S.; Erny, C.; Fitze, H.; Flechsig, U.; Follath, R.; Frei, F.; Gärtner, F.; Ganter, R.; Garvey, T.; Geng, Z.; Gorgisyan, I.; Gough, C.; Hauff, A.; Hauri, C. P.; Hiller, N.; Humar, T.; Hunziker, S.; Ingold, G.; Ischebeck, R.; Janousch, M.; Juranić, P.; Jurcevic, M.; Kaiser, M.; Kalantari, B.; Kalt, R.; Keil, B.; Kittel, C.; Knopp, G.; Koprek, W.; Lemke, H. T.; Lippuner, T.; Llorente Sancho, D.; Löhl, F.; Lopez-Cuenca, C.; Märki, F.; Marcellini, F.; Marinkovic, G.; Martiel, I.; Menzel, R.; Mozzanica, A.; Nass, K.; Orlandi, G. L.; Ozkan Loch, C.; Panepucci, E.; Paraliev, M.; Patterson, B.; Pedrini, B.; Pedrozzi, M.; Pollet, P.; Pradervand, C.; Prat, E.; Radi, P.; Raguin, J.-Y.; Redford, S.; Rehanek, J.; Réhault, J.; Reiche, S.; Ringele, M.; Rittmann, J.; Rivkin, L.; Romann, A.; Ruat, M.; Ruder, C.; Sala, L.; Schebacher, L.; Schilcher, T.; Schlott, V.; Schmidt, T.; Schmitt, B.; Shi, X.; Stadler, M.; Stingelin, L.; Sturzenegger, W.; Szlachetko, J.; Thattil, D.; Treyer, D. M.; Trisorio, A.; Tron, W.; Vetter, S.; Vicario, C.; Voulot, D.; Wang, M.; Zamofing, T.; Zellweger, C.; Zennaro, R.; Zimoch, E.; Abela, R.; Patthey, L.; Braun, H.-H. SwissFEL: The Swiss X-Ray Free Electron Laser. *Appl. Sci.* **2017,** *7,* 720.
64. Prat, E.; Dijkstal, P.; Ferrari, E.; Reiche, S. Demonstration of Large Bandwidth Hard X-Ray Free-Electron Laser Pulses at SwissFEL. *Phys. Rev. Lett.* **2020,** *124*, 074801.
65. Helliwell, J. R.; Habash, J.; Cruickshank, D. W. J.; Harding, M. M.; Greenhough, T. J.; Campbell, J. W.; Clifton, I. J.; Elder, M.; Machin, P. A.; Papiz, M. Z.; Zurek, S. The Recording and Analysis of Synchrotron X-Radiation Laue Diffraction Photographs. *J. Appl. Cryst.* **1989,** *22,* 483–497.
66. Rossmann, M. G.; Beek, C. G. V. Data processing. *Acta Cryst. Sect. D* **1999,** *55,* 1631–1640.
67. Rossmann, M. G. Processing Oscillation Diffraction Data for Very Large Unit Cells with an Automatic Convolution Technique and Profile Fitting. *J. Appl. Cryst.* **1979,** *12,* 225–238.
68. Ren, Z.; Moffat, K. Structure Refinement against Synchrotron Laue Data: Strategies for Data Collection and Reduction. *J. Appl. Cryst.* **1995,** *28,* 461–481.
69. Campbell, J. W. LAUEGEN, an X-Windows-Based Program for the Processing of Laue Diffraction Data. *J. Appl. Cryst.* **1995,** *28,* 228–236.
70. Šrajer, V.; Crosson, S.; Schmidt, M.; Key, J.; Schotte, F.; Anderson, S.; Perman, B.; Ren, Z.; Teng, T.-Y.; Bourgeois, D.; Wulff, M.; Moffat, K. Extraction of Accurate Structure Factor Amplitudes from Laue Data: Wavelength Normalization with Wiggler and Undulator X-Ray Sources. *J. Synchrotron Rad.* **2000,** *7,* 236–244.
71. Barty, A.; Kirian, R. A.; Maia, F. R. N. C.; Hantke, M.; Yoon, C. H.; White, T. A.; Chapman, H. Cheetah: Software for High-Throughput Reduction and Analysis of Serial Femtosecond X-Ray Diffraction Data. *J. Appl. Cryst.* **2014,** *47,* 1118–1131.
72. White, T. A.; Kirian, R. A.; Martin, A. V.; Aquila, A.; Nass, K.; Barty, A.; Chapman, H. N. CrystFEL: A Software Suite for Snapshot Serial Crystallography. *J. Appl. Cryst.* **2012,** *45,* 335–341.
73. Kalinowski, J. A.; Makal, A.; Coppens, P. The LaueUtil Toolkit for Laue Photocrystallography: I. Rapid Orientation Matrix Determination for Intermediate Size Unit-Cell Laue Data. *J. Appl. Cryst.* **2011,** *44,* 1182–1189.
74. Kalinowski, J. A.; Fournier, B.; Makal, A.; Coppens, P. The LaueUtil Toolkit for Laue Photocrystallography. II. Spot Finding and Integration. *J. Synchrotron Rad.* **2012,** *19,* 637–646.
75. Szarejko, D.; Kamiński, R.; Łaski, P.; Jarzembska, K. N. Seed-Skewness Algorithm for X-Ray Diffraction Signal Detection in the Time-Resolved Synchrotron Laue Photo-crystallography. *J. Synchrotron Rad.* **2020,** *27,* 405–413.
76. Bolotovsky, R.; Coppens, P. The 'seed-skewness' Method for Integration of Peaks on Imaging Plates II. Analysis of Bias Due to Finite Size of the Peak Mask and Treatment of α_1-α_2 Splitting. *J. Appl. Cryst.* **1997,** *30,* 244–253.
77. Bolotovsky, R.; White, M. E.; Darovsky, A.; Coppens, P. The 'seed-skewness' Method for Integration of Peaks on Imaging Plates. *J. Appl. Cryst.* **1995,** *28,* 86–95.
78. Darovsky, A.; Kezerashvili, V. Evaluation of The 'seed-skewness' Nethod of Peak Integration. *J. Appl. Cryst.* **1997,** *30,* 128–132.
79. Peters, J. The 'seed-skewness' Integration Method Generalized for Three-Dimensional Bragg Peaks. *J. Appl. Cryst.* **2003,** *36,* 1475–1479.
80. Straasø, T.; Müter, D.; Sørensen, H. O.; Als-Nielsen, J. Objective Algorithm to Separate Signal from Noise in a Poisson-Distributed Pixel Data Set. *J. Appl. Cryst.* **2013,** *46,* 663–671.
81. Pierre, S. *Morphological Image Anaysis*, Springer: Principles and Aplications, 2003.
82. Waterman, D.; Evans, G. Estimation of Errors in Diffraction Data Measured by CCD Area Detectors. *J. Appl. Cryst.* **2010,** *43,* 1356–1371.
83. Gevorkov, Y.; Barty, A.; Brehm, W.; White, T. A.; Tolstikova, A.; Wiedorn, M. O.; Meents, A.; Grigat, R.-R.; Chapman, H. N.; Yefanov, O. pinkIndexer - a Universal Indexer for Pink-Beam X-Ray and Electron Diffraction Snapshots. *Acta Cryst. Sect. A* **2020,** *76,* 121–131.
84. Paciorek, W. A.; Meyer, M.; Chapuis, G. On the Geometry of a Modern Imaging Diffractometer. *Acta Cryst. Sect. A* **1999,** *55,* 543–557.
85. Kamiński, R.; Szarejko, D.; Pedersen, M. N.; Hatcher, L. E.; Łaski, P.; Raithby, P. R.; Wulff, M.; Jarzembska, K. N. Instrument-Model Refinement in Normalised Reciprocal-Vector Space for X-Ray Laue Diffraction. *J. Appl. Cryst.* **2020,** *53,* 1370–1375.
86. Coppens, P.; Pitak, M.; Gembicky, M.; Messerschmidt, M.; Scheins, S.; Benedict, J. B.; Adachi, S.-I.; Sato, T.; Nozawa, S.; Ichiyanagi, K.; Chollet, M.; Koshihara, S.-Y. The RATIO Method for Time-Resolved Laue Crystallography. *J. Synchrotron Rad.* **2009,** *16,* 226–230.
87. Vorontsov, I. I.; Coppens, P. On the Refinement of Time-Resolved Diffraction Data: Comparison of the Random-Distribution and Cluster-Formation Models and Analysis of the Light-Induced Increase in the Atomic Displacement Parameters. *J. Synchrotron Rad.* **2005,** *12,* 488–493.

88. Vorontsov, I.; Pillet, S.; Kamiński, R.; Schmøkel, M. S.; Coppens, P. LASER - a Program for Response-Ratio Refinement of Time-Resolved Diffraction Data. *J. Appl. Cryst.* **2010,** *43,* 1129–1130.
89. Petříček, V.; Dušek, M.; Palatinus, L. Crystallographic Computing System JANA2006: General Features. *Z. Kristallogr.* **2014,** *229,* 345–352.
90. Ozawa, Y.; Pressprich, M. R.; Coppens, P. On the Analysis of Reversible Light-Induced Changes in Molecular Crystals. *J. Appl. Cryst.* **1998,** *31,* 128–135.
91. Puget, R.; Godefroy, L. Contribution à l'étude de l'ionicité des liaisons dans le rutile. *J. Appl. Cryst.* **1975,** *8,* 297–303.
92. Fujimoto, I. Direct Detection of Electric-Field-Induced Microscopic Structural Changes in $LiNbO_3$ by Modulation X-Ray Diffraction. *Phys. Rev. Lett.* **1978,** *40,* 941–944.
93. Paturle, A.; Graafsma, H.; Sheu, H.-S.; Coppens, P.; Becker, P. Measurement of the Piezoelectric Tensor of an Organic Crystal by the x-Ray Method: The Nonlinear Optical Crystal 2-Methyl 4-Nitroaniline. *Phys. Rev. B* **1991,** *43,* 14683–14691.
94. Paturle, A.; Graafsma, H.; Boviatsis, J.; Legrand, A.; Restori, R.; Coppens, P.; Kvick, Å.; Wing, R. M. The Influence of an External Electric Field on the X-Ray Scattering of 2-Methyl-4-Nitroaniline, an Organic Crystal with Nonlinear Optical Properties. *Acta Cryst. Sect. A* **1989,** *45,* fc25–fc28.
95. Hansen, N. K.; Fertey, P.; Guillot, R. Studies of Electric Field Induced Structural and Electron-Density Modifications by X-Ray Diffraction. *Acta Cryst. Sect. A* **2004,** *60,* 465–471.
96. Aoyagi, S.; Osawa, H.; Sugimoto, K.; Nakahira, Y.; Moriyoshi, C.; Kuroiwa, Y.; Takeda, H.; Tsurumi, T. Time-Resolved Structure Analysis of Piezoelectric Crystals by X-Ray Diffraction under Alternating Electric Field. *Jpn. J. Appl. Phys.* **2018,** *57,* 11UB06.
97. Gorfman, S.; Choe, H.; Shvartsman, V. V.; Ziolkowski, M.; Vogt, M.; Strempfer, J.; Łukasiewicz, T.; Pietsch, U.; Dec, J. Time-Resolved X-Ray Diffraction Reveals the Hidden Mechanism of High Piezoelectric Activity in a Uniaxial Ferroelectric. *Phys. Rev. Lett.* **2015,** *114,* 097601.
98. Coppens, P.; Kamiński, R.; Schmøkel, M. S. On R Factors for Dynamic Structure Crystallography. *Acta Cryst. Sect. A* **2010,** *66,* 626–628.
99. Fournier, B.; Coppens, P. On the Assessment of Time-Resolved Diffraction Results. *Acta Cryst. Sect. A* **2014,** *70,* 291–299.
100. Henn, J. On Predicted R Factors for Dynamic Structure Crystallography. *Z. Kristallogr.* **2018,** *233,* 689–694.
101. Afonine, P. V.; Grosse-Kunstleve, R. W.; Echols, N.; Headd, J. J.; Moriarty, N. W.; Mustyakimov, M.; Terwilliger, T. C.; Urzhumtsev, A.; Zwart, P. H.; Adams, P. D. Towards Automated Crystallographic Structure Refinement with Phenix.Refine. *Acta Cryst. Sect. D* **2012,** *68,* 352–367.
102. Murshudov, G. N.; Skubák, P.; Lebedev, A. A.; Pannu, N. S.; Steiner, R. A.; Nicholls, R. A.; Winn, M. D.; Long, F.; Vagin, A. A. REFMAC5 for the Refinement of Macromolecular Crystal Structures. *Acta Cryst. Sect. D* **2011,** *67,* 355–367.
103. Hajdu, J.; Raviacharya, K.; Stuart, D. I.; McLaughlin, P. J.; Barford, D.; Klein, H.; Johnson, L. N. Time-Resolved Structural Studies on Catalysis in the Crystal with Glycogen Phosphorylase b. *Biochem. Soc. Trans.* **1986,** *14,* 538–541.
104. Hajdu, J.; Machin, P. A.; Campbell, J. W.; Greenhough, T. J.; Clifton, I. J.; Zurek, S.; Gover, S.; Johnson, L. N.; Elder, M. Millisecond X-Ray Diffraction and the First Electron Density Map from Laue Photographs of a Protein Crystal. *Nature* **1987,** *329* (178–181), 178.
105. Teng, T.-Y.; Šrajer, V.; Moffat, K. Initial Trajectory of Carbon Monoxide after Photodissociation from Myoglobin at Cryogenic Temperatures. *Biochemistry* **1997,** *36,* 12087–12100.
106. Vitkup, D.; Petsko, G.; Karplus, M. A Comparison between Molecular Dynamics and X-Ray Results for Dissociated CO in Myoglobin. *Nat. Struct. Biol.* **1997,** *4,* 202–208.
107. Anderson, S.; Srajer, V.; Pahl, R.; Rajagopal, S.; Schotte, F.; Anfinrud, P.; Wulff, M.; Moffat, K. Chromophore Conformation and the Evolution of Tertiary Structural Changes in Photoactive Yellow Protein. *Structure* **2004,** *12,* 1039–1045.
108. Schmidt, M.; Rajagopal, S.; Ren, Z.; Moffat, K. Application of Singular Value Decomposition to the Analysis of Time-Resolved Macromolecular X-Ray Data. *Biophys. J.* **2003,** *84,* 2112–2129.
109. Schmidt, M. A Short History of Structure Based Research on the Photocycle of Photoactive Yellow Protein. *Struct. Dyn.* **2017,** *4*, 032201.
110. Pandey, S.; Poudyal, I.; Malla, T. N. Pump-Probe Time-Resolved Serial Femtosecond Crystallography at X-Ray Free Electron Lasers. *Crystals* **2020,** *10* (7), 628.
111. Nango, E.; Kubo, A. R. M.; Nakane, T.; CeciliaWickstrand; Kimura, T.; Tanaka, T.; Tono, K.; Song, C.; Tanaka, R.; Arima, T.; Yamashita, A.; Kobayashi, J.; Hosaka, T.; EiichiMizohata; Nogly, P.; Sugahara, M.; Nam, D.; Nomura, T.; Shimamura, T.; Im, D.; Fujiwara, T.; Yamanaka, Y.; Jeon, B.; Nishizawa, T.; Oda, K.; Fukuda, M.; Andersson, R.; Båth, P.; Dods, R.; Davidsson, J.; ShigeruMatsuoka; Kawatake, S.; MichioMurata; Nureki, O.; Owada, S.; Kameshima, T.; Hatsui, T.; Joti, Y.; Schertler, G.; Yabashi, M.; Bondar, A.-N.; Standfuss, J.; Neutze, R.; Iwata, S. A Three-Dimensionalmovie of Structural Changes in Bacteriorhodopsin. *Science* **2016,** *354,* 1552–1557.
112. Hoshino, M.; Nozawa, S.; Sato, T.; Tomita, A.; Adachi, S.-I.; Koshihara, S.-Y. Time-Resolved X-Ray Crystal Structure Analysis for Elucidating the Hidden 'over-Neutralized' Phase of TTF-CA. *RSC Adv.* **2013,** *3,* 16313–16317.
113. Hallmann, J.; Morgenroth, W.; Paulmann, C.; Davaasambuu, J.; Kong, Q.; Wulff, M.; Techert, S. Time-Resolved X-Ray Diffraction of the Photochromic α-Styrylpyrylium Trifluoromethanesulfonate Crystal Films Reveals Ultrafast Structural Switching. *J. Am. Chem. Soc.* **2009,** *131,* 15018–15025.
114. Hada, M.; Nishina, Y.; Kato, T. Exploring Structures and Dynamics of Molecular Assemblies: Ultrafast Time-Resolved Electron Diffraction Measurements. *Acc. Chem. Res.* **2021,** *54,* 731–743.
115. Li, Z.; Gyawali, S.; Ischenko, A. A.; Hayes, S.; Miller, R. J. D. Mapping Atomic Motions with Electrons: Toward the Quantum Limit to Imaging Chemistry. *ACS Photonics* **2020,** *7,* 296–320.
116. Jean-Ruel, H.; Cooney, R. R.; Gao, M.; Lu, C.; Kochman, M. A.; Morrison, C. A.; Miller, R. J. D. Femtosecond Dynamics of the Ring Closing Process of Diarylethene: A Case Study of Electrocyclic Reactions in Photochromic Single Crystals. *J. Phys. Chem. A* **2011,** *115,* 13158–13168.
117. Jean-Ruel, H.; Gao, M.; Kochman, M. A.; Lu, C.; Liu, L. C.; Cooney, R. R.; Morrison, C. A.; Miller, R. J. D. Ring-Closing Reaction in Diarylethene Captured by Femtosecond Electron Crystallography. *J. Phys. Chem. B* **2013,** *117,* 15894–15902.
118. Ishikawa, T.; Hayes, S. A.; Keskin, S.; Corthey, G.; Hada, M.; Pichugin, K.; Marx, A.; Hirscht, J.; Shionuma, K.; Onda, K.; Okimoto, Y.; Koshihara, S.-Y.; Yamamoto, T.; Cui, H.; Nomura, M.; Oshima, Y.; Abdel-Jawad, M.; Kato, R.; Miller, R. J. D. Direct Observation of Collective Modes Coupled to Molecular Orbital-Driven Charge Transfer. *Science* **2015,** *350,* 1501–1505.
119. Gao, M.; Lu, C.; Jean-Ruel, H.; Liu, L. C.; Marx, A.; Onda, K.; Koshihara, S.-Y.; Nakano, Y.; Shao, X.; Hiramatsu, T.; Saito, G.; Yamochi, H.; Cooney, R. R.; Moriena, G.; Sciaini, G.; Miller, R. J. D. Mapping Molecular Motions Leading to Charge Delocalization with Ultrabright Electrons. *Nature* **2013,** *496,* 343–346.
120. Kim, C. D.; Pillet, S.; Wu, G.; Fullagar, W. K.; Coppens, P. Excited-State Structure by Time-Resolved X-Ray Diffraction. *Acta Cryst. Sect. A* **2002,** *58,* 133–137.
121. Coppens, P.; Gerlits, O.; Vorontsov, I. I.; Kovalevsky, A. Y.; Chen, Y.-S.; Graber, T.; Gembicky, M.; Novozhilova, I. V. A Very Large rh-rh Bond Shortening on Excitation of the $[Rh_2(1,8\text{-Diisocyano-P-Menthane})4]^{2+}$ Ion by Time-Resolved Synchrotron X-Ray Diffraction. *Chem. Commun.* **2004,** 2144–2145.
122. Vorontsov, I. I.; Kovalevsky, A. Y.; Chen, Y.-S.; Graber, T.; Gembicky, M.; Novozhilova, I. V.; Omary, M. A.; Coppens, P. Shedding Light on the Structure of a Photoinduced Transient Excimer by Time-Resolved Diffraction. *Phys. Rev. Lett.* **2005,** *94*, 193003.
123. Benedict, J. B.; Makal, A.; Sokolow, J. D.; Trzop, E.; Scheins, S.; Henning, R.; Graber, T.; Coppens, P. Time-Resolved Laue Diffraction of Excited Species at Atomic Resolution: 100 Ps Single-Pulse Diffraction of the Excited State of the Organometallic Complex $Rh_2(\mu\text{-PNP})_2(PNP)_2 \cdot BPh_4$. *Chem. Commun.* **2011,** *47,* 1704–1706.
124. Vorontsov, I. I.; Graber, T.; Kovalevsky, A. Y.; Novozhilova, I. V.; Gembicky, M.; Chen, Y.-S.; Coppens, P. Capturing and Analyzing the Excited-State Structure of a Cu(I) Phenanthroline Complex by Time-Resolved Diffraction and Theoretical Calculations. *J. Am. Chem. Soc.* **2009,** *131,* 6566–6573.
125. Makal, A.; Benedict, J.; Trzop, E.; Sokolow, J.; Fournier, B.; Chen, Y.; Kalinowski, J. A.; Graber, T.; Henning, R.; Coppens, P. Restricted Photochemistry in the Molecular Solid State: Structural Changes on Photoexcitation of Cu(I) Phenanthroline Metal-to-Ligand Charge Transfer (MLCT) Complexes by Time-Resolved Diffraction. *J. Phys. Chem. A* **2012,** *116,* 3359–3365.
126. Collet, E.; Moisan, N.; Baldé, C.; Bertoni, R.; Trzop, E.; Laulhé, C.; Lorenc, M.; Servol, M.; Cailleau, H.; Tissot, A.; Boillot, M.-L.; Graber, T.; Henning, R.; Coppens, P.; Cointea, M. B.-L. Ultrafast Spin-State Photoswitching in a Crystal and slower Consecutive Processes Investigated by Femtosecond Optical Spectroscopy and Picosecond X-Ray Diffraction. *Phys. Chem. Chem. Phys.* **2012,** *14,* 6192–6199.

127. Jarzembska, K. N.; Kamiński, R.; Fournier, B.; Trzop, E.; Sokolow, J. D.; Henning, R.; Chen, Y.; Coppens, P. Shedding Light on the Photochemistry of Coinage-Metal Phosphorescent Materials: A Time-Resolved Laue Diffraction Study of an Ag^{I}-Cu^{I} Tetranuclear Complex. *Inorg. Chem.* **2014,** *53,* 10594–10601.
128. Jarzembska, K. N.; Hapka, M.; Kamiński, R.; Bury, W.; Kutniewska, S. E.; Szarejko, D.; Szczęśniak, M. M. On the Nature of Luminescence Thermochromism of Multinuclear Copper(I) Benzoate Complexes in the Crystalline State. *Crystals* **2019,** *9,* 36.
129. Coppens, P.; Vorontsov, I. I.; Graber, T.; Kovalevsky, A. Y.; Chen, Y.-S.; Wu, G.; Gembicky, M.; Novozhilova, I. V. Geometry Changes of a Cu(I) Phenanthroline Complex on Photoexcitation in a Confining Medium by Time-Resolved X-Ray Diffraction. *J. Am. Chem. Soc.* **2004,** *126,* 5980–5981.
130. Sperline, R. P.; Dickson, M. K.; Roundhill, D. M. New Route to the Directed Synthesis of Mixed Metal Chain Oligomers. Identification of a Platinum Complex Having an Intense Emission in the Visible Spectrum in Aqueous Solution. *J. Chem. Soc., Chem. Commun.* **1977,** 62–63.
131. Markert, J. T.; Clements, D. P.; Corson, M. R.; Nagle, J. K. Phosphorescent Lifetime and Quantum Yield Measurements of $K_4Pt_2(H_2P_2O_5)_4$ from 1.6 to 300 K. *Chem. Phys. Lett.* **1983,** *97,* 175–179.
132. Ribaud, L.; Wu, G.; Zhang, Y.; Coppens, P. A Modified Pinkerton-Type Helium Gas-Flow System for High-Accuracy Data Collection at the X3 SUNY Synchrotron Beamline at NSLS. *J. Appl. Cryst.* **2001,** *34,* 76–79.
133. Ozawa, Y.; Terashima, M.; Mitsumi, M.; Toriumi, K.; Yasuda, N.; Uekusa, H.; Ohashi, Y. Photoexcited Crystallography of Diplatinum Complex by Multiple-Exposure IP Method. *Chem. Lett.* **2003,** *32,* 62–63.
134. Rice, S. F.; Gray, H. B. Electronic Absorption and Emission Spectra of Binuclear Platinum(II) Complexes. Characterization of the Lowest Singlet and Triplet Excited States of $Pt_2(H_2P_2O_5)_4^{4-}$. *J. Am. Chem. Soc.* **1983,** *105,* 4571–4575.
135. van der Veen, R. M.; Milne, C. J.; El Nahhas, A.; Lima, F. A.; Pham, V.-T.; Best, J.; Weinstein, J. A.; Borca, C. N.; Abela, R.; Bressler, C.; Chergui, M. Structural Determination of a Photochemically Active Diplatinum Molecule by Time-Resolved EXAFS Spectroscopy. *Angew. Chem. Int. Ed.* **2009,** *48,* 2711–2714.
136. Christensen, M.; Haldrup, K.; Bechgaard, K.; Feidenhans'l, R.; Kong, Q.; Cammarata, M.; Russo, M. L.; Wulff, M.; Harrit, N.; Nielsen, M. M., Time-Resolved X-Ray Scattering of an Electronically Excited Etate in Solution. Structure of the $^3A_{2u}$ State of Tetrakis-μ-Pyrophosphitodiplatinate(II). *J. Am. Chem. Soc.* **2009,** *131,* 502–508.
137. Stevens, B. Some Effects of Molecular Orientation on Fluorescence Emission and Energy Transfer in Crystalline Aromatic Hydrocarbons. *Spectrochim. Acta* **1962,** *18,* 439–448.
138. Ferguson, J. Absorption and Fluorescence Spectra of Crystalline Pyrene. *J. Chem. Phys.* **1958,** *28,* 765.
139. Omary, M. A.; Sinha, P.; Bagus, P. S.; Wilson, A. K. Electronic Structure of Mercury Oligomers and Exciplexes: Models for Long-Range/Multicenter Bonding in Phosphorescent Transition-Metal Compounds. *J. Phys. Chem. A* **2005,** *109,* 690–702.
140. Kyle, K. R.; Ryu, C. K.; DiBenedetto, J. A.; Ford, P. C. Photophysical Studies in Solution of the Tetranuclear Copper(I) Clusters $Cu_4I_4L_4$ (L = Pyridine or Substituted Pyridine). *J. Am. Chem. Soc.* **1991,** *113,* 2954–2965.
141. Radjaipour, M.; Oelkrug, D. Kinetik der Lumineszenz-Thermochromie und Zuordnung der Tieftemperaturemission von Pyridino-Kupfer(I)-jodid. *Ber. Bunsen-Ges. Phys. Chem.* **1978,** *82,* 159–163.
142. Signal, I. S.; Mann, K. R.; Gray, H. B. Solar Energy Storage Reactions. Thermal and Photochemical Redox Reactions of polynuclear Rhodium Isocyanide Complexes. *J. Am. Chem. Soc.* **1980,** *102,* 7252–7256.
143. Mann, K. R.; Lewis, N. S.; Miskowski, V. M.; Erwin, D. K.; Hammond, G. S.; Gray, H. B. Solar Energy Storage. Production of Hydrogen by 546-Nm Irradiation of a Dinuclear Rhodium(I) Complex in Acidic Aqueous Solution. *J. Am. Chem. Soc.* **1977,** *99,* 5525–5526.
144. Miskowski, V. M.; Signal, I. S.; Mann, K. R.; Gray, H. B.; Milder, S. J.; Hammond, G. S.; Ryasson, P. R. Solar Energy Storage Reactions Involving polynuclear Rhodium Isocyanide Complexes. Flash Photolysis Studies in Aqueous Sulfuric Acid Solutions. *J. Am. Chem. Soc.* **1979,** *101,* 4383–4385.
145. Blakley, R. L.; Yin, Y.; Lloyd, C.; Mague, J. T.; McPherson, G. L. Photophysics of a Flexible Ligand Bridged Rhodium(I) Dimer: An Excited State Conformational Change in a Crystalline Solid. *Chem. Phys. Lett.* **1989,** *157,* 398–402.
146. Mague, J. T. Conformational Diversity in the Solid State Structures of $[Rh_2(\mu\text{-}CH_3N(P(OCH_3)_2)_2)_2(CH_3N(P(OCH_3)_2)_2)_2]X_2$ (X = O_3SCF_3, $B(C_6H_5)_4$). *Inorg. Chim. Acta* **1995,** *229,* 17–25.
147. Kamiński, R.; Schmøkel, M. S.; Coppens, P. Constrained Excited-State Structure in Molecular Crystals by Means of the QM/MM Approach: Toward the Prediction of Photocrystallographic Results. *J. Phys. Chem. Lett.* **2010,** *1,* 2349–2353.
148. Armaroli, N.; Accorsi, G.; Cardinali, F.; Listorti, A. Photochemistry and Photophysics of coordination compounds: Copper. In *Photochemistry and Photophysics of Coordination Compounds I. Topics in Current Chemistry;* Balzani, V., Campagna, S., Eds.; vol. 280; Springer: Berlin, Heidelberg, 2007; pp 69–115.
149. Sandroni, M.; Pellegrin, Y.; Odobel, F. Heteroleptic Bis-Diimine Copper(I) Complexes for Applications in Solar Energy Conversion. *C. R. Chim.* **2016,** *19,* 79–93.
150. Yersin, H.; Rausch, A. F.; Czerwieniec, R.; Hofbeck, T.; Fischer, T. The Triplet State of Organo-Transition Metal Compounds. Triplet Harvesting and Singlet Harvesting for Efficient OLEDs. *Coord. Chem. Rev.* **2011,** *255,* 2622–2652.
151. Armaroli, N. Photoactive mono- and polynuclear Cu(I)-phenanthrolines. A Viable Alternative to Ru(II)-Polypyridines? *Chem. Soc. Rev.* **2001,** *30,* 113–124.
152. Smolentsev, G.; Soldatov, A. V.; Chen, L. X. Three-Dimensional Local Structure of Photoexcited Cu Diimine Complex Refined by Quantitative XANES Analysis. *J. Phys. Chem. A* **2008,** *112,* 5363–5367.
153. Iwamura, M.; Takeuchi, S.; Tahara, T. Real-Time Observation of the Photoinduced Structural Change of Bis(2,9-Dimethyl-1,10-Phenanthroline)Copper(I) by Femtosecond Fluorescence Spectroscopy: A Realistic Potential Curve of the Jahn-Teller Distortion. *J. Am. Chem. Soc.* **2007,** *129,* 5248–5256.
154. Scaltrito, D. V.; Thompson, D. W.; O'Callaghan, J. A.; Meyer, G. J. MLCT Excited States of Cuprous Bis-Phenanthroline Coordination Compounds. *Coord. Chem. Rev.* **2000,** *208,* 243–266.
155. Kirchhoff, J. R.; McMillin, D. R.; Robinson, W. R.; Powell, D. R.; McKenzie, A. T.; Chen, S. Steric Effects and the Behavior of $Cu(NN)(PPh_3)_2^+$ Systems in Fluid Solution. Crystal and Molecular Structures of $[Cu(Dmp)(PPh_3)_2]NO_3$ and $[Cu(Phen)(PPh_3)_2]NO_3.1½EtOH$. *Inorg. Chem.* **1985,** *24,* 3928–3933.
156. Palmer, C. E. A.; McMillin, D. R. Singlets, Triplets, and Exciplexes: Complex, Temperature-Dependent Emissions from $Cu(Dmp)(PPh_3)_2^+$ and $Cu(Phen)(PPh_3)_2^+$ in Solution. *Inorg. Chem.* **1987,** *26,* 3837–3840.
157. Cunningham, K. L.; Hecker, C. R.; McMillin, D. R. Competitive Energy-Transfer and Reductive Quenching of the CT Excited States of Copper(I) phenanthrolines. *Inorg. Chim. Acta* **1996,** *242,* 143–147.
158. Cunningham, C. T.; Moore, J. J.; Cunningham, K. L. H.; Fanwick, P. E.; McMillin, D. R. Structural and Photophysical Studies of $Cu(NN)_2^+$ Systems in the Solid State. Emission at Last from Complexes with Simple 1,10-Phenanthroline Ligands. *Inorg. Chem.* **2000,** *39,* 3638–3644.
159. Cunningham, C. T.; Cunningham, K. L. H.; Michalec, J. F.; McMillin, D. R. Cooperative Substituent Effects on the Excited States of Copper phenanthrolines. *Inorg. Chem.* **1999,** *38,* 4388–4392.
160. Blasse, G.; Breddels, P. A.; McMillin, D. R. The Luminescence of Solid Bis(2,9-Diphenyl-1,10-Phenanthroline) Copper(I). *Chem. Phys. Lett.* **1984,** *109,* 24–26.
161. Berger, R. M.; McMillin, D. R.; Dallinger, R. F. Two-Photon Photochemistry of $[Cu(Dmp)_2]^+$. *Inorg. Chem.* **1987,** *26,* 3802–3805.
162. Kovalevsky, A. Y.; Gembicky, M.; Coppens, P. Cu(I)(2,9-Bis(Trifluoromethyl)-1,10-Phenanthroline)$_2^+$ Complexes: Correlation between Solid-State Structure and Photoluminescent Properties. *Inorg. Chem.* **2004,** *43,* 8282–8289.
163. Kovalevsky, A. Y.; Gembicky, M.; Novozhilova, I. V.; Coppens, P. Solid-State Structure Dependence of the Molecular Distortion and Spectroscopic Properties of the Cu(I) Bis(2,9-Dimethyl-1,10-Phenanthroline) Ion. *Inorg. Chem.* **2003,** *42,* 8794–8802.
164. Czerwieniec, R.; Kowalski, K.; Yersin, H. Highly Efficient Thermally Activated Fluorescence of a New Rigid Cu(I) Complex $[Cu(dmp)(phanephos)]^+$. *Dalton Trans.* **2013,** *42,* 9826–9830.
165. Kubiček, K.; Veedu, S. T.; Storozhuk, D.; Kia, R.; Techert, S. Geometric and Electronic Properties in a Series of Phosphorescent Heteroleptic Cu(I) Complexes: Crystallographic and Computational Studies. *Polyhedron* **2017,** *124,* 166–176.

166. Coppens, P.; Sokolow, J.; Trzop, E.; Makal, A.; Chen, Y. On the Biexponential Decay of the Photoluminescence of the Two Crystallographically-Independent Molecules in Crystals of [Cu(I)(phen)(PPh_3)$_2$][BF_4]. *J. Phys. Chem. Lett.* **2013,** *4,* 579–582.
167. Lorenc, M.; Hébert, J.; Moisan, N.; Trzop, E.; Servol, M.; Buron-Le Cointe, M.; Cailleau, H.; Boillot, M. L.; Pontecorvo, E.; Wulff, M.; Koshihara, S.; Collet, E. Successive Dynamical Steps of Photoinduced Switching of a Molecular Fe(III) Spin-Crossover Material by Time-Resolved X-Ray Diffraction. *Phys. Rev. Lett.* **2009,** *103,* 028301.
168. Chergui, M.; Collet, E. Photoinduced Structural Dynamics of Molecular Systems Mapped by Time-Resolved X-Ray Methods. *Chem. Rev.* **2017,** *117,* 11025–11065.
169. Collet, E.; Cammarata, M. Disentangling Ultrafast Electronic and Structural Dynamics with X-Ray Lasers. *Chem. Eur. J.* **2018,** *24,* 15696–15705.
170. Collet, E.; Lorenc, M.; Cammarata, M.; Guérin, L.; Servol, M.; Tissot, A.; Boillot, M. L.; Cailleau, H.; Cointe, M. B. L. 100 Picosecond Diffraction Catches Structural Transients of Laser-Pulse Triggered Switching in a Spin-Crossover Crystal. *Chem. Eur. J.* **2012,** *18,* 2051–2055.
171. Koshevoy, I. O.; Shakirova, J. R.; Melnikov, A. S.; Haukka, M.; Tunik, S. P.; Pakkanena, T. A. Coinage Metal Complexes of 2-Diphenylphosphino-3-Methylindole. *Dalton Trans.* **2011,** *40,* 7927–7933.
172. Schubert, H.; Wesemann, L. Silver Dimer, Tetramer, Polymer, and Network Structures with the Stannylene Stanna-Closo-Dodecaborate. *Organometallics* **2010,** *29,* 4906–4913.
173. Jarzembska, K. N.; Kamiński, R.; Dziubek, K. F.; Citroni, M.; Paliwoda, D.; Durka, K.; Fanetti, S.; Bini, R. Impact of High Pressure on Metallophilic Interactions and its Consequences for Spectroscopic Properties of a Model Tetranuclear Silver(I)-Copper(I) Complex in the Solid State. *Inorg. Chem.* **2018,** *57,* 8509–8520.
174. Filatov, A. S.; Hietsoi, O.; Sevryugina, Y.; Gerasimchuk, N. N.; Petrukhina, M. A. Reversible $Cu_4 \leftrightarrow Cu_6$ Core Interconversion and Temperature Induced Single-Crystal-to-Single-Crystal Phase Transition for Copper(I) Carboxylate. *Inorg. Chem.* **2010,** *49,* 1626–1633.
175. Ford, P. C.; Cariati, E.; Bourassa, J. Photoluminescence Properties of Multinuclear Copper(I) Compounds. *Chem. Rev.* **1999,** *99,* 3625–3647.
176. Plasser, F.; Lischka, H. Analysis of Excitonic and Charge Transfer Interactions from Quantum Chemical Calculations. *J. Chem. Theory Comput.* **2012,** *8,* 2777–2789.
177. Plasser, F.; Dreuw, A. High-Level Ab Initio Computations of the Absorption Spectra of Organic Iridium Complexes. *J. Phys. Chem. A* **2015,** *119,* 1023–1036.
178. Tretiak, S.; Mukamel, S. Density Matrix Analysis and Simulation of Electronic Excitations in Conjugated and Aggregated Molecules. *Chem. Rev.* **2002,** *102,* 3171–3212.
179. Deresz, K. A.; Łaski, P.; Kamiński, R.; Jarzembska, K. N. Advances in Diffraction Studies of Light-Induced Transient Species in Molecular Crystals and Selected Complementary Techniques. *Crystals* **2021,** *11,* 1345.
180. Casaretto, N.; Pillet, S.; Bendeif, E.-E.; Schaniel, D.; Gallien, A. K. E.; Klüfersc, P.; Woike, T. Photocrystallography and IR Spectroscopy of Light-Induced Linkage NO Isomers in [$RuBr(NO)_2(PCyp_3)2$]BF_4. *Acta Cryst. Sect. B* **2015,** *71,* 788–797.
181. Alle, P.; Wenger, E.; Dahaoui, S.; Schaniel, D.; Lecomte, C. Comparison of CCD, CMOS and Hybrid Pixel X-Ray Detectors: Detection Principle and Data Quality. *Phys. Scr.* **2016,** *91,* 063001.
182. Kaminski, R.; Benedict, J.; Trzop, E.; Jarzembska, K.; Fournier, B.; Coppens, P. First Steps towards Time-Resolved 'in-house' X-Ray Diffraction Experiments. *Acta Cryst. Sect. A* **2014,** *70,* C775.
183. Coppens, P.; Zhang, L.; Thomas, R.; Chen, Y.; Jarzembska, K.; Kaminski, R.; Trzop, E.; Fournier, B. Can we Deconvolute Electron Density Changes from the Dominant Influence of the Atomic Rearrangement on Molecular Excitation in Time-Resolved Diffraction Studies? *Phys. Scr.* **2016,** *91,* 023003.
184. Trzop, E.; Fournier, B.; Jarzembska, K.; Sokolow, J.; Kaminski, R.; Benedict, J.; Chen, Y.; Henning, R.; Coppens, P. Selective Time-Dependent Changes of Cu(DPPE)(DMP)·PF_6 on Photoexcitation. *Acta Cryst. Sect. A* **2014,** *70,* C776.
185. Poikela, T.; Plosila, J.; Westerlund, T.; Campbell, M.; Gaspari, M. D.; Llopart, X.; Gromov, V.; Kluit, R.; Beuzekom, M.v.; Zappon, F.; Zivkovic, V.; Brezina, C.; Desch, K.; Fu, Y.; Kruth, A. Timepix3: A 65K Channel Hybrid Pixel Readout Chip with Simultaneous ToA/ToT and Sparse Readout. *J. Instrum.* **2014,** *9,* C05013.
186. Yorke, B. A.; Beddard, G. S.; Owen, R. L.; Pearson, A. R. Time-Resolved Crystallography Using the Hadamard Transform. *Nat. Methods* **2014,** *11,* 1131–1134.
187. Mehrabi, P.; Müller-Werkmeister, H. M.; Leimkohl, J.-P.; Schikora, H.; Ninkovic, J.; Krivokuca, S.; Andričeк, L.; Epp, S. W.; Sherrell, D.; Owen, R. L.; Pearson, A. R.; Tellkamp, F.; Schulz, E. C.; Miller, R. J. D. The HARE Chip for Efficient Time-Resolved Serial Synchrotron Crystallography. *J. Synchrotron Rad.* **2020,** *27,* 360–370.
188. Lakowicz, J. R. *Principles of Fluorescence Spectroscopy,* 3rd ed.; Springer: New York, NY, 2006.

10.12 Direct observation of transient species and chemical reactions in a pore observed by synchrotron radiation

Hiroyoshi Ohtsu and Masaki Kawano, Department of Chemistry, School of Science, Tokyo Institute of Technology 2-12-1 Ookayama, Tokyo, Japan

© 2023 Elsevier Ltd. All rights reserved.

10.12.1	**Introduction**	**311**
10.12.2	**In situ crystallography**	**313**
10.12.2.1	Sampling	313
10.12.2.2	Diffractometer	313
10.12.2.3	Data processing	313
10.12.2.4	Structure determination	313
10.12.3	**In situ spectroscopy and theoretical calculations**	**314**
10.12.4	**Crystal design for in situ observation of unstable species by X-rays**	**314**
10.12.5	**Crystal packing approach**	**315**
10.12.5.1	Direct observation of photo-induced radicals	316
10.12.5.2	Direct observation of photo-induced triplet carbene	318
10.12.5.3	Direct observation of photo-induced triplet nitrene	319
10.12.5.4	Reaction intermediates for catalytic reactions	320
10.12.6	**Prison cell approach**	**321**
10.12.6.1	Direct observation of a photo-induced coordinatively unsaturated transition-metal complex in a M_6L_4 cage	321
10.12.6.2	Crystalline state solution-state-like reaction—Direct observation of selective photo-dimerization of acenaphthylene in a M_6L_4 cage	323
10.12.7	**Step III—Crystalline molecular flask**	**324**
10.12.7.1	Networking of M_6L_4 and in situ observation of the crystalline state photoreaction	324
10.12.7.2	Design of porous coordination networks—Cartridge synthesis	325
10.12.7.3	Pore modification by cartridge synthesis and single-crystal-to-single-crystal guest exchange	325
10.12.7.4	Direct observation of chemical reactions in a pore	325
10.12.7.5	Snapshots of transient species in pores	326
10.12.7.6	Unstable sulfur species observed by X-ray diffraction	329
10.12.7.7	X-ray snapshots of S_2 conversion in an interactive pore	336
10.12.7.8	Unstable phosphorus species: P_4	337
10.12.7.9	Reactive elements: Br_2	338
10.12.8	**Overview**	**340**
References		**341**

Abstract

Here, we have described the direct observation of transient chemical species and chemical reactions using synchrotron radiation. Direct observation of transient and unstable chemical species by X-ray diffraction can greatly enhance our understanding of chemical reactions. On top of that, the use of pores in coordination networks has various applications and is a promising method to elucidate the structure of molecular species that do not inherently crystallize. In particular, kinetic assembly of coordination networks can generate interactive sites in the pores, which is very useful for trapping unstable species. Thus, the methodology using porous coordination networks, i.e., crystalline molecular flasks, allows us to observe a variety of crystalline phase reactions. At the same time, the development of synchrotron radiation and X-ray detectors has made it possible to challenge the microscopic crystals found in MOF crystals. This means that structural analysis is now possible with a smaller amount of target guest sample. In addition, spectroscopic methods and theoretical calculations have been developed to elucidate the electronic structure of these chemical species.

10.12.1 Introduction

The conventional image of X-ray crystal structure analysis is one of routine methods to determine the structures of stable single crystal materials. In the late 1990s, X-ray diffractometers equipped with 2D area detectors like CCD, IP, semiconductor etc. took over from point-detector systems that opened up new research areas. Furthermore, extremely bright and parallel X-ray became

available at synchrotron facilities. High-energy synchrotron radiation is an ideal probe for determining electron density in a crystal. The combination of synchrotron radiation and the area detector system with a cryo-temperature controller enables fast collection of high-quality diffraction data, that is capable of structure determination of even reactive/metastable crystals. From structural studies of metastable systems one can gain deep insights of not only molecular structures but also chemical reactions. In general, chemical reactions between molecules are initiated by collision of molecules in any phases. Indeed, even reactive molecules generated by photo-irradiation are no exception. If molecular motion of reactive molecules is restricted, no chemical reactions occur, that is a golden rule. That means that if molecular motion in a crystal is frozen at cryo-temperatures, no successive chemical reactions occur, enabling the crystal structure determination by the conventional crystallography to be made as long as the crystal retains the long-range periodicity. Likewise, for the first time, Kawano et al. demonstrated that the crystal structures of reactive open-shell species such as radicals, triplet carbenes, and triplet nitrenes generated by photo-irradiation can be determined by X-ray cryo-crystallography. Structural information obtained by cryo-crystallography can give a clear vision of chemical reactions including the initial states, the intermediate states, and the final states. Such information provides the initial models for theoretical calculations to investigate the transient states in the structural changes. Infrared spectroscopic analysis using an inert matrix also provides very useful information about crystalline-state reactions, because whenever chemical reactions occur, the vibrational fingerprint must change. This review describes the development of studies by X-ray crystallography on in/ex situ observation of unstable species, chemical reactions and dynamic framework transformations, and trapping of unstable species in crystals. This review does not cover the study of intermediate species using time-resolved X-ray or Laue diffraction, although an X-ray laser like XFEL has been invented for monitoring extremely fast events.

The molecular structure obtained from a single-crystal X-ray diffraction analysis gives an averaged structure in which the unit cells in the crystal are convoluted by the Fourier transform of the Bragg diffraction. A single molecular crystal is usually obtained by slow crystallization of target molecules such as by layer diffusion, allowing molecules to align periodically in the crystal. This method can be applied when the target molecule is sufficiently stable during crystallization. In reality, most crystal structures reported in crystallographic databases can be categorized as stable compounds. It is rarely possible to crystallize unstable species with conventional crystallization methods. Therefore, in situ crystallographic techniques have been used to determine the crystal structures of unstable species by measuring X-ray diffraction during unstable species formation. In situ crystallography itself has a long history of over 40 years. However, most reactions are down-hill reactions, in which thermodynamically more stable products are generated in ongoing reactions in the crystal. Occasionally, the product can be even re-crystallized. Ohashi et al reported the pioneering works of crystalline state reactions in the late 1970[1,2] and Nakanishi et al. reported the first single-crystal-to-single-crystal (SCSC) reaction.[3] Such in situ crystallography revealed intriguing topological solid-state reaction mechanisms.[4–7] Unlike the solution phase, the solid phase allows for specific reactions such as stereoselective reactions, chiral induction, and the formation of metastable states.[8–10]

In sharp contrast to conventional SCSC reactions, a salient feature of in-situ studies for observing unstable species is derived from up-hill reactions, in which in situ-generated products cannot be recrystallized (**Fig. 1**). In order to observe unstable species, time-resolved pump-probe and cryo-trapping methods have been used.[11–14] The time-resolved pump-probe method requires exactly repeatable events triggered by external stimuli in a crystal. Practically speaking, this strict condition limits target samples, because a crystal can be readily damaged by excitation. Fascinating studies using state-of-the-art techniques have been reported, but unfortunately, only robust crystals can be studied with this method. In this case, to extend the lifetime of the reactive species, the cryo-trapping method is suitable for in situ crystallographic analysis. The cryo-trapping technique has been popular for matrix isolation spectroscopic studies to observe unstable species,[15] whereas it has not been widely used in crystallography.

Furthermore, Kawano et al. have developed a method to use cage-shaped complexes and voids in porous coordination networks for in situ observation of unstable species so that not only photoreactions but also chemical reactions can be observed using X-ray diffraction methods.

The methodology of in situ crystallography is described below.

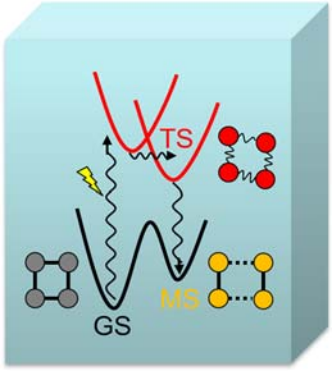

Fig. 1 Concept for in situ observation of up-hill reactions in a crystal.

10.12.2 In situ crystallography

Here we describe the general methodology of in situ crystallography.

In situ crystallography is a *synthetic* experiment performed in a crystal which can be assumed to be a crystalline flask. In order to observe unstable species or intermediates, we need to prepare a single crystal of starting materials (precursor molecules) to generate unstable species by photo-excitation or chemical reactions. If the crystal loses the periodicity of molecules (crystallinity) after excitation, diffraction technique cannot be applied. In principle, maintaining single crystallinity is essential for in situ diffraction study.

To maintain crystallinity and observe unstable species, cryo-temperatures are often required. The basic idea for the cryo-trapping method is to freeze unstable species generated from a precursor molecule by external stimuli using cryo-temperatures to suppress the thermal motion and prevent the intermediate from making successive reactions.[16a] Therefore, once intermediates are trapped at cryo-temperatures, X-ray data collection itself is the same as the standard X-ray measurement, as long as cryo-temperatures are maintained during the data collection. However, collecting high resolution data is essential to perform in situ crystallography, because excitation often results in disordered structures consisting of initial molecules and products. The structure determination of such disordered structures requires high resolution data to sharpen electron density peaks as much as possible. Otherwise, the least-squares refinement will not be stable, because of the broadening of electron density peaks. Strong correlations among parameters in the least-squares refinement will lead to physically meaningless results. Therefore, highly parallel and high-flux monochromatic X-ray synchrotron radiation are ideal for obtaining high-resolution data with well-resolved sharp diffraction spots. However, in situ study of small molecules is practically feasible with laboratory-based X-ray diffractometers. Most X-ray diffractometers can be used without any modification. Special equipment is not needed except possibly for a low temperature device. It is sometimes necessary to change temperatures rapidly right after excitation. In this case, a low temperature device using a gas flow rather than a vacuum type cryostat is preferable. Normally a nitrogen flow is used to cool samples, although ideally helium gas is most suitable to control sample temperatures because of its high thermal conductivity.

10.12.2.1 Sampling

Mounting crystals is important for obtaining useful data. Depending on target compounds, proper glue such as oil, epoxy glue, super glue etc. should be used to coat and mount a crystal. Especially for photo-excitation, the absorption of coating materials should be considered carefully to avoid filtering effects.

10.12.2.2 Diffractometer

Recent development of single crystal diffractometers has significantly contributed to in situ studies in that they enable rapid data collection covering high angle data on a timescale of hours. The advantage of area detectors like IP, CCD and semiconductor detectors are not only rapid data collection but also give photographic images of the diffraction pattern. The photographic image includes abundant information about changes in lattice parameters, diffuse scattering, superlattice parameters, emissions from the crystal, etc. Area detectors enable high throughput screening and prompt optimization of experimental conditions. At synchrotron facilities for single crystal crystallography, high throughput screening is quite important for chemists to be productive. In addition to area detectors, a three- or four-axis goniometer is essential to collect high resolution data with high coverage and high redundancy. Single axis goniometers are quite popular for protein crystallography, whereas they are not suitable for small molecule crystallography, because all vital areas of reciprocal space cannot be covered, sometime resulting in the generation of ghost peaks.

10.12.2.3 Data processing

Data processing itself is the same as conventional methods. It should be noted that crystal lattice, crystal system, or space group may change before and after excitation. It is necessary to generate products in a crystal uniformly. Data should be carefully examined, if diffractions attributable to domain structures or diffuse scattering are observed on excitation.

10.12.2.4 Structure determination

Structure determination is basically the same as for conventional determinations using single crystal X-ray analysis of small molecules. The best way to judge if a refined model is correct or not is to check bond distances, angles, displacement parameters, and a final difference Fourier electron density map rather than the final R factor. The displacement parameter, or thermal ellipsoids, are excellent parameters to detect problems with the modeling. There should not be any large residual electron density peaks remaining in the final electron density difference map. Severely disordered structures may cause some problems in refinement: in cases where the products are closely located to nearby precursor molecules, it is very difficult to refine those positional parameters correctly and the least-squares refinement will not converge. Sometime soft chemical restraints for rigid molecules can be applied to keep reasonable distances and angles. However, it is recommended not to use constraints, especially for displacement factors. Mistreatment of displacement parameters can lead to false modeling. Moreover, because displacement parameters are apt to have strong correlation with occupancy factors, it is not easy to determine reliable parameters when the occupancy factors are

refined. The conversion percentage between the precursor and the reaction product should be estimated by the other methods such as single crystal IR microspectroscopy using transmission optics.

10.12.3 In situ spectroscopy and theoretical calculations

In situ spectroscopy must be carried out under the same sample conditions as for the X-ray measurement including sample size, temperature, excitation conditions, the glue fixing a crystal, reaction time, etc. Itis essential to optimize X-ray measurement conditions and avoid false modeling in the X-ray structure determination. If excitation induces a reaction with structural changes, a vibrational spectrum must change before and after excitation. Because X-ray analysis is a method to provide bulk information from a crystal, transmission rather than reflection mode is desirable for spectroscopic measurements. Among various spectroscopic methods, single crystal IR microspectroscopy is most suitable for the quantitative evaluation of products, although UV-Vis and EPR spectroscopy can also be used but are not trivial. DFT calculation is very useful to simulate vibration spectra and analyze electronic states of products generated in a crystal. X-ray analysis reveals only a molecular structure but not the nature of molecules such as their electronic states. Theoretical calculations also can provide an energy diagram which is helpful for rationalization of reaction pathways and in-depth understanding of crystalline state reactions.

The next section will summarize the methodology of in situ crystal structure analysis.

10.12.4 Crystal design for in situ observation of unstable species by X-rays

In situ study of unstable species by X-rays has developed via three steps as shown in Fig. 2: Step I is the use of a crystal packing of target precursors (crystal packing approach); Step II is the use of a hollow void in a molecular cage compound (Prison Cell approach); Step III is the use of a confined space in a porous coordination network (crystalline molecular flask, crystalline sponge).[16b]

The crystal packing method in Step I is the most basic conventional method and uses a space bounded by nearest neighbor molecules. Crystal packing is formed by intermolecular interactions between precursor molecules. Many of solid-state reactions in Step I follow Schmidt's topochemical postulate which states that "reaction in the solid state occurs with a minimum amount of atomic or molecular movement".[17] In general, if a reaction cavity[5,18] around the reaction center is large enough to allow molecules to move around in the cavity, a reaction can occur. If not, a reaction can be suppressed, or a product can immediately return to the initial structure via recombination or annihilation. The advantage of the crystal packing approach can be applied to various photo-responsive crystalline materials. So long as a crystal of photo-responsive molecules is available, we can perform in situ study by X-ray diffraction. However, the disadvantage is that the conversion rate of photoproducts usually needs to be kept below 20% because the crystals degrade as the photoproduct conversion rate increases. The partial conversion also means that the photo-excited crystal always shows a disordered structure of the initial and photoproduct molecules. The severely disordered structure makes it more difficult to refine structural parameters and very often requires the use of restraints. One fatal problem is that target molecules are limited in crystalline materials. Molecules that do not form a crystal cannot be studied by the crystal packing approach.

In order to overcome those difficulties, the Prison Cell approach is proposed (Step II). The approach uses a hollow void of a discrete cage compound which can readily crystallize. If a target molecule can be encapsulated in a cage in a solution state, a cage compound encapsulating the target molecule can crystallize and the crystal structure can be determined by X-ray diffraction. Even if a target molecule itself never crystallizes, this method enables to determine the molecular structure of the target molecule as a guest in the cage. Furthermore, the target molecules can be sufficiently converted to photoproducts upon excitation without degrading the crystals. However, one of the disadvantages is that a crystal of a cage compound encapsulating guest is sometime fragile against photolysis because of the nature of a molecular crystal made up of discrete cage molecules.

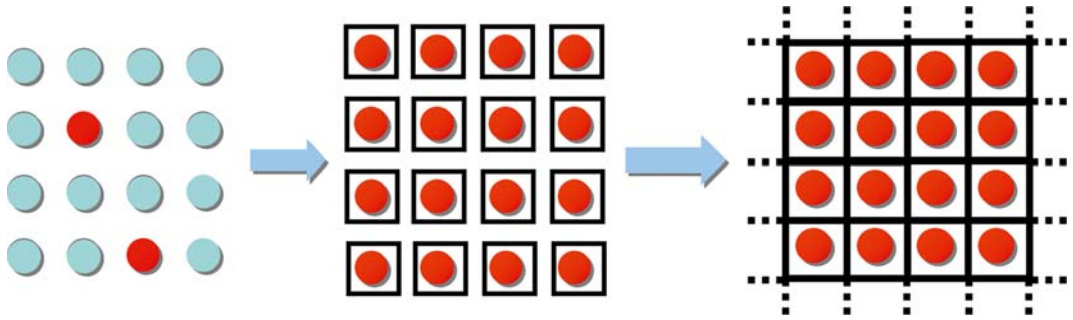

Fig. 2 Strategy for in situ crystallography. Modified from *Chem. Soc. Jpn.* Figure 2, *Bull. Chem. Soc. Jpn.* **87**, 577–592.

Then, to overcome the fragility of a molecular crystal, a crystalline molecular flask approach using a porous coordination network was proposed, now called the crystalline sponge method[19,20] (Step III). A single crystal of a porous coordination network can be more robust than that of a discrete cage molecule because of the infinite framework connectivity. Channels in porous coordination networks can be used as nanometer sized molecular flasks. A single crystal of a porous coordination network can be assumed as an aggregate of numerous nanometer sized flasks (crystalline molecular flask). In Step II, a homogeneous solution state is used for guest encapsulation, whereas in Step III, a heterogeneous state of single crystal and guest solution is used for guest encapsulation. The crystalline molecular flask method allows in situ observation of chemical reactions in single crystals as well as photoreactions because reagents can be easily introduced into the pores as guests. The solution-like environment of a pore and a flexible as well as robust framework play an important role in allowing reactions to occur smoothly in the pore without degrading the crystal. The method is characterized by its high designability of the porous coordination network, which makes it much more versatile in in situ observation than other methods. Each process is described in detail below.

10.12.5 Crystal packing approach

The first successful example of an in situ crystallographic study of unstable species is the determination of the photo-induced metastable states of sodium nitroprusside (SNP). The photo-excited states of a SNP crystal raised considerable attention because of the unique physical properties.[21–24] The history of the SNP study symbolizes the difficulty of direct observation of in situ generated unisolable species. In 1991, Rüdlinger et al. reported using neutron diffraction that the photo-induced metastable species of SNP (MS1) has slightly bent Fe-NO geometry.[25] In 1994, Pressprich et al. also concluded the same geometry for the metastable species by the charge-density method.[26,27] However, this slightly bent geometry of Fe—NO was controversial. In 1997, Carducci and Pressprich et al. reached the correct conclusion that the photo-induced metastable state is a linkage isomer with a Fe—ON coordination mode.[28] The key to success in obtaining the correct structure was the determination of the intermediate state (MS2), which is a side-on mode, as shown in Fig. 3. Finally, the Fe—ON model could explain all experimental results reasonably. The metastable SNP study clearly demonstrates the importance of direct observation of dynamic events and that in situ study of unstable species requires cooperation of crystallography, spectroscopy, and theoretical calculation. The photo-excited state study of SNP initiated many in situ studies of photo-induced linkage isomerization of various transition complexes including a family of SO_2 (Fig. 4) and NO_2 transition metal-based complexes.[29–31]

Another pioneering work on in situ crystallography is the study of a photo-excited triplet state of $[Pt_2(pop)_4]^{4-}$ (Pt-pop; pop = pyrophosphate, $(H_2P_2O_5)^{2-}$) shown in Fig. 5. This system is an important example in that, although it was characterized by several groups using different techniques, e.g. EXAFS, time-resolved X-ray diffraction, and photo-stationary X-ray diffraction methods, eventually they reached similar results. Initially, the triplet state of Pt-pop had been investigated by spectroscopic techniques: Gray et al. reported that a Pt-Pt bond distance in the photo-excited triplet state contracts by 0.21 Å from that of the ground state in the single crystal state.[32,33] In 1993, Thiel et al. reported 0.52 ± 0.13 Å contraction in the Pt-Pt distance in a liquid phase by EXAFS.[33] Other diffraction studies reached basically similar results indicating the contraction of Pt-Pt distance in the excited state. In 1980, X-ray diffraction studies of a ground state $K_4[Pt_2(pop)_4]$ crystal were first carried out by Sadler et al., who found the Pt—Pt distance to be 2.925 Å.[34] In 2002, Coppens et al. reported for tetraethylammonium salt of 2.913 Å shortening in the excited triplet state by using the time-resolved pump-probe X-ray diffraction method and density functional theory.[35,36] In 2002 and 2003, Ozawa, Toriumi, and Ohashi reported 2.942—2.973 Å shortening (for several organic counter ions) by using photo-stationary diffraction methods.[37,38] Even though their data collection strategies are different, they all identified a similar photo-excited triplet state structure.

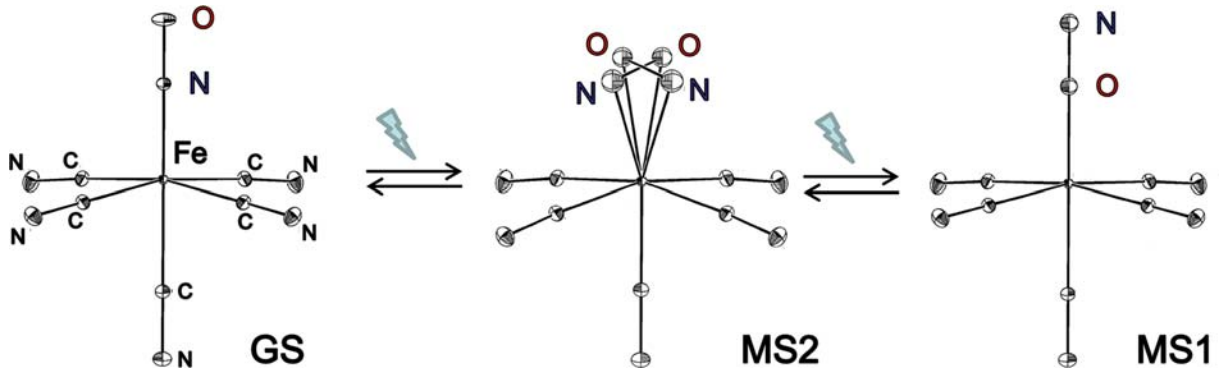

Fig. 3 Crystalline state photochemical linkage isomerization of SNP. Reprinted with permission from Kawano M. X-ray Direct Observation of Reactions and Labile Species on the Basis of Crystal Design. *Bull. Chem. Soc. Jpn.* 2014, **87**, 577–592. Copyright 2014 The Chemical Society of Japan.

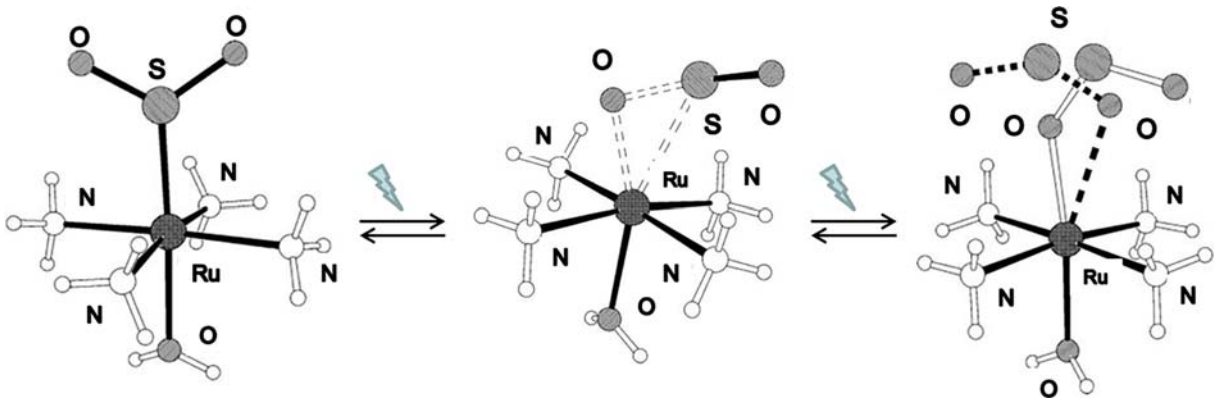

Fig. 4 Crystalline state photochemical linkage isomerization of SO_2 in a Ru complex. Reprinted with permission from Kawano M. X-ray Direct Observation of Reactions and Labile Species on the Basis of Crystal Design. *Bull. Chem. Soc. Jpn.* 2014, **87**, 577–593. Copyright 2014 The Chemical Society of Japan.

The next step of in situ crystallography was the observation of highly reactive species generated in a crystal. Since the late of 1990s, Kawano et al have studied highly reactive species formed in a crystal, e.g. open shell species including radicals, carbenes, and nitrenes, which are highly reactive and short-life intermediates in organic syntheses. They rarely crystallize under ambient conditions. Therefore, first, a crystal of a precursor of a target molecule should be prepared. Photolysis of the precursor crystal generates reactive species in a crystal. Most photo-chemical reactions are irreversible, that means that the time-resolved pump-probe method cannot be used. The only way to achieve direct observation of highly reactive species is by cryotrapping, which freezes reactive species and prevents successive reactions. In order to maintain crystallinity, as a rule of thumb, the conversion rate should be suppressed below 20%. Here are some examples.

10.12.5.1 Direct observation of photo-induced radicals

Radicals are representative open-shell reactive intermediates in chemical reactions and biological systems. Although many radicals have been studied by various spectroscopic techniques, a crystallographic approach is relatively rare in the study of unstable reactive radicals compared to stable radicals that can be crystallized. Kawano et al. reported the first crystallographic investigation of an unstable reactive radical pair (RP) generated in situ- in a crystal of 2,2′-di(orthochlorophenyl)-4,4′,5,5′-tetraphenyl biimidazole (*o*-Cl-HABI) as shown in Fig. 6[39,40] HABI derivatives have been used in industry as photo/thermochromic compounds and also polymerization photoinitiators in imaging materials and holographic photopolymers.[41] In general, it is difficult to observe a reactive intermediate generated in a single crystal of a small molecule by X-ray diffraction, because of difficulty in retaining crystallinity, the short lifetime of the species, retardation of the sample, and so on. However, it was possible to observe in situ generated planar radical pairs in a crystal at 103 K in 10% conversion ratio, when a color change is observed, that are in a thermally excited triplet state and recombine readily upon heating.[42–44] The crystalline state photo-chromic reaction is completely reversible unlike the solution state reaction that form several isomers. When a crystal of *o*-Cl-HABI is irradiated at room temperature, no color change occurs because the radical recombination process is very rapid at room temperature. The crystallographic analysis result of the RP also supports the mechanism in that the interatomic distance (3.1 Å) between C and N atoms corresponding to the photo-cleaved

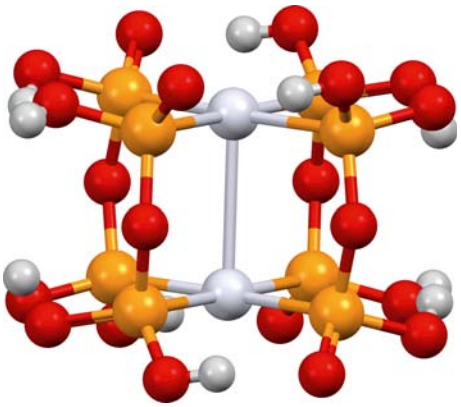

Fig. 5 Molecular structure of $[Pt_2(pop)_4]^{4-}$. Reprinted with permission from Kawano M. X-ray Direct Observation of Reactions and Labile Species on the Basis of Crystal Design. *Bull. Chem. Soc. Jpn.* 2014, **87**, 577–594. Copyright 2014 The Chemical Society of Japan.

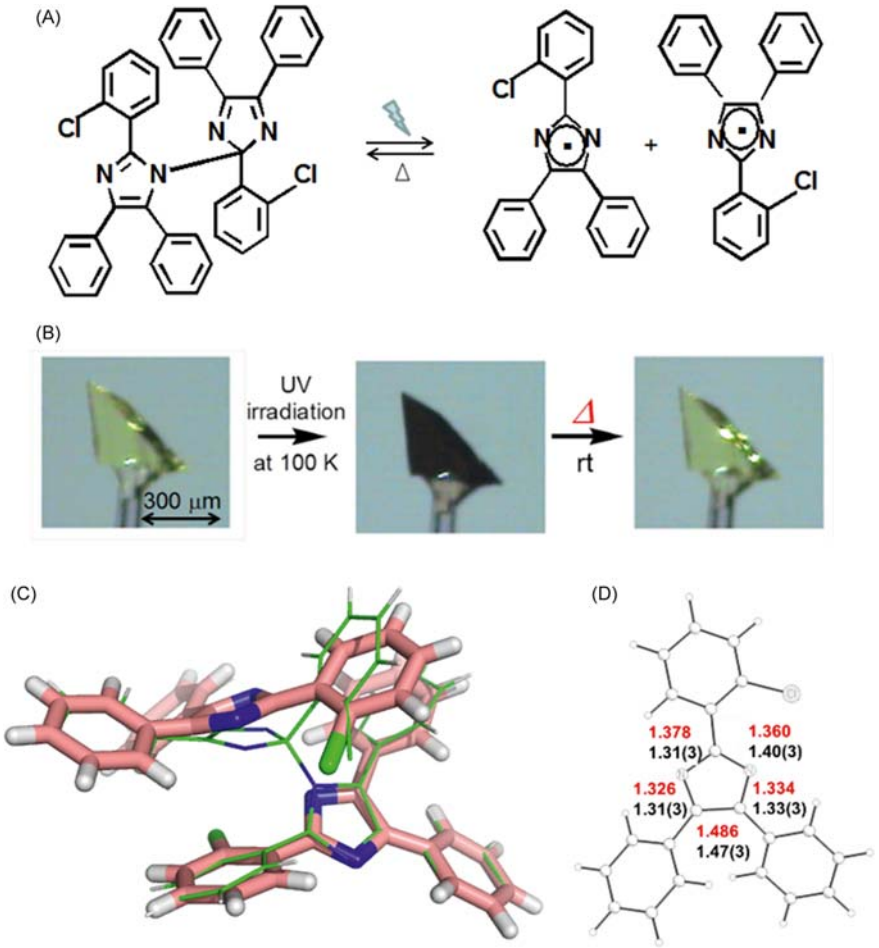

Fig. 6 Crystalline state photoreaction of *o*-Cl-HABI. (a) photoreaction scheme. (b) color changes of a single crystal on photo-irradiation at 100 K and thermal deactivation. (c) a disordered molecular structure of *o*-Cl-HABI after photo-irradiation; stick model, photoproduct, radical; line model, the initial structure. (d) bond distance comparison between DFT calculation (B3LYP/6-31G*) and X-ray analysis. Reprinted with permission from Kawano M. X-ray Direct Observation of Reactions and Labile Species on the Basis of Crystal Design. *Bull. Chem. Soc. Jpn.* 2014, **87**, 577–595. Copyright 2014 The Chemical Society of Japan.

C—N bond is quite short. CW-ESR measurements on both a powder sample and a single crystal of *o*-Cl-HABI indicated a triplet-state signal of RP and a very weak doublet derived from a trace of a free radical at 77 K and disappearance of the signal above 183 K due to the loss of the radicals by recombination. The distance between spins on RP estimated from ESR is ca. 6.2 Å, which corresponds to the distance between imidazolyl carbon atoms on RP in the crystal structure. The DFT calculation predicted that spin is highly populated at the carbon atoms of the imidazolyl ring. The molecular structure of radical calculated by DFT calculations also shows reasonable agreements with the X-ray structure of the imidazolyl ring well-separated from the initial molecule. Therefore, the structural information obtained by in situ X-ray analysis is consistent with spectroscopic data as well as theoretical calculations.

o-Cl-HABI is one of the most efficient polymerization photoinitiators among various HABI derivatives. In order to study their reactivity difference, pristine HABI crystals were investigated by in situ X-ray crystallography.[44] Photolysis of a HABI crystal shows crystalline state reactions different from that of *o*-Cl-HABI as shown in **Fig. 7**. The photolysis on a HABI crystal first produced radical pairs as expected. However, successive dimerization between radicals occurred so that 2,2′-dimer sandwiched by two radicals were produced. In situ X-ray crystallography, IR spectroscopy, and theoretical calculation revealed that 2,2′-dimer is an unstable piezochromic dimer. Although the existence of a HABI-derived piezochromic dimer was known, the molecular structure was unknown due to the difficulty of growing single crystals.[45] The 2,2′-dimer has an inversion center in the molecule, in which two imidazolyl rings are connected via a C—C bond. Therefore, the 2,2′-dimer is not photochromic but indeed piezochromic. Therefore, the formation of 2,2′-dimers during photolysis of HABI derivatives reduces their efficiency as polymerization photoinitiators. In situ X-ray analysis and IR spectroscopy combined with theoretical calculation can explain the reactivity difference of HABI derivatives as polymerization photo initiators.

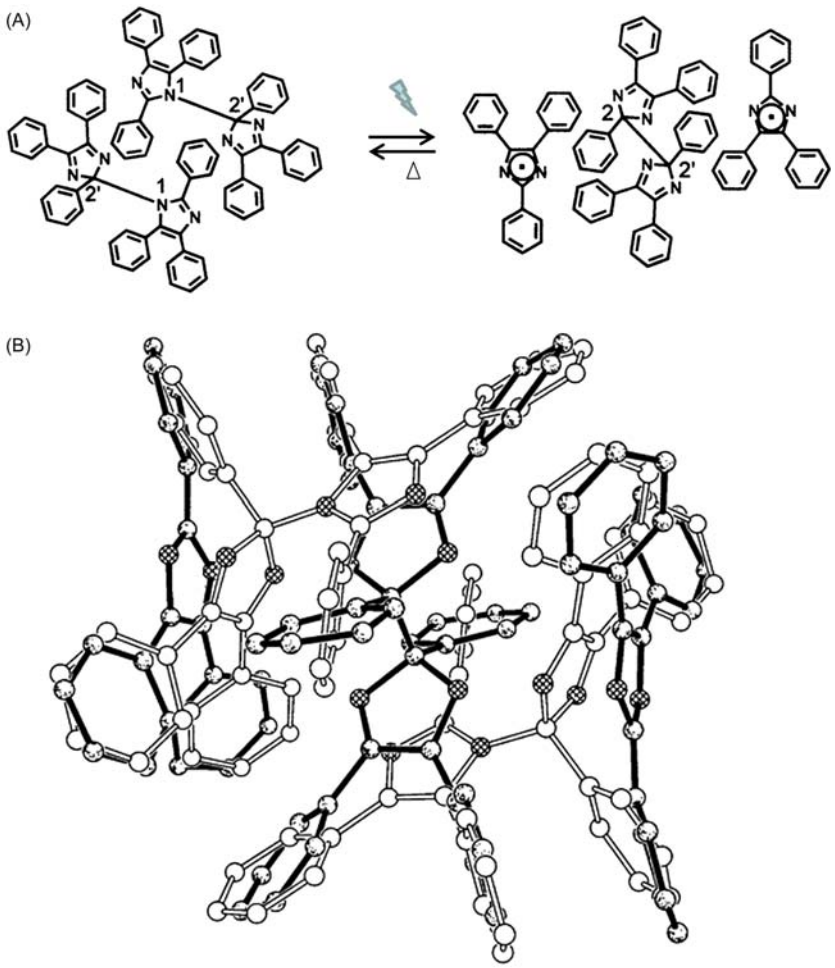

Fig. 7 Crystalline state photoreaction of HABI. (a) photoreaction scheme. (b) a disordered molecular structure of HABI after photo-irradiation: solid line, photoproducts; open line, the initial structure. Reprinted with permission from Kawano M. X-ray Direct Observation of Reactions and Labile Species on the Basis of Crystal Design. *Bull. Chem. Soc. Jpn.* 2014, **87**, 577–596. Copyright 2014 The Chemical Society of Japan.

10.12.5.2 Direct observation of photo-induced triplet carbene

Carbenes are neutral, divalent derivatives of carbon. The carbene atom has two electrons not involved in bonding which can be spin-paired (singlet state) or unpaired (triplet state). Thus, the species offers many unique challenging issues due to the labile electronic state[46–49] so that a number of spectroscopic[50–53] as well as theoretical studies[54] have been reported. However, there was no crystallographic structure for the reactive carbene because it is unstable and difficult to crystallize. Kawano et al. for the first time revealed triplet carbenes generated from diazomethane derivatives by in situ X-ray crystallography.[55] Photolysis of diazomethane derivatives produces carbenes and dinitrogen molecules by cleavage of C—N_2 bond. A key to maintaining crystallinity is keeping the conversion rate lower than 20% and preventing the dinitrogen molecules from escaping from the crystal at as low as liquid nitrogen temperature where liquid nitrogen should not cover a crystal because liquid nitrogen significantly increases the background of X-ray diffraction. Fig. 8a shows a difference electron density map before and after photo-irradiation on a crystal of bis(2,4,6-trichlorophenyl)diazomethane at 80 K where a solid line indicates a new peak, a dotted line a disappearing peak. On the basis of the difference electron density map it is possible to model a divalent molecule and a free dinitrogen molecule trapped in the crystal. Because of the relatively high temperature of 80 K, the dinitrogen molecule is moving around thermally in the reaction cavity. The atomic displacement factors of the dinitrogen molecule correspond to the shape of the reaction cavity around the diazo group of the initial molecule, which is reasonable (Fig. 8b). In order to investigate the electronic state of the carbene, an IR spectrum of bis(2,4,6-trichlorophenyl)diazomethane in a KBr matrix after 365 nm irradiation was measured at 80 K (Fig. 8c), which agrees with a simulated spectrum for a triplet carbene by the DFT calculation. In addition, the energy calculation indicates that a triplet carbene is more stable than a singlet one. Finally, Kawano et al. could confirm that the photoproduct in situ generated in the crystal of bis(2,4,6-trichlorophenyl)diazomethane is a triplet carbene. Kawano et al. subsequently succeeded in determining several crystal structures of triplet carbenes in situ generated from diazomethane derivatives.[56]

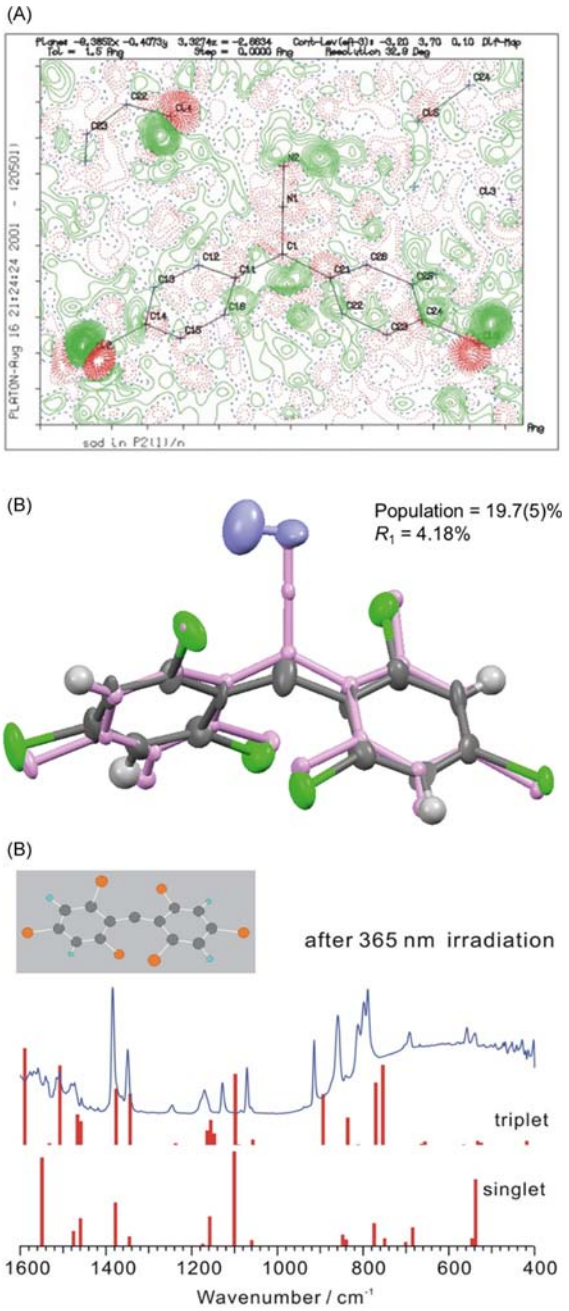

Fig. 8 Crystalline state in situ study of triplet carbene. (a) difference electron density map between before and after photo-irradiation: solid line, positive peaks; dotted line, negative peaks. (b) a disordered structure of a dinitrogen molecule, a triplet carbene (C, grey; Cl, green; H, light grey; N, blue) and the initial diazomethane (pink). (c) IR spectrum of diazomethane after photo-irradiation and simulated spectra for triplet and singlet states by the DFT calculation. Reprinted with permission from Kawano M. X-ray Direct Observation of Reactions and Labile Species on the Basis of Crystal Design. *Bull. Chem. Soc. Jpn.* 2014, **87**, 577–597. Copyright 2014 The Chemical Society of Japan.

10.12.5.3 Direct observation of photo-induced triplet nitrene

Triplet nitrenes are key intermediates in the photochemical reactions of phenylazide derivatives.[57–60] Because of the highly unstable nature of photoinduced nitrenes, many spectroscopic studies have been completed, but no crystallographic studies were carried out until 2003. Kawano et al. attempted to investigate triplet nitrenes photochemically in situ generated in 2-nitrophenylazide crystals.[61] Difference electron density maps of the azide crystal before and after photo-irradiation clearly show the crystalline state photoreaction. The X-ray analysis based on the electron density map revealed that the photoproduct is not a triplet nitrene but a benzofuroxan having a five-membered hetero-ring (Fig. 9). Although photolysis of the azide crystal generated a triplet nitrene as an

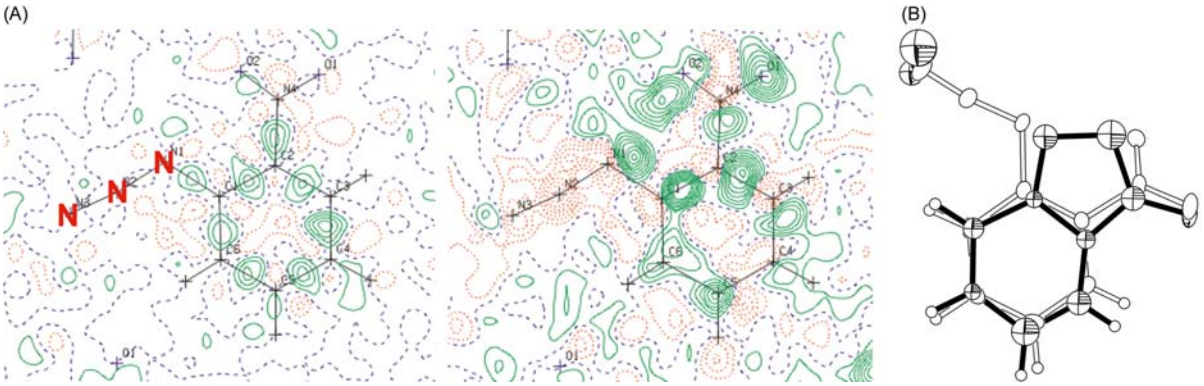

Fig. 9 Crystalline state in situ study of 2-nitrophenylazide. (a) difference electron density maps before (left) and after photo-irradiation (right): solid line, positive peaks; dotted line, negative peaks. (b) a disordered structure of a dinitrogen molecule, a benzofuroxan (solid line) and the initial azide (open line). Reprinted with permission from Kawano M. X-ray Direct Observation of Reactions and Labile Species on the Basis of Crystal Design. *Bull. Chem. Soc. Jpn.* 2014, **87**, 577–598. Copyright 2014 The Chemical Society of Japan.

intermediate species and a dinitrogen molecule, it smoothly reacted further to form a five-membered ring because of the short interatomic distance between a nitrate oxygen atom and a nitrene nitrogen atom.

Several phenylazide derivative crystals deteriorated on photo-irradiation (Fig. 10). In those cases, the reaction cavity volumes are too small to maintain crystallinity.[2,62] Molecular packing with larger reaction cavities through salt formation can overcome these situations; *m*-carboxylic phenyl azide formed a salt with dibenzylamine in a 1:1 ratio, successfully expanding the reaction cavity (2.2 $Å^3$) around the azide group (Fig. 11). As expected, the salt crystal showed single-crystal-to-single-crystal photoreaction to generate nitrenes, although the crystal of *m*-carboxylic phenyl azide itself (reaction cavity, 1.6 $Å^3$) was easily destroyed upon irradiation.[63] The triplet spin state was confirmed by IR spectroscopy combined with DFT theoretical calculations. When X-ray data were collected at 80 K, a free dinitrogen molecule could not be observed because of the severe thermal motion in the large reaction cavity. Therefore, the crystal structure analysis before and after photo-irradiation were performed at 25 K using the Toriumi X-ray vacuum camera set up at the BL02B1 station of SPring-8 (Fig. 12). In the difference Fourier map, a nitrene and a released dinitrogen molecule were clearly observed thanks to the high-resolution data without any background from air scattering and indeed the refinement converged well without any restraint for a nitrene molecule, although the occupancy factor of nitrene was only 7.5%.

Fig. 13 shows the bond lengths of triplet nitrene obtained by X-ray analysis at 25K and from theoretical calculations. There are several discrepancies between X-ray and UB3LYP/6-31G* results (red letters) for the triplet nitrene. The salient disagreements are found in the bond lengths around the C1R atom. To take into account the electronic correlation more precisely, the triplet nitrene structure was optimized at the CASSCF(6,6)/6-31G* level of theory. The CASSCF result (blue lettering) shows considerably better agreement with that obtained by X-rays (black lettering). The X-ray result was the first experimental one suggesting that the electronic correlation should be taken into consideration even in the ground state when the optimization of open-shell species such as a nitrene is performed.

10.12.5.4 Reaction intermediates for catalytic reactions

Reaction intermediates in catalytic reactions were observed by Powers et al especially for C–H functionalization.[64] Metal nitrides are one of the key intermediate species for C–H amination or olefin aziridination reactions. Powers et al determined the crystal

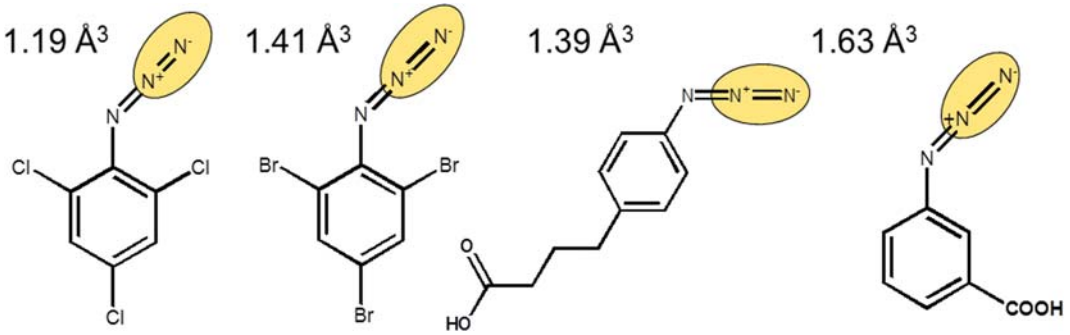

Fig. 10 Unsuccessful cases for crystalline-state in situ study of phenyl azide derivatives. Reprinted with permission from Kawano M. X-ray Direct Observation of Reactions and Labile Species on the Basis of Crystal Design. *Bull. Chem. Soc. Jpn.* 2014, **87**, 577–599. Copyright 2014 The Chemical Society of Japan.

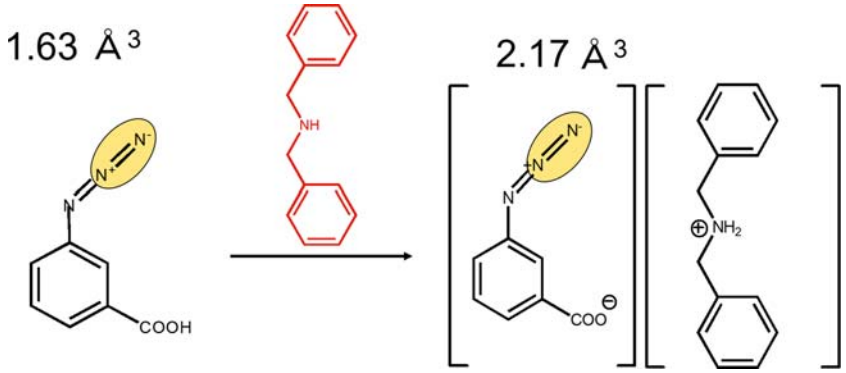

Fig. 11 Strategy for expansion of a reaction cavity around N_2. Reprinted with permission from Kawano M. X-ray Direct Observation of Reactions and Labile Species on the Basis of Crystal Design. *Bull. Chem. Soc. Jpn.* 2014, **87**, 577–600. Copyright 2014 The Chemical Society of Japan.

structure of Ru_2 nitrides by irradiating Ru_2-N_3 crystals.[65] When irradiated with 365 nm LED light, the azide groups in Ru_2-N_3 first linearize, followed by the formation of Ru_2 nitride (Fig. 14). Furthermore, they observed metal nitrenoid intermediate species using Rh_2 nitrenoid generated from Rh_2 alkylazide complexes by N_2 elimination.[66,67] In this research, reactive Rh_2 nitrenoids in the triplet state were directly observed by irradiating $Rh_2(esp)_2(AdN_3)_2$ with 365 nm light (Fig. 15).

10.12.6 Prison cell approach

The crystal packing approach has been successful for determination of unstable species as described above. However, it has a fatal limitation: it requires a crystal of a target molecule. If a target molecule does not crystallize, this approach cannot be used. The Prison Cell approach was proposed to overcome this drawback: a discrete cage compound, M_6L_4 ($M = Pd^{2+}$(diamino ligand); L = 2,4,6-tris(4-pyridyl)triazine, so-called TPT; Fig. 16)[68] was used as a Prison Cell, because M_6L_4 is highly soluble in water and can readily encapsulate various organic molecules in water and form a single crystal.[69] The solubility of M_6L_4 in water also can be adjusted by changing a protecting group on the metal center.

10.12.6.1 Direct observation of a photo-induced coordinatively unsaturated transition-metal complex in a M_6L_4 cage

Coordinatively unsaturated transition metals exist as key intermediates of a variety of organometallic reactions that are frequently involved in the catalytic cycles of organic transformations.[70,71] The direct observation of these reactive intermediates is particularly important for having the mechanistic insights of organometallic/organic reactions. To date, reactive intermediates have been investigated only by spectroscopic methods such as inert matrix isolation techniques and time-resolved IR spectroscopy, but rarely by crystallography because of their labile nature. Kawano and Fujita et al. succeeded in the in situ crystallographic observation of a coordinatively unsaturated manganese complex within a self-assembled coordination cage, M_6L_4.[72] Within the cavity of the cage, stable $Cp'Mn(CO)_3$ (Cp′ = methylcyclopentadienyl) liberates CO via photodissociation in the crystalline state and in situ generated

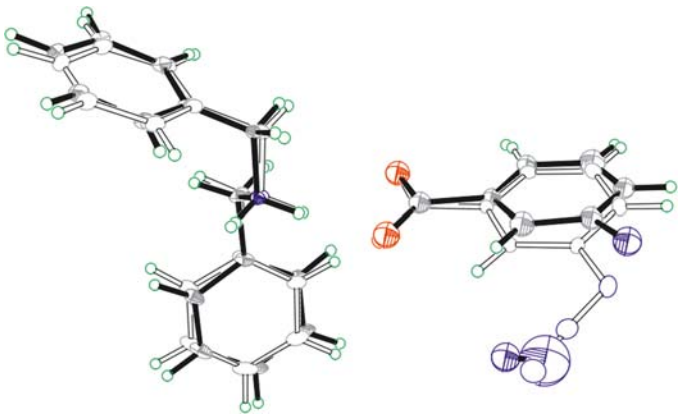

Fig. 12 Disordered structure of photoproducts including a dinitrogen molecule and a triplet nitrene (solid line) and the initial azide (open line). Reprinted with permission from Kawano M. X-ray Direct Observation of Reactions and Labile Species on the Basis of Crystal Design. *Bull. Chem. Soc. Jpn.* 2014, **87**, 577–601. Copyright 2014 The Chemical Society of Japan.

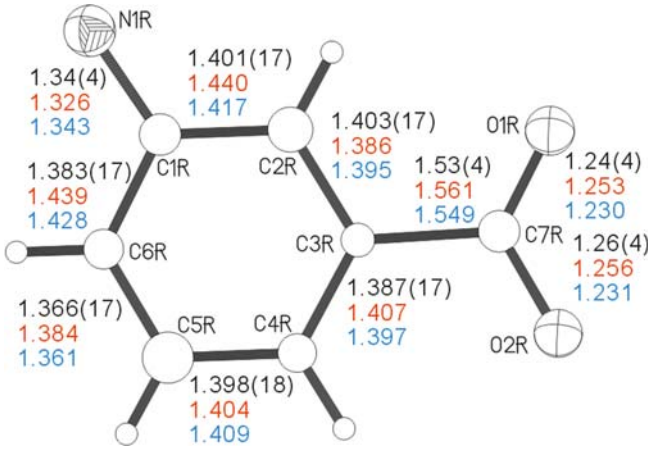

Fig. 13 Bond lengths (Å) of nitrene obtained by X-ray analysis at 25K and theoretical calculations: black with esd, X-ray; red, DFT UB3LYP/6-31G*; blue, CASSCF(6,6)/6-31G*. Reprinted with permission from Kawano M. X-ray Direct Observation of Reactions and Labile Species on the Basis of Crystal Design. *Bull. Chem. Soc. Jpn.* 2014, **87**, 577–602. Copyright 2014 The Chemical Society of Japan.

$Cp'Mn(CO)_2$ was directly observed by X-ray diffraction (Fig. 17). The crystallographic analysis clearly revealed that the 16-electron unsaturated manganese complex adopts a pyramidal rather than planer geometry. Another interesting observation is that, after CO cleavage on photolysis, one Cp′ ring rotates to a less bulky space to avoid steric repulsion. Only in situ X-ray analysis can provide three-dimensional information about this kind of structural changes on photo-irradiation.

It is noteworthy that the crystalline state reactivity of the Mn complex encapsulated in the M_6L_4 is totally different from that of Cp′Mn complex itself. In general, photolysis of the Cp′Mn complex in solution produces various photoproducts. However, only one among four Cp′Mn complexes encapsulated in M_6L_4 showed a Mn-CO bond cleavage reaction on photo-irradiation. Because a void in M_6L_4 can accommodate only one free CO, other CO ligands are no longer allowed to dissociate (or immediately recombined with the Mn center even if dissociated). Thus, only one CO ligand selectively dissociates. Indeed, in the case of $CpMn(CO)_3$ that has no methyl group on the ring and can be tightly packed in the cavity of M_6L_4, no photoreaction is observed in the crystalline state. These facts indicate that, depending on how the guest molecules are encapsulated in the cage, we can control the photo reactivity.

Even though $Cp'Mn(CO)_3$ itself is liquid at room temperature, the molecular structure can be determined by X-ray analysis by encapsulation to M_6L_4. This approach can be useful to determine the molecular structures of such liquid samples or non-crystalline materials. Nowadays, this approach has been developed as the crystalline sponge method by Fujita et al.[20,73] Furthermore, a cage

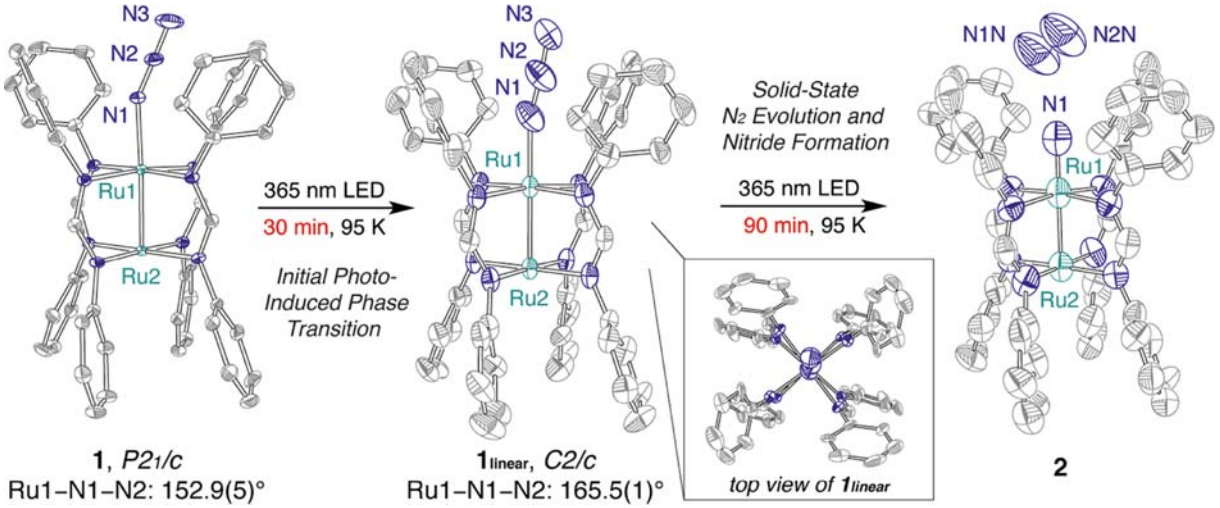

Fig. 14 Photocrystallographic characterization of reactive Ru_2 nitride **2**. Photolysis ($\lambda = 365$ nm) of a single crystal of Ru_2 azide **1** at 95 K results first in a phase transition ($P2_1/c$ to $C2/c$) to generate $\mathbf{1}_{linear}$, which is promoted by photoinduced crystal heating, and subsequently in extrusion of N_2 to generate Ru_2 nitride **2**. Thermal ellipsoids are drawn at 50% probability. H- and Cl-atoms are omitted for clarity. Reprinted with permission from Das A; Reibenspies JH; Chen Y-S; Powers DC. Direct Characterization of a Reactive Lattice-Confined Ru2 Nitride by Photocrystallography. *J. Am. Chem. Soc.* 2017, **139**, 2912–2915. Copyright 2017 American Chemical Society.

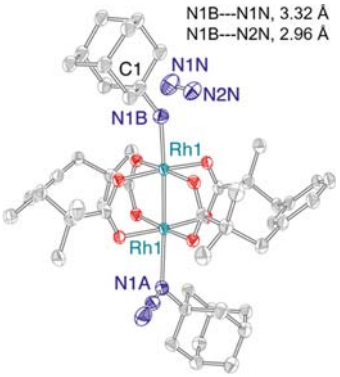

Fig. 15 Molecular structure of reactive Rh_2 nitrenoids in the triplet state directly observed by irradiating $Rh_2(esp)_2(AdN_3)_2$ with 365 nm light. Das A; Chen Y-S; Reibenspies JH; Powers DC. Characterization of a Reactive Rh2 Nitrenoid by Crystalline Matrix Isolation. *J. Am. Chem. Soc.* 2019, **141**, 16232–16236.

complex like M_6L_4 can be designed depending on target molecules, indicating that this Prison Cell approach can be widely applicable to various compounds.

10.12.6.2 Crystalline state solution-state-like reaction—Direct observation of selective photo-dimerization of acenaphthylene in a M_6L_4 cage

The M_6L_4 cage can provide a solution-like environment in a crystal.[74] Photochemical reactions are normally allowed to proceed only if the reaction centers of the substrates are well-arranged in close proximity, typically within 4.2 Å as required by the Schmidt rule.[4] However, the preorganization of the reaction centers is not required if substrates are accommodated in the cavity of a large hollow cage compound because they are allowed to tumble thermally in the cavity even in the solid-state. Therefore, various solid-state photoreactions in the cavity are expected to proceed without preorganization, like a solution-state reaction. In addition, such a solution-like behavior of the substrates can be directly observed by X-ray crystallographic analysis, if the molecular crystal of the rigid cage can remain crystalline during the reaction. To demonstrate this idea, the [2+2] photoaddition of acenaphthylene encapsulated in the M_6L_4 cage was selected as a model reaction. Despite the very unfavorable orientation of the substrates in the cage, the [2+2] photodimerization cleanly proceeds in a single-crystal-to-single-crystal fashion. The photolysis resulted in quantitative syn-dimer formation, although the two guests were disordered and located at three positions (Fig. 18). Photolysis of acenaphthylene without the M_6L_4 cage produces a mixture of syn-dimers and anti-dimers in different ratios depending upon the excitation conditions in either solution or solid.[75] This fact implies that the highly stereoselective photoreaction is due to the cage effect. The reaction

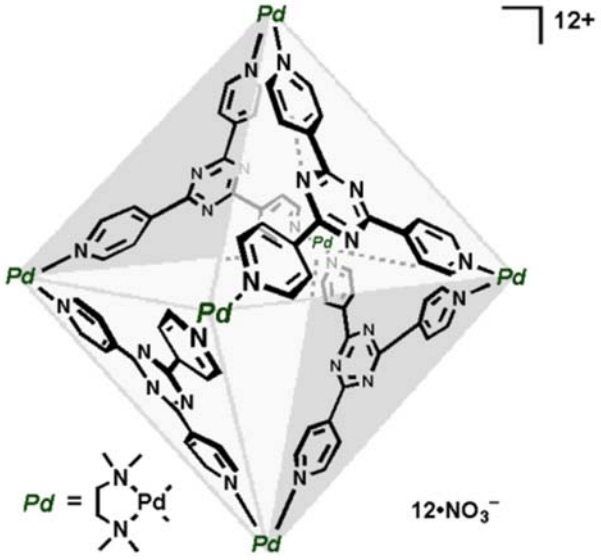

Fig. 16 Discrete cage compound of M_6L_4. Reprinted with permission from Kawano M. X-ray Direct Observation of Reactions and Labile Species on the Basis of Crystal Design. *Bull. Chem. Soc. Jpn.* 2014, **87**, 577–602. Copyright 2014 The Chemical Society of Japan.

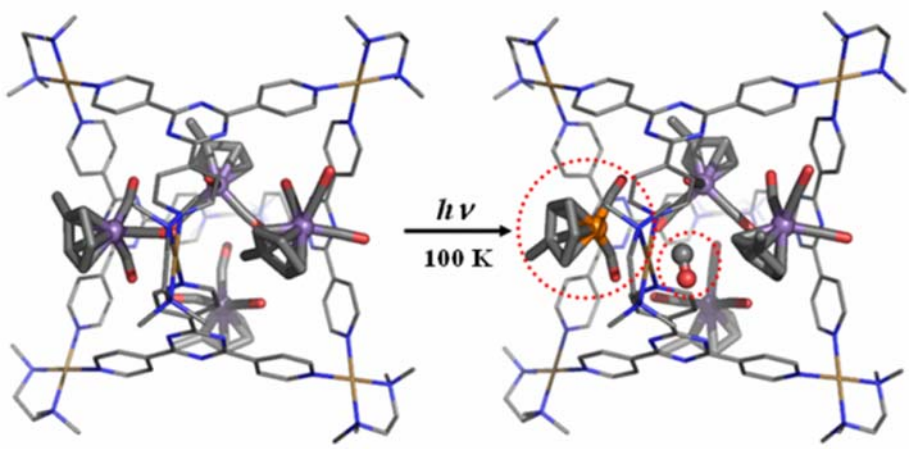

Fig. 17 In situ X-ray observation of the photodissociation reaction of Cp'Mn(CO)$_3$ in a M_6L_4 cage. Reprinted with permission from Kawano M. X-ray Direct Observation of Reactions and Labile Species on the Basis of Crystal Design. *Bull. Chem. Soc. Jpn.* 2014, **87**, 577–603. Copyright 2014 The Chemical Society of Japan.

completely differs from common solid-state photoreactions in that the reaction centers are not preorganized, but the reaction proceeds via thermal tumbling of the substrates.

10.12.7 Step III—Crystalline molecular flask

By using the Prison Cell approach, a 100% conversion reaction was achieved in a single-crystal-to-single-crystal fashion. However, because the M_6L_4 cage is a discrete molecule, the single crystal is a molecular crystal, which sometime is not robust enough for in situ crystallographic study. In order to make the in situ method more general, Kawano et al. proposed the usage of porous coordination networks and derived the concept of "crystalline molecular flask."[19,76] This concept has made it possible to visualize not only photoreactions but also chemical reactions by introducing reagents into the pore through guest exchange.

10.12.7.1 Networking of M_6L_4 and in situ observation of the crystalline state photoreaction

In order to utilize the void of the M_6L_4 cage in the solid state, M_6L_4 was incorporated in coordination network. When a host compound has a highly symmetric structure such as M_6L_4, it is often inevitable to observe disordered guests in the crystal structure. The site disorder problem hampers the accurate structure analysis of guests. Thus, ordering the guest orientation was achieved in a highly symmetrical host via guest networking.[77] When a guest molecule possesses appropriate coordination sites, a guest network can be generated by addition of connector (typically a metal ion) on crystallization, preventing the guest disorder (Fig. 19).

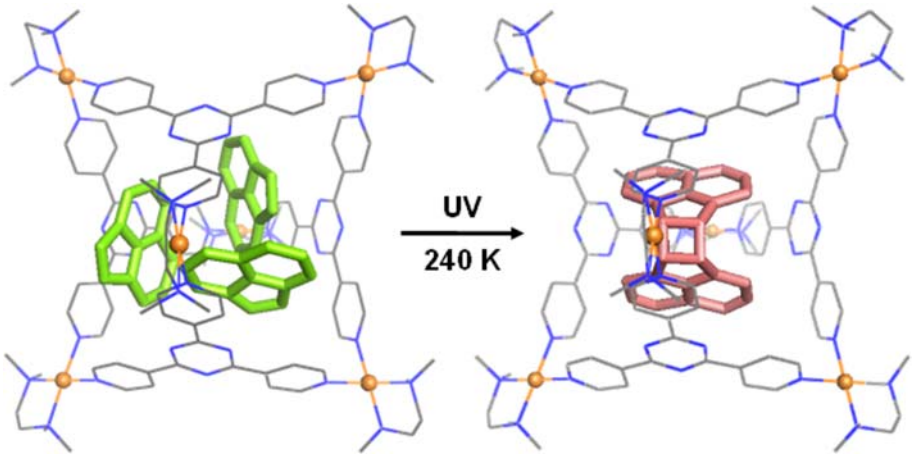

Fig. 18 In situ X-ray observation of [2+2] photoaddition of acenaphthylene encapsulated in the M_6L_4 cage. Two acenaphthylene molecules are disordered at three positions before photo-irradiation. Reprinted with permission from Ref. Kawano M. X-ray Direct Observation of Reactions and Labile Species on the Basis of Crystal Design. *Bull. Chem. Soc. Jpn.* 2014, **87**, 577–604. Copyright 2014 The Chemical Society of Japan.

The M_6L_4 cage has T_d symmetry. The guest disorder problem is often encountered in the crystallographic analysis of its host-guest complexes. To prevent the guest disorder, the guest networking was examined according to the strategy of Fig. 19. TPT was chosen as a coordinative guest on the basis of the knowledge that large planer aromatic compounds such as pyrene and perylene provide crystalline host-guest complexes with M_6L_4.[78] The advantage of TPT as a coordinative guest is that this planar guest efficiently stacks on one of the ligands of M_6L_4, still leaving a void capable of encapsulating the second guest. In this study, $Cp'Mn(CO)_3$ was used as the second guest. The pairwise selective recognition of two guests in the M_6L_4 cage was effectively carried out in an aqueous solution. However, a crystal of the discrete host-guest complex showed a severely disordered structure of guest molecules. Therefore, networking of the host-guest M_6L_4 complex was performed by forming coordination bonds between guest TPTs and Co(II) ions. Using this network, it was possible to obtain network crystals without severely disordered guest (Fig. 20). The crystallographic observation of the second guest, $Cp'Mn(CO)_3$, becomes easier and more accurate by the networking. Accordingly, the solution host-guest chemistry of the highly symmetric cage is easily translated into a solid-state chemistry which can be directly subjected to crystallographic analysis. Because a reaction cavity around the Mn complex in the M_6L_4 cage became larger, it was possible to observe a photochemically generated coordinatively unsaturated species by in situ X-ray crystallography (Fig. 20b).

10.12.7.2 Design of porous coordination networks—Cartridge synthesis

Porous coordination networks or metal-organic frameworks are prominent candidates for direct observation of guests in the pores. The method of direct observation using pores of the network is called the crystalline molecular flask approach. The first example of this method utilizes a biporous coordination network of ZnI_2 self-assembled with TPT and triphenylene, with two kinds of pores, A and B (Fig. 21).[79,80] Triphenylene molecules are alternatively stacked with TPTs via π-π stacking, forming a pillar structure. Even in guest exchange reactions, the non-covalently bound pillar structure remains. Importantly, the C—H groups of triphenylene molecules face the pore and compose part of the pore. This fact was exploited to develop a new pore modification strategy. If it is possible to prepare the same network connectivity using modified triphenylene molecules, a pore can be readily modified by functionalizing the triphenylene through simple organic reactions, just like exchange of cartridge (triphenylene derivative). This strategy is named "cartridge (modular) synthesis."[81] Various biporous networks were prepared by the cartridge method (Fig. 22).

10.12.7.3 Pore modification by cartridge synthesis and single-crystal-to-single-crystal guest exchange

Selective alcohol recognition by modified biporous coordination networks was reported to demonstrate the importance of pore modification.[81] When a triphenylene was used as a cartridge, propane-2-ol was not encapsulated at all. However, the biporous coordination network modified with hydroxyl groups successfully recognized propane-2-ol via hydrogen bond formation between the alcohol and hydroxyl groups (Fig. 23). Interestingly, 1- and 2-hydroxyl triphenylene show remarkably different recognition features for propane-2-ol: 1-hydroxyltriphenylene forms hydrogen bonds with alcohol directly, whereas 2-hydroxyl triphenylene recognizes the alcohol more efficiently due to hydrogen bonds of the water molecule intermediating between the alcohol and the 2-hydroxyltriphenylene (Fig. 24). Pores composed of only hydrogen atoms of triphenylene and TPT always recognize only cyclohexane. These facts indicate that slight modifications of the pore induce remarkably different guest recognition capabilities.

10.12.7.4 Direct observation of chemical reactions in a pore

Attempt to modify the pores using 1-salicylidenetriphenylene as a cartridge failed to produce a biporous network because the cartridge has chelating sites that trap metal ions and is relatively large compared to other cartridge molecules. To overcome this hurdle, application of the cartridge approach, nowadays called the post-synthetic method,[82] was applied: first biporous network crystals using 1-aminotriphenylene cartridge were produced, then, aldehyde reagents were introduced into the pores by guest exchange and quantitative condensation reactions of the amino group with aldehyde with 100% selectivity were performed in the pores at 100 °C in a single-crystal-to-single-crystal manner (Fig. 25). It was suggested that in this cartridge method, even chemical reactions in the pores can be visualized by X-ray diffraction. Prior to this work, most of researchers observed only photochemical reactions by in situ crystallography, because in general crystals are densely packed so that it is extremely difficult to introduce

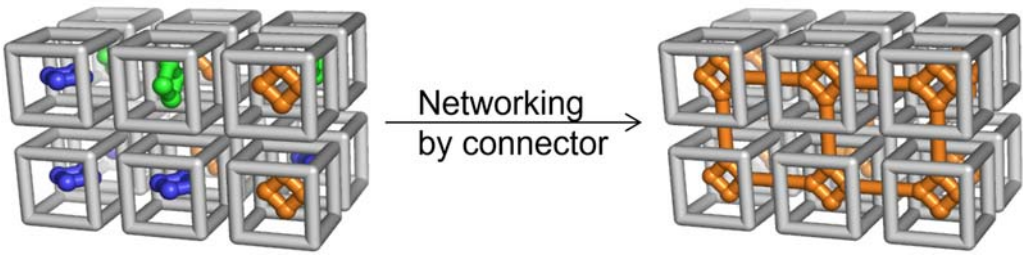

Fig. 19 Networking a hollow cage via guest coordination. Reprinted with permission from Kawano M. X-ray Direct Observation of Reactions and Labile Species on the Basis of Crystal Design. *Bull. Chem. Soc. Jpn.* 2014, **87**, 577–605. Copyright 2014 The Chemical Society of Japan.

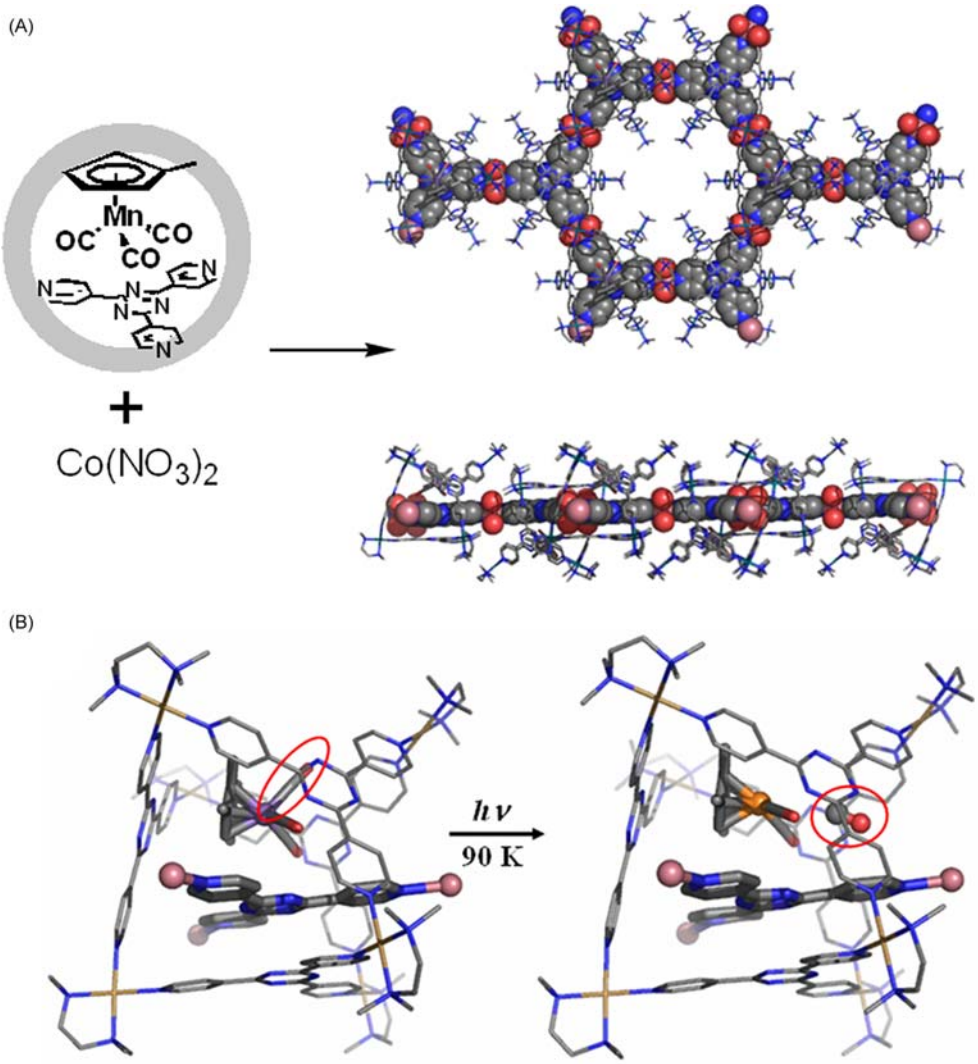

Fig. 20 (a) Networking of host-guest M_6L_4 complexes by forming coordination bonds between guest TPT and Co(II) ion and (b) crystalline state photoreaction of $Cp'Mn(CO)_3$. Reprinted with permission from Kawano M. X-ray Direct Observation of Reactions and Labile Species on the Basis of Crystal Design. *Bull. Chem. Soc. Jpn.* 2014, **87**, 577–606. Copyright 2014 The Chemical Society of Japan.

chemical reagents into the interior of crystals. However, pore channels increase the mobility of guest molecules and facilitate rapid diffusion. Even large organic molecules can be readily introduced into the pores by simple guest exchange.[74,83,84]

Thanks to the network's robust crystallinity, it is possible to perform the acylation and ureidation of aromatic amines, and imine formation from aromatic aldehydes within a single crystal (Fig. 26). The pores of the coordination networks thus act as crystalline molecular flasks. Porous network crystals modified with amines or aldehydes were immersed in reagent solutions to perform condensation reactions, and X-ray diffraction data were collected at low temperatures. Even a carboxyl acid is readily introduced as functional groups into pores, even though it is generally quite difficult to introduce with the conventional self-assembly method because the carboxyl group plays a role as a coordination site. Another important point is that it is possible to modify certain pores of the two types by the substrate (Fig. 26). Only in situ crystallography can prove this selective modification in porous network crystals.

10.12.7.5 Snapshots of transient species in pores

As mentioned above, it is possible to observe various condensation reactions by measuring X-ray diffraction data after chemical reactions. However, as described in organic text books, there are intermediate states during the condensation reactions. Therefore, it is intriguing to take crystallographic snapshots of chemical reactions. In the condensation reaction between amine and aldehyde, hemiaminal species should exist as a short-lived intermediate, followed by a dehydration reaction to form imine (Fig. 27). Kawano

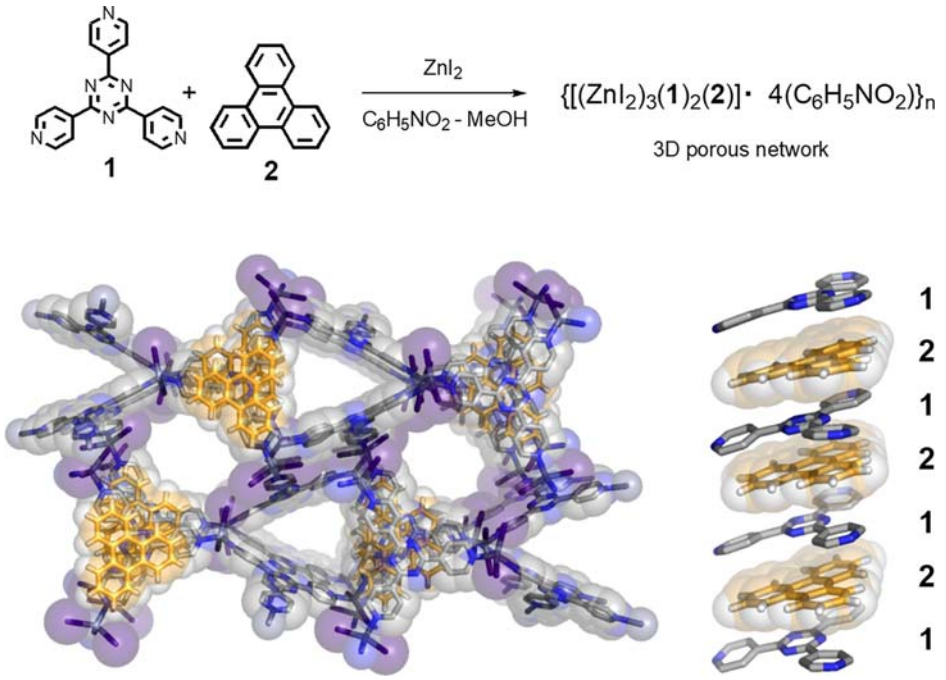

Fig. 21 Biporous network formation. Reprinted with permission from Kawano M. X-ray Direct Observation of Reactions and Labile Species on the Basis of Crystal Design. *Bull. Chem. Soc. Jpn.* 2014, **87**, 577–607. Copyright 2014 The Chemical Society of Japan.

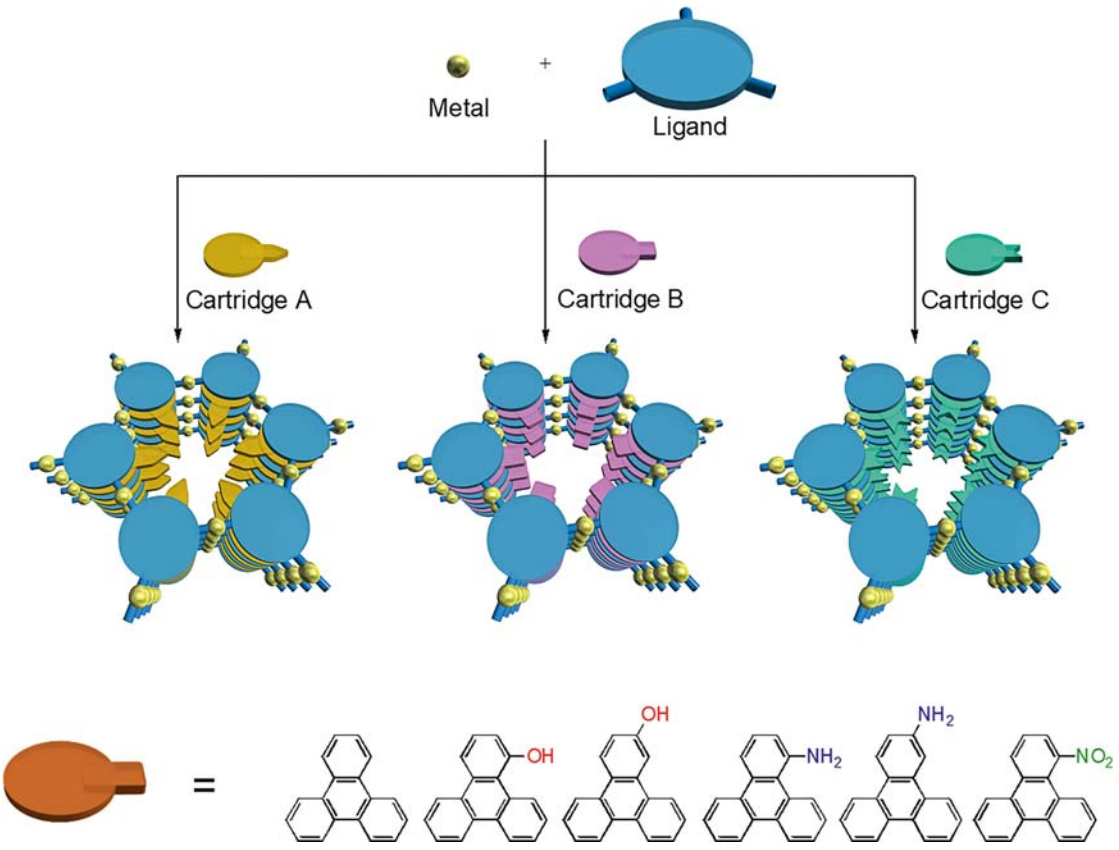

Fig. 22 Cartridge (modular) synthesis. Reprinted with permission from Kawano M. X-ray Direct Observation of Reactions and Labile Species on the Basis of Crystal Design. *Bull. Chem. Soc. Jpn.* 2014, **87**, 577–608. Copyright 2014 The Chemical Society of Japan.

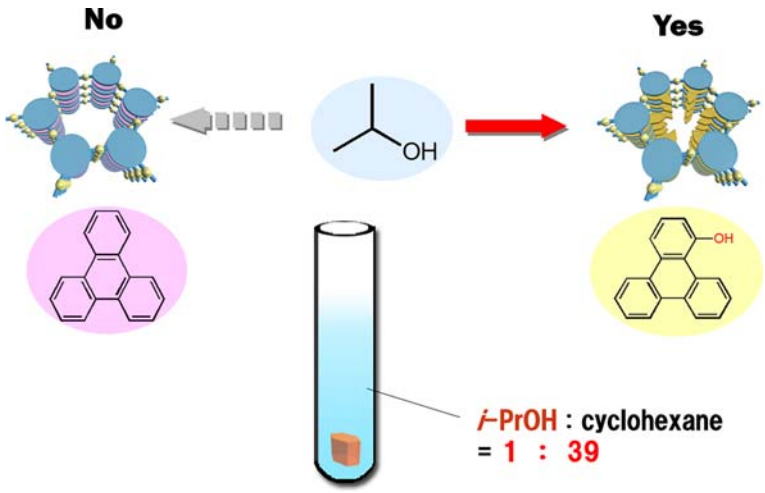

Fig. 23 Pore modification for selective alcohol recognition by cartridge approach. Reprinted with permission from Kawano M. X-ray Direct Observation of Reactions and Labile Species on the Basis of Crystal Design. *Bull. Chem. Soc. Jpn.* 2014, **87**, 577–609. Copyright 2014 The Chemical Society of Japan.

et al. succeeded in taking snapshots of the hemiaminal and the successive imine formation in the pores of the biporous coordination network by in situ X-ray crystallography.[85]

Using the cartridge synthesis method with 1-aminotriphenylene, a single crystal of the biporous coordination network was prepared as a platform of the reaction. The single crystal was mounted on a goniometer and acetaldehyde solution was introduced into the crystal by syringe pump at 215 K for 15 min (Fig. 28). Right after the hemiaminal formation reaction completed, the crystal was rapidly cooled down to 90 K to inhibit subsequent imine formation reactions. After X-ray data collection of hemiaminal species, the crystal temperature was raised to 270 K and held at that temperature for 30 min, which resulted in complete conversion of the hemiaminal to imine. Then, X-ray data were collected again at 90 K.

X-ray analysis of the 215 K reaction data revealed the crystal structure of hemiaminal with 36% yield. It should be noted that because hemiaminal is a chiral molecule, the appropriate model structure was constructed as only a racemic mixture with reasonable thermal ellipsoids. By introducing a racemic model with 18% R- and 18% S-form, all thermal parameters of hemiaminal groups converged to ideal values by full matrix least squares refinement (Fig. 29). It was not possible to obtain a proper model using the homochiral model. Thus, in the case of in situ crystallography, it is not possible to isolate and characterize the product by conventional methods, so the crystal structure must also be confirmed from the chemical perspective. Furthermore, in order to confirm in situ crystallographic results, spectroscopic analysis should be performed in that, as described above, an electron density map does not always provide a clear answer due to disorder and that short-lived reaction products are not isolable. Conventional analytical methods cannot be applied to characterize in situ generated products. Infrared microspectroscopy in transmission mode, rather than reflection mode, is the most powerful way to properly monitor crystalline state reactions. For spectroscopic measurements, crystals of the same size and crystallinity as those used for in situ X-ray observations must be used. Because infrared microspectroscopy requires a very thin crystal to avoid saturation, such a tiny crystal must be used for in situ crystallography as well.

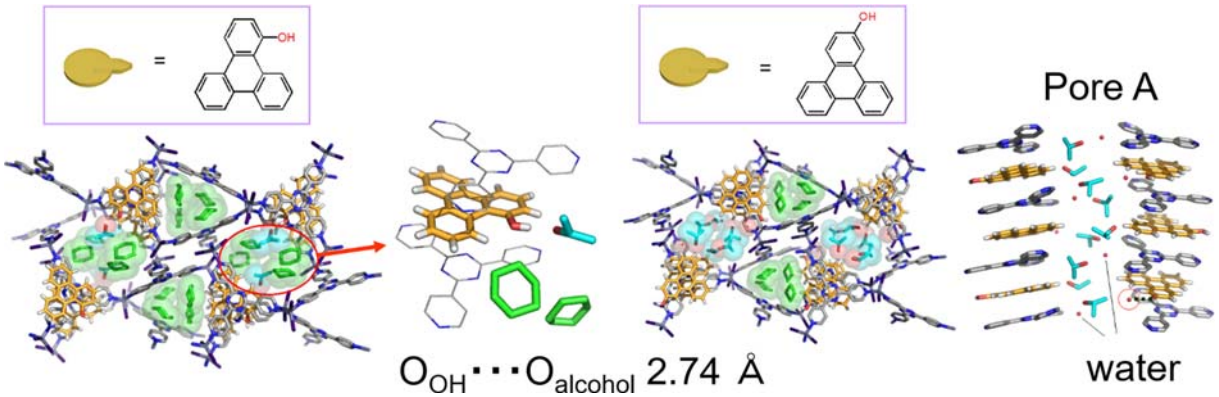

Fig. 24 Sophisticated pore modification for alcohol recognition by cartridge approach. Reprinted with permission from Kawano M. X-ray Direct Observation of Reactions and Labile Species on the Basis of Crystal Design. *Bull. Chem. Soc. Jpn.* 2014, **87**, 577–610. Copyright 2014 The Chemical Society of Japan.

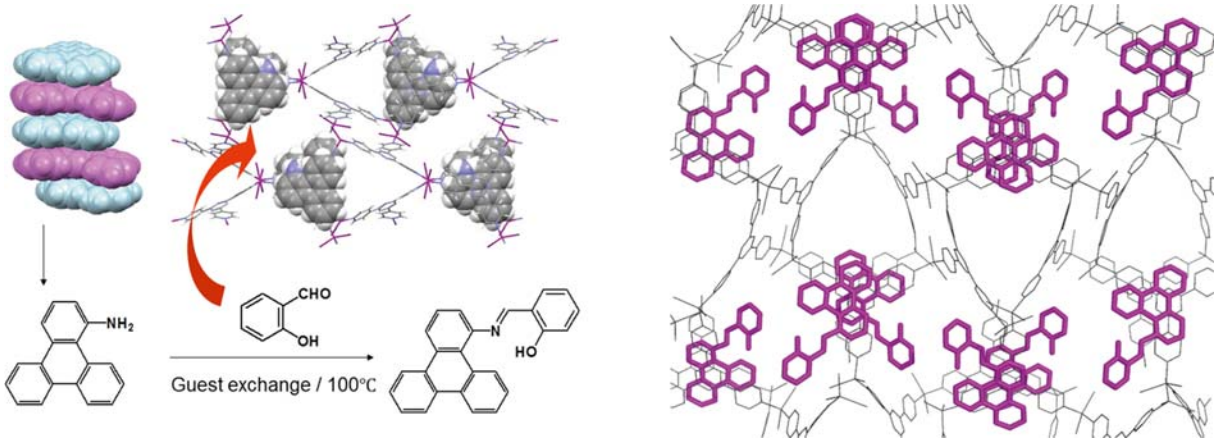

Fig. 25 Post-synthetic modification of a pore by cartridge approach (left) and a crystal structure of the modified porous network (right). Reprinted with permission from Kawano M. X-ray Direct Observation of Reactions and Labile Species on the Basis of Crystal Design. *Bull. Chem. Soc. Jpn.* 2014, **87**, 577–611. Copyright 2014 The Chemical Society of Japan.

Therefore, it is necessary to use high-flux synchrotron X-rays. In order to analyze the IR spectra, it is necessary to simulate the vibrational modes by means of theoretical calculations. In this study, excellent agreement was obtained between the results of the X-ray diffraction experiment and IR spectra (Fig. 30).

10.12.7.6 Unstable sulfur species observed by X-ray diffraction

The approach of observing unstable species or reaction intermediates propels the understanding of elemental allotropes. Elements have many allotropes, including unstable ones. For example, sulfur has the most stable and well-known allotrope S_8, while the unstable small sulfur allotropes, S_n ($n < 6$) that are unstable and cannot be isolated from the allotrope mixture either in the gas phase or in a solid Ar matrix.[86–88] These sulfur species are highly reactive and readily condense into heavier allotropes under ambient conditions. Therefore, their structures cannot be determined directly by X-ray diffraction. To solve this problem, crystalline molecular flasks can be used to confine these unstable species within a crystalline matrix.

For this purpose, interactive pore sites in a saddle porous coordination network, $[(ZnI_2)_3(TPT)_2]$, were used, in which the iodide groups facing the pore can interact with guest sulfur atoms to stabilize the reactive species.[89] Sulfur was encapsulated in the saddle network structure by vapor diffusion at 533 K under vacuum for 6 h. Under these conditions, the host network powder was fully equilibrated with gaseous sulfur. This treatment changed the light-yellow network powder to bright yellow and changed the PXRD pattern. The change in the position and relative intensity of the peaks indicates that sulfur was encapsulated in the network pores (Fig. 31).

This example represents the first crystal structure determination of a reactive sulfur allotrope smaller than S_6. The open-triangle C_{2v} structure of the observed S_3 is in good agreement with structure obtained by rotational spectroscopy.[90] The sulfur molecules in

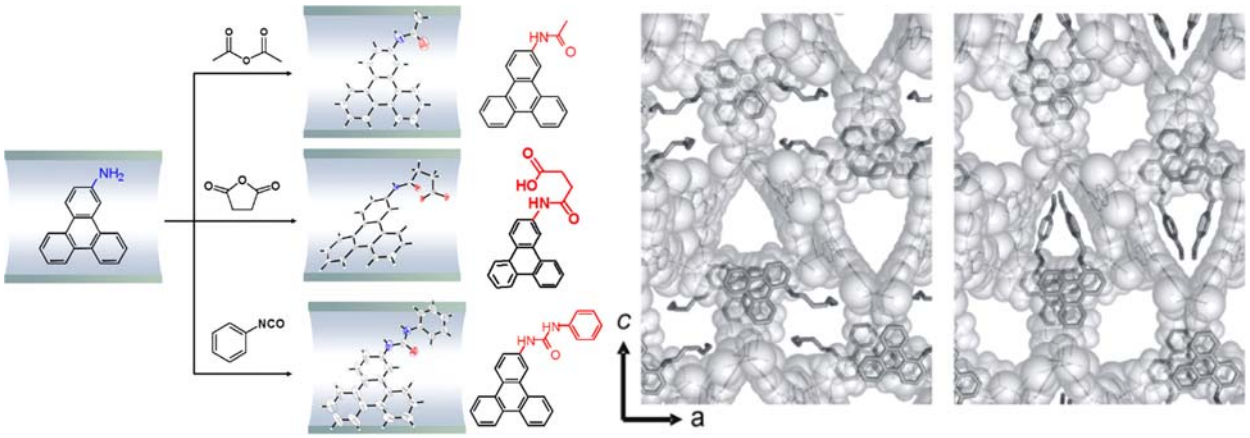

Fig. 26 Selective post-synthetic modification of a pore using various functional groups. Reprinted with permission from Kawano M. X-ray Direct Observation of Reactions and Labile Species on the Basis of Crystal Design. *Bull. Chem. Soc. Jpn.* 2014, **87**, 577–612. Copyright 2014 The Chemical Society of Japan.

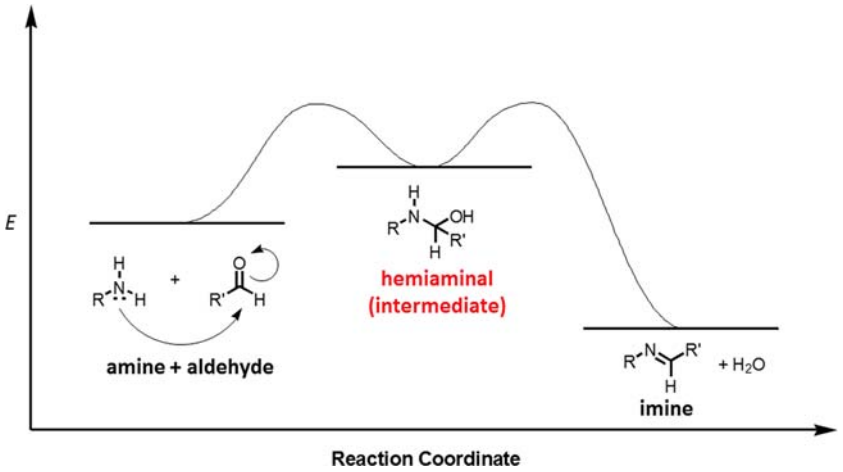

Fig. 27 Reaction pathway of imine formation via a hemiaminal intermediate. Reprinted with permission from Kawano M. X-ray Direct Observation of Reactions and Labile Species on the Basis of Crystal Design. *Bull. Chem. Soc. Jpn.* 2014, **87**, 577–613. Copyright 2014 The Chemical Society of Japan.

the pore were disordered in two positions. Notably, the short interatomic distances between iodide and sulfur, the major component of S_3, were 3.1 and 3.3 Å, which were considerably shorter than the sum of their van der Waals radii (3.8 Å), indicating a strong interaction between them (Figs. 32 and 33). It is postulated that this interaction enabled the encapsulation and stabilization of the highly reactive S_3 molecule.

Furthermore, the presence of S_3 in the pores was confirmed spectroscopically from the characteristic shoulder peak at about 680 cm^{-1} in the vibrational spectrum, which corresponds to asymmetric stretching of S_3. The encapsulated sulfur species exist in a neutral state, which was determined by the assignment of IR peaks and the lack of signal in the electron spin resonance spectrum.

The S_3 encapsulated in the pores was remarkably stable because of the interaction with the iodide sites facing the pores (Fig. 33). The PXRD pattern of the S_3-encapsulating network powder did not change significantly over three months of the exposure to air. Thermogravimetric analysis of the host-guest material showed a weight decrease at temperatures above 500 K, indicating that sulfur evaporation from the pores occurred at high temperatures. Furthermore, the S_3 molecules inside the network were found to be inert to the photo-irradiation. These results further highlight the remarkable stabilization of the S_3, an analog of ozone, inside the interactive pores of the saddle network.

Nevertheless, the encapsulated S_3 showed unique reactivity. Vacuum heating of this crystalline network powder at 473 K for 6 h with NH_4Cl changed the PXRD pattern, indicating a structural transformation had occurred. The crystal structure determined by *ab initio* PXRD analysis showed 0.5 S_6 molecules in each pore (Fig. 34). The product of this transformation was a six-membered ring

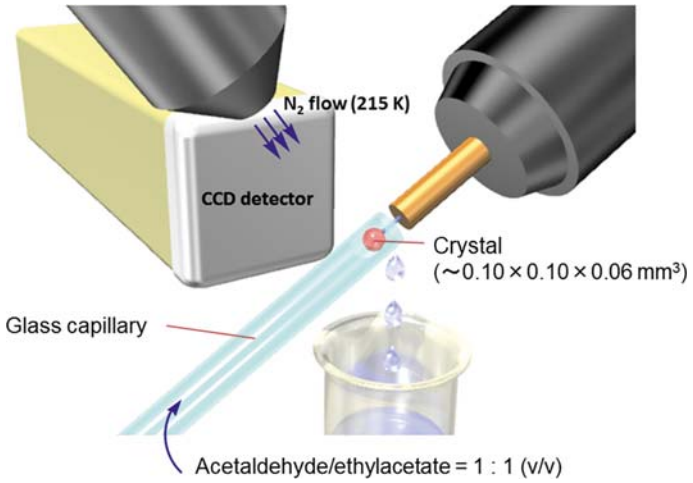

Fig. 28 Experimental setup for in situ crystallographic observation of chemical reactions in a porous network. Reprinted with permission from Kawano M. X-ray Direct Observation of Reactions and Labile Species on the Basis of Crystal Design. *Bull. Chem. Soc. Jpn.* 2014, **87**, 577–614. Copyright 2014 The Chemical Society of Japan.

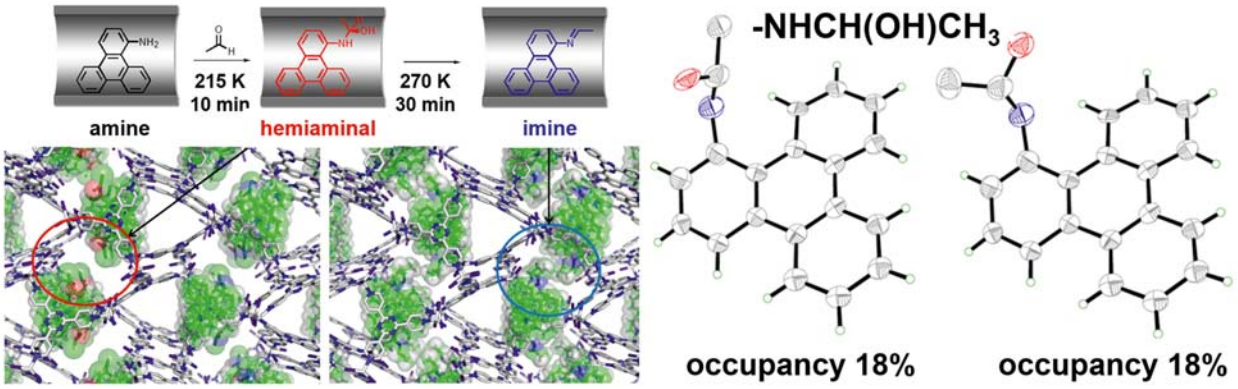

Fig. 29 Stepwise direct crystallographic observation of hemiaminal and imine formation. Reprinted with permission from Kawano M. X-ray Direct Observation of Reactions and Labile Species on the Basis of Crystal Design. *Bull. Chem. Soc. Jpn.* 2014, **87**, 577–615. Copyright 2014 The Chemical Society of Japan.

with a chair conformation characteristic of discrete S_6 molecules.[86] This result suggests that S_3 in the pores dimerized to produce S_6 as follows:

$$S_3 + S_3 \rightarrow S_6$$

The crystal structure reveals that the encapsulated S_6 also interacts with the iodide in the network as indicated by the fact that the interatomic distances between sulfur and iodide (3.1 and 3.4 Å) are shorter than the sum of their van der Waals radii (3.8 Å). The close proximity between S_6 and iodide indicates the presence of a strong host-guest interaction as in S_3. S_6 itself cannot enter the pore from the outside because the diameter of the opening is too small. Therefore, the only way to encapsulate S_6 is the ship-in-a-bottle approach,[91] starting from a small sulfur allotrope such as S_3. However, the S_3 dimerization cannot be achieved by simple heating and required catalysis with NH_4Cl. NH_4Cl is an impurity remaining from ligand synthesis and acts as a proton donor.[92] It is proposed that the hydrogen-bonding brings the sulfur trimers closer together and cyclization occurs. Furthermore, similar structural transformation could be induced by mechanical action during the grinding of the S_3-encapsulating network powder, indicating the flexibility of the saddle structure like a laundry net.

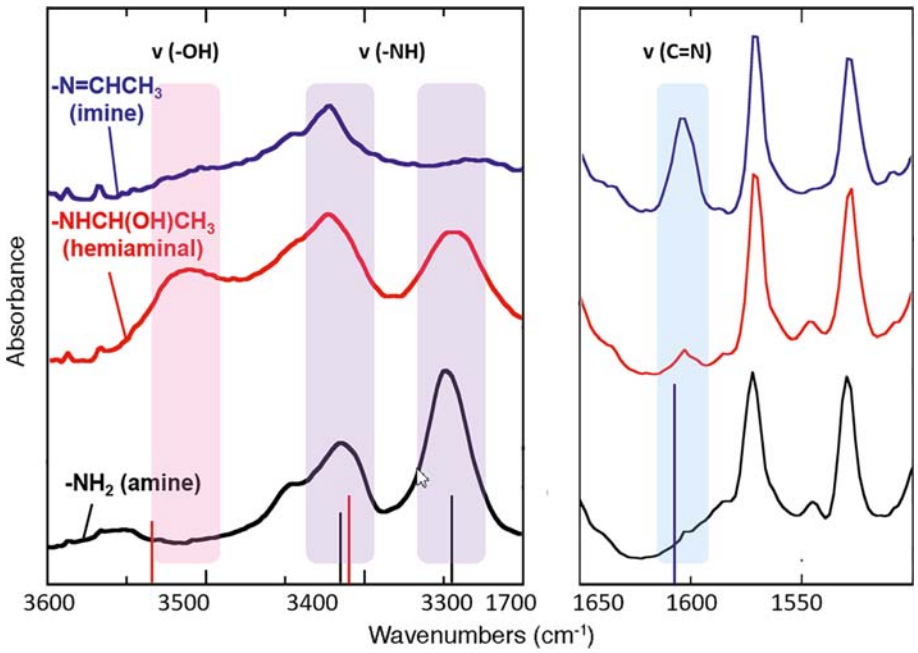

Fig. 30 Vibrational spectra obtained by IR microspectroscopy and simulated spectra by the DFT calculations for crystalline state chemical reactions of amine with aldehyde: black, amine; red, hemiaminal; blue, imine. Reprinted with permission from Kawano M. X-ray Direct Observation of Reactions and Labile Species on the Basis of Crystal Design. *Bull. Chem. Soc. Jpn.* 2014, **87**, 577–616. Copyright 2014 The Chemical Society of Japan.

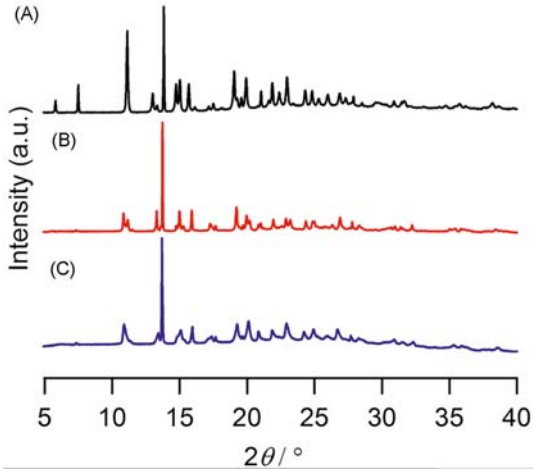

Fig. 31 Change in XRPD pattern of $[ZnI_2(TPT)_3]_n$ powder after sulfur encapsulation. (a) before encapsulation, (b) after encapsulation of sulfur: $[(ZnI_2)_3(TPT)_2(S_3)]_n$ and (c) after grinding $[(ZnI_2)_3(TPT)_2(S_3)]_n$: $[(ZnI_2)_3(TPT)_2(S_6)_{0.5}]_n$. 2θ is unified with $\lambda = 1.54056$ Å. From Ohtsu H; Choi W; Islam N; Matsushita Y; Kawano M. Selective Trapping of Labile S3 in a Porous Coordination Network and the Direct X-ray Observation. *J. Am. Chem. Soc.* 2013; **135**, 11449–11452.

Interestingly, this transformation is reversed by excitation at 365 nm, allowing full recovery of the starting S_3 molecule. This result indicates that inside the pore, S_3 is more stable toward light irradiation than S_6 (Fig. 34).

Overall, the interactivity of the pores is the key to the efficient trapping of small sulfur allotropes and their conversion, contributing to our understanding of the chemistry of these rare sulfur species.

The success of S_3 encapsulation has stimulated the design of materials that contain intrinsic interactivity within the pores using the principles of kinetic assembly. To produce coordination networks under kinetic control, labile metal connectors were employed. If metals can readily exchange ligands under reaction conditions, usually in solution, the presence of several intermediate metal complexes may give rise to multiple species during network formation. In particular, labile multinuclear metal clusters could give rise to multiple species existing simultaneously in solution. However, for most metal ions, the intermediate state geometries are predictable, which limits the number of easily accessible structures for the network metal connectors.

Therefore, to demonstrate kinetic control of network formation, labile metal connectors instead of the commonly used metal ions were used.[93,94] These were combined with rigid and highly symmetric ligands to produce structurally robust networks. In this study, $[Cu_4I_4(PPh_3)_4]$ was selected as a suitable metal precursor, because its central Cu_4I_4 cubane core is kinetically labile in solution and can be readily converted into other copper iodide clusters.[95,96] For the ligand, tetra-4-(4-pyridyl)phenylmethane (tppm) was used, which possesses all the required characteristics, namely structural rigidity, thermal stability and tetrahedral symmetry. Upon heating a suspension of $[Cu_4I_4(PPh_3)_4]$ and tppm in DMSO in air at 453 K for 30 min, a homogenous colorless solution was obtained. Depending on the cooling rate, two kinds of network crystals were obtained. Rapid cooling (*ca.* 20 K min^{-1}, kinetic assembly) exclusively produced yellow needles with the formula $[(CuI)_2(tppm)]$ in 99% yield. In contrast, slow cooling (*ca.* 3 K min^{-1}, thermodynamic assembly) resulted in the formation orange prisms with the formula $[(Cu_2I_2)(tppm)]$ in 95% yield. Although the two networks had exactly the same chemical composition, their connectivity and topology were markedly different. Therefore, these materials can be considered structural isomers (Fig. 35).

Single crystal structure analysis of the kinetic isomer revealed that CuI helical chains bridged by tppm ligands form a non-interpenetrating porous network along the *c*-axis, and each Cu(I) ion is coordinated by two nitrogen atoms of the tppm ligand and two bridging iodide groups. The helical chain network has 1D channels with pore windows of 5.8 × 5.5 Å and a 35% void space (without solvent) in the unit cell volume. The most important feature of this structure is that the bridging iodide in the connecting cluster faces into the 1D channel, and therefore can act as interactive pore sites (Fig. 35a, c and e). On the other hand, crystal structure analysis of the thermodynamic isomer revealed a quadruply interpenetrating network consisting of Cu_2I_2 dimer units and tppm ligands. The structure is a 4,4-connected grid with the PtS topology if the Cu_2I_2 dimer units are considered as square-planar sites and the central carbon atom of tppm as a tetrahedral node. In addition, this network contains 1D channels with pore windows of 4.0 × 3.9 Å and a 22% void space in the unit cell volume. The iodide groups in the Cu_2I_2 dimer are obscured by the tppm ligands from the interpenetrating nets, which is different from the kinetic structure. As a result, the channels in the thermodynamic network are not decorated by the interactive iodide sites, and thus are relatively featureless (Fig. 35b, d and f).

To elucidate the properties of the interactive pore sites, I_2 sorption experiments were performed on both solvated and desolvated networks. The crystallinity of the samples was retained after I_2 exposure. Single crystal structure analysis revealed that the pores of the kinetic network encapsulated I_2 via chemisorption mechanism converting I^- groups in the connector units into linear I_3^- (Fig. 36a and b). In contrast, the thermodynamic network only displayed physisorption of I_2 (Fig. 36c and d). Crystal structure analysis revealed that the I_2 molecules are arranged linearly along the 1D channel and are highly disordered. These results clearly demonstrate the importance of interactive pores in facilitating the chemical bond formation between bridging iodides and guest I_2.

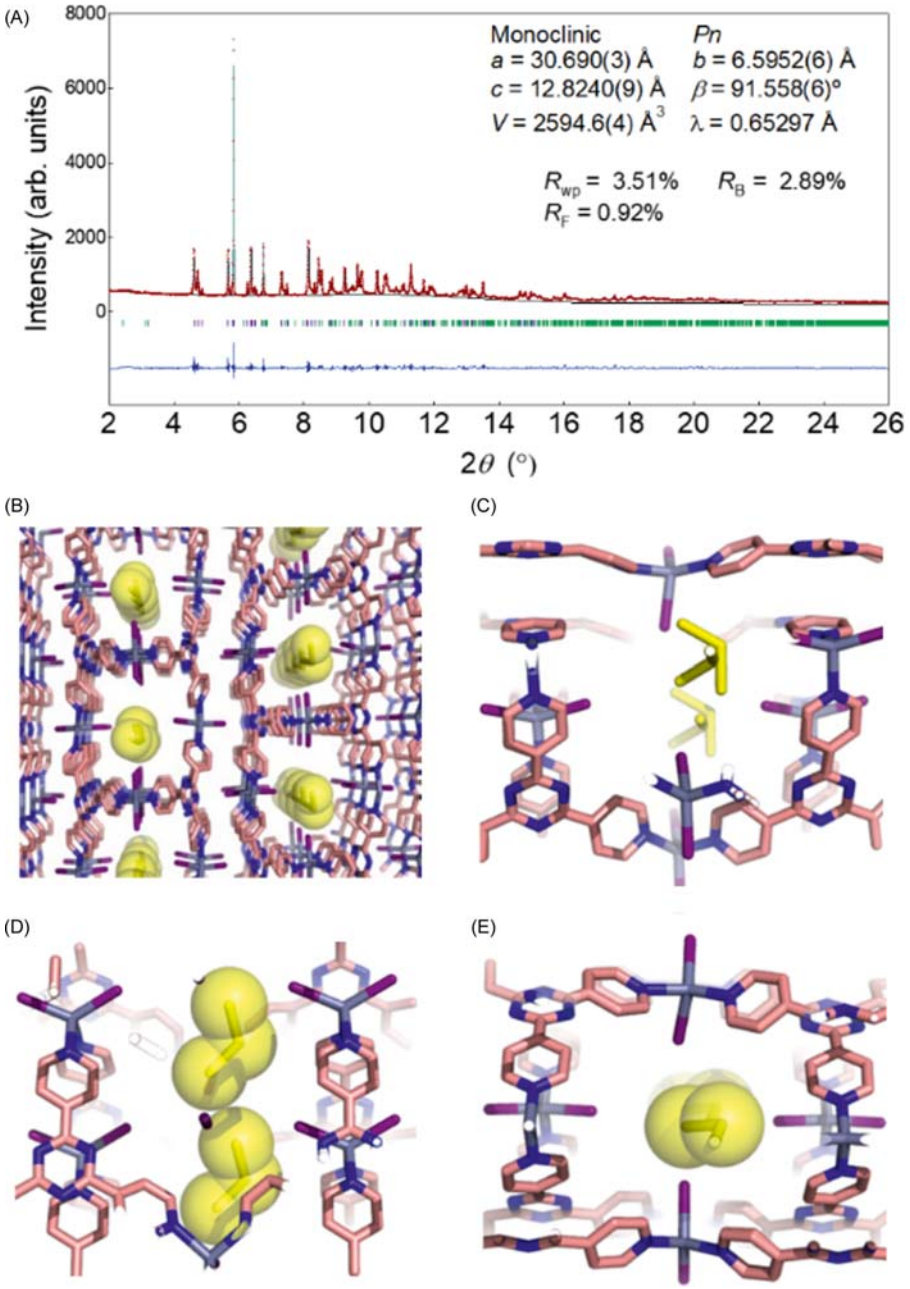

Fig. 32 (a) Experimental (red), calculated (black), and difference (blue) XRPD profiles from the final Rietveld refinement of $[(ZnI_2)_3(TPT)_2(S_3)]_n$. The experimental pattern was obtained at BL15XU in SPring-8. (b) View with a major component of S_3 along *b*-axis (Occupancy factor = 0.623). C, pink; N, blue; Zn, grey; I, purple; S, yellow. (c) Magnified view showing disordered S_3 molecules (Occupancy factor = 0.623 and 0.377). (d) View with a major component of S_3 along *c*-axis (Occupancy factor = 0.623). (e) View with a major component of S_3 along *b*-axis (Occupancy factor = 0.623). Reprinted with permission from Ohtsu H; Choi W; Islam N; Matsushita Y; Kawano M. Selective Trapping of Labile S3 in a Porous Coordination Network and the Direct X-ray Observation. *J. Am. Chem. Soc.* 2013, **135**, 11449–11452.

Remarkably, even though I_2 forms chemical bonds with the pores of helical network, its desorption temperature is unexpectedly lower than for the physisorbed I_2 inside the dimer network. This behavior is attributed to the steric repulsion between adsorbed I_2 molecules and the framework backbone. In particular, the pyridyl ring rotation is expected to become more rapid with increasing temperature, which would cause the collisions with the I_3^- units leading to their displacement.

Because the thermodynamic network has small pores, it is particularly suitable for small sulfur allotrope encapsulation. The small pore size cannot accommodate sulfur clusters larger than S_3, and it was expected to predominantly encapsulate disulfur, S_2. This favorable characteristic prompted us to study in depth the sulfur encapsulation in the dimer network.[97]

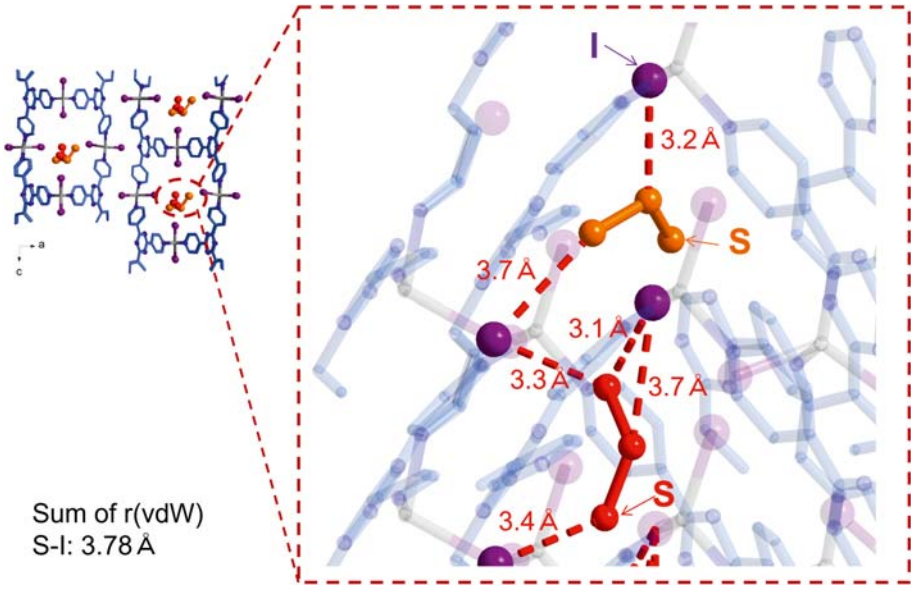

Fig. 33 Intermolecular interaction between iodide and S_3.

Sulfur was encapsulated from the gas phase by the kinetic trapping method, in which only sulfur vapor was present in the glassware while the network was kept at room temperature to create a temperature gradient. X-ray structure analysis of the sulfur containing network revealed that the S_2 molecules are physisorbed at two different sites in the channel: (i) highly disordered along the channel and (ii) within small cavities adjacent to the Cu_2I_2 units (Fig. 37).

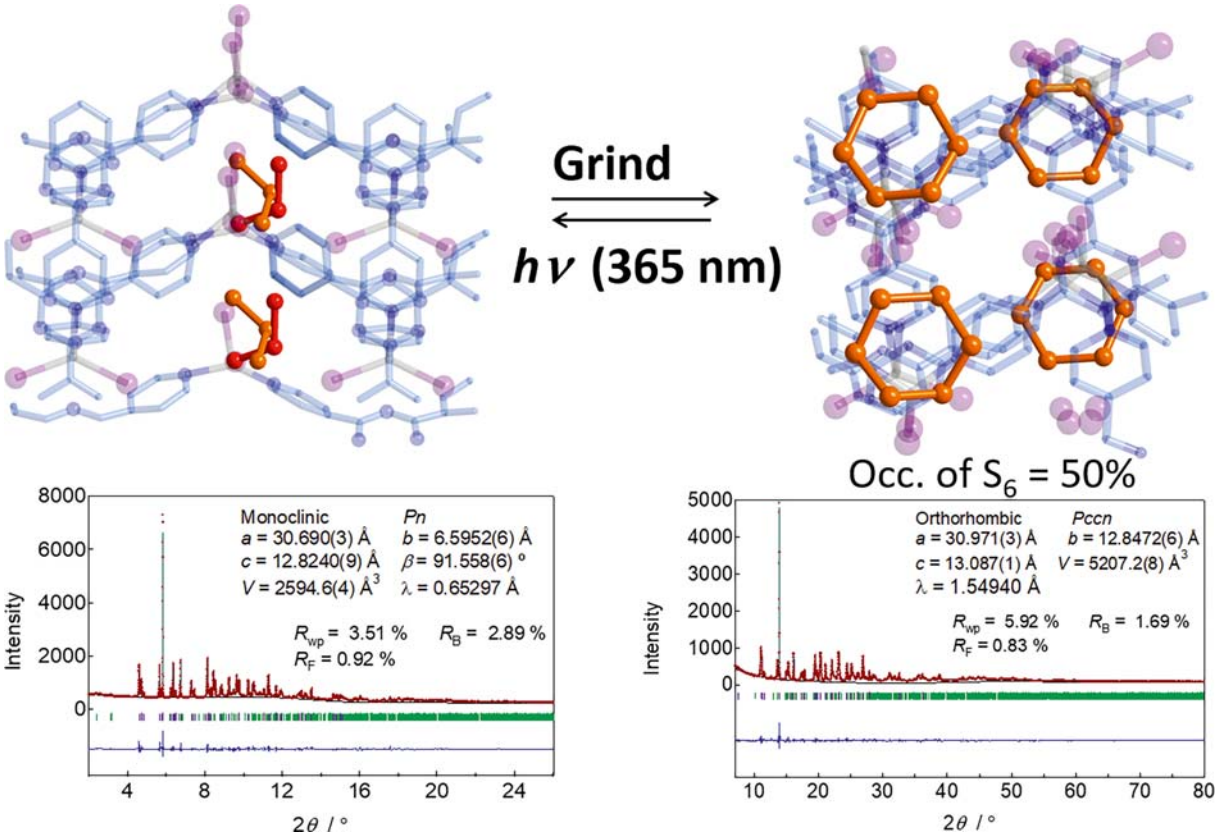

Fig. 34 Reversible transformation between S_3 and S_6 in a pore of $[ZnI_2(TPT)_3]_n$.

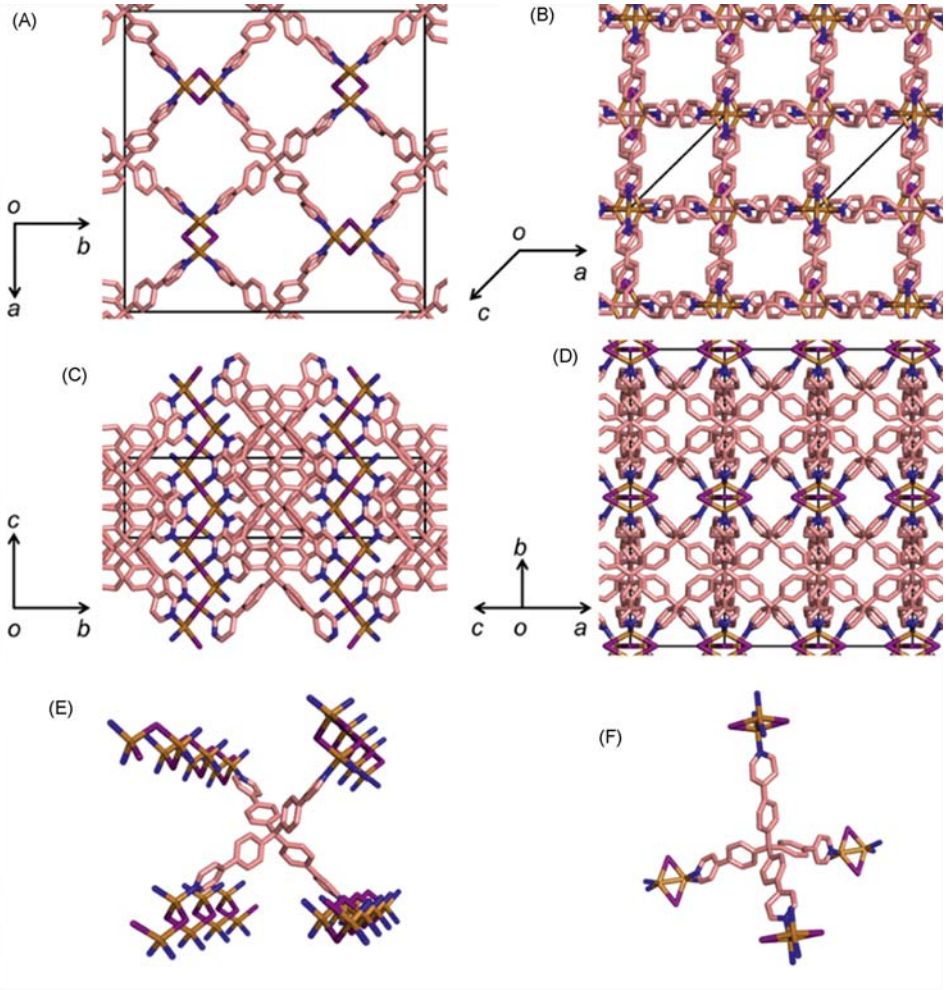

Fig. 35 Porous network structure and coordination geometry of CuI unit in isomer $[(CuI)_2(tppm)]$ and $[(Cu_2I_2)(tppm)]$. (a,b) Packing structures viewed from the 1D channel (the *c*-axis projection of isomer $[(CuI)_2(tppm)]$ (a), the *b*-axis projection of isomer $[(Cu_2I_2)(tppm)]$ (b), respectively). (c, d) Packing structures viewed from the direction perpendicular to the 1D channel (the *a*-axis projection of isomer $[(CuI)_2(tppm)]$ (c), the projection viewed from [102] direction of isomer $[(Cu_2I_2)(tppm)]$ (d), respectively). (e, f) Coordination geometries between the CuI unit (CuI helical chain unit in isomer $[(CuI)_2(tppm)]$ (e), and Cu_2I_2 dimer unit in isomer $[(Cu_2I_2)(tppm)]$ (f), respectively) and ligand tppm. Hydrogen atoms and solvent molecules are omitted for clarity. Kitagawa H; Ohtsu H; Kawano M. Kinetic Assembly of a Thermally Stable Porous Coordination Network Based on Labile CuI Units and the Visualization of I2 Sorption. *Angew. Chem. Int. Ed.* 2013, **52**, 12395–12399.

Only physisorption of S_2 was observed in the pore because of the steric hindrance around the iodide sites. The small size and linear shape of the 1D channels selectively trapped S_2 molecules and prevented further formation of larger sulfur allotropes. The presence of sulfur dimers in the network was confirmed by Raman spectroscopy at room temperature. A new band appeared at 728 cm^{-1} corresponding to the S_2 symmetric stretching mode. The encapsulated sulfur species remained stable inside the network up to 500 K because of the confinement effect of the pores.

The fact that the S_2 was detected in the pores implies that gas phase sulfur incorporation in other porous networks proceeds predominantly via sulfur dimers. This is consistent with the fact that the largest fraction of the gaseous sulfur is in the dimer state.[88] Therefore, the S_3 encapsulation in the saddle $[(ZnI_2)_3(TPT)_2]$ network likely occurred via a ship-in-a-bottle cluster assembly. First, S_2 (disulfur) molecules enter the pores of the network and then are converted to S_3 (trisulfur). Since encapsulation is conducted in equilibrium, it is difficult to determine the exact mechanism of disulfur molecule conversion. To observe these processes, the guest molecules should be kinetically trapped before they reach equilibrium. To this end, iodide sites may act as suitable interactive sites to capture small sulfur species and prevent aggregation. To explore this possibility, a kinetically assembled helical CuI network with interactive pores was employed.

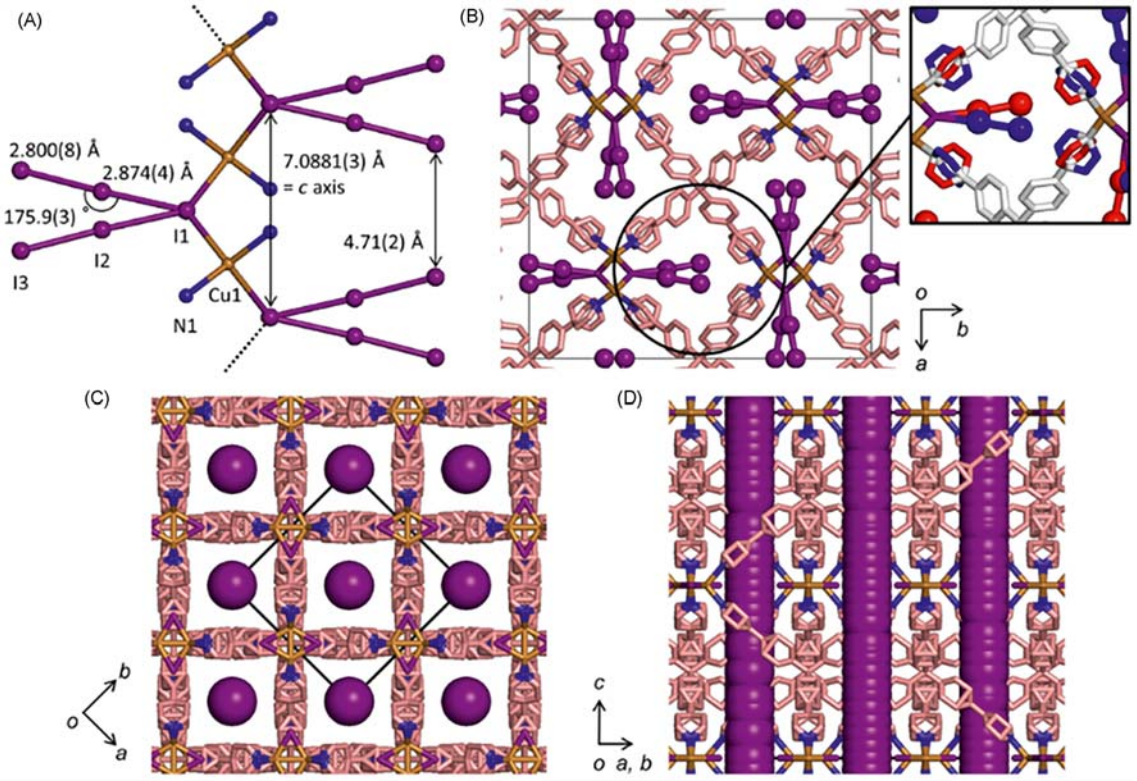

Fig. 36 Structure of iodine-encapsulating network isomer $(0.96I_2)$@$[(CuI)_2(tppm)]$ and $(2.125I_2)$@ $[(Cu_2I_2)(tppm)]$. (a) A CuI helical chain unit with chemisorbed Iodine molecules in $[(CuI)_2(tppm)]$. (b) the *c*-axis projection of $(0.96I_2)$@$[(CuI)_2(tppm)]$ (inset: different colored pairs of iodine molecules and pyridine ring showing corresponding disordered pair). (c, d) the *c*-axis projection of $(2.125I_2)$@ $[(Cu_2I_2)(tppm)]$ (c) and the projection viewed from [110] direction of $(2.125I_2)$@ $[(Cu_2I_2)(tppm)]$ (d). Hydrogen atoms and solvent molecules are omitted for clarity. Kitagawa H; Ohtsu H; Kawano M. Kinetic Assembly of a Thermally Stable Porous Coordination Network Based on Labile CuI Units and the Visualization of I2 Sorption. *Angew. Chem. Int. Ed.* 2013, **52**, 12395–12400.

10.12.7.7 X-ray snapshots of S_2 conversion in an interactive pore

As mentioned above, pores lined up with interactive iodide sites could serve as efficient traps to stabilize and visualize small sulfur species. Furthermore, sulfur encapsulation in the saddle ZnI network was performed under equilibrium conditions. Elemental sulfur and the network powder were kept at 533 K under vacuum for 6 h to encapsulate sulfur gas. Because of the equilibrium state,

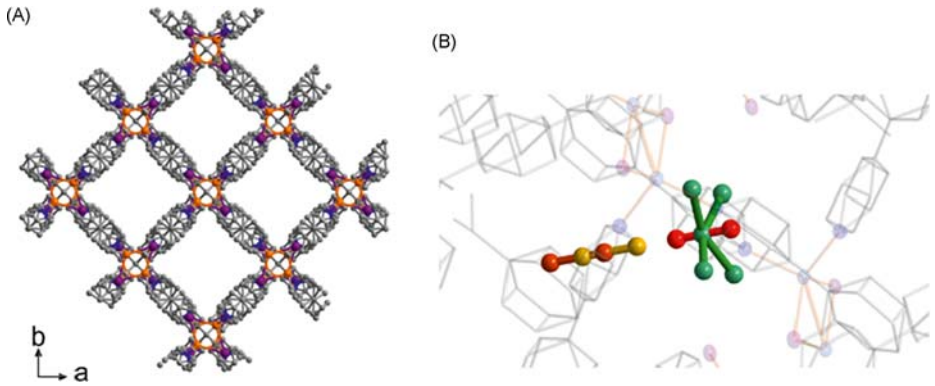

Fig. 37 Crystal structures for desolvated $[(Cu_2I_2)(tppm)]$ (a) and the structure after sulfur encapsulation at 30 K (b). The stoichiometry of the 30 K structure is $\{[(Cu_2I_2)(C_{45}H_{32}N_4)]\bullet(S_2)_{0.975}\}_n$. (b) shows a different view of disordered S_2 in the 1D-channel with a Ball and Stick model: each colored molecule corresponds to S_2. Atoms coloring: C, grey; N, blue; Cu, orange; I, purple, S, yellow, brown, red and green. Hydrogen atoms are omitted for clarity. Kitagawa H; Ohtsu H; Kawano M. Kinetic Assembly of a Thermally Stable Porous Coordination Network Based on Labile CuI Units and the Visualization of I2 Sorption. *Angew. Chem. Int. Ed.* 2013, **52**, 12395–12401.

it was difficult to determine the conversion mechanism before the sulfur species reached equilibrium inside the network pores. To overcome this limitation, small metastable sulfur allotropes were kinetically trapped and observed for conversion in the pores.

The CuI helical network was used for trapping experiments due to the presence of interactive iodide sites where the sulfur transformation could occur. Unlike previous encapsulation experiments, the sulfur trapping into the helical structure was carried out under kinetic conditions. Elemental sulfur and the desolvated network powder were placed at well-separated locations in a zigzag glass tube, followed by sealing it under vacuum ($\sim 10^{-6}$ Torr). By heating the sulfur side to generate sulfur vapor and keeping the network side at room temperature, a sharp temperature gradient could be generated. This arrangement enabled gaseous sulfur molecules to be kinetically trapped by the porous material. After the reaction was complete, single crystal X-ray diffraction of the resultant sample was performed sequentially at 250, 300, 350, and again 250 K using synchrotron radiation. Analysis of these diffraction patterns revealed the structure of transient small sulfur allotropes. The initial structure at 250 K showed the presence of two types of physisorbed guests in the network channel, S_2 and bent-S_3 species. Upon increasing the temperature to 300 K, crystal structure analysis revealed the formation of cyclo-S_3 chemisorbed at the bridging iodide site in addition to bent-S_3 and cyclo-S_3, both physisorbed on the channel. Theoretical investigations indicate that the more strongly interacting cyclo-S_3 specie should be in the dicationic state, cyclo-S_3^{2+}. Further heating to 350 K resulted in ring opening of the cyclic trimers, yielding two kinds of bent-S_3 species, one still bound to the network iodide sites and the other physisorbed inside the channel.

From these X-ray diffraction experiments, a tentative reaction mechanism for the temperature-induced interconversion of sulfur species inside the helical CuI network was proposed. First, S_2 is kinetically trapped by rapid absorption into the channel and then partially transformed into bent-S_3 structure. This dimer was only detected at 250 K, strongly indicating that this allotrope is the starting point for the next conversion reaction. Second, heating converts S_2 to several trimeric species: chemisorbed cyclo-S_3^{2+} and physisorbed cyclo-S_3 and bent-S_3. After that, the cyclic forms underwent ring opening to produce more stable bent-S_3 species (Fig. 38). Despite the kinetic nature of the experiments, the X-ray analysis results were generally reproducible.

10.12.7.8 Unstable phosphorus species: P_4

In addition, the saddle network was used to capture and stabilize other reactive elemental species, namely P_4, also known as white phosphorus.[98] The phosphorus tetramer was encapsulated into the pores using the phosphorus vapor generated by heating the red

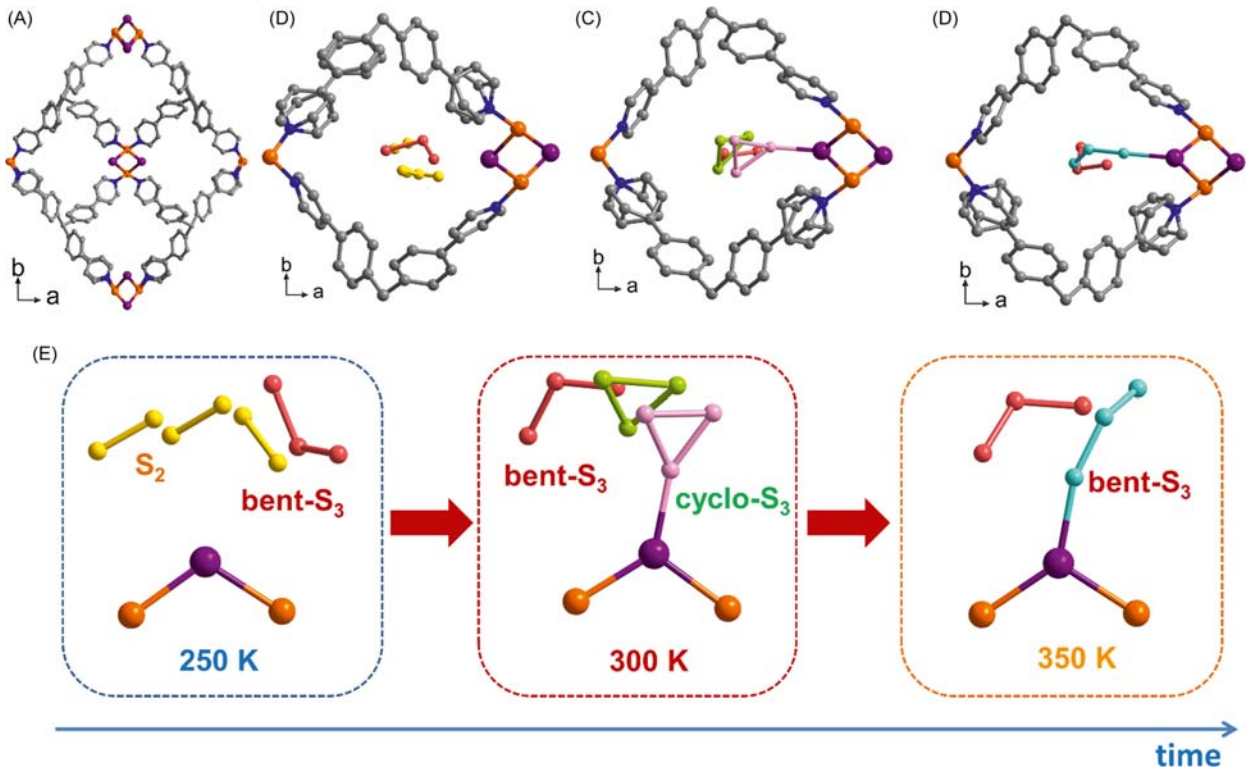

Fig. 38 Pore description in crystal structure of (a) [(Cu_2I_2)(tppm)], (b) the structure after sulfur encapsulation at 250 K, (c) 300 K and (d) 350 K. (e) The crystal structure of Sulfur-encapsulating showing parts of {CuI} unit and sulfur species. At 250 K, physisorbed S_2 and bent-S_3 were observed (left), at 300 K, chemisorbed cyclo-S_3^{2+}, physisorbed cyclo-S_3 and bent-S_3 was observed (middle), and at 350 K, bent-S_3 was observed. Bottom-arrow indicates time course of measurements showing molecular transformation mechanism from S_2 to bent-S_3 species. Atoms coloring: Cu, orange; I, purple; and S, yellow, red, green, pink and cyan to distinguish disordered molecules. Kitagawa H; Ohtsu H; Cruz-Cabeza AJ; Kawano M. Isolation and Evolution of Labile Sulphur Allotropes via Kinetic Encapsulation in Interactive Porous Networks. *IUCrJ* 2016, **3**, 232–236.

phosphorus polymer. The P_4 trapping was confirmed by X-ray diffraction, as shown in Fig. 39. This specie was stabilized by weak interactions with the pore walls and was stable under air at 300 K. This means that this network can be used as a versatile P_4 container. The removal and re-trapping process can be repeated, which is important for the molecular flask reusability. The presence of interactive sites inside the coordination network was demonstrated to be, once again, crucial for the efficient trapping and release of reactive species. As a result, chemically and thermally robust porous networks can be used as facile, reusable reagent containers.

10.12.7.9 Reactive elements: Br_2

The network may react with reactive guest molecules. For example, Br_2 reacts with the network to produce ZnBr network:[99]

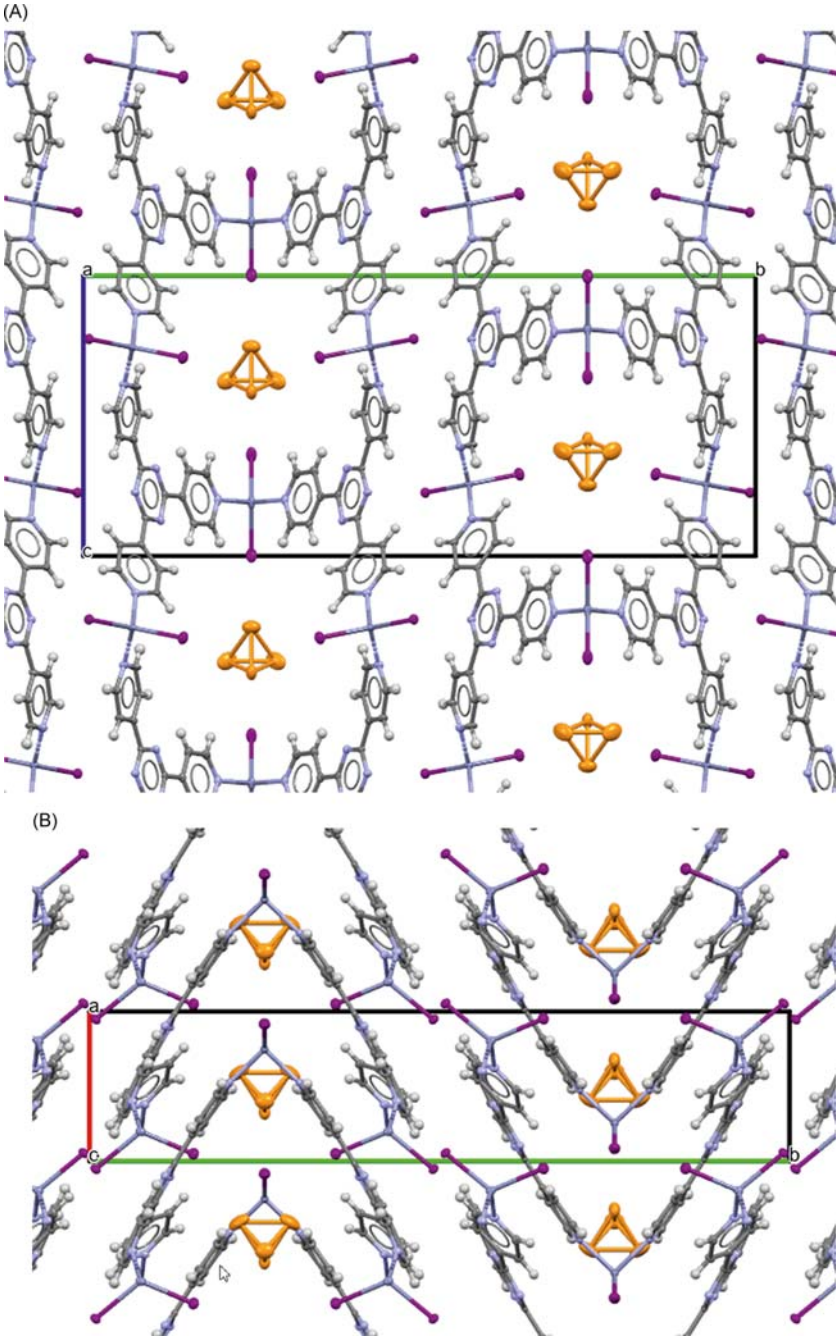

Fig. 39 Crystal structures (ORTEP plots, 50% probability) of $[(ZnI_2)_3(TPT)_2(P_4)]_n$ at 100 K: (a) view along *b*-axis. (b) view along *c*-axis. Color codes: C, gray; N, blue; P, orange; Zn, pale-blue; and I, purple.

$$\left[(ZnI_2)_3(TPT)_2\right] + 3Br_2 \rightarrow \left[(ZnBr_2)_3(TPT)_2(I_2)\right] + 2I_2$$

the new structure was confirmed by *ab initio* PXRD analysis (**Fig. 40**). The trapped I_2 showed strong interactions with the pores of the ZnBr network.

Furthermore, Raman spectroscopy proved the presence of I_2 inside the network.[100–102] The Raman spectrum showed sharp peaks at 174 and 194 cm^{-1}, corresponding to I_2 encapsulated in the pore and I_2 attached to the surface of crystal, respectively. I_2 in the pore interacts with Br^- sites of the network. The I···Br distance is 3.61 Å, shorter than the sum of the individual van der Waals radii of I and Br (3.75 Å).[103] Also, the I-I···Br angle is 153° (non-linear), indicating mainly a π-type interaction combined with some contribution of σ-type interactions. The brominated network shows a significantly stronger affinity for I_2 due to the contribution of π-interactions not present in the iodine analog. This post-synthetic modification of the pore is due to the strong oxidizing power of Br_2. The oxidation potential of Br_2/Br^- redox couple is 1.087 V vs SHE, which is higher than 0.54 V vs SHE of the I_2/I^- couple. Therefore, the encapsulated Br_2 readily oxidizes the constituent I^- to give I_2. This type of post-synthetic reaction is the first example of redox induced ligand transformation that results in the substitution of network components. As a result, the pore modification dramatically changed the nature of the interactive sites by switching from I^- to Br^-.

Furthermore, thermal treatment of the I_2-encapsulated ZnBr-network led to the guest removal affording an activated structure. When the I_2 loaded $[(ZnBr_2)_3(TPT)_2]$ network powder was heated at 573 K, the powder turned white, indicating the release of I_2 molecules from the pores. *Ab initio* PXRD structural analysis of the remaining white powder revealed that it is isostructural with the starting $[(ZnI_2)_3(TPT)_2]$ network (**Fig. 41**). The pore window of the bromide structure is 2.6 × 4.6 Å, which is larger compared to the iodide analog because of the smaller ionic radius of Br^- compared to I^-. The halide replacement preserved the overall saddle-type network structure and topology. Starting directly from $ZnBr_2$ and TPT did not yield the same structure, either by solution-phase synthesis or crystallization from vapor. In both cases, interpenetrating networks were the primary product. As a result, the only synthetic route to the $[(ZnBr_2)_3(TPT)_2]$ network is oxidative encapsulation and ligand substitution with Br_2.

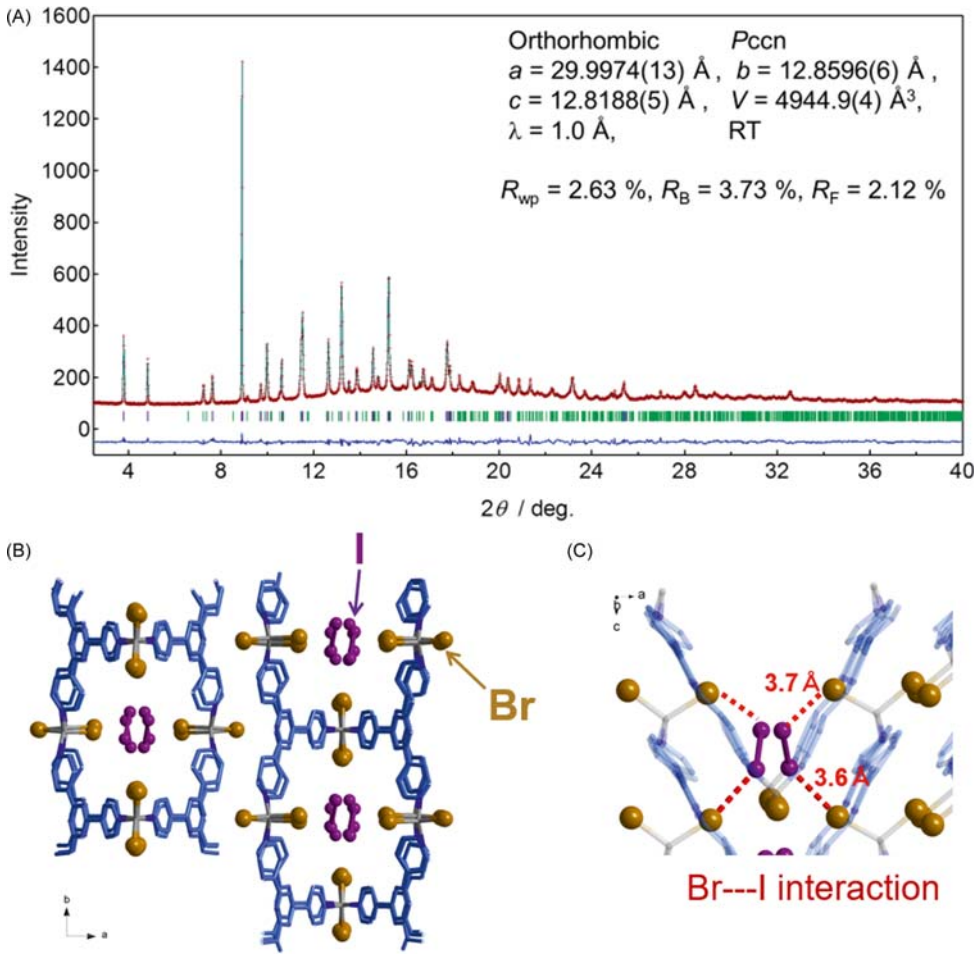

Fig. 40 Experimental (red), calculated (black), and difference (blue) XRPD profiles from the final Rietveld refinement of the $I_2@[(ZnBr_2)_3(TPT)_2]_n$. Crystal structure: (b) view along the *c*-axis. I_2 (occupancy 0.5) occupies two symmetrically related positions. (c) Br···I interaction. Color codes: C, gray; N, blue; Zn, pale-blue; I, purple; and Br, brown.

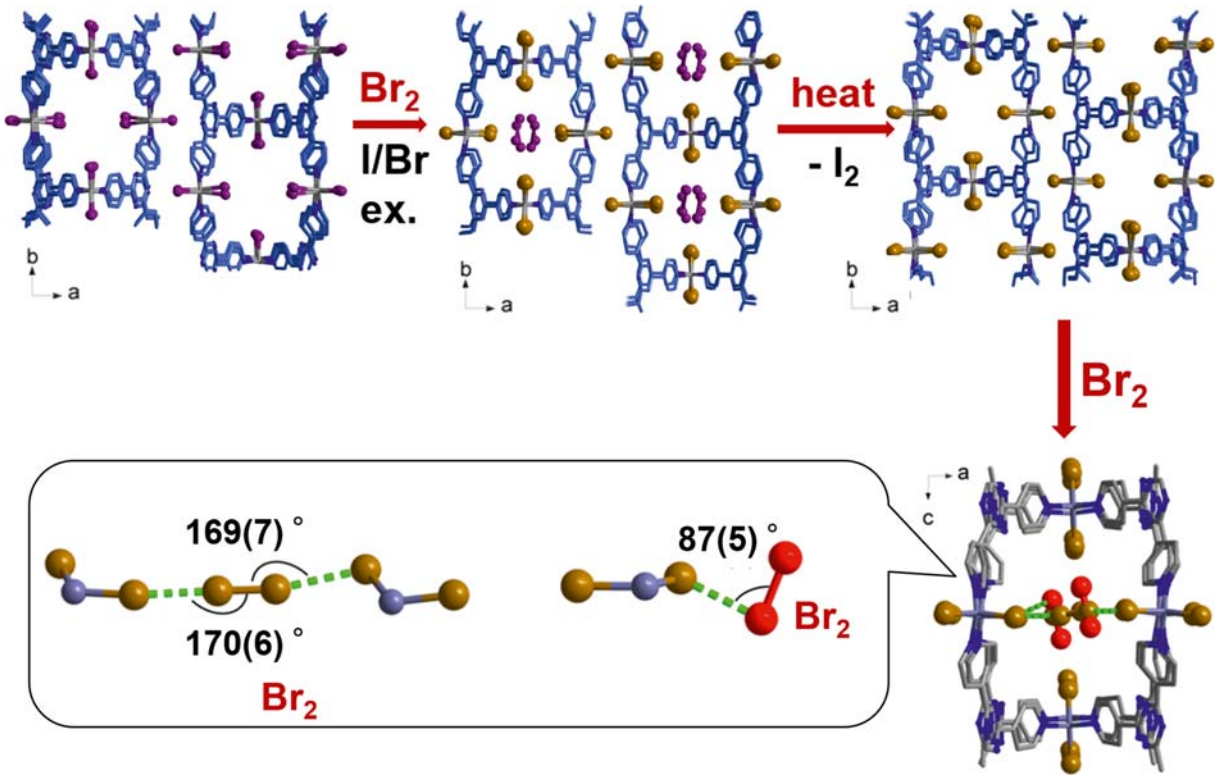

Fig. 41 Reaction scheme of $[(ZnI_2)_3(TPT)_2]_n$ to generate $[(ZnBr_2)_3nTPT)_2]_n$: Linear interactions between Br_2 and Br^- ions and perpendicular interactions between Br_2 and Br^- ions. Color codes: C, gray; N, blue; Zn, pale-blue; and Br, brown and red to distinguish disordered molecules.

Due to the presence of Br^- ions as interactive pore sites, trapping of Br_2 was attempted. In these experiments, Br_2 vapor diffusion was also performed under the same conditions as Br_2 encapsulation in $[(ZnI_2)_3(TPT)_2]$. After the vapor exposure, the white bromide network powder turned yellow, and the PXRD pattern changed accordingly. *Ab initio* PXRD structural analysis of the resultant yellow powder revealed that the material retains the basic ZnBr-network structure while also incorporating disordered Br_2 guests. These were physically adsorbed into the pore, strongly interacting with the network bromide groups. The observed Br···Br distances were 3.44, 3.55, and 3.22 Å, shorter than the sum of the van der Waals radii of Br (3.70 Å). One of the disordered Br_2 molecules exhibits an almost linear geometry, indicating σ-type halogen-halogen interaction (Fig. 41). In contrast, the other disordered Br_2 assumes an almost perpendicular geometry, indicating a π-type interaction with an elongated Br_2 bond (2.38(14) Å). Therefore, both σ-hole and π-orbitals based interactions can occur between the guest, Br_2, and the host, Br^-. These results highlight the diversity of halogen bonding possible inside the interactive pores and provide an opportunity to generate and study unusual halogenated polynuclear species that cannot exist outside.

10.12.8 Overview

Here, we have described the direct observation of transient chemical species and chemical reactions using synchrotron radiation. Direct observation of transient and unstable chemical species by X-ray diffraction can greatly enhance our understanding of chemical reactions. On top of that, the use of pores in coordination networks has various applications and is a promising method to elucidate the structure of molecular species that do not inherently crystallize. In particular, kinetic assembly can generate interactive sites in the pores, which is very useful for trapping unstable species. Thus, the methodology using porous coordination networks, i.e., crystalline molecular flasks, allows us to observe a variety of crystalline phase reactions. In addition, the development of coordination network (MOF) chemistry over the past quarter century has made it possible to utilize a wide variety of pores. At the same time, the development of synchrotron radiation and X-ray detectors has made it possible to study the microscopic crystals found in MOF crystals. This means that structural analysis is now possible with a smaller amount of target guest sample. In addition, spectroscopic methods and theoretical calculations have been developed to elucidate the electronic structure of these chemical species. It is expected that the development of synchrotron radiation technology, material synthesis, spectroscopic measurements, and theoretical calculations will enable us to observe a wide variety of chemical species and greatly expand this research area.

References

1. Ohashi, Y.; Sasada, Y. X-ray Analysis of Co-C Bond Cleavage in the Crystalline State. *Nature* **1977,** *267,* 142–144.
2. Ohashi, Y.; Yanagi, K.; Kurihara, T.; Sasada, Y.; Ohgo, Y. Crystalline State Reaction of Cobaloxime Complexes by X-Ray Exposure. 1. Direct Observation of Cobalt-Carbon Bond Cleavage in [(R)-1-Cyanoethyl][(S)-(-)-α-methylbenzylamine]bis(dimethylglyoximato)cobalt(III). *J. Am. Chem. Soc.* **1981,** *103,* 5805–5812.
3. Nakanishi, H.; Jones, W.; Thomas, J. M.; Hursthouse, M. B.; Motevalli, M. Monitoring the Crystallographic Course of a Single-Crystal → Single-Crystal Photodimerization by X-ray Diffractometry. *J. Chem. Soc. Chem. Commun.* **1980,** 611–612.
4. Cohen, M. D.; Schmidt, G. M. J.; Sonntag, F. I. Topochemistry. Part II. The Photochemistry of Trans-Cinnamic Acids. *J. Chem. Soc.* **1964,** 2000–2013.
5. Cohen, M. D. The Photochemistry of Organic Solids. *Angew. Chem. Int. Ed.* **1975,** *14,* 386–393.
6. Ohashi, Y., Ed.; *Reactivity in Molecular Crystals*, Kodansha-VCH: Tokyo-Berlin, 1993.
7. Tokitoh, N.; Arai, Y.; Sasamori, T.; et al. A Unique Crystalline-State Reaction of An Overcrowded Distibene With Molecular Oxygen: The First Example of a Single Crystal to a Single Crystal Reaction With an External Reagent. *J. Am. Chem. Soc.* **1998,** *120,* 433–434.
8. Ramamurthy, V.; Venkatesan, K. Photochemical Reactions of Organic Crystals. *Chem. Rev.* **1987,** *87,* 433–481.
9. Toda, F., Ed.; *Organic Solid-State Reactions*, Kluwer Academic Publishers: Dordrecht, 2002.
10. Leibovitch, M.; Olovsson, G.; Sceffer, J. R.; Trotter, J. An Investigation of the Yang Photocyclization Reaction in the Solid State: Asymmetric Induction Studies and Crystal Structure – Reactivity Relationships. *J. Am. Chem. Soc.* **1998,** *120,* 12755–12769.
11. Coppens, P.; Benedict, J.; Messerschmidt, M.; et al. Time-Resolved Synchrotron Diffraction and Theoretical Studies of Very Short-Lived Photo-Induced Molecular Species. *Acta Cryst.* **2010,** *A66,* 179–188.
12. Moffat, K. Time-Resolved Biochemical Crystallography: A Mechanistic Perspective. *Chem. Rev.* **2001,** *101,* 1569–1582.
13. Helliwell, J. R., Ed. Time-Resolved Chemistry: From Structure to Function. *Faraday Discuss.* **2003,** *122.*
14. Hoshino, M.; Uekusa, H.; Tomita, A.; et al. Determination of the Structural Features of a Long-Lived Electron-Transfer State of 9-Mesityl-10-methylacridinium Ion. *J. Am. Chem. Soc.* **2012,** *134,* 4569–4572.
15. Whittle, E.; Dows, D. A.; Pimentel, G. C. Matrix Isolation Method for the Experimental Study of Unstable Species. *J. Chem. Phys.* **1943,** *1954,* 22.
16. (a) Kawano, M. In situ Observation of Light-Induced Unstable Radical Species by X-ray Crystallography. *J. Cryst. Soc. Jpn.* **2001,** *43,* 164–168; (b) Kawano, M. X-ray Direct Observation of Reactions and Labile Species on the Basis of Crystal Design. *Bull. Chem. Soc. Jpn.* **2014,** *87,* 577–592.
17. Cohen, M. D.; Schmidt, G. M. J. Topochemistry. Part I. A Survey. *J. Chem. Soc.* **1964,** 1996–2000.
18. Weiss, R. G.; Ramamurthym, V.; Hammond, G. S. Photochemistry in Organized and Confining Media: A Model. *Acc. Chem. Res.* **1993,** *26,* 530–536.
19. Kawamichi, T.; Kodama, T.; Kawano, M.; Fujita, M. Single-Crystalline Molecular Flasks: Chemical Transformation With Bulky Reagents in the Pores of Porous Coordination Networks. *Angew. Chem. Int. Ed.* **2008,** *47,* 8030–8032.
20. (a) Inokuma, Y.; Yoshioka, S.; Ariyoshi, J.; et al. X-Ray Analysis on the Nanogram to Microgram Scale Using Porous Complexes. *Nature* **2013,** *495,* 461–466. Corrigendum: *Nature* **2013**, 501, 262; (b) Inokuma, Y.; Yoshioka, S.; Ariyoshi, J.; Arai, T.; Fujita, M. Preparation and Guest-Uptake Protocol for a Porous Complex Useful for 'Crystal-Free' Crystallography. *Nat. Protoc.* **2014,** *9,* 246–252.
21. Hauser, U.; Oestreich, V.; Rohrweck, H. D. On optical Dispersion in Transparent Molecular Systems, II. Properties of the New Kind of Isomeric Molecular States Generated by Coherent Light. *Z. Phys.* **1977,** *A280,* 125–130.
22. Hauser, U.; Oestreich, V.; Rohrweck, H. D. On Optical Dispersion in Transparent Molecular Systems, III. A New Kind of Inelastic Scattering of Polarized Light by Oriented Molecules Depending Upon the Coherence of the Radiation Field. *Z. Phys.* **1978,** *A284,* 9–19.
23. Woike, T.; Krasser, W.; Bechthold, P. S.; Hassühl, S. Extremely Long-Living Metastable State of $Na_2[Fe(CN)_5NO]_2H_2O$ Single Crystals: Optical Properties. *Phys. Rev. Lett.* **1984,** *53,* 1767.
24. Woike, T.; Kirchner, W.; Schetter, G.; et al. New Information Storage Elements on the Basis of Metastable Electronic States. *Opt. Commun.* **1994,** *106,* 6–10.
25. Rüdlinger, M.; Schefer, J.; Chevrier, G.; et al. Light-Induced Structural Changes in Sodium Nitroprusside ($Na_2(Fe(CN)_5NO)\cdot 2D_2O$) at 80 K. *Z. Phys. B.* **1991,** *83,* 125–130.
26. Pressprich, M. R.; White, M. A.; Coppens, P. Single-Crystal X-ray Analysis of an Electronic Excited State: The Structure Determination of a Metastable State of Sodium Nitroprusside. *J. Am. Chem. Soc.* **1993,** *115,* 6444–6445.
27. Pressprich, M. R.; White, M. A.; Coppens, P. Analysis of a Metastable Electronic Excited State of Sodium Nitroprusside by X-ray Crystallography. *J. Am. Chem. Soc.* **1994,** *116,* 5233–5238.
28. Carducci, M. D.; Pressprich, M. R.; Coppens, P. Diffraction Studies of Photoexcited Crystals: Metastable Nitrosyl-Linkage Isomers of Sodium Nitroprusside. *J. Am. Chem. Soc.* **1997,** *119,* 2669–2678.
29. Kawano, M.; Ishikawa, A.; Morioka, Y.; et al. X-ray Diffraction and Spectroscopic Studies of the Light-Induced Metastable State of a Ethylenediamine Nitrosyl Ruthenium Complex. *J. Chem. Soc. Dalton Trans.* **2000,** 2425–2431.
30. Bowes, K. F.; Cole, J. M.; Husheer, S. L. G.; et al. Photocrystallographic Structure Determination of a New Geometric Isomer of $[Ru(NH_3)_4(H_2O)(\eta^1\text{-OSO})][MeC_6H_4SO_3]_2$. *Chem. Commun.* **2006,** *2448-2450.*
31. Warren, M. R.; Brayshaw, S. K.; Johnson, A. L.; et al. Reversible 100% Linkage Isomerization in a Single-Crystal to Single-Crystal Transformation: Photocrystallographic Identification of the Metastable [Ni(dppe)(η^1-ONO)Cl] Isomer. *Angew. Chem. Int. Ed.* **2009,** *48,* 5711–5714.
32. Stiegman, A. E.; Rice, S. F.; Gray, H. B.; Miskowski, V. M. Electronic Spectroscopy of d^8-d^8 Diplatinum Complexes. $^1A_{2u}$ (d_σ* -> p_σ), ^3E_u (d_{xz},d_{yz} -> p_σ), and $^{3,1}B_{2u}$ (d_σ* -> d_{x2-y2}) Excited States of Tetrakis(diphosphonato)diplatinate(4-), $Pt_2(P_2O_5H_2)_4^{4-}$. *Inorg. Chem.* **1987,** *26,* 1112–1116.
33. Thiel, D. J.; Livins, P.; Stern, E. A.; Lewis, A. Microsecond-Resolved XAFS of the Triplet Excited State of $Pt_2(P_2O_5H_2)_4^{4-}$. *Nature* **1993,** *362,* 40–43.
34. Pinto, F. D. R. M. A.; Sadler, P. J.; Neidle, S.; et al. A Novel di-Platinum(II) Octaphosphite Complex Showing Metal–Metal Bonding and Intense Luminescence; A Potential Probe for Basic Proteins. X-Ray Crystal and Molecular Structure. *J. Chem. Soc. Chem. Commun.* **1980,** 13–15.
35. Kim, C. D.; Pillet, S.; Wu, G.; et al. Excited-State Structure by Time-Resolved X-ray Diffraction. *Acta Cryst.* **2002,** *A58,* 133–137.
36. Novozhilova, I. V.; Volkov, A. V.; Coppens, P. Theoretical analysis of the triplet excited state of the $[Pt_2(H_2P_2O_5)_4]^{4-}$ ion and comparison with time-resolved X-ray and spectroscopic results. *J. Am. Chem. Soc.* **2003,** *125,* 1079–1087.
37. Yasuda, N.; Kanazawa, M.; Uekusa, H.; Ohashi, Y. Excited-State Structure of a Platinum Complex by X-ray Analysis. *Chem. Lett.* **2002,** *31,* 1132–1133.
38. Ozawa, Y.; Terashima, M.; Mitsumi, M.; et al. Photoexcited Crystallography of Diplatinum Complex by Multiple-Exposure IP Method. *Chem. Lett.* **2003,** *32,* 62–63.
39. Hayashi, T.; Maeda, K. Preparation of a New Phototropic Substance. *Chem. Lett.* **1960,** *33,* 565–566.
40. Maeda, K. In *Processes in Photoreactive Polymers;* Krongauz, V. V., Trifunac, A. D., Eds., Chapman & Hall: New York, 1995; pp 90–110. and references therein.
41. Monroe, B. M.; Weed, G. C. Photoinitiators for Free-Radical-Initiated Photoimaging Systems. *Chem. Rev.* **1993,** *93,* 435–448.
42. Kawano, M.; Sano, T.; Abe, J.; Ohashi, Y. The First In Situ Direct Observation of the Light-Induced Radical Pair From a Hexaarylbiimidazolyl Derivative by X-ray Crystallography. *J. Am. Chem. Soc.* **1999,** *121,* 8106–8107.
43. Abe, J.; Sano, T.; Kawano, M.; et al. EPR and Density Functional Studies of Light-Induced Radical Pairs in a Single Crystal of a Hexaarylbiimidazolyl Derivative. *Angew. Chem. Int. Ed.* **2001,** *40,* 580–582.
44. Kawano, M.; Ozawa, Y.; Matsubara, K.; et al. Synchrotron Radiation Structure Analyses of the Light-Induced Radical Pair of a Hexaarylbiimidazolyl Derivative. Origin of the Spin-Multiplicity Change. *Chem. Lett.* **2002,** *31,* 1130–1131.
45. Kawano, M.; Sano, T.; Abe, J.; Ohashi, Y. In Situ Observation of Molecular Swapping in a Crystal by X-ray Analysis. *Chem. Lett.* **2000,** *29,* 1372–1373.

46. White, D. M.; Sonnenberg, J. Oxidation of Triarylimidazoles. Structures of the Photochromic and Piezochromic Dimers of Triarylimidazyl Radicals. *J. Am. Chem. Soc.* **1966,** *88,* 3825–3829.
47. Kirmse, W. *Carbene Chemistry,* 2nd ed.; Academic Press: New York, 1971.
48. Moss, R. A., Jones M. Jr., Eds.; *Carbenes*; Vols 1, 2; Wiley: New York, 1973, 1975.
49. Regitz, M., Ed.; *Carbene(oide) Carbine*, Thieme: Stuttgart, 1989.
50. Moss, R. S.; Turro, N. J. In *Kinetics and Spectroscopy of Carbenes and Biradicals;* Platz, M. S., Ed., Plenum Press: New York, 1990; pp 213–238.
51. Platz, M. S.; Maloney, V. M. In *Kinetics and Spectroscopy of Carbenes and Biradicals;* Platz, M. S., Ed., Plenum Press: New York, 1990; pp 239–352.
52. Moss, R. A. In *Advances in Carbene Chemistry;* Brinker, U. H., Ed., JAI Press: Greenwich, 1994; pp 59–88.
53. Jackson, J. E.; Platz, M. S. In *Advances in Carbene Chemistry;* Brinker, U. H., Ed., JAI Press: Greenwich, 1994; pp 89–160.
54. Bally, T.; Borden, W. T. In *Reviews in Computational Chemistry;* Lipowitz, K. B., Boyd, D. B., Eds., Wiley: New York, 1998.
55. Kawano, M.; Hirai, K.; Tomioka, H.; Ohashi, Y. Structure Analysis of a Transient Triplet Carbene Trapped in a Crystal. *J. Am. Chem. Soc.* **2001,** *123,* 6904–6908.
56. Kawano, M.; Hirai, K.; Tomioka, H.; Ohashi, Y. Structure Determination of Triplet Diphenylcarbenes by In Situ X-ray Crystallographic Analysis. *J. Am. Chem. Soc.* **2007,** *129,* 2383–2391.
57. Scriven, E. F. V., Ed.; *Azides and Nitrenes, Reactivity and Utility*, Academic Press: New York, 1984.
58. Kim, S. J.; Hamilton, T. P.; Shaefer, H. F., III Phenylnitrene: Energetics, Vibrational Frequencies, and Molecular Structures. *J. Am. Chem. Soc.* **1992,** *114,* 5349–5355.
59. Sasaki, A.; Mahé, L.; Izuoka, A.; Sugawara, T. Chemical Consequences of Arylnitrenes in the Crystalline Environment. *Bull. Chem. Soc. Jpn.* **1998,** *71,* 1259–1275.
60. Karney, W.; Borden, W. T. In *Advances in Carbene Chemistry;* Brinker, U. H., Ed.; 3; Elsevier, 2001; p 205.
61. Takayama, T.; Kawano, M.; Uekusa, H.; Ohashi, Y. Crystalline-State Photoreaction of 1-Azido-2-nitrobenzene–Direct Observation of Heterocycle Formation by X-Ray Crystallography. *Helv. Chim. Acta* **2003,** *86,* 1352–1358.
62. (a) Ohashi, Y. Dynamical Structure Analysis of Crystalline-State Racemization. *Acc. Chem. Res.* **1988,** *21,* 268; (b) Boldyreva, E. The Concept of the 'Reaction Cavity': A Link Between Solution and Solid-State Chemistry. *Solid State Ionics* **1997,** *101–103,* 843–849.
63. Kawano, M.; Takayama, T.; Uekusa, H.; et al. Structure Analysis of Photo-Induced Triplet Phenylnitrene Using Synchrotron Radiation. *Chem. Lett.* **2003,** *32,* 922–923.
64. Das, A.; Van Trieste, G. P., III; Powers, D. C. Crystallography of Reactive Intermediates. *Comments Inorg. Chem.* **2020,** *40,* 116–158.
65. Das, A.; Reibenspies, J. H.; Chen, Y.-S.; Powers, D. C. Direct Characterization of a Reactive Lattice-Confined Ru_2 Nitride by Photocrystallography. *J. Am. Chem. Soc.* **2017,** *139,* 2912–2915.
66. Das, A.; Maher, A. G.; Telserr, J.; Powers, D. C. Observation of a Photogenerated Rh_2 Nitrenoid Intermediate in C–H Amination. *J. Am. Chem. Soc.* **2018,** *140,* 10412–10415.
67. Das, A.; Chen, Y.-S.; Reibenspies, J. H.; Powers, D. C. Characterization of a Reactive Rh_2 Nitrenoid by Crystalline Matrix Isolation. *J. Am. Chem. Soc.* **2019,** *141,* 16232–16236.
68. Fujita, M.; Oguro, D.; Miyazawa.; et al. Self-Assembly of Ten Molecules Into Nanometre-Sized Organic Host Frameworks. *Nature* **1995,** *378,* 469–471.
69. Kusukawa, T.; Fujita, M. Self-Assembled M_6L_4-Type Coordination Nanocage With 2,2'-Bipyridine Ancillary Ligands. Facile Crystallization and X-ray Analysis of Shape-Selective Enclathration of Neutral Guests in the Cage. *J. Am. Chem. Soc.* **2002,** *124,* 131576–131582.
70. Geoffroy, G. L.; Wrighton, M. S. *Organometallic Photochemistry*, Academic: New York, 1979.
71. Moser, W. R.; Slocum, D. W. Homogeneous Transition Metal Catalyzed Reactions. *Am. Chem. Soc.* **1992**. Washington, DC.
72. Kawano, M.; Kobayashi, Y.; Ozeki, T.; Fujita, M. Direct crystallographic observation of a coordinatively unsaturated transition-metal complex in situ generated within a self-assembled cage. *J. Am. Chem. Soc.* **2006,** *128,* 6558–6559.
73. Hoshino, M.; Khutia, A.; Xing, H.; Inokuma, Y.; Fujita, M. The Crystalline Sponge Method Updated. *IUCrJ* **2016,** *3,* 139–151.
74. Takaoka, K.; Kawano, M.; Ozeki, T.; Fujita, M. Crystallographic Observation of an Olefin Photodimerization Reaction That Takes Place via Thermal Molecular Tumbling Within a Self-Assembled Host. *Chem. Commun.* **2006,** *1625–1627*.
75. Haga, N.; Takayanagi, H.; Tokumaru, K. Mechanism of Photodimerization of Acenaphthylene. *J. Org. Chem.* **1997,** *62,* 3734.
76. Inokuma, Y.; Kawano, M.; Fujita, M. Crystalline Molecular Flasks. *Nat. Chem.* **2011,** *3,* 349–358.
77. Kobayashi, Y.; Kawano, M.; Fujita, M. Networking a Hollow Cage Via Guest Coordination. *Chem. Commun.* **2006,** *4377–4379*.
78. Yoshizawa, M.; Tamura, M.; Fujita, M. AND/OR Bimolecular Recognition. *J. Am. Chem. Soc.* **2004,** *126,* 6846–6847.
79. Ohmori, O.; Kawano, M.; Fujita, M. A Two-in-One Crystal: Uptake of Two Different Guests Into Two Distinct Channels of a Biporous Coordination Network. *Angew. Chem. Int. Ed.* **2005,** *44,* 1962–1964.
80. Ohmori, O.; Kawano, M.; Fujita, M. Construction of Biporous Coordination Networks via π–π Interaction. *CrystEngComm* **2005,** *7,* 255–259.
81. Kawano, M.; Kawamichi, T.; Haneda, T.; Kojima, T.; Fujita, M. The Modular Synthesis of Functional Porous Coordination Networks. *J. Am. Chem. Soc.* **2007,** *129,* 15418–15419.
82. (a) Cohen, S. M.; Wang, Z. Postsynthetic Covalent Modification of a Neutral Metal-Organic Framework. *J. Am. Chem. Soc.* **2007,** *129* (41), 12368–12369; (b) Wang, Z.; Cohen, S. M. Postsynthetic Modification of Metal-Organic Frameworks. *Chem. Soc. Rev.* **2009,** *38,* 1315–1329.
83. Haneda, T.; Kawano, M.; Kawamichi, T.; Fujita, M. Direct Observation of the Labile Imine Formation Through Single-Crystal-to-Single-Crystal Reactions in the Pores of a Porous Coordination Network. *J. Am. Chem. Soc.* **2008,** *130,* 1578–1579.
84. Kawamichi, T.; Inokuma, Y.; Kawano, M.; Fujita, M. Regioselecitive Huisgen Cycloaddition Within Porous Coordination Networks. *Angew. Chem. Int. Ed.* **2010,** *49,* 2375–2377.
85. Kawamichi, T.; Haneda, T.; Kawano, M.; Fujita, M. X-ray Observation of a Transient Hemiaminal Trapped in a Porous Network. *Nature* **2009,** *461,* 633–635.
86. Steudel, R.; Eckert, B. Solid Sulphur Allotropes. *Top. Curr. Chem.* **2003,** *230,* 1–79.
87. Steudel, R.; Steudel, Y.; Wong, M. W. Speciation and Thermodynamics of Sulphur Vapor. *Top. Curr. Chem.* **2003,** *230,* 117–134.
88. Meyer, B. Elemental Sulphur. *Chem. Rev.* **1976,** *76,* 367–388.
89. Ohtsu, H.; Choi, W.; Islam, N.; Matsushita, Y.; Kawano, M. Selective Trapping of Labile S_3 in a Porous Coordination Network and the Direct X-ray Observation. *J. Am. Chem. Soc.* **2013,** *135,* 11449–11452.
90. McCarthy, M. C.; Thorwirth, S.; Gottlieb, C. A.; et al. Rotational Spectroscopy and Equilibrium Structures of S_3 and S_4. *J. Chem. Phys.* **2005,** *123*, 054326.
91. Ichikawa, M.; Kimura, T.; Fukuoka, A.; Inui, T. Ship-In-Bottle Synthesis of Sterically Crowded Fe-Phthalocyanines in NaY Zeolite Hosts and Their Catalytic Behaviour in Regioselective Oxidation of Alkanes. In *Studies in Surface Science and Catalysis;* Namba, S., Tatsumi, T., Eds.; 60; Elsevier, 1991; p C335-342.
92. Maleki, B.; Salehabadi, H. Ammonium Chloride; as a Mild and Efficient Catalyst for the Synthesis of Some 2-Arylbenzothiazoles and Bisbenzothiazole Derivatives. *Eur. J. Chem.* **2010,** *4,* 377–380.
93. Kitagawa, H.; Ohtsu, H.; Kawano, M. Kinetic Assembly of a Thermally Stable Porous Coordination Network Based on Labile CuI Units and the Visualization of I_2 Sorption. *Angew. Chem. Int. Ed.* **2013,** *52,* 12395–12399.
94. Ohtsu, H.; Kawano, M. Kinetic Assembly of Coordination Networks. *Chem. Commun.* **2017,** *53,* 8818–8829.
95. Hathaway, B. J. In *Comprehensive Coordination Chemistry;* Wilkinson, G., Gillard, R. D., McCleverty, J. A., Eds.; vol. 5; Pergamon: Oxford, 1987; pp 533–774.
96. Ohara, K.; Yamaguchi, K. Cold-Spray Ionization Mass Spectrometric Detection of a Coordination Oligomer. *Anal. Sci.* **2012,** *28,* 635–637.
97. Kitagawa, H.; Ohtsu, H.; Cruz-Cabeza, A. J.; Kawano, M. Isolation and Evolution of Labile Sulphur Allotropes via Kinetic Encapsulation in Interactive Porous Networks. *IUCrJ* **2016,** *3,* 232–236.
98. Choi, W.; Ohtsu, H.; Matsushita, Y.; Kawano, M. Safe P_4 Reagent in a Reusable Porous Coordination Network. *Dalton Trans.* **2016,** *45,* 6357–6360.

99. Ohtsu, H.; Kawano, M. Br_2 Induced Oxidative Pore Modification of a Porous Coordination Network. *Dalton Trans.* **2016,** *45,* 489–493.
100. Lang, J.-P.; Xu, Q. F.; Yuan, R. X.; Abrahams, B. F. $\{[WS_4Cu_4(4,4'\text{-bpy})_4][WS_4Cu_4I_4(4,4'\text{-bpy})_2]\}_\infty$—An Unusual 3D Porous Coordination Polymer Formed From the Preformed Cluster $[Et_4N]_4[WS_4Cu_4I_6]$. *Angew. Chem. Int. Ed.* **2004,** *43,* 4741–4745.
101. Holzer, W.; Murphy, W. F.; Bernstein, H. J. Resonance Raman Effect and Resonance Fluorescence in Halogen Gases. *J. Chem. Phys.* **1970,** *52,* 399–407.
102. Congeduti, A.; Nardone, M.; Postorino, P. Polarized Raman Spectra of a Single Crystal of Iodine. *Chem. Phys.* **2000,** *256,* 117–123.
103. Bondi, A. van der Waals Volumes and Radii. *J. Phys. Chem.* **1964,** *68,* 441–451.

10.13 X-ray transient absorption spectroscopies in the study of excited state structures

Stuart A. Bartlett, Diamond Light Source Ltd, Didcot, United Kingdom

© 2023 Elsevier Ltd. All rights reserved.

10.13.1	**Introduction**	**344**
10.13.2	**X-ray transient absorption experimental setups**	**345**
10.13.2.1	Sampling methods	346
10.13.2.2	Acquisition of X-ray transient absorption data	346
10.13.3	**A history of X-ray transient absorption spectroscopy**	**347**
10.13.4	**Recent studies and experiments using X-ray transient absorption spectroscopy**	**348**
10.13.4.1	Experiments at synchrotrons	348
10.13.4.1.1	Photosensitizers	348
10.13.4.1.2	Non- reversible photoreactions	354
10.13.4.1.3	Further EXAFS analysis using TR-XAS data collection method	355
10.13.4.1.4	Photoactive enzymes mimics	357
10.13.5	**TRXAS experiments at X-ray free electron lasers**	**361**
10.13.5.1	History of free-electron lasers	362
10.13.5.2	"Pump-probe" data collection at XFEL	364
10.13.5.3	TRXAS experiments conducted at XFEL	365
10.13.6	**Transient X-ray emission spectroscopy or pump-probe XES**	**367**
10.13.6.1	Transient X-ray emission studies of iron complexes in solution	367
10.13.7	**Transient X-ray spectroscopy of metalloporphyrin chemistry at XFEL**	**372**
10.13.8	**Final remarks**	**375**
References		**377**

Abstract

X-ray absorption spectroscopy (XAS) has become a very important analytical method for studying reactions under operating conditions and the method relies heavily on the use of tunable, high intensity X-ray radiation generated at synchrotron and X-ray Free Electron Laser (XFEL) facilities. Advances in methodology and instrumentation mean that X-ray absorption spectra can be measured in short time periods and can be used to probe catalytic reactions on a microsecond timescale. In this chapter the focus is TRansient X-ray Absorption Spectroscopy (TR-XAS) which operates effectively on submicrosecond timescales and is targeted at elucidating structural changes in molecular systems under photoactivation. The experimental set ups combine the use of laser pulses (to pump the reactions) with the X-ray pulses from the synchrotron (to probe the activated species) are described as well as the best methods to prepare and deliver the chemical samples into the reaction chamber. Recent results showing the benefits of using XAS in establishing the nature of catalytic processes are highlighted for a range of transition metal-based catalytic systems.

10.13.1 Introduction

X-ray absorption spectroscopy (XAS) has become an invaluable characterization method to study materials under working conditions. XAS can be collected in a wide variety of homogenous or inhomogeneous states and can provide key insights into the physical properties of materials or catalysts that may operate at elevated temperatures, pressures and in highly mixed medias for example. In catalysis, it is often the case that the starting material is a stable chemical material and requires some 'activation' step, in which it becomes a highly reactive species allowing it to circumvent high activation barriers to transform substrates to product. Due to constrains in conditions, it becomes very difficult to identify the active species which may only survive in harsh experimental conditions, have only a very short lifetime due to its reactive nature or there being only a small fraction of the true catalytic species present. Here XAS really comes into its own, where techniques such as X-ray scattering, although can provide very detailed structural analysis, become limited due to the sample constraints. Also other spectroscopies such as IR and UV can provide important physical data but often are unable to give the required detail that XAS can provide as a specific elemental probe. Recent advances in XAS now give very fast collection times, and with the versatility of the analysis, has become a critical technique in the study of catalytic metal-containing materials. With oscillating monochromators, specialist XAS techniques, such as so called Quick XAS, it is possible to obtain a full spectrum in 100s milliseconds.

This chapter will have a focus on timescales even shorter than Quick XAS. It will look at the current setups, methods and science using case studies conducted on microsecond timescales and faster, so called TRansient X-ray Absorption Spectroscopy (TR-XAS). This is a technique that specifically aims to elucidate the primary changes of chemicals after activation, in most cases using a laser to enact the first electron transitions that precede the subsequent reactive changes. It is these important changes that will dictate the reactivity and chemical prospect of highly important materials such as catalysts. On the microsecond timescale this often incorporates the first chemical bond formations and molecular rearrangements. On the picosecond timescale or less the investigations turn towards the first electronic changes and bond displacements of the chemical in question. On this timescale, guided by the ligand influences and environmental factors, the activation method will determine the path, the efficiency and the lifetime of important catalytic materials. By understanding the most fundamental changes after activation we can properly create new generations of materials that can help realize some important scientific challenges such as low cost and stable solar conversion, a wide variety of chemical energy storage materials or new highly efficient fuel cells.

10.13.2 X-ray transient absorption experimental setups

X-ray absorption spectroscopy (XAS) is a spectroscopic technique that provides electronic and structural information on materials out to commonly 5 or 6 Å of the absorbing element. It works by tuning the incoming X-ray photon energy into a sample using a crystalline monochromator, the X-rays can excite or eject core electrons of the element of interest. The electrons are held at different energies in their elemental orbitals, known as the binding energy. When the X-ray photons are at or above this binding energy, the electron is removed. Different electrons can be targeted creating so called 'edges' in the spectrum, observed as a dramatic rise in the absorption of the incoming X-rays as the energy is scanned over the binding energy of the electrons. The X-rays are being absorbed by the element and ejecting electrons as photo electrons as a result. The origin of the electrons dictate the name and type of XAS experiment, named by which core electron is excited corresponding to principal quantum numbered orbital from which it originates, most commonly 1,2 or 3, in XAS called the K-, L-, and M-edges, respectively. There are three main regions found on a spectrum generated by XAS data. Initially the pre-edge region consists of the first X-ray absorptions determined by the transition to the lowest unoccupied states of the element. Typically in a 3d transition metal K edge spectrum, this could be the promotion of 1s electron to unoccupied 3d orbitals, for example, typically occurring 20 eV before the absorption edge. The second is called the X-ray Absorption Near-Edge Structure (XANES) region. This is the appearance of the 'edge' in the spectrum and consist of dipole transitions between the core level to unoccupied molecular orbitals, core to quasi-bound states (virtual molecular orbitals just before the continuum where the electron escapes as a photoelectron. Multiple scattering states characterized by short lifetimes and broad peaks) and core to continuum (core electron has sufficient kinetic energy to escape into the continuum as a photoelectron, i.e., photoelectric effect). Often 50–100 eV above the absorption edge. The third region is classed as the EXAFS (Extended X-ray Absorption Fine Structure). This is where the initial excited electron has absorbed X-ray photons well above the binding energy giving it a high kinetic energy to escape the atom as a photoelectron. At this point the photoelectron can scatter and induce backscattering with neighboring atoms, where the backscattering off neighboring atoms can be approximated by single scattering events. This region is defined as roughly 100 eV and beyond the absorption edge. The probability of absorption of the X-ray is highest at the binding energy of the electron and so, as the energy of the incoming X-ray photon increases, the electron absorbs higher energy photons giving a greater kinetic energy to the resulting photoelectron. The greater the kinetic energy the further the photoelectron can travel giving more detailed structural analysis of the molecule through more detailed backscattering. Yet EXAFS data is hampered not only by mean free path of the electron as it travels further away from the absorbing atom, but also one must consider that the probability of the electron absorbing incident X-ray photons at energies above the binding energy decreases as the energy increases. Therefore, the signal decreases the higher in energy the scan reaches making EXAFS harder to distinguish especially when trying to resolve details that lie far from the absorbing atom. Once the X-ray spectrum has been collected, the data analysis involves modelling through a variety of different software systems using the XAS theory to generate model spectra to compare statistically to experimental data and get important physical information from the experiment.

In normal scanning XAS, getting a full range scan of the EXAFS region can take around 20 and 40 min for a stepping scan, where the monochromator adjusts the Bragg angle to select each energy point in turn, where the absorption of X-rays can be measured through the sample. Faster scans can be collected using quick EXAFS (QuEXAFS) where the monochromator is quickly oscillated through an energy range, being able in some cases to give full scans on the millisecond timescale. Faster still is an energy dispersive mode where the full energy range of the scan is collected by selecting an appropriate band width which covers the desired energy range of the element of interest and thus the data is collected completely in one shot. Although the energy dispersive mode does have its limitations in that it can only be run in transmission mode XAS where the detector must have a readout time on the millisecond timescale and a high energy resolution to accurately discern different incident energies.

Typically, TR-XAS will utilize a pump-probe setup to collect data from sub milliseconds down to picoseconds or femtoseconds at a XFEL. In a TR-XAS experiment setup, the beamline will move the monochromator in the same manner as for a step scan. The time resolution is provided by a fast readout detector. This will often be a simple detector allowing a faster collection speed. Here, the energy resolution is provided by the monochromator upstream on the beamline and the detector needs only to count the incoming photons in florescence mode, thus most commonly an avalanche photo diode is used. In the following section, the experimental setups will be introduced in general looking at how the samples are commonly presented to the beam, the types of detector used for the different setups and how the timing is discerned.

10.13.2.1 Sampling methods

Most studies to date have been carried out on samples in solution or crystals/nanoparticles suspended in solution. Solid samples tend to degrade quickly due to being exposed to laser and X-ray beam for long periods of time. Samples suspended or in solution can be refreshed and cycled during the data collection. The most common method to reduce sample degradation is by creating a flowing jet of the solution, where the solution is not held in any vessel or glass capillary but is ejected out of a nozzle to give a smooth jet to be collected after a few centimeters travel. This significantly decreases local heating and sample degradation due to beam exposure one would expect on a closed capillary for example. What is often the case with capillaries, is the glass surface heats with the X-ray and laser beam presenting a nucleation point for the sample in solution. This then heats and degrades quickly, and in some cases can cause damage to the capillary. Having an open jet circumvents these issues, where the heat is quickly dissipated by the flowing jet but the setup is often more complicated. Such a setup requires a large reservoir which must contain more than enough solution to fill the entire flow system. A pump is attached to flow the solution through a nozzle creating a jet. In most cases this a peristaltic pump which tends to have low pulsing flow and the added advantage that the solution can remain in PTFE tubing without having to flow into the pump. Here a gear is used to compress the tubing to push the solution through. There also are specifically designed Diaphragm pumps available that provide low pulsing by transferring the pulsing to the inlet of the pump rather than the flow outlet to the jet which would cause issues during data collection. The solution then flows from the pump through the jet nozzle, often a smoothly cut and strongly held metal or glass pipe that allows the solution to be ejected into the surrounding air. This is allowed to flow by gravity for 5–10 cm to keep a smooth laminar flow and adequate space for an X-ray and Laser beam to be lined up. A good rule of thumb is if the jet looks like it is not flowing, it is very stable with no pulsing that it will be good for pump-probe collection. Typically they are round and cylindrical but in some cases they can be flat.

In many cases, the jet will need to be housed in a closed chamber that will hold an inert atmosphere, ideally helium, as it is less absorbing to X-rays. In many cases the photoactive species may be oxygen sensitive and will degrade the sample or shorten the excited state lifetime after laser absorption. The jet is housed in a chamber with windows to allow for laser and X-ray entry and exit, along with the detector window. This should be easily assembled and disassembled as window fouling can be a common occurrence.

The jet is then captured into a wide mouth which allows for flowing back to the reservoir to be recycled. Here this is often done by gravity alone and so it is useful to have wide tubing diameter to allow easy flow back into the reservoir without any backfilling and overspill into the chamber.

10.13.2.2 Acquisition of X-ray transient absorption data

Key to a successful experiment is the methodology used in collecting the data and the synchronizing of the laser pulse and the X-ray data collection. The principle to get fast data time points to sub millisecond levels, is that the X-ray data is 'binned' into time frames as it is collected by the detector. At microsecond timescales this can be implemented through software as the data is collected using a Time Frame Generator at the beamline which essentially creates a designated number of time frames for the data as it is collected based on the selected time of each frame. If ultrafast timeframes are required, at the picoseconds level, for example, this is generally induced by the synchrotron clock. A working principle of the synchrotron is not that it is a continuous source and it actually operates as discrete electron bunches traveling around the ring. As each bunch passes through a bending magnet or undulator, it emits X-rays down the beamlines, typically each burst lasting $\sim$100 ps. There are then natural delays between bunches which provide a natural break between of the X-ray shots. Depending on the mode they can be smaller bunches at 2–5 ns or larger bunches on the 100s ns separation. There are also hybrid modes where there is one section which is a longer train of small electron bunches separated by 2–5 ns, followed by a long delay of 100s ns to one large bunch of electrons. At very fast time scales, generally the more isolated large bunch is utilized only to provide accurate time resolution, allowing for fine tuning of the laser pump-X-ray probe overlap whilst also providing a high enough flux for X-ray data.

It is important to accurately time the laser to the data collection, as there are two key phases of the data to be able to identify, the 'after' laser data and the 'before' laser data. Every laser flash is considered time zero and provides the restart of the reaction. One method for this setup is to take every laser pulse as the start of the reaction, the laser can become the 'master' to the rest of the data collection setup. For example, the Time Frame Generator (TFG) will fall in phase with the laser and tell the detector setup to appropriately time the data collection in line with when the laser was fired. When the data is output, the binning of the X-ray data is time stamped as to where the laser was pulsed. Another setup is that the TFG is the 'master' and signals to the laser when to fire to output the data in the same manner. On the picosecond timescale, the TFG is often too slow to signal and thus the laser linked to the synchrotron clock itself where it can inform the laser as each X-ray pulse is sent through the beamline and thus the laser can fire just before each bunch arrives. Once the X-ray data has been collected and appropriately time stamped, the time frames can be classed as 'before the laser has fired' (data consisting of the ground state or reactants only), and 'after the laser has fired' (data consisting of the excited state or photoproducts). Once the timing is setup, vitally it must be made sure that the before laser data only consists of unreacted ground state material. TRXAS is analyzed through data extraction arising as a difference between ground state and the excited state spectra. If the ground state spectra is a mix of excited state and ground state, the data will not be possible to accurately analyze. This requires consideration of the sample setup.

This relies on a set of variables of the sample setup itself, the solution flow speed, the jet size and the laser repetition rate. The setup consists of an overlapped X-ray and laser spot at the liquid jet, where the X-ray spot sits within the laser spot. One must be sure

that by the time the laser pulse hits the sample, the laser spot is entirely refreshed with new inactivated sample otherwise the 'before' laser data will not be pure. This requires consideration as to the amount of time frames collected. As an example setup, if every time frame collected is 1 μs and the detector is setup to collect for 40 μs between each laser pulse, the laser is operating on repletion rate of 25 KHz (laser pulse every 40 μs). This requires that following a laser pulse, the last 10 μs (30–40 μs) of the data collection period must be clean unreacted solution. To calculate this, assuming the jet is cylindrical, the volume of solution at time zero is calculated using height of the beam and size of the jet. From this a flow rate can be extrapolated given that the beam spot size needs to be refreshed after 30 μs. It becomes a careful play between high rep rate of the laser, meaning that per second more laser pulses are fired thus gaining data more quickly, making more efficient use of the X-rays, yet still allowing time for the solution to be entirely refreshed between laser pulses. Also, the flow speed cannot be too high otherwise all the excited state material is taken out of the beam too quickly. Hence experiments require very careful planning to get successful data collection.

Once the data has been collected and saved to file, the next process is to extract the difference spectrum. This is where the after laser data is averaged up to the desired time point after the laser pulse and subtracted from the before laser data. The normalization of the data is often done as the data is collected by normalizing with beam signal before it hits the sample, taking out any deviations from the synchrotron and optics of the beam line. What is observed is a so called bleaching of the ground state species seen as a negative absorption edge against energy axis.

Once this difference data has been collected, the difficult question arises of how it can be analyzed to gain useful information as clearly it cannot be analyzed in the typical manner of most XAS data. Over the following sections the various setups and data collection methods alongside the science cases will be discussed to highlight how the data is collected and analyzed to gain meaningful physical properties at ultrafast XAS timescales.

10.13.3 A history of X-ray transient absorption spectroscopy

TR-XAS as conducted by light activation, also known as the flash photolysis technique, was first described in 1950 by George Porter and Ronald Norrish (Fig. 1).[1] Using high intensity flash tubes as used in World War II for aerial photography, were applied to initiate photochemical reactions. The setup involved a flash photolysis tube as the pump source alongside a quartz reaction vessel filled with the substrate. Up steam sat the spectro-flash as the probe source to analyze the resultant photo reaction. Using this setup, substrates such as chlorine and carbon disulfide were investigated to look at the decomposition pathways after flash photolysis as a proof of concept. As quoted in the publication "The main purpose here has been to illustrate the power of this method for the investigation of fast reactions, and for this reason a wide range of substances has been studied. It is believed that the results are sufficient to show that the methods of flash photochemistry and spectroscopy provide a valuable weapon for the study of the more elusive of chemical compounds".

It was for studies such as these, investigating transient absorption spectroscopy on the microsecond timescale, for which George Porter and Ronald Norrish were awarded the 1967 Nobel Prize in Chemistry. This opened up a new time domain for experimental investigations and it continued to develop with increasing time resolution reaching femtoseconds in the 1990s. These were achieved by Ahmed Zewail winning Nobel Prize in 1999. Zewail used an ultrafast laser to inject two pulses, a powerful pump to initiate the excited state followed by a weaker probe pulse for detection. The time interval was varied between the pulses by rerouting the probe pulse to make a detour via mirrors. The data was then compared with theoretical simulations based on results of quantum chemical

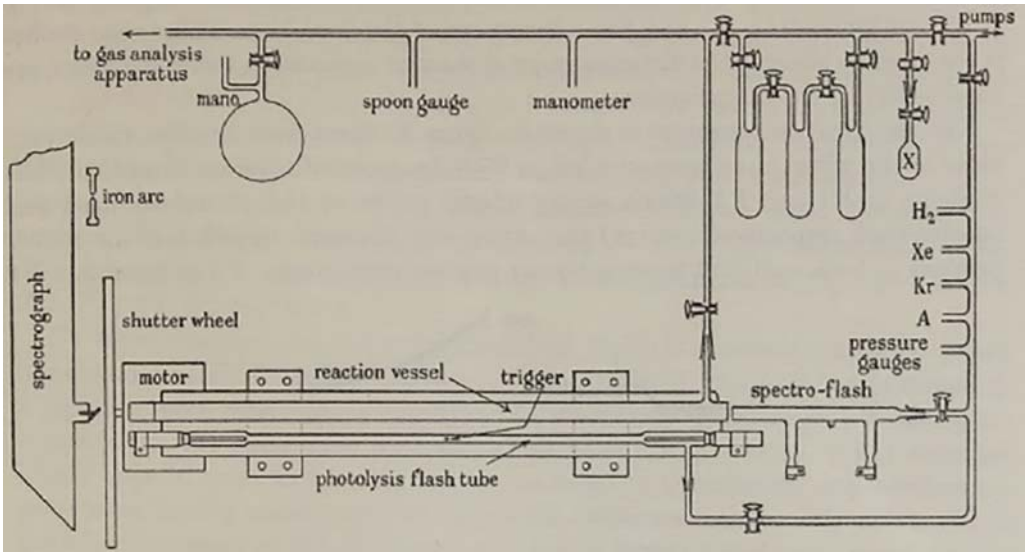

Fig. 1 Diagram of Porter and Norrish experimental setup for early flash photolysis measurements.[1]

calculations of spectra and energies for the molecules in their various states. This was proved by studying the disintegration of iodocyanide. He was able to observe the iodine-carbon bond breaking in the transition state, where the whole reaction takes place in 200 femtoseconds.[2] The press release of the Nobel Committee stated of Zewail's work: "We have reached the end of the road: no chemical reactions take place faster than this. With femtosecond spectroscopy we can for the first time observe in 'slow motion' what happens as the reaction barrier is crossed and hence also understand the mechanistic background to Arrhenius' formula for temperature dependence and to the formulae for which van't Hoff was awarded his Nobel Prize."[3] To date this setup is still typical of the experiments carried out in TR-XAS; using the pump-probe approach using signal synchronization to collect accurate data. The analysis of this data will often require comparisons with experimental reference data and theoretical simulations to elucidate the short lived transition states.

10.13.4 Recent studies and experiments using X-ray transient absorption spectroscopy

TR-XAS using pump-probe experiments often involve materials that will only have a fraction of the material that reaches the excited state after flash photolysis. Considering catalysis in general uses small concentrations of the catalyst, gaining information of a fraction of this concentration that has been activated is incredibly challenging and requires high flux X-ray sources. In the following case studies, two main facilities currently able to deliver useful information of light activated and excited state inorganic materials; synchrotrons and X-ray free electron lasers (XFEL), will be discussed.

10.13.4.1 Experiments at synchrotrons

10.13.4.1.1 Photosensitizers

A rich area of research in inorganic photochemistry is synthesizing complexes that can mimic photosynthetic transformations as observed in nature. Solar driven transformations are seen as a viable route to provide a sustainable sources of fuel through either directly producing fuel in the form of H_2 gas or as alternative to energy storage. This could, for example, involve splitting H_2O to produce H_2 and O_2 to be stored, where they are reacted at a later date to release the energy as an exothermic reaction. A potential alternative to batteries for long term and high power energy storage.[4–6] A popular route to achieve this transformation is the use of photosensitizers. A photosensitizer is a molecule that absorbs the incident photon and is elevated from the ground state to an excited singlet state, followed by a spin conversion by intersystem crossing from singlet to triplet state. The triplet state is much longer lived than the singlet excited state increasing the probability it will interact with a substrate inducing a chemical change. Once the energy transfer is completed the photosensitizer will return to the ground state to restart the process.[7] Organometallic photosensitizers typically contain a metal atom chelated to organic ligands with the ability to absorb photons paving routes for electrons to move from the metal bound electrons to anti-bonding, empty orbitals on the ligand frameworks, typically called metal to ligand charge transfers (MLCT). Identifying the key structural factors that can influence how easy electrons can make these relays through excited state structural dynamics and how long the electrons remain in a high energy state before decaying to a low energy state, i.e., the excited state lifetime, is critical to help towards a precise understanding and stabilization of these types of photosensitizers. Importantly, this field of research also looks to study a broad-range of earth abundant light-harvesting units with key properties such as controlled redox and luminescence, aiming to establish a detailed understanding of structure-function relationships.

The relationship between electronic and geometric changes of photoexcited materials is key to understanding charge-transfer processes. In metal complexes, understanding this fundamental process will be strongly influenced by the ligands. Research into the initial photo activation mechanism of organometallic compounds is an active area aiming to produce new generations of transition-metal-based compounds to perform the necessary reductive – oxidative photochemical transformations. Capturing the structural changes during photoexcitation is of special interest in order to provide efficient intermolecular charge transfer.[8,9] In H_2 evolution reactions these are often composed of electron rich, expensive transition metal such as ruthenium, iridium or platinum. These have electron rich d-orbitals with strained π-electron accepting ligands, often based on pyridyl motifs, having a nitrogen as a binding site of the metal. Recent advances have now looked towards cheaper metals such as chromium, copper and zinc.[10] One of the initial TR-XAS studies was performed on Ruthenium(II)-tris-2,2′-bipyridine, ($[Ru(bpy)_3]^{2+}$) complex in 2006.[11]

$[Ru(bpy)_3]^{2+}$ excited-state properties have been extensively studied by spectroscopy.[12–14] The key long lived so called triplet state is generated by light excitation of a metal-centered valence electron from the singlet ground state through a MLCT (metal to ligand charge transfer) to one of the bipyridine ligands. This undergoes intersystem crossing to a long-lived triplet state in less than 300 fs,[15,16] with a lifetime of about 600 ns.[17] TR-XAS was used to investigate the photoactivation of this widely studied complex, aiming to understand the underlying chemical properties which could then be applied to cheaper materials to provide the same outcome or better. TR-XAS was able to provide a picture of the electronic and molecular structure of the ground and excited states of $[Ru(bpy)_3]^{2+}$ using static and picosecond-resolved XANES and EXAFS. This research demonstrated particularly well how XAS is a vital tool in getting an insight into all the key physical properties of important inorganic compounds. It was the first picosecond resolved XANES and EXAFS study of a Ru-polypyridine compound probing both L_2 and L_3 edges of the metal atom. This was conducted at the Advanced Light Source (ALS) using a circulating free flowing jet of a salt of $[Ru(bpy)_3]^{2+}$ dissolved in deionized water. The experiment utilized a Ti:sapphire femtosecond laser at 1 kHz repetition rate to excite the sample at 400 nm, ranging 100–550 joules per pulse energy range. The X-ray probe from the synchrotron consisted of 70 ps pulses at 2 kHz repetition rate. This

experiment aimed to achieve X-ray data at 50 ps or less after laser excitation. At small time delays between laser and X-ray pulses, natural fluctuations in the timing of laser and X-rays pulses needs to be monitored and quantified to be sure the X-ray source is probing the desired excited state of the material at the chosen time. This is known as timing jitter. The limit of the time resolution was found to be 1 ps. Using this setup, a detailed analysis of the XANES of the L_2 and L_3 edges of the $[Ru(bpy)_3]^{2+}$ spectra were conducted. The difference spectra is shown below in Fig. 2.

Fig. 2 shows the ground state spectra of the $[Ru(bpy)_3]^{2+}$ complex (i.e., with no laser irradiation) and the difference spectra collected 50 ps after laser excitation. Previous laser studies had shown the triplet MLCT (^{3}MLCT) state is the dominant species in the 10–100 ps time range. Scanning time delays through 50 ps and 70 ps between laser and X-ray probe gave no significant change in the difference XAS, it was safely assumed that the XAS changes were due to the longer lived 3MLCT product state. From the difference the XAS spectrum of the photoproduct (Fig. 2c) was reconstructed using the equation[18]:

$$T(E,t) = f(t) \times \left[A_{es}(E,t) - A_{gs}(E)\right] \quad (1)$$

Where f(t) is the relative population of the excited complex species at time t, T(E,t) is the transient difference absorption spectrum consisting entirely of the photoinduced changes from the ground-state complex spectrum, $A_{gs}(E)$, to the excited complex spectrum, $A_{es}(E,t)$, at time t following photoexcitation. The time-dependent photolysis yield, f(t), influences the spectral shape of the excited-state XAS $[A_{es}(E,t)]$, where it was measured independently in laser-only transient absorption experiments. Thus Fig. 2c shows the recovered X-ray absorption spectrum of the photo excited species indicating an additional spectral feature (A') at both L-edges.

For the XANES analysis the line shapes were analyzed using a multiplet simulation code.[19] The starting point is to calculate the energy levels of the ground state, multiplet state and final state. The crystal field effects were then stepwise included with spin-orbit interactions. Finally the dipole selection rules of all states for the X-ray absorption process were applied and convoluted with the core hole lifetime and monochromator widths. This gave good agreement with the data that the 3MLCT state was dominant at 50 ps. The D from Fig. 1 (a) represents a clear EXAFS feature and is shifted to higher energy by 1 eV after photoexcitation, pointing to a bond contraction of the Ru-N nearest-neighbor distance. Natoli et al.[20] outlaid the theoretical details to precisely measure light-driven energetic shifts as a quantification of small transient structural changes. This analysis indicated a contraction of the Ru—N bonds by 0.03 Å on average. In the ground state the complex adopts a close to, but not exact octahedral geometry due to the rigidity of the ligands, and arrange in a propeller like geometry around the Ru atom. After photoexcitation there is a significant steric effect arising from the strain of the bipyridyl ligands which are constrained in the ground state as the Ru—N bond change is only very

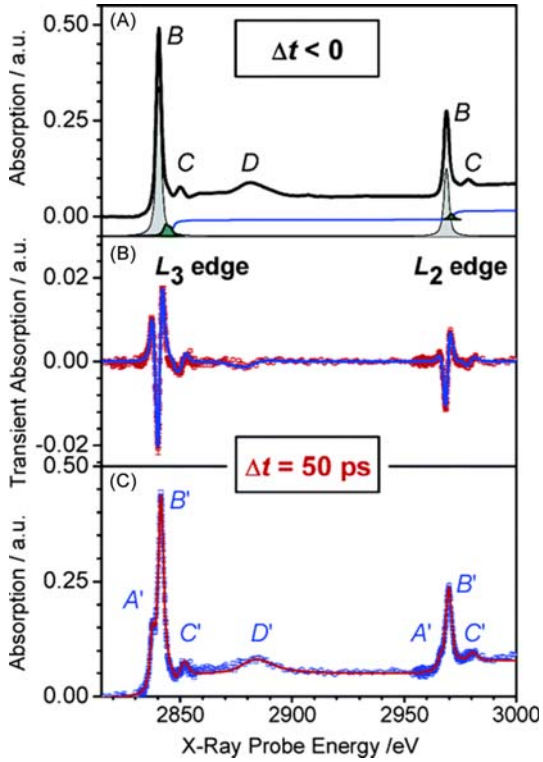

Fig. 2 (a) Ground state absorption spectrum of aqueous $[Ru(bpy)_3]^{2+}$ ions for the L_2 and L_3 edges with different regions indicated (b) Transient difference absorption spectrum measured 50 ps after photoexcitation. The solid line results from the fit analysis of the spectrum. (c) Excited-state XAS spectrum extracted from spectra (a) and (b) using Eq. (1). The red trace represents the results of the fit.[11]

small. Significant shortening of this bond would require a complete structural reorganization which is not energetically possible. Thus the conclusion indicated a small contraction due to the increased charge on the Ru ion after a MLCT.[18]

More recent investigations on metal complexes as photosensitizers have focused on iridium metal centers. As these were more recent studies, they have benefited from the development of powerful high repetition rate lasers creating a better signal-to-noise data on challenging systems. Investigations of an Ir complex with chromenopyridinone ligands $[Ir(Chp)_2(dtbbpy)]PF_6$, where Chp is 3-methyl-6-oxo-6H-isochromeno[4,3-*b*]pyridin-10-ide and dtbbpy is 4,4′-di-tert-butyl-2,2′-bipyridine (**Fig. 3**), was analyzed at the Swiss Light Source in Switzerland at the SuperXAS beamline.[21] This focused on a later timescale on processes occurring in the 100 ns to 100 μs time range. The Ir complex (**Fig. 3**) was dissolved in anhydrous acetonitrile to a concentration of 1 mM, circulated in a closed-cycle open jet flow system. The higher repetition rate of the laser system with short pulses allows increasing of the efficiency of the setup for short-lived transient species. The flow system for the sample was optimized in order to refresh the sample in the probed area during the time between two laser pulses. When using high repetition rate lasers this must be taken into account and is directly influenced by the flow rate of the sample. Thus optimization of the nozzle that forms the open jet is essential to obtain a stable flow at the correct flow rates. In this case a glass nozzle was developed with a contraction angle of more than 30° and a very short tip was utilized to keep a stable flow.

This experiment used a so called 'time-tagged single photon counting method' or DAQ, to obtain kinetic and structural information from XAS in the range between tens of nanoseconds to hundreds of microseconds. In order to obtain spectra of similar quality to an insertion device beamline, at a bending magnet beamline such as the SuperXAS beamline, where insertion device beamlines can give an order of magnitude higher flux,[21] using the DAQ process allows an efficient use of the X-rays to achieve that. The setup (see **Fig. 4**) is based on the multichannel digital X-ray processor, XIA XMAP. Here, information about each registered photon (arrival time, with respect to the trigger with a precision of 20 ns, and energy) is buffered and then saved to file. Two fluorescence detectors, avalanche photo diodes (APDs), were used coupled to signal amplifiers, with an additional APD used that is sensitive to the laser light, connected to one of the channels of the digital X-ray processor. This provides the reference signal of the timing of the laser pulse. Synchronization between X-rays, laser and acquisition setup was accurately achieved by following the radio frequency (RF) signal from the storage ring (500 MHz), which is intrinsically synchronized with the X-ray pulses. This serves as the input for the event receiver that generates signal to achieve the required repetition rate of the experiment. These signals

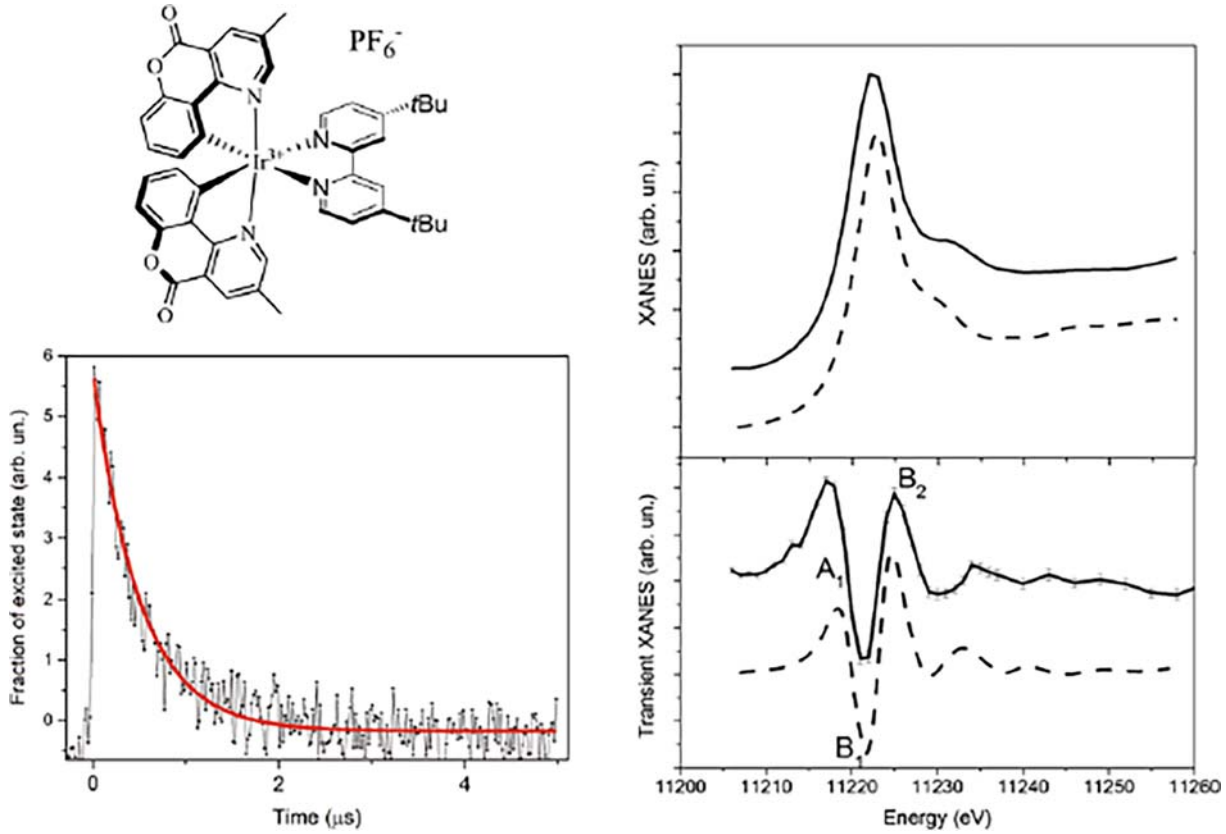

Fig. 3 The $[Ir(Chp)_2(dtbbpy)]PF_6$ complex (top left) and the ground state Ir L_3-edge XANES (top right) and the difference signal at 1 μs (bottom right) with associated fit (dashed). Kinetics were collected using principal component analysis of experimental time-resolved Ir L_3 XANES spectra (black line) and mono-exponential fit with lifetime 0.5 μs (bottom left).[21]

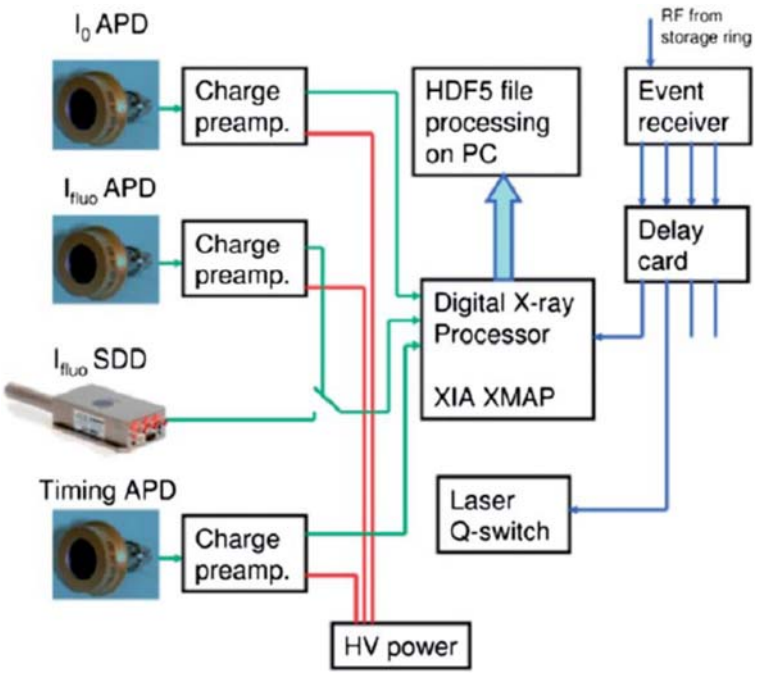

Fig. 4 Scheme of the data acquisition system for the pump-sequential-probes experiments.[22]

are further processed with the delay card generating pulses of required duration for laser and data collection. The signal sent to the laser to achieve synchronization between the actual laser pulse and the DAQ is better than 2 ns.

For the X-ray source, the SLS often uses 390 electron bunches separated by 2 ns forming a multi-bunch train with one additional more intense pulse, the so-called camshaft. This is located in the gap between the start and end of the multi-bunches. Despite this bunch structure, a uniform average incoming X-ray intensity distribution is achieved by shifting the synchronization between laser and the DAQ simultaneously, moving these two triggers relatively to the filling pattern of the synchrotron, as received from the RF signal. After each laser pulse intensities I_0 (X-ray beam before the sample) and I_f (detected X-ray fluorescence after the beam has passed through the sample) are measured as a function of time. A spectrum with good statistics can be obtained by averaging X-ray data following many laser pulses. The shifting of the laser/DAQ system ensures no intensity dips are observed in the X-ray pulses due to the longer delay between the multi-bunch train and the isolated camshaft bunch during the X-ray data collection. The APD detectors used for measuring the incoming and fluorescence X-ray radiation had Soller slits, with conical walls and a Z-1 filters to reduce the background noise caused by elastic scattering. Higher energy resolution detectors can be used such as silicon drift detectors but these are much slower in terms of data collection, thus the addition of the Soller slits provide added energy resolution to the APD.

Using this approach more than 500 time frames were collected at 20 ns time steps. Conducting a principal component analysis (PCA)[23] of this spectral series indicated two statistically significant components. One corresponds to the ground state, while the other one is a long-lived excited state. The kinetics of the excited state component was fitted as an exponential decay with a lifetime of 0.5 μs (**Fig. 3**). Using a density functional theory (DFT) based analysis, small structural differences between the ground and excited state were observed, indicating a change of <0.01 Å in the average Ir-ligand bond length that accompanies the transition from the ground singlet to the photo-excited triplet state. The theoretical spectrum replicated the peak A_1, indicating this feature arises from the transition from the Ir t_{2g} state, since an unoccupied state of such symmetry should appear after the electron transfer to the ligand.

As stated earlier, an overarching goal in investigating rare and expensive metal complexes are to understand the fundamental properties and apply to cheaper alternatives. As such, more recent research on photosensitizers have look towards trying to achieve this by using cheaper alternatives like Cu, Cr and Zn.[24–28] Copper(I) complexes with 1,10-phenanthroline ligand motif[29–35] have gained particular importance. These complexes are able to luminesce at room temperature in solution and undergo excited-state electron-transfer events comparable to that of the $[Ru(bpy)_3]^{2+}$ ion.[36]

In 2013, Cu K-edge XAS was used to investigate the MLCT states of a set of copper compounds, $[Cu(dmp)_2]^+$ (dmp = 2,9-dimethyl-1,10-phenanthroline) and $[Cu(dbtmp)_2]^+$ (dbtmp = 2,9-di-n-butyl-3,4,7,8- tetramethyl-1,10-phenanthroline), in this case using transmission XAS over that of the aforementioned studies which were all collected in florescence mode.[37] Difficulties tend to arise using transmission mode as the concentrations of the sample must be sufficiently high to achieve a good signal, placing strains on the solubility and also on the power of the laser pulse. In this case, energy dispersive XAS was used at ID24 at the European Synchrotron in Grenoble. This mode allows the simultaneous detection of $\sim$1000 eV in the X-ray bandwidth using a polychromator in the beamline and a position sensitive detector to discriminate the wavelength of the signal. This has the potential to

significantly reduce the total acquisition time so long as the flux of the X-ray beam is sufficiently high and the gating and repetition rates of the detector are fast enough to reach the desired time resolution of the experiment. These experiments used 4- bunch mode of the ESRF with 10 mA per bunch (compared to uniform filling mode of 200 mA) with a 700 ns interval between each bunch. A 10 Hz Nd:YAG laser, with a pulse width of 3 ns was used. The laser excitation was performed at 450 nm at a power of 12 mJ per pulse. With the XAS data collecting in transmission mode using a Si(111) polychromator, a Ge microstrip detector (XH) was used as the detector which was rapid enough in its acquisition time to isolate an individual electron bunch.[38] The detector was time-windowed (500 ns integration time) around the electron bunch, achieving a better than 100 kHz repetition rate. The X-ray and laser synchronization was achieved using an APD which linked to a fast oscilloscope and the ESRF machine clock signal drove the detector and the laser to vary the delay between excitation and recording. The concentrations measured were 15–20 mM solutions in acetonitrile in this case not using an open jet but in a continuous flow cell with quartz window. Using this energy dispersive setup, a high quality spectrum was obtained in about 2 h but limitations were due to the low repetition rate of the laser rather than the quality of the X-ray signal.

The use of a molecular orbital (MO) based approach to calculate XAFS spectra provided a quantitative analysis of the detected XANES region and gave a simple interpretation to key features of the spectra and corresponding peaks observed in the difference spectrum (**Fig. 5**).

These theoretical calculations of XANES spectra were compared with the experimental data for models of $[Cu(dbp)_2]^+$ using DFT optimization. Initial calculations of the ground state spectra indicated significant p-character binding around Cu with π orbitals of C and N atoms contributing to these MOs, producing a shoulder on the rising edge.[39] After laser excitation, one model assumed only flattening distortions of the complex in the MLCT state while a second corresponded to a state in which solvent molecules coordinated to the metal ion (**Fig. 5**). The theoretical spectra of these two excited state species were very different and a clear indication as to which model was viable could be drawn through comparison with the difference spectra. There was in strong agreement with theexperiment for the flattened structure. This model with flattening distortions has the same features as the ground state spectrum, but all of them are shifted to higher energy due to the changes of the core level as a result of an oxidation state change from Cu(I) to Cu(II). Thus, the negative peak in the difference spectrum within this model is related to the shift of the edge. In the difference spectrum for this model, it suggests the presence of a very small positive peak that at the relative energy −7 eV relative to the edge energy. This peak relates to the depopulation of the MOs (**Fig. 5**, bottom) with significant Cu d- character during the MLCT transition. What's more, this model describes several physical aspects of the data including the angle between the ligands (angle between two planes formed by the N atoms of the corresponding ligands and the Cu atom) changes from 83° in the ground state to 60° in the excited state and the average Cu—N bond length, which decreases by 0.03 Å after photoexcitation. Hence through XANES spectra with good theoretical calculations, many properties can be drawn about the system after photoexcitation.

In some very recent investigations of copper photosensitizers by TR-XAS, Cu(I) complexes of the type $[Cu(PP)(NN)]^+$ (PP represents a diphosphine ligand and NN a diimine ligand) have been reported.[10] These particular complexes have garnered a lot of

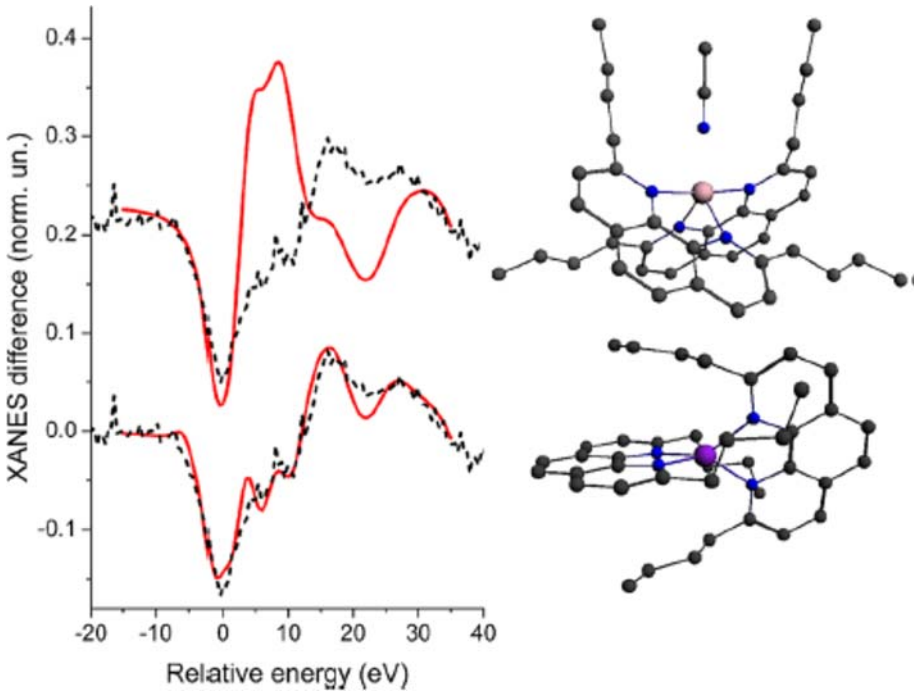

Fig. 5 Theoretical difference spectra (red, solid) between Cu Kedge XANES of photoexcited and ground state $[CuI(dbp)_2]^+$, compared to the experimental difference spectra of $[CuI(dbtmp)_2]^+$ (black, dashed). Calculations and corresponding models of the excited state are shown.[37]

interest as their ligands can easily be tuned to modify physical properties of the material such as their redox potentials, durability, luminescence properties and excited state lifetimes. These are understood to undergo singlet MLCT (1MLCT) followed by Jahn-Teller flattening distortion upon light excitation, towards forming the long lived triplet MLCT (^{3}MLCT) state.[40–42] It is postulated that discovering the details of the ^{3}MLCT state and how the ligand influences the complex towards radiative and non-radiative deactivation pathways is key to unlocking much of the understanding of how these photosensitizers operate and thus how to make further improvements. It is currently thought that the possible formation of a flattened geometry enables coordination by solvent molecules or counterions, promoting the formation of a low-energy excited state known as an "exciplex".[40–44]

The nature of the solvent itself is thought to effect the ^{3}MLCT lifetimes without a direct coordination to the metal center by tuning charge transfer excited state energies.[45] Studies such as TR-XAS were used to find direct evidence to resolve these ideas. This recent study looked at the ultrafast photo physical properties of a series of these Cu dimeric complexes. The aim was to explore two variables in order to understand the excited state dynamics of copper chromophores, changing solubilities via change of the counter ions and, exploring the effect of flexibility changing the 'spacer' chain length between copper centers. Using TR-XAS at the picosecond time resolution coupled with DFT calculations were applied to provide a detailed analysis.

The XAS measurements were collected at the Advanced Photon Source in Chicago, United States. The beamline that conducted this study, 11-ID-D, is an excellent example of a beamline setup for conducting pump-probe experiments at synchrotron allowing for users with relatively little experimental experience to setup experiments and conduct ultra-fast spectroscopy. The beamline has a permanent infrastructure for the setup of these transient experiments, where in most other beamlines, the apparatus and instruments are moved in for the experiment, setup and then removed once the beam time is complete. When experiments are conducted that make use of instruments such as lasers, they may not perform optimally if they are consistently being moved. Furthermore, there are major complexities with setting up the laser beam paths and ensure an accurate overlap with the X-ray spot. At 11-ID-D at the APS, there is a permanent laser installed at the beamline and the path to the cell fixed. With the beamline dedicated to ultrafast studies, it has delivered numerous scientific studies in this field at multiple time points of structural dynamics. Using a pulsed laser as an excitation source, providing X-ray pulse snapshots on chemical systems on time domains from 80 ps to 1 ms. The scientific program has integrated electronic and structural dynamics dictated by molecular and electron transfer processes in a broad range of scientific disciplines. This experiment was run at this beamline where the Cu samples were circulated through the beamlines stainless-steel nozzle into a free-flowing 650 mm cylindrical jet inside an airtight aluminium chamber. The X-ray fluorescence signals were collected with two APDs positioned at 90 degree on both sides of the liquid jet. The experiments were all carried out using the 24 bunch mode which consists of a train of X-rays separated at 6.5 MHz. The samples were pumped at 400 nm wavelength using a laser with 10 kHz repetition rate with a power of 650 mW.

Fig. 6 shows the three complexes under study and the subsequent transient signal that was observed, typical of the ^{3}MLCT state of the copper-based photosensitizers.[46–49] The major changes observed to produce the difference spectra indicated a change of the formal oxidation state, the electronic configurations and the copper coordination geometries. These were derived from the pre-edge region at energies around 8980 eV (Fig. 6). The spectra indicates a MLCT transition, a 3d electron promoted to a low-lying p* orbital of the ligand after light excitation. This indicates a d level occupational change moving from $3d^{10}$ to $3d^9$. The low energy pre-edge feature at 8980 eV corresponds to the resulting 1s to 3d quadrupole transition, although formally dipole forbidden, gains intensity

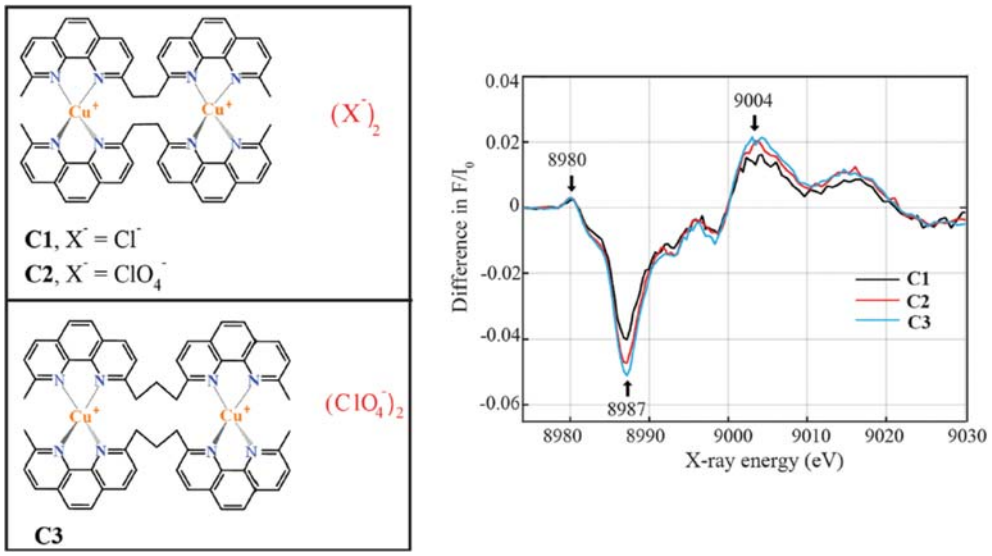

Fig. 6 General structures of the Cu(I) complexes. C_1 was investigated in a water solution (X = halide), C_2 and C_3 were both measured in acetonitrile solvent. Time-resolved XAS spectra (Laser ON-OFF) corresponding to the excited states of C_1 (black), C_2 (red) and C_3 (cyan) owing to metal-ligand charge transfer transitions at a delay of 100 ps between laser and X-ray pulses for a mixture of 2 mM Cu complex.[10]

due to 4 p mixing into the Cu 3d-shell.[50,51] The transient signal provides further features as an intense bleach transition at 8987 eV together with a broad positive peak at 9004 eV relating to the change in the 1s to 4pz and 1s to 4p transitions respectively (Fig. 7).

Theoretical DFT XAS spectra were calculated for the ground and excited state geometries for the Cu complexes displayed in Fig. 6. An analysis of the atomic contributions provided an assignment of the transitions observed in the experimental spectrum (Fig. 7). A small positive pre-edge peak corresponding to the 1s to 3d transition was identified in the transient signals. The negative shoulder at 8982 eV originates from transitions to the lowest lying acceptor orbitals delocalized over the ligands which contain traces of the copper 4p orbital contributions. The negative bleach feature at 8987 eV is most sensitive to the structural distortions around the CuN_4 core after photoexcitation.[9,45,52] As such, the differences between C_1–C_3 were assigned as geometrical changes arising from the flattening of the excited state core, which induces distortions to the neighboring copper center within the dimer. C_3 displayed the most negative bleach at 8987 eV in the experimental spectra indicating a larger flattening of its excited state core structure. This was attributed to greater flexibility of the propyl spacer in comparison to the ethyl ones of C_1 & C_2. These insights gained through TR-XAS provided a key insight as to how C_3 complex had a significantly longer lifetime at 1630 ps over that of C_1 and C_2 of 169 and 665 ps respectively. This study helped reveal the importance of designing more flexible and longer spacers in dimeric copper complexes gaining insights into the lifetimes of Cu(I) dimeric complexes with phenanthroline-based ligands, their ground and excited state conformations, and enables future rational schemes for their applications in different solar energy conversion schemes.

10.13.4.1.2 Non- reversible photoreactions

Another important class of photochemical reactions are the non-reversible reactions, where the absorption of light by a material sets off a chain of reactions rather than the initial excited complex returning to the ground state. In the case of photosensitizers, these often involve formal oxidation changes with changes in ligand conformations (i.e., flattening). In the case of non-reversible reactions, the absorption of light can facilitate the loss of a ligand to create a highly reactive species with a vacant coordination site. These species can then perform high energy barrier reactions such as CH activation reactions or light activated water splitting reactions. After photoactivation, the material absorbing the pump laser usually becomes a very different chemical species going through ligand substitutions and binding available substrates. In terms of the X-ray data, although difficult to collect, the EXAFS part of the XAS spectrum contains highly valuable information as this explicitly contains electron backscattering information of the neighboring atoms. This can be deconvoluted to provide the type, number and distance of donor atoms. EXAFS has become a hugely valuable tool in chemical activation and catalysis for this reason as often it is able to distinguish ligand losses and substitutions alongside formal changes of oxidation state. This rings true for photochemical reaction or photocatalytic processes where the light absorption can kick off a reaction chain. It is of key importance to try identify the earliest photoproducts in order to understand how the rest of the reaction mechanism will follow. In this way we can begin to tailor materials to perform specific transformations efficiently by using bursts of light or driven by solar radiation.

Tungsten hexacarbonyl is a widely used precursor to many tungsten organometallics compounds due to its reactivity with UV light. Exposing $W(CO)_6$ to UV in the presence of a solvent or substrate over 24 h will often produce $W(CO)_x(L)_x$. Recent studies using IR spectroscopy as a probe (using the C═O stretch as a marker) have also shown, under laser irradiation, it can bind to highly inert substrates such as alkanes, fluoroalkanes and even a noble gases.[53] Typically these complexes will last on the microsecond timescales before undergoing further substitution or decomposition. IR spectroscopy can inform us to the existence and the lifetimes of such complexes but cannot provide important information on how the ligands bind and the electronic state of the metal,

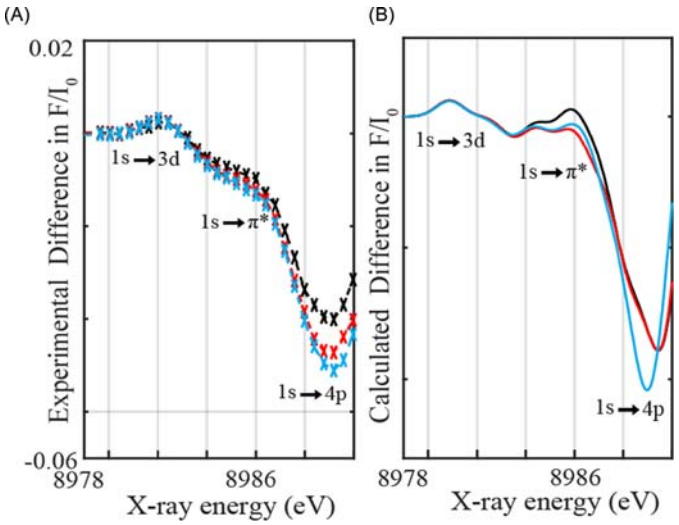

Fig. 7 XAS spectra of C_1-C_3 over the pre-edge and part of the rising-edge region for (a) Experimental and (b) Calculated TD-DFT transient.[10]

which will dictate as to how the substrate can be activated or how a highly reactive state can be longer lived using weakly binding ligands such as Kr.

In 2019 a study was published using pump-probe XAS to investigate just this, the photo activation of $W(CO)_6$ in a solvent to produce $W(CO)_5$(solvent).[53] This was conducted at the APS at beamline 11-ID-D as described earlier. This proved to be the perfect beamline for this study, as collecting an EXAFS signal is significantly more challenging than only the XANES but for this type of reaction, the EXAFS signal would contain very important physical information on the solvent bonding. Conventionally, the signal is very strong at or just over the absorption edge, the XANES region, because the probability of absorption of an X-ray by the absorbing atom is very high, producing a high fluorescence signal. The further you move away by increasing energy of the X-rays, from the absorption edge of the absorbing element, the probability of X-ray photons being absorbed decreases and thus the overall fluorescence signal is decreased. Furthermore, the photoelectron produced by the X-ray absorption by the atom, the photoelectric effect, has a defined mean free path and the further away it travels from the initial absorbing atom, the less likely it will contribute to a backscattering signal (i.e., the EXAFS). Essentially meaning the further away we want to 'see' from the absorbing atom, the lower that signal will be. In a normal solution EXAFS experiment for $W(CO)_6$ this is typically 5 Å away from the tungsten atom, taking 20 min data collection time. When conducting TR-XAS experiments, its likely only 1–5% will be activated for the $W(CO)_6$ experiments collecting on the nano to microsecond timescales, meaning to gain good signal-to-noise requires significant time to accumulate enough signal. A new way to use a conventional XAS analysis software package, Artemis (IFEFFIT),[54] helped to deconvolute the EXAFS signal gained through pump-probe data. This was again guided by other analysis methods particularly time-resolved IR data, providing information of timescales that needed to be analyzed and DFT calculations, providing viable models for the XAS. This method allowed for a more conventional EXAFS analysis, where normal analysis give key parameters such as disorder, bond distance and neighboring atoms despite the unusual way the data is presented to the software. In most other cases of EXAFS analysis of transient XAS data, as discussed in the following section, the analysis method does not resolve distances but rather a theoretical model is proposed and compared with no on-the-fly fitting analysis.

From the time resolved IR (TRIR) measurements of the light activation of $W(CO)_6$, it was understood after the initial absorption of the laser pulse at 256 nm, $W(CO)_6$ loses a CO ligand to form a triplet excited state [$W(CO)_5$*] and on the picosecond timescale this decays by coordinating to a solvent molecule. This can then be substituted for more donating solvent or a substrate over the following 30 μs.[53] In the TR-XAS study of this reaction, the initial solvent was heptane which was substituted by tributyl silane ($HSiBu_3$). Whilst this could be observed indirectly by TRIR, this was followed by using XANES linear component analysis and observe if the time matches the TRIR measurements. This method had been shown as a useful tool of reaction monitoring previously, seen for homocoupling reaction of bromobenzene by [Ni(cod)(bpy)] (cod = 1,5-cyclooctadiene; bpy = 2,2′-bipyridine).[55] If the product and the reactant are properly identified by XAS, they can act as standards to monitor the progress between the two over a time course XANES analysis and thus a lifetime can be estimated. Following the substitution from the heptane to the silane bound tungsten complex was successfully implemented using this methodology. It was essential that the TRIR had been performed to know when the heptane bound was formed and on what time scale the substitution to the silane occurred and finally a time point where the substitution had finished. Furthermore, the XAS studies need to align with the IR studies for confirmation. This principle is shown in Fig. 8.

Whilst XAS could confirm that TRIR was giving an accurate picture of the substitution, this study proved it is possible XAS could provide much more resolution in terms of the structural details of the tungsten complex itself. The TR-EXAFS data and its Fourier Transform is essentially the negative of W-CO scattering paths, as this is what has been lost and is a dominant part of the EXAFS of the parent compound $W(CO)_6$. In order to perform a proper analysis, a normal EXAFS spectrum of the product must be generated in the software and undergoes Fourier Transform which allows a fitting analysis to be conducted in Fourier space commonly done in the IFEFFET software package. In this manner, the software package can determine best fit parameters such as bond distances and neighboring atoms to the tungsten. This study presented an accurate method to do this. It follows the principle of how the difference data is initially generated. To give an accurate analysis of the photoproducts, the XAS experimental starting material data was collected and used to generate a highly accurate model of itself using the Artemis software package. This can then be input as a negative in the analysis of the difference data. If we consider this, thinking how the difference data is generated, the difference spectrum is equal to the photoproduct XAS spectrum minus the starting material spectrum. So in this system, for every mol of photoproduct that is generated, 1 mol of starting material is lost. When a model of the photoproduct is constructed in the software to provide a model EXAFS spectrum, this is then subtracted from the starting material model, generated from experimental data, and the output compared statistically with the experimental difference data. This is essentially copying the process to generate the difference data using models but comparing the output with real experimental data. Through this method, many tungsten compounds were accurately identified for $W(CO)_5$(solvent) where solvent was alkane, fluoroalkane, silane and even highly reactive noble gas coordination product as $W(CO)_5$(Xe) resolving to give a W—Xe bond length of 3.10 Å. Fig. 9 from the study shows the fit analysis and the details that were gained for this highly unusual complex, comparing with DFT analysis for further verification.

10.13.4.1.3 Further EXAFS analysis using TR-XAS data collection method

Extended X-ray Absorption Fine Structure (EXAFS) spectra is a rare occurrence in TR-XAS, this is mainly due the significantly reduced flux at increasing energy scan range, also that for many studies of photoactive materials, the electron transitions are all captured in the XANES region and the change in bond lengths are often quite minimal and so there is no much value in spending time to collect such data, as it is not often worth the effort. However, as in the aforementioned study, clearly in some cases the EXAFS does contain

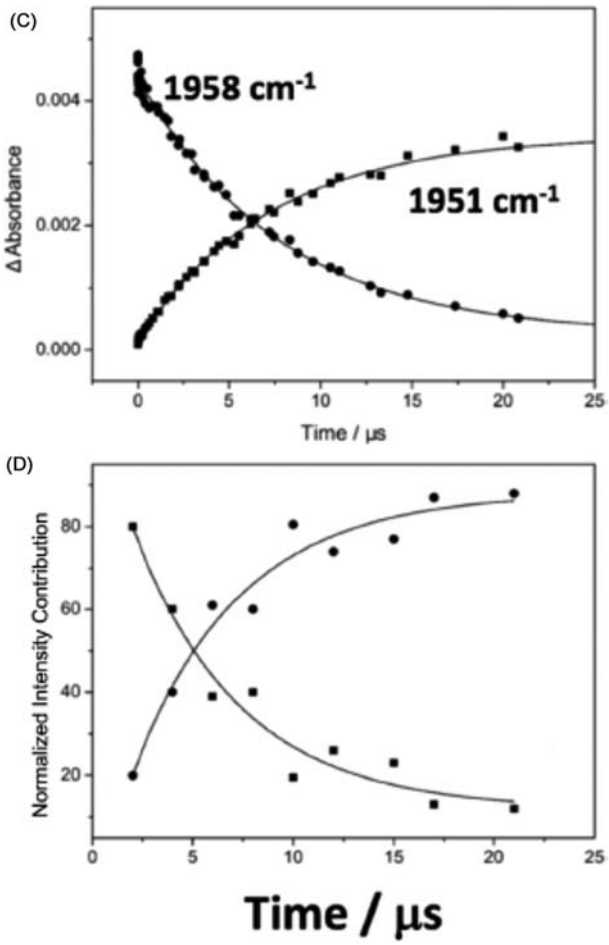

Fig. 8 Time-resolved IR (TRIR) spectra (TOP) obtained following photolysis (266 nm) of $W(CO)_6$ in n-heptane doped with $HSiBu_3$ (0.05 M) and (bottom) Linear combination XANES fitting analysis of the photolysis of $W(CO)_6$ in the presence of $HSiBu_3$ in heptane over first 20 μs. Using of the determined $W(CO)_5$(heptane) (decay) and $W(CO)_5(HSiBu_3)$ (growth) as standards.[53]

ligand	paths	EXAFS *R* (Å)	DFT *R* (Å)
trans W–CO	W–C	1.96(1)	1.96
	W–O	3.11(1)	3.11
4-*cis* W–CO	W–C	2.06(1)	2.06
	W–O	3.20(1)	3.20
W–Xe	W–Xe	3.10(2)	3.15

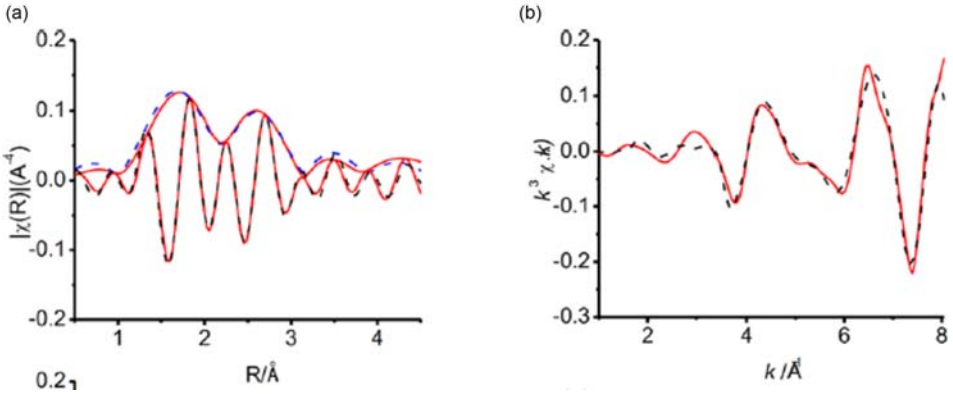

Fig. 9 The W L_3 edge difference extracted EXAFS (red) and fitting analysis (dashed) of (a) the Fourier transform data (red lines represent experimental data with the fit analysis as blue dashed line) of $W(CO)_6$ + fluroalkane under xenon atmosphere over the first 8 μs, and (b) associated EXAFS spectrum with black dashed line as the fit analysis. Above table shows the structural details of $W(CO)_5$(Xe) from over the first 8 μs.[53]

crucial information or added resolution to the study. When collecting EXAFS spectra comes the issue on how to accurately analyze the data as contained within are many structural details unable to be resolved by simply overlaying of data or fingerprinting. It requires modelling using the EXAFS equation and subtraction from the starting material or ground state (GS) data. An early example of structural elucidation tested a method using photo chemically induced spin-crossover complex of $[Fe(II)\text{-}\ (bpy)_3]^{2+}$ (bpy = bipyridyl) (Fig. 10).[56]

This method employs calculations of a series of EXAFS spectra, starting with the ground state (GS) iron complex using a model generated by FEFF code, derived from crystallographic data. In this case spectra is calculated in energy only (not Fourier transformed), in this way the X-ray energy shift relating to the photoproduct can be analyzed. Given the bpy ligand is essentially rigid, the ligand was moved stepwise radially further away from the Fe atom and each time the spectrum calculated and compared to the raw data. This was analyzed using least squares method for statistical verification. This methodology could also provide reasonable values for the chemical energy shift in the absorption edge between both states. These calculations demonstrated that only one of the three bpy ligands increased after photoexcitation by 0.2 Å after 50 ps.[56]

A similar approach was applied to the EXAFS analysis of the triplet excited state of the $[Pt_2(P_2O_5H_2)_4]^{4-}$ anion in solution at 150 ns after laser excitation.[57]

The antibonding-to-bonding nature of the electronic transition led to only the consideration of structural distortions involving a contraction along the Pt—Pt plane. Through this four chemically reasonable deformation models were applied (Fig. 11). In this case models III and IV imply a large structural change in the P—O—P bridging ligand angle, specifically considered as a mode in previous studies.[58,59] This analysis of these different models and their comparison to the difference XAS data demonstrated an elongation of Pt—P coordination bonds by 0.010(6) Å, in agreement with the DFT calculations. These insights let to a hypothesis that the elongation and weakening of the coordination bonds upon formation of the excited state served to reduce the overlap of the coordinating ligand orbitals with the Pt d orbitals. This allows the Pt atoms to come even closer, resulting in the relatively large distortion of 0.31(5) Å. This contraction of 0.31(5) Å was close to the value determined by time-resolved X-ray diffraction (0.28(9) Å)[60] and is within the range of values from DFT calculations.[61] This study demonstrated quantitative excited-state distortions in a dinuclear d8–d8 complex achieved through high sensitivity of the experiment together with a structural analysis of the transient EXAFS spectra.

10.13.4.1.4 Photoactive enzymes mimics

As seen above, XAS in general has a unique characteristic of being able to specifically probe transition metal of choice by tuning X-ray energy and thus used in extensively for transition metal based inorganic material characterization. It is not surprising this has crossed

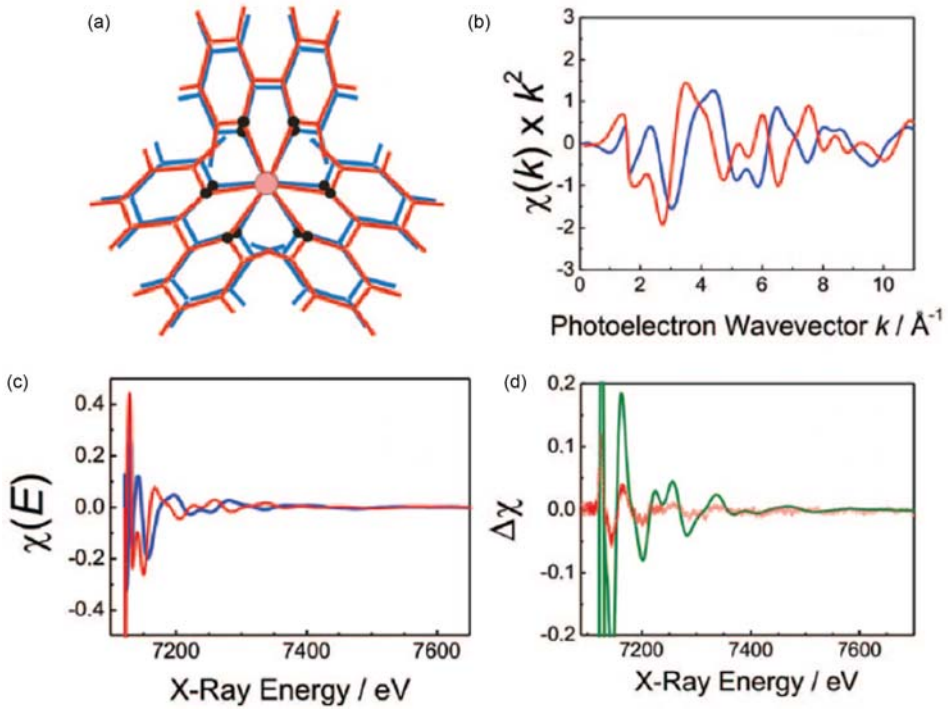

Fig. 10 Showing a procedure to generate transient EXAFS spectra as shown for two structures: (a) geometrical representation of the input structures used for calculating the EXAFS; (b) EXAFS spectra calculated from (a); (c) back-transformed EXAFS spectra to energy space so that the ground state EXAFS coincides with the ground state calculation; (d) for two different structures, the transient spectrum is calculated and shown for comparison with the actual transient data.[56]

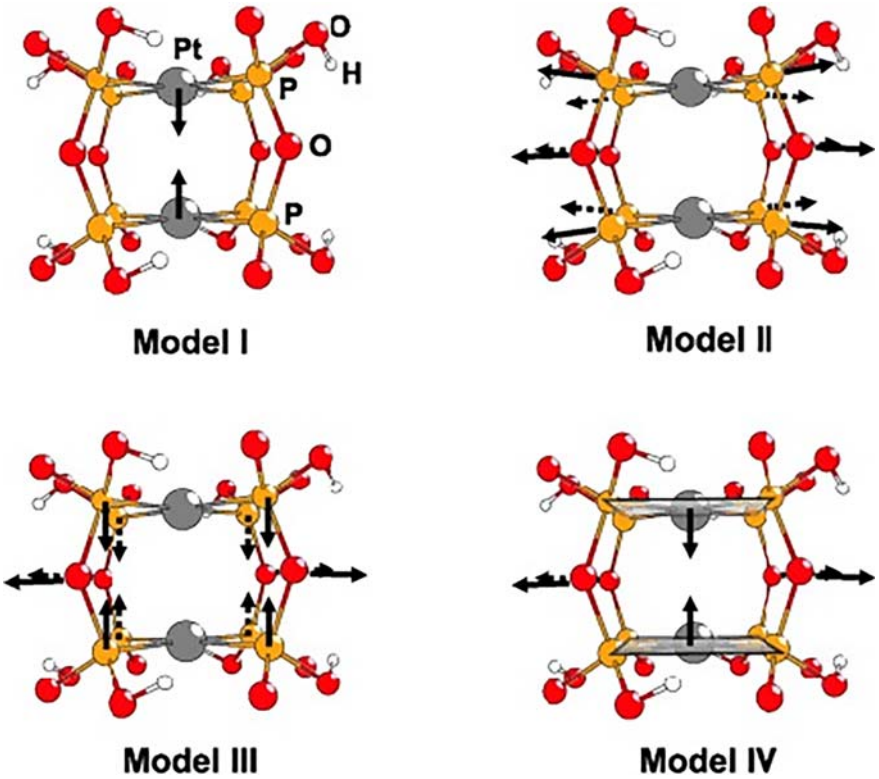

Fig. 11 Schematic representation of the structural distortion models I–IV considered in the statistical analysis (distortion indicated by arrows). The bridging P—O bond lengths are fixed for the distortions of models III and IV.[57]

over into biochemistry, where transition metals often play a critical role in a myriad of biological processes. Their ions and complexes serve as structural supports, electron transfer relays, oxygen transport and storage depots, and catalytic centers.

Fig. 12 and other transition metal based porphyrin complexes are often key components of metal based enzymes. To aid our understanding, "Model" compounds mimicking such chemistry are often synthesized in the lab help further our understanding of how such enzymes and biological agents accomplish chemistry that present high energy barriers whilst working at body temperature and pressure. The so called porphyrin macrocycles are nitrogen-containing pigments to which molecules such as heme (which

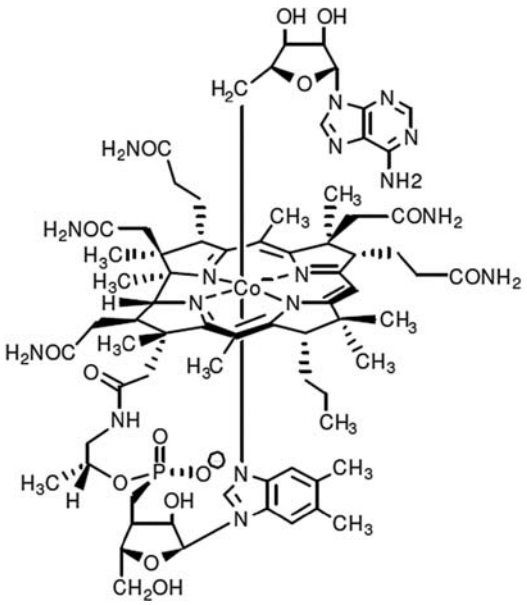

Fig. 12 The naturally occurring organometallic coenzyme B_{12} complex.

forms an integral part of haemoglobin), vitamin B_{12}, cytochrome P-450 and chlorophyll (photosynthesis) belong. All porphyrins have an excellent ability to strongly complex metal ions. The core aromatic ring system is planar and contains 18 delocalizable π-electrons. They form intensely colored materials with distinct absorption features.[62]

Investigating excited state dynamics of metalloporphyrins has been an emerging area using TR-XAS. These systems have strong light absorption properties, they can enable intra- and intermolecular energy/ electron redistribution, trigger chemical processes, often being dictated beyond the delocalized ring system but driven by the charge transfer mechanism between the coordinated metal and porphyrin ring system.[63–65] It is challenging to gain insights concerning the electronic configuration and molecular geometry of excited-state of metalloporphyrins, where excited-state dynamics for photoinduced energy transfers have largely been measured by ultrafast laser spectroscopy for various systems.[62] Yet it is considered that the structural factors and their excited-state dynamics have key influence on their ability to undergo energy or electron transfer, and the mechanisms of such exchanges, yet these kinetics are often unclear. The metal centered electronic states are often optically 'dark' or overlapped with stronger features, thus laser spectroscopy cannot reveal these important excited state transitions in many cases, unable to reveal any excited state electronic occupation and molecular orbital overlap. This leads to a overreliance on theoretical calculations in order to obtain molecular orbital energy levels and electronic configurations of excited state metalloporphyrins.[66–68] TR-XAS has proven to be a route to gain experimental evidence. This method is particularly suited for correlating molecular geometry with electronic configurations and MO energy levels when the excited state is optically dark or overwhelmed by other strongly absorbing or emitting states. An early example of this was published in 2007, investigating the excided state dynamics of nickel porphyrin systems which led to continuing research on this material through to the present day.[62] This initial study proved TR-XAS as a viable method to track the electronic and molecular configurations for the excited state of a Nickel porphyrin by studying a dilute toluene solution of nickeltetramesitylporphyrin (NiTMP). The excited state lifetime had been measured to last 200 ps providing a short window for TR-XAS measurements. NiTMP is a metalloporphyrins with open-shell transition metals whose excited states are short lived and thus poorly understood due to the coupling between the MOs involved in the initial (π, π*) excited state with metal d electron dominant MOs involved in light-activated redox reactions.[62] The proposed excited-state pathway of NiTMP in noncoordinating solvents outlined[69] as starting from a nearly square-planar ground state where the electronic configuration of Ni(II) ($3d^8$), having an empty $3d^2_{xy}$ MO and a doubly occupied $3d_{z^2}$.[70] The electronic transition after light absorption by exciting the Soret band in NiTMP, corresponding to a wavelength of maximum absorption at around 400 nm, arises due to an electron dipole movement that allows π-π* transitions common in porphyrin compounds. Within 350 fs following the excitation, the π to π* state is believed to convert, through energy transfer followed by intersystem crossing, to an intermediate state that then undergoes vibrational relaxation in less than 20 ps.[69,70] Finally, this state returns to the ground state in approximately 200 ps.

These mechanistic details have been assigned largely using to computational results that describe charge-transfer states of transition metalloporphyrins with unfilled d orbitals. The geometric structures of these excited states were inferred by Raman spectroscopy[71,72] and theoretical methods.[66,68] which still suffer many uncertainties. In these electron excitation studies, it is always desirable to simultaneously track electronic and molecular configurations determining an overall picture of the excited state in order to understand the correlations between electronic and molecular structural factors with reaction kinetics and pathways. The TR-XAS measurements aiming to resolve such information on NiTMP, were carried out at the APS on the 11-ID-D beamline. A 1 kHz repetition rate of the laser pulse (laser shot evert 1 ms) at wavelength 527 nm was used, which corresponds to the singlet to triplet state excitation as determined by the optical spectroscopy. These initial measurements also found a 45–50% fraction of excited state molecules of the NiTMP. The transient X-ray signals were averaged at each X-ray photon energy defined by an X-ray monochromators, which were extracted from a train of electron bunches circulating in the storage ring using a hybrid mode where an intense X-ray pulse with 16% of the total average photon flux was separated in time from other weak X-ray pulses with 84% of the total photon flux by ~1.59 μs (see **Fig. 13**). There was a limiting factor that only 0.06% of total X-ray photons could be used as the probe because the laser had a relatively slow 1 KHz repetition rate.

The TR-XAS spectra was collected at the Ni K-edge after 100 ps which gave two distinct features at 8331.0 eV and 8333.2 eV in the extracted excited state spectra. These were attributed to transitions from the Ni 1s orbital to the half-vacant predominantly 3d MOs. By this, the pre-edge spectrum directly depicts the electronic configuration of the primary excited state as singly occupied $3d^2_{xy}$ and $3d_{z^2}$.[64] TR-XAS was able to resolve electronic and structural dynamics by selectively monitoring time evolution of specific X-ray induced electronic transitions after the laser excitation. As the conversion of the excited NiTMP proceeds through the energy cascade after excitation, the excess energy from the (π, π*) generates vibrationally hot states accompanied with electron redistribution.[69,73] This results in molecular geometry rearrangements of the metalloporphyrin. These structural changes were able to be extracted from TR-EXAFS spectra in **Fig. 14**, where the spectrum after 100 ps is clearly different in frequency and phase to the ground state. The Fourier-transformed EXAFS spectra determined a lengthening of the average Ni—N and Ni—C distances after excitation as 0.08 Å and 0.07 Å, respectively, consistent with an expansion of the porphyrin ring. A mechanism was laid out in that one electron was promoted to the higher energy antibonding $3d^2_{xy}$ MO in the excited state, causing a stronger electrostatic repulsion serving to reduce the bond order for Ni—N bonds. This thereby increased the Ni—N bond distances. As the porphyrin ring expands, the electron density on Ni(II) through σ bonding and π conjugation decreases while its effective charge increases.

This is a good example that demonstrates how TR-XAS can aid in tracking the electronic transitions of important biological metalloporphyrins and metal complexes in general along their excited-state pathways. As the valence electrons are promoted to higher energy MOs by laser light, TR-XAS spectra is able to probe the electronic transitions from core to valence levels induced by X-rays. This provides a means for obtaining metal excited-state electronic configurations that are often inaccessible by optical transient

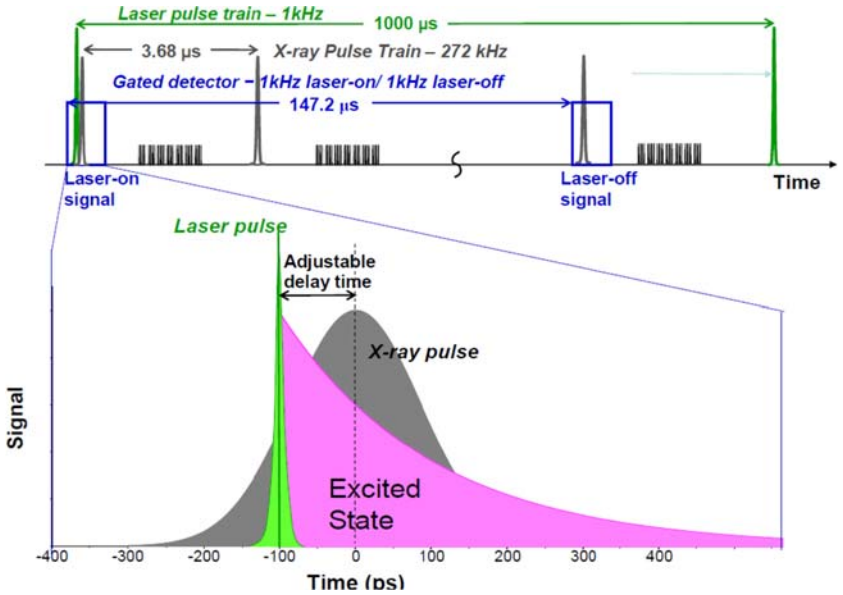

Fig. 13 The timing scheme of the TR-XAS experiment used at the APS synchrotron to measure excited state dynamics of NiTMP.[62]

absorption spectroscopy. As important as theoretical calculations are for these types of measurements, results such as these are required to directly verify and guide theoretical calculations and spectroscopic assignments for excited-state metal complexes.

A follow up study on the NiTMP focused on the molecular structural dynamics of the excited state in terms of how it is influenced by a coordinated axial ligand. This study used pyridine in a mixed toluene: pyridine solvent.[74] This experiments looked to provide a new mechanism for axial ligation after light activation, applicable to many other metalloporphyrins, potentially impacting future designs of photocatalysts for promoting binding to the metal center in a well-defined orientation, with an aim to selectively produce desirable products. The action of axial ligation can be thought of as a substrate binding to the photoactivated catalyst as the primary step of its transformation towards the product to begin.

Fig. 15 displays the transient XANES spectra of NiTMP in a mixed solvent of toluene and pyridine during the photoinduced ligation. This analysis focused strongly on the 1s to 4pz transition at 8337.5 eV. This peak feature has proven to be very sensitive to the ligation states of metalloporphyrins.[75–77] Based on the optical and the XANES spectra of the ground state NiTMP in the mixed, neat toluene and neat pyridine, the XANES spectra for the 100% dual-ligated NiTMP-Py_2 could be extracted (Fig. 15 inset). The XANES spectrum of NiTMP-Py_2 has no distinct 1s to 4pz transition peak compared to the non-ligated complex because it is at higher energy and thus shifts the peak feature into the white line transition. In the TR-XAS spectrum taken at a 100 ps delay, the loss of the ground

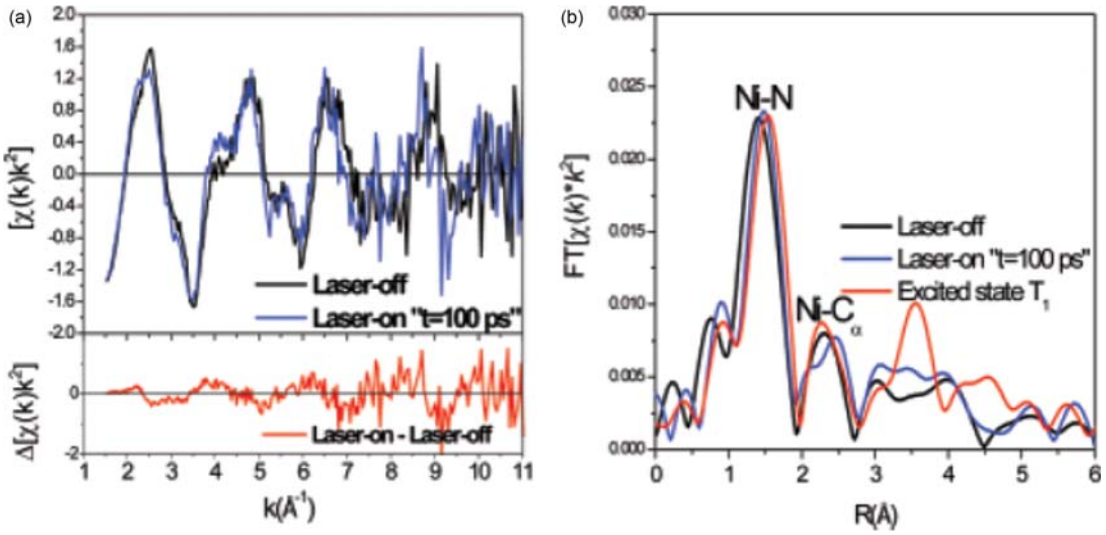

Fig. 14 (a) EXAFS spectra for NiTMP with the laser-off and laser-on conditions, respectively, at the delay time of 100 ps. The difference spectrum displayed in the bottom; (b) the Fourier transformed EXAFS spectra of NiTMP.[62]

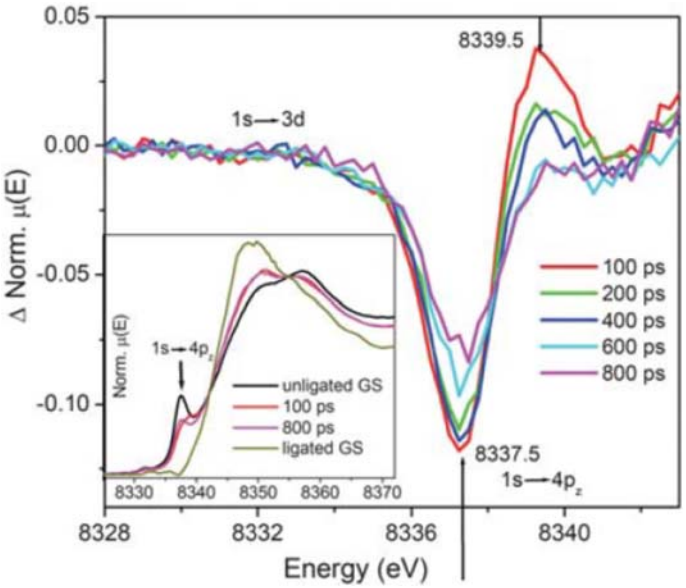

Fig. 15 Transient XANES spectra of NiTMP in a mixed solvent toluene:pyridine (3:1 by volume ratio). The edge feature focused on 1s/4pz for monitoring the spectral evolution as a function of the pump-probe delay times. Inset shows the XANES spectra measured at 100 ps, 800 ps, and the XANES spectra displays the pure ligated and unligated NiTMP in the ground state.[74]

state pre-peak at 8337.5 eV is due to the reduction of the 1s to 4pz transition for the unligated ground state upon the photoexcitation. A new absorption appears at 8339.5 eV which corresponds to the 1s to 4pz transition of the unligated excited NiTMP from the TR-XAS measurement on NiTMP in neat toluene.[62] During 200–400 ps after the excitation, both the excited state absorption and the ground state bleaching decreases. By the delay time of 600–800 ps after the excitation, the ground state bleaching is still changing while the absorption at 8339.5 eV remains largely unchanged.

This TR-XAS study found the dual ligated NiTMP has no 1s to 4pz feature at the Ni K-edge because the transition has been shifted to a higher energy due to the elevation of the 4pz MO energy.[39,75] The TR-XAS spectrum at 100 ps delay (Fig. 15) is very similar to that for the excited state of NiTMP in neat toluene without the ligation.[62] From this it was evident that solvent ligation happens after the formation of the initial excited state and the new absorption peak at higher energy is due to the formation of excited unligated NiTMP. The fact the intensity of the 8339.5 eV peak reduces and almost goes to zero after 600 ps indicated the diminishing population of the unligated excited state after 600 ps. The determined dual ligated NiTMP had shifted its 1s to 4pz peak to a higher energy, under the white line transition, it is unable to contribute to the intensity at 8337.5 eV. Thus the reduced intensity at 8337.5 eV indicates that ligation has occurred. These results provided strong evidence of the mechanism of photoinduced ligation. The solvent ligation happens much later after the vibrational relaxation of the initial excited state which agrees with a solvent diffusion process. The relatively long-lived ligated species indicates it is a triplet state that requires tens of nanoseconds to release the ligands and return to the ground state. These studies demonstrated that the photoexcited state favors solvent ligation compared to the ground state.

A more complete mechanism could be derived by bringing in the above discussed results on the NiTMP as to why the photoexcited state favored solvent coordination. From the pre-edge 1s to 3d transition in the XANES of NiTMP, finding the 3d orbitals become singly occupied after photoexcitation, in particular the $3d_z^2$ MO becomes singly occupied, allows the $3d_z^2$ to accommodate the axial ligation more easily. This results in a triplet degenerate $3d_z^2$ and $3d_{x^2-y^2}$ as expected for the pseudo-O_h symmetry in the hexacoordinated coordinated Ni(II). This state allows for a lone pair electrons from nitrogenated pyridine molecule to donate electrons to the Ni(II) center from above and below the porphyrin plane to achieve the dual ligation. Understanding the driving force and the time sequence of substrate binding, much as the pyridine binds to the NiTMP after photoexcitation, contributes significantly to understanding the correlations between electronic and geometric structures of molecules. This leads to future iterations to control molecular reactivity through structural variations, a main goal for catalysis in general.

10.13.5 TRXAS experiments at X-ray free electron lasers

A Free Electron Laser (FEL) is a light source that is similar to a synchrotron using a high-energy electron beam to produce coherent electromagnetic laser waves. Much like a synchrotron, X-Ray FELs allow a tunable X-ray source capable of high peak and average powers and can produce a wide variety of pulse formats. Hard X-ray FELs are considered as fourth-generation light sources.[78] The major advantage of XFELs is that they produce coherent light many orders of magnitude brighter than the light produced in synchrotrons, as such these are state of the art facilities in X-ray science. FELs are capable of operation over the entire electromagnetic

range at average powers up to several kilowatts and peak powers up to a gigawatt. The working principle of FELs use an electron beam that propagates through a periodic magnetic field, much like an insertion device commonly used at a synchrotron known as a wiggler or undulator. It uses similar principles as a laser, where excited state atoms of a lasing medium interact with photons to emit a new second photon identical to the initial photon causing the atom to return to the ground state. Thus, the first photon stimulates emission of a second photon and so on. As all the photons are identical, they are "in phase" and reinforce each other, so called constructive interference. This means that the amplitude of wave after constructive interference is the sum of the individual amplitudes. In a FEL source, the lasing occurs as a bunched electron beam passes through an alternating magnetic field of a wiggler, essentially a device that makes the electron path 'wiggle' as it travels through the alternating magnetic field with north—south alternations spaced often only a few millimeters apart (Fig. 16).

As the electron bunch moves from side to side, it emits electromagnetic waves. What this essentially does, is bring together the two separate components of electromagnetic radiation. An electronic part (the electrons) moving side to side in a wave with a magnetic part (the alternating magnets of a wiggler) perpendicular to this. This electromagnetic radiation falls in synchronization with the electrons, causing the electron bunch to form parallel lines in coherence with the emitted radiation, giving a significance boost to the power of the radiation. This microbunching is known as self-amplified spontaneous emission (SASE). This arises because the emitted photons will travel slightly faster than the electron bunch. As the electrons move periodically through the undulator device, the light either falls in or out of phase of the electrons. The electrons then either gain or lose energy (velocity) from this interaction, thus the electron bunches arrange into distinct parallel lines. These lines give spikes in X-ray flux at certain wavelengths against a lower amplitude background. The energies of the spikes can be modified by changing the gap of the undulator. The electrons can then be removed from the beam path allowing the radiation to be used further up the beam line. When the electrons are traveling close to the speed of light, this creates relativistic effects to provide high energy X-ray radiation. The LCLS facility has produced a well explained video of how X-rays are produced at an X-ray FEL source (XFEL).[81]

10.13.5.1 History of free-electron lasers

In the early 1950s, using a linear accelerator to accelerate electrons to produce visible light emission was demonstrated using a wiggler magnet.[82] Some years later a so called 'Ubitron' or Undulating Beam Interaction, produced peak power of 150 kW at a 5 mm wavelength,[83] by undulating an electron beam to give a new interaction mechanism (Fig. 17).

In 1971, an optical device subsequently referred to as a "free-electron laser" was proposed and it would operate in the near-infrared.[80,84,85] These Raman FELs were pioneered at numerous laboratories around the world and operated at microwave and millimeter wavelengths.[86–88] These were the first SASE FELs, although the term "super-radiant amplifiers" was commonly used. The interest in X-ray SASE FELs has fueled intense interest in infrared-, visible-, and ultraviolet-wavelength experiments in the field of physics and technology. These experiments were made possible by the use of high-brightness photocathode electron guns and were stepping stones to shorter wavelengths.

The development of linac-based FELs with both higher power and shorter wavelength were delayed by technological issues. In particular, the electron brightness was the principal limiting factor. The essential breakthrough was the development of laser-switched photocathode electron sources (photoinjectors) to replace thermionic cathodes, improving the electron beam brightness in linacs by two orders of magnitude.[89,90] Photoinjectors are used routinely in short-wavelength FELs.[78,91] High average power FELs also benefited from the application of photoinjectors. In the early 1990s the average power record for an FEL was 11 W.[92] An experiment at Boeing demonstrated the ability of photoinjectors to produce high average electron beam power and high beam quality (160 kW, 5 MeV) with a photoinjector designed as a driver for a high-power FEL.[93]

Currently, several XFELs are able to produce light in the hard-X-ray regime, which can produce intense, ultrashort pulses of radiation down to wavelengths of 0.1 nm.[94–96] The first hard X-ray XFEL went into operation at the Stanford Linear Accelerator Center in April 2009. For conducting XAS experiments, there are key design features of XFELs that are of particular interest, most important is the delivery of X-ray pulses with high peak brightness and short pulse duration (20–100 fs). This provides excellent setup for time-resolved studies of fast chemical dynamics. Also, the ability of flexible tuning of the X-ray wavelength for exploiting different X-ray absorption edges, conducted by varying the electron beam energy and/or the undulator gaps. XFELs can also operate in a "chirped"

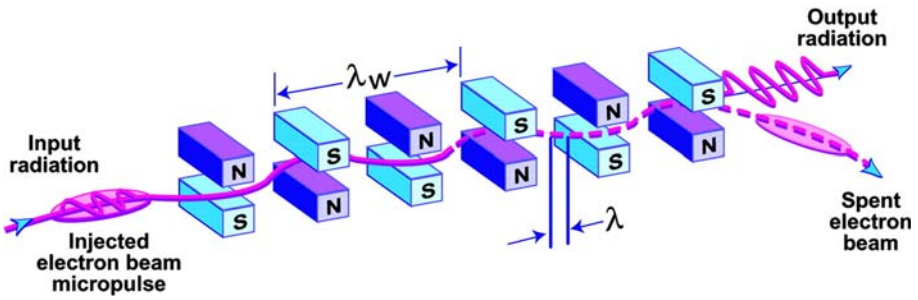

Fig. 16 Schematic illustration of the interaction between the electron beam and the wiggler in an FEL with a planar wiggler.[79,80]

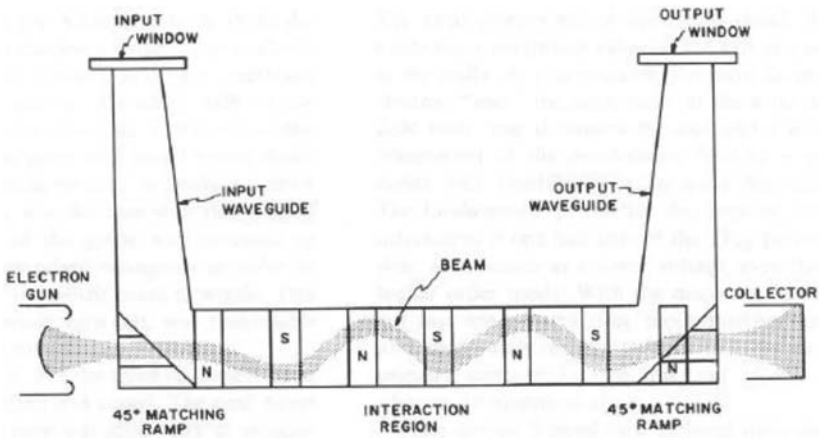

Fig. 17 The Ubitron is a high-power traveling-wave tube which makes use of the interaction between a magnetically undulated periodic electron beam and electromagnetic radiation, used for high-power wave amplification.[83]

mode to allow single shot measurements over an extended spectral range' with a synchronized optical laser source. With dedicated X-ray optics, the diameter of the X-ray spot at the sample can be varied over the range 0.1–100 mm. An XFEL facility with hard and soft X-ray capability will typically cover elemental K, L and M edges up to atomic number 85. At these facilities, collection of XANES data typically spans a region of photon energy within ± 50 eV of the absorption edge, where EXAFS measurements can be extended by scanning more than 500 eV above the edge.

An important aspect in absorption spectroscopy, particularly for XANES, is the bandwidth of the incoming X-rays, i.e., the measure of the photon wavelengths falling within the central or desired wavelength. The inherent bandwidth of an XFEL operating in the SASE mode is $\Delta E/E = 10^{-3}$. This can be reduced, typically by an order of magnitude by introducing a crystal or grating monochromator into the beamline optics. This mode tends to have the disadvantage of large shot-to-shot intensity fluctuations because the stochastic, spiky frequency spectrum will often lack spectral intensity at the monochromator energy. Although, narrowband monochromators may noticeably lengthen the duration of the XFEL pulse.[97] A feasible alternative for photon wavelengths longer than approximately 1 nm is to "seed" the XFEL, by introducing an external pulse of narrowband radiation which co-propagates with the electron pulse in the undulator pre-determining the wavelength of the micro-bunching (**Fig. 18**).

The issue with SASE generated X-ray radiation, generated from what is called electron beam "shot noise", is that it tends not to be very coherent and consists of slightly different wavelengths. A way of improving the X-ray flashes is to insert a monochromator between the undulators. The light generated in the first part of the undulator hits the monochromator at a certain angle, most of the light passes through the crystal, keeping the same properties as the incoming beam. However, because of the specific

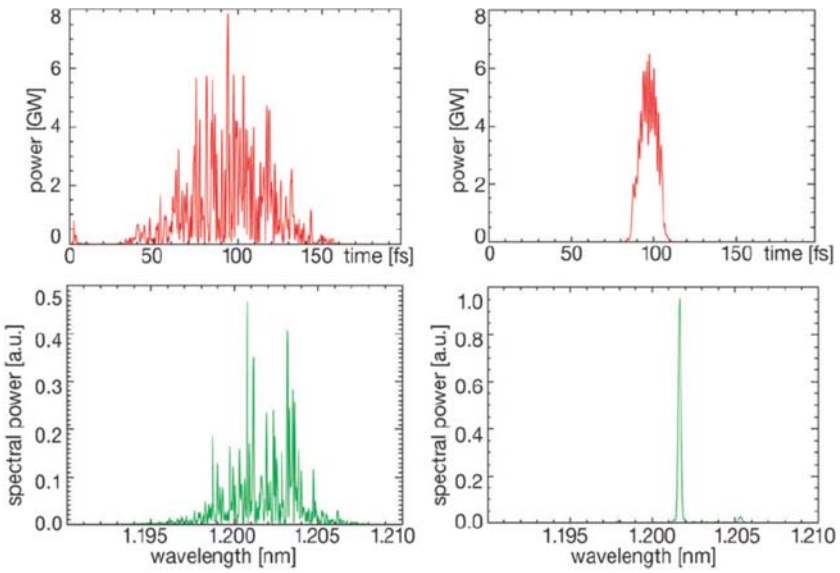

Fig. 18 A schematic seeding arrangement of SASE (left) and seeded (right) pulses at 1.2 nm wavelength showing both time and wavelength properties.[94]

properties of the crystal, the first pulse is followed by a second one, slightly delayed and monochromatic. These are the X-rays of most interest: if the electron beam that generates the light is also delayed using a magnetic chicane, and then set on top of the second light pulse, the electron beam will amplify this second pulse. Thus, only the high-quality X-rays seed the generation of very intense and coherent flashes in the second part of the undulator—a procedure that is known as "self-seeding". One feature of particular interest to time-resolved XAS experiments is the availability of a "broadband chirped" operation mode, in which the electron energy is made to vary along the length of the pulse.[97] A wide photon energy bandwidth in this mode, with a DE/E = 1–2%, will allow energy-dispersive, single-shot experiments.

10.13.5.2 "Pump-probe" data collection at XFEL

The very short, very intense photon pulses produced by an XFEL make it a highly attractive instrument for time-resolved experiments using X-ray absorption spectroscopy. The time-resolution achievable using this method is limited by the length of the pump and probe pulses and by the unavoidable synchronization jitter, being the deviation from a set periodic signal, often in relation to a reference clock signal. Typically, this can be as low as 50 fs. In order to achieve success with this type of experiment at XFEL, the pump pulse must produce a significant degree of excitation in the sample, but not produce excessive damage. With improved time resolution, this issue can be exacerbated as a sufficient level of excitation requires a minimum pump-pulse energy, where a better resolution means increasing the peak pump power. This can lead to multiphoton ionization of solvents, and for surface catalysis, ablation. Hence, careful pre-testing and adjustment of the pump wavelength and pulse energy is always required. If seeding of the XFEL is not implemented, the statistic nature of the SASE process will cause successive XFEL pulses to fluctuate in intensity, perhaps by as much as 50%. Using shot-to-shot intensity monitors can mitigate these fluctuations to some degree but can cause trouble when scanning the incoming photon wavelength or the pump-probe time delay.[98] Signal-to-noise will be an important issue, particularly for a low degree of sample excitation. In normal experiments, laboratory-based studies are first performed without X-rays in order to compare the effect of X-ray exposure on the sample, but for the XFEL, this will be complicated by the pulse-to-pulse intensity fluctuations. A possible solution to this problem is the "probe-pump-probe" method, schematically shown in Fig. 19. The so called "probe-pump-probe" method splits an incoming XFEL pulse delaying one of the pulses using mirrors, gratings or crystals. The Two identical pulses are then made to pass through the sample on delayed trajectories, and into separate detectors. By introducing an optical pump pulse between the two probe pulses, one detector sees an unexcited sample and the other an excited sample.

A challenge of XFEL facilities is the step-by-step tuning of the incoming X-rays often required for XAS experiments, especially true for EXAFS measurements. A goal of XFEL science is to shorten the time required to change the XFEL wavelength to the point where "on-the-fly" measurements are possible at the macro-pulse repetition rates. In some instances, it may be possible that "single shot" spectroscopic measurements is also feasible to collect full XANES spectrum at XFEL. This could be achieved through X-ray Emission Spectroscopy (XES), where the incoming X-ray energy is fixed just above an absorption edge-and the spectrum and the resulting fluorescent radiation is measured.[99] A full XANES spectrum could be collected in one shot using a dispersing element and an array detector used to provide the energy resolution of the emission signal, yielding information on the occupied electronic levels, orbital splitting energies and on spin and oxidation-states. Confining to the near-edge region, the broadband chirped mode of XFEL operation will allow single-shot XANES measurements.[98] A 1% bandwidth translates to $\Delta E = 100$ eV at 10 keV, entirely sufficient to sample an entire XANES region. Suitable dispersive detectors for single-shot XANES have been proposed.[100]

Clearly the high peak brightness and ultrashort pulse duration provided by X-ray Free Electron Lasers open dramatically new possibilities for time-resolved X-ray absorption spectroscopy measurements. These facilities incorporate several features of particular interest to the XAS community, including: a wavelength spectrum covering a multitude of absorption edges in the soft and hard spectral ranges, a pulse repetition rate which is consistent with detector readout and on-the-fly adjustments, flexible wavelength tuning by changes in both electron beam energy and undulator gap, synchronized pump sources and a broadband chirped operating mode with sufficient bandwidth to allow single-shot XANES spectroscopy.

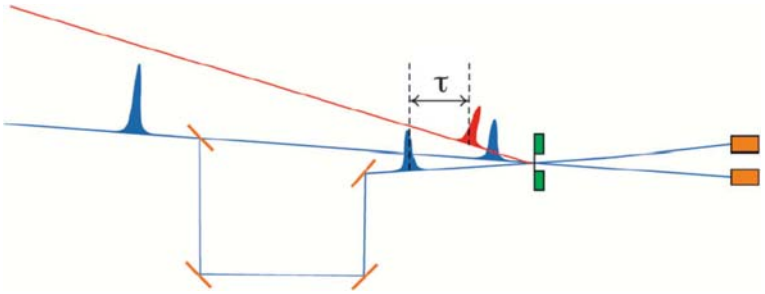

Fig. 19 The "probe-pump-probe" method, where an incoming XFEL pulse is split and delayed. By introducing an optical pump pulse between the two probe pulses, one detector sees an unexcited sample and the other an excited sample.[94]

10.13.5.3 TRXAS experiments conducted at XFEL

XFELS have introduced significant growth to the field of time-resolved (picosecond and femtosecond) X-ray spectroscopies over the past 10 years.[101–105] With the advent of XFELs bringing a significant improvement in time resolution matched with a several orders of magnitude increase in a photon flux per pulse compared to synchrotrons, these two aspects make XFELs a game changer for time-resolved X-ray spectroscopies. They have enabled femtosecond (fs) XAS to be carried out with reasonable data acquisition times,[106] perform fs photon-in/photon-out experiments such as X-ray emission (XES)[107,108] and resonant inelastic X-ray scattering (RIXS)[109,110] studies allowing the analysis of dilute systems. These types of experiments at the fs can only be carried out at XFELs, making these instruments unique. The first short wavelength FEL to be built was FLASH at DESY (Hamburg, Germany) in 2005, which provided vacuum ultraviolet (VUV) and soft X-ray radiation.[111] The first hard X-ray free electron laser Linac Coherent Light Source (LCLS) in the USA (Stanford) was launched in 2009, followed by the X-ray Ultraviolet (XUV)-FEL FERMI in Italy (Trieste)[112–116] and the hard X-ray FEL SACLA in Japan,[117–122] enabling many more studies to be carried on such instruments. The following section will review the technical aspects of these facilities in relation to pump-probe XAS studies bringing into focus the new science that have been realized thanks to them.

The very first fs XAS experiment was conducted on iron(II) tris(2,2′-bipyridine) salts in water ($[Fe(bpy)_3]^{2+}$).[106] This study demonstrated that despite the inherent instabilities of current SASE based XFELs, they can be used to measure high-quality X-ray absorption data. They reported femtosecond time-resolved XANES measurements of a spin-crossover system $[Fe(bpy)_3]^{2+}$ in water. This constituted an experimental study of the photoexcited spin transition dynamics in aqueous $[Fe(bpy)_3]^{2+}$, essentially proving the feasibility of the femtosecond XAS setup conducted at the Linear Coherent Light Source (LCLS) XFEL in Stanford. The XANES measurements were collected on a 50 mM aqueous solution of $[Fe(bpy)_3]Cl_2$ at the XPP station of the LCLS. The setup used a 0.1 mm thick liquid jet and the sample solution was excited with 400 nm laser light generated by a Ti:sapphire laser system with a pulse duration of 50 fs. Experimental setups must always be taken into consideration when measuring at ultrafast conditions, the 0.1 mm jet thickness at 45° led to a ~130 fs fwhm broadening of the time resolution due to the different refractive indices for X-ray and optical light in water. The detector used for X-ray fluorescence was a Si diode. The incoming intensity of polychromatic ("white") and monochromatic beams were measured using two non-invasive diagnostics (one before and one after the X-ray monochromator).[123] Through these diagnostic values, the total number of fluorescence photons at the detector could be calculated to around 10^7 photons per pulse. At ultrafast timescales the timing overlap must be accurately calculated and requires scanning between laser pulse arrival and X-ray pulse delay. Discerning the timing jitter between the pump and probe pulses was estimated to be between 100 and 200 fs full width half maximum (fwhm) through these timing scan measurements (and around 300–500 fs during spectral scans, **Fig. 20**).

XFELs use each electron bunch only once to generate X-rays before dumping the bunch making the X-ray source an inherently stochastic process.[124] This serves to make XFELs intrinsically less stable than storage ring-based X-ray sources. This "intrinsic instability" results in large variation of both the X-ray intensity and the spectrum for consecutive X-ray pulses. The fluctuations can bring a broad bandwidth (~0.3%, i.e., ~20 eV at 7 keV) and shot-to-shot jitter of the central wavelength (~20 eV during the experiment reported here). XANES experiments as required for this study require the use of an X-ray monochromator to precisely define the incoming X-ray wavelength. This still leaves large intensity fluctuations of the monochromatic beam and so a robust normalization must be obtained. This was achieved by taking "calibration runs" before acquiring the time-resolved data.

Spectra of the transient signal was acquired in the energy range 7105–7150 eV with 0.5 eV energy steps for time delays of −1 to +4 ps between the excitation laser pulse and the X-ray laser pulse. The difference XANES spectra were obtained from the experimental XANES spectra by subtracting signal measured at a negative time delay from a signal at various positive time delays. Scans were either performed at a fixed time delay varying the X-ray photon energy (**Fig. 20**a, "spectral scan") or at a fixed X-ray photon energy varying the time delay between the laser pump and the X-ray probe pulses (**Fig. 20**b, "time scan"). Each point in a spectral/time scan was averaged

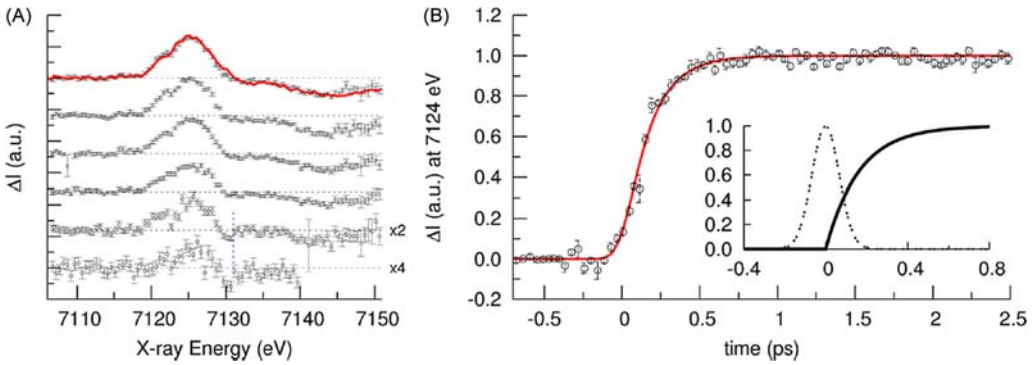

Fig. 20 (a) Difference XANES spectra (empty circles) of a $[Fe(bpy)_3]^{2+}$ salt was taken at time delays of −170 fs, 0 fs, 190 fs, 370 fs, 550 fs, and 1.25 ps. Previously measured transient XANES difference signal at 50 ps time delay is overlaid (red solid line). The disappearance of the negative peak and a shift of the zero-crossing at isosbestic point can be seen with increasing delay. (b) Time-dependent amplitude change of the feature at 7125.5 eV (open circles). The inset of (b) shows the instrument response function.[106]

over 120 or 240 shots (i.e., 2 or 4s because LCLS was running at 60 Hz). The rotary motion of the monochromator also adds a systematic energy dependent change of X-ray path length, corresponding to 48 fs in time over the entire energy range used in the experiment.

This study looked at a transition metal complexes exhibiting a photoinduced spin crossover (SCO) transition in order to provide a good example of the type of experiment and data that could be collected to study electronic dynamics coupled with nuclear motions. The $[Fe(bpy)_3]^{2+}$ cation has three bipyridine (bpy) ligands generating a ligand field, which splits the Fe(II) 3d molecular orbitals into $3d(t_{2g})$ at lower energy and $3d(e_g)$ at higher energy, which are respectively fully occupied and empty in the low-spin (LS) ground state.[17] The stability of the LS state depends critically on the distance of the bpy ligands, where expansion of the Fe—N coordination bonds by ~10% makes the high-spin (HS) quintet state the lowest energy configuration.[125] Due to the rather large energy difference between LS and HS states (0.6 eV), only photoexcitation can lead to an efficient conversion to the HS states.[126] Ultrafast optical transient absorption spectroscopy has been used to photoexcite their metal-to-ligand charge transfer (MLCT) absorption bands centered around 520 nm, resulting in shifting the electron density from Fe(II) center to the ligands. It has been previously reported that the photoexcitation of the MLCT absorption bands triggers a cascade of spin crossover transitions, eventually populating the lowest energy HS.[127] Transient absorption spectroscopy and femtosecond fluorescence studies have shown that population of the HS state occurs in <1 ps.[128–130] Despite this prior knowledge, the mechanism for SCO still remains unclear, in particular regarding the role of possible intermediate ligand-field states between the MLCT and the $^5T_2$ HS state.[131] This uncertainty is difficult to address using the ultrafast transient optical absorption spectroscopy, because the transitions to the involved intermediate spin states are all spin-forbidden and buried throughout the UV-vis spectral range by various allowed charge transfer transitions involving metal and ligand (i.e., MLCT) or ligands only. In contrast, time-resolved XAS makes use of the X-ray absorption properties of the atomic core electrons as an element-selective probe of the local geometrical and electronic structure, in particular the oxidation state of the absorber. Therefore, in principle, time-dependent changes of the nuclear structure and the oxidation state can be extracted from the transient XAS spectra in a robust manner and can complement the ultrafast optical measurements.

The shape of the difference spectra (Fig. 20) did not vary with the time delay. The spectrum at the longest measured delay in this data set (1.25 ps) strongly resembles a $^5T_2$ high-spin state at time delays ≥ 50 ps, the final long-lived high-spin ligand field state. The difference spectrum exhibits a peak at 7125.5 eV, which has been reported to be strongly correlated with the change in Fe—N bond distance.[132] By studying the time dependent rise in transient signal at 7125.5 eV, it was possible to monitor the rate for the formation of bond-elongated excited states like the $^5T_2$. The time dependence of the signal exhibits a fast rise followed by a slower increase. This asymmetric temporal behavior indicates that this measurement has sufficient time resolution to provide a rate of the metastable $^5T_2$ state formation giving an exponential rise time of 163 ± 6 fs. A close inspection at the shape of the difference spectra suggests a small spectral change that is especially noticeable around 7130 eV. Previous studies had suggested that upon photoexcitation, the system HS state is directly populated from the MLCT.[132] In this analysis, upon the photoexcitation of $[Fe(bpy)_3]^{2+}$ some of the electron density is shifted to the bpy ligands and thus the effective oxidation state of the central atom is changed from Fe(II) to Fe(III). Consequently, more energy is required to excite a core electron with an X-ray photon as in the photoexcited state. The XAS spectrum of a trivalent Fe would be expected to be shifted with respect to the one of the bivalent Fe. It has been suggested that the earliest initial photoexcited state is a MLCT state still existing as low spin (MLCT-LS) which would exhibit a spectrum represented as 2 eV shifted copy of the ground state. Fig. 21 is the calculated as difference between the MLCT-LS spectra and the GS spectra.

Fig. 21 demonstrated in this study that it was not possible to entirely resolve the early low-spin MLCT contribution at 7125 eV due to poor signal-to-noise at the earliest time points. The calculations propose the contribution of the MLCT-LS and other

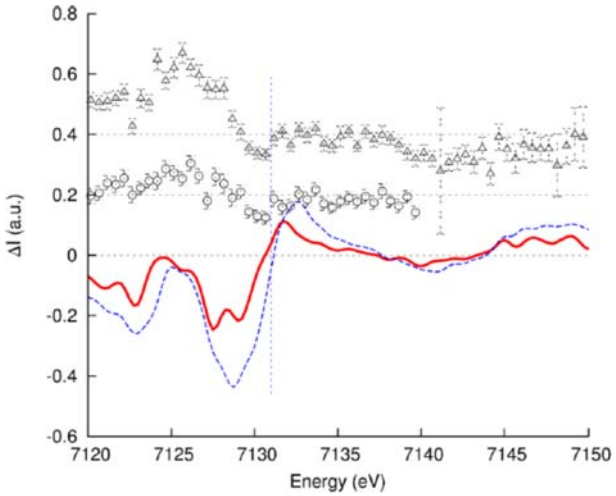

Fig. 21 Difference spectra at the two shortest time delays (points) together with the calculated difference spectrum as a (red) 1 eV shift and (blue) 2 eV shift of the photoexcited MLCT-LS state minus the ground state.[106]

intermediates to be large compared to the HS-state contribution around 7131 eV where the difference spectrum crosses zero. The spectral scans taken at the shortest time delay indicate a small blue shift of the zero-crossing and negative peak, which vanishes with increasing pump-probe time delay. The MLCT-LS model spectrum has a negative peak at ~7128 eV (Fig. 21) that might be responsible for the apparent shift of the zero crossing.

This interpretation does not deviate from the previous femtosecond Fe K-edge XANES measurements on $[Fe(bpy)_3]^{2+}$ salts and similar complexes.[132,133] These studies at the XFEL also had instrument response time-limited dynamics for the formation of the HS excited state. In these cases, with a higher S/N and better time resolution allowed determination of the rate of formation of the $^5T_2$ state more precisely. This study demonstrated a complete mapping of time resolved spectra on the femtosecond time. This is essential to disentangle the complex transient electronic and structural changes, where multiple intermediate excited states might play a role. A significant challenge demonstrated by this study was dealing with timing drifts (hundreds of fs per hour) allowing for collection of only few hundred shots per scan point to limit the duration of each scan to few minutes.

In 2017, this iron complex was further investigated using time resolved X-ray at LCLS. The jet was a 30 μm liquid jet in this case, where using a thin sample minimized the effect of temporal broadening due to inherit mismatching between optical and X-ray beams (~1 fs μm^{-1}). The overall time resolution was found to 60 fs full-width at half-maximum. This later study achieved sub-30-femtosecond resolution and high signal-to-noise ratio. The electronic decay from the initial optically excited electronic state towards the high spin state was distinguishable from the mode identified as molecular breathing. Disentangling these signals, revealed details of intramolecular vibronic coupling before a slower vibrational energy dissipation to the solution environment. Such findings illustrate how modern time-resolved X-ray absorption spectroscopy can provide key information to unravel dynamic details of photo-functional molecules.

10.13.6 Transient X-ray emission spectroscopy or pump-probe XES

Normal X-ray absorption spectroscopy employed for laser pump-X-ray probe studies tune the incident X-ray energy to the inner shell election of an element of interest within a molecule, and the transmission or total fluorescence yield, is measured. X-ray emission spectroscopy (XES) is still quite new in terms of pump-probe experiments. Non-resonant XES is where the incident X-ray energy is tuned above an inner shell edge, ejecting the electron from the element of interest and the fluorescence photon is emitted as an electron decays from an occupied higher-lying orbital to the core hole. This unresolved fluorescence signal will consist of all energies weighted by probabilities of which electron will decay from different occupied orbitals to fill the core hole. XES uses a wavelength-dispersive spectrometer to resolve the emitted fluorescence signal to gain high resolution spectral shapes of the different emission lines to provide accurate information about the occupied orbitals. Due to the more complicated setup combined with a significantly smaller signal makes XES more challenging than XAS especially when in conjunction with a pump-probe experiment. Laser-pump, X-ray-probe XES experiments tend to focus on measuring the core-to-core emission lines, Kα due to 2p → 1s transitions and, the Kβ1,3 and its satellite, Kβ′, due to 3p → 1s transitions. These spectra are sensitive to the unpaired electrons in the metal 3d orbitals, providing spin state information by probing the intra-atomic exchange interaction between the unpaired electron in the 2p (for Kα) or 3p (for Kβ) core hole final state and the unpaired metal 3d valence electrons.[134,135] Kα and Kβ spectroscopy is quite selective for spin state as other properties of the metal ion's chemical environment will not often have an appreciable impact on the core-to-core XES line-shapes.

10.13.6.1 Transient X-ray emission studies of iron complexes in solution

The first laser-pump, X-ray-probe XES experiment measured the iron Kα1 core-to-core emission line of iron, to study laser-induced spin-state switching in a $[Fe(bpy)_3]^{2+}$ salt, in an aqueous solution.[136] This was conducted in 2010 at the Swiss Light Source synchrotron.

This experiment overlapped the laser(L) and X-ray beams(X) on a 0.1 mm thick liquid jet(S) (Fig. 22). Using APDs to collect total fluorescence (D1), transmitted intensity (D2), and XES intensity (D3). The electron-bunch filling pattern at the Swiss Light Source used 2 ns spaced bunches followed by 200 ns gap, in which one densely packed electron bunch is placed (round trip time 960 ns). The monochromatized X-radiation consisted of essentially two different sections, an approximately 760 ns-long "superbunch" together with the well-separated 100 ps-long isolated pulse. A 1 kHz laser could be synchronized to this isolated pulse with an adjustable time delay. Using a gated integrator at twice the repetition rate of the femtosecond laser, created an alternating laser-on/laser-off X-ray intensities.

This was the first study to experimentally detect the spin state change of aqueous $[Fe(bpy)_3]^{2+}$ ions after a 60 ps ultrashort laser pulse excitation using time-resolved X-ray emission spectroscopy (XES). Here the laser excitation induced a spin transition of the central iron ion, from low spin (singlet) to high spin (quintet), detected as a broadening of the Fe Kα line shape, in agreement with static reference spectra and theoretical simulations. Subsequent experiments improved dramatically on the data quality by using a high-repetition-rate pump-probe scheme that used more of the available synchrotron X-ray flux.[137,138] In this way the weaker iron Kβ1,3 spectrum, which shows more sensitivity to the spin state, was also obtained with good signal-to-noise as well as 1s2p resonant X-ray emission (RXES) spectra.[137–139] This early study at synchrotron proved XES to be a valuable spectroscopic technique in order to discover the primary steps of involved in spin transition. It is of key importance to understand and detect both the

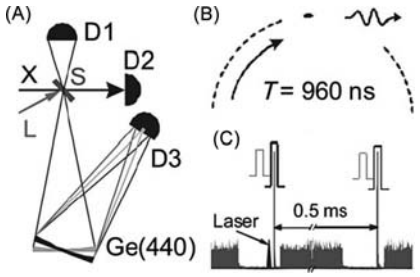

Fig. 22 Experimental setup for pump-probe XES measurement at the SLS.[136]

geometric and electronic changes in real time. Typically X-ray absorption has an emphasis on the structure of the materials, optical spectroscopy such as UV-Vis and IR, address a mixture of vibrational and electronic levels within the entire molecule. Whilst XES does have challenges regarding requirements of high photon flux, it has been demonstrated that it can provide a complete analysis in real time. The $[Fe(bpy)_3]^{2+}$ ion was again investigated with finer time resolution at the Linac Coherent Light Source in 2014.[108,140] By comparison of the transient core-to-core Kβ spectra with those from statically measured reference samples, this analysis observed an initial triplet state moving to a quintet state after excitation (Fig. 23). This study used XES transient difference spectra for $[Fe(2,2'\text{-bipyridine})_3]^{2+}$ measured at 50-fs and a 1-ps (picosecond) time delay. The spectrum in Fig. 23d identifies

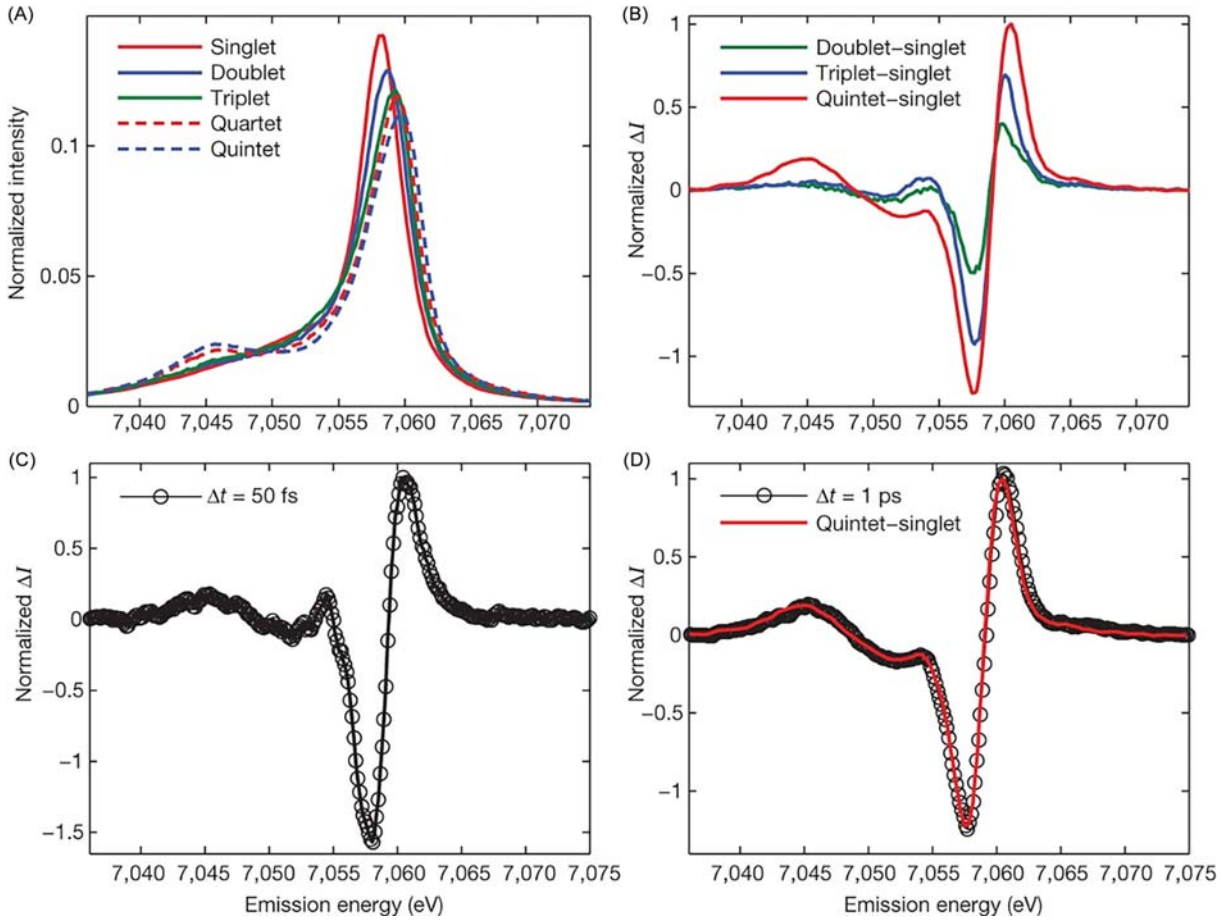

Fig. 23 (a) Displaying reference Kβ fluorescence spectra of ground-state iron complexes each with different spin states: singlet ($[Fe(2,2'\text{-bipyridine})_3]^{2+}$, red), doublet ($[Fe(2,2'\text{-bipyridine})_3]^{3+}$, blue), triplet (iron(II) phthalocyanine, green), quartet (iron(III) phthalocyanine chloride, red dashed), and quintet ($[Fe(phenanthroline)_2(NCS)_2]$, blue dashed). (b) Using spectra from (a), the subtracted difference spectra is displayed for the different spin states. (c) Kβ transient difference spectra obtained at 50-fs time delay for $[Fe(2,2'\text{-bipyridine})_3]^{2+}$ (black circles). (d) Kβ transient difference spectra obtained at 1-ps time delay for $[Fe(2,2'\text{-bipyridine})_3]^{2+}$ (black circles), closely matches the model complex difference spectra of the derived quintet-singlet state shown in (b).[108]

the quintet state with the Kβ fluorescence spectrum. The significant difference between the spectra in Fig. 23c and d, demonstrates the presence of excited-state species other than the quintet state.

XES provides several X-ray signals related to the different energies between molecular orbitals as the electrons redistribute to fill the core hole. Beyond the main core-to-core Kβ1,3 line in Fe XES, on the high energy tail of this transition line, lies the valence-to-core (vtc) region. This contains the Kβ2,5 and Kβ″ lines. This is a difficult spectral region to exploit using pump-probe experiments yet has potential to reveal a great deal of additional information about molecular structure, complementing that obtained from XAS and core-to-core XES. The main difficulty in measuring this feature is that the intensity is orders of magnitude weaker than those of the core-to-core Kβ lines. The theoretical calculations have advanced to show the valence-to-core region as a potential utility of this region where the advancement of the experimental data has been lacking.[141–143] The vtc XES features of transition metal complexes appear to be dominated by dipole transitions of the metal 1s orbital from valence molecular orbitals that are ligand s or p in character containing sufficient metal p mixing to make the transition viable. Thus, vtc XES probes directly valence molecular orbitals that undergo photoinitiated dynamics, whereas core-to-core XES probes the changes that take place in valence orbitals indirectly. Vtc XES also has been shown to overcome limitations in EXAFS spectroscopy in discrimination of the light atoms C, N, or O, which is of importance in areas such as catalysis.[143–148] Furthermore, vtc XES has sensitivity to detect chemical changes in the ligands themselves.[144–146] A key strength of vtc XES is that it can be well characterized by ground-state density functional theory (DFT), without the need for the inclusion of more complex physical descriptions that is usually required to model core-to-core XES or L- and M-edge XANES spectra.[142,149–153] Specific software exists that can aid experimentalists in extracting useful information about molecular orbitals from measured spectra, a user-friendly quantum chemistry software package, ORCA.[142] Having a relatively easy modelling package has allowed for more complex experiments to be conducted with an assurance the data can be understood as for the case in pump-probe measurements. Calculating XANES is often complex as its edge shape is dependent on a combination of electronic and geometric factors which may not be precisely known. For example, the pre-edge region is often a spectral feature that reflects 3d electronic structure and would be an important identifier in the overall spectrum; yet these are often quite small and may fall within the tail of the K-edge making them challenging to resolve experimentally. Vtc spectra has been shown to exhibit substantial spectral variation for different species, and in comparison with experimental spectra, has provided structural resolution when used with XANES and core-to-core XES.

One such study demonstrated the effectiveness of vtc XES using synchrotron X-rays, analyzing a very stable transition metal complex ion, the ferrocyanide $[Fe^{(II)}(CN)_6]^{4-}$ tetra-anion. In a water solution after laser excitation, ferrocyanide is known to undergo two common photoinitiated reactions: photooxidation and photoaquation.[154,155] At 266 nm excitation, the dominant reaction is photooxidation where a photon promotes an electron into a charge-transfer-to-solvent (CTTS) leading to an ejected electron and an oxidized parent ion, ferricyanide $[Fe^{(III)}(CN)_6]^{3-}$. For the photoaquation reaction, the iron ion is excited to the lowest singlet ligand field state, $^1T_{1g}$, which eventually leads to detachment of a CN^- ligand and substitution by H_2O producing $[Fe^{(II)}(CN)_5(H_2O)]^{3-}$. The ground state structure of ferrocyanide was known by XAS and this structure was used as a basis in laser-pump, X-ray-probe studies to understand its photoexcited dynamics.[50,156–158] This analysis focused on the laser-pump, X-ray-probe XES measurements of ferrocyanide, providing further resolution by analyzing the vtc and valence to valence XES resonances.

These experiments were carried out at the 7-ID-D beamline at the Advanced Photon Source, overlapping the X-rays and laser at a fast-flowing 100 μm thick liquid jet.[159] A hybrid singlet storage ring mode was used, where a single electron bunch with 16 mA circulates the ring separated by 1.6 μs on each side from a train of close-spaced bunches containing 86 mA. The singlet pulse was selected to be used solely for the pump-probe experiments. The laser pulses overlapped every other X-ray singlet pulse. The emission spectrometer was a bent Si(531) analyzer crystal, positioned relative to the sample on a 1 m Rowland circle focusing reflected radiation onto an APD detector.

The time-resolved Kβ measurement of ferrocyanide are shown in Fig. 24 at a 120 ps delay between laser and X-ray probe. At this time resolution the ligand field states and CN^- dissociation would be too fast to be resolved thus the measured transient signals are arise from the presence of photoproducts resulting after these changes. The difference is small but observable. For help in identifying the changes of the Kβ emission spectra after excitation, the transient difference between static $[Fe^{(II)}(CN)_6]^{4-}$ and $[Fe^{(III)}(CN)_6]^{3-}$ anionic reference samples were collected. This agreed with the interpretation that $[Fe^{(III)}(CN)_6]^{3-}$ anion would become the dominant photoproduct. However, the core-to-core Kβ's insensitivity to chemical environment means that the spectra of different chemical species with the same or similar spin of the transition metal ion would look very similar. In this case, as photoaquation is known to occur alongside the photo-oxidation, the photoaquated product $[Fe^{(II)}(CN)_5(H_2O)]^{3-}$ anion could contribute to the difference signal arising from a change in the metal-ligand covalency.[154,155,160] Alongside other permutations, separating contributions from multiple photoproducts in core-to-core Kβ emission spectra is a challenge and stands in the way of obtaining useful spin-state information for products involved in photochemical reactions.

At 50 eV to higher energy the vtc region is known to provide more sensitivity to the chemical environment of the absorbing metal ion. Measured and calculated vtc spectra of aqueous $[Fe^{(II)}(CN)_6]^{4-}$ anion are shown at the top of Fig. 25. The intensity is considerably weaker compared to the core-to-core Kβ1,3 fluorescence, with a peak count rate of 130 counts per second as compared to 4200 counts per second. The features arise from transitions to the Fe 1s core from molecular orbitals that are primarily ligand 2p in character.[142] The intensity is related to the amount of Fe p-orbital mixing with the ligand valence orbitals. As can be seen, the calculated spectrum reproduces the experimental features well. The DFT analysis indicates that the molecular orbitals probed are concentrated on the ligands which have dominantly p character. For comparison, the experimental and calculated vtc spectra

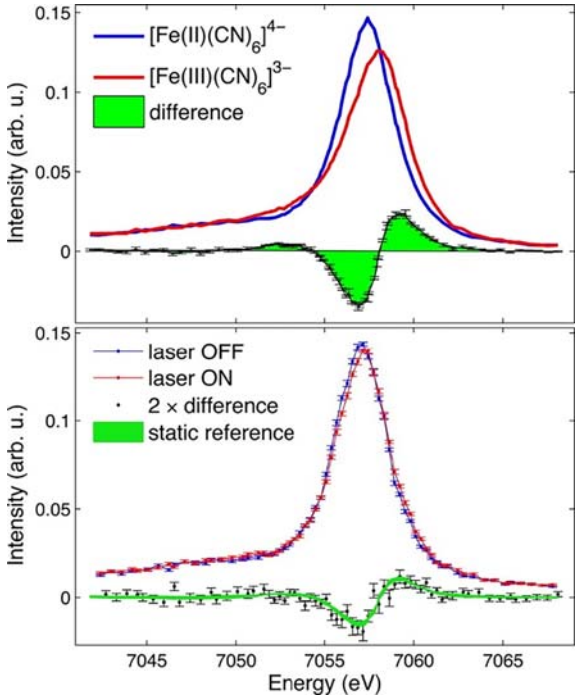

Fig. 24 Measured iron core-to-core (3p → 1s) Kβ emission spectra. Static measurements on 0.4 M aqueous $[Fe^{(II)}(CN)_6]^{4-}$ (blue) and $[Fe(III)(CN)_6]^{3-}$ (red) are shown in the top panel along with the difference. 0.05 M aqueous $[Fe^{(II)}(CN)_6]^{4-}$ pumped with 266 nm light, measured 120 ps after laser excitation is shown in the bottom pane and the differences are compared.[140]

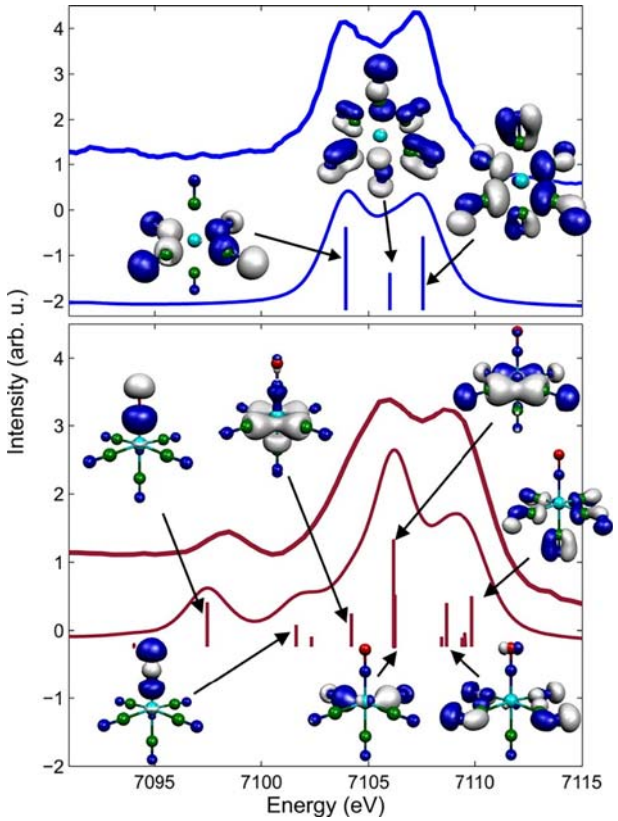

Fig. 25 Measured iron valence-to-1s core XES compared with DFT-simulated spectrum. (top) Measured vtc XES of 0.4 M aqueous $[Fe(CN)_6]^{4-}$ and the calculated spectrum for the same ion. (bottom) Spectrum of sodium nitroprusside, in solid form, and calculations for the $[Fe(CN)_5(NO)]^{2-}$ ion.[140]

of sodium nitroprusside are shown in the bottom panel of Fig. 25 to demonstrate the vtc signal sensitivity in ligand environments. $[Fe(CN)_5(NO)]^{2-}$ anion is very similar to $[Fe(CN)_6]^{4-}$, being low spin and having an iron oxidation state of +2, but differs only by replacing an NO^+ ligand in place of a CN^- ligand. Yet, this change does have a dramatic impact on the vtc spectrum which shows key satellite peaks due to transitions from ligand 2s orbitals.[142,148] The observed energy of the satellite peak is related to the ligand's 2s binding energy and can be used to identify the type of ligand. The intensity of this feature is linked with the metal-ligand bond distance. This is a large peak in the $[Fe(CN)_5(NO)]^{2-}$ spectrum, having a short Fe–N bond length (1.66 Å). For $[Fe(CN)_6]^{4-}$ this satellite peak is also observed but is smaller and broader, therefore not as clear from the background. The $[Fe(CN)_5(NO)]^{2-}$ vtc region is shifted to higher energy relative to the $[Fe(CN)_6]^{4-}$ spectrum, arising as the vtc spectrum is sensitive to the effective nuclear charge on the metal.[142] Here a negatively charged CN ligand has been replaced by a positively charged NO ligand leading to an effective charge difference of +2 between the two complexes. This is reflected by the corresponding shift of the vtc spectrum to higher energy.

The experimental measurements of time-resolved vtc XES is shown in the top panel of Fig. 26, as the difference between laser-on and laser-off after 120 ps excitation of 50 mM aqueous $[Fe^{(II)}(CN)_6]^{4-}$. The emission spectrometer was cycled through the four emission energies sitting at each point for 2 min at a time, making a total of 2-h integration time at each point. When the transient data is compared to the difference between static measurements of $[Fe^{(II)}(CN)_6]^{4-}$ and $[Fe^{(III)}(CN)_6]_3$ it appears the time-resolved points lie quite close to the derived transient signal. A photoaquated product $[Fe^{(II)}(CN)_5(H_2O)]^{3-}$ is also expected to be present but as this complex is unstable and difficult to measure even in a static measurement, its vtc spectrum had to be calculated computationally. The lower panel of Fig. 26 displays the calculations performed to generate $[Fe^{(II)}(CN)_6]^{4-}$, $[Fe^{(III)}(CN)_6]^{3-}$, and $[Fe^{(II)}(CN)_5(H2O)]^{3-}$ spectra. The $[Fe^{(II)}(CN)_6]^{4-}$ and $[Fe^{(III)}(CN)_6]^{3-}$ spectra agree with the experimental spectra. The calculated $[Fe^{(II)}(CN)_5(H_2O)]^{3-}$ spectrum is very similar to the $[FeII(CN)_6]^{4-}$, with only changes in intensity. This was suggested that as the Fe–O distance is rather large for $[Fe^{(II)}(CN)_5(H_2O)]^{3-}$(2.19 Å compared with 1.92 Å for the Fe–C distance in the Fe–CN bonds), hence little overlap of the O 2s and 2p orbitals with the Fe center. As a result, there is negligible contribution to the signal. The spectrum is dominated by five CN ligands as opposed to six, and therefore the intensity of the signal is less than expected. The symmetry of $[Fe^{(II)}(CN)_5(H_2O)]^{3-}$ is distorted relative to $[Fe^{(II)}(CN)_6]^{4-}$, which did not appear to influence the shape of the spectra as seen in previous similar measurements.[142] This study was conducted at a synchrotron and as such, only four transient points were investigated, taking a total of *ca.* 8 h collection time. This can be improved upon with the addition of adding more points to gain a complete transient vtc spectrum by increasing the fluorescence detection efficiency and incident X-ray flux, which can make vtc time-resolved spectra possible. By increasing the number of crystal analyzers, detection efficiency can be improved, where such

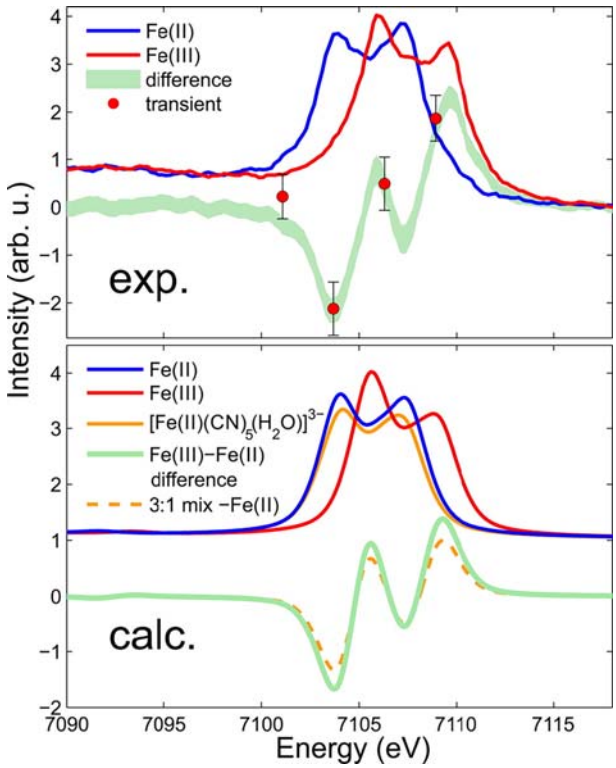

Fig. 26 Valence-to-core emission spectra of $[Fe^{(II)}(CN)_6]^{4-}$ (blue) and $[Fe^{(III)}(CN)_6]^{3-}$ (red). Measured spectra of the compounds in aqueous solution are shown in the top panel. DFT calculated spectra are shown in the bottom panel along with a third possible species, $[Fe^{(II)}(CN)_5(H2O)]^{3-}$. The differences between the $[Fe^{(II)}(CN)_6]^{4-}$ and $[Fe^{(III)}(CN)_6]^{3-}$ spectra are shown in green. The red data points are the difference between laser-on and laser-off, 120 ps after 266 nm laser excitation of $[Fe^{(II)}(CN)_6]^{4-}$.[140]

multi-crystal spectrometers have been implemented at the ESRF,[99,161] the Swiss Light Source,[162] the APS,[163] and the LCLS.[164] One must consider that as the number of analyzers increases, so does the complexity, and too many[165]can render the experiment too technically challenging.

These measurements were carried out with a monochromatic beam, lowering the bandwidth but also the incident flux of the X-ray beam. For XES, monochromaticity is perhaps not necessary for emission spectroscopy. The requirement is that the X-ray photon energy only needs to be a few hundred electron volts above the absorption edge making XES compatible with pink beam. Such conditions can be provided at certain synchrotrons but also at XFELs using SASE radiation. This can dramatically increase the flux per pulse but one must consider the significantly lower repetition rate at XFEL compared to synchrotron, despite a dramatic increase in pulse flux. Another route is to increase the laser repetition rate thereby making more efficient use of the available X-rays delivered. This can be dictated by the delivery mode set by the storage ring and the time taken for the samples to refresh before each proceeding laser pump. For the above study, the result was only 15% use of the available X-ray flux. With improved jet flow and appropriate laser and X-ray setups, this will move such an experiment from the kHz collection to the MHz collection regime. Clearly an increase in signal is required to make time-resolved valence-to-core spectroscopy feasible and routine, where the technical improvements to reach this are already available.

10.13.7 Transient X-ray spectroscopy of metalloporphyrin chemistry at XFEL

Metalloporphyrins have long been an area of study in inorganic chemistry. They have an ability to perform many different chemical transformations as light harvesting/electron transfer cofactors, both in biological processes (i.e., natural photosynthesis and[63] physiological oxygen transport[166]) and photocatalytic processes where they act as redox centers.[65,167,168] With often complex ligand framework around the metal, this allows for a high degree of chemical tunability in both the choice of metal center and the ligated macrocycle. Changes in macrocycle functionalization can dramatically impact metalloporphyrin ring conformation and rigidity, leading to varied redox and ligand binding properties, as well as the ability to impact relaxation dynamics by altering the energetic ordering of excited states. To understand and visualize the excited state dynamics, XFELs have proved themselves beyond capable of providing unprecedented detailed information on how metalloporphyrins operate because of their ability in producing femtosecond X-ray pulses.[169,170] Combining an ultrafast X-ray source with an ultrafast optical laser pulse capable of triggering photochemical processes allows quantitative analysis of the evolution of the electronic and nuclear dynamics of transition metal complexes. By implementing this experimental approach along with accurate theoretical modelling, rational control over transient, catalytically active transition metal complexes becomes a possibility.

In 2016, the ultrafast excited state dynamics of nickel(II) tetramesitylporphyrin (NiTMP) was studied using XFEL.[133] NiTMP which exists in the ground state as an ensemble of ring conformers and has been previously studied by optical absorption and Raman spectroscopy.[171–178] These studies proposed that within 20 ps of photoexcitation, this caused the S0 → S1 transition which is a porphyrin macrocycle based $\pi \rightarrow \pi^*$ transition. The newly promoted π^* orbital electron crosses to an empty $3d_{x^2-y^2}$ orbital. At which point, an electron from an originally filled $3d_{z^2}$ orbital moves to fill the hole in the porphyrin based π orbital left by the initial photoexcitation. This results in the lowest lying triplet state, ($3d_{z^2}$, $3d_{x^2-y^2}$) denoted as T(d,d) (**Fig. 27**).[173,179] Previous TR-XAS studies on the NiTMP system were performed at a synchrotron source (APS) at ~100 ps time resolution.[74,179] These could verify that the excited T(d,d) state has an $(3d_{x^2-y^2})^1$ $(3d_{z^2})^1$ electronic configuration as proposed through optical spectroscopy. This study was able to resolve the state's elongated Ni—N bond length and flattened macrocycle conformation using Extended X-ray Absorption Fine Structure (EXAFS).[74,179,180] However, the time resolution of the synchrotron X-ray pulses was unable to provide experimental information on the proposed excited state structural dynamics before the development of the relaxed T(d,d) state. Taking this system to XFEL, this missing time window in the evolution of excited Ni(*II*)TMP was obtained by collection of TR-XAS near the nickel K-edge (8333 eV) at sub-picosecond time resolution. The facility used was the Linac Coherent Light Source (LCLS).[106,181]

Fig. 28 shows the difference spectra of the photoactivated NiTMP complex at time delays of −5 to 20ps. The feature around 8337 eV in the difference spectra (E1) rises rapidly to its maximum amplitude at 400–800 fs, and decays within ~2 ps (**Fig. 28**b and c). After ~2 ps, the XANES difference reflects an increasing population of T(d,d) state, whose features are fully developed by 10 ps. A transient state was identified by observing that the loss of the ground state was at a different rate than that of the growth of the T(d,d) state. This intermediate state was denoted as T′ (**Fig. 27**) preceding the relaxed T(d,d) state (**Fig. 28**c). Another spectral feature on the ps time scale is an apparent delay between the rise of the white line peak feature at 8353 eV, which is an indication of the Ni—N bond elongation as seen in the T(d,d) state, and the rise of the 1s → 4pz transition peak associated with T(d,d). It appears that there is little growth of this feature until 2 ps delay time, suggested as a postponed nuclear geometry change. This could conceivably arise due to an expansion of the Ni—N bond. These measurements gave at the Ni K-edge gave sub picosecond optically excited mechanistic for Ni(*II*)TMP. Identifying importantly, a transient Ni(I) (π, d) electronic state (T′) is implicated as an intermediate through the interpretation of a short-lived excited state absorption. The assignment of this absorption is confirmed by agreement with calculated XAS transitions for the postulated (π, d) electronic states at this energy.

There have also been studies into photoactivation of porphyrin based cobalt metalloenzymes. Analysis of photoactivated cobalamins (Cbls) have garnered interest due to their applicability in controlling outcomes such as radical formation,[182] drug delivery,[183,184] gene activation,[185–187] and B_{12} bioavailability.[188,189] Photoinduced bond cleavage is central to both the engineered and the natural biological exploitations of cobalamin photochemistry. The use of ultrafast time-resolved X-ray spectroscopy at XFEL

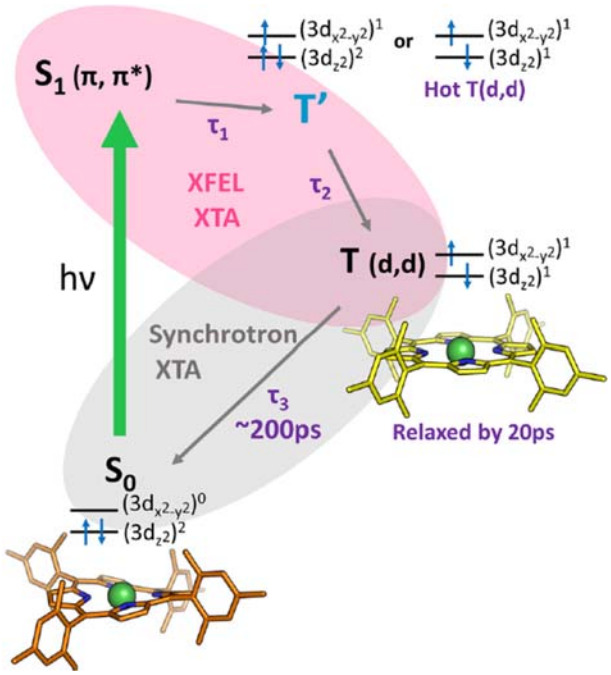

Fig. 27 Relaxation pathway of NiTMP following 527 nm excitation.[133]

provided an opportunity to probe structural changes in short-lived states. These studies analyzed the XANES region where the K-edge of 3d transition metals has proven to be particularly sensitive in identifying changes of bonding and oxidation state upon optical excitation.[190–193]

This work reported the excited state of Me-Cbl following excitation at 520 nm. A complementary measurement on coenzyme B_{12}, (AdoCbl) is used to characterize the cob(*II*)alamin product that forms in nearly 100% yield on a 100 ps time scale following photoexcitation of this compound.[194,195] These measurements could eliminate the ambiguity in assignment of features in the XANES spectrum to the MeCbl excited state or to cob(II)- alamin. By using polarized X-rays, the x, y and z axis components could be separated, and these difference spectra found that an expansion of the ring was a key contributor to the excited state, but little evidence for significant elongation of the Co—C bond (**Fig. 29**). Thus, the difference between the ground and excited-state structures is dominated by changes in the ring. In contrast, the XANES difference spectrum following photodissociation of AdoCbl is reflecting the loss of the upper axial ligand and the formation of cob(*II*)alamin.

A further study conducted at XFEL also used polarized X-ray absorption near-edge structure (XANES) at the Co K-edge to monitor the excited-state structure of coenzyme B_{12} (AdoCbl) over the first picosecond following excitation.[197] These measurements provided a cobalt-centered movie of the excited molecule as it evolves to the local excited-state minimum. Through femtosecond time-resolved XANES the excited-state dynamics followed excitation of AdoCbl in water and in ethylene glycol. They could demonstrate the rapid sequential distortion in the ring of the molecule in the initial optically bright state. An expansion of one or possibly both axial bonds occurs on a 214 fs time scale. Electronic changes resulting in a change of the UV-vis spectrum accompany the structural changes revealed in the XANES spectrum (**Fig. 30**). It was possible to identify the bright state and the changes correlated to its evolution.

Previous studies on similar compounds demonstrated an expansion to a maximum at 190 fs followed by a contraction to the excited-state minimum within 500 fs. For AdoCbl, the response of the axial nuclei is slower, reaching an expansion maximum around 450 fs. This was thought to be occurring due to the more massive adenosyl axial ligand. Calculations have shown that the shape of the excited-state potentials influenced by the different axial ligands are perhaps the more important factor.[198,199]

In 2021, the dynamics of photodissociation and recombination in heme proteins were investigated at an XFEL.[200] Iron porphyrin compounds in heme proteins represent an archetypical photochemical reaction widely used to understand the interplay between chemical dynamics and reaction environment. This report is a study of the photodissociation mechanism for the Fe(II)—S bond between the heme iron and methionine sulfur of ferrous cytochrome *c*. This bond dissociation is crucial in the conversion of cytochrome *c* from an electron transfer protein to a peroxidase enzyme. At XFEL, it was possible to follow the dynamics of Fe(II)—S bond dissociation and 1s3p (Kβ) X-ray emission spectroscopy to follow the dynamics of the iron charge and spin multiplicity during bond dissociation. Using the Kβ XES spectrum of 3d transition metal ions has proven to be sensitive to the effective 3d spin moment.[139,160] These attributes can be used to follow the femtosecond dynamics of charge transfer and intersystem crossing of transition metal complexes.[201]

This Kβ XES study investigated the potential role of electronic excited state optically generated through a π-π* transition and the quintet metal-centered (5MC) state, observed at time delays beyond 600fs. The appearance of a time-dependent difference signal

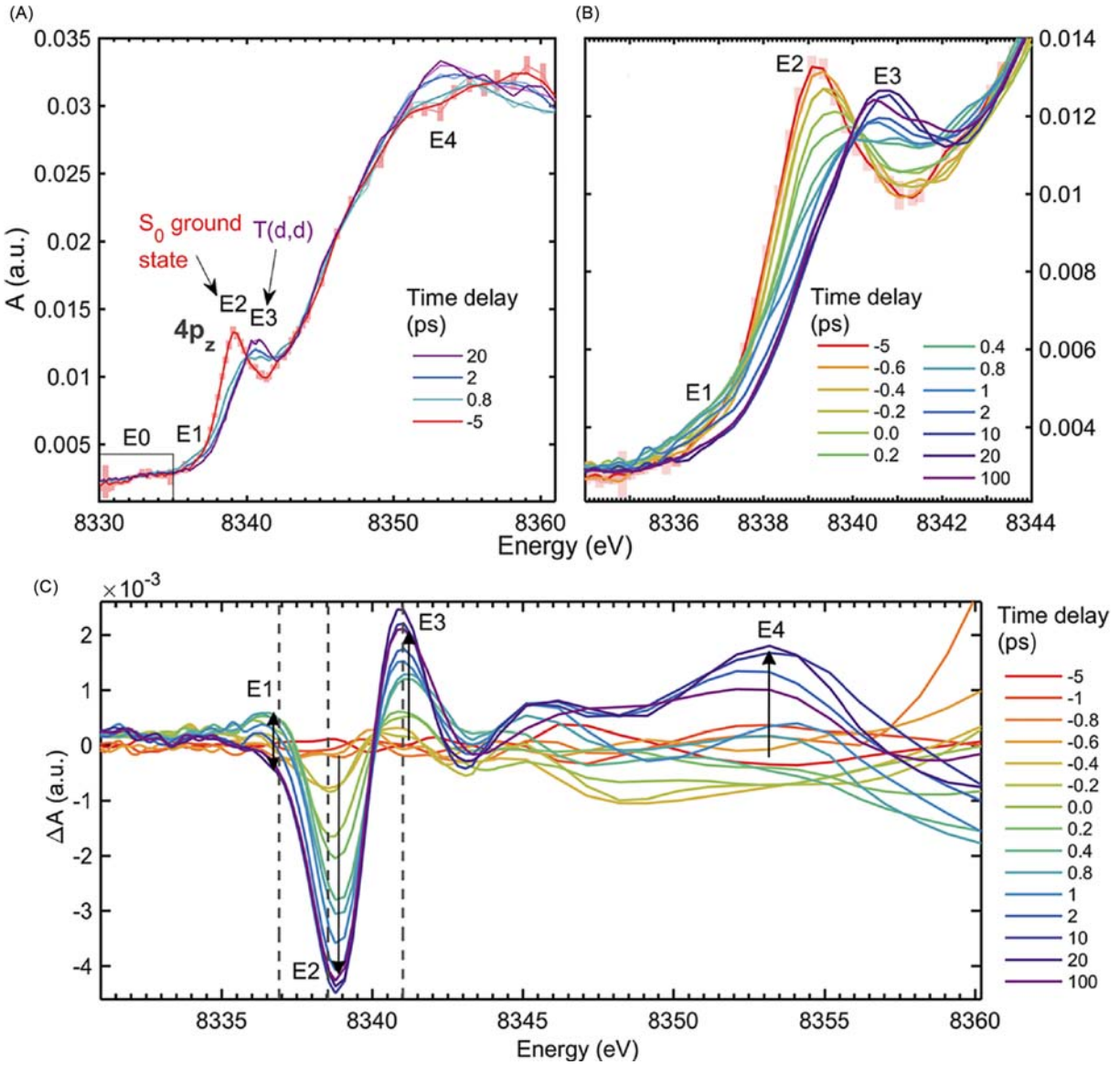

Fig. 28 Ni K-edge XANES spectra of NiTMP between −5 and 100 ps following 527 nm excitation. Numbered energies correspond to E0, the pre-edge region E1, a transient at the low-energy end of the 1s → 4pz region; E2, the S0 1s → 4pz transition; E3, the T(d,d) 1s → 4pz transition; and E4, the white-line feature associated with shortened Ni− N bonds in the T(d,d) state. (a) Time delays characteristic of (−5 ps) S0, (0.4 ps) the peak of the transient signal at 8337 eV, (2 ps) the partial disappearance of the transient at 8337 eV, the appearance of the T(d,d) 1s → 4pz peak at E2, and the shift of the primary white line feature to E4, and (20 ps) T(d,d). (b) The evolution of the XANES from −5 to 100 ps within the 1s → 4pz region. (c) Difference spectra relative to S0 spectrum for delays between −5 and 100 ps, showing the dynamics of the S0 bleach (E1), the rise of the T(d,d) 1s → 4pz peak (E2), the rise and fall of the transient at 8337 eV within 2 ps (E3) and the rise of the white line feature (E4).[133]

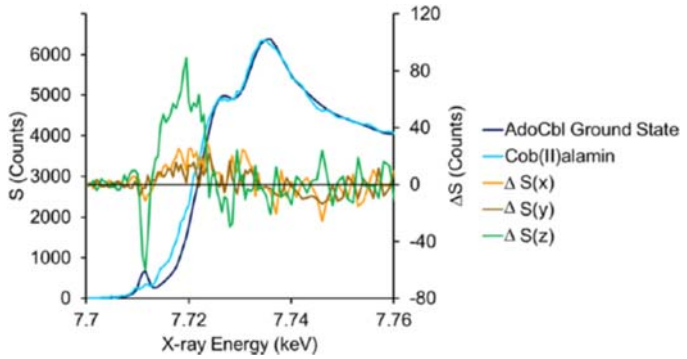

Fig. 29 XANES spectrum of AdoCbl obtained from the optical laser off a measurement at 250 ps time delays following excitation at 540 nm. XANES difference spectrum at 250 ps decomposed into contributions in the x, y, and z directions.[196]

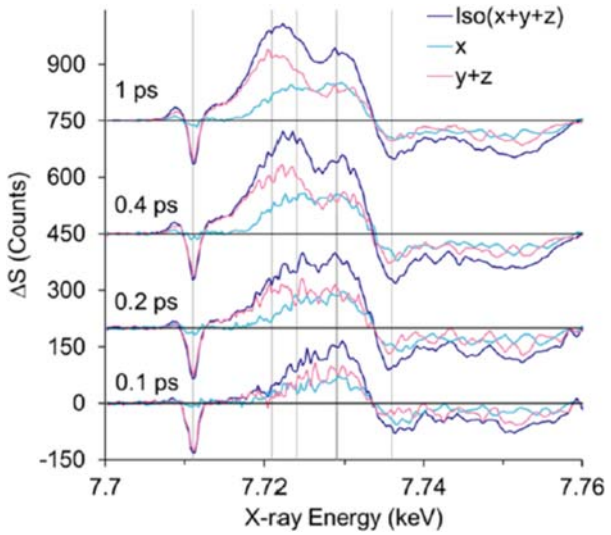

Fig. 30 XANES difference spectrum averaged around four key time delays as indicated on the plot. Both the isotropic spectrum and the decomposition into the x and y + z contributions are plotted.[197]

distinct from the 5MC state provided evidence for additional states involved in the excited state relaxation dynamics, where the π-π* state would not be expected to contribute to the difference spectra as it is not Fe centered. Fig. 31b–d is the difference signal during the first 850fs after excitation. The spectral shape of the difference signal at early time delays (Fig. 31c) is clearly distinct from the difference signal at later delay times. This indicates the presence of a short-lived excited state distinct from the π-π* and 5MC states. Using the reference spectra for different spin configurations as a guide, shown in Fig. 31a, the delayed negative difference signal at 7054 eV as compared to 7058 eV, shown in Fig. 31d, indicates an intermediate state has either a doublet, triplet or quartet configuration. This was the subject of a detailed computational analysis confirming the presence of a short-lived intermediate in the relaxation mechanism assigning it to a triplet metal-centered (3MC) state. The reference spectra as shown in Fig. 31a was used to fit the time-resolved XES difference spectra using a rate equation model.

Notably, detecting short-lived electronic excited states involved in ligand photolysis of heme compounds is very challenging.[202–207] Traditionally, excited states have been used to reconcile in-plane electronic redistribution associated with π-π* photoexcitation bringing dissociative motions along the axial ligand coordinate. Studies on CO photolysis from myoglobin have suggested that ultrafast CO dissociation proceed through a very short-lived, low-lying triplet excited state.[202,205] Yet these findings relied heavily on earlier theoretical work without support from experimental data.[208] In this analysis, using femtosecond resolution Kβ XES, a short lived triplet metal-centered intermediate state was identified having a $3[3d\pi,1d_z^2]$ configuration. Population of this state occurs from the $\pi - \pi^*$ excited state and decays with an 87fs lifetime to an Fe(II) quintet electronic excited state with a $5[2d\pi, 1d_z^2,1d_{xy}^2]$ configuration. With the use of structural modelling, assignments of the reduction in intensity between 0.4Å^{-1} and $1.1\ \text{Å}^{-1}$ were given as the axial Fe(II)−S bond dissociation and axial Fe(II)−N bond elongation. Thus, the conclusion of these measurements were that the formation of a triplet metal-centered excited state with anti-bonding Fe(II)−S interactions triggers the bond dissociation and precedes the formation of the metastable Fe high-spin quintet state.

10.13.8 Final remarks

TR-XAS can be a challenging experiment often requiring the synchronization of several instruments and detectors in order to obtain valid experimental data. Despite that, research is ever growing in attempting to define systems at the earliest time points after an initiation event. The main challenges in these experiments are often the sample delivery system and the accurate timing requirements. The sample delivery requires a constant refreshing of material before the next initiation event occurs, in most cases the laser pulse. The initiation event must be accurately timed in relation to the probe, in order to know at which time points the data is being collected on the system. The more these experiments are conducted at various facilities, the experimental setups can become more routine allowing a much easier standardized setup that can be applied to wider field of chemistry over that of just very specific systems. Furthermore, the more 'routine' the pump-probe experiments become, a greater confidence will be instilled into the non-specialist community, where such users feel assured that they can collect useful and meaningful data on their system of interest without having or needing the specialist knowledge required to setup the experiment. Also, it is important that to widen the field still further, is to explore systems than can be collected in pump-probe mode. In this discussion the focus has been on solution state sample as this is the majority, because practically it is much easier to refresh the material between each laser pulse, by flowing the solution. For solid state samples it becomes more difficult as the same spot is exposed to X-ray and laser radiation, it increases the

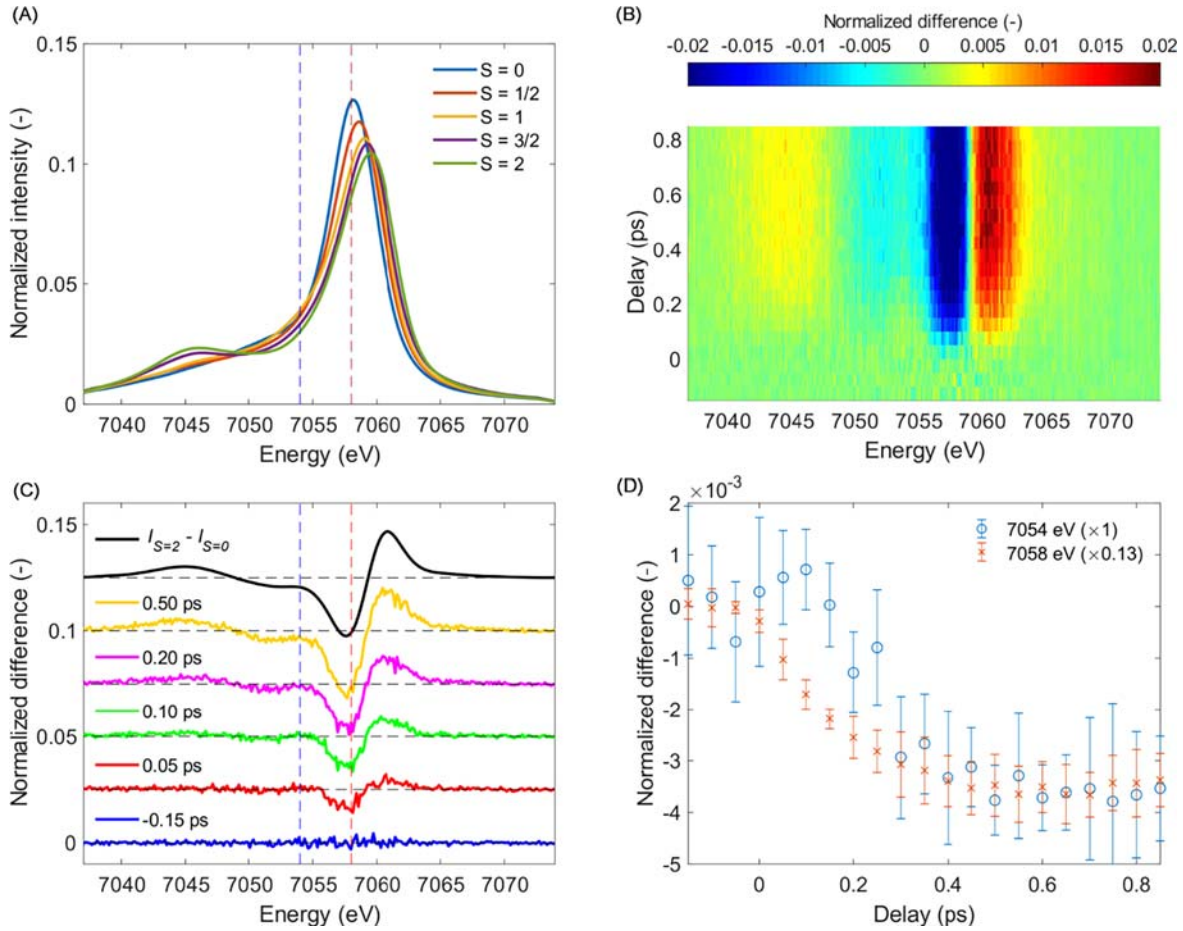

Fig. 31 (a) Area-normalized Kβ X-ray emission spectroscopy (XES). Singlet ($[Fe(2,2'\text{-bipyridine})_3]^{2+}$, blue), doublet ($[Fe(2,2'\text{-bipyridine})_3]^{3+}$, red), triplet ($Fe^{(II)}$phthalocyanine, orange), quartet ($Fe^{(III)}$phthalocyanine chloride, purple), quintet ($[Fe(phenanthroline)_2(NCS)_2]$, green). (b) Two-dimensional map of cytochrome *c* Kβ XES difference signal. (c) Difference spectra at various time delays. (d) Time-dependence for Kβ X-ray emission energies indicated by dashed vertical lines in c.[200]

risk of beam damage to samples. Typically, optical excitation is the reaction initiator but to apply this technique to as wide field as possible, alternative initiations should be considered, such as localized heating, electrical or reagent changes. These do become more challenging in terms of the timing accuracy and repeatability, where a laser pulse in terms of timing can be accurately characterized and synchronized.

Today, two major types of facility dominate the field on laser pump-X-ray probe analysis, X-ray Free Electron Lasers and synchrotron radiation light sources. The use of one facility does not provide a complete picture of a photochemical mechanism but rather operate in two separate time domains. The synchrotron studies can provide picoseconds measurements but at greatly reduced flux. Synchrotron measurements do excel at providing continued time points on the nanoseconds to microseconds being higher repetition rate probe source. Furthermore, this can extend beyond the XANES to EXAFS with a much larger scanning range allowable and providing a different level of detail of the system under analysis. XFELs have proven to really excel at the femtosecond time point providing such unprecedented flux per pulse. It is at these time points the range of energetics after laser excitation that can be explored before any molecular movements but are the fundamental transfer mechanism that will determine all subsequent steps the chemistry will take. Thus, XFEL and synchrotron should not be seen as competing sources in terms of pump-probe facilities but rather complimentary analysis.

Currently there are limited inorganic systems that have been studied at XFELs, the main systems being important biological enzymes and mimics and iron pyridyl based complexes. Regarding synchrotrons, with pump-probe studies truly beginning in the 1990s, there is now whole host of inorganic systems that have been studied, at various time points and at different sampling conditions. In the last 20 years synchrotron pump-probe analysis is reaching the more routine space with several facilities and beamlines offering such experiments. Currently XFELs appear to still be in the infancy of their capabilities in terms of inorganic systems but the potential is absolutely huge. Moving beyond the more typical XAS experiments, with such increased flux and short pulses, able to reach incredibly flux hungry methods like X-ray emission spectroscopy. At XFELs this is often collected complimentary to XAS at the very least as this is generated alongside traditional XAS measurements.

A common feature discussed in all TRXAS data analysis is the computational aspect of the analysis. This is so crucial in generating models that can be fit and statistically analyzed against experimental data. In as much as the field wants to expand experimentally, reaching ever faster timescales and more advanced detection methods, without the continued progress of computational analysis, the field would always be limited. Typically, 3d metals can be accurately modelled by many user-friendly software packages but often going outside this scope can present many difficult challenges to the data analysis. In as much as the experimental data has a reliance on the theoretical calculations, the theoretical calculations need experimental data to compare, contrast and adapt.

References

1. Porter, G. Flash Photolysis and Spectroscopy. A New Method for the Study of Free Radical Reactions. *Proc. R. Soc. A* **1950,** *2061* (200), 284.
2. El-Sayed, M. A.; Tanaka, I.; Molin, I. U. N. *Ultrafast Processes in Chemistry and Photobiology*, Blackwell Science, 1995.
3. Nobel Prize Outreach (2022) NobelPrize.org. https://www.nobelprize.org/prizes/chemistry/1999/press-release. Nobel Prize Outreach AB 2022.
4. Nocera, D. G. The Artificial Leaf. *Acc. Chem. Res.* **2012,** *45* (5), 767–776. https://doi.org/10.1021/ar2003013.
5. Teets, T. S.; Nocera, D. G. Photocatalytic Hydrogen Production. *Chem. Commun.* **2011,** *47* (33), 9268–9274. https://doi.org/10.1039/C1CC12390D.
6. Berardi, S.; Drouet, S.; Francàs, L.; Gimbert-Suriñach, C.; Guttentag, M.; Richmond, C.; Stoll, T.; Llobet, A. Molecular Artificial Photosynthesis. *Chem. Soc. Rev.* **2014,** *43* (22), 7501–7519. https://doi.org/10.1039/C3CS60405E.
7. Zhang, W.; Hong, J.; Zheng, J.; Huang, Z.; Zhou, J.; Xu, R. Nickel–Thiolate Complex Catalyst Assembled in One Step in Water for Solar H2 Production. *J. Am. Chem. Soc.* **2011,** *133* (51), 20680–20683. https://doi.org/10.1021/ja208555h.
8. Alperovich, I.; Moonshiram, D.; Concepcion, J. J.; Pushkar, Y. Electronic Structure Assessment: Combined Density Functional Theory Calculations and Ru L2,3-Edge X-Ray Absorption Near-Edge Spectroscopy of Water Oxidation Catalyst. *J. Phys. Chem. C* **2013,** *117* (37), 18994–19001. https://doi.org/10.1021/jp405648h.
9. Chen, L. X.; Zhang, X. Photochemical Processes Revealed by X-Ray Transient Absorption Spectroscopy. *J. Phys. Chem. Lett.* **2013,** *4* (22), 4000–4013. https://doi.org/10.1021/jz401750g.
10. Velasco, L.; Llanos, L.; Levín, P.; Vega, A.; Yu, J.; Zhang, X.; Lemus, L.; Aravena, D.; Moonshiram, D. Structure and Excited-State Dynamics of Dimeric Copper(i) Photosensitizers Investigated by Time-Resolved X-Ray and Optical Transient Absorption Spectroscopy. *Phys. Chem. Chem. Phys.* **2021,** *23* (5), 3656–3667. https://doi.org/10.1039/D0CP06080A.
11. Gawelda, W.; Johnson, M.; de Groot, F. M. F.; Abela, R.; Bressler, C.; Chergui, M. Electronic and Molecular Structure of Photoexcited [RuII(Bpy)3]$^{2+}$ Probed by Picosecond X-Ray Absorption Spectroscopy. *J. Am. Chem. Soc.* **2006,** *128* (15), 5001–5009. https://doi.org/10.1021/ja054932k.
12. Vlček, A. The Life and Times of Excited States of Organometallic and Coordination Compounds. *Coord. Chem. Rev.* **2000,** *200–202,* 933–978. https://doi.org/10.1016/S0010-8545(00)00308-8.
13. Balzani, V.; Juris, A.; Venturi, M.; Campagna, S.; Serroni, S. Luminescent and Redox-Active Polynuclear Transition Metal Complexes. *Chem. Rev.* **1996,** *96* (2), 759–834. https://doi.org/10.1021/cr941154y.
14. Juris, A.; Balzani, V.; Barigelletti, F.; Campagna, S.; Belser, P.; von Zelewsky, A. Ru(II) Polypyridine Complexes: Photophysics, Photochemistry, Eletrochemistry, and Chemiluminescence. *Coord. Chem. Rev.* **1988,** *84,* 85–277. https://doi.org/10.1016/0010-8545(88)80032-8.
15. Yeh, A. T.; et al. Ultrafast Electron Localization Dynamics Following Photo-Induced Charge Transfer. *Science* **2000,** *289* (5481), 935–938. https://doi.org/10.1126/science.289.5481.935.
16. Damrauer, N.; Cerullo, G.; Yeh, A.; Boussie, T.; Shank, C.; McCusker, J. Femtosecond Dynamics of Excited-State Evolution. *Science* **1997,** *275,* 54–57.
17. Creutz, C.; Chou, M.; Netzel, T. L.; Okumura, M.; Sutin, N. Lifetimes, Spectra, and Quenching of the Excited States of Polypyridine Complexes of Iron(II), Ruthenium(II), and Osmium(II). *J. Am. Chem. Soc.* **1980,** *102* (4), 1309–1319. https://doi.org/10.1021/ja00524a014.
18. Bressler, C.; Chergui, M. Ultrafast X-Ray Absorption Spectroscopy. *Chem. Rev.* **2004,** *104* (4), 1781–1812. https://doi.org/10.1021/cr0206667.
19. Stynes, H. C.; Ibers, J. A. Effect of Metal-Ligand Bond Distances on Rates of Electron-Transfer Reactions. Crystal Structures of Hexaammineruthenium(II) Iodide, [Ru(NH3)6]I2, and Hexaammineruthenium(III) Tetrafluoroborate, [Ru(NH3)6][BF4]3. *Inorg. Chem.* **1971,** *10* (10), 2304–2308. https://doi.org/10.1021/ic50104a043.
20. Natoli, C. R.; Benfatto, M.; Doniach, S. Use of General Potentials in Multiple-Scattering Theory. *Phys. Rev. A* **1986,** *34* (6), 4682–4694. https://doi.org/10.1103/PhysRevA.34.4682.
21. Smolentsev, G.; van Vliet, K. M.; Azzaroli, N.; van Bokhoven, J. A.; Brouwer, A. M.; de Bruin, B.; Nachtegaal, M.; Tromp, M. Pump–Probe XAS Investigation of the Triplet State of an Ir Photosensitizer with Chromenopyridinone Ligands. *Photochem. Photobiol. Sci.* **2018,** *17* (7), 896–902. https://doi.org/10.1039/C8PP00065D.
22. Smolentsev, G.; Guda, A. A.; Janousch, M.; Frieh, C.; Jud, G.; Zamponi, F.; Chavarot-Kerlidou, M.; Artero, V.; van Bokhoven, J. A.; Nachtegaal, M. X-Ray Absorption Spectroscopy with Time-Tagged Photon Counting: Application to Study the Structure of a Co(i) Intermediate of H2 Evolving Photo-Catalyst. *Faraday Discuss.* **2014,** *171,* 259–273. https://doi.org/10.1039/C4FD00035H.
23. Smolentsev, G.; Guilera, G.; Tromp, M.; Pascarelli, S.; Soldatov, A. V. Local Structure of Reaction Intermediates Probed by Time-Resolved x-Ray Absorption near Edge Structure Spectroscopy. *J. Chem. Phys.* **2009,** *130* (17), 174508. https://doi.org/10.1063/1.3125940.
24. Mejía, E.; Luo, S.-P.; Karnahl, M.; Friedrich, A.; Tschierlei, S.; Surkus, A.-E.; Junge, H.; Gladiali, S.; Lochbrunner, S.; Beller, M. A Noble-Metal-Free System for Photocatalytic Hydrogen Production from Water. *Chem. A Eur. J.* **2013,** *19* (47), 15972–15978. https://doi.org/10.1002/chem.201302091.
25. McCusker, C. E.; Castellano, F. N. Design of a Long-Lifetime, Earth-Abundant, Aqueous Compatible Cu(I) Photosensitizer Using Cooperative Steric Effects. *Inorg. Chem.* **2013,** *52* (14), 8114–8120. https://doi.org/10.1021/ic401213p.
26. Takeda, H.; Ohashi, K.; Sekine, A.; Ishitani, O. Photocatalytic CO_2 Reduction Using Cu(I) Photosensitizers with a Fe(II) Catalyst. *J. Am. Chem. Soc.* **2016,** *138* (13), 4354–4357. https://doi.org/10.1021/jacs.6b01970.
27. Yuan, Y.-J.; Yu, Z.-T.; Chen, D.-Q.; Zou, Z.-G. Metal-Complex Chromophores for Solar Hydrogen Generation. *Chem. Soc. Rev.* **2017,** *46* (3), 603–631. https://doi.org/10.1039/C6CS00436A.
28. Elder, R. C.; Hill, M. C. A Distorted Tetrahedral Copper(II) Complex of a Tetradentate Schiff Base Ligand. *Inorg. Chem.* **1979,** *18* (3), 729–732. https://doi.org/10.1021/ic50193a041.
29. Yao, Y.; Perkovic, M. W.; Rillema, D. P.; Woods, C. Structures and Properties of Copper(II) and Copper(I) Complexes Containing an Ethane-Bridged Dimeric Phenanthroline Ligand. *Inorg. Chem.* **1992,** *31* (19), 3956–3962. https://doi.org/10.1021/ic00045a019.
30. Blaskie, M. W.; McMillin, D. R. Photostudies of Copper(I) Systems. 6. Room-Temperature Emission and Quenching Studies of Bis(2,9-Dimethyl-1,10-Phenanthroline)Copper(I). *Inorg. Chem.* **1980,** *19* (11), 3519–3522. https://doi.org/10.1021/ic50213a062.
31. McMillin, D. R.; Buckner, M. T.; Tae Ahn, B. A Light-Induced Redox Reaction of Bis(2,9-Dimethyl-1,10-Phenanthroline)Copper(I). *Inorg. Chem.* **1977,** *16* (4), 943–945. https://doi.org/10.1021/ic50170a046.
32. Kirchhoff, J. R.; Gamache, R. E.; Blaskie, M. W.; del Paggio, A. A.; Lengel, R. K.; McMillin, D. R. Temperature Dependence of Luminescence from Cu(NN)$^{2+}$ Systems in Fluid Solution. Evidence for the Participation of Two Excited States. *Inorg. Chem.* **1983,** *22* (17), 2380–2384. https://doi.org/10.1021/ic00159a008.

33. Ahn, B.-T.; McMillin, D. R. Photostudies of Copper(I) Systems. 7. Studies of Bimolecular Reactions Involving Cobalt(III) Complexes, Chromium(III) Complexes, or Oxygen Following the Excitation of Bis(2,9-Dimethyl-1,10-Phenanthroline)Copper(I). *Inorg. Chem.* **1981,** *20* (5), 1427–1432. https://doi.org/10.1021/ic50219a020.
34. Phifer, C. C.; McMillin, D. R. The Basis of Aryl Substituent Effects on Charge-Transfer Absorption Intensities. *Inorg. Chem.* **1986,** *25* (9), 1329–1333. https://doi.org/10.1021/ic00229a008.
35. Ahn, B.-T.; McMillin, D. R. Studies of Photoinduced Electron Transfer from Bis(2,9-Dimethyl-1,10-Phenanthroline)Copper(I). *Inorg. Chem.* **1978,** *17* (8), 2253–2258. https://doi.org/10.1021/ic50186a048.
36. Lees, A. J. Luminescence Properties of Organometallic Complexes. *Chem. Rev.* **1987,** *87* (4), 711–743. https://doi.org/10.1021/cr00080a003.
37. Tromp, M.; Dent, A. J.; Headspith, J.; Easun, T. L.; Sun, X.-Z.; George, M. W.; Mathon, O.; Smolentsev, G.; Hamilton, M. L.; Evans, J. Energy Dispersive XAFS: Characterization of Electronically Excited States of Copper(I) Complexes. *J. Phys. Chem. B* **2013,** *117* (24), 7381–7387. https://doi.org/10.1021/jp4020355.
38. Headspith, J.; Groves, J.; Luke, P. N.; Kogimtzis, M.; Salvini, G.; Thomas, S. L.; Farrow, R. C.; Evans, J.; Rayment, T.; Lee, J. S.; Goward, W. D.; Amman, M.; Mathon, O.; Diaz-Moreno, S. First Experimental Data from XH, a Fine Pitch Germanium Microstrip Detector for Energy Dispersive EXAFS (EDE). 2007 IEEE Nuclear Science Symposium Conference Record; pp 2421–2428**.** https://doi.org/10.1109/NSSMIC.2007.4436647.
39. Kau, L. S.; Spira-Solomon, D. J.; Penner-Hahn, J. E.; Hodgson, K. O.; Solomon, E. I. X-Ray Absorption Edge Determination of the Oxidation State and Coordination Number of Copper. Application to the Type 3 Site in Rhus Vernicifera Laccase and Its Reaction with Oxygen. *J. Am. Chem. Soc.* **1987,** *109* (21), 6433–6442. https://doi.org/10.1021/ja00255a032.
40. Zhang, Y.; Schulz, M.; Wächtler, M.; Karnahl, M.; Dietzek, B. Heteroleptic Diimine–Diphosphine Cu(I) Complexes as an Alternative towards Noble-Metal Based Photosensitizers: Design Strategies, Photophysical Properties and Perspective Applications. *Coord. Chem. Rev.* **2018,** *356,* 127–146. https://doi.org/10.1016/j.ccr.2017.10.016.
41. Windisch, J.; Orazietti, M.; Hamm, P.; Alberto, R.; Probst, B. General Scheme for Oxidative Quenching of a Copper Bis-Phenanthroline Photosensitizer for Light-Driven Hydrogen Production. *ChemSusChem* **2016,** *9* (13), 1719–1726. https://doi.org/10.1002/cssc.201600422.
42. Armaroli, N. Photoactive Mono- and Polynuclear Cu(i)–Phenanthrolines. A Viable Alternative to Ru(ii)–Polypyridines? *Chem. Soc. Rev.* **2001,** *30* (2), 113–124 https://doi.org/10.1039/B000703J.
43. Moonshiram, D.; Garrido-Barros, P.; Gimbert-Suriñach, C.; Picón, A.; Liu, C.; Zhang, X.; Karnahl, M.; Llobet, A. Elucidating the Nature of the Excited State of a Heteroleptic Copper Photosensitizer by Using Time-Resolved X-Ray Absorption Spectroscopy. *Chem. A Eur. J.* **2018,** *24* (24), 6464–6472. https://doi.org/10.1002/chem.201800330.
44. Kohler, L.; Hadt, R. G.; Hayes, D.; Chen, L. X.; Mulfort, K. L. Synthesis, Structure, and Excited State Kinetics of Heteroleptic Cu(i) Complexes with a New Sterically Demanding Phenanthroline Ligand. *Dalton Trans.* **2017,** *46* (38), 13088–13100. https://doi.org/10.1039/C7DT02476B.
45. Penfold, T. J.; Karlsson, S.; Capano, G.; Lima, F. A.; Rittmann, J.; Reinhard, M.; Rittmann-Frank, M. H.; Braem, O.; Baranoff, E.; Abela, R.; Tavernelli, I.; Rothlisberger, U.; Milne, C. J.; Chergui, M. Solvent-Induced Luminescence Quenching: Static and Time-Resolved X-Ray Absorption Spectroscopy of a Copper(I) Phenanthroline Complex. *Chem. A Eur. J.* **2013,** *117* (22), 4591–4601. https://doi.org/10.1021/jp403751m.
46. Lockard, J. V.; Kabehie, S.; Zink, J. I.; Smolentsev, G.; Soldatov, A.; Chen, L. X. Influence of Ligand Substitution on Excited State Structural Dynamics in Cu(I) Bisphenanthroline Complexes. *J. Phys. Chem. B* **2010,** *114* (45), 14521–14527. https://doi.org/10.1021/jp102278u.
47. Chen, L. X.; Shaw, G. B.; Novozhilova, I.; Liu, T.; Jennings, G.; Attenkofer, K.; Meyer, G. J.; Coppens, P. MLCT State Structure and Dynamics of a Copper(I) Diimine Complex Characterized by Pump – Probe X-Ray and Laser Spectroscopies and DFT Calculations. *J. Am. Chem. Soc.* **2003,** *125* (23), 7022–7034. https://doi.org/10.1021/ja0294663.
48. Chen, L. X.; Jennings, G.; Liu, T.; Gosztola, D. J.; Hessler, J. P.; Scaltrito, D. V.; Meyer, G. J. Rapid Excited-State Structural Reorganization Captured by Pulsed X-Rays. *J. Am. Chem. Soc.* **2002,** *124* (36), 10861–10867. https://doi.org/10.1021/ja017214g.
49. Smolentsev, G.; Sundström, V. Time-Resolved X-Ray Absorption Spectroscopy for the Study of Molecular Systems Relevant for Artificial Photosynthesis. *Coord. Chem. Rev.* **2015,** *304–305,* 117–132. https://doi.org/10.1016/j.ccr.2015.03.001.
50. Westre, T. E.; Kennepohl, P.; DeWitt, J. G.; Hedman, B.; Hodgson, K. O.; Solomon, E. I. A Multiplet Analysis of Fe K-Edge 1s → 3d Pre-Edge Features of Iron Complexes. *J. Am. Chem. Soc.* **1997,** *119* (27), 6297–6314. https://doi.org/10.1021/ja964352a.
51. Loeb, K. E.; Westre, T. E.; Kappock, T. J.; Mitić, N.; Glasfeld, E.; Caradonna, J. P.; Hedman, B.; Hodgson, K. O.; Solomon, E. I. Spectroscopic Characterization of the Catalytically Competent Ferrous Site of the Resting, Activated, and Substrate-Bound Forms of Phenylalanine Hydroxylase. *J. Am. Chem. Soc.* **1997,** *119* (8), 1901–1915. https://doi.org/10.1021/ja962269h.
52. Katayama, T.; Northey, T.; Gawelda, W.; Milne, C. J.; Vankó, G.; Lima, F. A.; Bohinc, R.; Németh, Z.; Nozawa, S.; Sato, T.; Khakhulin, D.; Szlachetko, J.; Togashi, T.; Owada, S.; Adachi, S.; Bressler, C.; Yabashi, M.; Penfold, T. J. Tracking Multiple Components of a Nuclear Wavepacket in Photoexcited Cu(I)-Phenanthroline Complex Using Ultrafast X-Ray Spectroscopy. *Nat. Commun.* **2019,** *10* (1), 3606. https://doi.org/10.1038/s41467-019-11499-w.
53. Bartlett, S. A.; Besley, N. A.; Dent, A. J.; Diaz-Moreno, S.; Evans, J.; Hamilton, M. L.; Hanson-Heine, M. W. D.; Horvath, R.; Manici, V.; Sun, X.-Z.; Towrie, M.; Wu, L.; Zhang, X.; George, M. W. Monitoring the Formation and Reactivity of Organometallic Alkane and Fluoroalkane Complexes with Silanes and Xe Using Time-Resolved X-Ray Absorption Fine Structure Spectroscopy. *J. Am. Chem. Soc.* **2019,** *141* (29), 11471–11480. https://doi.org/10.1021/jacs.8b13848.
54. Ravel, B.; Newville, M. ATHENA, ARTEMIS, HEPHAESTUS: Data Analysis for X-Ray Absorption Spectroscopy Using IFEFFIT. *J. Synchrotron Radiat.* **2005,** *12* (4), 537–541.
55. Asakura, H.; Shishido, T.; Tanaka, T. In Situ Time-Resolved XAFS Study of the Reaction Mechanism of Bromobenzene Homocoupling Mediated by [Ni(Cod)(Bpy)]. *Chem. A Eur. J.* **2012,** *116* (16), 4029–4034. https://doi.org/10.1021/jp211627v.
56. Gawelda, W.; Pham, V.-T.; van der Veen, R. M.; Grolimund, D.; Abela, R.; Chergui, M.; Bressler, C. Structural Analysis of Ultrafast Extended X-Ray Absorption Fine Structure with Subpicometer Spatial Resolution: Application to Spin Crossover Complexes. *J. Chem. Phys.* **2009,** *130* (12), 124520. https://doi.org/10.1063/1.3081884.
57. van der Veen, R. M.; Milne, C. J.; El Nahhas, A.; Lima, F. A.; Pham, V.-T.; Best, J.; Weinstein, J. A.; Borca, C. N.; Abela, R.; Bressler, C.; Chergui, M. Structural Determination of a Photochemically Active Diplatinum Molecule by Time-Resolved EXAFS Spectroscopy. *Angew. Chem. Int. Ed.* **2009,** *48* (15), 2711–2714. https://doi.org/10.1002/anie.200805946.
58. Fordyce, W. A.; Brummer, J. G.; Crosby, G. A. Electronic Spectroscopy of a Diplatinum(II) Octaphosphite Complex. *J. Am. Chem. Soc.* **1981,** *103* (24), 7061–7064. https://doi.org/10.1021/ja00414a006.
59. Thiel, D. J.; Līviņš, P.; Stern, E. A.; Lewis, A. Microsecond-Resolved XAFS of the Triplet Excited State of Pt2(P2O5H2)4–4. *Nature* **1993,** *362* (6415), 40–43. https://doi.org/10.1038/362040a0.
60. Kim, C. D.; Pillet, S.; Wu, G.; Fullagar, W. K.; Coppens, P. Excited-State Structure by Time-Resolved X-Ray Diffraction. *Acta Crystallogr. A* **2002,** *58* (2), 133–137.
61. Novozhilova, I. V.; Volkov, A. V.; Coppens, P. Theoretical Analysis of the Triplet Excited State of the [Pt2(H2P2O5)4]4- Ion and Comparison with Time-Resolved X-Ray and Spectroscopic Results. *J. Am. Chem. Soc.* **2003,** *125* (4), 1079–1087. https://doi.org/10.1021/ja027857b.
62. Chen, L. X.; Zhang, X.; Wasinger, E. C.; Attenkofer, K.; Jennings, G.; Muresan, A. Z.; Lindsey, J. S. Tracking Electrons and Atoms in a Photoexcited Metalloporphyrin by X-Ray Transient Absorption Spectroscopy. *J. Am. Chem. Soc.* **2007,** *129* (31), 9616–9618. https://doi.org/10.1021/ja072979v.
63. Gust, D.; Moore, T. A.; Moore, A. L. Mimicking Photosynthetic Solar Energy Transduction. *Acc. Chem. Res.* **2001,** *34* (1), 40–48. https://doi.org/10.1021/ar9801301.
64. Holten, D.; Bocian, D. F.; Lindsey, J. S. Probing Electronic Communication in Covalently Linked Multiporphyrin Arrays. A Guide to the Rational Design of Molecular Photonic Devices. *Acc. Chem. Res.* **2002,** *35* (1), 57–69. https://doi.org/10.1021/ar970264z.
65. Rosenthal, J.; Bachman, J.; Dempsey, J. L.; Esswein, A. J.; Gray, T. G.; Hodgkiss, J. M.; Manke, D. R.; Luckett, T. D.; Pistorio, B. J.; Veige, A. S.; Nocera, D. G. Oxygen and Hydrogen Photocatalysis by Two-Electron Mixed-Valence Coordination Compounds. *Coord. Chem. Rev.* **2005,** *249* (13), 1316–1326. https://doi.org/10.1016/j.ccr.2005.03.034.
66. Patchkovskii, S.; Kozlowski, P. M.; Zgierski, M. Z. Theoretical Analysis of Singlet and Triplet Excited States of Nickel Porphyrins. *J. Chem. Phys.* **2004,** *121* (3), 1317–1324. https://doi.org/10.1063/1.1762875.

67. Nguyen, K. A.; Pachter, R. Jahn–Teller Triplet Excited State Structures and Spectra of Zinc Complexes of Porphyrin and Phthalocyanine: A Density Functional Theory Study. *J. Chem. Phys.* **2003,** *118* (13), 5802–5810. https://doi.org/10.1063/1.1540627.
68. Rosa, A.; Ricciardi, G.; Baerends, E. J.; Zimin, M.; Rodgers, M. A. J.; Matsumoto, S.; Ono, N. Structural, Optical, and Photophysical Properties of Nickel(II) Alkylthioporphyrins: Insights from Experimental and DFT/TDDFT Studies. *Inorg. Chem.* **2005,** *44* (19), 6609–6622. https://doi.org/10.1021/ic050838t.
69. Rodriguez, J.; Holten, D. Ultrafast Vibrational Dynamics of a Photoexcited Metalloporphyrin. *J. Chem. Phys.* **1989,** *91* (6), 3525–3531. https://doi.org/10.1063/1.456883.
70. Khalil, M.; Marcus, M. A.; Smeigh, A. L.; McCusker, J. K.; Chong, H. H. W.; Schoenlein, R. W. Picosecond X-Ray Absorption Spectroscopy of a Photoinduced Iron(II) Spin Crossover Reaction in Solution. *Chem. A Eur. J.* **2006,** *110* (1), 38–44. https://doi.org/10.1021/jp055002q.
71. Lemke, C.; Schweitzer-Stenner, R.; Shelnutt, J. A.; Quirke, J. M. E.; Dreybrodt, W. Vibrational Analysis of Metalloporphyrins with Electron-Withdrawing NO_2 Substituents at Different Meso Positions. *Chem. A Eur. J.* **2001,** *105* (27), 6668–6679. https://doi.org/10.1021/jp011137u.
72. Huang, Q.; Medforth, C. J.; Schweitzer-Stenner, R. Nonplanar Heme Deformations and Excited State Displacements in Nickel Porphyrins Detected by Raman Spectroscopy at Soret Excitation. *Chem. A Eur. J.* **2005,** *109* (46), 10493–10502. https://doi.org/10.1021/jp052986a.
73. Mizutani, Y.; Kitagawa, T. A Role of Solvent in Vibrational Energy Relaxation of Metalloporphyrins. *J. Mol. Liq.* **2001,** *90* (1), 233–242. https://doi.org/10.1016/S0167-7322(01)00126-X.
74. Chen, L. X.; Zhang, X.; Wasinger, E. C.; Lockard, J. V.; Stickrath, A. B.; Mara, M. W.; Attenkofer, K.; Jennings, G.; Smolentsev, G.; Soldatov, A. X-Ray Snapshots for Metalloporphyrin Axial Ligation. *Chem. Sci.* **2010,** *1* (5), 642–650. https://doi.org/10.1039/C0SC00323A.
75. Chen, L. X.; et al. Capturing a Photoexcited Molecular Structure Through Time-Domain X-Ray Absorption Fine Structure. *Science* **2001,** *292* (5515), 262–264. https://doi.org/10.1126/science.1057063.
76. Campbell, L.; Tanaka, S.; Mukamel, S. Ligand Effects on the X-Ray Absorption of a Nickel Porphyrin Complex: A Simulation Study. *Chemical Physics* **2004,** *299* (2), 225–231. https://doi.org/10.1016/j.chemphys.2003.08.032.
77. Campbell, L.; Mukamel, S. Simulation of X-Ray Absorption near Edge Spectra of Electronically Excited Ruthenium Tris-2,2′-Bipyridine. *J. Chem. Phys.* **2004,** *121* (24), 12323–12333. https://doi.org/10.1063/1.1814101.
78. Rossbach, J. A VUV Free Electron Laser at the TESLA Test Facility at DESY. *Nucl. Instrum. Methods Phys. Res.* **1996,** *375* (1), 269–273. https://doi.org/10.1016/0168-9002(95)01332-6.
79. O'Shea, P. G.; Freund, H. P. Free-Electron Lasers: Status and Applications. *Science* **2001,** *292* (5523), 1853–1858. https://doi.org/10.1126/science.1055718.
80. Elias, L. R.; Fairbank, W. M.; Madey, J. M. J.; Schwettman, H. A.; Smith, T. I. Observation of Stimulated Emission of Radiation by Relativistic Electrons in a Spatially Periodic Transverse Magnetic Field. *Phys. Rev. Lett.* **1976,** *36* (13), 717–720. https://doi.org/10.1103/PhysRevLett.36.717.
81. SLAC National Accelerator Laboratory (n.d.) X-ray Laser Animated Fly-through. https://www.youtube.com/watch?v=pgaG7f96SKM.
82. Motz, H.; Thon, W.; Whitehurst, R. N. Experiments on Radiation by Fast Electron Beams. *J. Appl. Phys.* **1953,** *24* (7), 826–833. https://doi.org/10.1063/1.1721389.
83. Phillips, R. M. History of the Ubitron. *Nucl. Instrum. Methods Phys. Res.* **1988,** *272* (1), 1–9. https://doi.org/10.1016/0168-9002(88)90185-4.
84. Deacon, D. A. G.; Elias, L. R.; Madey, J. M. J.; Ramian, G. J.; Schwettman, H. A.; Smith, T. I. First Operation of a Free-Electron Laser. *Phys. Rev. Lett.* **1977,** *38* (16), 892–894. https://doi.org/10.1103/PhysRevLett.38.892.
85. Madey, J. M. J. Stimulated Emission of Bremsstrahlung in a Periodic Magnetic Field. *J. Appl. Phys.* **1971,** *42* (5), 1906–1913. https://doi.org/10.1063/1.1660466.
86. Granatstein, V. L.; Schlesinger, S. P.; Herndon, M.; Parker, R. K.; Pasour, J. A. Production of Megawatt Submillimeter Pulses by Stimulated Magneto-Raman Scattering. *Appl. Phys. Lett.* **1977,** *30* (8), 384–386. https://doi.org/10.1063/1.89413.
87. Orzechowski, T. J.; Anderson, B.; Fawley, W. M.; Prosnitz, D.; Scharlemann, E. T.; Yarema, S.; Hopkins, D.; Paul, A. C.; Sessler, A. M.; Wurtele, J. Microwave Radiation from a High-Gain Free-Electron Laser Amplifier. *Phys. Rev. Lett.* **1985,** *54* (9), 889–892. https://doi.org/10.1103/PhysRevLett.54.889.
88. Kirkpatrick, D. A.; Bekefi, G.; DiRienzo, A. C.; Freund, H. P.; Ganguly, A. K. A Millimeter and Submillimeter Wavelength Free-electron Laser. *Phys. Fluids B: Plasma Phys.* **1989,** *1* (7), 1511–1518. https://doi.org/10.1063/1.858927.
89. Batchelor, K.; Ben-Zvi, I.; Fernow, R. C.; Fischer, J.; Fisher, A. S.; Gallardo, J.; Ingold, G.; Kirk, H. G.; Leung, K. P.; Malone, R.; Pogorelsky, I.; Srinivasan-Rao, T.; Rogers, J.; Tsang, T.; Sheehan, J.; Ulc, S.; Woodle, M.; Xie, J.; Zhang, R. S.; Lin, L. Y.; McDonald, K. T.; Russell, D. P.; Hung, C. M.; Wang, X. J. Performance of the Brookhaven Photocathode Rf Gun. *Nucl. Instrum. Methods Phys. Res.* **1992,** *318* (1), 372–376. https://doi.org/10.1016/0168-9002(92)91084-M.
90. Sheffield, R. L. Photocathode RF Guns. *AIP Conf. Proc.* **1989,** *184* (2), 1500–1531. https://doi.org/10.1063/1.38017.
91. O'Shea, P. G.; Bender, S. C.; Byrd, D. A.; Early, J. W.; Feldman, D. W.; Fortgang, C. M.; Goldstein, J. C.; Newnam, B. E.; Sheffield, R. L.; Warren, R. W.; Zaugg, T. J. Ultraviolet Free-Electron Laser Driven by a High-Brightness 45-MeV Electron Beam. *Phys. Rev. Lett.* **1993,** *71* (22), 3661–3664. https://doi.org/10.1103/PhysRevLett.71.3661.
92. Brau, C. A. The Vanderbilt University Free-Electron Laser Center. *Nucl. Instrum. Methods Phys. Res.* **1992,** *318* (1), 38–41. https://doi.org/10.1016/0168-9002(92)91020-A.
93. Dowell, D. H.; Davis, K. J.; Friddell, K. D.; Tyson, E. L.; Lancaster, C. A.; Milliman, L.; Rodenburg, R. E.; Aas, T.; Bemes, M.; Bethel, S. Z.; Johnson, P. E.; Murphy, K.; Whelen, C.; Busch, G. E.; Remelius, D. K. First Operation of a Photocathode Radio Frequency Gun Injector at High Duty Factor. *Appl. Phys. Lett.* **1993,** *63* (15), 2035–2037. https://doi.org/10.1063/1.110583.
94. Patterson, B. D.; Abela, R. Novel Opportunities for Time-Resolved Absorption Spectroscopy at the X-Ray Free Electron Laser. *Phys. Chem. Chem. Phys.* **2010,** *12* (21), 5647–5652. https://doi.org/10.1039/C003406A.
95. Shintake, T.; Tanaka, T.; Hara, T.; Togawa, K.; Inagaki, T.; Kim, Y. J.; Ishikawa, T.; Kitamura, H.; Baba, H.; Matsumoto, H.; Takeda, S.; Yoshida, M.; Takasu, Y. Status of SPring-8 Compact SASE Source FEL Project. *Nucl. Instrum. Methods Phys. Res.* **2003,** *507* (1), 382–387. https://doi.org/10.1016/S0168-9002(03)00949-5.
96. Cornacchia, M. Performance and Design Concepts of a Free-Electron Laser Operating in the X-Ray Region. Proceeding of SPIE; https://doi.org/10.1117/12.274368.
97. Krinsky, S.; Huang, Z. Frequency Chirped Self-Amplified Spontaneous-Emission Free-Electron Lasers. *Phys. Rev. ST Accel. Beams* **2003,** *6* (5), 50702. https://doi.org/10.1103/PhysRevSTAB.6.050702.
98. Bernstein, D. P.; Acremann, Y.; Scherz, A.; Burkhardt, M.; Stöhr, J.; Beye, M.; Schlotter, W. F.; Beeck, T.; Sorgenfrei, F.; Pietzsch, A.; Wurth, W.; Föhlisch, A. Near Edge X-Ray Absorption Fine Structure Spectroscopy with x-Ray Free-Electron Lasers. *Appl. Phys. Lett.* **2009,** *95* (13), 134102. https://doi.org/10.1063/1.3236540.
99. Bergmann, U.; Glatzel, P. X-Ray Emission Spectroscopy. *Photosynth. Res.* **2009,** *102* (2), 255. https://doi.org/10.1007/s11120-009-9483-6.
100. Siddons, D. P.; Zhong, Z. A Flash Spectrograph for XANES Measurements at SPPS/LCLS. *AIP Conf. Proc.* **2004,** *705* (1), 941–944. https://doi.org/10.1063/1.1757951.
101. Milne, C. J.; Penfold, T. J.; Chergui, M. Recent Experimental and Theoretical Developments in Time-Resolved X-Ray Spectroscopies. *Coord. Chem. Rev.* **2014,** *277–278,* 44–68. https://doi.org/10.1016/j.ccr.2014.02.013.
102. Bostedt, C.; Boutet, S.; Fritz, D. M.; Huang, Z.; Lee, H. J.; Lemke, H. T.; Robert, A.; Schlotter, W. F.; Turner, J. J.; Williams, G. J. Linac Coherent Light Source: The First Five Years. *Rev. Mod. Phys.* **2016,** *88* (1), 15007. https://doi.org/10.1103/RevModPhys.88.015007.
103. Hong, K.; Cho, H.; Schoenlein, R. W.; Kim, T. K.; Huse, N. Element-Specific Characterization of Transient Electronic Structure of Solvated Fe(II) Complexes with Time-Resolved Soft X-Ray Absorption Spectroscopy. *Acc. Chem. Res.* **2015,** *48* (11), 2957–2966. https://doi.org/10.1021/acs.accounts.5b00154.
104. Chergui, M. Emerging Photon Technologies for Chemical Dynamics. *Faraday Discuss.* **2014,** *171,* 11–40. https://doi.org/10.1039/C4FD00157E.
105. Zhang, W.; Gaffney, K. J. Mechanistic Studies of Photoinduced Spin Crossover and Electron Transfer in Inorganic Complexes. *Acc. Chem. Res.* **2015,** *48* (4), 1140–1148. https://doi.org/10.1021/ar500407p.
106. Lemke, H. T.; Bressler, C.; Chen, L. X.; Fritz, D. M.; Gaffney, K. J.; Galler, A.; Gawelda, W.; Haldrup, K.; Hartsock, R. W.; Ihee, H.; Kim, J.; Kim, K. H.; Lee, J. H.; Nielsen, M. M.; Stickrath, A. B.; Zhang, W.; Zhu, D.; Cammarata, M. Femtosecond X-Ray Absorption Spectroscopy at a Hard X-Ray Free Electron Laser: Application to Spin Crossover Dynamics. *Chem. A Eur. J.* **2013,** *117* (4), 735–740. https://doi.org/10.1021/jp312559h.

107. Canton, S. E.; Kjær, K. S.; Vankó, G.; van Driel, T. B.; Adachi, S.; Bordage, A.; Bressler, C.; Chabera, P.; Christensen, M.; Dohn, A. O.; Galler, A.; Gawelda, W.; Gosztola, D.; Haldrup, K.; Harlang, T.; Liu, Y.; Møller, K. B.; Németh, Z.; Nozawa, S.; Pápai, M.; Sato, T.; Sato, T.; Suarez-Alcantara, K.; Togashi, T.; Tono, K.; Uhlig, J.; Vithanage, D. A.; Wärnmark, K.; Yabashi, M.; Zhang, J.; Sundström, V.; Nielsen, M. M. Visualizing the Non-Equilibrium Dynamics of Photoinduced Intramolecular Electron Transfer with Femtosecond X-Ray Pulses. *Nat. Commun.* **2015,** *6* (1), 6359. https://doi.org/10.1038/ncomms7359.
108. Zhang, W.; Alonso-Mori, R.; Bergmann, U.; Bressler, C.; Chollet, M.; Galler, A.; Gawelda, W.; Hadt, R. G.; Hartsock, R. W.; Kroll, T.; Kjær, K. S.; Kubiček, K.; Lemke, H. T.; Liang, H. W.; Meyer, D. A.; Nielsen, M. M.; Purser, C.; Robinson, J. S.; Solomon, E. I.; Sun, Z.; Sokaras, D.; van Driel, T. B.; Vankó, G.; Weng, T.-C.; Zhu, D.; Gaffney, K. J. Tracking Excited-State Charge and Spin Dynamics in Iron Coordination Complexes. *Nature* **2014,** *509* (7500), 345–348. https://doi.org/10.1038/nature13252.
109. Kunnus, K.; Josefsson, I.; Rajkovic, I.; Schreck, S.; Quevedo, W.; Beye, M.; Weniger, C.; Grübel, S.; Scholz, M.; Nordlund, D.; Zhang, W.; Hartsock, R. W.; Gaffney, K. J.; Schlotter, W. F.; Turner, J. J.; Kennedy, B.; Hennies, F.; de Groot, F. M. F.; Techert, S.; Odelius, M.; Wernet, P.; Föhlisch, A. Identification of the Dominant Photochemical Pathways and Mechanistic Insights to the Ultrafast Ligand Exchange of Fe(CO)5 to Fe(CO)4EtOH. *Struct. Dyn.* **2016,** *3* (4), 043204. https://doi.org/10.1063/1.4941602.
110. Wernet, P.; Kunnus, K.; Josefsson, I.; Rajkovic, I.; Quevedo, W.; Beye, M.; Schreck, S.; Grübel, S.; Scholz, M.; Nordlund, D.; Zhang, W.; Hartsock, R. W.; Schlotter, W. F.; Turner, J. J.; Kennedy, B.; Hennies, F.; de Groot, F. M. F.; Gaffney, K. J.; Techert, S.; Odelius, M.; Föhlisch, A. Orbital-Specific Mapping of the Ligand Exchange Dynamics of Fe(CO)5 in Solution. *Nature* **2015,** *520* (7545), 78–81. https://doi.org/10.1038/nature14296.
111. Ackermann, W.; Asova, G.; Ayvazyan, V.; Azima, A.; Baboi, N.; Bähr, J.; Balandin, V.; Beutner, B.; Brandt, A.; Bolzmann, A.; Brinkmann, R.; Brovko, O. I.; Castellano, M.; Castro, P.; Catani, L.; Chiadroni, E.; Choroba, S.; Cianchi, A.; Costello, J. T.; Cubaynes, D.; Dardis, J.; Decking, W.; Delsim-Hashemi, H.; Delserieys, A.; di Pirro, G.; Dohlus, M.; Düsterer, S.; Eckhardt, A.; Edwards, H. T.; Faatz, B.; Feldhaus, J.; Flöttmann, K.; Frisch, J.; Fröhlich, L.; Garvey, T.; Gensch, U.; Gerth, C.; Görler, M.; Golubeva, N.; Grabosch, H.-J.; Grecki, M.; Grimm, O.; Hacker, K.; Hahn, U.; Han, J. H.; Honkavaara, K.; Hott, T.; Hüning, M.; Ivanisenko, Y.; Jaeschke, E.; Jalmuzna, W.; Jezynski, T.; Kammering, R.; Katalev, V.; Kavanagh, K.; Kennedy, E. T.; Khodyachykh, S.; Klose, K.; Kocharyan, V.; Körfer, M.; Kollewe, M.; Koprek, W.; Korepanov, S.; Kostin, D.; Krassilnikov, M.; Kube, G.; Kuhlmann, M.; Lewis, C. L. S.; Lilje, L.; Limberg, T.; Lipka, D.; Löhl, F.; Luna, H.; Luong, M.; Martins, M.; Meyer, M.; Michelato, P.; Miltchev, V.; Möller, W. D.; Monaco, L.; Müller, W. F. O.; Napieralski, O.; Napoly, O.; Nicolosi, P.; Nölle, D.; Nuñez, T.; Oppelt, A.; Pagani, C.; Paparella, R.; Pchalek, N.; Pedregosa-Gutierrez, J.; Petersen, B.; Petrosyan, B.; Petrosyan, G.; Petrosyan, L.; Pflüger, J.; Plönjes, E.; Poletto, L.; Pozniak, K.; Prat, E.; Proch, D.; Pucyk, P.; Radcliffe, P.; Redlin, H.; Rehlich, K.; Richter, M.; Roehrs, M.; Roensch, J.; Romaniuk, R.; Ross, M.; Rossbach, J.; Rybnikov, V.; Sachwitz, M.; Saldin, E. L.; Sandner, W.; Schlarb, H.; Schmidt, B.; Schmitz, M.; Schmüser, P.; Schneider, J. R.; Schneidmiller, E. A.; Schnepp, S.; Schreiber, S.; Seidel, M.; Sertore, D.; Shabunov, A. V.; Simon, C.; Simrock, S.; Sombrowski, E.; Sorokin, A. A.; Spanknebel, P.; Spesyvtsev, R.; Staykov, L.; Steffen, B.; Stephan, F.; Stulle, F.; Thom, H.; Tiedtke, K.; Tischer, M.; Toleikis, S.; Treusch, R.; Trines, D.; Tsakov, I.; Vogel, E.; Weiland, T.; Weise, H.; Wellhöfer, M.; Wendt, M.; Will, I.; Winter, A.; Wittenburg, K.; Wurth, W.; Yeates, P.; Yurkov, M. V.; Zagorodnov, I.; Zapfe, K. Operation of a Free-Electron Laser from the Extreme Ultraviolet to the Water Window. *Nat. Photon.* **2007,** *1* (6), 336–342. https://doi.org/10.1038/nphoton.2007.76.
112. Zangrando, M.; Cudin, I.; Fava, C.; Gerusina, S.; Gobessi, R.; Godnig, R.; Rumiz, L.; Svetina, C.; Parmigiani, F.; Cocco, D. First Results from the Commissioning of the FERMI@Elettra Free Electron Laser by Means of the Photon Analysis Delivery and Reduction System (PADReS). Proceeding of SPIE; https://doi.org/10.1117/12.886459.
113. Zangrando, M.; Abrami, A.; Cocco, D.; Fava, C.; Gerusina, S.; Gobessi, R.; Mahne, N.; Mazzucco, E.; Raimondi, L.; Rumiz, L.; Svetina, C.; Parmigiani, F. The Photon Beam Transport and Diagnostics System at FERMI@Elettra, the Italian Seeded FEL Source: Commissioning Experience and Most Recent Results. Proceeding of SPIE; https://doi.org/10.1117/12.929749.
114. de Ninno, G.; Mahieu, B.; Allaria, E.; Giannessi, L.; Spampinati, S. Chirped Seeded Free-Electron Lasers: Self-Standing Light Sources for Two-Color Pump-Probe Experiments. *Phys. Rev. Lett.* **2013,** *110* (6), 64801. https://doi.org/10.1103/PhysRevLett.110.064801.
115. Allaria, E.; Callegari, C.; Cocco, D.; Fawley, W. M.; Kiskinova, M.; Masciovecchio, C.; Parmigiani, F. The FERMI@Elettra Free-Electron-Laser Source for Coherent X-Ray Physics: Photon Properties, Beam Transport System and Applications. *New J. Phys.* **2010,** *12* (7), 075002. https://doi.org/10.1088/1367-2630/12/7/075002.
116. Hara, T. Fully Coherent Soft X-Rays at FERMI. *Nat. Photon.* **2013,** *7* (11), 852–854. https://doi.org/10.1038/nphoton.2013.279.
117. Juranić, P. N.; Stepanov, A.; Ischebeck, R.; Schlott, V.; Pradervand, C.; Patthey, L.; Radović, M.; Gorgisyan, I.; Rivkin, L.; Hauri, C. P.; Monoszlai, B.; Ivanov, R.; Peier, P.; Liu, J.; Togashi, T.; Owada, S.; Ogawa, K.; Katayama, T.; Yabashi, M.; Abela, R. High-Precision X-Ray FEL Pulse Arrival Time Measurements at SACLA by a THz Streak Camera with Xe Clusters. *Opt. Express* **2014,** *22* (24), 30004–30012. https://doi.org/10.1364/OE.22.030004.
118. Ohashi, H.; Yabashi, M.; Tono, K.; Inubushi, Y.; Sato, T.; Togashi, T.; Senba, Y.; Koyama, T.; Yumoto, H.; Miyokawa, K.; Ohsawa, T.; Goto, S.; Ishikawa, T. Beamline Mirrors and Monochromator for X-Ray Free Electron Laser of SACLA. *Nucl. Instrum. Methods Phys. Res.* **2013,** *710,* 139–142. https://doi.org/10.1016/j.nima.2012.10.094.
119. Obara, Y.; Katayama, T.; Ogi, Y.; Suzuki, T.; Kurahashi, N.; Karashima, S.; Chiba, Y.; Isokawa, Y.; Togashi, T.; Inubushi, Y.; Yabashi, M.; Suzuki, T.; Misawa, K. Femtosecond Time-Resolved X-Ray Absorption Spectroscopy of Liquid Using a Hard X-Ray Free Electron Laser in a Dual-Beam Dispersive Detection Method. *Opt. Express* **2014,** *22* (1), 1105–1113. https://doi.org/10.1364/OE.22.001105.
120. Tono, K.; Togashi, T.; Inubushi, Y.; Sato, T.; Katayama, T.; Ogawa, K.; Ohashi, H.; Kimura, H.; Takahashi, S.; Takeshita, K.; Tomizawa, H.; Goto, S.; Ishikawa, T.; Yabashi, M. Beamline, Experimental Stations and Photon Beam Diagnostics for the Hard x-Ray Free Electron Laser of SACLA. *New J. Phys.* **2013,** *15* (8), 083035. https://doi.org/10.1088/1367-2630/15/8/083035.
121. Kato, M.; Tanaka, T.; Kurosawa, T.; Saito, N.; Richter, M.; Sorokin, A. A.; Tiedtke, K.; Kudo, T.; Tono, K.; Yabashi, M.; Ishikawa, T. Pulse Energy Measurement at the Hard X-Ray Laser in Japan. *Appl. Phys. Lett.* **2012,** *101* (2), 023503. https://doi.org/10.1063/1.4733354.
122. Yabashi, M.; Tanaka, H.; Ishikawa, T. Overview of the SACLA Facility. *J. Synchrotron Radiat.* **2015,** *22* (3), 477–484. https://doi.org/10.1107/S1600577515004658.
123. Feng, Y.; Feldkamp, J. M.; Fritz, D. M.; Cammarata, M.; Aymeric, R.; Caronna, C.; Lemke, H. T.; Zhu, D.; Lee, S.; Boutet, S.; Williams, G.; Tono, K.; Yabashi, M.; Hastings, J. B. A Single-Shot Intensity-Position Monitor for Hard x-Ray FEL Sources. Proceeding of SPIE; https://doi.org/10.1117/12.893740.
124. Margaritondo, G.; Rebernik Ribic, P. A Simplified Description of X-Ray Free-Electron Lasers. *J. Synchrotron Radiat.* **2011,** *18* (2), 101–108. https://doi.org/10.1107/S090904951004896X.
125. Ordejón, B.; de Graaf, C.; Sousa, C. Light-Induced Excited-State Spin Trapping in Tetrazole-Based Spin Crossover Systems. *J. Am. Chem. Soc.* **2008,** *130* (42), 13961–13968. https://doi.org/10.1021/ja804506h.
126. Gütlich, P.; Goodwin, H. A. Spin Crossover—An Overall Perspective. In *Spin Crossover in Transition Metal Compounds I;* Gütlich, P., Goodwin, H. A., Eds., Springer Berlin Heidelberg: Berlin, Heidelberg, 2004; pp 1–47. https://doi.org/10.1007/b13527.
127. Bergkamp, M. A.; Chang, C. K.; Netzel, T. L. Quantum Yield Determinations for Subnanosecond-Lived Excited States and Photoproducts: Applications to Inorganic Complexes and Photosynthetic Models. *J. Phys. Chem.* **1983,** *87* (22), 4441–4446. https://doi.org/10.1021/j100245a024.
128. McCusker, J. K.; Walda, K. N.; Dunn, R. C.; Simon, J. D.; Magde, D.; Hendrickson, D. N. Subpicosecond 1MLCT. Fwdarw. 5T2 Intersystem Crossing of Low-Spin Polypyridyl Ferrous Complexes. *J. Am. Chem. Soc.* **1993,** *115* (1), 298–307. https://doi.org/10.1021/ja00054a043.
129. Gawelda, W.; Cannizzo, A.; Pham, V.-T.; van Mourik, F.; Bressler, C.; Chergui, M. Ultrafast Nonadiabatic Dynamics of $[FeII(Bpy)3]^{2+}$ in Solution. *J. Am. Chem. Soc.* **2007,** *129* (26), 8199–8206. https://doi.org/10.1021/ja070454x.
130. Consani, C.; Prémont-Schwarz, M.; ElNahhas, A.; Bressler, C.; van Mourik, F.; Cannizzo, A.; Chergui, M. Vibrational Coherences and Relaxation in the High-Spin State of Aqueous $[FeII(Bpy)3]^{2+}$. *Angew. Chem. Int. Ed.* **2009,** *48* (39), 7184–7187 https://doi.org/10.1002/anie.200902728.
131. de Graaf, C.; Sousa, C. Study of the Light-Induced Spin Crossover Process of the $[FeII(Bpy)3]^{2+}$ Complex. *Chem. A Eur. J.* **2010,** *16* (15), 4550–4556. https://doi.org/10.1002/chem.200903423.
132. Bressler, C.; Milne, C.; Pham, V.-T.; ElNahhas, A.; van der Veen, R. M.; Gawelda, W.; Johnson, S.; Beaud, P.; Grolimund, D.; Kaiser, M.; Borca, C. N.; Ingold, G.; Abela, R.; Chergui, M. Femtosecond XANES Study of the Light-Induced Spin Crossover Dynamics in an Iron(II) Complex. *Science* **2009,** *323* (5913), 489–492. https://doi.org/10.1126/science.1165733.

133. Shelby, M. L.; Lestrange, P. J.; Jackson, N. E.; Haldrup, K.; Mara, M. W.; Stickrath, A. B.; Zhu, D.; Lemke, H. T.; Chollet, M.; Hoffman, B. M.; Li, X.; Chen, L. X. Ultrafast Excited State Relaxation of a Metalloporphyrin Revealed by Femtosecond X-Ray Absorption Spectroscopy. *J. Am. Chem. Soc.* **2016,** *138* (28), 8752–8764. https://doi.org/10.1021/jacs.6b02176.
134. Peng, G.; deGroot, F. M. F.; Haemaelaeinen, K.; Moore, J. A.; Wang, X.; Grush, M. M.; Hastings, J. B.; Siddons, D. P.; Armstrong, W. H. High-Resolution Manganese X-Ray Fluorescence Spectroscopy. Oxidation-State and Spin-State Sensitivity. *J. Am. Chem. Soc.* **1994,** *116* (7), 2914–2920. https://doi.org/10.1021/ja00086a024.
135. Rovezzi, M.; Glatzel, P. Hard X-Ray Emission Spectroscopy: A Powerful Tool for the Characterization of Magnetic Semiconductors. *Semicond. Sci. Technol.* **2014,** *29* (2), 023002. https://doi.org/10.1088/0268-1242/29/2/023002.
136. Vankó, G.; Glatzel, P.; Pham, V.-T.; Abela, R.; Grolimund, D.; Borca, C. N.; Johnson, S. L.; Milne, C. J.; Bressler, C. Picosecond Time-Resolved X-Ray Emission Spectroscopy: Ultrafast Spin-State Determination in an Iron Complex. *Angew. Chem. Int. Ed.* **2010,** *49* (34), 5910–5912. https://doi.org/10.1002/anie.201000844.
137. Vankó, G.; Bordage, A.; Glatzel, P.; Gallo, E.; Rovezzi, M.; Gawelda, W.; Galler, A.; Bressler, C.; Doumy, G.; March, A. M.; Kanter, E. P.; Young, L.; Southworth, S. H.; Canton, S. E.; Uhlig, J.; Smolentsev, G.; Sundström, V.; Haldrup, K.; van Driel, T. B.; Nielsen, M. M.; Kjaer, K. S.; Lemke, H. T. Spin-State Studies with XES and RIXS: From Static to Ultrafast. *J. Electron Spectros. Relat. Phenomena* **2013,** *188,* 166–171. https://doi.org/10.1016/j.elspec.2012.09.012.
138. Haldrup, K.; Vankó, G.; Gawelda, W.; Galler, A.; Doumy, G.; March, A. M.; Kanter, E. P.; Bordage, A.; Dohn, A.; van Driel, T. B.; Kjær, K. S.; Lemke, H. T.; Canton, S. E.; Uhlig, J.; Sundström, V.; Young, L.; Southworth, S. H.; Nielsen, M. M.; Bressler, C. Guest–Host Interactions Investigated by Time-Resolved X-Ray Spectroscopies and Scattering at MHz Rates: Solvation Dynamics and Photoinduced Spin Transition in Aqueous Fe(Bipy)32+. *Chem. A Eur. J.* **2012,** *116* (40), 9878–9887 https://doi.org/10.1021/jp306917x.
139. Vankó, G.; Neisius, T.; Molnár, G.; Renz, F.; Kárpáti, S.; Shukla, A.; de Groot, F. M. F. Probing the 3d Spin Momentum with X-Ray Emission Spectroscopy: The Case of Molecular-Spin Transitions. *J. Phys. Chem. B* **2006,** *110* (24), 11647–11653. https://doi.org/10.1021/jp0615961.
140. March, A. M.; Assefa, T. A.; Bressler, C.; Doumy, G.; Galler, A.; Gawelda, W.; Kanter, E. P.; Németh, Z.; Pápai, M.; Southworth, S. H.; Young, L.; Vankó, G. Feasibility of Valence-to-Core X-Ray Emission Spectroscopy for Tracking Transient Species. *J. Phys. Chem. C* **2015,** *119* (26), 14571–14578. https://doi.org/10.1021/jp511838q.
141. Gallo, E.; Glatzel, P. Valence to Core X-Ray Emission Spectroscopy. *Adv. Mater.* **2014,** *26* (46), 7730–7746. https://doi.org/10.1002/adma.201304994.
142. Lee, N.; Petrenko, T.; Bergmann, U.; Neese, F.; DeBeer, S. Probing Valence Orbital Composition with Iron Kβ X-Ray Emission Spectroscopy. *J. Am. Chem. Soc.* **2010,** *132* (28), 9715–9727. https://doi.org/10.1021/ja101281e.
143. Bauer, M. HERFD-XAS and Valence-to-Core-XES: New Tools to Push the Limits in Research with Hard X-Rays? *Phys. Chem. Chem. Phys.* **2014,** *16* (27), 13827–13837 https://doi.org/10.1039/C4CP00904E.
144. Delgado-Jaime, M. U.; Dible, B. R.; Chiang, K. P.; Brennessel, W. W.; Bergmann, U.; Holland, P. L.; DeBeer, S. Identification of a Single Light Atom within a Multinuclear Metal Cluster Using Valence-to-Core X-Ray Emission Spectroscopy. *Inorg. Chem.* **2011,** *50* (21), 10709–10717. https://doi.org/10.1021/ic201173j.
145. Safonov, V. A.; Vykhodtseva, L. N.; Polukarov, Y. M.; Safonova, O. V.; Smolentsev, G.; Sikora, M.; Eeckhout, S. G.; Glatzel, P. Valence-to-Core X-Ray Emission Spectroscopy Identification of Carbide Compounds in Nanocrystalline Cr Coatings Deposited from Cr(III) Electrolytes Containing Organic Substances. *J. Phys. Chem. B* **2006,** *110* (46), 23192–23196. https://doi.org/10.1021/jp064569j.
146. Bergmann, U.; Horne, C. R.; Collins, T. J.; Workman, J. M.; Cramer, S. P. Chemical Dependence of Interatomic X-Ray Transition Energies and Intensities—A Study of Mn Kβ″ and Kβ2,5 Spectra. *Chem. Phys. Lett.* **1999,** *302* (1), 119–124. https://doi.org/10.1016/S0009-2614(99)00095-0.
147. Lancaster, K. M.; Roemelt, M.; Ettenhuber, P.; Hu, Y.; Ribbe, M. W.; Neese, F.; Bergmann, U.; DeBeer, S. X-Ray Emission Spectroscopy Evidences a Central Carbon in the Nitrogenase Iron-Molybdenum Cofactor. *Science* **2011,** *334* (6058), 974–977. https://doi.org/10.1126/science.1206445.
148. Swarbrick, J. C.; Kvashnin, Y.; Schulte, K.; Seenivasan, K.; Lamberti, C.; Glatzel, P. Ligand Identification in Titanium Complexes Using X-Ray Valence-to-Core Emission Spectroscopy. *Inorg. Chem.* **2010,** *49* (18), 8323–8332. https://doi.org/10.1021/ic100755t.
149. Pollock, C. J.; DeBeer, S. Valence-to-Core X-Ray Emission Spectroscopy: A Sensitive Probe of the Nature of a Bound Ligand. *J. Am. Chem. Soc.* **2011,** *133* (14), 5594–5601. https://doi.org/10.1021/ja200560z.
150. Bordage, A.; Pápai, M.; Sas, N. S.; Szlachetko, J.; Nachtegaal, M.; Vankó, G. On the Sensitivity of Hard X-Ray Spectroscopies to the Chemical State of Br. *Phys. Chem. Chem. Phys.* **2013,** *15* (26), 11088–11098. https://doi.org/10.1039/C3CP50367D.
151. Beckwith, M. A.; Roemelt, M.; Collomb, M.-N.; DuBoc, C.; Weng, T.-C.; Bergmann, U.; Glatzel, P.; Neese, F.; DeBeer, S. Manganese Kβ X-Ray Emission Spectroscopy As a Probe of Metal–Ligand Interactions. *Inorg. Chem.* **2011,** *50* (17), 8397–8409. https://doi.org/10.1021/ic200970t.
152. Gallo, E.; Lamberti, C.; Glatzel, P. Investigation of the Valence Electronic States of Ti(Iv) in Ti Silicalite-1 Coupling X-Ray Emission Spectroscopy and Density Functional Calculations. *Phys. Chem. Chem. Phys.* **2011,** *13* (43), 19409–19419. https://doi.org/10.1039/C1CP21556F.
153. Delgado-Jaime, M. U.; DeBeer, S.; Bauer, M. Valence-to-Core X-Ray Emission Spectroscopy of Iron–Carbonyl Complexes: Implications for the Examination of Catalytic Intermediates. *Chem. A Eur. J.* **2013,** *19* (47), 15888–15897. https://doi.org/10.1002/chem.201301913.
154. Shirom, M.; Stein, G. Excited State Chemistry of the Ferrocyanide Ion in Aqueous Solution. I. Formation of the Hydrated Electron. *J. Chem. Phys.* **1971,** *55* (7), 3372–3378. https://doi.org/10.1063/1.1676587.
155. Shirom, M.; Stein, G. Excited State Chemistry of the Ferrocyanide Ion in Aqueous Solution. II. Photoaquation. *J. Chem. Phys.* **1971,** *55* (7), 3379–3382. https://doi.org/10.1063/1.1676588.
156. Penfold, T. J.; Reinhard, M.; Rittmann-Frank, M. H.; Tavernelli, I.; Rothlisberger, U.; Milne, C. J.; Glatzel, P.; Chergui, M. X-Ray Spectroscopic Study of Solvent Effects on the Ferrous and Ferric Hexacyanide Anions. *Chem. A Eur. J.* **2014,** *118* (40), 9411–9418. https://doi.org/10.1021/jp5055588.
157. Lee, T.; Jiang, Y.; Rose-Petruck, C. G.; Benesch, F. Ultrafast Tabletop Laser-Pump–x-Ray Probe Measurement of Solvated Fe(CN)64−. *J. Chem. Phys.* **2005,** *122* (8), 084506 https://doi.org/10.1063/1.1852455.
158. Reinhard, M.; Penfold, T. J.; Lima, F. A.; Rittmann, J.; Rittmann-Frank, M. H.; Abela, R.; Tavernelli, I.; Rothlisberger, U.; Milne, C. J.; Chergui, M. Photooxidation and Photoaquation of Iron Hexacyanide in Aqueous Solution: A Picosecond X-Ray Absorption Study. *Struct. Dynam.* **2014,** *1* (2), 024901. https://doi.org/10.1063/1.4871751.
159. Dufresne, E. M.; Adams, B.; Arms, D. A.; Chollet, M.; Landahl, E. C.; Li, Y.; Walko, D. A.; Wang, J. Time-Resolved Research at the Advanced Photon Source Beamline 7-ID. *AIP Conf. Proc.* **2010,** *1234* (1), 181–184. https://doi.org/10.1063/1.3463168.
160. Pollock, C. J.; Delgado-Jaime, M. U.; Atanasov, M.; Neese, F.; DeBeer, S. Kβ Mainline X-Ray Emission Spectroscopy as an Experimental Probe of Metal–Ligand Covalency. *J. Am. Chem. Soc.* **2014,** *136* (26), 9453–9463. https://doi.org/10.1021/ja504182n.
161. Verbeni, R.; Pylkkänen, T.; Huotari, S.; Simonelli, L.; Vankó, G.; Martel, K.; Henriquet, C.; Monaco, G. Multiple-Element Spectrometer for Non-Resonant Inelastic X-Ray Spectroscopy of Electronic Excitations. *J. Synchrotron Radiat.* **2009,** *16* (4), 469–476. https://doi.org/10.1107/S090904950901886X.
162. Kleymenov, E.; van Bokhoven, J. A.; David, C.; Glatzel, P.; Janousch, M.; Alonso-Mori, R.; Studer, M.; Willimann, M.; Bergamaschi, A.; Henrich, B.; Nachtegaal, M. Five-Element Johann-Type x-Ray Emission Spectrometer with a Single-Photon-Counting Pixel Detector. *Rev. Sci. Instrum.* **2011,** *82* (6), 065107. https://doi.org/10.1063/1.3600452.
163. Gog, T.; Seidler, G. T.; Casa, D. M.; Upton, M. H.; Kim, J.; Stoupin, S.; Nagle, K. P.; Balasubramanian, M.; Gordon, R. A.; Fister, T. T.; Heald, S. M.; Toellner, T.; Hill, J. P.; Coburn, D. S.; Kim, Y.-J.; Said, A. H.; Alp, E. E.; Sturhahn, W.; Yavas, H.; Burns, C. A.; Sinn, H. Momentum-Resolved Resonant and Nonresonant Inelastic X-Ray Scattering at the Advanced Photon Source. *Synchrotron Radiat. News* **2009,** *22* (6), 12–21. https://doi.org/10.1080/08940880903397009.
164. Alonso-Mori, R.; Kern, J.; Sokaras, D.; Weng, T.-C.; Nordlund, D.; Tran, R.; Montanez, P.; Delor, J.; Yachandra, V. K.; Yano, J.; Bergmann, U. A Multi-Crystal Wavelength Dispersive X-Ray Spectrometer. *Rev. Sci. Instrum.* **2012,** *83* (7), 073114. https://doi.org/10.1063/1.4737630.
165. Sokaras, D.; Weng, T.-C.; Nordlund, D.; Alonso-Mori, R.; Velikov, P.; Wenger, D.; Garachtchenko, A.; George, M.; Borzenets, V.; Johnson, B.; Rabedeau, T.; Bergmann, U. A Seven-Crystal Johann-Type Hard x-Ray Spectrometer at the Stanford Synchrotron Radiation Lightsource. *Rev. Sci. Instrum.* **2013,** *84* (5), 053102. https://doi.org/10.1063/1.4803669.

166. Frauenfelder, H.; McMahon, B. H.; Fenimore, P. W. Myoglobin: The Hydrogen Atom of Biology and a Paradigm of Complexity. *Proc. Natl. Acad. Sci.* **2003,** *100* (15), 8615–8617. https://doi.org/10.1073/pnas.1633688100.
167. Graham, D. J.; Nocera, D. G. Electrocatalytic H2 Evolution by Proton-Gated Hangman Iron Porphyrins. *Organometallics* **2014,** *33* (18), 4994–5001. https://doi.org/10.1021/om500300e.
168. Yang, J. Y.; Nocera, D. G. Catalase and Epoxidation Activity of Manganese Salen Complexes Bearing Two Xanthene Scaffolds. *J. Am. Chem. Soc.* **2007,** *129* (26), 8192–8198. https://doi.org/10.1021/ja070358w.
169. Emma, P.; Akre, R.; Arthur, J.; Bionta, R.; Bostedt, C.; Bozek, J.; Brachmann, A.; Bucksbaum, P.; Coffee, R.; Decker, F.-J.; Ding, Y.; Dowell, D.; Edstrom, S.; Fisher, A.; Frisch, J.; Gilevich, S.; Hastings, J.; Hays, G.; Hering, P.; Huang, Z.; Iverson, R.; Loos, H.; Messerschmidt, M.; Miahnahri, A.; Moeller, S.; Nuhn, H.-D.; Pile, G.; Ratner, D.; Rzepiela, J.; Schultz, D.; Smith, T.; Stefan, P.; Tompkins, H.; Turner, J.; Welch, J.; White, W.; Wu, J.; Yocky, G.; Galayda, J. First Lasing and Operation of an Ångstrom-Wavelength Free-Electron Laser. *Nat. Photon.* **2010,** *4* (9), 641–647. https://doi.org/10.1038/nphoton.2010.176.
170. Berrah, N.; Bozek, J.; Costello, J. T.; Düsterer, S.; Fang, L.; Feldhaus, J.; Fukuzawa, H.; Hoener, M.; Jiang, Y. H.; Johnsson, P.; Kennedy, E. T.; Meyer, M.; Moshammer, R.; Radcliffe, P.; Richter, M.; Rouzée, A.; Rudenko, A.; Sorokin, A. A.; Tiedtke, K.; Ueda, K.; Ullrich, J.; Vrakking, M. J. J. Non-Linear Processes in the Interaction of Atoms and Molecules with Intense EUV and X-Ray Fields from SASE Free Electron Lasers (FELs). *J. Mod. Opt.* **2010,** *57* (12), 1015–1040. https://doi.org/10.1080/09500340.2010.487946.
171. Zamyatin, A. V.; Gusev, A. V.; Rodgers, M. A. J. Two-Pump – One-Probe Femtosecond Studies of Ni(II) Porphyrins Excited States. *J. Am. Chem. Soc.* **2004,** *126* (49), 15934–15935. https://doi.org/10.1021/ja0448059.
172. Zhang, X.; Wasinger, E. C.; Muresan, A. Z.; Attenkofer, K.; Jennings, G.; Lindsey, J. S.; Chen, L. X. Ultrafast Stimulated Emission and Structural Dynamics in Nickel Porphyrins. *Chem. A Eur. J.* **2007,** *111* (46), 11736–11742. https://doi.org/10.1021/jp0751763.
173. Kim, D.; Kirmaier, C.; Holten, D. Nickel Porphyrin Photophysics and Photochemistry. A Picosecond Investigation of Ligand Binding and Release in the Excited State. *Chemical Physics* **1983,** *75* (3), 305–322. https://doi.org/10.1016/0301-0104(83)85199-4.
174. Retsek, J. L.; Drain, C. M.; Kirmaier, C.; Nurco, D. J.; Medforth, C. J.; Smith, K. M.; Sazanovich, I. V.; Chirvony, V. S.; Fajer, J.; Holten, D. Photoinduced Axial Ligation and Deligation Dynamics of Nonplanar Nickel Dodecaarylporphyrins. *J. Am. Chem. Soc.* **2003,** *125* (32), 9787–9800. https://doi.org/10.1021/ja020611m.
175. Song, Y.; Haddad, R. E.; Jia, S.-L.; Hok, S.; Olmstead, M. M.; Nurco, D. J.; Schore, N. E.; Zhang, J.; Ma, J.-G.; Smith, K. M.; Gazeau, S.; Pécaut, J.; Marchon, J.-C.; Medforth, C. J.; Shelnutt, J. A. Energetics and Structural Consequences of Axial Ligand Coordination in Nonplanar Nickel Porphyrins. *J. Am. Chem. Soc.* **2005,** *127* (4), 1179–1192. https://doi.org/10.1021/ja045309n.
176. Shelnutt, J. A.; Majumder, S. A.; Sparks, L. D.; Hobbs, J. D.; Medforth, C. J.; Senge, M. O.; Smith, K. M.; Miura, M.; Luo, L.; Quirke, J. M. E. Resonance Raman Spectroscopy of Non-Planar Nickel Porphyrins. *J. Raman Spectros.* **1992,** *23* (10), 523–529. https://doi.org/10.1002/jrs.1250231004.
177. Gentemann, S.; Nelson, N. Y.; Jaquinod, L.; Nurco, D. J.; Leung, S. H.; Medforth, C. J.; Smith, K. M.; Fajer, J.; Holten, D. Variations and Temperature Dependence of the Excited State Properties of Conformationally and Electronically Perturbed Zinc and Free Base Porphyrins. *J. Phys. Chem. B* **1997,** *101* (7), 1247–1254. https://doi.org/10.1021/jp9631137.
178. Jia, S.-L.; Jentzen, W.; Shang, M.; Song, X.-Z.; Ma, J.-G.; Scheidt, W. R.; Shelnutt, J. A. Axial Coordination and Conformational Heterogeneity of Nickel(II) Tetraphenylporphyrin Complexes with Nitrogenous Bases. *Inorg. Chem.* **1998,** *37* (17), 4402–4412. https://doi.org/10.1021/ic980289+.
179. Jeong, D. H.; Kim, D.; Cho, D. W.; Jeoung, S. C. Picosecond Transient Resonance Raman Study on the Excited-State Conformational Dynamics of a Highly Ruffled Nickel Porphyrin. *J. Raman Spectros.* **2001,** *32* (6–7), 487–493. https://doi.org/10.1002/jrs.713.
180. Chen, L. X. Probing Transient Molecular Structures with Time-Resolved Pump/Probe XAFS Using Synchrotron X-Ray Sources. *J. Electron Spectros. Relat. Phenom.* **2001,** *119* (2), 161–174. https://doi.org/10.1016/S0368-2048(01)00289-4.
181. Katayama, T.; Inubushi, Y.; Obara, Y.; Sato, T.; Togashi, T.; Tono, K.; Hatsui, T.; Kameshima, T.; Bhattacharya, A.; Ogi, Y.; Kurahashi, N.; Misawa, K.; Suzuki, T.; Yabashi, M. Femtosecond X-Ray Absorption Spectroscopy with Hard x-Ray Free Electron Laser. *Appl. Phys. Lett.* **2013,** *103* (13), 131105. https://doi.org/10.1063/1.4821108.
182. Shell, T. A.; Lawrence, D. S. A New Trick (Hydroxyl Radical Generation) for an Old Vitamin (B_{12}). *J. Am. Chem. Soc.* **2011,** *133* (7), 2148–2150. https://doi.org/10.1021/ja111585c.
183. Shell, T. A.; Lawrence, D. S. Vitamin B_{12}: A Tunable, Long Wavelength, Light-Responsive Platform for Launching Therapeutic Agents. *Acc. Chem. Res.* **2015,** *48* (11), 2866–2874. https://doi.org/10.1021/acs.accounts.5b00331.
184. Shell, T. A.; Shell, J. R.; Rodgers, Z. L.; Lawrence, D. S. Tunable Visible and Near-IR Photoactivation of Light-Responsive Compounds by Using Fluorophores as Light-Capturing Antennas. *Angew. Chem. Int. Ed.* **2014,** *53* (3), 875–878. https://doi.org/10.1002/anie.201308816.
185. Kutta, R. J.; Hardman, S. J. O.; Johannissen, L. O.; Bellina, B.; Messiha, H. L.; Ortiz-Guerrero, J. M.; Elías-Arnanz, M.; Padmanabhan, S.; Barran, P.; Scrutton, N. S.; Jones, A. R. The Photochemical Mechanism of a B_{12}-Dependent Photoreceptor Protein. *Nat. Commun.* **2015,** *6* (1), 7907. https://doi.org/10.1038/ncomms8907.
186. Jost, M.; Fernández-Zapata, J.; Polanco, M. C.; Ortiz-Guerrero, J. M.; Chen, P. Y.-T.; Kang, G.; Padmanabhan, S.; Elías-Arnanz, M.; Drennan, C. L. Structural Basis for Gene Regulation by a B_{12}-Dependent Photoreceptor. *Nature* **2015,** *526* (7574), 536–541. https://doi.org/10.1038/nature14950.
187. Padmanabhan, S.; Jost, M.; Drennan, C. L.; Elías-Arnanz, M. A New Facet of Vitamin B12: Gene Regulation by Cobalamin-Based Photoreceptors. *Annu. Rev. Biochem.* **2017,** *86* (1), 485–514. https://doi.org/10.1146/annurev-biochem-061516-044500.
188. Miller, N. A.; Wiley, T. E.; Spears, K. G.; Ruetz, M.; Kieninger, C.; Kräutler, B.; Sension, R. J. Toward the Design of Photoresponsive Conditional Antivitamins B_{12}: A Transient Absorption Study of an Arylcobalamin and an Alkynylcobalamin. *J. Am. Chem. Soc.* **2016,** *138* (43), 14250–14256. https://doi.org/10.1021/jacs.6b05299.
189. Kräutler, B. Antivitamins B_{12}—A Structure- and Reactivity-Based Concept. *Chem. A Eur. J.* **2015,** *21* (32), 11280–11287. https://doi.org/10.1002/chem.201502072.
190. Miller, N. A.; Deb, A.; Alonso-Mori, R.; Garabato, B. D.; Glownia, J. M.; Kiefer, L. M.; Koralek, J.; Sikorski, M.; Spears, K. G.; Wiley, T. E.; Zhu, D.; Kozlowski, P. M.; Kubarych, K. J.; Penner-Hahn, J. E.; Sension, R. J. Polarized XANES Monitors Femtosecond Structural Evolution of Photoexcited Vitamin B_{12}. *J. Am. Chem. Soc.* **2017,** *139* (5), 1894–1899. https://doi.org/10.1021/jacs.6b11295.
191. Zerdane, S.; Cammarata, M.; Balducci, L.; Bertoni, R.; Catala, L.; Mazerat, S.; Mallah, T.; Pedersen, M. N.; Wulff, M.; Nakagawa, K.; Tokoro, H.; Ohkoshi, S.; Collet, E. Probing Transient Photoinduced Charge Transfer in Prussian Blue Analogues with Time-Resolved XANES and Optical Spectroscopy. *Eur. J. Inorg. Chem.* **2018,** *2018* (3–4), 272–277. https://doi.org/10.1002/ejic.201700657.
192. Subramanian, G.; Zhang, X.; Kodis, G.; Kong, Q.; Liu, C.; Chizmeshya, A.; Weierstall, U.; Spence, J. Direct Structural and Chemical Characterization of the Photolytic Intermediates of Methylcobalamin Using Time-Resolved X-Ray Absorption Spectroscopy. *J. Phys. Chem. Lett.* **2018,** *9* (7), 1542–1546. https://doi.org/10.1021/acs.jpclett.8b00083.
193. Lemke, H. T.; Kjær, K. S.; Hartsock, R.; van Driel, T. B.; Chollet, M.; Glownia, J. M.; Song, S.; Zhu, D.; Pace, E.; Matar, S. F.; Nielsen, M. M.; Benfatto, M.; Gaffney, K. J.; Collet, E.; Cammarata, M. Coherent Structural Trapping through Wave Packet Dispersion during Photoinduced Spin State Switching. *Nat. Commun.* **2017,** *8* (1), 15342. https://doi.org/10.1038/ncomms15342.
194. Shiang, J. J.; Walker, L. A.; Anderson, N. A.; Cole, A. G.; Sension, R. J. Time-Resolved Spectroscopic Studies of B_{12} Coenzymes: The Photolysis of Methylcobalamin Is Wavelength Dependent. *J. Phys. Chem. B* **1999,** *103* (47), 10532–10539. https://doi.org/10.1021/jp992358r.
195. Walker, L. A.; Shiang, J. J.; Anderson, N. A.; Pullen, S. H.; Sension, R. J. Time-Resolved Spectroscopic Studies of B_{12} Coenzymes: The Photolysis and Geminate Recombination of Adenosylcobalamin. *J. Am. Chem. Soc.* **1998,** *120* (29), 7286–7292. https://doi.org/10.1021/ja981029u.
196. Michocki, L. B.; Miller, N. A.; Alonso-Mori, R.; Britz, A.; Deb, A.; Glownia, J. M.; Kaneshiro, A. K.; Konar, A.; Koralek, J.; Meadows, J. H.; Sofferman, D. L.; Song, S.; Toda, M. J.; van Driel, T. B.; Kozlowski, P. M.; Kubarych, K. J.; Penner-Hahn, J. E.; Sension, R. J. Probing the Excited State of Methylcobalamin Using Polarized Time-Resolved X-Ray Absorption Spectroscopy. *J. Phys. Chem. B* **2019,** *123* (28), 6042–6048. https://doi.org/10.1021/acs.jpcb.9b05854.

197. Miller, N. A.; Michocki, L. B.; Konar, A.; Alonso-Mori, R.; Deb, A.; Glownia, J. M.; Sofferman, D. L.; Song, S.; Kozlowski, P. M.; Kubarych, K. J.; Penner-Hahn, J. E.; Sension, R. J. Ultrafast XANES Monitors Femtosecond Sequential Structural Evolution in Photoexcited Coenzyme B_{12}. *J. Phys. Chem. B* **2020,** *124* (1), 199–209. https://doi.org/10.1021/acs.jpcb.9b09286.
198. Toda, M. J.; Lodowski, P.; Al Mamun, A.; Jaworska, M.; Kozlowski, P. M. Photolytic Properties of the Biologically Active Forms of Vitamin B_{12}. *Coord. Chem. Rev.* **2019,** *385,* 20–43. https://doi.org/10.1016/j.ccr.2018.12.017.
199. Kozlowski, P. M.; Garabato, B. D.; Lodowski, P.; Jaworska, M. Photolytic Properties of Cobalamins: A Theoretical Perspective. *Dalton Trans.* **2016,** *45* (11), 4457–4470. https://doi.org/10.1039/C5DT04286K.
200. Reinhard, M. E.; Mara, M. W.; Kroll, T.; Lim, H.; Hadt, R. G.; Alonso-Mori, R.; Chollet, M.; Glownia, J. M.; Nelson, S.; Sokaras, D.; Kunnus, K.; van Driel, T. B.; Hartsock, R. W.; Kjaer, K. S.; Weninger, C.; Biasin, E.; Gee, L. B.; Hodgson, K. O.; Hedman, B.; Bergmann, U.; Solomon, E. I.; Gaffney, K. J. Short-Lived Metal-Centered Excited State Initiates Iron-Methionine Photodissociation in Ferrous Cytochrome C. *Nat. Commun.* **2021,** *12* (1), 1086. https://doi.org/10.1038/s41467-021-21423-w.
201. Kjær, K. S.; van Driel, T. B.; Harlang, T. C. B.; Kunnus, K.; Biasin, E.; Ledbetter, K.; Hartsock, R. W.; Reinhard, M. E.; Koroidov, S.; Li, L.; Laursen, M. G.; Hansen, F. B.; Vester, P.; Christensen, M.; Haldrup, K.; Nielsen, M. M.; Dohn, A. O.; Pápai, M. I.; Møller, K. B.; Chabera, P.; Liu, Y.; Tatsuno, H.; Timm, C.; Jarenmark, M.; Uhlig, J.; Sundström, V.; Wärnmark, K.; Persson, P.; Németh, Z.; Szemes, D. S.; Bajnóczi, É.; Vankó, G.; Alonso-Mori, R.; Glownia, J. M.; Nelson, S.; Sikorski, M.; Sokaras, D.; Canton, S. E.; Lemke, H. T.; Gaffney, K. J. Finding Intersections between Electronic Excited State Potential Energy Surfaces with Simultaneous Ultrafast X-Ray Scattering and Spectroscopy. *Chem. Sci.* **2019,** *10* (22), 5749–5760. https://doi.org/10.1039/C8SC04023K.
202. Negrerie, M.; Cianetti, S.; Vos, M. H.; Martin, J.-L.; Kruglik, S. G. Ultrafast Heme Dynamics in Ferrous versus Ferric Cytochrome c Studied by Time-Resolved Resonance Raman and Transient Absorption Spectroscopy. *J. Phys. Chem. B* **2006,** *110* (25), 12766–12781. https://doi.org/10.1021/jp0559377.
203. Consani, C.; Bräm, O.; van Mourik, F.; Cannizzo, A.; Chergui, M. Energy Transfer and Relaxation Mechanisms in Cytochrome C. *Chem. Phys.* **2012,** *396,* 108–115. https://doi.org/10.1016/j.chemphys.2011.09.002.
204. Bräm, O.; Consani, C.; Cannizzo, A.; Chergui, M. Femtosecond UV Studies of the Electronic Relaxation Processes in Cytochrome C. *J. Phys. Chem. B* **2011,** *115* (46), 13723–13730. https://doi.org/10.1021/jp207615u.
205. Petrich, J. W.; Poyart, C.; Martin, J. L. Photophysics and Reactivity of Heme Proteins: A Femtosecond Absorption Study of Hemoglobin, Myoglobin, and Protoheme. *Biochemistry* **1988,** *27* (11), 4049–4060. https://doi.org/10.1021/bi00411a022.
206. Chernoff, D. A.; Hochstrasser, R. M.; Steele, A. W. Geminate Recombination of O_2 and Hemoglobin. *Proc. Natl. Acad. Sci.* **1980,** *77* (10), 5606–5610. https://doi.org/10.1073/pnas.77.10.5606.
207. Ye, X.; Demidov, A.; Rosca, F.; Wang, W.; Kumar, A.; Ionascu, D.; Zhu, L.; Barrick, D.; Wharton, D.; Champion, P. M. Investigations of Heme Protein Absorption Line Shapes, Vibrational Relaxation, and Resonance Raman Scattering on Ultrafast Time Scales. *Chem. A Eur. J.* **2003,** *107* (40), 8156–8165. https://doi.org/10.1021/jp0276799.
208. Waleh, A.; Loew, G. H. Quantum Mechanical Studies of the Photodissociation of Oxyheme Complexes. *J. Am. Chem. Soc.* **1982,** *104* (9), 2352–2356. https://doi.org/10.1021/ja00373a003.

Всё для победы! НАРОДНЫЙ ФРОНТ
https://pobeda.onf.ru/
LET'S HELP THE RUSSIA

10.14 X-ray and neutron diffraction from glasses and liquids

Chris J. Benmore, Advanced Photon Source, Argonne National Laboratory, Lemont, IL, United States

Published by Elsevier Ltd.

10.14.1	**Introduction**	**384**
10.14.2	**Neutron diffraction**	**386**
10.14.2.1	Neutron scattering lengths and cross sections	389
10.14.2.2	Time-of-flight neutron instrumentation	391
10.14.2.3	Analysis of neutron diffraction data	393
10.14.2.4	Faber Ziman formalism	395
10.14.2.5	Pair Distribution Functions	398
10.14.2.6	The effect of Q_{max} on real space resolution	400
10.14.3	**X-ray diffraction**	**400**
10.14.3.1	X-ray form factors	404
10.14.3.2	High energy X-ray Instrumentation	404
10.14.3.3	Analysis of X-ray diffraction data	406
10.14.4	**Complementary Techniques**	**411**
10.14.4.1	Anomalous X-ray scattering	412
10.14.4.2	Anomalous neutron diffraction	412
10.14.4.3	Isomorphic substitution	412
10.14.4.4	Neutron Diffraction with Isotopic Substitution	412
10.14.4.4.1	The Partial Structure Factors of Water	414
10.14.4.4.2	The Partial Structure Factor analysis of silica glass	415
10.14.5	**The first sharp diffraction peak**	**416**
10.14.5.1	Bhatia and Thornton formalism	418
10.14.6	**Atomistic modeling**	**419**
10.14.6.1	Reverse Monte Carlo (RMC)	420
10.14.6.2	Empirical Potential Structure Refinement (EPSR)	420
10.14.6.3	Classical Molecular Dynamics (CMD)	420
10.14.6.4	Density Functional Theory (DFT) and Ab initio Molecular Dynamics (AIMD)	421
10.14.6.5	Machine Learning interatomic potentials	421
10.14.7	**Outlook**	**422**
Acknowledgments		**422**
References		**422**

Abstract

This chapter lays out an intuitive approach to the determination of the differential scattering cross section using both neutrons and X-rays, for the study of disordered materials using the pair distribution function technique. It covers neutron scattering processes, cross sections and scattering lengths, time-of-flight neutron instrumentation, neutron pair distribution function analyses, the basics of X-ray diffraction, X-ray form factors, high energy X-ray instrumentation, and X-ray pair distribution function analyses. Detailed corrections to the measured neutron and X-ray data are presented, with an emphasis on spallation neutron and hard synchrotron X-ray diffraction methods. The Faber-Ziman and Bhatia-Thornton representations of measured structure factors are also described in the context of liquid and glass science. There is a concise assessment of related complementary techniques, including anomalous X-ray scattering, anomalous neutron scattering and isomorphic substitution. Emphasis is given to the neutron diffraction isotopic substitution method, and combining neutron and X-ray data for extracting partial structure factors. Detailed examples are given for liquid water and glassy silica, followed by a discussion of the first sharp diffraction peak. Throughout the chapter, the strong links between experiment and theory are underlined. It concludes with a brief overview of the latest computer atomistic modeling and simulation methods, and an outlook for future areas of liquid and glass science research.

10.14.1 Introduction

The liquid state covers a wide expanse of phase space, where the structures are not restricted by the symmetry associated with long range order. This can lead to very different local and packing arrangements for the atoms and molecules when compared to

crystalline phases of the same composition, and yield structures varying over a wide range of densities. The translational and orientational degrees of freedom associated with the structural entities that constitute stable melts and metastable glasses generally lead to a broad distribution of local polyhedra, and reduced steric hinderance effects, see Fig. 1. This disorder makes structural characterization difficult and, typically, a combination of several techniques are required to obtain a complete structural picture. Of the methods available, neutron and X-ray Pair Distribution Function (PDF) analyses represent some of the most powerful and established techniques for probing local ($\leq$5 Å) and intermediate range structural order ($\sim$20 Å and beyond) in a material.[1,2]

The scattering of radiation by condensed matter is related to the atomic positions if the wavelength of the incoming radiation is of the order of the interatomic spacing.[3] While X-rays scatter from the electrons in materials, neutrons scatter from the atomic nuclei, and typically offer complementary information. Both radiation sources provide a direct relation to the atomic positions in a material, and in practice the nuclear interaction generally provides a higher sensitivity to light elements and the electron interaction a higher sensitivity to heavier elements. Pioneering X-ray diffraction PDF experiments examining non-crystalline forms of matter were performed by Warren in the 1930s.[4,5] Narten and colleagues[6,7] made considerable progress in the 1970s by carefully refining the data analysis techniques associated with the X-ray pair distribution function method, using conventional X-ray sources. Meanwhile, the PDF technique gained much popularity within the field of neutron scattering in the 1960s, where the majority of early neutron diffraction experiments were performed on reactor sources using thermal ($\sim$25 meV) neutrons.[8,9] More energetic "hot" reactor sources ($\sim$80–800 meV) extended measurements to larger Q values, and provided high quality liquid diffraction data. The energy range was extended with the advent of spallation neutron sources and the use of "epithermal" neutrons enabled access to very high momentum transfers for high-resolution glass and amorphous materials measurements.[10] A similar leap in instrumentation occurred for X-ray diffraction with the development of the high energy X-ray technique on synchrotron radiation sources in the mid-1990s. Here we define the term "high energy" as energies in excess of 60 keV.[11] Based on a 60 keV γ-ray diffraction technique,[12] the breakthrough was made by Poulsen and Neuefeind,[13] when they first used synchrotron radiation of $\sim$100 keV to study the structure of glasses out to high momentum transfers i.e. $Q > 20$ Å^{-1}. The high-energy X-ray PDF technique has become widespread in the last two decades and synchrotron beamlines routinely perform measurements on glass, liquids and amorphous materials using large area detectors.

A distinct advantage of the PDF technique is the direct relation to theory and the stringent test of atomistic models. At low densities the minimum in the interatomic pair potential corresponds to the peak position in the PDF i.e. the average distance between pairs. The distance of shortest approach is determined by the repulsive part of the potential, as shown in Fig. 2, corresponding to the diameter σ for hard spheres of equal sizes. The precise shape of the pair potential and depth of the energy well, ε, define the interaction between atom pairs that is reflected in the 3-D structure and shape of the corresponding PDF. In this chapter, we start with an intuitive derivation of the scattering formula for neutrons and X-rays, based on the so-called "orange book" of unpublished scattering notes given by Prof. Peter Egelstaff at the University of Guelph, Canada during the early 1990s. The chapter is organized in the following way: The first section contains a description of the scattering and absorption processes during a typical neutron scattering experiment and the relation to the static total structure factor S(Q). There is a discussion of neutron scattering lengths and cross sections in comparison to X-ray diffraction. Time-of-flight neutron diffraction instrumentation and the analysis procedures are outlined with a view of extracting the Faber-Ziman total and partial neutron structure factors. The Fourier transformation procedure from S(Q) to the corresponding pair distribution functions G(r) is presented. The second section describes analogous X-ray diffraction processes, photon cross sections, X-ray form factors and X-ray instrumentation. The analysis of high-energy X-ray diffraction data and extraction of the Faber-Ziman total and partial X-ray structure factors is presented. The third section contains a brief

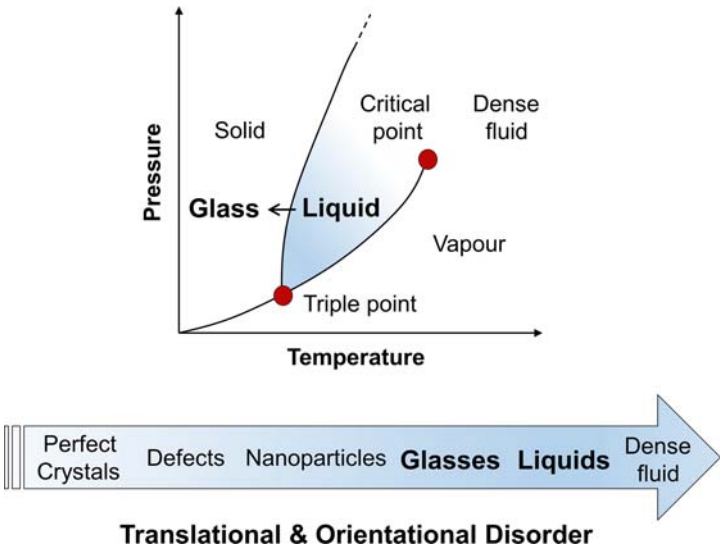

Fig. 1 Increasing pressure and temperature lead to increased translational and orientational disorder within a material.[3]

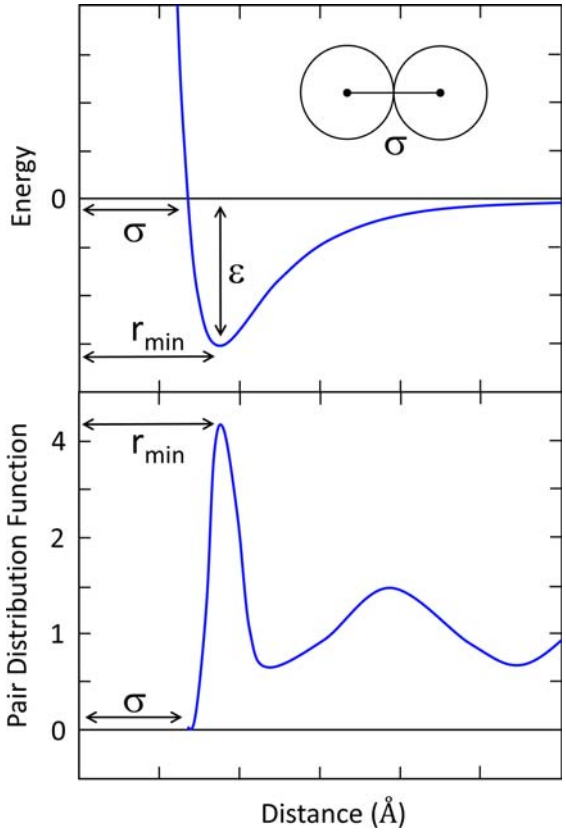

Fig. 2 The relationship between the atom-atom pair potential and the pair distribution function at low density.[3]

overview of anomalous X-ray and neutron methods and isomorphic substitution. Partial structure factor examples are given for the cases of liquid water and glassy silica. Next, there is a discussion of the first sharp diffraction peak, ranges or order within liquids and glasses and the Bhatia-Thornton formalism. Finally, an account of current computer modeling methods and a look toward future developments is given.

10.14.2 Neutron diffraction

Here we consider the atomic scattering of wavelets of radiation with similar amplitudes and phases, which interfere to produce a pattern as if the sample were a diffraction grating. We isolate the scattered coherent neutron intensity in terms of an interference function, which provides information on the average short, intermediate and long-range order in disordered materials.[14] To determine the nuclear positions in a sample by scattering a neutron beam from the nuclei, the incident and final wave-vectors k_0 and k_f are considered together with the scattering angle 2θ (Fig. 3).

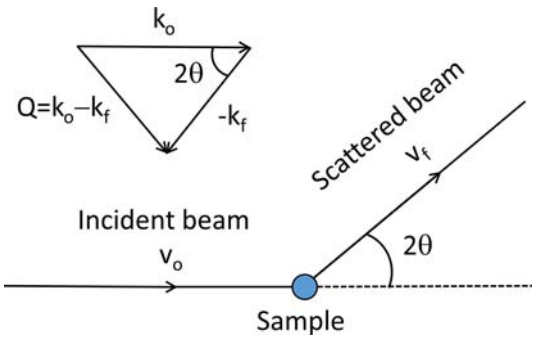

Fig. 3 Elastic scattering in real and reciprocal space where the incoming neutron velocity v_0 and associated wave-vector k_0 are related through $mv = hk$. For elastic scattering $|k_0| = |k_f|$ such that $Q = 2 \mid k_0 \mid \sin\theta$.[10]

Regardless of whether the experiment is performed with a monochromatic or polychromatic beam of radiation, the measured intensity is proportional to the structure factor S(Q), where Q is given by,

$$Q = \frac{4\pi \sin\theta}{\lambda}$$

In a typical neutron reactor scattering experiment, four measurements are made; the sample (S) in a container, empty container (C), vanadium (*V*) in a holder, empty holder (H). Vanadium has a neutron cross section that is almost entirely incoherent, making it an ideal calibration standard for most neutron diffraction experiments.[10] The scattering pattern from vanadium does exhibit some small Bragg peaks due to a small coherent cross section, but these are typically removed by smoothing or modeling. For each of these measurements, a background is subtracted with a piece of cadmium, the same size and shape as the sample, blocking the beam, in an effort to determine the differential cross section $d\sigma/d\Omega$ using the *intuitive* formula,

$$\mathrm{I}(2\theta) = aH\frac{d\sigma}{d\Omega}N$$

which is measured in barns per steradian per atom/4π, where.

I(θ) is the measured sample intensity per unit time over a solid angle dΩ at the angle 2θ.
a is the diffractometer calibration factor determined from a standard e.g. vanadium and other information.
H is the self-absorption factor i.e. absorption of radiation in the sample.
N is the number of atoms in the beam.

Neglecting inelastic scattering effects for the moment, the differential cross section can be split into self and distinct parts

$$\frac{d\sigma}{d\Omega} = \frac{d\sigma}{d\Omega_{self}} + \frac{d\sigma}{d\Omega_{distinct}}$$

The ratio, γ, of the coherent to total scattering cross sections can be written as

$$\gamma = \frac{\sigma_{coh}}{\sigma_{coh} + \sigma_{incoh}} = \frac{\sigma_{coh}}{\sigma_{scatt}}$$

where

$$\frac{d\sigma}{d\Omega} = \{(S(Q) - 1)\gamma + 1\}\frac{\sigma_{scatt}}{4\pi}$$

and S(Q) is the structure factor we are trying to extract.

If we include inelasticity effects, the so called Placzek[15] correction term P is added, to allow for the changes in neutron energy on scattering,

$$I(\theta) = aH\{(S(Q) - 1)\gamma + 1 + P\}\frac{N\sigma_{scatt}}{4\pi}$$

In addition, some neutrons will be scattered two or more times within the sample. The ratio of these multiply scattered neutrons to the singly scattered ones is denoted by Δ, and if we assume that the self-absorption factor is H we obtain,

$$I(\theta) = aH\{(S(Q) - 1)\gamma + 1 + P + \triangle\}\frac{N\sigma_{scatt}}{4\pi}$$

Considering the vanadium results first, we can write the absorption factors in the notation of[16] e.g. $A_{V,VH}$ denotes scattering by V and absorption by V and H, and we obtain

$$I_{VH}(\theta) - I_H(\theta)\frac{A_{H,VH}}{A_{H,H}} = a(\theta)A_{V,VH}N_V\left\{\frac{d\sigma}{d\Omega} + \frac{\triangle\,\sigma_{scatt}}{4\pi}\right\}_V$$

where $d\sigma/d\Omega$ is given by 1 + P and a(θ) may be calculated, since S(Q) = 1 for vanadium. If the instrument is well designed a(θ) can be independent of θ. These scattering and absorption process in a sample are depicted in **Fig. 4**.

Attenuation and multiple scattering corrections have been discussed by numerous authors, and are illustrated in **fig. 4**. Several approaches have been used including numerical integrations[17,18] and Monte Carlo simulations.[19] The Paalman and Pings[16] attenuation factors can also be written for the sample in a container using the terms $A_{S,SC}$, $A_{C,SC}$ and $A_{C,C}$. Similarly, the quantities M_{SC} and M_C can be used to represent the total multiple scattering differential cross sections for the sample plus container and empty container respectively. The attenuation factors depend on the sample geometry and the total neutron cross section, and can be expanded for additional shielding arising from furnace or cryostat walls for example. However, the multiple scattering terms are much more difficult to calculate since, in principle, they require a detailed knowledge of the sample structure. For samples that scatter $< 20\%$, an isotropic approximation is often used which assumes that for a particular energy the scattering at each angle is isotropic.[20]

The experimental data for the sample and container can be treated in a similar way as just described, by defining the primed quantities in the following equations as intensities which have been properly normalized and corrected for multiple scattering. Such that,

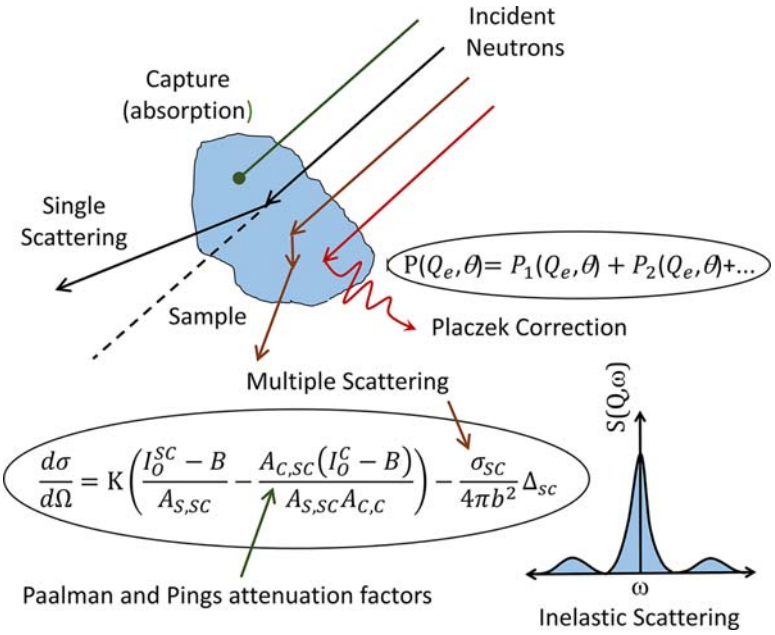

Fig. 4 The scattering and absorption processes that can occur during a neutron scattering experiment.

$$\frac{I_{SC}(\theta)}{a(\theta)} = I'_{SC}(\theta) + \triangle_{SC}\left\{A_{S,SC}\left(\frac{N\sigma_{scatt}}{4\pi}\right)_S + A_{C,SC}\left(\frac{N\sigma_{scatt}}{4\pi}\right)_C\right\}$$

and

$$\frac{I_C(\theta)}{a(\theta)} = I'_C(\theta) + \triangle_C\left\{A_{C,C}\left(\frac{N\sigma_{scatt}}{4\pi}\right)_C\right\}$$

The differential cross section can now be written as,

$$N\left\{\frac{d\sigma}{d\Omega}\right\}_S = \left\{I'_{SC}(\theta) - I'_C(\theta)\frac{A_{C,SC}}{A_{C,C}}\right\}\frac{1}{A_{S,SC}}$$

An alternative, and important way of checking that the calculation has been performed correctly, is to ensure that S(Q) tends to 1.0 at high Q. Absorption and multiple scattering corrections for a flat plate geometry have been discussed by,[21] considering infinite slabs positioned at various angles to the beam. A wide uniform beam incident on a cylindrical sample gives simpler corrections but generates a higher background. For cases where it is necessary to access smaller scattering angles, smaller beams are required making the corrections more complex.

Turning to the structure factor S(Q) itself, this is defined as the integral of S(Q,ω) over all energies. However, in neutron scattering inelastic collisions also occur between the neutron and the nucleus of the atom. So strictly speaking we cannot measure the required S(Q,ω) over all the energy transfers required, and we are left with the problem that,

$$b^2\int_0^\infty \frac{k_f}{k_0}\varepsilon S(Q,\omega)dE \neq b^2 S_{expt}(Q)$$

where E is the energy of the scattered neutrons.

ε is the detector efficiency.
b is the neutron scattering length.

It has been shown by Placzek[15] that for heavier nuclei a model can often provide a good approximation to S(Q,ω). The Placzek correction is labelled $P(Q,\theta)$, and approximates the neutron recoil that depends on the nuclear mass, sample temperature, incident neutron energy, geometry and detector efficiency. However, it cannot always be directly applied to thermal neutron diffraction experiments in which only some vibrational levels are excited by the neutron as illustrated in Fig. 5. Placzek's arguments were based on the fact that the first two moments in S(Q,ω) for a classical fluid can be described by,

$$S_1(Q) = \sum_\alpha \frac{c_\alpha\langle b_\alpha^2\rangle\hbar Q^2}{2M_\alpha} \text{and} S_2(Q) = \sum_\alpha c_\alpha\langle b_\alpha^2\rangle\left(\frac{K_B T Q^2}{M_\alpha} + \frac{\hbar^2 Q^2}{4M_\alpha^2} + \ldots.\right)$$

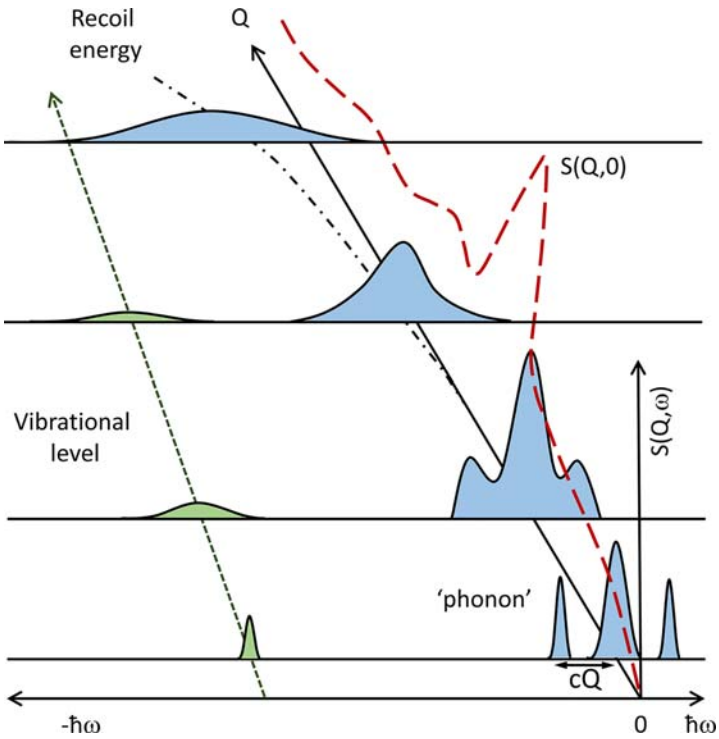

Fig. 5 The scattering law S(Q,ω) for a liquid. Collective excitations equivalent to phonon-like modes are observed at the lowest Q-values before the first peak in S(Q,0). A quasi-elastic peak is also present from self-diffusion. At higher Q values, peaks merge forming a Gaussian distribution centered on the recoil energy line $\hbar^2Q^2/2M$.[10]

which leads to the first and second order correction terms $P_1(Q_e,\theta)$ and $P_2(Q_e,\theta)$.

Placzek[15] pointed out that the cases where the incident energy $\gg \hbar\omega$ (the energy transfer), corresponded to those where the mass of the scattering atom M was much greater than the mass of a neutron, m_n. By writing the differential cross section as an asymptotic power series in m_n/M, where the leading term is S(Q), the higher order terms in this series have become called the "Placzek corrections". Two points to note about this series are that it does not converge under all conditions i.e. if M = 1 or 2 (hydrogen or deuterium) other methods are required, and for large values of M/m_n the terms higher than the second are small. Details of this expansion for a liquid at high-Q values measured on a reactor and time-of-flight source have been given by Powles[22] and implemented using the method of Howe et al.[23]

Strictly speaking, a model neutron scattering law S(Q,ω) is needed to describe the system under study over the range of energies probed in the experiment. However, when this is not known e.g. for systems containing hydrogen or deuterium, the shape of the inelastic signal has been successfully approximated and removed by the use of low-order polynomials. This is illustrated in Fig. 6, for the case of D_2O measured on a reactor source, using the empirical formula $P(\lambda, 2\theta) = A + BQ^2 + C^4$.[24] In the case of time-of-flight data, Chebyshev polynomials are commonly used to approximate the Placzek contribution.[25]

10.14.2.1 Neutron scattering lengths and cross sections

A knowledge of the scattering lengths and absorption cross sections for the elements is vital to the application of thermal neutron scattering to the structure and dynamics of materials. This information is needed to obtain absolute normalization and correction of the measured functions, see Fig. 7. In certain cases, the *v*alues for particular isotopes are also required.[27] Typically, scattering lengths and cross sections for nuclides are independent of the incident neutron wave vector, k_0, in the thermal neutron regime, and the absorption cross sections are inversely proportional to k_0. By convention, these values are listed for $k = 3.494\ \text{Å}^{-1}$ i.e. $\lambda = 1.798$ Å, E = 25.3 meV or v = 2200 m/s. ^{113}Cd is an important exception to these proportionalities, as it has an energy-dependent resonance in the thermal region. The imaginary parts of the scattering lengths are only appreciable in the case of strongly absorbing nuclides. Our knowledge of neutron scattering lengths and cross sections is not complete, and the accuracy of the measurements are continually being improved and the listed values updated.[2,28]

Away from nuclear resonances, the total neutron cross section has contributions from two primary processes; scattering σ_{scatt} and absorption σ_{abs}. The probability of absorption is proportional to the neutron wavelength. The scattering cross section represents the integral of the differential scattering cross section at a fixed wavelength over all scattering angles and varies between the so-called "bound" value at low energies where only diffusional type motions are excited and "free" values where all possible modes are accessible.

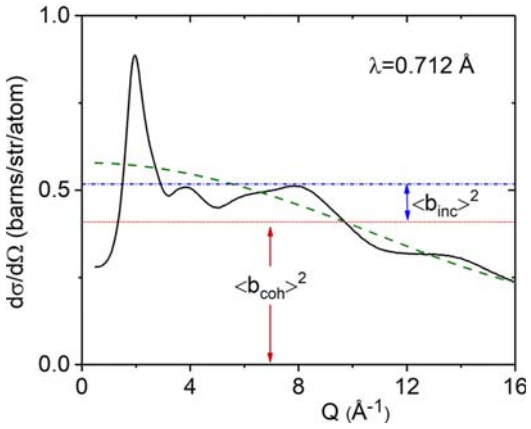

Fig. 6 A representation of the total differential scattering cross section from D_2O measured at fixed wavelength. $\langle b_{coh}\rangle^2$ is the coherent cross section per atom/4pi, and $\langle b_{inc}\rangle^2$ is the incoherent cross section per atom/4pi.[26] The green dashed line includes the Placzek term $P(\lambda, 2\theta)$ calculated using a polynomial expansion.

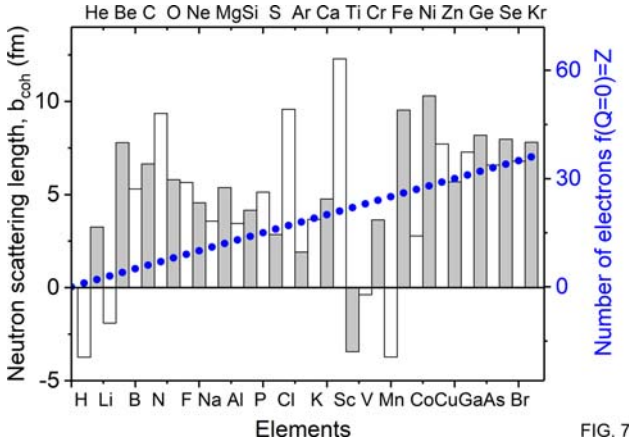

Fig. 7 Neutron coherent scattering lengths for light natural elements (bars) taken from Ref. 27 These are compared to the linear relation for X-ray diffraction that has been scaled to illustrate that the neutron and X-ray scattering is essentially equivalent for $GeSe_2$ glass.[10] Sears, V. F. Neutron Scattering Lengths and Cross Sections. *Neutron News* **1992**, *3*(3), 26–37. 10.1080/10448639208218770.

The total neutron cross section σ_{total} is given by,

$$\sigma_{total}(\lambda) = \sigma_{scatt}(\lambda) + \sigma_{abs}(\lambda)$$

A nuclear resonance occurs when the neutron excites the nucleus to an excited state somewhat analogous to an absorption edge in X-ray scattering. The possible nuclear states can be complicated and can exhibit changes in scattering, absorption or both. Within the Born approximation, the Fermi pseudopotential describes the scattering of a neutron by a single bound nucleus,

$$V(r) = \frac{2\pi\hbar^2}{m} b\delta(r)$$

where m is the mass of the neutron, b is the bound scattering length and r is the position of the neutron relative to the nucleus. b is complex where $b' = -ib'' = (A + 1/A)$, where A is the nucleus/neutron mass ratio, and

$$\sigma_{scatt,bound} = \left(\frac{A+1}{A}\right)^2 \sigma_{scatt,free}$$

This ratio has a value of 0.25 for hydrogen and 0.44 for deuterium denoting a significant fall in cross section with increasing energy. For heavier atoms this factor is close to unity.

The neutron also has spin s, which can generally be expressed by

$$b = b_{coh} + \frac{2b_{inc}}{\sqrt{I(I+1)}} s.I$$

where I is the spin of the nucleus, b_{coh} and b_{inc} are the bound coherent and incoherent scattering lengths. Consequently, the scattering length depends both on the isotopic mass of the nucleus and the relative orientation of the isotope's nuclear spin state with respect to the incident neutron's spin state.

The total scattering cross section is given by $\sigma_{scatt} = 4\pi\langle b^2\rangle$ and the absorption cross section by $\sigma_{abs} = 4\pi\langle b''\rangle/k$.

For unpolarized neutrons, or nuclei, the total scattering cross section can be written as

$$\sigma_{scatt} = \sigma_{coh} + \sigma_{inc}$$

where σ_{coh} and σ_{inc} are the bound coherent and incoherent scattering cross sections, such that

$\sigma_{coh} = 4\pi\langle b_{coh}\rangle^2$ and $\sigma_{inc} = 4\pi\langle b_{inc}\rangle^2$.where $\sigma_{inc} = \sigma_{spin} + \sigma_{isotope}$. Calculations of cross sections from nuclear data using the Breit-Wigner formulation are given in Ref. 3.

10.14.2.2 Time-of-flight neutron instrumentation

The main instrument components for reactor and time-of-flight diffraction experiments are shown in Fig. 8. The process starts with the production of radiation and selection of the incident energy using a monochromator or moderator, followed by collimation (and possibly focusing) into a well-defined beam incident onto the sample. A detector array measures the scattered diffraction pattern, and is positioned at a distance chosen to balance the needs of resolution versus count-rate. The signals are counted and binned within a data acquisition electronics system and viewed using dedicated data analysis software.

At spallation neutron sources, accelerators produce high energy protons, which when fired into a target such as uranium or mercury can produce up to 30 neutrons per proton. Other targets such as tantalum or tungsten produce half this number.[29] Neutrons produced by spallation from a target material are too energetic for most diffraction experiments, and require slowing

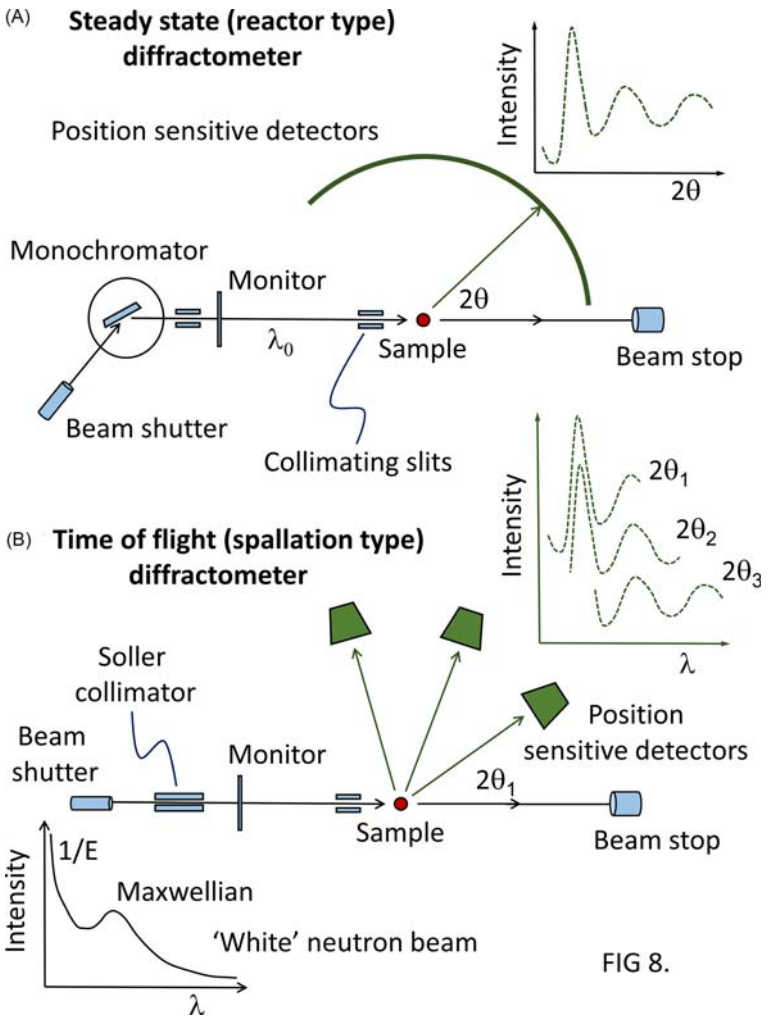

Fig. 8 Schematic diagrams of the components for (A) a monochromatic, steady state, diffractometer, (B) compared to a spallation time-of-flight diffractometer.

down and thermalization by a moderator to be useful. Moderators usually contain light atoms. Hydrogen-rich materials such as H_2O, CH_4, are commonly employed because hydrogen has a similar mass to the incoming neutron, thereby maximizing the energy transferred in each collision. Moderators are typically surrounded by beryllium, which acts as a neutron reflecting material.[9] Consequently, the typical neutron incident beam spectrum contains an epithermal region, in which the intensity varies as 1/E, and a Maxwellian region characterized by a peak whose position and width are determined by the moderator parameters. Spallation neutrons emerge from the moderator in pulses in all directions and a full spectrum of all energies impinges on the sample. This is in contrast to a continuous beam monochromatic reactor-based neutron experiment, see Fig. 8. Cadmium and gadolinium are often the preferred neutron absorbing (shielding) materials for monochromatic reactor based diffraction experiments, but boron is more widely used to reduce scatter in spallation time-of-flight measurements.

For liquids and amorphous materials, the measured structure factor consists of a few broad peaks, which merge together continuously, and detailed analysis of this spectra requires absolute measurements. Spallation time-of-flight experiments can be very sensitive to sample positioning effects. Ideally the container is constructed of a material that is (almost) a completely incoherent scatterer such as vanadium or titanium-zirconium alloy, or has a weakly scattering (non-hydrogen containing) amorphous structure. Removing sharp Bragg reflections from a diffuse signal is problematic if not impossible, largely due to the slightly different scattering angles emerging from the front and back of the container and attenuation effects from the sample being present. Common neutron detector types include gas counters where, for example, He^3 or BF_3 is the main neutron absorber, or scintillator detectors. The measured events are recorded in the data acquisition electronics, which time stamps the event in a time-of-flight experiment.

With neutrons or high energy X-rays, a beamstop is needed to absorb the main beam that does not interact with the sample. Comprehensive shielding around the beamline is essential for human protection from exposure to radiation. A primary consideration in building any diffractometer is the trade-off between count rate and resolution. For powder diffraction from ordered materials there are many sharp peaks close to each other so high resolution is required, whereas for glasses, liquids and amorphous materials the peaks are weaker, broader and overlap continuously, so lower resolution, and high count rates are needed.

Consider a neutron of wavevector $\vec{k}_O$ emitted by a pulsed source and traveling an initial distance of "L_o" units before impinging on a sample. After scattering through angle 2θ, and having a new wavevector $\vec{k}_f$, it travels a final distance of L_f before being captured by a detector. We can then write the relation between these events using the time-of-flight equation;

$$\frac{L_o}{\vec{k}_o}+\frac{L_f}{\vec{k}_f}=\frac{L_o+L_f}{\vec{k}_e}$$

where $\vec{k}_e$ is the wavenumber for elastic scattering. The differential cross section for this experiment can be written,

$$\frac{4\pi}{\sigma_{scatt}}.\frac{d\sigma}{d\Omega}=\vec{K}_f\int\phi\left(\frac{1}{\vec{k}_o}\right)f\left(\vec{k}_f\right)\frac{\vec{k}_f}{\vec{k}_o}S(Q,\omega)\left.\frac{\partial\omega}{\partial\left(1/\vec{k}_e\right)}\right|_k.d\left(\frac{1}{\vec{k}_o}\right)$$

where a neutron's time of flight is proportional to $1/\vec{k}$ and $\phi\left(1/\vec{k}_o\right)d\left(1/\vec{k}_o\right)$ is the incident time of flight spectrum and $f\left(\vec{k}_f\right)$ is the detector efficiency. After normalizing ϕ and f by their values for elastic scattering, replacing $1/\vec{k}_o$ with ω using a Jacobian and combining with the relation

$$\omega=\frac{\hbar}{2m}\left(\vec{k}_o^{\,2}-\vec{k}_f^{\,2}\right).$$

the time-of-flight differential cross section becomes

$$\frac{4\pi}{\sigma_{scatt}}.\frac{d\sigma}{d\Omega}=\vec{K}_f\int_{-\infty}^{\infty}N\left(\vec{k}_o,\vec{k}_e\right)\left.\frac{\partial\left(1/\vec{k}_o\right)}{\partial\left(1/\vec{k}_e\right)}\right|_\omega S(Q,\omega)d\omega$$

where $\vec{K}_f=\left(\vec{k}_f\right)_{sample}/\left(\vec{k}_f\right)_{vanadium}$, $N\left(\vec{k}_o,\vec{k}_e\right)$ represents the incident time of flight spectrum and detector efficiency terms and

$$\left.\frac{\partial\left(1/\vec{k}_o\right)}{\partial\left(1/\vec{k}_e\right)}\right|_\omega=\frac{L_o+L_f}{L_o+\left(\vec{k}_o/\vec{k}_f\right)^3}.$$

Since the integration is complicated by the fact that experimentally only a selection of incident and scattered energies are measured, Egelstaff[29] has called the latter term the "sampling factor" because it determines how S(Q,ω) is sampled. In addition, it is important to note that the measured differential cross section is normalized to a vanadium standard and remains a function of scattering angle, with each 2θ covering a different Q-range. The Placzek, absorption and multiple scattering corrections need to be

applied at each 2θ before they can be merged together. In comparison with the steady state method, the same formulae are obtained in the limit $L \rightarrow \infty$ i.e. the incident flight path becomes much longer than the scattered flight path. However, the sampling factor reduces to unity for $\hbar\omega \leq E_e$ and to zero for $\hbar\omega > E_e$.

10.14.2.3 Analysis of neutron diffraction data

Several of the corrections required for neutron scattering data have already been discussed. These, and others, mainly arise from three aspects of the experiment. Namely the source, the sample and the diffractometer. Firstly, we consider the source and sample errors. Variations in the incident radiation source flux need to be accounted for. The measured neutron intensity needs to be divided by the incident monitor neutron counts (or spectrum in the case of a time-of-flight neutron experiment) to account for small variations in incident beam intensity. Regarding the diffractometer itself, instrument calibrations are normally performed using standard powders such as Ni, MgO or diamond to calibrate the Q scale. Also, detector dead time corrections can be important in both neutron and X-ray experiments. Detectors do not count for a short time after an event has occurred and during high intensity scattering experiments this dead time can miss a significant proportion of the counts. Diffractometer stability, due to electronic drifts and other effects, is important for accurate neutron diffraction data. One way to minimize these effects is to rapidly switch between different samples and vanadium standards to reduce the level of systematic error.

Variation in the angle of scatter is an important correction in high energy, low angle experiments typically optimized for high-Q PDF measurements. A geometric correction is necessary for out-of-plane scattering errors due to the finite size of the detector. To calculate the angle θ' to the midpoint of a neutron detector above or below the scattering plane, we can use the following equation to give the angle θ' in the tilted plane

$$\cos\theta' = \frac{l\cos\theta}{\sqrt{l^2 + d^2}}$$

where θ is the normal scattering angle and l the normal path length and d is ¼ the length of the counter e.g. ^{3}He tube counter.

For an accurate S(Q), resolution corrections are also required. If the width ΔQ represents the instrumental resolution in the measured S(Q) and we assume that the contributions are made up of deviations in λ and θ, we can write

$$\frac{\triangle Q}{Q} = \left\{ \left(\frac{\triangle \lambda}{\lambda} \right)^2 + \left(\frac{\triangle \theta}{2\tan\theta/2} \right)^2 \right\}^{1/2}$$

Where $\Delta\lambda$ is due to the angular spread α of either the incident or reflected beams from the monochromator and the monochromator's mosaic spread, η.

Frequently the deviations in λ and θ are independent such that

$$\frac{\triangle \theta_{Beam}}{\theta_{Beam}} = \left\{ \left(\frac{\triangle \eta}{\eta} \right)^2 + \left(\frac{\triangle \alpha}{\alpha} \right)^2 \right\}^{1/2}$$

and

$$\frac{\triangle \lambda}{\lambda} = \frac{\triangle \theta_{Beam}}{\tan\theta_{Beam}}$$

The scattering angle θ_{Beam} is uncertain because of the angular spread of the incident beam, the size of the sample and the size of and distance to the detector. Sometimes the wavelength deviation is correlated with the angular deviation of the incident beam (if $\Delta\alpha << \eta$) and this case should be considered separately. Usually when considering diffraction from disordered materials the angular deviations are large, so we can neglect this case and the effects of sample size and detector size can be combined into one angular deviation $\Delta\phi$. Because a section of the 3-dimensional diffraction pattern is being taken there will not be a symmetric resolution function, but one which is biased towards lower-Q. In addition, the individual resolution elements will vary from case to case.

In considering the sample related corrections, transmission measurements are important for estimating the amount of material in the beam. Transmission is determined by measuring the ratio of the number of neutrons passing directly through the sample (at zero scattering angle), to the number passing through with no sample present. When normalized to the incident neutron monitor, the fraction of neutrons absorbed by the sample is proportional to the neutron cross section and sample density (including the packing fraction if a powdered sample). For a flat plate sample uniformly covering the beam, the transmission of the sample is given by,

$$T = e^{-\rho\sigma_{total}(\lambda)t}$$

where ρ is the atomic number density and t is the sample thickness.

The transmission of cylindrical samples is related to the Paalman and Pings[16] absorption correction at $2\theta = 0$, such that $T_C = A_{C,C}$ $(2\theta = 0)$ and $T_S = A_{S,S}$ $(2\theta = 0)$ and, $A_{s,sc} \approx A_{C,SC} \approx A_{C,C} \times A_{S,S} \approx T_C \times T_S$. Since the beam path through a cylindrical

container is longer at the edges than in the middle, and the opposite is true for the sample, it follows that $A_{c,sc} < A_{s,sc}$. In practice the difference between these two quantities is ~1% for A ~ 0.5 indicating these inequalities work well.

Absorbing slits and masks positioned in front of the sample are important for defining the height and width of the incident beam necessary for accurate multiple scattering calculations. The multiple scattering cross section for a sample and a container are given by

$$\sigma_{MS} = \left[(N\sigma)_S A_{S,SC} + (N\sigma)_C A_{C,SC}\right] \frac{\triangle_{SC}}{4\pi}$$

where N is the effective number of atoms in the beam and $\triangle_{SC}$ is the ratio of multiply to singly scattered neutrons arising from both the sample and container. Examples of representative Placzek, absorption and multiple scattering corrections for liquid CCl_4 measured on a time-of-flight diffractometer are shown in Fig. 9. The overall neutron data analysis procedure is described in Fig. 10.

Next, we consider the uncertainties involved. The error on any cross section, structure factor, normalization constant or any other quantity is made up of two components. The first being statistical counting errors, and the other systematic errors such as instrumental drift, etc. For statistical counting errors, the number of counts N recorded over a certain time can be described by a Poisson distribution and has a standard deviation of $\sqrt{N}$. Adding or subtracting datasets yields combined standard deviations of

$$N_1 + N_2 \pm \sqrt{N_1 + N_2} \text{and} N_1 - N_2 \pm \sqrt{N_1 + N_2}$$

and multiplications and divisions are described by,

$$N_1 \times N_2 \pm N_1 \times N_2 \sqrt{\frac{1}{N_1} + \frac{1}{N_2}} \text{ and } \frac{N_1}{N_2} \pm \frac{N_1}{N_2} \sqrt{\frac{1}{N_1} + \frac{1}{N_2}}.$$

In addition to the statistical errors, after the application of corrections to the data, the observed structure factor $S_{obs}(Q)$ will be subject to a number of systematic errors. These are of two general types (i) additive errors due to inadequate subtractions or additions. Such errors may vary with Q and are denoted β(Q) (ii) multiplicative errors due to uncertainties in cross sections denoted α, the number of atoms in the beam, attenuation coefficients denoted by a factor γ, which to a first approximation are independent of Q. Therefore, the observed structure factor is related to S(Q) by

$$s_{obs}(Q) = \frac{[S(Q) - 1]\gamma + 1 + \beta(Q)}{\alpha} = [S(Q) - 1]\frac{\gamma}{\alpha} + \frac{1 + \beta(Q)}{\alpha}$$

this procedure depends on two unknown constants. Some examples of how to determine α and β(Q) are considered below: (i) For the case where β(Q) is believed to be nearly constant and one node of S(Q)-1 is known (denoted Q′) then $S_{obs}(Q') = 1 + \beta/\alpha$. This leaves the ratio of γ/α to be determined either by assuming the published value of γ and that α = 1 or by fitting to another known point. (ii) By determining the density derivative of S(Q), if the dependence of α and β on ρ is weak, then

$$\frac{\partial S_{obs}(Q)}{\partial \rho} = \frac{\gamma}{\alpha} \cdot \frac{\partial S(Q)}{\partial \rho}$$

such that β(Q) is not important. If several S(Q) derivatives are measured for the same material only one choice of γ/α will be acceptable. (iii) If the range of Q covered in the experiment is large enough, the traditional limits can be usedi.e. S(Q) → 1 as Q → ∞ and g(r) → 0 as r → 0.

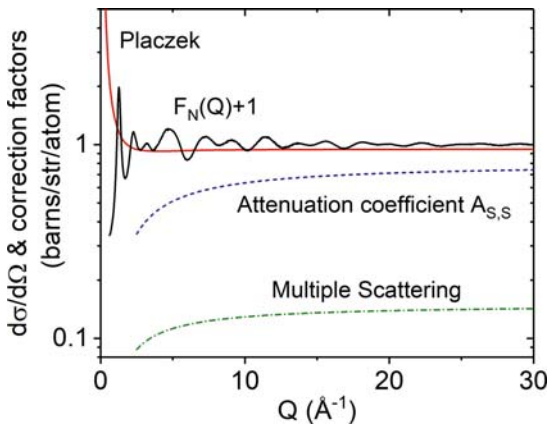

Fig. 9 The measured intensity and correction factors associated with analyzing data for CCl_4 from a time-of-flight diffractometer at $2\theta = 113.6^o$ with data taken from Ref. 30. The figure shows a dimensionless ratio between the Placzek corrected scattering cross section and the uncorrected one (red line), the corrected distinct scattering (black line), the calculated coefficient of neutrons scattered by sample and then attenuated by sample (blue dotted line), and the calculated multiple scattering in terms of secondary scattering fraction (green dash-dot line). Tao, J.; Benmore, C. J.; Worlton, T. G.; Carpenter, J. M.; Mikkelson, D.; Mikkelson, R.; Siewenie, J.; Hammonds, J.; Chatterjee, A. Time-of-Flight Neutron Total Scattering Data Analysis Implemented in the Software Suite ISAW. *Nucl. Instrum. Methods Phys. Res. A Accel. Spectrom. Detect. Assoc. Equip.* **2006**, *562*(1), 422–432.

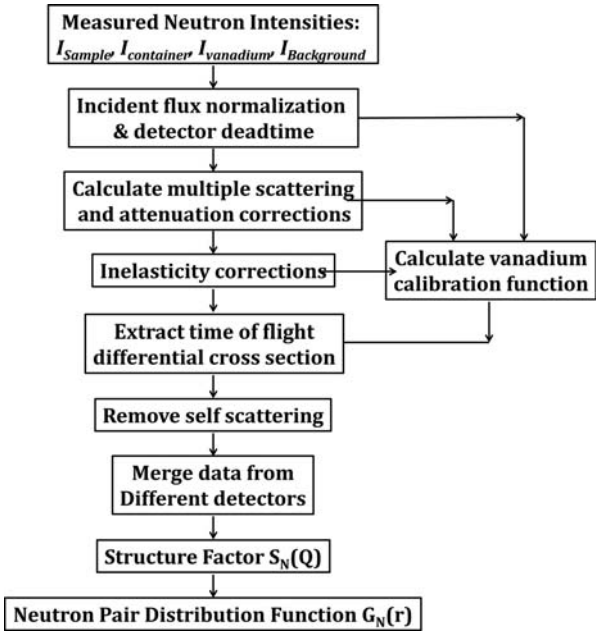

Fig. 10 Overview of neutron total scattering data analysis.[30]

The first gives $S_{obs}(\infty) = [1 + \beta(\infty)]/\alpha$ and if the dependence of β on Q is not large, then

$$\frac{\gamma}{\alpha} = -\frac{1}{2\pi^2\rho}\int_0^\infty [S_{obs}(Q) - S_{obs}(\infty)]Q^2 dQ$$

so that the ratio γ/α can be determined from the density, provided the data is of good quality.

Lastly, as the measured scattered intensity from glasses, liquids and amorphous materials results in a broad pattern compared to those from crystals, high count rates are vital in order to measure their weak diffuse features. For different neutron diffractometers the count rate for a given sample can be compared by evaluating the so-called "C-number".[29] This is particularly useful when comparing reactor and pulsed source diffractometers, because the count rate is almost independent of Q for reactor experiments but for pulsed sources the flux decays as 1/Q in the epithermal region of pulsed experiments and the detector efficiency also falls away in a similar manner. The C-number provides a measure of the scattered count rate per unit detector solid angle i.e. neutrons/$Å^{-1}$/s/cm^3V.

$$C(Q) = \Phi(E)\frac{I_{Scatt}}{I_{total}}\Omega\eta$$

where $\Phi(E)$ is the neutron flux,I_{scatt}/I_{total} represents the fraction of neutrons scattered by the sample, Ω is the detector solid angle and η is the detector efficiency.

10.14.2.4 Faber Ziman formalism

Static structure factor measurements have been routine for the study of liquid and amorphous systems since the seminal X-ray work of Warren.[4,5] In the wider context of powdered disordered crystalline or nanocrystalline materials, the technique has become known as total scattering because both the Bragg scattering as well as the underlying diffuse component are utilized in describing the structure. However, the notation of these measurements has evolved differently within the different communities and led to confusion in the literature. To clarify the situation, Keen[31] detailed the different nomenclatures which arises from the desire to emphasize different parts of the pair distribution function (albeit with some typographic errors). The emphasis mainly arises from the desire to highlight local structure in liquids, versus medium range order in crystals and not from any fundamental difference in theory. Here we will discuss the most commonly encountered forms of the element specific Faber Ziman formalism[32] used in the modern day literature. The majority of the glass, liquids and amorphous materials community use the Hannon, Howells and Soper formalism definitions,[29,31,33] whereas those from a crystalline background often use the (PDFFIT) nomenclature.[34]

Starting with the differential cross section definition, as illustrated in Fig. 11 we find

$$\frac{1}{N}\frac{d\sigma}{d\Omega} = \sum_{\alpha,\beta=1}^{n} c_\alpha c_\beta b_\alpha b_\beta \left[S_{\alpha\beta}(Q) - 1\right] + \sum_{\alpha=1}^{n} c_\alpha b_{\alpha,scatt}^2 + P = F_N(Q) + \sum_{\alpha=1}^{n} c_\alpha b_{\alpha,scatt}^2 + P$$

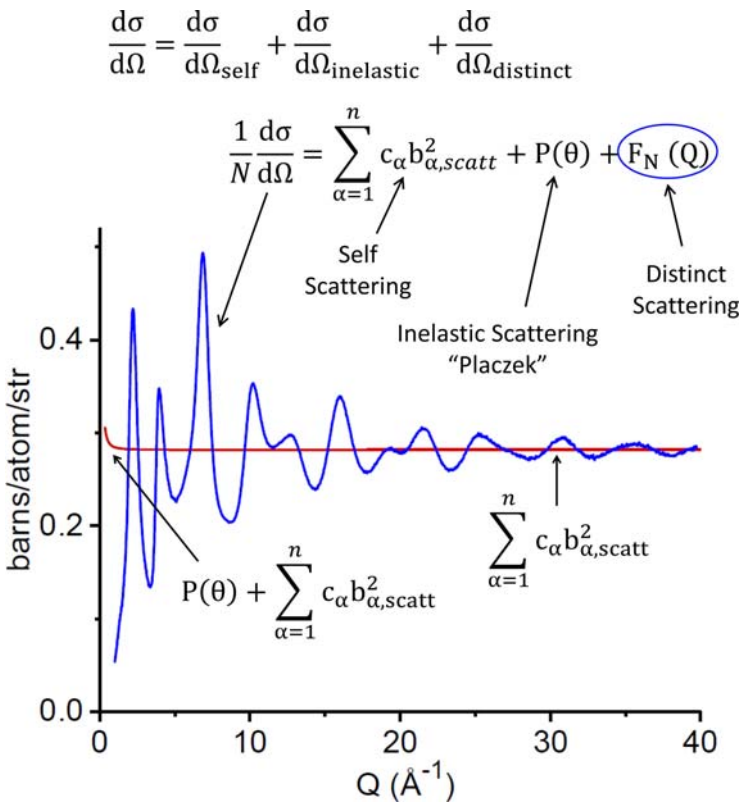

Fig. 11 A graphical representation of the components in the total neutron differential cross section for glassy SiO_2, as measured on a spallation source time-of-flight diffractometer. The instrument is designed for optimal extraction of the distinct scattering part of the measured data, $F_N(Q)$, out to high-Q values.

Where for brevity we write $b_\alpha = \langle b_\alpha \rangle$ and $b_\beta = \langle b_\beta \rangle$ corresponding to the coherent scattering lengths of α and β. P is the Placzek correction, $4\pi\sum_\alpha c_\alpha b^2_{\alpha,\,scatt}$ is the total scattering cross section and $S_{\alpha\beta}(Q)$ are the partial structure factors which are related to the corresponding partial pair distribution functions $g_{\alpha\beta}(r)$.

For isotropic scatterers, S(Q) and the pair distribution function g(r) depend solely on the magnitude of Q and r, so by integrating over azimuthal angular coordinates we obtain (see discussion in the next section for details of the inversion)

$$S_{\alpha\beta}(Q) - 1 = \rho_0 \int_0^\infty 4\pi r^2 \left[g_{\alpha\beta}(r) - 1\right] \frac{\sin Qr}{Qr} dQ$$

Where $\rho_0 = N/V$ represents the atomic number density of the material in atoms Å^{-3}, and the $g_{\alpha\beta}(r)$ are defined as

$$g_{\alpha\beta}(r) = \frac{n_{\alpha\beta}(r)}{4\pi c_\beta \rho_0 r^2 dr}$$

Where $n_{\alpha\beta}(r)$ are the number of atoms of type β that lie between distances of r and r + dr from an atom of type α at the origin and c_β is the atomic fraction of atoms of type β, see Fig. 12.

Here it is important to recognize that S(Q) is a dimensionless quantity in reciprocal space and represents a one dimensional integral which describes a 3-dimensional structure. G(r), the pair distribution function in real space, represents the probability of finding an atom at a radial distance r from an atom at the origin.

For a multicomponent system the total scattering structure factor, $F_N(Q)$, is the so-called interference or distinct scattering term,

$$F_N(Q) = \sum_{\alpha,\beta=1}^{n} c_\alpha c_\beta \langle b_\alpha \rangle \langle b_\beta \rangle \left[S_{\alpha\beta}(Q)\right]$$

which when normalized relates to the dimensionless structure factor S(Q),

$$S(Q) - 1 = \left(\sum_{\alpha=1}^{n} c_\alpha \langle b_\alpha \rangle\right)^{-2} \sum_{\alpha,\beta=1}^{n} c_\alpha c_\beta \langle b_\alpha \rangle \langle b_\beta \rangle \left[S_{\alpha\beta}(Q) - 1\right]$$

Which corresponds to the normalized total pair distribution function G(r)

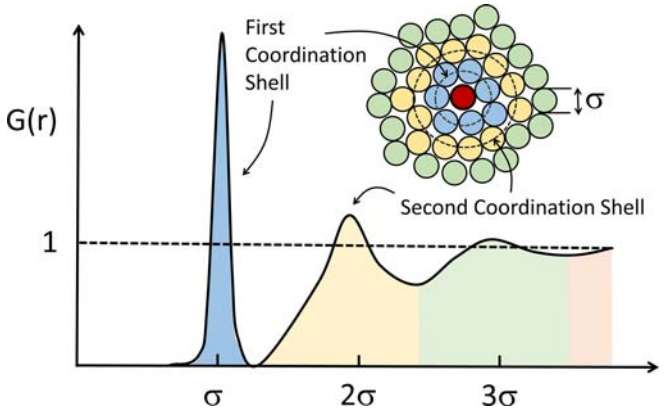

Fig. 12 The probability pair distribution function, G(r), which describes the probability of finding an atom of diameter σ surrounding another atom at the origin. Note the probability is zero below the distance of closest approach, where the atoms exhibit hard core repulsion, such that the atom positions cannot overlap.

$$G(r) - 1 = \left(\sum_{\alpha=1}^{n} c_\alpha \langle b_\alpha \rangle \right)^{-2} \sum_{\alpha,\beta=1}^{n} c_\alpha c_\beta \langle b_\alpha \rangle \langle b_\beta \rangle \left[g_{\alpha\beta}(r) - 1 \right]$$

An example of the relationship between the total neutron structure factor and the individual weighted partial structure factors for GeO_2 glass is shown in Fig. 13.

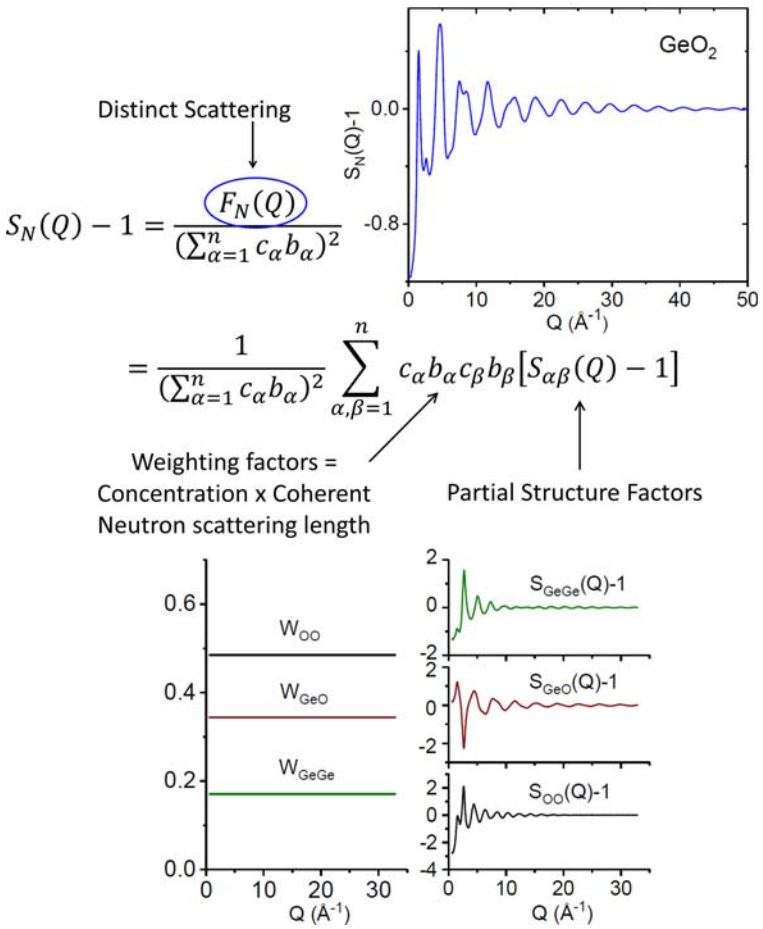

Fig. 13 A graphical representation of contributions to the distinct scattering part of the measured neutron differential cross section for glassy GeO_2.

For a two component system such as MX_2 glasses and liquids, for example SiO_2, and $GeSe_2$, there are three partial structure factors, MM, MX and XX. M representing the (often metal) positively charged cations and X representing the negatively charged anions. This requires three measurements to solve the three simultaneous equations. This can be written in matrix form as,

$$\begin{bmatrix} F_{\alpha_1\beta_1}(Q) \\ F_{\alpha_2\beta_2}(Q) \\ F_{\alpha_3\beta_3}(Q) \end{bmatrix} = \begin{bmatrix} c_\alpha^2\langle b_{\alpha_1}\rangle^2 & 2c_\alpha c_\beta\langle b_{\alpha_1}\rangle\langle b_{\beta_1}\rangle & c_\beta^2\langle b_{\alpha_1}\rangle^2 \\ c_\alpha^2\langle b_{\alpha_2}\rangle^2 & 2c_\alpha c_\beta\langle b_{\alpha_2}\rangle\langle b_{\beta_2}\rangle & c_\beta^2\langle b_{\alpha_2}\rangle^2 \\ c_\alpha^2\langle b_{\alpha_3}\rangle^2 & 2c_\alpha c_\beta\langle b_{\alpha_3}\rangle\langle b_{\beta_3}\rangle & c_\beta^2\langle b_{\alpha_3}\rangle^2 \end{bmatrix} \begin{bmatrix} S_{\alpha\alpha}(Q)-1 \\ S_{\alpha\beta}(Q)-1 \\ S_{\beta\beta}(Q)-1 \end{bmatrix}$$

if we denote the middle "weighting factor" matrix as

$$[A] = \begin{bmatrix} c_\alpha^2\langle b_{\alpha_1}\rangle^2 & 2c_\alpha c_\beta\langle b_{\alpha_1}\rangle\langle b_{\beta_1}\rangle & c_\beta^2\langle b_{\alpha_1}\rangle^2 \\ c_\alpha^2\langle b_{\alpha_2}\rangle^2 & 2c_\alpha c_\beta\langle b_{\alpha_2}\rangle\langle b_{\beta_2}\rangle & c_\beta^2\langle b_{\alpha_2}\rangle^2 \\ c_\alpha^2\langle b_{\alpha_3}\rangle^2 & 2c_\alpha c_\beta\langle b_{\alpha_3}\rangle\langle b_{\beta_3}\rangle & c_\beta^2\langle b_{\alpha_3}\rangle^2 \end{bmatrix}$$

then the equation can be reduced to

$$[F(Q)] = [A][S(Q)-1]$$

such that the matrix can be inverted to solve for the partial structure factors $S_{\alpha\beta}(Q)$

$$[S(Q)-1] = [A]^{-1}[F(Q)].$$

Similarly, in real space we can write,

$$[g(r)-1] = [A]^{-1}[G(r)].$$

10.14.2.5 Pair Distribution Functions

The structure factor S(Q) and pair distribution function G(r) are related to each other by a direct Fourier transform. However, the inversion can be problematic due to the finite extent of the data, given that the integral goes from zero to infinity, and compounded by the presence of statistical noise and systematic errors. Truncation of the data over a finite Q-range can severely limit the resolution in real space, especially at low-r. Truncating at a node after a trough (following an integer number of full periods of oscillation) can minimize some spurious oscillations in real space but in some cases a modification or window function[35,36] is used to reduce Fourier artifacts. In addition, the resolution function of the instrument may cause additional broadening, as previously discussed, arising from the incident energy spread, small path uncertainties related to the detector geometry and the finite size of the sample.[10]

The relationship between S(Q) and G(r) can be written as,

$$S(Q) = \int_0^\infty 4\pi\rho_0 r^2 G(r)\frac{\sin Qr}{Qr}dr$$

And

$$G(r) = \int_0^\infty \frac{1}{2\pi^2\rho_0}Q^2F(Q)\frac{\sin Qr}{Qr}dQ$$

Limiting values can be defined at the lowest and highest Q values. It is a clear condition at high-Q that $S(Q\rightarrow\infty)=1$. For a homogeneous monoatomic liquid system (or assuming that density fluctuations frozen in at the glass transition temperature T_g are governed only by the diffusive part of the isothermal compressibility in a quenched glass[14]), the corrected structure factor may be written as

$$S(0) = \langle b_{coh}\rangle^2\rho_0 k_B T\chi_T + \langle b_{inc}\rangle^2$$

Where χ_T is the isothermal compressibility.

Similarly in real space $G(r\rightarrow\infty)=1$ and $G(r<r_{\alpha\beta}^0)=0$, where $r_{\alpha\beta}^0$ is the closest approach between the two atoms α and β (as shown in Fig. 2). In practice, long wavelength systematic errors in Q-space are manifested as oscillatory functions in real space, which are greatest at low-r.

The coordination number $N_{\alpha\beta}$ is defined as the number of atoms of type β that lie between distances of r_1 and r_2 from an atom of type α at the origin i.e.

$$N_{\alpha\beta} = \int_{r_1}^{r_2} 4\pi r^2 c_\beta\rho_0 g_{\alpha\beta}(r)dr$$

Extraction of the coordination number from a single partial pair distribution function is straightforward. It is also possible to extract accurate coordination numbers where peaks arising from one partial are isolated. For overlapping correlations, peak fitting may be used to estimate the contributions from differing correlations.

Typically, the G(r) notation emphasizes the low-r region of distribution function, which is the most relevant to short range ordering in liquids. The Hannon-Howells-Soper[31] formalisms define the differential distribution function D(r) and total correlation function T(r) (Fig. 14) to highlight the mid-range ordering through,

$$D(r) = 4\pi\rho_0 r[G(r) - 1]$$

and

$$T(r) = 4\pi\rho_0 rG(r)$$

Both D(r) and T(r) have the benefit that, in the harmonic approximation, peaks are broadened symmetrically by thermal motions, making them useful notations for peak fitting. Wright and co-workers[31,37] used a less common definition of concentration to define the same functions in terms of composition units i.e. $i^{Wright}(Q) = (N/N_u)S(Q)$, where N_u is the number of composition units in the sample. For example, in the case of SiO_2 there are three atoms or composition units.

For crystalline and nanocrystalline materials, Proffen and Billinge[34] have redefined S(Q) to be,

$$S(Q) - 1 = \int_0^\infty 4\pi r^2 \left[\rho^{PDF}(r) - \rho_0(r)\right] \frac{\sin Qr}{Qr} dr$$

Where

$$G^{PDF}(r) = 4\pi r\left[\rho^{PDF}(r) - \rho_0(r)\right] = D(r)\left(\sum_{\alpha=1}^{n} c_\alpha \langle b_\alpha \rangle\right)^{-2}$$

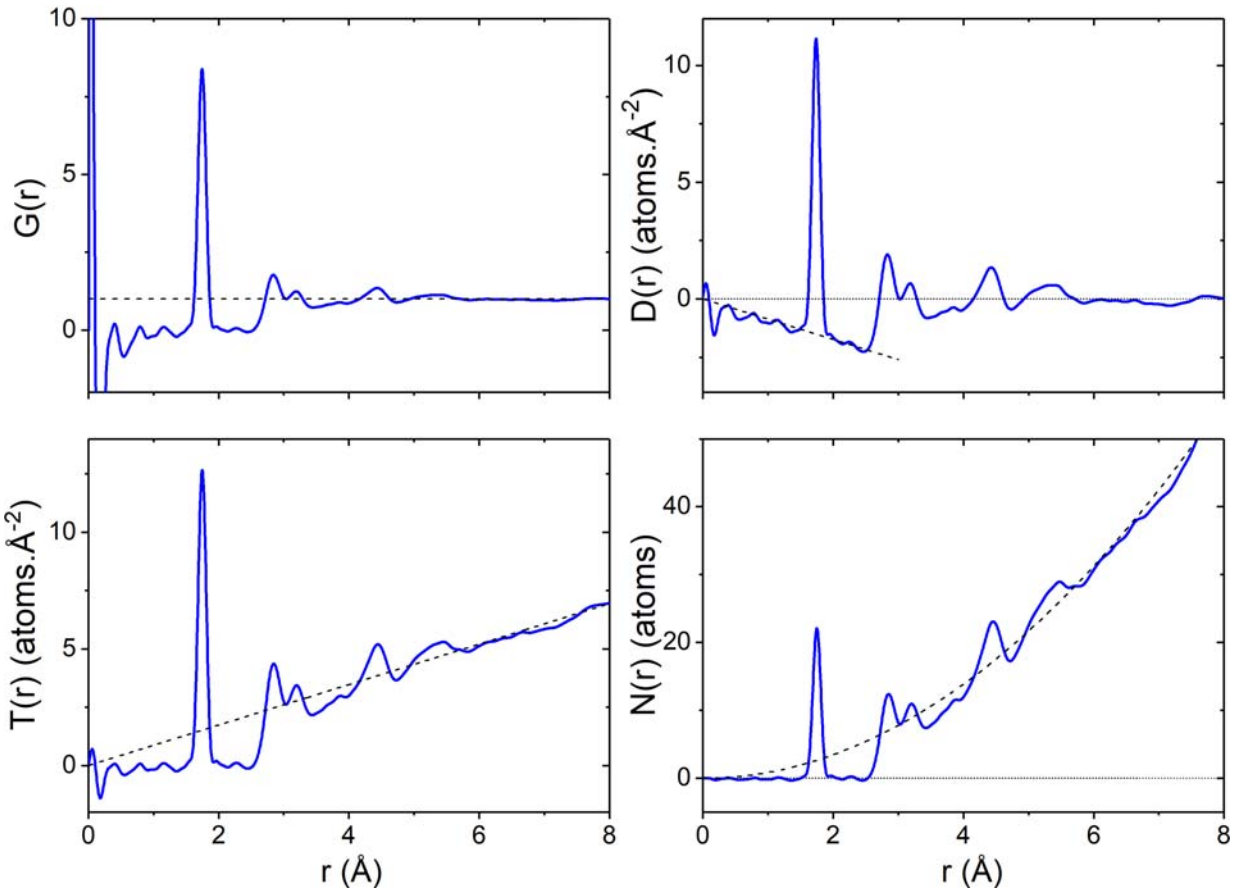

Fig. 14 Different representations of the neutron pair distribution function for GeO_2 glass; G(r) oscillating about unity at high-r and zero at low-r, T(r) oscillating about zero at low-r and $4\pi\rho r$ at high-r, D(r) oscillating about $-4\pi\rho r$ at low-r and zero at high-r, and the number of atoms, N(r).

10.14.2.6 The effect of Q_{max} on real space resolution

Here we address the fact that although the upper limit of the integral in the Fourier transform is infinity, in practice this value has to be a finite value. The high-Q limit of diffraction data can have a marked effect on the real space resolution of G(r), and generally the larger the value of Q_{max} the better (see Fig. 15). However, practically there will come a point where either the resolution becomes much greater than the width of the peaks in the pair distribution function and/or the inclusion of greater statistical noise at high Q-values will start to degrade G(r). A guide to choosing a first estimate of Q_{max} is to truncate the data at a node beyond which no underlying oscillations are visible outside of the noise in the structure factor. Performing the Fourier transform at $Q_{max} \pm \delta$ (corresponding to a node) will give an idea if subtle features are real or due to experimental errors.

$G_X(r)$ is obtained via a Sine Fourier transformation of $S_X(Q)$ using,

$$G_X(r) - 1 = \frac{1}{2\pi^2 r\rho}\int_{Qmin}^{Qmax} Q[S_X(Q) - 1]M(Q, \triangle)\sin(Qr)dQ$$

In the equation above Q_{min} and Q_{max} represent the finite range in reciprocal space over which the X-ray data are measured and ρ is the atomic (or molecular) number density in Å^3. Of these two limits, Q_{max} often has the most noticeable effect on the shorter range correlations in the Fourier transform. If $S_X(Q)$ is not truncated at a node corresponding to unity, a step function is Fourier transformed into real space and large "ringing" oscillations are superimposed on the pair distribution function masking out structural features. In addition, missing features between the measured Q_{min} and $Q = 0$ can lead to omitted long wavelength oscillations due to density fluctuations or particle sizes at high-r values in $G_X(r)$.

A Lorch,[35] or other modification function, $M(Q, \triangle)$ is often used to minimize the oscillations generated during the Fourier transform over a finite Q-range, where the parameter $\triangle$ describes the average width in real space. The Lorch modification function takes the form of a zeroth order spherical Bessel function e.g.

$$M\left(Q, \triangle\right) = \sin\left(\frac{\pi Q}{Q_{max}}\right)/\left(\frac{\pi Q}{Q_{max}}\right)$$

A severe example of its application is shown in Fig. 16. This function can be offset to start at a particular Q value and end at the maximum value of the scattering data Q_{max}. Soper and Barney[36] have proposed a revised Lorch modification function, based on a first order spherical Bessel function, to suppress spurious oscillations more rapidly with increasing r, which has the form,

$$M(Q, \triangle) = \left[\frac{3}{(Q\triangle_1)^3}\right]\left[\sin(Q\triangle_1) - Q\triangle_1\cos(Q\triangle_1)\right] \quad \text{where } \triangle_1 = \left(\frac{4.4934}{Q_{max}}\right).$$

10.14.3 X-ray diffraction

The scattering of X-rays by a free atom involves the excitation of atomic energy levels rather than the nuclear energy levels in neutron scattering. X-rays have sufficient energy to induce inelastic processes such as fluorescence and Compton scattering, see Fig. 17. Egelstaff[38] has noted that Compton scattering is frequently referred to as incoherent scattering in X-ray texts, but in practice it can exhibit coherent effects and can be considered as inelastic scattering using neutron definitions. Nonetheless, the pair distribution function is

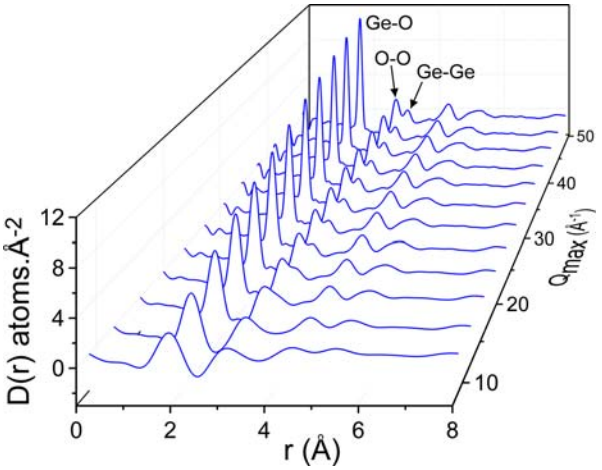

Fig. 15 The effect of truncating the structure factor S(Q) at different nodes. Reducing Q_{max} below 35 Å^{-1}, for the example GeO_2 glass data set, starts to significantly affect the resolution of the overlapping O—O and Ge—Ge peaks. For $Q_{max} < 24$ Å^{-1} these peaks become indistinguishable.

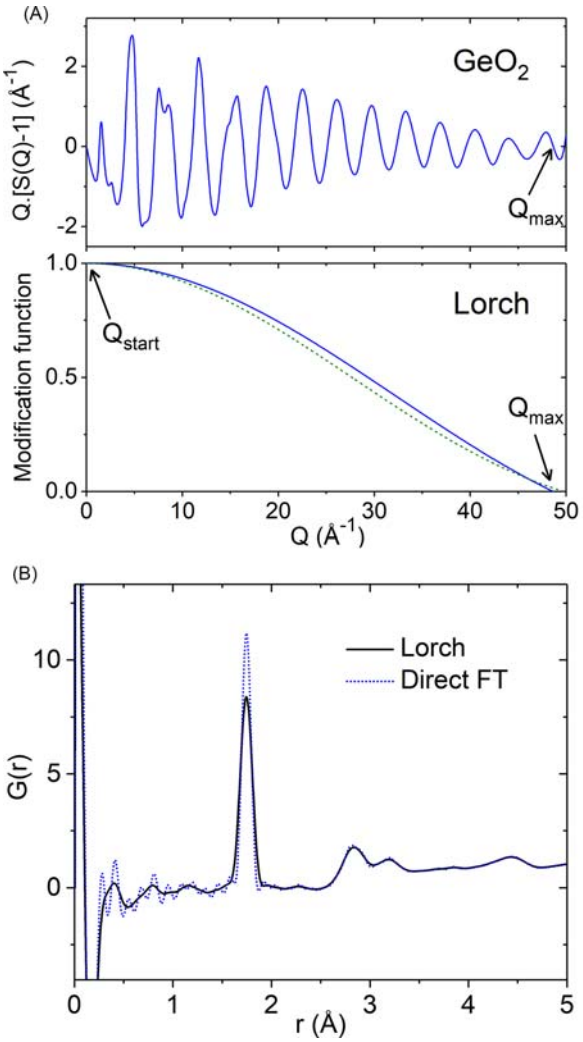

Fig. 16 (A) The structure factor of GeO_2 glass multiplied by Q to highlight the extent of the measured oscillations. An example of the original Lorch[35] modification function starting at Q_{start} and ending at the node in the data defined by Q_{max} (solid line) and a revised Lorch function proposed by Soper and Barney[36] (dashed line). (B) A direct Fourier transform of the GeO_2 data shown above convoluted with a Lorch modification function to reduce the Fourier oscillations. It also has the effect of significantly broadening the first peak in real space.

still related to the elastic differential cross section. The classical scattering by a single free electron is often referred to as Thomson scattering,[39] and for X-rays the Thomson differential cross section for unpolarized radiation is given by,

$$\frac{d\sigma_T}{d\Omega} = \left(\frac{q^2}{4\pi\varepsilon_0 mc^2}\right)^2 \frac{1+\cos^2 2\theta}{2}$$

where 2θ is the angle between the incident and scattered light, m_e is the mass of an electron, c is the speed of light and ε_0 is the permittivity. For a group of electrons clustered in a volume centered around the nucleus of an atom, many levels can be excited by X-rays, electrons can be treated as free particles to a good approximation, and the factor $1/Q^2$ arises from electron scattering due to the range of the Coulomb potential. While the angular dependent scattering amplitude is straightforward to measure in an experiment, the phase is not normally determined. However, the polarization of an X-ray photon is source dependent and can vary drastically with scattering angle.

An example of the photon scattering cross sections for $GeSe_2$ glass as a function of energy is shown in Fig. 18. In a typical X-ray scattering experiment three measurements are made; the sample in a container, empty container, and a background to determine the differential cross section $d\sigma/d\Omega$ using the intuitive formula

$$I(\theta) = a\frac{H}{P}\frac{d\sigma}{d\Omega}$$

which is measured in barns per steradian per atom/4 π, where

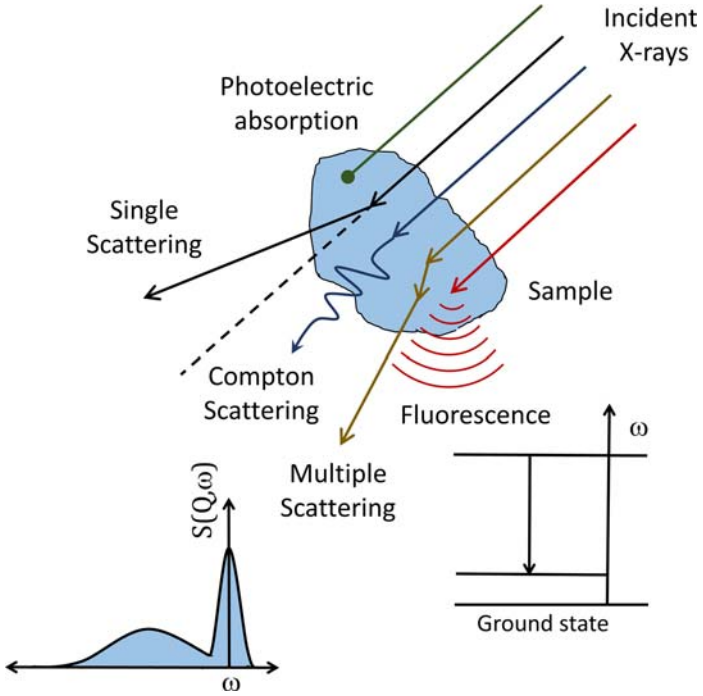

Fig. 17 X-ray scattering processes that occur during a diffraction experiment.

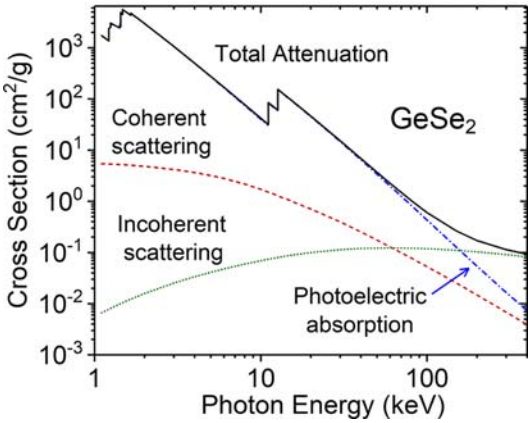

Fig. 18 Photon scattering cross-sections for $GeSe_2$ as a function of incident energy using data taken from Ref. 41. The coherent scattering (blue dash-dot line) dominates for energies below ~60 keV, above which the incoherent Compton scattering dominates (red dotted line). Saloman, E. B.; Hubbell, J. H.; Scofield, J. H. X-Ray Attenuation Cross Sections for Energies 100 EV to 100 KeV and Elements Z = 1 to Z = 92. *Atomic Data and Nuclear Data Tables*; Academic Press, 1988; pp. 1–196.

$I(2\theta)$ is the measured intensity per unit time over a solid angle $d\Omega$ at the angle 2θ
a is the diffractometer calibration factor determined by normalization to the sum of the self and Compton scattering.
H is the absorption factor and P is the polarization factor.

Since X-rays scatter from the electrons, the measured differential cross section is related to an electron-electron correlation function, rather than a nuclear one. The differential X-ray cross section itself can be split into self, Compton and distinct parts,

$$\frac{d\sigma}{d\Omega} = \frac{d\sigma}{d\Omega_{self}} + \frac{d\sigma}{d\Omega_{Compton}} + \frac{d\sigma}{d\Omega_{distinct}}$$

The sample dependent absorption corrections to the scattered X-ray intensity $I_X(Q)$ from a liquid or glass can be reliably applied using the method of Paalman and Pings, by independently measuring the sample scattering in a container I_0^{SC}, the empty container I_0^C and the background B. The corrected sample scattering, $I_X^S(\theta)$,is therefore given by,[40]

$$I_X^S(\theta) = \left(\frac{I_0^{SC} - B}{A_{S,SC}} - \frac{A_{C,SC}\left(I_0^C - B\right)}{A_{S,SC}A_{C,C}}\right)$$

After background subtractions, the measured intensity, $I_X(Q)$, needs to be scaled to the sum of the X-ray form factor (self-scattering) plus the Compton scattering $C(\theta)$ and also corrected for multiple experimental effects $M(\theta,\lambda)$. These effects include; geometry $G(\theta)$, polarization $P(\theta,\phi)$, fluorescence $Fl(\theta,\lambda)$, multiple scattering Δ and attenuation by air, filters and the detector, where ϕ represents the azimuthal angle describing the plane of the beam,

$$I_X(\theta) = a\left(\frac{I_X^S(\theta)G(\theta)}{M(\theta,\lambda)P(\theta,\phi)}\right) - C(\theta) - \triangle - Fl(\theta,\lambda)$$

For thin samples with few electrons, the multiple scattering of the sample in the container, $\triangle$, is negligible at high energies, so this can often be discarded. However, at the energies used in conventional laboratory sources both absorption and multiple scattering effects can be significant and require geometry-dependent computational algorithms to calculate their Q-dependence accurately, since the volume of the sample probed varies with scattering angle. Low energy X-ray measurements in reflection geometry may also be more sensitive to surface effects and thereby probe a different aspect of the materials structure. The incoherent Compton signal dominates the scattering at high-Q values and can be eliminated using an energy discriminating detector at high scattering angles, provided the peak is sufficiently separated from the elastic scattering peak (**Fig. 19**). However, at low-Q values there is overlap between the elastic and Compton scattering peaks, and the peak fitting of the energy spectrum at each Q-value is required for their separation.[42] For this reason, in most cases the entire energy spectrum is measured and the element-specific tabulated Compton cross sections are used for correction instead.[43,44] At high energy synchrotron sources, the Compton scattering contributions are subject to a relativistic quantum correction as described by the Klein-Nishina formula.[45] The normalization factor "a" is required to normalize $I_X(Q)$ to the number of electrons, such that $S_X(Q)$ oscillates about unity at high Q values. Once the appropriate corrections have been applied, for isotropic scatterers, by integrating over azimuthal angular coordinates this leads to the final expression,

$$I_X(Q) = \left\langle f^2(Q)\right\rangle + \left\langle f(Q)\right\rangle^2 \rho_0 \int_0^\infty 4\pi r^2[G(r) - 1]dr$$

where $f(Q)$ represents the X-ray form factors for each element.

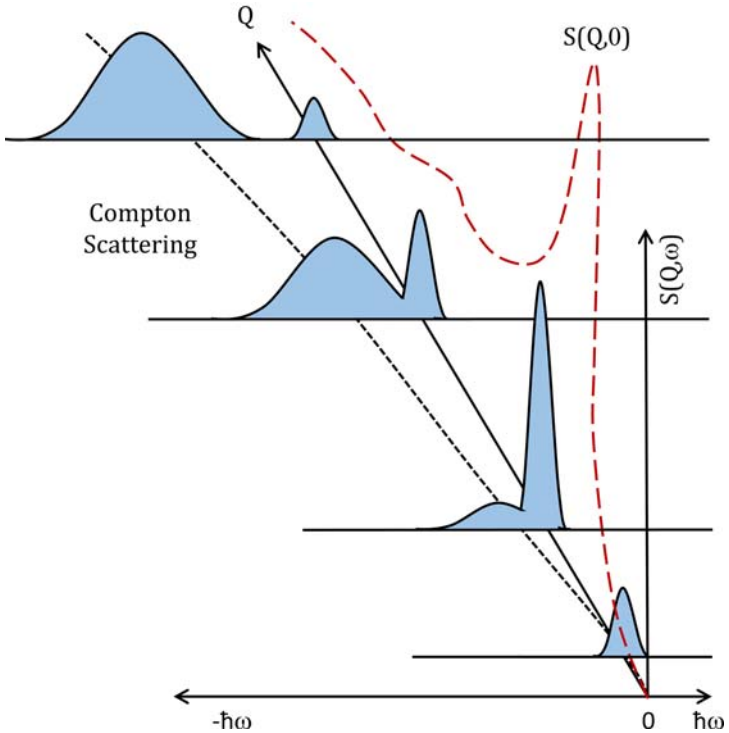

Fig. 19 The scattering law S(Q,ω) for a liquid. The elastic scattering is modulated by the X-ray scattering amplitude or form factor. At lower Q values the Compton scattering overlaps with the elastic scattering but becomes separated in energy at higher Q-values.

10.14.3.1 X-ray form factors

Photons scatter from the electron cloud surrounding an atom such that the scattering amplitude increases with atomic number Z. Atomic X-ray form factors,[43,44] denoted $f(Q)$, therefore represent an important parameter in describing the scattering in a diffraction experiment. To calculate $f(Q)$ the radial dependence of the electron density needs to be known such that

$$\sum_n \int_0^\infty 4\pi r^2 \rho_n(r) dr = Z$$

where Z is the number of electrons in the atom and $f(0) = Z$ assuming the free atom approximation.

For X-ray scattering from a spherical electron distribution at a wavelength in the vicinity of an absorption edge, it is necessary to include a dispersion correction term,[2]

$$f(Q) = f_0(Q) + \triangle f'(Q) + i \triangle f''(Q)$$

where $f_0(Q)$ is the atomic form factor, $\triangle f'(Q)$ and $i \triangle f''(Q)$ are the real and imaginary parts of the dispersion correction, where the imaginary part is associated with a small shift in phase upon scattering. The quantum mechanical treatment of these terms is given in detail elsewhere and not considered here.[2] A simplified example of the electron charge distribution calculated for a neutral Lithium atom is shown in Fig. 20.

The decrease in the form factor with increasing Q largely defines the maximum value of Q that it is obtainable with X-rays, and this is the fundamental reason why high-resolution measurements on low-Z materials are difficult. The Q-dependent behavior of normalized $f(Q)$'s for representative elements using the free atom approximation is shown in Fig. 21. For heavier elements, significant amplitude persists to larger Q-values. For hydrogen, the function rapidly falls to zero. In comparison, electron form factors in electron diffraction experiments, which can be calculated from the X-ray form factors using the Mott-Bethe formula, primarily differ only in the low-Q region.[46]

Fig. 21 shows that the majority of the high-Q scattering amplitude comes from core electrons. The non-spherical shape of the valence electron cloud in liquids or glasses with few electrons and directional bonding, such as hydrogenous or light element materials, requires the re-distribution of charge to be taken into account. This effects the shape of S(Q) at low Q-values, typically $Q \leq 1$ Å^{-1}. In the case of water, the spherical independent atom approximation form factors have been successfully corrected using a modified atomic form factor (MAFF) equation of the form,[49]

$$f_\alpha^{MAFF}(Q) = \left[1 - \frac{Z_\alpha}{f_\alpha(0)} \exp\left(-\frac{Q^2}{2\delta_\alpha^2}\right)\right] f_\alpha(Q)$$

where Z is the fractional electron charge on the α atoms and it is required that $\sum_{\alpha=1}^{n} Z_\alpha = 0$ to conserve charge. Hydrogen-related correlations represent a worst-case scenario for extracting reasonable atom-atom bond lengths and coordination numbers from X-ray PDF data because the scattering electrons reside part-way along the bond i.e. there is a high ratio of electrons involved in bonding divided by the total number of electrons.

10.14.3.2 High energy X-ray Instrumentation

Monochromatic X-ray beams generally provide the most accurate PDF data because the correction procedures are more straightforward. For laboratory X-ray tubes the diffractometer is most commonly configured in Bragg-Brentano reflection geometry (see Fig. 22)[39] and can be arranged in either of two ways. For a fixed tube the geometry is θ-2θ, whereas if the tube and detector

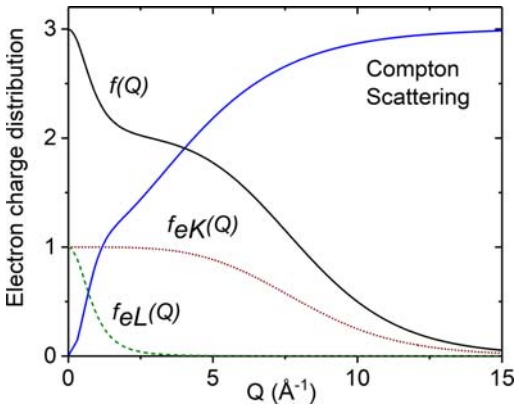

Fig. 20 Contributions to the form factor from the K and L shell electrons of a neutral Li atom, where $f(Q) = f_{eK}(Q) + f_{eL}(Q)$, compared to the Compton Scattering. The data were taken from Ref. 43. Hubbell, J. H.; Veigele, W. J.; Briggs, E. A.; Brown, R. T.; Cromer, D. T.; Howerton, R. J. Atomic Form Factors, Incoherent Scattering Functions, and Photon Scattering Cross Sections. *J. Phys. Chem. Ref. Data* **1975**, *4*(3), 471–538.

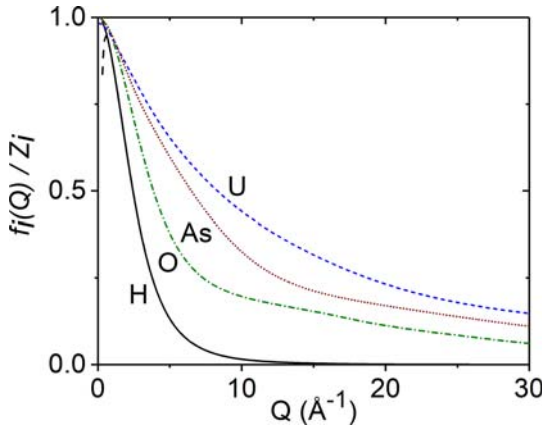

Fig. 21 The free atom form factors for the elements H, O, As and U normalized to their number of electrons Z at Q = 0, using data taken from Ref. 43. The dashed black line for H denotes the modified atomic form factor[47] obtained using the MAFF equation with $Z_\alpha = 0.5$ corresponding to the electron residing halfway along the bond and $\delta = 2.0$ obtained from fitting to the quantum mechanical calculations of Wang et al. for H_2O.[48] Hubbell, J. H.; Veigele, W. J.; Briggs, E. A.; Brown, R. T.; Cromer, D. T.; Howerton, R. J. Atomic Form Factors, Incoherent Scattering Functions, and Photon Scattering Cross Sections. *J. Phys. Chem. Ref. Data* **1975**, *4*(3), 471–538.

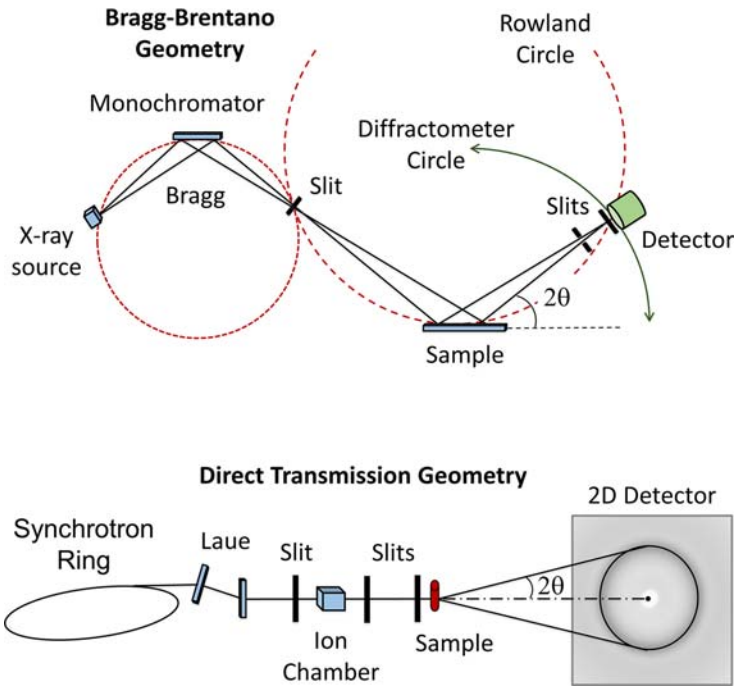

Fig. 22 Bragg-Brentano reflection geometry (top) versus high-energy transmission (direct) geometry.

move, but the sample is fixed, the geometry is referred to as θ-θ. The essential characteristics are that (i) a Mo or Ag K_α source is used to access a reasonable maximum momentum transfer range, (ii) the angle between the specimen surface and the incident X-ray beam (θ) and the angle between the incident beam and the detector slit (2θ) is maintained throughout the experiment. (iii) the source slit-to sample and sample-to-detector distance are fixed and equal defining a diffractometer circle with the sample at the center. The main issues with this type of PDF experiment arise from sample-dependent corrections due to the low energies involved.

In contrast, in a synchrotron experiment, a monochromatic beam of high energy X-rays scatters in the forward direction in transmission geometry (Fig. 22), passing through the entire sample into a detector.[11] High energy X-rays (or "hard" X-rays) at synchrotron sources typically have energies of 60–120 keV and very high fluxes. Despite the fall off in coherent scattering and increase in incoherent scattering (Fig. 18), there are many advantages to conducting PDF experiments on liquids and glasses using high energy photons, namely: (i) Much higher momentum transfers can be accessed, leading to high real space resolution at short distances in the pair distribution function. This can lead to more accurate determination of bond distances at low-r, particularly between two average bond distances which are very close together e.g. chalcogenide glasses such as $GeSe_2$. (ii) The high penetration allows

experiments to be conducted in air and the scattering is concentrated in the forward direction with minimal polarization effects. The penetration also allows for the use of a variety of bulky sample environments and a large area flat-plate detector arrangement (iii) Photo-absorption strongly depends on the atomic number of the material and is greatly reduced at higher energies, so millimeter sized samples that contain heavy elements can be studied. (iv) The radiation damage in biological samples is massively reduced. (v) The measured X-ray structure factors and pair distribution functions are directly comparable to neutron diffraction studies measured over comparable Q-ranges.

Fig. 23 illustrates the additional information obtained in a high-energy X-ray experiment at a synchrotron source compared to a lower energy laboratory X-ray tube apparatus or synchrotron experiment. Taking, for example, the high-energy X-ray beamlines at the Advanced Photon Source, these diffractometers generally operate at a fixed energy between 60 and 120 keV ($\sim$0.1–0.2 Å where $d\lambda/\lambda$ is $\sim 10^{-3}$) and have multiple pairs of horizontal and vertical collimating slits. The wavelength is calibrated using standard gamma-ray sources when using a solid state Ge point detector or by using the radial plots of crystalline LaB_6 and CeO_2 at several different sample-detector distances when using a 2D area detector.[40] For area detectors the asymmetry of the powder patterns at the longer (high resolution) distances are used to determine the perpendicular tilt of the detector panel, which is usually <1 m radian. An ion chamber measures the incident flux from the direct beam. The incident beam is typically blocked by a tungsten rod which is mounted in front of the detector. The sample is positioned on a goniometer with three-dimensional motor control. Alignment is initially performed using an optical telescope and laser beam system, and precise adjustments are made using the X-ray beam and a moveable photodiode detector, which also measures the sample transmission. For some detectors regular dark current measurements are necessary to minimize the effects of electronic drift.

There are nonetheless several pitfalls when performing high energy synchrotron experiments, which include: (i) keeping the count-rate to below $\sim$60,000 counts/s, above which detector dead time corrections become difficult for most solid state detectors or area detectors begin to saturate. (ii) The sample thickness needs to be considered carefully to balance the optimum signal versus absorption and multiple scattering effects, (iii) Careful consideration of the incident collimation is needed in order to reduce slit scattering and secondary background scattering into the detector. (iv) One of the most vital issues is beam stop alignment. Tilted beam stops can lead to asymmetric background scatter and so beam stops should be perfectly aligned prior to the experiment. If the beam stop alignment is altered during the experiment, the background may change significantly making previous measurements worthless. (v) At the current time, most high energy area detectors are integrating and do not carry out energy discrimination, thus suffering from memory effects where residual images from (previously measured) strongly scattering crystals remain as trapped excited states in the detector pixels.[40] These memory effects are usually only a few percent of the measured signal, but can ruin the measurements from a diffuse and weakly scattering glass. Care therefore needs to be taken to eliminate detector memory effects, as they decay slowly with time over hours or days, before the experiment starts, by exposing the detector to a high flat field of radiation to release the trapped excited states in the detector, thus evening out the pixels response.

10.14.3.3 Analysis of X-ray diffraction data

Here we consider the differing origins of effects that can influence the accuracy of the extracted X-ray static structure factor and the associated PDF. These effects include those related to (i) the source (polarization, energy resolution and beam size); (ii) sample and environmental effects (container, attenuation, multiple scattering, fluorescence); and (iii) detector effects (geometrical arrangements, oblique incidence, detector efficiency, flat field, electronic dark currents). Many of these have already been discussed in detail[40,53] and the order they are applied must be considered carefully (see Fig. 24), together with the removal of the background scattering (air or vacuum plus any windows) and the composition-dependent Compton scattering contribution.

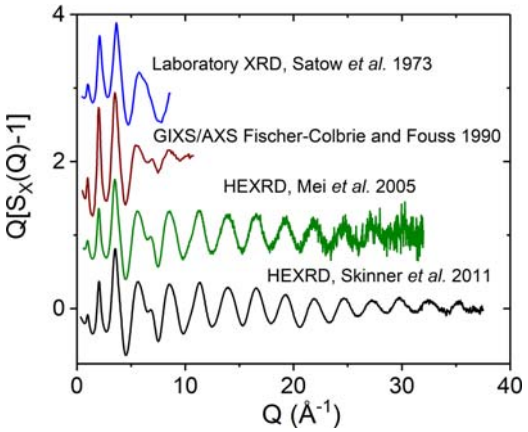

Fig. 23 X-ray structure factors, $Q[S_X(Q)-1]$, from experiments on glassy $GeSe_2$ made with laboratory Cu-K_α radiation (XRD),[50] Grazing Incidence X-ray Scattering (GIXS) for anomalous scattering measurements at a synchrotron,[51] and High Energy X-ray Diffraction (HEXRD).[40,52]

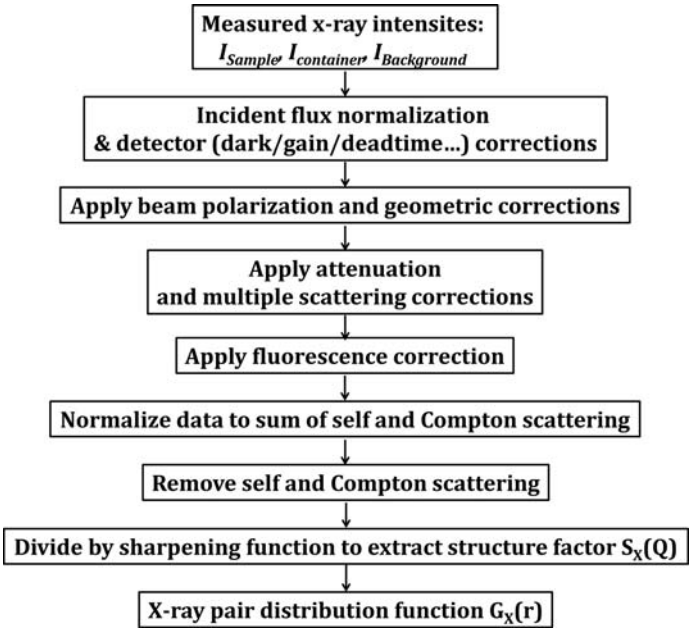

Fig. 24 Overview of total X-ray scattering data analysis.

Many of the sample-related corrections described previously, which are so prominent in neutron scattering, can be minimized to a fraction of 1% when using state-of-the-art monochromatic high energy X-ray synchrotron sources, but cumulatively they often result in overall accuracies of one or 2% (at best) in $S_X(Q)$. In addition, it has been demonstrated[40] that many of the Q-dependent source and detector-related corrections have similar shapes at high energies when using flat plate area detectors (Fig. 25) and are inter-dependent, so tracking data analysis errors is often problematic. The sample dependent corrections often become much more difficult to calculate using lower energy X-ray tube sources and consequently the overall accuracy is not as high as for synchrotron X-rays, although the detector efficiencies often improve at lower energies. The situation for energy dispersive X-ray diffraction is exacerbated, since the myriad of corrections need to be performed over a wide range of energies. However, this technique has the advantage that measurements can be made very quickly, and are very useful in mapping out large regions of pressure or temperature space, for example.

The energy resolution of an X-ray diffraction experiment is ultimately limited by the quality of the monochromator and optics, but for the study of diffuse diffraction peaks in glasses, for most powder diffractometers, this generally has a negligible effect on the quality of the data, unless performing anomalous X-ray diffraction measurements. Similarly, X-ray beam sizes of <0.5 mm, when compared to the sample-to-detector distances of ca. 500 mm, are usually well below the limit for detecting significant peak broadening. Beam polarization effects depend solely on the X-ray source. For synchrotrons the incident photons are almost completely

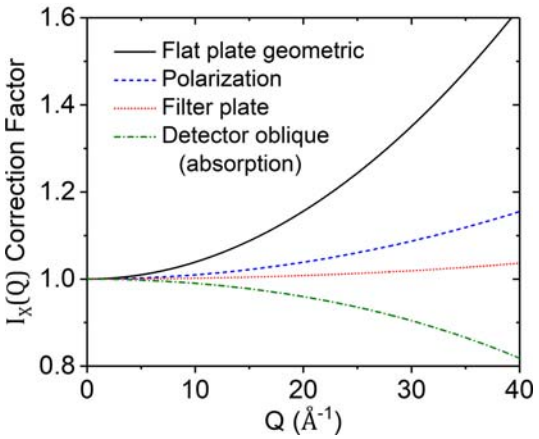

Fig. 25 Relative multiplicative correction factors for an amorphous silicon area detector at 115 keV. Calculated using equations in Ref. 40. Skinner, L. B.; Benmore, C. J.; Parise, J. B. Area Detector Corrections for High Quality Synchrotron X-Ray Structure Factor Measurements. *Nucl. Instrum. Methods Phys. Res. A Accel. Spectrom. Detect. Assoc. Equip.* **2012**, *662*(1), 61–70.

polarized, such that corrections in the vertical plane are minimal. However, a strong angular dependence occurs in the plane of scattering, falling to zero at 90° when complete linear polarization is produced. On a laboratory diffractometer, which uses unpolarized X-rays, the case is the average of these two extremes. The beam polarization can be calculated by,

$$pol(\theta) = \frac{1}{2}\left[1 + \cos^2(2\theta) - f\cos(\varphi)\sin^2(2\theta)\right]$$

Where φ is the azimuthal angle, and f is the polarization factor which is typically 0.90–0.99 for synchrotron X-rays.

The detector response to scattered radiation can vary drastically depending upon the type and details of the detection mechanism used. For energy discriminating solid state detectors, bremsstrahlung background radiation can be minimized during the experiment, but dead time effects need to be carefully considered if moderate to high intensity fluxes are used. Modern photon-counting pixel detectors have become widespread at synchrotron light sources, and as many sources plan for significant brilliance upgrades, detector dead time corrections are becoming increasingly important. Blaj[54] has described the influence of synchrotron fill patterns on photon-counting linearization methods and found an empirical formula to obtain the linearized counting rate, given by

$$N = \frac{C}{g[f(r)]}$$

Where C represents counts, g is the relative pixel gain and f(r) is the normalized photon rate.

Accurate geometrical corrections are essential in any X-ray experiment since different paths thorough absorbing filters, sample shapes and detector elements can alter the measured signal significantly. For 2D flat plate area detectors, which have been used in many of the example illustrations in this chapter, dark currents need to be regularly monitored for electronic drift throughout the experiment. Also, flat field experiments (**Fig. 26**) need to be performed to obtain a detector gain map of different pixel efficiencies within the detector paneling.[40,55] In addition, an oblique incidence correction due to vastly different path lengths of hard X-rays at the edges of area detectors are required.

With several Q-dependent corrections to the X-ray data, normalization of the measured intensity is more difficult than for neutrons, and, accurate normalization in absolute units can sometimes be problematic, although this becomes less of an issue when higher energy X-rays are used. This is because for hard X-rays the measured data tends towards the number of electrons in the system corresponding to the dominant Compton scattering contribution at high-Q. By analogy with neutron scattering, the normalization process of the corrected $I_X(Q)$ to the self plus Compton scattering is illustrated in **Fig. 27**.

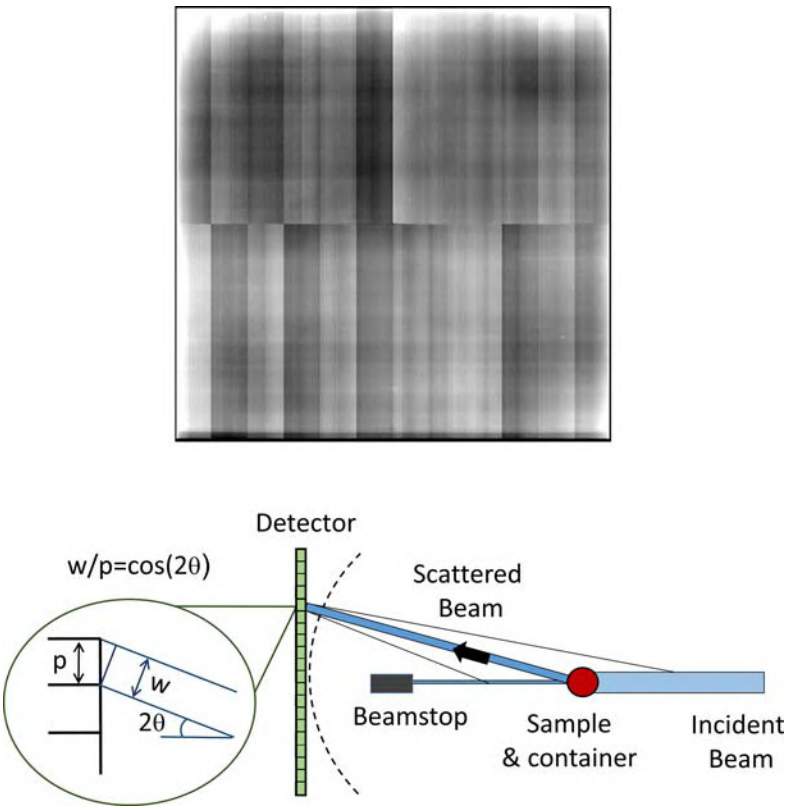

Fig. 26 The flat-field correction for panellation effects in an amorphous silicon area detector. A schematic of the geometric correction associated with flat area detectors and background air-scattering from before and after the sample position.

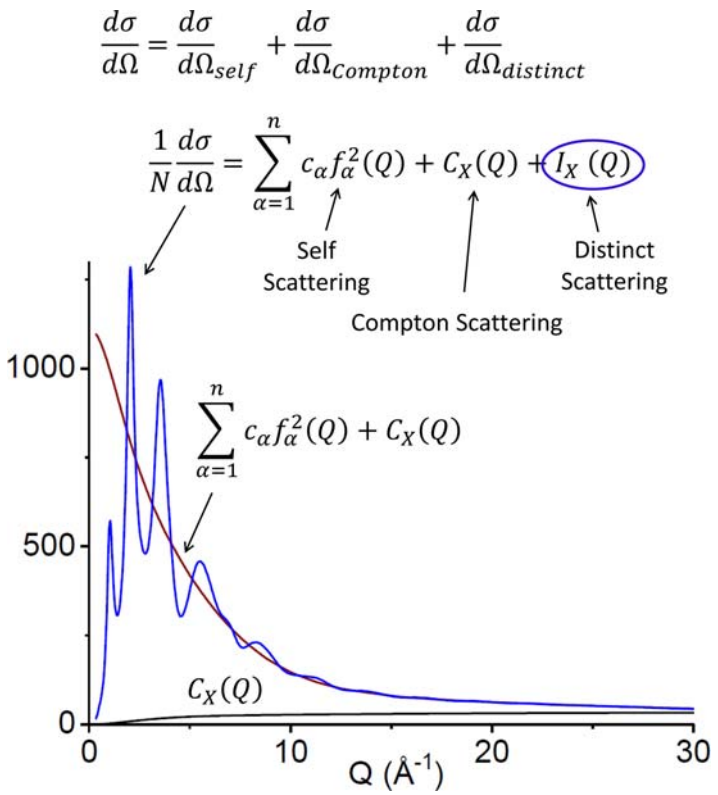

Fig. 27 A graphical representation of the components of the total X-ray differential cross section for glassy $GeSe_2$, measured on a high energy X-ray diffractometer. The purpose of the high energy X-ray instrumentation is to optimize and extract the distinct scattering part of the measured spectra, $F_X(Q)$, out to high-Q values.

For X-rays, a direct Sine Fourier transformation of the corrected and normalized intensity $I_X(Q)$ yields the electron distribution function, which contains information on the shape of the electron cloud surrounding the nucleus. In order to obtain a pseudo-atomic function it is necessary to divide by a so-called "sharpening function".[6,7] The most common formalism is to divide by the average scattering $\langle f(Q)\rangle^2$,

$$S_X(Q) - 1 = \frac{I_X(Q) - \left(\sum_{\alpha=1}^{n} \langle f_\alpha^2(Q)\rangle\right) - C(Q)}{\langle f(Q)\rangle^2}$$

where α and β represent the different atomic species in the material, and the average scattering is given by,

$$\langle f(Q)\rangle^2 = \left[\sum\nolimits_{\alpha,\beta=1}^{n} c_\alpha f_\alpha(Q)\right]^2$$

However, some recent work has suggested division by $\langle f^2(Q)\rangle$.[49] The measured $S_X(Q)$ is most commonly expressed using the Faber-Ziman formalism[32] as the sum of the X-ray weighted element specific partial structure factors $S_{ij}(Q)$ (as shown in Fig. 28 for GeO_2 glass), where

$$S_X(Q) - 1 = \left(\frac{\sum_{\alpha,\beta} c_\alpha c_\beta f_\alpha(Q) f_\beta(Q)\left[S_{\alpha\beta}(Q) - 1\right]}{\langle f(Q)\rangle^2}\right).$$

For materials where the density is well known, the Krogh-Moe/Norman technique[56,57] can be used, which employs sum rules to normalize the $S_X(Q)$ data for a given density using the low-r region, but this can become difficult for data containing a significant amount of systematic or statistical error. The approximate statistical error in S(Q) is shown in Fig. 29 for various well known liquids and glasses, determined simply by the dominant effect of the sharpening function.[40] Ultimately, there are consistency checks which can be applied to fully analyzed X-ray diffraction data to assess the effects of systematic errors, such as the isothermal compressibility limit at $Q = 0$ (which usually corresponds to that of the liquid at T_g for a glass). However, the quality of the experimental data can be most easily evaluated by the behavior of the Fourier transform at low-r, below the first real peak in the pair distribution function. If the oscillations in this region are small compared to the magnitude of the first real peak and alternate about the theoretical limit,

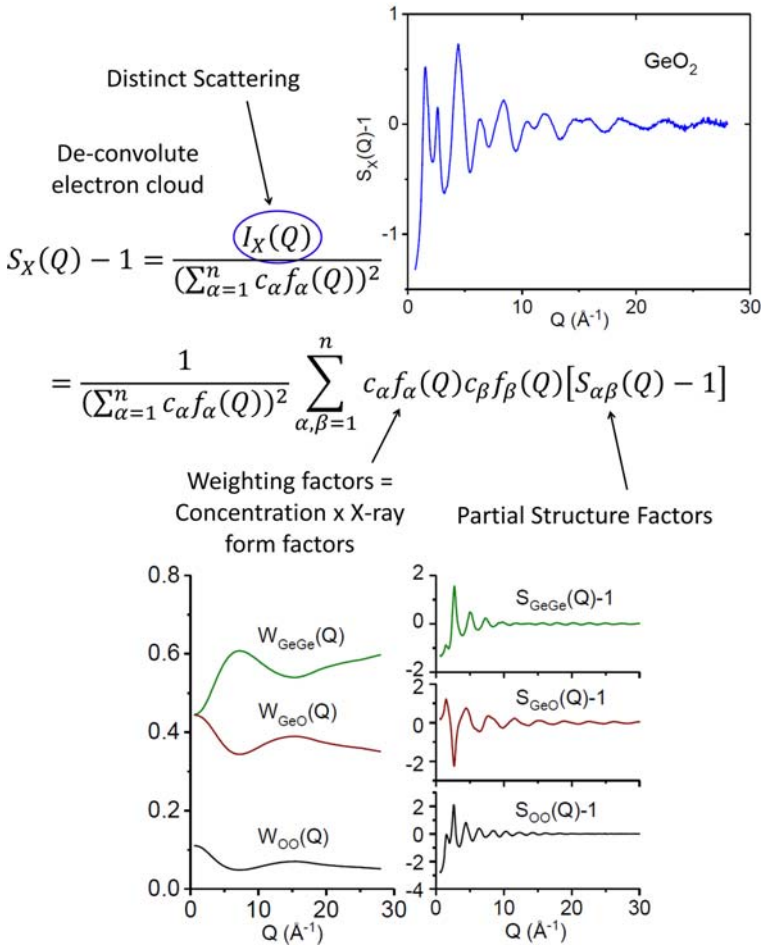

Fig. 28 A graphical representation of the breakdown of the distinct scattering part of the measured X-ray differential cross section for GeO_2 into the component partial structure factors and associated weighting factors.

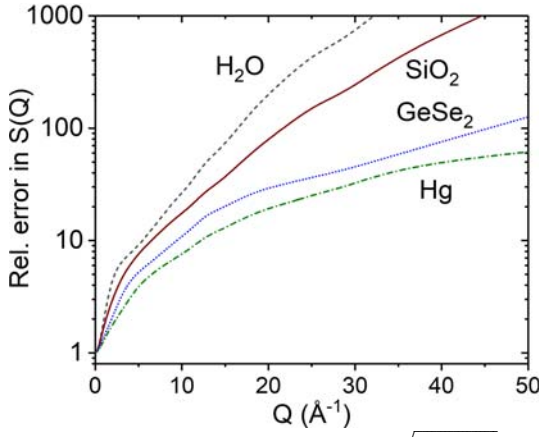

Fig. 29 The approximate error in S(Q) due to X-ray form factor decay with Q, given by $\sqrt{\langle Z\rangle^2/\langle f\rangle^2}$ using data.[43] Currently, the effective limit to Q_{max} is estimated to be associated with errors in the region of 200 (i.e. 0.5%). Hubbell, J. H.; Veigele, W. J.; Briggs, E. A.; Brown, R. T.; Cromer, D. T.; Howerton, R. J. Atomic Form Factors, Incoherent Scattering Functions, and Photon Scattering Cross Sections. *J. Phys. Chem. Ref. Data* **1975**, *4*(3), 471–538.

the data can be assessed as being of good quality. However, it has been pointed out that there are many ways to disguise poorer quality data,[58] including omitting the data in this region from the published figure.

The Fourier transformation from $S_X(Q)$ to $G_X(r)$ can sometimes appear to be a black art to those unfamiliar with the technique. Truncation effects due to data sets not ending at precisely unity or from limited Q-ranges can lead to Fourier artifacts, which take the

form of strongly varying periodic oscillations superimposed on the real space structure. As a starting point, useful information for the interpretation of $G_X(r)$ can often be obtained from a comparison with the corresponding crystalline structures of a similar density. This does not imply crystalline models are suitable for describing glass structure, as the local structural units are usually more distorted in the glass and the range of connectivity considerably broader. However, the local bonding arrangements are often similar between glass and crystal analogs. A comprehensive discussion of the validity of crystal based models (quasi-crystalline, strained-crystalline and para-crystalline) as well as cluster, molecular and layered models for amorphous materials has previously been given.[58]

Although the $G_X(r)$ function if often used to extract bond distances and local coordination numbers, the appropriate X-ray weighting factors need to be accounted for to accurately obtain this information. In many studies in the literature the Q-dependent weighting factor is replaced with a constant approximation when evaluating the coordination number. This can be done either by taking the average value over the Q-range of the experiment (which can lead to misleading coordination numbers) or more commonly the value at the $Q = 0$ limit i.e. $f(Q = 0) = Z$. Although the latter method is accurate for high-Z materials, there is still the question of knowing the effective number of electrons associated with each atomic species. The flaws in the averaging approximation are illustrated in Fig. 28, which shows a significant Q-dependence in the weighting factors for each specific partial structure factor in glassy GeO_2. For X-rays, local structural peaks can be fitted in Q-space using a Gaussian approximation to take into account the Q-dependent variation in the weighting factor[59] or the Q-dependence must be divided out in Q-space before inversion to real space. For molecules or well-defined "molecular units" we can fit individual "intra-molecular" peaks to the X-ray $S_X(Q)$ through,[7]

$$S_{intra}(Q) = \sum_{\alpha,\beta=1}^{n} \frac{Nc_\alpha c_\beta f_\alpha(Q) f_\beta(Q)}{2} \mathrm{sinc}(Qr_{\alpha\beta}) \exp(-Q^2\sigma_{\alpha\beta})$$

$$\text{where } S_X(Q) = S_{intra}(Q) + S_{inter}(Q)$$

N denotes the coordination number, $r_{\alpha\beta}$ are the atomic separations of the intra-molecular interactions, and $\sigma_{\alpha\beta}$ are the associated values for half the mean square variation, where $\sigma_{\alpha\beta} = <r_{\alpha\beta}^2>/2$. Using this method has the advantage that the area under all the Fourier termination oscillations either side of the main peak in real space are accounted for e.g. see Fig. 16. In addition, the model fit can be applied to the same momentum transfer range as the measured data, and truncated at the same Q_{max}. The disadvantage is that the real space peak is assumed to be symmetric, which could lead to errors if it is asymmetric and only partially resolved. Also, overlapping correlations from neighboring peaks need to be accounted for when fitting. Finally, we stress that the information extracted from the PDF method corresponds to average values. This is because diffraction is generally not sensitive to the speciation of elements in the same way as NMR i.e. the relative populations of species like AlO_4, AlO_5 and AlO_6, cannot be uniquely determined since their peaks completely overlap in the PDF. Rather the bond distances and coordination numbers extracted from the PDF fit will correspond to the sum of individual speciation contributions, corresponding to the average from the bulk material.

Although Rietveld refinement is unsuitable for the structure determination of liquids and glasses, it is important to point out a distinction between the total scattering (PDF) method and traditional crystal structure refinements. In crystallographic analyses, the bond length is generally taken as the distance between mean atomic positions. It has been shown that for β-cristobalite, taking the Si−O bond length to be halfway between neighboring Si−Si atoms, leads to a significantly shorter (ca. 2%) Si−O bond length than the true distance obtained from PDF.[60] Also, since the entire X-ray PDF function provides an average correlation function of the bulk structure over a range of distances, the information from several complimentary experimental techniques can, and should, be used in combination. The use of additional information for data interpretation is important because for a system of n atom types there are $n(n+1)/2$ contributing partial structure factors,[8] although low Z partial contributions can often be neglected since they are weakly weighted by X-rays. Neutron diffraction in particular is a sister technique to X-ray diffraction and the data are generally combined directly to eliminate specific partial structure factors and deconvolute overlapping peaks in G(r).

10.14.4 Complementary Techniques

Many other element-specific techniques can be used to help interpret X-ray PDF data. These include NMR spectroscopy, which has made great strides in glass science in recent decades and provides information not obtainable using the PDF technique, such as speciation and molecular conformation.[61] Two other common element specific X-ray absorption methods include; Extended X-ray Absorption Fine Structure (EXAFS)[62] and X-ray Absorption Near-Edge Structure (XANES).[63] More sophisticated X-ray difference techniques such as Anomalous X-ray Scattering (AXS) and Isomorphic Substitution (IS) are very powerful in determining partial structure factor information, but can only be applied to a limited range of elements and are often limited by the accuracy of the corrections or approximations used.[64] In any glass diffraction study, the interpretation can become clearer if a systematic study is made. Variations in composition, pressure or temperature, for example, can aid in the extraction of useful information.

10.14.4.1 Anomalous X-ray scattering

At wavelengths where specific atoms strongly absorb i.e. K, L or M absorption edges, the X-ray scattering form factor changes due to anomalous dispersion. Both the magnitude and phase of the scattering are changed. Anomalous X-ray Scattering (AXS) has long held the promise of extracting partial structure factor information, by varying the incident photon energy in the vicinity of an absorption edge of one of the constituent elements in the glass. The resulting change in X-ray form factor can readily provide differential structure factors for glass forming elements using high energy resolution photon beams, provided the data can be reliably corrected for Compton scattering and fluorescence problems.[64] However, $S_X(Q)$ cannot be obtained at $Q > 10$ Å^{-1} for elements lighter than Ga, making normalization difficult. Recently, it has been shown that high-energy AXS can extend the accessible Q-range and provide high resolution PDF data, even though the anomalous dispersion is much smaller.[65] However, the accessible absorption edges at energies >40 keV are largely limited to the rare earths and heavier elements, these edges could be applied to find modifier environments in glasses (see **Fig. 30**).

10.14.4.2 Anomalous neutron diffraction

Large variations in the bound coherent scattering lengths occur close to low energy neutron absorption resonances for a small number of nuclei.[67,68] This enables the determination of element specific structural information by carrying out diffraction experiments on the same sample at different wavelengths, provided the absorption corrections are manageable i.e. if the samples can be made thin enough or the concentration of the resonant atom is dilute. Such experiments are rare, and more difficult than their X-ray anomalous X-ray scattering counterparts. Anomalous neutron diffraction is accompanied by a phase shift in the scattered wave from the resonant nucleus. A list of potentially useful neutron resonance energies are given in **table 1**.

10.14.4.3 Isomorphic substitution

In X-ray diffraction studies the scattering contrast can also be changed by substituting two elements belonging to the same column in the periodic table with similar atomic radii.[69] Families of elements that have the same chemical behavior generally have the ability to attract a similar number of valence electrons, leading to comparable electronegativities. Indications of isomorphic characteristics can also include the substituted elements having the same crystal structures with similar ionic radii and similar melting points.[70] **Fig. 31** shows the variation in electronegativity and cation radius for elements in their oxides with different oxidation states.[71] A self-consistency check can be made to ensure the cation-oxygen peak has cancelled out in the isomorphic first order difference function discussed in the next section.

10.14.4.4 Neutron Diffraction with Isotopic Substitution

Isotopic substitution, for the study of liquids and glasses, has been in routine use by the community since its inception in 1966.[8] Of the many methods for extracting partial structure factors, neutron diffraction with isotopic substitution (NDIS) has proven to be one of the most successful. A number of "ideal" elements such as Li, Ti, Cl, Ni and N have isotopes with significantly different coherent neutron scattering lengths, enabling the isolation of partial structure factors of interest. A version of the periodic table shown in **Fig. 32** outlines the nuclides and extent of the contrast possible using NDIS. As the number of components increases, the ability

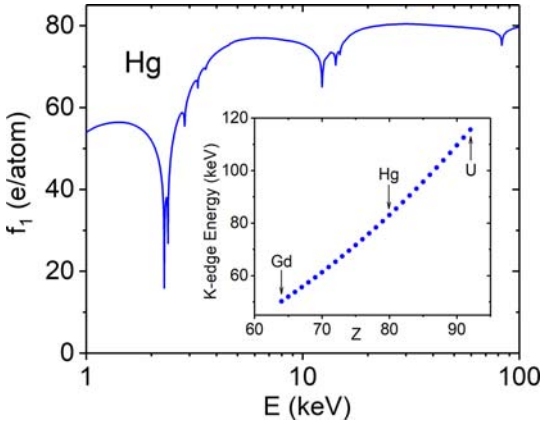

Fig. 30 The energy dependence of the X-ray form factor for mercury. The inset shows the K-edge energies for heavier elements above 50 keV.[66] Chantler, C. T. Theoretical Form Factor, Attenuation, and Scattering Tabulation for Z=1–92 from E=1–10 EV to E=0.4–1.0 MeV. *J. Phys. Chem. Ref. Data* **1995**, *24*(1), 71–643.

Table 1 Neutron resonance energies of elements below 1 eV.[29]

Element	*Resonance (eV) (isotope)*	*Element*	*Resonance (eV) (isotope)*	*Element*	*Resonance (eV) (isotope)*
Sm	0.1 (149)	Pu	0.3(239, 241)	Ra	0.5
Lu	0.14	Pa	0.4	Np	0.5
Cd	0.18	Er	0.45, 0.58	Yb	0.6
Am	0.3, 0.6	Eu	0.5	Ir	0.66

Soper, A.K.; Howells, W.S.; Hannon, A.C. *ATLAS-Analysis of Time-of-Flight Diffraction Data from Liquid and Amorphous Samples*; Rutherford Appleton Laboratory, 1989.

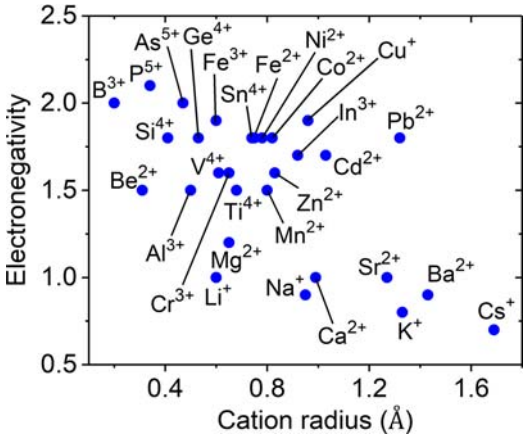

Fig. 31 The electronegativity of various cations in oxide materials as a function of cation radius.[71] Waseda, Y.; Toguri, J. M. *The Structure and Properties of Oxide Melts*; World Scientific, 1998.

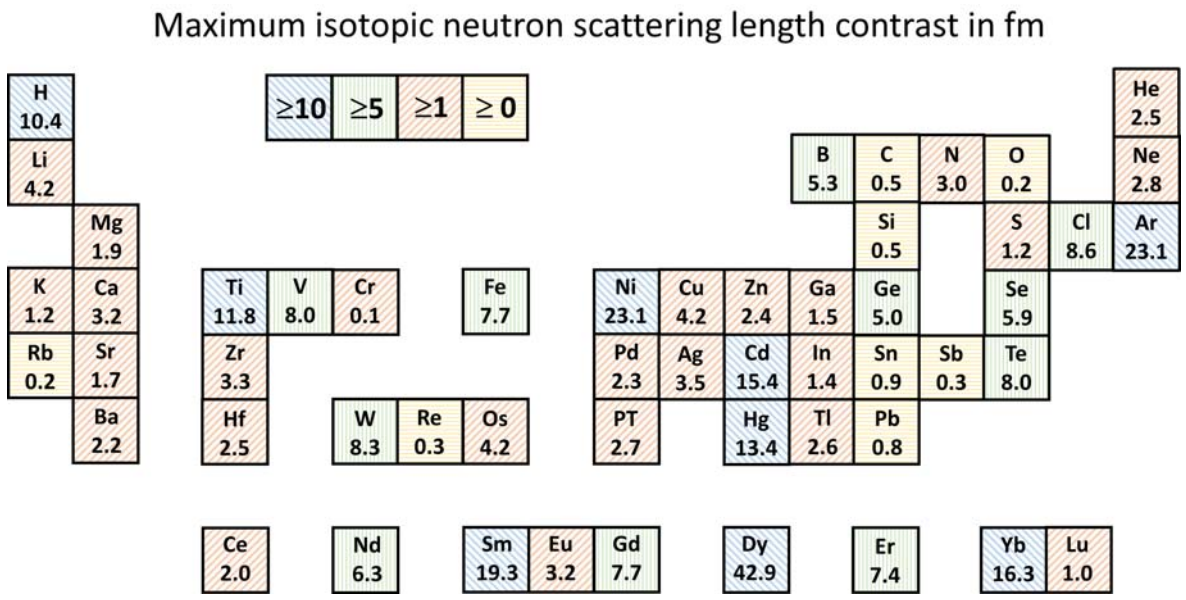

Fig. 32 Selected parts of the periodic table shown in terms of the maximum coherent neutron scattering length contrast from natural nuclides. Adapted and updated from **Table 1** by Enderby.[72] The natural abundance is not taken into consideration, but usually those with low abundance (<1%) are expensive. They are nonetheless listed here given that the large neutron fluxes now available at the latest generation spallation sources enable the use of small samples. Enderby, J. E. Isotopic Substitution and Partial Structure Factors. In *Methods in the Determination of Partial Structure Factors of Disordered Matter by Neutron and Anomalous X-ray Diffraction*, Suck, J.B.; Chieux, P.; Raoux, D.; Riekel, C., Eds.; *World Scientific*, **1993**; pp. 16–29.

to make a complete determination of all the individual partial structure functions becomes increasingly difficult. For a system containing n chemical species there are $n(n+1)/2$ measurements needed if all the partial structure factors are to be determined. Often, only a few are important to characterize the salient bonding mechanisms, or signature structural arrangements can be targeted. Applications of the NDIS technique are described for the cases of liquid water and glassy silica in the following sections.

10.14.4.4.1 The Partial Structure Factors of Water

Of all materials, water plays an essential role in our lives. Consequently, water has a central role in many disciplines, including physics, chemistry, biology and geology. Despite the molecule's relatively simple structure, the number and variety of ice phases that can be formed demonstrates the complexity of the structures that can be made. The ability to form up to four hydrogen bonds leads to its many anomalous properties. So here we choose water as the example of our 1st and 2nd order neutron diffraction isotopic substitution (NDIS) cases.

10.14.4.4.1.1 Oxygen isotope first order difference in water

As pointed out by Zeidler et al.,[28] using oxygen isotopic substitution and deuterium instead of hydrogen has the benefit of minimizing the Placzek correction. However, the coherent scattering length contrast between ^{18}O, $b_c(^{18}O) = 6.009$ fm and ^{17}O, $b_c(^{17}O) = 5.867$ fm is very small, making a first order difference difficult but none the less feasible, see **Fig. 33**. In this case we can write,

$$\begin{bmatrix} F_{H_2O(18)}(Q) \\ F_{H_2O(17)}(Q) \end{bmatrix} = \begin{bmatrix} 19.779 & -9.986 & 4.012 \\ 19.779 & -17.395 & 3.825 \end{bmatrix} \begin{bmatrix} S_{HH}(Q)-1 \\ S_{OH}(Q)-1 \\ S_{OO}(Q)-1 \end{bmatrix}$$

and solve for oxygen interactions OX, where X = O or H, by eliminating the HH partial structure factor i.e.

$$\triangle F_{OX}(Q) = F_{H_2O(17)}(Q) - F_{H_2O(18)}(Q)$$

$$= 17.395 \times [S_{OH}(Q)-1] - 0.187 \times [S_{OO}(Q)-1].$$

This leaves a first order difference function that is dominated by OH correlations with a small amount of negatively contributing OO correlations.

10.14.4.4.1.2 Hydrogen/Deuterium second order difference in water

To perform a second order difference and completely solve for all three partials, 3 measurements are necessary. The H/D substitution technique has been developed by Soper[74,75] and exploits the large coherent scattering length contrast between H, $b_c(H) = -3.739$ fm and D, $b_c(D) = 5.867$ fm. In this example we take HDO, which maximizes the contrast with $b_c(HD) = 1.466$ fm, as it represents the mid-point between the two extremes of H_2O and D_2O. It is equally valid to take the "null" scattering mixture sample where the proportions of H and D are combined in the exact ratio of 64.1%H and 35.9%D to achieve a scattering length of $b_c(H_{null}) = 0$ fm, thereby eliminating the hydrogen correlations. The drawback being the Placzek correction is still present on the data, whereas for the HDO case the Placzek correction cancels to a first approximation when extracting $S_{HH}(Q)$, since

$$S_{HH}(Q) \propto F_{H_2O}(Q) + F_{D_2O}(Q) - 2F_{HDO}(Q)$$

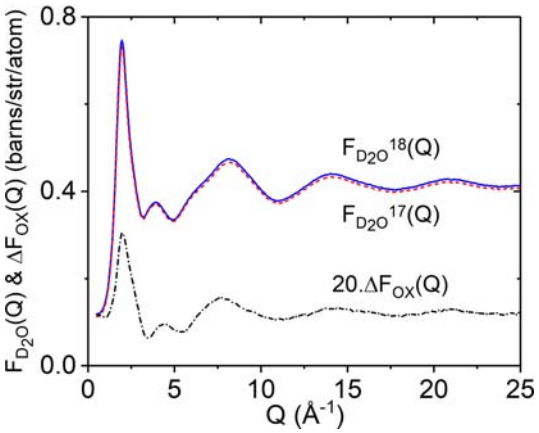

Fig. 33 The top two curves show the idealized neutron differential interference cross sections for $D_2{}^{18}O$ and $D_2{}^{17}O$ which are very similar due to the small scattering length contrast of oxygen.[28,73] Below is shown the first order difference function taken as $D_2{}^{18}O$ minus $D_2{}^{17}O$ and multiplied by a factor of $\times 20$ for clarity. The $\Delta F_{OX}(Q)$ function contains oxygen interactions only, as the HH interactions cancel in the difference.

Using the matrix notation, the three H_2O, D_2O, HDO measured structure factors are solved to find three element specific, Faber Ziman, partial structure factors. Of these OO has the least weighting and is the most ill-conditioned to extract.

$$\begin{bmatrix} F_{H_2O}(Q) \\ F_{HDO}(Q) \\ F_{D_2O}(Q) \end{bmatrix} = \begin{bmatrix} 6.213 & -9.643 & 3.742 \\ 0.955 & 3.781 & 3.742 \\ 19.779 & 17.205 & 3.742 \end{bmatrix} \begin{bmatrix} S_{HH}(Q)-1 \\ S_{OH}(Q)-1 \\ S_{OO}(Q)-1 \end{bmatrix}$$

For the HH and OH partial structure factors there are both intra- and inter-molecular contributions. The intra-molecular contributions can be separated to remove the molecular shape from the spectra as shown in Fig. 34.

10.14.4.4.2 The Partial Structure Factor analysis of silica glass

Given the different weighting factors for the neutron and X-ray diffraction measurements illustrated in Figs. 13 and 28, the techniques are most powerful when combined. Benmore et al.[76] have exploited this contrast to extract the Faber-Ziman partial structure factors of SiO_2 glass using isotopic neutron diffraction and high energy X-ray diffraction, to obtain element specific pair distribution function information. Combined X-ray and neutron measurements are particularly useful in the study of oxide liquids, chalcogenide glasses and molten salts, where there is significant contrast between the scattering of the constituent atoms. Again, using the matrix notation, the three measured structure factors $^{Nat}SiO_2$ (neutron and X-ray) and $^{29}SiO_2$ (neutron) are solved to find the three element specific Faber Ziman partial structure factors. Here $b^{NatSi} = 4.1491$ (10) fm, $b^{29Si} = 4.80$ (10) fm and $b^{O} = 5.803$ (4) fm, $I_X(Q) = F_X(Q)$ and the full Q-dependence is required to solve for SiSi, SiO and OO, since $f_\alpha(Q) \neq Z_\alpha$ for $Q > 0$.[76]

$$\begin{bmatrix} F_N^{NatSi}(Q) \\ F_N^{29Si}(Q) \\ I_X^{NatSi}(Q) \end{bmatrix} = \begin{bmatrix} 1.913 & 10.700 & 14.965 \\ 2.560 & 12.378 & 14.965 \\ 0.111 f_{Si}^2(Q) & 0.444 f_{Si}(Q) f_O(Q) & 0.444 f_O^2(Q) \end{bmatrix} \begin{bmatrix} S_{SiSi}(Q)-1 \\ S_{SiO}(Q)-1 \\ S_{OO}(Q)-1 \end{bmatrix}$$

The Si—Si, Si—O and O—O partial pair distribution functions for glassy SiO_2 are shown in Fig. 35 along with the representative "element specific" interactions that they correspond to.

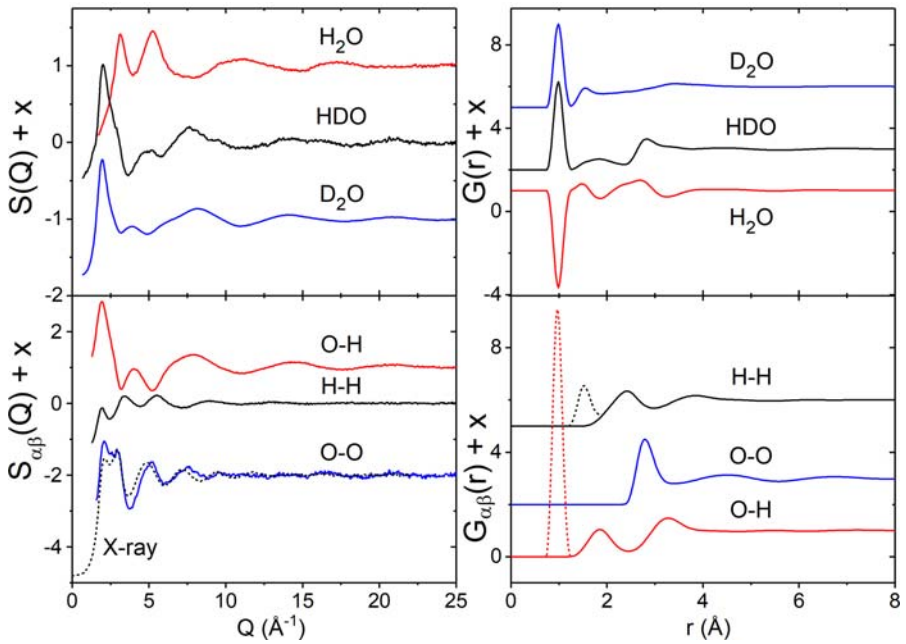

Fig. 34 Top: The total neutron structure factors for H_2O, D_2O, HDO (left) and their corresponding total pair distribution functions (right), shifted for clarity.[74] Note that the negative coherent scattering length of hydrogen results in a negative peak at the intra-molecular distance $r_{OH} \sim 1$ Å, in contrast to the positive r_{OH} peak in D_2O. Bottom: The extracted partial atom-atom structure factors O—H, H—H and O—O (left), with the O—O compared to the X-ray structure factor (dashed line).[47] The corresponding partial atom-atom pair distribution functions. The intra-molecular contributions are shown as dotted lines and the inter-molecular interactions as solid lines. Soper, A. K. Partial Structure Factors from Disordered Materials Diffraction Data: An Approach Using Empirical Potential Structure Refinement. *Phys. Rev. B Condens. Matter Mater. Phys.* **2005**, *72*(10), 104204.

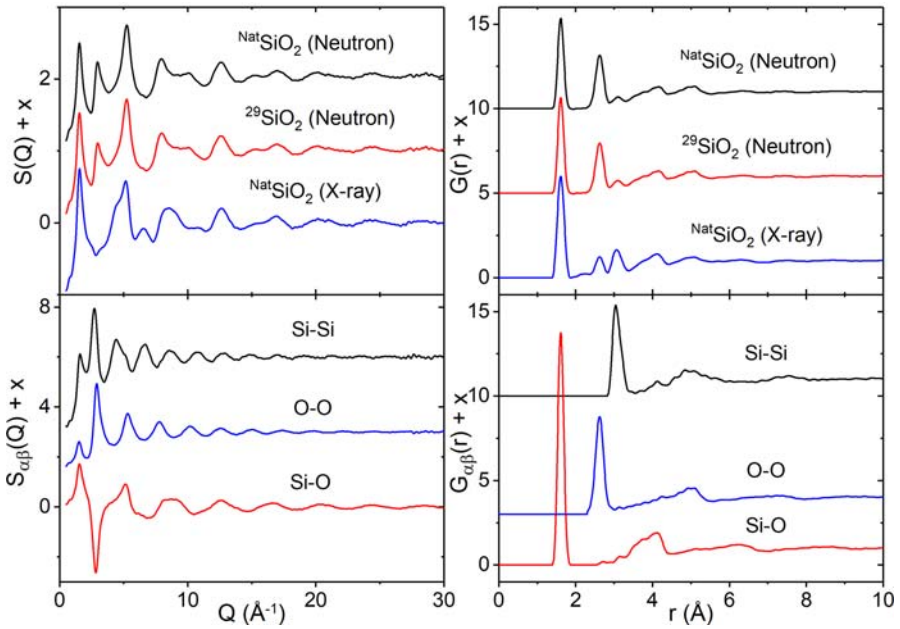

Fig. 35 Top: Idealized total neutron structure factors for natural isotopic abundance $^{Nat}SiO_2$ and $^{29}SiO_2$ glass (left), and their corresponding total pair distribution functions (right), shifted for clarity.[77] Also shown is the X-ray S(Q) for $^{Nat}SiO_2$ glass. Bottom: The extracted partial atom-atom structure factors (left) and the corresponding partial atom-atom pair distribution functions. Kohara, S.; Suzuya, K. Intermediate-Range Order in Vitreous SiO_2 and GeO_2. *J. Phys. Condens. Matter.* **2005**, *17*, S77.

10.14.5 The first sharp diffraction peak

In this section we consider the information that can be extracted from the measured S(Q) and G(r) functions for liquids and glasses. The First Sharp Diffraction Peak (FSDP) or pre-peak in the low-Q region, $Q_{FSDP} < 2$ Å^{-1}, in the X-ray or neutron S(Q) is associated with the existence of intermediate or medium range order in a liquid or glass. A FSDP at position Q_1 is associated with a structural feature with periodicity $2\pi/Q_1$, although its' origin is still controversial.[14,78,79] Medium range order has been loosely defined as covering the region ~5–20 Å.[78,79] The FSDP is often fitted with a Lorentzian or Gaussian peak in the diffraction data to accurately extract Q_1 as well as the peak width, which is related to the coherence of the structural units giving rise to it, as described by the Scherrer equation.[80] For tetrahedral network glasses, the Q_2 peak has been associated with chemical ordering within the bulk glass.[81,82] However, it is worth noting that in reciprocal space the highest frequency Fourier components decay the most rapidly, and for a glass the peaks invariably become broader with increasing-Q, until only the one arising from the sharpest real space peak remains, which is often related to the first interatomic distance in real space.

Network formation in glasses that give rise to intermediate range order is commonly associated with the clustering, alignment or layering of low coordinated polyhedra. These are typically trigonal or tetrahedral units arranged in an open packed fashion. A convenient way to compare the structures of different glassy and liquid systems with varying bond lengths and packing arrangements is to plot the quantity S(Q) versus Q_1r_1, where r_1 is the nearest neighbor distance in the corresponding radial distribution function G(r) (see Fig. 36). It has been pointed out by Price et al.[79] that most MX_2 tetrahedral glasses such as SiO_2 have a FSDP at $Q_1r_1 \sim 2.5$ and a second (principal peak) at $Q_2r_1 \sim 4.5$. Despite their name, "FSDPs" do not always occur, and are distinct from the principal peak. This is particularly important for many molten salts and metallic liquids where the principal peak is usually the lowest-Q peak in the diffraction pattern. As explained in the next section the FSDP is typically associated with orientational correlations between entities in the glass, whereas the principal peak can be linked to the repeated chemical ordering of atoms. The principal peak is also the largest feature in the Faber–Ziman partial structure factors of non-molecular liquids and glasses, whereas the pre-peak is often small or absent. We note that the principal peak in metallic glasses, generally agrees with the well-known Ehrenfest relation for a dense packing of hard spheres. Correlations associated with the peak at $Qr_1 \sim 4.5$ may also correspond to intermediate range ordering, as in the example of very high density amorphous ice.

The origin of the FSDP in vitreous archetypal SiO_2, and other tetrahedral glasses, has long been debated in the literature. Quasi-crystalline silica models have been rejected by several authors as a viable explanation of the FSDP, since no single crystalline polymorph can adequately reproduce all the features of the diffraction pattern. Similarly, layered structures often found in crystalline analogs of chalcogenide glasses have been found to provide an inappropriate description of the FSDP in vitreous SiO_2. Probably the two most widely used explanations for the FSDP in vitreous SiO_2 were those proposed by Ref. 14,79,85. Wright[14] has associated the first sharp diffraction peak in vitreous silica with "the periodicity arising from the boundaries between a succession of the cages which comprise the structure of a three-dimensional covalent network." In this scenario the cages are described as "irregular groups

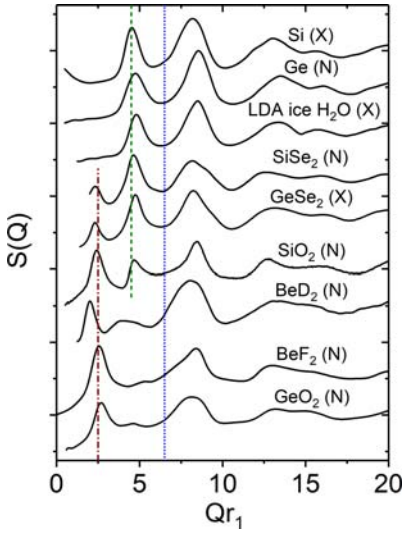

Fig. 36 A comparison of several glassy and amorphous MX_2 tetrahedral systems plotted as a function of Qr_1.[83] Price et al.[79] have argued that in MX_2 glasses the peak at $Qr_1 \sim 2.5$ can usually be associated with cages surrounding open regions in the network and ring statistics which give rise to intermediate range order. Whereas the peak at $Qr_1 \sim 4.5$ corresponds to the packing of the atoms or molecules. The peaks at $Qr_1 > 7$ correspond to details of the tetrahedral unit.[84] Wilding, M. C.; Benmore, C. J. Structure of Glasses and Melts. In *Neutron Scattering in Earth Sciences*, Wenk, H. R., Ed.; Mineralogical Society of America, 2006; pp. 275–312.

of 10–20 atoms enclosing the empty regions of the network," and three element-specific partial structure factors may be expected to contribute in the region of the FSDP for SiO_2 glass, particularly the oxygen-related partials due to the high concentration of oxygen. According to the data tabulated by Price et al.,[79] the Q_1 position at which the FSDP occurs in MX_2 or M_2X_3 oxide, halide and chalcogenide liquids and glasses, is sensitive to the competition between the form factor for the structural unit, which falls rapidly with increasing Q, and a structure factor for the positions of these units, which rises with increasing Q over the same region. This is illustrated in Fig. 37 for the case of tetrahedral SiO_2 glass, where the measured total structure factor is compared to the intra-molecular contribution representative of the SiO_2 tetrahedra, and the difference due to inter-molecular packing arrangements of the tetrahedral are predominantly at lower Q-values. Elliott's explanation of the FSDP differs from the previous authors[78,85] and suggests that "the FSDP in the structure factor of network glasses and liquids is a pre-peak in the concentration-concentration structure factor $S_{CC}(Q)$ using the Bhatia-Thornton formalism[86] (see next section) due to the chemical ordering of interstitial voids around cation-centered clusters." The void-cluster model is based on two main observations: (i) the representation of Bletry[87] that "shows the structure of tetravalent monoatomic amorphous materials can be represented approximately as a mixture of spherical atoms and holes, having the same diameter and concentration, arranged in a packing which maximizes the local chemical short range order of holes and atoms" and (ii) an FSDP in $S_{CC}(Q)$ will arise from pronounced void-cation cluster ordering in real space.

The explanations for the FSDP in SiO_2 glass may be reconciled to some extent because cages by definition create voids and vice-versa. From a more practical standpoint, suffice to say that there are varying ranges of order in liquids and glasses, with the first few

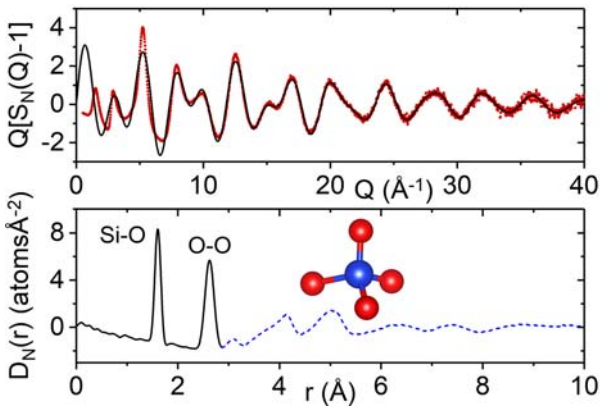

Fig. 37 Upper panel: The red circles represent the measured total structure factor for SiO_2 glass and the black line the SiO_4 tetrahedral intra-molecular structure factor $S_{intra}(Q)$, corresponding to contributions from Si—O and O—O only as depicted below in real space. Lower panel: The corresponding intra-molecular SiO_4 unit is shown as a solid line for $r < 3$ Å and intermolecular packing shown as a dashed line for $r > 3$ Å.

peaks in the PDF arising from a distribution of local polyhedra, followed by correlations between edge-, corner- (and even face-) sharing polyhedra at longer distances. These packing arrangements often lead to preferred orientations and produce a distribution of ring sizes as illustrated in Fig. 38, and atomistic modeling is required to extract these 3D structures from the PDF.

10.14.5.1 Bhatia and Thornton formalism

Bhatia and Thornton[86] defined the partial structure factors in a completely different way to the element specific Faber-Ziman formalism[32] discussed so far. The element specific FZ functions are directly related to the Bhatia-Thornton (BT) partial structure factors $S_{NN}(Q)$, $S_{CC}(Q)$ and $S_{NC}(Q)$ through,

$$S_{NN}(Q) = c_\alpha^2 S_{\alpha\alpha}(Q) + c_\beta^2 S_{\beta\beta}(Q) + 2c_\alpha c_\beta S_{\alpha\beta}(Q)$$

$$S_{NC}(Q) = c_\alpha\left(S_{\alpha\alpha}(Q) - S_{\alpha\beta}(Q)\right) - c_{\beta\beta}\left(S_{\beta\beta}(Q) - S_{\alpha\beta}(Q)\right)$$

$$S_{CC}(Q) = c_\alpha c_\beta\left(S_{\alpha\alpha}(Q) + S_{\beta\beta}(Q) - 2S_{\alpha\beta}(Q)\right)$$

In the Bhatia-Thornton formalism the number–number function, $S_{NN}(Q)$ provides a global description of the topological order within the structure and is identical to the structure factor of the monoatomic network. For two element systems, $S_{NN}(Q)$ is therefore the structure factor that would be measured if both atomic species scattered the incident neutron or X-ray beam with equal cross sections i.e. $\langle b_\alpha \rangle = \langle b_\beta \rangle$ for a binary mixture of chemical species α and β. The concentration–concentration structure factor, $S_{CC}(Q)$, describes the chemical ordering i.e. whether a given separation distance is likely to contain like or unlike atomic species, see Fig. 39. For an ideal binary mixture of atoms represented as spheres of the same diameter and occupying the same molar volume $S_{CC}(Q)$ is constant and equal to $c_\alpha c_\beta$. For a chemical mixture, where the atoms have very different diameters and directional heteropolar or

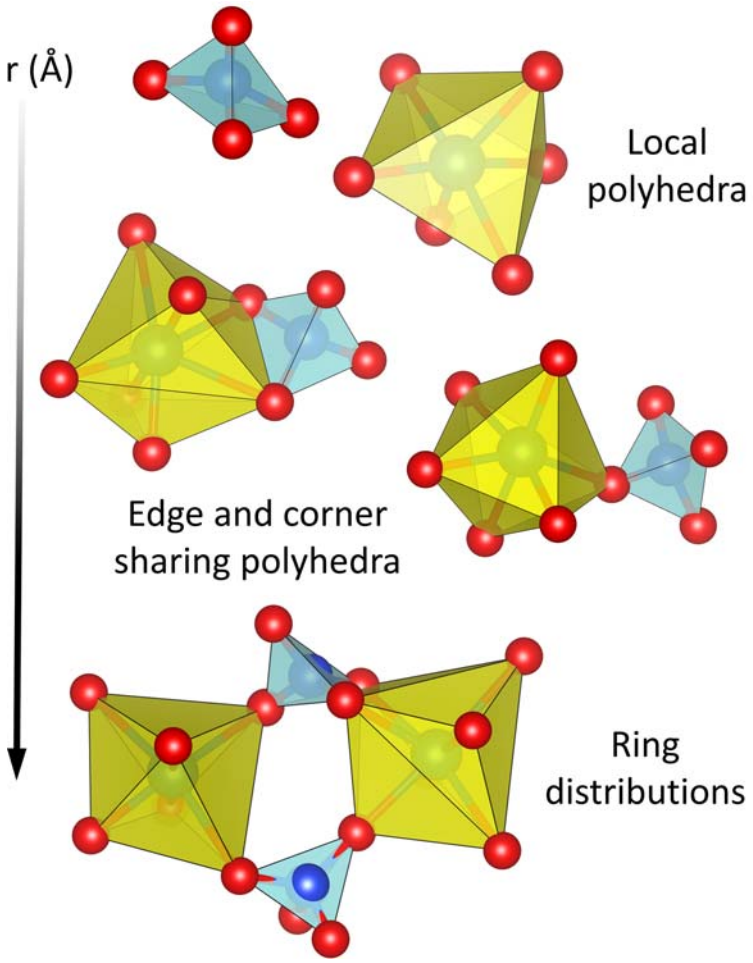

Fig. 38 An illustration of short and medium range order in liquids and glasses, moving from local polyhedral shapes, to edge and corner sharing polyhedra and onto ring distributions.

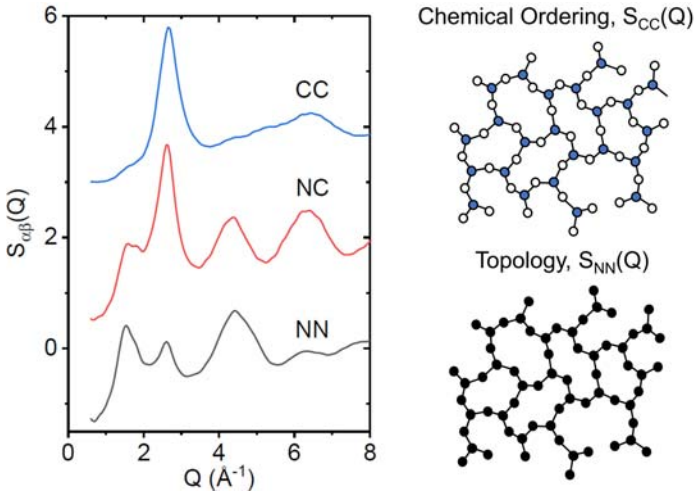

Fig. 39 The Bhatia-Thornton partial structure factors for glassy GeO_2, obtained using the data of,[77] which can be compared to the element specific Faber-Ziman structure factors shown in **Figs. 13 and 28**. An idealized glass structure is shown to differentiate between the atomic chemical ordering of atoms described by the chemical ordering $S_{CC}(Q)$ and the topology, given by $S_{NN}(Q)$.[81] Kohara, S.; Suzuya, K. Intermediate-Range Order in Vitreous SiO_2 and GeO_2. *J. Phys. Condens. Matter* **2005**, *17*, S77.

homopolar bonding it is possible to interpret the concentration-concentration variation in terms of chemical ordering. For example, if $S_{CC}(Q) < c_\alpha c_\beta$ heteropolar interactions such as α-β are preferred. Alternatively, if $S_{CC}(Q) > c_\alpha c_\beta$ homopolar interactions such as α-α or β-β are preferred. Or if $\langle b \rangle = 0$ then $S_{CC}(Q) = S(Q)$. $S_{NC}(Q)$ describes the correlation between the number and concentration fluctuations. In other words, if the scattering centers are occupied by chemical species that yield very different partial structure factors, the larger the influence of $S_{NC}(Q)$ on $S(Q)$. In contrast, for an ideal mixture $S_{NC}(Q) = 0$ and the system is completely described by $S_{NN}(Q)$. In matrix form this can be written as,

$$\begin{bmatrix} S_{NN}(Q)-1 \\ S_{NC}(Q)-1 \\ S_{CC}(Q)-1-c_\alpha c_\beta \end{bmatrix} = \begin{bmatrix} c_\alpha^2 & 2c_\alpha c_\beta & c_\beta^2 \\ c_\alpha^2 c_\beta & c_\alpha c_\beta (c_\beta - c_\alpha) & -c_\alpha c_\beta^2 \\ c_\alpha^2 c_\beta^2 & -2c_\alpha^2 c_\beta^2 & c_\alpha^2 c_\beta^2 \end{bmatrix} \begin{bmatrix} S_{\alpha\alpha}(Q)-1 \\ S_{\alpha\beta}(Q)-1 \\ S_{\beta\beta}(Q)-1 \end{bmatrix}$$

Since the weighting factors are purely concentration dependent the generic transformation for a MX_2 system is given by,

$$[A] = \frac{1}{81}\begin{bmatrix} 9 & 36 & 36 \\ 6 & 6 & -12 \\ 4 & -8 & 4 \end{bmatrix}$$

The Bhatia-Thornton formalism[86] has been successfully used to explore the extent of longer-range correlations in real space known as "extended range ordering" which relates to feint correlations persisting out to long distances e.g. r ~ 60 Å.[81] However, it should be noted that the magnitude of these oscillations show that the degree of ordering only represents a very small fraction of the bulk material.[88] For a binary ionic mixture, we can calculate the charge-charge, $S_{ZZ}(Q)$ and number-charge, $S_{NZ}(Q)$ partial structure factors through,

$$S_{ZZ}(Q) = \frac{S_{CC}(Q)}{c_\alpha c_\beta} \text{ and } S_{NZ}(Q) = \frac{Z_\alpha S_{NC}(Q)}{c_\beta}$$

where Z_α represents the charge on the chemical species α, bearing in mind that charge neutrality in the system must be preserved such that $c_\alpha Z_\alpha + c_\beta Z_\beta = 0$.

10.14.6 Atomistic modeling

One of the most important uses of the neutron and X-ray PDF techniques is that S(Q), or G(r), provide a rigorous test of structural models over a range of length scales, typically from 1 to 20 Å. In the first instance, the average number density is a simple yet strong indicator of the soundness of any structural model. Beyond that, it has been suggested a goodness of fit R-factor for χ-squared fitting of models to real space data should be used to assess the accuracy of the model.[14] With modern day computers, ball-and-stick or Percus-Yevick[89] models are rarely used. Modeling approaches fit broadly into three categories: methods that aim to fit the neutron and/or X-ray as accurately as possible using chemical and other constraints, classical molecular dynamics simulations based on an

effective inter-atomic pair-potential that can predict both structure and dynamics, and ab initio methods that take into account the materials electronic behavior based on quantum chemistry.

10.14.6.1 Reverse Monte Carlo (RMC)

Widely used methods to model PDF data using computer generated models include Reverse Monte Carlo (RMC) modeling[90,91] and Empirical Potential Structural Refinement (EPSR).[49,74] The RMC method uses random and/or crystalline starting structures and iteratively refines a three-dimensional atomistic model of the material that is consistent with PDF data sets. During the RMC process, favorable changes in structure are accepted, and unfavorable changes are allowed with some probability to avoid local minima, on the basis of a χ-squared fit to S(Q). The technique can be very powerful for modeling pairwise additive interactions, provided enough constraints are used from other sources, such as chemical knowledge, density, neutron, NMR or EXAFS data. If too few constraints are used, unrealistic chemical structures may be obtained that still fit perfectly with the X-ray diffraction pattern. In addition, RMC will often fit the data with the most disordered models possible. A 3-D RMC or EPSR model can provide access to bond angle distributions (**Fig. 40**), which represent the populations of atoms at specific angles and are often broader in the case of the more distorted local polyhedra found in glasses compared to their crystalline counterparts. Bond angle information has important implications for ring size distributions, since narrower angles could correspond to smaller ring sizes and vice-versa.

10.14.6.2 Empirical Potential Structure Refinement (EPSR)

EPSR is, in concept, similar to RMC or Rietveld refinement, targeting mainly molecular liquids, whereby it refines an arbitrary interatomic potential until the three-dimensional atomic model for the system is in agreement with the measured PDF data. Both EPSR and RMC modeling techniques can be considered as analogous to a Rietveld refinement in crystallography. Here, the EPSR model interatomic potential is perturbed in a non-physical way to reach the desired fit with diffraction data i.e. the potential itself has no meaning, but is used as a mechanism to adjust the 3-D arrangement of atoms. From the EPSR or RMC model the ring size distribution (see **Fig. 41**) can be determined using a shortest-path criteria, which describes the topology of the glass structure.[93] Good glass forming ability is often associated with a broad range of ring sizes, in contrast to crystals, which normally only have a few well-defined ring sizes. For systems made up of non-spherical molecules, orientational correlation functions can also be obtained from the EPSR model that depends on the relative arrangements of neighboring molecules. Although this information cannot be extracted from diffraction data alone, the EPSR modeling technique[74] bridges this gap by using diffraction data as a constraint on the 3-dimensional model used to extract the angular correlation functions.

10.14.6.3 Classical Molecular Dynamics (CMD)

Classical molecular dynamics (MD) can predict the neutron and X-ray PDFs by moving atoms within a simulation box according to predefined inter-atomic potentials.[94] The main advantage is that the essential underlying forces within the system can be determined and used to predict both the structure and dynamical behavior. The simplest interatomic interaction potential is the Lennard-Jones potential, which consists of two terms: a $1/r^{12}$ repulsion term that prevents two atoms from occupying the same space, and a $1/r^6$ attractive term simulating the attractive van der Waals forces between atoms. More complex, Morse, Buckingham and Coulombic potential terms are commonly used in simulating PDF data for liquids and glasses. Potential parameters such as bond-lengths and bond strengths are often fitted to appropriate crystal structures, and transferred to simulate behavior in the liquid state. The potential parameters are largely based on effective two-body (pair interactions) but can also explicitly include many body

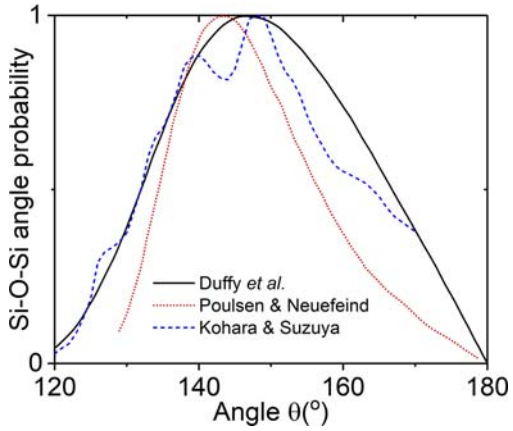

Fig. 40 The Si—O—Si bond angle distribution in SiO_2 glass obtained from ^{29}Si MAS-NMR data (solid black line),[92] a fit to high energy X-ray diffraction data (dotted red line),[13] and extracted from an RMC model constrained by neutron and X-ray data (blue dashed line).[77]

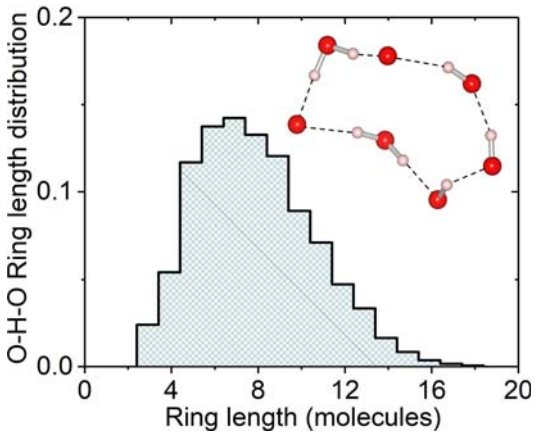

Fig. 41 The —O—H—O— ring distribution from an EPSR model of water at 293 K based on the shortest path criteria.[93] Shi, C.; Alderman, O. L. G.; Benmore, C. J. Network Topology of Deeply Supercooled Water. *Mol. Phys.* **2019**, *117*(22), 3217–3226.

terms. A main advantage of classical MD potentials is the huge computational cost saving associated with using empirically derived approximations to describing complex quantum mechanical interactions. The goal is often to describe the underlying physics of an interatomic interaction rather than obtain perfect agreement with the neutron or X-ray PDF e.g. see Fig. 42. Dynamical information such as the diffusion coefficient can also be extracted from the model. An example of the variation in fit to the PDF of several different classical MD potentials is shown in Fig. 42 for the case of liquid iron-oxide.

10.14.6.4 Density Functional Theory (DFT) and Ab initio Molecular Dynamics (AIMD)

Ab initio molecular dynamics (AIMD) simulations of liquids and glasses combine the advantages of MD and density functional theory (DFT), and generally provide more accurate models than classical MD simulations with the added cost of computational time and smaller system sizes. AIMD is based on the Schrodinger equation rather than Newton's equation that is used in classical MD. DFT calculates the electronic structure using a potential acting on the systems electrons using quantum mechanics, and addresses the difficulty of describing many-body interactions. It can predict the formation and breaking of bonds between atoms, and uses density functionals to describe the electronic interactions. In Car-Parrinello MD the core electrons are described by a pseudopotential and a plane wave basis set is used to describe the valence electrons.[96] A drawback of comparing limited size DFT atomistic models with PDF data is that artificial broadening in reciprocal space and Fourier transform artifacts arise from the restricted r_{max} due to the limited number of atoms.

10.14.6.5 Machine Learning interatomic potentials

More recently, Machine Learning algorithms that run on supercomputers are able to generate energies and forces with quantum mechanical accuracy that are comparable to DFT, but with a much lower computational cost. Gaussian approximation potentials

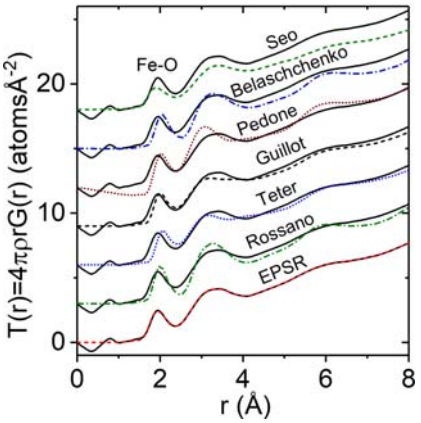

Fig. 42 The X-ray total pair distribution functions $T(r)$ for liquid FeO i.e. containing 100% Fe^{2+} or the closest available composition, modelled using classical MD simulations at a temperature of ~2000 K using various inter-atomic potentials taken from the literature, based on fig. S6a from Ref. 95. The black solid lines represent experimental data for a melt with 95% Fe^{2+}. Also shown is the EPSR fit to the data (bottom curve). Shi, C.; Alderman, O. L. G.; Tamalonis, A.; Weber, R.; You, J.; Benmore, C. J. Redox-Structure Dependence of Molten Iron Oxides. *Commun. Mater.* **2020**, *1*(1), 80.

with a smooth overlap of atomic positions descriptor have been successfully used to simulate the amorphous PDF forms of carbon and silicon.[97] Machine learnt, coarse grained bond order potentials have been used on boxes containing millions of water molecules to simulate the crystallization of supercooled water.[98] PDF data can be used to validate ML-based interatomic potentials of binary oxides.[99] Indeed, if all phases could be used in the algorithm, a "global" interatomic potential could be generated, which would represent a major breakthrough in predicting the atomic and electronic structures of liquid and glassy materials.

10.14.7 Outlook

X-ray and neutron diffraction is often the first step in characterizing glass structure, since the measurements are straightforward and generally robust. Information on both the intermediate range order (~5–20 Å) as well as the short range order (1–5 Å) can be obtained. This includes accurate bond distances, local coordination numbers and bond angles, provided overlapping correlations from neighboring peaks are adequately taken into account. Some care needs to be taken because the PDF only measures an average distribution function, making extrapolation to a three dimensional structure problematic. The main difficulty with the analysis of neutron and X-ray diffraction data from glasses is that of uniqueness, as even if the model precisely fits the measured data, other models may also fit just as well. Nonetheless, the PDF technique does, perhaps most importantly of all, provide a stringent test of any model and if the model is not consistent with the X-ray data it is wrong and needs to be modified or rejected.

The potential future for the application of neutron and X-ray diffraction to liquid and glass science lies in advances in three main areas (i) instrumentation (ii) dedicated sample environment equipment and (iii) software development and modeling.

(i) Advances in focusing optics and more intense sources will lead to smaller beam sizes, which may address the question of structural heterogeneity between the ergodic and non-ergodic regimes during glass formation. The combination of simultaneous neutron or X-ray small and wide angle scattering experiments is already possible, but it has not yet been fully utilized by the glass community to explore local structure concurrently with longer-range density fluctuations. Neutron instruments have well established energy discriminating detectors, but energy discrimination is not currently available for large X-ray detectors. Such an innovation would significantly improve the accuracy of X-ray data at high-Q values, and significantly extend the Q-range achievable to those obtainable at spallation neutron sources. Newly developed Grazing Incidence PDF has enabled the study of nanometer-sized thin films, and represents another area of research, which may extend to the study of amorphous materials at interfaces. Coherent high energy photons from X-ray free electron lasers (X-FEL) hold the promise of extracting 3-dimensional images of glass structures using the technique of ankylography,[100] although at the time of writing the limitations of this technique are still under debate.[101]

(ii) Aerodynamic levitation with laser heating[102] is already an established technique for studying the structure of both stable melts and the supercooling of liquids through the glass transition temperature.[103,104] The use of reduced gas atmospheres, or a few hundred bar pressure, could extend this technique to the study of nitride and carbide systems. Similarly, the study of liquids and glasses at high pressures using both neutrons and X-rays has been shown to be feasible,[105] but both techniques are still in their infancy and to date there are only a handful of PDF studies on phenomena such as pressure induced amorphization. The study of liquid and glassy materials under realistic operating conditions including stress/strain, high/low humidity, as well as high magnetic or electric fields also offer future avenues of exploration.

(iii) More sophisticated software is needed to *accurately* process the huge amounts of data that are now generated at high flux neutron spallation and X-ray synchrotron sources. It follows from the detailed discussions in this chapter, that the accuracy of the correction procedures should not be compromised, at the expense of bulk processing. Unfortunately, this is the current trend, and is problematic in the case of PDF measurements from liquids and glasses, where important yet subtle structural effects are commonplace. Advances in computational scattering science are also necessary to make full use of the data we already measure through combination with computer simulation. Combinations of RMC with DFT have been demonstrated to be particularly powerful[106] and provide a direct link to NMR spectroscopy and the dynamical behavior of glasses. Moreover, Machine Learned global interatomic potentials hold the promise of large scale DFT-type simulations that are guided by experimental PDF data.[99]

Acknowledgments

This research used resources of the Advanced Photon Source, a U.S. Department of Energy (DOE) Office of Science User Facility operated for the DOE Office of Science by Argonne National Laboratory under Contract No. DE-AC02-06CH11357.

References

1. Benmore, C. J. In *Modern Glass Characterization;* Affatigato, M., Ed., John Wiley & Sons, Inc.: Hoboken, NJ, 2015.
2. Fischer, H. E.; Barnes, A. C.; Salmon, P. S. Neutron and X-Ray Diffraction Studies of Liquids and Glasses. *Rep. Prog. Phys.* **2006,** *69* (1), 233–299.
3. Egelstaff, P. A. *An Introduction to the Liquid State*, Elsevier, 1994.
4. Warren, B. E. The Diffraction of X-Rays in Glass. *Phys. Rev.* **1934,** *45* (10), 657–661.

5. Warren, B. E. X-Ray Determination of the Structure of Liquids and Glass. *J. Appl. Phys.* **1937,** *8* (10), 645–654.
6. Narten, A. H.; Levy, H. A. Liquid Water: Molecular Correlation Functions from x-Ray Diffraction. *J. Chem. Phys.* **1971,** *55* (4), 2263–2269.
7. Narten, A. H. Diffraction Pattern and Structure of Noncrystalline BeF_2 and SiO_2 at 25°C. *J. Chem. Phys.* **1972,** *56* (5), 1905–1909.
8. Enderby, J. E.; North, D. M.; Egelstaff, P. A. The Partial Structure Factors of Liquid cu-Sn. *Philos. Mag.* **1966,** *14* (131), 961–970.
9. Carpenter, J. M.; Loong, C.-K. *Elements of Slow-Neutron Scattering*, Cambridge University Press, 2015.
10. Windsor, C. G. *Pulsed Neutron Scattering*, Taylor & Francis: London, 1981. Halsted Press: New York.
11. Benmore, C. J. A Review of High-Energy X-Ray Diffraction from Glasses and Liquids. *ISRN Mater. Sci.* **2012,** *2012,* 1–19.
12. Root, J. H.; Egelstaff, P. A.; Hime, A. Quantum Effects in the Structure of Water Measured by Gamma Ray Diffraction. *Chem. Phys.* **1986,** *109* (2–3), 437–453.
13. Neuefeind, J.; Poulsen, H. F. Diffraction on Disordered Materials Using "Neutron-Like" Photons. *Phys. Scr.* **1995,** *1995* (T57), 112–116.
14. Wright, A. C. Neutron Scattering from Vitreous Silica. V. The Structure of Vitreous Silica: What Have We Learned from 60 Years of Diffraction Studies? *J. Non Cryst. Solids* **1994,** *179* (C), 84–115.
15. Placzek, G. The Scattering of Neutrons by Systems of Heavy Nuclei. *Phys. Rev.* **1952,** *86* (3), 377–388.
16. Paalman, H. H.; Pings, C. J. Numerical Evaluation of X-Ray Absorption Factors for Cylindrical Samples and Annular Sample Cells. *J. Appl. Phys.* **1962,** *33* (8), 2635–2639.
17. Soper, A. K.; Egelstaff, P. A. Multiple Scattering and Attenuation of Neutrons in Concentric Cylinders: I. Isotropic First Scattering. *Nucl. Instrum. Methods* **1980,** *178* (2–3), 415–425.
18. Soper, A. K. Multiple Scattering from an Infinite Plane Slab. *Nucl. Instrum. Methods Phys. Res. A* **1983,** *212* (1–3), 337–347.
19. Copley, J. R. D. Monte Carlo Calculation of Multiple Scattering Effects in Thermal Neutron Scattering Experiments. *Comput. Phys. Commun.* **1974,** *7* (6), 289–317.
20. Blech, I. A.; Averbach, B. L. Multiple Scattering of Neutrons in Vanadium and Copper. *Phys. Rev.* **1965,** *137* (4A), A1113.
21. Vineyard, G. H. Multiple Scattering of Neutrons. *Phys. Rev.* **1954,** *96* (1), 93–98.
22. Powles, J. G. The Analysis of a Time-of-Flight Neutron Diffractometer for Amorphous Materials: The Structure of a Molecule in a Liquid. *Mol. Phys.* **1973,** *26* (6), 1325–1350.
23. Howe, M. A.; McGreevy, R. L.; Howells, W. S. The Analysis of Liquid Structure Data from Time-of-Flight Neutron Diffractometry. *J. Phys. Condens. Matter* **1989,** *1* (22), 3433–3451.
24. Bellissent-Funel, M. C.; Bosio, L.; Teixeira, J. The Inelasticity Correction for Liquid Water in Neutron Scattering. *J. Phys. Condens. Matter* **1991,** *3* (22), 4065–4074.
25. Soper, A. K. Inelasticity Corrections for Time-of-Flight and Fixed Wavelength Neutron Diffraction Experiments. *Mol. Phys.* **2009,** *107* (16), 1667–1684.
26. Montague, D. G. H/D Substitution in Neutron Diffraction. In *Hydrogen-Bonded Liquids*, Springer: Netherlands, 1991; pp 129–137.
27. Sears, V. F. Neutron Scattering Lengths and Cross Sections. *Neutron News* **1992,** *3* (3), 26–37.
28. Zeidler, A.; Salmon, P. S.; Fischer, H. E.; Neuefeind, J. C.; Simonson, J. M.; Lemmel, H.; Rauch, H.; Markland, T. E. Oxygen as a Site Specific Probe of the Structure of Water and Oxide Materials. *Phys. Rev. Lett.* **2011,** *107* (14), 145501.
29. Soper, A. K.; Howells, W. S.; Hannon, A. C. *ATLAS-Analysis of Time-of-Flight Diffraction Data from Liquid and Amorphous Samples*, Rutherford Appleton Laboratory, 1989.
30. Tao, J.; Benmore, C. J.; Worlton, T. G.; Carpenter, J. M.; Mikkelson, D.; Mikkelson, R.; Siewenie, J.; Hammonds, J.; Chatterjee, A. Time-of-Flight Neutron Total Scattering Data Analysis Implemented in the Software Suite ISAW. *Nucl. Instrum. Methods Phys. Res. A Accel. Spectrom. Detect. Assoc. Equip.* **2006,** *562* (1), 422–432.
31. Keen, D. A. A Comparison of Various Commonly Used Correlation Functions for Describing Total Scattering. *J. Appl. Cryst.* **2001,** *34* (2), 172–177.
32. Faber, T. E.; Ziman, J. M. A Theory of the Electrical Properties of Liquid Metals. *Philos. Mag.* **1965,** *11* (109), 153–173.
33. Susman, S.; Volin, K. J.; Montague, D. G.; Price, D. L. The Structure of Vitreous and Liquid $GeSe_2$: A Neutron Diffraction Study. *J. Non Cryst. Solids* **1990,** *125* (1–2), 168–180.
34. Proffen, T.; Billinge, S. J. L. PDFFIT, a Program for Full Profile Structural Refinement of the Atomic Pair Distribution Function. *J. Appl. Cryst.* **1999,** *32* (3), 572–575.
35. Lorch, E. Neutron Diffraction by Germania, Silica and Radiation-Damaged Silica Glasses. *J. Phys. C Solid State Phys.* **1969,** *2* (2), 229–237.
36. Soper, A. K.; Barney, E. R. On the Use of Modification Functions When Fourier Transforming Total Scattering Data. *J. Appl. Cryst.* **2012,** *45* (6), 1314–1317.
37. Wright, A. C. The Structure of Amorphous Solids by X-Ray and Neutron Diffraction. In *Advances in Structure Research by Diffraction Methods*, Elsevier, 1974; pp 1–84.
38. Egelstaff, P. A. Notes on the X-Ray and Neutron Scattering Nomenclature. In *Methods in the Determination of Partial Structure Factors of Disordered Matter by Neutron and Anomalous X-ray Diffraction;* Suck, J. B., Chieux, P., Raoux, D., Riekel, C., Eds., World Scientific, 1993; p 243.
39. Klug, H. P.; Alexander, L. E. *X-Ray Diffraction Procedures: For Polycrystalline and Amorphous Materials,* 2nd Ed.; 1974; p Wiley.
40. Skinner, L. B.; Benmore, C. J.; Parise, J. B. Area Detector Corrections for High Quality Synchrotron X-Ray Structure Factor Measurements. *Nucl. Instrum. Methods Phys. Res. A Accel. Spectrom. Detect. Assoc. Equip.* **2012,** *662* (1), 61–70.
41. Saloman, E. B.; Hubbell, J. H.; Scofield, J. H. X-Ray Attenuation Cross Sections for Energies 100 EV to 100 KeV and Elements $Z = 1$ to $Z = 92$. *Atomic Data and Nuclear Data Tables* **1988,** *38,* 1–196.
42. Laaziri, K.; Kycia, S.; Roorda, S.; Chicoine, M.; Robertson, J. L.; Wang, J.; Moss, S. C. High-Energy x-Ray Diffraction Study of Pure Amorphous Silicon. *Phys. Rev. B Condens. Matter Mater. Phys.* **1999,** *60* (19), 13520–13533.
43. Hubbell, J. H.; Veigele, W. J.; Briggs, E. A.; Brown, R. T.; Cromer, D. T.; Howerton, R. J. Atomic Form Factors, Incoherent Scattering Functions, and Photon Scattering Cross Sections. *J. Phys. Chem. Ref. Data Monogr.* **1975,** *4* (3), 471–538.
44. Waasmaier, D.; Kirfel, A. New Analytical Scattering-Factor Functions for Free Atoms and Ions. *Acta Crystallogr. A* **1995,** *51* (3), 416–431.
45. Klein, O.; Nishina, T. Über Die Streuung von Strahlung Durch Freie Elektronen Nach Der Neuen Relativistischen Quantendynamik von Dirac. *Z. Phys.* **1929,** *52* (11–12), 853–868.
46. Cowley, J. M.; Goodman, P.; Vainshtein, B. K.; Zvyagin, B. B.; Dorset, D. L. Electron Diffraction and Electron Microscopy in Structure Determination. In *International Tables for Crystallography,* International Union of Crystallography, 2006; pp 276–345.
47. Skinner, L. B.; Huang, C.; Schlesinger, D.; Pettersson, L. G. M.; Nilsson, A.; Benmore, C. J. Benchmark Oxygen-Oxygen Pair-Distribution Function of Ambient Water from X-Ray Diffraction Measurements with a Wide Q-Range. *J. Chem. Phys.* **2013,** *138* (7), 074506.
48. Wang, J.; Tripathi, A. N.; Smith, V. H. Chemical Binding and Electron Correlation Effects in X-Ray and High Energy Electron Scattering. *J. Chem. Phys.* **1994,** *101* (6), 4842–4854.
49. Soper, A. K. Joint Structure Refinement of X-Ray and Neutron Diffraction Data on Disordered Materials: Application to Liquid Water. *J. Phys. Condens. Matter* **2007,** *19* (33), 335206.
50. Satow, T.; Uemura, O.; Sagara, Y. Study on the Amorphous Structure of Se-$GeSe_2$ Alloys by X-Ray Diffraction. *J. Japan Inst. Metals* **1973,** *37* (12), 1348–1351.
51. Fischer-Colbrie, A.; Fuoss, P. H. X-Ray Scattering Studies of Intermediate-Range Order in Amorphous $GeSe_2$. *J. Non Cryst. Solids* **1990,** *126* (1–2), 1–34.
52. Mei, Q.; Benmore, C. J.; Hart, R. T.; Bychkov, E.; Salmon, P. S.; Martin, C. D.; Michel, F. M.; Antao, S. M.; Chupas, P. J.; Lee, P. L.; Shastri, S. D.; Parise, J. B.; Leinenweber, K.; Amin, S.; Yarger, J. L. Topological Changes in Glassy $GeSe_2$ at Pressures up to 9.3 GPa Determined by High-Energy X-Ray and Neutron Diffraction Measurements. *Phys. Rev. B Condens. Matter Mater. Phys.* **2006,** *74* (1), 014203.
53. Soper, A. K.; Barney, E. R. Extracting the Pair Distribution Function from White-Beam X-Ray Total Scattering Data. *J. Appl. Cryst.* **2011,** *44* (4), 714–726.
54. Blaj, G. Dead-Time Correction for Spectroscopic Photon-Counting Pixel Detectors. *J. Synchrotron Radiat.* **2019,** *26* (5), 1621–1630.
55. Chupas, P. J.; Chapman, K. W.; Lee, P. L. Applications of an Amorphous Silicon-Based Area Detector for High-Resolution, High-Sensitivity and Fast Time-Resolved Pair Distribution Function Measurements. *J. Appl. Cryst.* **2007,** *40* (3), 463–470.
56. Krogh-Moe, J. A Method for Converting Experimental X-Ray Intensities to an Absolute Scale. *Acta Crystallogr.* **1956,** *9* (11), 951–953.
57. Norman, N. The Fourier Transform Method for Normalizing Intensities. *Acta Crystallogr.* **1957,** *10* (5), 370–373.
58. Wright, A. C. In *Experimental Techniques of Glass Science;* Simmons, C. J., El-Bayoumi, O. H., Eds., American Ceramic Society, 1993. Chapter 8.

59. Pickup, D.; Moss, R.; Newport, R. *NXFit*: A Program for Simultaneously Fitting X-Ray and Neutron Diffraction Pair-Distribution Functions to Provide Optimized Structural Parameters. *J. Appl. Cryst.* **2014,** *47* (5), 1790–1796.
60. Dove, M. T.; Tucker, M. G.; Keen, D. A. Neutron Total Scattering Method: Simultaneous Determination of Long-Range and Short-Range Order in Disordered Materials. *Eur. J. Mineral.* **2002,** *14* (2), 331–348.
61. Youngman, R. NMR Spectroscopy in Glass Science: A Review of the Elements. *Materials* **2018,** *11* (4), 476.
62. Filipponi, A. EXAFS for Liquids. *J. Phys. Condens. Matter* **2001,** *13* (7), R23.
63. Alderman, O. L. G.; Wilding, M. C.; Tamalonis, A.; Sendelbach, S.; Heald, S. M.; Benmore, C. J.; Johnson, C. E.; Johnson, J. A.; Hah, H. Y.; Weber, J. K. R. Iron K-Edge X-Ray Absorption near-Edge Structure Spectroscopy of Aerodynamically Levitated Silicate Melts and Glasses. *Chem. Geol.* **2017,** *453,* 169–185.
64. Bienenstock, A. In *Methods in the Determination of Partial Structure Factors of Disordered Matter by Neutron and Anomalous X-Ray Diffraction;* Suck, J. B., Chieux, P., Raoux, D., Riekel, C., Eds., World Scientific Pub Co Pte Ltd., 1993; p 123.
65. Petkov, V.; Shastri, S. D. Element-Specific Structure of Materials with Intrinsic Disorder by High-Energy Resonant x-Ray Diffraction and Differential Atomic Pair-Distribution Functions: A Study of PtPd Nanosized Catalysts. *Phys. Rev. B Condens. Matter Mater. Phys.* **2010,** *81* (16), 165428.
66. Chantler, C. T. Theoretical Form Factor, Attenuation, and Scattering Tabulation for Z = 1–92 from E = 1–10 EV to E = 0.4–1.0 MeV. *J. Phys. Chem. Ref. Data Monogr.* **1995,** *24* (1), 71–643.
67. Wright, A. C.; Etherington, G.; Erwin Desa, J. A.; Sinclair, R. N. Neutron Diffraction Studies of Rare Earth Ions in Glasses. *J. Phys. Colloq.* **1982,** *43,* C9-31–C9-34.
68. Cole, J. M.; Wright, A. C.; Newport, R. J.; Sinclair, R. N.; Fischer, H. E.; Cuello, G. J.; Martin, R. A. The Structure of the Rare-Earth Phosphate Glass $(Sm_2O_3)_{0.205}(P_2O_5)_{0.795}$ Studied by Anomalous Dispersion Neutron Diffraction. *J. Phys. Condens. Matter* **2007,** *19* (5), 056002.
69. Maret, M. Isomorphous Substitution in Neutron Diffraction for the Determination of Partial Structure Factors in Glasses, Liquids and Quasicrystals. In *Methods in the Determination of Partial Structure Factors of Disordered Matter by Neutron and Anomalous X-Ray Diffraction;* Suck, J. B., Chieux, P., Raoux, D., Riekel, C., Eds.*;* 1993; pp 86–98.
70. Skinner, L. B.; Benmore, C. J.; Weber, J. K. R.; Du, J.; Neuefeind, J.; Tumber, S. K.; Parise, J. B. Low Cation Coordination in Oxide Melts. *Phys. Rev. Lett.* **2014,** *112* (15).
71. Waseda, Y.; Toguri, J. M. *The Structure and Properties of Oxide Melts*, World Scientific, 1998.
72. Enderby, J. E. Isotopic Substitution and Partial Structure Factors. In *Methods in the Determination of Partial Structure Factors of Disordered Matter by Neutron and Anomalous X-ray Diffraction;* Suck, J. B., Chieux, P., Raoux, D., Riekel, C., Eds.*;* 1993; pp 16–29.
73. Skinner, L. B.; Benmore, C. J.; Neuefeind, J. C.; Parise, J. B. The Structure of Water Around the Compressibility Minimum. *J. Chem. Phys.* **2014,** *141* (21), 214507.
74. Soper, A. K. Partial Structure Factors from Disordered Materials Diffraction Data: An Approach Using Empirical Potential Structure Refinement. *Phys. Rev. B Condens. Matter Mater. Phys.* **2005,** *72* (10), 104204.
75. Finney, J. L.; Soper, A. K. Solvent Structure and Perturbations in Solutions of Chemical and Biological Importance. *Chem. Soc. Rev.* **1994,** *23,* 1–10.
76. Mei, Q.; Benmore, C. J.; Sen, S.; Sharma, R.; Yarger, J. L. Intermediate Range Order in Vitreous Silica from a Partial Structure Factor Analysis. *Phys. Rev. B Condens. Matter Mater. Phys.* **2008,** *78* (14), 144204.
77. Kohara, S.; Suzuya, K. Intermediate-Range Order in Vitreous SiO_2 and GeO_2. *J. Phys. Condens. Matter* **2005,** *17,* S77–S86.
78. Elliott, S. R. Origin of the First Sharp Diffraction Peak in the Structure Factor of Covalent Glasses. *Phys. Rev. Lett.* **1991,** *67* (6), 711–714.
79. Price, D. L.; Moss, S. C.; Reijers, R.; Saboungi, M. L.; Susman, S. Intermediate-Range Order in Glasses and Liquids. *J. Phys. C Solid State Phys.* **1988,** *21* (32), L1069.
80. Patterson, A. L. The Scherrer Formula for X-Ray Particle Size Determination. *Phys. Rev.* **1939,** *56* (10), 978–982.
81. Salmon, P. S. Amorphous Materials: Order within Disorder. *Nat. Mater.* **2002,** 87–88.
82. Price, D. L.; Saboungi, M. L.; Barnes, A. C. Structure of Vitreous Germania. *Phys. Rev. Lett.* **1998,** *81* (15), 3207–3210.
83. Wilding, M. C.; Benmore, C. Structure of Glasses and Melts. *Rev. Mineral. Geochem.* **2006,** *63,* 275–312.
84. Benmore, C. J.; Hart, R. T.; Mei, Q.; Price, D. L.; Yarger, J.; Tulk, C. A.; Klug, D. D. Intermediate Range Chemical Ordering in Amorphous and Liquid Water, Si, and Ge. *Phys. Rev. B Condens. Matter Mater. Phys.* **2005,** *72* (13), 132201.
85. Elliott, S. R. Medium-Range Structural Order in Covalent Amorphous Solids. *Nature* **1991,** *354,* 445–452.
86. Bhatia, A. B.; Thornton, D. E. Structural Aspects of the Electrical Resistivity of Binary Alloys. *Phys. Rev. B* **1970,** *2* (8), 3004–3012.
87. Bletry, J. Sphere and Distance Models for Binary Disordered Systems. *Philos. Mag. B* **1990,** *62* (5), 455–467.
88. Wright, A. C. Longer Range Order in Single Component Network Glasses? *Phys. Chem. Glasses Eur. J. Glass Sci. Technol. B* **2008,** *49* (3), 102–117.
89. Cusack, N. *The Physics of Structurally Disordered Matter: An Introduction.* (Reprinted, Hilger: Bristol, 1988.
90. McGreevy, R. L. Reverse Monte Carlo Modelling. *J. Phys. Condens. Matter* **2001,** R877.
91. Keen, D. A.; McGreevy, R. L. Structural Modelling of Glasses Using Reverse Monte Carlo Simulation. *Nature* **1990,** *344* (6265), 423–425.
92. Duffy, M. G.; Boudreaux, D. S.; Polk, D. E. Systematic Generation of Random Networks. *J. Non Cryst. Solids* **1974,** *15* (3), 435–454.
93. Shi, C.; Alderman, O. L. G.; Benmore, C. J. Network Topology of Deeply Supercooled Water. *Mol. Phys.* **2019,** *117* (22), 3217–3226.
94. Allen, M. P.; Tildesley, D. J. *Computer Simulation of Liquids,* 2nd Ed.; Oxford University Press, 2017.
95. Shi, C.; Alderman, O. L. G.; Tamalonis, A.; Weber, R.; You, J.; Benmore, C. J. Redox-Structure Dependence of Molten Iron Oxides. *Commun. Mater.* **2020,** *1* (1), 80.
96. Sarnthein, J.; Pasquarello, A.; Car, R. Structural and Electronic Properties of Liquid and Amorphous SiO_2: An Ab Initio Molecular Dynamics Study. *Phys. Rev. Lett.* **1995,** *74* (23), 4682–4685.
97. Deringer, V. L.; Bernstein, N.; Bartók, A. P.; Cliffe, M. J.; Kerber, R. N.; Marbella, L. E.; Grey, C. P.; Elliott, S. R.; Csányi, G. Realistic Atomistic Structure of Amorphous Silicon from Machine-Learning-Driven Molecular Dynamics. *J. Phys. Chem. Lett.* **2018,** *9* (11), 2879–2885.
98. Chan, H.; Cherukara, M. J.; Narayanan, B.; Loeffler, T. D.; Benmore, C.; Gray, S. K.; Sankaranarayanan, S. K. R. S. Machine Learning Coarse Grained Models for Water. *Nat. Commun.* **2019,** *10* (1), 1–14.
99. Sivaraman, G.; Krishnamoorthy, A. N.; Baur, M.; Holm, C.; Stan, M.; Csányi, G.; Benmore, C.; Vázquez-Mayagoitia, Á. Machine-Learned Interatomic Potentials by Active Learning: Amorphous and Liquid Hafnium Dioxide. *NPJ Comput. Mater.* **2020,** *6* (1), 104.
100. Raines, K. S.; Salha, S.; Sandberg, R. L.; Jiang, H.; Rodríguez, J. A.; Fahimian, B. P.; Kapteyn, H. C.; Du, J.; Miao, J. Three-Dimensional Structure Determination from a Single View. *Nature* **2010,** *463* (7278), 214–217.
101. Wei, H. Fundamental Limits of "Ankylography" Due to Dimensional Deficiency. *Nature* **2010,** *480* (7375), E1.
102. Price, D. L. *High-Temperature Levitated Materials*, Cambridge University Press, 2010. ISBN 9780521880527.
103. Hennet, L.; Pozdnyakova, I.; Bytchkov, A.; Cristiglio, V.; Zanghi, D.; Brassamin, S.; Brun, J. F.; Leydier, M.; Price, D. L. Fast X-Ray Scattering Measurements on High Temperature Levitated Liquids. *J. Non Cryst. Solids* **2008,** *354* (47–51), 5104–5107.
104. Benmore, C. J.; Weber, J. K. R.; Wilding, M. C.; Du, J.; Parise, J. B. Temperature-Dependent Structural Heterogeneity in Calcium Silicate Liquids. *Phys. Rev. B Condens. Matter Mater. Phys.* **2010,** *82* (22), 224202.
105. Benmore, C. J.; Soignard, E.; Amin, S. A.; Guthrie, M.; Shastri, S. D.; Lee, P. L.; Yarger, J. L. Structural and Topological Changes in Silica Glass at Pressure. *Phys. Rev. B Condens. Matter Mater. Phys.* **2010,** *81*, 054105.
106. Kohara, S.; Akola, J.; Morita, H.; Suzuya, K.; Weber, J. K. R.; Wilding, M. C.; Benmore, C. J. Relationship between Topological Order and Glass Forming Ability in Densely Packed Enstatite and Forsterite Composition Glasses. *Proc. Natl. Acad. Sci. U. S. A.* **2011,** *108* (36), 14780–14785.

10.15 An overview of platon/pluton crystal structure validation

Anthony L. Spek, Utrecht University, Utrecht, The Netherlands

© 2023 Elsevier Ltd. All rights reserved.

10.15.1	**Introduction**	**426**
10.15.2	**Crystal structure determination**	**427**
10.15.2.1	Data collection and data reduction	427
10.15.2.2	Solution of the phase problem	427
10.15.2.3	Structure refinement	427
10.15.2.4	Analysis of the results, illustrations and validation	428
10.15.3	**The programPLATON**	**428**
10.15.3.1	PLATON tools and functions	428
10.15.3.1.1	CALC ALL	429
10.15.3.1.2	PLUTON	429
10.15.3.1.3	ORTEP	430
10.15.3.1.4	CONTOUR	430
10.15.3.1.5	Simulated powder pattern	430
10.15.3.1.6	LEPAGE, DELRED and ADDSYM	430
10.15.3.1.7	CALC SOLV	434
10.15.3.1.8	SQUEEZE	434
10.15.3.1.9	TWINROTMAT	435
10.15.3.1.10	ASYM-VIEW	435
10.15.3.1.11	BIJVOET-PAIR	436
10.15.4	**Crystal structure validation**	**437**
10.15.4.1	The PLATON/checkCIF report	438
10.15.4.1.1	CIF-validation	439
10.15.4.1.2	FCF-validation	439
10.15.4.2	A PLATON/checkCIF report example	439
10.15.4.3	Some common validation issues	443
10.15.4.3.1	Reflection dataset completeness	443
10.15.4.3.2	Negative or large K values	443
10.15.4.3.3	Residual density peaks	443
10.15.4.3.4	Hydrogen atoms	443
10.15.5	**Implementation and availability**	**443**
10.15.6	**Concluding remarks**	**444**
References		**444**

Abstract

The number of new crystal structure reports submitted to the International Union of Crystallography (IUCr) journals started to explode in the early 1990s. This became a challenge for the journals and their refereeing process and similarly for the archival and validation of the numerical results in databases such as the Cambridge Structural Database (CSD). There were various reasons for this. A limiting factor, the slow X-ray data collection with point detectors, was resolved with the introduction of 2D detectors that changed the data collection time and effort from weeks to days or even hours. More recently, the use of synchrotron X-ray facilities has speeded up data collections further, with the high intensity X-ray sources allowing for complete data collections on large, complex molecules to be carried out in minutes. Easy to use software to address a longtime limitation, known as the *phase-problem*, had become widely available as was the access to local computing power. A growing number of structure determinations started to be carried out by non-specialists, mainly in support of their chemical research rather than out of pure crystallographic interest by experts. Structure validation and the handling of the numerical data, traditionally (re)typed from the manuscript, were now the bottleneck for publication. As a first step to automate that process, the CIF standard was introduced in 1991 to facilitate electronic data exchange and archival. CIF also opened the way to automated validation with a new utility named checkCIF. That tool was pioneered by the IUCr journals and is now part of their refereeing and publication process. Its initial goal was to check a structure report for completeness of information, consistency of the supplied data and the quality of the analysis. That effort was soon extended by adding more involved checks based on tools and facilities, such as ADDSYM and VOID, available in the program PLATON. The WEB-based checkCIF system is now called IUCr/checkCIF and the validation report that it produces is currently required by most journals publishing crystal structures. CheckCIF provides authors, referees and journal editors with a list of issues, called

ALERTS, to be checked or acted on. PLATON based structure validation is closely identical to IUCr/checkCIF. PLATON/checkCIF can be used locally as part of the structure determination process, either stand-alone or as part of structure determination packages. This chapter provides an overview of the current crystal structure determination process, structure validation and the tools available in the program PLATON for that task. Common issues such as missed symmetry, twinning and disordered solvent treatment are discussed with examples.

10.15.1 Introduction

Crystal structure studies are often essential as proof for new reported inorganic and metal-organic chemistry. Nowadays, single crystal X-ray crystallography, the most used analysis technique for that, is often conceived as being routine, highly automated and reliable. For that reason, the main result of such a study is often just summarized in the printed part of a non-crystallographic journal with an ORTEP illustration showing the three-dimensional molecular geometry without presenting the supporting numerical details: *Seeing is Believing*. Fortunately, such a figure gives also, apart from the three-dimensional molecular geometry, an overall impression of the quality of the structure determination and may point experts at possible unresolved problems. Issues with the structure model and its refinement often show up in such a picture as unusual Atomic Displacement Parameter (ADP) ellipsoidal shapes. The full analysis details are expected to be made available as supplementary material to the printed paper, mostly with a reference to the archived CIF in the Cambridge Structural Database (CSD).[1] At least one of the referees of such a paper is expected to also inspect that material for validity and completeness. This applies in particular when unusual structural results are claimed to be sure that those results are not based on a misinterpretation of the experimental data or just refinement artifacts. In addition, future readers should be able to make use of the deposited data to allow them to repeat or improve on the analysis or to use the experimental data for an alternative or more detailed investigation beyond the original purpose of the study. The experimental data might also be unique or not easily obtainable again from scratch. Some interesting metastable polymorphs are good examples for that since they cannot always be reproduced.

Validation of the result of a crystal structure determination is not trivial. Expertise is often required to evaluate whether the available data support the authors analysis and claims. Various types of avoidable pitfalls that may invalidate a claimed result need to be recognized. The available refereeing expertise is limited for the handling of the exploding number of reports of routinely obtained crystal structures determined by insufficiently trained analysts using mainly GUI driven black box software. Unfortunately, also the relatively rare cases of faked structure reports should be detected.[2]

The time-consuming and proper validation of structure reports became problematic in the early 1990s due to their increasing numbers. New software requiring less user input made structure solution and refinement easier. At that time, the results were still mainly available only in printed form, often incomplete and with typos introduced with the preparation of the manuscript. Using those data for additional calculations and archival in databases such as the CSD required retyping again and was time consuming. Newer data collection hardware started to generate an explosion of new structure reports, making their proper processing soon unmanageable.

One of the problems was that the various refinement program systems had their own I/O formats. Of those, a still popular and surviving exchange format for selected refinement results is the free format RES file of the SHELXL program[3] that is often used for data exchange with molecular graphics programs. The same applies for the fixed format HKL file containing the reflection data on which the refinement model is based and used by other refinement programs. The information in those files is not complete.

Early attempts to standardize electronic data exchange involving a fixed formatted computer readable archival style, based on the 80 column IBM punched card model, were not widely adopted. The solution for the data exchange and archival issue of the crystallographic results was eventually found in the creation of the flexible computer readable Crystallographic Information Framework (CIF) file format.[4]

The free format CIF file is flexible with a data-name keyword and associated data-value structure. This standard was pioneered by the International Union of Crystallography (IUCr) with their Acta Crystallographica section B, C and E journals. Syd Hall, co-author of a at that time popular structure determination package, XTAL,[5] and section editor of Acta Crystallographica, section C, was very influential in pushing CIF as a data exchange and archival standard. He managed to convince George Sheldrick to be one of the first adopters of this standard in his still today widely used SHELXL refinement program, either in its native form or as part of free software packages such as OLEX2,[6] WINGX[7] and commercial software packages that are provided with the diffractometer hardware. CIF style crystal structure data deposition is now adopted as a standard requirement by all major journals. The CSD also requires CIF as deposition standard. Most current crystallographic programs can read and/or write CIF formatted files.

The CIF standard also opened the way to the publication of structure reports where both the manuscript and the relevant data are submitted electronically as a single file. The IUCr journals Acta Cryst. C and E were among the early adopters. It was their answer to the exponential growth of manuscripts received by the journals reporting crystal structure reports due to advances in data collection hardware, structure solution software and computing facilities.

In view of the large increase in the number of received manuscripts, often reporting routine structure reports, it was also clear that the classical refereeing process was inadequate. Automated validation of the CIF data was therefore introduced to facilitate that process. Initially, that involved tests that checked for the completeness of the data and their internal consistency. Subsequently, more detailed content related tests as supplied by the PLATON program[8] were included in the IUCr/checkCIF server (https://checkcif.iucr.org) based report. Currently several hundreds of tests have been implemented and their result collected in the form

of a set of ALERT messages with four levels of potential relevance. This validation report is easily available for the structure analyst, authors, referees and reader. Details about IUCr/checkCIF can be found on the IUCr journals WEB-site (https://journals.iucr.org). This chapter will give an overview of the multiple tests done by the program PLATON (http://platonsoft.nl). In addition, several PLATON tools will be discussed that can be used to investigate ALERTed issues in more detail.

10.15.2 Crystal structure determination

A crystal Structure determination can be divided into several stages: data collection, data reduction, solution of the phase problem, structure refinement, analysis of the 3D structure, graphical presentation of the result and validation. Though very important for the validity of a structure report, the first three are currently only marginally validated. Work is going on for standardized archival of the primary experimental data, i.e., the diffraction images.[9] Archived diffraction images may be useful to resolve problems encountered with a structure determination by looking for details in the diffraction images that are not accounted for as part of the standard block-box image processing and data reduction.

10.15.2.1 Data collection and data reduction

Today, most 3D structure determinations of organic and metal-organic compounds are based on the collection of diffraction data on a single crystal using MoKα, CuKα or synchrotron X-ray radiation and 2D diffraction images produced by 2D detectors. Alternatives are the less routine neutron diffraction and electron diffraction. The diffraction images are processed, based on the diffraction spots in those images, into information about the translation lattice (cell dimensions, space group) and the intensity of the indexed diffraction spots, to be used in the subsequent structure determination. In that data-reduction process, valuable information may be lost such as diffraction spots that do not fit for various reasons in the assumed translation lattice or the diffuse scattering and streaks in between diffraction spots. The latter may provide information about multiple types of structural disorder and twinning. It is important to be able to go back to the primary experimental data, i.e., the diffraction images, to try to resolve unexplained problems with a structure determination such as twinning or poor structure refinement issues.

10.15.2.2 Solution of the phase problem

Crystal structure determination in essence amounts to obtaining a three-dimensional electron density map of the unit cell content from the experimental set of diffraction spot intensities. Such a map can be analyzed in terms of isolated atomic densities from which the three-dimensional coordinates of their centers can be extracted and used, after refinement, for molecular geometry calculations such as bond distances and angles and for illustrations of the crystal structure.

The electron density map can be calculated with a Fourier synthesis, based on the amplitudes and phases of the reflections as coefficients. The amplitudes are easily derived as proportional to the square root of the intensity of the diffraction spots. Unfortunately, the corresponding phases are lost in the experiment. However, as it turns out, in most cases approximate phases can be recovered from the set of observed intensity data, given that the number of observations is usually much larger than the number of atomic parameter values to be determined. Those preliminary phases are subsequently improved iteratively in the refinement stage. Early approaches to the phase recovery issue relied on the introduction of a heavy atom into the molecule to be studied, when not already present next to the otherwise light atoms, or co-crystallized with a molecule containing a heavy atom. Subsequently, statistical methods were developed (symbolic addition, tangent formula) that no longer needed the introduction of heavy atoms in the compound to be investigated. Those methods are today again mostly superseded by even more powerful black-box techniques such as the charge flipping algorithm[10] or the intelligent brute force procedure as implemented in the program SHELXT.[11]

10.15.2.3 Structure refinement

Most of the reported structures are today refined into a final set of atomic parameters using the least-squares program SHELXL, either in its native form or as part of a structure solution package [WINGX, OLEX2]. Alternative software packages such as CRYSTALS,[12] JANA2006[13] and OLEX2 include refinement options not available in SHELXL.

Traditional refinement programs such as SHELXL use the AIM (Atom-in-Molecule) model where the electron density map is approximated as a collection of spherical atomic densities with associated anisotropic displacement parameters. Such a model is usually sufficient for the purpose of most studies. However, they ignore the bonding and lone pair effects that will show up as residual density peaks in difference electron density maps, in particular in case of refinement with high quality and high-resolution diffraction data. More involved refinement techniques, e.g., NoSpherA2,[14] and IDEAL,[15] that use aspherical scattering models (involving quantum chemical calculations) will not be discussed here. The same applies to incommensurate structures that can be modeled and refined with JANA2006.

10.15.2.4 Analysis of the results, illustrations and validation

Multiple programs are available for the calculation of a variety of derived geometry parameters such as bond distances and angles and molecular illustrations. This chapter will concentrate on those available in the program PLATON, some of which are also used as part of the checkCIF structure validation.

10.15.3 The programPLATON

PLATON[16–18] is a computer program that has been developed and extended over a period of more than 40 years since 1980 and is used in the context of the National Service Facility for single crystal structure determinations in the Netherlands. It grew out of a geometry analysis tool by adding multiple new options that were found to be useful for our service facility or suggested by outside users along with its involvement in the IUCr/checkCIF project. Some of those tools are unique such as TwinRotMat, others such as ADDSYM [MISSYM[19]] and ORTEP[20] are adaptations and extensions of pre-existing programs that we found useful to include. PLATON can be seen as a collection of knowledge and experience assembled over more than 50 years in this field. As a single program, PLATON is designed to be as much as possible to be independent from external libraries. It is available on the three common computer platforms: LINUX, MacOS and MS-WINDOWS. PLATON is developed and updated on the current FORTRAN platform that is also used by other widely used programs such as SHELXL and SHELXT.

The central subject of this overview chapter is the validation tool checkCIF in PLATON. That tool makes use of a selection of the other available tools in PLATON. PLATON/checkCIF creates a validation report in the form of a set of so-called ALERTS, short messages that need to be further investigated and possibly acted upon. Also there, PLATON tools can be helpful for that task.

10.15.3.1 PLATON tools and functions

Fig. 1 shows the opening window of PLATON when it is invoked with a CIF file, in this example the file yk2161.cif. Alternatively, it can be invoked with a <name>.ins or <name>.res file, being the standard input or output files from the SHELXL refinement

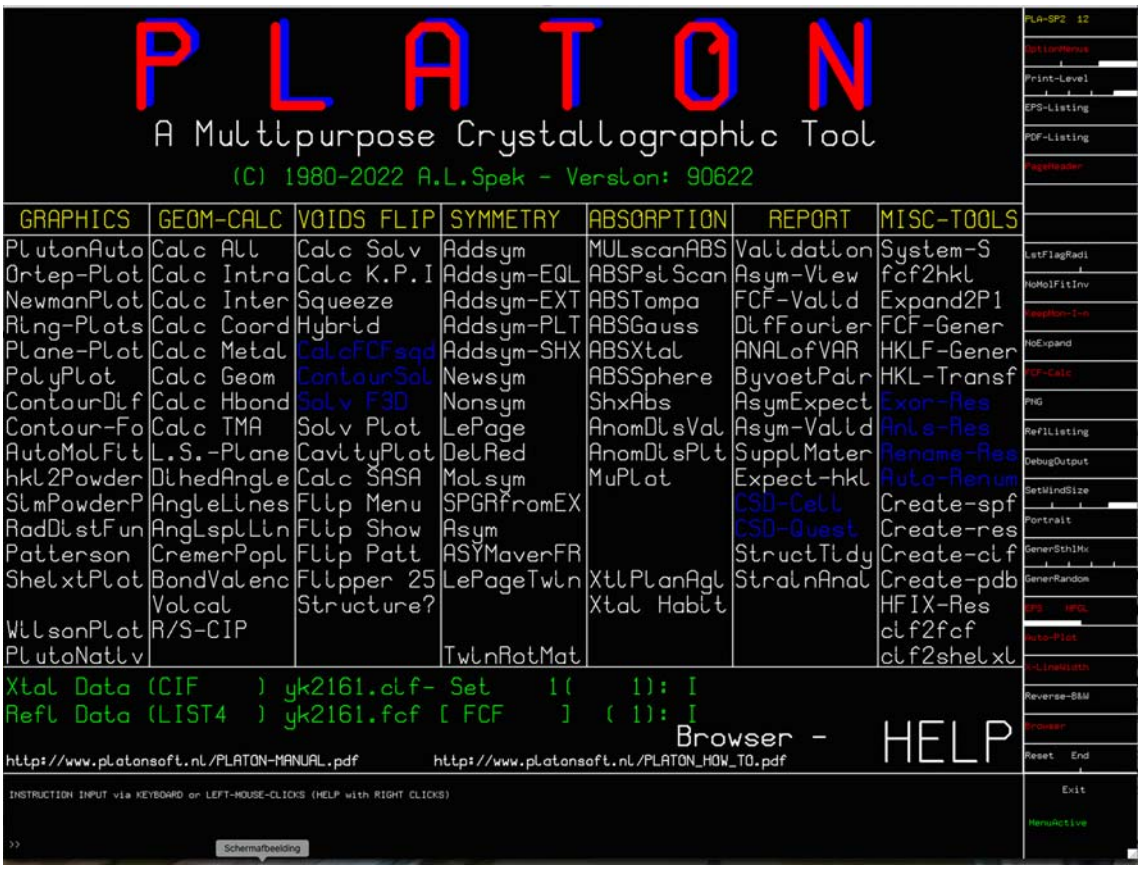

Fig. 1 Opening window of the PLATON program with in the central box an overview of the clickable tools (Blue when currently not applicable). The side menu gives access to various program options. The lower section lists the active data files. The box at the bottom provides an option for keyboard input of instructions.

program. The program attempts to automatically search for an associated reflection file such as <name>.fcf or <name>.hkl. The center of the PLATON overview window displays a tableau showing the available tools and functions that can be invoked by left-clicking on their respective names. Right-clicking on an item will offer info, downloaded from the internet, on that item in a new window. As an example, left-clicking on VALIDATION, [1, 6], will produce a validation report for data set <name>.cif and optionally <name>.fcf in the report files <name>.chk and <name>.ckf respectively. Note that the notation [1, 6] indicates the position row 1, column 6 in the tools tableau. The validation tool invokes in the background several of the other tools for its report. Examples are ADDSYM, [1, 4], Calc Solv, [1, 3], TwinRotMat [17, 4] and BijvoetPair, [6, 6]. Those tools can also be used directly to investigate ALERTed for issues in more detail.

On the right of the tool tableau there is a left clickable submenu with options and features such as listing symmetry details, symm, (10,13,2). Note that the latter code indicates its click position in submenu 10, vertical option 13, horizontal box 2. Most tools have one or more sub-menus. The main PLATON tool has three submenus [Fig. 1, (12,1,3)]. Below the tools tableau there is a box where information is displayed about the associated data files and some help pointers to more information. Instructions to the program can be given either by clicking on menu options or by keyboard data entry in the bottom window box after "≫."

10.15.3.1.1 CALC ALL

A single click on CALC ALL [1, 2] will create an extensive listing file with a large range of detailed geometrical information such a bond distances, bond angles, torsion angles, least-squares planes, dihedral angles, ring puckering parameters, coordination geometry, intermolecular contacts including hydrogen bonds and many other descriptors such as tentative valence and chirality assignments. CALC INTRA [2, 2], CALC INTER [3, 2], CALC COORD [4, 2], CALC METAL [5, 2], CALC METAL [6, 2], HBOND [7, 2] and CALC TMA [8, 2] will create subset listings.

The graphical tool L.S.-PLANE [9, 2] can be used to calculate the least-squares plane though a set of atoms along with their deviations from that plane by clicking on the partaking atoms in the graphical molecular display. Similarly dihedral angles [DihedAngle [10, 2]], the angle between lines (or bonds) [AngleLines [11, 2]] and the angle between a line and a plane [AngLsplLin [12, 2]] can be calculated interactively.

10.15.3.1.2 PLUTON

PLUTON is a molecular graphical tool that visualizes the 3D connectivity of the atom sites as derived from the electron density map with associated atom types and atom labels. By default, atoms are represented by balls and bonds by sticks in a minimum overlap orientation. Alternatively, space-filling models can be created. There are two clickable options to invoke this tool. PlutoNative [17, 1] to start building the content and style of the molecular display from scratch and PlutonAuto [1, 1] for an automatic preliminary display that can also be extended with additional interactively supplied instructions. Fig. 2 gives an example of a unit-cell content illustration in space group P-1. PLUTON can be used to investigate polymeric and hydrogen bond networks and as interface to external programs such as POVRAY for ray-traced images or RASMOL for dynamic rotations of the structure.

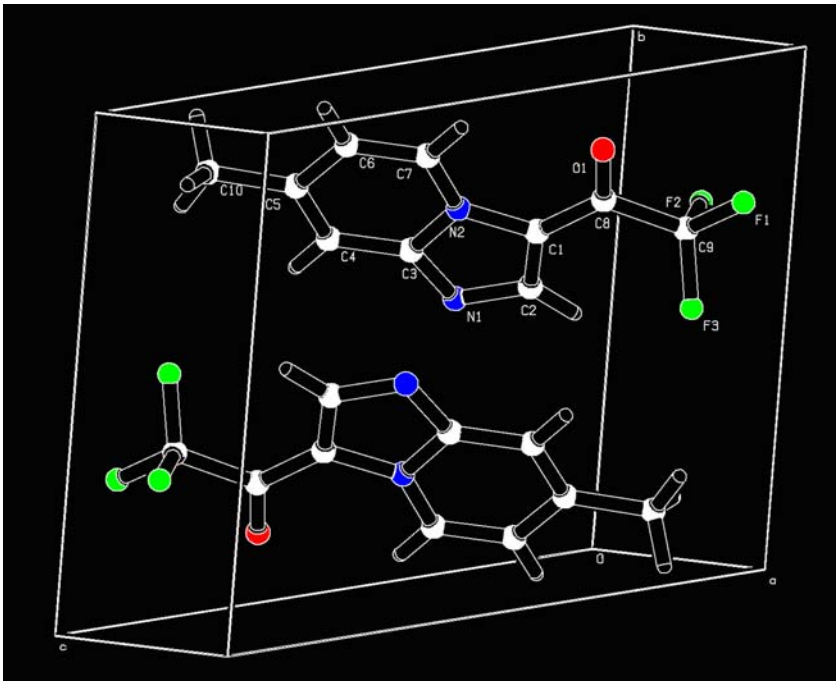

Fig. 2 A PLUTON style ball-and-stick packing plot of the content of the triclinic unit-cell.

10.15.3.1.3 ORTEP

ORTEP is a molecular graphics tool [2, 1] similar to PLUTON with the difference that not only the position and connectivity of the atoms are shown but also the Atomic Displacement Parameters (ADPs). Atoms are represented with an ellipsoidal probability surface drawn at a given probability level (usually 50%). Those ellipsoids do not represent the electron density but the refined atomic thermal motion parameters that can be convoluted by systematic factors such as unaccounted for disorder or unsuitable correction for absorption. Fig. 3 gives an example of a 50% probability ellipsoid plot. Atoms with severely elongated or flattened ellipsoids or with a size that deviates significantly from those of neighboring atoms may indicate model and/or refinement issues to be investigated. The components of the ellipsoids along a bond are expected to have similar values.[21]

10.15.3.1.4 CONTOUR

Fourier transformation of the square root of the experimental diffraction intensity data, F_{obs}(hkl), together with associated phases obtained with one of the available methods to recover them from the same intensity data results in a 3D electron density map. Such a map represents the electron density averaged over all unit cells in the crystal, i.e., space and time averaged. CONTOUR is a tool for displaying density level contoured sections of that map. The CONTOUR-Fo option [8, 1] displays a section of the F_{obs} map (Fig. 4a) defined by the 6-membered ring atoms in the structure shown in Fig. 3. For validation purposes, the related CONTOUR-DIF option [7, 1] can be used to create a density map that displays the difference electron density between a map calculated with observed data and a map calculated using the derived model parameters (Fig. 4b). Nonzero densities in such a map may indicate several types of problems such as misplaced hydrogen atoms, missing hydrogen atoms, wrong element type assignment, unresolved twinning and inadequate correction for absorption. The residual density on the bonds in Fig. 4b is due to refinement based on the AIM refinement model.

10.15.3.1.5 Simulated powder pattern

Fig. 5 shows a simulated powder pattern for the compound illustrated in Fig. 3. Such a pattern can be calculated based on the experimental reflection data with hkl2Powder [10, 1] or based on reflection data as calculated with the structure model parameters with SimPowderP [11, 1]. This tool can be useful for checking whether two structures are identical but described in different settings or space groups or compared with experimental powder patterns.

10.15.3.1.6 LEPAGE, DELRED and ADDSYM

The assignment of the proper space group to a crystal structure is not always obvious. A preliminary structure may have been obtained (or obtainable only) in a lower symmetry space group then the actual higher symmetry space group. In that case, atoms that are related by symmetry are refined as independent. This might lead to refinement artifacts and distorted geometry, in particular when the missing symmetry elements are an inversion center or a lattice translation.

The LEPAGE [CREDUC[22]] or DELRED [DELOS[23]] tools can be used to investigate the lattice symmetry of a supplied unit cell parameter set for higher lattice symmetry within applied tolerances. The actual content of the unit cell will determine whether this is the actual symmetry or just accidental. Both tools are inspired by the respective tools in square brackets.

ADDSYM is a tool for checking the correctness of the preliminary space group assignment by inspection of the structure model coordinate set for additional symmetry elements. Invoking the ADDSYM option [1, 4] will report on the possible additional symmetry elements along with a proposed revised space group. The related option ADDSYM-PLT [4, 4] will show an updated model when applicable and the ADDSYM-SHX [5, 4] option will create an averaged coordinate set suitable for a test refinement in the

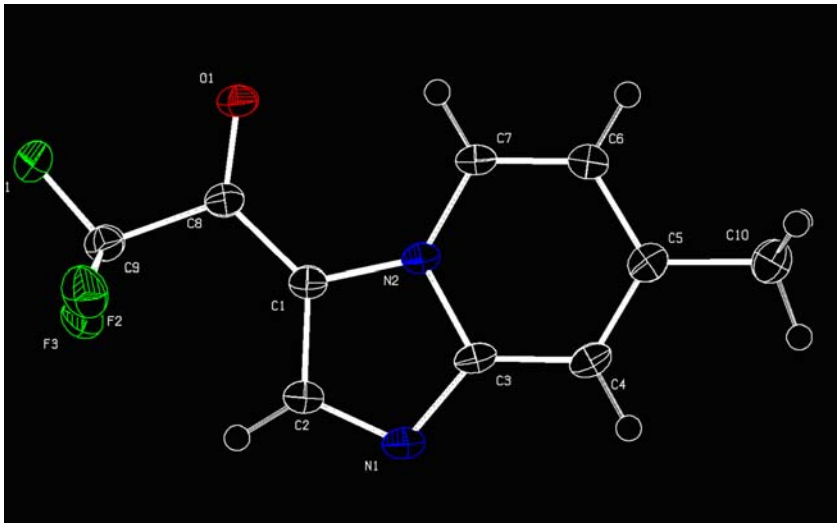

Fig. 3 A labeled ORTEP plot with ellipsoids drawn at the 50% probability level.

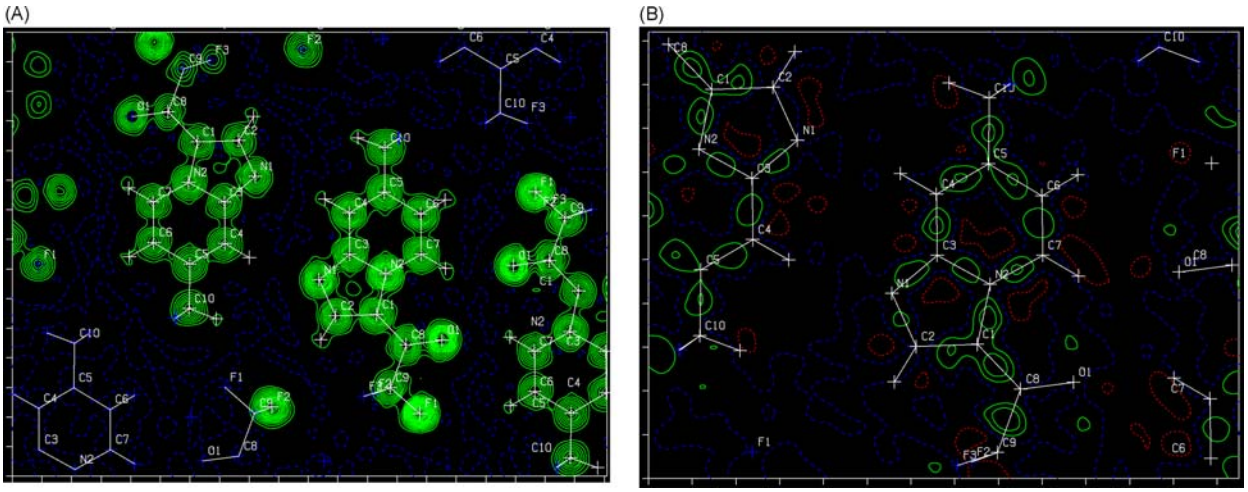

Fig. 4 (a) A contoured electron density map section with contour levels 1.0 e/Å^3 apart. (b) Difference electron density map showing residual densities on bonds that are not accommodated by the AIM model. Contour levels 0.1 e/Å^3 apart.

proposed new space group. Comparison of the old and new refinement results should determine which one provides the best description of the structure. The reported higher symmetry elements can be either only approximate (pseudo-symmetry) or to be implemented, depending on the applied distance tolerances and experimental error. Poor data quality, disorder, pseudo-symmetry and twinning may complicate the analysis. In those cases, all possibilities should be investigated and the best one reported with an associated discussion.

Example 1: The structure shown in Fig. 6 with CSD code BAMYEU was originally reported in monoclinic non-centrosymmetric space group Cc. Interestingly, the associated publication included an ORTEP illustration in approximately the same

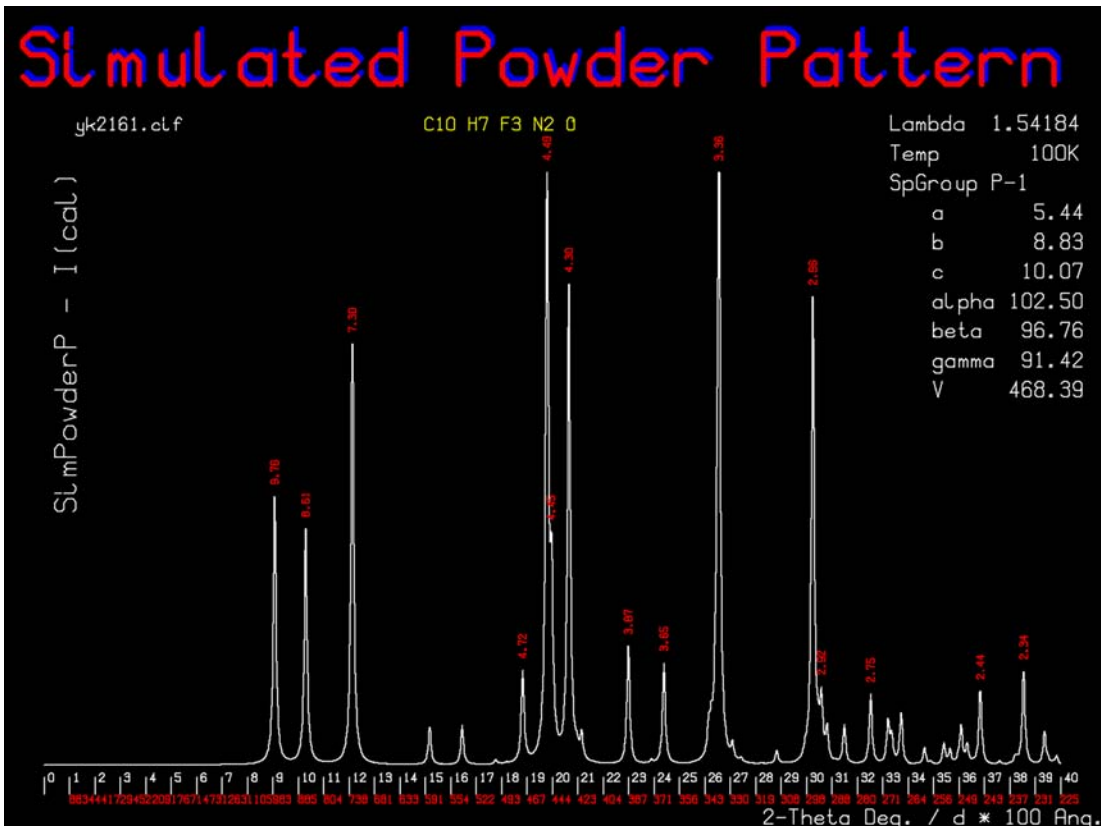

Fig. 5 A Simulated Powder Pattern based on intensities calculated from the structure model parameters.

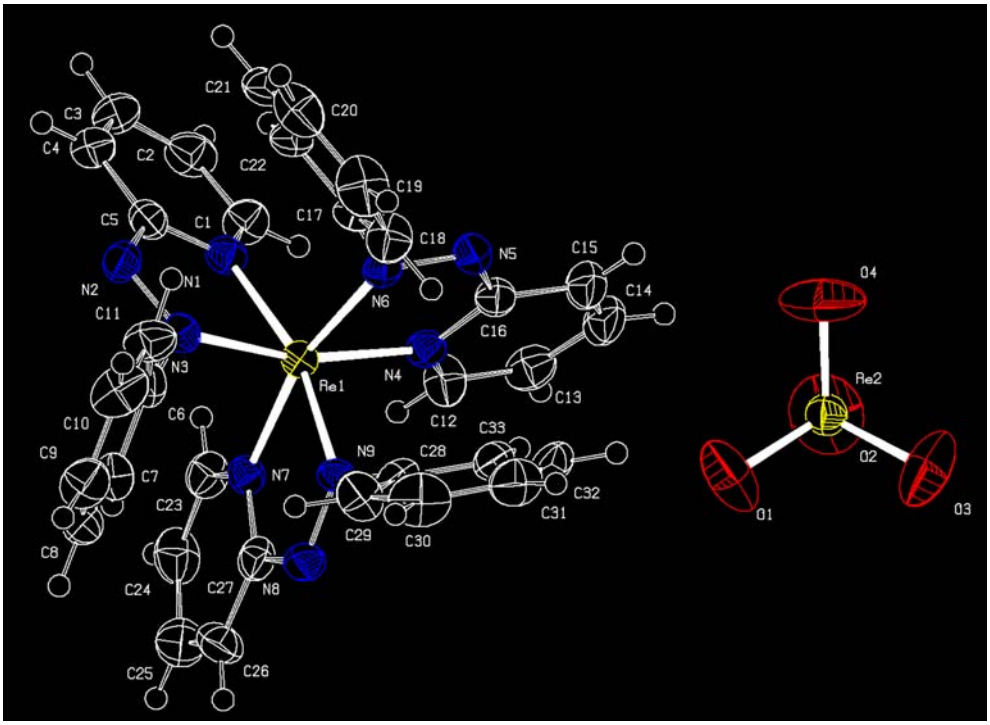

Fig. 6 Structure of CSD entry BAMYEU published in the monoclinic space group Cc that suggests threefold axes as additional symmetry elements of both the cation and the anion.

orientation as in Fig. 6, clearly suggesting an additional threefold symmetry axis. ADDSYM indeed points out (Fig. 7) that the real space group is P31c in the trigonal system (Fig. 8). A correction was published by Dick Marsh[24] who has also corrected hundreds of similar published cases of missed higher symmetry. Adding a threefold axis does not change the structure into centrosymmetric thus no drastic changes in the molecular geometry are to be expected for this structure other than averaging for systematic errors in the reflection data.

Example 2: The structure with CSD code EKOKOE was published with two independent molecules in the non-centrosymmetric space group P1. Inspection of Fig. 9 and ADDSYM clearly suggest an additional center of inversion. Fitting both molecules with the AUTOMOLFIT [9, 1] routine in PLATON shows a good configurational fit (Fig. 10). A description in the centrosymmetric space group P-1 is indicated[25] but should be investigated with a refinement in that space group for a definite proof.

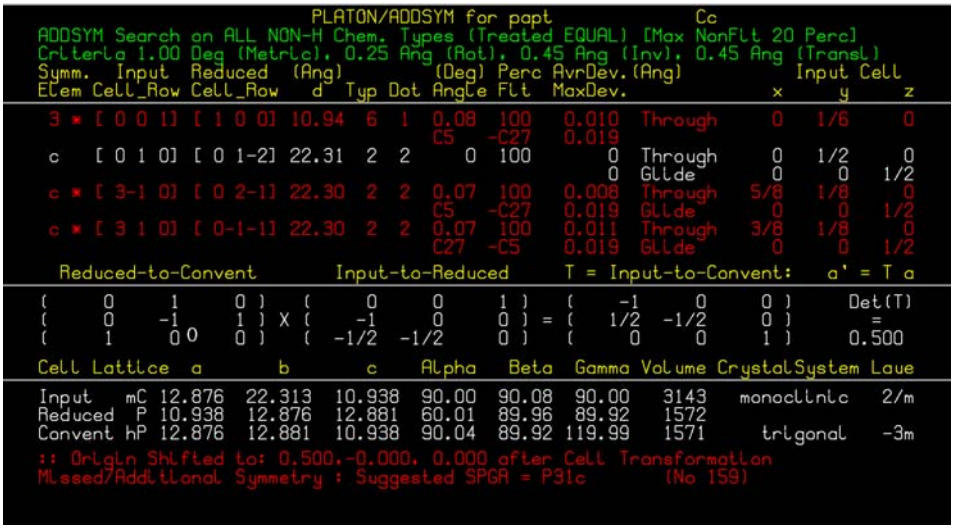

Fig. 7 ADDSYM suggests the higher trigonal P31c space group symmetry based on the detection of three more symmetry elements. The proposed additional symmetry elements are shown in red. The transformation matrix from the C-centered to P-trigonal lattice is also shown. The new symmetry applies to 100% of the atoms, subject to the distance and angle tolerances shown in green.

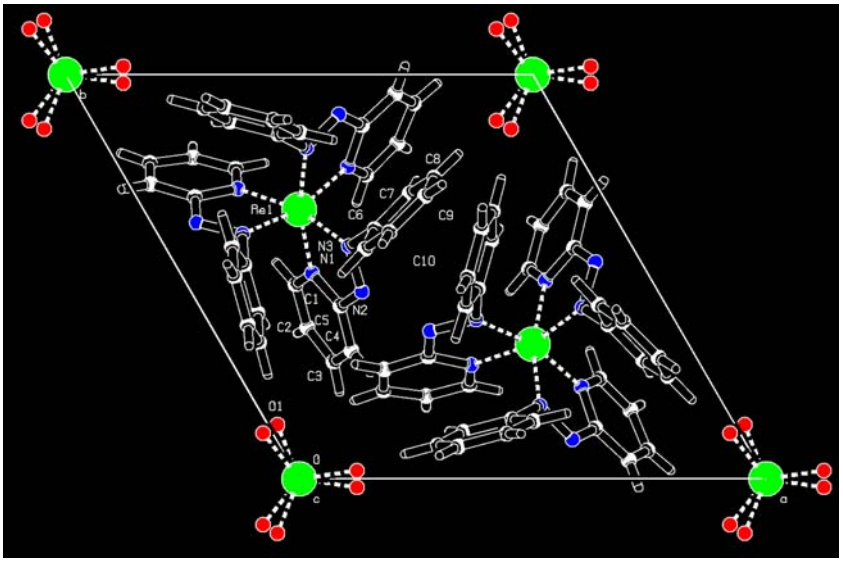

Fig. 8 Packing diagram of the unit cell content in the trigonal space group P31c with all molecular species on threefold axial sites. The symmetry independent atoms are labeled.

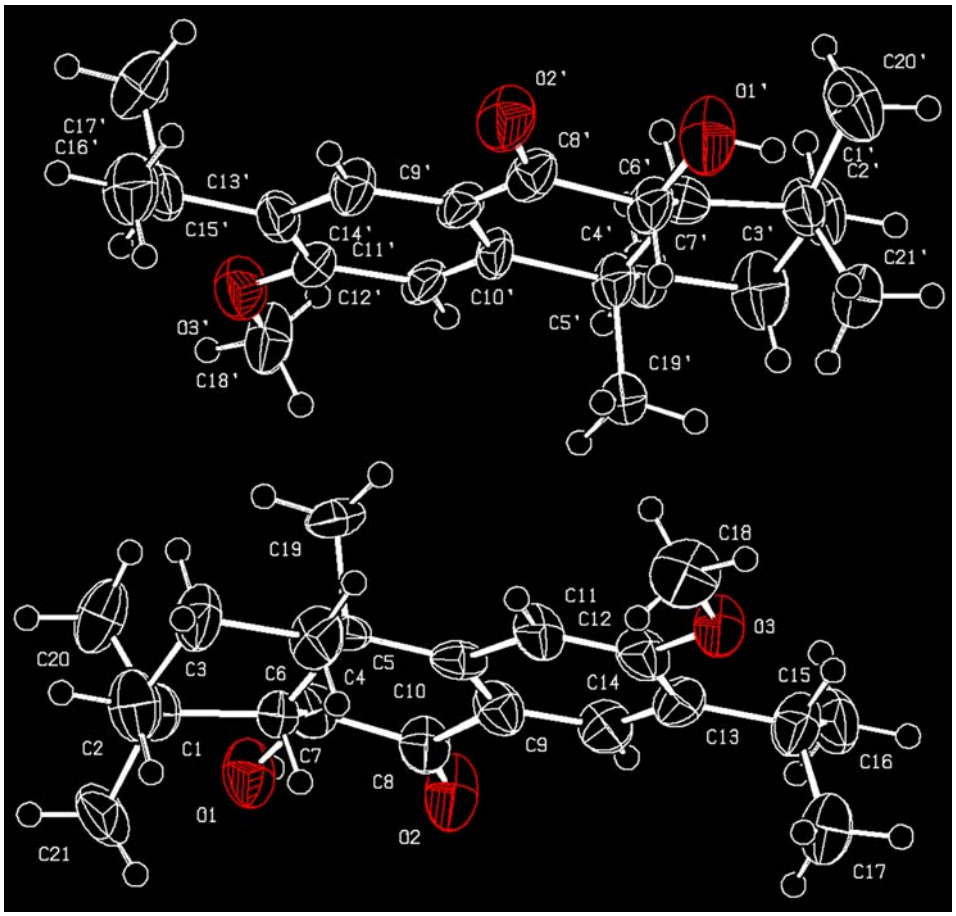

Fig. 9 Displacement ellipsoid plot of the two independent molecules of CSD entry EKOKOE published in space group P1. Corresponding ADP ellipsoids tend to be perpendicular (e.g., C10 and C10′) suggest inversion symmetry and space group P-1.

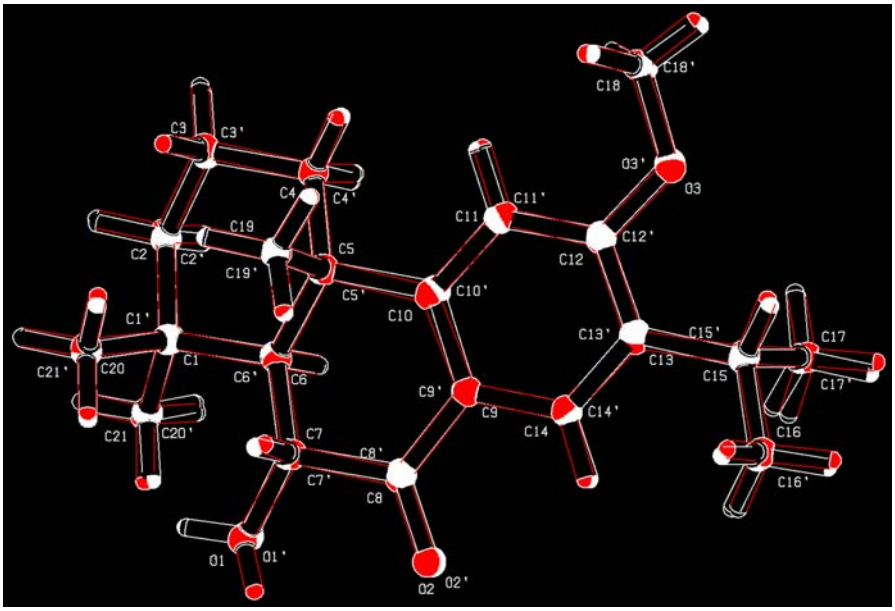

Fig. 10 Quaternion based fitting of the two independent molecules of EKOKOE shows a close configurational consistency.

Unfortunately, no reflection data are available for that. Refinement of a centrosymmetric structure in a non-centrosymmetric space group usually leads to refinement artifacts due to numerical instability. This is clearly shown in **Fig. 11** where corresponding bond distances are compared. As an example, C10-C11 and C10′-C11′ differ significantly by 12.1 s.u. units. Their average is near the expected value for such a bond. Another signal is the observation that corresponding ADP ellipsoids tend to be perpendicular due to the numerical instability.

Example 3: See **Section 10.15.4.2**. That example shows that additional symmetry proposed by ADDSYM, representing the (approximate) symmetry in the coordinate set of the refined model, should always be checked with the symmetry in the reflection data set (i.e., systematic absences and statistical tests for an inversion center). The latter can be done with the SPGRfromEx [11, 4] tool. In addition, there is the Newsym [6, 4] tool to investigate the reflection data symmetry of reflection data calculated from the refined model parameters, which may differ from the symmetry of the observed reflection set. A detailed statistical analysis for inversion symmetry is available with the WilsonPlot [17, 1] tool.

10.15.3.1.7 CALC SOLV

The crystal structure of a compound of interest often includes solvents of crystallization in voids left by the packing of the main molecules. Those solvent molecules are often disordered when there is limited interaction with the framework of the main molecules or might even have been partly evaporated. Disordered density in those voids is easily missed. Peak search algorithms that are used to identify atoms in an electron density map assume ellipsoidal atomic density shapes. Disordered solvents often do not satisfy that assumption. Missed solvent contributions to the structure model may lead to unsatisfactory refinement results. CALC SOLV reports on solvent accessible voids in a structure model. That information is used in the SQUEEZE tool (**Section 10.15.3.1.8**). CAVITYPLOT [9, 3] creates a crude image of those voids and their location in the structure (**Fig. 12**).

Even when there are no solvent accessible voids in a structure there is still space in pockets in between molecules. The volume of the molecules in the unit-cell is usually characterized with the value of the Kitaigorodskii[26] packing index. That value can be calculated with the related CALC K.P.I instruction and is based on the volume taken by the molecules in the unit cell with van der Waals radii assigned to the atoms. Typical packing indices are in the order of 0.65.

10.15.3.1.8 SQUEEZE

It is not always possible to model the content of voids meaningfully with a discrete set of parameters due to severe disorder, in particular when the nature of the solvent is unknown, a mixture of solvents or even an impurity with its origin in earlier synthesis steps. Channels that are incommensurately filled with molecules are difficult to model meaningfully with a disorder model. Ignoring their contribution will result in higher R-values and low-quality structural parameter values of the molecules of interest. The SQUEEZE [3, 3] tool provides an alternative method to handle the scattering contribution of disordered solvents in a crystal structure to the total scattering of the structure model in the least-squares refinement. The geometry of the molecules of interest and R-values generally improve with the application of SQUEEZE.

Preliminary, the Calc Solv [1, 3] option can be invoked to investigate whether a structure contains solvent accessible volumes. When that is the case, the SQUEEZE tool can be used to find out how much density can be found in those voids. SQUEEZE generates

Resd#1	Resd#2	Dist#1	Dist#2	Dif	Dif/Sig
O1 -C7	O1' -C7'	1.435(10)	1.384(11)	0.051	3.431
O2 -C8	O2' -C8'	1.193(11)	1.248(10)	-0.055	-3.700
O3 -C12	O3' -C12'	1.357(10)	1.353(9)	0.004	0.297
O3 -C18	O3' -C18'	1.453(12)	1.352(13)	0.101	5.709
C1 -C2	C1' -C2'	1.561(13)	1.498(14)	0.063	3.298
C1 -C6	C1' -C6'	1.582(9)	1.553(10)	0.029	2.156
C1 -C20	C1' -C20'	1.576(11)	1.518(16)	0.058	2.987
C1 -C21	C1' -C21'	1.551(14)	1.511(12)	0.040	2.169
C2 -C3	C2' -C3'	1.552(14)	1.482(15)	0.070	3.412
C3 -C4	C3' -C4'	1.544(11)	1.507(12)	0.037	2.273
C4 -C5	C4' -C5'	1.540(10)	1.548(11)	-0.008	-0.538
C5 -C6	C5' -C6'	1.578(9)	1.559(10)	0.019	1.412
C5 -C10	C5' -C10'	1.485(8)	1.567(7)	-0.082	-7.714
C5 -C19	C5' -C19'	1.539(9)	1.570(10)	-0.031	-2.304
C6 -C7	C6' -C7'	1.525(10)	1.556(10)	-0.031	-2.192
C7 -C8	C7' -C8'	1.495(9)	1.560(8)	-0.065	-5.398
C8 -C9	C8' -C9'	1.486(11)	1.427(9)	0.059	4.151
C9 -C10	C9' -C10'	1.394(10)	1.416(9)	-0.022	-1.635
C9 -C14	C9' -C14'	1.387(11)	1.407(9)	-0.020	-1.407
C10-C11	C10'-C11'	1.464(9)	1.318(8)	0.146	12.125
C11-C12	C11'-C12'	1.368(10)	1.426(8)	-0.058	-4.529
C12-C13	C12'-C13'	1.427(11)	1.389(9)	0.038	2.674
C13-C14	C13'-C14'	1.341(11)	1.402(10)	-0.061	-4.103
C13-C15	C13'-C15'	1.517(10)	1.524(9)	-0.007	-0.520
C15-C16	C15'-C16'	1.560(14)	1.497(13)	0.063	3.298
C15-C17	C15'-C17'	1.515(14)	1.550(12)	-0.035	-1.898

Fig. 11 Comparison of corresponding bond distances in both molecules in EKOKOE as reported in space group P1. Bond distances such as those of C10-C11 and C10′-C11′ differ up to 12 times the estimated error in the bond.

a new set of instruction files suitable for implementing the solvent contribution to the calculated structure factors with the final refinement using SHELXL. More details about SQUEEZE and examples can be found in Ref. 27.

10.15.3.1.9 TWINROTMAT

Twinned crystals can often be detected at the experimental stage, either by inspection of the crystal under polarized light or by inspection of the diffraction images, but not always. When twinned, the main diffraction lattice is overlayed with one or more similar lattices in a different orientation. The different lattices may be completely overlapping or only partial. In the latter case it is often possible to deconvolute the data for a preliminary structure determination. In many other cases, it is still possible to preliminary solve such a structure but with unsatisfactory high R-values and significant residual density peaks in the difference density map. TwinRotMat [17, 4] is a tool to detect a twinned structure in such a dataset and to provide information about the type of twinning model needed for a proper final refinement. **Fig. 13** shows the result of such an analysis. A twofold rotation about the a-axis is detected causing a 100% lattice overlap resulting in a close to 50:50 racemic mixture. Taking the reported rotation matrix into account in the subsequent least-squares refinement is expected to lower the R-value by in the order of 17%. **Fig. 14** illustrates the lattice overlap. See also **Fig. 2** in Ref. 28.

10.15.3.1.10 ASYM-VIEW

ASYM-VIEW [2, 6] is a graphical tool to inspect the reciprocal lattice for missing data and the distribution of weak data. It can be used with either HKL or FCF data. ASYM-VIEW is one of the options of the ASYM [12, 4] tool. It can be used to create an averaged/unique reflection file. The <name>.cfk file (see **Section 10.15.4.1.2**) includes a listing of the merged reflections and excluded systematic absences.

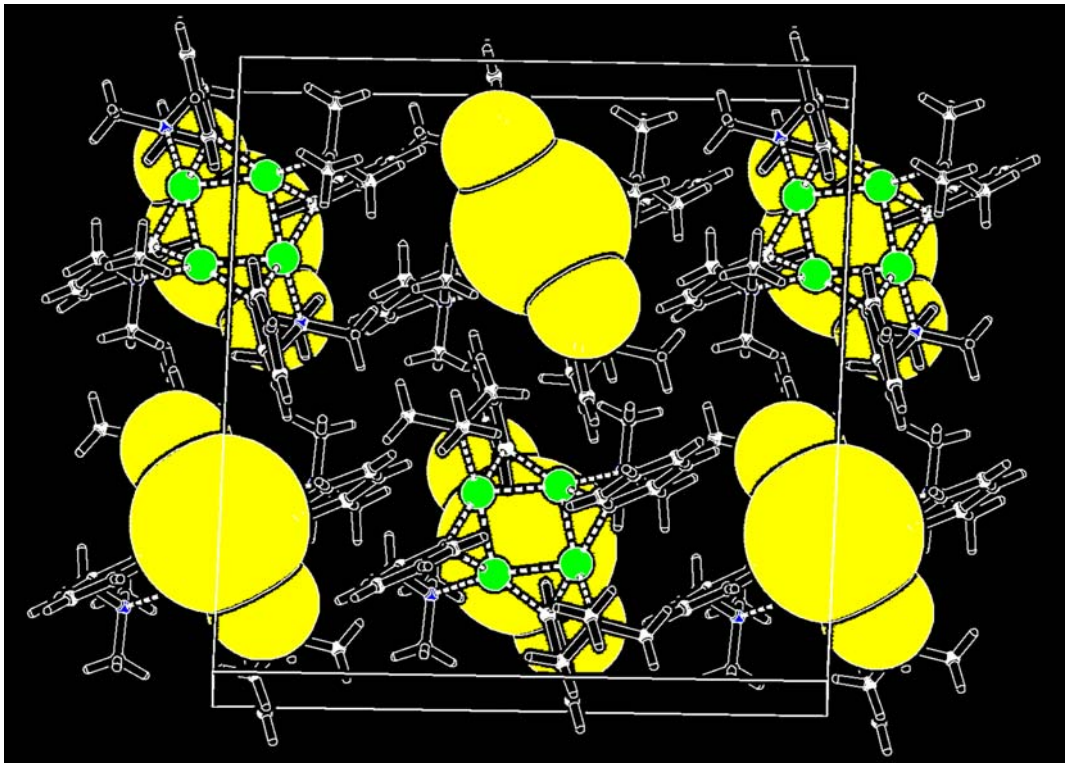

Fig. 12 Visualization of the solvent accessible voids in the unit-cell. Voids are represented by yellow spheres of variable radius.

10.15.3.1.11 BIJVOET-PAIR

X-Ray crystallography allows the determination of the absolute structure of crystal structures missing an inversion center. In such a case, the intensities of Friedel pairs of reflections (hkl and -h-k-l), or more generally Bijvoet pairs, have slightly different intensities, depending on the atomic resonant scattering parameter values f′ and f″. This implies, in the absence of a mirror plane, the determination of the chirality of the molecules in the structure or the polarity of the crystal otherwise. The absolute structure can be determined as a special case of twinning with the refinement of a inversion twinning parameter = Flack parameter.[29] Values of 0 and 1 represent enantiopure structures where 1 indicates that the reported structure model needs to be inverted to be consistent with the diffraction data. A value of 0.5 indicates a racemic mixture. The refined Flack parameter comes with an s.u. (standard uncertainty) to be used as a reliability indicator for the absolute structure assignment. Refinement with a complete set of Friedel pairs is advised to avoid correlation effects with the positional parameters.

Alternatively, post-refinement estimates of the Flack parameter value can be determined based on the comparison of the observed differences in the Friedel pair intensities vs the corresponding calculated differences. Those Flack parameter value estimates tend to have smaller s.u.'s than the refined Flack parameter value. The BIJVOET-PAIR tool [6, 6] reports the values of two of those estimates: The PARSONS parameter[30] and the HOOFT parameter.[31–33]

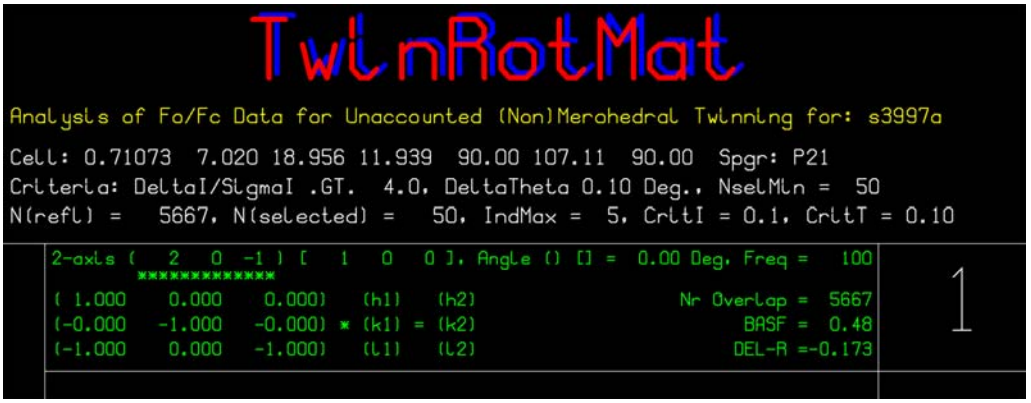

Fig. 13 Example output of TwinRotMat reporting a twinning operation and its estimated reduction of the R-factor when applied.

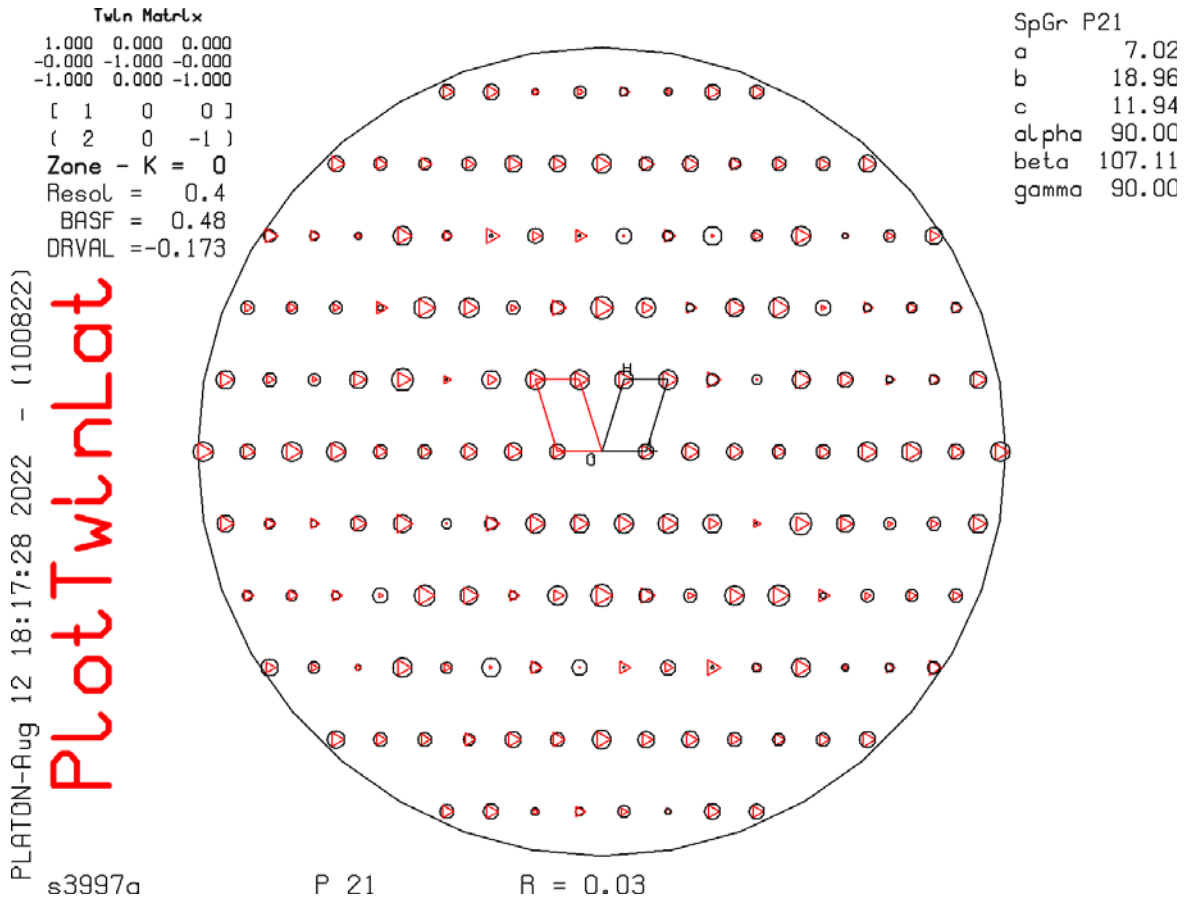

Fig. 14 Display of the two overlapping reciprocal lattices in the h0l section. The twin operation is a twofold rotation about the vertical a-axis.

Fig. 15 gives an overview of the result of the various absolute structure determination approaches for a gold containing compound in space group P1. Relevant numerical results are collected in the table on the right. The Hooft and Parsons estimates of the Flack parameter value show indeed lower s.u. values than the refined Flack parameter value. All values are close to zero, indicating that the structure is essentially enantiopure. The Friedel pair coverage of 0.98 is also high. A scatter plot of observed vs calculated Friedel pair differences is shown on the left. The slope of the least-squares line (green) though the data point is positive, again indicating the correct absolute structure assignment. Individual counter indications are shown in red. The data points on the right are shown with one sigma error bars. The same datapoints, but now without error bars, are shown on the left.

10.15.4 Crystal structure validation

To quote Dorothy Hodgkin in her 1964 Nobel Lecture: "… [The] great advantage of X-ray analysis as a chemical structure analysis is its power to show some totally unexpected and surprising structure with, at the same time, complete certainty …." The catch with this statement is the implicit assumption that all procedures have been carried out correctly. That is the task of structure validation to certify.

A key step in a crystal structure determination is the interpretation of the preliminary 3D electron density map of the unit cell content in terms of discrete atomic densities. The next and critical step is the correct assignment of an element type to that atomic density. That is done based on peak height, chemical knowledge and assumed chemistry such as the expected element types. The preliminary assignment of the non-hydrogen atoms is today mostly done by computer software such as SHELXT. In general, this works well with good experimental diffraction data with reasonable resolution. Twinning, when not detected at the experimental stage, may hamper a smooth structure determination. Disorder, either configurational, conformational, partial occupation or substitutional, will need human intervention. The correct assignment of atom types differing by only one electron, such as C, N and O, can be a problem when not known beforehand from the chemistry. The same applies for nearby transition elements such as Cu and Zn and the lanthanides. The assignment of hydrogen atoms can be trivial with good data and involved in other cases. Notorious are problems with hydrogens on water molecules and -O-H moieties, when the hydrogen atoms are disordered over more than one site. Mis-assignment of atom types may lead to different assumed chemistry. Attempts to synthesize such

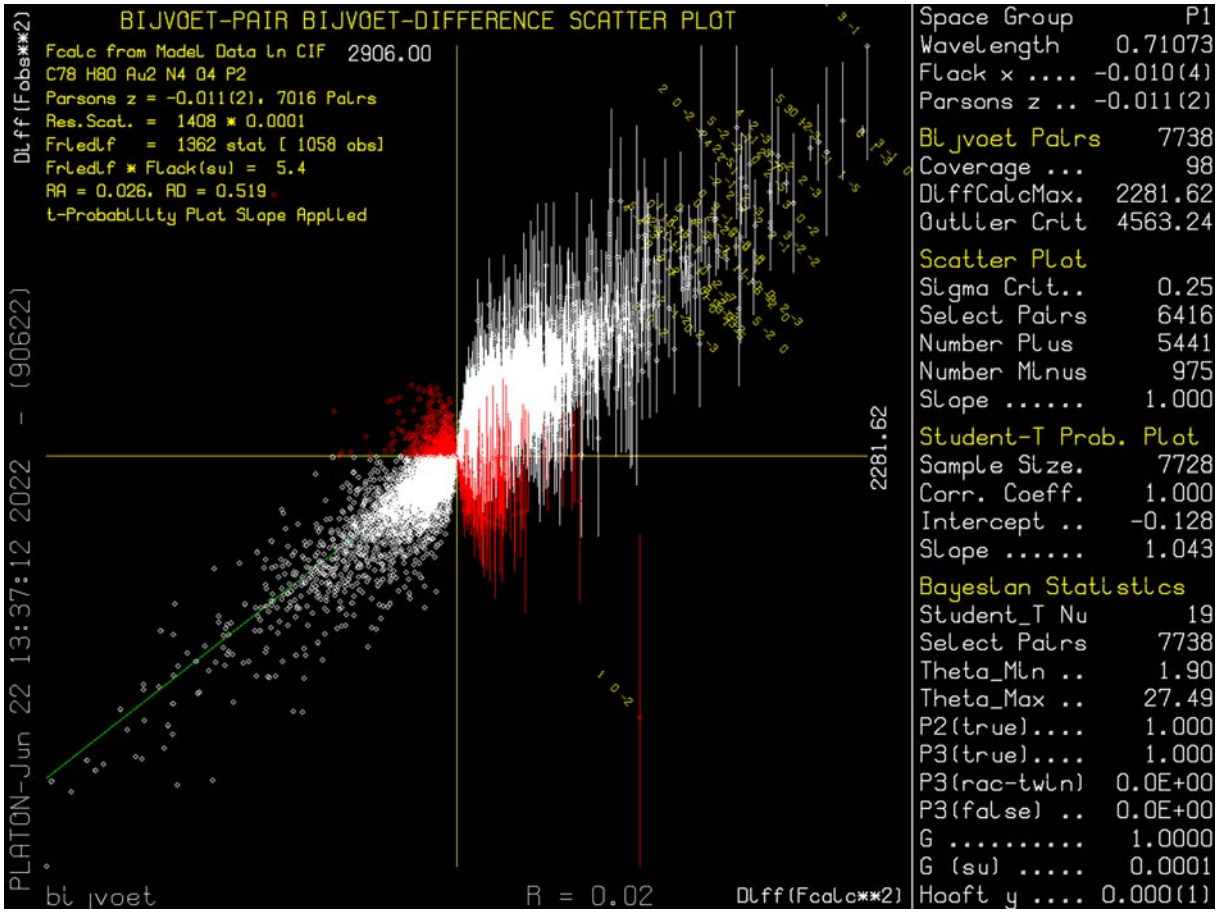

Fig. 15 Overview of the Bijvoet-pair absolute structure analysis results.

a compound may lead to one with completely different properties than the original compound. A famous example is the complete synthesis of a natural product based on an incorrect crystal structure report.[34]

Wrong symmetry assignment may also lead to unusual geometry claims based on artifacts. Solution of the phase problem may only lead to an interpretable structure in a particular space group such as P1. However, that space group may be a subgroup of the correct higher symmetry one. Refinement in a too low symmetry group may lead to refinement artifacts and "interesting chemistry." See Fig. 2 in Ref. 16 where an example is shown where the authors claim significantly different coordination bond lengths that are chemically expected to be identical. CheckCIF validation includes multiple checks to detect artifacts as described above. Newly discovered issues often lead on a regular basis to the addition of new ALERTS.

10.15.4.1 The PLATON/checkCIF report

A full PLATON/checkCIF report for a compound <name> consists of two parts. The first one is the file <name>.chk file with an overview of relevant data of the analysis and a list of ALERT messages about the structure analysis, mainly based on the structure model parameters as supplied in the supplied <name>.cif file, being *the authors interpretation of the experimental data*. An example is shown in Section 10.15.4.2, Fig. 18. That information is also displayed in a graphical window when validation is invoked from the main PLATON main menu. The second one is the <name>.cfk file with extensive details on the quality of the refinement and the reflection data, as supplied with the <name>.fcf file, on which the structure model is based. This file contains more explicit information on issues reported in the <name>.chk file such as data set resolution, missing reflections, twinning, absolute structure and details of the refinement and reflection merging.

CheckCIF validation reports on issues such as missing information, inconsistencies, quality, potential errors, unusual results, possible improvements or interesting features. Those messages come as ALERT messages but are not necessarily errors. They come with three levels of relative importance, A, B and C, and a mainly informative G level. Level A messages may be serious or simple to address when pointing to missing relevant information. A set of low-level G ALERTS in combination may point to a serious issue after all.

PLATON based checkCIF ALERTS are included in IUCr/checkCIF with an identifier PLATxyz, where xyz is an ALERT number. ALERT messages are compact. More details and suggestions are listed on the terminal window in the background.

10.15.4.1.1 CIF-validation

Structure validation aims at providing information on (1) The quality of the data on which the study is based (i.e., based on the best attainable data quality or sufficient for the purpose of the study). (2) The quality of the refined model (i.e., are all issues such as disorder resolved or sufficient to prove the structural features of interest). (3) Details on the experimental, data reduction and handling procedures used (allowing to repeat the analysis or to use the experimental data for follow-up research). (4) Messages about interesting, unusual or erroneous structural features.

10.15.4.1.2 FCF-validation

CIF-validation mainly addresses the result of the structure determination. FCF-validation inspects the diffraction data on which that analysis is based and the refinement in more detail. The key to that analysis is the FCF file containing the (merged) observed and calculated diffraction data on which the refinement is based. That file should be provided and archived explicitly along with the CIF unless when that file can be easily recreated automatically from the relevant (embedded RES, HKL, FAB file) information in the CIF as is the case with current SHELXL version-based refinements.

The FCF file is checked for missing reflection data, sufficient resolution, outliers, signs for unresolved twinning, absolute structure, checking of a normal distribution of errors with a Normal Probability Plot (Fig. 16) or of deviating Analysis-of-Variance values (Section 10.15.4.3.2, Fig. 23). Relevant ALERTS are added to the <name>.chk file with more details in the <name>.ckf file.

10.15.4.2 A PLATON/checkCIF report example

Fig. 17 shows the packing diagram of a structure that refined to an R-factor of 3% in the non-centrosymmetric space group $Pca2_1$. This figure suggests an additional center of inversion at the nickel atom. Notice that the whole structure can be moved in this space group freely in the c-axis direction to have the Ni atom close to a center of inversion of the lattice. A PLATON based validation report

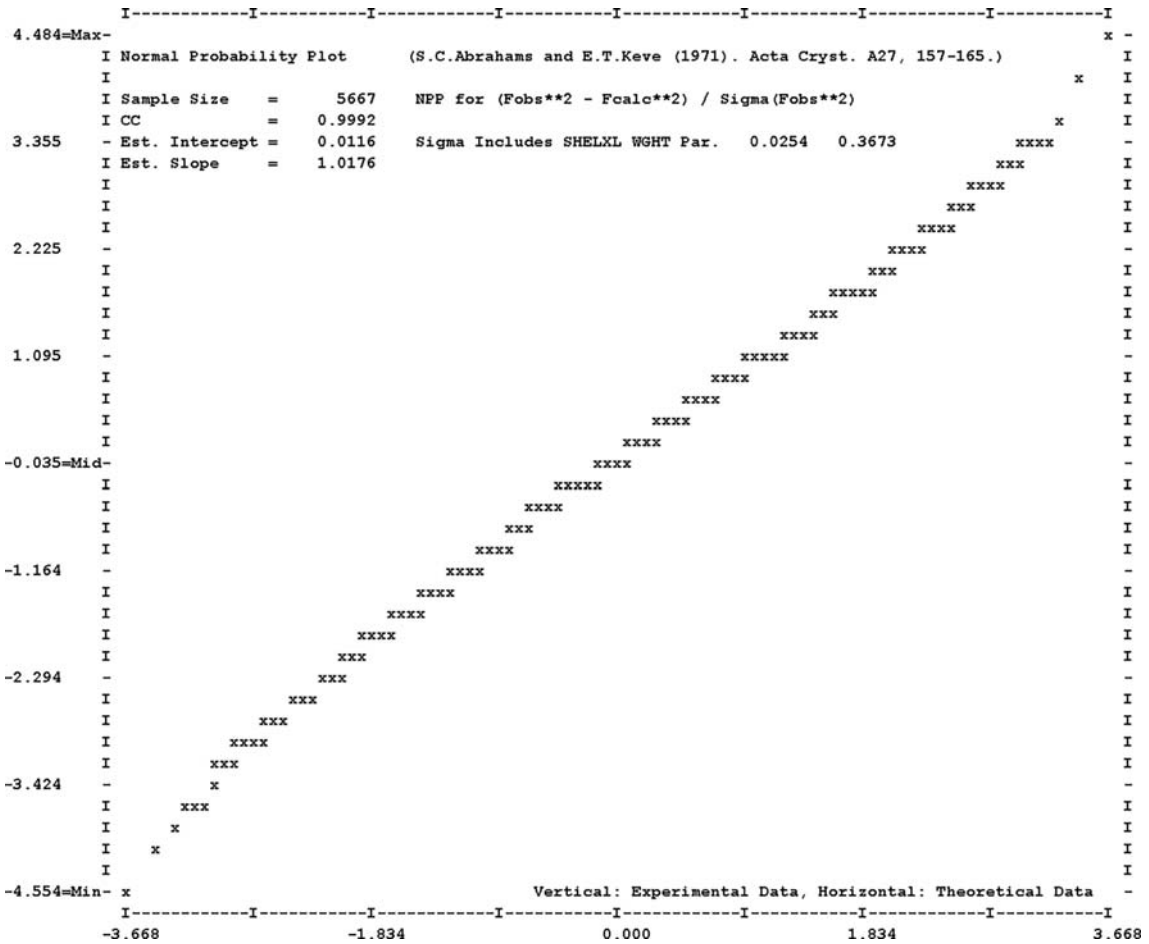

Fig. 16 Normal Probability Plot testing the normal error distribution between F_o^2 and F_c^2 that is expected to be close to linear.

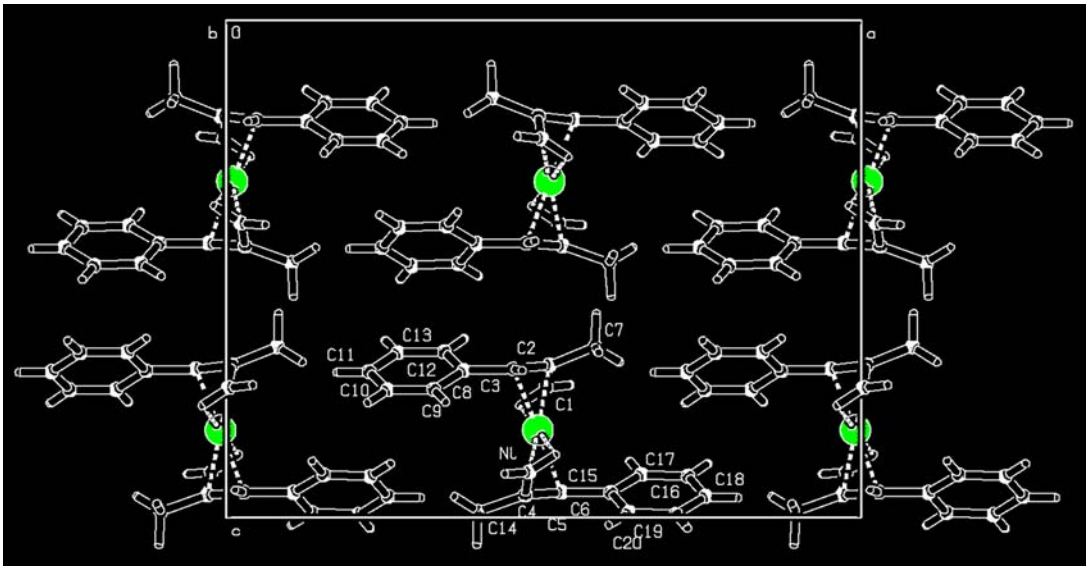

Fig. 17 Projection of a structure in the non-centrosymmetric space group Pca21, suggesting an additional center of inversion on Ni.

for this structure is shown in Fig. 18. The checkCIF report starts with an overview of some relevant data for this structure (Fig. 18a). It reports that structure was refined with SHELXL-2018/3 and that both the CIF and FCF are provided. For most displayed items, both the data as reported in the CIF and those as calculated from the content of the CIF are shown. Those values should be (close to) identical. The best choice of the formula unit is not always obvious. The choice made by the algorithm in checkCIF may differ from that of the authors. When a different formula unit has been reported, the values of Z, Z′ and M_r should be consistent with that choice. The reported residual difference map density should be similar to that calculated by checkCIF. Three sets of R, wR2 and S values are reported. The first one reports values calculated from the data in the CIF and FCF. The second set is calculated based on the observed and calculated F^2 values in the FCF. The third set are those values as reported in the CIF. All three should be consistent. A large difference may indicate that the FCF is not created in the same job where the CIF was created. The value of the Flack parameter is the one reported in the CIF. Those for Parsons and Hooft are calculated estimates.

Fig. 18b lists the various ALERTS. The first eight ALERTS are easy to address. ALERT_907 can be ignored for this racemic structure. ALERT_111 and ALERT_113 need some more work since they seem to confirm a missing inversion center within the default distance tolerances in ADDSYM. The PLATON tool ADDSYM-SHX can be used to create the input for a test refinement in the suggested new space group Pbca. That resulted in a refined structure as shown in Fig. 19 with an unsatisfactory R value of 22% and some poor displacement ellipsoids. From this, it can be concluded that this is a case of pseudo-symmetry which could also be verified by re-running ADDSYM with more strict distance tolerances. Further support for description of the structure in space group $Pca2_1$ comes from the NZ test (Fig. 20) that clearly shows a non-centrosymmetric intensity distribution. Finally, space group Pbca is not supported by the required set of systematic absences for that space group. Only two of the three glide-planes are fully supported.

(A)

```
VALIDATION REPORT FOR CURRENT CIF
PLATON/CHECK-( 90822) versus check.def version 220517, Entry: jv06a_sx
Data: validcif - Type: CIF18                    Bond Precision   C-C = 0.0041 A
Refl: validcif - Type: LIST4                                     Temp = 100 K
AuditSHELXL-2018/3
ReflnSHELXL-2018/3 (SHELDRICK, 2018)
X-ray CuKa                 R1(Int) = 0.000.  wR2/R1(Int) =  0.0.  Nref/Npar =   9.0
Cell  18.5993(6)   5.8559(2)  14.5773(4)   90          90          90
Wavelength 1.54184  Volume Reported     1587.70(9) Calculated      1587.70(9)
SpaceGroup from Symmetry P c a 21      HallP 2c -2ac              orthorhombic
                Reported P c a 21          P 2c -2ac              orthorhombic
MoietyFormula C20 H22 NI
     Reported ?
   SumFormula C20 H22 NI
     Reported C20 H22 NI
Mr          =     321.07[Calc].     321.08[Rep]      Volume/NonHatoms = 19 Ang**3
Dx,gcm-3    =       1.343[Calc].      1.343[Rep]
Z           =           4[Calc].          4[Rep]
Mu (mm-1)   =       1.656[Calc].      1.656[Rep]  Xtal Size =  0.030x0.040x0.090 mm
F000        =     680.0[Calc].      680.0[Rep]  or F000' =    669.32[Calc]
Calculated T Limits: Tmin=0.924 Tmax=0.852  Tmin'=0.852  Tmax=0.952
Measured   HKL: Reported    3307, Embedded    3307, <Mult>  1.9
Reported   Hmax=  0, Kmax=  0, Lmax=  0, Nref=    3307          , Th(max)= 76.095
Obs in FCF Hmax= 23, Kmax=  7, Lmax= 18, Nref=    3307[  1732], Th(max)= 76.095
Calculated Hmax= 23, Kmax=  7, Lmax= 18, Nref=    3328[  1734], Ratio=1.91/0.99
Reported   Rho(min) = -0.42, Rho(max) =  0.47 e/Ang**3 (From CIF)
Calculated Rho(min) = -0.38, Rho(max) =  0.42 e/Ang**3 (From CIF+FCF data)
w=1/[\s^2^(Fo^2^)+(0.0524P)^2^+0.0482P], P=(Fo^2^+2Fc^2^)/3
R= 0.0316(  3150), wR2= 0.0905(  3307), S = 1.298          (From CIF+FCF data)
R= 0.0316(  3150), wR2= 0.0905(  3307), S = 1.297          (From FCF data only)
R= 0.0316(  3150), wR2= 0.0905(  3307), S = 1.297, Npar=  193, Flack   0.51(4)
Number BIJvoet Pairs = 1575 ( 99%),          1445 Selected for:  Parsons 0.501(12)
          P3(tr) 0.000, P3(tw) 1.000, Student-T Nu =  99,  Hooft 0.500(11)
For Documentation:http://www.platonsoft.nl/CIF-VALIDATION.pdf
```

(B)

```
>>> The Following Improvement and Query ALERTS were generated - (Acta-Mode) <<<
   Format: alert-number_ALERT_alert-type_alert-level text

103_ALERT_1_A Missing _cell_measurement_reflns_used Value ....      Please Do !
104_ALERT_1_A Missing _cell_measurement_theta_min Value .....      Please Do !
105_ALERT_1_A Missing _cell_measurement_theta_max Value .....      Please Do !
699_ALERT_1_A Missing _exptl_crystal_description Value .....       Please Do !
901_ALERT_1_A No Datum for _diffrn_reflns_av_R_equivalents ...     Please Do !

025_ALERT_1_B Hmin..Lmax Data Incomplete or Missing .........      Please Check

048_ALERT_1_C MoietyFormula Not Given (or Incomplete) ........     Please Check
052_ALERT_1_C Info on Absorption Correction Method   Not Given     Please Do !
907_ALERT_2_C Flack x > 0.5. Structure Needs to be Inverted? .       0.51 Check
977_ALERT_2_C Check Negative Difference Density on H1A    .        -0.32 eA-3

069_ALERT_1_G Atom Label Without Numerical Part ..............        NI Do !
111_ALERT_2_G ADDSYM Detects New (Pseudo) Centre of Symmetry .       100 %Fit
113_ALERT_2_G ADDSYM Suggests Possible Pseudo/New  Space Group      Pbca Check
303_ALERT_2_G Full Occupancy Atom H1A       with # Connections      2.00 Check
303_ALERT_2_G Full Occupancy Atom H4A       with # Connections      2.00 Check
883_ALERT_1_G No Info/Value for _atom_sites_solution_primary .     Please Do !
912_ALERT_4_G Missing # of FCF Reflections Above STh/L=  0.600        2 Note
941_ALERT_3_G Average HKL Measurement Multiplicity .........        1.9 Low
965_ALERT_2_G The SHELXL WEIGHT Optimisation has not Converged     Please Check
978_ALERT_2_G Number C-C Bonds with Positive Residual Density.      11 Info

      ALERT_Level and ALERT_Type Summary
      ==================================
 5 ALERT_Level_A = Most Likely a Serious Problem - Resolve or Explain
 1 ALERT_Level_B = A Potentially Serious Problem - Consider Carefully
 4 ALERT_Level_C = Check. Ensure it is Not caused by an Omission or Oversight
10 ALERT_Level_G = General Info/Check that it is not Something Unexpected
```

Fig. 18 Validation output: (a) Overview of selected information about the structure determination. (b) Validation ALERT messages listing.

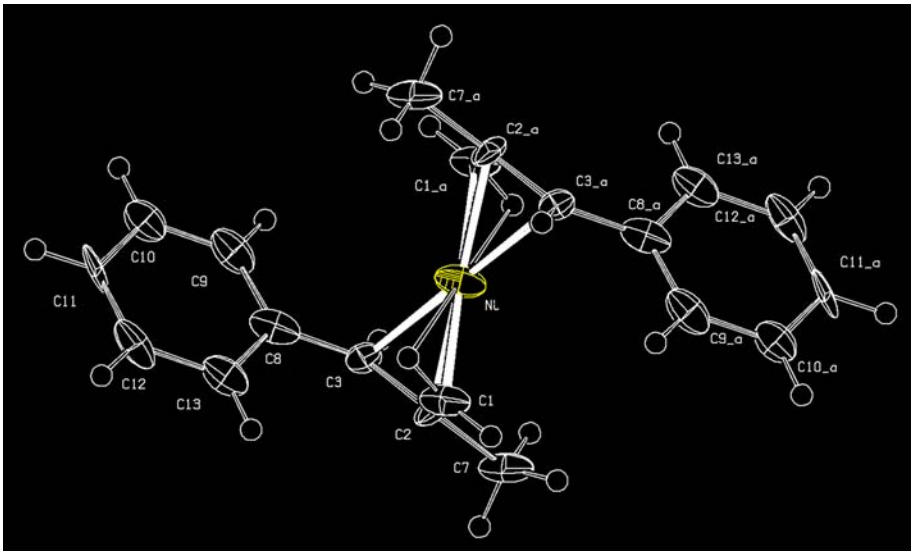

Fig. 19 Refinement result when the $Pca2_1$ structure shown in **Fig. 17** is refined in space group Pbca, based on the inclusion of a center of inversion, as suggested by ADDSYM.

This can be investigated with the SPGRfromEX [11, 4] tool. Close inspection of the Pbca structure shows that layers of molecules perpendicular to the c-axis have slightly shifted to an average position, consistent with the direction of the elongation of the ADP ellipsoids as shown in the obviously averaged structure shown in **Fig. 19**.

ALERT_977 and ALERT_303 are related. **Fig. 21** suggests agostic Ni…H interactions what would be chemically interesting when true. Inspection of the difference density map (**Fig. 22**) shows negative density (red) at the H1A and H4A atom sites, indicating that there is too much density put in the model at that site. The nearby green density maxima indicate the proper location of those hydrogen atoms. Refinement with the hydrogen atoms at the proposed positions removes both ALERTs, thus removing the agostic interaction issue.

ALERT_941 reports about low measurement multiplicity. Sufficient reflection multiplicity, i.e., the same reflection measured in different orientations multiple times, is required for a meaningful application of the multi-scan type correction for absorption with programs such as SADABS or MULABS [1, 5]. The positive and negative peaks around Ni may indicate inadequate absorption correction for that reason (**Fig. 22**).

ALERT_978 reports residual density on bonds. This generally indicates good quality data and result. There absence may indicate non-AIM type refinement, poor data or "observed" data "erroneously?" based on calculated structure factors.

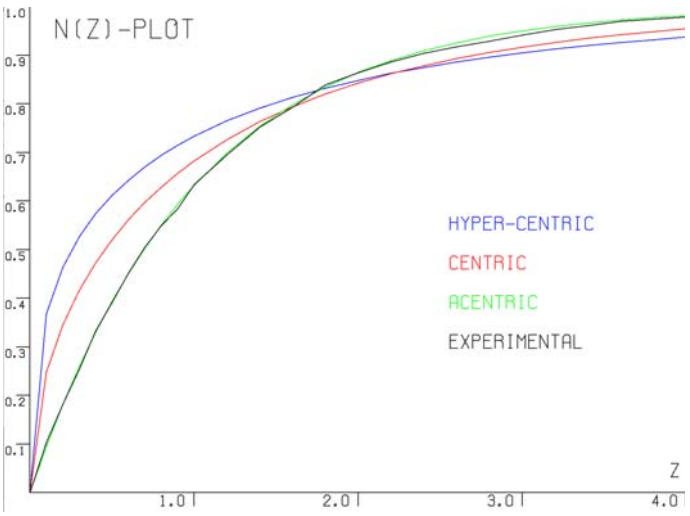

Fig. 20 NZ-Plot test showing that the investigated structure is likely non-centrosymmetric. The experimetal data based curve closely coincides the theoretical green curve for a non-centrosymmetric structure.

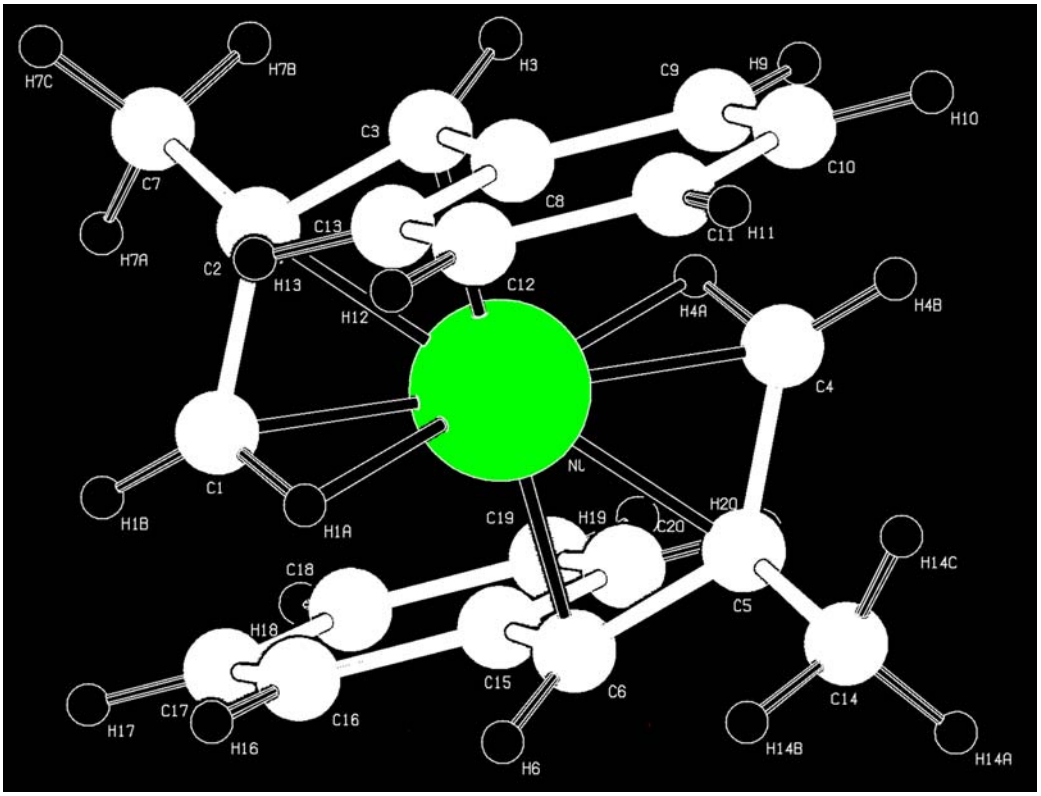

Fig. 21 PLUTON illustration showing erroneous short Ni-H contacts.

ALERT_965 suggests that the reflection weighting scheme should be optimized. The target is a GOOF = S value close to 1, both globally and as a function of intensity or resolution. The ANALofVAR [8, 6] tool provides such an overview (Fig. 23).

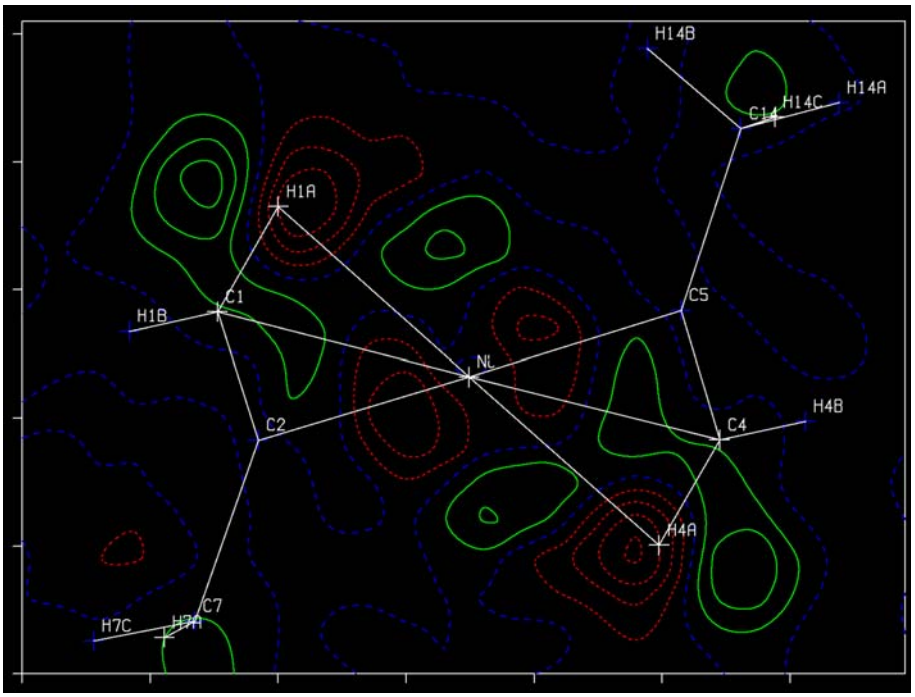

Fig. 22 Difference density map showing negative density (red) at the location where H1A and H4A are in the refined structure model and nearby positive density (green) for their correct position.

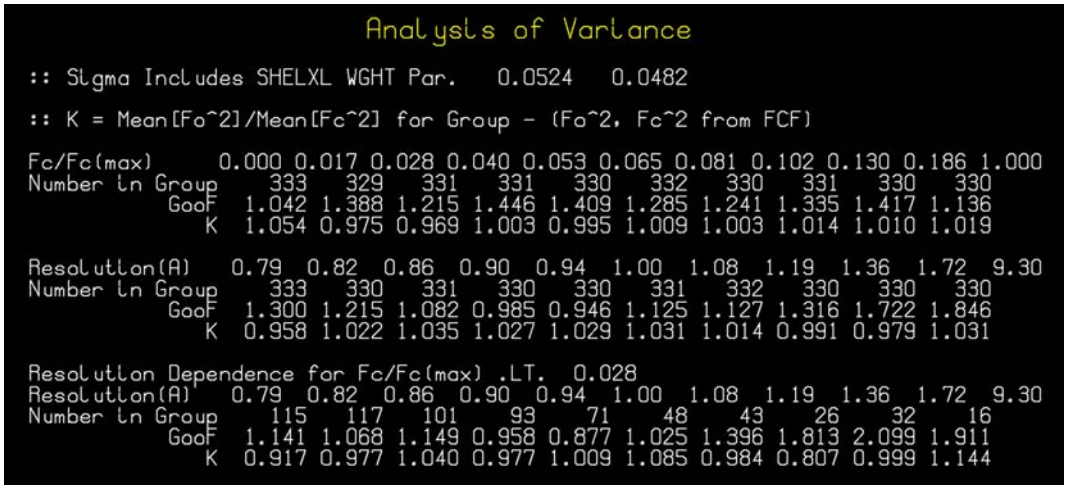

Analysis of Variance

:: Sigma Includes SHELXL WGHT Par. 0.0524 0.0482

:: K = Mean[Fo^2]/Mean[Fc^2] for Group - (Fo^2, Fc^2 from FCF)

Fc/Fc(max)	0.000	0.017	0.028	0.040	0.053	0.065	0.081	0.102	0.130	0.186	1.000
Number in Group	333	329	331	331	330	332	330	331	330	330	
GooF	1.042	1.388	1.215	1.446	1.409	1.285	1.241	1.335	1.417	1.136	
K	1.054	0.975	0.969	1.003	0.995	1.009	1.003	1.014	1.010	1.019	

Resolution(A)	0.79	0.82	0.86	0.90	0.94	1.00	1.08	1.19	1.36	1.72	9.30
Number in Group	333	330	331	330	330	331	332	330	330	330	
GooF	1.300	1.215	1.082	0.985	0.946	1.125	1.127	1.316	1.722	1.846	
K	0.958	1.022	1.035	1.027	1.029	1.031	1.014	0.991	0.979	1.031	

Resolution Dependence for Fc/Fc(max) .LT. 0.028

Resolution(A)	0.79	0.82	0.86	0.90	0.94	1.00	1.08	1.19	1.36	1.72	9.30
Number in Group	115	117	101	93	71	48	43	26	32	16	
GooF	1.141	1.068	1.149	0.958	0.877	1.025	1.396	1.813	2.099	1.911	
K	0.917	0.977	1.040	0.977	1.009	1.085	0.984	0.807	0.999	1.144	

Fig. 23 Analysis-of-Variance statistics. Values of GooF and K are expected to be close to 1.

10.15.4.3 Some common validation issues

10.15.4.3.1 Reflection dataset completeness

Two types of information are expected to be given in the CIF: (a) The completeness of the dataset at theta_max, the maximum theta value of the reflection set, (b) The theta value (theta_full) at which the dataset is essentially complete. A dataset is expected to be complete to at least 25.2° (MoKα) radiation. SHELXL reports by default the completeness at 25.2° (MoKα). A completeness ALERT will be issued when lower than 95%. Proper theta_full values where near completeness is reached can be gleaned from the <name>.ckf listing associated with the checkCIF report (Section 10.15.4). A lower than 25.2° theta_full value needs a valid justification such as no significant reflections beyond that value or experimental restriction such as data collected with high-pressure gadgets.

10.15.4.3.2 Negative or large K values

The K values in Fig. 23 are expected to be close to 1. Strongly deviating values are reported with an ALERT in the checkCIF report. The most common ones are those associated with relatively weak F_c^2 values. A value much larger than 1 may indicate unresolved twinning, model errors or integration problems. A negative value may indicate problems with the background handling.

10.15.4.3.3 Residual density peaks

The difference electron density map should be essentially clean as mentioned in Section 10.15.3.1.4. Large positive and negative peaks often appear near heavy atoms. Most of those densities are caused by inadequate correction for absorption. Such peaks on atom sites may indicate wrong atom type assignments or partial site occupation. Other causes may be disorder or twinning. The argument of diffraction ripples does not apply for difference density maps.

10.15.4.3.4 Hydrogen atoms

Hydrogen atoms are often introduced at calculated positions according to the assumed hybridization of the atom they are attached to. ALERTS will be issued when either negative or positive density is found in the difference density map on those sites. Short intermolecular contacts due to such a mis-assignment may also result in an ALERT.

10.15.5 Implementation and availability

PLATON is developed on the UNIX platforms LINUX and MacOS with graphics and GUI based on the X-Windows system. Hardcopy versions of the molecular graphics may be either PostScript or HPGL. The program is provided in source code and is easily compiled on UNIX platforms using free of charge compilers such as gfortran. For the MS-Windows platform there are two options. A compiled version with additional GUI is available from http://chem.gla.ac.uk/~louis/software/platon/. That version does not include, due to implementation issues, the System-S tool. The current WINDOWS11 platform also allows to install a virtual LINUX machine in it. In that way, a full LINUX version of PLATON can be compiled and installed as well on that platform.

Some PLATON tools rely on the availability of readily available external programs such as SHELXL, SHELXT, RASMOL and POVRAY.

Some program packages such as OLEX2, CRYSTALS and SHELXLE[35] use PLATON tools and features in the background. The same applies to IUCr/checkCIF. The latter facility includes most of the PLATON based ALERTS. The PLATON software and more details are available from http://platonsoft.nl.

10.15.6 Concluding remarks

PLATON/checkCIF validation is designed to validate mainly supposedly routine 3D structure determination reports. Powder diffraction studies are validated mainly for the reported 3D geometry. For a cautionary tale see Ref. 36. Incommensurate structure reports will need a specialist reviewer and are currently not covered by checkCIF. Similarly, the details of reports based on (quantum-mechanical) methods to address the non-spherical atomic density distribution are validated only partly.

CheckCIF is not only useful as part of the refereeing process. It should also not be used only in that late finalization stage but also at various points of the structure determination. Issues with a structure determination might be easier to address at that time than years later when submitted for publication. Not all ALERTS are errors that can be corrected. A good scientific explanation should suffice.

References

1. Groom, C. R.; Bruno, I. J.; Lightfoot, M. P.; Ward, S. C. *Acta Crystallogr.* **2016,** *B72,* 171–179.
2. Harrison, W. T. A.; Simpson, J.; Weil, M. *Acta Crystallogr.* **2010,** *E66,* e1–e2.
3. Sheldrick, G. M. *Acta Crystallogr.* **2015,** *C71,* 3–8.
4. Hall, S. R.; Allen, F. H.; Brown, I. D. *Acta Crystallogr.* **1991,** *A47,* 655–685.
5. Stewart, M.; Hall, S. R. *J. Appl. Cryst.* **1985,** *18,* 283.
6. Dolomanov, O. V.; Bourhis, L. J.; Gildea, R. J.; Howard, J. A. K.; Puschmann, H. *J. Appl. Cryst.* **2009,** *42,* 339–341.
7. Farrugia, L. J. *J. Appl. Cryst.* **2012,** *45,* 849–854.
8. Spek, A. L. *J. Appl. Cryst.* **2003,** *36,* 7–13.
9. Kroon-Batenburg, L. M. J.; Helliwell, J. R.; McMahon, B.; Terwilliger, T. C. *IUCrJ* **2017,** *4,* 87–99.
10. Palatinus, L.; Chapuis, G. *J. Appl. Cryst.* **2007,** *A60,* 604–610.
11. Sheldrick, G. M. *Acta Crystallogr.* **2015,** *A71,* 3–8.
12. Betteridge, P. W.; Carruthers, J. R.; Cooper, R. I.; Prout, K.; Watkin, D. J. *J. Appl. Cryst.* **2003,** *36,* 1487.
13. Petricek, V.; Dusek, M.; Palatinus, L. *Z. Kristallogr.* **2014,** *229* (5), 345–352.
14. Kleemiss, F.; Dolomanov, O. V.; Bodensteiner, M.; Peyerimhoff, N.; Midgley, M.; Bourhis, L. J.; Genoni, A.; Malaspina, L. A.; Jayatilaka, D.; Spencer, J. L.; White, F.; Grundkoetter-Stock, B.; Steinhauer, S.; Lentz, D.; Puschmann, H.; Grabowsky, S. *Chem. Sci.* **2021,** *12,* 1675–1692.
15. Lübben, J.; Wandike, C. M.; Hübschle, C. B.; Ruf, M.; Sheldrick, G. M.; Dittrich, B. *Acta Crystallogr.* **2019,** *A75,* 50–62.
16. Spek, A. L. *Acta Crystallogr.* **2009,** *D65,* 148–155.
17. Spek, A. L. *Inorg. Chim. Acta* **2018,** *470,* 232–237.
18. Spek, A. L. *Acta Crystallogr.* **2020,** *E76,* 1–11.
19. Le Page, Y. *J. Appl. Cryst.* **1987,** *20,* 264–269.
20. Johnson, C. K. *ORTEP-II*, Oak Ridge National Laboratory: Oak Ridge, TN, ORNL-3794, 1965.
21. Hirshfeld, F. L. *Acta Crystallogr.* **1976,** *A32,* 239–244.
22. LePage, Y. *J. Appl. Cryst.* **1982,** *15,* 255–259.
23. Zimmermann, H.; Burzlaff, Z. *Z. Kristallogr.* **1985,** *170,* 231–246.
24. Marsh, R. E. *Acta Crystallogr.* **2004,** *B60,* 252–253.
25. Marsh, R. E. *Acta Crystallogr.* **2005,** *B61,* 359.
26. Kitaigorodskii, A. I. *Molecular Crystals and Molecules*, Academic Press: New York, 1973.
27. Spek, A. L. *Acta Crystallogr.* **2015,** *C71,* 9–18.
28. Linden, A. *Acta Crystallogr.* **2020,** *E76,* 765–775.
29. Flack, H. D. *Acta Crystallogr.* **1983,** *A39,* 876–881.
30. Parsons, S.; Flack, H. D.; Wagner, T. *Acta Crystallogr.* **2013,** *B69,* 249–259.
31. Hooft, R. W. W.; Straver, L. H.; Spek, A. L. *J. Appl. Cryst.* **2008,** *41,* 96–103.
32. Hooft, R. W. W.; Straver, L. H.; Spek, A. L. *Acta Crystallogr.* **2009,** *A65,* 319–321.
33. Hooft, R. W. W.; Straver, L. H.; Spek, A. L. *J. Appl. Cryst.* **2010,** *43,* 665–668.
34. Li, J.; Burgett, W. G.; Esser, L.; Amezcua, C.; Harran, P. G. *Angew. Chem.* **2001,** *113,* 4906–4909.
35. Hübschle, C. B.; Sheldrick, G. M.; Dittrich, B. *J. Appl. Cryst.* **2011,** *44,* 1281–1284.
36. Schlesinger, C.; Fitterer, A.; Buchsbaum, C.; Habermehl, S.; Chierotti, M. R.; Nervi, C.; Schmidt, M. U. *IUCrJ* **2022,** *9,* 406–424.

Всё для Победы! НАРОДНЫЙ ФРОНТ
https://pobeda.onf.ru/
LET'S HELP THE RUSSIA

10.16 Ab initio structure solution using synchrotron powder diffraction

James A. Kaduk, Department of Physics, North Central College, Naperville, IL, United States; and Department of Chemistry, Illinois Institute of Technology, Chicago, IL, United States

© 2023 Elsevier Ltd. All rights reserved.

10.16.1	**Introduction**	**446**
10.16.2	**Indexing**	**447**
10.16.3	**Solve by analogy**	**448**
10.16.3.1	Hexaaquairon(II) trifluoromethanesulfonate, $Fe(H_2O)_6(CF_3SO_3)_2$	448
10.16.3.2	$Al_4H_2(SO_4)_7(H_2O)_{24}$	450
10.16.3.3	$(NH_4)Fe(CO_3)(OH)_2$	450
10.16.3.4	$(NH_4)Fe_2S_3$	450
10.16.3.5	$Fe(BF_4)_2(H_2O)_6$	454
10.16.3.6	$[Fe(H_2O)_6]_2[FeF_6][FeF_4(H_2O)_2]$	454
10.16.3.7	$Na(NH_4)Mo_3O_{10}(H_2O)$	454
10.16.3.8	*bis*(Ethylammonium) tetrachloroiron(II)	457
10.16.4	**Reciprocal space methods**	**457**
10.16.4.1	Direct methods	457
10.16.4.1.1	Hydrated sodium aluminate, $NaAlO_2(H_2O)_{5/4}$	457
10.16.4.1.2	Potassium aluminium borate, $K_2Al_2B_2O_7$	459
10.16.4.1.3	Magnesium hydrogen citrate, $Mg(H_2C_6H_5O_7)_2$	461
10.16.4.1.4	Calcium hydrogen citrate dihydrate, $[Ca(HC_6H_5O_7)(H_3CH_5O_7)(H_2O)](H_2O)$	461
10.16.4.1.5	Calcium citrate hexahydrate, $Ca_3(C_6H_5O_7)_2(H_2O)_6$	461
10.16.4.2	Charge flipping	462
10.16.4.2.1	Antimony oxalate hydroxide, $Sb(C_2O_4)(OH)$	466
10.16.4.2.2	Tamsulosin hydrochloride, $C_{20}H_{29}N_2O_5SCl$	466
10.16.4.2.3	$Fe_{25}Sn_{28}Ti_{47}$	466
10.16.5	**Real space methods**	**466**
10.16.6	**Hybrid methods – Monte Carlo simulated annealing**	**469**
10.16.6.1	$Na_{1-x}Ge_{3+z}$	471
10.16.6.2	$MoO_2(O_2)(H_2O)\cdot H_2O$	471
10.16.6.3	$(CH_3)_3AsO(H_2O)_2$	471
10.16.6.4	$[Ba_3(C_6H_5O_7)_2(H_2O)_4](H_2O)$	475
10.16.6.5	$M(C_8H_4O_4)(H_2O)_2$, M = Mg, Mn, Fe, and Co	475
10.16.7	**Stealth and guile?**	**475**
10.16.7.1	Diammonium 2,6-naphthalenedicarboxylate	475
10.16.7.2	Poly(tyrosol carbonate), $(C_2H_4C_6H_4CO_3)_n$	475
10.16.8	**Microcrystals/polycrystals**	**478**
10.16.9	**Resonant diffraction**	**480**
10.16.10	**Accuracy and precision**	**480**
Acknowledgments		**481**
References		**481**
Further reading		**484**
Relevant websites		**484**

Abstract

The ways of solving crystal structures ab initio using synchrotron X-ray powder diffraction data are illustrated, primarily via examples. Since indexing (determining the unit cell from the powder pattern) can be a bottleneck, common indexing algorithms are described. With a unit cell, lattice matching techniques can be used to identify structural analogs, and avoid the ab initio solution problem. Examples of structure solution using reciprocal space techniques (direct methods and charge flipping), real space techniques (crystal structure prediction), and hybrid techniques (Monte Carlo simulated annealing) are provided, as well as examples using model building. The possibilities of using microcrystals and polycrystals are described. An example of resonant scattering is given. The accuracy and precision which can be expected from synchrotron powder crystallography are summarized.

10.16.1 Introduction

Knowledge of a material's crystal structure permits understanding, computing, and rationalizing its chemical and physical properties. A single crystal experiment is generally considered the "gold standard" for structural characterization, but when single crystals are not available, powder diffraction can be a good "Plan B." Most materials in commerce are polycrystalline, so when structures of real materials need to be determined (especially in situ and/or *in operando*), powder diffraction is the only option.

Of the 250,343 crystal structures in the Inorganic Crystal Structure Database (ICSD[1]), 74,705 are experimental structures determined using X-ray powder diffraction data. The number of powder structures per year generally varies between 1000 and 1500 (Fig. 1). These database entries include variable-temperature studies and structures solved by analogy, so the true number of unique structures is lower. The number of powder organic crystal structures archived in the Cambridge Structural Database[2] is smaller. Checking "exclude powder structures" yields 1,153,527 of the 1,155,595 total structures, or 2068 hits. Doing an all-text search on "powder" yields 969 hits. The true number of powder structures is the CSD is almost certainly higher, but is only a small fraction of the contents of the CSD. The number of organic/organometallic/coordination complex structures in the CSD determined using powder data starts to increase only in the last 15 years (Fig. 1), indicating that organic powder crystallography is a relatively-new field.

Although many structures are solved using laboratory X-ray powder diffraction data, synchrotron radiation almost always makes the process easier, and can amply repay the extra investment to carry out an experiment at a national user facility. Synchrotron radiation permits experiments at higher reciprocal space resolution (narrower peaks, when the specimen permits), higher real-space resolution (smaller samples), and finer time resolution (more-rapid measurements). Access to synchrotron beamlines is generally obtained through a proposal system, though some beamlines run a mail-in program, which makes access relatively rapid and easy. Dedicated powder diffraction beamlines divide into two classes: high-resolution, with multiple analyser crystals/detectors, and high-throughput, with area or strip detectors. Consultation with beamline staff before an experiment is always helpful.

In this Chapter, I summarize through examples the variety of structural results that can be obtained using synchrotron powder diffraction (although a few examples involve laboratory experiments), and illustrate the process of powder crystallography.

In a powder diffraction experiment, the three dimensions of reciprocal space are compressed into a one-dimensional powder diffraction pattern. Ultimately the overlap of powder diffraction peaks causes loss of information; there is less information in a powder pattern than in a single crystal dataset, limiting the accuracy and precision of the results which can be obtained. But since the physics underlying the experiment is well-understood, considerable information can still be gleaned.

The process of solving a crystal structure ab initio using powder diffraction data has been liked to traversing a maze[3] (Fig. 2). A radiation probe is used to collect data. Determining the unit cell (indexing) is often a bottleneck, so some discussion of this process is provided below. In general, individual peak integrated intensities, obtain by Le Bail and/or Pawley methods, are used to solve the

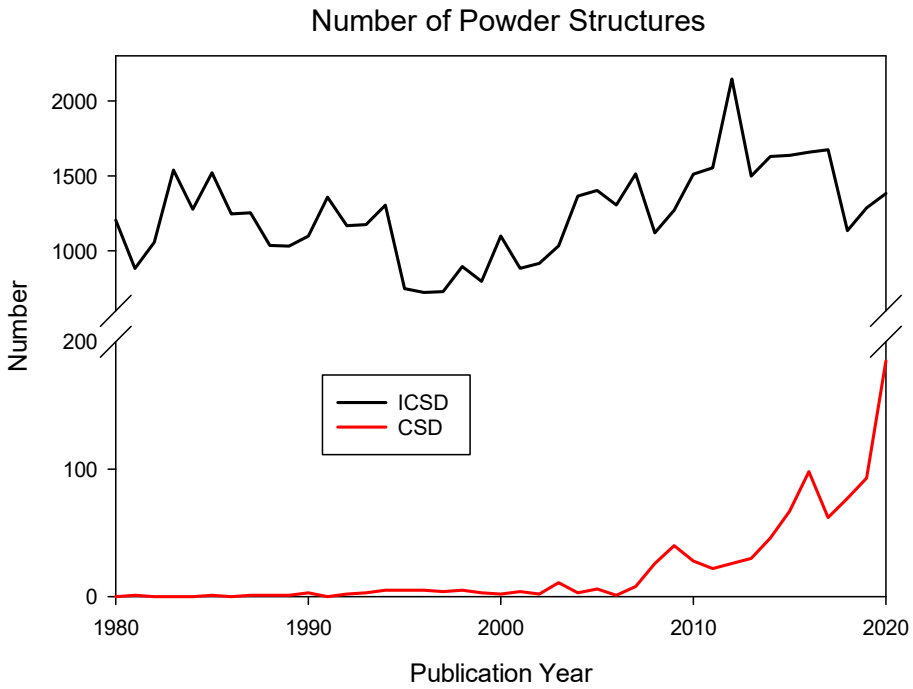

Fig. 1 Number of crystal structures from powder data in the Inorganic Crystal Structure Database (ICSD, black) and Cambridge Structural Database (CSD, red) per year.

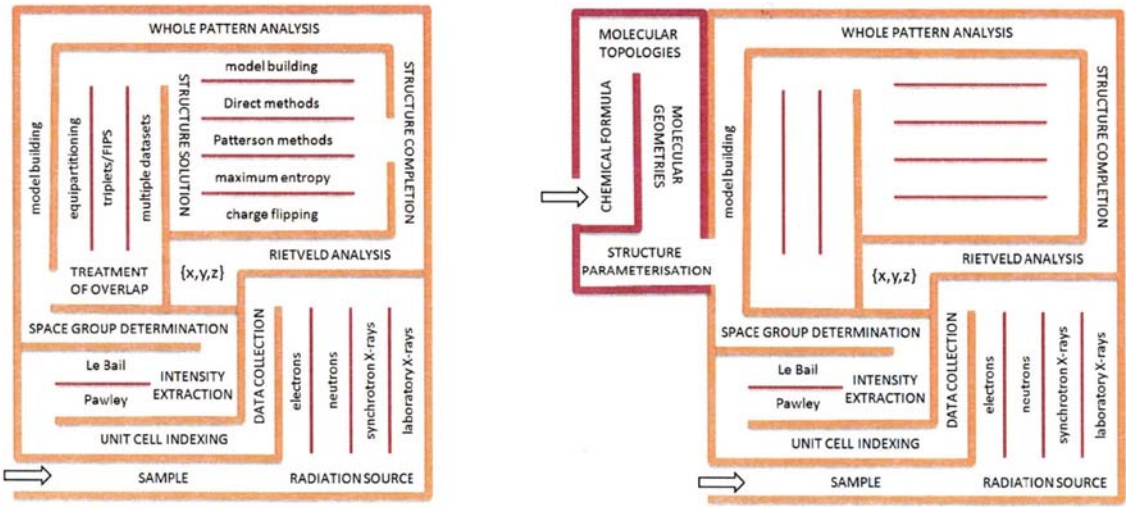

Fig. 2 (A) The maze of strategies associated with the determination of crystal structures from powder diffraction data (after[4]) and (B) the modified "global optimization" maze showing the double start point and simplification of the principal maze. From David, W. I. F. Real-Space Methods for Structure Solution from Powder-Diffraction Data: Application to Molecular Structures. *International Tables for Crystallography Volume H: Powder Diffraction*. Chester: International Union of Crystallography, Chapter 4.3, 2019.

structure. This speeds the process compared to using the raw data. Several methods, discussed below, can be used to solve the structure. Sometimes only a partial structure is obtained, so it must be completed.

Ab initio structure solution is an example of a global minimization problem (Fig. 3). For a given compound, there are many terrible crystal structures (whose calculated diffraction patterns yield poor agreement to the experimental data). Generally, there are several potentially reasonable crystal structures, which occur at the bottoms of very narrow and deep wells in a hypersurface. The challenge of structure solution is to find the global minimum (best structure), rather than being trapped in a local minimum.

Refinement of crystal structures using powder diffraction data is done by the Rietveld method, and will not be discussed here in detail. This methodology is well-established, but we often need to supplement the experimental diffraction data with chemical information, in the form of constraints and restraints.

10.16.2 Indexing

As noted in Fig. 2, the first step in structure solution after data collection is indexing – determining the lattice constants. Without a unit cell and space group, it hard to make further progress. Since the lattice parameters determine the positions of the peaks in a powder pattern, indexing uses the peak positions (not the intensities) to deduce the lattice parameters. The space group (or potential space groups) is determined by automated and manual analysis of the systematic absences. Indexing is strongly-dependent on

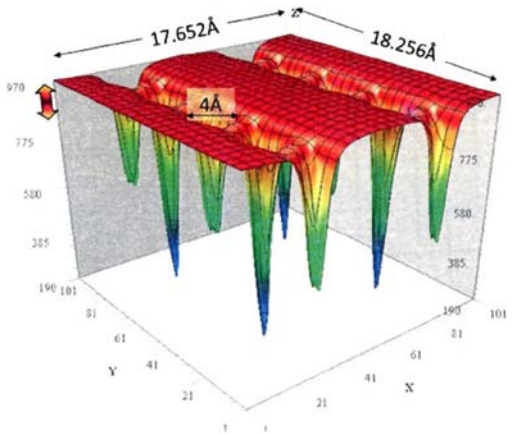

Fig. 3 A 2D section of the χ^2 hypersurface (quality of fit of observed and calculated powder patterns) as a function of x and z translations of a fragment. From David, W. I. F. Real-Space Methods for Structure Solution from Powder-Diffraction Data: Application to Molecular Structures. *International Tables for Crystallography Volume H: Powder Diffraction*. Chester: International Union of Crystallography, Chapter 4.3, 2019.

accurate peak positions. The algorithms are generally less-sensitive to random errors, but a systematic error of even 0.02° 2θ can prevent indexing. Thus, care should be taken to obtain accurate peak positions, perhaps including the use of an internal standard and/or a thin specimen. High-resolution multi-analyser synchrotron powder diffractometers eliminate such systematic errors as displacement and transparency. Higher resolution makes accurate peak location easier. Thus, synchrotron patterns are generally much easier to index than those from laboratory diffractometers. More times than I care to admit, I thought I knew the unit cell before taking a sample to the synchrotron, but only obtained the correct cell from the synchrotron data (!).

Even though at most six lattice parameters (for a triclinic lattice) need to be determined, indexing is a harder problem than it seems. Only the first (lowest-angle) 20–30 peaks contain really useful information, because they are less-sensitive to small changes in cell dimensions and higher-angle peaks are often multiplets, even though they may seem to be single peaks.

If the positions of all of the peaks in a powder pattern can be explained by a single unit cell, this is strong evidence than the sample is phase-pure. Conversely, attempting to index the pattern of a mixture on a single unit cell is hopeless. Determining the unit cell is a necessary prelude to determining the crystal symmetry and structure; indexing has been called "a gateway technology." Knowledge of the unit cell permits phase identification by lattice matching techniques, as illustrated in the following section. Traditional methods for phase identification use both the intensities and positions of the peaks in a powder pattern. Atoms vary less in size than they do in scattering power, so the unit cells of isostructural compounds can be more similar than the intensities of peaks in their powder patterns.

Indexing methods are summarized in Altomare et al.[5] The three most-common methods (because they are embedded in many commercial and free software packages) are zone indexing, successive dichotomy, and index heuristics. Other methods are described in this reference.

The zone indexing method derives from ideas of Runge[6] and Ito,[7,8] was generalized by de Wolff,[9,10] and enhanced by Visser.[11] The ITO program uses the law of cosines to search for zones (reciprocal lattice planes, which contain lattice points). The *d*-spacings of low-angle peaks are used to suggest potential vector magnitudes. In combination with small integers, these are used to calculate potential angles between lattice vectors. Angles which occur frequently identify potential crystallographic zones. Since lattice planes must intersect in a lattice vector, common zone vectors are used to derive inter-zone angles, and thus lattices.

The peak positions in a powder pattern are determined by the lattice parameters. If instead of single values, we apply ranges to the potential lattice parameters, we obtain ranges of potential peak positions. The search proceeds from high to low symmetry, and low to high cell volumes, successively incrementing the lattice parameters. If the observed peaks all fit in at least one range, the ranges are halved, and the comparison is done again, up to seven times (successive dichotomy). If the proposed ranges do not explain the peak positions, the lattice parameters are incremented, and the process is repeated. The DICVOL algorithm was first developed by Louër and Louër,[12] and has been extended many times.[13–16]

The index heuristics strategy searches for the correct unit cell by a trial-and-error approach (TREOR), by assigning Miller indices to the lowest-angle peak positions (the number of peaks varies with the crystal system), calculating the unit cell, and seeing if this unit cell explains the positions of higher-angle peaks. Since low-angle peaks have low Miller indices, maximum limits are placed on trial *hkl*. The method was first proposed by Werner,[17] then refined,[18] and made more robust and effective by Altomare et al.[19–21]

A potential unit cell should have a high figure of merit (as described in[5]; basically, this indicates the agreement between the observed and expected peak positions). A match of the cell to that of a compound with similar chemistry provides additional confidence. If the systematic absences correspond to a common space group and the cell volume indicates an integer number of formula units, confidence is further increased. Obtaining the same solution from multiple programs (using very different algorithms) further increases that chances of the cell being correct. Ultimately, the true test of the cell is if it permits solution and refinement of the crystal structure.

10.16.3 Solve by analogy

Once a unit cell has been obtained, it is wise to search in the appropriate database for chemically-sensible analogs which have a similar unit cell. Often such an analog can provide a good-enough model to begin a Rietveld refinement of the new compound. Lattice matching provides a powerful alternative (to traditional search-match) for phase identification, and saves the labor of ab initio structure solution for cases in which it is truly necessary. Many protein structures are solved by "isomorphous replacement," which is perhaps a fancier name for this technique.

10.16.3.1 Hexaaquairon(II) trifluoromethanesulfonate, $Fe(H_2O)_6(CF_3SO_3)_2$

A pilot plant reactor, which contained a supported triflic acid catalyst, developed severe corrosion after it was emptied. The responsible engineer wanted to know if the deposit contained iron triflate.[22] Analysis of the powder pattern of the as-received deposit indicated the presence of the typical corrosion phases magnetite, hematite, wüstite, goethite, and lepidocrocite, but the major peaks of the pattern were not matched by any database entry. Since triflate is a well-known "noncoordinating" anion, it seemed likely that an iron triflate would be soluble. The majority of the deposit was indeed soluble in ethanol. The slurry was filtered to remove the oxides, and allowed to evaporate, which yielded a white solid with the same diffraction pattern.

A portion of the white solid was blended with NIST 640b silicon internal standard, to obtain accurate peak positions for indexing. The pattern could be indexed[11] on a C-centered monoclinic cell having $a = 18.6415(14)$, $b = 6.9291(5)$, $c = 6.5938(5)$ Å,

$\beta = 104.742(6)^\circ$, and $V = 823.68(10)\text{Å}^3$. A reduced cell search against the old NIST Crystal Data Identification File yielded a good match to hexaaquavanadium(II) trifluoromethanesulfonate[23]. Today we would do the search in the Cambridge Structural Database, the Inorganic Crystal Structure Database, and/or the Powder Diffraction File. A Rietveld refinement (Fig. 4A) was carried

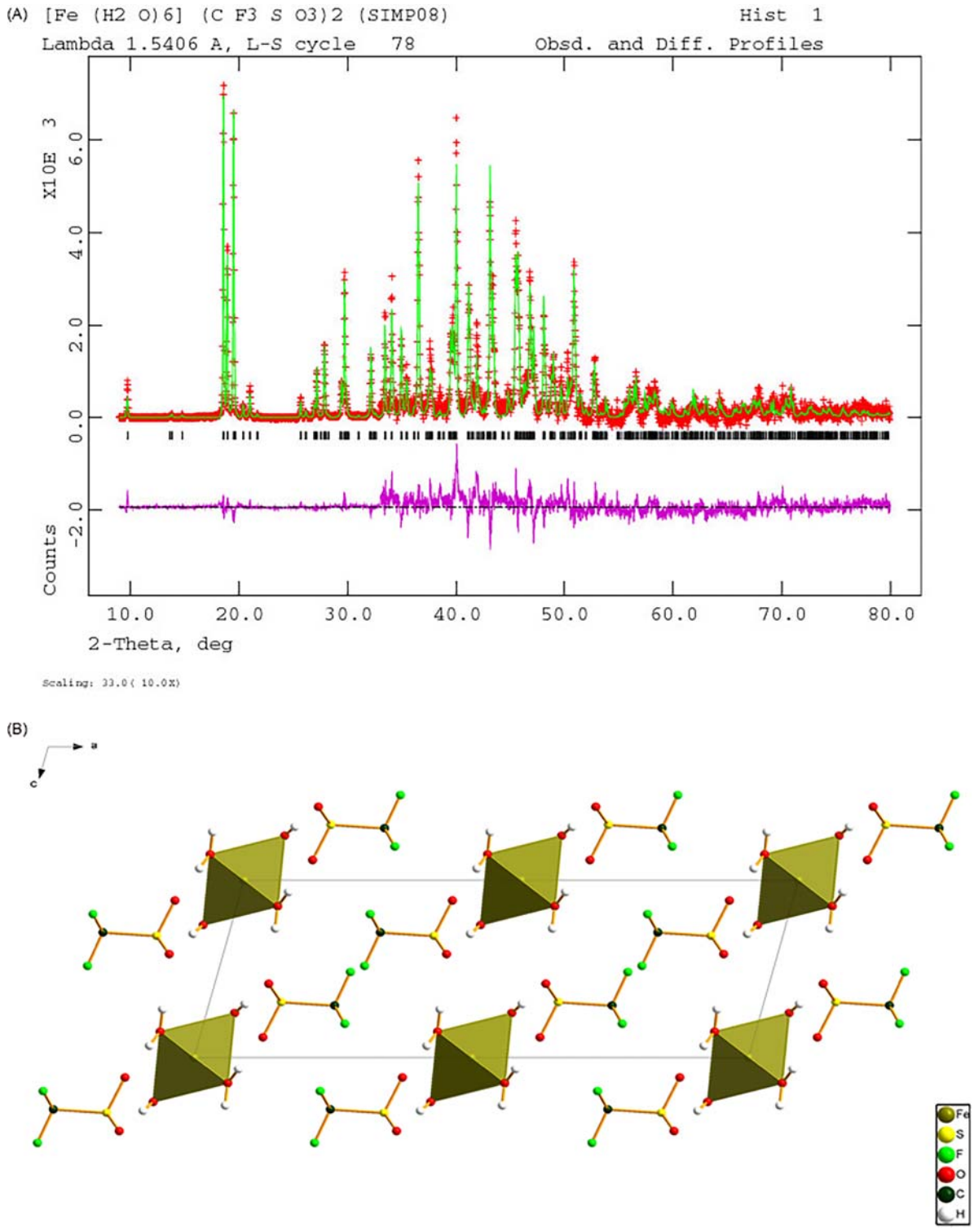

Fig. 4 (A) The Rietveld plot for the refinement of hexaaquairon(II) trifluoromethanesulfonate, $[Fe(H_2O)_6](CF_3SO_3)_2$. The red crosses represent the observed data points, and the green line is the calculated pattern. The magenta curve is the error plot. The vertical scale has been multiplied by a factor of $10\times$ for $2\theta > 33.0^\circ$. (B) The crystal structure of hexaaquairon(II) trifluoromethanesulfonate, $[Fe(H_2O)_6](CF_3SO_3)_2$, viewed down the *b*-axis. Image generated with Diamond.[24]

out, replacing the V with Fe. The crystal structure (Fig. 4B) is dominated by hydrogen bonding and the packing of the trifluoromethyl groups.

With this phase identification by analogy we could conclude that the presence of residual triflic acid, combined with exposure to atmospheric moisture, can cause steel to corrode rapidly, with the formation of iron oxides, hydrous oxides, and hexaaquairon(II) trifluoromethanesulfonate.

10.16.3.2 $Al_4H_2(SO_4)_7(H_2O)_{24}$

The black tar recovered from a pump seal at BP's Texas City refinery was surprisingly crystalline, although it did contain amorphous components which could be removed by washing with acetone. Traditional search/match techniques identified three crystalline phases: $Al_4H_2(SO_4)_7(H_2O)_{24}$ (Powder Diffraction File entry 00-022-0006), szomolnokite $FeSO_4(H_2O)$ (01-074-1332), and alunogen $Al_2(SO_4)_3(H_2O)_{17}$ (00-026-2010). At the time, the crystal structure of $Al_4H_2(SO_4)_7(H_2O)_{24}$ had not been reported, so before a Rietveld refinement for quantitative phase analysis could be carried out, the structure had to be derived.[25]

Both the ICSD and PDF include a data item "structure type," ANX. By the rules for defining the structure type, $Al_4H_2(SO_4)_7(H_2O)_{24}$ has ANX = A4B7X52: four A cations of one type, seven B cations of another type, and 52 X anions. Searching the ICSD for this structure type yielded only one hit, $Cr_4H_2(SO_4)_7(H_2O)_{24}$. Even though the powder patterns (00–022-0006 and 01–072-0981) were different, it seemed reasonable that Cr^{3+} and Al^{3+} compounds might be isostructural, and the Cr compound proved to be a good model to begin the Rietveld refinement (Fig. 5A). None of the three structures included hydrogen positions, so approximate locations were derived by analysis of potential hydrogen bonding patterns, and accurate positions were determined later by DFT optimizations. The refined structure (Fig. 5B) shows that the compound is more accurately formulated as $[Al(H_2O)_6][Al(H_2O)_5(SO_4)](H_3O)_2(SO_4)_5$. After this work was done, a crystal structure was reported.[26]

Examination of old literature showed that $Al_4H_2(SO_4)_7(H_2O)_{24}$ forms around 50–60 °C under acid-rich conditions, and is *metastable*. Sulfuric acid leaked into this pump, and reacted with both the aluminium housing and steel pump parts. The problem was thus probably a current one, that needed immediate remediation, rather than waiting for the next scheduled unit shutdown.

10.16.3.3 $(NH_4)Fe(CO_3)(OH)_2$

After the liquid ammonia supply to one of BP Chemicals' plants had changed, deposits began to form in a liquid ammonia heat exchanger. Such deposits reduce the efficiency of the exchanger, and thus affect the process economics. The deposits consisted of mixtures of phases,[25] including PDF entry 00–022-0052, "$(NH_4)_2Fe_2(OH)_4(CO_3)_2(H_2O)$."[27]

The compound was prepared almost phase-pure according to the method of Dvořák and Feitknecht. The pattern could be indexed[11] on a C-centered orthorhombic unit cell having $a = 6.6154(6)$, $b = 12.0639(10)$, and $c = 6.0263(5)$ Å. A traditional reduced cell search of the Crystal Data Identification File yielded no hits. Both from the process chemistry and the synthesis, we could reasonably assume that the compound contained C, H, N, and O. A search of the ICSD for (inorganic) compounds containing these elements and having a C-centered orthorhombic unit cell yielded 25 hits. Most of these could be discarded, as they were cyanide complexes, but among them was "NH4-dawsonite," $(NH_4)Al(CO_3)(OH)_2$[28] (dawsonite is $NaAl(CO_3)(OH)_2$), which had been reported as a corrosion product of aluminium by Erdös and Altorfer.[29] This compound crystallizes in C*mcm*, with $a = 6.618(3)$, $b = 11.944(5)$, and $c = 5.724(2)$ Å, and thus represented a plausible structural model for the Fe compound.

This Al compound was a suitable model to begin the Rietveld refinement (Fig. 6A). The original authors had thus misformulated their compound. The crystal structure (Fig. 6B) consists of chains (parallel to the *c*-axis) of edge-sharing octahedral Fe atoms. The equatorial plane is composed of four bridging hydroxyl groups, and the axial positions are occupied by bridging carbonate anions.

Synthesis of $(NH_4)Fe(CO_3)(OH)_2$ requires CO_2 and H_2O, neither of which should have been present in the liquid ammonia feed system. After careful examination of the system for leaks (and finding none), we concluded that these deposits were a start-up problem, rather than a failure of the system.

10.16.3.4 $(NH_4)Fe_2S_3$

A black solid from a pump screen (filter) in an alkylation unit in one of BP's refineries was highly-crystalline, and contained minor concentrations of many typical corrosion phases: sulfur, pyrite, pyrrhotite, magnetite, and hematite. The peaks of the major phase, however, were a good match to those of rasvumite, KFe_2S_3 (04-011-6818). This was very strange, as there should be no potassium in a refinery stream (and there was none detected by bulk chemical analysis). When the Mason jar containing the sample was opened, there was a strong smell of ammonia. Infrared spectroscopy revealed strong bands from the ammonium cation. Remembering that NH_4^+ and K^+ are about the same size, and can form isostructural compounds, rasvumite then seemed to be a good initial model for an isostructural $(NH_4)Fe_2S_3$.

This model permitted a reasonable Rietveld refinement (Fig. 7A), which yielded a quantitative phase analysis of this not-unreasonable refinery corrosion deposit. The structure (Fig. 7B) consists of double chains of edge-sharing Fe octahedra, with ammonium ions between the chains.

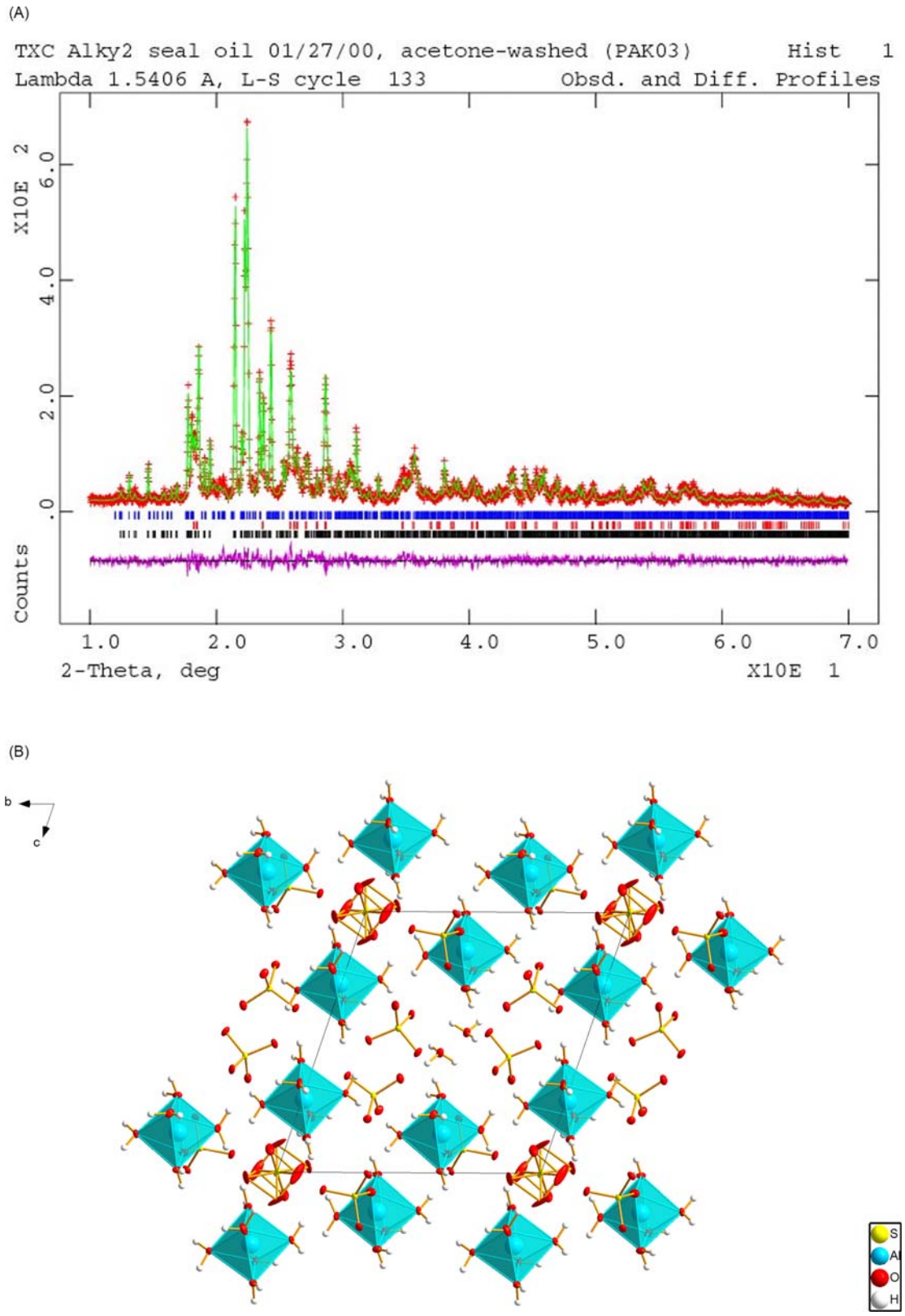

Fig. 5 (A) The Rietveld plot for the refinement of an alkylation unit pump deposit. The red crosses represent the observed data points, and the green line is the calculated pattern. The magenta curve is the error plot. The rows of black, red, and blue tick marks indicate the reflection positions for $Al_4H_2(SO_4)_7(H_2O)_{24}$, szomolnokite $FeSO_4(H_2O)$, and alunogen $Al_2(SO_4)_3(H_2O)_{17}$, respectively. (B) The crystal structure of $Al_4H_2(SO_4)_7(H_2O)_{24}$, viewed down the *a*-axis. Image generated with Diamond.[24]

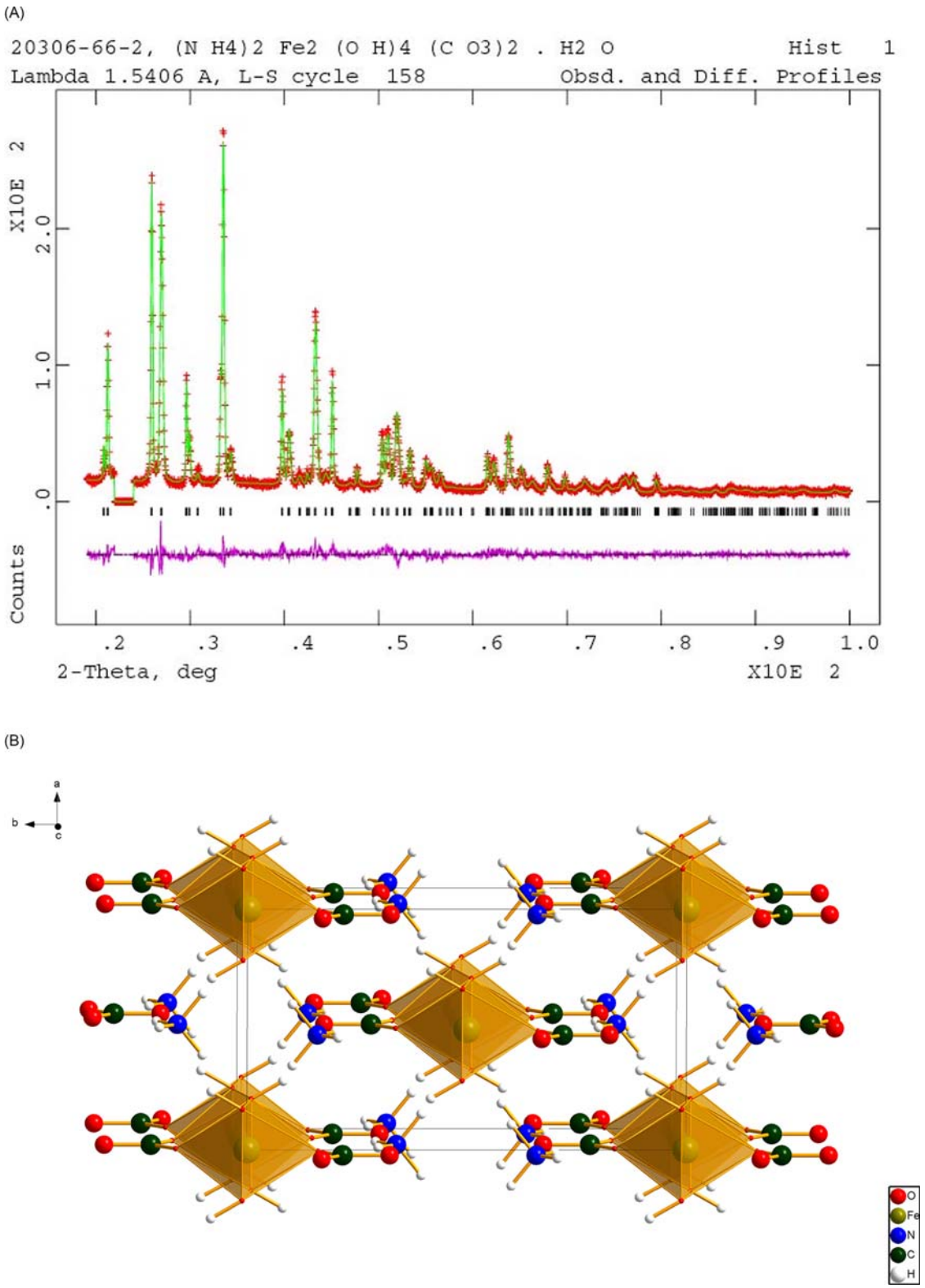

Fig. 6 (A) The Rietveld plot for the refinement of $(NH_4)Fe(CO_3)(OH)_2$. The red crosses represent the observed data points, and the green line is the calculated pattern. The magenta curve is the error plot. The row of black tick marks indicates the calculate reflection positions. (B) The crystal structure of $(NH_4)Fe(CO_3)(OH)_2$, viewed down the *c*-axis. Image generated with Diamond.[24]

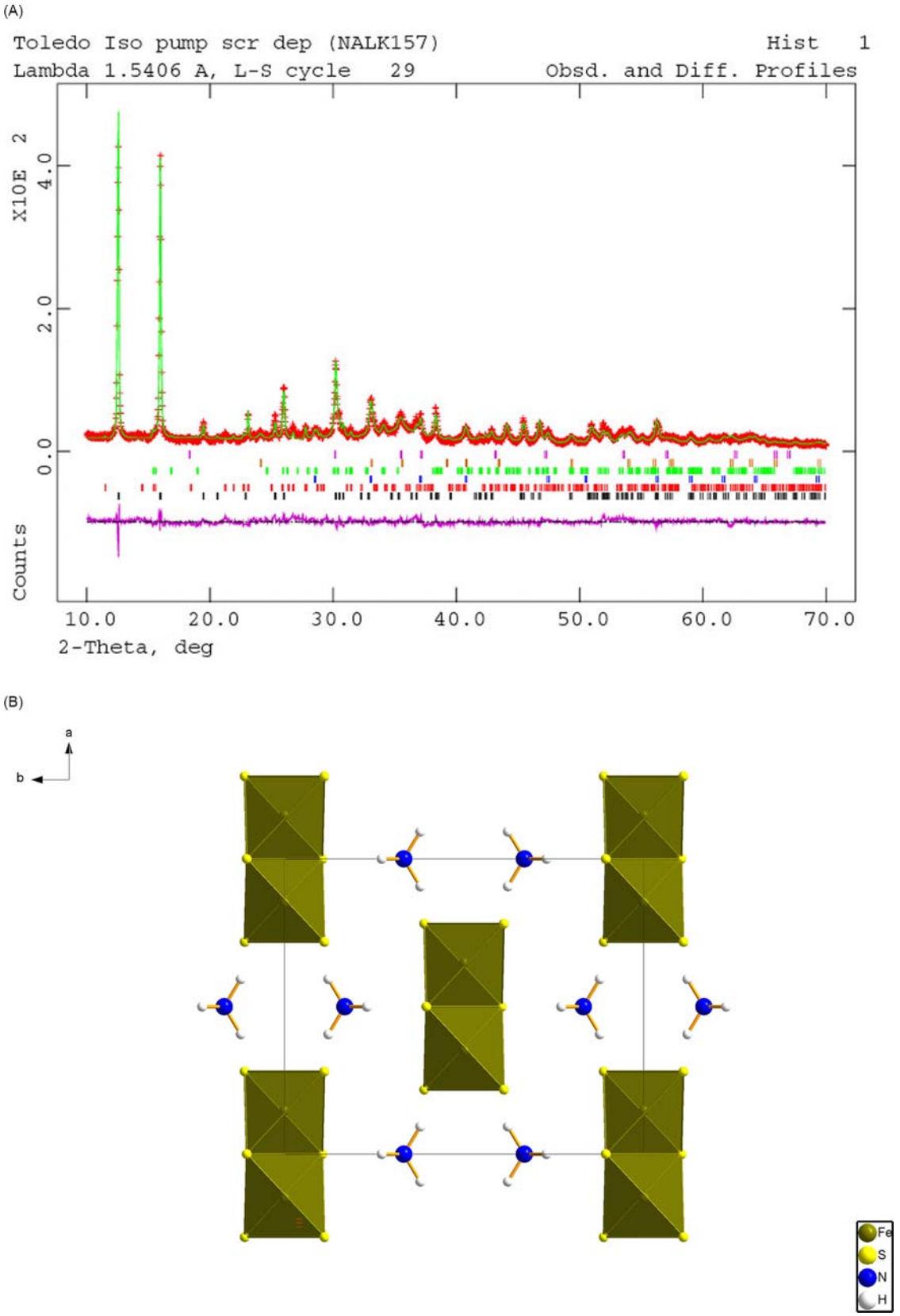

Fig. 7 (A) The Rietveld plot for the refinement of an alkylation unit pump screen deposit. The red crosses represent the observed data points, and the green line is the calculated pattern. The magenta curve is the error plot. The rows of black, red, blue, green, brown, and magenta tick marks

10.16.3.5 $Fe(BF_4)_2(H_2O)_6$

Linear alpha-olefins (LAO) are short/medium hydrocarbon chains with a double bond at the 1,2-position. They are useful as comonomers in polyolefins, and in many other applications. LAO are made commercially using a BF_3 catalyst, which needs to be decomposed at the end of the process stream. Since this process generates HF, many "interesting" corrosions deposits can be observed. One such deposit was mainly boric acid, with a few extra impurity peaks. Most of the boric acid could be washed away with methanol, leaving white and red hygroscopic solids after evaporation of the solution.

The powder pattern of the white solid showed that it still contained a small amount of sassolite, $B(OH)_3$, but the major phase was not matched by any entry in the PDF. Most of the peaks could be indexed[11] on a primitive orthorhombic cell having $a = 7.686$, $b = 13.286$, $c = 5.376$ Å, and $V = 548.95$ Å^3. Visser's Ito program (run natively) is good at using the reduced cell relationships found in Volume A of the International Tables for Crystallography to suggest possible higher symmetry. In this case, the program suggested that the true cell was probably hexagonal, with $a = 15.34$ and $c = 5.38$ Å. In this case, however, the program was wrong. A reduced cell search of both cells in the ICSD (using the large tolerance of 0.5 Å) yielded no hits. A similar search in the old NIST Crystal Data Identification File yielded hexagonal unit cells for several transition metal tetrafluoroborate and perchlorate hexahydrates.[30] Since these cells were determined using film data from a 9 cm diameter camera, they should be considered only approximate.

The PDF contains an experimental pattern for $Fe(BF_4)_2(H_2O)_6$ (00-021-0427) and a few other tetrafluoroborates, but no crystal structures. This pattern did not match the observed one well. The NBS*LATTICE program used by the CDIF (Crystal Data Identification File) provided the ability to search for sub- and super-cells; this capability is now included in the PDF. A sub-cell search yielded the structure of $Fe(ClO_4)_2(H_2O)_6$, which was reported in space group $P6_3mc$ with $a = 7.815$ and $c = 5.13$ Å.[31] I converted this structure to space group P1, built a 2x2x1 supercell (to correspond to the suggested cell), and removed every other Fe atom, because the comments in the ICSD entry indicated that the structure was determined in the supergroup of a three-component twin. Analysis of the resulting structure using PLATON[32] suggested that the space group was $Pmn2_1$. A search on this orthorhombic cell in the ICSD yielded entry 24,250 for $Mg(ClO_4)_2(H_2O)_6$,[33] so this structure was used as the initial model for the Rietveld refinement (Fig. 8A). (It probably would have been easier to solve the structure ab initio!)

The crystal structure (Figs. 8B) looked reasonable, but the BF_4 U_{iso} were high (0.159 and 0.095 Å^2). It turns out that this compound, and several other transition metal tetrafluoroborate hexahydrates, melt close to room temperature, and that such high displacement coefficients are typical for compounds within 5 K of their melting temperature.

10.16.3.6 $[Fe(H_2O)_6]_2[FeF_6][FeF_4(H_2O)_2]$

The pattern of the red solid isolated from the LAO deposit matched well that of PDF entry 00-045-0883, $Fe_2F_5(H_2O)_7$.[34] This entry reports a primitive triclinic unit cell with $a = 8.849$, $b = 8.988$, $c = 6.582$ Å, $\alpha = 97.07$, $\beta = 95.17$, and $\gamma = 103.47°$. A reduced cell search in the ICSD (0.5 Å tolerance) yielded several C-centered monoclinic $[M(H_2O)_6][MF_5(H_2O)]$, but these patterns did not match the observed pattern. Among the hits was $ZnInF_5(H_2O)_7$. The Zn^{2+} and In^{3+} were plausible analogs for Fe^{2+} and Fe^{3+}, so a Rietveld refinement (Fig. 9A) was begun from this model. The refined structure (Fig. 9B) shows that the compound is more-correctly formulated as $[Fe(H_2O)_6]_2[FeF_6][FeF_4(H_2O)_2]$.

10.16.3.7 $Na(NH_4)Mo_3O_{10}(H_2O)$

This compound was isolated during development of Mo recycling procedures for accelerator-based production of ^{99}Mo.[36] The synchrotron pattern (measured at beamline 08B1–1 at the Canadian Light Source) could be indexed using DICVOL06[37] on a primitive orthorhombic cell having $a = 13.5570$, $b = 9.3063$, and $c = 7.6188$ Å. CheckCell[38] suggested space groups $Pnam$ and $Pna2_1$ as equally-plausible options. A reduced cell search in the ICSD (using an unusually large tolerance of 3% of the longest cell dimension) yielded the structure of diammonium trimolybdate, $(NH_4)_2Mo_3O_{10}$.[39] The observed lattice parameters were also reasonably similar to those of orthorhombic $Na(NH_4)Mo_3O_{10}(H_2O)$ observed by Förster et al.,[40] with $a = 9.25$, $b = 7.58$, and $c = 13.47$ Å.

Since the exact composition was uncertain, structure solution was carried out with FOX using both space groups and three combinations of cations: two Na^+, two NH_4^+, and a mixed cation composition. The mixed cation compositions yielded clearly superior results, but both space groups yielded comparable solutions, the $Pnma$ structure was chosen as it yielded comparable agreement factors with fewer parameters.

Rietveld refinement (Fig. 10A) was performed with GSAS. The crystal structure (Fig. 10B) is characterized by edge-sharing molybdate chains running parallel to the b-axis. The cations and water molecules provide links between the chains.

indicate the calculated reflection positions of $(NH_4)Fe_2S_3$, sulfur, pyrite, pyrrhotite, hematite, and magnetite. (B) The crystal structure of $(NH_4)Fe_2S_3$, viewed down the c-axis. Image generated with Diamond.[24]

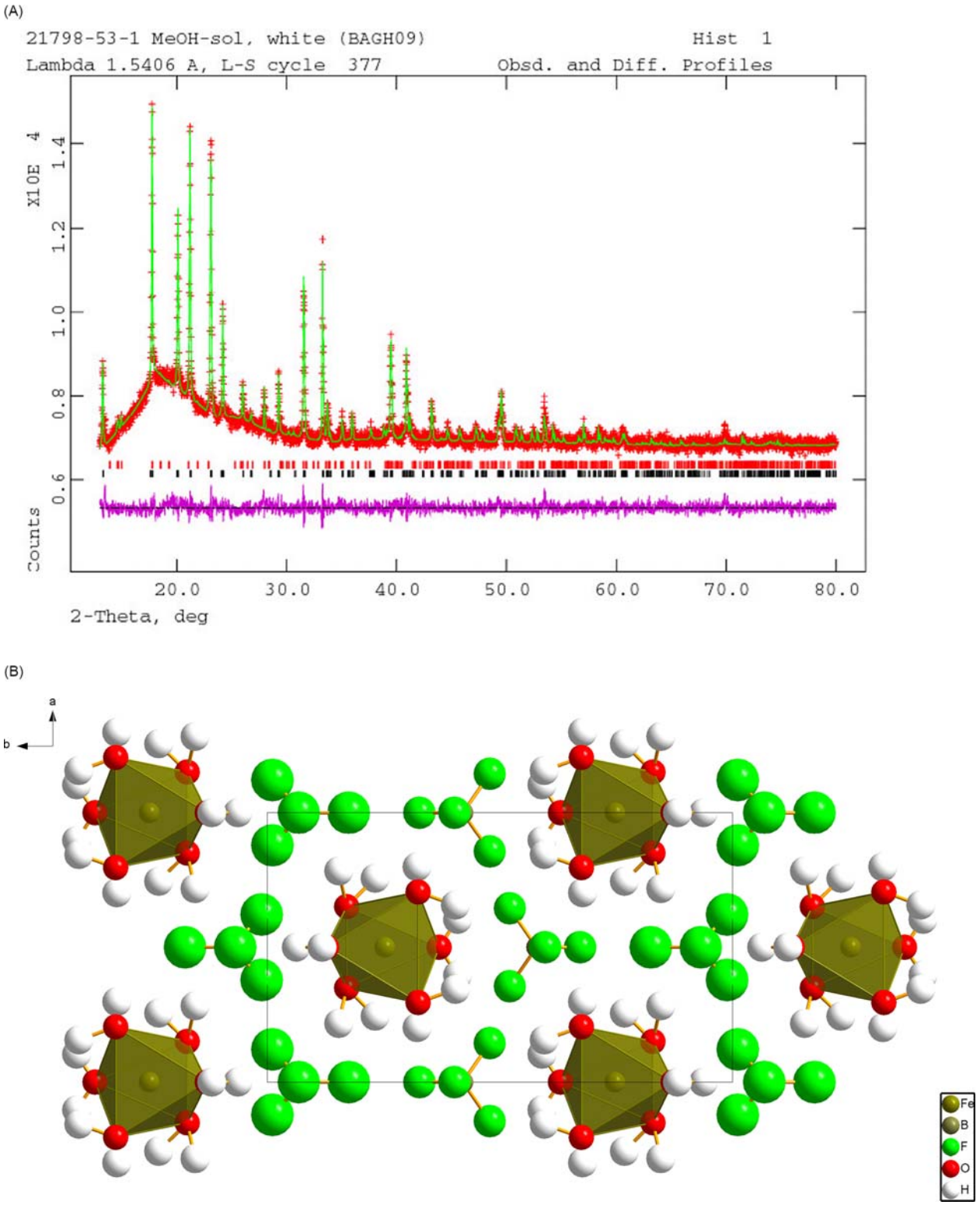

Fig. 8 (A) The Rietveld plot for the refinement of $[Fe(H_2O)_6](BF_4)_2$. The red crosses represent the observed data points, and the green line is the calculated pattern. The magenta curve is the error plot. The rows of black and red tick marks indicate the reflection positions for $[Fe(H_2O)_6](BF_4)_2$ and sassolite, $B(OH)_3$, respectively. (B) The crystal structure of $[Fe(H_2O)_6](BF_4)_2$, viewed down the *c*-axis. Image generated with Diamond.[24]

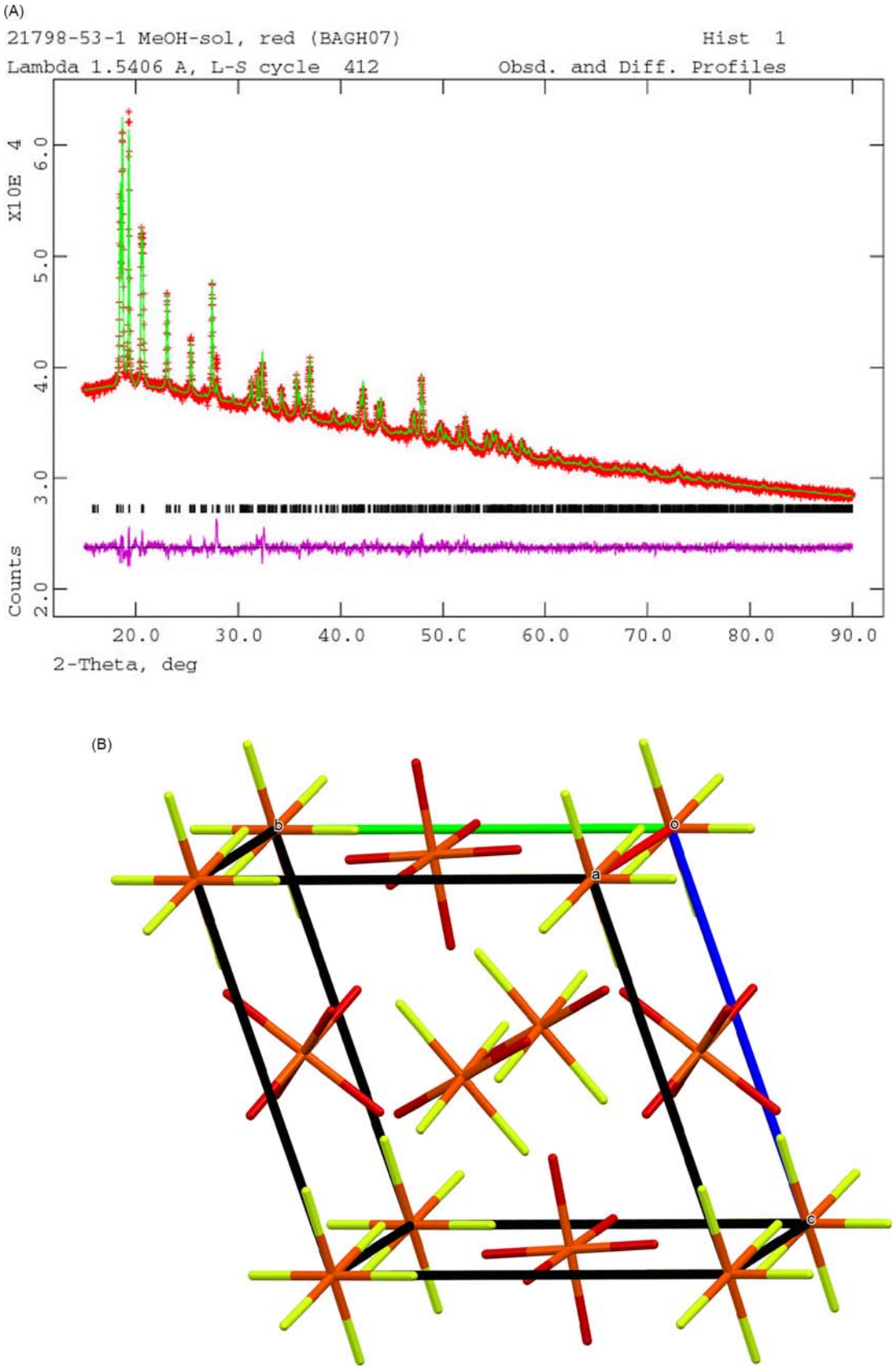

Fig. 9 (A) The Rietveld plot for the refinement of $[Fe(H_2O)_6]_2[FeF_6][FeF_4(H_2O)_2]$. The red crosses represent the observed data points, and the green line is the calculated pattern. The magenta curve is the error plot. The row of black tick marks indicates the calculated reflection positions. (B) The

10.16.3.8 *bis*(Ethylammonium) tetrachloroiron(II)

The powder pattern of a gray deposit isolated from the head end of a vapor recovery compressor in a commercial polyolefins unit did not match any entry in the PDF.[42] The appearance of the raw pattern indicated the presence of preferred orientation. Since preferred orientation affects only the intensities but not the positions of the diffraction peaks, lattice matching techniques can be useful in identifying oriented materials.

The pattern could be indexed[11] on a primitive orthorhombic unit cell having $a = 7.3291(6)$, $b = 7.2603(7)$, $c = 21.7544(9)$ Å, and $V = 1157.59$ Å^3. A default search of the CDIF yielded no hits, but increasing the tolerances on the cell edges from the default 0.1 Å to 0.3 Å yielded a match to the low-temperature γ-form of bis(ethylammonium) tetrachloromanganese(II).[43] The coordinates were retrieved from the CSD,[2] and proved to be a suitable model for the Rietveld refinement (Fig. 11A). This Fe compound had been synthesized previously by Mostafa and Willet,[44] but its structure had not been reported.

The structure (Fig. 11B) consists of single corner-sharing ruffled layers of $FeCl_6$ octahedra parallel to the *ab*-plane. The layers are separated by bilayers of ethylammonium cations. The layers resemble perovskite layers.

10.16.4 Reciprocal space methods

Reciprocal space methods use the diffraction data (without assumptions about the chemical structure) using these steps:

(1) The unit cell is assumed to be known; the pattern is indexed. There may be ambiguity about the space group, in which all of the possibilities may need to be explored.
(2) The structure factor amplitude associated with each reflection is derived from the intensity. Two common methods for intensity extraction are the Pawley and Le Bail methods.[45] Ultimately overlap of peaks limits the accuracy of intensity extraction.
(3) The phases of the structure factors are estimated by methods which use the experimental amplitudes.[46–49]
(4) An electron density map is computed by the inverse Fourier transform of the structure factors (amplitudes and phases) and interpreted as a collection of atoms.

Although reciprocal space methods include the Patterson function,[50] and some Patterson ideas have been incorporated into direct methods,[51] as well as maximum entropy methods,[52] most reciprocal space powder structure solutions have been carried out using direct methods and charge flipping.

10.16.4.1 Direct methods

10.16.4.1.1 Hydrated sodium aluminate, $NaAlO_2(H_2O)_{5/4}$

Hydrated sodium aluminate, $NaAlO_2(H_2O)_{5/4}$, is an important industrial chemical, used in water treatment systems and also as a convenient source of aluminium in synthetic applications, such as the synthesis of zeolites. Although powder diffraction data had been reported, the crystal structure had not until it was solved using synchrotron powder data.[53] Both laboratory and synchrotron patterns (from beamline X3B1 at NSLS at Brookhaven National Laboratory) could be indexed on a primitive tetragonal unit cell with $a = 10.53396(4)$, $c = 5.33635(3)$ Å, $V = 592.14$ Å^3, and $Z = 8$. Manual analysis of the systematic absences suggested possible space groups P-42_1m or P42_12. Solution in both was attempted using EXPO2014, and only P-42_1m was successful.

A Le Bail fit was carried out using GSAS[54] to obtain 357 structure factor amplitudes ($d_{min} = 0.83$ Å). This limit was chosen, because visually it appeared that peak overlap was not too severe beyond this point. For a single crystal dataset with this resolution, the structure would solve easily. Overlap of peaks (some peaks that appeared to be single were really multiplets) ultimately limited the accuracy of the extracted intensities. These intensities were used to create a SHELX "hklF 4" pseudo-single crystal data file. Solution by direct methods yielded one peak in the *E*-map which was stronger than the others. This was assigned as the Al atom, as that is the heaviest atom in the structure. Refinement by least squares and calculation of a difference Fourier map yielded two peaks near the Al; the peak-Al distances were ~1.74 Å, and the peak-Al-peak angle was ~109°. At this point, knowledge (from ^{27}Al MASNMR) that the Al coordination was tetrahedral permitted manual addition of the remaining two O atoms of the tetrahedral coordination structure. This 5-atom model was sufficient to permit location of the Na atom and the O atoms of the water molecules in difference Fourier maps, and begin Rietveld refinement (Fig. 12A) using the powder data. The positions of 3 of the 4 independent H atoms could be deduced by analysis of potential hydrogen bonding patterns, but the last could only be located confidently by neutron powder diffraction using a deuterated sample (Fig. 12B). The sample contained three "impurities": a Si internal standard, corundum from the grinding elements in the micronizing mill used to prepare the powder, and thermonatrite, $Na_2CO_3(H_2O)$ (a product of reaction with the atmosphere).

crystal structure of $[Fe(H_2O)_6]_2[FeF_6][FeF_4(H_2O)_2]$, viewed approximately down the *a*-axis. Hydrogen atoms have been omitted for clarity. Image generated by Mercury.[35]

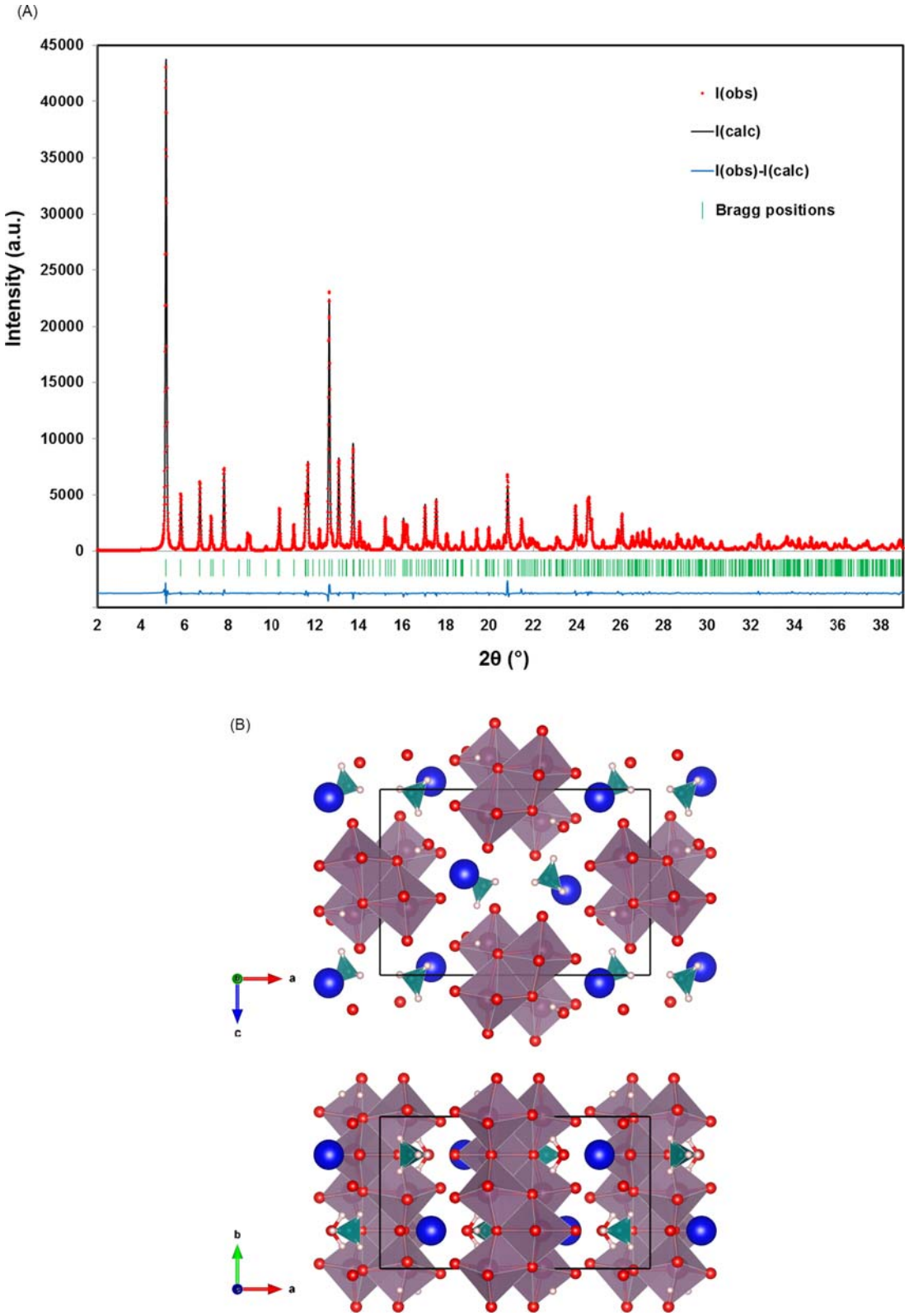

Fig. 10 (A) A plot illustrating the final Rietveld refinement of $Na(NH_4)Mo_3O_{10}\cdot H_2O$ obtained with GSAS. (B) The crystal structure of $Na(NH_4)Mo_3O_{10}\cdot H_2O$, viewed along the *b*-axis (top) and *c*-axis (bottom). The polyhedra and atom types can be identified by color including NH_4 (green tetrahedra), MoO_6 (purple octahedra), Na (dark blue), hydrogen (pink) and O (red). The unit cell is outlined in black. The figure was prepared with VESTA.[41] From Reid, J. W.; Kaduk, J. A.; Olson, J. A. The Crystal Structure of $Na(NH_4)Mo_3O_{10}\cdot H_2O$. *Powder Diffr.* **2017**, *32,* 140–147.

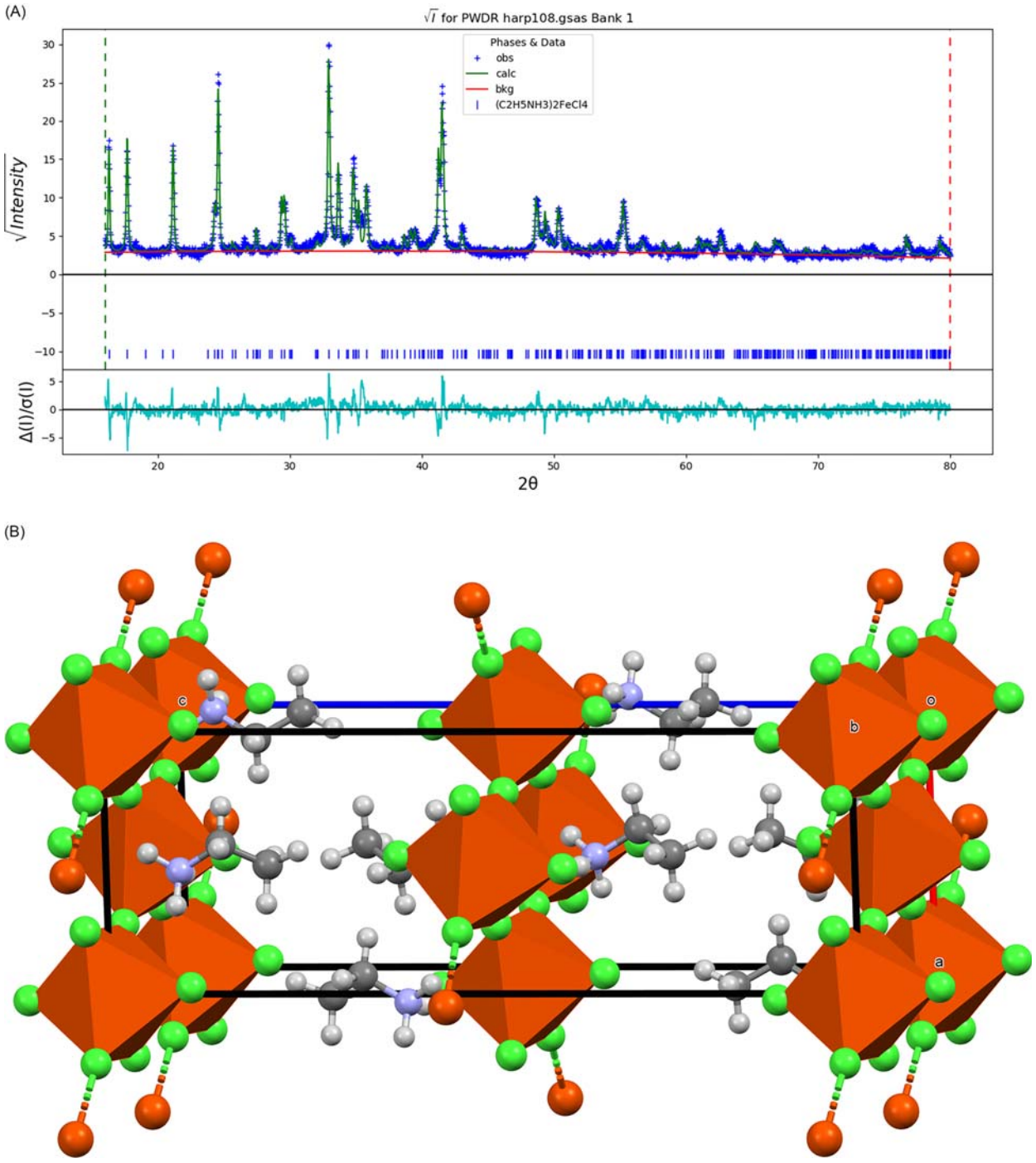

Fig. 11 (A) The Rietveld plot for the refinement of bis(ethylammonium) tetrachloroiron(II). The blue crosses represent the observed data points, and the green line is the calculated pattern. The vertical scale is the square root of intensity. The cyan curve is the normalized error plot. The row of blue tick marks indicates the calculated reflection positions. (B) The crystal structure of bis(ethylammonium) tetrachloroiron(II), viewed approximately down the *a*-axis. Image generated by Mercury.[35]

10.16.4.1.2 Potassium aluminium borate, $K_2Al_2B_2O_7$

Crystalline $K_2Al_2B_2O_7$ occurs in the K_2O-Al_2O_3-B_2O_3 phase diagram near a black amorphous semiconducting phase. We[55] hoped that knowledge of the crystal structure would provide insight into the structure of the amorphous phase and the mechanisms of conductivity. Both laboratory and synchrotron (X3B1 at NSLS) patterns could be indexed on a very high quality trigonal/hexagonal unit cell having $a = 8.55802(2)$, $c = 8.45576(3)$ Å, $V = 536.328$ Å^3, and $Z = 3$. No systematic absences were observed, limiting the possible space groups to 16, in 5 different Laue classes. In all of the Laue classes but 6/mmm, there are inequivalent reflections

(A)

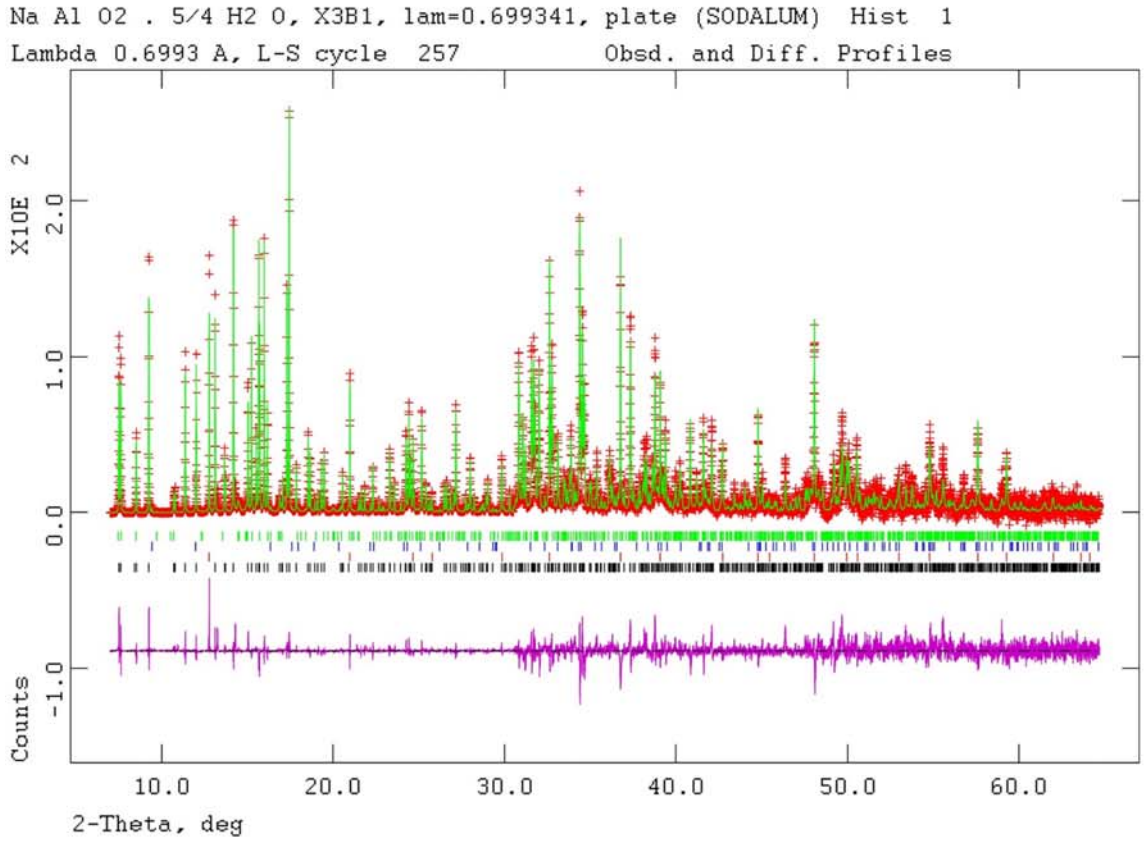
Na Al O2 . 5/4 H2 O, X3B1, lam=0.699341, plate (SODALUM) Hist 1
Lambda 0.6993 A, L-S cycle 257 Obsd. and Diff. Profiles
X10E 2
2.0
1.0
0.0
-1.0
Counts
10.0
20.0
30.0
40.0
50.0
60.0
2-Theta, deg
Scaling: 30.5(10.0X) 47.5(20.0X)

(B)

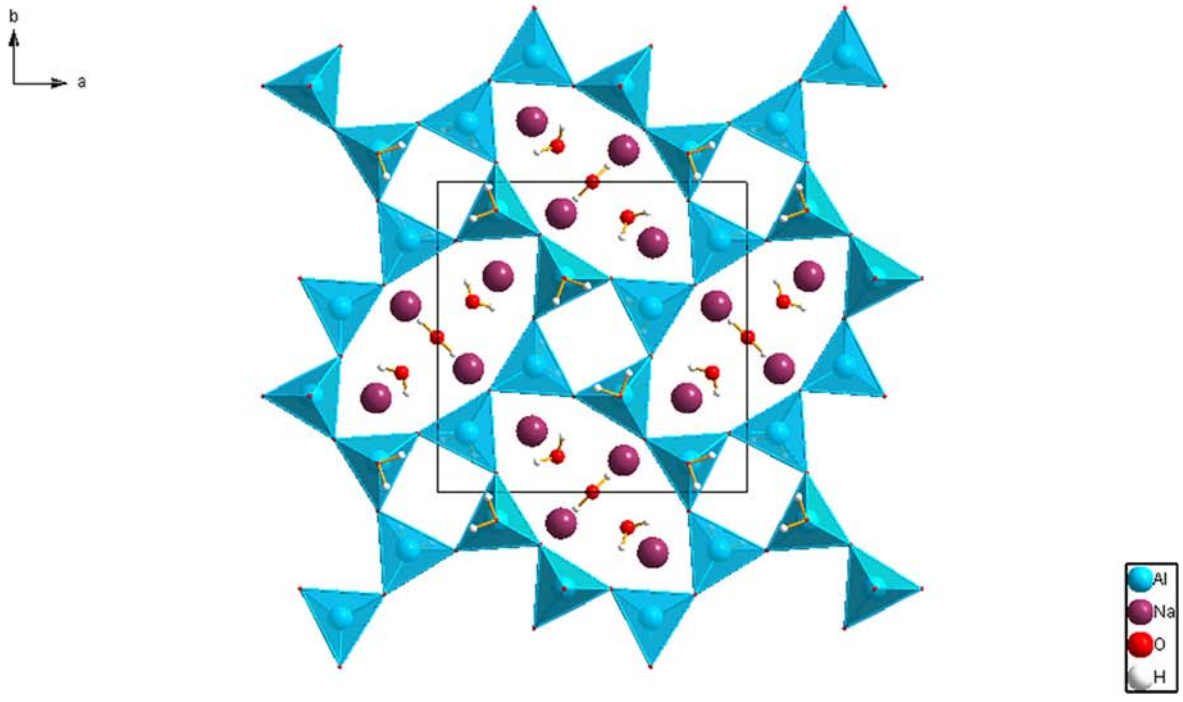
b
a
Al
Na
O
H

which overlap exactly, making extraction of accurate intensities difficult. Many reflections which would be absent in a rhombohedral unit cell were absent or very weak in the observed pattern, suggesting the likely presence of pseudosymmetry, and that the structure solution would be difficult. Magic angle spinning NMR indicated that the Al atoms were tetrahedral and that the B coordination was trigonal.

Consideration of the coordination requirements of the cations and the approximate number of atoms in the unit cell suggested that a 6-fold rotation axis was unlikely. Attempts to solve the structure with the laboratory pattern in space groups P-*62m* and P-*6m2* suggested a hexagonal array of heavy atoms, but all attempt to locate additional atoms were unsuccessful. The strategy followed, therefore, was to solve and refine the structure in the lowest symmetry possible space group, P3, and seek additional symmetry elements later. A Le Bail extraction of the synchrotron pattern yielded 426 structure factor amplitudes ($d_{min} = 0.96$ Å). These structure factors were used to create a SHELX "hklf 4" pseudo-single crystal data file. Attempts to solve the structure by direct methods were unsuccessful, but a Paterson synthesis suggested the presence of a K atom at the origin and an additional K atom at 1/3,2/3,0.5148. Successive cycles of least squares refinement and difference Fourier maps gradually yielded the remaining atoms. The structure was refined using GSAS.[54] One of the B atoms was non-planar (sum of O-B-O angles = 330°) and the Al-O-Al angles in the Al_2O_7 units were 180°. These unusual geometrical features suggested that the space group was incorrect.

The structure was examined for the presence of additional symmetry elements by application of the MISSYM program of the NRCVAX system[56]; today we would use PLATON.[32] A number of additional symmetry elements were found to relate the K, Al, and B atoms, but when the default tolerances were applied to all atoms, no additional symmetry was detected. Increasing the tolerances slightly suggested the presence of additional 2-fold axes parallel to [010], [100], and [110], and thus that the space group was P*321*. Refinement of this model yielded more-satisfactory results, but a large displacement coefficient suggested that one of the O atoms was disordered off of a 3-fold axis. This disordered model was used for the final refinement (**Fig. 13**A). The crystal structure (**Fig. 13**B) consists of a 3-dimensional network of corner-sharing BO_3 triangles and Al_2O_7 units.

10.16.4.1.3 Magnesium hydrogen citrate, $Mg(H_2C_6H_5O_7)_2$

Although traditional (single crystal) direct methods tools can be used for ab initio powder structure solution, it is better to use tools optimized for powder diffraction. These include EXPO2014[57] and XLENS.[51] Both contain features intended to overcome some of the limits imposed by limited data and overlap.

The crystal structure of bis(dihydrogencitrato)magnesium, $Mg(H_2C_6H_5O_7)_2$, was solved by direct methods (EXPO2014,[57]) using synchrotron powder diffraction data collected at beamline 11-BM[58–60] at the Advanced Photon Source, Argonne National Laboratory.[61] The sample was obtained by dissolving the scale (magnesian calcite, $Ca_{0.85}Mg_{0.16}CO_3$) from a home water still in aqueous citric acid. This compound was the last to crystallize after evaporating at ambient conditions for 5 months. It proved difficult to index the laboratory pattern, though in retrospect the correct cell was included in the list of suggestions by DICVOL06.[14] The synchrotron pattern was indexed on a primitive monoclinic unit cell with N-TREOR[57]: $a = 23.24944(8)$, $b = 10.97739(3)$, $c = 5.92449(1)$ Å, $\beta = 97{,}186(3)°$, $V = 1500.267(6)$ Å^3, and $Z = 4$. The systematic absences determined the space group as $P2_1/c$. The structure (**Fig. 14**A) was solved by direct methods using EXPO2014, assuming that it was a Ca salt. During the refinement (**Fig. 14**B) using GSAS-II,[62] the electron density of the metal site and the metal-oxygen bond distances made it clear that it was a Mg salt rather than a Ca compound. Analysis of the refined structure using PLATON[32] suggested the presence of additional symmetry, and that the true space group was *C2/c* (transformation matrix 101/0–10/00–1). The structure was then re-refined in the correct space group.

10.16.4.1.4 Calcium hydrogen citrate dihydrate, $[Ca(HC_6H_5O_7)(H_3CH_5O_7)(H_2O)](H_2O)$

Among the other crystalline phases obtained by evaporating the solution from cleaning the scale from the water still (after 90 days) is "aquabis(dihydrogencitrato)calcium hydrate," better formulated as aqua(citric acid)(hydrogen citrato)calcium monohydrate, $[Ca(HC_6H_5O_7)(H_3CH_5O_7)(H_2O)](H_2O)$.[63] Indexing[14] (DICVOL06) both the laboratory and synchrotron (11-BM) patterns yielded a triclinic unit cell (space group P-*1*) having $a = 8.37267(11)$, $b = 10.9032(3)$, $c = 11.0629(3)$ Å, $\alpha = 105.2029(6)$, $\beta = 100.6847(4)$, $\gamma = 110.7096(3)°$, $V = 867.24(1)$ Å^3, and $Z = 2$. Structure solution using EXPO2014 and the Rietveld refinement (**Fig. 15**A) were straightforward. The positions of the heavy atoms were clear from the refinement, but identification of the citric acid ligand required a DFT optimization (**Fig. 15**B).

10.16.4.1.5 Calcium citrate hexahydrate, $Ca_3(C_6H_5O_7)_2(H_2O)_6$

A laboratory pattern of calcium citrate hexahydrate, $Ca_3(C_6H_5O_7)_2(H_2O)_6$,[64] could be indexed on a C-centered monoclinic unit cell having $a = 21.424$, $b = 6.344$, $c = 17.316$ Å, $\beta = 109.30°$, and $V = 2234.37$ Å^3, but attempts to solve the structure were unsuccessful, because this was the wrong unit cell. The synchrotron pattern (from 11-BM at APS) could be indexed on a C-centered monoclinic cell with $a = 33.015$, $b = 10.777$, $c = 5.957$ Å, $\beta = 91.71°$, $V = 2118.4$ Å^3, and $Z = 4$. Analysis of the systematic absences using EXPO2014 suggested the space groups *C2/c* or *Cc*. *C2/c* was assumed, and confirmed by straightforward successful solution

Fig. 12 (A) The Rietveld plot for the refinement of $NaAlO_2(H_2O)_{1.25}$. The red crosses represent the observed data points, and the green line is the calculated pattern. The magenta curve is the error plot. The vertical scale has been multiplied by a factor of 10× for $2\theta > 30.5°$, and by a factor of 20× for $2\theta > 47.5°$. The rows of black, red, blue, and green tick marks indicate the calculated reflection positions for $NaAlO_2(H_2O)_{1.25}$, silicon, corundum, and thermonatrite. (B) The crystal structure of $NaAlO_2(H_2O)_{1.25}$, viewed down the *c*-axis. Image generated with Diamond.[24]

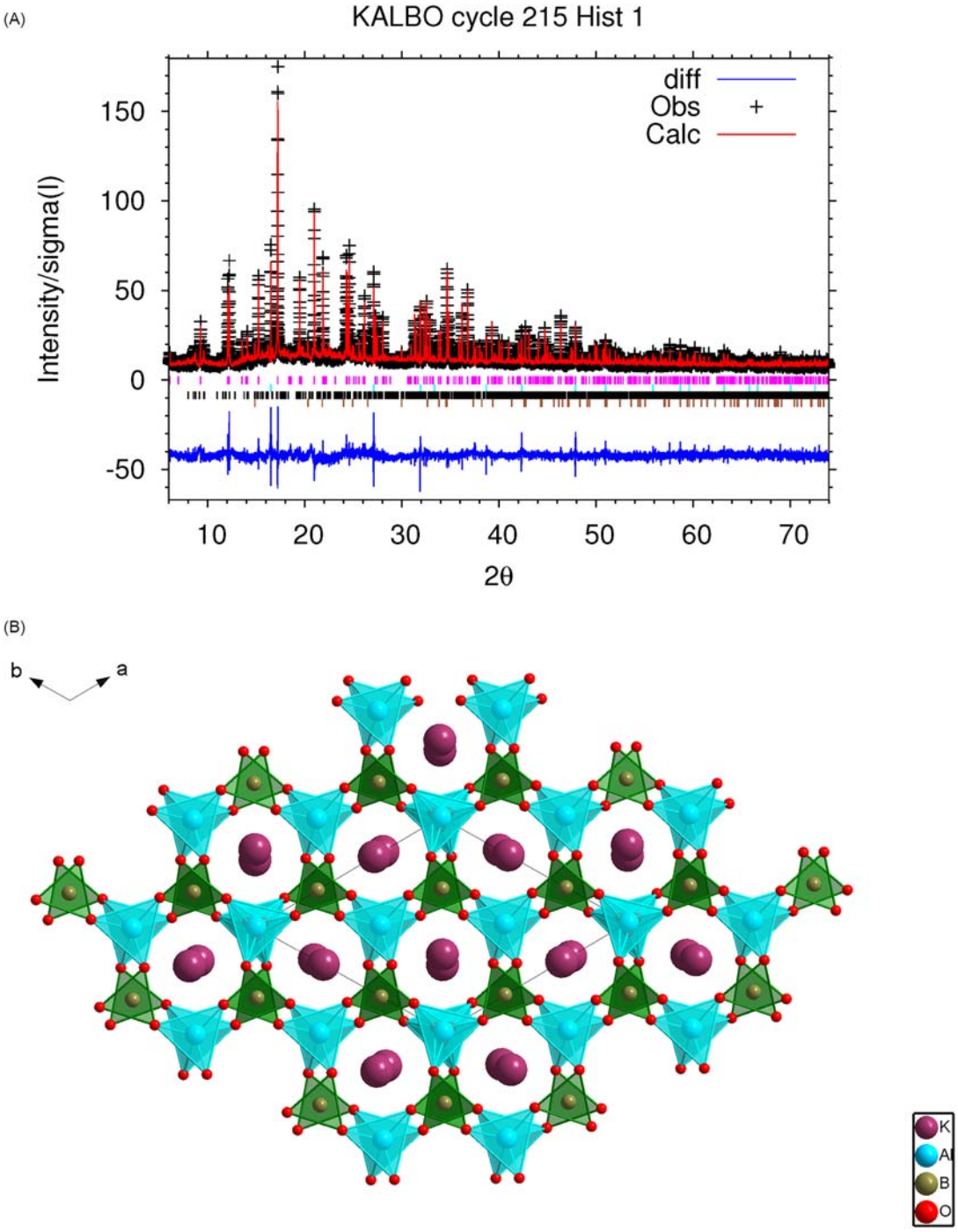

Fig. 13 (A) The Rietveld plot for the refinement of $K_2Al_2B_2O_7$. The black crosses represent the observed data points, and the red line is the calculated pattern. The vertical scale is normalized counts, that is I_{obs} or $I_{cal}/\sigma(I_{obs})$. The blue curve is the normalized error plot. The rows of magenta, cyan, black, and brown tick marks indicate the calculated reflection positions for $K_2Al_2B_2O_7$, silicon, $K_2B_4O_5(OH)_4(H_2O)_2$, and corundum. (B) The crystal structure of $K_2Al_2B_2O_7$, viewed down the *c*-axis. Image generated with Diamond.[24]

using direct methods and refinement (Fig. 16A). The layered structure (Fig. 16B) proved to be essential in working out the structures of the related compounds calcium citrate tetrahydrate (encountered in vitamin supplements) and anhydrous calcium citrate.

10.16.4.2 Charge flipping

The charge flipping algorithm[65,66] is much newer than direct methods. It was originally included in a standalone program SUPERFLIP,[67] but has since been incorporated into a variety of commercial and public-domain packages, so it is readily available. It has

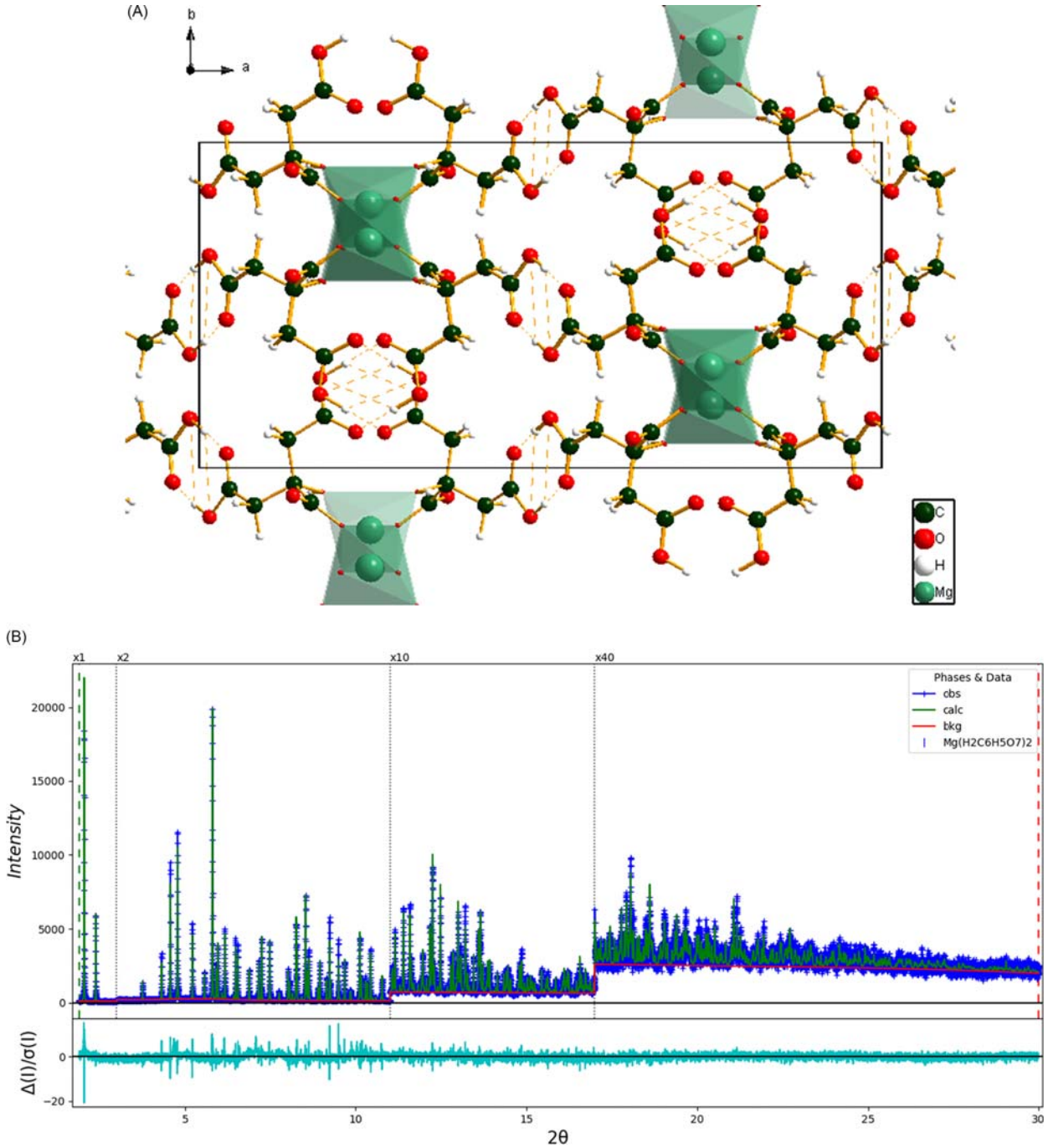

Fig. 14 (A) The crystal structure of magnesium hydrogen citrate, $Mg(H_2C_6H_5O_7)_2$, viewed down the *c*-axis. Image generated with Diamond.[24] (B) The Rietveld plot for the refinement of $Mg(H_2C_6H_5O_7)_2$. The blue crosses represent the observed data points, and the green line is the calculated pattern. The cyan curve is the error plot. The vertical scale has been multiplied by a factor of $10\times$ for $2\theta > 12.0°$, and by a factor of $40\times$ for $2° > 17.0°$.

been used to solve some very complex inorganic structures,[68,69] and continues to provide an alternate (to direct methods) method for structure solution.

The method involves assigning a set of random phases to a set of experimental structure factor amplitudes (single crystal or powder). The method is easily extended to multiple dimensions, and so is often used to solve aperiodic structures. An electron density map is calculated. The map has no physical reality because of the use of random phases, and contains regions of both positive and negative electron density. Since (for X-rays) the electron density cannot be negative, the sign of the regions of negative density is inverted (flipped) to generate a new electron density map. The threshold is generally not zero, but a small positive value;

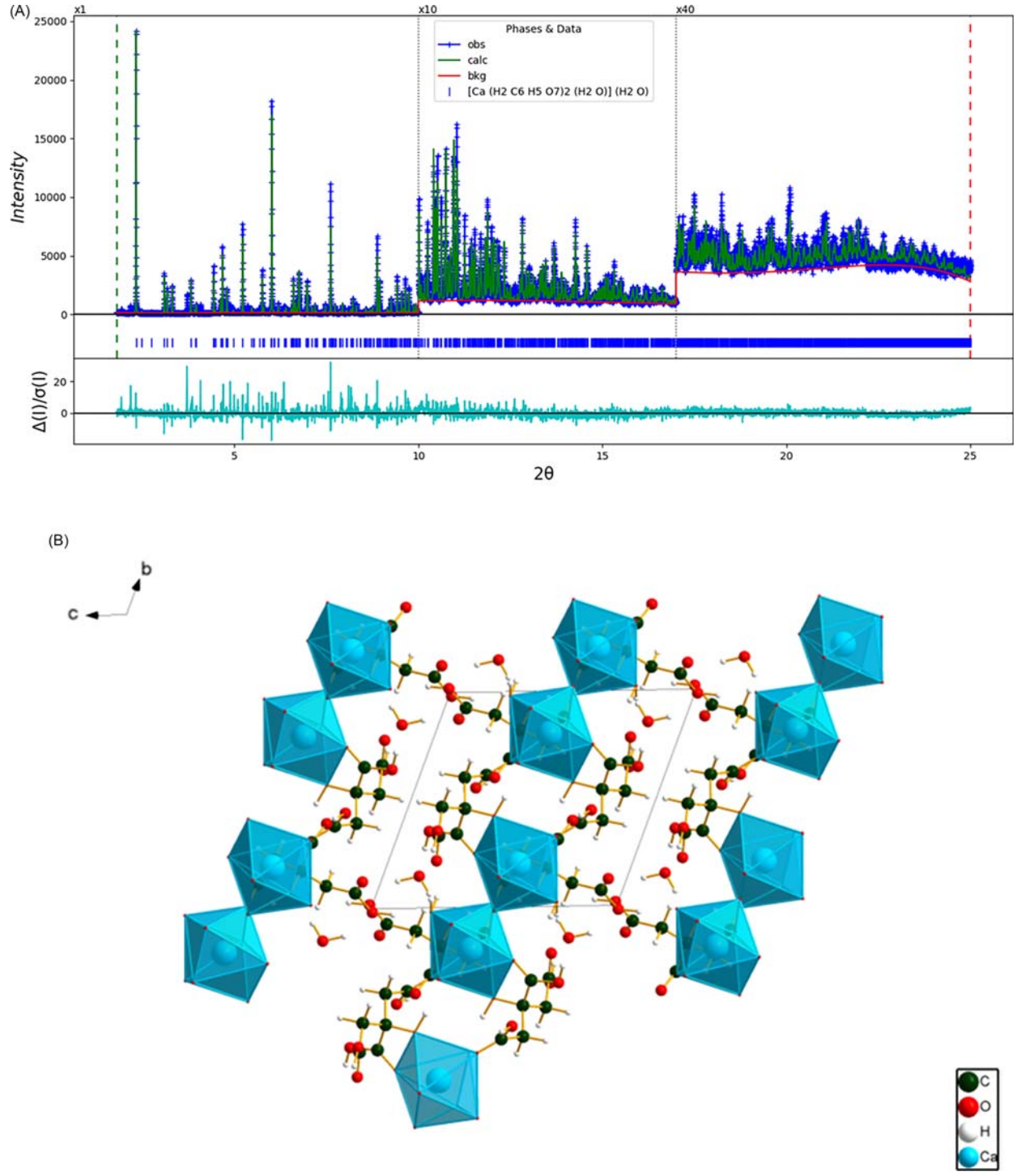

Fig. 15 (A) The Rietveld plot for the refinement of calcium hydrogen citrate dihydrate, $[Ca(HC_6H_5O_7)(H_3CH_5O_7)(H_2O)](H_2O)$. The blue crosses represent the observed data points, and the green line is the calculated pattern. The cyan curve is the normalized error plot. The vertical scale has been multiplied by a factor of $10\times$ for $2\theta > 10.0°$, and by a factor of $40\times$ for $2° > 17.0°$. (B) The crystal structure of aqua(citric acid)(hydrogen citrato)calcium monohydrate, viewed down the *a*-axis.

this is the only user-controllable parameter. This electron density map is Fourier transformed to yield a new set of structure factors. The magnitudes are discarded, but the new phases are used with the experimental amplitudes to compute a new Fourier map. The negative density in this new map is flipped as before, and the process is repeated until convergence. (Direct methods are magical, but charge flipping is a different order of magic!).

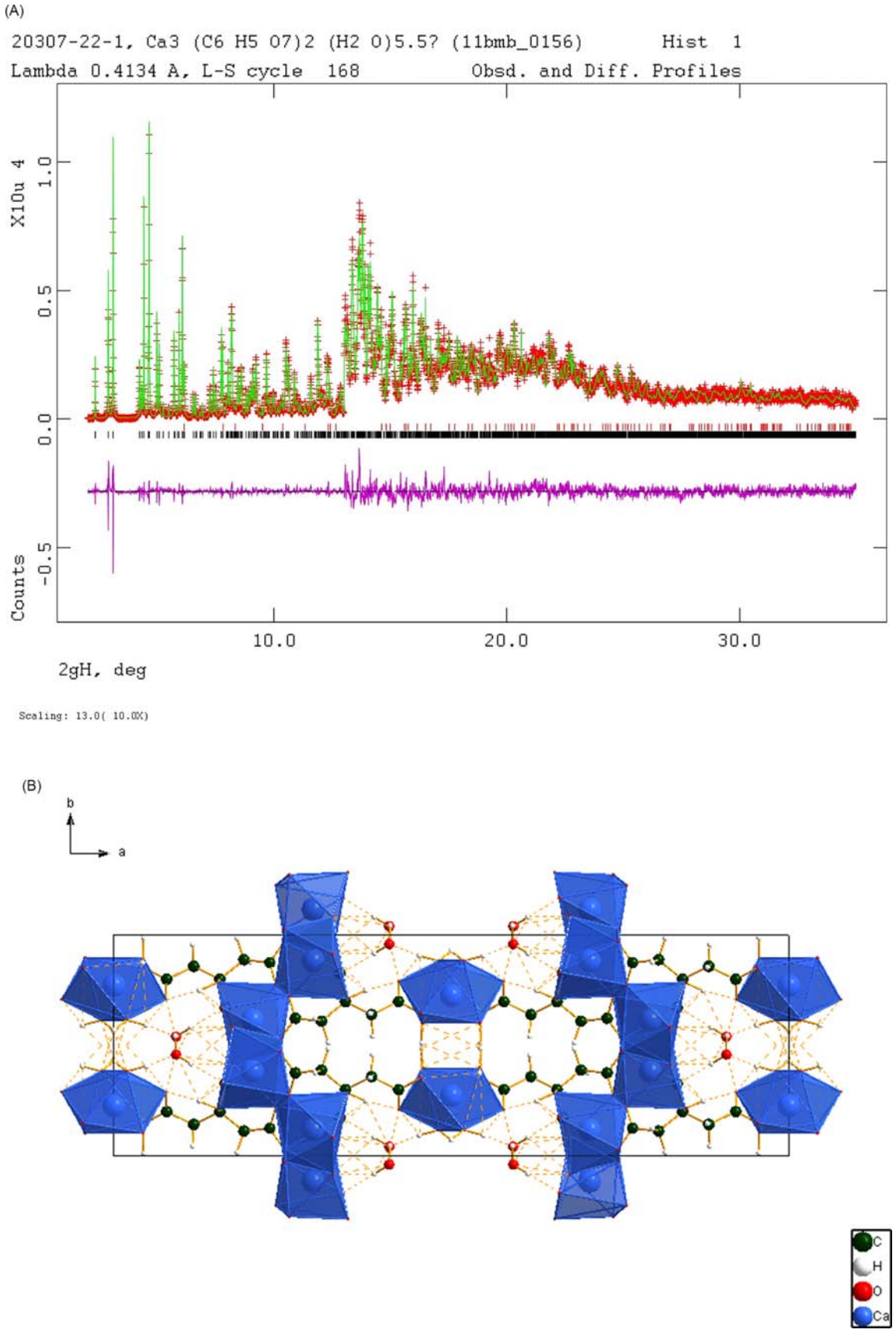

Fig. 16 (A) The Rietveld plot for the refinement of $Ca_3(C_6H_5O_7)_2(H_2O)_6$. The red crosses represent the observed data points, and the green line is the calculated pattern. The magenta curve is the error plot. The vertical scale has been multiplied by a factor of $10\times$ for $2\theta > 13.0^\circ$. The rows of black and red tick marks indicate the calculated reflection positions for $Ca_3(C_6H_5O_7)_2(H_2O)_6$ and a calcite impurity. (B) The crystal structure of $Ca_3(C_6H_5O_7)_2(H_2O)_6$, viewed down the *c*-axis. Image generated with Diamond.[24]

10.16.4.2.1 Antimony oxalate hydroxide, $Sb(C_2O_4)(OH)$

Antimony oxalate hydroxide, $Sb(C_2O_4)(OH)$, was of interest as a soluble stoichiometric antimony source for use in catalyst preparation.[70] Although a powder pattern (00–037-0646) was contained in the Powder Diffraction File,[71] no crystal structure was available. The laboratory powder pattern could be indexed using DICVOL06[14] on a primitive orthorhombic unit cell (space group P*nma*) with $a = 5.82713(3)$, $b = 11.29448(10)$, $c = 6.31377(3)$ Å, $V = 415.537(5)$ Å^3, and $Z = 4$. Both direct methods and Monte Carlo simulated annealing methods were unsuccessful in solving the structure, though both located the Sb atom on the mirror plane. Structure factor amplitudes from a Le Bail extraction using GSAS[72] were used to create a SHELX "hklf 4" file, which was used as input to SUPERFLIP as incorporated into JANA2006.[73] The Sb and the hydroxyl oxygen atoms were located easily. These two atoms were fixed in GSAS, and a difference Fourier map yielded the positions of the oxalate C and one of the O atoms. Another O (the strongest peak in the difference map) was located only 1.06 Å from the Sb, but in a direction expected for the remaining oxalate O. This atom was moved manually into the approximately correct position and the refinement (Fig. 17A) begun. The crystal structure (Fig. 17B) apparently contains voids, but these are filled by the lone pairs of the Sb^{3+} cations. The refined texture index was 1.441, which indicated that significant preferred orientation was present, though not obvious visually. Such preferred orientation tends to concentrate electron density into planes or lines in a difference map, thus mis-locating the last O atom and causing difficulty in structure solution. It is always better to minimize preferred orientation experimentally, but it can be included in refinement models.

10.16.4.2.2 Tamsulosin hydrochloride, $C_{20}H_{29}N_2O_5SCl$

Even though tamsulosin is an organic molecule, tamsulosin hydrochloride provides an example of a complex crystal structure solved by charge flipping.[74] The synchrotron pattern (from 11-BM at APS) was indexed using N-TREOR on a primitive monoclinic unit cell (space group $P2_1$) with $a = 7.62988(2)$, $b = 9.27652(2)$, $c = 31.84996(12)$ Å, $\beta = 93.2221(2)^\circ$, $V = 2250.734(7)$ Å^3, and $Z = 4$. The cell volume corresponded to 4 molecules, so the asymmetric unit contained two independent tamsulosin cations and 2 chloride anions. The structure was solved using the raw pattern by charge flipping as incorporated into JANA2006. All of the non-H atoms, apart from two ring carbon atoms were located, and the missing atoms were added using Materials Studio.[75] Although the initial structure picture looked unpromising (Fig. 18A), once a packing diagram was generated, the fragments were joined together into two recognizable cations. The refinement (Fig. 18B) yielded an excellent crystal structure (Fig. 18C), which was in good agreement with a DFT-optimized structure and could be used to develop a detailed understanding of the hydrogen bonds in the structure.

10.16.4.2.3 $Fe_{25}Sn_{28}Ti_{47}$

This phase was synthesized during an investigation of the phase diagram of the ternary system Fe–Sn–Ti.[76] The experimental pattern (Fig. 19A) permitted identification of small concentrations of several known phases, but the major peaks did not match any phase in the Powder Diffraction File. These peaks could be indexed using DICVOL14[15] on a primitive hexagonal unit cell with $a = 7.531$ and $c = 6.112$ Å. There were no systematic absences, "limiting" the possible space groups to 16, in 5 Laue classes (Fig. 19B). For structure solution, the composition of the phase was approximated as Cr_3Sn (Cr is the average of Ti and Fe, which can be considered equivalent in this step, and distinguished later during refinement). The space groups were tested in decreasing order of frequency in the Metals and Alloys subfile of the PDF. The structure was solved by charge flipping as implemented in Jana2006[73]; several space groups yielded equivalent structures, and subsequent analysis suggested that space group P-*62 m* was the most reasonable. Refinement (Fig. 19C) was carried out using GSAS.[54] The structure (Fig. 19D) consists of columns of atoms along the *c*-axis. Some sites could clearly be identified as Ti or Fe only. One site had mixed Ti/Fe occupation, and is displaced from the columns of the other metal atoms.

Both direct methods and charge flipping generally require "atomic resolution data," that is, a set of accurate structure factor amplitudes (intensities) to *d*-spacings as low as 1.3–1.0 Å or less. In a powder diffraction experiment, the falloff of atomic scattering factors (especially for organic systems), the experiment geometry (a smaller fraction of the Debye ring is sampled as angle increases), and peak overlap generally mean that this ideal is not attained, even for synchrotron data, though it certainly makes it easier to achieve. Thus, these reciprocal space methods succeed in only a minority of cases, but when they do it means that the structure solution is not "biased" by our chemical expectations. In many cases, however, a partial structure can be obtained, generally of the heavy atoms. This partial information can be valuable when the compound's stoichiometry is not known (yet), and can be useful in hybrid methods.

10.16.5 Real space methods

In this section, I use the term "real space methods" for structure solutions that do not use the diffraction data, but use the data in the refinement stage once a model has been obtained. An example of this sort of real space structure solution is provide by trimellitic anhydride.[77]

Trimellitic anhydride (TMA), 1,2,4-benzenetricarboxylic acid 1,2-anhydride, is a versatile intermediate for chemicals and polymer applications. It is produced by homogeneous catalytic oxidation of pseudocumene (1,2,4-trimethylbenzene). Although worldwide capacity was over 150 million pounds/year, the crystal structure had not been determined, at least in part because all attempts to grow single crystals yielded solvates. The laboratory and synchrotron (from X3B1 at NSLS) powder patterns could be indexed (DICVOL91,[78]) to a primitive orthorhombic unit cell having $a = 5.3684$, $b = 6.8628$, $c = 21.6999$ Å, and $V = 799.47$ Å^3. The observed density of ~ 1.6 gcm^{-3} suggested that $Z = 4$. The systematic absences were ambiguous, limiting the space group to the

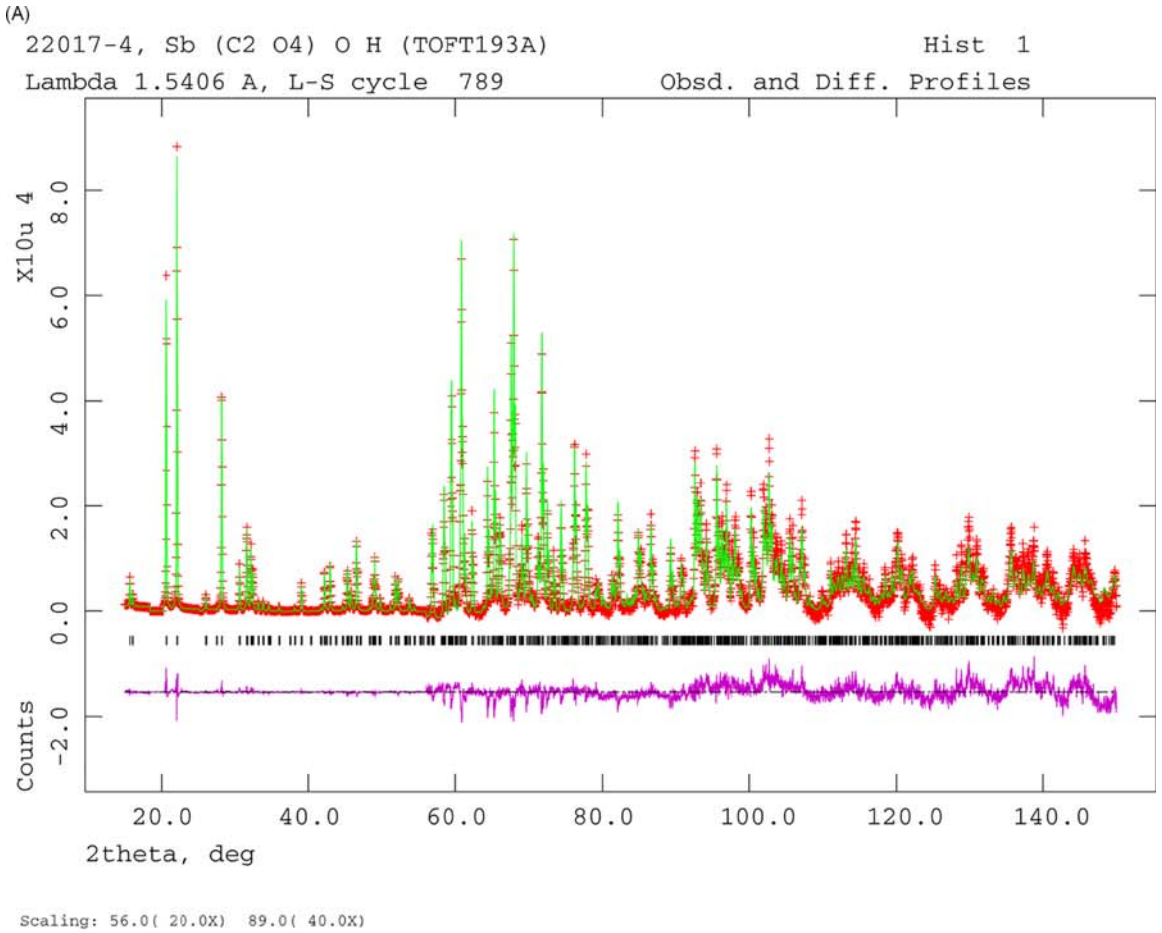

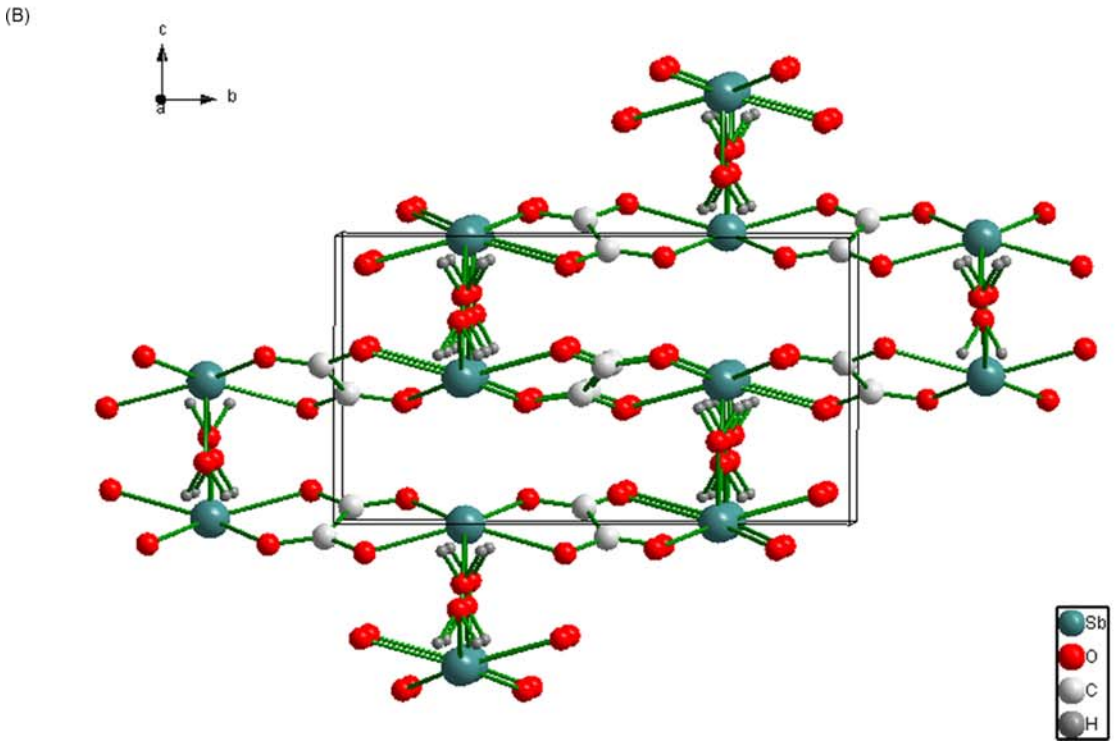

Fig. 17 (A) The Rietveld plot for the refinement of $Sb(C_2O_4)(OH)$. The red crosses represent the observed data points, and the green line is the calculated pattern. The magenta curve is the error plot. The vertical scale has been multiplied by a factor of $20\times$ for $2\theta > 56.0^\circ$, and by a factor of $40\times$ for $2\theta > 89.0^\circ$. (B) The crystal structure of $Sb(C_2O_4)(OH)$, viewed down the *a*-axis. Image generated with Diamond.[24]

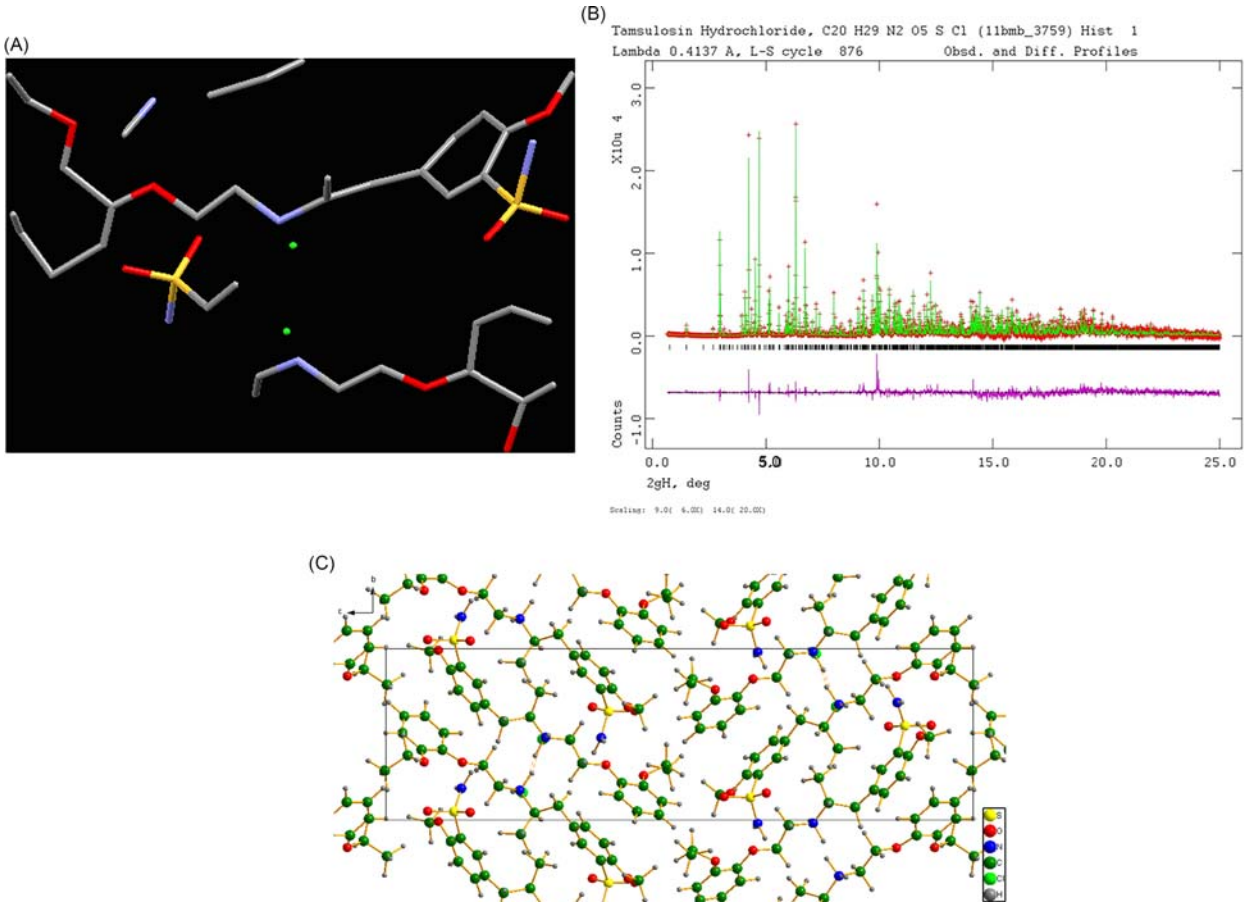

Fig. 18 (A) The initial result of solving the structure of tamsulosin hydrochloride by charge flipping using synchrotron powder diffraction data. (B) The Rietveld plot for the refinement of tamsulosin hydrochloride. The red crosses represent the observed data points, and the green line is the calculated pattern. The magenta curve is the error plot. The vertical scale has been multiplied by a factor of $6\times$ for $2\theta > 9.0°$, and by a factor of $20\times$ for $2\theta > 14.0°$. (C) The crystal structure of tamsulosin hydrochloride, viewed down the *a*-axis. Image generated with Diamond.[24]

general form $P2_1xx$. This restricts the possible space groups to seven, three of which are rare. The most likely space groups were thus $P2_12_12_1$, $P2_12_12$, $Pna2_1$, and $Pca2_1$. The TMA molecule has two possible minimum energy conformations, corresponding to 180° rotation of the 4-carboxyl group. Each conformation was optimized using Gaussian92,[79] and each conformation was used as the base molecule in a polymorph prediction sequence in each space group using the Cerius^{2}™ Polymorph module.[80] This force-field based approach yielded an energy-ranked list of potential structures. The lattice parameters of the second most stable structure in space group $P2_12_12_1$ closely matched the experimental lattice parameters, and was used to begin the Rietveld refinement. The refinement (**Fig. 20**A) also included a Si internal standard, corundum (from the grinding elements of the micronizing mill used to prepare the sample), and trimellitic acid (a reaction product with the atmosphere). The crystal structure (**Fig. 20**B) is characterized by helical O-H • • • O hydrogen-bonded chains, as well as C-H • • • O hydrogen bonds.

The distinction between real space structure solution and what is normally called structure prediction is fuzzy. The current state of organic crystal structure prediction is summarized in the report on the sixth blind test of organic structure prediction, organized by CCDC.[81] Results of previous blind tests can be found at https://www.ccdc.cam.ac.uk/Community/initiatives/cspblindtests/past-csp-blind-tests/. Submissions to the seventh blind test are due by 31 May 2022.

Advanced inorganic materials have been identified as a fundamental national need,[82] and the US government has provided funding for a variety of resources to accelerate the development of such materials. Sample resources are:

The Materials Project (https://materialsproject.org/[83]) is an open-access database offering DFT-computed materials properties and crystal structures. The system includes many modules, including a Structure Predictor.[84]

The Center for Hierarchical Materials Design (CHiMaD; https://chimad.northwestern.edu/) is a NIST-sponsored center of excellence for advanced materials research, part of the Materials Genome Initiative. Among the tools are the Materials Data Facility (https://materialsdatafacility.org/) and the Open Quantum Materials Database (http://oqmd.org).

Recent advances in the prediction of protein[85] (AlphaFold2, https://predictioncenter.org/casp14/zscores_final.cgi) and RNA[86] molecular structures may give hope that such artificial intelligence techniques may be applied to inorganic structures also. The

(A)

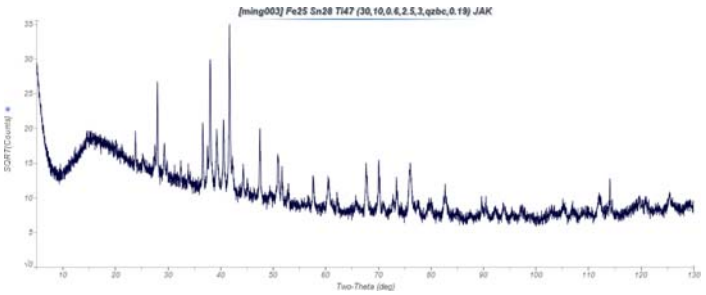

(B)

S. G.	S. G. #	#	S. G.	S. G. #	#
P3	143	45	P6	168	3
P3	147	207	P6	174	297
			P6/m	175	156
P321	150	49			
P3m1	156	184	P622	177	11
P-3m1	164	1915	P6mm	183	21
			P62m	189	1900
P312	149	12	P6m2	187	495
P31m	157	28	P6/mmm	191	5217
P-31m	162	70			

(C)

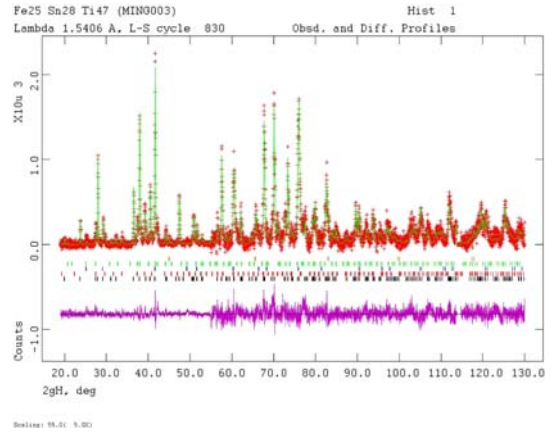

(D)

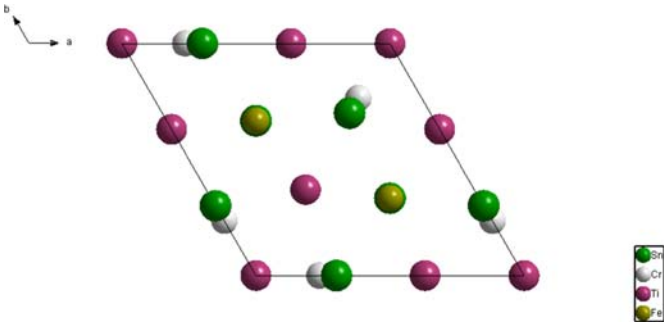

Fig. 19 (A) Experimental laboratory powder pattern for the composition $Fe_{25}Sn_{28}Ti_{47}$. The vertical scale is the square root of the intensity. (B) Space group frequencies in the Metals and Alloys subfile of the PFD-4+ database. (C) The Rietveld plot for the refinement of $Fe_{25}Sn_{28}Ti_{47}$. The red crosses represent the observed data points, and the green line is the calculated pattern. The magenta curve is the error plot. The vertical scale has been multiplied by a factor of 5× for $2\theta > 55.0°$. The rows of black, red, blue, green, and brown tick marks indicate the calculated reflection positions of $Fe_7Sn_{10}Ti_{17}$, Ti_6Sn_5, $TiFe_2Sn$, $(Fe,Ti)_{22}Sn$, and α-Fe. (D) The crystal structure of $Fe_7Sn_{10}Ti_{17}$, viewed down the *c*-axis. The site labelled "Cr" is a mixture of Ti and Fe. Image generated with Diamond.[24]

greater variety of inter-fragment connectivity and crystallographic symmetry will present a real challenge. These approaches depend on the availability of large training sets, so the existing databases of inorganic crystal structures will prove to be a vital resource.

The output of a crystal structure prediction is generally a set of potential crystal structures with similar energy. A powder pattern can be calculated for each of these structures. Thus, it does not take much experimental diffraction data to distinguish among these possibilities, and use the correct structure to begin a refinement. This structure prediction strategy is especially useful when the diffraction data are poor (as is often the case for synthetic polymers), or when the sample is a mixture of polymorphs.

10.16.6 Hybrid methods – Monte Carlo simulated annealing

Often referred to as real space methods,[3] I prefer to think of Monte Carlo simulated annealing (and its close relative, parallel tempering) as hybrid methods, as the moves are performed in real space but the metric is the reciprocal space agreement of observed and calculated powder diffraction patterns. The key feature of these global optimization methods is the use of chemical connectivity information (of a molecule and/or chemical fragments) in the structure solution process.

The methods require prior determination of the unit cell and space group. If the space group is ambiguous, several possible space groups may have to be tested. Molecules or fragments are built or extracted from a crystallographic database, and saved/converted into the appropriate format for the program being used. Although most builders will use reasonable bond distances and angles, torsion angles in an organic fragment may be far from their optimum values. It is generally advisable to optimize the fragment structure (using molecular mechanics or quantum mechanics), including determining the global minimum-energy conformation, to improve the speed and success rate of the structure solution.

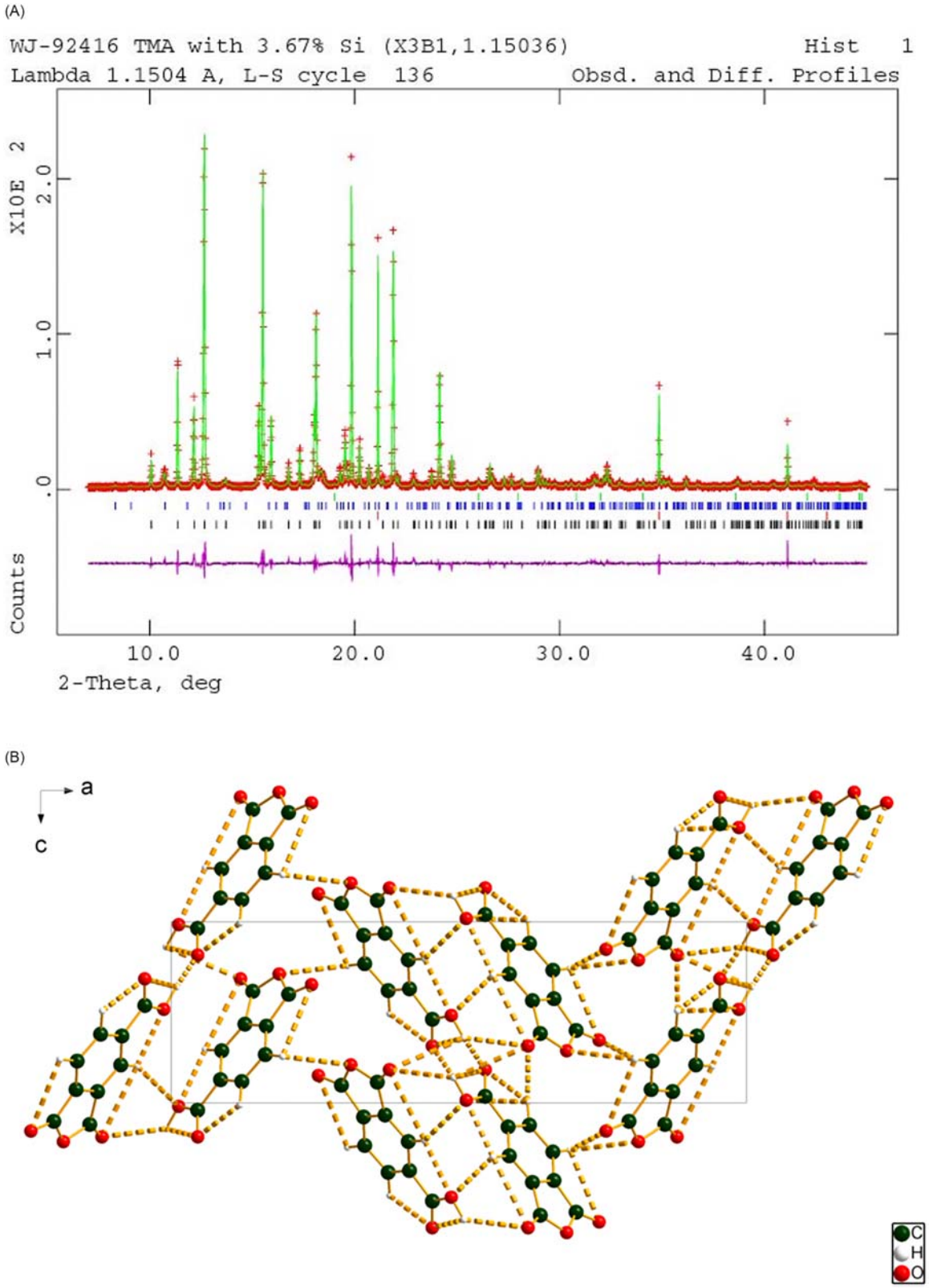

Fig. 20 (A) The Rietveld plot for the refinement of trimellitic anhydride. The red crosses represent the observed data points, and the green line is the calculated pattern. The magenta curve is the error plot. The rows of black, red, blue, and green tick marks indicate the calculated reflection positions for trimellitic anhydride, Si, trimellitic acid, and corundum. (B) The crystal structure of trimellitic anhydride, viewed down the *b*-axis. The dashed lines indicate O-H···O and C-H···O hydrogen bonds. Image generated with Diamond.[24]

The complexity of the problem is often expressed in terms of the number of variable parameters: three for the center of mass of each fragment, three orientation angles for each fragment (except for single atoms), and one parameter for each variable torsion angle. The success rate is often reasonable for up to about 30 variables, but above that the success rate drops markedly.

The process begins by placing each fragment at a random position and orientation in the unit cell, with random torsion angles. The powder pattern is calculated and compared to the observed pattern. (In general, a table of hklI generated by a Le Bail or Pawley fit is used instead of the raw data, to speed up the process.) Then one of the parameters is changed ("making a move"), and the calculated and observed patterns are compared again. If the agreement is better, the move is accepted and other moves are made. If the agreement is poorer, the move is mainly rejected, but is accepted with a probability which gradually decreases though the process. The mathematics of this step resembles that for annealing, hence "simulated annealing." Acceptance of "poorer" moves provides a way of sampling all possible local minima (this is a global optimization technique) and not becoming trapped in a particular local minimum. Many (hundreds of thousands, millions, or tens of millions) moves are made until the best fit is obtained. The process if generally repeated many times, given the random nature of many of the steps. Computers are good at such repetitive calculations, and one only needs to succeed once (!); repeatedly obtaining a similar solution improves confidence in the result.

10.16.6.1 $Na_{1-x}Ge_{3+z}$

This phase was synthesized by thermal decomposition of Na_4Ge_4.[87,88] Bulk chemical analysis indicated a composition close to $NaGe_3$. Synchrotron X-ray powder diffraction data were collected at beamline 32-ID of the Advanced Photon Source, Argonne National Laboratory using a wavelength of 0.4958 Å (25 keV). The pattern was indexed on a primitive hexagonal unit cell using DICVOL04.[37] There were no systematic absences, so structure solution was attempted in all trigonal and hexagonal space groups having no extinctions.

The structure was solved using Monte Carlo simulated annealing techniques as implemented in Endeavour 1.3,[89] using individual Na and Ge atoms as fragments. Several space groups yielded essentially the same structure. The lowest residual was obtained in space group P6, but analysis of the refined structure[32] suggested that P6/*m* was the correct space group. Rietveld refinement (Fig. 21A) was carried out using GSAS.[54] The zeolite-like structure (Fig. 21B) is composed of a framework of fully-occupied Ge sites, with fully- and partially-occupied Na and Ge sites in the hexagonal channels.

10.16.6.2 $MoO_2(O_2)(H_2O)\cdot H_2O$

Preparation of the medically-important isotope ^{99m}Tc, which is a daughter of ^{99}Mo, using production routes that do not involve highly-enriched uranium has become of interest. Chemistry development for target processing related to linear accelerator (LINAC) production of ^{99}Mo led to the synthesis of this phase.[90]

Powder patterns were collected using the Canadian Macromolecular Crystallography Facility beamline 08B1-1[91] at the Canadian Light Source. The 2D patterns were calibrated and integrated using GSAS-II.[62] Phase identification using the Powder Diffraction File[71] yielded an indexed experimental pattern for $H_2MoO_5\cdot H_2O$ (00-041-0060,[92]). The space group is I2/*m*, with $a = 17.156(1)$, $b = 3.8749(3)$, $c = 6.5506(4)$ Å, and $\beta = 90.832(4)^\circ$, but no atom coordinates were reported. An impurity phase was also present; its peaks could be indexed using DICVOL06, and it was included in the refinement as a Le Bail phase.

A reduced cell search of the PDF yielded a hydrated tungsten peroxide, $WO_2(O_2)(H_2O)_{2.66}$ (04-011-4401,[93]) as a potentially analogous structure. However, Rietveld refinements based on this model were unsuccessful, and the structure was solved using FOX,[94] using the unit cell and space group from PDF entry 00–041-0060. Rietveld refinement (Fig. 22A) was carried out using GSAS.[54] The structure (Fig. 22B) is characterized by double zig-zag molybdate chains running parallel to the *b*-axis.

10.16.6.3 $(CH_3)_3AsO(H_2O)_2$

Trimethylarsine oxide (TMAO) is one of several biochemically-important methylated arsenic species. The structure of TMAO dihydrate was determined from a commercial sample of TMAO.[95] The powder pattern was collected at beamine 08B1-1 of the Canadian Light Source.[91] The pattern was indexed using DICVOL06[37] on a primitive orthorhombic unit cell with $a = 13.3937(4)$, $b = 9.5302(3)$, $c = 11.5951$ Å, $Z = 8$, and space group P*bca*.

A TMAO molecule was extracted from CSD entry ASOXCA.[96] The molecule was converted to a Fenske-Hall *Z*-matrix using Open Babel[97] for structure solution using parallel tempering in FOX.[94] The material is quite hygroscopic, so different levels of hydration (different number of O atoms = water molecules) were tested during structure solution. Two water molecules proved optimal; inclusion of more O atoms led to overlap and occupancy adjustment during parallel tempering.

Rietveld refinement (Fig. 23A) was carried out using GSAS.[54] The crystal structure (Fig. 23B) is characterized by alternating layers of TMAO and water molecules parallel to the ab-plane. The hydrogen bonds were characterized using the results of a DFT geometry optimization using CRYSTAL14.[98] The limited information content of an X-ray powder pattern makes determining hydrogen atom positions difficult, so it is better to rely on other techniques.

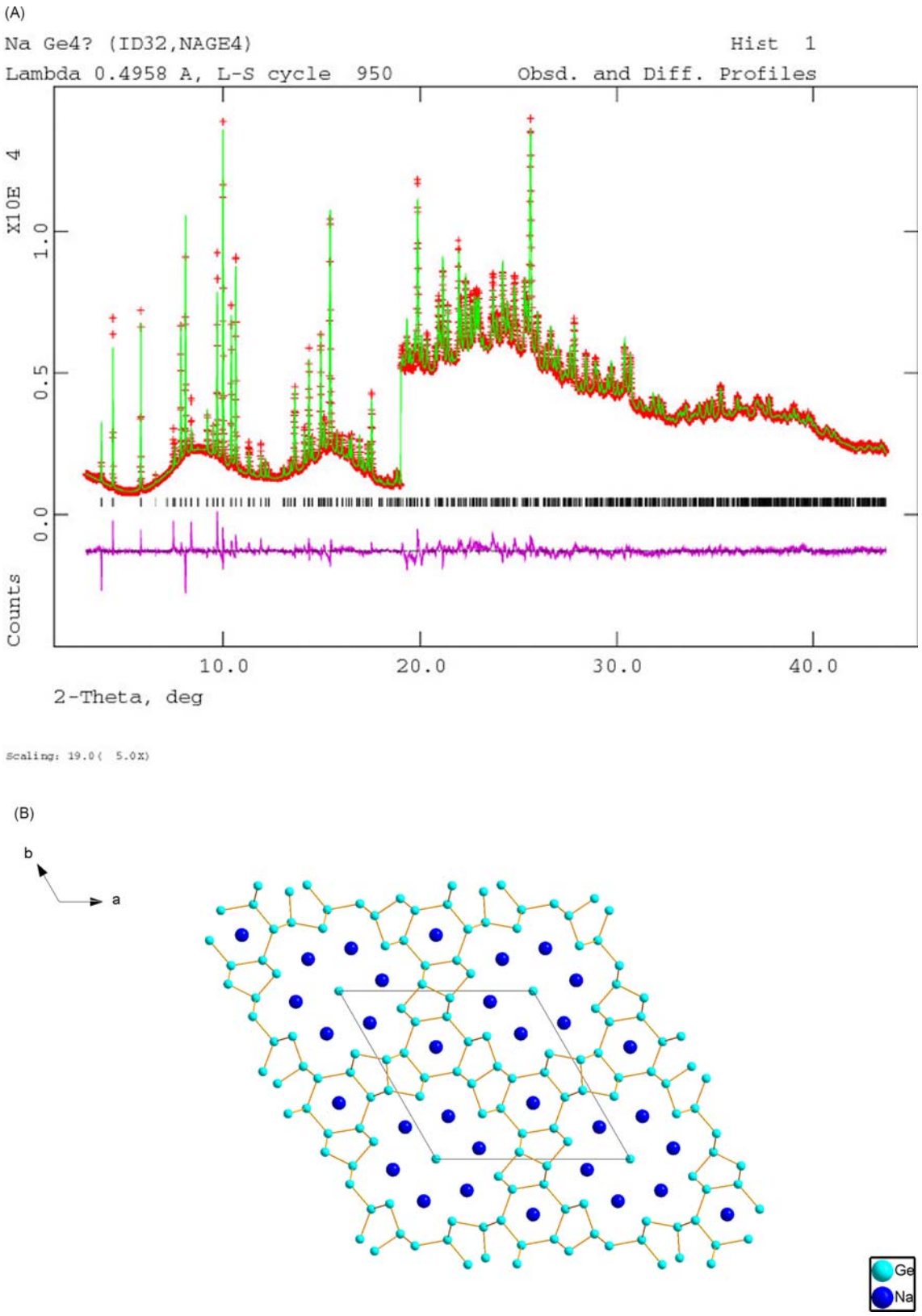

Fig. 21 (A) The Rietveld plot for the refinement of $Na_{1-x}Ge_{3+z}$. The red crosses represent the observed data points, and the green line is the calculated pattern. The magenta curve is the error plot. (B) The crystal structure of $Na_{1-x}Ge_{3+z}$, viewed down the c-axis. Image generated with Diamond.[24] The vertical scale has been multiplied by a factor of $5\times$ for $2\theta > 19.0$ deg.

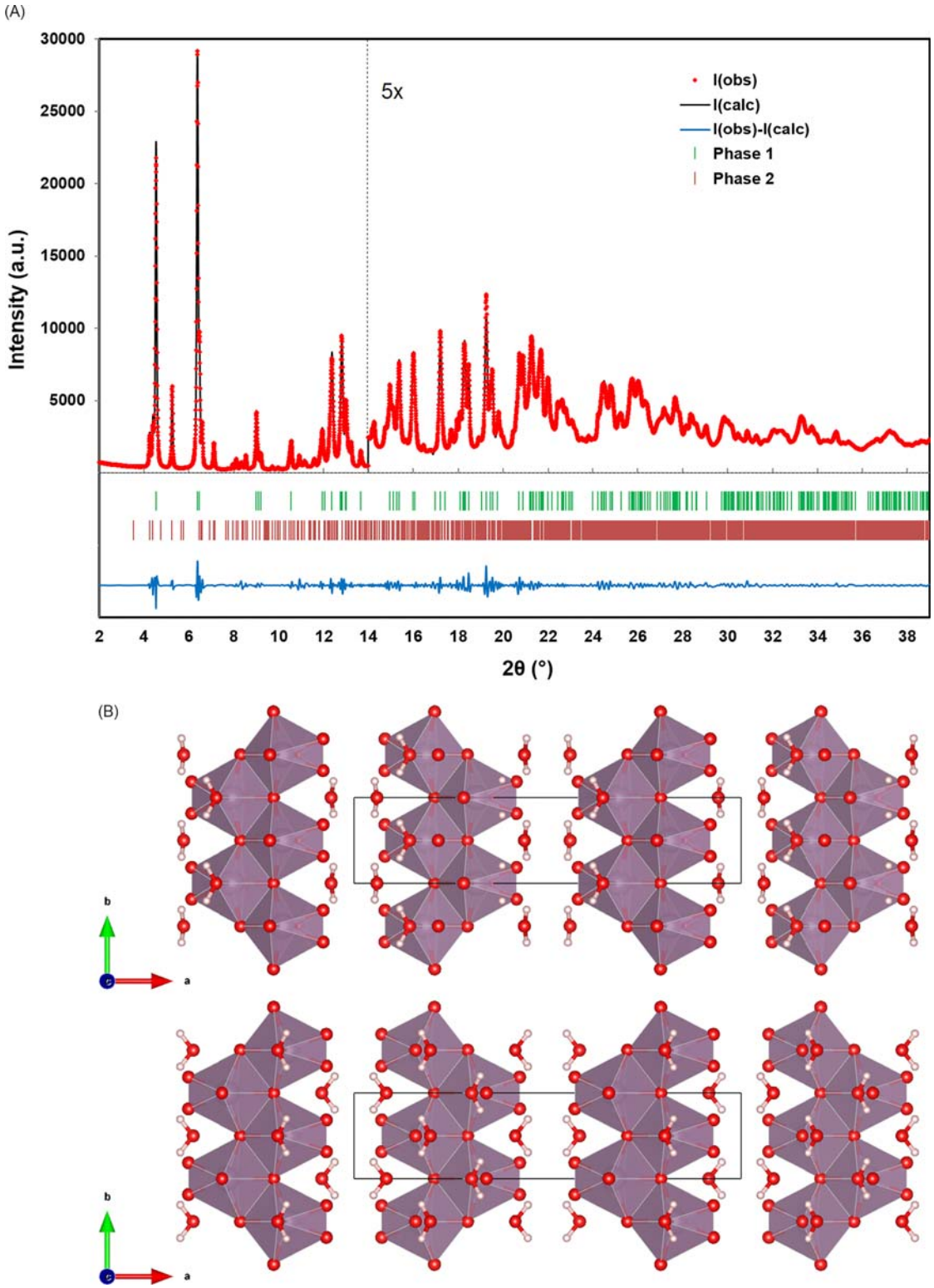

Fig. 22 (A) A plot illustrating the final Rietveld refinement of $MoO_2(O_2)(H_2O)\cdot H_2O$ (Phase 1) obtained with GSAS. Phase 2 refers to the unknown monoclinic phase refined with Le Bail refinement. The data is magnified by a factor of 5 for the region above 14° (2θ). (B) The DFT optimized crystal structure of $MoO_2(O_2)(H_2O)\cdot H_2O$, viewed along the *c*-axis with water hydrogen atoms associated with O2 (top) and O4 (bottom). The polyhedra and atom types can be identified by color including MoO_6 (purple octahedra), hydrogen (pink) and O (red). The unit cell is outlined in black. The figure was prepared with VESTA.[41] From Reid, J. W.; Kaduk, J. A.; Matei, L. The Crystal Structure of $MoO_2(O_2)(H_2O)\cdot H_2O$. *Powder Diffr.* **2019**, *34*, 44–49.

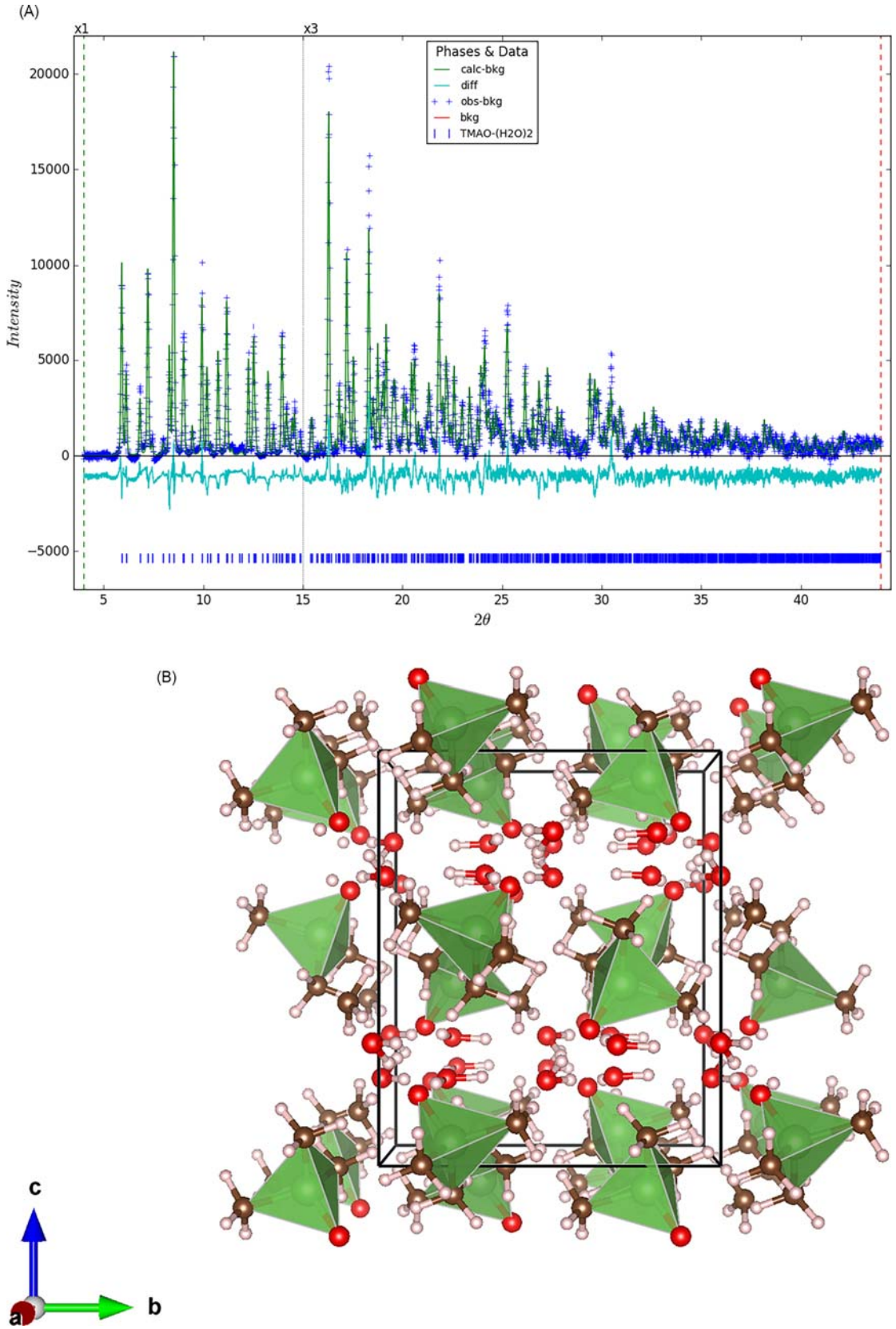

Fig. 23 (A) A plot illustrating the final Rietveld refinement of $(CH_3)_3AsO \cdot 2H_2O$ obtained with GSASII. The data is presented background subtracted and magnified by a factor of 3 for the region above 15°, 2θ. (B) The DFT optimized crystal structure of $(CH_3)_3AsO \cdot 2H_2O$, viewed along the *a*-axis. The atom types can be identified by color including arsenic (green tetrahedra), carbon (brown), oxygen (red) and hydrogen (pink). The unit cell is outlined in black. The figure was prepared with VESTA.[41] From Reid, J. W.; Kaduk, J. A.; Blanchard, P. E. R. Crystal Structure and X-Ray Absorption Spectroscopy of Trimethylarsine Oxide Dihydrate, $(CH_3)3AsO \cdot 2H_2O$. *Powder Diffr.* **2020**, *35*, 190–196.

10.16.6.4 $[Ba_3(C_6H_5O_7)_2(H_2O)_4](H_2O)$

Barium citrate pentahydrate was synthesized[99] as part of a systematic study of citrate salts of Group 1 and Group 2 cations.[100] A laboratory powder pattern of this compound, measured using Cu radiation, was indexed using DICVOL06 on a primitive monoclinic cell (space group $P2_1/a$) with $a = 11.4741$, $b = 13.7366$, $c = 15.0626$ Å, $\beta = 107.944°$, $V = 2258.62$ Å^3, and $Z = 4$. After attempts to solve the structure using the laboratory data were unsuccessful, the powder pattern was measured at beamline 11-BM at the Advanced Photon Source, Argonne National Laboratory, and was indexed on a similar cell. It is not uncommon to find that, although one thought the laboratory pattern had been indexed, the true cell was only obtained from the synchrotron data.

The structure was solved using Monte Carlo simulated annealing techniques as implemented in DASH.[101] Three Ba atoms and two citrate anions were used as fragments. Oxygen atoms of water molecules were placed in voids located by Mercury.[35] Approximate positions of the hydrogen atoms were determined by analysis of potential hydrogen bonding patterns. Final hydrogen positions were determined by a DFT optimization of the Rietveld-refined structure (Fig. 24A). The 10-, 9-, and 10-coordinate Ba coordination polyhedra share edges and corners to form a three-dimensional network (Fig. 24B). One water molecule is uncoordinated.

10.16.6.5 $M(C_8H_4O_4)(H_2O)_2$, M = Mg, Mn, Fe, and Co

Terephthalic acid, 1,4-benzenedicarboxylic acid, is often used as a reagent in the synthesis of metal organic framework (MOF) materials. Metal terephthalate salts are sometimes isolated from process streams during the commercial production of terephthalic acid. The crystal structures of these four isostructural compounds were solved using synchrotron powder data for the Mg complex.[25,102]

The patterns (collected at beamlines X3B1 at NSLS and 10-ID at APS) could be indexed on a C-centered monoclinic cell having $a = 18.511$, $b = 6.536$, $c = 7.317$ Å, $\beta = 99.734°$, and V = 872.5 Å^3. The systematic absences were consistent with space groups *C2/c* or *Cc*. To obtain a reasonable density, $Z = 4$. Space group *C2/c* was selected and confirmed by successful solution and refinement of the structure. A terephthalate anion was built and optimized in *Cerius*^{2}[103] and fixed at the origin. The orientation of the anion was determined using Monte Carlo simulated annealing techniques as implemented in the *STRUCTURE_SOLVE* module of *InsightII*[104]. With Z = 4, the Mg cation also occupies a special position (like the center of the terephthalate). The only special position that yielded a reasonable coordination geometry was 1/4,1/4,0, and the position of the coordinated water molecules could be deduced easily. The structure was refined using GSAS (Fig. 25A), and a DFT optimization was carried out using *CASTEP*[105] as implemented in *Cerius*^{2}. The crystal structure (Fig. 25B) consists of alternating layers (perpendicular to the *a*-axis) of terephthalate anions and octahedrally-coordinated Cations. The octahedra are isolated.

10.16.7 Stealth and guile?

It is perhaps more elegant to refer to these approaches as "model building" and/or the use of chemical intuition. They can be useful when the powder diffraction data is limited.

10.16.7.1 Diammonium 2,6-naphthalenedicarboxylate

This compound was synthesized for use as a (water-soluble) reagent in the synthesis of metal carboxylate salts. The laboratory powder pattern could not be indexed (the peaks are fairly broad), but the synchrotron pattern (measured at 10-ID at APS) could be indexed on a primitive triclinic unit cell with $a = 4.1531(3)$, $b = 5.9937(3)$, $c = 12.2752(10)$ Å, $\alpha = 79.123(7)$, $\beta = 81.040(9)$, $\gamma = 86.781(5)°$, and $V = 296.31(4)$ Å^3. The space group was assumed to be P-*1*. With $Z = 1$, the density is 1.402 g/mL. This made the compound interesting, as a search of the CSD for compounds containing only C, H, N, and O suggests that the density should be about 1.6.

The unit cell is about 1 molecule (2,6-NDA) long x 1 molecule wide x 1 molecule thick. An NDA anion was built, and fixed at the origin. The orientation of the anion was adjusted manually so that they did not overlap. There was a small void between the anions, so the nitrogen atom of an ammonium cation was placed there, and Rietveld refinement (Fig. 26A) begun. Final hydrogen positions were determined by a DFT optimization. The structure (Fig. 26B) consists of alternating layers of anions and cations. The density is lower than usual for the same reason that ice is less dense than liquid water; there is an open network of strong N-H • • • O hydrogen bonds.

10.16.7.2 Poly(tyrosol carbonate), $(C_2H_4C_6H_4CO_3)_n$

Model building is often used to solve the crystal structures of synthetic polymers, for which the quantity of diffraction data is very limited. An example of the approach is the structure of poly(tyrosol carbonate), even though a combination of laboratory and synchrotron (measured at 5-ID-D, APS) data was used.[106]

The 2D patterns of stretched and annealed films were measured using a Bruker AXS Hi-Star area detector. The patterns were processed using the GADDS software to obtain 1D scans. Eleven peaks were used to index the 1D pattern using DICVOL06 on a primitive monoclinic cell with $a = 7.3518$, $b = 8.0647$, $c = 13.7958$ Å, $\beta = 92.308°$, and $V = 817.29$ Å^3. Analysis of the systematic absences using both EXPO2014 and FOX suggested the space group $P2_1$. The cell volume suggested that there were two independent

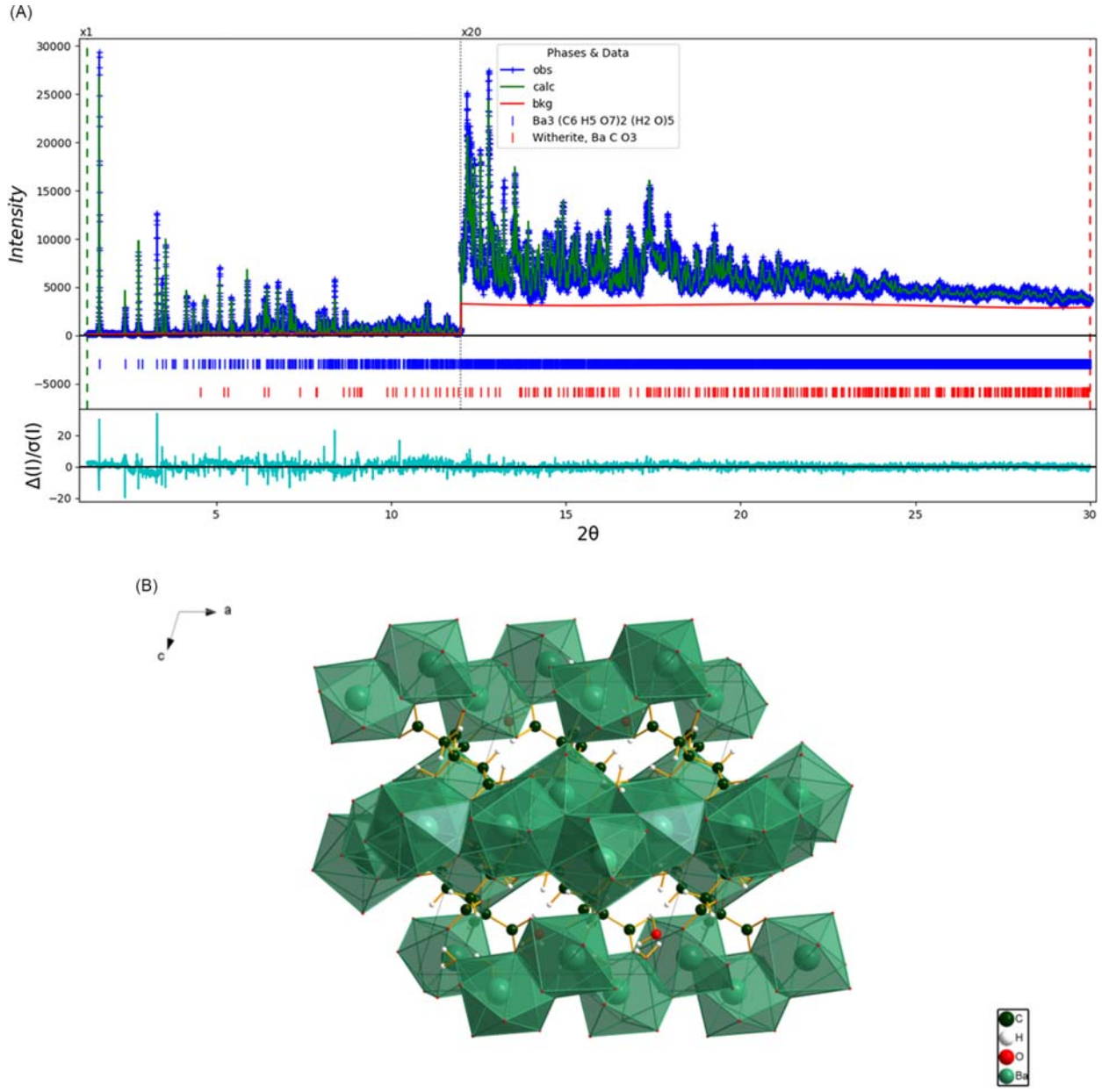

Fig. 24 (A) Rietveld plot for tribarium dicitrate pentahydrate. The blue crosses represent the observed data points, and the green line is calculated pattern. The cyan curve is the normalized error plot. The vertical scale has been multiplied by a factor of 20 × for $2\theta > 12.0°$. The row of blue tick marks indicates the calculated reflection positions, and the red tick marks indicate the peak positions for the $BaCO_3$ impurity. The red line is the background curve. (B) The crystal structure of $[Ba_3(C_6H_5O_7)_2(H_2O)_4](H_2O)$, viewed down the *b*-axis. Image generated with Diamond.[24]

tyrosol carbonate monomers in the asymmetric unit, so a C_2H_4-C_6H_4-CO_3-C_6H_4-C_2H_4-CO_3 fragment was built using Spartan.[107] Initial attempts to solve the structure were made by manually orienting this fragment in the unit cell using Materials Studio,[75] but ultimately it was easier to use Monte Carlo simulated annealing techniques in FOX to solve the structure with this fragment. The structure was refined using GSAS (Fig. 27A), modelling the two phenyl rings as rigid bodies, and optimized using CRYSTAL09.[108] The structure consists of extended polymer chains along the *c*-axis, as is conventional in polymer chemistry (Fig. 27B).

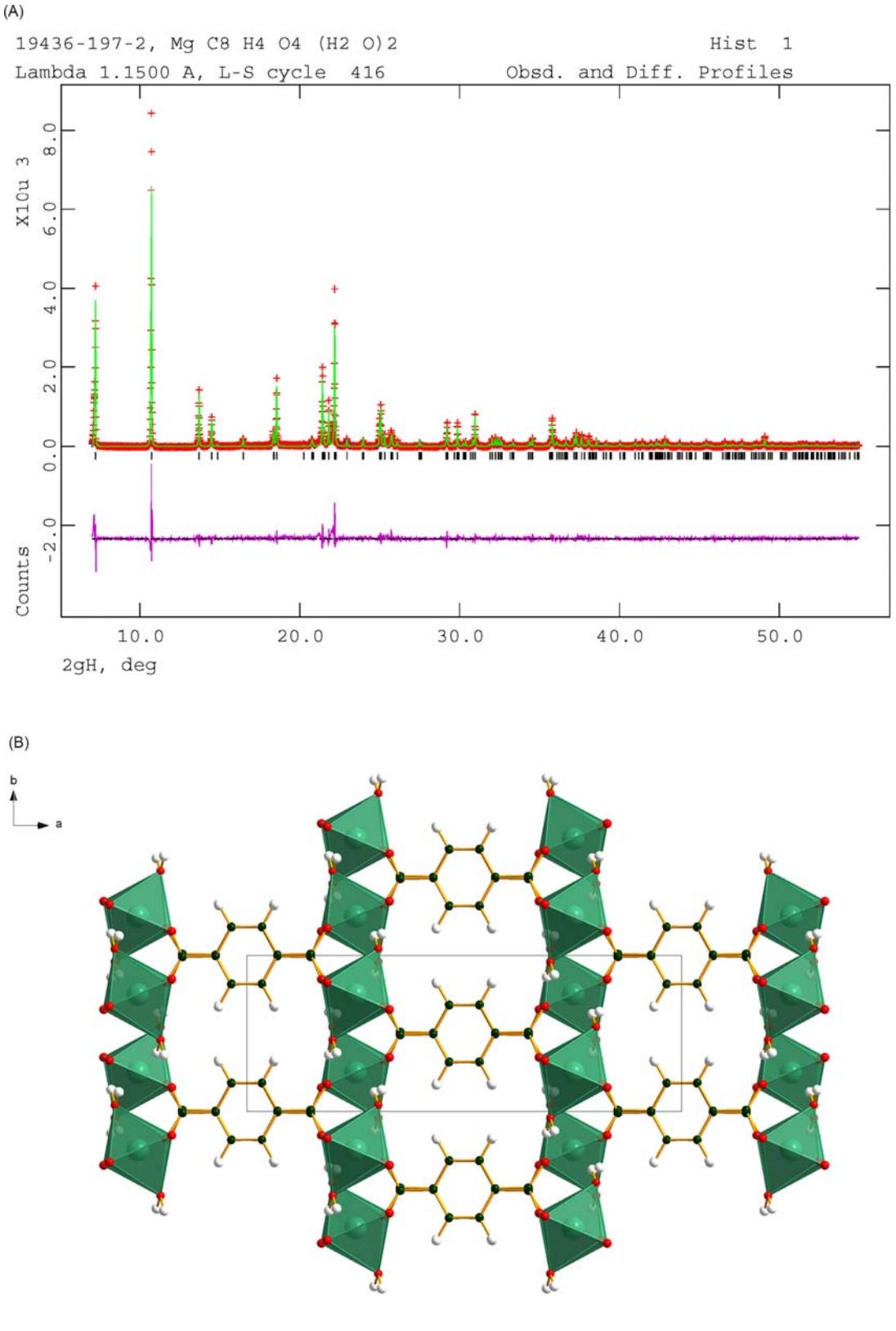

Fig. 25 (A) The Rietveld plot for the refinement of magnesium terephthalate dihydrate. The red crosses represent the observed data points, and the green line is the calculated pattern. The magenta curve is the error plot. (B) The crystal structure of magnesium terephthalate dihydrate, viewed down the *c*-axis. Image generated with Diamond.[24]

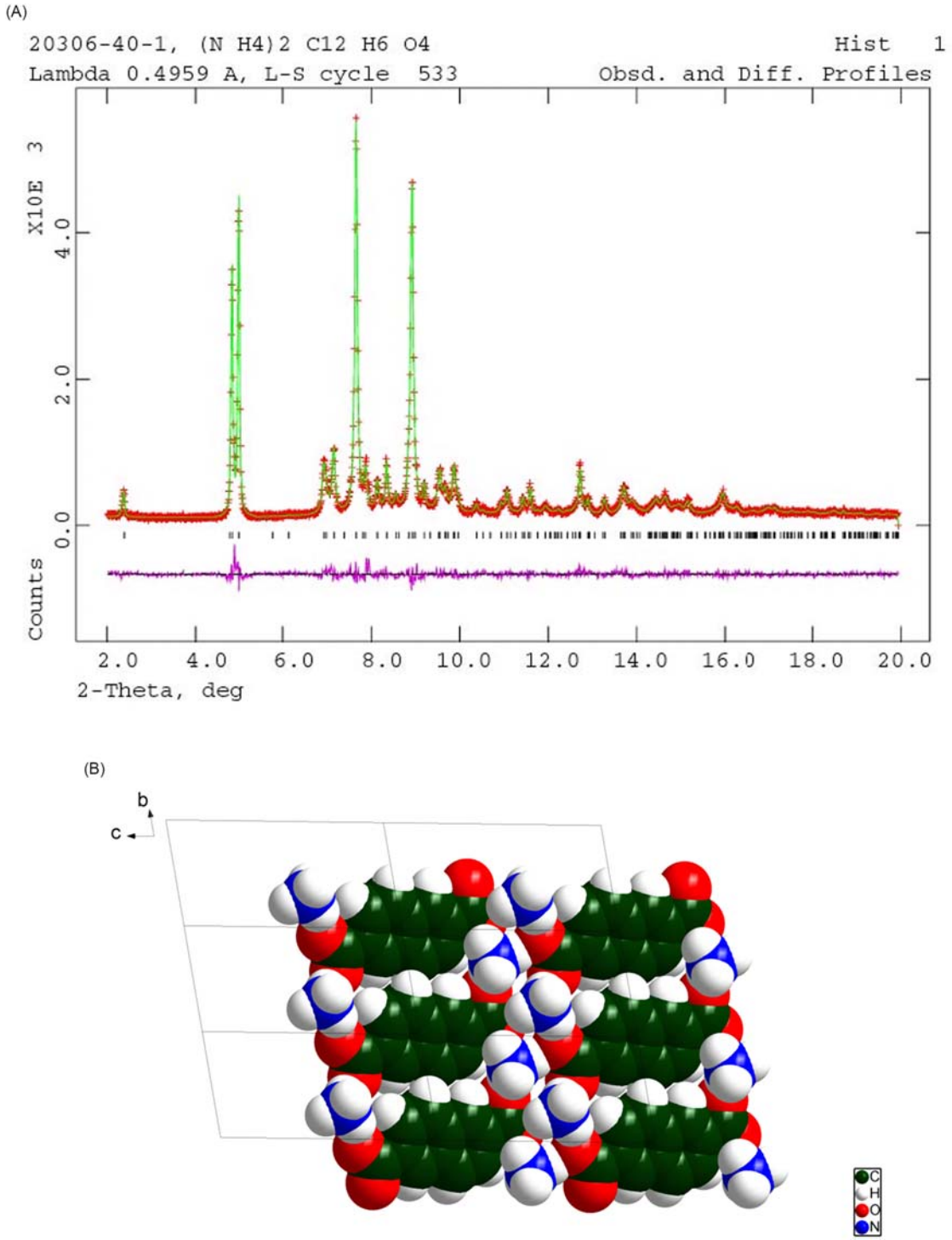

Fig. 26 (A) The Rietveld plot for the refinement of diammonium 2,6-naphthalenedicarboxylate. The red crosses represent the observed data points, and the green line is the calculated pattern. The magenta curve is the error plot. The row of black tick marks indicates the calculated reflection positions. (B) The crystal structure of diammonium 2,6-naphthalenedicarboxylate, viewed down the *a*-axis. Image generated with Diamond.[24]

10.16.8 Microcrystals/polycrystals

Ideally the crystals in a powder diffraction sample should be < 5 μm in size. Often, the finest sieve through which a sample has been passed is 325 mesh (~ 40 μm). Improvements in both laboratory and synchrotron single crystal instrumentation provide the opportunity to convert the ab initio powder structure solution problem into another problem, a micro single-crystal problem.

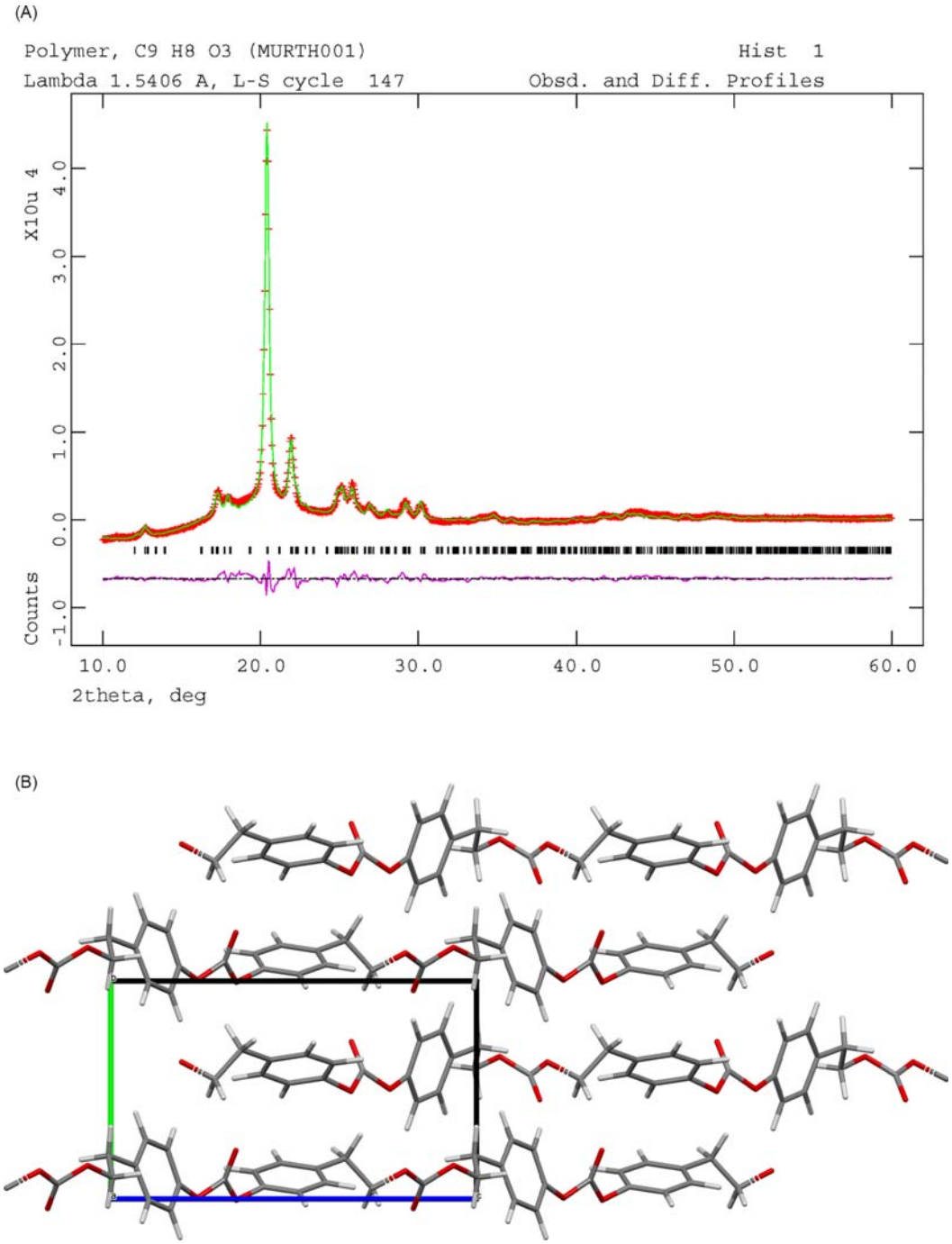

Fig. 27 (A) The Rietveld plot for the refinement of poly(tyrosol carbonate), $(C_2H_4C_6H_4CO_3)_n$. The red crosses represent the observed data points, and the green line is the calculated pattern. The magenta curve is the error plot. The row of black tick marks indicates the calculated reflection positions. () The crystal structure of poly(tyrosol carbonate), $(C_2H_4C_6H_4CO_3)_n$, viewed down the *a*-axis. Image generated with Mercury.[35]

The average size of the crystals used in laboratory experiments has been decreasing. Even in a laboratory experiment, good results are obtained from crystals of the order of 0.1–0.2 mm in size. Many structures are determined from crystals having 1 or 2 dimensions <100 μm; 30–60 μm dimensions are common (needles or plates). It should be possible to do a single crystal experiment at a synchrotron on a sub-5 μm single crystal. Mounting and centering such small crystals in the traditional way can be a challenge. Serial diffraction, as is done at X-ray lasers,[109] is something to consider. This is "diffract and destroy," in which the single shot of X-rays destroys the crystallite. Many diffraction patterns of different crystals in different orientations are measured, and then combined to obtain one single crystal data set, on which traditional techniques can be used.

Another way to convert the ab initio powder problem into another one is to use microcrystal electron diffraction.[110] An example of this technique, which also involved synchrotron powder diffraction, is the solution and refinement of the structure of the drug linagliptin.[111]

Yet another approach to consider is multigrain crystallography.[112] As in serial crystallography, an orientation matrix is generated for each individual crystallite in a polycrystalline specimen. The individual single-crystal datasets are normalized and merged into a single dataset, and the structure solved by traditional single-crystal techniques.

10.16.9 Resonant diffraction

While resonant diffraction (anomalous scattering) techniques are well-established for single-crystal protein structure determination, their application to powder diffraction seems at first to be counterintuitive. The Friedel pairs hkl and -h-k-l overlap exactly in a single powder line. Methods for exploiting the change in the average intensity as a function of wavelength have been used in combination with maximum entropy methods to solve the structure of $SrSO_4$.[113] The need to tune the wavelength restricts resonant scattering techniques to synchrotron radiation.

Performing measurements near the absorption edge of an element and away from the edge exploits the variation of the resonant scattering factor terms $\Delta f'$ and $\Delta f''$ near the edge to vary the scattering power of that element, and thus obtain selectivity to that element. Since X-rays scatter off the electrons, it can be difficult to distinguish elements close in atomic number. Resonant scattering experiments using several wavelengths can vary the scattering power of an element by enough to permit distinguishing the occupation of close elements on specific sites. Since $\Delta f'$ and $\Delta f''$ vary rapidly near an absorption edge, high energy resolution is required, as well as the ability to tine the wavelength continuously. These features require the use of synchrotron radiation. While values for $\Delta f'$ and $\Delta f''$ are tabulated, shifts in the position of the edge from atomic environment and oxidation state make it highly desirable to measure the position of the edges (essentially to do a simultaneous XANES/XAFS/XRD experiment) and use the Kramers-Kroning relation to calculate the actual values of $\Delta f'$ and $\Delta f.''$

An example of a resonant scattering study is an in situ characterization of the cation site occupancies in the Zn/Na-exchanged faujasite (Zeolite Y) $Na_{13}Zn_{19}Al_{52}Si_{140}O_{384}(H_2O)_{220}$, which was a diamagnetic model for more catalytically-interesting transition metal exchanged zeolite Y.[114] A similar system had been studied previously by Wilkinson et al.[115] Powder patterns were collected in the laboratory using Cu K_α radiation at beamline X3B1 at NSLS using the wavelengths of 1.14982 and 1.28520 Å. This last wavelength is just below the Zn K edge, and resulted in a variation of $\sim$20% in the Zn scattering power. Synchrotron measurements were made both at ambient conditions (hydrated) and in situ at 300 °C (dehydrated).

In hydrated ZnNa-FAU, the Zn ions occupy sites II′ and II, with the Na ion at site I′ (Fig. 28). There is significant electron density at the center of the sodalite cage, which likely represent an O atom coordinated to the Zn ions at site II′. At 300 °C, the Zn move to site I′, and site II′ moves closer to the framework. The Na ions are displaced to site II in the supercage. The resonant study permitted unambiguous determination of the occupancies of these partially-occupied sites. This study demonstrated that cation occupancies and positions differ at ambient conditions and at a catalytically-relevant temperature. To develop a valid structure/activity correlation, the correct structure must be used, and catalyst structures must be determined in situ.

10.16.10 Accuracy and precision

Assessing the accuracy of a crystal structure determination is generally referred to as structure validation. The various ways of assessing the accuracy of a structure determination are summarized in Kaduk.[116] These include statistical and graphical measures of the quality of a Rietveld refinement, which are useful for quantifying better or poorer refinements carried out under the same conditions, but are more difficult to apply on an absolute basis in comparing different instruments. More important is what can be called chemical reasonableness.

Since the true value of a structural parameters is typically not known, another approach must be used to assess accuracy. With over 250,000 inorganic crystal structures determined, we have a good idea of the normal values for bond distances and bond angles in most chemical environments. Tools for determining the "normal" value of a structural parameter in organic and organometallic structures are well-developed, and are included with the Cambridge Structural Database.[2] Tools for inorganic structures are less well-developed. Knowledge of inorganic bond distances is conveniently summarized in the bond valence formalism[117] and tables of ionic radii.[118] The Pearson's Crystal Data database[119] contains information about the distribution of interatomic distances between any pair of atoms, and similar histograms of interatomic distances derived from the Inorganic Crystal Structure Database[1] are contained in the Build/Connectivity menu of the Diamond visualization software.[24] Bond valence sums of all atoms should certainly fall within the expected ranges.

The current state of the art for automated structure validation is the *checkCIF* web utility.[32] At my last count, this utility runs over 460 checks of a crystal structure, and generates various levels of alerts. These are not necessarily errors, but highlight unusual features that should be considered by the user. Although the tools are developed for single crystal structures (and thus many alerts are not appropriate for powder refinements), powder crystallography is still crystallography, and many of the tests are still relevant.

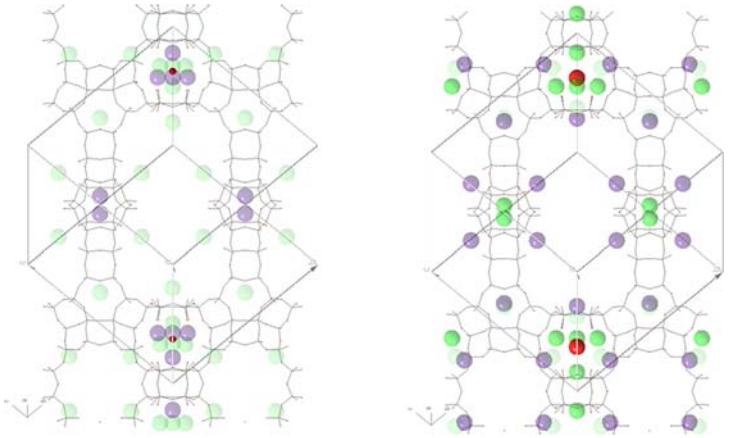

Fig. 28 Extraframework sites in ZnNa-FAU. The Na are purple, and the Zn are colored green. The color intensity is proportional to the site occupancy. The 3-fold axis along the body diagonal of the cubic unit cell is vertical. From Kaduk, J. A. Extraframework Species in Zeolite Y at Nonambient Conditions. *Crystallogr. Rev.* **2005**, *11*, 1–19.

If two different techniques converge to the same answer, there is increased confidence that the answer is accurate. Dispersion-corrected density functional calculations have been shown to be essentially equivalent to single crystal structures.[120] Somewhat larger tolerances must be used in comparing DFT and powder structure,[121] but agreement of DFT-optimized and Rietveld-refined structures is good evidence that the experimental structure is correct.

A comparison of single crystal and powder (both laboratory and synchrotron) refinements obtained from the same sample of cobalt acetate tetrahydrate has been made.[122] Compared to the single crystal refinement, refinement using laboratory powder data yielded an average difference in bond distances of 0.02 Å, in bond angles of 3°, and root-mean-square displacements of 0.07 Å. The standard uncertainties of the bond distances were ~ 0.01 Å, in contrast to the 0.001–0.002 Å in the single crystal refinement. The use of synchrotron powder data (both individually and in combination with other datasets) resulted in improvement both in precision (0.005 Å on distances and 0.2° on angles) and accuracy (0.02 Å on distances and 0.9° on angles). Powder structures can be as accurate as single crystal structures (though there are exceptions), and accurate enough to answer most chemical questions, such as whether a bond is single or double. Ultimately the overlap of powder reflections limits the accuracy and precision which can be obtained.

Acknowledgments

Use of the Advanced Photon Source at Argonne National Laboratory was supported by the U. S. Department of Energy, Office of Science, Office of Basic Energy Sciences, under Contract No. DE-AC02-06CH11357. I thank Lynn Ribaud and Saul Lapidus for their assistance in the data collection at beamline 11-BM. This work represents work carried out in part at the National Synchrotron Light Source at Brookhaven National Laboratory, which was supported by the U.S. Department of Energy, division of Materials Sciences, and Division of Chemical Sciences. The SUNY X3 beamline at NSLS was supported by the Division of Basic Energy Sciences of the U.S. Department of Energy (DE-FG02-86ER45231). I thank Peter W. Stephens for his assistance in data collection at beamline X3B1.

References

1. Hellenbrandt, M. The Inorganic Crystal Structure Database (ICSD) – Present and Future. *Crystallogr. Rev.* **2004,** *10*, 17–22.
2. Groom, C. R.; Bruno, I. J.; Lightfoot, M. P.; Ward, S. C. The Cambridge Structural Database. *Acta Crystallogr.* **2016,** *B72*, 171–179.
3. David, W. I. F. Real-Space Methods for Structure Solution from Powder-Diffraction Data: Application to Molecular Structures. Chapter 4.3. In *International Tables for Crystallography Volume H: Powder Diffraction*, International Union of Crystallography: Chester, 2019.
4. Baerlocher, C.; McKusker, L. B. In *The Structure Determination Process. Structure Determination from Powder Diffraction Data;* David, W. I. F., Shankland, K., McKusker, L. B., Baerlocher, C., Eds., Oxford University Press, 2002; pp 4–7.
5. Altomare, A.; Cuocci, C.; Moliterni, A.; Rizzi, R. Indexing a Powder Diffraction Pattern. Chapter 3.4. In *International Tables for Crystallography Volume H: Powder Diffraction*, International Union of Crystallography: Chester, 2019.
6. Runge, C. Die Bestimmung eines Kristallsystems durch Rontgen-strahlen. *Phys. Z.* **1917,** *18*, 509–515.
7. Ito, T. A General Powder X-Ray Photography. *Nature* **1949,** *164*, 755–756.
8. Ito, T. *X-Ray Studies on Polymorphism*, Maruzen Company: Tokyo, 1950.
9. de Wolff, P. M. On the Determination of Unit-Cell Dimensions from Powder Diffraction Patterns. *Acta Crystallogr.* **1957,** *10*, 590–595.
10. de Wolff, P. M. Detection of Simultaneous Zone Relations among Powder Diffraction Lines. *Acta Crystallogr.* **1958,** *11*, 664–665.
11. Visser, J. W. A Fully Automatic Program for Finding the Unit Cell from Powder Data. *J. Appl. Cryst.* **1969,** *2*, 89–95.
12. Louër, D.; Louër, M. Méthode d'essais et erreurs pour l'indexation automatique des diagrammes de poudre. *J. Appl. Cryst.* **1972,** *5*, 271–275.

13. Louër, D.; Boultif, A. Indexing with the Successive Dichotomy Method, DICVOL04. *Z. Kristallogr. Suppl.* **2006,** *23,* 225–230.
14. Louër, D.; Boultif, A. Powder Pattern Indexing and the Dichotomy Algorithm. *Z. Kristallogr. Suppl.* **2007,** *26,* 191–196.
15. Louër, D.; Boultif, A. Some Further Considerations in Powder Diffraction Pattern Indexing with the Dichotomy Method. *Powder Diffr.* **2014,** *29* (S2), S7–S12.
16. Louër, D.; Vargas, R. Indexation automatique des diagrammes de poudre par dichotomies successives. *J. Appl. Cryst.* **1982,** *15,* 542–545.
17. Werner, P.-E. Trial-and-Error Computer Methods for the Indexing of Unknown Powder Patterns. *Z. Kristallogr.* **1964,** *120,* 375–387.
18. Werner, P.-E.; Eriksson, L.; Westdahl, M. TREOR, a Semi-Exhaustive Trial-and-Error Powder Indexing Program for all Symmetries. *J. Appl. Cryst.* **1985,** *18,* 367–370.
19. Altomare, A.; Giacovazzo, C.; Guagliardi, A.; Moliterni, A. G. G.; Rizzi, R.; Werner, P.-E. New Techniques for Indexing: N-TREOR in EXPO. *J. Appl. Cryst.* **2000,** *33,* 1180–1186.
20. Altomare, A.; Giacovazzo, C.; Moliterni, A. Indexing and space group determination. In *Powder Diffr. Theory and Practice;* Dinnebier, R. E., Billinge, S. J. L., Eds., RSC Publishing: Cambridge, 2008; pp 206–226.
21. Altomare, A.; Campi, G.; Cuocci, C.; Eriksson, L.; Giacovazzo, C.; Moliterni, A.; Rizzi, R.; Werner, P.-E. Advances in Powder Diffraction Pattern Indexing: N-TREOR09. *J. Appl. Cryst.* **2009,** *42,* 768–775.
22. Kaduk, J. A. Combining CDIF and PDF Information in Problem Solving: Crystal Structure of a Corrosion Deposit, Hexaaquairon(II) Trifluoromethanesulfonate. *Powder Diffr.* **1999,** *14,* 166–170.
23. Holt, D. G. L.; Larkworthy, L. F.; Povey, D. C.; Smith, G. W.; Jeffery Leigh, G. Preparation, properties, and crystal and molecular structures of trans-tetrakis (acetic acid) dichlorovanadium (II) and hexakis (acetic acid) vanadium (II) dibromide. *J. Chem. Soc., Dalton trans.* **1990,** *11,* 3229–3233.
24. Crystal Impact; Putz, H.; Brandenburg, K. *Diamond - Crystal and Molecular Structure Visualization*. Kreuzherrenstr. 102, 53227 Bonn, Germany. https://www.crystalimpact.de/diamond, 2021.
25. Kaduk, J. A. Use of the Inorganic Crystal Structure Database as a Problem Solving Tool. *Acta Crystallogr.* **2002,** *B58,* 370–379.
26. Fischer, T.; Kniep, R.; Wunderlich, H. Crystal Structure of Dioxonium Bis (Tris (Sulfato) Dialuminate) Sulfate Docosahydrate, $(H_3O)_2\cdot[Al_2(SO_4)_3]_2\cdot(SO_4)\cdot 22H_2O$. *Z. Kristallogr.* **1996,** *211,* 469–470.
27. Dvořák, V.; Feitknecht, W. Sur les carbonates basiques de fer (III): II. Préparation, radiocristallographie et spectres IR. du $(NH_4)_2Fe_2(OH)_4(CO_3)_2\cdot H_2O$. *Helv. Chim. Acta* **1969,** *52,* 515–522.
28. Iga, T.; Kato, S. Crystal Structure of NH4-Dawsonite. *J. Cerma. Soc. Jpn.* **1978,** *86,* 509–512.
29. Erdos, E.; Altorfer, H. On the Corrosion of Mild Steel and Aluminum in Aqueous Solutions of Ammonia and Carbon Dioxide. Pt. 1. *Corrosion Products. Werks. Korros.* **1976,** *27,* 611–618.
30. Moss, K. C.; Russell, D. R.; Sharp, D. W. A. The Lattice Constants of some Metal-Fluoroborate Hexahydrates. *Acta Crystallogr.* **1961,** *14,* 330.
31. Ghosh, M.; Ray, S. Twinning, Disorder and Phase Transition in Ferrous Perchlorate Hexahydrate Crystals. *Z. Kristallogr.* **1981,** *155,* 129–137.
32. Spek, A. L. checkCIF Validation ALERTS: What they Mean and how to Respond. *Acta Crystallogr.* **2020,** *E76,* 1–11.
33. West, C. D. Crystal Structures of Hydrated Compounds. *Z. Krist. Krist. Krist. Krist.* **1935,** *91,* 480–493.
34. Gallagher, K. J.; Ottaway, M. R. Mixed-Valent Iron Fluoride Hydrates and their Thermal-Decomposition Products. *J. Chem. Soc. Dalton Trans.* **1975,** *11,* 978–982.
35. Macrae, C. F.; Sovago, I.; Cottrell, S. J.; Galek, P. T. A.; McCabe, P.; Pidcock, E.; Platings, M.; Shields, G. P.; Stevens, J. S.; Towler, M.; Wood, P. A. *Mercury 4.0*: From Visualization to Design and Prediction. *J. Appl. Cryst.* **2020,** *53,* 226–235.
36. Reid, J. W.; Kaduk, J. A.; Olson, J. A. The Crystal Structure of $Na(NH_4)Mo_3O_{10}\bullet H_2O$. *Powder Diffr.* **2017,** *32,* 140–147.
37. Boultif, A.; Louër, D. Trial and Error Method for the Automatic Indexing of Powder Diffraction Patterns-Variation of Parameters by Successive Dichotomy. *J. Appl. Cryst.* **2004,** *37,* 724–731.
38. Laugier, J.; Bochu, B. LMGP-Suite Suite of Programs for the Interpretation of X-Ray Experiments. In *ENSP/Laboratoire des Matériaux et du Génie Physique*, Saint Martin d'Hères: France, 2000.
39. Range, K.-J.; Fässler, A. Diammonium trimolybdate(VI), $(NH_4)_2Mo_3O_{10}$. *Acta Crystallogr.* **1990,** *C46,* 488–489.
40. Förster, A.; Kreusler, H. U.; Fuchs, J. Die kristallen Phasen der Alkalitrimolybdate. *Z. Naturforsch.* **1985,** *40b,* 1139–1148.
41. Momma, K.; Izumi, F. VESTA 3 for Three-Dimensional Visualization of Crystal, Volumetric and Morphology Data. *J. Appl. Cryst.* **2011,** *44,* 1272–1276.
42. Kaduk, J. A.; Harper, J. J. Crystal Structure of an Unusual Corrosion Deposit, *Bis*(Ethylammonium)Tetrachloroiron(II). *Powder Diffr.* **1999,** *14,* 261–266.
43. Depmeier, W. The Uniqueness of the Propyl Compound in the Series $(C_2H_{2n+1}NH_3)_2MnCl_4$ with N = 1-10. *J. Solid State Chem.* **1979,** *29,* 15–26.
44. Mostafa, M.; Willet, R. D. Magnetic Properties of Ferrous Chloride Complexes with Two-Dimensional Structures. *Phys. Rev. B* **1971,** *4,* 2213–2215.
45. Le Bail, A. Data Reduction to $|F_{hkl}|$ Values. Chapter 3.5. In *International Tables for Crystallography Volume H: Powder Diffraction*, International Union of Crystallography: Chester, 2019.
46. Giacovazzo, C. Direct Methods and Powder Data: State of the Art and Perspectives. *Acta Crystallogr.* **1996,** *A52,* 331–339.
47. Giacovazzo, C. *Direct Phasing in Crystallography*, IUCr/Oxford University Press: Oxford, 1998.
48. Giacovazzo, C. Direct Methods. Chapter 2.2. In *International Tables for Crystallography Volume B: Reciprocal Space,* 2nd ed;, IUCr/Kluwer Academic Publishers: Dordrecht, 2001.
49. Giacovazzo, C. *Phasing in Crystallography: A Modern Perspective*, IUCr/Oxford University Press: Oxford, 2013.
50. Patterson, A. L. A Fourier Series Method for the Determination of the Components of Interatomic Distances in Crystals. *Phys. Rev.* **1934,** *46,* 372–376.
51. Rius, J. Patterson-Function Direct Methods for Structure Determination of Organic Compounds from Powder Data. XVI. *Acta Crystallogr.* **2011,** *A67,* 63–67.
52. Gilmore, C.; Dong, W.; Bricogne, G. A Multisolution Method of Phase Determination by Combined Maximization of Entropy and Likelihood. VI. The Use of Error-Correcting Codes as a Source of Phase Permutation and their Application to the Phase Problem in Powder, Electron and Macromolecular Crystallography. *Acta Crystallogr.* **1999,** *A55,* 70–83.
53. Kaduk, J. A.; Pei, S. The Crystal Structure of Hydrated Sodium Aluminate, NaAlO2.5/4H2O, and its Dehydration Product. *J. Solid State Chem.* **1995,** *115,* 126–139.
54. Larson, A. C.; Von Dreele, R. B. GSAS, The General Structure Analysis System. Los Alamos National Laboratory Report*;* 1994; pp 86–748.
55. Kaduk, J. A.; Satek, L. C.; McKenna, S. T. Crystal Structures of Metal Aluminum Borates. *Rigaku J.* **1999,** *16,* 17–30.
56. Larson, A. C.; Lee, F. L.; LePage, Y.; Webster, M.; Charland, J. P.; Gabe, E. J. *The NRCVAC Crystal Structure System*, NRC Chemistry Division: Ottawa, 1988.
57. Altomare, A.; Cuocci, C.; Giacovazzo, C.; Moliterni, A.; Rizzi, R.; Corriero, N.; Falcicchio, A. EXPO2013: A Kit of Tools for Phasing Crystal Structures from Powder Data. *J. Appl. Cryst.* **2013,** *46,* 1231–1235.
58. Antao, S. M.; Hassan, I.; Wang, J.; Lee, P. L.; Toby, B. H. State-of-the-Art High-Resolution Powder X-Ray Diffraction (HRPXRD) Illustrated with Rietveld Refinement of Quartz, Sodalite, Tremolite, and Meionite. *Can. Mineral.* **2008,** *46,* 1501–1509.
59. Lee, P. L.; Shu, D.; Ramanathan, M.; Preissner, C.; Wang, J.; Beno, M. A.; Von Dreele, R. B.; Ribaud, L.; Kurtz, C.; Antao, S. M.; Jiao, X.; Toby, B. H. A Twelve-Analyzer Detector System for High-Resolution Powder Diffraction. *J. Synchrotron Radiat.* **2008,** *15,* 427–432.
60. Wang, J.; Toby, B. H.; Lee, P. L.; Ribaud, L.; Antao, S. M.; Kurtz, C.; Ramanathan, M.; Von Dreele, R. B.; Beno, M. A. A Dedicated Powder Diffraction Beamline at the Advanced Photon Source: Commissioning and Early Operational Results. *Rev. Sci. Instrum.* **2008,** *79*, 085105.
61. Kaduk, J. A. Crystal Structures of Two Magnesium Citrates from Powder Diffraction Data. *Acta Crystallogr.* **2020,** *E76,* 1611–1616.
62. Toby, B. H.; Von Dreele, R. B. GSAS II: The Genesis of a Modern Open Source all Purpose Crystallography Software Package. *J. Appl. Cryst.* **2013,** *46,* 544–549.
63. Kaduk, J. A. Crystal Structure of Aqua(Citric Acid)(Hydrogen Citrato)Calcium Monohydrate, $[ca(HC_6H_5O_7)(H_3C_6H_5O_7)(H_2O)](H_2O)$, from Synchrotron X-Ray Powder Data, and DFT-Optimized Crystal Structure of Existing Calcium Hydrogen Citrate Trihydrate, $[ca(HC_6H_5O_7)(H_2O)_3]$. *Acta Crystallogr.* **2020,** *E76,* 1689–1693.
64. Kaduk, J. A. Crystal Structures of Tricalcium Citrates. *Powder Diffr.* **2018,** *33,* 98–107.

65. Coelho, A. A. A Charge-Flipping Algorithm Incorporating the Tangent Formula for Solving Difficult Structures. *Acta Crystallogr.* **2007,** *A63,* 400–406.
66. Oszlányi, G.; Sűtó, A. The Charge Flipping Algorithm. *Acta Crystallogr.* **2008,** *A64,* 123–134.
67. Palatinus, L.; Chapuis, G. SUPERFLIP – A Computer Program for the Solution of Crystal Structures by Charge Flipping in Arbitrary Dimensions. *J. Appl. Cryst.* **2007,** *40,* 786–790.
68. Baerlocher, C.; Gramm, F.; Massűger, L.; McCusker, L. B.; He, Z.; Hovmöller, S.; Zou, X. Structure of the Polycrystalline Zeolite Catalyst IM-5 Solved by Enhanced Charge Flipping. *Science* **2007,** *315,* 1113–1116.
69. Gies, H. Charge Flipping and Beyond. *Science* **2007,** *315,* 1087–1088.
70. Kaduk, J. A.; Toft, M. A.; Golab, J. T. Crystal Structure of Antimony Oxalate Hydroxide, sb(C_2O_4)OH. *Powder Diffr.* **2010,** *25,* 19–24.
71. Gates-Rector, S.; Blanton, T. The Powder Diffraction File: A Quality Materials Characterization Database. *Powder Diffr.* **2019,** *39,* 352–360.
72. Larson, A. C.; Von Dreele, R. B. *General Structure Analysis System, (GSAS)*, Alamos National Laboratory Report LAUR: Los, 2004; pp 86–784.
73. Petříček, V.; Dušek, M.; Palatinus, L. Crystallographic Computing System JANA2006: General Features. *Z. Krist.* **2014,** *229,* 345–352.
74. Patel, N. V.; Golab, J. T.; Kaduk, J. A.; Gindhart, A. M.; Blanton, T. N. Crystal Structure of Tamsulosin Hydrochloride, $C_{20}H_{29}N_2O_5SCl$. *Powder Diffr.* **2021,** *36,* 85–91.
75. Dassault Systèmes. *Materials Studio 2021*, BIOVIA: San Diego CA, 2021.
76. Yin, M.; Nash, P.; Kaduk, J. A.; Schuster, J. C. Experimental Investigation of the Fe-Sn-Ti Ternary Isothermal Section at 873 K. *J. Alloys Compd.* **2017,** *693,* 76–86.
77. Kaduk, J. A.; Golab, J. T.; Leusen, F. J. J. The Crystal Structures of Trimellitic Anhydride and Two of its Solvates. *Cryst. Eng.* **1998,** *1,* 277–290.
78. Boultif, A.; Louër, D. Indexing of Powder Diffraction Patterns for Low-Symmetry Lattices by the Successive Dichotomy Method. *J. Appl. Cryst.* **1991,** *24,* 987–993.
79. Gaussian Inc. *Gaussian92*, A Program for Quantum Mechanical Calculations: Pittsburgh PA, 1992.
80. Molecular Simulations, Inc. *Cerius ^{2}™, Version 2.0. San Diego, CA,* 1995.
81. Reilly, A. M.; et al. Report on the Sixth Blind Test of Organic Crystal Structure Prediction Methods. *Acta Crystallogr.* **2016,** *B72,* 439–459.
82. Subcommittee on the Materials Genome Initiative, Committee on Technology, National Science and Technology Council. *Materials Genome Initiative Strategic Plan,* 2021.
83. Jain, A.; Ong, S. P.; Hautier, G.; Chen, W.; Richards, W. D.; Dacek, S.; Cholia, S.; Gunter, D.; Skinner, D.; Ceder, G.; Persson, K. A. The Materials Project: A Materials Genome Approach to Accelerating Materials Innovation. *APL Mater.* **2013,** *1*, 011002.
84. Hautier, G.; Fischer, C.; Ehrlacher, V.; Jain, A.; Ceder, G. Data Mined Ionic Substitutions for the Discovery of New Compounds. *Inorg. Chem.* **2011,** *50,* 656–663.
85. Baek, M.; DiMaio, F.; Anishchenko, I.; Dauparas, J.; Ovchinnikov, S.; Lee, G. R.; Wang, J.; Cong, Q.; Kinch, L. N.; Schaeffer, R. D.; Millan, C.; Park, H.; Adams, C.; Glassman, C. R.; DeGiovanni, A.; Pereira, J. H.; Rodrigues, A. V.; van Dijk, A. A.; Ebrecht, A. C.; Opperman, D. J.; Sagmeister, T.; Buhlheller, C.; Pavkov-Keller, T.; Rathinaswamy, M. K.; Dalwadi, U.; Yip, C. K.; Burke, J.; Garcia, K. C.; Grishin, N. V.; Adams, P. D.; Read, R. J.; Baker, D. Accurate Prediction of Protein Structures and Interactions Using a Three-Track Neural Network. *Science* **2021,** *373,* 871–876.
86. Townshend, R. J. L.; Eismann, S.; Waykins, A. M.; Rangan, R.; Karelina, M.; Das, R.; Dror, R. O. Geometric Deep Learning of RNA Structure. *Science* **2021,** *373,* 1047–1051.
87. Beekman, M.; Kaduk, J. A.; Huang, Q.; Wong-Ng, W.; Yang, Z.; Wang, D.; Nolas, G. S. Synthesis and Crystal Structure of $Na_{1-x}Ge_{3+z}$: A Novel Zeolite-like Framework Phase in the Na-Ge System. *Chem. Commun.* **2007,** 837–839.
88. Beekman, M.; Stefanoski, W.-N.; W., Kaduk, J. A., Huang, Q., Reeg, C., Bowers, C. R. and Nolas, G. S. Structure and Thermal Conductivity of $Na_{1-x}Ge_{3+z}$. *J. Solid State Chem.* **2010,** *183,* 1272–1277.
89. Brandenburg, K.; Putz, H. *Endeavour V1.3*, Crystal Impact, 2004. Kreuzherrenstr. 102, 53227 Bonn, Germany.
90. Reid, J. W.; Kaduk, J. A.; Matei, L. The Crystal Structure of $MoO_2(O_2)(H_2O)\cdot H_2O$. *Powder Diffr.* **2019,** *34,* 44–49.
91. Fodje, M.; Grochulski, P.; Janzen, K.; Labiuk, S.; Gorin, J.; Berg, R. 08B1-1: An Automated Beamline for Macromolecular Crystallography Experiments at the Canadian Light Source. *J. Synchrotron Radiat.* **2014,** *21,* 633–637.
92. Sonneveld, E. $H_2MoO_5\cdot H_2O$. In *Powder Diffr. File Entry 00–041-0060*, ICDD Grant-in-Aid, 1989.
93. Pecquenard, B.; Castro-Garcia, S.; Livage, J.; Zavalij, P. Y.; Whittingham, S.; Thouvenot, R. Structure of Hydrated Tungsten Peroxides $[WO_2(O_2)H_2O]\cdot nH_2O$. *Chem. Mater.* **1998,** *10,* 1882–1888.
94. Favre-Nicolin, V.; Černý, R. FOX, Free Objects for Crystallography: A Modular Approach to Ab Initio Structure Determination from Powder Diffraction. *J. Appl. Cryst.* **2002,** *35,* 734–743.
95. Reid, J. W.; Kaduk, J. A.; Blanchard, P. E. R. Crystal Structure and X-Ray Absorption Spectroscopy of Trimethylarsine Oxide Dihydrate, $(CH_3)_3AsO\cdot 2H_2O$. *Powder Diffr.* **2020,** *35,* 190–196.
96. Ng, Y. S.; Rodley, G. A.; Robinson, W. T. Tri-μ-(Trimethyl)Arsine Oxide-Hexakis(Trimethylarsine Oxide)Dicalcium(II) Tetraperchlorate – A Dinuclear Calcium Complex. *Acta Crystallogr.* **1977,** *B33,* 931–934.
97. O'Boyle, N.; Banck, M.; James, C. A.; Morley, C.; Vandermeersch; Hutchison, G. R. Open Babel: An open chemical toolbox. *J. Chem. Inf.* **2011,** *3,* 33. https://doi.org/10.1186/1758-2946-3-33.
98. Dovesi, R.; Orlando, R.; Erba, A.; Zicovich-Wilson, C. M.; Civalleri, B.; Casassa, S.; Maschio, L.; Ferrabone, M.; De La Pierre, M.; D-Arco, P.; Noël, Y.; Causà, M.; Kirtman, B. CRYSTAL14: A Program for the Ab Initio Investigation of Crystalline Solids. *Int. J. Quantum Chem.* **2014,** *114,* 1287–1317.
99. Kaduk, J. A. Tribarium dicitrate pentahydrate, $[Ba_3(C_6H_5O_7)_2(H_2O)_4]\cdot H2O$. *Acta Crystallogr.* **2021,** *E77,* 251–254.
100. Rammohan, A.; Kaduk, J. A. Crystal Structures of Alkali Metal (Group 1) Citrate Salts. *Acta Crystallogr.* **2018,** *B74,* 239–252. https://doi.org/10.1107/S2052520618002330.
101. David, W. I. F.; Shankland, K.; van de Streek, J.; Pidcock, E.; Motherwell, W. D. S.; Cole, J. C. DASH: A Program for Crystal Structure Determination from Powder Diffraction Data. *J. Appl. Cryst.* **2006,** *39,* 910–915.
102. Kaduk, J. A. Terephthalte Salts of Dipositive Cations. *Acta Crystallogr.* **2002,** *B58,* 815–822.
103. Molecular Simulations (2000). Cerius2. Version 4.2MS. Molecular Simulations, 9685 Scranton Road, San Diego CA 92121, USA
104. Molecular Simulations (1996). InsightII. Version 4.0. Molecular Simulations, 9685 Scranton Raod, San Diego CA 92121, USA.
105. Milman, V.; Winkler, B.; White, J. A.; Pickard, C. J.; Payne, M. C.; Akhmatskaya, E. V.; Nobes, R. H. Electronic Structure, Properties, and Phase Stability of Inorganic Crystals: A Pseudopotential Plane-Wave Study. *Int. J. Quantum Chem.* **2000,** *77,* 895–910.
106. Sommerfeld, S. D.; Murthy, N. S.; Cohen, J.; Zhang, Z.; Kaduk, J. A.; Kohn, J. Structural Investigations of Polycarbonates whose Mechanical and Erosion Behavior Can Be Controlled by their Isomer Sequence. *Macromolecules* **2020,** *53,* 9878–9889.
107. Wavefunction, I. *Spartan '18 Version 1.4.5*, Wavefunction Inc., 2020, 18401 Von Karman Ave., Suite 370, Irvine CA 92612.
108. Dovesi, R.; Orlando, R.; Civalleri, B.; Roetti, C.; Saunders, V. R.; Zicovich-Wilson, C. M. CRYSTAL: A Computational Tool for the *Ab Initio* Study of the Electronic Properties of Crystals. *Z. Kristallogr.* **2005,** *220,* 571–573.
109. Wolff, A. M.; Young, I. D.; Sierra, R. G.; Brewster, A. S.; Martynowycz, M. W.; Nango, E.; Sugahara, M.; Nakane, T.; Ito, K.; Aquila, A.; Bhowmick, A.; Biel, J. T.; Carbajo, S.; Cohen, A. E.; Cortez, S.; Gonzalez, A.; Hino, T.; Im, D.; Koralek, J. D.; Kubo, M.; Lazarou, T. S.; Nomura, T.; Owada, S.; Samelson, A. J.; Tanaka, T.; Tanaka, R.; Thompson, E. M.; van den Bedem, H.; Woldeyes, R. A.; Yumoto, F.; Zhao, W.; Tono, K.; Boutet, S.; Iwata, S.; Gonen, T.; Sauter, N. K.; Fraser, J. S.; Thompson, M. C. Comparing Serial X-Ray Crystallography and Microcrystal Electron Diffraction (MicroED) as Methods for Routine Structure Determination from Small Macromolecular Crystals. *IUCrJ* **2020,** *7,* 306–323.
110. Barringer, R. Illuminating the Secrets of Crystals: Microcrystal Electron Diffraction in Structural Biology. *Biosci. Horiz.* **2019,** *12,* 1–12.

111. Das, P. P.; Andrusenko, I.; Mugnaioli, E.; Kaduk, J. A.; Nicolopoulos, S.; Gemmi, M.; Boaz, N. C.; Gindhart, A. M.; Blanton, T. N. Crystal Structure of Linagliptin Hemihydrate Hemiethanolate, $(C_{25}H_{28}N_8O_2)_2(H_2O)(C_2H_5OH)$ from 3D Electron Diffraction Data, Rietveld Refinement, and Density Functional Optimization. *Cryst. Growth Des.* **2021,** *21,* 2019–2027.
112. Poulsen, H. F.; Vaughan, G. B. M. Multigrain Crystallography and Three-Dimensional Grain Mapping. Chapter 5.5. In *International Tables for Crystallography Volume H: Powder Diffraction*, International Union of Crystallography: Chester, 2019.
113. Burger, K.; Cox, D.; Papoular, R.; Prandl, W. The Application of Resonant Scattering Techniques to Ab Initio Structure Solution from Powder Data Using $SrSO_4$ as a Test Case. *J. Appl. Cryst.* **1998,** *31,* 789–797.
114. Kaduk, J. A. Extraframework Species in Zeolite Y at Nonambient Conditions. *Crystallogr. Rev.* **2005,** *11,* 1–19.
115. Wilkinson, A. P.; Cheetham, A. K.; Tang, S. C.; Reppart, W. J. Cation Distribution in Zeolite Zinc/Sodium-Y by Resonant X-Ray Diffraction. *J. Chem. Soc. Chem. Commun.* **1992,** 1485–1487.
116. Kaduk, J. A. Structure Validation. Chapter 4.9. In *International Tables for Crystallography Volume H: Powder Diffraction*, International Union of Crystallography: Chester, 2019.
117. Brown, I. D. In *The Chemical Bond in Inorganic Chemistry: The Bond Valence Model*. International Union of Crystallography Monographs on Crystallography 12, Oxford University Press: Oxford, 2002.
118. Shannon, R. D.; Prewitt, C. T. Effective Ionic Radii in Oxides and Fluorides. *Acta Crystallogr.* **1969,** *B25,* 925–946.
119. Villars, P.; Onodera, N.; Iwata, S. The Linus Pauling File (LPF) and its Applications to Materials Design. *J. Alloys Compd.* **1998,** *279,* 1–7.
120. van de Streek, J.; Neumann, M. A. Validation of Experimental Molecular Crystal Structures with Dispersion-Corrected Density Functional Theory. *Acta Crystallogr.* **2010,** *B66,* 544–558.
121. van de Streek, J.; Neumann, M. A. Validation of Molecular Crystal Structures from Powder Diffraction Data with Dispersion-Corrected Density Functional Theory (DFT0D). *Acta Crystallogr.* **2014,** *B70,* 1020–1032.
122. Kaduk, J. A. Chemical Accuracy and Precision in Rietveld Analysis: The Crystal Structure of Cobalt(II) Acetate Tetrahydrate. *Powder Diffr.* **1997,** *12,* 27–39.

Further reading

Gilmore, C. J.; Kaduk, J. A.; Schenk, H. *International Tables for Crystallography Volume H: Powder Diffraction*, International Union of Crystallography: Chester, 2019.

Relevant websites

https://www.aps.anl.gov/Education/Powder-Diffraction-Educational_Materials —Beamline 11-BM, Advanced Photon Source.
https://www.cryst.ehu.es —Bilbao Crystallography Server.
https://www.icdd.com/methodfield-tutorials —ICDD, International Centre for Diffraction Data.
https://www.iucr.org/education —International Union of Crystallography.
https://www.dxcicdd.com —Denver X-ray Conference.
https://lightsources.org —lightsources.com.

INDEX

Notes

Cross-reference terms in *italics* are general cross-references, or refer to subentry terms within the main entry (the main entry is not repeated to save space). Readers are also advised to refer to each article for additional cross-references − not all of these cross-references have been included in the index cross-references.

The index is arranged in set-out style with a maximum of three levels of subheading. Major discussion of a subject is indicated by bold page numbers. Page numbers suffixed by t, f, and b refer to Tables, Figures, and Boxes respectively. *vs.* indicates a comparison.

The index entries are presented in word-by-word alphabetical sequence in which a group of letters followed by a space is filed before the same group of letters followed by a letter. For example, entries beginning 'air density' are alphabetized before 'aircraft.' Prefixes and terms in parentheses are excluded from the initial alphabetization.

A

A-site
  A-site-ordered quadruple perovskite **4**:698−705
  cation **3**:15
  columnar-ordered quadruple perovskites **4**:705−707
  perovskite oxides with A-site ordering **4**:698−707
A-type antiferromagnet $CaCo_2P_2$ **9**:236−241
  background of $CaCo_2P_2$ **9**:236
  ^{59}Co and ^{31}P NMR in $CaCo_2P_2$ **9**:237−238
  external magnetic-field dependence of direction of ordered moments in $CaCo_2P_2$revealed by NMR line-width **9**:239−240
  magnetic phase diagram of $CaCo_2P_2$determined by NMR **9**:241
  magnetic structure o/$CaCo_2P_2$ **9**:238−239
$A^{11}B$ NMR-derived structural model of borosilicate glasses **9**:624
AA platform **2**:647
Ab initio molecular dynamics (AIMD) **10**:421
ABC transporters. *See* ATP-binding cassette transporters (ABC transporters)
absolute shielding scales **9**:777
absorbance and luminescence **2**:511
acceptor doping **4**:146−147
acetyl-CoA synthases **2**:123−124
acid-base considerations on potential binding sites **2**:633
aconitase **2**:132−133
acquisition of X-ray transient absorption data **10**:346−347
actinides, luminescence properties of **8**:789−808
actinium complex **9**:666
actinoid complexes **1**:406−407
actinyls, luminescence properties of **8**:789−808
activated carbon **7**:230−232
activation wavelengths **2**:511−512
active metal hydrides **4**:387−388
active site
  mobility in zeolites
    computational assessment of **6**:183−193
    enhanced sampling methods over static methods **6**:183−185
    experimental and theoretical evidence for **6**:167−183
  mobility of active site in H-SSZ13 during fast NH_3-SCR-NOx **6**:187−191
activity metrics **7**:525−530
  onset potential and half-wave potential **7**:526−528
  overpotential at defined current density **7**:525−526
acyclic polychalcogenide anions **1**:974−975
  general **1**:974
  polysulfide radical anions **1**:975
  preparation **1**:974
  structures **1**:974−975
acyclic sulfur **1**:971−973
AD. *See* adaptive design (AD). *See* Alzheimer's disease (AD)
adaptive design (AD) **5**:12−13
  techniques **5**:7−9
AdcA and AdcAII zincophores **2**:568
ADDSYM **10**:430−434
adenosylcobamide-dependent aminomutases **2**:286
adenosyltransferases **2**:288
ADP-ribosyltransferases **2**:136−137
adsorption free energy, contribution of **6**:297−299
advanced NMR techniques and methods **9**:717−720
aging phenomena **3**:359
AHNP-platinum conjugates targeting HER2 **2**:826−827
^{27}Al (S=5/2) NMR **9**:618−620
^{27}Al-O-^{27}Al linkages in aluminosilicate glasses **9**:635
$^{27}Al^{(p)}$ NMR parameters, extracting **9**:619
albumin
  delivery of platinum drugs by **2**:827−828
alcohol oxidation **2**:380−382
ALD. *See* atomic layer deposition (ALD)
aliphatic diselenolate linkers, synthetic complexes with **1**:557−567
  hexacarbonyl complexes **1**:557−567
alkali metal alloy materials and compounds for Li-, Na-, and K-ion batteries **7**:110−112
alkaline
  alkaline-based batteries **4**:318−319
  earth metals **1**:387−388
  lattices **3**:250−251
  playing with alkaline ion **7**:23−26
alkane(s) **2**:374−375
  analogues **1**:125−138
  catalytic oxidation of **6**:390−391
alkenyl involved metal clusters with μ_4-η^1, μ_4-η^1, η^1, η^2, η^2 and μ_5-η^1, η^1, η^1, η^1, η^2 modes **1**:1060−1061
alkenyl ligands **1**:1051−1062

alkyl benzenes **2**:375–378
alkyl carbons
  centered metal clusters
    with μ_2-η^1 and m_3-h^1 modes **1**:1066–1067
    with μ_4-η^1 mode **1**:1067–1069
  as coordination sites **1**:1065–1069
alkyl iodine(I) $[L–X–L]^+$ complexes **1**:589–590
alkynyl involved metal clusters with μ_4-η^1, μ_4-η^1, η^1, η^2, η^2 and μ_5-η^1, η^1, η^1, η^1, η^2 modes **1**:1060–1061
alkynyl ligands **1**:1051–1062
alkynyl metal clusters with μ_3-η^1; μ_3-η^1, η^1, η^2 and μ_3-η^1, η^2, η^2 modes **1**:1053–1058
all-solid-state Li batteries (ASSLBs) **4**:672–676
allene analogues **1**:140–141
  group 14 element derivatives **1**:140–141
alloyed nanoparticles **9**:430–433
alloyed systems **4**:511
alloys **7**:71–75
  alloy-type materials **5**:205–206
  group 14 **7**:71–73
  group 15 **7**:73–75
alluaudite(s) **7**:54–56, **7**:256
  phosphates **7**:250–251
  sulfates **7**:253–255
alpha-synuclein (AS) **2**:607–610
AlPOs. *See* aluminophosphates (AlPOs)
alternative anode materials **7**:342
aluminium (Al) **3**:410, **4**:193–196
  Al-based complex intermetallics **3**:95–96
  Al-doped yttrium-iron garnet **9**:441
  Al-NBO bonding in aluminosilicate glasses **9**:639
  Al/Si framework materials, proton activity of **6**:285–289
    Al substitution by Fe^{3+} and Ga^{3+} **6**:285–286
    non framework substituted systems **6**:286–289
  Al/Si intermixing **9**:627
  speciations of common glass systems **9**:618–619
alumino(boro)silicates **9**:640–641
aluminophosphates (AlPOs) **9**:562, **9**:640
aluminosilicate
  glasses **9**:642–643
  zeolites, ^{29}Si NMR of **9**:119
aluminum
  aluminum-doped MnO_2 **9**:433–434
  centered biradical **1**:193
  cluster compounds **1**:822–824
aluminum nitride (AlN) **4**:160
aluminum oxide/alumina (Al_2O_3) **9**:416
Alzheimer's disease (AD) **2**:590–605
  metal ions as therapeutic target for **2**:605
  prion protein in **2**:603–605
Amber **9**:826–827
ambient pressure chemistry and strategies **4**:380–381
americium(III) **8**:801–802
amino acids **2**:514
  sensors **8**:172–173
aminopeptidase N (APN) **2**:824
aminopeptidases **2**:247–248
ammonia **3**:410
  ammonia-water mixtures **3**:410
  lyase **2**:284–285
  synthesis **3**:129–130
    catalytic activity of hydride catalysts for **3**:131
    on ionic compound surfaces **3**:130–131
amorphous materials **5**:121–122
  and preparation **5**:195–196
amorphous precursor **2**:80–82
amorphous systems **10**:237–238
amorphous *vs.* crystalline materials **9**:127–128
amphoteric germanium **3**:61–65
amphoteric silicon **3**:60
amyloid beta (Aβ) **2**:595–601
  Aβ (4-x) and Aβ (11-x) fragments **2**:598–600
  Aβ (p3-x) and Aβ (p11-x) fragments **2**:600
amyloid precursor protein (APP) **2**:590–594
anaerobic methane metabolism, corrinoid methyl group transferases in **2**:276–277
Anderson lattice model in periodic systems **3**:475–476
angle-resolved photoemission spectroscopy (ARPES) **4**:534
anion
  ANION–cation redox competition **7**:8–9
  binding and recognition **1**:630–631
  order-disorder **4**:438–439
  polymerization **7**:8–9
  substitutions in first coordination sphere **9**:603
  transport **1**:632–633
anionic $[N–I–O]^-$complexes **1**:593
anionic $[O–I–O]^-$complexes **1**:593
anionic activity from O (2p)-M(nd) p-type interaction **7**:18
anionic redox
  chemistry **7**:8–14
    birth of insertion chemistry based on dichalcogenides **7**:8–14
    practical issues **7**:13
    theoretical progresses **7**:12
  fundamentals **7**:15–21
    anionic redox activity from O 2p "NB states" or "lone-pair states" **7**:16
    band structure descriptions **7**:15
    charge-transfer vs. Mott–Hubbard classification **7**:16–17
  materials chemistry **7**:21–30
    increasing Li/M and O/M ratio in layered rock-salt compounds **7**:21–23
anisotropy of pressure field **10**:205–206
ANN. *See* artificial neural network (ANN)
anode(s) **7**:434
  anode/liquid electrolyte interfaces, structure and charge transfer at **7**:159–164
  for LIBs **4**:339–342
    conversion oxides **4**:348
    intercalation anode materials **4**:339–341
  materials **5**:199–206
anomalous neutron diffraction **10**:412
anomalous X-ray scattering **10**:412
anti-stokes properties of lanthanide compounds **8**:492
antibodies, delivery of platinum drugs by **2**:828–829
anticancer
  gold complexes with improved anti-cancer potency **2**:861–864
  gold compounds
    anti-arthritic gold(I) drugs with anti-cancer activities **2**:848
    anti-cancer gold(I) complexes **2**:848–854
    anti-cancer gold(III) complexes **2**:854–861
  metal-based drugs **2**:794–797
    chemical proteomics approach to disclose protein targets for ruthenium complex RAPTA **2**:802–803
    emerging technologies for target identification in metallodrugs' research **2**:801–804
    proteins as alternative targets for **2**:797–798, **2**:800
  therapy **2**:717–722
antiferromagnetic oxides **4**:240–243
antiferromagnets **9**:198–200, **9**:232–241
  A-type antiferromagnet $CaCo_2P_2$ **9**:236–241
  G-type antiferromagnet $BaMn_2As_2$ **9**:232–235
antimony chalcogenides **5**:149
antimony oxalate hydroxide **10**:466
antimony-donor ligands **1**:68
  monodentate ligands **1**:68
antivitamins B_{12}, B_{12}-analogs with **2**:292
apatites **9**:441–442
APN. *See* aminopeptidase N (APN)
APP. *See* amyloid precursor protein (APP)
approach-to-equilibrium molecular dynamics **3**:452
aqueous solution
  aqueous solution-gel synthesis **7**:189–191
  behavior of metal oxides dispersed in **7**:211–212
arc-melting **5**:188–189
arginine deiminase and nitrate reduction (ANR) **2**:146
argon compounds **1**:519–521
aromatic bromine(I) $[L–Br–L]^+$ complexes **1**:589
aromatic diselenolate linkers
  general aspects for structures and syntheses of iron mimetic complexes with aromatic diselenolate linkers **1**:567–568
  synthetic complexes with **1**:567–568
aromatic heavy group 14 atom frameworks **1**:844–859
  benzene and polycyclic aromatic hydrocarbon analogs **1**:851–858

cyclobutadiene dianion and dication analogs **1**:859
cyclopentadienyl analogs **1**:844–851
cyclopropenyl cation analogs **1**:858
pioneering works **1**:844
aromatic iodine(I) $[L–I–L]^+$ complexes **1**:588
ARPES. *See* angle-resolved photoemission spectroscopy (ARPES)
arsenic (As) **2**:66–69
arsenic-donor ligands **1**:67–68
bidentate ligands **1**:67–68
monodentate ligands **1**:67
battery electrolytes **1**:428–432
ionic liquids **1**:425–426
supporting electrolytes **1**:427–428
arsenides **5**:80–82
artificial drugs **3**:363
artificial intelligence for quantification of single atom images **6**:229–232
artificial neural network (ANN) **5**:18
artificial nucleobases **2**:689–700
artificial nucleosides, nucleic acids involving **2**:705–706
artificial shell **2**:91
artificial water oxidation **8**:337–347
catalyst design **8**:343–346
development of artificial water oxidation catalysts **8**:337–341
material catalysts **8**:339–341
aryl
bridged gem-dimetal moieties in metal clusters **1**:1062–1064
metal clusters with μ_3-η^1 mode **1**:1064–1065
aryl ligands **1**:1062–1065
with adjacent two or three coordination sites **1**:1065
AS. *See* alpha-synuclein (AS)
assisted metathesis **5**:31
ASSLBs. *See* all-solid-state Li batteries (ASSLBs)
ASYM-VIEW **10**:435
atom under pressure **3**:422–424
atomic diffusion requires very high temperatures **10**:202
atomic layer deposition (ALD) **7**:3–4
atomically dispersed supported metal catalysts
challenges with **6**:87–108
effects
metal nuclearity **6**:94–98
non-support ligands **6**:87–89
promoters **6**:98–101
supports as ligands **6**:89–94
limited ability
to control stability **6**:101–104
to tune catalytic performance **6**:87–101
limited metal loadings **6**:106–108
atomistic modeling **10**:419–422
atomistic thermodynamics, surface stability from DFT and **3**:83–86
ATP-binding cassette transporters (ABC transporters) **2**:566
attenuation-based imaging **5**:354–356
attractive Hubbard model **3**:480
auranofin reductase **2**:800
averaged bonding descriptors **3**:171–175
$AVPO_4F$ **7**:60–61
Aβ. *See* amyloid beta (Aβ)

B

^{11}B (S=3/2) NMR **9**:620–624
^{11}B-^{11}B COSY NMR spectroscopy **9**:97–98
B-B coupling and relaxation **9**:71–75
^{11}B-O-^{11}B linkages **9**:635–636
B-site cation **3**:14
B_{12}-analogs with metals and antivitamins B_{12} **2**:292
B_{12}-dependent dehalogenases **2**:290–291
B_{12}-dependent methyl transferases **2**:275–279
B_{12}-dependent radical-SAM methyl group transferases **2**:278–279
B_{12}-derivatives
as ligands of proteins and nucleic acids **2**:291–292
organometallic and redox-chemistry of **2**:271–275
structures of **2**:269–271
B_{12}-processing enzymes **2**:288–290
bacteria, metallomics studies disclose main bismuth binding proteins in **2**:804
bacterial acetate metabolism, corrinoid methyl group transferases in **2**:277–278
bacterial cell wall remodeling enzymes **2**:47–49
bacterial siderophores **2**:4–5
bacterial zincophores–Substrate-binding proteins (SBPs) **2**:566–569
ball-milling induced amorphization **5**:292–294
defect introduction **5**:294
mechanistic aspects of collapse **5**:293
mechanosynthesis **5**:292
structural collapse upon ball-milling **5**:292
band dispersion and effective masses of charge carriers **4**:620–623
band gaps and band edge positions **4**:617–620
tuning band gaps of nitride semiconductors **4**:617–618
tuning conduction band energy of metal nitrides **4**:618–619
tuning valence band energy of metal nitrides **4**:619–620
bare mononuclear transition metal ions **6**:151–155
β-barium borate (β-BBO) **4**:19–20
barium titanate ($BaTiO_3$) **4**:155–156
BAS. *See* Brønsted acid sites (BAS)
"base-on/base-off" switch of "complete" corrinoids **2**:271
basin hopping **3**:402–403
BaSn alloy **3**:254
batch in-situ NMR **9**:500–503
battery
application in battery electrolytes for zinc ion batteries **1**:431–432
characteristics **7**:408–409
dislocation dynamics during battery cycling **10**:177–179
electrode materials under cycling **10**:225–226
energy storage of batteries *vs.* electrochemical capacitors **7**:226–227
materials
battery basics **4**:309–311
battery performance metrics **4**:313–314
C rates **4**:314–315
co precipitation **7**:191–196
commercial Na^+ batteries **4**:351
different applications require different synthesis routes **7**:188–189
early battery chemistry **4**:318–319
early binary transition metal oxides **4**:324–325
first battery **4**:311–312
intercalation cathode materials **4**:320–338
intercalation chemistry and lithium revolution **4**:319–338
intercalation-based anode structures **4**:341–342
interfacial deposition mechanisms of ionic species on solid surfaces **7**:212–214
layered transition metal disulfides **4**:321–322
layered transition metal oxides **4**:323–330
mixed anion cathode materials **4**:335
multivalent intercalation **4**:351–356
post-synthesis thermal treatment **7**:216
precipitation **7**:191–193
single-phase reaction **4**:316–317
strategies for surface modification **7**:210–211
surface modification **7**:210–216
surface modification through deposition-precipitation **7**:214–216
synthesis of **7**:197–210
synthesis of surface modified lithium-ion battery cathode materials **7**:211–216
two-phase reaction **4**:317–318
Bayesian optimization (BO) **5**:7–9, **5**:19
non-BO **5**:9–11
BCDI. *See* Bragg coherent X-ray diffraction imaging (BCDI)
benzannulated group 14 metallolide dianion equivalents **1**:850–851
benzene and polycyclic aromatic hydrocarbon analogs **1**:851–858
germanium analogs of benzene and related polycyclic aromatic hydrocarbons containing germanium atom **1**:852–853
heavy analogs of phenyl anions **1**:856
heavy group 14 atoms **1**:856–858

benzene and polycyclic aromatic hydrocarbon analogs (*continued*)
silicon analogs of benzene and related polycyclic aromatic hydrocarbons containing silicon atom **1**:851–852
tin analogs of benzene and related polycyclic aromatic hydrocarbons containing tin atom **1**:855
benzochalcogenadiazoles **1**:616–620
benzochalcogenazoles **1**:616–620
BEP relationship. *See* Brønsted–Evans–Polanyi relationship (BEP relationship)
beryllium **4**:183–184
complexes **1**:516–517
Bhatia formalism **10**:418–419
bi-dimensional zeolites **6**:28
bidentate C^N-type gold(III) complexes **2**:859
bidentate ligands **1**:88
arsenic-donor ligands **1**:67–68
nitrogen-donor ligands **1**:44–53
oxygen-donor ligands **1**:75–83
phosphorus-donor ligands **1**:65–66
selenium-donor ligands **1**:89–90
bidentate N^N-type gold(III) complexes **2**:859
bifunctional catalysts **6**:8–11
activation of short alkanes by Ga or Zn **6**:9–10
methane to aromatics catalysis **6**:10–11
bifunctional mediators **7**:346
BIJVOET-PAIR **10**:436–437
bimetallic nanoalloys **6**:389–390
bimetallic nanoparticle catalysts, classes of **6**:384–387
bimetallic species
interrogation of **10**:127–130
selective oxidation using bimetallic catalysts **10**:127–128
bimolecular reactivity **8**:734
binary glasses **9**:128–129
binary inter-metalloid clusters
of group 14 elements **1**:908–911
of group 15 elements **1**:918–919
binary Li_2S–P_2S_5-type electrolytes **7**:206–208
binary metal oxides **4**:399
binary oxides **5**:65–69
binary products **5**:25–30
binuclear zinc hydrolases **2**:247–251
bio-derived furanics, oxidation of **6**:395–398
bioactive glasses **9**:420
bioactive phosphosilicate glasses **9**:618
biocompatibility **8**:164–166
bioelectrocatalysis **7**:457–458
applications **7**:471–483
bioelectrocatalysts
bioelectrocatalyst-electrode connections **7**:468–471
principles of **7**:458–466
bioelectrosynthesis **7**:480–483
advances in enzymatic electrosynthesis **7**:481–483
characterization of enzymatic electrosynthesis performance **7**:480–481
cofactor regeneration **7**:481
principles **7**:480
bioenergy **2**:94
biohybrid systems **2**:392
bioimaging
phosphorescent metal complexes for **2**:461–473
advantages of **2**:461–462
organelle imaging and tracking **2**:462–470
bioinorganic complexes **9**:52–53
vanadium and oxygen centers in **9**:35–38
bioinspired bond-forming reactions **2**:393–400
bioinspired carbon dioxide reduction **2**:388–390
bioinspired C–C bond-forming reactions **2**:395–396
bioinspired energy-relevant catalysis **2**:383–393
bioinspired hydrogen evolution reaction **2**:390–393
bioinspired oxidation **2**:374–383
bioinspired oxygen reduction reactions **2**:383–388
biological inorganic chemistry **2**:1
biological nitrogen fixation **2**:304–318
See also synthetic nitrogen fixation
biogenesis of nitrogenase cofactors **2**:309–310
hydride formation and unproductive H_2 release **2**:312
nitrogenase enzymes **2**:304–310
properties and function of nitrogenase cofactors **2**:310–314
reductive elimination of H_2 generates super-reduced state **2**:312
role of Fe protein **2**:304–305
biological probes **8**:196–224
biological systems **9**:50, **9**:53–54
biomass
oxidation **6**:391
valorization **6**:31–32
biomaterials **9**:566–567
biomedical therapy **2**:96–98
cancer treatment **2**:98
vaccine improvement **2**:96–98
biomineralization
application of biomineralization for tissue regeneration **2**:87–91
crystallization in **2**:78–85
bioorthogonal probes **8**:200–209
biosensors **7**:471–476
characterization of analytical performance of electrochemical enzymatic biosensors **7**:473–474
principles **7**:471–473
biotin-platinum conjugates targeting SMVT **2**:822
2,2′-biphosphinine **1**:66
2,2′-bipyridine **1**:53
biradicaloids **1**:13–14
biradicals **1**:13–14, **1**:168
applications of biradicals as molecular switches **1**:221–222
character **1**:184–187
chemical interpretation of biradical states **1**:172–175
classifications of **1**:187–188
degenerate frontier orbitals **1**:175–180
dynamic *vs.* non-dynamic correlation **1**:168–169
electrons in orbitals **1**:169
energetic ordering of biradical states **1**:170–172
four and five-membered heterocyclic **1**:224
frontier orbitals **1**:169–170
general aspects **1**:188–189
group analogs of cyclobutane-1, 3-diyls **1**:189–210
main group **1**:188–221
non-symmetric **1**:183–184
orbital transformations **1**:180–183
theoretical description of **1**:168–188
bis-noble-gas hydrides **1**:513–515
bismuth (Bi) **2**:63–65
Bi···Bi metallophilic interactions **1**:718–720
binding proteins in bacteria, metallomics studies disclose main **2**:804
bismuth-based layered structure **4**:161
chalcogenides **5**:149
intermolecular Bi···Bi metallophilic interactions **1**:718–720
bismuth ferrite ($BiFeO_3$, BF) **4**:158
bismuth telluride (Bi_2Te_3) **4**:54–55
bismuthides **4**:384–385
bisulfates **7**:251–253
black box, peering into **10**:249–252
Bloch's theorem **3**:148–149
blue emissive iridium(III) complexes **8**:5–15
BO. *See* Bayesian optimization (BO)
BO↔NBO substitutions in first coordination sphere **9**:602–603
Boltzmann transport equation **3**:449–451
bond activation on metal surfaces **3**:106–114
bond angles **9**:604
distributions in silicate glasses **9**:128
bond dissociation viewed as bond formation **3**:128–129
bond formation
bond dissociation viewed as **3**:128–129
on metal surfaces **3**:114–119
bond lengths **9**:604
bond reorganization, photochromism with **8**:365–366
bond valence site energy (BVSE) **7**:411
software for BVSE modeling **7**:418
bond valence sum energy modeling **7**:413–414
bonding analysis
in boron rich borides
borides with capping vertices **3**:43
borides with missing vertices **3**:42–43
classical bonding **3**:28–32

in condensed polyhedral **3**:40–41
delocalized monopolyhedral bonding **3**:32–39
localized 3c–2e bonding **3**:32
in non-deltahedral borides **3**:44–45
in single-vertex sharing macropolyhedra **3**:41
localization and delocalization indices for **3**:232–233
between molecules H and X bonding **3**:178–179
in position space
electron density for **3**:223–224
bone **9**:814–816
borate(s) **4**:18–19, **4**:410–412, **4**:647, **7**:255
glasses **9**:643
starting materials to introduce **1**:383–384
borenium cations **1**:344–346
borides
with B_{12} units **3**:36–38
with B_6 units **3**:35–36
with B_n deltahedra **3**:38–39
with sp hybridized boron **3**:28–29
with sp^2 hybridized boron **3**:29–30
with sp^3 hybridized boron **3**:30
of transition metals **4**:381–382
boron **3**:410, **4**:191–193, **9**:780
centered biradicals **1**:190–193
borophosphates **9**:642
bottom-up assembly **5**:223–226
bottom-up zeolite synthetic strategies **6**:49–51
Bragg coherent X-ray diffraction imaging (BCDI) **10**:155–160
active site determination using **10**:166–167
crystal growth and dissolution studied via **10**:170–174
at fourth-generation synchrotron sources **10**:183
in-situ/operando capabilities **10**:160–165
resolution **10**:157
sensitivity to lattice displacement **10**:157–159
strain tensor **10**:160
studies
of catalytic materials **10**:165–170
of energy storage materials **10**:174–179
ultrafast dynamics using **10**:179–183
Bragg geometry, coherent X-ray diffraction imaging in **10**:152–165
Bridgman method **4**:519
Bridgman single crystal growth **5**:185
broken bond model
apply at intermetallic compound surfaces **3**:88–89
at metal surfaces **3**:87–88
bromoxenate cage anions **1**:503–504
Bronsted acid **9**:45
Brønsted acid sites (BAS) **6**:167
mobility in pristine zeolite framework **6**:167–169
protic molecules mediated hopping and solvation of **6**:169–170
proton mobility in **6**:167–170
Brønsted–Evans–Polanyi relationship (BEP relationship) **6**:211
Brown millerites **5**:262
bulk crystals **4**:450–451
growth from melt **4**:519
bulk-truncated surfaces **3**:78–80
BVSE. *See* bond valence site energy (BVSE)

C

C-terminal $(4Fe4S)_{AUX}$ of HydG **2**:183–184
C=C oxidation **2**:378–380
CA. *See* carbonic anhydrases (CA)
cadmium **2**:71, **4**:188–190, **9**:850–853
complexes **9**:711–713
sulfide nanoparticles **9**:405
cage compounds **3**:96
CALC
ALL **10**:429
SOLV **10**:434
calcium
calcium-binding properties of α-synuclein and biological implications **2**:608
citrate hexahydrate **10**:461–462
hydrogen citrate dihydrate **10**:461
cancer stem cells (CSCs) **2**:771
targeted **2**:751, **2**:771–772
canvas paintings **9**:802
capsules **1**:625–626
carbamazepine dihydrate (CBZ dihydrate) **9**:425
carbide(s) **4**:389–397
materials **4**:394–395
mechanism **6**:364
of transition metals **4**:381–382
carbine
ligand-based copper(I) complexes **8**:49–51
transfer reactions **2**:222–225
triplet harvesting by thermally-activated delayed fluorescence using carbene metal amides **8**:662–664
carbohydrate probes **8**:196
carbon dioxide (CO_2) **7**:481–482
catalysts for CO_2 hydrogenation **10**:117–122
palladium catalysts for emissions abatement **10**:122–127
supported catalysts measured at atmospheric pressure **10**:117–118
supported catalysts measured at elevated pressures **10**:118–122
dissociation from carboxylato 3d TMCs **8**:762
carbon dioxide reduction reaction (CO_2RR) **10**:138
carbon monoxide (CO)
reduction by V-dependent nitrogenase **2**:314–317
CO-bound structures are dead-end adducts **2**:315
continuous electron and proton supply in three phases **2**:316–317
insertion of hydride **2**:315–316
N_2 binds to E4 state **2**:317
product release **2**:317
provision of electrons and protons in nitrogenase cofactors **2**:314–315
reductive elimination of H_2 is linked to N_2 binding **2**:317–318
requirements for binding different substrates **2**:314
carbon(s) **4**:198–200, **5**:82
based materials, unsaturated moieties as precursors for **4**:394–397
C-donor functionalized carbenes **1**:243–247
carbon-based negative electrode materials **7**:65–69
carbon-centered biradicals **1**:212–213
carbon-doped MgB_2 **9**:433
carbon-skeleton mutases **2**:282–284
C–C bond formation **2**:394–396, **8**:85–90
centered biradicals **1**:193–195, **1**:210–212
C–H activation of methane on IrO_2 surface **3**:120–122
C–H bond
activation on late transition metal oxide surfaces **3**:119–129
oxidations **2**:374–378
C–N
bond formation **2**:396, **8**:92–93
materials **4**:395
C–O bond formation **2**:396, **8**:90–91
C–P bond formation **8**:93–94
electrode degradation **7**:343–344
magnetoplumbite-related phases **4**:691
materials **4**:394–395, **7**:104–110
electrochemical properties of graphite **7**:106–107
hard and soft carbon **7**:108–110
K Alloys and potassiatable compounds **7**:110–114
K intercalation into graphite **7**:104–105
monoxide
Co^{3+} perovskites **4**:691
Co^{4+} perovskites **4**:690–691
dehydrogenases **2**:123–124
oxides **4**:690–691
RP phases **4**:691
nanoparticles **9**:402
nanotubes **9**:451–453
ophosphates **7**:263–264
valence and conduction band dispersion of carbon nitrides **4**:622–623
carbonates **4**:410–412, **4**:646
carbonate-phosphates **7**:61–63
carbonic anhydrases (CA) **2**:44–45, **2**:241–244
carbonyl **8**:179–189
carboranes, NMR of **9**:62–106
carboxylates **1**:78–80
linkers **5**:231
carboxypeptidases (CPDs) **2**:244–245
Carr-Purcell Meiboom-Gill sequence (CPMG sequence) **9**:148
cartridge synthesis **10**:325
catalysis
FLP in **1**:315–377

catalysis (*continued*)
by intermolecular chalcogen bonding **1**:635–639
of methylations by rlmn and cfr **2**:129
and polymerization chemistry **1**:421–424
applications in homogenous catalysis **1**:421–423
applications in polymerization chemistry **1**:423–424
of sulfur insertion-biotin synthase **2**:127–128
catalyst
loading and utilization **7**:538
self-assembly **10**:127
catalytic active sites within zeolite catalysis, dynamic evolution of **6**:165–200
catalytic chemistry of proton activation **6**:293–310
catalytic layer (CL) **7**:531–538
conductivity of **7**:535–536
catalytic materials, BCDI studies of **10**:165–170
sample environments for in-situ/operando studies **10**:166
strain and defect evolution during catalysis **10**:168–170
catalytic oxidation of alkanes **6**:390–391
catalytic reactions, reaction intermediates for **10**:320–321
catalytic sites
chemical shift and quadrupolar patterns for investigating sites **9**:480–483
investigation of catalytic sites via internuclear correlations **9**:484–499
isotropic chemical shift for revealing **9**:481–482
NMR principles and basic interactions **9**:474–480
quadrupolar interaction for revealing catalytic sites **9**:483
catechol **2**:8, **2**:18
catena-polypnictogens, reactions forming **1**:898
catenanic copper complexes **8**:363–364
catenanic ruthenium complexes **8**:364
cathode(s) **7**:432–434
See also anodes
cathode/liquid electrolyte interface, structure and charge transfer at **7**:164–166
sulfur host structures **7**:432–433
materials **5**:206–212
cation disorder **7**:28–30
cation ordering **5**:258–260
in structure types, and summary **5**:260
cationic $[S–X–S]^+$ complexes **1**:594
CBO. *See* cesium triborate (CBO)
CBZ dihydrate. *See* carbamazepine dihydrate (CBZ dihydrate)
CDI. *See* coherent X-ray diffraction imaging (CDI)
CE. *See* cross effect (CE)
cell(s)
biology of zinc **2**:234–236
for electrochemical reactions **10**:115–116
for gas-liquid and gas-liquid-solid reactions **10**:116
for gas-solid reactions **10**:115
for grazing incidence measurements **10**:116
organelles **2**:470
cellular accumulation **2**:813
cellular molecule labelling **2**:470–473
cellular physical state detection **2**:470–473
ceria-based catalysts
catalysis by single-atom ceria-based catalysts **6**:262–266
characterization of ceria materials **6**:250–257
metal-support interfaces in ceria catalysts **6**:257–262
structure and redox properties **6**:244–247
synthesis of ceria **6**:247–249
cerium(IV) oxide/ceria (CeO_2) **9**:414–416
cesium lead iodide perovskites (CsPbI3)
halide perovskite photovoltaic **3**:12–13
cesium lithium borate (CLBO) **4**:22–24
cesium triborate (CBO) **4**:22
CEST. *See* chemical exchange saturation transfer (CEST)
CH_2NCH_2 moiety of azapropanedithiolate bridge derives from serine amino acid residue **2**:187–188
chain compounds with direct E-E-single bonds **1**:779–807
chalcogen
in aromatic systems **1**:610
biradicals **1**:209–210
bonding
in catalysis and synthesis **1**:634–642
definition of interaction energy, choice of basis sets and methods **1**:643–644
interaction energies and potential energy surfaces **1**:644
model systems **1**:644–647
in solid state **1**:603–625
theoretical and computational studies **1**:642–647
chalcogen-anion coordination **1**:630–634
chalcogen-arsenic, -antimony, and-bismuth compounds and complexes **1**:998–1005
chalcogen-chalcogen interactions **1**:603–613
linear systems with chalcogen centers **1**:603–605
chalcogen-halogen
cations **1**:1010–1013
interactions **1**:620–621
chalcogen-hydrogen interactions **1**:625
chalcogen-iodine cations **1**:960
chalcogen-nitrogen compounds **1**:988–994
chalcogen-oxygen interactions **1**:623–625
chalcogen-phosphorus compounds **1**:994–998
chalcogen-pnictogen interactions **1**:613–620
donor functionalized nonclassical carbenes **1**:257–262
halogenides **1**:1005–1014
interactions **1**:621–625
in catalysis, special **1**:641–642
self-assembly by **1**:625–629
linkers **5**:227–228
rings as ligands in metal complexes **1**:948–952
chalcogenides **10**:192–196, **4**:10–11, **4**:648–649, **5**:52–55
clusters, $T_{p,\,q}$ type of **5**:223
chalcogenocyanates **1**:613–616
channels **2**:357–359
identifying **2**:357–359
characterization techniques
combination of **5**:321–322
modeling **7**:440
used in Li-S battery mechanistic research **7**:436–447
charge density studies **10**:99–100
charge flipping algorithm **10**:462–466
charge neutralization reactions **1**:925
charge process **7**:334–335
charge transfer
cross solid/solid interfaces **7**:154–157
kinetics
apparent activation energies for interfacial charge transfer **7**:143–148
experimental studies of **7**:137–148
in ion intercalation processes **7**:132–137
modeling charge transfer in metal-ion batteries **7**:148–166
Chatt cycle **2**:321–322
chemical bonding analyses **3**:213–220
basic examples **3**:202–213
basis functions **3**:155–157
complicated molecules, LCAO in general **3**:147–148
concept of charges and bonding indicators **3**:151–155
interplay of bonding and structure **3**:194–196
materials mapping **3**:191–193
methods **3**:155–175
principles in magnetic topological quantum materials
combined with SOC effects **3**:495
derived from semiconductors and semimetals **3**:494–495
design novel intrinsic magnetic topological materials from chemistry perspectives **3**:494–499
expanding magnetic behaviour **3**:502–504
fixed by symmetry and crystal structures **3**:495–496
manipulating magnetic and electronic states with pressure **3**:502–505
tuned by chemical substitutions **3**:498–499
tuning fermi level **3**:504–505
utilizing neutron scattering to understand magnetic topological materials **3**:499–502
projected DOS, COOP, COHP, fatband, and k-dependent COHP and time-reversal symmetry **3**:163–166

for simplest molecule **3**:143–144
chemical exchange saturation transfer (CEST) **2**:441–442
chemical insights from total scattering experiments **10**:259–262
challenges and limitations for in situ total scattering experiments **10**:262
PDF studies of particle nucleation **10**:260–262
chemical isolation of reactants is critical **10**:204
chemical modeling, optimal parameters for **3**:364–365
chemical noninnocence **1**:242–262
chemical pressure approach
assessment of anion positions in metallic structures in light of chemical pressure formalism **3**:250–254
chemical pressure-DFT formalism **3**:241–243, **3**:245–248
contextualization of **3**:240–241
chemical proteomics approach to disclose protein targets for ruthenium complex RAPTA **2**:802–803
chemical reactions **3**:320, **3**:351
in pore, direct observation of **10**:325–326
chemical shielding **9**:284
chemical shift
chemical shift ranges and Ramsey's equation **9**:749–751
of network modifiers **9**:605
temperature sensitivity of **9**:751–755
chemical shift anisotropy (CSA) **9**:475–476
and dipolar coupling interactions **9**:477–478
powder patterns **9**:476–477
and quadrupolar patterns for investigating catalytic sites **9**:480–483
for revealing catalytic sites **9**:482–483
structural information from **9**:614–616
chemical stability
of garnet **4**:666–667
of NASICON-type Li ion electrolytes **4**:664
of perovskite-type Li ion electrolytes **4**:662–663
chemical synthesis with in situ X-ray diffraction, high-pressure apparatus for **10**:206–217
chemical vapor deposition (CVD) **5**:153–154
chemicals, inorganic catalysis for methane conversion to **6**:327–353
chemosensors **8**:167–196
chemotherapeutic agents, metal complexes as **2**:744–793
chemotherapy **2**:2
phosphorescence in **2**:474
phosphorescent metal complexes for **2**:473–480
Cherenkov radiation with inorganic lumiphores **2**:422–425
chiral noninnocence **1**:268–275
chloro-xenate cage anions **1**:503–504
chlorotoxin (CTX) **2**:825
CTX-platinum conjugates targeting chlorotoxin receptors **2**:825
chromatographic analysis **7**:440–441
chromium (Cr) **2**:342
complexes **9**:675–676
Cr (III) complexes **8**:73
Cr (III) polypyridines **8**:133–135
Cr oxides **4**:686
photoNORMs **8**:276–277
CL. *See* catalytic layer (CL)
classical molecular dynamics (CMD) **10**:420–421, **7**:414–415
clathrates **10**:28, **4**:70–71
clathrate-like hydrides **3**:434–435
CLBO. *See* cesium lithium borate (CLBO)
close-packed solids, EZKC in **3**:67–70
closed shell binary oxides **4**:634–637
closo-borate anions and derivatives **1**:741–763
closo-decaborate anion ($[B_{10}H_{10}]^{2-}$) **1**:755–762
derivatives with
B–C bonds **1**:761–762
B–N bond **1**:759–761
B–O bond **1**:757–758
B–P bonds **1**:761
B–S bond **1**:758–759
general aspects **1**:755–756
halogen derivatives **1**:756–757
oxidation reactions **1**:762
closo-dodecaborate anion ($[B_{12}H_{12}]^{2-}$) **1**:741–755
derivatives with
B–C bonds **1**:754
B–N bonds **1**:748–754
B–O bond **1**:745–747
B–P bonds **1**:754
B–S bond **1**:747–748
B–Se bond **1**:748
general aspects **1**:741–742
halogen derivatives **1**:743–744
oxidation reactions **1**:754–755
closo-heneicosaborate anion **1**:768
closo-heptaborate anion ($[B_7H_7]^{2-}$) **1**:763
closo-hexaborate anion ($[B_6H_6]^{2-}$) **1**:763
closo-nonaborate anion ($[B_9H_9]^{2-}$) **1**:762
closo-octaborate anion ($[B_8H_8]^{2-}$) **1**:762–763
closo-undecaborate anion($[B_{11}H_{11}]^{2-}$) **1**:755
cluster
beam deposition catalyst synthesis **6**:387–389
clusters based on architectures **4**:88–91
fluxionality **6**:205–208
intercluster or intracluster charge transfer in cluster-based chalcogenides **5**:239–240
with p-block (semi)metals from different groups **4**:130–131
from supertetrahedral cluster to cluster-based superlattice **5**:226–235
cluster resolution feature selection (CR-FS) **5**:13–15
CMD. *See* classical molecular dynamics (CMD)
C*n*-P*n* hybrid assembly **5**:233
C*n*-type of chalcogenide clusters **5**:221–222
cobalamins
cobalamin-deligase CblC **2**:289–290
as gene-regulatory RNA-ligands **2**:291
cobalt (Co) **2**:333–338, **9**:438
catalysts **6**:358–360
co-catalytic materials **7**:536–538
co-crystalline derivative **9**:425
Co-related metal complexes **2**:386–387
Co/Rh/Ir-Sn **4**:222–223
cobalt reduction in Co Fischer-Tropsch catalysts **10**:128
cobalt-bound methyl groups, radical-induced abstraction of **2**:275
cobalt-containing nanoparticles **9**:437–438
cobalt-corrins as cofactors and intermediates in enzymes **2**:275–291
cobalt(III) complexes **8**:137–139
Co–C bond
homolytic cleavage and formation of **2**:274
nucleophile-induced heterolysis and formation of **2**:274–275
complexes **9**:689–693
dissociation from 3d TMC **8**:754
enzymes
B_{12}-derivatives as ligands of proteins and nucleic acids **2**:291–292
cobalt-corrins as cofactors and intermediates in enzymes **2**:275–291
organometallic and redox-chemistry of B_{12}-derivatives **2**:271–275
structures of B_{12}-derivatives **2**:269–271
hemoprotein reconstituted with cobalt porphyrinoid **2**:226
insertion mechanism **6**:364–366
reactions by and Ni porphyrinoids in hemoproteins **2**:225–227
reduction in Co Fischer-Tropsch catalysts **10**:128
stripping **7**:508–509
cobamide-dependent methionine synthase (MetH) **2**:275–276
coenzyme B_{12}
coenzyme B_{12}-dependent isomerases **2**:284–286
coenzyme B_{12}-dependent ribonucleotide reductases **2**:287–288
as light-sensitive ligand in photo-regulatory proteins **2**:291–292
and related adenosylcobamides **2**:279–288
coherent X-ray diffraction imaging (CDI) **10**:153
in Bragg geometry **10**:152–165
fundamentals of **10**:153–154
coherent X-rays **10**:149–152
applications of **10**:151–152
diffraction studies of inorganic crystalline nanomaterials **10**:149–186
source of X-rays **10**:149–151

collapse, pressure and temperature **5**:302–304
collossal magnetoresistance **4**:254–255
color **4**:562–570
  due to band to band (band gap) transitions **4**:567–569
  due to charge transfer transitions **4**:564–567
  due to *d-d* transitions **4**:563–564
  due to defects **4**:569
  due to other reasons **4**:569–570
combinations of mechanisms **2**:514
combinatorial chemistry approach **4**:300–301
combined imaging and therapy-image-guided therapy **2**:411
combined therapy and theranostics, MOFs **2**:735–736
combustion synthesis **7**:197
complementary spectroscopic techniques **10**:11, **10**:411–415
complete corrinoids **2**:269–271
  base-on/base-off switch of **2**:271
complex doping **4**:147
complex hydrides **10**:20–27
  history and nomenclature **10**:20
  neutron scattering studies of **10**:21–26
complex modeling, combination of **5**:321–322
complexed free elemental clusters **1**:412–415
complexed mixed-transition metal-element clusters **1**:416–419
composite materials **5**:89–90
compositional complexity **3**:409–410
compositional stability **3**:404–405
compound P **9**:423
compounds with oxoanions and mixed anion groups **7**:61–63
computation of NMR parameters for inorganic nuclides, advances in **9**:837–868
computational alchemy **3**:361
computational design
  of ion conducting materials **7**:410–419
  of materials for metal-ion batteries **7**:404–429
  state of art and role of **7**:404–406
computational methods for perovskite electronic structure **3**:8–9
computational modeling and characterization of secondary bonding in compounds of late p-block elements **1**:572–585
computer-aided approaches of metallomics and metalloproteomics **2**:60
condensed materials **5**:65–85
conduction band dispersion of metal oxide **4**:610
conductors **9**:41–43
  dynamics **9**:43
  structure **9**:42–43
confinement **6**:300–305
  micro pore equilibration **6**:303–305
  stereoselectivity **6**:303
  transition state stabilization **6**:300–301
π-conjugated aromatic ligands, gold(III) complexes with coordination of **2**:858
conjugates **8**:408–409
conjuncto-boranes **1**:766–768
continuous wave (CW) **8**:495–497
CONTOUR **10**:430
contrast agents **2**:436
contrast transfer function (CTF) **10**:64–65
conventional platinum(II) complexes **2**:745–747
  clinically used anticancer agents **2**:745–747
conversion anodes **4**:347–348
conversion batteries **4**:343–348
conversion cathodes **4**:343–347
conversion materials **5**:205–206
conversion-alloying reactions **7**:120
cooperative photoredox catalysts **8**:142
coordination cages **8**:635–638
coordination chemistry of P_4 and As_4 tetrahedra **1**:887–888
coordination compounds **1**:913–915, **8**:419–421
  of group 14 elements **1**:911–918
  of group 15 elements **1**:919–921
  as photoactive triggers **8**:422–427
  as structural and photoactive components **8**:428–435
  as structural elements **8**:421–422
  of substituted Zintl anions **1**:915–918
  of Tt_4^{4-}, $Tt_5^{2-}$and Tt_9^{4-} **1**:911–913
coordination environment around metal center, regulation of **8**:387–391
coordination number **9**:601–602
coordination polymers **5**:56–57
copals **9**:826–827
copper (Cu)
  binding
    to amyloid precursor protein and biological implications **2**:591–593
    to prion protein and biological implications **2**:584–586
    properties of tau protein and its biological implications **2**:601
    properties of α-synuclein and biological implications **2**:609
    properties to amyloid-β peptide and biological implications **2**:596–598
  complexes **9**:704–706
  copper(I) complexes **8**:48–55, **8**:598–606
    clusters **8**:598–604
    four-coordinate copper(I) complexes **8**:52–55
    metallacycles Cu-related metal complexes **2**:387, **8**:605–606
    three-coordinate copper(I) complexes **8**:51
  Cu oxides **4**:693–695
  Cu-related metal complexes **2**:387
  Cu···Cu interactions **1**:704–708
  heteroleptic complexes **8**:125–132
  intermolecular Cu···Cu metallophilic interactions **1**:705–708
  mobility of Cu sites in Cu-CHA during low-temperature NH_3-SCR-NOx **6**:173–180
    catalytically relevant mobile $[Cu(NH_3)_2]^+$ under low-temperature standard SCR **6**:173–175
    mobilized copper in oxidation half-cycle during NH_3-SCR-NOx **6**:175–180
corrinoid methyl group transferases
  in anaerobic methane metabolism **2**:276–277
  in bacterial acetate metabolism **2**:277–278
corundum-derived $LiNbO_3$-type materials **5**:259–260
corundum-derived Ni_3TeO_6-type materials **5**:260
corundum-derived ordered-ilmenite materials **5**:260
corundum-derived structures **5**:258–260
cost function as combination of potential energy and experimental data **3**:350
cost function landscapes, robustness of **3**:306–307
COT. *See* cyclooctatetraene (COT)
coupled non-polar distortions **5**:264–266
covalent bonding indicators **3**:171–173
covalent crystalline oxides and glasses **9**:189–191
covalent hydrides **3**:435–437
CP. *See* cross-polarization (CP)
CPDs. *See* carboxypeptidases (CPDs)
CPMG sequence. *See* Carr-Purcell Meiboom-Gill sequence (CPMG sequence)
CR-FS. *See* cluster resolution feature selection (CR-FS)
Crewe's Z-contrast **10**:67
cross effect (CE) **9**:368–369
  mechanism **9**:389
cross-polarization (CP) **9**:148–149, **9**:636–638
cross-validation (CV) **5**:19
cryo-electron microscopy (cryo-EM) **2**:369
cryo-EM. *See* cryo-electron microscopy (cryo-EM)
crystal **4**:450–459
  atom under pressure **3**:422–424
  chemistry at high pressure **3**:421–422
  design for in situ observation of unstable species by X-rays **10**:314–315
  mechanical exfoliation of **4**:452
  orbital bond index **3**:168–170
  packing approach **10**:315–321
  under pressure **3**:424–432
    compounds of noble gases **3**:427–428
    electronic structure **3**:424–425
    geometries and bonding **3**:429–432
    high pressure electrides **3**:425–427
    miscibility under pressure **3**:428–429
  superconductivity **3**:432–437
  symmetry, effects of **4**:139–140
crystalline
  amorphous *vs.* crystalline materials **9**:127–128

configuration space **3**:394–396
inorganic materials from supertetrahedral chalcogenide clusters **5**:216–245
molecular flask **10**:324–340
state photoreaction, networking of M_6L_4 and in situ observation of **10**:324–325
state solution-state-like reaction–direct observation of photo-dimerization of acenaphthylene in M_6L_4 cage **10**:323
crystallites, nucleation of **10**:238–240
crystallization **5**:223–226
in biomineralization **2**:78–85
classical crystallization **2**:79
nonclassical crystallization **2**:80–85
mechanism **5**:91–94
crystallographic image processing **10**:65–66
CSA. *See* chemical shift anisotropy (CSA)
CSCs. *See* cancer stem cells (CSCs)
CTF. *See* contrast transfer function (CTF)
CTX. *See* chlorotoxin (CTX)
Curie temperature **4**:138
Curie-Weiss law **4**:138, **4**:238
curium (III) **8**:802–804
CV. *See* cross-validation (CV)
CVD. *See* chemical vapor deposition (CVD)
CW. *See* continuous wave (CW)
cyclic (alkyl)(amino)carbine **1**:238–241
cyclic chalcogen anions **1**:962–964
cyclic chalcogen-halogen cations **1**:959–960
cyclic radical anions **1**:963
cyclic selenoethers **1**:531–532
adducts and coordination compounds **1**:531–541
crown-ether analogs **1**:540–541
cyclic selenoether cations **1**:541–543
molecular structures **1**:529–531
saturated selenoethers **1**:527–543
selenoethers
with alkene spacers **1**:543–550
with alkyne spacers **1**:552–553
synthesis **1**:527–529
unsaturated selenoethers **1**:543–553
cyclic systems with chalcogen centers **1**:605–609
cyclic voltammetry **7**:436–437, **7**:478
cycloalkanes **2**:374–375
cyclobutadiene dianion and dication analogs **1**:859
cycloheptaselenium, Se_7 **1**:941
cycloheptasulfur, S_7 **1**:937–939
cyclohexaselenium, Se_6 **1**:941
cyclohexasulfur, S_6 **1**:936–937
cyclooctaselenium Se_8 **1**:941–942
cyclooctasulfur, S_8 **1**:939–940
cyclooctatetraene (COT) **9**:224–226
cyclooxygenase inhibition **2**:762–764
cyclopentadienyl analogs **1**:844–851
benzannulated group 14 metallolide dianion equivalents **1**:850–851
group 14 metallole anion equivalents **1**:844–845
group 14 metallolide dianion equivalents **1**:846–849
cyclopentadienyllithium CpLi) **1**:845
cyclopentane-1,3-diyls, main group 15 analogs of **1**:210–221
cyclopropenyl cation analogs **1**:858
cytochrome P450 **2**:198–207
catalyzing monooxygenation **2**:198–203
catalyzing peroxygenase **2**:204–207
modification of substrate specificity of cytochrome P450BM3 **2**:222
cytoplasm **2**:467–468

D

d-block metal ions in neurodegenerative diseases **2**:575–628
d-block SMMs **9**:219
d-PDF studies **5**:321
d^0 ions, SOJT for **5**:252–254
d^0 transition metals, emission from **4**:269–270
DAC. *See* diamond anvil cell (DAC)
dangling bonds **3**:90–91
at elemental semiconductor surfaces **3**:90–91
at intermetallic and oxide surfaces **3**:91
DARR. *See* dipolar-assisted rotational resonance (DARR)
data
acquisition methods **9**:147–152
analysis **10**:114–115
in real space **5**:310
and reporting **7**:545
collection **10**:278–283
data-driven approaches **4**:301–302
processing **10**:313
science and TE materials **3**:456–457
databases **3**:456
informed methods **3**:400–401
of ion conducting materials **7**:419
DDR. *See* DNA damage response (DDR)
decaborane(14) **1**:764–765
decision tree (DT) **5**:19
deep-red emissive iridium(III) complexes **8**:21–27
deep-ultraviolet NLO materials (DUV NLO materials) **4**:27–35
dehydration–synthesis of ribonucleotide–viperin **2**:129–130
dehydrogenative aromatization **8**:98
dehydrogenative olefination **8**:97
dehydrogenative oxonation of alcohols **8**:95–97
delocalized carbocations **1**:397
DELRED **10**:430–434
deltahedral clusters with 9, 10, 11 and 12 vertices **1**:908–910
demetallization **6**:51–52
densities of states **3**:336–337
free energies and **3**:336–338
density **9**:393
density functional theory (DFT) **10**:421, **2**:514, **3**:81, **3**:144–147, **4**:508–510
calculations **2**:514, **7**:415–417
DFT-chemical pressure methodology **3**:243–245
structural models for surfaces within DFT **3**:82–83
surface stability from DFT and atomistic thermodynamics **3**:83–86
density-dependence of gas-phase NMR spectrum **9**:772
dephasing curves for distance measurement **9**:497–498
deprotonation energy **6**:279–281
desferrioxamine B (DFOB) **2**:16–18
designing new polar materials
in context **5**:247
displacive polar phases **5**:249–250
experimental methods **5**:268–270
order parameter **5**:250
order-disorder
and displacive descriptions of **5**:248–250
polar phases **5**:248
property measurements **5**:269–270
strategies for **5**:251–268
structural characterization **5**:269
synthesis methods and sample preparation **5**:268–269
theoretical background and definitions **5**:247–251
DET. *See* direct electron transfer (DET)
detection techniques of metallomics and metalloproteomics **2**:58–59
detonation nanodiamonds (DNDs) **9**:402
DFOB. *See* desferrioxamine B (DFOB)
DFT. *See* density functional theory (DFT)
diammonium 2,6-naphthalenedicarboxylate **10**:475
diamond anvil cell (DAC) **10**:209–214
advantages and disadvantages of **10**:213
using DAC for chemical synthesis **10**:211–212
examples of synthesis with **10**:213–214
1,2-Diaza-4-silacyclopentane-3,5-diyls **1**:212
1,2-Diaza-cyclopentane-3,5-diyls **1**:210–212
diazenides **4**:392
dichalcogenides, birth of insertion chemistry based on **7**:8–14
dielectrics **5**:122–123, **5**:247
hysteresis loop **4**:138–139
1,3-diene analogues **1**:139–140
heteronuclear derivatives **1**:139–140
differential scanning calorimetry **5**:296–297
diffraction techniques **7**:505
pattern **3**:478
of X-ray\synchrotron radiation **5**:347–358
diffuse and total scattering **4**:529
diffusion rates are greatly diminished under pressure **10**:204–205
diffusion-ordered spectroscopy (DOSY) **9**:28, **9**:718
digermenes **1**:128–130
digermyne **1**:144
β-diketiminates **1**:50–52
β-diketonates **1**:77–78
1,2-dimethoxyethane **1**:75–76

dinitrogen (N_2) **7**:482
dinuclear binding site for substrates **2**:313–314
dinuclear iron systems **2**:332–333
dinuclear molybdenum systems **2**:322–327
diol dehydratase **2**:284–285
diol ligands **1**:76–77
diolato ligands **1**:76–77
Dion-Jacobson phases (DJ phases) **5**:266
  hybrid-improper mechanisms in **5**:266
diphosphene derivatives **1**:145–151
diplumbenes **1**:132
diplumbyne **1**:145
dipnictogens **1**:866–871
  non-supported, cyclic dipnictogens **1**:868–869
  non-supported, non-cyclic dipnictogens **1**:866–867
  supported, heterocyclic dipnictogens **1**:869–870
  supported, metalated dipnictogens **1**:870–871
dipolar coupling plays **9**:485–486
dipolar interaction **9**:284–285
dipolar-assisted rotational resonance (DARR) **9**:541–543
direct dipolar interaction **9**:265
direct E-E-single bonds, chain and ring compounds with **1**:779–807
  synthesis and structures of compounds
    with E-E′ bonds **1**:806–807
    with E_3-units **1**:794–799
    with higher E_n-units **1**:799–806
    with solitary E_2-units **1**:779–794
direct electron transfer (DET) **7**:467
direct methane conversion **6**:331–343
  low and medium temperature methane conversion **6**:331–335
direct polarization **9**:386
discharge process **7**:327–334
  general reaction pathway **7**:327–328
  superoxide anion formation and solvation **7**:328–329
disconnectivity graphs **3**:356
discrete anions **1**:963
discrete clusters in crystal lattice and dispersibility in solvent **5**:235–236
discrete multinuclear platinum(II) complexes **8**:591–592
discrete structure modeling of nanomaterials **5**:314–317
disilenes **1**:125–128
disilynes **1**:144
display panels, phosphors for **4**:289–290
disproportionation **6**:2–4
distannenes **1**:130–132
distannyne **1**:144–145
distribution of quadrupolar parameters **9**:607–609
1,2-Dithiolylium-4-olates **1**:212–213
divalent oxides **4**:634
DJ phases. *See* Dion-Jacobson phases (DJ phases)
DJ-1 protein **2**:606
  metal-binding properties of DJ-1 protein **2**:606
d^n transition metals, emission from **4**:270–271
DNA **2**:514
  damage repair **2**:813–814
  from paramagnetic metal ions to inorganic samples, applications of **9**:388–389
  repair glycosylases **2**:149–150
DNA damage response (DDR) **2**:772
  disrupters **2**:772
DNDs. *See* detonation nanodiamonds (DNDs)
DNP. *See* dynamic nuclear polarization (DNP)
donor doping **4**:146
doped nanoparticles **9**:433–435
doped semiconductor photocatalysts **6**:401–418
DOSY. *See* diffusion-ordered spectroscopy (DOSY)
double layer capacitance **7**:510
double perovskites **4**:503–505, **4**:514–516
drug delivery
  MOFs **2**:730–732
  photoactivated metal complexes for **8**:254–297
  SCCs **2**:722–725
  systems for photoactive metallodrugs **2**:537–542
DT. *See* decision tree (DT)
dual mediators **7**:346
dual-action complexes **8**:270–272
dual-electrode methods **7**:518–521
DUV NLO materials. *See* deep-ultraviolet NLO materials (DUV NLO materials)
dynamic NMR spectroscopy **9**:101–103
dynamic nuclear polarization (DNP) **9**:50–52, **9**:130–133, **9**:151–152, **9**:277–278, **9**:368–370
  NMR in presence of paramagnetic species **9**:370–375
  practical considerations **9**:389–394
^{29}Si NMR **9**:129–134
dynamic temperature NMR from chemical exchanges and reactions **9**:718–719

E

E_2R_4 compounds **1**:780–786
EA. *See* evolutionary algorithms (EA)
early transition metal oxides **9**:300–302
ECL behavior. *See* electrochemiluminescence behavior (ECL behavior)
ECs. *See* electrochemical capacitors (ECs)
EDE mode. *See* energy dispersive EXAFS mode (EDE mode)
EDL capacitance. *See* electric double layer capacitance (EDL capacitance)
EDNMR. *See* electron-electron double resonance-detected NMR (EDNMR)
EDS. *See* energy dispersive x-ray spectroscopy (EDS)
EELS. *See* electron-energy loss spectroscopy (EELS)
EFAL. *See* extra framework aluminum (EFAL)
EGFR. *See* epidermal growth factor receptor (EGFR)
EIS. *See* electrochemical impedance spectroscopy (EIS)
electric double layer capacitance (EDL capacitance) **7**:227–229
electric field, special aspects associated with **3**:316
electric hotspot generation through dielectric superlensing modulation **8**:459–464
electrical resistivity **4**:223–225
electrically neutral molecules **1**:1005–1010
electrides **3**:406
electrocatalysis
  benchmarking in **7**:492–550
  coupling photoredox catalysis with **8**:83–84
  direct instrumental investigation of active sites **6**:429
  fundamentals of **6**:419–421
  generalized coordination number **6**:423–429
  structural change of catalysts during reaction **6**:431–434
  structure-reactivity relations **6**:422–429
electrocatalysts
  best practice for evaluating performance of **7**:530–545
    ascertaining materials stability **7**:531–533
    electrode conditioning and pretreatment **7**:533–534
    homogeneity of thin catalyst film **7**:534–535
  evaluation of real surface area of **7**:504–510
  of hydrogen peroxide reduction, transition metal hexacyanoferrates as **7**:175–176
electrocatalytic activity, experimental measurement of **7**:510–525
electrocatalytic conversion of methane **6**:343–351
  to C_{2+} oxygenates **6**:350
  to ethylene and ethane **6**:346–347
  to fuels and chemicals **6**:346–350
  fundamentals of **6**:345–346
  to methanol **6**:348–350
electrocatalytic materials **7**:501–504
electrocatalytic reaction
  charge-transfer overpotential for single electron step **7**:495–497
  double-layer effects **7**:498–499
  in electrolyzers and fuel cells **6**:421–422
  factors affecting rate of **7**:494–501
  influence of adsorption **7**:497–498
  mass-transport effects **7**:499–500
  multi-electron processes **7**:497
  Ohmic effects **7**:500

overpotential and nature **7**:494–495
electrochemical capacitors (ECs) **7**:225–227
applications **7**:227
energy storage of batteries *vs.* electrochemical capacitors **7**:226–227
examples of devices **7**:226
future directions and opportunities **7**:237
materials and applications **7**:230–237
mechanisms **7**:227–230
electrochemical cell, counter and reference electrode, choice of **7**:541–544
electrochemical data **4**:314–318
electrochemical enzymatic biosensing applications **7**:475–476
biosensors
for analysis of food and beverage quality **7**:475
for clinical sensing and medical diagnostics **7**:476
for environmental sensing **7**:475
electrochemical impedance spectroscopy (EIS) **7**:440, **7**:479
electrochemical Li^+ intercalation mechanism in graphite **4**:341
electrochemical methods **7**:506–510
for characterization of enzymatic fuel cells **7**:477–479
electrochemical quartz crystal microbalance (EQCM) **7**:438–439
electrochemical reactions
cells for **10**:115–116
in situ and operando observations of **7**:309–315
electrochemical stability
of garnet **4**:666–667
of NASICON-type Li ion electrolytes **4**:664
of perovskite-type Li ion electrolytes **4**:662–663
electrochemical techniques **7**:436–440
electrochemiluminescence behavior (ECL behavior) **5**:239
electrochemistry **4**:176
XAFS and **10**:134–138
electrochromism triggered by redox switching of metal moieties **8**:393–394
3-electrode liquid electrolyte cell, measurements in **7**:511–521
electrode(s) **7**:468–471
design **7**:342
materials **7**:468–471
in battery applications, in situ/in operando diffraction studies of **5**:329–368
characterization of **5**:338–359
negative electrode materials **7**:63–75
phase boundaries, grain boundaries and surfaces **7**:301–304
planar defects **7**:297–301
point defects and order-disorder in **7**:292–297
positive electrode materials **7**:48–63
Prussian blue analogues as **7**:93–94
structurally related to katiarsite **7**:390–398
structurally related to natisite **7**:379–384
electroluminescence, device architectures and working mechanisms of **8**:4
electrolyte(s) **7**:434–435
choice of supporting **7**:539–541
decomposition **7**:342–343
design **7**:342
for supercapacitors **1**:432
electrolyzers, electrocatalytic reactions in **6**:421–422
electromagnetic forces **3**:315–317
electromagnetic radiation **3**:317
electron pair-distribution function analysis (ePDF) **10**:78–81
electron paramagnetic resonance spectroscopy (EPR spectroscopy) **2**:363–365, **6**:151, **7**:447
characterization of metal ions with **9**:390–391
on Cu^{2+} **6**:151–152
electron-electron double resonance-detected NMR (EDNMR) **9**:718
electron-energy loss spectroscopy (EELS) **6**:232–234
electron-nuclear double resonance (ENDOR) **9**:718
electron(s)
with 3d TMCs **8**:734
beam damage in transmission electron microscopy **7**:284
counting rules **3**:92–94
involving d electrons **3**:92–93
at oxide surfaces **3**:93–94
at sp semiconductor surfaces **3**:92
crystallography
data processing **10**:59–61
decoding atomic arrangements from high resolution images **10**:64–72
detecting light elements by 3D ED and imaging **10**:77
mixed occupancies and vacancies **10**:74–75
orientation and secondary phases maps **10**:81
outside realm of perfectly periodic crystals **10**:74–77
phase analysis **10**:62
phase analysis and serial ED **10**:81
planar discontinuities **10**:75–76
STEM for electron crystallography applications **10**:67–69
structure determination and phase analysis **10**:59–62
structure determination by electron diffraction **10**:53–62
structure refinement **10**:62
structure solution **10**:61
for studies of inorganic and functional materials **10**:73–81
superstructures and aperiodic structures **10**:76–77
techniques of zonal-axis 2D electron diffraction acquisition **10**:56–57
three-dimensional electron diffraction **10**:57–58
density
analysis **1**:576–580
for bonding analysis in position space **3**:223–224
diffraction **5**:358–359
formation of **10**:53–56
techniques for metal-ion battery electrodes **7**:285–291
electron-localizability approach **3**:227–228
holes **7**:19–21
localizability indicator-electron density basin intersection **3**:228–229
microscopy **4**:544–545, **6**:121–122
relaxation **9**:372
scattering methods in inorganic chemistry **10**:1–2
spectroscopy with **7**:305–309
transfer
chain **2**:350–351
in electrochemical enzymatic biosensors **7**:474–475
mechanisms **7**:466–467
electronegativity **3**:254–258
electronic absorption and emission spectroscopy **1**:726
electronic communication in MV states, modulation of **8**:380–382
electronic conductivity **4**:545–546
electronic spectroscopy **4**:534–542
electronic states at surface **3**:96–97
electronic structure
of oxide and halide perovskites
common perovskite distortions **3**:6–7
effect of composition on band structure **3**:13–15
conceptualizing cubic perovskite band structures **3**:9–13
effects of distortions on band structure **3**:15–18
high pressure and epitaxial strain **3**:19
perovskite structure and composition **3**:5–7
strategies for tuning band structure **3**:18–20
superstructures with reduced dimensionality **3**:19–20
unifying messages **3**:17–18
theory for inorganic complexes **8**:656–657
electronic transitions in inorganic solids **4**:264–267
electrophilic phosphonium cations **1**:346–347
electrostatic influence of metal ions **2**:656
element-rich cluster compounds **1**:821–835
elemental boron **3**:95
bonding in elemental boron polymorphs **3**:45–48
elemental composition, cubic perovskite structure and variety in **3**:5–6
elementary proton activated reactions **6**:294–296
elements
gases and mixtures of gases **3**:341

elements (*continued*)
or organic groups, group 14 Zintl anions functionalized with **1**:906–907
elongating excited-state lifetime **2**:483
embryonic zeolites (EZ) **6**:28
Empirical Potential Structure Refinement (EPSR) **10**:420
empirical potentials **3**:365
encapsulation materials **10**:205
endogenous metal ions, differences between exogenous organic radicals and **9**:387–388
endohedral lanthanide-fullerene SMMs **9**:226
endoplasmic reticulum (ER) **2**:465–467, **2**:832
ER-targeted Pt complexes **2**:832
stains **8**:230–233
ENDOR. *See* electron-nuclear double resonance (ENDOR)
endosome stains **8**:239–244
energy **4**:314
of atoms and between atoms within position space approach **3**:233–235
BCDI studies of energy storage materials **10**:174–179
fast *vs.* slow variation **3**:304–306
functions **3**:290–293
with building units and molecules **3**:292
and state space, choice of **3**:290–293
general methods to explore and classify cost function and energy landscapes **3**:325–339
landscapes in inorganic chemistry
barrier structure **3**:276–277
basic features of cost function landscapes **3**:271–277
characteristic regions and inherent structures **3**:275
definition of cost function landscapes **3**:271–273
densities of states and minima **3**:276
fundamental elements of cost function landscapes **3**:273–277
general cost function landscape concepts **3**:271–281
graph representations **3**:278–281
landscape pockets **3**:274
locally ergodic regions **3**:276
minima **3**:274
order parameters **3**:281
projections on subsets of configuration space **3**:277–278
representation of landscapes **3**:277–281
saddle points **3**:274
landscapes in interaction with environment **3**:307–325
changes in composition **3**:317–322
general aspects **3**:308–310
general stress tensor **3**:314–315
high *vs.* low temperature **3**:312–313
mechanical forces **3**:313–315
pressure **3**:313–314
system with thermal gradient **3**:313
temperature **3**:310–313
landscapes of isolated chemical systems **3**:282–293
choice of moveclass **3**:289–290
clusters and molecules on surfaces **3**:289
continuous state space **3**:284–285
dimensionality of chemical systems **3**:287–290
discrete state space **3**:285–286
empirical potentials **3**:291
beyond empirical potentials **3**:291–292
finite system **3**:283–286
infinite system **3**:286–287
non-periodic approximants **3**:287
periodic approximants **3**:286–287
locally ergodic regions in general statistical ensembles **3**:298–300
materials **5**:119–121
measurements in experiment and simulations **3**:293–295
noisy cost function landscapes **3**:306
periodic variation **3**:306
time dependence of cost function/energy landscapes **3**:303–306
variation of
cost function **3**:304
state space and moveclass **3**:303–304
energy dispersive EXAFS mode (EDE mode) **10**:113–114
energy dispersive x-ray spectroscopy (EDS) **6**:234
energy transfer (EnT) **8**:734
with 3d TMCs **8**:734
EnT. *See* energy transfer (EnT)
environmental health and toxicology, application of metallomics and metalloproteomics for **2**:69–71
environmental protection **2**:94
enzymatic bioelectrocatalysis, fundamentals and applications of **7**:456–491
enzymatic bioelectrocatalysts **7**:463
enzymatic bioelectrochemical CO_2 conversion **7**:481–482
enzymatic biofuel cells, applications of **7**:479–480
enzymatic electrochemical H_2 production **7**:483
enzymatic electrochemical N_2 reduction **7**:482–483
enzymatic fuel cells **7**:477–480
electrochemical methods for characterization of **7**:477–479
principles **7**:477
enzyme(s) **7**:458–463
bioelectrocatalyst-electrode connections and immobilization strategies **7**:469–471
cascades **7**:464
chemical nature of **7**:458–459
classifications **7**:462–463
directed evolution **7**:466
engineering **7**:464–466
factors impacting enzyme activity **7**:461–462
fundamentals of enzyme kinetics **7**:460–461
principles of enzyme catalysis **7**:459–460
sensors **8**:195–196
cobalt-corrins as cofactors and intermediates in **2**:275–291
specificity **7**:459
ePDF. *See* electron pair-distribution function analysis (ePDF)
epidermal growth factor receptor (EGFR) **2**:825–826
peptide-platinum conjugates targeting EGFR **2**:825–826
EPR spectroscopy. *See* electron paramagnetic resonance spectroscopy (EPR spectroscopy)
EPSR. *See* Empirical Potential Structure Refinement (EPSR)
EQCM. *See* electrochemical quartz crystal microbalance (EQCM)
equilibration trees **3**:302–303, **3**:358
Equimolar tetrel chalcogenides **4**:57–63
ER. *See* endoplasmic reticulum (ER)
estrogen-platinum conjugates targeting estrogen receptors **2**:819–820
ethene hydrogenation & oligomerization, mobility of Rh in zeolite Y and consequences for **6**:181
ethene oligomerization, Ni-SSZ-24 for **6**:187
evolutionary algorithms (EA) **3**:398–400
EXAFS. *See* extended X-ray absorption fine structure (EXAFS)
exchange current density **7**:528–529
exchange-correlation functional **4**:510
excited-state nuclear dynamics **8**:659–660
excited-state rate theory **8**:658–659
exogenous organic radicals and endogenous metal ions, differences between **9**:387–388
exotic halide compounds **4**:403–405
experimental considerations **10**:13
extended Anderson lattice model **3**:475
extended X-ray absorption fine structure (EXAFS) **10**:109, **10**:111–112, **10**:355–357
analysis using TR-XAS data collection method **10**:355–357
catalysis in liquid phase **10**:133–134
in combination with techniques **10**:132–133
combined XAFS/UV-vis study of catalyst synthesis and reaction **10**:133
combined XAFS/vibrational spectroscopic study of catalyst synthesis and reaction **10**:132
combined XAFS/XRD **10**:133
to determine metal particle size and shape **10**:130
imaging studies **10**:139–140
novel analysis methods for determining active species present **10**:140–141
obtaining more information on state of catalyst **10**:139–141
supported catalysts **10**:116–138
extra framework aluminum (EFAL) **6**:170–172

extra framework oxygen atoms, complexes of metal ions in zeolites with **6**:156–161
eye towards extraordinary predictions **5**:19–20
EZ. *See* embryonic zeolites (EZ)
EZKC in close-packed solids **3**:67–70

F

^{19}F NMR on polymers **9**:26
  experimental considerations **9**:27–28
  liquid-state NMR **9**:28–29
  NMR relaxation **9**:31–32
  radiation chemistry of fluoropolymers **9**:29–30
  semicrystallinity **9**:32–34
^{19}F probes **2**:442–443
f-block SMMs **9**:220–226
Faber Ziman formalism **10**:395–398
Faradaic efficiency (FE) **7**:500–501, **7**:530
fast MAS **9**:150–151
FCC. *See* fluid catalytic cracking (FCC)
FCS. *See* Fermi-contact shift (FCS)
FE. *See* Faradaic efficiency (FE)
Fe protein **2**:304–305
(2Fe-2S) cluster **2**:108–111
(3Fe-4S) cluster **2**:111–112
(4Fe-4S) cluster **2**:112–113
Fe-only nitrogenase **2**:307–309
(1Fe) cluster **2**:107–108
(FeFe)-hydrogenases **2**:119–120
  HydE structure **2**:185
  leads from sequence alignments **2**:182
  radical-SAM enzyme HydE **2**:184–188
    acts on HydG product **2**:185–187
  radical-SAM enzyme HydG **2**:181–184
  reaction mechanism of **2**:178–180
  scaffold HydF protein **2**:188–189
  structural features of **2**:177–178
  structure and mechanism **2**:177–180
  structure of HydG **2**:181–182
[FeFe]-hydrogenase mimics containing heavy p block elements **1**:556–557
  synthetic complexes with aliphatic diselenolate linkers **1**:557–567
  synthetic complexes with aromatic diselenolate linkers **1**:567–568
FeMo cofactor, electronic structure of resting state **2**:310–312
Fermi-contact shift (FCS) **9**:212
  in absence of ZFS **9**:213–214
  methods for determination of **9**:216
  in presence of ZFS **9**:214
  purely NMR based methods for separations of **9**:216
  separation of FCS and PCS contributions to hyperfine shift **9**:215–216
  simplified treatment of **9**:212–215
ferrimagnetic nanomagnet Mn12 **9**:250–253
ferrimagnetic oxides **4**:243–245
ferroelectric(s) **5**:123–124, **5**:247–248
  applications of ferroelectric materials **4**:167–168
    automotive **4**:168
    consumer electronics **4**:168
    industrial manufacturing, processing and detection **4**:168
    medical and health care **4**:167
    piezoelectric devices and application **4**:167
  basic theories of **4**:140–143
  distortion **3**:16–17
  domain **4**:138–139
  materials **4**:137
    classification of **4**:143
ferroelectricity **4**:136–137
ferrofluids **5**:181–182
ferromagnetic oxides **4**:239–240
ferromagnets **9**:198–200
few-layer 2D materials, preparation of **4**:451–459
Fibonacci lattice **3**:463–464
finite-time thermodynamics for chemical processes **3**:361
first principles crystal structure prediction **3**:393–394
  accelerating search process **3**:406–408
  challenges **3**:411–413
  crystalline configuration space **3**:394–396
  examples **3**:409–411
  first principles calculations in solids **3**:396–397
  fitness functions **3**:403–406
  modern approaches **3**:397–403
  visualizing PES **3**:408–409
first row transition metals **8**:125–141
  oxides **4**:639–640
first sharp diffraction peak (FSDP) **10**:416–419
first-generation biosensors **7**:474–475
first-order quadrupolar interaction **9**:597–598
first-order recoupling **9**:540
Fischer-Tropsch catalysts **6**:354–361
  carbide mechanism **6**:364
  chain growth **6**:362
  chain termination and product desorption **6**:363
  Co catalysts **6**:358–360
  Fe catalysts **6**:358
  Fischer-Tropsch to chemicals **6**:371–375
  future role of FT in achieving net zero carbon **6**:360–361
  kinetics of **6**:368–371
  mechanism of **6**:361–366
  mechanistic insights **6**:369–371
  mechanistic models **6**:363–366
  monomer formation and chain initiation **6**:362
  past, historical perspective **6**:355–356
  present commercial operations **6**:356–360
  and processes **6**:357–358
  reactant adsorption **6**:361–362
  readsorption and further reaction **6**:363
  structure sensitivity **6**:366–368
fitness functions **3**:403–406
  compositional stability **3**:404–405
  electronic properties **3**:405–406
  structural and mechanical properties **3**:405
FLPs. *See* frustrated Lewis pairs (FLPs)
fluid catalytic cracking (FCC) **6**:29–30
fluoride sulfates ($LiMSO_4F$) **7**:388–390
fluorinated alkoxy-aluminates
  and–borates, chemistry with **1**:383–432
    applications in catalysis and polymerization chemistry **1**:421–424
    complexation of weak ligands **1**:407–421
    material science and electrochemical applications **1**:425–432
    reactive cations stabilized by $[pf]^-$aluminates **1**:384–407
    starting materials to introduce $[M(OR^F)_4]^-$aluminates and borates **1**:383–384
  as WCAs **1**:380–383
fluorine **9**:845–850
fluoro-anion salts **1**:487–497
fluorooxoborates **4**:31–33
fluorophosphates **7**:257–260
fluoropolymers, radiation chemistry of **9**:29–30
fluorosulfates **7**:262–263
flux(es) **5**:153
  assisted synthesis **4**:175–176
  method **4**:149
  single crystal growth **5**:187
FNR. *See* fumarate and nitrate reductase (FNR)
Fock's equation **3**:144–147
Folate-platinum conjugates targeting folate receptors **2**:822
Förster resonance energy transfer with luminescent lanthanide compounds **8**:491–492
Fourier difference maps and alternatives to rietveld refinement **10**:9–11
framework-associated aluminium **6**:170–172
free electron model extended to surface **3**:86–87
free energy
  calculations **3**:337–338
    and densities of states **3**:336–338
  landscape **3**:356
    clusters and molecules **3**:356
    phase transition via free energy landscape investigation **3**:354
    3D solids **3**:356
free oxygen ions, detection of **9**:640
free-electron lasers **10**:362–364
frequency-swept pulses **9**:149
frustrated Lewis pairs (FLPs) **1**:315–316
  See also metal-mediated base pairs
  FLP-mediated catalytic hydrogenation **1**:316–349
    of non-polar substrates **1**:332–338
    of polar substrates **1**:316–332
  FLP-mediated C–H borylation **1**:363–366

frustrated Lewis pairs (FLPs) (*continued*)
FLP-mediated cyclization reactions **1**:366–369
FLP-mediated dehydrogenation **1**:342–344
FLP-mediated hydroamination **1**:362–363
FLP-mediated hydrosilylation **1**:349–352
FLP-mediated reduction
of amides to amines via hydrosilylation **1**:359–361
of CO_2 **1**:369–373
FLP-mediated transfer hydrogenation **1**:338–342
unusual FLP systems for catalytic hydrogenation **1**:344–349
FSDP. *See* first sharp diffraction peak (FSDP)
fuel cells, electrocatalytic reactions in **6**:421–422
fulvalene-containing organometallics **8**:365–366
fumarate and nitrate reductase (FNR) **2**:144–146
functionalized silica materials, DNP-enhanced ^{29}Si NMR of **9**:133–134
(Functionalized) adenine **2**:679–683
(Functionalized) cytosine **2**:671–679
(Functionalized) guanine **2**:683–687
(Functionalized) thymine **2**:667–671
fungal siderophores **2**:4–5
fungal zincophores **2**:564–566

G

G-N7 macrochelation **2**:646
G-quadruplex targeted **2**:748–749
G-type antiferromagnet $BaMn_2As_2$ **9**:232–235
background of $BaMn_2As_2$ **9**:232–234
magnetic structure of $BaMn_2As_2$ **9**:234–235
^{55}Mn NMR in $BaMn_2As_2$ **9**:234
GA. *See* genetic algorithms (GA)
gallium (Ga) **4**:196–197
cluster compounds **1**:824–832
Ga_8, clusters **1**:824–828
Ga_9 clusters **1**:824–828
Ga_{10} clusters **1**:824–828
Ga_{11} clusters **1**:828
Ga_{13} clusters **1**:828
Ga_{16} clusters **1**:828–829
Ga_{18} clusters **1**:828–829
Ga_{19} clusters **1**:828–829
Ga_{22} clusters **1**:829–831
Ga_{23} and higher clusters **1**:831–832
galvanostatic cycling **4**:315–318
gamma-ray conversion to light production **4**:292–294
garnet(s) **4**:282–283, **4**:639, **9**:302–303
garnet-type solid electrolytes **4**:665–667
gas
cells for gas-solid reactions **10**:115
gas otransmitters **8**:272–291
gas-liquid and gas-liquid-solid reactions **10**:116
gas-phase adsorption techniques **7**:505–506
gas-phase NMR of nuclei
applications of **9**:777–778
determination of nuclear magnetic dipole moments **9**:777
gas-phase NMR of particular nuclei **9**:778–785
gas-diffusion electrode (GDE) **7**:511
half-cell measurements with **7**:524
gaseous ligand, transition metal cations with **1**:411
GC base pairs **2**:641–642
GDE. *See* gas-diffusion electrode (GDE)
generalized stress-redox equivalence **3**:254–256
genetic algorithms (GA) **3**:398–400
base pairs **2**:644
mismatch base pair **2**:644
genetic engineering of hemoproteins toward abiological reactions **2**:223–224
geometric ferroelectrics **5**:257
geometrical/topological analysis **7**:412–413
software for **7**:417–418
germanates **4**:643–645
germanides **4**:383
germanium **4**:201–202, **9**:780
analogs of benzene and related polycyclic aromatic hydrocarbons containing germanium atom **1**:852–853
centered biradicals **1**:201–202
chalcogenides **5**:148–149
complexes **1**:987
germanium selenide (GeSe) **4**:62
germanium(II) telluride (GeTe) **4**:60–61
GG stacking **2**:648
glass(es) **9**:48–50, **9**:567–568
with multiple network formers **9**:643–644
structure **9**:585–588
basic building blocks **9**:585–586
extended Q^n notation for second coordination sphere **9**:588
F–O–F′ bonding "rules" **9**:586–587
NBO distribution among network formers and Q^n notation **9**:587–588
global hydrogen energy economy **10**:3–7
global optimization techniques **3**:327–331
calculation of mesoscopic properties **3**:338–339
exhaustive methods **3**:327
genetic and evolutionary algorithms **3**:330
intermetallics **3**:342
jump methods, taboo methods, accelerated dynamics **3**:330–331
locally ergodic regions **3**:335–336
multiple local minimization methods **3**:327–328
pockets of landscape and characteristic regions **3**:333
probability flows **3**:335
saddle point techniques **3**:332
transition path analysis **3**:333–335
glucose
glucose-platinum conjugates targeting glucose transporters **2**:820–821
oxidation **6**:392–394
glutamate mutase (GM) **2**:283–284
glutathione S-transferases (GSTs) **2**:767
inhibition **2**:767–768
glycerol **6**:394–395
glycopolymers **9**:429–430
glycyl radical enzyme activation-pyruvate formate-lyase activating enzyme **2**:128–129
GM. *See* glutamate mutase (GM)
gold (Au) **2**:65–66, **9**:400
Au/Al nanocomposite **9**:436–437
Au···Au metallophilic interactions **1**:689–695
complexes **1**:516, **2**:783–784, **9**:710
with improved anti-cancer potency **2**:861–864
gold(I/III) complexes **8**:42–48
with carbene ligand **8**:42–44
with tetradentate ligand **8**:46–48
with tridentate ligand **8**:44–46
gold(I) complexes **2**:861–862, **8**:614–623
clusters **8**:617–623
low-nuclearity gold(I) complexes **8**:614–616
gold(I)-alkynyl complexes **2**:853–854
gold(I)-dithiocarbamate complexes **2**:854
gold(I)-NHC complexes **2**:850–853
gold(I)-phosphine complexes **2**:848–850
gold(I)-thiourea complexes **2**:853
gold(III) complexes **2**:863–864, **8**:597–598
with coordination of π-conjugated aromatic ligands **2**:858
gold(III)-dithiocarbamate complexes **2**:860–861
porphyrins **2**:854–855
intermolecular Au···Au metallophilic interactions **1**:690–695
Golgi apparatus **2**:465–467
stains **8**:233
gram-negative bacteria **2**:18–19
gram-positive bacteria **2**:19–20
graphene **4**:460–463, **9**:453–456
graphite **9**:297
electrochemical properties of graphite **7**:106–107
as intercalation host **4**:339–341
K intercalation into graphite **7**:104–105
gravimetric capacity **4**:313–314
green emissive iridium(III) complexes **8**:16–21
Green-Kubo approach **3**:451
group 10 transition metals, photoactive nonclassical carbene complexes of **1**:299
group 11 transition metals, photoactive nonclassical carbene complexes of **1**:300–303
group 12 metals **1**:388–389
group 13 chalcogenide clusters **4**:81–91
general synthesis methods of group 13 chalcogenide clusters **4**:81–82
reactivity and application **4**:82–85
group 13 monochalcogenides (TrCh) **4**:468–469
group 14 chalcogenide clusters **4**:91–126

compounds based on purely inorganic $[T_4E_{10}]^{4-}$supertetrahedra **4**:92–98
group 14 elements
and compounds **7**:112–113
coordination compounds and heterometallic clusters of **1**:911–918
group 14 metallole anion equivalents **1**:844–845
group 14 metallolide dianion equivalents **1**:846–849
group 15 chalcogenide clusters **4**:128–129
group 15 elements
binary intermetalloid clusters of **1**:918–919
and compounds **7**:113–114
coordination compounds and heterometallic clusters of **1**:919–921
group 4 donor functionalized nonclassical carbenes **1**:243–247
group 4 MNX **4**:486–487
group 5 donor functionalized nonclassical carbenes **1**:247–257
group 8 transition metals, photoactive nonclassical carbene complexes of **1**:297–298
group 9 transition metals, photoactive nonclassical carbene complexes of **1**:298–299
GSTs. *See* glutathione S-transferases (GSTs)
GTP-binding protein **2**:189
GU wobble **2**:647
pairs **2**:643–644
guanidinate ligands **1**:46–49
gums **9**:826–828

H

^{1}H chemical shifts **9**:606–607
H-cluster
of (FeFe)-hydrogenase **2**:189
biosynthetic proteins **2**:180–189
hafnium complexes **9**:669
Half-Heusler compounds **4**:248–249
halide(s) **4**:647–648, **5**:83–85
based solid electrolytes **4**:669–672
conductivity **4**:547–548
coordination **1**:634
solid electrolytes
with metal element **4**:669–670
with non-metallic element **4**:670–672
halogen(s) **9**:781–783
halogen-bonded halogen(I) ion complexes
halogen(I) complexes in solid-state **1**:588–592
halogen(I) ion complexes in solution **1**:595–598
halogen(I)ion complexes **1**:593–594
loss **4**:547–548
SSNMR spectroscopy of **9**:273
haptotropic rearrangement **8**:366
hard carbons **5**:200–205
heteroatom doping **5**:201–202
hydrothermal synthesis **5**:204–205
precursor choice **5**:200–201
structure and sodiation mechanism **5**:200
thermal treatment **5**:202–203
hard sphere potentials and volumes **3**:406–407
hBN. *See* hexagonal boron nitride (hBN)
HD. *See* Huntington's disease (HD)
HDAC. *See* histone deacetylases (HDAC)
heat capacity **4**:227–231
heating **4**:175
heavy analogs of phenyl anions **1**:856
heavy metal-based chalcogenides **5**:148–151
bismuth and antimony chalcogenides **5**:149
lead, tin and germanium chalcogenides **5**:148–149
ternary metal chalcogenides **5**:150–151
thallium and indium chalcogenides **5**:149
heavy nuclei **9**:783–785
heavy transition metal oxides **4**:640–641
heavy-metal soaps **9**:808–811
$EuCo_2As_2$ **9**:245–246
$EuCo_2P_2$ **9**:242–245
helical antiferromagnets **9**:241–247
helium compounds **1**:518
helix center, metal ion binding in **2**:650–651
hematite (α-Fe_2O_3) **9**:416
heme cofactor, metal substitutions of **2**:224
heme framework, modification of **2**:219–220, **2**:224–225
heme-containing proteins **2**:194
cytochrome P450 **2**:198–207
heme acquisition protein **2**:208–211
myoglobin **2**:195–198
heme-propionate side chains, modification of **2**:218–219
hemoproteins **2**:216
hemoprotein reconstituted with nickel porphyrinoid **2**:227
modification of **2**:217–218
oxidation **2**:218–221
reactions by Co and Ni porphyrinoids in hemoproteins **2**:225–227
reconstituted with cobalt porphyrinoid **2**:226
toward abiological reactions, genetic engineering of **2**:223–224
HER. *See* hydrogen evolution reaction (HER)
HETCOR. *See* heteronuclear correlation (HETCOR)
hetero-cyclobutane-1,3-diyls with radical centers on elements
of group 13 **1**:190–193
of group 14 **1**:193–202
of group 15 **1**:202–208
of group 16 **1**:208–210
hetero-cyclopentane-1,3-diyls with radical centers on elements
of group 14 **1**:210–213
of group 15 **1**:213–221
heteroanionic metathesis **5**:31–32
heteroatomic p-block hosts **1**:653–661
group 14 host-guest chemistry **1**:657–660
group 15 host-guest chemistry **1**:653–657
other systems **1**:660–661
heteroatomic zintl anions **1**:905–906
heterobimetallic cooperativity **1**:287–288
heterocubane-type and related cluster cores **4**:81–85
heterocyclic chalcogen molecules **1**:942–945
heterocyclic ligands
selenium-donor ligands **1**:90
sulfur-donor ligands, **1**:87–88
heterodinuclear $M^1\cdots M^2$ complexes with metallophilic interactions **1**:721–725
intermolecular $M^1\cdots M^2$ metallophilic interactions **1**:721–725
heterogeneous catalysts
deriving 3-D information on single atoms in **6**:235–240
non-oxidative dehydroaromatization of methane **6**:313–318
oxidative dehydrodimerization of methane **6**:318–323
heterogeneous charge transfer
kinetics **7**:134–136
mechanism **7**:132–134
heterogeneous ORR/OER catalysts **7**:335–336
heterogenous catalysts, imaging single atoms in **6**:225–232
heteroleptic compounds **1**:788–794
heteroleptic units **5**:262–264
heterometallic clusters **1**:908–924
of group 14 elements **1**:911–918
of group 15 elements **1**:919–921
heteronuclear chalcogen rings **1**:934–969
heteronuclear connectivities
involving ^{17}O **9**:639–640
network formers **9**:640–642
probed by NMR **9**:636–642
heteronuclear correlation (HETCOR) **9**:636–638
spectroscopy **9**:98–99, **9**:491–495
^{11}B-^{19}F correlation spectroscopy **9**:99
^{11}B-^{1}H correlation spectroscopy **9**:98–99
heteronuclear derivatives **1**:132–138
heteronuclear experiments targeting network modifiers **9**:640
heteronuclear NMR techniques **9**:636–638
Heusler compounds **4**:248–249
hexaaquairon(II) trifluoromethanesulfonate **10**:448–450
hexagonal boron nitride (hBN) **4**:460–463
sheets **9**:459–460
hexagonal tungsten bronzes (HTBs) **5**:253–254
hexammine complexes with Co^{3+} and metal ions **2**:651
high energy X-ray Instrumentation **10**:404–406
high field NMR **9**:152–173
high ionic conductivity in solids, prerequisites for **7**:410–411
high pressure **3**:410–411
allotropes **1**:971–973
apparatus for chemical synthesis with in situ X-ray diffraction **10**:206–217

high pressure (*continued*)
chemistry, devices for **4**:378–380
electrides **3**:425–427
NMR **9**:719–720
studies of transition metal oxides
HPHT synthesis of 3d-transition metal oxides and investigations at HT conditions **4**:684–695
mixed-anion oxides **4**:707–710
perovskite oxides with A-site ordering **4**:698–707
synthesis **4**:434
inorganic materials from **4**:381–415
tool for open frameworks **4**:415
x-ray diffraction methods for high-pressure solid-state synthesis **10**:200–221
high pressure and high temperature (HPHT) **4**:681
synthesis of 3d-transition metal oxides and investigations at HT conditions **4**:684–695
synthesis of 4d, 5d transition metal oxides **4**:695–698
high resolution NMR of quadrupolar nuclei **9**:609–610
high surface area electrodes **7**:469
high temperature hydrothermal synthesis of inorganic compounds **4**:628–657
high temperature methane conversion **6**:336–343
high-density lipoprotein nanoparticles **9**:426–427
high-pressure noble-gas chemistry **1**:518–521
high-resolution transmission electron microscopy mode (HRTEM mode) **10**:52–53
and HRSTEM investigations, advantages of aberration correction for **10**:71–72
image formation **10**:64
and contrast transfer **10**:64–65
high-temperature
batteries **4**:318
piezoelectric materials **4**:159–163
need for **4**:159
perspectives and challenges of **4**:161–163
polycrystalline piezoelectric materials **4**:161
solid-state synthesis **4**:518
higher alcohol synthesis **6**:374–375
higher coordination numbers **1**:786–788
HisI **2**:40–41
histone deacetylases (HDAC) **2**:758
inhibition **2**:758–762
HOIPs. *See* hybrid organic-inorganic perovskites (HOIPs)
σ-hole bonding **1**:646–647
homo-atomic zintl anions **1**:904–905
homoatomic p-block hosts **1**:661–662
homocyclic chalcogen molecules **1**:935–942
homocyclic oxygen molecules **1**:942
homocyclic sulfur oxides **1**:947–948
homocyclic tellurium molecules **1**:942
homodinuclear *d*-block (groups 8–12) M···M complexes with metallophilic interactions **1**:669–711
homodinuclear p-block (groups 13–15) M···M complexes with metallophilic interactions **1**:711–720
homogeneous photocatalytic systems **8**:299–310
homoleptic TMCCs **1**:410
homoleptic units **5**:261–262
homonuclear chalcogen rings **1**:934–969
homonuclear cooperativity **1**:275–287
network formers **9**:630–636
homonuclear correlation spectroscopy **9**:490–491
homonuclear derivatives **1**:125–132
host-guest chemistry **5**:240
host-guest systems **10**:230–231
HPHT. *See* high pressure and high temperature (HPHT)
HRTEM mode. *See* high-resolution transmission electron microscopy mode (HRTEM mode)
HTBs. *See* hexagonal tungsten bronzes (HTBs)
Hume-Rothery phases **4**:179–180
Huntington's disease (HD) **2**:611–613
copper in **2**:611–612
iron in **2**:612
manganese in **2**:612
metal ions as therapeutic targets in **2**:613
zinc in **2**:613
hybrid assemblies of different supertetrahedral clusters into chalcogenide frameworks **5**:231–233
hybrid cluster protein **2**:115–116
hybrid framework materials **5**:290–292
hybrid group 14/group 15 element derivatives **1**:141
hybrid melt quenched glass examples **5**:298–302
hybrid mesoporous materials **6**:45–47
hybrid metal oxides **5**:56–57
hybrid methods **10**:469–475
hybrid networks with B_{12} and B_6 units **3**:38
hybrid organic-inorganic materials **5**:56–63
hybrid organic-inorganic perovskites (HOIPs) **5**:300
hybrid systems comprising metal complexes and solid materials **8**:310–313
hybrid-improper ferroelectricity **5**:264–266
hybrid-improper mechanisms
in Dion-Jacobson phases **5**:266
in Ruddlesden-Popper phases **5**:265–266
hybrids with light-harvesting materials **8**:310
HydF **2**:188
structure **2**:188–189
HydG enzyme mechanism **2**:184
hydrated inorganic cation-assisted solvothermal synthesis **5**:225–226
hydrated sodium aluminate **10**:457
hydride(s) **4**:385–389, **5**:129
catalysts for ammonia synthesis, catalytic activity of **3**:131
as reducing agents for synthesis of reduced oxides and oxyhydrides **5**:130–134
oxyhydrides **5**:134
reduced oxides **5**:132–133
reduced oxides obtained from non-perovskite phases **5**:133
as source of alkali, alkaline earth, and rare earth metals **5**:137–139
in SPS and high-pressure synthesis **5**:140–141
for synthesis of nanoparticles **5**:142–143
as unintentional source of hydrogen and hydrogenous Zintl phases **5**:134–136
hydrogen (H_2) **3**:410, **3**:434, **7**:483
adsorption at coordinatively-unsaturated metal centers in MOFs **10**:36–37
adsorption/desorption **7**:506
bonding **3**:410
chloride **3**:410
hydrogen/deuterium second order difference in water **10**:414–415
in situ applications of H_2in dehydrogenation reaction **8**:98–100
storage **10**:3–7
experimental techniques **10**:6
hydrogen around world **10**:4–5
remaining sections **10**:6–7
research considerations **10**:5–6
transition metal hexacyanoferrates as electrocatalysts of H_2 peroxide reduction **7**:175–176
hydrogen evolution reaction (HER) **10**:135–136
hydrogenases **2**:118–123
hydrolytic cleavage experiments **2**:639
hydrosilylation **1**:349–361
asymmetric FLP-mediated hydrosilylation **1**:352–359
FLP-mediated hydrosilylation **1**:349–352
FLP-mediated reduction of amides to amines via hydrosilylation **1**:359–361
hydrothermal methods **4**:523
for preparative solid-state chemistry **5**:40–110
hydrothermal synthesis
of gems and minerals **4**:649
routes **7**:196
surface modification by **7**:216
hydrous minerals **3**:410
hydroxamic acid **2**:7–8, **2**:17–18
hydroxyapatite/reduced graphene oxide **9**:438
hydroxylation **2**:221–222
hydroxyosulfates **7**:263
hyperfine NMR shifts, temperature dependence of **9**:215
hyperfine shift,

separation of FCS and PCS contributions to **9**:215–216
hyperfine sub-level correlation (HYSCORE) **9**:718
hyperpolarization **9**:778
hyphenated ESI-MS/XRD investigative protocol for adducts characterization **2**:798–800
hypoxia
promoting performance in **2**:486
reinforcing phototherapeutic potency in **2**:492–494
HYSCORE. *See* hyperfine sub-level correlation (HYSCORE)

I

i-MAX **5**:281–282
ICD. *See* immunogenic cell death (ICD)
identification techniques of metallomics and metalloproteomics **2**:59
iDPC. *See* integrated differential phase-contrast (iDPC)
IEDDA reaction. *See* inverse electron-demand Diels–Alder reaction (IEDDA reaction)
IM. *See* imidazolate (IM)
imaging **2**:408
magnetic resonance imaging **2**:436–444
modes **6**:225–228
MPI **2**:426–430
optical and near-IR imaging **2**:412–425
PET **2**:444–448
probes
MOFs **2**:732–735
SCCs **2**:727
reagents **8**:225–248
single atoms in heterogenous catalysts **6**:225–232
SPECT **2**:444–448
ultrasound and photoacoustic imaging **2**:431–436
X-ray computed tomography **2**:408–412
imidazol-4-ylidene **1**:235–236
nonmetal redox active moieties appended to **1**:266–267
imidazolate (IM) **5**:230
imidazole **1**:43
imidoamidate ligands **1**:46–49
immobilization strategies **7**:469–471
immunogenic cell death (ICD) **2**:754–755
stimulators **2**:754–756
immunostimulators **2**:768–771
imparting tumor targeting and uptake ability **2**:486–487
in situ crystallography **10**:313
data processing **10**:313
diffractometer **10**:313
sampling **10**:313
structure determination **10**:313
in situ electrochemical cells for X-ray scattering **5**:330–332
in situ NMR
analysis of reaction media during ball-milling **9**:529
methods **9**:288–289
in situ observation of unstable species by X-rays, crystal design for **10**:314–315
in situ pair distribution function (in situ PDF) **5**:352–354
in situ PDF. *See* in situ pair distribution function (in situ PDF)
in situ powder diffraction studies
changes in crystal structure during material formation **10**:257–258
chemical insight from **10**:252–259
identifying complex reaction pathways **10**:253
mapping of synthesis parameters **10**:258–259
nanoparticle growth **10**:255–256
phase transformations **10**:253–255
in situ scattering studies of material formation **10**:248–272
in situ spectroscopy and theoretical calculations **10**:314
in situ studies **10**:248–249
of solvothermal crystallization **5**:94–99
in situ total scattering experiments, challenges and limitations for **10**:262
in situ X-ray diffraction
in DAC **10**:212–213
high-pressure apparatus for chemical synthesis with **10**:206–217
in MAP **10**:216
in PEP **10**:207
radiography **5**:354–358
tomography **5**:354–358
in situ/in operando behavior of $LiFePO_4$ olivine-type cathode **5**:350–352
in situ/in operando characterization
of electrode materials with neutron diffraction **5**:339–341
of structural evolution for selected electrode materials **5**:347–352
in situ/in operando diffraction studies of electrode materials in battery applications **5**:329–368
in situ/in operando neutron
diffraction studies on commercial cells **5**:341–343
imaging **5**:336–337
reflectometry **5**:336
in situ/in operando neutron depth profiling (NDP) **5**:338
in situ/in operando small angle neutron scattering (SANS) **5**:335
in situ/in operando spatially-resolved neutron diffraction studies cells **5**:344–347
in situ\in operando electrochemical cells for neutron scattering **5**:333–338
in-situ NMR
under flow reaction condition **9**:503–504
use of **9**:499–508
incomplete corrinoids **2**:269–271
indirect methane conversion **6**:330–331
indirect methods **2**:639
indirect spin-spin coupling **9**:775–777
indirect spin-spin interactions **9**:267–268
indium **4**:197–198
chalcogenides **5**:149
cluster compounds **1**:833–835
indomethacin polymorphs **9**:425
inelastic neutron scattering **3**:501–502
techniques **10**:11
inelastic X-ray and neutron scattering **4**:530
infrared spectroscopy **2**:368
inorganic and bioinorganic chemistry, applications of ^{17}O and ^{51}V NMR in **9**:35–61
inorganic anion sensors **8**:170–172
inorganic catalysis for methane conversion to chemicals **6**:327–353
inorganic chemistry **1**:1–3
neutron and electron scattering methods in **10**:1–2
in 20th century **1**:3–4
volume 1 of comprehensive inorganic chemistry III **1**:15–17
inorganic chromophore ions, structure, geometry and color of **4**:571–572
inorganic complexes **4**:628–657, **9**:52–53
advantages and disadvantages **4**:630
and covalent crystalline oxides **9**:181–182
development in electronic structure theory for **8**:656–657
early history and commercial efforts **4**:631–633
morphologies and electronic structures of inorganic compound surfaces **3**:95–97
techniques **4**:629–630
vanadium and oxygen centers in **9**:35–38
inorganic crystalline nanomaterials, coherent x-ray diffraction studies of **10**:149–186
inorganic crystals
Al lattices **3**:252–253
alkaline-earth structures **3**:251–252
chemical bonding in inorganic solids **3**:239–240
chemical pressure formalism **3**:240–248
contextualization of chemical pressure approach **3**:240–241
guest-host electronegativity equalization **3**:256–258
linking pressure **3**:254–258
mapped and non-mapped contributions **3**:244
pressure field calculation **3**:243–244
structures of **3**:249–258
unwarping procedure **3**:244–245
inorganic electrochemistry **7**:1–5
inorganic functional materials, spark plasma sintering routes to consolidated **5**:111–127
inorganic glasses **9**:182
inorganic materials **9**:54–55
chemistry **5**:1–2
from high pressure synthesis **4**:381–415
intermetallic compounds **4**:381–385
synthesis routes for **7**:188–197

inorganic molecular cluster structures **10**:228
inorganic nanocarriers **2**:540–542
inorganic non-molecular systems **3**:1–3
inorganic nonlinear optical materials
  main mid-and far-infrared nonlinear optical materials **4**:6–8
  materials **4**:26–27, **4**:33–35
  mid-and far-infrared nonlinear optical materials **4**:5–12
  near-infrared and visible nonlinear optical materials **4**:12–19
  newly developed deep-ultraviolet nonlinear optical materials **4**:29–35
  newly developed mid-and far-infrared nonlinear optical materials **4**:8–12
  newly developed near-infrared and visible nonlinear optical materials **4**:16–19
  newly developed ultraviolet nonlinear optical materials **4**:24–27
  representative deep-ultraviolet nonlinear optical materials **4**:28–29
  representative near-infrared and visible nonlinear optical materials **4**:12–16
inorganic nuclides, advances in computation of NMR parameters for **9**:837–868
inorganic photochemistry **8**:1
  computational considerations for **8**:655–660
  impact of machine learning in **8**:658
  using ultrafast pulses of X-rays **8**:664–670
inorganic pigments with transition metal chromophores
  at tetrahedral, octahedral, square pyramidal and square planar environments **4**:572–575
  at trigonal bipyramidal coordination **4**:576–589
    Y(Al, M)O_3 pigments **4**:585–586
    Y(In, Cu/Ti)O_3 green **4**:583
    Y(In, Fe)O_3 orange **4**:583
    Y(In, Mn/Ti/Zn/Al)O_3 purple **4**:580–582
    Y(In, Mn)O_3 blue **4**:578–579, **4**:587–589
inorganic solids
  characterization **9**:535
    applications **9**:561–568
    correlations between distinct nuclei **9**:544–561
    correlations between identical nuclei **9**:536–544
  chemical bonding in **3**:239–240
  electrolytes for all-solid-state batteries **4**:661–672
  electronic transitions in **4**:264–267
inorganic systems, high field solid-state NMR of challenging nuclei in **9**:138–177
inorganic thermoelectric materials
  data science and TE materials **3**:456–457
  electron transport properties **3**:452–453
  figure of merit, *ZT* **3**:447
  parameters **3**:453–456
  thermal transport properties **3**:447–452
insertion-type materials **7**:234–237
insulating electroceramics **5**:122–124
integrated differential phase-contrast (iDPC) **10**:68–69
inter-metalloid **1**:908–924
interaction of light and matter **10**:275–276
intercluster
  assembly into cluster-based chalcogenide frameworks **5**:227–231
  charge transfer in cluster-based chalcogenides **5**:239–240
interfaces
  construction of slabs with **7**:149–150
  solid-liquid interfaces **7**:150
  solid-solid interfaces **7**:149–150
  stability of **7**:149
intermetallic compounds **3**:214–220
intermetallic materials
  See also magnetocaloric materials
  container materials **4**:174–175
  elements & derivatives of closed packed structures **4**:176–178
  group 2/12 **4**:183–191
  group 13 **4**:191–198
  group 14 **4**:198–204
  Hume-Rothery phases **4**:179–180
  laves-phases **4**:178–179
  selected binary and ternary phases **4**:183–204
  starting materials **4**:174
  synthesis **4**:174–176
  terminology and classification **4**:173–174
intermetallic(s) **5**:85
  clathrates **4**:383–384
  compounds **4**:381–385, **9**:182–188
  dangling bonds at intermetallic surfaces **3**:91
  magnets **4**:246–249
    binary intermetallics **4**:247–248
    general considerations **4**:246–247
    Heusler and Half-Heusler compounds **4**:248–249
    $ThCr_2Si_2$-type intermetallics **4**:249
  superconductors
    critical charge transfer pairs in representative superconductors **4**:218–223
    three basic characterizations when reporting new superconductors **4**:223–231
intermolecular chalcogen bonding, catalysis by **1**:635–639
internet of things (IoT) **4**:168
internuclear distances **9**:496–499
intracellular biomacromolecule **2**:473
intracellular redox small molecule **2**:472
intracluster charge transfer in cluster-based chalcogenides **5**:239–240
intramolecular chalcogen bonding, synthesis and structure rigidification by **1**:634
intramolecular ligand exchange reactions, photochromism with **8**:363–364
intramolecular photosensitizer **8**:428–432
intrinsic basicities **2**:633–635
inverse electron-demand Diels–Alder reaction (IEDDA reaction) **8**:206–209
inverse FLP **1**:347–349
iodates **4**:17–18
ion
  charge transfer kinetics in ion intercalation processes **7**:132–137
  classification of ion conducting materials **7**:406–408
  computational design of ion conducting materials **7**:410–419
    prerequisites for high ionic conductivity in solids **7**:410–411
  ion-exchange **5**:240, **6**:34
  phenomenological description of ion intercalation kinetics **7**:136–137
ionic and covalent compounds **3**:341–342
ionic bonding indicators **3**:173–175
ionic compounds
  ammonia synthesis ionic compound surfaces on **3**:130–131
  Pauling rules extended to surfaces of **3**:89–90
ionic conductivity **4**:545–546
ionization **3**:321
ionothermal synthesis **5**:226
IoT. *See* internet of things (IoT)
Ir-Ge **4**:220–221
iridium (Ir)
  complexes **9**:696
  intermolecular Ir···Ir metallophilic interactions **1**:670–671
  Ir···Ir metallophilic interactions **1**:670–671
  iridium(III) complexes **8**:5–29
    with bidentate ligand **8**:5–27
    with tridentate/tetradentate ligand **8**:27–29
  iridium(III) cyclometalated complexes **8**:111–117
iron (Fe)
  binding to amyloid-β peptide and its biological implications **2**:598
  catalysts **6**:358
  chalcogenides **5**:157–160
  complexes **8**:135–137, **9**:683–685
  Fe oxides **4**:688–690
  Fe-As **4**:219
  Fe-related metal complexes **2**:384–385
  Fe(II) carbenes photosensitisers, ultrafast dynamics of **8**:667–670
  Fe(III)–siderophore complexes, characterization of **2**:6–9
  germanium tellurides **4**:478–479
  homeostasis, post-transcriptional regulation of **2**:138–140
  iron-binding properties of α-synuclein and biological implications **2**:608–609
  iron-cobalt nanoparticles for MPI **2**:427
  iron-sulfur (de)hydratases **2**:132–136
  iron-sulfur clusters
    basic structures and cluster coordination modes **2**:106–114
    complex iron-sulfur clusters **2**:114–124

direct catalysis at iron-sulfur clusters **2**:124–137
enzymatic activities **2**:137
involved in metabolic regulation **2**:138–149
linear clusters and cluster interconversions **2**:113–114
organometallic and mixed-metal clusters **2**:118–124
redox and spectroscopic properties of A-cluster **2**:124
redox and spectroscopic properties of C-cluster **2**:123–124
role of iron-sulfur clusters in DNA processing enzymes **2**:149–150
transcription regulators **2**:140–149
type of centers and variability of coordination **2**:106–124
unique clusters **2**:115–118
iron(II/III) complexes **8**:69–71
oxide agents **2**:440–441
siderophores in microbial battle for **2**:555–563
and tau hyperphosphorylation **2**:602–603
transport, siderophores and **2**:3–29
iron-sulfur cluster biogenesis regulator (IscR) **2**:141–142
isolated chemical system
locally ergodic regions for **3**:295–298
variation of composition within **3**:320–321
corrosion **3**:322
defects in equilibrium with environment **3**:322
enforced currents **3**:323–325
insertion/removal of atoms from system in non-equilibrium situations **3**:321
order-disorder phase transitions **3**:320
particle radiation and radioactive decay as source of particles **3**:321–322
isolated triangular antiferromagnet V15 **9**:247–249
isomorphic substitution **10**:412
isothiourea catalysis **1**:639–641
isotropic chemical shift
distribution **9**:607
for revealing catalytic sites **9**:481–482
isovalent substitutions **4**:147
IspG involved in isoprenoid biosynthesis **2**:133–134
IspH involved in isoprenoid biosynthesis **2**:133–134
I–V characteristics **3**:486–488

J

J-coupling **9**:71–75
plays **9**:486–487
Jablonski diagram **4**:264–265
absorption **4**:264–265
fluorescence and phosphorescence **4**:265
interactions between activator ion and host structure **4**:265–267
non-radiative relaxation **4**:265
jet **9**:826–827
jump methods and accelerated dynamics **3**:330

K

KBe_2-BO_3F_2 (KBBF) **4**:27
family **4**:29–30
ketone oxidation **2**:382
kinetic analyses of material formation **10**:253–255
kinetic current density **7**:528
kinetic modeling **6**:368–369
kinetic Monte Carlo simulations **7**:414–415
knight shift interaction **9**:286
Kohn-Sham equations **3**:144–147
Kok cycle **2**:352–353, **8**:321–325
krypton
compounds **1**:519–521
hydrides **1**:509–513
krypton(II) compounds **1**:443–466
$KTiOPO_4$ structure types **7**:60–61
$KZr_2(PO_4)_3$ **7**:371–379

L

langasite family **4**:160
lanthanide (Ln) **8**:486
lanthanide-based luminescence imaging **8**:494–505
materials for **8**:494
lanthanide-doped upconversion nanomaterials
anti-stokes properties of lanthanide compounds **8**:492
blocking energy leakage **8**:444–446
choice of physical state lanthanide compounds as luminescent probes **8**:492–494
emerging applications **8**:464–481
enhancing NIR energy harvesting **8**:441–442
functional principles of lanthanide upconversion **8**:440–441
manipulation of energy transfer **8**:441–446
multiplexed microscopy **8**:500
nanocavity-assisted surface plasmon coupling **8**:455–459
optimization of energy transfer pathways **8**:442–444
recent strategies for enhancing upconversion luminescence **8**:447–464
super-resolution imaging **8**:465–472
upconversion optogenetics **8**:477–481
MOFs as luminescent probes **8**:494
nanoparticles NPs as luminescent probes **8**:493–494
P_4 and As_4 with lanthanide and actinide reagents **1**:894
upconversion lasing **8**:472–477
lanthanide complexes ($LnPc_2$) **1**:406–407, **9**:220–222
as luminescent probes **8**:493
spectroscopic properties of **8**:487–492
lanthanum **9**:192–197
complexes **9**:665–666
larger intermetalloid clusters of the group 14 elements **1**:911
larger sulfur rings S_9-S_{16}, S_{18}, and S_{20} **1**:940–941
laser pump pulses **8**:685–686
late actinides Bk-Es **8**:804–806
late p-block elements
energy **1**:573–575
polarization and charge transfer **1**:581–582
structure **1**:573
lateral flow assays, persistent luminescent phosphors for **4**:292
lateral heterostructures **4**:456
latex **9**:827–828
Laue data processing
for macromolecular crystals **10**:283–284
for small-molecule crystals **10**:284–286
Laue method **10**:279–283
layered carbon nitrides **4**:616
layered materials **5**:85–88
layered metal sulfides **5**:169–170
layered oxides as positive electrode materials **7**:87–93
classification of layered structures **7**:87
P2-and P3-type binary and ternary transition-metal systems **7**:91–93
single transition metal oxides **7**:89–91
stable structure types of layered $AxMO_2$ **7**:87–89
layered perovskite structure **4**:161
layered perovskite-related materials **5**:255–257
aurivillius phases **5**:255–257
DJ phases **5**:257
LDs. *See* lipid droplet stains (LDs)
lead (Pb) **2**:71, **4**:203–204, **9**:783–785, **9**:860–861
chalcogenides **5**:148–149
complexes **1**:987
intermolecular Pb···Pb metallophilic interactions **1**:713–717
lead-free perovskite piezoelectric materials **4**:154–159
with better performance **4**:154–155
chemical modification and phase boundary engineering **4**:154–155
lead-free piezoelectric materials **4**:154
microstructure engineering **4**:155
perspectives and challenges of **4**:158–159
restriction of lead components in applications **4**:154
lead-free piezoelectric material systems **4**:155–158
Pb-acid battery **4**:319
Pb-based electrode materials **7**:71–73
Pb···Pb metallophilic interactions **1**:713–717
lead zirconate-titanate ceramics (PZT ceramics) **4**:143–147
effect of chemical modifications **4**:146–147
and morphotropic phase boundary **4**:143–144

lead zirconate-titanate ceramics (PZT ceramics) (*continued*)
perovskite structure **4**:143
perspectives and challenges for **4**:153–154
piezoelectric response in PZT near MPB region **4**:145
leathers **9**:816–817
LECs. *See* light-emitting electrochemical cells (LECs)
LED. *See* light-emitting diode (LED)
LEPAGE **10**:430–434
Lewis acidity **1**:786–788
Lewis base catalysis by transient chalcogen bonding interactions **1**:634–635
Li-S batteries. *See* lithium–sulfur batteries (Li-S batteries)
lid methods **3**:331
LIESST. *See* light-induced excited spin state trapping (LIESST)
$LiFePO_4$ **4**:317–318
ligand(s)
centered radicals, delocalization from **9**:213
effects of supports as **6**:89–94
exchange reactions **1**:925
hole chemistry **7**:8–9
ligand-field theory **10**:87
manipulation **7**:26–28
reported in metal-mediated base pairing **2**:667–706
TMCs as complex ligands **1**:411
light harvesting antennas based on metal complexes subunits **8**:629–634
light-driven assembly of manganese cluster **2**:360–363
light-element nuclei **9**:757–758
light-emitting diode (LED) **4**:295–296
phosphors for LED-based white lighting **4**:288–289
light-emitting electrochemical cells (LECs) **8**:4
light-harvesting ability **2**:483–484
light-induced charge transfer-induced spin transition **8**:369–373
light-induced electron transfer-induced second-order nonlinear optical switching **8**:373
light-induced excited spin state trapping (LIESST) **10**:89, **8**:366–369
effect studies using synchrotron diffraction **10**:97–98
light-induced halide segregation **4**:548–549
lignin **9**:427–428
$LiMn_2O_4$ cathode material (LMO cathode material) **7**:197–199
$LiNi_{0.5}Mn_{1.5}O_4$ cathode material (LNMO cathode material) **7**:199–201
$LiNi_{x-y-z}Co_yAl_zO_2$ (NCA) **4**:329–330
$LiNi_{x-y-z}Mn_yCo_zO_2$ (NCM) **4**:329
$LiNi_{x-y-z}Mn_yCo_zO_2$ (NMC) **4**:329
linkage isomerization complexes **8**:363
with organic ambidentate ligands **8**:362–363
lipid droplet stains (LDs) **8**:244–245
lipid nanoparticles **9**:425–426
liquid(s)
catalysis in liquid phase **10**:133–134
effects **1**:1034–1035
electrolyte
first stages of liquid electrolyte decomposition **7**:158–159
physicochemical properties determination **7**:441
and glasses **3**:358–360
liquid-state NMR **9**:28–29
modeling of liquid solutions **7**:157–158
LISICON-type solid electrolytes **4**:664–665
lithiated nanoparticles **9**:433–435
lithiated Sn (LixSn) **9**:434
lithium (Li)
electrochemical impedance spectroscopy of Li-ion battery **7**:140–143
iodate α-$LiIO_3$ **4**:16
Li-air batteries, chemistry of **7**:324–362
Li-based batteries **1**:428–429
Li-ion battery **4**:312–313
strain energy landscape in Li-ion battery cathode nanoparticles **10**:174–176
Li-rich cathode materials involving multi-electron redox **4**:336–338
Li-rich disordered rocksalt phases **9**:297
Li-rich layered oxides **9**:295–297
Li-rich metal oxides **4**:337–338
Li-rich metal sulfides **4**:336–337
Li-S battery
mechanism **7**:447–448
characterization techniques used in Li-S battery mechanistic research **7**:436–447
Li/M ratio in layered rock-salt compounds **7**:21–23
Li(Na)-based anionic redox materials for better batteries
chemical and electrochemical irreversibility **7**:30–33
practical issues and fundamental understandings **7**:30–38
Li_2MnO_3 cathode material **7**:199
Li_2MnO_3-based compounds **7**:11–12
Li_2S cathode **7**:433–434
$Li_4Ti_5O_{12}$ **7**:202–205, **9**:419
$LiCoO_2$ **4**:316–317
$LiN_{i-x-y}Mn_xCo_yO_2$ **7**:201–202
many shapes of **7**:338–339
metal **4**:347, **9**:299–300
beyond Li **4**:348–356
peroxide
deposition in porous electrode **7**:333–334
fundamental aspects of lithium peroxide crystallization **7**:330–332
lithium cobalt oxide (LCO) **4**:325–328
lithium niobate ($LiNbO_3$) **4**:14–16, **4**:160
lithium phosphorus oxynitride (LiPON) **9**:307
lithium tantalate ($LiTaO_3$, LT) **4**:160
lithium tetraborate ($Li_2B_4O_7$) **4**:160
lithium triborate LiB_3O_5 (LBO) **4**:21–22
lithium–sulfur batteries (Li-S batteries) **7**:430–448
See also metal-ion batteries
common materials and parameters **7**:432–436
operational principles **7**:431
problems and challenges **7**:432
LMO cathode material. *See* $LiMn_2O_4$ cathode material (LMO cathode material)
LNMO cathode material. *See* $LiNi_{0.5}Mn_{1.5}O_4$ cathode material (LNMO cathode material)
LOBSTER, atomic basis sets in **3**:162–163
local approaches **3**:401–403
basin hopping **3**:402–403
metadynamics **3**:401–402
minima hopping **3**:402
soft modes **3**:403
low nuclearity, catalysis using ions of **10**:130–132
low-coordinate compounds
doubly bonded derivatives **1**:125–143
heavier dipnictene derivatives **1**:151–153
of heavier group 14 elements **1**:125–145
of heavier group 15 elements **1**:145–153
of heavier group 16 elements **1**:153–157
multiple bonds between group 13 element and heavier group 16 element **1**:153–155
multiple bonds between group 14 element and heavier group 16 element **1**:155–156
multiple bonds between group 15 element and heavier group 16 element **1**:156–157
multiple bonds between group 16 element and heavier group 16 element **1**:157
theoretical aspects **1**:119–125
triply bonded derivatives **1**:144–145
low-nuclearity gold(I) complexes **8**:614–616
Lowe-Thorneley model **2**:310
lower dimensional coordination polymers **5**:302
lower olefin synthesis **6**:372–373
luminescence
chemosensors
chirality **8**:159–160
counterion **8**:160
formal charge **8**:155–156
lipophilicity **8**:153–155
molecular size **8**:157–159
receptor-mediated uptake **8**:160–164
structure–property relationships **8**:153–166
in solid state
electronic transitions in inorganic solids **4**:264–267
luminescent transition metal and main group materials **4**:267–273
scintillators **4**:292–294
semiconductors **4**:294–298
luminescent lanthanide
FRET with luminescent lanthanide compounds **8**:491–492
spectroscopic properties of luminescent lanthanide complexes **8**:487–492

luminescent materials
discovery of 4:298–302
identification of host crystal structures 4:299–301
rational synthesis through atomic substitution 4:298–299
luminescent probes
choice of physical state lanthanide compounds as 8:492–494
lanthanide NPs as 8:493–494
luminescent supramolecular assemblies 8:574–575
of d^{10} metal complexes 8:598–623
copper(I) 8:598–606
gold(I) 8:614–623
silver(I) 8:606–614
of d^8 metal complexes 8:575–598
gold(III) 8:597–598
palladium(II) 8:592–596
platinum(II) 8:575–592
rhodium(I) 8:596–597
luminescent transition metal
for electroluminescence luminescent transition-metal complexes 8:4–73
and main group materials 4:267–273
lutetium 9:200–203
complexes 9:666
lysosomes 2:465
lysosome stains 8:239–244
lysosome-targeted Pt complexes 2:832

M

$[M(OR^F)_4]^-$aluminates 1:383–384
machine learned potentials 3:407–408
machine learning
accelerating calculation electron transport coefficients with 3:457
accelerating calculation of lattice thermal conductivity with 3:456–457
interatomic potentials 10:421–422
impact of machine learning in inorganic photochemistry 8:658
methods in nanocluster catalysis 6:214–218
aided global optimizations 6:214–215
experimental and computational machine learning validation 5:5–6
for extracting structural information for x-ray adsorption spectroscopy 6:215–218
101–10,000 training datapoints 5:12–17
1–100 training datapoints 5:6–11
for surface chemistry of nanoclusters 6:215
10,000D training datapoints 5:18–19
training dataset size organization of validation articles 5:6–19
macrocyclic and cage ligands 1:58–60
macrocyclic ligands
oxygen-donor ligands 1:85
selenium-donor ligands 1:91–92
sulfur-donor ligands 1:88–89
macromolecular TR photocrystallography 10:288–290
maghemite (g-Fe_2O_3) 9:417
magic angle spinning (MAS) 9:286–287, 9:367, 9:535, 9:593–594
acquisition of MAS NMR spectra with MIDNP 9:391–392
reporting dopant concentrations 9:393–394
cross effect 9:381–384
MAS-DNP at high fields 9:375–389
Overhauser effect 9:375–377
solid effect 9:377–381
spreading hyperpolarization throughout sample 9:385–387
magnesium (Mg) 4:184–186
hydrogen citrate 10:461
ion
binding motifs 2:646
classification of Mg^{2+} binding sites 2:641
metal ion binding motifs in RNA by 2:641–646
Mg^{2+} clamp 2:644–645
Mg-containing thermoelectric materials 4:64–68
magnesium silicide (Mg_2Si) 4:64–66
magnetic crystals 10:240
magnetic elements, incorporated into 3:497–498
magnetic field, special aspects of 3:316–317
magnetic materials
applications of 4:253–257
Curie-Weiss law 4:238
definitions, units, and equations 4:237–239
diamagnetism and paramagnetism 4:237
magnetic ordering 4:238–239
magnetic units 4:237
magnetic-field control of domains in 9:253–258
detwinning in $EuFe_2As_2$ 9:253–256
magnetization and susceptibility 4:237
magnetic order 5:266
magnetic oxides 4:239–245
magnetic particle imaging (MPI) 2:426–430
iron-cobalt nanoparticles for 2:427
variation on nanoparticle coatings and construction in 2:427–430
magnetic refrigeration 5:178–179
magnetic resonance imaging (MRI) 2:436–444, 9:778
^{19}F probes 2:442–443
CEST 2:441–442
contrast agents 2:436
Gd^{III}-containing contrast agents and alternatives 2:436–440
iron oxide agents 2:440–441
PARASHIFT probes 2:442
responsive contrast agents 2:443–444
magnetic susceptibility 4:225–227
magnetic systems 3:184–187
magnetism, control over 8:382–387
magnetite (Fe_3O_4) 9:417
magnetocaloric effect (MCE) 5:178–179
in bulk crystalline materials 5:179–180
measurements of 5:180–181
thermodynamics of 5:179–182
magnetocaloric materials 4:255–257, 5:178–183
See also intermetallic materials
material design criteria 5:183
preparation in sealed Nb 5:190–191
preparation of bulk magnetocaloric materials 5:188–196
single crystal growth of 5:184–187
sintering 5:189–190
tri-arc single crystal growth 5:185
magnetoelectric(s) 5:266–268
fluids 5:181–182
magnetoplumbite-related phases 4:691
magnetostriction-driven polarization 5:267
main group metal coordination chemistry 1:19–117
manganese (Mn)
1(I/II) complexes 8:67–69
binding to prion protein and biological implications 2:587
complexes 9:679–680
manganese-rich spinel cathodes 9:294–295
oxides 7:232–234
oxides 4:687
photoNORMs 8:275–276
manganese dioxide (MnO_2) 4:355–356
many-body Schrödinger equation 3:80
MAP. *See* multi-anvil press (MAP)
maricite 7:51–52
marine organisms 2:13
mass spectroscopy 2:365
master equation dynamics 3:300–303, 3:361
time evolution and 3:300–303
materials
design 3:363
property driven design 3:363
synthesis routes and 3:361–364
and main characteristics of batteries 7:406–409
with noncollinear magnetic structures 4:250–253
synthesis
chalcogenides 10:192–196
compositions 10:197
experimental techniques and analytical methods 10:188–189
oxides 10:191–192
matrix isolation, noble-gas molecules characterized by 1:509–517
matrix metalloproteinases (MMPs) 2:246
max phases
bulk MAX phases 5:283–285
microwave heating 5:283–284
and mxenes 5:278–279
ordered MAX phases 5:280–282
stability/formability/exfoliability 5:282–283
synthesis of=p0o98u7y70 5:283–287
thin film MAX phases 5:285
variations to standard techniques 5:287
maximally localized Wannier functions (MLWFs) 3:202

maximally localized Wannier functions (MLWFs) (*continued*)
constructed from entangled bands **3**:207−213
constructed from multiple isolated bands **3**:205−207
constructed from single isolated band **3**:202−205
Maya blue **9**:811−812
MBLs. *See* metallo-β-lactamases (MBLs)
MC simulations. *See* Monte Carlo simulations (MC simulations)
MCE. *See* magnetocaloric effect (MCE)
MCM. *See* methylmalonyl-CoA-mutase (MCM)
MCs. *See* metal chalcogenides (MCs)
MEA. *See* membrane-electrode assembly (MEA)
mean distance **9**:394
mechanical alloying **5**:191−192
mechanism of O−O bond formation **8**:333−336
mechanisms of S-state transitions and **8**:330−336
mechanochemical enrichment of molecules and materials in NMR-active isotopes **9**:521−524
mechanochemical treatment, change in nuclear relaxation rates through **9**:524−526
mechanochemistry
and NMR, synthetic and instrumental developments performed at interface of **9**:526−529
ssNMR
for study of crystallinity and microstructure of nanomaterials prepared by **9**:518−520
for understanding properties of materials prepared by **9**:520
as synthetic method for enabling new developments in solid state NMR **9**:521−526
mediated electron transfer (MET) **7**:466−467
membrane-electrode assembly (MEA) **7**:522−523
mercury (Hg) **2**:69−71, **4**:190−191, **9**:857−860
complexes **9**:713−715
Hg···Hg metallophilic interactions **1**:709−711
intermolecular Hg···Hg metallophilic interactions **1**:709−711
meso-to nanoscale description of MPB **4**:145
meso-to nanoscopic understanding **4**:153
mesoporous
materials
catalytic applications of **6**:53−62
catalytic applications of representative ordered **6**:56−59
synthesis of **6**:42−53
metals **6**:42−43
for catalysis **6**:53−56
zeolites **6**:48−53
for catalysis **6**:60−62
mesoporous metal-organic frameworks **6**:46−47
for catalysis **6**:59−60
mesoscopic models, output maximization using **3**:361
mesostructured materials **6**:41−66
MET. *See* mediated electron transfer (MET)
metadynamics **3**:401−402
metadynamics and metashooting **3**:352−354
studies **3**:352
metal chalcogenides (MCs) **5**:147−148
crystal structures **5**:148−151
properties and applications **5**:157−170
synthetic methodologies **5**:151−157
metal chalcohalides (MChX) **4**:486−487
metal ion(s) **2**:470−471, **2**:664−665
and aggregation of prion protein **2**:588
and Aβ aggregation and its pathological implications **2**:600−601
binding in helix center **2**:650−651
characterization of metal ions with EPR **9**:390−391
chemical shifts and temperature dependence **9**:749−755
distribution, determining homogeneity of **9**:389−390
homeostasis **2**:30−32
DksA/DksA2 **2**:35−36
HisI **2**:40−41
metal-independent paralogs **2**:34−36
metalloenzyme paralogs **2**:33−49
nutritional immunity and pathogen adaptation **2**:32−33
obligatory Zn-dependent paralogs **2**:36−41
ribosomal C−paralogs **2**:34−35
Zn-independent or metal-promiscuous paralogs **2**:41−44
interactions with nucleic acids
binding of metal ion complexes **2**:651−653
electrostatic influence of **2**:656
GA mismatch base pair **2**:644
general considerations **2**:632−635
GU wobble pairs **2**:643−644
kinetically inert metal ions **2**:649−650
loop E motive or **2**:644
metal ion affinities of individual sites of single-stranded nucleic acids **2**:635−637
metal ion binding in helix center **2**:650−651
metal ion binding motifs in RNA by Mg^{2+} **2**:641−646
metal ion binding motifs in RNA of monovalent metal ions **2**:646−649
metal ion binding to RNAs **2**:637−653
metal ions and role in folding and dynamics of RNA **2**:653−654
metal ions and role in RNA catalysis **2**:654−656
metal-ion sensing by riboswitches **2**:654
sheared GA base pairs **2**:644
solvation content of **2**:638−639
tandem GC base pairs **2**:641−642
thermodynamics of metal ion binding to RNA **2**:639−641
and proteolytic processing of amyloid precursor protein **2**:593−594
and tau kinases **2**:603
as therapeutic target in prion diseases **2**:588
in zeolites with extraframework oxygen atoms, complexes of **6**:156−161
metal ions DNP (MIDNP) **9**:367
acquisition of MAS NMR spectra with **9**:391−392
metal nitride semiconductors **4**:612−623
See also oxide semiconductors; nitride semiconductors
crystal structures and photoelectrochemical properties **4**:612−616
perovskite-type oxynitride structures **4**:613−614
wurtzite-type oxynitride structures **4**:614−615
metal nitrohalides (MNX) **4**:486−487
metal oxide catalysts **9**:564−565
metal oxide semiconductors **4**:597−612
See also oxide semiconductors; nitride semiconductors
band dispersion and effective masses of charge carriers **4**:607−612
band gaps and band edge positions **4**:602−607
crystal structures and photoelectrochemical properties **4**:598−602
layered perovskite structures with 2D B-cation connectivity **4**:599−600
perovskite type structures with 3D B-cation connectivity **4**:598−599
structures with 2D B-cation and extended A-cation connectivity **4**:600−601
structures with extended A-cation connectivity and isolated B-cations **4**:602
structures with only 1D A-cation and B-cation connectivity **4**:601−602
tuning band gaps of oxide semiconductors **4**:603
tuning conduction band energy of metal oxides **4**:603−604
tuning valence band energy of metal oxides **4**:605−607
metal-ion batteries **7**:404−406
See also Lithium−sulfur batteries (Li-S batteries)
electron diffraction techniques for metal-ion battery electrodes **7**:285−291
interphases and electron transfer in **7**:129−132
materials and main characteristics of batteries **7**:406−409
mineral inspired electrode materials for **7**:363−403
modeling charge transfer in **7**:148−166
modeling methods **7**:148−149
modeling *vs.* experiment **7**:419−421
metal-mediated base pairs **2**:665

See also frustrated Lewis pairs (FLPs)
early **2**:665–666
ligands reported in metal-mediated base pairing **2**:667–706
metal-mediated base pairs involving canonical nucleobases **2**:700–705
structures of oligonucleotides bearing metal-mediated base pairs **2**:700–706
metal-metal interactions in bimetallic transition metal complexes **8**:695–696
metal-organic frameworks (MOFs) **10**:2–3, **10**:28–36, **10**:230–231, **2**:727–730, **5**:57–63, **8**:494, **9**:47–48, **9**:330, **9**:563–564
biomedical applications of **2**:730–736
^{43}Ca **9**:341–343
enhanced physisorption using small pores and flexible **10**:30–32
$^{69/71}$Ga **9**:354–356
hybrid melt quenched glass examples **5**:298–302
hydrogen adsorption at coordinatively-unsaturated metal centers in **10**:36–37
^{39}K **9**:341
^{115}In **9**:358–361
^{139}La **9**:361–362
literature review **9**:336–362
melting and glass formation in **5**:297–302
melting in coordination polymers and **5**:297
^{25}Mg **9**:337–340
NMR background and quadrupolar NMR considerations **9**:331–336
polymorphism in PT space **5**:303
^{45}Sc **9**:343–349
scope **9**:336–337
theory **5**:297
thermal characterization of **5**:294–297
$^{47/49}$Ti **9**:350
^{67}Zn **9**:350–354
^{91}Zr **9**:356–358
metal-to-ligand-charge-transfer (MLCT) **8**:689–691
excited states of TMCs **8**:689–693
metal(s) **5**:85, **8**:141–142
alkynyl clusters with μ-η1 and μ-η^1, η^2 modes **1**:1051–1053
B_{12}-analogs with **2**:292
carbene complex heterogenization **1**:288–297
cation **5**:229–230
sensors **8**:167–170
chlorin **2**:392
clusters protected by alkynyl ligands in multiple coordination modes **1**:1061–1062
complex(es)
as chemotherapeutic agents **2**:744–793
linkers **5**:229–230
other than porphyrins and porphyrinoids **2**:198
containing nanoclusters in zeolites **6**:112–147
delocalization of metal centered unpaired electrons **9**:213
electrochromism triggered by redox switching of metal moieties **8**:393–394
hydrides **10**:13–19
chemistry of **10**:14–15
neutron scattering studies of **10**:15–19
hydroxides **3**:410
metal-containing supramolecular compounds based on non-covalent linkages **8**:638–644
metal-iodide/iodine compounds **1**:1032–1034
metal-ion diffusion inside inorganic SEI phases **7**:153–154
metal-ligand hybridization driven polarization **5**:268
metal-promiscuous paralogs **2**:41–44
FolE/FolE2 **2**:41–43
HemB/HemB2 **2**:43–44
metal-support interfaces in ceria catalysts **6**:257–262
nanoparticles
NMR of **9**:399–401
and surfaces stabilized by nonclassical carbenes **1**:296–297
nitride
semiconductors **4**:623
valence and conduction band dispersion of **4**:621–622
nuclearity, effects of **6**:94–98
oxide(s) **6**:42–43
for catalysis **6**:53–56
metal oxide-based catalysts **6**:321–322
and modified metal oxides **9**:507–508
nanoparticles **9**:407–419
oxyanion building blocks **4**:641–647
phosphides and metal nitrides **6**:322–323
role in homeostasis of **2**:555–563
sulfides based on conversion **7**:120
surfaces
bond activation on **3**:106–114
bond formation on **3**:114–119
transport in vivo and lighting up metallophore–metal–metal transporter interactions and infection **2**:563
trichalcogenides **4**:472–473
UPD **7**:508–509
metalated polycyclic catena-pnictogens, chemistry of **1**:897–898
metalation process of individual proteins **2**:798–800
metallo-β-lactamases (MBLs) **2**:249–251
metallocenyl-appended carbenes **1**:263–266
metallodrug research, application of metallomics and metalloproteomics for **2**:60–69
metalloenzyme **7**:462–463
metalloid oxide nanoparticles **9**:407–419
metallomics **2**:54
application
for environmental health and toxicology **2**:69–71
for metallodrug research **2**:60–69
technical platform for **2**:55–60
metallophilic interactions
heterodinuclear $M^1\cdots M^2$ complexes with **1**:721–725
homodinuclear *d*-block (groups 8–12) M···M complexes with **1**:669–711
homodinuclear p-block (groups 13–15) M···M complexes with **1**:711–720
metallophilicity **1**:666–669
scope and organization **1**:669
spectroscopy **1**:726–727
synthesis **1**:725
metallophilicity **1**:666–669
computational studies on **1**:669
history of **1**:666–669
requirements for **1**:668
metallophore(s)
biomimetics **2**:562–563
implications of siderophores secretion for social relations between microorganisms and with host **2**:558–560
interactions of siderophores with metal ions **2**:560–562
metalloproteins with experiment and theory, structure-function relationships of **8**:670
metalloproteomics **2**:55
application for
environmental health and toxicology **2**:69–71
metallodrug research **2**:60–69
technical platform for **2**:55–60
metaphosphates **7**:250
metashooting of ZnO **3**:354
metadynamics and **3**:352–354
metathesis
reaction **6**:2–4
routes to materials
assisted metathesis **5**:31
descriptive chemistry of metathesis reactions **5**:25–32
kinetics **5**:32–33
targeting metastable phases via **5**:34–37
ternary metathesis **5**:30–31
thermally-controlled metathesis **5**:28
thermodynamics and kinetics of metathesis reactions **5**:32–37
transport-promoted metathesis **5**:28–30
methane
borylation **6**:333
development of methane activation and conversion technologies **6**:329–351
halogenation/oxy-halogenation **6**:331–333
inorganic catalysis for methane conversion to chemicals **6**:327–353
non-oxidative dehydroaromatization of **6**:313–318
oxidative dehydrodimerization of **6**:318–323
physicochemical properties of **6**:329

methane (*continued*)
  sulfonation **6**:331
  thermo-catalytic conversion of **6**:330–343
methanol to olefins (MTO) **6**:30
methylene glutarate mutase (MGM) **2**:284
methylmalonyl-CoA-mutase (MCM) **2**:282–283
MGM. *See* methylene glutarate mutase (MGM)
micro acidity constants **2**:633–635
micro crystals **10**:478–480
micro pore equilibration **6**:303–305
micro-kinetic modeling and dynamics **6**:139–141
microelectrode techniques **7**:524–525
microporous materials **9**:562–564
  AlPOs **9**:562
  MOFs **9**:563–564
  zeolites **9**:562–563
microscopic environment **8**:346
microscopy **4**:542–545, **7**:445–446, **7**:505
microstructure engineering **4**:155
microtubule stains **8**:245–246
microwave synthesis **5**:194
microwave-assisted methods **4**:523–524
mid-gap states
  visible light absorption via excitation of **6**:404–413
MIDNP. *See* metal ions DNP (MIDNP)
mineralizers **4**:631
minerals **9**:566–567
  inspired electrode materials for metal-ion batteries
    electrode materials structurally related to katiarsite **7**:390–398
    electrode materials structurally related to natisite **7**:379–384
    NASICON–type materials, structurally related to kosnarite **7**:371–379
    olivine-type cathode materials $LiMPO_4$ **7**:365–371
    phosphate minerals in pegmatites **7**:364–365
    tavorite based electrode materials **7**:385–390
minima hopping **3**:402
miscibility under pressure **3**:428–429
mitochondria **2**:463–464
  mitochondria-targeted Pt complexes **2**:830–831
  stains **8**:234–239
mixed anion materials **4**:431–448
mixed krypton/xenon compounds **1**:454–460
mixed metal
  nanoparticles, selective oxidation by **6**:381–400
  tellurides **4**:481–485
  transition metal oxides **4**:399–403
mixed phosphates **7**:57–58, **7**:260–261
mixed polyanionic cathodes **7**:256–266
mixed spectroscopies **8**:544–545
mixed synthetic strategy **6**:52–53
mixed-anion oxides **4**:707–710
mixed-anion positive electrode materials **7**:58–61
mixed-ligand **2**:8–9
mixed-solvent methods **4**:522–523
MLCT. *See* metal-to-ligand-charge-transfer (MLCT)
MLWFs. *See* maximally localized Wannier functions (MLWFs)
MMPs. *See* matrix metalloproteinases (MMPs)
MNX. *See* metal nitrohalides (MNX)
mobilized copper in oxidation half-cycle during NH_3-SCR-NOx **6**:175–180
model free analysis of total scattering data **5**:310
model Li-rich systems **7**:12
model Na systems **7**:12
modeling ion conducting materials, software for **7**:417–419
modeling magnetic shielding tensors **9**:838–839
modified Bridgman method **4**:150
modifier cation intermixing around the BO and NBO sites **9**:627
modular decomposition **3**:407
modulation excitation methods **10**:141
  of photoresponsive wavelength **8**:398–401
MOFs. *See* metal-organic frameworks (MOFs)
molecular anion compounds **4**:410–414
molecular boron clusters
  closo-Borate anions and derivatives **1**:741–763
  closo-Decaborate anion $[B_{10}H_{10}]^{2-}$ **1**:755–762
  closo-Heptaborate anion $[B_7H_7]^{2-}$ **1**:763
  closo-Hexaborate anion $[B_6H_6]^{2-}$ **1**:763
  closo-Nonaborate anion $[B_9H_9]^{2-}$ **1**:762
  closo-Octaborate anion $[B_8H_8]^{2-}$ **1**:762–763
  closo-Undecaborate anion $[B_{11}H_{11}]^{2-}$ **1**:755
  conjuncto-Boranes **1**:766–768
  polyhedral boranes with open structure **1**:763–766
molecular catalysts **8**:337–339
molecular crystalline oxides and glasses **9**:189–191
molecular crystals **3**:343
molecular dynamics **3**:451–452
  based methods **3**:329
molecular inorganic catalysts, photoredox organic transformations using **8**:108–142
molecular inorganic chemistry
  biradicals and biradicaloids **1**:13–14
  current trends in **1**:5–14
  multiple bonding in p-block compounds **1**:6–8
  SBIs **1**:8–9
  small-molecule activation **1**:9–12
  weakly coordinating anions **1**:12–13
molecular machines **8**:417–419
molecular materials
  See also thermoelectric materials
  ([3,5- (CF_3) 2pz]Cu)$_3$ trimer complex **10**:295–296
  Ag_2Cu_2(dpi) $_4$ multicenter complex **10**:301–302
  Cu(dppe)(dmp) PF_6 and Cu(phen)$(P(Ph)_3)_2$ BF_4 photoactive complexes **10**:298–300
  $Cu_4(PhCO_2)_4$ carboxylate complex **10**:302–303
  data processing and analysis **10**:283–288
  examples of time-resolved studies **10**:288–305
  Fe(tpa)(tcc) PF_6 spin-crossover complex **10**:300–301
  importance of solid-state studies **10**:276
  in-house time-resolved photocrystallographic studies **10**:304–305
  methods **10**:277–288
  photodifference maps **10**:286–287
  $Pt(pop)_2(popH)_2$ $N(Et)_4$ cage complex **10**:292–293
  Rh_2(dimen) $_4$ $(PF_6)_2$ cage complex **10**:293–295
  Rh_2(m-pnp)$_2$(pnp)$_2$ $(B(Ph)_4)_2$ half-cage complex **10**:296–297
  structure-model refinement **10**:287–288
molecular multi-chromophoric systems for photoinduced charge separation **8**:634–635
molecular nanomagnets **9**:247–253
  ferrimagnetic nanomagnet Mn12 **9**:250–253
  isolated triangular antiferromagnet V15 **9**:247–249
molecular organic nanoparticles **9**:423–428
molecular photocatalysis, photophysical and mechanistic aspects of **8**:104–108
molecular systems **3**:176–177
molecules
  dissociative activation of **3**:107–109
  non-dissociative activation of **3**:109–114
molybdates **4**:645–646
molybdenum complexes **9**:676–677
molybdenum trioxide (MoO_3) **4**:355–356
molybdenum(0) isocyanides **8**:120–123
monochromatic method **10**:278–279
monocyclic catena-pnictogens **1**:875–886
monocyclic heterocycles containing catena-pnictogen groups **1**:885–886
monodentate acetato ligands **1**:75
monodentate heterocyclic ligands **1**:39–44, **1**:73–74
monodentate ligands
  arsenic-donor ligands **1**:67–68
  nitrogen-donor ligands **1**:23–44
  oxygen-donor ligands **1**:68–75
  phosphorus-donor ligands **1**:61–64
  selenium-donor ligands **1**:89–90
  sulfur-donor ligands **1**:85–88
monofunctional complexes **2**:751–752
monofunctional platinum(II) anticancer agents **2**:815
monolayer **4**:450–459

preparation of **4**:451–459
mononuclear iron systems **2**:327–332
mononuclear molybdenum systems **2**:319–322
mononuclear photocatalysts **8**:108–142
mononuclear SCO materials **10**:92–93
mononuclear zinc hydrolases **2**:244–246
Monte Carlo simulated annealing **10**:469–475
Monte Carlo simulations (MC simulations) **7**:414
morphotropic phase boundary **4**:143–144
conventional pictures of **4**:145
meso-to nanoscale description of **4**:145
monoclinic phase and high piezoelectricity **4**:145
MPB facilitating polarization rotation **4**:151–153
piezoelectric response in PZT near MPB region **4**:145
Mott transition **3**:471–475
on Penrose tiling **3**:472–473
in periodic systems **3**:471–472
MPI. *See* magnetic particle imaging (MPI)
MRI. *See* magnetic resonance imaging (MRI)
MTO. *See* methanol to olefins (MTO)
Mulliken and Löwdin population analysis **3**:166–167
multi-action prodrugs **2**:758–774
multi-anion systems **4**:405–410
multi-anvil press (MAP) **10**:214–217
See also Paris–Edinburgh press (PEP)
advantages and disadvantages of **10**:216
examples of synthesis with **10**:216–217
using MAP for chemical synthesis **10**:215–216
multi-halogen(I) ion structures **1**:590–591
multi-nuclear platinum complexes **2**:747–748, **2**:815
multi-photon activation **2**:512
multi-pulse experiments **8**:545–560
T2D-IR **8**:545–550
UV pump–IR pump–IR probe spectroscopy **8**:550–560
multi-walled carbon nanotubes (MWCNTs) **9**:437–438
multicomponent phosphate-based glasses **9**:617
multicomponent silicate glasses **9**:611–614
multicomponent supramolecular photochemistry **8**:628–629
metal-containing supramolecular compounds based on non-covalent linkages **8**:638–644
polynuclear metal complexes **8**:629–638
supramolecular systems based on host-guest interactions **8**:645–650
multidentate pyridine linkers **5**:230
multimetallic nanoparticle catalysts **6**:383–384
multimodal imaging **2**:410–411
multimodal therapy **2**:494–495
for enhanced cancer therapy **2**:488
multimolecular systems **1**:582–583
multinary oxides **5**:69–77
multinary products **5**:30–32
multinary transition metal oxides **4**:399–403
multinuclear cooperativity **1**:275–297
multinuclear Cu sites in chabazites for selective catalytic reduction of nitrogen oxides, mobility of **6**:192–193
multinuclear photoredox catalysts **8**:142
multinuclear SCO complexes and frameworks **10**:93–97
multiphotochromic systems **8**:406
multiple bonding in p-block compounds **1**:6–8
multiple network formers, glasses with **9**:643–644
mummies **9**:812–814
MWCNTs. *See* multi-walled carbon nanotubes (MWCNTs)
MXenes **4**:464–465, **5**:278–279, **5**:282, **5**:285–287, **9**:461–467
myoglobin **2**:195–198
heme analogs with different central metal or modified side chain **2**:195–197
to hydroxylase **2**:221
metal complexes other than porphyrins and porphyrinoids **2**:198
modification of heme pocket of **2**:218
porphyrinoids with modified heme (porphyrin) skeleton **2**:197–198

N

N-heterocyclic carbene (NHC) **1**:207
coordination of N-heterocyclic carbene ligand **2**:849–850
stabilized phosphorus centered biradicals **1**:207–208
N-nitroso-*N*-hydroxylamine **2**:10–11
N-terminal $(4Fee4S)_{RS}$ mediates radical chemistry **2**:182–183
NA mechanism. *See* nucleophilic attack mechanism (NA mechanism)
Na superionic conductor (NASICON) **9**:303–305
NASICON-structured electrode materials **7**:52–54
NASICON-type phosphates **7**:246
NASICON-type solid electrolytes **4**:663–664
structurally related to kosnarite NASICON–type materials **7**:371–379
nano-size materials, NMR of **9**:435–443
nano-sized metal-organic frameworks (nanoMOFs) **9**:443
nano-sized metal-organics **9**:443
nanocarriers and delivery mechanisms **8**:288–291
nanocluster
heterogeneous catalysts
cluster fluxionality **6**:205–208
descriptors for adsorption **6**:208–211
global optimization methods to explore structures of **6**:211–214
machine learning methods in **6**:214–218
methods **6**:208–218
reactant induced cluster reconstruction **6**:202–205
unique properties in **6**:202–208
machine learning for surface chemistry of **6**:215
nanocomposites **9**:435–438
NMR of **9**:435–443
nanocrystalline
cellulose **9**:442–443
inorganic compounds **9**:438–442
NMR of **9**:435–443
oxides **9**:46–47
nanocrystals **5**:155–157
nanomaterials, total scattering and pair distribution function analysis for studies of **5**:307–328
nanoMOFs. *See* nano-sized metal-organic frameworks (nanoMOFs)
nanoparticles
analysis of nanoparticle structure from scattering data in Q-space **5**:308–309
NMR of **9**:399–435
size and shape **10**:262–264
time-and position-resolved studies of nanoparticle chemistry **5**:322–324
nanosheets **5**:155–157
nanosized zeolites
alternative reaction conditions for synthesis of **6**:28–29
conventional synthesis of **6**:25–26
properties of **6**:20
seed-assisted synthesis of **6**:26–27
special cases of **6**:27–28
synthesis **6**:25–29
by modifying initial precursor **6**:27
via interzeolite conversion **6**:26
nanostructure in r-space, analysis of **5**:309–321
nanostructured electrodes **7**:469
nanostructured materials for electrochemical capacitors **7**:225–240
nanozeolites
See also zeolites
adsorption and gas separation **6**:33–34
application **6**:29–34
catalysis **6**:29–32
reactions **6**:33–34
NASICON. *See* Na superionic conductor (NASICON)
natural bond orbital analyses (NBO analyses) **1**:645
natural polymeric nanocarriers **2**:537–538
natural water oxidation **8**:318–336
NBO. *See* non-bridging oxygen (NBO)
NBO analyses. *See* natural bond orbital analyses (NBO analyses)
NDP. *See* neutron depth profiling (NDP)
near infra-red emissive iridium(III) complexes **8**:21–27
near infrared microscopy (NIR microscopy) **8**:501–504
near surface alloys **6**:386–387

near-IR imaging **2**:412–425
  with 4d and 5d transition metal complexes **2**:419–422
  Cherenkov radiation with inorganic lumiphores **2**:422–425
  with inorganic compounds and materials **2**:412
  trivalent lanthanide-based luminescence and imaging **2**:412–418
NEB. *See* nudged elastic band method (NEB)
NEET proteins **2**:111
negative electrode **7**:336–342
  See also positive electrode
  materials **7**:63–75, **7**:104–120
    transition metal oxides as **7**:115–117
  mechanisms of morphological instability **7**:339–341
  uniform deposition **7**:341–342
neon compounds **1**:518
neptunyl ions **8**:799–801
networks
  formers
    heteronuclear connectivities among **9**:640–642
    homonuclear connectivities among **9**:630–636
  as templates **3**:342
    atoms, molecules and clusters on surfaces and substrates **3**:344–346
    atoms on surfaces **3**:352
    barrier studies **3**:350–354
    clusters and large molecules **3**:346
    clusters on surfaces **3**:345
    compositional variation restricted to prescribed sub-lattices **3**:348
    fixed composition, as function of pressure and/or temperature **3**:348
    graph representations of energy landscapes **3**:356–358
    low-dimensional solids **3**:343
    mixed types of interactions **3**:342
    particles on closed surfaces **3**:344–345
    phase diagram prediction **3**:346–348
    prediction including compositional variation without experimental input **3**:347
    prescribed path method **3**:352
    probability flows **3**:354
    reorganization of surfaces **3**:344
    thin films on surfaces **3**:345–346
neural networks **3**:364–365
neutron
  diffraction **10**:386–400, **4**:529, **5**:333–335, **5**:339–347
    analysis of neutron diffraction data **10**:393–395
    with isotopic substitution **10**:412–415
    role of magnetic symmetry **3**:499–501
    situ/in operando characterization of electrode materials with neutron diffraction **5**:339–341
  radiation
    cell designs for **5**:330–338
    in situ/in operando characterization of electrode materials using **5**:330–338
  scattering
    cross section techniques **10**:7–8
    lengths and cross sections **10**:389–391
    methods in inorganic chemistry **10**:1–2
neutron depth profiling (NDP) **5**:338
NgF_2
  main-group coordination complexes of **1**:452–454
  transition-metal coordination complexes of **1**:444–452
NGR-platinum conjugates targeting APN **2**:824
$NH_4B_4O_6F$ (ABF) **4**:31
  ABF family **4**:31–33
  ABF-STEM **10**:68
NHC. *See* N-heterocyclic carbene (NHC)
Ni_3TeO_6 (NTO) **5**:260
nickel (Ni)
  complexes **9**:696–697
  hemoprotein reconstituted with nickel porphyrinoid **2**:227
  Ni oxides **4**:691–693
  Ni-based batteries **4**:318–319
  nickel(0/II) complexes **8**:71–72
  nickel(II) multidentate complexes **8**:139–141
NICS. *See* nucleus independent chemical shift (NICS)
nido-Octadecaborane(22) **1**:766–767
Niecke's 1,3-diphospha-cyclobutane-2,4-diyl **1**:190
(NiFe) hydrogenases **2**:120–123
NIIs. *See* nucleophilic iodine(I) interactions (NIIs)
niobium complexes **9**:673–674
NIR microscopy. *See* near infrared microscopy (NIR microscopy)
NIS pathways. *See* nonribosomal peptide synthetase-independent siderophore pathways (NIS pathways)
Nishibayashi's systems **2**:331–332
nitrene transfer reactions **2**:222–225
nitric oxide **8**:273–279
nitride semiconductors **4**:620–623
  See also oxide semiconductors
  general trends **4**:620–621
nitrides **4**:389–397, **5**:80–82
  materials **4**:395–397
  in supercritical ammonia **4**:649–650
  of transition metals **4**:381–382
nitridophosphates **4**:413–414, **7**:264
nitridosilicates **4**:412–413
nitriles **1**:31–32
nitrite-sensitive transcription repressor (NsrR) **2**:143–144
nitrito complexes **8**:357
nitrogen **8**:179–189, **9**:780
  centered biradicals **1**:202–203
  materials **4**:395–397
  N-donor functionalized carbenes **1**:247–257
  N-truncation of amyloid-b and its impact in metal-binding properties **2**:598
  N_2 splitting with 3d TMCs **8**:770
  N–H bond formation on early transition metal hydride surfaces **3**:129–136
  nitrogen-^{14} NMR spectroscopy
    ^{14}N in solid-state NMR **9**:9–19
    ^{14}N in solution NMR **9**:8–9
    quadrupolar interaction **9**:5–8
    structural insights obtained by ^{14}N NMR **9**:15–19
  nitrogen-donor ligands **1**:23–60
    bidentate ligands **1**:44–53
    monodentate ligands **1**:23–44
    polydentate open-chain, macrocyclic and cage ligands **1**:58–60
    tridentate ligands **1**:53–58
  N–N bond formation **2**:396–400
  oxides **6**:31
    mobility of multinuclear Cu sites in chabazites for SCR of **6**:192–193
  unsaturated moieties as precursors for nitrogen based materials **4**:394–397
  xenon trioxide adducts of N-donor ligands **1**:498–502
nitrogenase enzymes **2**:304–310
nitrogenise **2**:117–118
NLO. *See* nonlinear optics (NLO)
NMC electrodes, structural behavior of **5**:347–348
NMR spectroscopy. *See* nuclear magnetic resonance spectroscopy (NMR spectroscopy)
NO isomerization and dissociation in 3d TMC **8**:758
noble gases **9**:778–780
  compounds **3**:427–428, **4**:403–405
  chemistry
    and periodic table **1**:440–441
    reviews **1**:441
    synthesis and reactivity of XeF_2 **1**:441–442
    xenon(II) and krypton(II) compounds **1**:443–466
  insertion compounds **1**:515
  molecules characterized by matrix isolation **1**:509–517
non Li metal anodes **7**:434
non-bridging oxygen (NBO) **9**:586
  distribution among silicate groups **9**:611
non-centrosymmetric structural units **5**:261–264
non-conventional mechanism of action **2**:752–754
non-conventional platinum(II)anticancer complexes **2**:814–815
  monofunctional platinum(II) anticancer agents **2**:815
  multi-nuclear platinum(II) anticancer complexes **2**:815
  trans-platinum compounds **2**:814–815
non-covalent mechanism of action **2**:756–757
non-cyclic catena-pnictogens **1**:871–875

branched, metalated catena-pnictogens **1**:874–875
linear, metalated catena-pnictogens **1**:873–874
linear, non-metalated catena-pnictogens **1**:872–873
non-cyclic dipnictogens **1**:866–867
non-deltahedral cluster with 10 and 12 vertices **1**:910
non-electrochemical methods **7**:504–506
non-integer spin quadrupolar nuclei **9**:265–267
non-linear optical properties **5**:166–167
non-metal oxides **4**:397–399
non-metalated polycyclic catena-pnictogens **1**:896
non-metalloenzymes **7**:462–463
non-oxidative dehydroaromatization of methane **6**:313–318
alternative catalysts **6**:316–317
Mo/ZSM-5 **6**:313–316
induction period and catalyst deactivation **6**:315
preparation of **6**:313–314
reaction mechanism **6**:315–316
non-oxidative methane conversion to olefins, aromatics and hydrogen (MTOAH) **6**:341–343
non-oxidative methane dehydroaromatization to aromatics (MDA) **6**:337–338
non-oxide p-block metal chalcogenide cage compounds
clusters with p-block (semi)metals from different groups **4**:130–131
group 13 chalcogenide clusters **4**:81–91
group 14 chalcogenide clusters **4**:91–126
group 15 chalcogenide clusters **4**:128–129
non-platinum anticancer agents **2**:780–784
non-polar substrates **1**:332–338
See also polar substrates
reduction of alkenes and allenes **1**:333–335
reduction of alkynes **1**:336–338
non-porphyrinoid metal complex into apomyoglobin, insertion of **2**:220–221
non-radiative relaxation **4**:265
non-reversible photoreactions **10**:354–355
non-sacrificial photocatalysis systems **8**:81–85, **8**:95
acceptorless intramolecular dehydrogenation **8**:95–98
coupling photoredox catalysis with electrocatalysis **8**:83–84
merging photocatalysts and cobaloximes **8**:81–82
non-sacrificial photocatalytic reactions **8**:85–95
non-support ligands, effects of **6**:87–89
non-supported dipnictogens **1**:866–867
non-zeolite based catalysts **6**:317
nonclassical carbenes
emerging applications of **1**:297–305
biological and medicinal applications of **1**:303–305
light-harvesting and-emitting applications **1**:297–303
metal nanoparticles and surfaces stabilized by **1**:296–297
stabilized metal clusters **1**:294–296
noncollinear magnetic ordering **4**:249–253
general considerations **4**:249–250
materials with noncollinear magnetic structures **4**:250–253
nonequilibrium molecular dynamics **3**:451
nonhalide derivatives **1**:800–806
nonlinear optics (NLO) **8**:391–393
switching **8**:373
nonmetal redox active moieties appended to triazolylidenes and imidazol-4-ylidenes **1**:266–267
nonribosomal peptide synthetase pathways (NRPS pathways) **2**:13–15
nonribosomal peptide synthetase-independent siderophore pathways (NIS pathways) **2**:15–16
NRPS pathways. *See* nonribosomal peptide synthetase pathways (NRPS pathways)
ns^2np^0 ions, SOJT for **5**:254–257
NsrR. *See* nitrite-sensitive transcription repressor (NsrR)
nuclear magnetic dipole moments, determination of **9**:777
nuclear magnetic resonance spectroscopy (NMR spectroscopy) **1**:726, **7**:447, **9**:36, **9**:139, **9**:283–290, **9**:331, **9**:367, **9**:584–585, **9**:772
See also solid-state nuclear magnetic resonance spectroscopy (SSNMR spectroscopy)
achieving fields **9**:145–146
acquisition of NMR spectra **9**:283–284
applications in cultural heritage science
biological remains and materials **9**:812–818
case studies **9**:790–830
cleaning methods **9**:794–795
cleaning treatments **9**:802
drying oils **9**:806
mock films **9**:806–807
model samples of paper **9**:818–819
paintings **9**:799–806
paints and constituent parts **9**:806–812
paper **9**:818–822
paper artifacts and conservation treatments **9**:819–822
parchment **9**:817–818
porosity, water absorption, and distribution **9**:790–792
pottery **9**:799
salts and pollutants **9**:795–796
science and cultural heritage **9**:789
solid-state NMR characterization and provenance **9**:796–799
stone and ceramics **9**:790–799
wall paintings **9**:799–802
based methods for separations of PCS and FCS **9**:216
basics of **9**:231–232
hyperfine interactions **9**:231–232
NMR spectrum **9**:232
of carboranes
^{10}B NMR spectroscopy **9**:75–76
^{11}B NMR spectroscopy **9**:63–75
^{13}C NMR **9**:77–84
^{19}F NMR **9**:88–89
^{1}H NMR **9**:84–88
antipodal effect **9**:69–70
chemical shift **9**:63–70
computational studies **9**:64–69
experimental techniques **9**:95–103
central and satellite transitions **9**:597
chemical shifts and NMR shift scale **9**:591–592
conventional superconducting magnets **9**:145
crystallography of zeolites **9**:123–125
definitions and scope **9**:139
detection methods **9**:180–181
electric quadrupolar interaction **9**:141–144
fundamentals **9**:283
on glass powders **9**:607–609
heteronuclear connectivities probed by **9**:636–642
high field magnet development **9**:145–147
high field NMR **9**:152–173
interactions and magnetic field dependence **9**:139–145
of ligand nuclides in complexes **9**:715–716
magnetic shielding **9**:140–141
measurements of internuclear metal-to-ligand distances involving vanadium centers **9**:55
mechanosynthesis through **9**:526–529
of metals in complexes **9**:715
of nanocomposites, nanocrystalline, and nano-size materials **9**:435–443
of nanoparticles **9**:399–435
NMR of metal nanoparticles **9**:399–401
NMR-active isotopes, mechanochemical enrichment of molecules and materials in **9**:521–524
NMR-signal dephasing techniques **9**:638
paramagnetic interactions **9**:144–145
parameters of solids **9**:839–845
on powders **9**:592–597
in presence of paramagnetic species **9**:370–375
principles and basic interactions **9**:474–480
CSA and dipolar coupling interactions **9**:477–478
NMR sensitivity **9**:480
NMR spectroscopy without interactions **9**:475
NMR spectrum with internal spin interactions **9**:475–476
powder patterns—Beyond isotropic chemical shift **9**:476–477
quadrupolar interaction **9**:478–479
principles of **9**:588–592
properties shared by complexes of more than two transition metals **9**:715–717

nuclear magnetic resonance spectroscopy (NMR spectroscopy) (*continued*)
pulsed magnets **9**:147
quadrupolar NMR considerations **9**:331–336
on quadrupolar nuclei **9**:597–601
relaxation **9**:31–32, **9**:372–375
and sensitivity concerns of solid-state NMR **9**:594–595
on selected network modifiers **9**:628–630
^{23}Na (S=3/2) **9**:628
^{25}Mg (S=5/2) **9**:629
^{45}Sc (S= 7/2) and ^{89}Y (S=1/2) **9**:630
series-connected hybrid magnets **9**:146
signatures of $^{11}BO_3$ and $^{11}BO_4$ groups **9**:620–621
spectroscopy **4**:542, **7**:447, **9**:1–3, **9**:789
provide unique perspective **9**:789–790
spectrum of gaseous sample **9**:772–777
on static powders **9**:592–593
strategies for spectral acquisition **9**:334–336
studies of 2D and pseudo-2D systems **9**:450–470
studies of lithium batteries **9**:290–309
anodes **9**:297–302
cathodes **9**:291–297
electrolytes **9**:302–307
fundamentals of batteries **9**:290–291
interfaces **9**:307–309
studies of supercapacitors **9**:310–317
dynamics and diffusion of adsorbed species **9**:312–313
fundamentals **9**:310
NMR studies of pore size and electrode structure **9**:311–312
observation of adsorbed species **9**:310–311
supercapacitor charging mechanisms **9**:313–317
studies using parahydrogen **9**:719
synthetic and instrumental developments performed at interface of mechanochemistry and **9**:526–529
theoretical and computational studies of **9**:717
of transition metal nuclei **9**:746–749
relevant NMR transition **9**:747–749
nuclear magnetic shielding **9**:772–774
nuclear relaxation **9**:774–775
change in nuclear relaxation rates through mechanochemical treatment **9**:524–526
nuclear spectroscopy **4**:534–542
nuclear spin **9**:588
and quadrupolar interactions **9**:747
nucleic acids **2**:664–665
B_{12}-derivatives as ligands of **2**:291–292
involving artificial nucleosides **2**:705–706
metal-mediated base pairs in nucleic acid duplexes **2**:664–713
sensors **8**:189–195
nucleobase tetrads **2**:648–649
nucleolus **2**:462–463
stains **8**:225–229
nucleophilic attack mechanism (NA mechanism) **8**:333
nucleophilic iodine(I) interactions (NIIs) **1**:592
nucleophilic O–O coupling mechanism **8**:335
nucleotides **2**:514
nucleus **2**:462–463, **8**:225–229
nucleus-targeted Pt complexes **2**:829–830
nucleus independent chemical shift (NICS) **9**:89–95
nudged elastic band method (NEB) **3**:351–352
nutritional immunity and pathogen adaptation **2**:32–33
N_x dissociation from azido 3d TMCs **8**:765

O

^{17}O (S=5/2) NMR **9**:624–627
dependence of 17O NMR parameters on local structure **9**:624–626
^{17}O chemical shifts **9**:606
^{17}O NMR
applications of **9**:41–52
background and common techniques **9**:38–40
calculations of NMR parameters **9**:40–41
methodologies **9**:39–40
peak-assignments in aluminoborosilicate glasses **9**:639
practical considerations for **9**:38–41
sample preparation and challenges **9**:38
^{17}O solid state NMR measurements **9**:36–38
o-MAX **5**:280–281
o-Tn type of chalcogenide clusters **5**:222–223
(o-T*n*)-T*n* hybrid assembly **5**:232
O/M ratio in layered rock-salt compounds **7**:21–23
O4-W1 radical coupling mechanism **8**:335
obligatory Zn-dependent paralogs **2**:36–41
PyrC/PyrC2 **2**:38–40
QueD/QueD2 **2**:36–38
octadecahydro-*closo* anion **1**:768
octahedral APn_2Te_4 family **4**:475–478
octahedral rotation **3**:17
OE. *See* overhauser effect (OE)
OEC. *See* oxygen-evolving complex (OEC)
OER. *See* oxygen evolution reaction (OER)
OH chemical bond **6**:279–285
OIL. *See* ordered-ilmenite (OIL)
OLEDs. *See* organic light-emitting diodes (OLEDs)
oligonucleotides bearing metal-mediated base pairs, structures of **2**:700–706
olivine
cathodes **9**:293–294
olivine-type cathode materials $LiMPO_4$ **7**:365–371
phosphates **7**:246–248
OMCs. *See* ordered mesoporous carbons (OMCs)
OMOS. *See* ordered mesoporous organosilicas (OMOS)
OMS. *See* ordered mesoporous silicas (OMS)
ON/OFF switching
of luminescence **8**:376–380
of photochromism via redox switching of metal centers **8**:395–397
one-dimensional systems **3**:149–151
one-photon activation **2**:512
open circuit voltage **7**:477–478
open shell oxides **4**:639–641
open-chain and tripodal **1**:66
open-chain tridentate N-donor ligands **1**:53–54
open-framework inorganic materials **5**:55–56
open-framework oxides **5**:52–55
operando thermodynamic analysis, structure prediction by **6**:136
optical band gap **3**:406
optical imaging **2**:412–425
with 4d and 5d transition metal complexes **2**:419–422
Cherenkov radiation with inorganic lumiphores **2**:422–425
with inorganic compounds and materials **2**:412
trivalent lanthanide-based luminescence and imaging **2**:412–418
optical spectroscopy **4**:534–544, **7**:444–445
OPV. *See* organic photovoltaics (OPV)
orbital free DFT **3**:407
orbital interaction between methane and IrO_2 surface **3**:122–128
order-disorder in electrode materials **7**:292–297
ordered mesoporous carbons (OMCs) **6**:47–48
for catalysis **6**:57–59
ordered mesoporous organosilicas (OMOS) **6**:45
for catalysis **6**:56–57
ordered mesoporous silicas (OMS) **6**:42–43
for catalysis **6**:56
ordered-ilmenite (OIL) **5**:260
corundum-derived ordered-ilmenite materials **5**:260
organelle-targeted platinum complexes **2**:829–832
organic ambidentate ligands, linkage isomerization with **8**:362–363
organic dye sensitization **8**:448–455
organic groups
group 14 Zintl anions functionalized with main group elements or organic groups **1**:906–907
group 15 Zintl anions functionalized with **1**:907–908
zintl anions functionalized with **1**:906–908
organic light-emitting diodes (OLEDs) **8**:1, **8**:4, **8**:655

computational insights into phosphorescent molecules used for **8**:661–662
photophysical properties of **8**:660–664
triplet harvesting by thermally-activated delayed fluorescence using carbene metal amides **8**:662–664
organic matrix **2**:86–87
confinement effect **2**:87
organic-inorganic interface **2**:86
template effect **2**:86
organic nanocarriers **2**:537–540
organic photochromics **8**:376
control over photo-, electro-, and magneto-properties of transition metal complexes and organometallics via photoisomerization of **8**:376–393
interplay among **8**:374–409
by transition metal complexes and organometallics, control over isomerization behavior of **8**:393–401
organic photovoltaics (OPV) **1**:432
organic polychalcogenides **1**:981–986
organism improvement **2**:91–98
organometallics **8**:357–373
of B_{12}-derivatives **2**:271–275
clusters **1**:1050–1072
interplay among **8**:374–409
nitrito complexes and **8**:357
nitrosyl complexes and **8**:358
organotetrel chalcogenide clusters
based on adamantane-type $\{T_4E_6\}$ or semicubane-type $\{T_3E_4\}$ cores **4**:98–121
synthesis and structures of **4**:100–121
OrpR σ^{54}-dependent activator **2**:148–149
ORR. *See* oxygen reduction reaction (ORR)
ORTEP **10**:430
osmium **2**:338–341
osmium complexes **9**:687–688
osmium(II) complexes **8**:57–58
overhauser effect (OE) **9**:368
mechanism **9**:388
oxalate
derivatives **7**:264–265
dianion **1**:80–82
oxidation
of bio-derived furanics **6**:395–398
catalysis with nanoclusters **6**:8
mobilized copper in oxidation half-cycle during NH_3-SCR-NOx **6**:175–180
reactions **1**:925
state schemes **8**:321–325
oxidative cleavage experiments **2**:640
oxidative coupling of methane to C_2 hydrocarbon (OCM) **6**:336–337
oxidative dehydrodimerization of methane **6**:318–323
oxide semiconductors **4**:607–612
See also nitride semiconductors
general trends **4**:608–610
oxides **10**:191–192, **4**:323–331, **4**:349, **4**:354–356, **4**:397–403, **4**:634–641
ammonolysis of **4**:432
based solid Li ion electrolytes **4**:661–667
dangling bonds at **3**:91
oxide-containing nanoparticles **9**:420
from oxides to sulfides/selenides **7**:26–28
surfaces **3**:96
oxidized O^{2-}, nature of **7**:19–21
oxo-oxyl radical coupling mechanism (RC mechanism) **8**:334
oxo/oxyl-catalysis **6**:161–162
oxoanion-based compounds **7**:51–58
oxonitridophosphates **4**:413–414
oxonitridosilicates **4**:412–413
oxyanion analogs of minerals **5**:64–65
oxychalcogenides **4**:443–444
oxyfluorides **4**:335, **4**:439–443
electrochemical synthesis **4**:441
high pressure synthesis **4**:443
solvothermal synthesis **4**:442–443
topochemical synthesis **4**:440–441
oxyfluoro-anion salts **1**:479–487
oxygen **4**:345–347, **9**:780–781
centers in inorganic and bioinorganic complexes **9**:35–38
channel **2**:359
detection of oxygen triclusters **9**:640
and hypoxic environment **2**:471–472
isotope first order difference in water **10**:414
O-donor functionalized carbenes **1**:257–261
O-donor ligands, xenon trioxide adducts of **1**:498–502
O-O dimers **7**:19–21
oxygen-donor ligands **1**:68–85
bidentate ligands **1**:75–83
monodentate ligands **1**:68–75
probes **8**:209–217
redox activity in $LiCoO_2$ **7**:9–11
release **7**:19–21
oxygen evolution reaction (OER) **10**:136–137
oxygen reduction reaction (ORR) **10**:137–138
oxygen-evolving complex (OEC) **8**:318–321
artificial analogs **8**:347
oxyhalides **4**:708–709
oxyhydrides **4**:436–439, **4**:709–710, **5**:134
anion order-disorder **4**:438–439
high pressure synthesis **4**:438
high temperature synthesis **4**:436
thin films **4**:439
topochemical synthesis **4**:434, **4**:436–438
oxynitrides **4**:406–408, **4**:432–435, **4**:589, **4**:710
anion order in **4**:434–435
oxypnictides **4**:443–444

P

^{31}P MAS NMR **9**:616–618
^{31}P *vs.* 29Si NMR **9**:616–617
^{31}P-^{31}P connectivities **9**:632–633
p-block elements
heteroatomic p-block hosts **1**:653–661
homoatomic p-block hosts **1**:661–662
polychalcogenide derivatives of **1**:976–1014
chalcogen halogenides **1**:1005–1014
group 13 complexes **1**:976–981
group 14 derivatives and complexes **1**:981–987
group 15 derivatives and complexes **1**:988–1005
p-element hydrides **4**:388–389
packaging systems for Ln^{III} imaging probes **2**:414–415
PACT. *See* photoactivated chemotherapy (PACT)
pair distribution function (PDF) **10**:1–3, **10**:103, **10**:222, **10**:398–399, **5**:307
analysis **5**:309–321
formal description of **10**:224
palladium (Pd) **9**:399–400
catalysts for emissions abatement **10**:122–127
active state of Pd revealed under in situ and operando conditions **10**:123–127
rationalizing effect of preparation method on properties and performance **10**:122–123
complexes **9**:697–698
intermolecular Pd···Pd metallophilic interactions **1**:682–689
interrogation of bimetallic species **10**:127–130
palladium(II) **8**:592–596
complexes **8**:59–63
Pd···Pd metallophilic interactions **1**:681–689
sites in SSZ-13 **6**:181
solvation and mobility of **6**:181
Panov oxidation reaction **6**:7–8
parahydrogen (p-H_2) **9**:719
paramagnetic broadening **9**:622
paramagnetic interactions **9**:286
paramagnetic metal complexes (Pnmr) **9**:211
pNMR of single molecule magnets in solution **9**:212
selected solution pNMR studies of SMMs **9**:219–226
paramagnetic relaxation enhancement **9**:372–375
paramagnetically shifted (PARASHIFT) **3**:456
probes **2**:442
parameters **3**:453–456
defects concentration **3**:455–456
distributions **9**:607–609
quality factor **3**:454–455
PARASHIFT. *See* paramagnetically shifted (PARASHIFT)
PARIS. *See* phase-alternated recoupling irradiation scheme (PARIS)
Paris–Edinburgh press (PEP) **10**:206–209
See also multi-anvil press (MAP)
advantages and disadvantages of **10**:207

Paris–Edinburgh press (PEP) (*continued*)
example syntheses with **10**:208–209
using PEP for chemical synthesis **10**:207
Parkinson's disease (PD) **2**:605–610
metal ions as therapeutic targets in **2**:610
particle swarm optimization (PSO) **3**:398
particular elements, theoretical calculations applied to **9**:845–863
Pauling rules extended to surfaces of ionic compounds **3**:89–90
PBAs. *See* Prussian blue analogs (PBAs)
PbSe **4**:60
PbTe **4**:60
Pc multidecker complexes **9**:222–224
PCs. *See* photocatalysts (PCs)
PCS. *See* pseudocontact shift (PCS)
PD. *See* Parkinson's disease (PD)
PDF. *See* pair distribution function (PDF)
PDK. *See* pyruvate dehydrogenase kinases (PDK)
PDSD. *See* proton-driven spin diffusion (PDSD)
PDT. *See* photodynamic therapy (PDT)
penrose tiling **3**:464
noninteracting case on **3**:476
RDMFT results for EALM on **3**:476–478
pentonate dehydratases **2**:134–136
PEP. *See* Paris–Edinburgh press (PEP)
peptides **2**:514
peptide-based zincophores in tug-of-war over zinc **2**:563–569
permanent magnets **4**:253–254
pernitrides **4**:393–394
perovskites **4**:505–506, **4**:637–638, **5**:253, **5**:255, **9**:305
under high pressure **4**:546–547
oxides with A-site ordering **4**:698–707
perovskite-type solid electrolytes **4**:661–663
structure **4**:143
system **4**:161
with unusual ordering **4**:505
persistent luminescence, role of defects and rise of **4**:286–287
PET. *See* positron emission tomography (PET)
Peters' systems **2**:327–331
[*pf*]$^{-}$aluminates, reactive cations stabilized by **1**:384–407
lanthanide and actinoid complexes **1**:406–407
low valent group 14 cations **1**:398–400
reactive group 13 cations **1**:389–396
reactive group 14 cations **1**:396–398
reactive group 15 cations **1**:400–406
reactive group 16 cations **1**:406
reactive group 2 and related group 12 cations **1**:387–389
unusual group 1 M^{+}-complexes **1**:387
PGSE. *See* pulsed-field gradient spin-echo (PGSE)
pH probes **8**:217–219
phase stability very sensitive to temperature **10**:204
phase-alternated recoupling irradiation scheme (PARIS) **9**:541–543
phase-transformation-based crystallization **2**:82–84
1,1′-phenanthroline **1**:53
phenomenological models **3**:86–95
free electron model extended to surface **3**:86–87
phenomenological theory **4**:140–142
phosphates ($LiFePO_4$) **4**:16, **4**:331–334, **4**:410–412, **4**:643
class of polyanionic cathodes **7**:246–251
glasses **9**:643
minerals in pegmatites **7**:364–365
phosphides **5**:80–82
phosphonate-platinum conjugate targeting bone cancers **2**:823
phosphonitrates **7**:266
phosphorescence in chemotherapy **2**:474
phosphorescent
iridium complexes as chemotherapeutic agents **2**:477–479
metal complexes
for bioimaging **2**:461–473
as chemotherapeutic agents **2**:480
for chemotherapy **2**:473–480
for photodynamic therapy **2**:480–497
phosphorescent Ir(III) complexes for PDT **2**:489–495
phosphorescent Ru(II) complexes for PDT **2**:482–488
ruthenium complexes as chemotherapeutic agents **2**:474–477
phosphors **5**:119
phosphorus **9**:780
centered biradical dianions **1**:206
phosphorus-carbon-centered heterocyclopentane-1, 3-diyl **1**:219–221
phosphorus-centered benzo-fused cyclopentane-1, 3-diyls **1**:219
phosphorus-centered heterocyclopentane-1, 3-diyls **1**:214–215
phosphorus-donor ligands **1**:61–66
bidentate ligands **1**:65–66
monodentate ligands **1**:61–64
tris(phosphane) ligands **1**:66
phosphosilicates **9**:641
phosphosulfates **7**:265
photo-dimerization of acenaphthylene in M_6L_4 cage, crystalline state solution-state-like reaction–direct observation of **10**:323
photo-induced coordinatively unsaturated transition-metal complex in M_6L_4 cage **10**:321–322
photo-induced radicals, direct observation of **10**:316–317
photo-induced triplet carbine, direct observation of **10**:318
photo-induced triplet nitrene, direct observation of **10**:319–320
photo-regulatory proteins, coenzyme B_{12} as light-sensitive ligand in **2**:291–292
photo-uncaging
of cancer therapeutics **8**:266–270
fundamental issues in **8**:256
photoacoustic imaging **2**:431–436
photoactivatable platinum(IV) complexes **2**:817–819
photoactivatable prodrugs **2**:774–778
photoactivated chemotherapy (PACT) **2**:510, **2**:525–534, **8**:265–266
photoactivated metal complexes for drug delivery **8**:254–297
photoactivation
of ligands **2**:514
mechanisms and pathways **2**:513–514
photoactive anticancer metallodrugs **2**:515–535
photoactive antimicrobial metallodrugs **2**:535–537
photoactive components **8**:428–435
photoactive enzymes mimics **10**:357–361
photoactive metallodrugs, drug delivery systems for **2**:537–542
photoactive structural components **8**:432–434
photocatalysis **2**:513
mechanisms of **8**:107–108
photocatalysts (PCs) **8**:103–104
characteristics of successful **8**:105
doping effects on physicochemical and semiconducting properties of **6**:402–415
electronic structures **8**:105–107
with LMCT excited states **8**:107
with MC spin-flipped states **8**:107
with MLCT excited states **8**:105–107
modification of electronic states via aliovalent ion doping **6**:402–404
modification of particle morphology **6**:413–415
visible light absorption via excitation of mid-gap states **6**:404–413
photochemical CO_2 reduction **8**:299
mixed system of photosensitizer and catalyst **8**:300–304
photochemical kinetics **8**:256–257
photochemically driven molecular machines based on coordination compounds **8**:417–438
photochemistry of metallodrugs **2**:511–514
photochromic materials **8**:356–416
photochromic transition metal complexes and organometallics **8**:357–373
photochromism (photoCORMs) **8**:279–288
with bond reorganization **8**:365–366
group 6 photoCORMs **8**:282
group 7 photoCORMs **8**:283–286
group 8 photoCORMs Fe and Ru **8**:287–288
with intramolecular ligand exchange reactions **8**:363–364
without large structural changes **8**:366–373
with linkage isomerization **8**:357–363
photocrystallography **10**:276

photodynamic therapy (PDT) **2**:480–481, **2**:509–510, **2**:515–525, **8**:258–262
candidate PDT metallodrugs **2**:516–525
metallodrugs entered clinical trials **2**:515–516
phosphorescent Ir(III) complexes for **2**:489–495
phosphorescent metal complexes for **2**:480–497
phosphorescent metal complexes/polymetallic complexes for **2**:495–497
phosphorescent Ru(II) complexes for **2**:482–488
promoting photophysical performance for **2**:489–491
targeted PDT by Ir(III) complexes **2**:491–492
photoelectric performance **5**:236
photoelectrocatalytic conversion of methane **6**:350–351
photoelectrochemical materials for solar energy conversion **4**:594–627
photoemission spectroscopy **4**:532–534
photoinduced electron transfer from and to 3d TMCs **8**:735
photoinduced energy transfer from and to 3d TMC **8**:745
photoinduced isomerization in excited state TMCs **8**:693–694
photoisomerization of organic photochromics, control over photo-, electro-, and magneto-properties of transition metal complexes and organometallics via **8**:376–393
photoluminescence (PL) **5**:235
performance **5**:236–239
spectroscopy **4**:538–540
photoNORMs based on iron **8**:273–275
photophysics of metallodrugs **2**:511–514
photoreactions with biomolecules **2**:514
photoredox organic transformations using molecular inorganic catalysts **8**:108–142
photoreduction **2**:513
photorelease of H_2S **8**:288
photosensitizers **10**:348–354
mixed system of photosensitizer and catalyst **8**:300–304
photosubstitution **2**:513
photosynthesis **2**:348, **8**:318–321
channels **2**:357–359
function of photosystem II **2**:349–352
architecture **2**:349–350
electron transfer chain **2**:350–351
energetics of water oxidation reaction **2**:351–352
light-driven assembly of manganese cluster **2**:360–363
mechanism of photosynthetic O_2 evolution **2**:359–360
perspective **2**:369
photosynthetic reaction centers **2**:349
S-state transition of oxygen evolving complex **2**:352–357
techniques **2**:363–369
photosystem II (PSII) **8**:318–321
phototherapeutic window, extending absorption profile to **2**:484–486
phototherapy **2**:509–510
photothermal therapy (PTT) **2**:510, **2**:535
phototrigger of supramolecular transformations **8**:434–435
piezo-materials
applications of **4**:167–168
automotive **4**:168
consumer electronics **4**:168
industrial manufacturing, processing and detection **4**:168
medical and health care **4**:167
piezoelectric devices and application **4**:167
piezoelectric equations **4**:137–138
piezoelectric materials **4**:136–137
classification of **4**:143
era of **4**:148
piezoelectricity **4**:136–137
piezoelectrics **5**:123
pigments through ages **4**:561–562
pincer ligands **1**:57–58
pincer-type gold(III) complexes **2**:856–858
PL. *See* photoluminescence (PL)
planar defects **7**:297–301
plane waves **3**:148–149
plane-wave-based quantum chemistry programs **3**:159–160
plant growth, phosphors for promoting **4**:290
plant products **9**:826–828
plasma membrane stains **8**:246–248
platinum (Pt) **9**:861–863
anticancer drugs **2**:61–62, **2**:809–819, **9**:400–401
challenges and future perspectives of platinum chemotherapeutics **2**:778–779
complexes **2**:814–819, **8**:83, **9**:698–704
delivery of platinum drugs
by albumin **2**:827–828
by antibodies **2**:828–829
by proteins **2**:827–829
intermolecular Pt···Pt metallophilic interactions **1**:675–679
platinum drug-based nano-delivery systems **2**:832–838
Pt···Pt metallophilic interactions **1**:675–681
platinum(II) **8**:575–592
action mechanism of **2**:810–812
aquation, DNA binding, and cell death **2**:812
with bidentate ligand **8**:29–34
cellular uptake of **2**:812
circulation of **2**:810–811
complexes **8**:29–42
complexes as anticancer agents **2**:745–757
complexes with chelating cyclometalating ligands **8**:587–591
complexes with chelating N-donor ligands **8**:578–587
complexes with cyanide and/or isocyanide ligands and platinum(II) double salts **8**:575–578
development of **2**:809–810
discrete multinuclear platinum(II) complexes **8**:591–592
drug resistance of **2**:813–814
limitations of **2**:813–814
platinum(II) anticancer drugs **2**:809–814
side effects of **2**:813
with tetradentate ligand **8**:39–42
with tridentate ligand **8**:34–38
platinum-conjugated nano-systems **2**:836–838
platinum-incorporated nano-systems **2**:833–836
platinum-self-assembled nano-systems **2**:836
platinum(IV) prodrugs **2**:815–819
as anticancer agents **2**:757–779
in cells **2**:816–817
in clinical trials **2**:816
clinically trialed prodrugs **2**:757–758
photoactivatable platinum(IV) complexes **2**:817–819
platon/pluton **10**:426–437
crystal structure determination **10**:427–428
analysis of results, illustrations and validation **10**:428
data collection and data reduction **10**:427
solution of phase problem **10**:427
structure refinement **10**:427
crystal structure validation **10**:437–443
PLATON/checkCIF report **10**:438–439
PLATON/checkCIF report example **10**:439–442
validation issues **10**:443
implementation and availability **10**:443
tools and functions **10**:428–437
PLD. *See* pulsed laser deposition (PLD)
PLGA. *See* poly(lactic-co-glycolic acid) (PLGA)
plutonyl ions **8**:799–801
*P*n-type of chalcogenide clusters **5**:220–221
pnictides **4**:8
Pnictogen centered biradicals **1**:202–206, **1**:208
Pnictogen-centered heterocyclopentane-1, 3-diyls **1**:215–218
point defects in electrode materials **7**:292–297
polar crystalline materials, symmetry requirements for **5**:250–251
polar substrates **1**:316–332
See also non-polar substrates
enantioselective reduction of C–N multiple bonds and silyl enols **1**:323–326
reduction
amides and phosphine oxides **1**:319–320
of carbonyls **1**:326–330

polar substrates (*continued*)
of C–N multiple bonds and silyl enols **1**:317–319
reductive alkylation of amines with carbonyls **1**:330–332
reductive etherification of carbonyls **1**:330
substrates serve Lewis basic components of FLPs **1**:320–323
polarity probes **8**:219–221
polarization **7**:477–478
poly(lactic-co-glycolic acid) (PLGA) **9**:428
poly(tyrosol carbonate) **10**:475–476
polyanion cathode materials **4**:331–335
polyanionic cathodes **7**:255–256
mixed polyanionic cathodes **7**:256–266
phosphate class of **7**:246–251
sulfate class of **7**:251–255
polyanionic compounds **5**:210
as positive electrode materials **7**:99–104
polyanionic sodium-ion battery insertion materials **7**:241–271
polyanions **4**:349
polyatomic chalcogen cations **1**:952–959
polybromides **1**:1036–1038
polycationic group 13 clusters, formation of **1**:395–396
polychalcogen molecules, ligands, and ions **1**:934–969
polychalcogen-halogen anions **1**:1013–1014
polychalcogenide derivatives of p-block elements **1**:976–1014
polycrystalline materials, synthesis of **5**:188–194
polycrystalline thin films **10**:233–236
polycrystals **10**:478–480
polycyclic catena-pnictogens **1**:886–898
from P_4 and As_4 tetrahedra **1**:888–894
synthesis of polycyclic catena-pnictogens from sources **1**:895–896
polydentate ligands
oxygen-donor ligands **1**:84–85
polydentate open-chain **1**:58–60
polyhalides **1**:1038–1040
applications **1**:1040–1044
doping of polymers and carbons **1**:1041
in energy applications **1**:1042–1044
for metal extraction **1**:1041–1042
optical applications **1**:1040
triiodide detection **1**:1041
polyhedral bonding, perturbations in **3**:41–43
polyhedral boranes with open structure **1**:763–766
polyhedral cluster compounds **1**:807–820
polyhydride superconductors **3**:411
polyiodides **1**:1027–1030
structural confinement **1**:1030–1032
trends in polyiodide chemistry **1**:1030–1034
polymer nanoparticles **9**:428–430
polymerization catalysis **6**:2–4
polymers and materials **1**:626–629
polymorphism, pressure and temperature **5**:302–304
polynuclear metal complexes **8**:629–638
coordination cages **8**:635–638
light harvesting antennas based on metal complexes subunits **8**:629–634
molecular multi-chromophoric systems for photoinduced charge separation **8**:634–635
polystyrene (PS) **9**:428–429
polysulfide radical anions **1**:975
polytelluride networks, extended **1**:963–964
porous coordination networks–cartridge synthesis, design of **10**:325
porous electrode, lithium peroxide deposition in **7**:333–334
porous frameworks as reaction containers for pressure induced reactions **4**:415
porous inorganic materials **5**:44–56
porous materials **10**:27–37
to high pressure conditions **4**:415
zeolites and clathrates **10**:28
porphyrinoids with modified heme (porphyrin) skeleton **2**:197–198
position space
chemical bonding analysis in
electron density for bonding analysis in **3**:223–224
electron localizability indicator-electron density basin intersection **3**:228–229
electron-localizability approach **3**:227–228
energy of atoms and between atoms within **3**:233–235
extended 8–N rule in position-space representation **3**:229–231
localization and delocalization indices for bonding analysis in **3**:232–233
volume chemistry **3**:224–227
representation
extended 8–N rule in **3**:229–231
positive electrode **7**:327–336
materials **7**:48–63, **7**:87–104
layered oxides as **7**:87–93
layered oxides of transition metals **7**:48–51
polyanionic compounds as **7**:99–104
Prussian blue analogues **7**:93–98
positron emission tomography (PET) **2**:444–448
post reaction data analysis methods **10**:140–141
post-synthetic transformations **4**:525–526
posttranslational modification α-synuclein and impact on metal-binding properties **2**:610
potassium (K)
intercalation anodes **4**:351
intercalation cathodes **4**:349–350
ion batteries **4**:349–351
K-ion battery **7**:84–87
Prussian blue analogues for **7**:95
potassium aluminum borate (KBBF) **10**:459–461, **4**:28–29
potassium dihydrogen phosphate (KDP) **4**:12–13
potassium manganese sulfides (KMS) **5**:170
potassium metal chalcophosphates (KMPS) **5**:170
potassium niobate (KN) **4**:15–16
potassium tin sulfides (KTS) **5**:169–170
potassium titanyl phosphate (KTP) **4**:13–14
potentiostatic chronoamperometric experiments **7**:437–438
powder X-ray diffraction **4**:527–528
power **4**:314
curves **7**:477–478
generation **7**:477–478
power-to-liquids **6**:360–361
praseodymium to thulium **9**:198–200
pre-formed layers, zeolite synthesis by assembly of **6**:24
precursor-directed biosynthesis and mutasynthesis **2**:17–18
pressure
be measured alongside temperature **10**:205
pressure-induced SCO **10**:89, **10**:100–102
prion diseases **2**:579–588
prion protein **2**:581–588
prion protein in Alzheimer's disease **2**:603–605
prison cell approach **10**:321–323
pristine zeolite framework, BAS mobility in **6**:167–169
probe molecules, use of **9**:504–508
prodrugs with unconventional cytotoxic cores **2**:772–774
projection method **3**:160–162
projector augmented wave method **3**:158–159
propylene epoxidation **6**:4–7
proteins **2**:514
as alternative targets for anticancer metal-based drugs **2**:797–798, **2**:800
B_{12}-derivatives as ligands of **2**:291–292
delivery of platinum drugs by **2**:827–829
and nucleic acids, B_{12}-derivatives as ligands of **2**:291–292
probes **8**:197–200
protein-based zincophores in tug-of-war over zinc **2**:563–569
rational design of **7**:465–466
targets for anticancer metal based drugs **2**:794–807
proteolytic processing of cellular prion protein and impact in metal-binding properties **2**:587–588
protic molecules mediated hopping and solvation of BAS **6**:169–170
protocols for acquisition of electron diffraction data **10**:56–59
proton
bond as function of zeolite lattice Al/Si concentration ratio **6**:277–279
channel **2**:359
mobility in zeolites **6**:186–187
proton-driven spin diffusion (PDSD) **9**:541–543

protonated organic amines-assisted solvothermal synthesis **5**:224–225
protonic bond, physical chemistry of **6**:274–279
Prussian blue analogs (PBAs) **4**:350, **5**:211–212, **7**:61–63, **7**:93–98
  as electrode materials **7**:93–94
  for K-ion batteries **7**:95
  Li, Na, and K insertion into **7**:94–95
  particle size and anion vacancy effect on electrochemical performance **7**:97–98
  structural evolution during K^+ insertion **7**:95–97
Prussian blue based biosensors **7**:176–177
  nanozymes and applications **7**:178–180
PS. *See* polystyrene (PS)
pseudocapacitance **7**:229–230
pseudocontact shift (PCS) **9**:212, **9**:214–215
  methods for determination of **9**:216
  purely NMR based methods for separations of **9**:216
  separation of FCS and PCS contributions to hyperfine shift **9**:215–216
  simplified treatment of **9**:212–215
pseudopotentials
  basis functions and **4**:511
  in general **3**:157–158
PSO. *See* particle swarm optimization (PSO)
PTT. *See* photothermal therapy (PTT)
pulsed laser deposition (PLD) **7**:3–4
pulsed magnets **9**:147
pulsed-field gradient spin-echo (PGSE) **9**:718
pump-probe data collection at XFEL **10**:364
pump-probe XES **10**:367–372
  transient X-ray emission studies of iron complexes in solution **10**:367–372
pump–probe spectroscopy **8**:512–525
  principles **8**:512–514
  TAS **8**:514–518
  time-resolved Raman spectroscopy **8**:524–525
  TRIR **8**:518–524
pure silica zeolites, ^{29}Si NMR of **9**:119–122
purine
  and derivatives **2**:679–689
  purine N7-seat **2**:646
putrebactin **2**:17
pym. *See* pyrimidine (pym)
pyoverdine **2**:9
  chromophore **2**:14–15
pyrazine (pyz) **1**:41–42
pyrazole **1**:43–44
pyridine **1**:39–41
pyrimidine (pym) **1**:41–42
  and derivatives **2**:667–679
pyrochlores **4**:638–639
pyroelectrics **5**:247–248
pyrophosphates **7**:56–57, **7**:248
pyruvate dehydrogenase kinases (PDK) **2**:765
  inhibition **2**:765–767
pyz. *See* pyrazine (pyz)

Q

q-space, analysis of nanoparticle structure from scattering data in **5**:308–309
(3Q)MAS spectral resolution and NMR peak assignments **9**:626–627
2Q–1Q correlation NMR experiments **9**:630–632
QCPMG. *See* quadrupolar CPMG (QCPMG)
Qmax effect on real space resolution **10**:400
QPM semiconductors. *See* quasi-phase-matched semiconductors (QPM semiconductors)
quadrupolar coupling, impact of **9**:267–268
quadrupolar CPMG (QCPMG) **9**:545–546
quadrupolar interaction **9**:5–8, **9**:265–267, **9**:285–286
quadrupolar nuclei
  enhancements for **9**:276–277
  high resolution NMR of **9**:609–610
  NMR on **9**:597–601
  and Rf fields **9**:599–601
quadrupolar-product trends among $27Al^{(p)}$ sites **9**:619–620
quantum dots **4**:296–298
quantum efficiency **2**:352
quantum materials **4**:365–366
  chemical definition of **4**:364–365
  classification of **4**:367–370
  frontiers **4**:372
  ideality meets reality **4**:371
  preparation of **4**:372
quantum pressure formalism **3**:240–241
quartz **4**:159
  analogs **4**:160
  commercial development of **4**:631
quasi-1D systems **3**:288–289
quasi-2D systems **3**:288–289
quasi-harmonic approximation **3**:449
quasi-harmonic Debye model **3**:449
quasi-phase-matched semiconductors (QPM semiconductors) **4**:11–12
quasicrystals **3**:462–463
  correlated electronic states **3**:462
  crossover of superconducting states **3**:484
  emergence of superconductivity at low temperature **3**:481
  framework of DMFT **3**:468–469
  local density of states **3**:485
  numerical solvers for effective impurity problem **3**:469–470
  phase diagram **3**:473
  quasiperiodic structure **3**:463–465
  site-dependent quantities **3**:473
  specific heat **3**:486
  strong electron correlation effects in **3**:467
  theoretical framework **3**:468–471
  tilings **3**:464–465
  unconventional cooper pairing **3**:482–483
  valence distribution **3**:477–478
quasielastic neutron scattering **10**:12–13

R

RAD. *See* radio frequency assisted diffusion (RAD)
radiation chemistry of fluoropolymers **9**:29–30
radicals **1**:622–623
  radical-SAM enzymes **2**:125–132
    atypical SAM-dependent enzymes **2**:130–132
    examples of **2**:126–132
  SAM mutases-lysine 2, 3-aminomutase **2**:126
radio frequency assisted diffusion (RAD) **9**:541–543
radio-frequency driven-recoupling (RFDR) **9**:540
Ramsey's equation, chemical shift ranges and **9**:749–751
random forest (RF) **5**:19
random structure searching **3**:397–398
rapid-injection NMR **9**:720
rapidly exploring random tree based methods (RRT based methods) **3**:331
  based explorations **3**:352
RAPTA, chemical proteomics approach to disclose protein targets for ruthenium complex **2**:802–803
rare earth nuclei
  NMR detection methods **9**:180–181
  nuclei and properties and interactions **9**:178–180
  scope of review **9**:180
rare earth oxides based pigments **4**:589
rare earth-calcium oxyborate (ReCOB) **4**:160
rare-earth substituted materials **4**:273–284
  emission from 4f↔4f transition in **4**:273–279
  emission from $Ce^{3+}$and Eu^{2+} **4**:279–280
  notable rare-earth substituted phosphors families **4**:282–284
  thermal stability of 4f↔5d electronic transitions **4**:280–282
rare-earth substituted phosphors, application of **4**:288–292
rate-limiting steps, electrochemical signatures of **7**:137–140
RC mechanism. *See* oxo-oxyl radical coupling mechanism (RC mechanism)
RCS. *See* reactive carbonyl species (RCS)
RDC. *See* residual dipolar coupling (RDC)
RDE. *See* rotating disk electrode (RDE)
RDMFT. *See* real-space DMFT (RDMFT)
re-arrangement reactions **1**:925
reactant interfaces dictate product yield **10**:203
reactive carbonyl species (RCS) **8**:186–187
reactive elements **10**:338–340
reactive nitrogen species (RNS) **8**:183–186
reactive oxygen **8**:179–189
reactive oxygen species (ROS) **8**:179–182
  reactions with **7**:342–344
reactive sulfur species (RSS) **8**:188–189

real space methods **10**:466–469
real space rietveld refinement on total scattering data **5**:311–314
real-space DMFT (RDMFT) **3**:470–471
  results for EALM on Penrose tiling **3**:476–478
  for superconducting state **3**:480–481
rechargeable battery electrode materials **3**:187–189
rechargeable calcium batteries **1**:431
rechargeable magnesium batteries (RMBs) **1**:429–431
reciprocal space methods **10**:457–466
  direct methods **10**:457–462
recrystallization **5**:186
red emissive iridium(III) complexes **8**:21–27
redox
  mediators **7**:344–346
    basic principles **7**:344
    for charge **7**:345–346
    for discharge **7**:346
  noninnocence **1**:262–267
  photocatalysis **8**:103–151
  potential **2**:351
  redox-chemistry of B_{12}-derivatives **2**:271–275
  redox pseudocapacitance **7**:509–510
redox-sensitive response regulator (RsrR) **2**:144
reduced oxides **5**:132–133
  multinary perovskites and perovskites-like oxides with substitution in A-site **5**:132–133
  multinary perovskites and perovskites-like with substitution in B-site **5**:132
  obtained from non-perovskite phases **5**:133
  ternary perovskites and perovskite-like **5**:132
reductive coupling mechanism **7**:17–18
relaxation time, measurement of **9**:718
relaxors **5**:247–248
  ferroelectrics **4**:147–148
  relaxor-based piezoelectric single crystals **4**:147–154
    growth of **4**:148–150
    property anisotropy and domain engineering **4**:151
    tailoring properties of **4**:150–151
    ultrahigh piezoelectric response in **4**:151–153
  relaxor-PT piezoelectric single crystals **4**:148
residual dipolar coupling (RDC) **9**:216–217
residual quadrupolar coupling (RQC) **9**:216–217
resins **9**:826–828
responsive contrast agents **2**:443–444
reverse Monte Carlo (RMC) **10**:420, **5**:318–321
reversible sodium ions de/intercalation, electrode materials for **7**:46–82
RF. *See* random forest (RF)
RFDR. *See* radio-frequency driven-recoupling (RFDR)
RGD-platinum conjugates targeting integrin **2**:823–824
rhenium **2**:341
  complexes **9**:682–683
  rhenium(I) complexes **8**:56–57
rhizobial iron regulator A (RirA) **2**:142–143
rhodium (Rh)
  complexes **9**:693–696
  dithionite cluster complexes **8**:361–362
  intermolecular Rh···Rh metallophilic interactions **1**:671–673
  Rh···Rh metallophilic interactions **1**:671–674
  rhodium(I) **8**:596–597
  rhodium(III) complexes **8**:59
  in zeolite Y and consequences for ethene hydrogenation & oligomerization, mobility of **6**:181
α-rhombohedral boron, inter-and intra-cluster bonds in **3**:213–214
ribonucleotide reductases, coenzyme B_{12}-dependent **2**:287–288
riboswitches, metal-ion sensing by **2**:654
rich materials chemistry, anionic redox opening new **7**:21–30
Rieske proteins **2**:109–111
rietveld refinement techniques **10**:9
ring compounds with direct E-E-single bonds **1**:779–807
RirA. *See* rhizobial iron regulator A (RirA)
RMBs. *See* rechargeable magnesium batteries (RMBs)
RMC. *See* reverse Monte Carlo (RMC)
RNA
  metal ion
    binding motifs in RNA by Mg^{2+} **2**:641–646
    binding to **2**:637–653
    and role in folding and dynamics of **2**:653–654
    and role in RNA catalysis **2**:654–656
  potential liganding atoms on **2**:633–635
    acid-base considerations on potential binding sites **2**:633
    micro acidity constants, intrinsic basicities, and tautomeric equilibria **2**:633–635
  thermodynamics of metal ion binding to **2**:639–641
RNS. *See* reactive nitrogen species (RNS)
room-temperature mechanochemical methods **4**:518–519
ROS. *See* reactive oxygen species (ROS)
rotating disk electrode (RDE) **7**:511–521
  application of RDE for studies
    of modified electrodes **7**:512–515
    of nanoparticles and porous materials **7**:515–518
    of planar electrodes **7**:512
  voltammetry **7**:478–479
rotaxanic copper complexes **8**:363–364
RP. *See* Ruddlesden-Popper (RP)
RQC. *See* residual quadrupolar coupling (RQC)
Rrf2 family **2**:140–144
RRT based methods. *See* rapidly exploring random tree based methods (RRT based methods)
RsrR. *See* redox-sensitive response regulator (RsrR)
RSS. *See* reactive sulfur species (RSS)
rubber **9**:827–828
Ruddlesden-Popper (RP) **5**:265
  hybrid-improper mechanisms in Ruddlesden-Popper phases **5**:265–266
ruthenium (Ru) **2**:62–63, **2**:338–341
  complexes **2**:651–653, **2**:781–783, **9**:685–686
  intermolecular Ru···Ru metallophilic interactions **1**:669
  photoNORMs **8**:278–279
  Ru-P **4**:221–222
  Ru···Ru metallophilic interactions **1**:669
  ruthenium(II) complexes **8**:55–56
  ruthenium(II) polypyridine complexes **8**:108–110
  sulfoxide complexes **8**:358–361

S

S-donor functionalized carbenes **1**:261–262
S-state transition of oxygen evolving complex **2**:352–357
  capturing intermediate S-states **2**:354
  Kok cycle **2**:352–353
  OEC structure **2**:354–357
    S_0 state **2**:356
    S_1 state **2**:355–356
    S_2 state **2**:356
    S_3 state **2**:356
    structural changes during S-state transitions **2**:357
    structural/spin isomers **2**:356–357
(S)TEM image simulation **7**:283–284
s^2 transition metals, emission from **4**:272–273
SAAs. *See* single atom alloys (SAAs)
SACs. *See* single atom catalysts (SACs)
sample homogeneity is difficult to control **10**:205
SANS. *See* small-angle neutron scattering (SANS)
SBIs. *See* secondary bonding interactions (SBIs)
SBP. *See* siderophore binding protein (SBP)
scandium (Sc) **9**:181–188
  complexes **9**:662–663
  inorganic complexes and covalent crystalline oxides **9**:181–182
  inorganic glasses **9**:182
  intermetallic compounds **9**:182–188
  oxides **4**:684
scanning mode **10**:112–113
scattering **10**:265
scavenger-free photocatalytic systems, particle-based **8**:84–85
SCCs. *See* supramolecular coordination complexes (SCCs)
Schrock catalyst **2**:319–320

Schrödinger's equation **3**:144–147
scintillators **4**:292–294
  gamma-ray conversion to light production **4**:292–294
SCR. *See* selective catalytic reduction (SCR)
SE. *See* solid effect (SE)
second coordination sphere **9**:604
second row transition metals **8**:108–125
second-generation biosensors **7**:475
second-order Jahn-Teller effect (SOJT) **5**:252
  for d^0 ions **5**:252–254
  for ns^2np^0 ions **5**:254–257
second-order quadrupolar interaction **9**:598–599
second-order recoupling **9**:541
second-shell ligands in zinc reactivity **2**:238–239
secondary bonding interactions (SBIs) **1**:8–9
SEI. *See* solid electrolyte interphase (SEI)
selective catalytic oxidation, importance of **6**:382–383
selective catalytic reduction (SCR) **6**:192–193
selective oxidation **6**:4–8
  by mixed metal nanoparticles **6**:381–400
  oxidation reactions catalyzed by zeolites **6**:7–8
  propylene epoxidation **6**:4–7
  reactions **6**:390–394
selective oxidation of methane to methanol (SOM) **6**:333–335
selenides **5**:77–80
selenium (Se) **1**:941–942, **1**:950–951, **1**:971–973
  $Se(CH_2)_4$ **1**:532–534
  $Se_2(CH_2)_4$ **1**:532–534
  $Se_2(CH_2)_6$ **1**:534–538
  $Se_3(CH_2)_3$ **1**:532–534
  $Se_4(CH_2)_{12}$ **1**:538–540
  $Se_6(CH_2)_{18}$ **1**:538–540
  selenium-chlorine cations **1**:959
  selenium-donor ligands **1**:89–92
    monodentate and bidentate ligands **1**:89–90
  sulphides **1**:942–943
self-powered biosensors **7**:476
self-propagating reactions **5**:26–28
semi-empirical methods **3**:448
semiconductors **3**:180–184, **4**:294–298
  hybrids with **8**:310–313
  nanoparticles **10**:226–227, **9**:402–407
    interfacial charge transfer from TMCs to **8**:694–695
  surfaces
    electron counting rules at sp **3**:92
semicrystallinity **9**:32–34
sensing oxygen by NreBC two component system **2**:148
separation techniques of metallomics and metalloproteomics **2**:55–57
separator **7**:435–436
serial electron diffraction (SerialED) **10**:58–59
series-connected hybrid magnets **9**:146
shuttle effect **7**:346
^{29}Si MAS NMR **9**:610–616
  limitations of **9**:611–614
^{29}Si-^{29}Si connectivities **9**:633–635
sideromycins **2**:4–5
siderophore binding protein (SBP) **2**:558
  SBP-metallophores **2**:569
siderophores
  adaptations **2**:11–13
  applications of **2**:21
  bacterial and fungal siderophores **2**:4–5
  biosynthesis of **2**:13–18
  characterization of Fe(III)–siderophore complexes **2**:6–9
  environmental aspects of siderophore production **2**:555
  functional group **2**:10–11
  in infection and stealth siderophores **2**:20–21
  in microbial battle for iron and role in homeostasis of metals **2**:555–563
  transport systems **2**:556–558
  uptake and transport **2**:18–20
SiGe **4**:56–57
signal enhancement methods **9**:287–288
signal quenching **9**:375
silica glass, partial structure factor analysis of **10**:415
silicates **4**:283–284, **4**:334–335, **4**:410–412, **4**:642–643, **7**:61–63, **7**:255–256
  ^{29}Si NMR of **9**:113–116
    ^{29}Si chemical shifts and notation for silicates and functionalized silica **9**:114–116
  glasses **9**:642–643
    bond angle distributions in **9**:128
  sheets **9**:460–461
  silicate-glass network models **9**:633–635
  speciations **9**:610
silicides **4**:382–383
silicon **4**:200–201, **4**:348, **9**:298–299, **9**:402–403, **9**:780
  analogs of benzene and related polycyclic aromatic hydrocarbons containing one silicon atom **1**:851–852
    structures and aromaticity **1**:852
    synthesis **1**:851–852
  centered biradicals **1**:195–201
  derivatives **1**:981–986
  NMR spectroscopy
    ^{29}Si NMR of aluminosilicate zeolites **9**:119
    ^{29}Si NMR of pure silica zeolites **9**:119–122
    chemical shifts **9**:109–111
    DNP-enhanced ^{29}Si NMR of functionalized silica materials **9**:133–134
    dynamic nuclear polarization ^{29}Si NMR **9**:129–134
    general features of **9**:108–113
    isotope **9**:108–109
    NMR crystallography of zeolites **9**:123–125
    of siloxanes and silicates **9**:113–116
    solid-state ^{29}Si NMR experiments **9**:111–113
    solid-state ^{29}Si NMR of glasses **9**:127–128
    solid-state ^{29}Si NMR of zeolites **9**:116–126
    two dimensional ^{29}Si NMR of zeolites **9**:122–123
  oxides **9**:298–299
  silicon-based electrode materials **7**:71
silicon dioxide/silica (SiO_2) **9**:407–409
siloxanes
  ^{29}Si chemical shifts and notation for **9**:113–114
  ^{29}Si NMR of **9**:113–116
silver (Ag) **2**:65
  Ag sites in MFI during C_3H_8-SCR reactivity, mobility of **6**:182–183
  Ag···Ag metallophilic interactions **1**:697–704
  complexes **9**:706–710
  intermolecular Ag···Ag metallophilic interactions **1**:697–704
  silver(I) **8**:606–614
    clusters **8**:607–611
    complexes **8**:63–65
    four-coordinate silver(I) complexes **8**:64–65
    metallacycles **8**:611–614
    two-coordinate silver(I) complexes **8**:63–64
silver gallium selenide $AgGaSe_2$ (AGSe) **4**:6–7
silver thiogallate $AgGaS_2$ (AGS) **4**:6
simulated powder pattern **10**:430
simulation techniques **7**:411–417
single atom alloys (SAAs) **6**:384–385
single atom catalysis **6**:11–12
  reducible supports **6**:11–12
  solid solution catalysts **6**:12
single atom catalysts (SACs) **10**:128–130
  adding rigor to imaging of single atom catalysts **6**:240–241
  applying artificial intelligence for quantification of single atom images **6**:229–232
  deriving chemical information from single atom catalysts **6**:232–234
  determining concentration of surface atoms **6**:228
  determining identity of surface atoms **6**:229
  development of electron microscopy for achieving atomic resolution **6**:222–224
single crystal growth **5**:155
single molecule magnet (SMM) **9**:210
  choice of solvent and sample concentration **9**:217
  cluster compounds **9**:219
  line widths, magnetic field and acquisition parameters **9**:218
  magnetic anisotropy and energy barriers in d-and f-block SMMs **9**:211–212

single molecule magnet (SMM) (*continued*)
pNMR of single molecule magnets in solution **9**:212
practical aspects for solution NMR measurements of **9**:217–218
selected solution pNMR studies of SMMs **9**:219–226
theoretical background **9**:211–217
single particle diagnosis approach **4**:299–300
single perovskites **4**:502–503, **4**:512–514
single photon emission computed tomography (SPECT) **2**:444–448
single site catalysts **6**:2–13
bifunctional catalysts **6**:8–11
disproportionation or metathesis reaction, polymerization catalysis **6**:2–4
selective oxidation **6**:4–8
single atom catalysis **6**:11–12
solid state to molecular nano-clusters catalysts **6**:13
single transition metal oxides **7**:89–91
single-atom ceria-based catalysts, catalysis by **6**:262–266
single-crystal reflectance **4**:536
single-crystal X-ray diffraction **4**:528–529
single-crystal-to-single-crystal guest exchange **10**:325
single-pulse NMR experiment **9**:590–591
single-stranded nucleic acids, metal ion affinities of individual sites of **2**:635–637
site dependence **6**:282–285
site selective spectroscopy **6**:161–162
on Fe^{2+} and Fe^{3+} **6**:153–155
Skutterudites **4**:70–71
sluggish kinetics **7**:13
small molecule bioregulators **8**:272–291
small-angle neutron scattering (SANS) **5**:335
small-angle X-ray scattering, information from **10**:262–264
small-molecule activation **1**:9–12
small-molecule models, lessons from **2**:342
SMM. *See* single molecule magnet (SMM)
Sn-based electrode materials **7**:71–73
SnTe **4**:62
SOC. *See* spin orbit coupling (SOC)
sodium (Na) **3**:410
approaches for describing mechanisms of sodium ion storage **7**:67–69
intercalation anodes **4**:351
intercalation cathodes **4**:349–350
ion batteries **4**:349–351
Na_2MPO_4F **7**:59–60
$Na_3V_2(PO_4)_2(O, F)_3$ **7**:58
$NaMPO_4$ **7**:51–52
sodium-ion batteries **5**:199
anode materials **5**:199–206
cathode materials **5**:206–212
transition metal oxides **5**:206–210
sodium sulfide (Na_2S) **9**:438
sodium tantalate ($NaTaO_3$) **6**:413–415
sodium vanadium fluorophosphates ($NaVPO_4F$) **7**:257–258
soft inorganic structures **10**:229
soft X-ray spectroscopy **8**:696–697
soft-mode theory **4**:142–143
software
for BVSE modeling **7**:418
for classical MD and KMC simulations **7**:418
for DFT modeling **7**:418–419
for geometrical/topological analysis **7**:417–418
for modeling ion conducting materials **7**:417–419
SOJT. *See* second-order Jahn-Teller effect (SOJT)
sol-gel based synthesis **5**:284–285
solar energy conversion, photoelectrochemical materials for **4**:594–627
solid effect (SE) **9**:368, **9**:377–381
mechanism **9**:388–389
solid electrolyte interphase (SEI) **4**:340, **7**:337
design **7**:341–342
solid-state chemistry, solvothermal and hydrothermal methods for preparative **5**:40–110
solid-state crystal growth (SSCG) **4**:150
solid-state nuclear magnetic resonance spectroscopy (SSNMR spectroscopy) **6**:129–131, **9**:99–101, **9**:262–269
See also nuclear magnetic resonance spectroscopy (NMR spectroscopy)
ABX_3 **9**:273–274
advanced SSNMR techniques **9**:274–278
analytical tool for structure, texture and properties of materials prepared under mechanochemical c as onditions **9**:515–518
cross polarization **9**:275–276
emerging interest **9**:262
enhancement techniques **9**:275–277
experimental techniques **9**:286–290
of fundamental properties **9**:269–274
of glasses
chemical-shift/structure relationships **9**:601–607
distribution of modifier cations **9**:642–644
simplified model for chemical-shift predictions **9**:601
of halogens **9**:273
historical background **9**:261–262
of I=1 nuclei **9**:268–269
isolated spin pairs **9**:265
magnetic shielding **9**:263–265
maximizing SSNMR response **9**:274–275
mechanochemistry as synthetic method for enabling new developments in **9**:521–526
^{14}N in **9**:9–19
direct detection **9**:9–11
indirect detection **9**:11–15
NMR relaxation and sensitivity concerns of **9**:594–595
of perovskites **9**:269–274
of rare earth nuclei **9**:178–208
spin interactions in **9**:284–286
structure/property relationships via SSNMR **9**:270–273
study of crystallinity and microstructure of nanomaterials prepared by mechanochemistry **9**:518–520
for understanding properties of materials prepared by mechanochemistry **9**:520
solid-state structures of XeO_3 **1**:498
solids
acid catalysis **6**:271–310
calculating NMR parameters of **9**:839–845
electrolytes
desired functional properties of **4**:658–660
fundamentals of **4**:658–660
ion transport mechanism in **4**:659–660
halogen(I) complexes in **1**:588–592
alkyl iodine(I) $[L–X–L]^+$ complexes **1**:589–590
aromatic bromine(I) $[L–Br–L]^+$ complexes **1**:589
aromatic iodine(I) $[L–I–L]^+$ complexes **1**:588
multi-halogen(I) ion structures **1**:590–591
NIIs **1**:592
preamble **1**:588
melting method **5**:151–153
solid-liquid interfaces **7**:150
solid-solid interfaces **7**:149–150
solid-solid transitions **3**:351
solid-state ^{29}Si NMR
experiments **9**:111–113
of glasses **9**:127–128
of zeolites **9**:116–126
solid-vapor synthesis **5**:193–194
solid/solid interfaces **7**:150–153
on cathode **7**:152–153
charge transfer across solid/solid interfaces **7**:154–157
structure and energetics of **7**:150–152
solutions between relaxors and ferroelectric $PbTiO_3$ **4**:148
state batteries **5**:120–121
state inorganic chemistry **4**:1–2
state inorganic color pigments **4**:560–561
color **4**:562–570
inorganic pigments with transition metal chromophores at tetrahedral, octahedral, square pyramidal and square planar environments **4**:572–575
inorganic pigments with transition metal chromophores at trigonal bipyramidal coordination **4**:576–589
pigments through ages **4**:561–562
rare earth oxides based pigments **4**:589
structure, geometry and color of inorganic chromophore ions **4**:571–572
sulfides and oxynitrides **4**:589

synthesis
and crystallization from melt **4**:518–519
from solid nitridation sources **4**:433
review of some fundamental concepts in **10**:202–204
wide line NMR spectra for **9**:277
solution NMR
^{14}N in **9**:8–9
of transition metal complexes **9**:660–744
solution-gel synthesis, surface modification by **7**:216
solution-mediated mechanism **7**:328–329
solution-state synthesis **4**:519–524
solvent
effects **1**:1034–1035
evaporation methods **4**:522
solvothermal conditions, classes of materials prepared under **5**:44–90
solvothermal crystallization, mechanistic aspects of **5**:90–99
solvothermal methods **4**:523
for preparative solid-state chemistry **5**:40–110
solvothermal synthesis
routes **7**:196
surface modification by **7**:216
SOM. *See* selective oxidation of methane to methanol (SOM)
SOMC. *See* surface organometallic chemistry (SOMC)
sound waves, imaging with **2**:431
SoxR. *See* superoxide response regulator (SoxR)
spark plasma sintering (SPS) **5**:112, **5**:192–193
from bulk powder to dense pellet **5**:115–117
considerations for densifying new material using **5**:114–118
context and understanding of **5**:112–114
from dense pellet to characterization **5**:118
example applications of SPS routes to inorganic functional materials **5**:118–124
influence of temperature **5**:113–114
material chemistry considerations **5**:114–115
simultaneous reaction and consolidation **5**:117–118
SPECT. *See* single photon emission computed tomography (SPECT)
spectroscopic ellipsometry **4**:536–537
spectroscopic methods **2**:640–641
spectroscopic properties
of lanthanide complexes **8**:487–492
of luminescent lanthanide complexes **8**:487–492
spectroscopy **10**:265, **1**:726–727
with electrons **7**:305–309
spin
diffusion **9**:385–386
experimentally assessing role of **9**:387
echoes **9**:147–148
glasses **3**:360
Hamiltonian **9**:370–372
polarization **9**:213–214
polarization systems **3**:184–187
spin-current driven polarization **5**:268
spin-decoupling experiments **9**:96
^{11}B{^{1}H} experiments **9**:96
^{13}C{^{11}B, ^{1}H} experiments **9**:96
^{1}H{^{11}B} experiments **9**:96
spin-driven polarization **5**:268
spin-spin relaxation **9**:756–757
time **9**:756
spin orbit coupling (SOC) **3**:495
combined with SOC effects **3**:495
relativistic effects and **4**:511
spinel oxides (LiM_2O_4) **4**:330–331
SPS. *See* spark plasma sintering (SPS)
SPSAC. *See* strain-promoted sydnone–alkyne cycloaddition (SPSAC)
SQUEEZE **10**:434
$Sr_2Be_2B_2O_7$ (SBBO family) **4**:24–26
SrTiO3, d^0 oxide perovskite **3**:9–11
SSCG. *See* solid-state crystal growth (SSCG)
SSNMR spectroscopy. *See* solid-state nuclear magnetic resonance spectroscopy (SSNMR spectroscopy)
stable heating relies on sophisticated apparatus **10**:203
state-of-the-art quantum mechanical computations, validation of results of **9**:777
steady-state microscopy **8**:495–497
STEM for electron crystallography applications **10**:67–69
stoichiometric layered oxides **9**:291–293
strain energy landscape in lithium-ion battery cathode nanoparticles **10**:174–176
strain-promoted alkyne–nitrone cycloaddition **8**:203–205
strain-promoted azide–alkyne cycloaddition **8**:200–202
strain-promoted sydnone–alkyne cycloaddition (SPSAC) **8**:205–206
structural dimensionality **7**:28–30
structural models of borate-based glasses **9**:622–623
structural motifs of inorganic cores of organotetrel chalcogenide clusters, and general synthetic approach **4**:98–100
structure analysis techniques of metallomics and metalloproteomics **2**:59–60
subhalides **1**:799–800
substrate
identifications **8**:326–330
substrate-water exchange **8**:326–330
SufR transcription repressor **2**:148
sulfate class of polyanionic cathodes **7**:251–255
sulfides **4**:589, **5**:77–80, **7**:14, **9**:305–307
sulfide based solid electrolytes **4**:668
sulfide solid-state electrolytes **7**:205–210
sulfides/selenides, from oxides to **7**:26–28
sulfite reductase **2**:116–117
sulfur **1**:971, **9**:780–781
species sensors **8**:179–189
sulfur-bromine cations **1**:959
sulfur-donor ligands **1**:85–89
monodentate ligands **1**:85–88
sulfur-nitrogen centered biradical **1**:209
sulphates **4**:334
sulphides **4**:321–323, **4**:352–354
sulphur **1**:935–941, **1**:948–949, **4**:343–345
supercapacitors, electrolytes for **1**:432
superconducting properties **3**:484–488
superconducting order parameter and gap **3**:484–485
superconductivity **3**:432–437, **3**:479–488, **4**:217–218, **5**:157–161
clathrate-like hydrides **3**:434–435
covalent hydrides **3**:435–437
elements **3**:433–434
hydrogen **3**:434
iron chalcogenides **5**:157–160
spatial inhomogeneity in superconducting state **3**:481–482
transition metal dichalcogenides **5**:160–161
superoxide anion formation and solvation **7**:328–329
superoxide response regulator (SoxR) **2**:146–147
superstructure **7**:28–30
supertetrahedral chalcogenide clusters
classification of **5**:219–223
functionalization and applications **5**:236–242
origin of **5**:217–219
supertetrahedral clusters **4**:85–88
to cluster-based superlattice, from **5**:226–235
non-bonding packing **5**:226–227
support vector machine (SVM) **5**:12–15
general SVM **5**:15–17
non-SVM **5**:17
supramolecular
chemistry involving chalcogen rings **1**:946–947
photocatalysts **8**:304–310
systems based on host-guest interactions **8**:645–650
supramolecular coordination complexes (SCCs) **2**:715–717
biomedical applications of **2**:717–727
synthesis **2**:715–717
of helicates **2**:717
surface
basics of surface science **3**:76–80
coordination chemistry
characterization techniques utilized in SOMC approach **6**:74–76
complexity of heterogeneous catalysis **6**:67–68
core principles of SOMC approach **6**:68
single-site catalyst concept **6**:68
success stories in SOMC single site catalysis **6**:76–78

surface (*continued*)
surface of supporting material as ligand **6**:69–74
tailored molecular precursors for well-defined surface species **6**:74–76
within DFT, structural models for **3**:82–83
convergence issues **3**:82–83
supercell slab generation **3**:83
surface stability from DFT and atomistic thermodynamics **3**:83–86
electronic states at **3**:96–97
energy **3**:76–78
amount of reversible work to create **3**:76–77
of clean surfaces **3**:83–84
modified by adsorption **3**:85–86
surface energy anisotropy and wulff construction **3**:77–78
thermodynamic approach **3**:77
first principles modeling of **3**:80–86
free electron model extended to **3**:86–87
impact of functional in surface computations **3**:81–82
surface morphologies **3**:95–96
surface-mediated mechanism **7**:328–329
symmetries **3**:78
surface (hydr)oxides, formation/reduction of **7**:507–508
surface organometallic chemistry (SOMC) **6**:68
characterization techniques utilized in SOMC approach **6**:74–76
complexity of heterogeneous catalysis **6**:67–68
core principles of surface organometallic chemistry approach **6**:68
single-site catalyst concept **6**:68
success stories in SOMC single site catalysis **6**:76–78
surface of supporting material as ligand **6**:69–74
tailored molecular precursors for well-defined surface species **6**:74–76
SVM. *See* support vector machine (SVM)
synchrotron
cell designs for in situ/in operando characterization of electrode materials using **5**:330–338
diffraction studies on spin crossover materials **10**:86–104
charge density studies **10**:99–100
LIESST **10**:89
LIESST effect studies using synchrotron diffraction **10**:97–98
ligand-field theory and thermal spin-crossover **10**:87
mononuclear SCO materials **10**:92–93
multinuclear SCO complexes and frameworks **10**:93–97
PDF **10**:103
pressure-induced SCO **10**:89, **10**:100–102
structure and properties of SCO complexes **10**:87–88
synchrotron GIXRD and in-plane XRD studies **10**:103–104
thermal SCO **10**:88–89
time-resolved synchrotron studies of SCO materials **10**:98–99
types of SCO complex **10**:89–90
X-ray induced excited spin state trapping **10**:99
GIXRD and in-plane XRD studies **10**:103–104
powder diffraction
accuracy and precision **10**:480–481
indexing **10**:447–448
reciprocal space methods **10**:457–466
resonant diffraction **10**:480
solve by analogy **10**:448–457
stealth and guile **10**:475–476
synthesis routes **3**:364
and materials design **3**:361–364
synthetic nitrogen fixation **2**:319–342
See also biological nitrogen fixation
dinuclear iron systems **2**:332–333
lessons from small-molecule models **2**:342
mononuclear iron systems **2**:327–332
mononuclear molybdenum systems **2**:319–322
systems with other transition metals **2**:333–342
synthetics **9**:828
exploration of synthetic variables **5**:90–91
materials **9**:812
polymeric nanocarriers **2**:538–540
substances associated with human life **9**:828–830
systems with other transition metals **2**:333–342

T

T2D-IR spectroscopy. *See* Transient 2D-IR spectroscopy (T2D-IR spectroscopy)
Ta tubes, RF induction heating **5**:190–191
taboo searches **3**:331
tafel slope **7**:529–530
tamsulosin hydrochloride **10**:466
tantalum
complexes **9**:674
nitride **4**:615–616
oxynitride **4**:615–616
tantalum-nickel group chalcogenides **4**:480–481
targeted imaging **2**:409–410
using Ln^{III} luminescent probes **2**:412–413
TAS. *See* transient electronic absorption spectroscopy (TAS)
tau protein **2**:601–603
tautomeric equilibria **2**:633–635
tavorite based electrode materials **7**:385–390
tavorite structure types **7**:60–61
TD-DFT. *See* time-dependent DFT (TD-DFT)
TE materials. *See* thermoelectric materials (TE materials)
technetium complexes **9**:680–682
tellurides **5**:77–80
tellurium **1**:941–942, **1**:951–952, **1**:971, **9**:856–857
allotropes **1**:971–973
tellurium-containing chalcogen rings **1**:943–945
temperature
effects **3**:84–85
probes **8**:223–224
sensitivity
of chemical shift **9**:751–755
electronic structure influence on **9**:751–752
molecular structure influence on **9**:752–753
persisting need for understanding **9**:755
vibrational structure **9**:753–755
temperature-controlled methods **4**:521–522
temperature-dependent relaxation dynamics **9**:755–757
templated grain growth, mechanism of **4**:165–166
ternary clusters **1**:922–924
containing lanthanides, actinides and early transition metal atoms **1**:923–924
containing post transition metal atoms **1**:922–923
ternary metal chalcogenides **5**:150–151
ternary metathesis **5**:30–31
ternary mixed element oxides **4**:637–639
ternary products **5**:30–32
ternary sulfide electrolytes **7**:209–210
2, 2′:6′, 2″-Terpyridines **1**:58
tethered nonclassical metal carbene complexes **1**:290–293
tetradecahydro-*arachno*-nonaborate anion **1**:765–766
tetradecahydro-*nido*-undecaborate anion **1**:764
tetradymites **4**:473–475
derivatives **4**:475
tetragonal tungsten bronzes (TTBs) **5**:253–254
tetrahedral E_4R_4 cluster compounds and derivatives **1**:808–813
aromaticity of $[EnRn]^{x-}$ cluster compounds **1**:817–820
bonding **1**:810–812
higher $[EnRn]^{x-}$ cluster compounds **1**:814–817
reactivity **1**:812–813
synthesis and structures **1**:808–810
tetrahedral MTr_2Ch_4 family **4**:478
tetrahedron-based network compounds **4**:410–414
tetravalent oxides **4**:636–637
tetrel chalcogenide clusters with or without organic ligands based on architectures **4**:121–126
textiles **9**:824–826
textured ceramics
piezoelectric properties of **4**:166
single crystals and preparation of **4**:155
textured piezoelectric ceramics **4**:163–166

mechanism of templated grain growth **4**:165–166
motivation for developing textured ceramics **4**:163
progress in **4**:163–166
texturing techniques by TGG and RTGG **4**:164
TG microscopy. *See* time-gated microscopy (TG microscopy)
TGA. *See* thermogravimetric analysis (TGA)
thallium (Tl) **4**:198
chalcogenides **5**:149
cluster compounds **1**:833–835
intermolecular Tl···Tl metallophilic interactions **1**:711–712
Tl···Tl metallophilic interactions **1**:711–712
thermal decomposition **5**:294–295
thermal SCO **10**:88–89
thermal spin-crossover **10**:87
thermally-controlled metathesis **5**:28
thermo-catalytic conversion of methane **6**:330–343
direct methane conversion **6**:331–343
indirect methane conversion **6**:330–331
thermodynamics
approach **3**:77
avoiding thermodynamic sinks **5**:33–34
of material requirements **5**:179–182
thermoelectric materials (TE materials) **3**:446, **4**:46–50
See also molecular materials
basic thermoelectric parameters related to efficiency **4**:48–50
classic thermoelectric materials **4**:53–57
common approaches to thermoelectric materials development and optimization **4**:50–53
complex crystal structures for **4**:68–72
complex intermetallics of $R_{117}Fe_{52}Ge_{112}$ structure-type **4**:71–72
complex tetrel chalcogenide thermoelectric materials **4**:62–63
crystal structure–phonon structure–thermal conductivity relationship **4**:68–69
data science and **3**:456–457
large unit cells in 14-1-11 compounds **4**:69–70
thermoelectrics **5**:119–120, **5**:162–166
phases **3**:189–191
thermogravimetric analysis (TGA) **5**:294–295
thin films **4**:439
deposition **4**:524–525
forms **4**:450–459
growth methods **4**:454–456
thiol sensors **8**:173–179
thiol-containing molecules **2**:813
thioredoxin reductase **2**:800
thiospinels (CuM_2S_4) **4**:322–323
third generation biosensors **7**:475
third row transition metals **8**:108–125
thornton formalism **10**:418–419
three-dimension (3D)
coordination framework materials **5**:300–301
crystallographic information **10**:69–71
framework topology of 3D cluster-based open frameworks **5**:233–235
halide perovskites
alloyed perovskites **4**:505–506
computational approximations **4**:510–511
density functional theory **4**:508–510
double perovskites **4**:503–505
electronic structure **4**:506–516
elemental analysis **4**:526–527
measurement **4**:526–546
peculiar properties **4**:546–549
perovskites with unusual ordering **4**:505
single perovskites **4**:502–503
structure and composition **4**:501–506
synthesis **4**:516–526
HPHT synthesis of 3d-transition metal oxides and investigations at HT conditions **4**:684–695
imaging in **7**:304–305
metal sulfides **5**:168–169
solids **3**:341–343
TM
charge transfer emitters **8**:726
spin-flip emitters **8**:716
TMC
electron and energy transfer with **8**:734
luminescent **8**:716
photodissociations and rearrangements of **8**:772
photoinduced electron transfer from and to **8**:735
photoinduced energy transfer from and to **8**:745
photophysical background and specific considerations for **8**:712
unimolecular reactivity of **8**:753
transition metal dichalcogenides **7**:118–119
through-bond heteronuclear correlations **9**:544–546
between spin-1/2 and half-integer quadrupolar isotopes **9**:545–546
without high-resolution **9**:545–546
with high-resolution **9**:546
between spin-1/2 isotopes **9**:544–545
between two half-integer quadrupolar isotopes **9**:546
through-bond homonuclear correlations **9**:537–539
through-bond J interactions **9**:596
through-space dipolar interactions **9**:595–596
through-space heteronuclear correlations **9**:547–561
between spin-1/2 and quadrupolar isotopes **9**:555–561
between half-integer quadrupolar isotopes **9**:561
without high-resolution **9**:555–559
with high-resolution **9**:559–561
between spin-1/2 isotopes **9**:547–555
through-space homonuclear correlations **9**:539–544
between half-integer quadrupolar nuclei **9**:543–544
between spin-1/2 nuclei **9**:539–543
thulium
praseodymium to thulium **9**:198–200
TI. *See* topological insulator (TI)
time
crystals **3**:348–349
evolution **3**:300–303
landscapes **3**:293–307
fast *vs.* slow variation **3**:304–306
locally ergodic regions in general statistical ensembles **3**:298–300
measurements in experiment and simulations **3**:293–295
noisy cost function landscapes **3**:306
periodic variation **3**:306
time dependence of cost function/energy landscapes **3**:303–306
variation of cost function **3**:304
variation of state space and moveclass **3**:303–304
time-dependent DFT (TD-DFT) **2**:514
calculations **2**:514
time-gated microscopy (TG microscopy) **8**:497–500
time-of-flight neutron instrumentation **10**:391–393
time-resolved (TR) **8**:497–500
electronic structure and dynamics for time-resolved X-ray spectra **8**:664–667
emission spectroscopy **8**:525–528
Raman spectroscopy **8**:524–525
structural methods **8**:528–533
studies **10**:288–305
of coordination compounds **10**:290–292
of small organic molecules **10**:290–292
synchrotron studies of SCO materials **10**:98–99
tin **4**:202–203, **9**:783–785, **9**:853–856
analogs of benzene and related polycyclic aromatic hydrocarbons containing one tin atom **1**:855
centered biradicals **1**:202
chalcogenides **5**:148–149
complexes **1**:987
comprehensive example on growth of tin cluster **1**:925–926
tin monoselenide (SnSe) **4**:61–62
TiS_2 **4**:353
tissue
application of biomineralization for tissue regeneration **2**:87–91
bone repair **2**:90–91
collagen mineralization **2**:87–88
tooth repair **2**:88–89
transmission of light through **8**:257
titanium (Ti) **2**:341
complexes **9**:667–668
oxides **4**:684–685
titanium-based materials **7**:69–71

titanium dioxide/titania (TiO_2) **9**:409–411
titanocenes **8**:132–133
TM. *See* transition metal (TM)
TMCCs. *See* transition metal carbonyl cations (TMCCs)
TMCs. *See* transition metal carbonyls (TMCs)
TMDs. *See* transition metal dichalcogenides (TMDs)
TME. *See* tumor microenvironment (TME)
TMIs. *See* transition metal ions (TMIs)
T*n*-P*n* hybrid assembly **5**:233
T*n*-T*m* hybrid assembly **5**:232
T*n*-T*p, q* hybrid assembly **5**:233
*T*n-type chalcogenide clusters **5**:219–220
TOF. *See* turnover frequency (TOF)
top-down synthetic strategy via demetallization **6**:51–52
top-seeded solution growth method (TSSG method) **4**:149–150
topological ferroelectrics **5**:257
topological insulator (TI) **5**:161
total scattering analysis, from rietveld refinement to **5**:308–309
total scattering data, local structure determination using
  amorphous systems **10**:237–238
  battery electrode materials under cycling **10**:225–226
  formal description of PDF **10**:224
  inorganic molecular cluster structures **10**:228
  layered materials **10**:231–233
  magnetic crystals **10**:240
  MOF and host-guest systems **10**:230–231
  nucleation of crystallites **10**:238–240
  polycrystalline thin films **10**:233–236
  semiconductor nanoparticles **10**:226–227
  soft inorganic structures **10**:229
  structural phase transitions **10**:224–225
  total scattering measurements **10**:224
tourmaline **4**:159–160
$T_{p,\,q}$ type of chalcogenide clusters **5**:223
TPP. *See* tumor penetrating peptide (TPP)
TR. *See* time-resolved (TR)
trans-platinum compounds **2**:814–815
Transient 2D-IR spectroscopy (T2D-IR spectroscopy) **8**:545–550
transient electronic absorption spectroscopy (TAS) **8**:514–518
transient infrared spectroscopy (TRIR) **8**:518–524
transient species in pores, snapshots of **10**:326–329
transient X-ray emission spectroscopy **10**:367–372
  transient X-ray emission studies of iron complexes in solution **10**:367–372
transient X-ray spectroscopy of metalloporphyrin chemistry at XFEL **10**:372–375
transition metal (TM) **6**:172
  application of transition metal substituted phosphors **4**:288–292
  borides, carbides and nitrides of **4**:381–382
  cations with gaseous ligands **1**:411
  chalcogenides **7**:117–120
  complexes **1**:419–420
  hexacyanoferrates
    as electrocatalysts of hydrogen peroxide reduction **7**:175–176
    structure and electroactivity **7**:172–174
    synthesis **7**:174–175
  hydrides **4**:385–387
    N–H bond formation on early **3**:129–136
  mobility of active sites in TM-exchanged zeolites **6**:172–183
  nitrides **4**:391–392
  NMR thermometry
    literature survey **9**:757–767
    metal ion chemical shifts and temperature dependence **9**:749–755
    NMR spectroscopy of transition metal nuclei **9**:746–749
    temperature-dependent relaxation dynamics **9**:755–757
  nuclei **9**:758–767
  oxide surfaces
    C–H bond activation on late **3**:119–129
  oxides as negative electrode materials **7**:115–117
    based on conversion reaction **7**:117
    Ti, Mo, and Nb oxides **7**:115–117
  oxyfluorides **4**:408
  oxyhydrides **4**:408–409
  oxynitrides **4**:407–408
  P4 and As4 with transition-metal reagents **1**:891–894
  phospho-/silico-/germano-trichalcogenides **4**:470–471
  single ion magnets of **9**:219
  systems
    P2-and P3-type binary and ternary transition-metal systems **7**:91–93
  transition metal-based chalcogenides **5**:151
transition metal carbonyl cations (TMCCs) **1**:410
  as starting materials **1**:411–412
transition metal carbonyls (TMCs) **1**:411, **8**:679
  absorption in **4**:267–269
  as complex ligands **1**:411
  data analyses **8**:687–688
  detector systems **8**:686
  excited state structural characterization examples **8**:688–695
  experimental methods **8**:684–688
  interplay among **8**:374–409
  photoinduced ligand dissociation **8**:688–689
  sample considerations **8**:686–687
  to semiconductor nanoparticles, interfacial charge transfer from **8**:694–695
  signal processing **8**:686
  solution NMR of **9**:660–744
  studied by L-edge XTA spectroscopy and soft X-ray spectroscopy **8**:696–697
transition metal dichalcogenides (TMDs) **4**:465–467, **5**:160–161
4d transition metal dichalcogenides **7**:120
5d transition metal dichalcogenides **7**:120
transition metal halides (MX_3) **4**:469–470
transition metal ions (TMIs) **6**:148–149
  in zeolites **6**:149–150
4d transition metal oxides, HPHT synthesis of **4**:695–698
5d transition metal oxides, HPHT synthesis of **4**:695–698
transition-metal coordination complexes of NgF_2 **1**:444–452
transmission electron microscopy
  data visualization, manipulation and treatment **7**:283
  electron beam damage in **7**:284
  electron diffraction techniques for metal-ion battery electrodes **7**:285–291
  imaging of local crystal and defect structure **7**:291–305
  (S)TEM image simulation **7**:283–284
  techniques in brief **7**:273–284
transport-promoted metathesis **5**:28–30
transuranic actinide ions **8**:801–806
trapped O_2 molecules **7**:19–21
tree/disconnectivity graphs **3**:356
  3D solids **3**:356
  clusters and molecules **3**:356
triazenide ligands **1**:52–53
1,2,3-triazol-5-ylidene **1**:236–238
triazolylidenes, nonmetal redox active moieties appended to **1**:266–267
tricoordinate carbenium ions **1**:396–397
tridentate **1**:68
  ligands
    oxygen-donor ligands **1**:83
    selenium-donor ligands **1**:91
    sulfur-donor ligands **1**:88
triel dihalides **1**:780
trihylite $LiFePO_4$ **7**:365–370
triiodide ion and lighter congeners **1**:1022–1027
  bonding in trihalide ions **1**:1025
  bonding trends in trihalides **1**:1025–1027
triphylite **7**:51–52
triple quantum MAS (3QMAS) **9**:609–610
triplet harvesting by thermally-activated delayed fluorescence using carbene metal amides **8**:662–664
tripod ligands **1**:68
tripodal **1**:66
  ligands **1**:54–57
TRIR. *See* transient infrared spectroscopy (TRIR)
tris(pyrazolyl)borates **1**:54–57
trivalent lanthanide-based luminescence and imaging **2**:412–418
  applications **2**:416–418
  packaging systems for Ln^{III} imaging probes **2**:414–415
  targeted imaging using Ln^{III} luminescent probes **2**:412–413
trivalent oxides **4**:635–636
TRXAS experiments

conducted at XFEL **10**:365–367
at X-ray free electron lasers **10**:361–367
TSSG method. *See* top-seeded solution growth method (TSSG method)
T–T bonds in transition metal (T) **3**:214–220
TTBs. *See* tetragonal tungsten bronzes (TTBs)
tumor microenvironment (TME) **2**:768
regulators **2**:768
tumor penetrating peptide (TPP) **2**:824–825
TPP-platinum conjugates targeting memHSP70 **2**:824–825
tumor-targeted platinum complexes **2**:819–829
tumor-targeted platinum-peptide conjugates **2**:823–827
tumor-targeted small molecule-platinum conjugates **2**:819–823
tungsten **9**:783–785
bronze system **4**:161
complexes **9**:677–679
tungsten(VI) complexes **8**:66
tungsten(VI) oxo complexes **8**:123–125
tuning zeolite acidity **6**:317–318
turnover frequency (TOF) **7**:529
TWINROTMAT **10**:435
two-dimension (2D) **9**:596
dispersions of 2D materials in solution **4**:452–453
existence and embedding 2D and 1D systems, of **3**:288
materials and thin films **10**:78
NMR **9**:596–597, **9**:717
correlations **9**:489–495
phosphorus sheets **9**:456–458
^{29}Si NMR of zeolites **9**:122–123
van der waals materials
canonical families of **4**:459–471
in crystal, monolayer, and thin film forms **4**:450–459
emerging families of **4**:471–488
vdW materials **4**:488
two-dimensional electronic spectroscopy (2D-ES) **8**:543–544
two-dimensional electronic-vibrational spectroscopies (2D-EV spectroscopies) **8**:544–545
two-dimensional infrared spectroscopy (2D-IR spectroscopy) **8**:535–542
two-dimensional vibrational-electronic spectroscopies (2D-VE spectroscopies) **8**:544–545
two-metal ion mechanism **2**:655

U

UCr_4C_4-type materials **4**:284
ultrafast dynamics of photoinduced processes in coordination compounds **8**:511–512
multi-pulse experiments **8**:545–560
pump–probe spectroscopy **8**:512–525
time-resolved emission spectroscopy **8**:525–528
time-resolved structural methods **8**:528–533
ultrafast multidimensional spectroscopy **8**:533–545
ultrasound imaging **2**:431–436
ultrasound-assisted methods **4**:523–524
ultraviolet nonlinear optical materials (UV NLO material) **4**:19–27
ultraviolet photoelectron spectroscopy (UPS) **4**:533–534
ultraviolet-visible-near infrared (UV-vis-NIR) **4**:534–538, **6**:151–152
spectroscopy on Co^{2+} **6**:155
uncaging
of chemotherapeutic drugs and photoactivated chemotherapy **8**:265–272
neurotransmitters **8**:262–265
unconventional cytotoxic cores, prodrugs with **2**:772–774
unconventional platinum(II) complexes **2**:747–757
unit cell volume **9**:393
unstable phosphorus species **10**:337–338
unusual solvent complexes of the Ga-, Cu- and Ag-salts **1**:420–421
upconversion (UC)
materials **4**:284–286
familiar upconversion systems **4**:285–286
mechanisms of **4**:284–285
for temperature sensing **4**:290–291
microscopy **8**:504–505
UPS. *See* ultraviolet photoelectron spectroscopy (UPS)
uracil **2**:667–671
uranium **8**:791–799
uranium(IV) **8**:797–799
uranyl(*V*) **8**:796–797
uranyl(*VI*) **8**:792–796
UV NLO material. *See* ultraviolet nonlinear optical materials (UV NLO material)
UV-vis-NIR. *See* ultraviolet-visible-near infrared (UV-vis-NIR)

V

^{51}V NMR
application of **9**:52–55
practical considerations for **9**:38–41
^{51}V solid state NMR **9**:38–40
^{51}V solid state NMR measurements **9**:36–38
V-dependent nitrogenase **2**:306–307
V_2O_5 **4**:354–355
valence
band dispersion of metal oxides **4**:610–612
and conduction band dispersion of carbon nitrides **4**:622–623
metal nitrides **4**:621–622
fluctuation **3**:475–479
Van der Waals complexes **1**:517
van der Waals compounds, alloys of **4**:487
Van Vleck paramagnets **9**:198
vanadates **4**:645–646
vanadium (V) **2**:341
centers in inorganic and bioinorganic complexes **9**:35–38
complexes **9**:669–673
V oxides **4**:685–686
vanadium-based fluorophosphates **7**:257–259
vanadium(V) oxo complexes **8**:133
variable offset cumulative spectrum acquisition **9**:149
variable-temperature NMR from chemical exchanges and reactions (VT NMR from chemical exchanges and reactions) **9**:718–719
vertical heterostructures
via mechanical exfoliation **4**:456
via thin film growth **4**:457–459
vibrational spectroscopy **1**:727, **4**:534–542, **6**:126–129
of zeolite hydroxyls **6**:274–277
vinylidene analogues **1**:141–143
violins **9**:824
viscosity probes **8**:221–223
voltage
fade **7**:13, **7**:33–36
hysteresis **7**:13, **7**:36–38
volume editor **2**:1–2, **8**:1
volumetric capacity **4**:313–314
VS_4 (linear chain compound) **4**:354

W

water
channel **2**:359
delivery channels **8**:326–330
energetics of water oxidation reaction **2**:351–352
quantum efficiency **2**:352
redox potential **2**:351
hydrogen/deuterium second order difference in **10**:414–415
oxidation catalysis
crystallographic structures **8**:320–321
first coordination sphere **8**:345–346
high-valent Mn(VII)-dioxo mechanism **8**:335–336
Kok cycle, oxidation state schemes and structural flexibility **8**:321–325
mechanisms of S-state transitions and O–O bond formation **8**:330–336
role of metal **8**:344–345
second coordination sphere **8**:346
structural flexibility **8**:324–325
oxidation mechanisms **8**:341–343
oxygen isotope first order difference in **10**:414
partial structure factors of **10**:414–415
purification **5**:167–170
layered metal sulfides **5**:169–170
three-dimensional metal sulfides **5**:168–169
WCAs. *See* weakly coordinating anions (WCAs)
weak ligands
complexation of **1**:407–421

weak ligands (*continued*)
complexed free elemental clusters **1**:412–415
complexed mixed group 15/16 cages **1**:415–416
complexed mixed-transition metal-element clusters **1**:416–419
complexed olefins and acetylenes **1**:408–410
homoleptic TMCCs **1**:410
TMCs as complex ligands **1**:411
transition metal carbonyl cations as starting materials **1**:411–412
transition metal cations with gaseous ligands **1**:411
transition-metal complexes **1**:419–420
unusual solvent complexes of the Ga-, Cu- and Ag-salts **1**:420–421
weakly coordinating anions (WCAs) **1**:12–13, **1**:379–380
fluorinated alkoxyaluminates as WCAs **1**:380–383
wearable electrochemical biosensors **7**:476
wet-chemical syntheses **10**:248–272
wet-chemical synthesis studies, development of experimental setups for **10**:249–252
WhiB-family of transcription factors regulators **2**:147–148
wood **9**:822–824
artifacts **9**:822–823
wulff construction, surface energy anisotropy and **3**:77–78

X

X-ray Absorption Fine Structure (XAFS) **10**:2, **10**:109
data acquisition **10**:112–114
and electrochemistry **10**:134–138
X-ray absorption near edge structure (XANES) **10**:110–111
X-ray absorption spectroscopy (XAS) **10**:344–345, **4**:531–532, **6**:122–126
history of X-ray transient absorption spectroscopy **10**:347–348
experiments at synchrotrons **10**:348–361
recent studies and experiments **10**:348–361
machine learning methods for extracting structural information for **6**:215–218
transient X-ray emission spectroscopy or pump-probe XES **10**:367–372
transient X-ray spectroscopy of metalloporphyrin chemistry at XFEL **10**:372–375
TRXAS experiments at X-ray free electron lasers **10**:361–367
x-ray transient absorption experimental setups **10**:345–347
acquisition of X-ray transient absorption data **10**:346–347
sampling methods **10**:346
X-ray free-electron laser (XFEL) **10**:276
prospects **10**:283
X-ray photoelectron spectroscopy (XPS) **4**:532–533
X-ray transient absorption spectroscopy (XAS) **8**:681–684
X-rays **10**:1–2
computed tomography **2**:408–412
combined imaging and therapy-image-guided therapy **2**:411
multimodal imaging **2**:410–411
targeted imaging **2**:409–410
contrast agents **1**:1040–1041
crystal design for in situ observation of unstable species by **10**:314–315
crystallography **2**:7–9
N-nitroso-*N*-hydroxylamine **2**:10–11
at X-ray free electron lasers **2**:368–369
diffraction **10**:400–411
analysis of X-ray diffraction data **10**:406–411
methods for high-pressure solid-state synthesis **10**:200–221
research possibilities with X-ray diffraction methods **10**:276
tomography **5**:356–358
unstable sulfur species observed by **10**:329–335
form factors **10**:404
induced excited spin state trapping **10**:99
inorganic photochemistry using ultrafast pulses of **8**:664–670
and neutron scattering **4**:527–531
scattering techniques **4**:531
snapshots of S_2 conversion in interactive pore **10**:336–337
sources with intense short pulses **8**:684–685
spectroscopy **2**:365–368
techniques **7**:441–444
X-site anion **3**:14
XAFS. *See* X-ray Absorption Fine Structure (XAFS)
xanes **4**:463–464
XANES. *See* X-ray absorption near edge structure (XANES)
XAS. *See* X-ray absorption spectroscopy (XAS). *See* X-ray transient absorption spectroscopy (XAS)
xenes **4**:463–464
xenon compounds **1**:519–521
xenon difluoride (XeF_2)
room-temperature non-irradiative synthesis of **1**:441
synthesis and reactivity of **1**:441–442
XeF_2/fluoride-ion acceptors as versatile one-electron oxidants **1**:442
xenon fluorides **1**:467–471
xenon hexafluoride hexafluoroxenon (XeF_6)
and coordination complexes of XeF_6 **1**:471–478
vibrational study of XeF_6 and $XeOF_4$ **1**:477–478
xenon hydrides **1**:509–513
xenon oxide fluorides **1**:466–467
xenon tetroxide (XeO_4)
photolysis of **1**:507–509
xenon trioxide (XeO_3)
chemistry of **1**:498–504
solid-state structures of **1**:498
stable chloro-and bromoxenate cage anions **1**:503–504
stable crown ether complex with noble-gas compound **1**:502–503
xenon trioxide adducts of N-and O-donor ligands **1**:498–502
xenon(II) compounds **1**:443–466
main-group ligand compounds of **1**:443–444
xenon(II)cations **1**:461–466
xenon(IV) compounds **1**:466–471
xenon(VI) compounds **1**:471–504
xenon(VIII) compounds **1**:504–509
infrared spectra of XeO_4 and $Na_4[XeO_6]$ in Ne and Ar matrices **1**:506
XFEL. *See* X-ray free-electron laser (XFEL)
XPS. *See* X-ray photoelectron spectroscopy (XPS)

Y

Y-clamp **2**:645
Y(Al, M)O_3 pigments **4**:585–586
Y(In, Cu/Ti)O_3 green **4**:583
Y(In, Fe)O_3 orange **4**:583
Y(In, Mn/Ti/Zn/Al)O_3 purple **4**:580–582
Y(In, Mn)O_3 blue **4**:578–579, **4**:587–589
$Yb_{14}MgSb_{11}$ **4**:67–68
yellow emissive iridium(III) complexes **8**:16–21
ytterbium **9**:200
yttrium **9**:189–192
complexes **9**:664–665
molecular and covalent crystalline oxides and glasses **9**:189–191
organometallic complexes to intermetallic compounds **9**:191–192
yttrium(III) oxide/yttria (Y_2O_3) **9**:417–419

Z

Z^{2-x} contrast **10**:68
Zeeman interaction **9**:588
zeolites **10**:28, **3**:342–343, **3**:363, **5**:44–49, **6**:18–19, **9**:44–46, **9**:420, **9**:505–507, **9**:562–563
See also nanozeolites
active site cooperation and multifunctionality in confined space **6**:132–135
advanced characterization techniques for zeolite encapsulated metal species **6**:120–131
C1 molecules conversion **6**:131–132
catalytic applications **6**:131–136
complexes of metal ions in zeolites with extraframework oxygen atoms **6**:156–161
components of synthesis mixture **6**:21–22

computational assessment of active site mobility in **6**:183–193
computational modeling **6**:136–141
confined space for selectivity control **6**:135–136
encapsulation of nanoclusters in **6**:113–117
experimental and theoretical evidence for active site mobility in **6**:167–183
flexibility of zeolite lattice **6**:281–282
interzeolite conversion **6**:23
isolated single metal atom sites in **6**:117–120
locating guest species in **9**:125–126
micro-kinetic modeling and dynamics **6**:139–141
modification **6**:317–318
nanosheets **6**:28
NMR crystallography of **9**:123–125
nucleation and crystal growth **6**:22–23
oxidation reactions catalyzed by **6**:7–8
properties of **6**:19–20
proton bond as function of zeolite lattice Al/Si concentration ratio **6**:277–279
proton mobility in **6**:186–187
proton strength of zeolite Brønsted acid **6**:274–290
reactivity scaling relationship and beyond **6**:136–139
Rh in zeolite Y and consequences for ethene hydrogenation & oligomerization **6**:181
solid-state ^{29}Si NMR of **9**:116–126
structure **9**:44–45
structure of **6**:19
structure prediction by operando thermodynamic analysis **6**:136
synthesis **6**:20–29, **6**:113–120
by assembly of pre-formed layers **6**:24
transition metal ions in **6**:149–150
two dimensional ^{29}Si NMR of **9**:122–123
vibrational spectroscopy of zeolite hydroxyls **6**:274–277
zeolite-based catalysts **6**:316–317, **6**:323
zeolitic imidazolate frameworks **5**:299–300
zeotypes **5**:49–52
zero-field splitting (ZFS) **9**:211
FCS in absence of **9**:213–214
FCS in presence of **9**:214
ZFS. *See* zero-field splitting (ZFS)
ZGP. *See* zinc germanium phosphide $ZnGeP_2$ (ZGP)
zinc **4**:186–188
alcohol dehydrogenases **2**:253–254
atomic disorder in zinc antimonides **4**:70
binding properties to amyloid precursor protein and biological implications **2**:593
binding properties to amyloid-β peptide and biological implications **2**:598
binding to prion protein and its biological implications **2**:586–587
chemical properties of **2**:236–237
complexes **9**:710–711
distribution and ubiquity of zinc proteins in proteomes **2**:234–235
enzymes
cell biology of zinc **2**:234–236
chemistry of **2**:236–241
zinc essential transition metal ion for life **2**:233–234
zinc-dependent enzymes **2**:241–258
homeostasis **2**:235–236
pK_a of zinc-bound water molecules **2**:239–241
reactivity
second-shell ligands in **2**:238–239
transferases **2**:254–255
zinc hydrolases **2**:244–251
zinc ion batteries, application in battery electrolytes for **1**:431–432
zinc isomerases **2**:256
zinc ligands and role in modulating activity of catalytic zinc centers **2**:237–238
zinc ligases **2**:256–258
zinc lyases **2**:241–244
zinc-binding properties of tau protein, aggregation, and toxicity **2**:601–602
zinc-dependent oxidoreductases **2**:253–254
Zn-independent paralogs **2**:41–44
FolE/FolE2 **2**:41–43
HemB/HemB2 **2**:43–44
zinc germanium phosphide $ZnGeP_2$ (ZGP) **4**:7–8
zinc oxide (ZnO) **9**:411–412
ZinT periplasmic SBPs **2**:566–568
zintl
anions functionalized with organic groups **1**:906–908
coordination compounds of substituted **1**:915–918
group 14 Zintl anions functionalized with main group elements or organic groups **1**:906–907
group 15 Zintl anions functionalized with organic groups **1**:907–908
chemistry
definitions **1**:904
development of **1**:903–904
electronic structure and bonding **1**:926–927
new members of main group zintl polyanions **1**:904–906
potential applications of Zintl ions/clusters in materials science and catalysis **1**:927–929
formation of zintl clusters in solution **1**:924–926
new members of main group zintl polyanions **1**:904–906
phases **3**:189–191
potential applications of zintl ions/clusters in materials science and catalysis **1**:927–929
zintl-phases **4**:180–182
Zintl-Klemm concept (ZKC) **3**:52
amphoteric germanium **3**:61–65
amphoteric silicon **3**:60–61
branched silicates **3**:59
closed packed arrays **3**:65–70
extended ZKC **3**:55–60
EZKC in close-packed solids **3**:67–70
four connected networks **3**:55–57
structure and bonding in Zintl phases **3**:52–55
three-connected networks **3**:57
two-connected networks **3**:57–59
zirconium complexes **9**:668–669
zirconium dioxide/zirconia (ZrO_2) **9**:413
zirconium(IV) complex **8**:72–73
zirconium(IV) pincer complexes **8**:117–120
ZKC. *See* Zintl-Klemm concept (ZKC)
ZnuA periplasmic SBPs **2**:566–568
zonal-axis 2D electron diffraction acquisition, techniques of **10**:56–57

AUTHOR INDEX

A

Abakumov, Artem M.
Electrode materials viewed with transmission electron microscopy
Introduction: Inorganic electrochemistry

Abul-Futouh, Hassan
[FeFe]-Hydrogenase mimics containing heavy p block elements

Acharyya, Paribesh
Metal chalcogenide materials: Synthesis, structure and properties

Adeyemi, Adedoyin N.
Hydride precursors in materials synthesis

Agote-Arán, Miren
EXAFS studies of inorganic catalytic materials

Aiba, Yuichiro
Heme-containing proteins: Structures, functions, and engineering

Aksyonov, Dmitry A.
Charge transfer through interfaces in metal-ion intercalation systems

Al-ani, Enas
Imaging

Aldrich-Wright, J.R.
Metal complexes as chemotherapeutic agents

Alkan, Fahri
Advances in the computation of nmr parameters for inorganic nuclides

Allen, Lisa
EXAFS studies of inorganic catalytic materials

Allen, Matthew J.
Imaging

Amoureux, Jean-Paul
Advances in the characterization of inorganic solids using NMR correlation experiments

Andreoni, Leonardo
Photochemically driven molecular machines based on coordination compounds

Antipov, Evgeny V.
Introduction: Inorganic electrochemistry
Mineral inspired electrode materials for metal-ion batteries

Arcos-López, Trinidad
The role of *d*-block metal ions in neurodegenerative diseases

Ariyasu, Shinya
Heme-containing proteins: Structures, functions, and engineering

Atta, Mohamed
[FeFe]-hydrogenases: Structure, mechanism, and metallocluster biosynthesis

Au, Vonika Ka-Man
Luminescent supramolecular assemblies

Augustyn, Veronica
Nanostructured materials for electrochemical capacitors

Azuma, Masaki
High pressure studies of transition metal oxides

B

Bahr, Guillermo
The biochemistry and enzymology of zinc enzymes

Baird, Sterling G.
Data-driven materials discovery and synthesis using machine learning methods

Balakrishnarajan, Musiri M.
Bonding in boron rich borides

Bandarenka, Aliaksandr S.
Structure-reactivity relations in electrocatalysis

Bao, Xinhe
Inorganic catalysis for methane conversion to chemicals

Baroncini, Massimo
Photochemically driven molecular machines based on coordination compounds

Barpanda, Prabeer
Development of polyanionic sodium-ion battery insertion materials

Barthélemy, Antoine
Chemistry with weakly coordinating aluminates $[Al(OR^F)_4]^-$ and borates $[B(OR^F)_4]^-$: From fundamentals to application

Bartlett, Stuart A.
X-ray transient absorption spectroscopies in the study of excited state structures

Beale, Andrew M.
EXAFS studies of inorganic catalytic materials

Belik, Alexei A.
High pressure studies of transition metal oxides

Benmore, Chris J.
X-ray and neutron diffraction from glasses and liquids

Bennett, Thomas Douglas
Amorphization of hybrid framework materials

Berger, Robert F.
Electronic structure of oxide and halide perovskites

Bernard, Guy M.
Solid-state nmr studies of halide perovskite materials with photoconversion potential

Bernhard, Stefan
Redox photocatalysis

Bezuglov, Iliya A.
Computational design of materials for metal-ion batteries

Bezuidenhout, Daniela I.
Nonclassical carbenes as noninnocent ligands

Bhaskar, Gourab
Hydride precursors in materials synthesis

Billinge, Simon J.L.
Local structure determination using total scattering data

Birchall, Lee T.
Synchrotron diffraction studies on spin crossover materials

Birkel, Christina S.
Max phases and mxenes

Biros, Elizabeth S.
Imaging

Biswas, Kanishka
Metal chalcogenide materials: Synthesis, structure and properties

Blatov, Vladislav A.
Computational design of materials for metal-ion batteries

Bocus, Massimo
Dynamic evolution of catalytic active sites within zeolite catalysis

Bolia, R.
Conventional and less conventional solution-based synthesis of battery materials: Cathodes, anodes and electrolytes

Bols, Max L.
Single site spectroscopy of transition metal ions and reactive oxygen complexes in zeolites

Bortolus, Mark R.
Noble-gas chemistry

Bresien, Jonas
Biradicals in main group chemistry: Synthesis, electronic structure, and application in small-molecule activation

Brgoch, Jakoah
Luminescence in the solid state

Brouwer, Darren H.
Applications of silicon-29 NMR spectroscopy

Brown, C.M.
Neutron scattering studies of materials for hydrogen storage

Bryce, David L.
Introduction: NMR of inorganic nuclei

Bu, Xianhui
Crystalline inorganic materials from supertetrahedral chalcogenide clusters

C

Campagna, Sebastiano
Multicomponent supramolecular photochemistry

Cancelliere, Ambra M.
Multicomponent supramolecular photochemistry

Capdevila, Daiana A.
Metal ion homeostasis: Metalloenzyme paralogs in the bacterial adaptative response to zinc restriction

Carden, Jamie L.
Frustrated lewis pairs in catalysis

Carepo, Marta S.P.
Iron-sulfur clusters — functions of an ancient metal site

Carnevale, Diego
Nitrogen-14 NMR spectroscopy

Casini, Angela
Supramolecular metal-based molecules and materials for biomedical applications

Catalano, Jaclyn
Applications of NMR spectroscopy in cultural heritage science

Centeno, Silvia A.
Applications of NMR spectroscopy in cultural heritage science

Cha, Wonsuk
Coherent x-ray diffraction studies of inorganic crystalline nanomaterials

Chagnot, Matthew
Nanostructured materials for electrochemical capacitors

Chan, Michael Ho-Yeung
Luminescent supramolecular assemblies

Chao, Hui
Phosphorescent metal complexes for biomedical applications

Charbonnière, Loïc J.
Lanthanides as luminescence imaging reagents

Che, Chi-Ming
Anti-cancer gold compounds

Chen, Yu
Phosphorescent metal complexes for biomedical applications

Chen, Lin X.
Structural characterization of excited state transition metal complexes by x-ray transient absorption spectroscopies

Chen, Jiaye
Lanthanide-doped upconversion nanomaterials

Chen, Kuizhi
NMR of catalytic sites

Chestnut, Jessica
Photoelectrochemical materials for solar energy conversion

Chivers, Tristram
Polychalcogen molecules, ligands, and ions Part 2: Catenated acyclic molecules, ions, and p-block element derivatives

Choi, Sungwook
Coherent x-ray diffraction studies of inorganic crystalline nanomaterials

Clark, Judith K.
Magnetic materials

Cnudde, Pieter
Dynamic evolution of catalytic active sites within zeolite catalysis

Codd, Rachel
Siderophores and iron transport

Coles, Martyn P.
Chain, ring, and cluster compounds of group 15 elements (P, As, Sb, Bi)

Cong, Peixi
EXAFS studies of inorganic catalytic materials

Constable, Edwin C.
Main group metal coordination chemistry

Conway, Lewis J.
First principles crystal structure prediction

Cook, Tabitha M.
Solution NMR of transition metal complexes

Cooper, Susan R.
Total scattering and pair distribution function analysis for studies of nanomaterials

Copéret, Christophe
Surface organometallic and coordination chemistry approach to formation of single site heterogeneous catalysts

Corbin, Brooke A.
Imaging

Cox, Tori
Hydride precursors in materials synthesis

Credi, Alberto
Photochemically driven molecular machines based on coordination compounds

Cussen, Serena A.
Introduction: Inorganic materials chemistry

D

Dabringhaus, Philipp
Chemistry with weakly coordinating aluminates $[Al(OR^F)_4]^-$ and borates $[B(OR^F)_4]^-$: From fundamentals to application

Dar, Sohail H.
Bonding in boron rich borides

Datye, Abhaya K.
Imaging of single atom catalysts

Dehnen, Stefanie
Non-oxide p-block (semi-)metal chalcogenide cage compounds

Delevoye, Laurent
Advances in the characterization of inorganic solids using NMR correlation experiments

Del Rosario, Cathlene
Metallophilic interactions

Deng, Zhiqin
Platinum anticancer drugs: Targeting and delivery

Deo, K.M.
Metal complexes as chemotherapeutic agents

De Sloovere, D.
Conventional and less conventional solution-based synthesis of battery materials: Cathodes, anodes and electrolytes

Ding, Ran
Nanostructured materials for electrochemical capacitors

Dissanayaka Mudiyanselage, Ranuri S.
Critical charge transfer pairs in intermetallic superconductors

Di Tullio, Valeria
Applications of NMR spectroscopy in cultural heritage science

Doerrer, Linda H.
Metallophilic interactions

Domen, Kazunari
Doped semiconductor photocatalysts

Dominko, Robert
Lithium sulfur batteries: Electrochemistry and mechanistic research

Dorn, Matthias
d-d and charge transfer photochemistry of 3d metal complexes

Dronskowski, Richard
Chemical bonding with plane waves

Drozhzhin, Oleg A.
Mineral inspired electrode materials for metal-ion batteries

Drvaric Talian, Sara
Lithium sulfur batteries: Electrochemistry and mechanistic research

Dujovne, Matias Villarruel
Metal ion homeostasis: Metalloenzyme paralogs in the bacterial adaptative response to zinc restriction

Duong, Nghia Tuan
Advances in the characterization of inorganic solids using NMR correlation experiments

Dutta, Prabir
Metal chalcogenide materials: Synthesis, structure and properties

Dybowski, Cecil
Advances in the computation of nmr parameters for inorganic nuclides
Applications of NMR spectroscopy in cultural heritage science

E

East, Nathan Roy
d-d and charge transfer photochemistry of 3d metal complexes

Eckert, Hellmut
Solid state nmr of the rare earth nuclei: Applications in solid-state inorganic chemistry

Edén, Mattias
Solid-state nmr of glasses

Ehrenberg, Helmut
In situ/in operando diffraction studies of electrode materials in battery applications

Eickhoff, Liesa
Biradicals in main group chemistry: Synthesis, electronic structure, and application in small-molecule activation

Einsle, Oliver
Biological and synthetic nitrogen fixation

Ellis, David
NMR of carboranes

Enders, Markus
Solution NMR spectroscopy of single-molecule magnets

Eng, Julien
Recent progress and application of computational chemistry to understand inorganic photochemistry

Engesser, Tobias A.
Biological and synthetic nitrogen fixation

Entwistle, Jake
Materials synthesis for Na-ion batteries

Erdélyi, Mate
Halogen-bonded halogen(I) ion complexes

Ertural, Christina
Chemical bonding with plane waves

Evans, H.A.
Neutron scattering studies of materials for hydrogen storage

F

Fan, Alice
Metallophilic interactions

Fang, Guangzong
Inorganic catalysis for methane conversion to chemicals

Fazliji, Besim
Metal ion interactions with nucleic acids

Fdez Sanz, Javier
In silico modeling of inorganic thermoelectric materials

Fedotov, Stanislav S.
Electrode materials for reversible sodium ions de/intercalation

Feng, Pingyun
Crystalline inorganic materials from supertetrahedral chalcogenide clusters

Fernández-Terán, Fernandez-Teran Ricardo J.
Ultrafast dynamics of photoinduced processes in coordination compounds

Ferreira Rodrigues, Carla
Metal ion interactions with nucleic acids

Fichtner, Maximilian
Development of polyanionic sodium-ion battery insertion materials

Filot, Ivo A.W.
Promoted Fischer-Tropsch catalysts

Fischer, Roland A.
Supramolecular metal-based molecules and materials for biomedical applications

Fontecave, Marc
[FeFe]-hydrogenases: Structure, mechanism, and metallocluster biosynthesis

Ford, Peter C.
Photoactivated metal complexes for drug delivery

Förster, Christoph
d-d and charge transfer photochemistry of 3d metal complexes

Francés-Soriano, Laura
Lanthanides as luminescence imaging reagents

Frandsen, Benjamin A.
Local structure determination using total scattering data

Freakley, Simon J.
Selective oxidation by mixed metal nanoparticles

Fredrickson, Daniel C.
Introduction: Theory and bonding of inorganic non-molecular systems

Fukuda, Masayuki
High pressure studies of transition metal oxides

Furukawa, Yuji
Nmr of magnetic materials: Determination of magnetic structures by "on-site" nmr measurements

G

Gao, Shenghan
Mixed anion materials

Gao, Dunfeng
Inorganic catalysis for methane conversion to chemicals

Garakani, Mohammad Akbari
Solid-state electrolytes for lithium-ion batteries

Garbacz, Piotr
Gas-phase NMR of nuclei other than ^{1}H and ^{13}C

Garcia, John V.
Photoactivated metal complexes for drug delivery

Garlyyev, Batyr
Structure-reactivity relations in electrocatalysis

Gast, Michael
Chain, ring, and cluster compounds of heavy group 13 elements (Al, Ga, In, Tl)

Gaudry, Émilie
An introduction to the theory of inorganic solid surfaces

Gaultois, Michael W.
Spark plasma sintering routes to consolidated inorganic functional materials

Giedroc, David P.
Metal ion homeostasis: Metalloenzyme paralogs in the bacterial adaptative response to zinc restriction

Goldberger, J.E.
The zoology of two-dimensional van der waals materials

Grazina, Raquel
Iron-sulfur clusters — functions of an ancient metal site

Griffin, John M.
Solid-state NMR of energy storage materials

Griffith, Kent J.
Solid-state NMR of energy storage materials

Grin, Yuri
Chemical bonding analysis in position space

Grundy, Josef V.
Transition metal nmr thermometry

Guan, Ruilin
Phosphorescent metal complexes for biomedical applications

Gubanova, Elena
Structure-reactivity relations in electrocatalysis

Gumienna-Kontecka, Elzbieta
Metallophores: How do human pathogens withdraw metal ions from the colonized host

Guo, Zijian
Introduction: Bioinorganic chemistry and homogeneous biomimetic inorganic catalysis

Guo, Yu
Water oxidation catalysis in natural and artificial photosynthesis

Gupta, Rupal
Applications of ^{17}O and ^{51}V NMR in inorganic and bioinorganic chemistry

Guzman, Camilo
Photoactivated metal complexes for drug delivery

Gvozdetskyi, Volodymyr
Hydride precursors in materials synthesis

H

Halasyamani, P. Shiv
Introduction: Solid state inorganic chemistry

Hamm, Christin M.
Max phases and mxenes

Hardy, A.
Conventional and less conventional solution-based synthesis of battery materials: Cathodes, anodes and electrolytes

Hariyani, Shruti
Luminescence in the solid state

Harris, Kristopher J.
NMR studies of 2D and pseudo-2D systems

Häussermann, Ulrich
High pressure chemistry

Hayashi, Takashi
Engineering of hemoproteins

Hebenbrock, Marian
Metal-mediated base pairs in nucleic acid duplexes

Hecel, Aleksandra
Metallophores: How do human pathogens withdraw metal ions from the colonized host

Heinze, Katja
d-d and charge transfer photochemistry of 3d metal complexes

Hensen, Emiel J.M.
Heterogeneous catalysts for the non-oxidative conversion of methane to aromatics and olefins
Introduction: A short history of single site catalysis
Metal-support interfaces in ceria-based catalysts

Hermann, Andreas
First principles crystal structure prediction

Heyer, Alexander J.
Single site spectroscopy of transition metal ions and reactive oxygen complexes in zeolites

Hildebrandt, Niko
Lanthanides as luminescence imaging reagents

Hilleke, Katerina P.
Crystal chemistry at high pressure

Hisatomi, Takashi
Doped semiconductor photocatalysts

Holmes, Sean T.
Advances in the computation of nmr parameters for inorganic nuclides

Hong, Sangki
Hydride precursors in materials synthesis

Hosaka, Tomooki
Electrode materials for K-ion batteries

Hou, Guangjin
NMR of catalytic sites

Housecroft, Catherine E.
Main group metal coordination chemistry

Hu, Di
Anti-cancer gold compounds

Huang, Zhehao
Structural studies of inorganic materials by electron crystallography

Huang, Chunmei
Inorganic nonlinear optical materials

Huang, Yining
A review of exotic quadrupolar metal nmr in mofs

I

Ingo, Krossing
Chemistry with weakly coordinating aluminates $[Al(OR^F)_4]^-$ and borates $[B(OR^F)_4]^-$: From fundamentals to application

Inozemtseva, Alina
Chemistry of Li-air batteries

Isaev, Valerii
Chemistry of Li-air batteries

Ishitani, Osamu
Photochemical CO_2 reduction

Itkis, Daniil
Chemistry of Li-air batteries

Iton, Zachery W.B.
Battery materials

J

Jacob, Eike
Chemistry with weakly coordinating aluminates $[Al(OR^F)_4]^-$ and borates $[B(OR^F)_4]^-$: From fundamentals to application

Janka, Oliver
Intermetallic materials

Jardón-Álvarez, Daniel
Dynamic nuclear polarization in inorganic solids from paramagnetic metal ion dopants

Jarzembska, Katarzyna Natalia
Time resolved structural studies in molecular materials

Jensen, Kirsten M.Ø.
In situ scattering studies of material formation during wet-chemical syntheses
Total scattering and pair distribution function analysis for studies of nanomaterials

Jiang, Guibin
Metallomics and metalloproteomics

Jin, Biao
Biomineralization

Joos, B.
Conventional and less conventional solution-based synthesis of battery materials: Cathodes, anodes and electrolytes

Jordan, Matthew R.
Metal ion homeostasis: Metalloenzyme paralogs in the bacterial adaptative response to zinc restriction

Juelsholt, Mikkel
In situ scattering studies of material formation during wet-chemical syntheses

K

Kabanov, Artem A.
Computational design of materials for metal-ion batteries

Kaduk, James A.
Ab initio structure solution using synchrotron powder diffraction

Kagalwala, Husain N.
Redox photocatalysis

Kageyama, Hiroshi
Mixed anion materials

Kaminski, Radosław
Time resolved structural studies in molecular materials

Kammampata, Sanoop Palakkathodi
Solid-state electrolytes for lithium-ion batteries

Kanatzidis, Mercouri G.
Panoramic (in beam) studies of materials synthesis

Karhu, Aino J.
Nonclassical carbenes as noninnocent ligands

Karmakar, Abhoy
Solid-state nmr studies of halide perovskite materials with photoconversion potential

Karns, John P.
Imaging

Karunadasa, Hemamala I.
A practical guide to Three-dimensional halide perovskites: Structure, synthesis, and measurement

Karyakin, Arkady A.
Transition metal hexacyanoferrates as catalysts for (bio)sensors

Kato, Shunsuke
Engineering of hemoproteins

Kato, Daichi
Mixed anion materials

Kaur, Navjot
NMR of nanoparticles

Kawano, Masaki
Direct observation of transient species and chemical reactions in a pore observed by synchrotron radiation

Kelchtermans, A.S.
Conventional and less conventional solution-based synthesis of battery materials: Cathodes, anodes and electrolytes

Kelly, Paul F.
Polychalcogen molecules, ligands, and ions Part 1: Homo- and heteronuclear chalcogen rings
Polychalcogen molecules, ligands, and ions Part 2: Catenated acyclic molecules, ions, and p-block element derivatives

Kern, Jan
Photosynthesis

Khasanova, Nellie R.
Mineral inspired electrode materials for metal-ion batteries

Kim, Hyunjung
Coherent x-ray diffraction studies of inorganic crystalline nanomaterials

Kim, Seong Shik
Battery materials

King, Roberto S.P.
Polychalcogen molecules, ligands, and ions Part 1: Homo- and heteronuclear chalcogen rings
Polychalcogen molecules, ligands, and ions Part 2: Catenated acyclic molecules, ions, and p-block element derivatives

Kitahara, Koichi
Chemical bonding analyses using wannier functions

Kitzmann, Winald Robert
d-d and charge transfer photochemistry of 3d metal complexes

Klein, R.A.
Neutron scattering studies of materials for hydrogen storage

Kleinhans, George
Nonclassical carbenes as noninnocent ligands

Klimczuk, Tomasz
Critical charge transfer pairs in intermetallic superconductors

Kloo, Lars
Catenated compounds in group 17—polyhalides

Koger, Hendrik
Chemistry with weakly coordinating aluminates $[Al(OR^F)_4]^-$ and borates $[B(OR^F)_4]^-$: From fundamentals to application

Kolb, Simon
Chalcogen bonding in supramolecular structures, anion recognition, and catalysis

Kolis, Joseph W.
High temperature hydrothermal synthesis of inorganic compounds

Komaba, Shinichi
Electrode materials for K-ion batteries

Komkova, Maria A.
Transition metal hexacyanoferrates as catalysts for (bio)sensors

Korzynski, Maciej Damian
Surface organometallic and coordination chemistry approach to formation of single site heterogeneous catalysts

Kosinov, Nikolay
Heterogeneous catalysts for the non-oxidative conversion of methane to aromatics and olefins
Metal-support interfaces in ceria-based catalysts

Kovnir, Kirill
Thermoelectric materials

Kozlowski, Henryk
Metallophores: How do human pathogens withdraw metal ions from the colonized host

Kräutler, Bernhard
Cobalt enzymes

Kravberg, Alexander
Water oxidation catalysis in natural and artificial photosynthesis

Kubota, Kei
Electrode materials for K-ion batteries

Kulkarni, Sheila
Photoactivated metal complexes for drug delivery

Kurtoglu-Öztulum, Samira Fatma
Challenges with atomically dispersed supported metal catalysts: Controlling performance, improving stability, and enhancing metal loading

L

Lafon, Olivier
Advances in the characterization of inorganic solids using NMR correlation experiments

La Ganga, Giuseppina
Multicomponent supramolecular photochemistry

Laitinen, Risto S.
Introduction: Significance of molecular inorganic chemistry
Polychalcogen molecules, ligands, and ions Part 1: Homo- and heteronuclear chalcogen rings
Polychalcogen molecules, ligands, and ions Part 2: Catenated acyclic molecules, ions, and p-block element derivatives
Syntheses and molecular structures of cyclic selenoethers and their derivatives

Laurencin, Danielle
The expanding frontier between mechanochemistry & solid state NMR: Special focus on inorganic components of materials

Lazzaro, Giuliana
Multicomponent supramolecular photochemistry

Lee, Vladimir
Low-coordinate compounds of heavier group 14−16 elements

Lee, Yoo Seok
Fundamentals and applications of enzymatic bioelectrocatalysis

Lee, Lawrence Cho-Cheung
Luminescence chemosensors, biological probes, and imaging reagents

Leroy, César
The expanding frontier between mechanochemistry & solid state NMR: Special focus on inorganic components of materials

Leskes, Michal
Dynamic nuclear polarization in inorganic solids from paramagnetic metal ion dopants

Li, Hongyan
Metallomics and metalloproteomics

Li, Jun
Solid state inorganic color pigments: Ancient to modern

Li, Guanna
Metal containing nanoclusters in zeolites

Li, Biao
Status of Li(Na)-based anionic redox materials for better batteries

Liang, Liangliang
Lanthanide-doped upconversion nanomaterials

Lin, Xinlin
Phosphorescent metal complexes for biomedical applications

Lindquist, Kurt P.
A practical guide to Three-dimensional halide perovskites: Structure, synthesis, and measurement

Linti, Gerald
Chain, ring, and cluster compounds of heavy group 13 elements (Al, Ga, In, Tl)

Liu, Jiangping
Phosphorescent metal complexes for biomedical applications

Liu, Zenghui
Piezoelectric and ferroelectric materials: Fundamentals, recent progress, and applications

Liu, Marianne
Data-driven materials discovery and synthesis using machine learning methods

Liu, Xiaogang
Lanthanide-doped upconversion nanomaterials

Liu, Qiang
Non-sacrificial photocatalysis

Lo, Kenneth Kam-Wing
Luminescence chemosensors, biological probes, and imaging reagents

Lobato, Álvaro
The Zintl-Klemm concept and its broader extensions
The structures of inorganic crystals: A rational explanation from the chemical pressure approach and the anions in metallic matrices model

Lochab, Shubham
Development of polyanionic sodium-ion battery insertion materials

Lok, Chun-Nam
Anti-cancer gold compounds

López-Guerrero, Víctor E.
The role of *d*-block metal ions in neurodegenerative diseases

Lopez-Odriozola, Laura
Luminescence properties of the actinides and actinyls

Lucier, Bryan E.G.
A review of exotic quadrupolar metal nmr in mofs

Lutter, Jacob C.
Imaging

M

Maeda, H.
Photochromic materials

Maggard, Paul A.
Photoelectrochemical materials for solar energy conversion

Makulski, Włodzimierz
Gas-phase NMR of nuclei other than ^{1}H and ^{13}C

Marquez, Antonio
In silico modeling of inorganic thermoelectric materials

Marshall, Madalynn
Chemical bonding principles in magnetic topological quantum materials

Marzo, Tiziano
Protein targets for anticancer metal based drugs

McCabe, Emma E.
Designing new polar materials

McClain, Rebecca
Panoramic (in beam) studies of materials synthesis

McGeachie, Liam
Polychalcogen molecules, ligands, and ions Part 1: Homo- and heteronuclear chalcogen rings
Polychalcogen molecules, ligands, and ions Part 2: Catenated acyclic molecules, ions, and p-block element derivatives

McGrady, John E.
Zintl chemistry: From zintl ions to zintl clusters

McMillen, Colin D.
High temperature hydrothermal synthesis of inorganic compounds

McQueen, Tyrel M.
The chemistry of quantum materials

Mediavilla-Madrigal, Sofia
EXAFS studies of inorganic catalytic materials

Melen, Rebecca L.
Frustrated lewis pairs in catalysis

Mercier, Hélène P.A.
Noble-gas chemistry

Messori, Luigi
Protein targets for anticancer metal based drugs

Métro, Thomas-Xavier
The expanding frontier between mechanochemistry & solid state NMR: Special focus on inorganic components of materials

Michaelis, Vladimir K.
Solid-state nmr studies of halide perovskite materials with photoconversion potential

Minteer, Shelley D.
Fundamentals and applications of enzymatic bioelectrocatalysis

Moll, Johannes
d-d and charge transfer photochemistry of 3d metal complexes

Moreno-Alcántar, Guillermo
Supramolecular metal-based molecules and materials for biomedical applications

Morisako, Shogo
Low-coordinate compounds of heavier group 14−16 elements

Morkhova, Yelizaveta A.
Computational design of materials for metal-ion batteries

Morozov, Anatolii V.
Electrode materials viewed with transmission electron microscopy

Moura, José J.G.
Iron-sulfur clusters − functions of an ancient metal site

Moura, Isabel
Iron-sulfur clusters − functions of an ancient metal site

Mozharivskyj, Yurij
Preparation of magnetocaloric materials

Müller, Jens
Metal-mediated base pairs in nucleic acid duplexes

Müller, Peter C.
Chemical bonding with plane waves

Muravev, Valery
Metal-support interfaces in ceria-based catalysts

Mylavarapu, S.K.
Conventional and less conventional solution-based synthesis of battery materials: Cathodes, anodes and electrolytes

N

Nagahora, Noriyoshi
Low-coordinate compounds of heavier group 14−16 elements

Nastasi, Francesco
Multicomponent supramolecular photochemistry

Nath, Pinku
In silico modeling of inorganic thermoelectric materials

Natrajan, Louise S.
Luminescence properties of the actinides and actinyls

Neale, Samuel E.
Dynamic evolution of catalytic active sites within zeolite catalysis

Neilson, James R.
Metathesis routes to materials

Nelson, Ryky
Chemical bonding with plane waves

Nikitina, Victoria A.
Charge transfer through interfaces in metal-ion intercalation systems

Nishihara, H.
Photochromic materials

Nishikawa, M.
Photochromic materials

Niu, H.-C.
Supramolecular chemistry of p-block elements

O

Ohtsu, Hiroyoshi
Direct observation of transient species and chemical reactions in a pore observed by synchrotron radiation

Oilunkaniemi, Raija
Polychalcogen molecules, ligands, and ions Part 1: Homo- and heteronuclear chalcogen rings
Polychalcogen molecules, ligands, and ions Part 2: Catenated acyclic molecules, ions, and p-block element derivatives
Syntheses and molecular structures of cyclic selenoethers and their derivatives

Oliver, Gwyndaf A.
Chalcogen bonding in supramolecular structures, anion recognition, and catalysis

Onoda, Hiroki
Heme-containing proteins: Structures, functions, and engineering

Orlova, Elena D.
Electrode materials viewed with transmission electron microscopy

Oshchepkov, Alexandr G.
Benchmarking in electrocatalysis

Osman, Hussien H.
The structures of inorganic crystals: A rational explanation from the chemical pressure approach and the anions in metallic matrices model

O'Donnell, Shaun
Photoelectrochemical materials for solar energy conversion

Ozvat, Tyler M.
Transition metal nmr thermometry

P

Palcic, Ana
Synthesis and application of (nano) zeolites

Pan, Shilie
Inorganic nonlinear optical materials

Pan, Xiulian
Inorganic catalysis for methane conversion to chemicals

Pancharatna, Pattath D.
Bonding in boron rich borides

Paterson, Alexander L.
High field solid-state nmr of challenging nuclei in inorganic systems

Patheria, Eshaan S.
Battery materials

Pauleta, Sofia R.
Iron-sulfur clusters — functions of an ancient metal site

Paulus, A.
Conventional and less conventional solution-based synthesis of battery materials: Cathodes, anodes and electrolytes

Pauly, Magnus
Photoelectrochemical materials for solar energy conversion

Pecoraro, Vincent L.
Introduction: Bioinorganic chemistry and homogeneous biomimetic inorganic catalysis

Penfold, Thomas
Recent progress and application of computational chemistry to understand inorganic photochemistry

Perez-Cruz, Claudia
The role of *d*-block metal ions in neurodegenerative diseases

Perras, Frédéric A.
High field solid-state nmr of challenging nuclei in inorganic systems

Piasta, Karolina
Metallophores: How do human pathogens withdraw metal ions from the colonized host

Pickard, Chris J.
First principles crystal structure prediction

Pidko, Evgeny A.
Metal containing nanoclusters in zeolites

Pigliapochi, Roberta
Applications of NMR spectroscopy in cultural heritage science

Plata, José J.
In silico modeling of inorganic thermoelectric materials

Plessers, Dieter
Single site spectroscopy of transition metal ions and reactive oxygen complexes in zeolites

Porter, Stephen
Imaging of single atom catalysts

Posadas, Yanahi
The role of *d*-block metal ions in neurodegenerative diseases

Pourpoint, Frédérique
Advances in the characterization of inorganic solids using NMR correlation experiments

Price, Stephen W.T.
EXAFS studies of inorganic catalytic materials

Puntoriero, Fausto
Multicomponent supramolecular photochemistry

Q

Qian, Michelle D.
Battery materials

Qiao, Lei
Zintl chemistry: From zintl ions to zintl clusters

Quintanar, Liliana
The role of *d*-block metal ions in neurodegenerative diseases

R

Raithby, Paul R.
Introduction: X-ray, neutron and electron scattering methods in inorganic chemistry

Rakita, Yevgeny
Local structure determination using total scattering data

Rankin, Andrew G.M.
Advances in the characterization of inorganic solids using NMR correlation experiments

Rankine, Conor
Recent progress and application of computational chemistry to understand inorganic photochemistry

Recio, J. Manuel
The structures of inorganic crystals: A rational explanation from the chemical pressure approach and the anions in metallic matrices model

Reichenauer, Florian
d-d and charge transfer photochemistry of 3d metal complexes

Ren, Wei
Piezoelectric and ferroelectric materials: Fundamentals, recent progress, and applications

Reuter, Thomas
d-d and charge transfer photochemistry of 3d metal complexes

Rhoda, Hannah M.
Single site spectroscopy of transition metal ions and reactive oxygen complexes in zeolites

Rinn, Niklas
Non-oxide p-block (semi-)metal chalcogenide cage compounds

Rissanen, Kari
Halogen-bonded halogen(I) ion complexes

Rogers, Hannah
Selective oxidation by mixed metal nanoparticles

Röhner, David
Chemistry with weakly coordinating aluminates $[Al(OR^F)_4]^-$ and borates $[B(OR^F)_4]^-$: From fundamentals to application

Roslova, Maria
Structural studies of inorganic materials by electron crystallography

Rowinska-Zyrek, Magdalena
Metallophores: How do human pathogens withdraw metal ions from the colonized host

Rulev, Alexey
Chemistry of Li-air batteries

S

Sadler, Peter J.
Photoactive metallodrugs

Saeed, Saeed
Nanostructured materials for electrochemical capacitors

Saito, Masaichi
Aromatic compounds bearing heavy group 14 atoms in their molecular frameworks

Sakai, Shiro
Correlated electronic states in quasicrystals

Sakamoto, R.
Photochromic materials

Salvadó, Miguel Ángel
The structures of inorganic crystals: A rational explanation from the chemical pressure approach and the anions in metallic matrices model

Samarin, Aleksandr Sh.
Electrode materials for reversible sodium ions de/intercalation

Sánchez-López, Carolina
The role of *d*-block metal ions in neurodegenerative diseases

Sandhya Kumari, L.
Solid state inorganic color pigments: Ancient to modern

Sarkar, Arka
Thermoelectric materials

Sarkar, Debattam
Metal chalcogenide materials: Synthesis, structure and properties

Sasamori, Takahiro
Low-coordinate compounds of heavier group 14−16 elements

Sautet, Philippe
Nanocluster heterogeneous catalysts: Insights from theory

Savinova, Elena R.
Benchmarking in electrocatalysis

Sayeed, Hasan M.
Data-driven materials discovery and synthesis using machine learning methods

Sayler, Richard I.
The role of *d*-block metal ions in neurodegenerative diseases

Scheler, Ulrich
^{19}F NMR on polymers

Schmitt, Manuel
Chemistry with weakly coordinating aluminates $[Al(OR^F)_4]^-$ and borates $[B(OR^F)_4]^-$: From fundamentals to application

Schön, J. Christian
Energy landscapes in inorganic chemistry

Schoonheydt, Robert A.
Single site spectroscopy of transition metal ions and reactive oxygen complexes in zeolites

Schrobilgen, Gary J.
Noble-gas chemistry

Schulz, Axel
Biradicals in main group chemistry: Synthesis, electronic structure, and application in small-molecule activation

Schwarz, Ulrich
High pressure chemistry

See, Kimberly A.
Battery materials

Segovia, José
The role of *d*-block metal ions in neurodegenerative diseases

Sellin, Malte
Chemistry with weakly coordinating aluminates $[Al(OR^F)_4]^-$ and borates $[B(OR^F)_4]^-$: From fundamentals to application

Sels, Bert F.
Single site spectroscopy of transition metal ions and reactive oxygen complexes in zeolites

Senyshyn, Anatoliy
In situ/in operando diffraction studies of electrode materials in battery applications

Seshadri, Ram
Introduction: Inorganic materials chemistry

Shatruk, Michael
Magnetic materials

Shepherd, Helena J.
Synchrotron diffraction studies on spin crossover materials

Shi, Huayun
Photoactive metallodrugs

Shoji, Osami
Heme-containing proteins: Structures, functions, and engineering

Sigel, Roland K.O.
Metal ion interactions with nucleic acids

Silvi, Serena
Photochemically driven molecular machines based on coordination compounds

Simoska, Olja
Fundamentals and applications of enzymatic bioelectrocatalysis

Singh, Shashwat
Development of polyanionic sodium-ion battery insertion materials

Sivaev, Igor B.
Molecular boron clusters

Skjaervoe, Sandra H.
Local structure determination using total scattering data

Skjærvø, Susanne L.
In situ scattering studies of material formation during wet-chemical syntheses

Solomon, Edward I.
Single site spectroscopy of transition metal ions and reactive oxygen complexes in zeolites

Sparks, Taylor D.
Data-driven materials discovery and synthesis using machine learning methods

Spek, Anthony L.
An overview of platon/pluton crystal structure validation

Spektor, Kristina
High pressure chemistry

Stefkova, Katarina
Frustrated lewis pairs in catalysis

Stein, Laura
d-d and charge transfer photochemistry of 3d metal complexes

Stevenson, Keith J.
Introduction: Inorganic electrochemistry

Su, Alexander C.
A practical guide to Three-dimensional halide perovskites: Structure, synthesis, and measurement

Subramanian, M.A.
Solid state inorganic color pigments: Ancient to modern

Sun, Zhong-Ming
Zintl chemistry: From zintl ions to zintl clusters

Sun, Hongzhe
Metallomics and metalloproteomics

Sun, Geng
Nanocluster heterogeneous catalysts: Insights from theory

Sun, Licheng
Water oxidation catalysis in natural and artificial photosynthesis

Sun, Yuting
NMR of catalytic sites

Sutrisno, Andre
A review of exotic quadrupolar metal nmr in mofs

T

Takemori, Nayuta
Correlated electronic states in quasicrystals

Tamaki, Yusuke
Photochemical CO_2 reduction

Tamerius, Alexandra D.
X-ray diffraction methods for high-pressure solid-state synthesis

Tang, Ruikang
Biomineralization

Tao, Songsheng
Local structure determination using total scattering data

Tao, Peng
Luminescent transition-metal complexes and their applications in electroluminescence

Tapia-Ruiz, Nuria
Materials synthesis for Na-ion batteries

Tarascon, Jean-Marie
Status of Li(Na)-based anionic redox materials for better batteries

Taticchi, Chiara
Photochemically driven molecular machines based on coordination compounds

Terban, Maxwell W.
Local structure determination using total scattering data

Thangadurai, Venkataraman
Solid-state electrolytes for lithium-ion batteries

Thiel, Scott D.
X-ray diffraction methods for high-pressure solid-state synthesis

Tomatis, Pablo E.
The biochemistry and enzymology of zinc enzymes

Tong, Ka-Chung
Anti-cancer gold compounds

Trump, B.A.
Neutron scattering studies of materials for hydrogen storage

Truong, Khai-Nghi
Halogen-bonded halogen(I) ion complexes

Trussov, Ivan A.
Electrode materials for reversible sodium ions de/intercalation

Tsuji, Yuta
Bond activation and formation on inorganic surfaces

Tuczek, Felix
Biological and synthetic nitrogen fixation

U

Udovic, T.J.
Neutron scattering studies of materials for hydrogen storage

Ulu, F.
Conventional and less conventional solution-based synthesis of battery materials: Cathodes, anodes and electrolytes

Üngör, Ökten
Transition metal nmr thermometry

Uzun, Alper
Challenges with atomically dispersed supported metal catalysts: Controlling performance, improving stability, and enhancing metal loading

V

Valtchev, Valentin
Synthesis and application of (nano) zeolites

Vanam, Sai Pranav
Development of polyanionic sodium-ion battery insertion materials

Van Bael, M.K.
Conventional and less conventional solution-based synthesis of battery materials: Cathodes, anodes and electrolytes

van Santen, Rutger A.
Introduction: A short history of single site catalysis
Solid acid catalysis; Part I, the zeolite protonic site
Solid acid catalysis; Part II, catalytic chemistry of proton activation

Van Speybroeck, Véronique
Dynamic evolution of catalytic active sites within zeolite catalysis

Vargas-Baca, Ignacio
Computational modeling and characterization of secondary bonding in compounds of late p-block elements

Vegas, Ángel
The Zintl-Klemm concept and its broader extensions
The structures of inorganic crystals: A rational explanation from the chemical pressure approach and the anions in metallic matrices model

Vigil, Julian A.
A practical guide to Three-dimensional halide perovskites: Structure, synthesis, and measurement

Vila, Alejandro J.
The biochemistry and enzymology of zinc enzymes

Viswanathan, Gayatri
Thermoelectric materials

Vizintin, Alen
Lithium sulfur batteries: Electrochemistry and mechanistic research

Vranken, T.
Conventional and less conventional solution-based synthesis of battery materials: Cathodes, anodes and electrolytes

W

Wagner, Frank R.
Chemical bonding analysis in position space

Wagner, Molly
Applications of NMR spectroscopy in cultural heritage science

Walker, Lauren
Luminescence properties of the actinides and actinyls

Walsh, James P.S.
X-ray diffraction methods for high-pressure solid-state synthesis

Walton, Richard I.
Solvothermal and hydrothermal methods for preparative solid-state chemistry

Wan, Pui-Ki
Anti-cancer gold compounds

Wang, Zhigang
Platinum anticancer drugs: Targeting and delivery

Wang, Haibo
Metal ion interactions with nucleic acids

Wang, Jian
Thermoelectric materials

Wang, Guoxiong
Inorganic catalysis for methane conversion to chemicals

Wang, Qian
Applications of ^{17}O and ^{51}V NMR in inorganic and bioinorganic chemistry

Ward, Jas S.
Halogen-bonded halogen(I) ion complexes

Ware, Skyler D.
Battery materials

Watzele, Sebastian A.
Structure-reactivity relations in electrocatalysis

Webb, Paul B.
Promoted Fischer-Tropsch catalysts

Wei, Wei
Bio-inspired catalysis

Weigand, Wolfgang
[FeFe]-Hydrogenase mimics containing heavy p block elements

Wein, Emily
Photoactivated metal complexes for drug delivery

Weinstein, Julia A.
Ultrafast dynamics of photoinduced processes in coordination compounds

Werz, Daniel B.
Chalcogen bonding in supramolecular structures, anion recognition, and catalysis

Wesley Surta, T.
Spark plasma sintering routes to consolidated inorganic functional materials

White, Susan A.
Imaging

Widdifield, Cory M.
NMR of nanoparticles

Wilkinson, Angus P.
Introduction: X-ray, neutron and electron scattering methods in inorganic chemistry

Williams, A.J.
The zoology of two-dimensional van der waals materials

Wong, Wai-Yeung
Luminescent transition-metal complexes and their applications in electroluminescence

Woodward, Patrick M.
Introduction: Solid state inorganic chemistry

Wright, D.S.
Supramolecular chemistry of p-block elements

Wu, Xue
Bio-inspired catalysis

Wu, Hua
Piezoelectric and ferroelectric materials: Fundamentals, recent progress, and applications

Wu, Tao
Crystalline inorganic materials from supertetrahedral chalcogenide clusters

Wu, Li-Zhu
Non-sacrificial photocatalysis

Wustrow, Allison
Metathesis routes to materials

X

Xiao, Kui
Synthesis, carbon-polymetal bonding and applications of organometallic clusters

Xiao, Feng-Shou
Mesostructured materials

Xie, Weiwei
Chemical bonding principles in magnetic topological quantum materials
Critical charge transfer pairs in intermetallic superconductors

Xue, Chaozhuang
Crystalline inorganic materials from supertetrahedral chalcogenide clusters

Xue, Zi-Ling
Solution NMR of transition metal complexes

Y

Yachandra, Vittal K.
Photosynthesis

Yakubovich, Olga V.
Mineral inspired electrode materials for metal-ion batteries

Yam, Vivian Wing-Wah
Introduction: Inorganic photochemistry
Luminescent supramolecular assemblies

Yamada, Ikuya
High pressure studies of transition metal oxides

Yamamoto, Takafumi
High pressure studies of transition metal oxides

Yamaura, Kazunari
High pressure studies of transition metal oxides

Yan, Xueting
Metallomics and metalloproteomics

Yang, Long
Local structure determination using total scattering data

Yano, Junko
Photosynthesis

Yao, Houzong
Platinum anticancer drugs: Targeting and delivery

Yashina, Lada
Chemistry of Li-air batteries

Ye, Zuo-Guang
Piezoelectric and ferroelectric materials: Fundamentals, recent progress, and applications

Yox, Philip
Thermoelectric materials

Yu, Feng
Mesostructured materials

Z

Zadrozny, Joseph M.
Transition metal nmr thermometry

Zaikina, Julia V.
Hydride precursors in materials synthesis

Zakharchenko, Tatiana
Chemistry of Li-air batteries

Zander, Edgar
Biradicals in main group chemistry: Synthesis, electronic structure, and application in small-molecule activation

Zhang, Fangfang
Inorganic nonlinear optical materials

Zhang, Zheyu
Solid-state electrolytes for lithium-ion batteries

Zhang, Li
Materials synthesis for Na-ion batteries

Zhang, Hengyi
Materials synthesis for Na-ion batteries

Zhang, Hao
Heterogeneous catalysts for the non-oxidative conversion of methane to aromatics and olefins

Zhang, Wanli
A review of exotic quadrupolar metal nmr in mofs

Zhao, Liang
Synthesis, carbon-polymetal bonding and applications of organometallic clusters

Zhao, Yueqi
Biomineralization

Zhao, Xinyang
Bio-inspired catalysis

Zhao, Jing
Bio-inspired catalysis

Zhou, Ying
Metallomics and metalloproteomics

Zhu, Guangyu
Platinum anticancer drugs: Targeting and delivery

Zhu, Lu
Bio-inspired catalysis

Zhu, Tong
Mixed anion materials

Zhuang, Jianqin
Applications of ^{17}O and ^{51}V NMR in inorganic and bioinorganic chemistry

Zou, Xiaodong
Structural studies of inorganic materials by electron crystallography

Zumbulyadis, Nicholas
Applications of NMR spectroscopy in cultural heritage science

Zurek, Eva
Crystal chemistry at high pressure